The Archean Cu-Zn magnetite-rich Gossan Hill VHMS deposit, Western Australia: Evidence of a structurally-focussed, exhalative and sub-seafloor replacement mineralising system

Robina Sharpe
B.Sc. Hons.

Submitted in fulfilment of the requirements
for the degree of Doctor of Philosophy

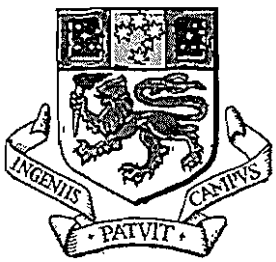

UNIVERSITY OF TASMANIA

Hobart, Australia
September, 1999

Declaration

This Thesis contains no material which has been accepted for the award of any other degree or diploma in any tertiary institution and, to the best of my knowledge and belief, contains no copy or paraphrase of material previously published or written by another person, except where due reference is made in the text of this Thesis.

Robina Sharpe
September 1999

This thesis may be made available for loan. Copying of any part of this thesis is prohibited for two years from the date this statement was signed; after that time limited copying is permitted in accordance with the *Copyright Act 1969*

Robina Sharpe
Date: 24/9/99

"Within the snares of making truth a pawn,
Whiles not doubting where it enters,
Lie true proof and knowledge"

William Shakespeare

Abstract

The Archean Cu-Zn Gossan Hill volcanic-hosted massive sulphide deposit is situated on the northeast flank of the Warriedar Fold Belt in the Yilgarn Craton, Western Australia. The deposit is hosted within re-deposited rhyodacitic tuffaceous volcaniclastics of the Golden Grove Formation and is overlain by rhyodacite-dacite lavas and intrusive domes of the Scuddles Formation. The Gossan Hill deposit consists of two discrete subvertical ore zones situated stratigraphically 150 m apart in the middle and upper Golden Grove Formation. The stratigraphically lower Cu-rich ore zone (7.0 Mt @ 3.4% Cu) consists of stratabound, podiform to discordant massive pyrite-chalcopyrite-pyrrhotite-magnetite. In addition to massive sulphides, the lower ore zone also contains discordant to sheet-like zones of massive magnetite-carbonate-chlorite-talc (~12 Mt). The upper Zn-Cu ore zone (2.2 Mt @ 11.3% Zn, 0.3% Cu, 1.5 g/t Au and 102 g/t Ag) is mound-shaped with sheet-like, stratabound, massive sphalerite-pyrite-chalcopyrite overlying discordant massive pyrite-pyrrhotite-chalcopyrite-magnetite. A sulphide-rich vein stockwork connects the upper and lower ore zones. Metal zonation grades from Cu-Fe (±Au) in the lower ore zone to Zn-Cu-rich sulphides at the base of the upper ore zone. The upper ore zone grades upwards and laterally from Zn-Cu to Zn-Ag-Au (±Cu, ±Pb)-rich sulphides.

Regional preservation of primary tuffaceous volcanic textures within the Golden Grove Formation is attributed to an early syndepositional, quartz-chlorite alteration. Induration and differential permeability/porosity reduction of the succession during the early alteration likely promoted more-focussed pathways for successive hydrothermal fluids. Subsequent hydrothermal alteration related to mineralisation at Gossan Hill has a limited lateral extent, and forms a narrow Fe-chlorite-ankerite-siderite envelope to the massive magnetite and sulphide of the lower ore zone, and an intense siliceous envelope surrounding the stockwork and upper ore position. Pervasive calcite-muscovite alteration is recognised in the hangingwall volcanics of the Scuddles Formation.

The nature of deformation and metamorphism (greenschist facies: 454 ± 4°C at 1 kbar based on andalusite-chloritoid-quartz equilibrium) is uniform throughout the massive magnetite, massive sulphide and host succession. Sediment-sulphide-magnetite relationships at Gossan Hill suggest the formation of magnetite and sulphide during deposition of the upper Golden Grove Formation. Massive magnetite formed entirely by sub-seafloor replacement processes as inferred from gradational upper and lower contacts and interdigitating volcaniclastics. Replacement occurred along permeable tuffaceous strata outward from a discordant feeder. Massive magnetite was later veined, replaced

and cut by massive sulphide. The synchronous formation of both upper and lower sulphide ore zones is indicated by the connecting sulphide stockwork. Both sulphide ore zones formed by sub-seafloor replacement, although stratiform hydrothermal chert-sulphide-sediment layers in, and adjacent to, the upper sulphide zone attest to some exhalation of fluids onto the seafloor.

The thickest occurrence of massive magnetite, massive sulphide and stringer stockwork spatially coincide and support a common feeder conduit during massive magnetite and sulphide mineralisation. The asymmetry of hydrothermal alteration envelopes, massive magnetite and massive and veins sulphide zones are consistent with synvolcanic structural controls, with a growth structure occupied and obscured by a younger dacite dome from the Scuddles Formation.

A systematic increase in sulphide $\delta^{34}S$ values (range of -4.0 to 7.8‰, average 2.1 ± 1.7‰) stratigraphically upwards through massive and vein sulphide is suggestive of progressive mixing of upwelling ore fluids with entrained seawater. Homogeneous $\delta^{34}S$ values of ~1.5‰ in the lower ore zone have a consistent homogeneous rock sulphur source with possible magmatic contributions.

The $\delta^{18}O_{H2O}$ values of ore fluids responsible for deposition of magnetite in massive magnetite and disseminated magnetite in the sulphide zones range from 6‰ to 13‰. This data is inconsistent with the direct input of Archean seawater, and favours derivation of hydrothermal fluids by rock buffering of circulating fluids, or by direct magmatic contribution.

Thermodynamic considerations suggest massive magnetite and sulphide formed from high temperature (300° to 350°C), reduced (low $f\ O_2$), slightly acidic hydrothermal fluids. H_2S-deficient fluids formed massive magnetite, whilst H_2S-rich fluids formed massive sulphides. Fluid chemistry differences are attributed to magmatic sulphur contributions during sulphide mineralisation. Precipitation of sub-seafloor sulphide in the lower ore zone resulted from chemical entrapment by the interaction of upwelling H_2S-rich fluids with pre-existing massive magnetite. It is suggested that shallow parental magma chambers to the Scuddles Formation drove hydrothermal convection of seawater and may have supplied volatiles and H_2S to the ascending hydrothermal fluids.

The Gossan Hill sulphide-magnetite deposit represents an evolving hydrothermal system in an environment characterised by rapid volcaniclastic sedimentation and changing structural and magmatic processes. An important influence on this hydrothermal system was the creation and destruction of porosity and permeability in the host succession. The hydrothermal system initiated as part of a regional seawater convection-alteration system that led to VHMS mineralisation at Gossan Hill by (1) synsedimentary metasomatism and progressive heating of convecting fluids, (2) formation of massive magnetite by host rock replacement above a buried synvolcanic conduit, and (3) structural re-activation and tapping of deeper H_2S-rich and metal-bearing fluids, leading to the sub-seafloor sulphide replacement and local exhalation of hydrothermal fluids forming sulphide and chert. Burial by proximal felsic volcanism led to preservation of the deposit.

Contents

Abstract i
Contents iii
Figures ix
Tables xii
Appendices xiii
Acknowledgements xiv
Nomenclature and frequently used abbreviations xv

Chapter 1: Introduction
1.1 Preamble 1
1.2 Exploration history and mining status 3
1.3 Previous studies at Golden Grove 4
1.4 Objectives of this study 4
1.5 Methodology 5
1.6 Thesis strategy 5

Chapter 2: Regional Geology
2.1 Introduction 6
2.2 The Murchison Province 6
2.3 Regional intrusions 11
2.3.1 Pegmatite banded gneiss 12
2.3.2 Recrystallised monzogranite 12
2.3.3 Post-folding granitoids 12
2.3.4 Mafic intrusions 13
2.4 Structure of the Murchison Province 13
2.5 Regional metamorphism 14
2.6 The Warriedar Fold Belt 14
2.6.1 Tectonostratigraphic Domains of the WFB 15
Gnows Nest Domain 15
Golden Grove Domain 15
Chulaar Domain 17
Windaning Domain 17
Fields Find Domain 17
2.7 Stratigraphy of the Golden Grove Domain 18
2.7.1 Gossan Hill Group 18
Shadow Well Formation 18
Gossan Valley Formation 18
Golden Grove Formation 18
Scuddles Formation 21
Cattle Well Formation 21
2.7.2 Thundelarra Group 21
2.7.3 Minjar Group 22
2.7.4 Depositional setting of the Golden Grove Domain 22
2.7.5 Association of the Golden Grove Domain to other domains in the WFB 23
2.8 Age Dating 23
2.8.1 VHMS Pb-model ages 24
2.9 Tectonic setting 24
2.10 The Scuddles and Gossan Hill VHMS deposits 25
2.11 Summary 27

Chapter 3: Stratigraphy
3.1 Introduction 28
3.1.1 The implementation of a stratigraphic framework 28

3.1.2 Aims 29
3.2 The Gossan Valley Formation 32
3.2.1 Member 4 (GVF M4) 32
3.3 The Golden Grove Formation 35
3.3.1 Member 1 (GGF M1) 35
Thinly bedded sandstone facies 35
Pebble breccia facies 37
Interpretation 39
3.3.2 Members 2 (GGF M2) and 3 (GGF M3) 41
3.3.3 Member 4 (GGF M4) 41
Polymict breccia facies 44
Interpretation 44
3.3.4 Member 5 (GGF M5) 46
Interpretation 50
3.3.5 Member 6 (GGF M6) 50
Sandstone and siltstone 51
Breccia 51
Tuffaceous strata 51
Interpretation 51
3.3.6 GGF M6: The M1 Marker 52
Discussion 54
3.4 Scuddles Formation 55
3.4.1 SCF M2: Rhyodacite (RD2) 55
3.4.2 SCF M2: Rhyodacite breccia facies 58
3.4.3 Rhyodacite facies interpretation 58
3.4.4 SCF M2: Dacite (DAC3) 60
3.4.5 SCF M2: Dacite breccia facies 60
3.4.6 Dacite facies interpretation 61
3.5 Intrusions 61
3.5.1 Dacite porphyries 61
3.5.2 Dolerite 61
3.5.3 Rhyolite 62
3.6 Geometry and distribution of the GGF 62
3.7 Deposition of the Golden Grove Formation 62
3.7.1 Mechanisms of emplacement 63
3.7.2 A question of hiatus: When and how many? 64
3.7.3 Devitrification state of the tuffaceous strata 65
3.7.4 Diagenetic alteration 66
3.7.5 Textural preservation: Diagenetic or hydrothermal alteration? 66
3.7.6 Porosity and permeability 67
3.8 Summary 67

Chapter 4: Structure and metamorphism
4.1 Introduction 69
4.2 Aims 69
4.3 Synvolcanic structures 69
4.3.1 Geological constraints 71
4.3.2 Synvolcanic structures at the Scuddles deposit 73
4.3.3 Gossan Hill and Scuddles: A structural model 76
4.4 Bedding 78
4.5 Dolerite intrusions 78
4.6 Rhyolite intrusions 81
4.7 Faults 81
4.7.1 Southeast faults 81
4.7.2 East faults 83
4.7.3 North-south faults 86
4.7.4 Southwest faults 86
4.8 Veins 86
4.8.1 Pre-mineralising quartz veins 88
4.8.2 Sulphide veins 88
4.8.3 Southeast veins 90
4.8.4 East-west veins 90
4.8.5 North-south veins 90
4.8.6 Southwest veins 92
4.9 Cleavage 92
4.9.1 Folded veins 94

4.9.2 Boudinage structures 97
4.10 Metamorphism 97
4.10.1 Chlorite 97
4.10.2 Muscovite 97
4.10.3 Talc 99
4.10.4 Carbonate 100
4.10.5 Epidote and clinozoisite 100
4.10.6 Sphene 100
4.10.7 Ilmenite-rutile 100
4.10.8 Chloritoid 100
4.10.9 Andalusite 102
4.10.10 Actinolite 102
4.10.11 Discussion 102
4.10.12 Timing of peak metamorphism 104
4.10.13 Temperature indicator minerals 104
4.11 Summary of deformation and metamorphism at Gossan Hill 104
4.12 Regional considerations and exploration ramifications 106

Chapter 5: Magnetite and sulphide mineralisation
5.1 Introduction 107
5.2 Ore types 108
5.3 Terminology 108
5.4 Mineralisation in GGF M6: The upper stratigraphic association 110
5.4.1 Geometry and distribution 110
5.4.2 Upper contacts 113
5.4.3 Lower contacts 116
5.4.4 Massive sphalerite 119
5.4.5 Massive pyrite 119
5.4.6 Stringer veins 119
5.4.7 Indicators of relict wall rock 120
5.4.8 Porosity and permeability controls of the wall rock 122
5.4.9 Discussion 124
5.5 Massive magnetite 125
5.5.1 Distribution and geometry 129
5.5.2 Upper contacts 129
5.5.3 Lower contacts 131
5.5.4 Massive magnetite 131
5.5.5 Discussion 132
5.6 Mineralisation in GGF M4: The lower stratigraphic association 133
5.6.1 Distribution and geometry 133
5.6.2 Upper contacts 133
5.6.3 Lower contacts 135
5.6.4 Massive pyrite 135
5.6.5 Stringer veins 136
5.6.6 Discussion 139
5.7 The relationship of the lower and upper massive sulphide zones 141
5.8 The distribution of chalcopyrite 141
5.9 Mineralogy and association of the stringer veins 142
5.9.1 Vein form 144
5.9.2 Vein mineralogy 144
5.9.3 Type I 144
5.9.4 Type II 144
5.9.5 Type III 144
5.9.6 Type IV 146
5.9.7 Type V 146
Type V(A): Pyrite-pyrrhotite-chalcopyrite-rich veins 146
Type V(B): Pyrite-sphalerite-rich veins 147
5.9.8 Type VI 147
5.9.9 Summary 147
5.10 Mineralisation at the Scuddles deposit 149
5.11 Discussion 150
5.12 Summary 152

Chapter 6: Ore minerals and their textures
6.1 Introduction 154
6.2 Sphalerite 154

6.2.1 Recrystallisation and deformation of sphalerite 156
6.2.2 Composition of sphalerite 156
6.3 Pyrite 158
6.3.1 Pyrite in massive sphalerite 158
6.3.2 Massive pyrite (GGF M4 and GGF M6) 160
6.3.3 Pyrite in stringer veins 161
6.3.4 Disseminated pyrite (GGF M4 and GGF M6) 161
6.3.5 Deformation textures 163
6.3.6 Marcasite 163
6.3.7 Composition of pyrite 163
6.3.8 Discussion 164
6.4 Chalcopyrite 164
6.4.1 Discussion 165
6.5 Pyrrhotite 165
6.5.1 Discussion 166
6.6 Magnetite 166
6.6.1 Disseminated magnetite in sulphide 166
6.6.2 Magnetite in massive magnetite 166
Granular magnetite 166
Inclusion-rich and skeletal magnetite 167
Lath-shaped magnetite 167
Banded textures 167
6.6.3 Deformation textures 169
6.6.4 Discussion 169
6.7 Ilmenite and rutile 170
6.7.1 Discussion 170
6.8 Galena 172
6.9 Tetrahedrite 172
6.10 Native silver 173
6.11 Electrum 173
6.12 Cobaltite 173
6.13 Arsenopyrite 173
6.14 Gangue mineralogy and textures 174
6.14.1 Quartz 174
6.14.2 Chlorite 174
6.14.3 Carbonate 174
6.14.4 Talc 174
6.14.5 Apatite 176
6.15 Discussion and Summary 176

Chapter 7: Alteration mineralogy, distribution and timing
7.1 Introduction 178
7.2 Alteration mineralogy 178
7.3 Regional alteration 179
7.3.1 Alteration of the footwall (GGF M1) 181
7.3.2 Alteration of the host rocks (GGF M4, GGF M5 and GGF M6) 181
7.3.3 Nodular siliceous alteration 183
7.3.4 Textural preservation: A discussion 186
7.3.5 Laminar alteration 187
7.3.6 Timing constraints and origin of nodular alteration 188
7.3.7 Timing of regional quartz-chlorite alteration in the GGF 188
7.4 Local siliceous alteration 190
7.4.1 Timing of local siliceous alteration 192
7.5 Local chlorite alteration 192
7.5.1 Composition of chlorite 194
7.5.2 Timing of localised chlorite alteration 195
7.6 Carbonate alteration 197
7.6.1 Distribution and textures 197
7.6.2 Composition of carbonate 199
7.6.3 Timing of carbonate alteration 199
7.7 Muscovite alteration 200
7.8 Minor alteration minerals 202
7.8.1 Talc 202
7.8.1 Apatite 202
7.8.1 Chloritoid and andalusite 202
7.9 Alteration zonation 202
7.9.1 Alteration zonation at the Scuddles deposit 205

7.10 Alteration paragenesis 205
7.11 Synthesis 207

Chapter 8: Lithogeochemistry
8.1 Introduction 209
8.2 Aims 209
8.3 Previous geochemical investigations 209
8.4 Sample details 209
8.4.1 Analytical techniques 210
8.5 Immobile element characterisation 212
8.5.1 Immobile element geochemistry summary 214
8.6 Alteration geochemistry 217
8.6.1 Major element variations 217
8.6.2 Down hole variations 223
8.6.3 Summary of major element geochemistry 227
8.6.4 Trace element variations 227
8.6.5 Down hole variation of trace elements 229
8.6.6 Trace element summary 229
8.7 ICPMS data 229
8.7.1 Down hole variation 233
8.7.2 Discussion 233
8.8 The M1 Marker 239
8.8.1 Discussion 241
8.8.2 Summary 244
8.9 Discussion 244
8.9.1 Geochemistry of the hangingwall (SCF M2) 244
8.9.2 Geochemistry of the host sequence (GGF M4, M5 and M6) 246
8.9.3 Geochemistry of the footwall (GGF M1) 246
8.9.4 Review of geochemical characteristics of the Scuddles deposit 247
8.10 Conclusions 248

Chapter 9: Metal zonation
9.1 Introduction 249
9.2 Previous work 250
9.3 Methods 250
9.4 Metal contours 251
9.4.1 Results 251
9.5 Zn and Cu ratio values 259
9.5.1 The upper ore zone 260
9.5.2 The lower ore zone 262
9.6 Metal associations 264
9.6.1 Variation in metals with stratigraphy 264
9.6.2 Inter-element associations 268
9.6.3 Gold 268
9.6.4 Silver 271
9.7 Discussion 271
9.7.1 Magnetite-sulphide (Cu-Fe) association of the lower ore zone 273
9.7.2 Location of feeder zones 273
9.7.3 Metal zonation at Scuddles 274
9.8 Summary 275

Chapter 10: Sulphur isotopes
10.1 Introduction 276
10.2 Methods 277
10.3 Results 278
10.3.1 Isotopic differences between the upper and lower ore zones 278
10.3.2 Isotopic differences between ore types 278
10.3.3 Isotopic differences between sulphide veins 281
10.3.4 Spatial variation of $\delta^{34}S$ values 283
10.3.5 Intra-grain $\delta^{34}S$ variation in pyrite 285
10.4 Discussion 286
10.4.1 Phanerozoic VHMS deposits 286
10.4.2 The Archean perspective 288
10.4.3 Interpretation of $\delta^{34}S$ values in Archean VHMS deposits 289
10.4.4 Variation in $\delta^{34}S$ values 290
10.4.5 Geothermometry 291

10.4.6 Gossan Hill sulphur isotope model 292
10.5 Summary 294

Chapter 11: Oxygen, hydrogen and carbon isotopes
11.1 Introduction 295
11.2 Methods 296
11.3 Results 296
11.3.1 Oxygen isotope composition of magnetite 296
11.3.2 Whole rock oxygen isotopes 298
11.3.3 Oxygen isotope composition of chlorite 298
11.3.4 Hydrogen isotope composition of chlorite 298
11.3.5 Oxygen isotope composition of carbonate 298
11.3.6 Carbon isotope composition of carbonate 299
11.4 Oxygen isotope mineral pair geothermometry 299
11.5 Oxygen and hydrogen variation in chlorite 302
11.6 Isotopic variation in carbonate 302
11.6.1 VHMS deposits 305
11.6.2 Temperature gradients 305
11.6.3 Isotopic constraints on Archean seawater 305
11.6.4 Archean Au deposits 306
11.6.5 Organic contributions–examples from Archean BIF deposits 306
11.6.6 Metamorphic effects 307
11.6.7 Discussion 307
11.7 Summary 307

Chapter 12: The genesis of the Gossan Hill deposit
12.1 Introduction 309
12.1.1 VHMS deposits: Definition, classifications and styles 309
12.1.2 Differences between Archean and Phanerozoic VHMS deposits 313
12.2 The Gossan Hill deposit 313
12.2.1 Depositional environment 313
12.2.2 Deformation and metamorphism 314
12.2.3 Synvolcanic structural control on the siting of mineralisation 317
12.2.4 Replacement *versus* seafloor deposition 318
12.2.5 The role of sedimentation 319
12.2.6 Timing and formation of massive magnetite 320
12.2.7 Timing and formation of massive sulphide 321
12.2.8 Ground preparation and hydrothermal alteration 322
12.2.9 Geochemical constraints on alteration at Gossan Hill 324
12.3 Archean environments 324
12.4 Geochemical constraints 325
12.4.1 Ore fluid origins 325
12.4.2 Source of metals 325
12.4.3 Temperatures of formation 327
12.4.4 Characteristics of Fe 327
12.4.5 Sulphur and oxygen activity 328
12.4.6 Chemical control on formation of the lower sulphide zone 331
12.5 Gossan Hill: A genetic model 331
12.5.1 Stage I: Initiation 332
12.5.2 Stage II: Ground preparation 332
12.5.3 Stage III: Massive magnetite 339
12.5.4 Stage IV: Synvolcanic structure re-activation and sulphide initiation 340
12.5.5 Stage V: The main sulphide event 341
12.5.6 Stage VI: Burial and waning 342
12.6 Gossan Hill and Scuddles: Contrasting deposits 342
12.7 Exploration ramifications 343

Chapter 13: Conclusions 345

References 351

Figures

Figure 1.1 Location of the Gossan Hill VHMS deposit, Western Australia 2

Figure 2.1 Geology of the Murchison Province 7
Figure 2.2 Stratigraphic schemes used in the Murchison Province 9
Figure 2.3 Stratigraphy of the Murchison Supergroup 9
Figure 2.4 Depositional and structural events in the Murchison Province 10
Figure 2.5 Structure and stratigraphy of the Warriedar Fold Belt 16
Figure 2.6 Stratigraphy of the Golden Grove Domain 19
Figure 2.7 Stratigraphy and megascopic structure of the Golden Grove Domain 20
Figure 2.8 Local geology of the Gossan Hill and Scuddles deposits 26

Figure 3.1 Stratigraphy of the Golden Grove Domain 30
Figure 3.2 Facies variation at the Gossan Hill deposit 31
Figure 3.3 Photographs of GVF M4 and GGF M1 33
Figure 3.4 Underground mapping of the GVF M4-GGF M1 contact 34
Figure 3.5 Underground mapping of unconformable contacts within GGF M1 36
Figure 3.6 Photographs of GGF M1, GGF M2 and GGF M4 38
Figure 3.7 Photographs of GGF M1 40
Figure 3.8 Facies variation within GGF M2 and GGF M3 across Gossan Hill 42
Figure 3.9 Mapping of polymict breccia facies within GGF M4 45
Figure 3.10 Facies variation within GGF M5 across Gossan Hill 47
Figure 3.11 Photographs of GGF M5 and GGF M6 48
Figure 3.12 East-west cross sections in the south of the Gossan Hill deposit 49
Figure 3.13 Photographs of the M1 Marker and the SCF M2 rhyodacite 53
Figure 3.14 Facies variation diagram of the SCF M2 rhyodacite at Gossan Hill 56
Figure 3.15 Photographs of SCF M2 rhyodacite, dacite and late intrusions 57
Figure 3.16 Cross sections through the central and northern zones of Gossan Hill 59

Figure 4.1 Geological level plan at 10,100 RL (250 metres below surface) 72
Figure 4.2 Longitudinal north-south projection of stratigraphic surfaces at the Gossan Hill deposit 74
Figure 4.3 Longitudinal north-south projection of stratigraphic surfaces at Scuddles 75
Figure 4.4 Structural model for Gossan Hill and Scuddles 77
Figure 4.5 Stereonet projections of bedding, late intrusions and sulphide veins 79
Figure 4.6 Photographs of slump folding and faults 80
Figure 4.7 Stereonet projections of faults and kinematic indicators 82
Figure 4.8 Photographs of vein types 84
Figure 4.9 Mapping of the faulted GVF M4-GGF M1contact 85
Figure 4.10 Stereonet projections of faults, kinematic indicators on faults and veins 87
Figure 4.11 Underground wall mapping of early quartz and sulphide veins 89
Figure 4.12 Photographs of brittle veins and cleavage structures 91
Figure 4.13 Photographs of cleavage and related deformation structures 93
Figure 4.14 Photographs of vein deformation and boudinage structures 95
Figure 4.15 Schematic illustration of vein deformation systematics 96
Figure 4.16 Photographs of boudinage structures and metamorphic minerals 98

Figure 4.17 Photographs of metamorphic minerals 101

Figure 5.1 Plan projection at 10,200 RL through the Gossan Hill deposit 111
Figure 5.2 Transform section (17,766 N) at the south of Gossan Hill 112
Figure 5.3 Sections through the upper ore zone 114
Figure 5.4 Graphic logs through the upper ore zone contacts 115
Figure 5.5 Graphic logs through the upper ore zone 117
Figure 5.6 Photographs of massive and vein sulphide from the upper ore zone 118
Figure 5.7 Photographs of sulphide veins from the upper ore zone 121
Figure 5.8 Photographs of massive magnetite in the lower ore zone 123
Figure 5.9 Plan projection at 10,150 RL through the central part of Gossan Hill 126
Figure 5.10 East-west cross sections through the lower ore zone 127
Figure 5.11 East-west cross sections through the lower ore zone 128
Figure 5.12 Stratigraphic logs through the lower ore zone 130
Figure 5.13 Photographs of massive magnetite and sulphide in the lower ore zone 134
Figure 5.14 Photographs of sulphide veins in the lower ore zone 138
Figure 5.15 East-west cross section 18,820 N 140
Figure 5.16 Schematic paragenesis of the veins 143
Figure 5.17 Photographs of the vein types 145
Figure 5.18 Cross section and plan through the Scuddles deposit 148

Figure 6.1 Photomicrographs of sphalerite and its composition 155
Figure 6.2 Photomicrographs of pyrite textures 159
Figure 6.3 Photomicrographs of pyrite, chalcopyrite and magnetite textures 162
Figure 6.4 Photomicrographs of magnetite textures in massive magnetite 168
Figure 6.5 Photomicrographs of minor and accessory sulphide minerals 171
Figure 6.6 Electrum fineness 173
Figure 6.7 Photomicrographs of gangue minerals in massive sulphide and magnetite 175

Figure 7.1 Photographs of regional quartz-chlorite alteration of the GGF 180
Figure 7.2 Alteration of the footwall GGF M1 at Gossan Hill 182
Figure 7.3 Photographs of quartz, chlorite and carbonate alteration in GGF M6 184
Figure 7.4 Nodular siliceous alteration 185
Figure 7.5 Intense siliceous alteration surrounding the upper ore zone 191
Figure 7.6 Intense chlorite alteration surrounding the lower ore zone 193
Figure 7.7 Compositional variation of chlorite at Gossan Hill 195
Figure 7.8 Carbonate alteration textures and its composition 196
Figure 7.9 Carbonate nodular alteration in GGF M5 198
Figure 7.10 Photographs of minor alteration minerals in the GGF 201
Figure 7.11 The distribution of alteration at Gossan Hill 203
Figure 7.12 Schematic illustration of alteration surrounding the Scuddles deposit 206
Figure 7.13 Relative timing of alteration at Gossan Hill 206

Figure 8.1 Location of geochemical samples on plan projection 10,200 RL 211
Figure 8.2 Y *versus* Nb and Zr *versus* Nb 213
Figure 8.3 Al_2O_3 *versus* TiO_2 213
Figure 8.4 Nb/Y *versus* Zr/TiO_2 215
Figure 8.5 TiO_2 *versus* Zr 215
Figure 8.6 Stratigraphic variation in the Ti/Zr ratio 216
Figure 8.7 SiO_2 *versus* FeO 218
Figure 8.8 Whole rock geochemistry plots of SiO_2, MgO, MnO and CaO 220
Figure 8.9 Na_2O+K_2O-FeO-MgO ternary plot 222
Figure 8.10 Chlorite-Carbonate alteration index (CCI) *versus* SiO_2 222
Figure 8.11 Major element variation along drill hole GG132 224
Figure 8.12 Major element variation along drill hole GG165 225
Figure 8.13 Major element variation along drill hole GG070 226
Figure 8.14 Trace element variation diagrams 228

Figure 8.15 Trace element variation along drill hole GG132 230
Figure 8.16 Trace element variation along drill hole GG165 231
Figure 8.17 Trace element variation along drill hole GG070 232
Figure 8.18 ICPMS trace element variation diagrams 234
Figure 8.19 ICPMS trace element variation diagrams 235
Figure 8.20 ICPMS trace element variation along drill hole GG132 236
Figure 8.21 ICPMS trace element variation along drill hole GG165 237
Figure 8.22 ICPMS trace element variation along drill hole GG070 238
Figure 8.23 Immobile element variation in the M1 Marker 240
Figure 8.24 Major element spiderdiagram of the M1 Marker geochemistry 241
Figure 8.25 Correlation of major and trace elements in the M1 Marker 242
Figure 8.26 Al-Fe-Mn ternary plot of the M1 Marker samples 243

Figure 9.1 Distribution of Cu at Gossan Hill 252
Figure 9.2 Distribution of Pb at Gossan Hill 253
Figure 9.3 Distribution of Zn at Gossan Hill 254
Figure 9.4 Distribution of Ag at Gossan Hill 255
Figure 9.5 Distribution of Au at Gossan Hill 256
Figure 9.6 Distribution of Fe at Gossan Hill 257
Figure 9.7 Distribution of specific gravity at Gossan Hill 258
Figure 9.8 Distribution of the Cu and Zn ratios in the upper and lower ore zones 261
Figure 9.9 Cu-Pb-Zn ternary diagrams 263
Figure 9.10a Stratigraphic variation of metals in the upper ore zone 265
Figure 9.10b Stratigraphic variation of metals in the lower ore zone 266
Figure 9.11 Scatter diagrams illustrating the association between metals 267
Figure 9.12 Scatter diagrams of the association between Ag and Au 269
Figure 9.13 Scatter diagrams of the association between Ag and Au 270
Figure 9.14 Schematic illustration of the metal zonation at Gossan Hill 272

Figure 10.1 Sulphur isotope variation at Gossan Hill 279
Figure 10.2 Sulphur isotope variation of the different ore zones 280
Figure 10.3 Sulphur isotope variation within sulphide veins 282
Figure 10.4 Stratigraphic variation of sulphur isotope values along drill holes 284
Figure 10.5 Summary of the stratigraphic variation 285
Figure 10.6 Intra-grain sulphur isotope variation 286
Figure 10.7 Changes in the sulphur isotope composition of VHMS deposit over time 287
Figure 10.8 Frequency histogram of sulphide isotope mineral pair temperatures 292
Figure 10.9 Schematic illustration of the sulphur isotope variation at Gossan Hill 293

Figure 11.1 Oxygen, hydrogen and carbon isotope compositions of minerals 297
Figure 11.2 Oxygen-hydrogen isotope variation of chlorite 303
Figure 11.3 Carbon-oxygen isotope composition of carbonate 304

Figure 12.1 Schematic representation of the major Australian VHMS deposit types 311
Figure 12.2 Genesis of the Kuroko deposits 312
Figure 12.3 Stratigraphic and facies variation between Gossan Hill and Scuddles 315
Figure 12.4 Depositional setting of the Gossan Hill Group 316
Figure 12.5 Stability fields of Fe-S-O minerals in fO_2-pH space 329
Figure 12.6 Stability fields of Fe-S-O minerals in fO_2-pH space 330
Figure 12.7 Stage I: Intiation 333
Figure 12.8 Stage II: Ground preparation 334
Figure 12.9 Stage III: Massive magnetite 335
Figure 12.10 Stage IV: Synvolcanic structural reactivation and sulphide initiation 336
Figure 12.11 Stage V: Main sulphide stage 337
Figure 12.12 Stage VI: Burial 338

Tables

Table 2.1 Precambrian geological history of the Murchison Province 11

Table 3.1 Previous stratigraphic subdivisions of the Golden Grove Domain 29

Table 4.1 Regional structural framework for the Murchison Province 70
Table 4.2 Metamorphic mineral occurrences at Gossan Hill 99

Table 5.1 Estimated resource of the Gossan Hill deposit 109
Table 5.2 Mineralogy of massive sphalerite, massive pyrite and massive magnetite 109
Table 5.3 Major veins types at Gossan Hill 142

Table 6.1 Summary of the FeS and ZnS composition of sphalerite 157

Table 7.1 Distribution of alteration minerals in the strata at Gossan Hill 179
Table 7.2 Average chlorite compositions in alteration surrounding Gossan Hill 194
Table 7.3 Average carbonate compositions 199

Table 8.1 Details of the Gossan Hill geochemical sample suite 210
Table 8.2 Immobile element summary 212
Table 8.3 Geochemical characteristics of alteration at Gossan Hill 245
Table 8.4 Geochemical characteristics of alteration at Scuddles 247

Table 9.1 Grade and tonnage data of various VHMS deposits 260

Table 10.1 Analytical details of the laser ablation technique 277
Table 10.2 Summary of sulphur isotope values of sulphides 278
Table 10.3 Sulphur isotope variation within sulphide veins 281

Table 11.1 Oxygen isotope composition of magnetite 296
Table 11.2 Oxygen and hydrogen isotope composition of chlorite 298
Table 11.3 Carbonate and oxygen isotope composition of carbonate 299
Table 11.4 Oxygen isotope geothermometry 300
Table 11.5 Fractionation systematics of magnetite applied to Gossan Hill 301

Appendices

Appendix A1.1	Examples of logging practices, codes and symbols used during field work
Appendix A2.2	Rock catalogue
Appendix A2.1	Electron microprobe analsysis of andalusite
Appendix A2.2	Temperature and pressure calculations of peak metamorphism
Appendix A3.1	Underground mapping of the 300 level
Appendix A3.2	Underground mapping of the 250 level
Appendix A4.1	Electron microprobe analysis of sphalerite
Appendix A4.2	Electron microprobe analysis of pyrite
Appendix A4.3	Electron microprobe analysis of chalcopyrite
Appendix A4.4	Electron microprobe analysis of pyrrhotite
Appendix A4.5	Electron microprobe analysis of magnetite
Appendix A4.6	Electron microprobe analysis of ilmenite-rutile
Appendix A4.7	Electron microprobe analysis of galena
Appendix A4.8	Electron microprobe analysis of tetrahedrite
Appendix A4.9	Electron microprobe analysis of native silver
Appendix A4.10	Electron microprobe analysis of electrum
Appendix A4.11	Electron microprobe analysis of cobaltite
Appendix A4.12	Electron microprobe analysis of arsenopyrite
Appendix A5.1	Electron microprobe analysis of chlorite
Appendix A5.2	Electron microprobe analysis of carbonate
Appendix A5.3	Electron microprobe analysis of apatite
Appendix A5.4	Electron microprobe analysis of chloritoid
Appendix A6.1	Geochemcial analysis of least altered samples
Appendix A6.2	Geochemcial analysis of least altered samples
Appendix A7.1	Grid line geometry sepcifications for metal contour plots
Appendix A7.2	Drill holes used in metal ratio, contour and relational plots
Appendix A7.3	Ore types in metal ratio, contour and relational plots
Appendix A7.4	Zn and Cu ratio plots of GGF M6 and the upper ore zone
Appendix A7.5	Zn and Cu ratio plots of GGF M4 and the lower ore zone
Appendix A8.1	Sulphur isotope data of sulphides at Gossan Hill
Appendix A9.1	Oxygen, hydrogen and carbon isotope data

Acknowledgments

Many people have provided advice, assistance, support and friendship over the last four years, and although the following list attempts to cite and thank all these, I extend a general acknowledgment to any I may have overlooked.

First and foremost I am indebted to my supervisor, Dr. Bruce Gemmell, who has given me immeasurable encouragement, scientific and moral support, and the opportunity to work on the modern seafloor deposits. I am also grateful to Dr. Gemmell for his enthusiasm, reading the manuscript, keeping me on track, and helping to improve many aspects of this work. Drs. Ross Large, Paul Kitto, Khin Zaw, Garry Davidson, Mike Solomon, Ron Berry and Alicia Verbeeten are also thanked for reading various chapters of this thesis. The careful and tedious corrections by Dr. Fernando Della-Pasqua were invaluable. Thanks are also extended to Dr. David Cooke and Dr. Grant Garven for helpful discussions with the genesis chapter.

This study would not have been possible without the financial and logistical support of Normandy through the Murchison Zinc Company. The geologists at Golden Grove are a great team to work with and they are all thanked for their helpful discussions and enthusiastic support. In particularly thanks are extended to Lucy Moorfield, Stefan Gawlinski, Mike Northcotte, Scott Findlay, Chris Robinson, Flackey, Cathy Small, Miles Dunkin, John Winterbottom and Steve Johansen, Ian Stewart and Mark Flemming. Logistical support in the core yard by Scranno, Brett and Rob was greatly appreciated.

Invaluable technical assistance was provided by June Pongratz, Mike Blake, Mike Harlow, Darren Turner, Chris Higgins, Peter Cornish, Nilar Hilang, Di Steffans, Marilyn Feast, Phil Robinson (XRF), Simon Stevens (lapidary), Wislaw Jablonski (CSL electron microprobe), Dr. David Steele (CSL electron microprobe), Dr. Mike Powers Snr. (CSL stable isotopes), Christine (CSL, stable isotopes) and Keith Harris (CSL stable isotopes). I gratefully acknowledge the CIS at CSIRO, Sydney, and Anita Andrews, for oxygen isotope analyses in this thesis.

Alteration studies in this thesis were part of the AMIRA P439 project, and to the university and industry members of this team, I extend a general thanks. Funding for the ICP-MS analyses through the AMIRA P439 project are gratefully acknowledged.

Numerous post doctoral fellows and fellow Ph.D. students at the School of Earth Science and CODES SRC have provided friendship, a helpful discussion forum and support over the past years. I thank Anthea Hill, Ali Raos, David Rawlings (Rowdster), Holger Paulick, Peter Winefield, Steve Bodon, Andrew Rae, Briony Sinclair, Karin Orth, Andrew McNeil, Matt White, Mark Doyle, David Selley, Jamie Rogers, Catherine Reid, Steve Hunns, Bill Wyman, Meng, Owen Hatton, Dene Caroll, Oilver Holm, Leonoid Danushevsky, Vanessa Lickfold, Dima Kamenetsky, Mark Duffett, Aung Pwa, Sarah Jones, Kirstie Simpson, Andrew Davies and Rick Squire. In particular I am grateful to the past and present residents of room 338 for providing a stimulating work environment: Alicia Verbeeten, Cathryn Gifkins, Rohan Wolfe, Fernando Della-Pasqua, Xu Li and Giovanni Parente.

I am indebted to my brother Ian, and my close friends for keeping me sane, putting up with the emotional trauma, feeding me, and their unlimited support and love. Thank you Miss King, Mr Blake, Miss Verbeeten, Dr. Kitto and Miss Raos. I am eternally grateful to Ray and Elvie Baker at 'Pondorosa' for looking after me and 'Sharpe's Siding' and giving me a home away from home. A special thankyou to Fernando Della-Pasqua for his patience, love and for just being there. Finally, this thesis is dedicated to my father Stan Sharpe (1904-1996) and my mother Joan Watson (1930–1984) who instilled within me the importance of patience and persistence.

Nomenclature and frequently used abbreviations

Grid references in this thesis refer to the local mine grid used by MZC at Golden Grove. These co-ordinates can be translated to Australian Map Grid (AMG) co-ordinates using the base point of the Golden Grove Grid at AMG 6,805,374 N, 492,404 E and a grid north of 308 degrees.

Megaquartz refers to quartz grains that have equant to elongate forms and sizes greater than ~0.02 mm.

Microcrystalline quartz refers to mosaics of equidimensional quartz grains that are less than ~0.02 mm in size. These mosaics are characterised by patchy, undulatory extinction and pinpoint birefringence.

Abbreviations:

bx	breccia
chl	chlorite
cm	centimetres
co	carbonate
cp	chalcopyrite
DAC3	Scuddles Formation Member 2 dacite
ds	disseminated
FeO*	total iron
footwall	strata below massive sulphide (GGF M1)
Ga	billion years
GGF	Golden Grove Formation
hangingwall	strata above massive sulphide (SCF)
host horizon	strata containing massive sulphide (GGF M4-GGF M6)
Kbar	Kilo bar ($=10^8 N/m^2$)
km	kilometres
m	metres
mas	massive
Mg#	(Mg+Fe)/Mg
mgt	magnetite
mm	millimetres
Mt	million tonnes
musc	muscovite
p	pervasive
po	pyrrhotite
ppm	parts per million
py	pyrite
qz	quartz
RL	reduced level
RD2	Scuddles Formation Member 2 rhyodacite
SCF	Scuddles Formation
si	siliceous alteration
slt	siltstone
sp	sphalerite
sst	sandstone
VHMS	volcanic-hosted massive sulphide
WFB	Warriedar Fold Belt
µ	micron
~	approximately

Chapter 1

Introduction

1.1 Preamble

This research thesis focuses on primary mineralisation of the Gossan Hill volcanic-hosted massive sulphide (VHMS) deposit situated in the Archean Yilgarn Craton of Western Australia. The Gossan Hill deposit is a Cu-Zn-rich VHMS consisting of weathered oxidised mineralisation (5.3 Mt at 1.5% Cu and 2.2 Mt at 2.2 g/t Au and 86 g/t Ag), which overlies primary Cu and Zn mineralisation (7 Mt at 3.4% Cu and 2.2 Mt at 11.3% Zn, 1.5 g/t Au and 102 g/t Ag) within a tuffaceous volcaniclastic host sequence. Geographically, the Gossan Hill deposit (latitude 28°45' S, longitude 116°59' E) is approximately 500 km north-northeast of Perth and 140 km east of Geraldton, and is located in the southern part of the Yalgoo-Singleton greenstone belt of the Murchison granite-greenstone province (Fig. 1.1).

In the Yilgarn Craton, Cu-Zn-Pb mineralisation has two main occurrences as (1) stratabound VHMS deposits, and (2) shear-hosted vein deposits (Watkins and Hickman, 1990a). Despite the extensive geographic expanse of the Yilgarn Craton, surprisingly few VHMS deposits are known when compared with the Canadian Archean. To date, the Murchison Province is the largest base metal producer in the Yilgarn Craton and hosts the two largest Australian Archean VHMS deposits, namely the Gossan Hill and Scuddles deposits (Watkins and Hickman, 1990a; Barley, 1992). Elsewhere in the Yilgarn Craton, known VHMS deposits include the Murrin Murrin, Teutonic Bore, Yindarlgooda, Nimbus and Trilogy deposits (Barley, 1992). Exploration for VHMS mineralisation in the Yilgarn Craton has been hindered by the concealment of bedrock by alluvial sand plains and deep weathering profiles, often up to 100 m below the current surface. At Gossan Hill, the discovery outcrop rose 60 m above the sand plains as a magnetite gossan, first identified in 1971 (Pitt, 1990).

Elevated Au and abundant magnetite (estimated at 12 Mt) make Gossan Hill an atypical example of an Australian polymetallic VHMS deposit (Large, 1992). Although such features are unusual in Australian polymetallic VHMS deposits, similar attributes are documented in many Canadian Archean deposits (*e.g.*, Franklin *et al.*, 1975; Roberts, 1975; Galley *et al.*, 1995; Zaleski and Peterson, 1995) and these similarities are addressed in the course of this thesis.

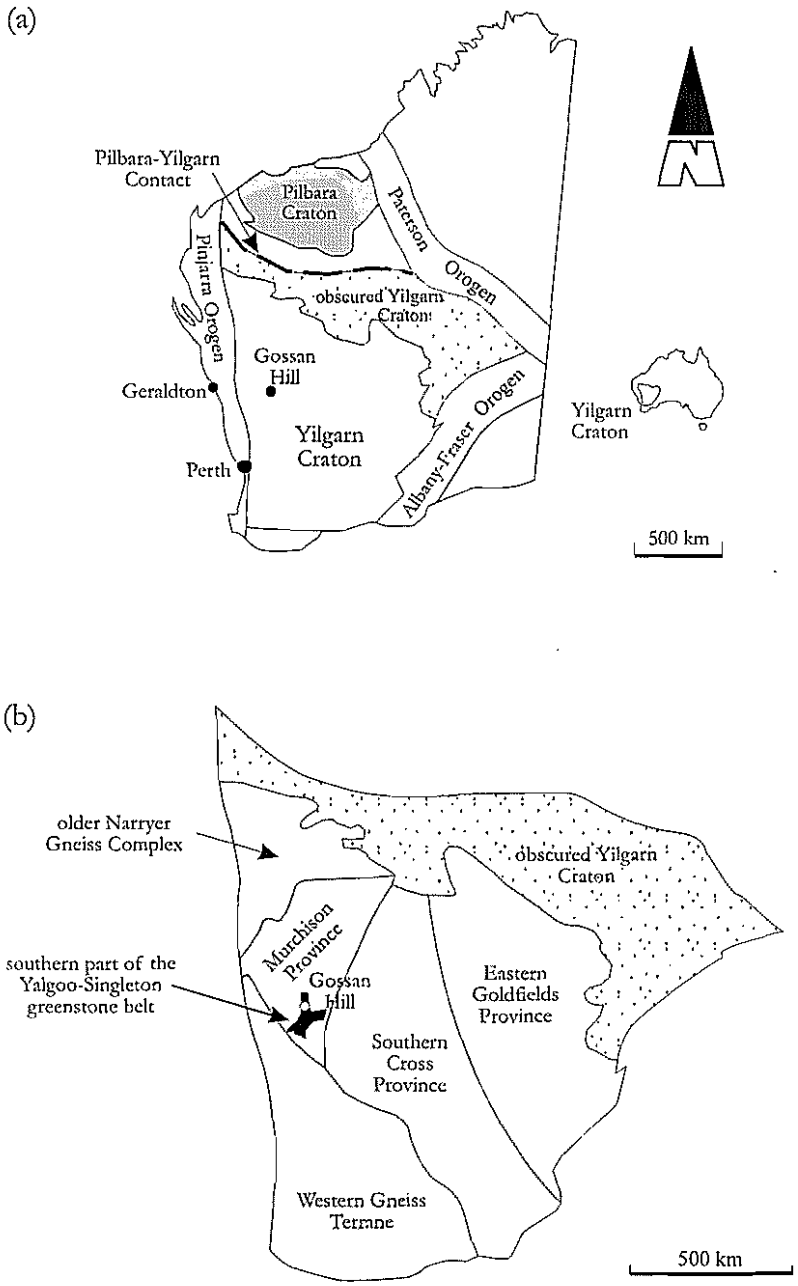

Figure 1.1: (a) Location of the Gossan Hill VHMS deposit in the Yilgarn Craton, Western Australia. (b) Subdivision of the Yilgarn Craton to four geological provinces (the Murchison, Southern Cross and Eastern Goldfields Provinces), the Western Gneiss Terrane and the older Narryer Gneiss Complex. The Golden Grove area, which hosts the Gossan Hill VHMS deposit, is located in the south of the Murchison Province within the southern part of the Yalgoo-Singleton greenstone belt (after Myers, 1990; Clifford, 1992).

1.2 Exploration history and mining status

Gossan Hill has had a long exploration history since its discovery in 1971 (Pitt, 1990) and the commencement of mining in 1998. Factors that have contributed to this history include changes in exploration philosophy, the remote location, difficulties in resource evaluation, and economic viability due to changes in metal prices. A brief summary of the exploration history at Gossan Hill is given below.

Anomalous gossan outcrop on Gossan Hill (Pitt, 1990) initiated a prospecting campaign by Aztec Exploration to evaluate the Cu-Zn prospectivity of the area known as Golden Grove. Amax Exploration Australia entered the joint venture with Aztec in 1972, following the recognition of similarities between outcropping magnetite-rich gossan at Gossan Hill to Cu-Zn volcanogenic mineralisation in Canada. Initial drilling of Gossan Hill was completed in 1972 and demonstrated a broad zone of podiform Cu-enriched mineralisation (Pitt, 1990). The Electrolytic Zinc Company of Australia joined the venture in 1973, which led to the systematic diamond drill delineation testing of the Gossan Hill prospect between 1973 and 1976. Early resource estimates of the Gossan Hill deposit were 12.1 Mt at 3.4% Cu, however, the resource was considered uneconomic at this time (Clifford *et al.*, 1990; Pitt, 1990).

The identification of Zn-rich sulphides overlying Cu-rich zones at Gossan Hill significantly modified exploration programs in the area. Zinc not only became an exploration target, but the concept of multiple 'favourable' stratigraphic horizons as potential hosts to Cu-Zn mineralisation was emphasised in subsequent exploration programs (Mill, 1990; Mill *et al.*, 1990; Sheppy and Clifford, 1991; Sheppy *et al.*, 1992). Subsequent exploration focussed on more regional programs within the Golden Grove area.

Esso Exploration and Production Australia Incorporated entered the joint venture in 1978 and conducted drilling programs both regionally and locally at Gossan Hill. In 1979, the discovery of the Scuddles VHMS deposit 4 km north of Gossan Hill eventuated from the culmination of anomalous geochemistry and geology, coincident with anomalous aeromagnetics (Mill, 1990). Initial drill testing at Scuddles intersected sub-economic Cu-rich sulphide. However, this was followed up by downhole EM, which identified a conductive target and resulted in an intersection through the massive sphalerite of the Scuddles deposit (Robinson and Belford, 1991; Boyd and Frankcombe, 1994). The pre-mining Scuddles resource was estimated to be 21 Mt at 1.2% Cu, 0.6% Pb, 8.2% Zn, 1 g/t Au, 67 g/t Ag (Dudley *et al.*, 1984) and is presently mined via shaft and decline access.

Renegotiations of the Golden Grove joint venture in 1987 modified the interests of the partners to 45% for Australian Consolidated Minerals (ACM) (formerly held by Amax), 35% for Esso, and 20% for Aztec, with operations carried out under the Murchison Zinc Company (MZC). In 1991, Normandy (formerly Normandy Poseidon) through its takeover of ACM, managed MZC and in 1995, Normandy also absorbed the equity of Aztec. In 1997, MZC became a wholly owned subsidiary of Normandy after Normandy's absorption of the interest formerly held by Esso in the Golden Grove joint venture.

Between 1994 and 1997, a feasibility program was completed at Gossan Hill by MZC. This feasibility study aimed to assess the resource and economic viability of mining Gossan Hill, and involved the development of an underground decline from which, delineation drilling and metallurgical testing was carried out. Production at Gossan Hill commenced in early 1998 using the on site processing and concentrating facilities previously established for mining the Scuddles deposit.

1.3 Previous studies at Golden Grove

The Gossan Hill deposit, formerly cited in the literature as Golden Grove (Frater, 1983a; 1985a;b), was the focus of two major studies and a component of many other studies in the area. Doctoral studies by Frater (1978) were based on early drilling results from Gossan Hill and examined the petrology, mineralogy, structure and chemistry of the deposit. The thrust of Frater's study was the mineralogical and textural variation of sulphide mineralogies and their response to deformation. Publications arising from Frater's (1978) work include Frater (1983a;b; 1985a;b) and Seccombe and Frater (1981). Despite this comprehensive study, the stratigraphic framework of the area was unresolved and consequently, the distribution and association of alteration and mineralisation within the host rocks was not defined. The second major study (Clifford, 1992), focussed on the volcanology of the area and resulted in the development of a consistent lithostratigraphic framework. The work by Clifford (1992) permitted correlation of the volcanic host sequence throughout the region and invoked a similar stratigraphic framework for massive sulphides at both the Gossan Hill and Scuddles deposits.

Processes of laterisation near Gossan Hill were investigated by Smith *et al.* (1980) and Smith and Pedrix (1983). Investigations on wall rock alteration and geochemistry by Ashley (1983; 1984), Ashley *et al.* (1988) and Whitford and Ashley (1992) examined alteration zonation patterns proximal to the Scuddles deposit, in order to identify primary dispersion haloes for exploration targeting. Potter (1991) geochemically defined dacite intrusions in the volcaniclastic footwall at Scuddles, whilst Ford (1992) reviewed the metal zonation patterns at Scuddles. Everett (1990) provided descriptive and analytical information on the nature, timing, mineralogy and geochemistry of the Au associated with base metal mineralisation at Gossan Hill. This study builds upon these earlier investigations.

1.4 Objectives of this study

The major objectives of this study at the Gossan Hill deposit were to:

(1) describe and characterise the geology and structural setting of the deposit;
(2) determine the lithostratigraphic context, geometry and distribution of massive magnetite and massive sulphide;
(3) describe the textures, composition and zonation within the massive magnetite and sulphide;
(4) delineate the distribution, type, timing and textural, mineralogical and geochemical variation of alteration associated with massive magnetite and massive sulphide;

(5) evaluate the timing and role of syngenetic *versus* epigenetic mineralisation;
(6) geochemically constrain formational fluids responsible for massive magnetite and massive sulphide;
(7) develop a genetic model for the formation of the Gossan Hill deposit and identify useful criteria for the exploration of similar resources in the Golden Grove Domain and elsewhere in the Yilgarn Craton.

1.5 Methodology

The objectives of this study were achieved by means of the following investigations:

(1) detailed logging (1:250) and sampling of diamond drill core at Gossan Hill (logging examples and rock catalogue are given in Appendix A1.1 and A1.2 respectively);
(2) 1:250 scale underground mapping of the exploration decline and ground checking of surface mapping completed by previous studies and MZC geologists;
(3) petrographic and textural studies on host rocks, massive magnetite and massive sulphide using polished and doubly polished thin sections;
(4) microprobe analyses to determine the composition of minerals within massive magnetite, massive sulphide and alteration;
(5) whole rock and trace element geochemistry of altered and least altered rocks;
(6) examination of metal zonation patterns in massive magnetite and massive sulphide using routine drill core assays provided by MZC;
(7) measurement of stable isotope compositions of sulphides (sulphur isotopes), carbonate (carbon and oxygen isotopes), magnetite (oxygen isotopes) and chlorite (hydrogen and oxygen isotopes) within massive magnetite, massive sulphide and hydrothermal alteration zones.

1.6 Thesis strategy

Chapter 2 reviews the regional geological setting of the Golden Grove area and its context within the Murchison Province and is a summary of regional granitoid intrusion history, structural setting, deformation, metamorphism and age constraints on the volcanic rocks. Chapter 3 is a critical descriptive analysis of the stratigraphy at Gossan Hill, which gives the stratigraphic framework and context of mineralisation. Structural and metamorphic studies (Chapter 4) examine syn- and post-mineralising structure, proposing synvolcanic structural control to the localisation of mineralisation at Gossan Hill. The metamorphic mineralogy, its timing and peak temperature estimates are also given. Chapter 5 focuses on the distribution, geometry and relative timing between wall rocks and massive sulphide and massive magnetite at Gossan Hill. The textural and compositional variation of minerals in massive magnetite and sulphide are given in Chapter 6. Chapters 7 and 8 address hydrothermal alteration including mineralogy, distribution, relative timing of events and geochemical characteristics. Chapter 9 summarises metal zonation patterns, whilst investigations in Chapters 10 and 11 deal with the stable isotope systematics of sulphide (Chapter 10) and carbonate, magnetite and chlorite (Chapter 11). A genetic model for the formation of the Gossan Hill deposit is given in Chapter 12 and the major conclusions of this thesis are summarised in Chapter 13.

Chapter 2

Regional geology

2.1 Introduction

The Gossan Hill and Scuddles VHMS deposits, and several other regional base metal prospects such as Luisini, Cullens, Felix and Flying Hi are all located within the Warriedar Fold Belt (WFB) (Baxter, 1982; Ashley *et al.*, 1988; Clifford, 1992). The WFB is part of the Yalgoo-Singleton greenstone belt that is located in the southern area of the Murchison Province (Fig. 2.1). This chapter presents a summary of the regional geology of the Murchison Province, its context within the Yilgarn Craton, and the geological setting of VHMS mineralisation within the WFB.

The Archean Yilgarn Craton consists of linear to arcuate greenstone belts within an extensive terrane of intrusive granitoid and gneiss. Based upon lithostructural criteria, the Yilgarn Craton is subdivided into three Provinces (Murchison, Southern Cross and Eastern Goldfields) and one terrane (Western Gneiss Terrane) (Gee *et al.*, 1981) (Fig. 2.1a). The Murchison Province shares many characteristics with the Southern Cross and Eastern Goldfields Provinces and consequently, the evolution of each of these provinces reflect the evolution of the Yilgarn Craton.

Based on conventional zircon U-Pb dating, the evolution of the Yilgarn Craton took place in three main stages, commencing with the development of a ~3.4 Ga stable granitic nucleus. This was followed by two separate episodes of greenstone formation and granitoid emplacement, both of which spanned the time interval between ~3.0 and ~2.6 Ga (Pidgeon and Wilde, 1990; Watkins and Hickman, 1990a; Myers, 1992; 1995; Nelson *et al.*, 1994). During this time, intense tectonic, volcanic, plutonic and metamorphic activity formed the various tectonstratigraphic terranes of the Yilgarn Craton. Greenstone-granitoid formational episodes were characterised by the accretion of these terranes at the margins of the stable craton, resulting in cratonisation of the diverse crustal fragments that now form the Yilgarn Craton (Gee *et al.*, 1981; Myers, 1990; 1995).

2.2 The Murchison Province

The Murchison Province (Fig. 2.1) is bounded to the north by the older Narryer Gneiss Complex (>3.0 Ga, Myers, 1988; 1992). To the northeast, the Murchison Province greenstone-granitoid sequence is overlain by Proterozoic rocks of the Nabberu Basin (Elias *et al.*, 1982). East of the Murchison Province lies the Southern Cross Province,

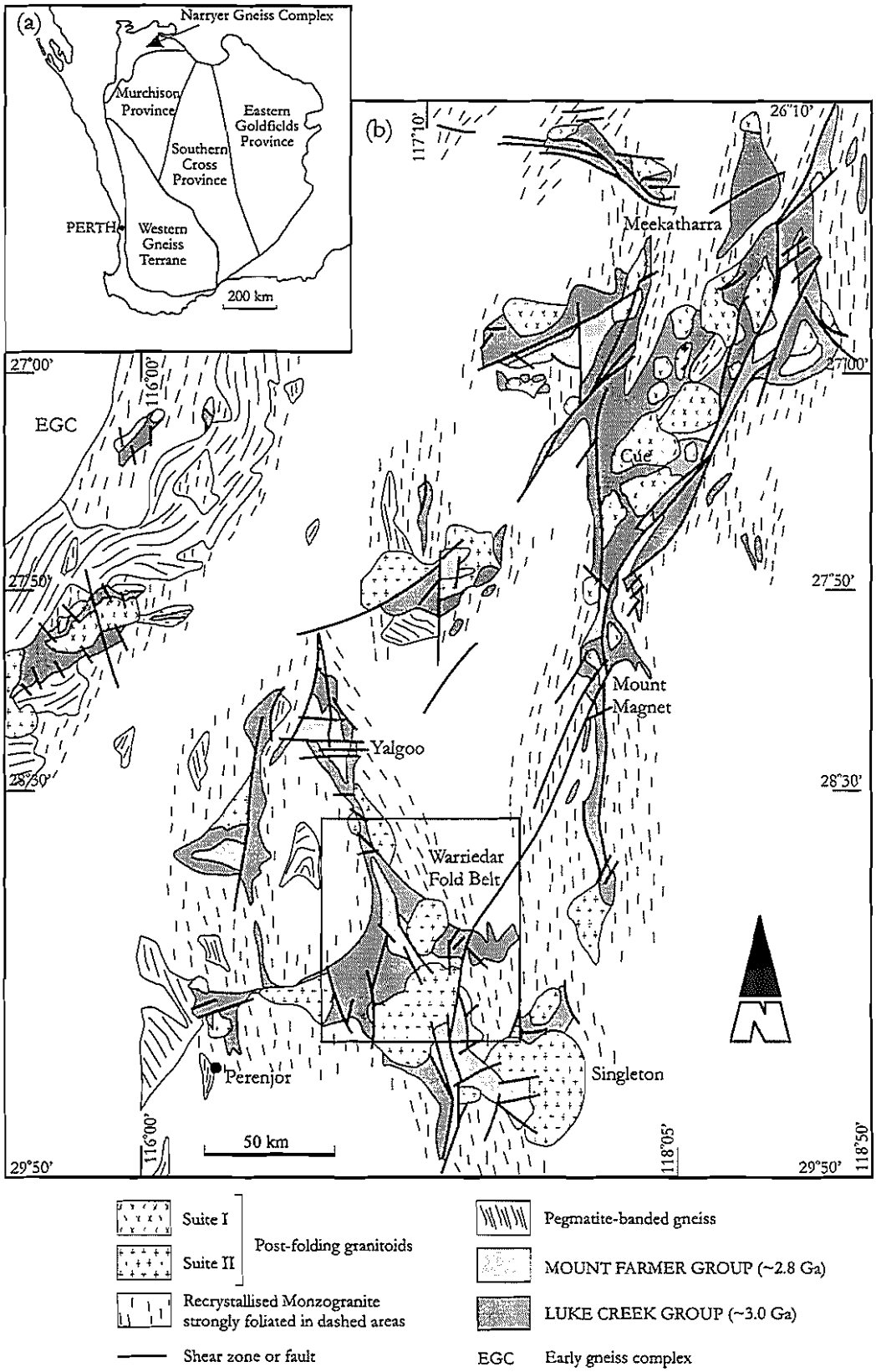

Figure 2.1: (a) Subdivision of the Yilgarn Craton into the Murchison Province, Southern Cross Province, Eastern Goldfields Province and the Western Gneiss Terrane. (b) Geology of the Murchison Province illustrating the distribution of the major crustal components (after Watkins and Hickman, 1990a; Myers, 1990)

whilst to the south is the Western Gneiss Terrane (Fig 2.1a). These eastern and southern boundaries of the Murchison Province are imprecisely located, but are defined by the differing tectonic trends within each province (Gee *et al.*, 1981).

The Murchison Province consists of six major crustal components that comprise two greenstone sequences (~3.0 to 2.8 Ga) and four granitoid suites (2.92 to 2.62 Ga) (Watkins and Hickman, 1990a) (Fig. 2.1b). The main components of the greenstone sequences in the Murchison Province are mafic volcanics and intrusions. However, the rarity of ultramafic rocks within the Murchison Province contrasts markedly with the Eastern Goldfields Province where they abound (Giles, 1981; Gee *et al.*, 1981; Hallberg and Giles, 1986; Barley and Groves, 1990).

Formal stratigraphic subdivision of the Murchison Province was first completed by de la Hunty (1973) and Baxter (1974). This early stratigraphic scheme was modified during a major geological campaign in the Murchison Province by the Western Australia Geological Survey (Watkins and Hickman, 1990a). Early stratigraphic subdivisions within the Murchison Province identified an unconformity that separated two fundamentally different greenstone sequences (*e.g.*, Hallberg *et al.*, 1976; Frater, 1978; Baxter, 1982; Lipple *et al.*, 1983; Baxter and Lipple, 1985) (Fig. 2.2). Nonetheless, it was not until the work by Watkins and Hickman (1990a;b) that a province-wide stratigraphic framework for the greenstone sequences in the Murchison Province was developed. This framework proposed two distinct greenstone sequences; the **Luke Creek Group** and the **Mount Farmer Group**, which form the Murchison Supergroup (Figs. 2.2 and 2.3).

The Luke Creek Group has a thickness of 10 km and consists of four laterally extensive formations. These are the Murrouli Basalt and the Golconda, Gabanintha and Windaning Formations (Fig. 2.3). The Luke Creek Group lithologies include tholeiitic (low- and high-Mg) basalt, banded iron-formation (BIF), komatiite, felsic volcanics and sedimentary rocks (Fig. 2.3). Tholeiitic basalt in the Luke Creek Group represents regionally extensive lava plain volcanism (Myers, 1995; Watkins and Hickman, 1990a).

Unconformably overlying the Luke Creek Group is the Mount Farmer Group. The Mount Farmer Group is up to 5 km thick, and consists of nine separate volcanic centres and one epiclastic sedimentary basin, all of which have a local distribution (Myers, 1995; Watkins and Hickman, 1990a). The main rock types in the Mount Farmer Group are low- and high-Mg tholeiitic basalt, felsic volcanics and sedimentary rocks (Fig. 2.3).

The four granitoids suites within the Murchison Province are (1) granodiorite-monzogranite metamorphosed to pegmatite banded gneiss (~2.9 Ga), (2) recrystallised monzogranite (~2.7 Ga), and (3-4) two contemporaneous post-folding granitoids (~2.6 Ga) (Watkins *et al.*, 1991). Pegmatite banded gneiss and recrystallised monzogranite intruded the base of the Murchison Supergroup (Luke Creek Group) as thick subhorizontal tabular bodies (Watkins and Hickman, 1990a). Post-folding granitoids intrude both the Luke Creek and Mount Farmer Groups. The timing of greenstone formation, granitoid emplacement and regional deformational events are summarised in Table 2.1 and Figure 2.4.

<table>
<tr><th>Frater (1978)</th><th>Baxter (1982)</th><th colspan="4">Watkins and Hickman (1990a)</th><th>Clifford (1992)</th></tr>
<tr><td>WFB Unit 6
WFB Unit 5
WFB Unit 4</td><td>Mungada Group
Chulaar Group
Warriedar Group</td><td rowspan="6">Murchison Supergroup</td><td rowspan="2">Mount Farmer Group</td><td>Singleton Basalt</td><td>Mougooderra Formation</td><td colspan="2">Upper Sedimentary Succession</td></tr>
<tr><td>WFB Unit 3</td><td rowspan="2">Thundelarra Group</td><td rowspan="4">Luke Creek Group</td><td colspan="2">Windaning Formation</td><td rowspan="2">Upper Mafic Succession</td><td>Minjar Group</td></tr>
<tr><td>WFB Unit 2</td><td colspan="2" rowspan="2">Gabanintha Formation</td><td>Thundelarra Group</td></tr>
<tr><td>WFB Unit 1</td><td>Gossan Hill Group</td><td colspan="2">Gossan Hill Group</td></tr>
<tr><td></td><td>Fields Find Group</td><td colspan="2">Golconda Formation
Murrouli Basalt</td><td colspan="2">Lower Mafic Succession</td></tr>
</table>

Figure 2.2: Differing stratigraphic schemes used within the Murchison Province, Western Australia. There is general agreement of two greenstone sequences separated by an unconformity, and of at least four stratigraphic components within both greenstone sequences. These stratigraphic schemes illustrate the differing interpretations of thickness and contact relations between the stratigraphy in the Murchison Province (Watkins and Hickman, 1990a) to that of the Warriedar Fold Belt (Frater, 1978; Baxter, 1982; Clifford, 1992).

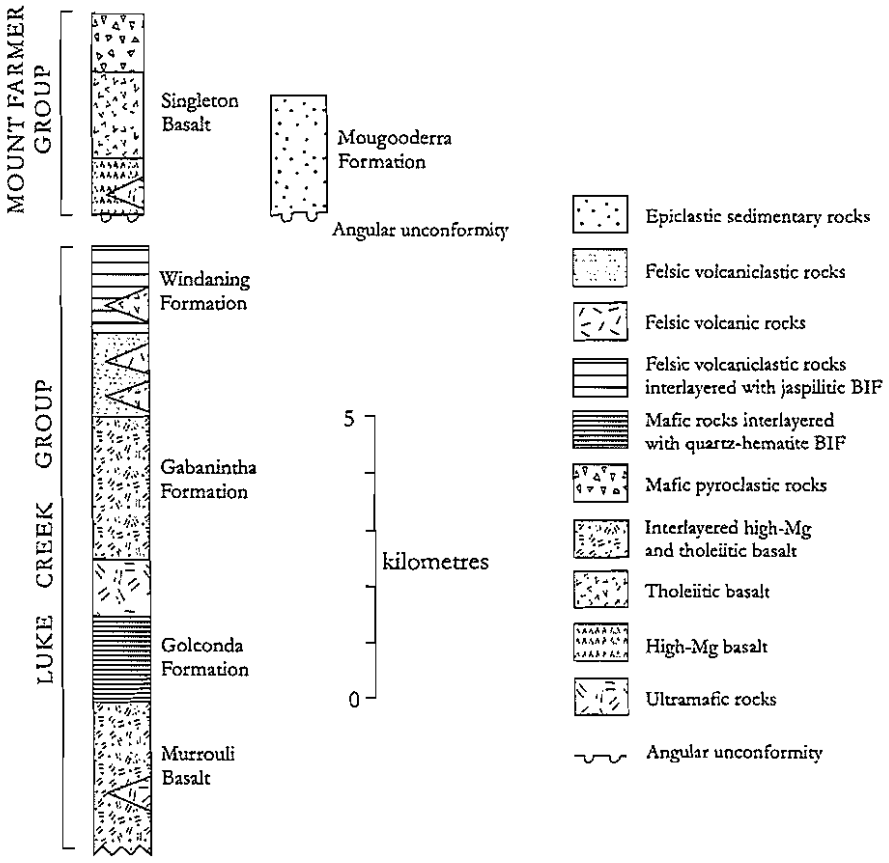

Figure 2.3: Stratigraphy of the Murchison Supergroup illustrating the different formations and rock types within the Luke Creek Group and the Mount Farmer Group. Stratigraphic thicknesses are approximate (after Watkins and Hickman, 1990a).

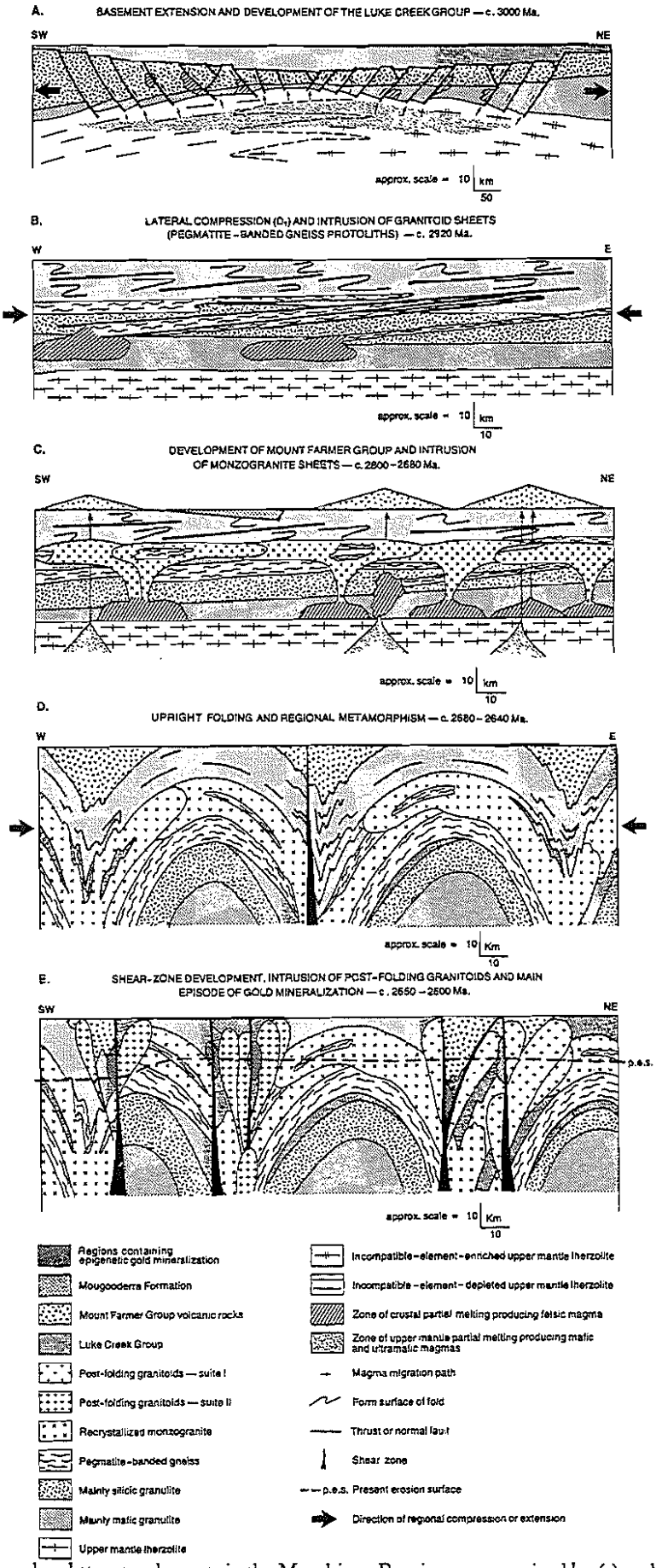

Figure 2.4: Depositional and structural events in the Murchison Province summarised by (a) early extension and deposition of the Luke Creek Group, (b) intrusion of granitoid, (c) deposition of the Mount Farmer Group and intrusion of monzogranite sheets, (d) upright folding and regional metamorphism (D3), and (e) shear zone development and intrusion of post-folding granitoids (D4) (from Watkins and Hickman, 1990a).

Table 2.1: Precambrian geological history of the Murchison Province (from Watkins and Hickman, 1990a).

Event	Age	Details
1	3.0 Ga	Deposition of the Luke Creek Group on inferred basement Note: VHMS mineralisation formed during this event
2	2.92 Ga	Intrusion of monzogranite and granodiorite
3		D1: development of major recumbent folds and thrusts in the Luke Creek Group; deformation of granitoid sheets and subsequent development of pegmatite banded gneiss Note: events (2) and (3) could be contemporaneous
4	2.8 Ga	Deposition of the Mount Farmer Group unconformably on the Luke Creek Group and pegmatite banded gneiss
5	2.69-2.68 Ga	Intrusion of voluminous monzogranite as thick sheets into the base of the Murchison Supergroup; development of amphibolite facies contact metamorphic aureoles around monzogranite
6		D2: tight east-west trending upright folding of granitoids and greenstones
7		D3: tight and isoclinal north, northwest to northeast trending folds, upright folding of granitoids and greenstones Note: D3 more intensely developed than D2
8	2.68-2.64 Ga	Regional metamorphism of granitoids and greenstones, mainly in greenschist facies
9	2.64-2.62 Ga	Intrusion of post-folding granitoid plutons into greenstone belts, mainly along contacts between greenstone belts and earlier granitoids
10		D4: development of northwest to northeast trending steeply inclined shear zones and faults Note: shear zones were probably initiated during late D3
11	2.42 Ga	Intrusion of the west to south trending mafic dyke suite
12		D5: development of east to southeast trending shear zones and faults Note: D5 confined to the northwest part of the Murchison Province

Watkins and Hickman (1990a) propose two main cycles in the crustal evolution of the Murchison Province. Each cycle consists of (1) deposition and volcanism in an extensional sialic setting followed by, (2) the intrusion of large volume regional lacoliths of monzogranite and granodiorite at relatively shallow crustal levels, and (3) compressional deformation events (Fig. 2.4).

2.3 Regional intrusions

Granitoids form over 85% of the current exposure in the Murchison Province and reflect three phases of granitoid magmatism (Table 2.1). Geochemical and isotopic studies indicate that each of these granitoids was derived from partial melting of crustal rocks (Watkins and Hickman, 1990a; Watkins *et al.*, 1991). The source of pegmatite banded gneiss and recrystallised monzogranite was derived from a uniform mafic crustal source, whilst post-folding granitoids were derived from siliceous crustal material (Watkins *et al.*, 1991; Clifford, 1992).

Within the Murchison Province, the arcuate outcrop patterns of greenstone belts against granitoids has two interpretations, both of which infer strong tectonic and structural control. Earlier interpretations have favoured diapiric emplacement of granitoid batholiths (*e.g.*, Gee *et al.*, 1981; Baxter and Lipple, 1985) whilst more recent work favours dome-and-basin fold interference structures (Myers and Watkins, 1985; Myers, 1995).

2.3.1 Pegmatite banded gneiss

Pegmatite banded gneiss forms a northeast trending belt in the west of the Murchison Province and elsewhere occurs as enclaves and rafts within recrystallised monzogranite (Fig. 2.1b). Pegmatite banded gneiss does not occur adjacent to the WFB (Fig. 2.1b). The intrusive contacts between pegmatite banded gneiss and recrystallised monzogranite, together with common xenoliths of gneiss within later recrystallised monzogranite (Section 2.3.2) indicate that the gneiss formed earlier than the monzogranite (Watkins and Tyler, 1985).

Pegmatite banded gneiss consists of quartz, oligoclase, microcline and biotite. Gneissic layering within this granitoid is defined by variation in biotite contents and subparallel pegmatite bands (several cm thick) interlayered with compositionally banded, medium grained monzogranite and granodiorite (<10 cm thick) (Watkins and Hickman, 1990b). The injection of pegmatite to banded monzogranite and granodiorite was synchronous with D1 deformation (Watkins and Hickman, 1990b).

U-Pb zircon dates of ~2.9 Ga mean that pegmatite banded gneiss is the earliest recognised granitoid within the Murchison Province (Watkins and Hickman, 1990a; Wiedenbeck and Watkins, 1993). Comparatively, Rb-Sr whole rock and mineral isochrons yield ages of ~2.6 Ga (Arriens, 1971; de Laeter *et al.*, 1981). These younger Rb-Sr ages however, represent post-metamorphic cooling contemporaneous with post-folding granitoid intrusion (Watkins and Hickman, 1990a; Watkins *et al.*, 1991).

2.3.2 Recrystallised monzogranite

Recrystallised monzogranite occurs in most regions between the greenstone sequences (Fig. 2.1b) and was emplaced as thick (several km) subhorizontal tabular sheets of a regional extent (Watkins and Hickman, 1990a; Clifford, 1992). Large rafts of greenstone within the recrystallised monzogranite indicate that the monzogranite intrudes the base of greenstone sequences (Myers and Watkins, 1985). The contacts between recrystallised monzogranite and greenstone sequences are complex, high strain zones up to 1 km wide (Watkins and Hickman, 1990a;b). Ubiquitous granoblastic and lepidoblastic textures within monzogranite are the result of recrystallisation during regional metamorphism (Watkins and Hickman, 1990b). Near the WFB, recrystallised monzogranite is strongly foliated and has greenschist facies metamorphism (Watkins and Hickman, 1990a; Clifford, 1992).

U-Pb zircon dating from recrystallised monzogranite yield ages of 2.68 Ga to 2.7 Ga (Wiedenbeck and Watkins, 1993; Mueller *et al.*, 1996). Rb-Sr isochron ages however, range from 2.55 to 2.71 Ga and have a mean age of 2.61 Ga (de Laeter *et al.*, 1981). As with Rb-Sr ages in pegmatite banded gneiss, these younger Rb-Sr ages reflect post-metamorphic cooling (Watkins *et al.*, 1987; Watkins and Hickman, 1990a;b).

2.3.3 Post-folding granitoids

Post-folding granitoids have subcircular discordant outcrop patterns that truncate stratigraphic units and earlier tectonic features associated with folding. However, most

shear zones and faults cross cut these granitoids and the contact between the granitoids and greenstone sequences are sharp, commonly with contact hornfels aureoles of less than 100 m wide (Clifford, 1992). The intrusion of post-folding granitoids occurred syn- to post-peak regional metamorphism (Watkins and Hickman, 1990a; Watkins *et al.*, 1991).

Compositionally, post-folding granitoids vary from monzogranite to syenogranite with a mineral assemblage of quartz, orthoclase, plagioclase and biotite (Watkins and Hickman, 1990a). Based upon petrography and geochemistry, these granitoids are divided into two contemporaneous suites; Suite I and II (Watkins and Hickman, 1990a;b). Suite I granitoids vary from tonalite, granodiorite, monzogranite to trondgjemite, all of which occur in the northeast of the Murchison Province. Suite II granitoids are quartz-rich monzogranite and syenogranite that occur in the southwest of the Murchison Province (Watkins *et al.*, 1991).

Suite I and II post-folding granitoids have contemporaneous U-Pb zircon ages of ~2.68 Ga (Wiedenbeck and Watkins, 1993). Rb-Sr isochrons yield ages from 2.51 to 2.6 Ga (Watkins and Hickman, 1990a), giving a slightly younger age than the U-Pb zircon dates. Wang *et al.* (1993) conclude that Rb-Sr isochron ages from post-folding granitoids are indistinguishable from regional post metamorphic cooling, which occurred at ~2.6 Ga.

2.3.4 Mafic intrusions

Mafic intrusions in the Murchison Province consist of concordant to subconcordant gabbro and dolerite sills and dykes (Frater, 1978; Watkins and Hickman, 1990a;b; Clifford, 1992). Multiple phases of these mafic intrusions are synvolcanic to mafic volcanism during the evolution of the WFB (Hallberg and Wilson, 1983). Some mafic intrusions however, post-date post-folding granitoid emplacement.

Late stage cross cutting dolerite and gabbro sills and dykes are the main mafic intrusion type within the WFB (Frater, 1978; Clifford, 1992). These intrusions are up to 120 m wide, lack a regional penetrative fabric and are metamorphosed to greenschist facies (Clifford, 1992). Their intrusion is interpreted to be prior to or synchronous with peak metamorphism, possibly associated with contemporaneous faulting. However, Rb-Sr isochrons on these mafic dykes, yield ages ~2.42 Ga indicating that they are early Proterozoic in age (Watkins and Hickman, 1990a).

2.4 Structure of the Murchison Province

Five deformational events are recognised within the Murchison Province (Table 2.1) and are summarised in Figure 2.4. The first four of these events (D1 to D4) are ubiquitous throughout the Murchison Province. The last deformation event (D5) is only identified in the northwest of the Murchison Province (Watkins and Hickman, 1990a) and is not discussed further.

The earliest deformational event (D1) is characterised by recumbent folding and thrusting without significant penetrative cleavage development. However, gneissic layering within pegmatite banded gneiss and weak layer parallel foliation in some areas of

the Luke Creek Group formed during D1 (Baxter, 1982; Watkins and Hickman, 1990a). The time interval separating D1 and D2, corresponds to the deposition of the Mount Farmer Group (Table 2.1) and is considered to have been substantial (Watkins and Hickman, 1990a). D2 deformation generated east-west trending folds with subvertical axial surfaces and subhorizontal fold axes within granitoids and the Murchison Supergroup (Myers and Watkins, 1985; Watkins and Hickman, 1990a;b; Clifford, 1992). An east-west directed compressional event (D3) occurred soon after D2. This event formed northwest to northeast trending, upright isoclinal folds (D3) (Watkins and Hickman, 1990a). Continued compression during and after D3 followed, with the development of brittle-ductile shear during D4. The penetrative fabric resultant from D3 is strongly developed in north-south fold limbs (Clifford, 1992). The D2 structures were refolded during D3, forming dome and basin fold interference structures (Myers and Watkins, 1985).

The WFB is characterised by narrow heterogeneous deformational zones of high strain. These zones separate less deformed areas that have a consistent stratigraphic framework (Frater, 1978; Baxter, 1982; Clifford, 1992). Folds characteristic of the two regional folding events (D2 and D3) are identified throughout the WFB (Frater, 1978; Archibald, 1990; Clifford, 1992). However, penetrative deformation associated with D2 in the WFB has a limited distribution, as do D2 mesoscopic folds (Archibald, 1990; Clifford, 1992). The regional schistosity within the WFB is a north-south directed fabric, which was developed during D3 (Frater, 1978; Ashley, 1983; Clifford, 1992). Notably, the D1 deformational event interpreted by Watkins and Hickman (1990a) remains contentious within the WFB (Frater, 1978; Archibald, 1990; Clifford, 1992).

2.5 Regional metamorphism

Prograde regional metamorphism in the Murchison Province overprints all Archean thermal intrusive and deformational events (Watkins and Ahmat, 1988). Metamorphic facies throughout the Murchison Province range from prehnite-pumpellyite to granulite (Watkins and Ahmat, 1988). Nonetheless, the majority of rocks have greenschist to lower amphibolite facies, with amphibolite facies (hornblende-biotite-garnet) generally restricted to the margins of granitoid intrusions. Peak metamorphism occurred less than 2.64 Ga, as indicated by late stage faults with greenschist facies assemblages that truncate post folding granitoids (Myers, 1995).

Within the WFB, metamorphism is predominantly greenschist facies. Greenschist facies is defined by a chlorite, albite and quartz (±biotite, tremolite, actinolite, epidote, clinozoisite) assemblage in mafic lithologies, and by a quartz, albite, white mica and chlorite (±biotite) assemblage in felsic volcanics and volcano-sedimentary rocks (Watkins and Ahmat, 1988; Clifford, 1992).

2.6 The Warriedar Fold Belt

The term Warriedar Fold Belt (WFB) was first used by Baxter (1982) to describe an area of supracrustal rocks within the Murchison Province that is bounded by the Mongers

Fault to the east and by granitoids elsewhere (Fig. 2.5a). Stratigraphic and structural interpretations consistently recognise two volcanic-sedimentary successions within the WFB (Frater, 1978; Gee *et al.*, 1981; Baxter, 1982; Watkins and Hickman, 1990a; Clifford, 1992) (Fig. 2.2). Despite this consistency, the regional stratigraphic framework of the Murchison Province (Watkins and Hickman, 1990a) differs markedly from that of the WFB (*e.g.*, Frater, 1978; Ashley *et al.*, 1988; Clifford, 1992) (Fig. 2.2). The regional stratigraphic framework of Watkins and Hickman (1990a) relates the relative superposition of greenstone belts within the Murchison Province. However, despite good geochronological control on granitoid magmatism, similar geochronological data for the greenstone sequences in the Murchison Province is lacking (Pidgeon and Wilde, 1990; Clifford, 1992). Therefore, a definitive terrane-wide stratigraphic correlation between greenstone sequences cannot be made. Moreover, the potential of thrust stacking within the Murchison Province, as exemplified in the Archean Superior Province of Canada (*e.g.*, Thurston and Chivers, 1990; Ayres and Corfu, 1991) must also be considered.

The stratigraphic framework devised by Clifford (1992) for the WFB, addresses these issues by means of a tectonic evaluation criteria. Clifford (1992) subdivides the WFB into five tectonostratigraphic domains, using techniques similar to those employed by Ludden and Hubert (1986) and Card (1990). This methodology results in the most comprehensive stratigraphic framework of the WFB to date.

2.6.1 Tectonostratigraphic Domains of the WFB

Within the WFB, five major faults representing structural discontinuities separate unrelated tectonostratigraphic domains (Clifford, 1992). These faults are the Mongers, Mougooderra, Pincer, Windaning and Rothsay Faults (Fig. 2.5a). From north to south the WFB tectonostratigraphic domains are the Gnows Nest, Golden Grove, Chulaar, Windaning and Fields Find Domains (Fig. 2.5a). Each of these domains is briefly described below.

Gnows Nest Domain

The Gnows Nest Domain is located in the northern WFB (Fig. 2.5a). Domain bounding faults are the Mougooderra (east), Pincer (south) and Windaning (southwest) Faults, with recrystallised monzogranite intruding the succession to the northwest (Fig. 2.5a). The Gnows Nest Domain lies on the western limb of a north trending F3 syncline, which overprints an earlier F2 anticline. Bedding within this domain is subvertical and eastward younging. Stratigraphic components within the Gnows Nest Domain are up to 2 km thick and consist dominantly of tholeiitic (low- and high-Mg) basalt with minor banded iron formation (BIF) and felsic to mafic arenites (Fig. 2.5b). All of these lithofacies lie within the Golconda Formation of the Luke Creek Group (Watkins and Hickman, 1990a).

Golden Grove Domain

The Golden Grove Domain hosts the Gossan Hill and Scuddles VHMS deposits and lies along the northeast flank of the WFB (Fig. 2.5a). The Mougooderra Fault (west),

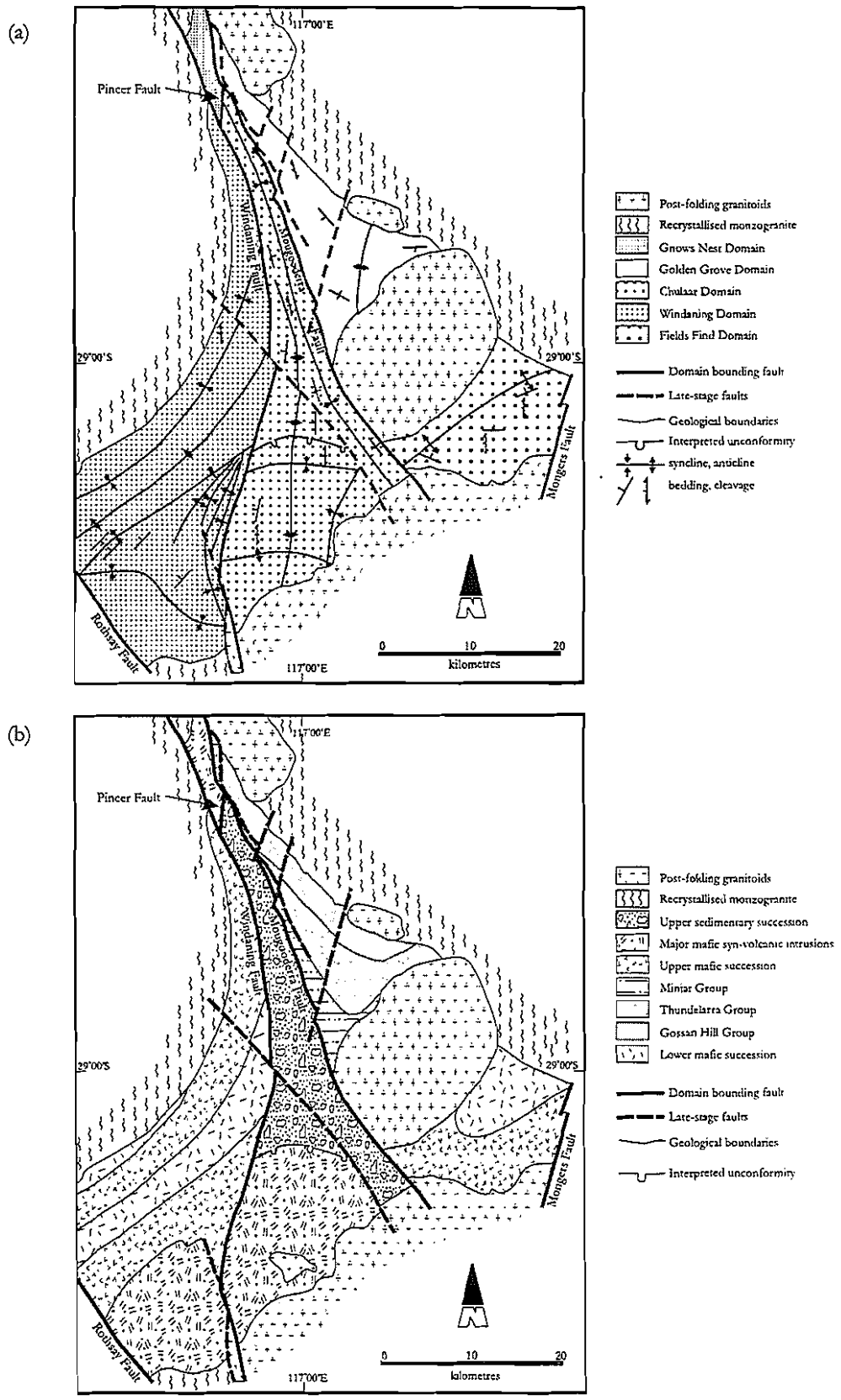

Figure 2.5: Structure and stratigraphy of the Warriedar Fold Belt. (a) Tectonostratigraphic domains and structures within the Warriedar Fold Belt. (b) Stratigraphy of each of the tectonostratigraphic domains within the Warriedar Fold Belt (after Clifford, 1992).

recrystallised monzogranite (east) and post-folding granitoids (north and south) bound this domain. The dominant megascopic structural feature of this domain is a north trending, subvertically plunging F3 anticline. The majority of the Golden Grove Domain is located on the western limb of this anticline and has westward younging and steeply dipping strata. Clifford (1992) defines the stratigraphy of the Golden Grove Domain as having three groups; the Gossan Hill, Thundelarra and Minjar Groups (Fig. 2.5b), all of which occur within the Gabanintha Formation (Watkins and Hickman, 1990a). These stratigraphic components are further discussed in Section 2.7.

Chulaar Domain

The Chulaar Domain has a northerly trend and forms the central part of the WFB (Fig. 2.5a). It is bounded by the Mougooderra (east), Windaning (west) and Pincer (north) Faults. A post-folding granitoid truncates this domain to the south. The dominant megascopic structures of the Chulaar Domain are a north to northwest-trending F3 anticline and syncline. Two distinct lithofacies are present within the Chulaar Domain and have an estimated thickness of 1.8 km. To the south of this domain, basalt and dolerite sills abound with subordinated ultramafic, BIF and sedimentary rocks. To the north of the Chulaar Domain, the main lithologies are quartz sandstone to conglomerate and breccia (Fig. 2.5b), all of which fine upwards to volcanogenic sandstone and black shale (Clifford, 1992). The contact between these two lithotypes is an unconformity (Clifford, 1992). Watkins and Hickman (1990a) classify this strata within the Gabanintha and Windaning Formations (Fig. 2.2).

Windaning Domain

The Windaning Domain forms the western margin of the WFB and is bounded by the Windaning Fault (east), the Rothsay Fault (southwest), and elsewhere by recrystallised monzogranite (Fig. 2.5a). The dominant structures of this domain are tight, north to northeast trending upright F3 synclines and anticlines. Two distinct lithofacies occur within the Windaning Domain, and are separated by an inferred fault or unconformity (Clifford, 1992). Lithologies within this domain include mafic volcanics and a thick succession of interbedded felsic volcanogenic sedimentary rocks (Fig. 2.5b), with minor BIF and high-Mg tholeiitic basalt (Clifford, 1992). Strata within the Windaning Domain lie within the Gabanintha and Windaning Formations of Watkins and Hickman (1990a).

Fields Find Domain

The Fields Find Domain is located on the southeast flank of the WFB (Fig. 2.5a). It is bounded by intrusive contacts against post-folding granitoids (south and northwest) and by recrystallised monzogranite (northeast). The Mongers and Mougooderra Faults form the east and west domain boundaries respectively. The main structure within the Fields Find Domain is a megascopic west-trending subvertical F2 anticline (Fig. 2.5a). Mesoscopic upright F3 folds indicate that this domain lies on the western limb of a F3 anticline. Lithofacies within the Fields Find Domain consist of mafic intrusives, which are overlain by a thick pile of tholeiitic (low- and high-Mg) basalt (Fig. 2.5b) as well as minor BIF and litharenite. Watkins and Hickman (1990a) interpreted these rocks to lie

within the Windaning Formation (Luke Creek Group) and the Singleton Basalt (Mount Farmer Group) (Fig. 2.3).

2.7 Stratigraphy of the Golden Grove Domain

The stratigraphy of the Golden Grove Domain was formally defined by Clifford (1992), and is illustrated in Figures 2.6 and 2.7. This stratigraphy consists of three conformable stratigraphic groups; (1) the Gossan Hill Group, (2) the Thundelarra Group, and (3) the Minjar Group. The following stratigraphic descriptions are summarised from Clifford (1992).

2.7.1 Gossan Hill Group

The Gossan Hill Group is a sequence of felsic volcaniclastic and coherent volcanic rocks that has an average thickness of 3 km. This sequence lies within the Gabanintha Formation and represents the lowest preserved stratigraphic component of the Golden Grove Domain (Fig. 2.6). VHMS mineralisation is located in the central parts of the Gossan Hill Group. The strata within the Gossan Hill Group has a north-south strike extent of 28 km (Fig. 2.7). The Gossan Hill Group has five formations. From base to top these are the (1) Shadow Well, (2) Gossan Valley, (3) Golden Grove, (4) Scuddles, and (5) Cattle Well Formations (Fig. 2.6). The distribution of each of these formations is summarised in Figure 2.6 and illustrated in Figure 2.7.

Shadow Well Formation

The Shadow Well Formation is the lowest stratigraphic formation of the Gossan Hill Group and has an estimated thickness varying from 150 to 1100 m. This formation strikes northwest (Fig. 2.7) and has intrusive contacts against recrystallised monzogranite (northeast) and conformable contacts with the overlying Gossan Valley Formation (southwest). A post-folding granitoid also intrudes the Shadow Well Formation to the south (Fig. 2.7). The lithology of the Shadow Well Formation consists of poorly sorted quartz-feldspathic sandstone.

Gossan Valley Formation

The Gossan Valley Formation occurs in the eastern part of the Golden Grove Domain, has a northwest trend (Fig. 2.7) and ranges in thickness from 170 to 920 m. This formation has conformable upper and lower contacts to the Golden Grove and Shadow Well Formations respectively. Post-folding granitoid intrusions truncate this formation to the southeast. The Gossan Valley Formation consists of matrix and clast supported polymict sandstone and breccia, with minor felsic and mafic volcanic facies. This formation is divided into four members based on facies associations (Harris *et al.*, 1982; Dudley *et al.*, 1984; Ashley *et al.*, 1988; Clifford, 1992) and detailed descriptions are given in Clifford (1992).

Golden Grove Formation

The Golden Grove Formation (GGF) hosts VHMS mineralisation (Fig. 2.6), has a northwest trend (Fig. 2.7) and a thickness that varies between 75 to 800 m. This

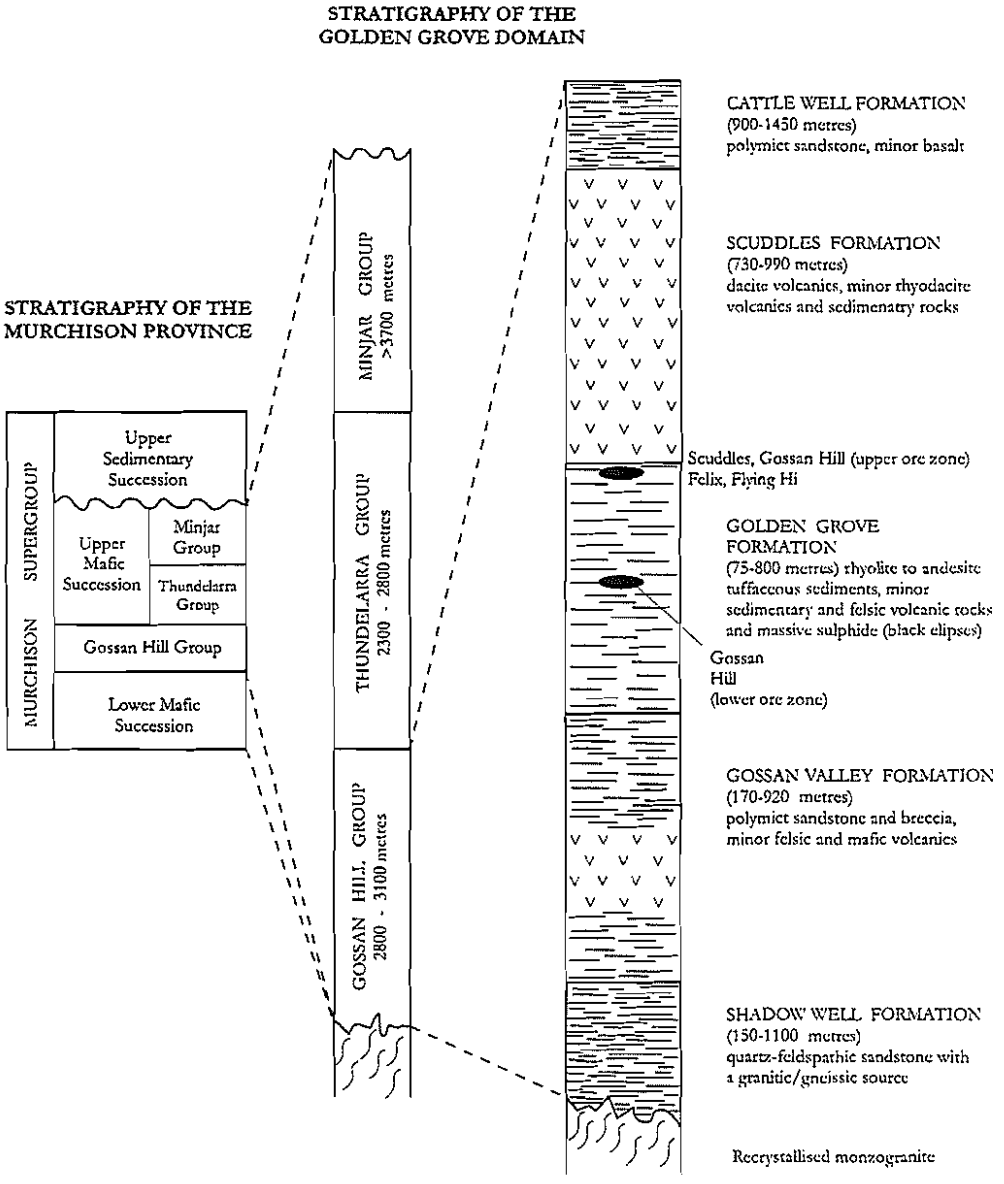

Figure 2.6: Stratigraphy of the Golden Grove Domain (after Clifford, 1992) and its relation to the regional stratigraphy of the Murchison Province. The stratigraphic location of massive sulphides is indicated (black elipses) and occurs within the Golden Grove Formation of the Gossan Hill Group.

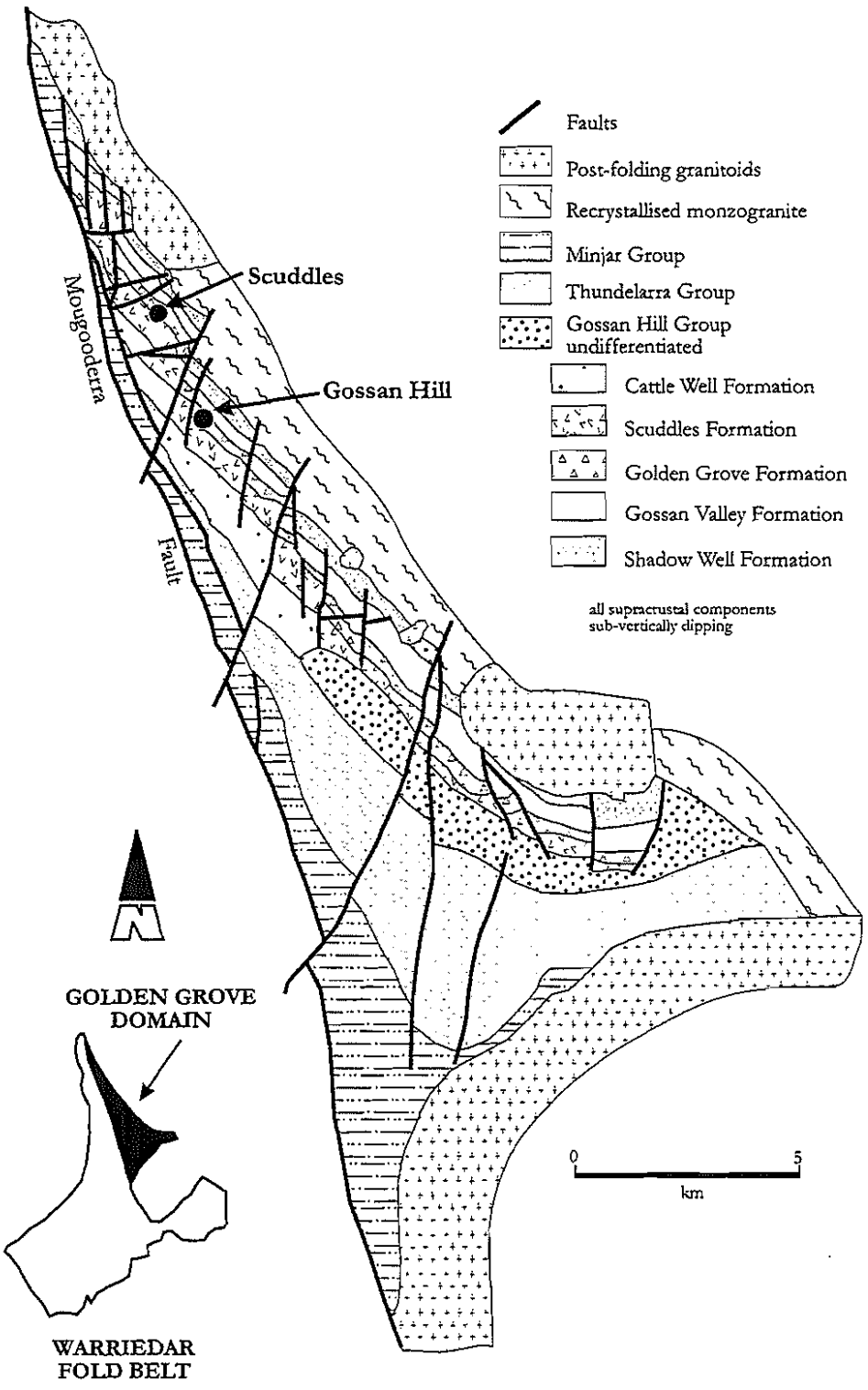

Figure 2.7: Distribution of stratigraphic components and megascopic structure of the Golden Grove Domain (after Clifford, 1992). The Golden Grove Domain is located on the northeast flank of the Warriedar Fold Belt. The location of the Gossan Hill and Scuddles VHMS deposits is also shown.

formation has conformable lower contacts against the Gossan Valley Formation (east), and passive to interactive, discordant to conformable contacts with volcanics of the Scuddles Formation (west). Volcanics of the Scuddles Formation commonly cross cut the contact of the GGF, intruding underlying sedimentary rocks from above or transgressing the contact as dykes feeding volcanic flows and intrusive-extrusive domes from below. Post-folding granitoids intrude and truncate the GGF in the southeast (Fig. 2.7).

The GGF stratigraphic subdivision is equivalent to the Mineralised Horizon of Frater (1978) and Ashley *et al.* (1988) and the Mineralised Succession of Mill *et al.* (1990). Lithologies within the GGF consist of resedimented juvenile tuffaceous debris of rhyolite to andesite composition, as well as minor sedimentary rocks and volcanic rocks varying from andesite to rhyodacite. Economically significant chemical horizons in the GGF include massive sulphide and massive magnetite (Section 2.10), and hydrothermal alteration associated with these horizons is widespread. The GGF is divided into six members, which are the focus of Chapter 3.

Scuddles Formation

The Scuddles Formation (SCF) varies in thickness from 730 to 990 m and forms a northwest trending belt in the central part of the Golden Grove Domain (Fig. 2.7). The SCF is bounded by conformable contacts against the overlying Cattle Well Formation and conformable to transgressive contacts with the underlying GGF. The lithology of the SCF is dominated by dacite volcanic facies with minor rhyodacite volcanics and sedimentary rocks. The SCF consists of four members, which are described in Chapter 3.

Cattle Well Formation

The Cattle Well Formation has northwest trending outcrop within the Golden Grove Domain (Fig. 2.7) and varies in thickness from 900 to 1450 m. It is bounded to the northeast by conformable contacts to the underlying SCF and to the southwest by the overlying Thundelarra Group. Lithologies in the Cattle Well Formation vary from poorly to moderately sorted polymict sandstone and breccia, with minor coherent basalt.

2.7.2 Thundelarra Group

In the Golden Grove Domain, the Thundelarra Group was first defined by Baxter (1982) and occurs within the Gabanintha Formation of Watkins and Hickman (1990a) (Fig. 2.3). Its thickness is estimated to vary between 2.3 and 2.8 km. The Thundelarra Group is bounded by the Mougooderra Fault (west), the Gossan Hill Group (northeast) and the overlying Minjar Group (south and southwest) (Fig. 2.7). Recrystallised monzogranite intrudes the Thundelarra Group to the southeast. The Thundelarra Group is a mafic succession that is dominated by tholeiitic (low- to high-Mg) basalt and concordant synvolcanic sills with minor ultramafic rocks and interflow sedimentary rocks (Watkins and Hickman, 1990a; Clifford, 1992). Interflow mafic litharenite sedimentary rocks and minor BIF and epiclastics led Clifford (1992) to imply a deep subaqueous setting for the Thundelarra Group.

2.7.3 Minjar Group

The Minjar Group is bounded by the Mougooderra Fault (west) and the Gnows Nest (northwest) and Chulaar (west) Domains. This group also has intrusive contacts with post-folding granitoids to the south (Fig. 2.7). The maximum preserved thickness of this group is 3.7 km and it is conformable to the underlying Thundelarra Group. The lower parts of the Minjar Group are dominated by a thick succession of epiclastic and BIF rocks with an overlying mafic to ultramafic sequence.

In the classification of Watkins and Hickman (1990a), the Minjar Group in the Golden Grove Domain spans the Windaning Group (Luke Creek Group) and the Singleton Basalt (Mount Farmer Group), which are separated by an unconformity. Work by Clifford (1992) however, indicates limited disruption and interdigitation of these rocks within the Mougooderra Fault in the Golden Grove Domain. Clifford (1992) argues that there is a lack of evidence to infer an unconformity between these lithologies and instead suggest these facies are either related or juxtaposed as fault blocks.

2.7.4 Depositional setting of the Golden Grove Domain

The lithofacies within the Golden Grove Domain are interpreted to form a coherent stratigraphic succession that was deposited within a deep subaqueous environment (Clifford, 1992). The subaqueous mass-flow style of sedimentation and the effusive styles of proximal volcanism support this inference. The depositional environment of the Golden Grove Domain is summarised below from the work of Clifford (1992).

The subdivision of the Gossan Hill Group into five formations represents five distinct phases of basinal development. The Shadow Well Formation at the base of the Gossan Hill Group records the influx of granitic and gneissic sediments into the basin. The Gossan Valley Formation represents an abrupt change in sediment source to mixed provenance reworked andesitic volcanic debris, emplaced *via* mass-flow sedimentation. The GGF records ongoing mixed provenance litharenite sedimentation that was periodically interrupted by large volume influx and rapid mass flow emplacement of juvenile rhyodacitic pyroclastic debris. This interpretation of the GGF contrasts with earlier interpretations by Frater (1978) and Ashley *et al.* (1988) and is reviewed in Chapter 3. Minor proximal volcanism during deposition of the GGF is reflected by sparse rhyodacite to andesite volcanics. The SCF represents a major pulse of effusive felsic volcanism and produced laterally extensive composite flows and domes with interdigitating autoclastic facies. The cessation of volcanism is marked by the upper contact of the SCF, with the Cattle Well Formation sedimentary sequence representing a return to mass-flow sedimentation.

Effusive basaltic volcanism of the Thundelarra Group supercedes sedimentation of the Gossan Hill Group. This volcanism reflects rapid eruption of large volumes of basaltic magma within a deep subaqueous environment, as indicated by interflow sediments and hyaloclastite. Overlying the Thundelarra Group, epiclastic sedimentary facies of the Minjar Group are interpreted to represent ongoing background sedimentation in a deep subaqueous environment (*i.e.*, significant mudstone facies within the Minjar Group).

Tholeiitic (low- and high-Mg) basalt in the upper parts of the Minjar Group indicate epiclastic deposition giving way to basaltic volcanism.

2.7.5 Association of the Golden Grove Domain to other domains in the WFB

The main contrast between the Golden Grove Domain and other tectonostratigraphic domains in the WFB is the absence of lithofacies equivalent to the Gossan Hill Group (Clifford, 1992). Similarly, the Golden Grove Domain does not contain mafic lithofacies equivalent to the Upper Sedimentary Succession, which abound in the adjacent Chulaar Domain. Additionally, the lithologies in the Golden Grove Domain are dominated by felsic to andesitic volcaniclastic and volcanic rocks with subordinate mafic volcanics, whilst the WFB is dominated by mafic volcanic successions with subordinate epiclastics (*c.f.* Figs. 2.5b and 2.7). Despite these differences, Clifford (1992) proposed a correlation between the mafic-dominated Thundelarra Group within the Golden Grove Domain and the mafic successions elsewhere in the WFB (the Lower and Upper Mafic Successions) (Figs. 2.3 and 2.5). As a consequence, the Gossan Hill Group, which underlies the Thundelarra Group, could reflect an additional lithostratigraphic component that is only exposed in the Golden Grove Domain. However, geochronological data is currently lacking to substantiate this conclusion.

2.8 Age dating

The time span of greenstone belt formation within the Murchison Province is poorly constrained and a range of dating techniques yield a range of ages. Zircon U-Pb investigations for the Yilgarn Craton indicate at least two distinct episodes of felsic volcanism at ~3.0 and ~2.7 Ga. Each of these episodes spans an interval of ~79 Ma (Pidgeon *et al.*, 1988; Pidgeon and Wilde, 1990). Within the WFB, U-Pb zircon dating on the Gabanintha Formation give crystallisation ages varying from 2.93 Ga to 3.01 Ga (Pidgeon and Wilde, 1990). Sm-Nd isochron ages from the Yalgoo-Singleton greenstone belt also yield 2.98 Ga and 2.82 Ga ages (Fletcher *et al.*, 1994), all of which are broadly consistent and considered to reflect the broad formational age of the Luke Creek Group at ~3.0 Ga (Watkins and Hickman, 1990a).

Within the Golden Grove Domain, a U-Pb zircon date of 2.94 Ga was obtained from the Gossan Valley Formation (Member 3) (Pidgeon and Wilde, 1990; Wang *et al.*, 1998) and dates of 2.96 Ga and 2.95 Ga from the SCF (Member 1) (Pidgeon *et al.*, 1994; Wang *et al.*, 1998). These dates are inferred to represent a maximum age difference of ~10 Ma between the Gossan Valley and the Scuddles Formations, which correspond to 550 m of sedimentary facies (Pidgeon *et al.*, 1994; Clifford, 1992). This estimate of depositional time is consistent with high sedimentation rates (50 to 300 m per Ma) in modern extensional marginal basins (Carey and Sigurdsson, 1984; Clifford, 1992).

Recent U-Pb zircon dating by Wang *et al.* (1996; 1998) identify stratigraphic correlation problems within the Murchison Supergroup, previously highlighted by Clifford (1992). The U-Pb zircon dating within the Yalgoo-Singleton greenstone belt yield dates of 2.95 Ga for the Gabanintha Formation and 2.8 Ga for the Windaning Formation (Wang *et al.*, 1996; 1998). Additionally, dates from the nearby Meekatharra-Wydgee greenstone belt

yield ages of 2.7 and 2.8 Ga for the Windaning and Gabanintha Formations respectively (Wang *et al.*, 1996). This work is in agreement with geochronology by Schiotte and Campbell (1996) and Wiedenbeck and Watkins (1993), whose results indicate that parts of the Mount Farmer Group are as young as 2.7 Ga.

Age dating of greenstone sequences within the Murchison Province is therefore broadly consistent with the relative timing of greenstone formation as proposed by Watkins and Hickman (1990a). The range in ages however, suggests that the relative timing of volcanic episodes is not well constrained and that stratigraphic correlation problems exist. Nonetheless, age determinations from greenstone sequences in the Murchison Province indicate that these volcanic episodes were broadly contemporaneous with granitoid plutonism (Wiedenbeck and Watkins, 1993; Wang *et al.*, 1996).

2.8.1 VHMS Pb-model ages

Galena, syngenetic with VHMS mineralisation at the Gossan Hill and Scuddles deposits (Frater, 1978; 1983a; Ashley, 1983; Ashley *et al.*, 1988; Clifford, 1992), yield mean Pb-model ages of ~3.0 Ga, ranging from 3.05 Ga (Scuddles and Gossan Hill) to 2.97 Ga (Yerecion 2 base metal prospect) (Browning *et al.*, 1987). These Pb-model ages are older than U-Pb zircon ages obtained for the Gabanintha Formation (Section 2.8). Vaasjoki (1984) obtained a Pb-model age from wall rock samples at Scuddles and Gossan Hill of ~2.73 Ga. This age of mineralisation is too young and is similar to U-Pb zircon dates for the younger overlying Mount Farmer Group (Section 2.8). Therefore, Pb model ages for syngenetic VHMS mineralisation at Gossan Hill and Scuddles yield dates that are both too old and too young. However, these ages demonstrate a ~3.0 to ~2.8 Ga age for volcanism and mineralisation (Vaasjoki, 1984; Pidgeon and Wilde, 1990).

2.9 Tectonic setting

Watkins and Hickman (1990a;b) proposed that the Murchison Province began its tectonic history as a single large-scale, extensional, ensialic basin in an intra-plate setting. This interpretation is based on (1) the inferred siliceous to mafic granulite nature of basement rocks, and (2) the layered stratigraphy of the Luke Creek Group. Nonetheless, contention still remains on the origin and tectonic significance of volcanic rocks in Archean supracrustal sequences and whether the Archean had unique tectonism (Watkins and Hickman, 1990a) or tectonic regimes comparable to modern analogues (Gee *et al.*, 1981; Hallberg and Giles, 1986; Clifford, 1992; Myers, 1995). Barley and Groves (1990) and Barley *et al.* (1992) suggest a range of tectonic settings within the evolution of individual terranes of the Yilgarn Craton based upon the heterogeneous distribution of Archean mineral deposits.

Evolutional models of granite-greenstone terranes depend critically on the nature of the basement and the tectonic regime in operation. Both of these parameters are poorly understood in the Murchison Province. As the basement rocks of the Murchison Supergroup are not exposed, two types of basement have been inferred; (1) a simatic "oceanic" type, and (2) a sialic "continental" type (*e.g.*, Archibald *et al.*, 1981; Gee *et al.*, 1981; Groves and Batt, 1984; Watkins and Hickman, 1990a; Shackleton, 1995).

Geophysical evidence, combined with lithological, geochemical and isotopic evidence from overlying stratigraphic sequences, led Watkins and Hickman (1990a) to infer a heterogeneous, layered basement assemblage consisting of mafic and siliceous granulite, with a significant garnet amphibolite and tonalite component. This conclusion is in agreement with other authors on Archean geology in Western Australia (*e.g.*, Archibald *et al.*, 1981; Gee *et al.*, 1981; Hallberg and Giles, 1986).

The preservation of Archean greenstone sequences requires that they be erupted on to buoyant silialic crust, which prevents their destruction by subduction (Nisbet and Fowler, 1983; Watkins and Hickman, 1990b). Tectonic models involving development of greenstone as oceanic crust are therefore excluded. Volcanological and geochemical evidence within the WFB support early rifting in response to extensional tectonic processes (Watkins and Hickman, 1990a; Clifford, 1992) (Fig. 2.4a). The abundance of deep submarine facies and mafic rocks in the WFB favours an oceanic arc setting with derivation from a continental source due to the lack of ophiolitic rocks within the WFB. Clifford (1992) interprets the WFB to have evolved as a rifting island-arc with a significant continental component. This tectonic setting is therefore comparable to modern tectonic island-arc rift or back-arc settings that contain VHMS mineralisation (*e.g.*, the Tertiary Hokuroko Basin, Japan in Cathles *et al.*, 1983; the Manus Basin, Papua New Guinea in Binns and Scott, 1993).

2.10 The Scuddles and Gossan Hill VHMS deposits

The Gossan Hill and Scuddles deposits are the largest VHMS deposits in the Yilgarn Craton (Watkins and Hickman, 1990a). They occur within the Golden Grove Domain and are hosted by the GGF of the Gossan Hill Group (Figs. 2.6 and 2.7). The Golden Grove Formation consists of a layered volcaniclastic sequence with minor volcanic rocks. At Scuddles, VHMS mineralisation occurs in the uppermost part of the Golden Grove Formation near the contact with the overlying Scuddles Formation volcanics (Fig. 2.8). This stratigraphic location corresponds to the site of VHMS mineralisation at Gossan Hill and Scuddles, as well as a number of uneconomic base metal prospects along strike within the GGF (*e.g.*, Felix and Flying Hi). The occurrence of these deposits along a single strata supports the concept of a favourable stratigraphic interval for mineralisation (*e.g.*, Franklin *et al.*, 1981) in the Golden Grove Domain. However, VHMS mineralisation at Gossan Hill spans a greater stratigraphic interval than mineralisation at Scuddles and occurs within the central to the uppermost parts of the GGF (Figs. 2.6 and 2.8).

The local geology and proximity (<4 km) of the Gossan Hill and Scuddles deposits is illustrated in Figure 2.8. Stratigraphy trends northwest and dips steeply to the west. A series of north to northeast trending D4 faults dissect the Archean geology, with faults having small strike-slip displacements. Dolerite intrusions in this area are common and have similar orientations to late D4 faults. In the east, recrystallised monzogranite intrudes the base of the Shadow Well Formation to within 400 m of VHMS mineralisation at the Gossan Hill and Scuddles deposits (Fig. 2.8).

VHMS mineralisation in the Golden Grove Domain is characteristically Zn- and Cu-rich,

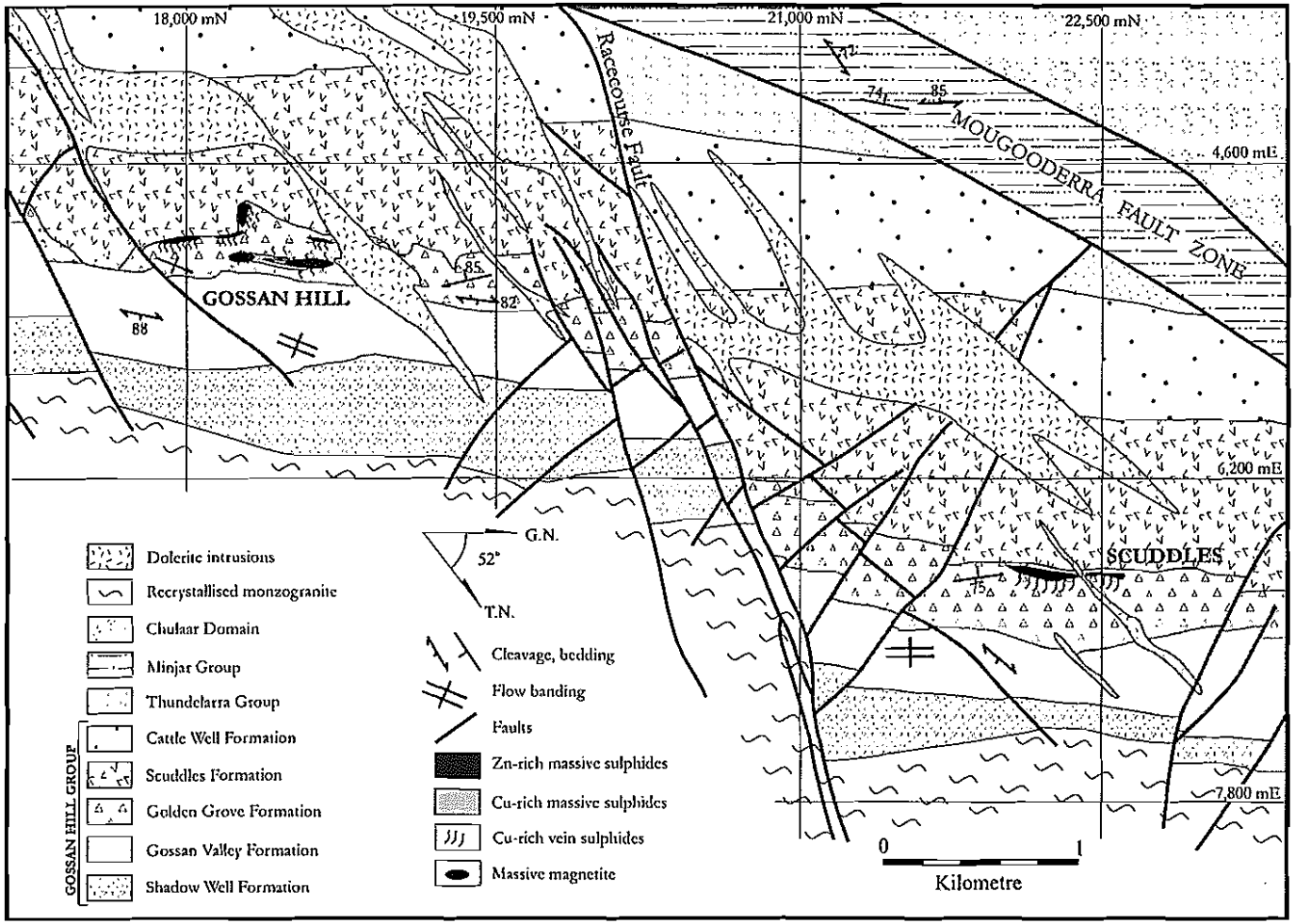

Figure 2.8: Local geology of the Gossan Hill and Scuddles deposits within the Golden Grove Domain. Massive sulphides are hosted within the Golden Grove Formation of the Gossan Hill Group. Zn-rich sulphides at Gossan Hill are located near the upper contact of the Golden Grove Formation and the Scuddles Formation, whilst massive magnetite and Cu-rich sulphides occur lower in the Golden Grove Formation (after Clifford, 1992).

having low Pb and barite contents, and Cu-rich stringer stockwork developed below the Zn-rich massive sulphides. The morphology of the Scuddles and Gossan Hill deposits differs. Scuddles is a relatively stratiform sheet-like deposit that has a discordant underlying Cu-rich stockwork. Gossan Hill varies from a sheet-like deposit in its upper stratigraphic parts, to a large discordant stockwork zone in its lower parts. Gossan Hill also contrasts to the Scuddles deposit due to the occurrence of podiform massive magnetite bodies associated with discordant Cu-rich mineralisation at Gossan Hill (Chapter 5).

2.11 Summary

- The Murchison Province contains four episodes of granitoid emplacement and two episodes of greenstone formation. These greenstone episodes formed the Murchison Supergroup that consists of the older Luke Creek Group (~3.0 Ga), which is unconformably overlain by the younger Mount Farmer Group (~2.8 Ga). VHMS mineralisation is correlated to the Luke Creek Group.
- Four granitoid suites intrude the Murchison Province. From oldest to youngest these are (1) granodiorite-monzogranite metamorphosed to pegmatite banded gneiss (~2.9 Ga), which intruded the base of the Luke Creek Group, (2) recrystallised monzogranite (~2.7 Ga), which also intruded the base of the Luke Creek Group, and (3-4) two contemporaneous post-folding granitoids (~2.6 Ga) that truncate all stratigraphy and fold structures.
- Four phases of deformation are identified with recumbent folds and thrusts of D1 predating deposition of the Mount Farmer Group and intrusion of recrystallised monzogranite. The major structural features of the Murchison Province are however tight east-west folds (D2) and tight north to northwest folds (D3). The main penetrative fabric (S3) formed during the north to northwest D3 folding event. Shear zones (northwest to northeast) were developed during D4.
- Prograde metamorphism in the Murchison province ranges from prehnite-pumpellyite to granulite facies, however rocks in the Warriedar Fold Belt have greenschist to lower amphibolite facies.
- The Warriedar Fold Belt is an arcuate greenstone sequence in the central part of the Murchison Province. This greenstone belt contains five tectonostratigraphic domains, with economic base metal mineralisation located within the Golden Grove Domain, on the northeast flank of the WFB.
- The Golden Grove Domain is a coherent succession of felsic to mafic volcaniclastic and volcanic rocks deposited in a deep subaqueous environment. This domain has a layered stratigraphy with a strike extent of 28 km.

Chapter 3

Stratigraphy

3.1 Introduction

The Golden Grove Formation (GGF) is part of the Gossan Hill Group volcano-sedimentary succession and forms a layered sequence of felsic volcaniclastics that underlies and hosts massive sulphide mineralisation at Gossan Hill. Coherent volcanic rocks are absent from the GGF near Gossan Hill, but the main rock type of the overlying Scuddles Formation (SCF). The SCF consists of massive volcanic lavas, intrusions and related breccia facies, with minor volcaniclastics. Both the GGF and the SCF have a steep west to subvertical dip and a northwest strike.

It is difficult to describe the stratigraphy of the GGF at Gossan Hill without some precursory introduction to the alteration systematics of these rocks, as all rocks within the GGF are altered. As a result of alteration, primary mineralogies are not preserved and the rocks consist almost entirely of alteration assemblages, excepting volcanic quartz. Consequently, mineralogy is not a diagnostic criteria for the subdivision of strata. The stratigraphic classification of the GGF in this thesis is based on three main characteristics. These are (1) the proportions of volcanic quartz, (2) preserved volcanic textures, and (3) physical attributes including bedding and grading. The most important criteria used for lithologic and stratigraphic orientation, is the abundance, morphology, distribution and size of volcanic quartz. In the GGF, volcanic quartz is the most chemically resistant and stable phase against the effects of alteration, having diagnostic attributes for each stratigraphic subdivision. Preserved volcanic textures also yield much information about the original lithology and lithofacies. However, textural preservation is variable and limited within intense alteration near mineralisation.

3.1.1 The implementation of a stratigraphic framework

Early workers in the Golden Grove Domain encountered many difficulties in resolving a consistent stratigraphy (*e.g.*, Table 3.1). These difficulties arose from the massive homogeneous appearance of strata within the Gossan Hill Group and resulted in conflicting interpretations of rock type and origin. For example, the stratigraphic subdivisions of Frater (1978) and Ashley (1983) were divided between a pyroclastic origin and a mixed pyroclastic-epiclastic origin respectively. In an attempt to resolve the stratigraphic context of sulphide-magnetite mineralisation at Gossan Hill, Frater (1978) and Ashley *et al.* (1988) each developed a subdivision termed the "Mineralised Horizon"

Table 3.1: Correlation and nomenclature of previous stratigraphic subdivisions devised by workers in the Golden Grove Domain. Abbreviated terms used by previous workers refer to (1) the interpreted relative stratigraphic position to mineralisation; U = upper, W = hangingwall, L = lower, FW = footwall, (2) lithological features; F = feldspathic, Q = quartz, X = crystal, C = cherty, (3) facies interpretation; T = tuff, AF = ashflow cycles, and (4) stratigraphic units; MH = mineralised horizon.

Frater (1978; 1983a)	Frater (1978)	Clifford (1987)	Harris *et al.*, (1982)	Ashley *et al.*, (1988)	Clifford (1992); this study
Cycle 3					**Scuddles Formation**
felsdpathic volcorudite		Unit 12	UFAF	UFAF	Member 4
		Unit 11		UFAT	Member 3
Cycle 2		Unit 10	UQAF	UQAF	Member 2
Dacite sill and UQXT		Unit 9		UAFV	Member 1
					Golden Grove Formation
HWC	Cycle 5	Unit 8	MH (upper)	UMHT and MH	Member 6
upper MH	Cycle 5	Unit 7	MH (middle)	LMAF	Member 5
lower MH	MH	Unit 6	MH (lower)	LAF(C)	Member 4
lower MH	MH	Unit 5	transition	LAF	Member 3
	MH	Unit 4			Member 2
FWLT	Cycle 4	Unit 3	FLT/LAF		Member 1
					Gossan Valley Formation
Cycle 1					
LCT	Cycle 1-3	Unit 2	LAF(C)		Member 4
LQXT	Cycle 1	Unit 1	LAFQ		Member 3
basal tuff	Cycle 1		LAF		Member 2
basal tuff	Cycle 1				Member 1

(Table 3.1), which was based on the assumption that all the mineralisation at Gossan Hill occurred contemporaneously. The "Mineralised Horizon" encompassed all mineralised rocks to a single stratigraphic unit due to difficulties in differentiating between similar altered volcaniclastic lithologies.

The implementation of facies analysis by Clifford (1992) proved to be highly successful in the Golden Grove Domain and resulted in the development of a consistent stratigraphic division. Based upon critical examination of volcanic textures and primary facies characteristics, Clifford (1992) divided the Gossan Hill Group into five formations (Fig. 3.1). In Clifford's (1992) scheme, the Gossan Hill Group represents a coherent volcano-sedimentary succession that consists of coherent facies, tuffaceous volcaniclastics and epiclastic sediments. This definition means that mineralisation at Gossan Hill is hosted by tuffaceous and epiclastic strata and that stratigraphic separation exists between Cu- and Zn-rich mineralisation.

3.1.2 Aims

This chapter examines the stratigraphy proximal to mineralisation at the Gossan Hill deposit, from Gossan Valley Formation Member 4 in the footwall to SCF Member 2 in the hangingwall (Fig. 3.2). The stratigraphic investigations of this thesis test and complement the regional stratigraphic studies of Clifford (1992). This study uses facies

FACIES ASSOCIATIONS

1. Epiclastic facies

(a) Quartz Arenite Facies: Poorly sorted, quartzo-feldspathic, fine to coarse sandstone, minor interbedded pelite. Eroding gneissic/granitic source terrain. Facies lensoidal when interbedded with other epiclastic or volcanic facies. Distribution limited: Shadow Well and Gossan Valley Formation Member 1.

(b) Mixed Provenance Litharenite Facies: Moderate to poorly sorted, polymict-lithic, fine sandstone to cobble breccias; the breccias being subordinate. Source area dominated by eroding andesitic volcanics, with subordinate plutonic, dacitic, basaltic and ultramafic volcanic sources. Bedded centimetres to 15 metres, partial Bouma sequences and scoured bases. The facies is lensoidal when interdigitating with volcanic facies. Stratigraphic distribution: upper four formations of the Gossan Hill Group.

(c) Tuffaceous Volcaniclastic Facies Association: Poorly sorted breccias composed of resedimented juvenile magmatic and phreatomagmatic tuffaceous debris. Massive to bedded, depositional units centimetres to 9 metres massive to crudely graded (A2A3 Bouma sequences), and scoured bases. Individual facies are laterally continuous on a scale of kilometres. Stratigraphic distribution: Golden Grove Formation

2. Volcanic facies

(a) Coherent Basalt Facies: Thin laterally discontinuous, aphyric, amygdaloidal, coherent basalt flows and some associated synvolcanic intrusives. Stratigraphic distribution: Gossan Valley and Cattle Well Formations

(b) Andesite Facies Association: Three related facies are defined, the Coherent Andesite, Massive Andesite Breccia and Stratified Andesite Breccia Facies. All facies are weakly porphyritic, amygdaloidal, laterally discontinuous and together form a genetically related facies group. Stratigraphic distribution: Golden Grove Formation Member 2.

(c) Dacite Facies Association: Three facies, the Coherent Dacite, Massive Dacite Breccia and Stratified Dacite Sandstone and Breccia Facies, are defined within this facies association. Six distinct eruptives have been identified (Dacite 1-6). These vary from aphyric to quartz-feldspar porphyritic and are locally amygdaloidal. Stratigraphic distribution: Golden Grove Formation Member 2, Scuddles Formation Members 1-4.

(d) Rhyodacite Facies Association: Three facies, the Coherent Rhyodacite, Massive Rhyodacite Breccia and Stratified Rhyodacite Breccia Facies, are defined within this facies association. Three distinct eruptives have been identified (Rhyodacite 1-3). All are quartz-feldspar porphyritic and locally amygdaloidal. Stratigraphic distribution: Golden Grove Formation Member 2, Scuddles Formation Member 2 and 4.

(e) Rhyolite Facies Association: Three facies, the Coherent Rhyolite, Massive Rhyolite Breccia and Stratified Pebbly Rhyolite Sandstone Facies, are defined within this facies association. The association includes a single eruptive, which is quartz-feldspar porphyritic and restricted in stratigraphic distribution to Gossan Valley Formation Member 3.

3. Chemical sediment facies

(a) Chert Facies: Fine grained silica, commonly with finely disseminated carbonate, sulphide and oxide impurities, defining delicate laminations. Geometry of the facies is thin (<5 metres) lensoidal occurrences of limited (<200 metres) lateral continuity. Isolated occurrences known, but most abundant as a lateral equivalent of, or in the hangingwall to significant Massive Sulphide Facies occurrences. Most stratigraphically widespread chemical sedimentary facies: Golden Grove and lower Scuddles Formation

(b) Massive Oxide Facies: The facies has two end-member varieties. Variety 1 - coarse-grained (1-2 millimetres) subhedral magnetite, beds of <2 centimetres interbedded with Chert Facies. Variety 2 - fine-grained (<0.01 millimetres) magnetite, massive stratiform lenses of <10 metres thickness and <80 metres lateral continuity overlying epigenetic magnetite stockwork, footwall to significant massive sulphide facies. Stratigraphic distribution: Golden Grove and lower Scuddles Formation (var. 1) and Golden Grove Formation Member 4 (var. 2)

(c) Massive Sulphide facies: Primary and recrystallised Fe, Zn, Cu, Pb sulphides. Geometry varies from thin (<2 centimetres) lensoidal occurrences interbedded with chert and massive magnetite, through to stratiform massive sulphide lenses <40 centimetres thick, with lateral dimensions of <400 metres. Major occurrences exhibit zoned metal distributions and underlying well developed epigenetic stockwork. Stratigraphic distribution: Golden Grove Formation Members 4 and 6 and Scuddles Formation Member 3.

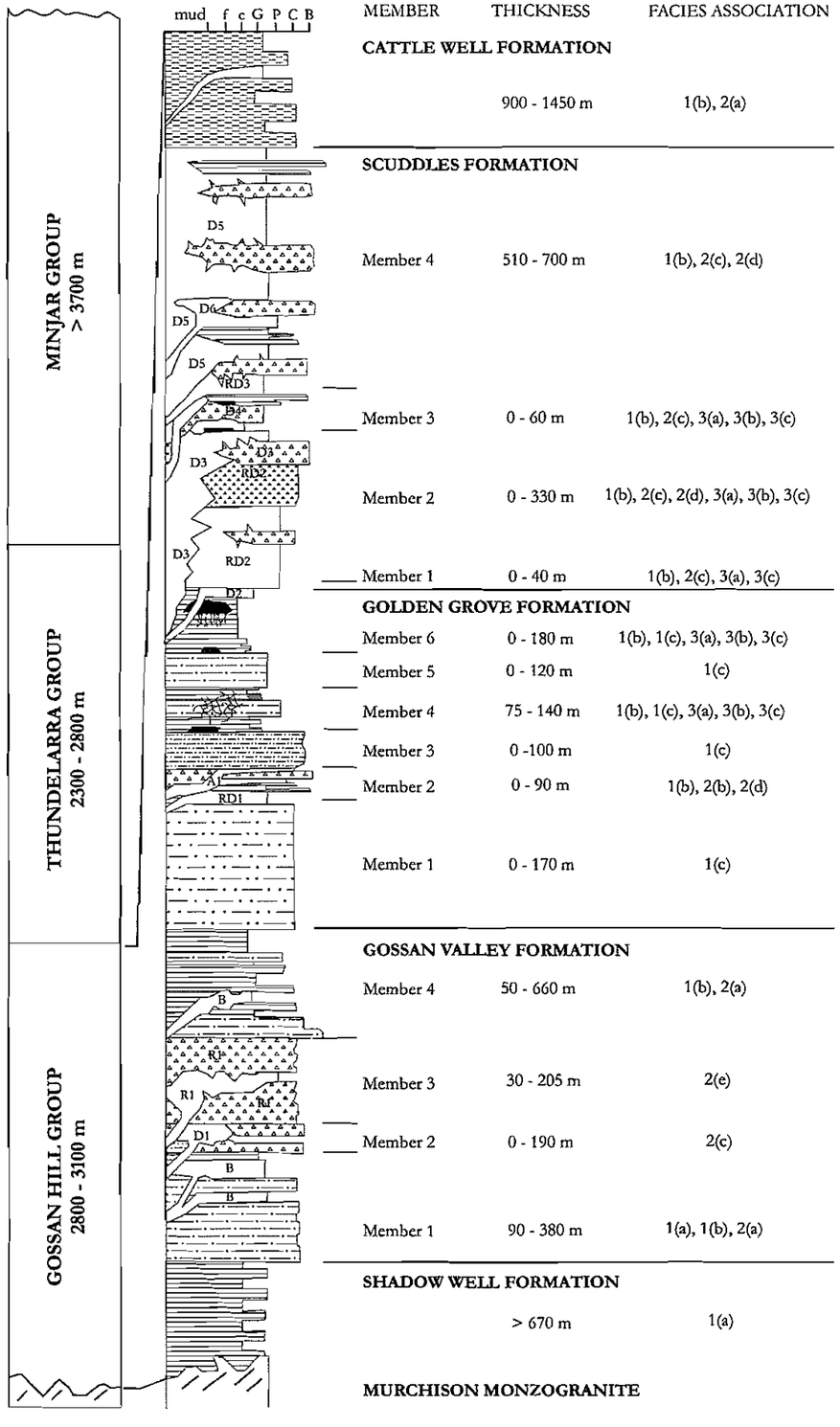

Figure 3.1: Stratigraphy of the Golden Grove Domain and the stratigraphic subdivision and nomenclature devised by Clifford (1992) for the Gossan Hill Group.

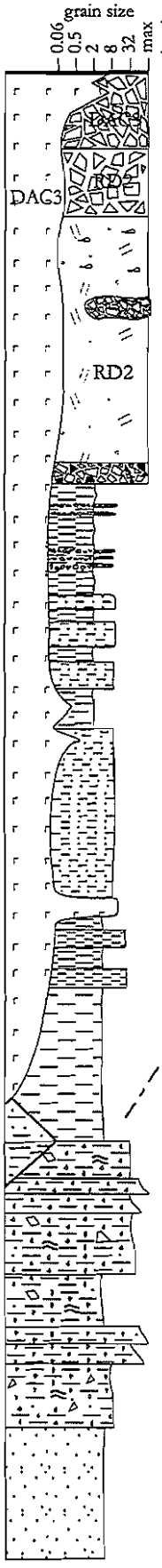

Scuddles Formation Member 2 (SCF M2)

Dacite (DAC3): Massive feldspar, quartz-phyric extrusive-intrusive lava and associated breccia facies. Intrudes GGF M4 to GGF M6 and rhyodacite (RD2) and sills parallel to the GGF M4-GGF M5 contact (thickness 0 to 330 metres).

Rhyodacite (RD2): Massive quartz, feldspar-phyric lava and associated breccia facies. Large 5 to 8 mm fractured and embayed quartz phenocrysts are distinctive. Upper parts may be amygdaloidal. Lower and upper rhyodacite breccia facies are poorly sorted and clast supported. Clasts include rhyodacite, bedded volcaniclastics and rare massive sulphide (thickness 0 to 330 metres).

Golden Grove Formation Member 6 (GGF M6)

Thinly to thickly bedded siltstone, sandstone and polymict pebble breccia. Some sandstone and pebble breccia are tuffaceous. Normal grading, scoured basal contacts, syndepositional faulting and mantling are common. Lower part is interbedded with GGF M5 (thickness 0 to 180 metres).

Golden Grove Formation Member 5 (GGF M5)

Massive, clast supported, lithic-rich sandstone and granule to pebble breccia with minor volcanic quartz (<2%). Lithics include <4 mm, pumiceous and formerly glassy clasts including tube and vesicular pumice, bubble wall fragments and shards (thickness 0 to 120 metres).

Golden Grove Formation Member 4 (GGF M4)

Quartz-rich, clast supported bedded sandstone, siltstone and granule to pebble breccia. Volcanic quartz forms 5 to 15%, forming up to 2 millimetre sized angular quartz fragments and euhedral grains. Formerly pumiceous-glassy lithics include relict tube pumice, vesicular glassy clasts and shards and pumiceous shreds (thickness 50 to 140 metres).

Golden Grove Formation Members 2 and 3 (GGF M2 and GGF M3)

Bedded siltstone, sandstone and pebble breccia, some of which are tuffaceous (thickness 0 to 190 metres, but less than 25 metres at Gossan Hill).

Golden Grove Formation Member 1 (GGF M1)

Massive, clast supported, poorly sorted pumiceous granule to pebble breccia interbedded with sandstone. A monomict lithic population of tube pumice with fragments up to 100 mm, but generally less than 20 mm. Blocky and angular volcanic quartz grains generally form less than 2% modal, but rarely up to 15%. Thinly bedded zones have normal and reverse grading and common scoured basal contacts (thickness 100 to 170 metes).

Gossan Valley Formation Member 4 (GVF M4)

Massive quartz-rich sandstone to clast supported, polymict conglomerate-breccia. Quartz is less than 3 mm in size and forms up to 8% modal (thickness 50 to 660 metes).

Figure 3.2: Facies variation of the stratigraphy proximal to the Gossan Hill deposit, from Gossan Valley Formation Member 4 to Scuddles Formation Member 2. The Golden Grove Formation is a thick sequence of felsic volcaniclastics that are overlain and intruded by coherent felsic volcanics of the Scuddles Formation. Stratigraphic subdivision and nomenclature are from Clifford (1992) (refer Fig. 3.1). Golden Grove Formation Members 4 and 6 host Cu- and Zn-rich massive sulphide at Gossan Hill respectively.

analysis techniques similar to those described in McPhie *et al.* (1993) and implements the stratigraphic nomenclature devised by Clifford (1992).

Lithological, facies and textural variations at Gossan Hill are address constraints on the (1) volcano-sedimentary depositional processes, (2) environment of deposition, (3) longevity of the hydrothermal-mineralising system, and (4) mechanisms by which VHMS mineralisation was preserved. Investigations in this chapter are therefore focused on the GGF due to its footwall, host and in part, hangingwall association to massive sulphide at Gossan Hill. Each of the six stratigraphic members of the GGF (Fig. 3.2) are discussed in detail with critical examination of their facies and textural variation. As mineralisation spans a stratigraphic interval within the GGF, these investigations also address depositional hiatus that may have provided time windows for the accumulation of sulphide mineralisation. Furthermore, the stratigraphy at Gossan Hill highlights a genetic link between preservation of volcanic textures and alteration (Chapter 7).

3.2 The Gossan Valley Formation

The Gossan Valley Formation (GVF) underlies the GGF and has four members that consist of mixed provenance litharenite, coherent basalt, rhyodacite, dacite and quartz arenite facies (Fig. 3.1; Clifford, 1992). The GVF Member 4 is the uppermost stratigraphic subdivision of the GVF and is the only Member investigated here due to its exposure underground.

3.2.1 Member 4 (GVF M4)

GVF M4 is a sequence of interbedded normally graded breccia, conglomerate and sandstone, with beds up to 1 m thick. Breccia and conglomerate are typically polymict, poorly sorted and clast supported, with subrounded to subangular quartz-phyric lithic clasts (Fig. 3.3a) that are silicified or chlorite altered. Volcanic quartz in conglomerate and breccia form phenocrysts within lithic clasts and scattered grains in the matrix. Matrix quartz is typically less than 3 mm in size and forms between 3 to 10% modal. Pumiceous clasts were not observed within breccia and conglomerate.

Massive sandstone within GVF M4 consist of euhedral to subrounded, fractured and embayed volcanic quartz grains (<10% modal) in a fine-grained muscovite, quartz and chlorite altered matrix (Fig. 3.3b). In these sandstones, volcanic quartz is commonly recrystallised to megaquartz. GVF M4 sandstone commonly has a muscovite-quartz and chlorite-muscovite-quartz alteration banding (Fig. 3.3b), which obscures primary bedding but may itself reflect relict bedding. Nonetheless, the modal abundance and size of quartz between the chlorite-muscovite-quartz and muscovite-quartz alteration bands does not vary.

The upper stratigraphic contact between GVF M4 and the Golden Grove Formation (Member 1) is interbedded over a thickness of 10 m (Fig. 3.4) or is faulted. Breccia beds within the interbedded contact zone are poorly sorted, polymict and clast supported, with beds up to 4 m consisting dominantly of GVF M4 sandstone clasts. These sandstone clasts are up to 1 m in size, angular to subangular with jigsaw fit textures and contain

Figure 3.3

(a) GVF M4: poorly sorted, clast supported conglomerate with broad normal grading. Clasts are rounded to subrounded and consist of white siliceous and green chlorite altered quartz-phyric clasts in a fine-grained, quartz-rich matrix (5,223 E, 18,858 N, Pump Access Cuddy 190 level).

(b) GVF M4: massive sandstone containing abundant rounded quartz grains in a fine-grained matrix. Alteration banding in this sandstone consists of alternating light grey muscovite-quartz bands and green chlorite-muscovite-quartz bands. Although bedding is not evident in this sandstone, alteration banding may reflect bedding. Minor disseminated pyrite is present in the sandstone as are narrow pyrite veins that parallel cleavage. Scale in cm (sample 97U046). Note: sample location details are given in Appendix A1.2.

(c) Contact between GVF M4 and GGF M1. Coarse-grained sandstone and pebble breccia interbedded with coarse-grained breccia. The contact between pebble breccia (right) and overlying coarse-grained breccia (left) is undulose and scoured (dashed line). The overlying coarse-grained breccia contains clasts up to 0.5 m that are quartz-rich and have muscovite-chlorite alteration banding similar to sandstone in (b). The differential orientation of this banding supports banding as an early alteration of the sandstone in the underlying GVF. Breccia beds are clast supported and poorly sorted. Location of this sample is indicated in Figure 3.4. Width of rock bolt plates is approximately 40 cm (Cuddy #13, 5,154.2 E, 18,283.6 N).

(d) Thinly bedded sandstone of GGF M1. Sandstone beds vary from 0.1 to 1 cm thickness. Sandstone beds are pumiceous-rich (white flecks) in a fine-grained quartz-chlorite altered, quartz and shard-rich matrix. Bed contacts vary from planar to undulose. The light grey bands are shard-rich siltstone beds. Scale in cm (sample 97U005).

(e) Bedded pebble breccia, sandstone and siltstone from the base of GGF M1. Pebble breccia beds have normal to reverse grading, are clast supported and contain pumiceous lithics in a fine-grained quartz-rich matrix. Basal contacts are sharp and planar. Siltstone (Slt) and sandstone (Sst) beds are fine-grained, shard-rich beds. Scale in cm (sample 97U047).

(f) Photomicrograph of sandstone within GGF M1. The sandstone consists entirely of preserved shard textures that are replaced by quartz. Shards have cuspate to rod-like shapes and some are bubble wall junctions with relict vesicle structures (arrow). The interstitial matrix to the altered shards is chlorite that contains minor disseminated pyrite (Py) (sample 97U013).

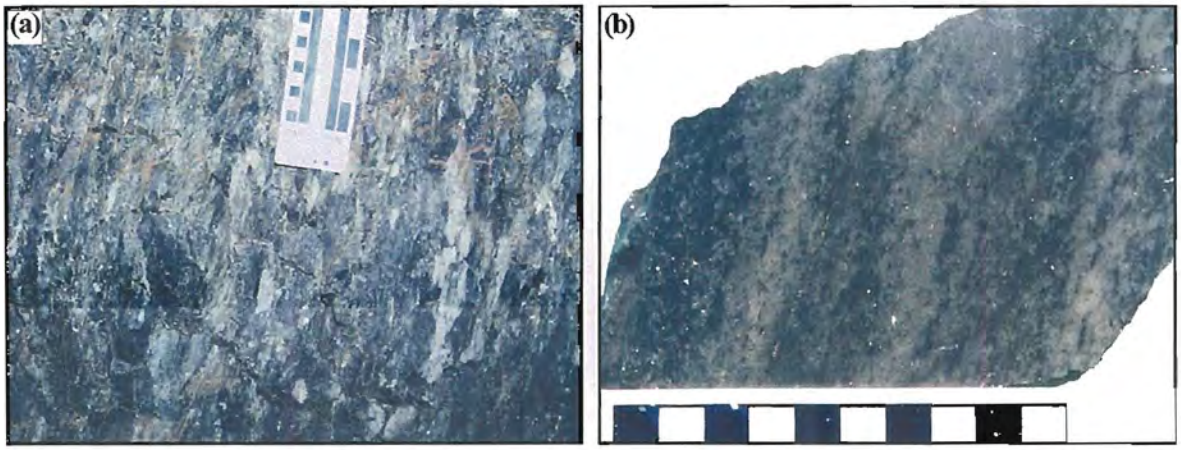
(a)
(b)

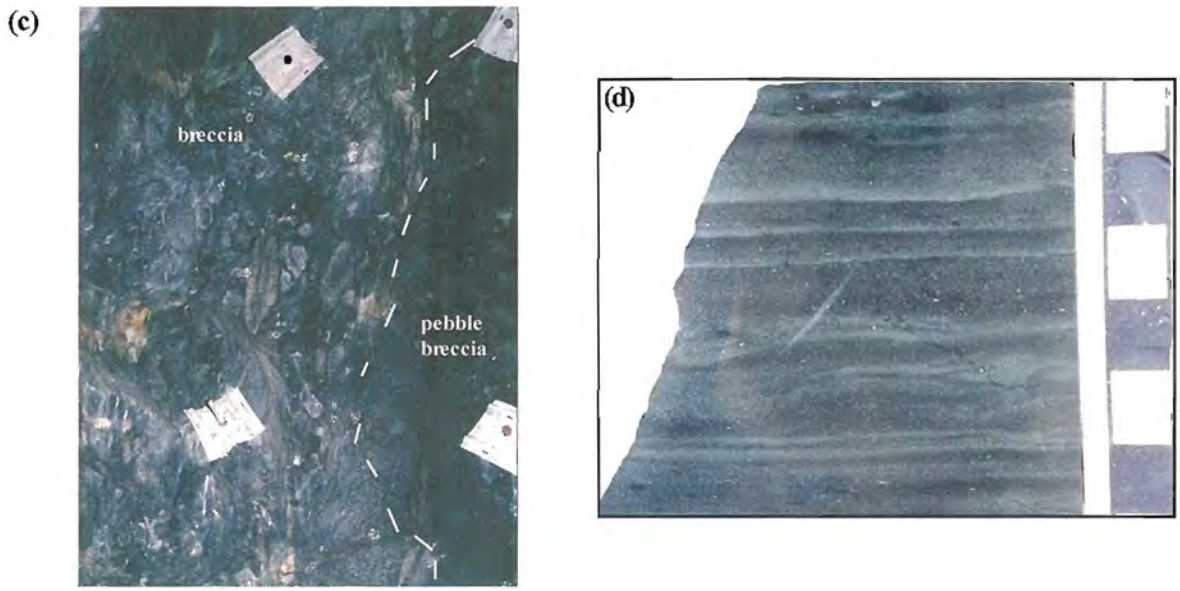
(c)
breccia
pebble
breccia
(d)

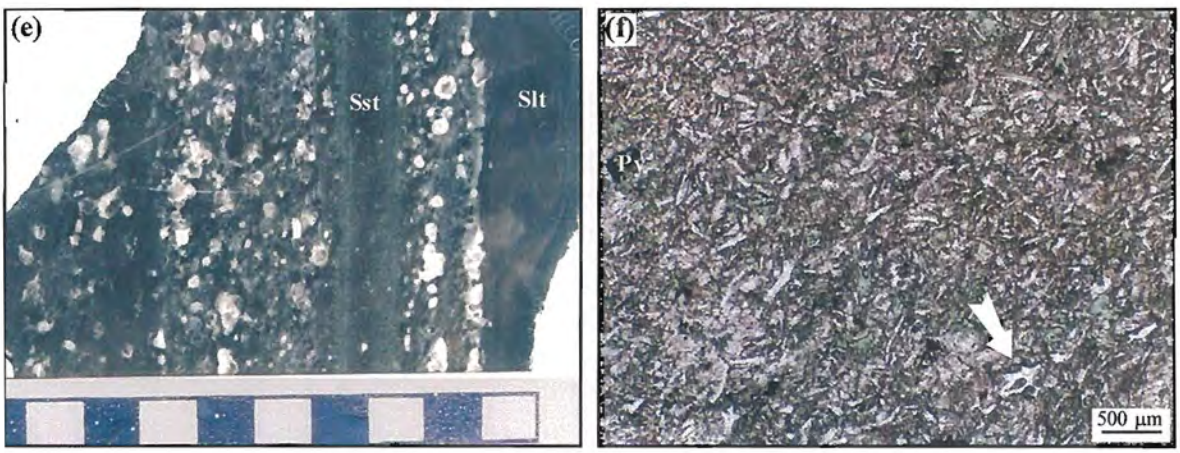
(e)
Sst
Slt
(f)
Py
500 µm

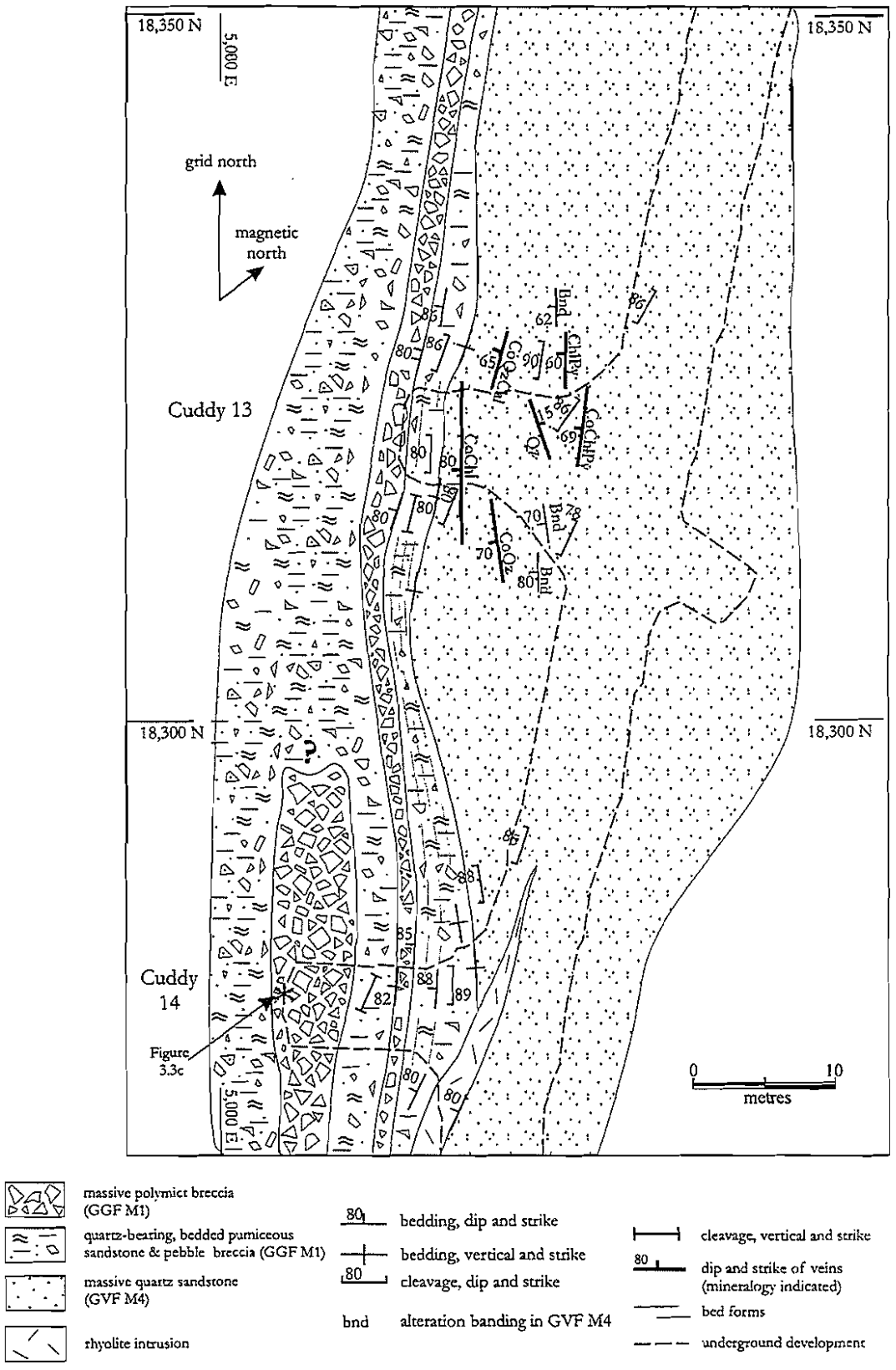

Figure 3.4: Plan view of underground mapping of Cuddy 13 and 14. The contact between GVF M4 and GGF M1 is unconformable, but broadly conformable to strike. GVF M4 is a massive quartz-bearing sandstone that has muscovite-quartz and chlorite-muscovite-quartz alteration banding subparallel to bedding. GGF M1 consists of massive, poorly sorted, interbedded pebble and cobble breccia with tuffaceous pebble breccia units at the base. Cobble breccia beds contain large, less than 1 m clasts of banded quartz-rich sandstone. These clasts have a similar lithology to underlying massive banded quartz sandstone in GVF M4. Thinly to medium bedded sandstone to pebble breccias of the overlying GGF M1 contain abundant volcanic quartz and altered pumiceous lithics. Decline indicated by dashed lines.

variably oriented muscovite-quartz and chlorite-muscovite-quartz alteration banding (Fig. 3.3c), identical to underlying sandstone. Due to the matching lithology between these clasts and underlying strata, sandstone clasts were likely derived from underlying GVF M4 sandstone, with alteration banding reflecting alteration prior to incorporation. The lower contact of GVF M4 is not exposed.

3.3 The Golden Grove Formation

The Golden Grove Formation (GGF) is a sequence of bedded, felsic, tuffaceous volcaniclastics and epiclastic sediments. The GGF has six stratigraphic members (Members 1 to 6 inclusive; Fig. 3.2) that are subdivided based on lithofacies characteristics including size and abundance of lithics and volcanic quartz, as well as bed thickness. The lithofacies of each member of the GGF are discussed in the following sections.

3.3.1 Member 1 (GGF M1)

Within the Golden Grove Domain, GGF M1 has a strike continuance in excess of 15 km and a thickness of less than 170 m (Clifford, 1992). At Gossan Hill, the thickness of GGF M1 averages 120 m, although its lower stratigraphic contact is not well constrained by drilling. The upper contact of GGF M1 is conformable and sharp or interbedded with the tuffaceous units of GGF M3 and GGF M4 or epiclastics of GGF M2 (Section 3.3.2).

Formal stratigraphic nomenclature classifies GGF M1 as the stratified, rhyodacite, lithic breccia facies (Clifford, 1992). GGF M1 is a sequence of tuffaceous volcaniclastics, which form the footwall to Cu-rich mineralisation at Gossan Hill. GGF M1 consists of bedded, pumiceous-rich pebble breccia (>4 mm), granule breccia (2 to 4 mm) and sandstone (<2 to 0.1 mm). Occurrences of cobble breccia, with lithics up to 30 cm in size are observed, but rare. At Gossan Hill, GGF M1 is subdivided to two lithofacies based on grain size and bedding. These two facies form an interbedded sequence of (1) thinly bedded sandstone and pebble breccia facies, and (2) thickly bedded lithic-rich pebble breccia facies. The thinly bedded sandstone sequence dominantly occurs in the basal parts of GGF M1, whilst massive pebble breccia facies abound in its upper parts. Each of these facies are described below.

Thinly bedded sandstone facies

Fine- to coarse-grained sandstone form the basal 20 to 30 m of GGF M1. Sandstone may be laminated (<2 mm), thinly bedded (<10 cm) (Fig. 3.3d) to medium bedded (<30 cm) with conformable, rhythmic, planar beds or locally undulose and scoured contacts. Narrow (10 to 50 cm) pebble breccia beds are interbedded within this sandstone sequence (Fig. 3.3e). Sandstone commonly has normal grading and rare cross bedding. Reverse grading may also occur in coarse-grained sandstone and pebble breccia, and syndepositional faults are common on a metre to millimetre scale. The basal contacts of pebble breccia beds against bedded sandstone are commonly undulose and scoured, to convolute and disconformable, indicating locally erosional contacts. These erosional contacts are often associated with syndepositional faulting (*e.g.*, Fig. 3.5a at 2 m) and

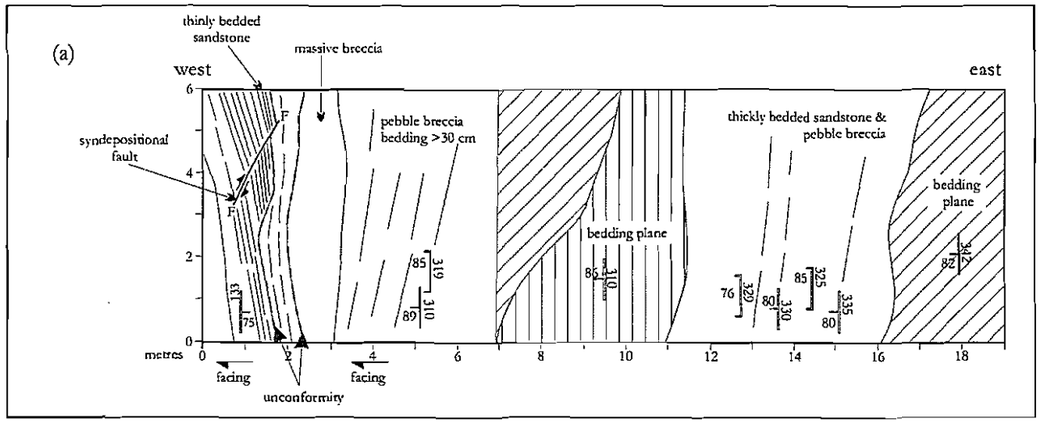

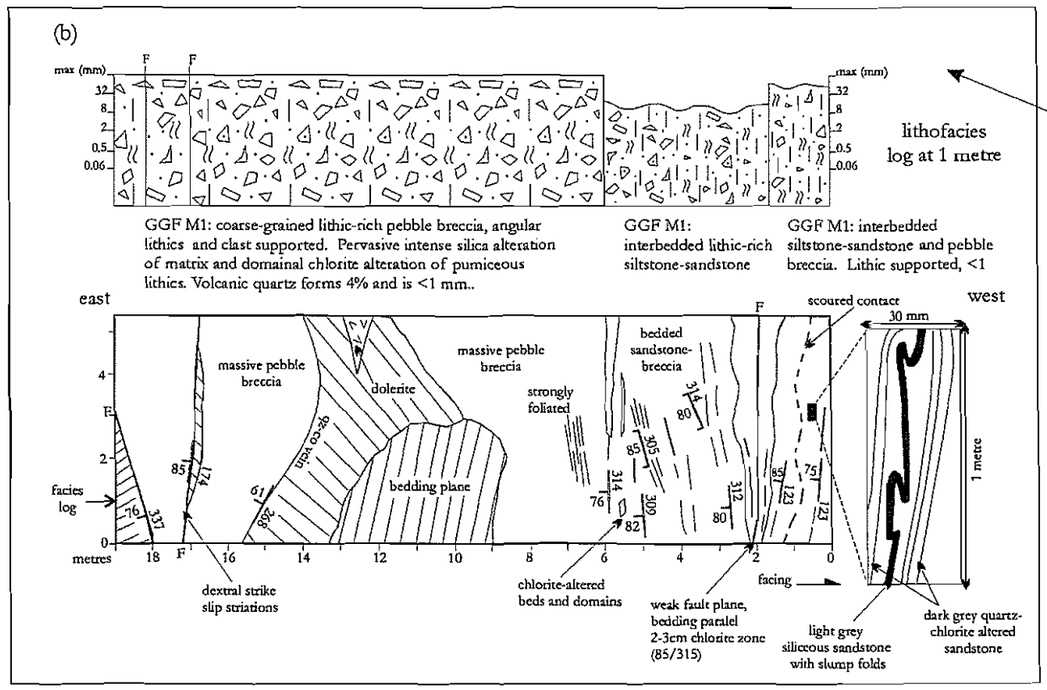

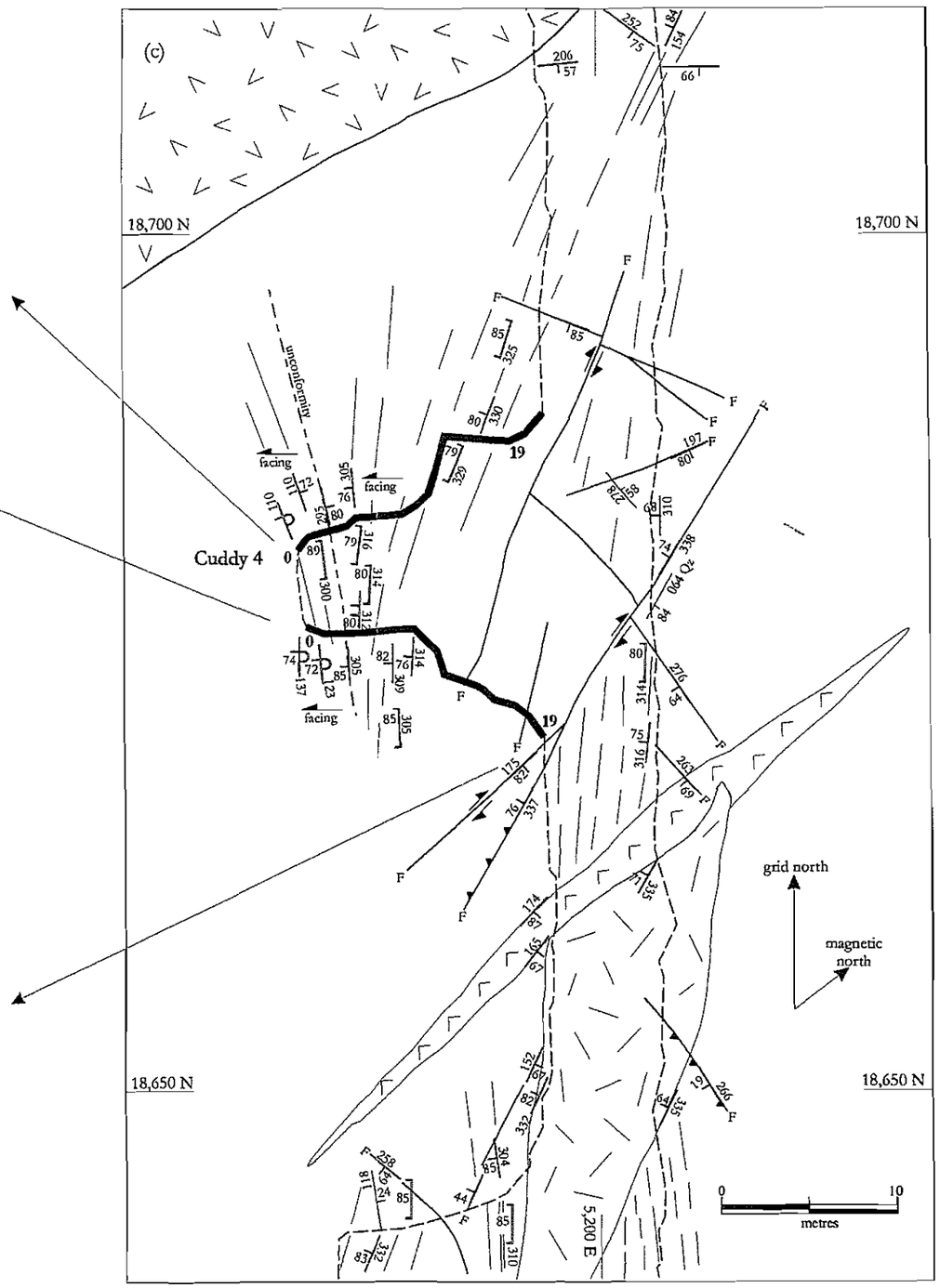

GGFM1: massive to bedded pebble breccia and sandstone

Intrusions

feldspar porphyritic dacite intrusion

dolerite intrusion

rhyolite intrusion

bedding, dip and strike

bedding, vertical and strike

cleavage, dip and strike

alteration banding in GVF M4

cleavage, vertical and strike

dip and strike of veins (mineralogy indicated)

bed form lines

fault, dip and strike

normal fault

reverse fault

decline outline

Figure 3.5: Underground mapping of Cuddy 4. (a) and (b) are maps of the north and south walls of Cuddy 4 respectively with a facies log given along the wall in (b), and (c) is a plan projection. Apparent changes in the dip of strata are the result of locally unconformable stratigraphic contacts caused by scoured and erosional basal bed contacts, associated with syndepositional faulting. GGF M1 is intruded by late stage dacite, dolerite and rhyolite intrusions. GGF M1 consists of interbedded lithic-rich tuffaceous pebble breccia and sandstone.

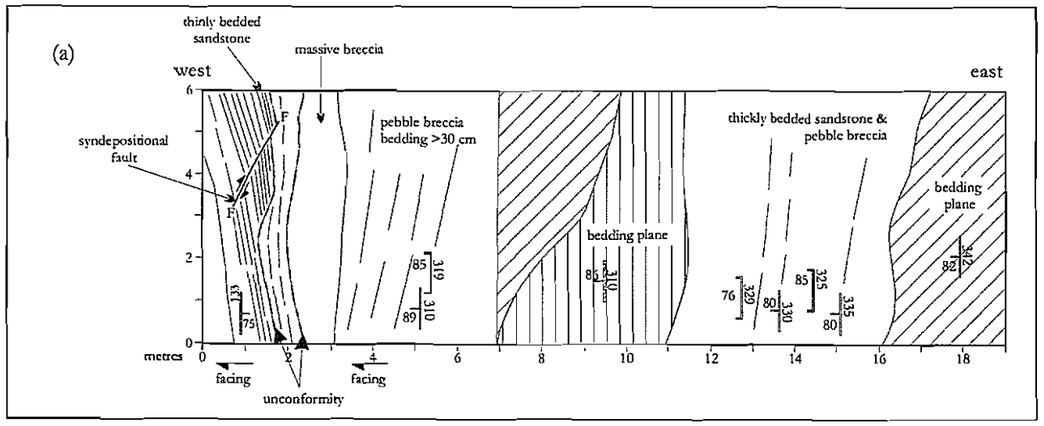

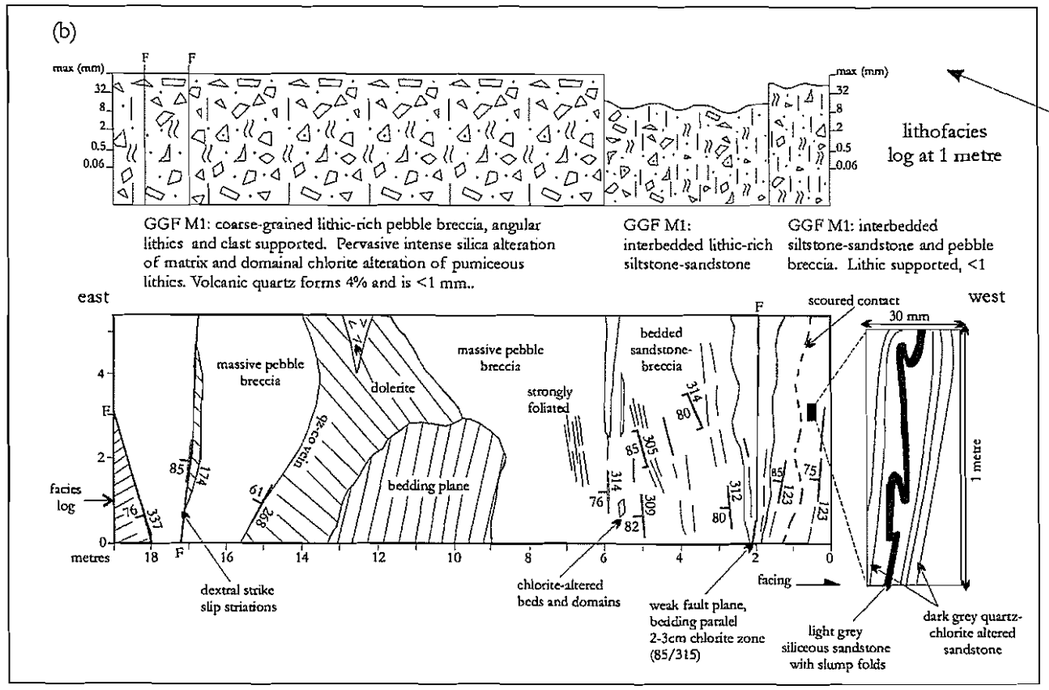

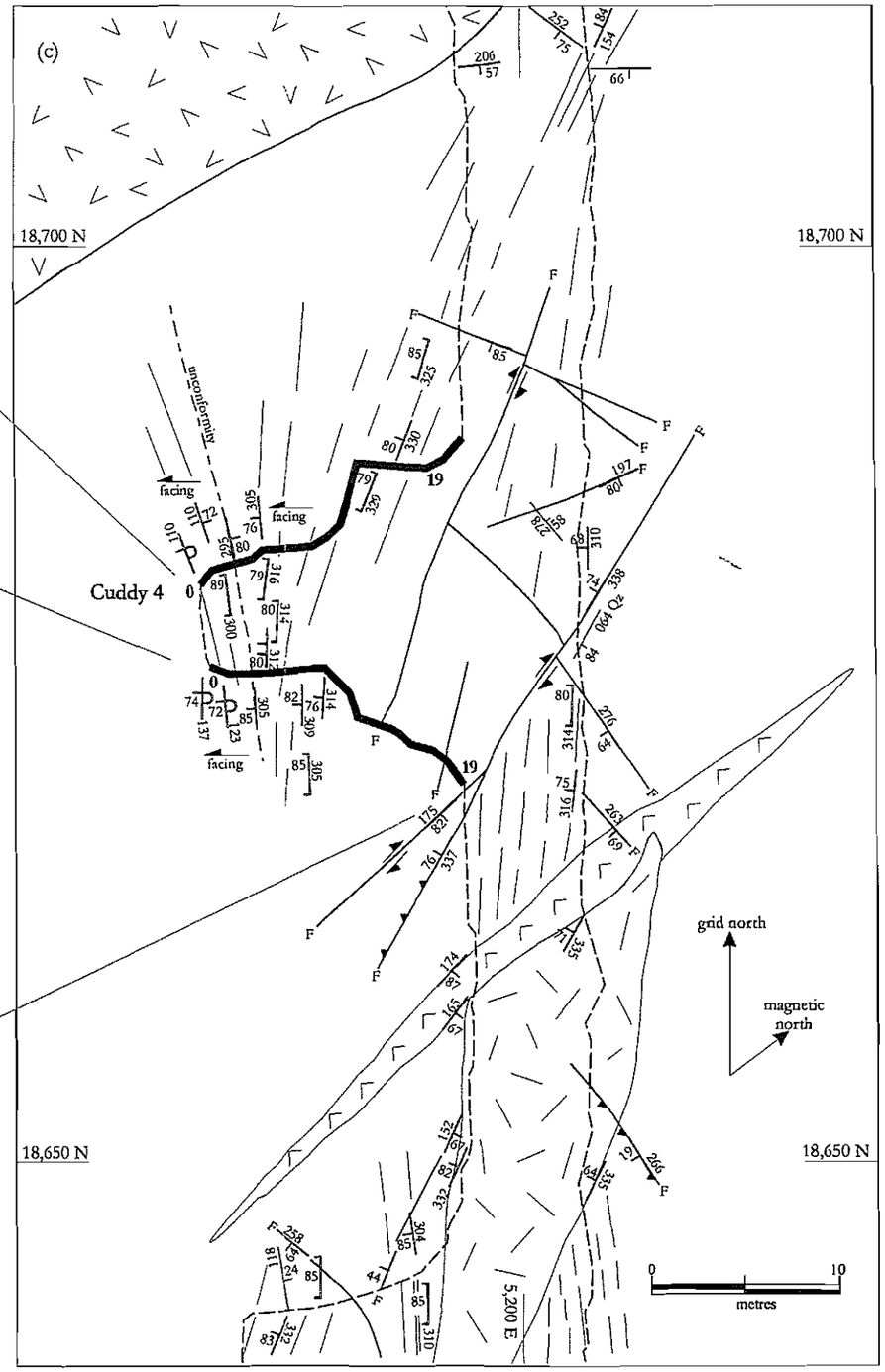

GGFM1: massive to bedded pebble breccia and sandstone

Intrusions

feldspar porphyritic dacite intrusion

dolerite intrusion

rhyolite intrusion

bedding, dip and strike

bedding, vertical and strike

cleavage, dip and strike

alteration banding in GVF M4

cleavage, vertical and strike

dip and strike of veins (mineralogy indicated)

bed form lines

fault, dip and strike

normal fault

reverse fault

decline outline

Figure 3.5: Underground mapping of Cuddy 4. (a) and (b) are maps of the north and south walls of Cuddy 4 respectively with a facies log given along the wall in (b), and (c) is a plan projection. Apparent changes in the dip of strata are the result of locally unconformable stratigraphic contacts caused by scoured and erosional basal bed contacts, associated with syndepositional faulting. GGF M1 is intruded by late stage dacite, dolerite and rhyolite intrusions. GGF M1 consists of interbedded lithic-rich tuffaceous pebble breccia and sandstone.

reflect locally undulose, partly eroded surfaces, mantled by overlying thinly bedded sandstone. The combined effect of these erosional surfaces and syndepositional faulting results in an apparent overturning of strata as exemplified in Figure 3.5. Nonetheless, consistent west facing (Fig. 3.5) mean that the east dips of beds result from the mantling of erosional contacts. These scoured, erosional contacts likely reflect the development of local channels during deposition of this sandstone and breccia sequence.

Thinly bedded sandstone facies in GGF M1 consist of volcanic quartz and angular to subrounded pumiceous lithics or shards. Quartz abundances range from 2 to 15% modal with quartz having blocky to angular morphologies and a grain size of less than 1 mm. The changes in the modal abundance, morphology and size of volcanic quartz are sharp and define bedding. Generally, volcanic quartz grains have reaction margins to micron-sized microcrystalline quartz overgrowths along grain boundaries and fractures. Embayment and undulose extinction of quartz is also common.

Lithic clasts in sandstone are completely altered to quartz and chlorite mosaics. Where preserved, clasts are quartz altered and have morphologies that vary from rounded, angular, and blocky to tabular, often with cuspate or curviplanar margins. Some lithic clasts contain quartz phenocrysts less than 1 mm in size. Preserved volcanic textures within clasts are principally tube striation structures and less commonly vesicle structures. The morphology and size of these clasts varies between beds and coarser-grained sandstone and pebble breccia beds are lithic-rich, clast supported with a closed framework. Comparatively, fine-grained sandstone and the finer fractions of coarse sandstone and pebble breccia contain preserved shard and rod textures and bubble wall fragments (Fig. 3.3f). Fine-grained sandstone are matrix supported and consist of formerly glassy, shard-rich material.

Although coarse-grained sandstone and pebble breccia are lithic-rich with a closed framework, relict pore spaces are indicated by the rare occurrence of vugs. Figure 3.6a illustrates an angular 3 mm cavity structure in coarse-grained, lithic-rich sandstone, infilled by subhedral to euhedral carbonate and quartz. These cavity structures are interpreted to represent original pore spaces in the sandstone that were infilled by secondary minerals after emplacement.

Pebble breccia facies

Pebble breccia facies are the main rock type in the upper 100 m of GGF M1 and are interbedded with up to 10 m thick sequences of fine-grained sandstone. Pebble breccia facies are thinly to thickly bedded (>1 m) and have broad normal grading. The distribution, size and morphology of volcanic quartz varies between and within pebble breccia beds. The proportion of volcanic quartz varies from 2 to 7% modal and its grain shape is distinctly bimodal between blocky euhedral to angular quartz (Fig. 3.6b). Blocky euhedral quartz forms up to 5% modal and consist of grains between 0.2 to 1.4 mm in size. Euhedral quartz have reaction textures that include less than 0.05 mm quartz overgrowths (optically continuous), embayment, grain fracture often with jigsaw fit textures, recrystallisation of quartz to microcrystalline quartz along and outward from

Figure 3.6

(a) Photomicrograph of a vug within coarse-grained, lithic-rich sandstone of GGF M1. The vug is symmetric and subrounded. A rim of subhedral megaquartz forms the outermost part of the cavity, which is in filled by euhedral quartz and subhedral carbonate. This vug represents the in fill of primary porosity in the pebble breccia by secondary quartz and carbonate minerals (sample 97U047).

(b) Photomicrograph of a quartz-rich sandstone from the base of GGF M1. Volcanic quartz grains are euhedral to angular grains. Some euhedral quartz grains are fractured whilst some angular grains have curviplanar grain margins (arrow). Both euhedral and angular quartz have narrow quartz overgrowth rims around their grain margins. The matrix to this sandstone is a closely packed array of altered pumiceous lithic clasts and shards that are altered to quartz and chlorite (sample 769088).

(c) Photomicrograph of a vesicular pumiceous lithic clast within a pebble breccia of GGF M1. The pumiceous lithic clast consists entirely of microcrystalline quartz and has well-preserved volcanic textures. These textures include vesicle walls, with vesicles in filled by chlorite or quartz (sample 97U078).

(d) Contact between a fine-grained and coarse-grained sandstone of GGF M2. The fine-grained sandstone is intensely quartz altered (chert) and the coarse-grained sandstone is a quartz- and pumiceous-rich sandstone (Sst). Scale in cm (sample 769018).

(e) Bedded sandstone and siltstone typical of the basal parts of GGF M4. Sandstone (Sst) is quartz-rich and contains euhedral to angular vitric quartz crystals scattered in a fine-grained shard-rich matrix. Siltstone (Slt) has a conformable contact with sandstone and is shard-rich but lacks volcanic quartz. Both the siltstone and sandstone have strong pervasive chlorite alteration. Scale bar in cm (sample 769095).

(f) Bedded pebble breccia and sandstone typical of the upper parts of GGF M4. The pebble breccia is moderately sorted, clast supported with the lithic clast population consisting entirely of quartz altered pumice. Within the silicified pumiceous lithic clasts (white clasts), tube striations are visible, as are their irregular clast margins. The contact between the pumiceous pebble breccia and tuffaceous sandstone (arrow) is conformable. Scale in cm (sample 760308).

(g) Photomicrograph of a quartz-rich sandstone within GGF M4. Volcanic quartz varies from euhedral to angular grains, the later which have cuspate margins and *in situ* jigsaw fit textures (arrow). The matrix of this sample is chlorite (sample 760357).

(h) Photomicrograph of quartz-rich sandstone typical of the upper parts of GGF M4. Quartz grains have angular grain shapes with cuspate to curviplanar grain margins. The matrix of this sandstone consists of smaller quartz crystal fragments in a fine-grained quartz-altered shard-rich meshwork (sample 762085).

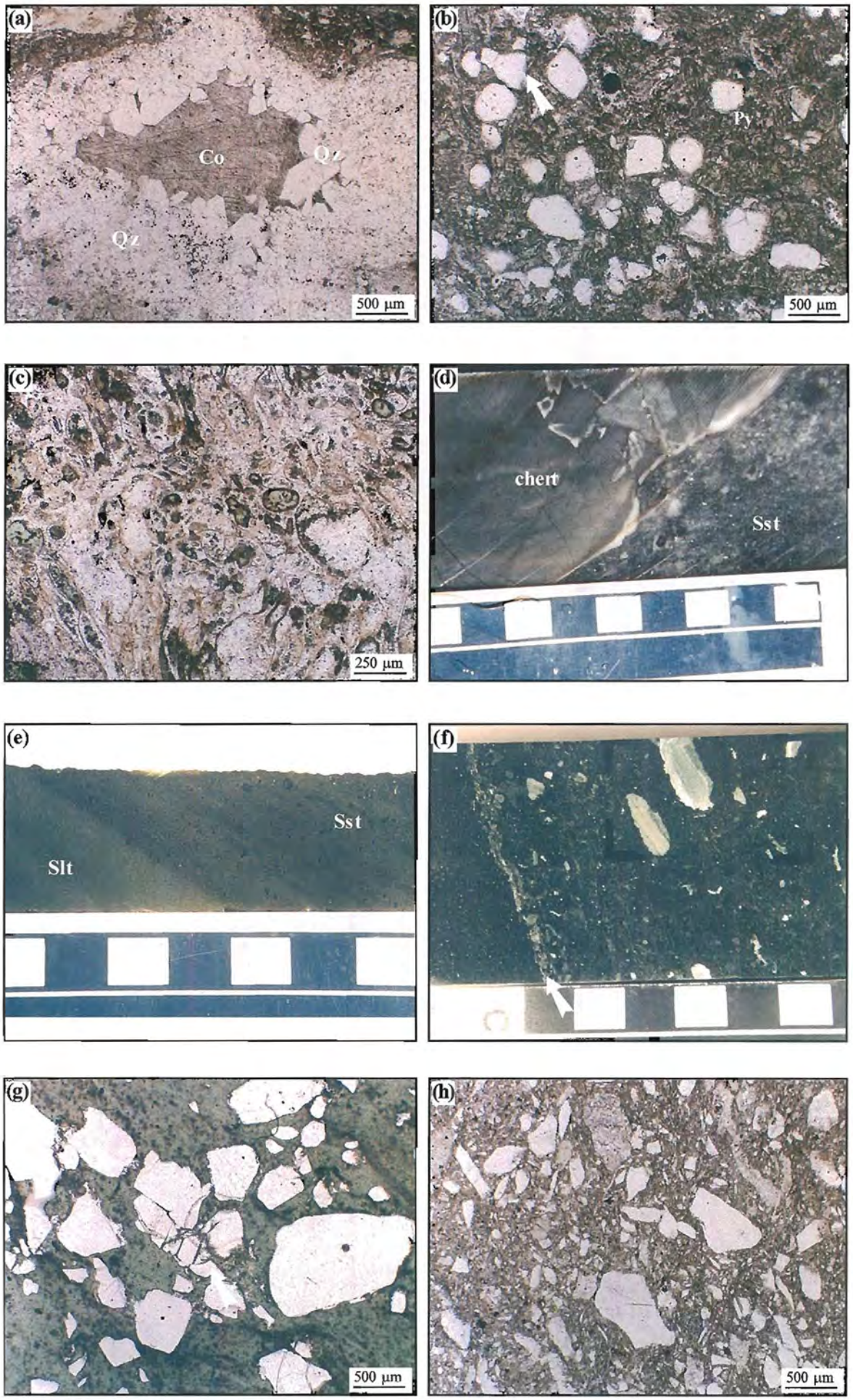
(a)
Co
Qz
Qz
500 µm
(b)
Py
500 µm
(c)
250 µm
(d)
chert
Sst
(e)
Sst
Slt
(f)
(g)
500 µm
(h)
500 µm

fractures and undulose extinction. Comparatively, angular volcanic quartz grains have a smaller grain size variation (<1 mm) and a modal abundance in any given bed of up to 3%. Curviplanar to cuspate grain margins are a distinctive characteristic of angular quartz (*e.g.*, Fig. 3.6b). Reaction textures of angular quartz include less than 0.1 mm quartz overgrowths, corroded irregular grain margins, embayment, undulose extinction and common recrystallisation to microcrystalline quartz mosaics.

The clast supported framework of pebble breccia beds in GGF M1 is denoted by abundant pumiceous lithic clasts, which form in excess of 90% of this facies (Fig. 3.7a). These lithic clasts consist entirely of interlocking mosaics of megaquartz, microcrystalline quartz and chlorite (Fig. 3.7b). Lithic clasts altered to chlorite rarely contain volcanic textures, however, quartz altered clasts commonly have good textural preservation. Preserved volcanic textures include clast morphology, vesicle structures (Fig. 3.6c) and tube striation textures, the later which is characterised by delicate sub-parallel striations that impart a fibrous texture (Figs. 3.7b and 3.7c). Within pebble breccia, pumiceous lithics vary in size from 8 to 300 mm in size, however, the majority of lithic clasts are generally less than 2 mm and indicate generally good sorting. Pumiceous lithic clasts have blocky to tabular morphologies with no evidence of flattening or welding (Fig. 3.7b) and a random orientation is denoted by the variable orientations of tube structures. Pumiceous lithics are commonly quartz-phyric and spherulitic textures are rare.

It is not possible to modally quantify the proportion of matrix in pebble breccia facies due to alteration. The fine-grained matrix (<0.1 mm) of the pebble breccia facies consists of formerly glassy fragments that lack evidence of flattening or welding. These fine-grained fractions include vesicular pumice shreds, tube pumice shreds, cuspate vesicle junctions, bubble wall shards, curviplanar to arcuate shards and rod-like shards. This fine-grained tuffaceous matrix is closely packed and consists of ash- and sand-sized formerly glassy detritus that also contains minor angular quartz grains.

Interpretation

GGF M1 consists of two facies; a sandstone and pebble breccia facies. Thinly bedded sandstone form a fine-grained, strongly stratified basal section to GGF M1 and is rich in angular quartz and formerly glassy sand and ash. The upper parts of GGF M1 are dominated by pebble breccia facies but contain abundant interbedded sandstone. Pebble breccia facies are clast supported with a closed framework and contain abundant formerly glassy tube pumice and vesicular lithic clasts; both of which may be quartz-phyric. The matrix of the pebble breccia beds consist of angular volcanic quartz fragments and sand- to ash-sized glassy shard detritus.

It is now well established that pumice and shards form during the explosive disruption of vesiculating magma (Cas and Wright, 1988; McPhie *et al.*, 1993). As facies within GGF M1 consist of tube pumice, shards and volcanic quartz, their derivation is from an explosive pyroclastic felsic source. Well-preserved pumiceous lithics and shard-rich matrix material of GGF M1 are indicative of juvenile tuffaceous debris that experienced

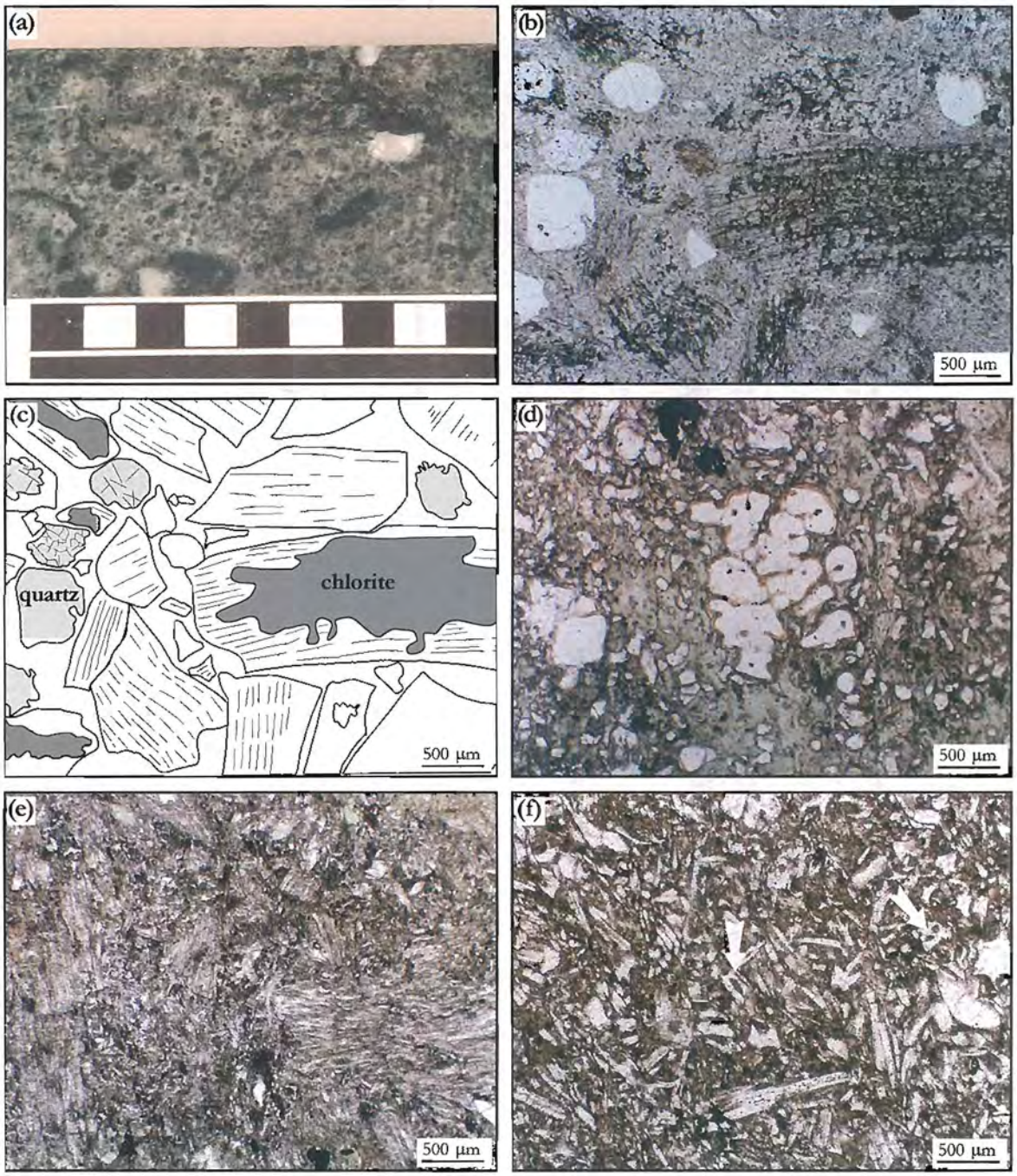
(a)
(b)
500 µm
(c)
quartz
chlorite
500 µm
(d)
500 µm
(e)
500 µm
(f)
500 µm

(g)
500 µm

little internal reworking (*e.g.*, Heiken and Wohletz, 1991). Shattered quartz crystals are common in pyroclastic debris and have angular shapes with curviplanar margins (Fisher, 1984; Gimeno, 1994). Angular quartz crystals in breccia and sandstone of GGF M1 share these characteristics and were likely generated from the explosive eruption of a quartz-phyric magma source. This volcanic source lies outside of the current exposure within the Golden Grove Domain (Clifford, 1992). The absence of welded textures and gas pipe structures within GGF M1 indicate a cold state of emplacement. Additionally, cuspate to curviplanar margins of many lithic clasts and quartz grains, could have resulted from the quenching of initially hot fragments. A consistent pumiceous clast population also indicates a relatively homogeneous provenance for GGF M1.

The interbedded breccia and sandstone tuffaceous debris forming GGF M1 was likely transported by mass flow processes and emplaced by deposition from water saturated, high density turbidity currents. The dominance of normal grading in GGF M1 indicates the influence of gravity sorting mechanisms and therefore pumiceous debris was likely water saturated. Turbidity current deposits can extend over tens of kilometres (McPhie *et al.*, 1993) and is consistent with the 15 km strike continuance of GGF M1. Additionally, strongly stratified sandstone facies may result from the suspension settling of fine-grained debris, particularly shards, thrown into suspension during transport (Fisher, 1965; Lowe, 1982; Fisher, 1984; McPhie *et al.*, 1993).

3.3.2 Members 2 (GGF M2) and 3 (GGF M3)

GGF M2 and M3 represent a quiescent period of ambient sedimentation associated with minor volcanism (Clifford, 1992). GGF M2 consists of mixed provenance litharenite facies and andesite facies, whilst GGF M3 consists entirely of tuffaceous volcaniclastic facies (Clifford, 1992) (Fig. 3.1). At Gossan Hill, GGF M2 consists of intensely silicified, thinly bedded sandstone to siltstone (Fig. 3.6d) and polymict pebble breccia. GGF M3 consists of thinly to medium bedded, pumiceous and quartz-bearing sandstone and pebble breccia. In both members, normal grading is common.

At Gossan Hill, GGF M2 and GGF M3 are laterally discontinuous and are either absent or form a narrow interbedded zone (Fig. 3.8). The maximum thickness of GGF M2 and GGF M3 at Gossan Hill is 22 m, which occurs directly below Cu-magnetite mineralisation and adjacent to a DAC3 dacite intrusion (Fig. 3.8). In the south and north of Gossan Hill, GGF M2 and M3 are absent and GGF M1 is conformably overlain or interbedded with GGF M4 (Fig. 3.8). The distribution of facies within GGF M2 and GGF M3 at Gossan Hill, likely reflects the local paleo seafloor topography during deposition, with their thickest development corresponding to local seafloor depressions, and their absence to topographically elevated areas.

3.3.3 Member 4 (GGF M4)

The thickness of GGF M4 varies from 75 to 140 m over a strike in excess of 24 km (Clifford, 1992). At Gossan Hill, the maximum thickness of GGF M4 reaches 100 m in the vicinity of massive sulphide and massive magnetite. To the south and north of Gossan Hill, GGF M4 thins to less than 30 m (<18,250 N and >18,700 N). The lower

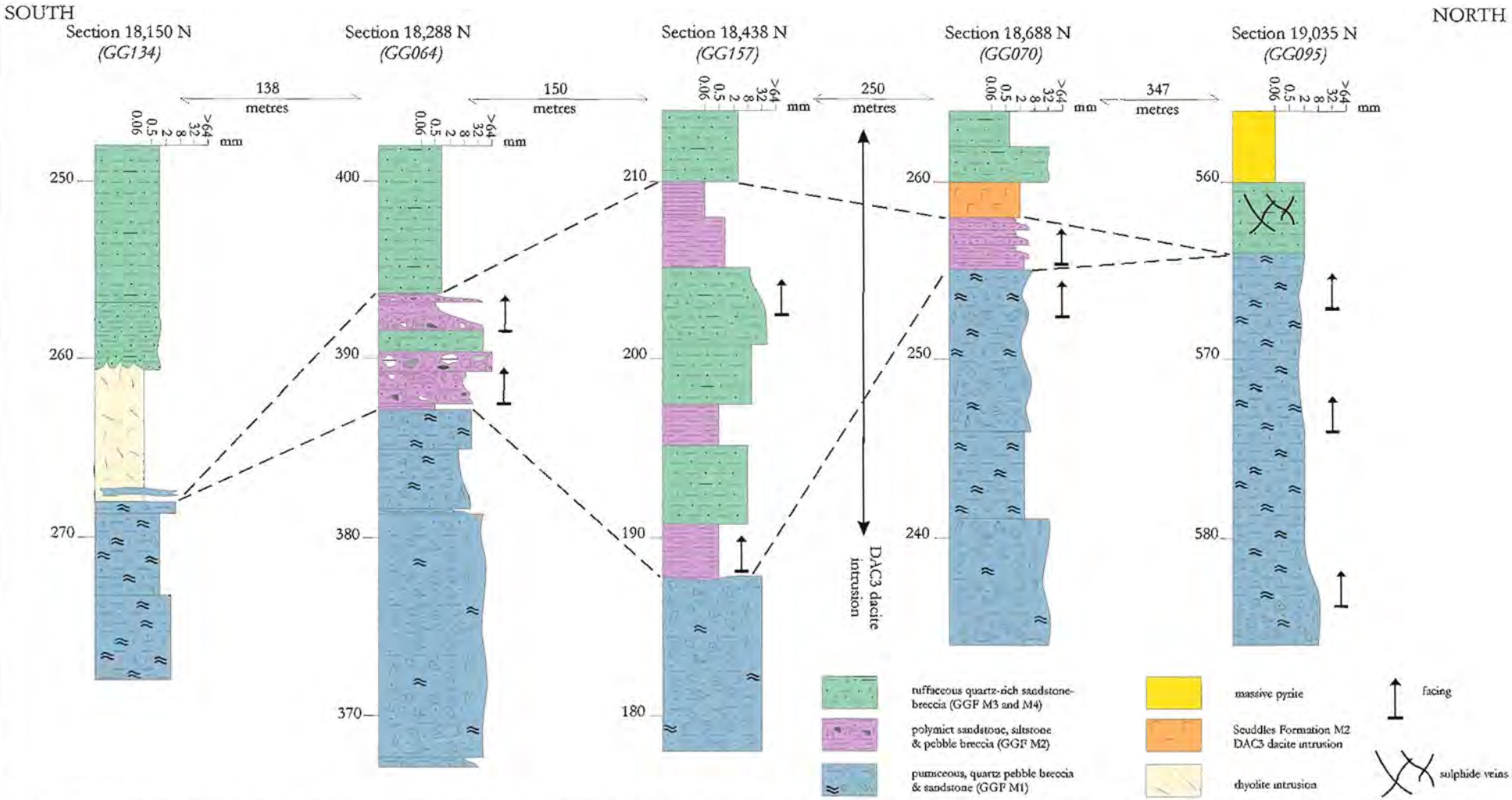

Figure 3.8: Facies variation and distribution of mixed provenance litharenite facies (GGF M2) and interbedded tuffaceous facies (GGF M3). At Gossan Hill these members have a discontinuous and lensoidal occurrence. In the north (>19,035 N) and south (<18,150 N) of Gossan Hill GGF M2 and GGF M3 are absent. The thickest development of GGF M2 and GGF M3 coincides with the central mineralised area at Gossan Hill (between 18,400 N and 18,700 N) where they are interbedded. A DAC3 dacite intrusion, of the hangingwall Scuddles Formation occurs at ~18,500 N (arrow). Distance down hole is in metres and drill holes are indicated in italic. The horizontal distances between drill holes are not to scale.

contact between GGF M1 and GGF M4 is faulted, intruded or locally conformable and interbedded. GGF M2 and M3, where present, have a sharp conformable contact with GGF M4 (Fig. 3.8). The upper contact of GGF M4 with GGF M5 is sharp and conformable and defined by the changes in quartz abundance and bedding.

GGF M4 is defined as the stratified, rhyolite, pumice-lithic breccia facies (Clifford, 1992). The dominant rock types within GGF M4 are bedded siltstone to sandstone in its basal parts (Fig. 3.6e), and bedded sandstone to granule or pebble lithic-rich breccias in its upper parts (Fig. 3.6f). The lower siltstone to sandstone volcaniclastic sequence is quartz-rich and thinly (<2 mm) to thickly bedded (<1 m). Comparatively the upper sandstone to breccia sequence is more thickly bedded (<5 m). Throughout GGF M4, bed contacts vary from planar to locally undulose and scoured.

Volcanic quartz is a diagnostic characteristic of GGF M4 and has grain size of less than 2 mm and commonly forms up to 10% modal, but can form up to 15% in crystal-rich sandstone. Within intense chlorite alteration, quartz is the only primary grain preserved and changes in its modal abundance indicate bedding (*e.g.*, Fig 3.6e). Based on its grain shape, quartz has two populations that are blocky to euhedral quartz (Fig. 3.6g) and angular to subangular quartz that have curviplanar grain margins (Fig. 3.6h). Blocky to euhedral volcanic quartz has grains that are generally larger than angular quartz (<2 mm) and form up to 5% modal. These quartz grains are commonly embayed (Fig. 3.7d) or fractured, with *in situ* fracture textures denoted by jigsaw fit (Fig. 3.6g) and optically continuous quartz overgrowths. Quartz overgrowths around embayed grains indicate that these quartz overgrowths formed after embayment (Fig. 3.7d). Deformation of blocky quartz is characterised by undulose extinction, cleavage wrapping and quartz-chlorite pressure shadows. Angular quartz textures also include fractured grains, jigsaw fit textures, quartz overgrowths, fractures, undulose extinction and embayment textures.

Lithic clasts in bedded sandstone and breccia of GGF M4 are quartz-phyric, pumiceous clasts that have preserved tube striations (Fig. 3.7e). These lithic clasts consist of megaquartz and microcrystalline quartz, and are unflattened tabular to blocky clasts up to 4 mm in size, but generally less than 2 mm. Within intense chlorite alteration, primary volcanic textures are poorly preserved and the morphology of pumiceous lithic clasts is obscured. Where preserved however, pumiceous clasts have randomly oriented tube striations. Quartz phenocrysts within pumiceous clasts are euhedral and up to 2 mm in size. Rare subangular to subrounded clasts consisting entirely of megaquartz likely represent formerly dense glassy lithic clasts.

Finer-grained clast fractions (<0.6 mm) within siltstone, sandstone and breccia include vesicular fragments, bubble wall and cuspate fragments, rod-like shards and smaller pumice shreds (Fig. 3.7f). Spherulitic textures within GGF M4 are rare (Fig. 3.7g). These fine-grained lithic-rich fractions form siltstone and sandstone beds and the matrix to coarser-grained sandstone and breccia. In zones of good textural preservation, this matrix consists entirely of megaquartz and microcrystalline quartz, but is poorly preserved within chlorite alteration. These fine-grained fractions in siltstone, sandstone

and pebble to granule breccia were formerly glassy arrays of sand- and ash-sized shards, pumice shreds and bubble wall fragments, which are moderately to well sorted.

Polymict breccia facies

Polymict breccia facies within GGF M4 has a rare occurrence and is only identified in the underground workings. In this locality, polymict breccia facies forms two narrow (up to 2 m wide), discontinuous boudinaged lenses (Fig. 3.9). Both lenses lie adjacent to the lower stratigraphic contact of GGF M4 and are either enclosed by massive pyrite or are conformable to quartz-rich sandstone (Fig. 3.9). The polymict breccia facies is coarse grained, poorly sorted and clast supported. Lithic clasts are angular to subrounded and less than 30 cm. Clast types include massive pyrite, chert and most commonly silicified, bedded sandstone and siltstone. Massive pyrite clasts are less than 20 cm in size and consist of fine-grained pyrite. The matrix of these breccias is a dark grey-green, fine-grained intensely silicified sandstone. Cleavage wraps around these more competent breccia lenses and there is no evidence to support structural emplacement of the breccias.

Interpretation

GGF M4 is a sequence of bedded, quartz-rich sandstone to granule breccia with minor pebble breccia. This sequence consists of angular and euhedral volcanic quartz, pumiceous clasts, bubble wall junctions and shards derived from a relatively homogeneous juvenile pyroclastic source. Normally graded, thinly bedded strata indicate deposition by suspension settling and density sorting or from high density turbidity currents with limited reworking. Moreover, the abundance of quartz in some beds (up to 15% modal) is suggestive of crystal enrichment epiclastic processes. The generally fine-grained nature of GGF M4 reflects a high proportion of fine-grained, well-sorted ash- and sand-sized shard and pumiceous shreds. GGF M4 is interpreted by Clifford (1992) to contain interbeds of mixed provenance litharenite facies, which represents background sedimentation. The rare interbeds of polymict pebble breccia facies within the GGF M4 sequence therefore represent breaks in the depositional continuity of GGF M4.

The polymict breccia facies has a clast supported, poorly sorted framework with a lensoidal occurrence and these are characteristics of talus breccia formed by local slumping. Similar breccia facies, which also contain massive sulphide clasts, were observed overlying mineralisation at the Scuddles deposit. The deposition of talus breccia facies occurs within many VHMS deposits and indicates seafloor talus accumulation (*e.g.*, Eldridge *et al.*, 1983; Kuroda, 1983). At Gossan Hill, the massive sulphide and altered sandstone clasts in polymict breccia, of GGF M4, were likely derived from underlying strata, indicating the formation of minor pyrite-rich sulphide prior to formation of these breccias. Moreover, the occurrence of polymict breccia facies within massive pyrite (Fig. 3.9) also indicates massive sulphide formation after breccia formation. The close proximity of polymict breccia facies to the GGF M4-M1 stratigraphic contact means that some sulphide deposition within GGF M4 had commenced by the onset of GGF M4 deposition. At Gossan Hill, polymict breccia

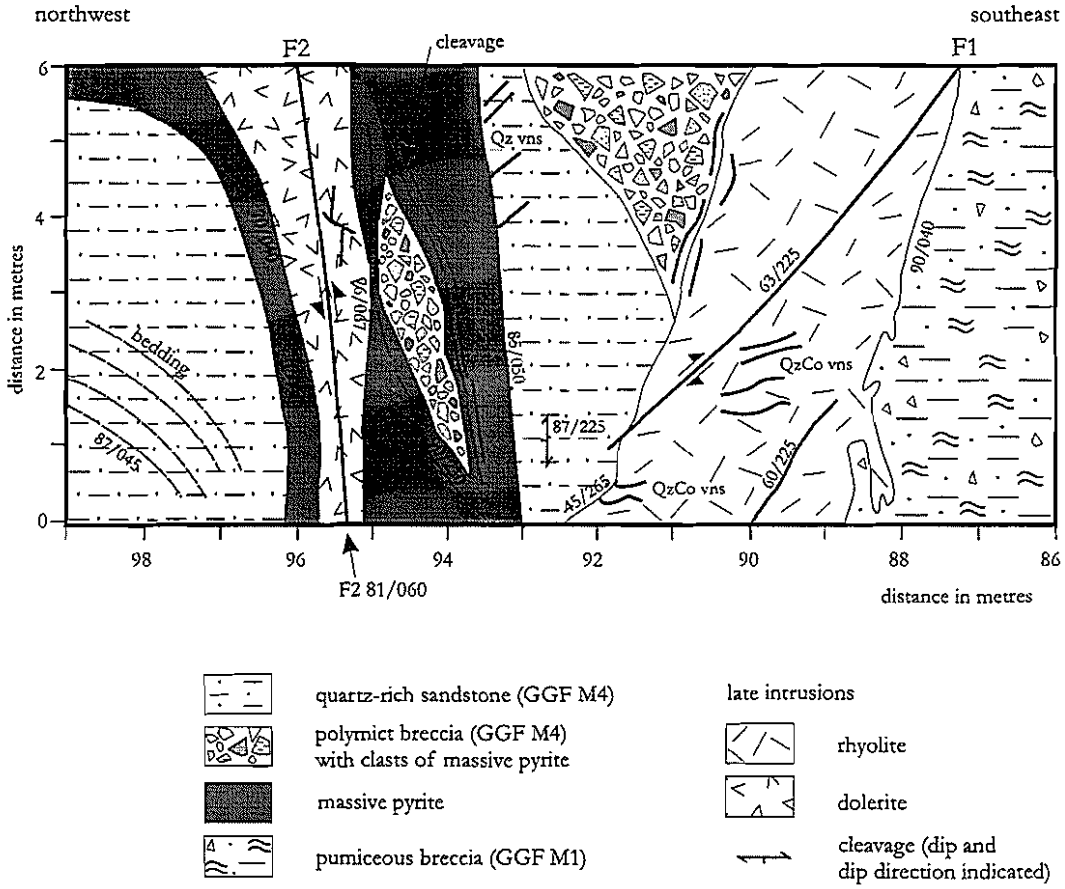

Figure 3.9: Underground mapping (wall map) of the lower stratigraphic contact between massive pumiceous-rich pebble breccia (GGF M1) and quartz-rich sandstone of GGF M4. The contact is intruded by a late stage rhyolite and offset by a late brittle fault (F1). Two polymict, poorly sorted, clast supported lenses of breccia occur. One is intruded by the rhyolite intrusion, but is conformable to massive quartz-rich sandstone. The second breccia lens forms a narrow zone (<1 m) that is enclosed within massive pyrite. These breccia lenses are discontinuous podiform beds that contain lithic clasts of massive pyrite and intensely silicified sandstone and siltstone in a sandstone matrix. Dip and dip direction of faults, cleavage and stratigraphic contacts are also given.

within GGF M4 indicates at least one seafloor site associated with pyrite-rich mineralisation during the deposition of GGF M4.

3.3.4 Member 5 (GGF M5)

Regionally, GGF M5 is up to 120 m thick and has a strike continuance in excess of 26.5 km (Clifford, 1992). At Gossan Hill, GGF M5 varies in thickness from less than 10 m in the south of Gossan Hill, to 50 m adjacent to a dacite intrusion (Fig. 3.10), where it underlies and overlies the thickest development of Zn-rich and Cu-rich massive sulphide mineralisation respectively.

GGF M5 is termed the massive rhyolite pumice breccia facies by Clifford (1992) and is a sequence of dark grey, massive sandstone to granule breccia with minor volcanic quartz (<1%) and infrequent visible lithic clasts. This member is typified by its massive and relatively homogeneous appearance, having minor variation in quartz or lithic clast constituents (Fig. 3.11a). Grading and bedding indicators are rare within GGF M5, but may be masked by the strong ubiquitous quartz-chlorite alteration. Rare thin interbeds (<20 cm thick) of coarse-grained pumiceous breccia occur within GGF M5. The basal contact of GGF M5 is sharp and conformable to GGF M4 (Fig. 3.10). The upper contact of GGF M5 is conformable and interbedded. This upper contact is denoted by the first appearance of thinly bedded sandstone, siltstone and pebble breccia characteristic of GGF M6. The DAC3 dacite of the SCF M2 (refer Fig. 3.2) intrudes the GGF M5 and has sharp, planar, fine-grained and weakly chilled contacts. These DAC3 intrusions form sills and dykes and the former commonly parallel stratigraphic contacts of GGF M5 (*e.g.*, Figs. 3.12a and 3.12b).

Volcanic quartz in GGF M5 forms less than 1% modal and has angular to subhedral shapes. Angular quartz (<0.3 mm) is generally smaller than subhedral quartz, which ranges up to 0.8 mm in size. Angular quartz has curviplanar grain margins commonly with optically continuous 0.05 mm microcrystalline quartz overgrowths. In subhedral quartz, grain fracture and embayment are common, as are quartz overgrowths (up to 0.2 mm), which contour embayed grains. Undulose extinction in both quartz populations is uncommon. Therefore, angular and subhedral quartz populations have similar histories to quartz in GGF M4 (Section 3.3.3), with embayment pre-dating quartz overgrowth.

Lithic clasts in GGF M5 consist of altered tube pumice, shards and fine-grained pumiceous shreds (Figs. 3.11b and 3.11c). These lithic clasts are generally less than 1 mm in size, but range up to 4 mm with larger clasts scattered through the fine-grained shard-rich matrix. Pumiceous clasts have blocky to tabular shapes and commonly contain well-preserved tube striations (Fig. 3.11b), particularly where altered to quartz. Vesicle structures of up to 0.2 mm in size are preserved in some lithics and indicate the occurrence of vesicular pumice in addition to tube pumice. In these examples, quartz replaced vesicle walls are filled by quartz-chlorite. Other relict glassy textures include small (<0.6 mm) cuspate pumiceous shreds, rod-like shards and bubble wall junctions (Fig. 3.11c). Some sandstone within GGF M5 consist of greater than 70% sand- to ash-sized shard-rich fractions. In zones of strong alteration, pumiceous lithic clasts and relict

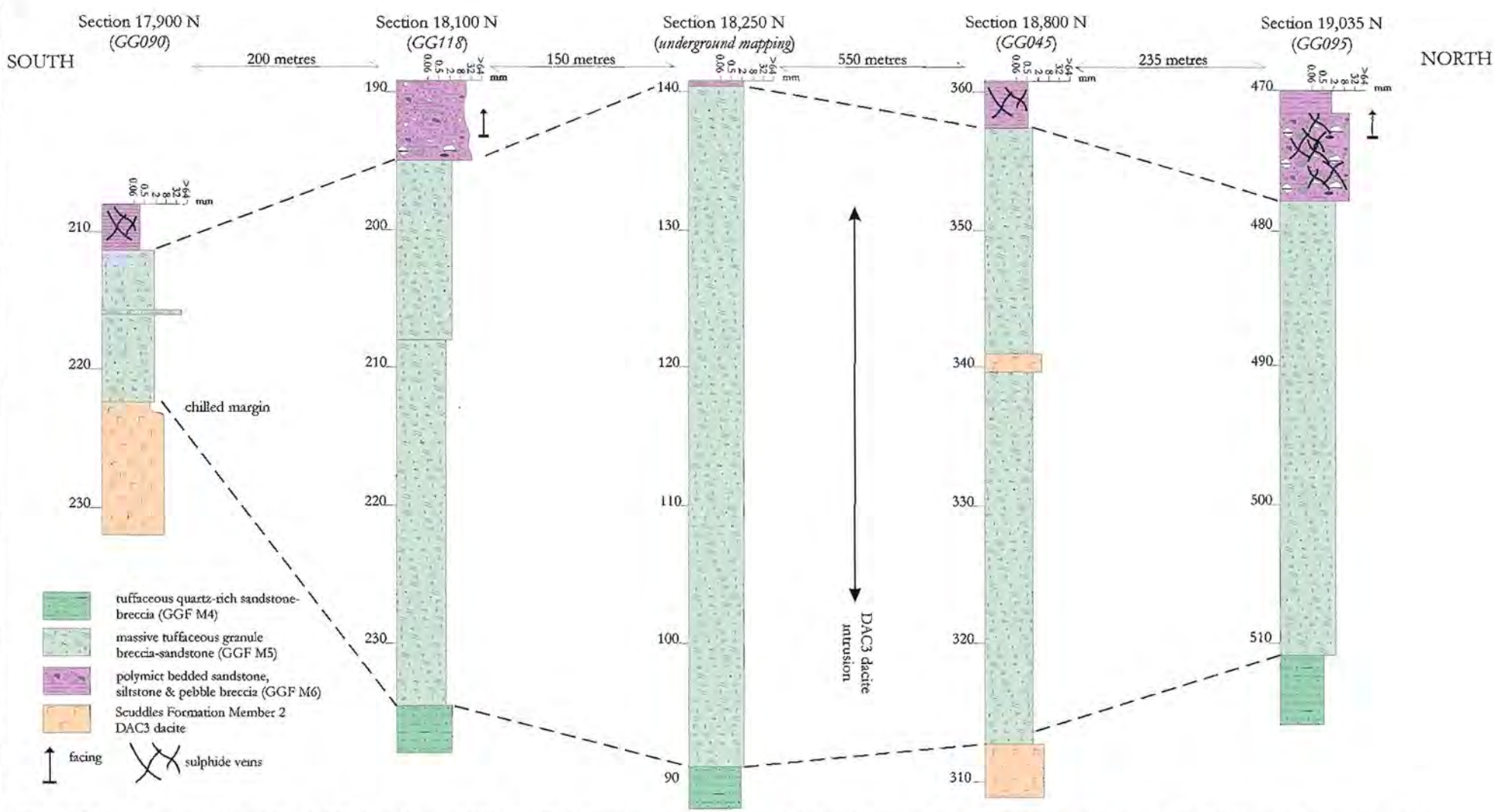

Figure 3.10: Facies variation within GGF M5 at Gossan Hill. GGF M5 gradually thickens toward the north, attains its greatest thickness adjacent to a DAC3 dacite intrusion of the hangingwall Scuddles Formation (arrow). A gradual thinning of GGF M5 northwards from the DAC3 dacite intrusion is inferred. Bedding within GGF M5 is rare (*e.g.*, GG090). The lower and upper contacts of GGF M5 with GGF M4 and GGF M6 are conformable. GGF M5 is also intruded by SCF M2 DAC3 (*e.g.*, GG090 and GG045). Vertical distances are down hole depths in metres. Drill holes are given in italic. Horizontal distances between drill holes are not to scale.

Figure 3.11

(a) Massive sandstone typical of GGF M5. This sandstone contains rare visible volcanic quartz and scattered, silicified pumiceous lithic clasts (white flecks up to 2 mm) within a massive homogeneous matrix that has little internal variation. Scale in cm (sample 760389).

(b) Photomicrograph of granule breccia within GGF M5. This breccia consists of meshwork of pumiceous lithic clasts in a fine-grained shard- and pumiceous shred-rich matrix. Tube striations are well preserved in some clasts, however, the clasts margins are poorly preserved. Some pumiceous clasts (arrows) consist of a number of pieces, which probably formed a larger pumiceous lithic clast. Lithic clasts vary in size and shape and also include highly angular vesicular clasts. The pumice and vesicular clasts now consist of microcrystalline quartz and the matrix is quartz-chlorite altered (sample 769286).

(c) Photomicrograph of sandstone within GFF M5. This sandstone consists of quartz-replaced pumice shreds and shards. Shard textures include cuspate to rod-like shard and vesicle junctions (sample 97U066).

(d) Thinly bedded sandstone within GGF M6. Sandstone beds are less than 1 cm thick and have planar conformable contacts. Syndepositional faulting and mantling occurs within this sample (arrow). The grey to white colour of sandstone beds is the result of differential pervasive quartz and chlorite alteration. Scale in cm (sample 762094).

(e) Pebble breccia within the upper bedded sequence of GGF M6. This pebble breccia has broad normal grading and an undulatory upper contact to sandstone. The pebble breccia varies from matrix to clast supported and contains angular to subrounded clasts of chert and siliceous bedded sandstone and siltstone. The brown clast (arrow) contains finely disseminated sphalerite. Pyrite is also disseminated through the breccia matrix. Scale in cm (sample 760364).

(f) Photomicrograph of (e). Lithic clasts within the pebble breccia bed are quartz-altered thinly bedded to laminated sandstone and siltstone. The brown clast in (e) (arrow) contains micron-sized disseminated sphalerite in microcrystalline quartz. The matrix of this sample is strongly chlorite and quartz altered and contains smaller clasts and rare quartz grains.

(g) Example of a clast within a pebble breccia bed within GGF M6. This clast is subrounded and has well-preserved relict glassy textures. The matrix is intensely silicified (sample 760435).

(h) Tuffaceous sandstone bed from thinly bedded strata within GGF M6. Volcanic textures, including tube pumice and shards are moderately preserved by quartz and chlorite alteration. Volcanic quartz grains are scattered through the sandstone and have rounded to angular shapes (sample 760293).

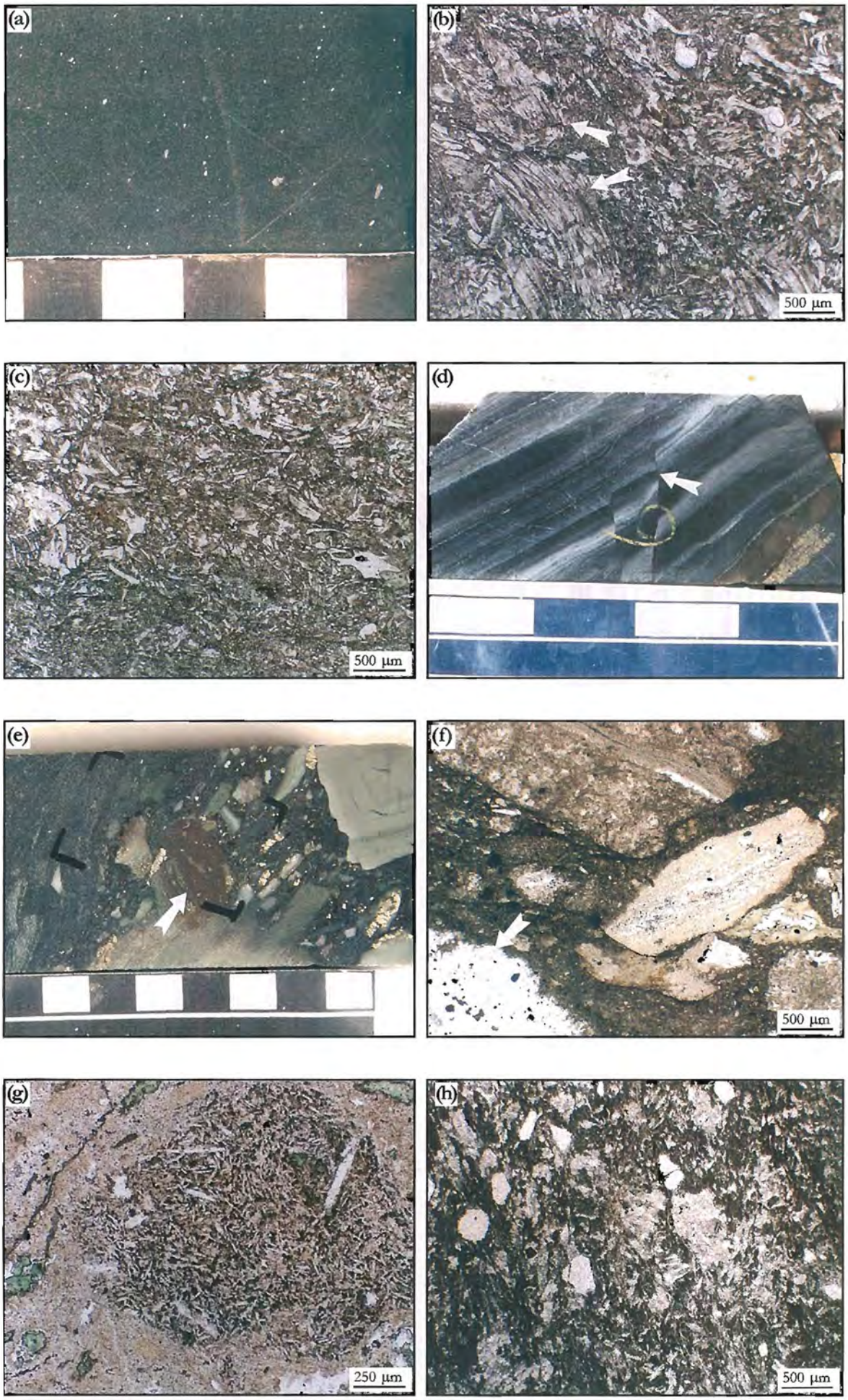
(a)
(b)
500 µm
(c)
500 µm
(d)
(e)
(f)
500 µm
(g)
250 µm
(h)
500 µm

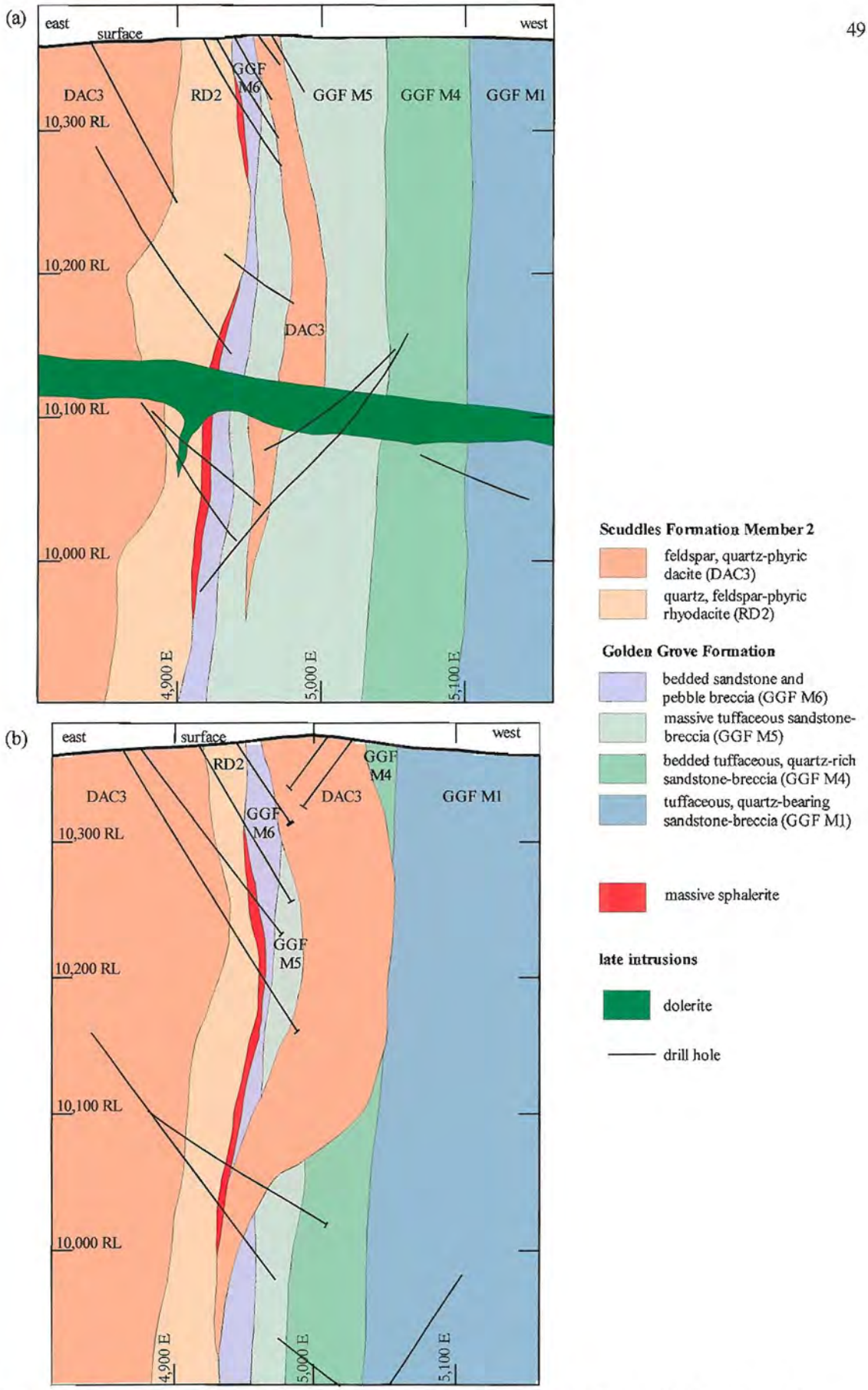

Figure 3.12: East-west cross sections (25 m data window) through the southern end of the Gossan Hill deposit. The DAC3 dacite intrudes all Members of the GGF and RD2. (a) Section 17,800 N at the south end of Gossan Hill. Massive sphalerite forms a narrow sheet that subparallels the RD2-GGF M6 contact. In this area, DAC3 dacite sills GGF M5. (b) Section 17,900 N, 100 m north of (a). DAC3 dacite intrudes the lower part of GGF M5 and partly subparallels the GGF M4-M5 stratigraphic contact. DAC3 dacite varies from weakly to strongly discordant to GGF M5. Mine grid in metres.

shards often form "ghosts" and lack preserved volcanic textures.

Interpretation

Volcanic textures indicate GGF M5 is a massive pumiceous and shard-rich sandstone to granule breccia. The closely packed, moderately sorted array of pumiceous lithic clasts and formerly glassy shard detritus indicate a relatively open framework. As all the constituents of GGF M5 are tuffaceous in origin, GGF M5 had an explosive felsic volcanic source, but lacks the abundant quartz observed in other tuffaceous members of the GGF. Texturally unmodified pumiceous and shard debris within GGF M5 have little evidence of reworking and no evidence of diagenetic compaction, flattening or welding. Therefore, a cold state of emplacement is interpreted from the absence of welded and steam disrupted textures. The massive nature of GGF M5 is consistent with a rapid deposition by mass flow processes. Notably, Clifford (1992) also proposed the possibility that deposition of GGF M5 could have taken place by the transformation of a gas-supported pyroclastic flow into a water supported flow.

3.3.5 Member 6 (GGF M6)

GGF M6 consists of five distinct facies (refer Fig. 3.1; Clifford, 1992). These are the (1) mixed provenance litharenite facies, (2) tuffaceous volcaniclastic facies, (3) chert facies, (4) massive oxide facies, and (5) massive sulphide facies. The later two facies form the VHMS mineralisation at Gossan Hill. Due to contention between their exhalative or replacement origin, these chemical facies are described and discussed in Chapter 5. However, intense alteration associated with this mineralisation within GGF M6 at Gossan Hill hinders lithological studies.

The contact between GGF M6 and GGF M5 is conformable and interbedded over a width of up to 53 m. This interbedded contact consists of thinly bedded sandstone, siltstone and breccia (GGF M6) forming narrow (<1 m) intervals between massive tuffaceous beds of GGF M5 (up to 10 m thick). Within this interbedded contact, the width of tuffaceous interbeds (GGF M5) decrease away from the basal contact, from 10 m thick beds at the base to beds less than 1 m in the upper parts. Overlying this interbedded contact is a medium to thinly bedded sequence of siltstone, sandstone and pebble breccia. The upper contact of GGF M6 is locally unconformable against RD2 rhyodacite of SCF M2 (Section 3.4.1).

GGF M6 consists principally of mixed provenance litharenite facies that has a lensoidal distribution within the Golden Grove Domain (Clifford, 1992). The thickness of GGF M6 can vary by 10's of metres, whilst its lateral continuity varies on a scale of kilometres (Clifford, 1992). At Gossan Hill, GGF M6 is laterally continuous over the 2 km strike length of the study area, except where it is intruded by DAC3 dacite of SCF M2 (~18,300 N to 18,400 N). In the south of Gossan Hill (18,000 N), GGF M6 has a thickness of less than 10 m, which gradually thickens to the north. This increased thickness is accompanied by a thickening of the interbedded basal contact zone between GGF M6 and GGF M5. The true thickness of GGF M6 in the north is difficult to estimate, due to the occurrence of massive sulphides within it. GGF M6 is however,

thickest adjacent to the DAC3 dacite intrusion, where it contains massive sulphide and is estimated to be 100 m thick. North of the DAC3 dacite intrusion (>18,700 N), GGF M6 is approximately 30 m thick.

Sandstone and siltstone

Intense ubiquitous alteration of sandstone and siltstone within GGF M6 has resulted in poor textural preservation of these lithologies. Nonetheless, this alteration generally preserves their stratification (Fig. 3.11d). Sandstone and siltstone in GGF M6 are thinly to rhythmically bedded (from 1 to 20 mm) and rarely contain relict quartz grains or lithic clasts. Due to their thinly bedded nature, these units are inferred to have been fine-grained sandstone and siltstone and presently consist entirely of microcrystalline quartz, megaquartz, chlorite and carbonate. Bedding contacts between sandstone and siltstone are planar and conformable and common syndepositional faulting and bed mantling is observed (Fig. 3.11d).

Breccia

Breccia beds within GGF M6 are interbedded with sandstone and siltstone and vary from granule breccia to cobble breccia (lithics up to 10 cm in size). Breccia beds generally have normal grading, from a clast supported, closed framework base to a relatively open framework, granule breccia or sandstone top. Basal breccia contacts are typically scoured and undulose. Sorting within breccia beds is poor in cobble breccia to moderate in granule breccia and clast morphologies vary from subrounded to angular (Fig. 3.11e). Lithic clasts have a polymict population and consist predominantly of fine-grained thinly bedded siltstone to sandstone clasts and intensely silicified chert clasts (Fig. 3.11f). Less common lithic clasts include tuffaceous clasts of altered dense glass (Fig. 3.11g), altered tube and vesicular pumiceous clasts and feldspar-phyric clasts. Within GGF M6 breccia, all lithic clasts are intensely quartz and/or chlorite altered. The matrix to breccia beds is generally fine-grained and strongly chlorite-quartz altered, but may contain rare volcanic quartz.

Tuffaceous strata

Intense quartz-chlorite alteration of bedded siltstone, sandstone and pebble breccia within GGF M6, obscure primary lithofacies. Granule to pebble breccia beds and sandstone often have relict tuffaceous volcanic textures, which support a glassy precursor to these beds (Fig. 3.11h). As such, it is possible that fine-grained sandstone and siltstone had glassy precursors and were sand- to ash-sized tuffaceous beds. The ubiquitous intense alteration has transformed these lithologies to quartz-chlorite alteration mosaics and destroyed primary volcanic textures. Textural and alteration investigations in this thesis indicate that GGF M6 consisted of a larger component of formerly glassy tuffaceous material than previously recognised by Clifford (1992).

Interpretation

Bedded fine-grained sandstone, siltstone and breccia of GGF M6 form the mixed provenance litharenite facies and are interpreted to represent background sedimentation

(Clifford, 1992). The polymict nature of breccia and sandstone indicate derivation from multiple sources. Notably, mudstone facies are absent from GGF M6, indicating that although deposition of this GGF M6 succession represents background sedimentation, significant quiescent periods did not occur.

The interbedded lower contact of sandstone, siltstone and pebble breccia (GGF M6) with massive tuffaceous sandstone (GGF M5), likely represents a transitional change in the sediment source and depositional style. During this transitional period, intermittent pulses of high density tuffaceous turbidite sedimentation (GGF M5) interrupted ongoing low volume sedimentation (GGF M6). The pulses of tuffaceous sedimentation are separated by periods of background sedimentation during which time sequences of bedded sandstone, siltstone and breccia formed by the settlement from suspension of fine-grained tuffaceous material and by low volume turbidite sedimentation. Common tuffaceous constituents within GGF M6 siltstone, sandstone and breccia are expected due to the concurrent deposition of tuffaceous and epiclastic facies. Away from the lower contact of GGF M6, the tuffaceous interbeds (GGF M5) thin. The thinning of these tuffaceous beds reflects the decreasing influx volume of tuffaceous detritus, with sedimentation giving way to epiclastic sedimentation. The upper parts of GGF M6 are a bedded sequence of siltstone, sandstone and polymict breccia and reflect the termination of large volume tuffaceous sedimentation. Normal grading of sandstone and breccia within GGF M6 indicate the influence of gravity sorting mechanisms.

Within GGF M6, the lithology of lithic clasts in breccia is similar to enclosing sandstone and siltstone lithologies. The intense quartz-chlorite alteration of these sandstone and siltstone beds matches the alteration of siltstone and sandstone lithic clasts within breccia beds. The matrix of these breccia beds in GGF M6 is less intensely altered that sandstone and siltstone clasts within them. It is likely that alteration (mainly silicification) of these sandstone and siltstone lithic clasts within breccia of GGF M6 occurred prior to their incorporation. The lithological similarity of these clasts to siltstone and sandstone lithologies within GGF M6 supports their local derivation. This local derivation may have resulted from slumping and erosion of underlying strata.

3.3.6 GGF M6: The M1 Marker

Distinctive bedded chert-chlorite units are identified at both Gossan Hill and Scuddles and consist of thinly bedded quartz and chlorite-carbonate. These chert-chlorite units were first identified at Scuddles and termed the M1 Marker (Ashley *et al.*, 1988). At Gossan Hill, the M1 Marker occurs both within and overlying massive sulphide in GGF M6 and is an important stratigraphic correlation tool in identifying the stratigraphic time equivalent to massive sulphide formation. Although volumetrically insignificant, the M1 Marker represents the only marker unit in the GGF and is interpreted to have formed from hydrothermal fluids responsible for sulphide mineralisation (Ashley, 1983; Clifford, 1992). This section reviews the lithological variation of the M1 Marker at both Gossan Hill and Scuddles, whilst its hydrothermal origin is investigated in Chapter 8.

At Scuddles, the M1 Marker is rhythmically bedded, having alternating green chlorite-

Figure 3.13

(a) Example of the M1 Marker at the Scuddles deposit within GGF M6. Rhythmically bedded chert and chlorite-rich beds. Chlorite beds contain finely disseminated magnetite and minor pyrite. Discontinuous carbonate veins cut chert and chlorite beds. Scale in cm (sample SCD007).

(b) Photomicrograph of (a). Chert beds (chert) consist of microcrystalline quartz mosaics and contain disseminated carbonate and minor pyrite. The chlorite bed (Chl) is strongly chlorite-carbonate altered and contains magnetite.

(c) Example of the M1 Marker at the Gossan Hill deposit within GGF M6. Thinly bedded chert (chert) and chlorite-rich beds overly a disrupted chert-chlorite breccia bed (Bx). The chert bands contain discontinuous white carbonate veins. Disseminated pyrite occurs within the chlorite altered beds and in the breccia. Scale bar in cm (sample 760490).

(d) Photomicrograph of (c). The chert band (chert) consists of microcrystalline quartz mosaics, which are strongly veined by fine-grained anhedral carbonate (Co). Lithic-rich beds are intensely chlorite (Chl) and carbonate altered.

(e) Photomicrograph of M1 Marker chert and carbonate beds at Gossan Hill. These chert and carbonate beds are finely laminated with a pyrite-rich band in a carbonate bed (sample 762064).

(f) M1 Marker chert-lithic breccia bed at Gossan Hill. Chert clasts have *in situ* jigsaw fit textures and are cut by discontinuous carbonate veins. Chert fragments have angular shapes and are enclosed by a chlorite-carbonate-rich matrix that contains disseminated pyrite. Scale in cm (sample 760489).

(g) Massive quartz and feldspar-phyric rhyodacite (RD2) from SCF M2. Quartz phenocrysts are large rounded grains that are fractured and up to 5 mm in size. Feldspars are muscovite altered. This sample contains angular clasts of grey chert (chert) within massive rhyodacite. Scale in cm (sample 760254).

(h) Contact between massive quartz and feldspar-phyric rhyodacite (RD2) and sandstone/breccia of GGF M6. The basal contact of the rhyodacite has a 10 cm thick breccia zone that grades in to massive rhyodacite (arrow). This breccia contact contains clasts of sandstone within a quartz, feldspar-phyric matrix (~4929 E, 18,748 N, 10,179 RL, from drill hole GG141 at ~201m).

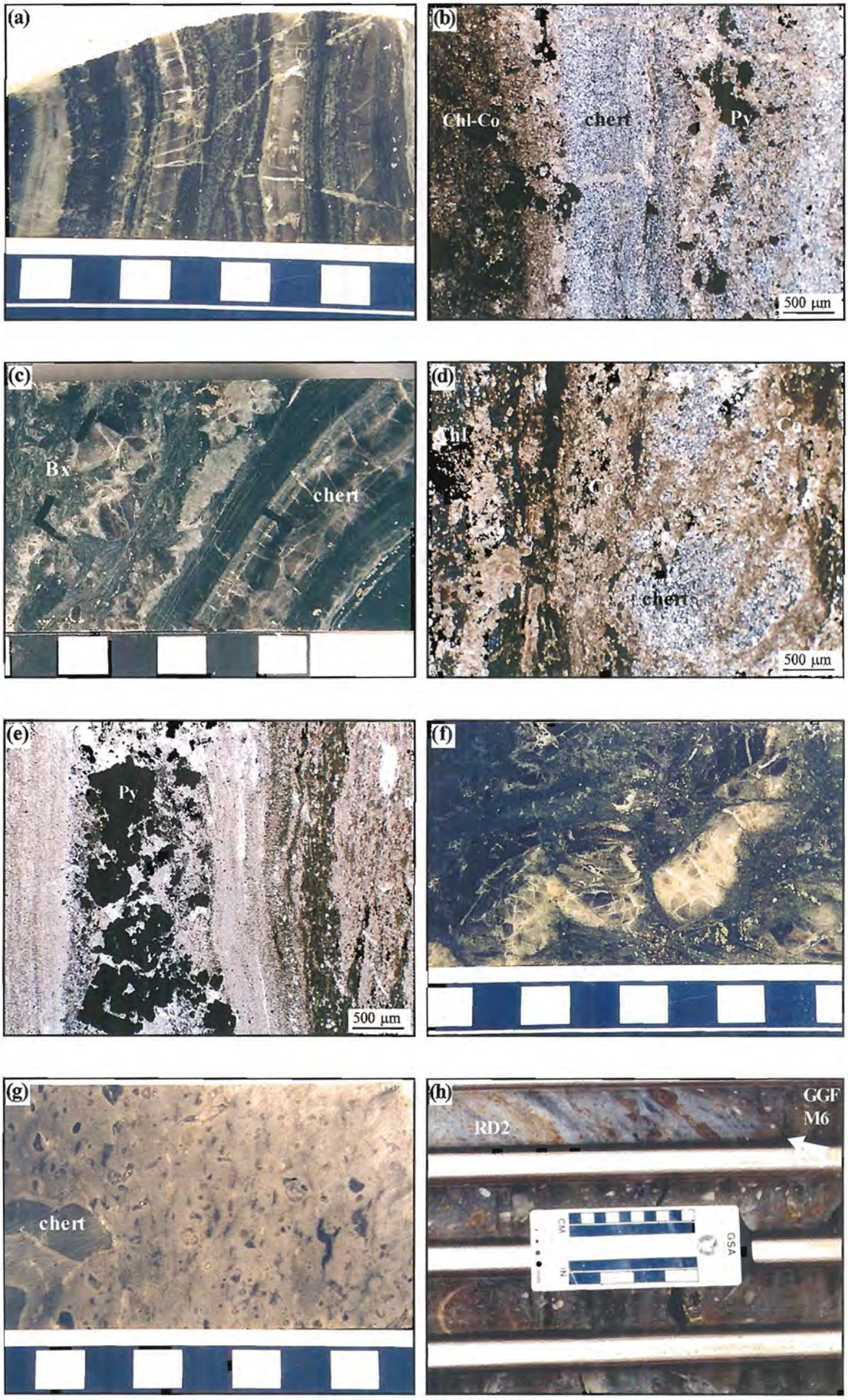
(a)
(b)
Chl-Co
chert
Py
500 µm
(c)
Bx
chert
(d)
Chl
Co
Co
chert
500 µm
(e)
Py
500 µm
(f)
(g)
chert
(h)
RD2
GGF
M6
CM
GSA
IN

carbonate-rich beds and milky-white to translucent quartz beds (Fig. 3.13a). Chlorite beds within the M1 Marker at Scuddles consist entirely of chlorite and carbonate, with abundant disseminated euhedral magnetite and sulphide (Fig. 3.13b). No relict volcanic textures are preserved in these chlorite beds, which themselves represent intensely chlorite-carbonate altered siltstone beds. Quartz beds are up to 2 cm thick and consist of interlocking microcrystalline quartz mosaics (Fig. 3.13b). Quartz beds typically contain minor sulphide.

At Gossan Hill, similar M1 Marker units are identified (Fig. 3.13c). These units occur throughout the upper thinly bedded sandstone, siltstone and breccia sequence of GGF M6. Chert beds are thinly interbedded with fine-grained green chlorite-carbonate altered and quartz-chlorite altered siltstone-sandstone (Figs. 3.13c and 3.13d). Chert beds vary from 1 mm to 6 cm thickness and are translucent and planar beds that consist of microcrystalline quartz and carbonate (Fig. 3.13d). At Gossan Hill, these chert beds are commonly discontinuous and lensoidal, having sharp conformable bases and irregular upper contacts. Delicately laminated, less than 10 μm wide carbonate laminae parallel bedding within the chert-chlorite M1 Marker units at Gossan Hill (Figs. 3.13d and 3.13e), suggestive of carbonate deposition during M1 Marker formation. Altered lithic-rich beds within the M1 Marker are thinly bedded siltstone, sandstone to poorly sorted, clast supported pebble breccia that contain translucent chert clasts (Figs. 3.13c and 3.13f). These breccia beds have undulose scoured bases and conformable upper contacts and contain chert clasts that range up to 4 cm in size. Chert clasts within breccia beds have an identical lithology to the M1 Marker chert bands, often with angular shapes and jigsaw fit textures (Fig. 3.13f).

Significant differences between the M1 Marker at the Gossan Hill and Scuddles deposits occur. At Gossan Hill, chert-chlorite units of the M1 Marker occur throughout the upper bedded sequence of GGF M6, whilst at Scuddles, the M1 Marker predominantly overlies massive sulphides. In addition, the M1 Marker at Scuddles has a greater proportion of magnetite and sulphide than equivalent units at Gossan Hill. The presence of carbonate laminae and chert breccia beds at Gossan Hill were not observed in the M1 Marker from Scuddles. Nonetheless, chert beds of the M1 Marker are distinct from the quartz altered siltstone-sandstone within GGF M6.

Discussion

Interbedded chert-chlorite units of the M1 Marker reflect a mixed hydrothermal-epiclastic source. Chert beds represent hydrothermally precipitated quartz, whilst the chlorite and quartz altered beds represent hydrothermally altered epiclastics. Similar chert-lithic units associated with VHMS mineralisation are reported from the Kuroko deposits (Kalogeropoulos and Scott, 1983; 1989) and the Noranda deposits (Peter and Goodfellow, 1996). The textural similarity and occurrence of the M1 Marker at both the Gossan Hill and Scuddles deposits support a common origin for these units, as well as a similar timing for their formation during the deposition of GGF M6. However, the occurrence of multiple chert-chlorite units within GGF M6 at Gossan Hill indicates

concurrent deposition of these units with deposition of the upper bedded sequence of GGF M6.

Precipitation of hydrothermal chert requires low sedimentation rates (Kalogeropoulos and Scott, 1983). Therefore, multiple chert-lithic units throughout an epiclastic sequence, such as GGF M6, indicate multiple sedimentation time breaks during which time, hydrothermal activity formed the M1 Marker cherts. The interbedded sandstone, siltstone and pebble breccia with M1 Marker chert beds indicate their alternating and synchronous formation. Pebble breccia beds that contain M1 Marker chert lithic clasts likely formed from local slumping and disruption of underlying chert beds. As a result, sedimentation depositing GGF M6 must have operated in conjunction with quiescent periods of hydrothermal activity that formed these cherts.

3.4 Scuddles Formation

The Scuddles Formation (SCF) overlies the GGF and consists of massive felsic volcanics rocks and associated autoclastic facies of a dacite to rhyodacite composition. The SCF has four members (Fig. 3.1), but only Member 2 (SCF M2) is considered in this thesis as it forms the hangingwall to mineralisation at Gossan Hill. SCF M1 only occurs at the Scuddles deposit and detailed facies descriptions of SCF M1, M3 and M4 are given in Clifford (1992). SCF M2 consists of two rock types; rhyodacite (RD2) and dacite (DAC3), both of which have associated breccia facies (Fig. 3.2).

3.4.1 SCF M2: rhyodacite (RD2)

Rhyodacite (RD2) is a grey, quartz, feldspar-phyric massive rock with distinctive large quartz phenocrysts (Fig. 3.13g). The upper contact of RD2 is sharp against a rhyodacite breccia facies (Section 3.4.2) or massive dacite (DAC3) of SCF M2. RD2 overlies GGF M6 and massive sulphides (Fig. 3.14). At Gossan Hill, RD2 commonly has a narrow zone (<3 m thick) of poorly sorted, clast supported polymict breccia at its base, indicating a scoured basal contact. Breccia along this contact contains lithic clasts (<10 cm in size) of siltstone, sandstone (Fig. 3.13h) and massive sulphide (Fig. 3.15a) within a quartz, feldspar-phyric matrix. Some of these clasts have soft sediment deformation textures indicating RD2 emplacement prior to their lithification.

Despite its locally unconformable lower contact, RD2 is broadly conformable against the underlying GGF at Gossan Hill. The continuity of the RD2 is interrupted between 18,300 N to18,500 N, by an intrusion of DAC3 dacite. South of 18,300 N, RD2 varies from 50 m (17,700 N) to 100 m (18,300 N) thick, whilst north of 18,500 N it is less than 30 m thick. This thickness change from 100 to 30 m occurs across the DAC3 intrusion, with RD2 thickest against its southern margin (18,300 N). On the southern side of DAC3, RD2 is amygdaloidal and has an overlying breccia facies (Fig. 3.14). To the north and south of the mineralised area at Gossan Hill, RD2 is also intruded by a number of smaller DAC3 bodies, however they do not disrupt the continuity of RD2.

Within RD2, large quartz phenocrysts (2 to 8 mm in size) form up to 4% modal and are rounded, embayed and contain curviplanar fractures. A second smaller quartz phenocryst

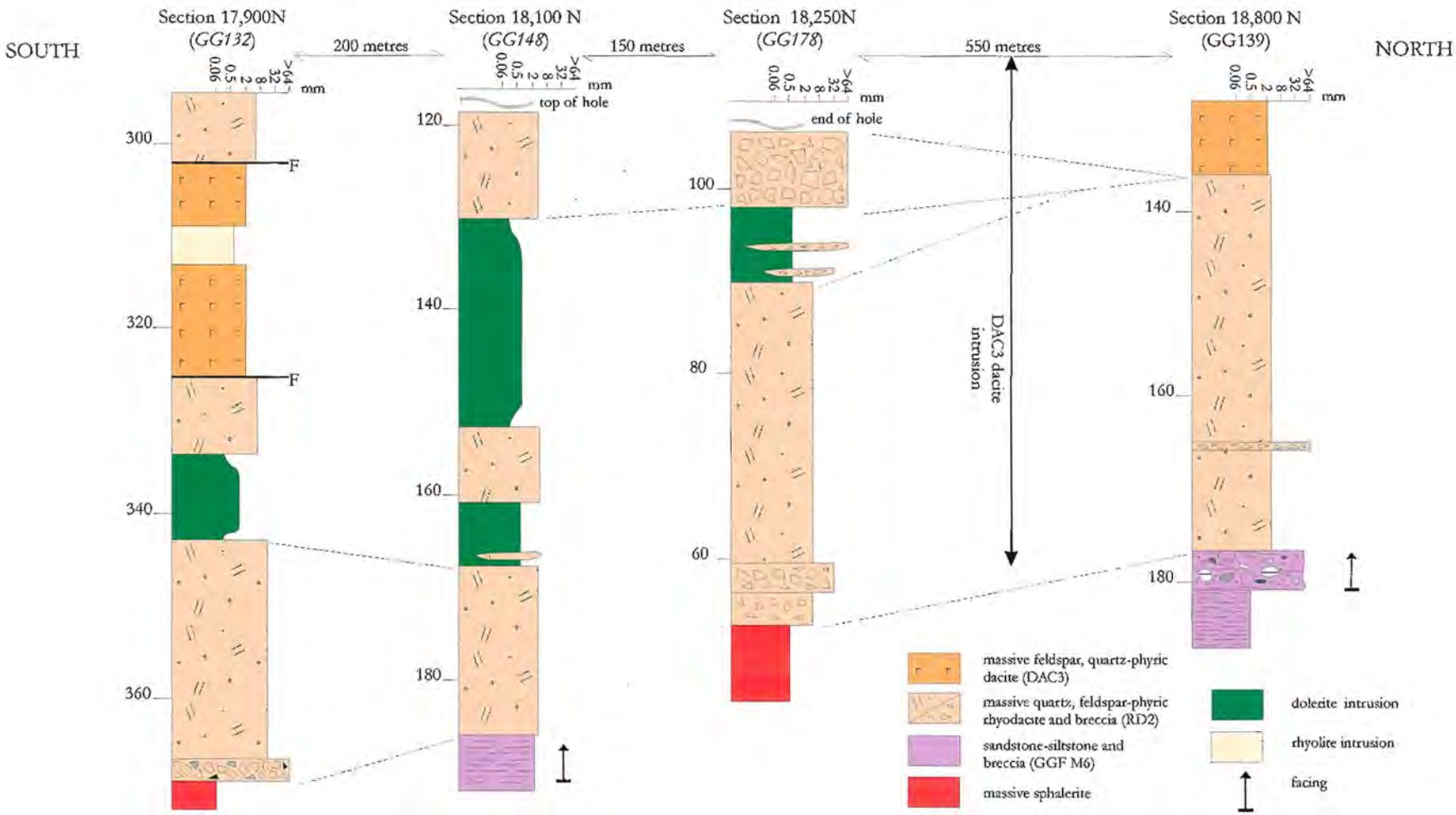

Figure 3.14: Facies variation diagram illustrating the distribution of RD2 rhyodacite within SCF M2. RD2 rhyodacite is intruded by flat lying dolerite in the south and central part of Gossan Hill (*e.g.*, GG132, GG148 and GG178). RD2 is overlain by DAC3 in the north (*e.g.*, GG139). The lower contact of RD2 commonly has a narrow zone of polymict rhyodacite breccia or may be in direct contact with sandstone-siltstone-breccia of GGF M6 (*e.g.*, GG139) or massive sulphides. Monomict rhyodacite breccia facies is best developed in the central parts of Gossan Hill (*e.g.*, Gg178), where RD2 breccia facies occurs on the south side adjacent to the DAC3 intrusion (arrow). Vertical scale indicates depth down strata in metres. Horizonatal distances between drill holes is not to scale. Drill hole identification given in italics.

Figure 3.15

(a) Polymict breccia at the base of rhyodacite (RD2). This breccia is poorly sorted, clast supported and contains a massive sphalerite clast as well as sandstone and rhyodacite clasts. The matrix to this breccia is a quartz, feldspar-rich rhyodacite (RD2) matrix. Scale bar in cm (4,784.6 E, 18,230.7 N, 10,061.1 RL, drill hole G96/184 at 89 m).

(b) Photomicrograph of a quartz (Qz) and feldspar (Fd)-phyric massive rhyodacite (RD2). Quartz phenocrysts are fractured and have quartz overgrowth rims. Feldspar phenocrysts are altered to interlocking patches of muscovite and the groundmass is a fine-grained interlocking quartz-feldspar mosaic that has pervasive muscovite alteration (sample 760487).

(c) Massive feldspar, quartz-phyric dacite (DAC3) from SCF M2. Feldspar within these dacites are strongly chlorite-carbonate altered and form patches up to 1 cm in size. The matrix is fine-grained and strongly carbonate-muscovite altered. Scale in cm (sample 760207).

(d) Photomicrograph of (c) showing small rounded quartz phenocrysts in a fine-grained pervasively carbonate-muscovite altered matrix. Feldspar phenocrysts (Fd) are intensely carbonate-chlorite-muscovite altered.

(e) Dacite hyaloclastite (DAC3) breccia facies from SCF M2. The clasts and matrix are feldspar, quartz-phyric. Clasts have curviplanar margins and jigsaw fit textures (4,784 E, 18,180 N, 10,180 RL, drill hole GG171 at ~201 m).

(f) Late stage feldspar-porphyritic dacite intrusion. Scale in cm (sample 769076).

(g) Photomicrograph of late dacite intrusion in (f) showing large plagioclase phenocrysts in a fine-grained feldspathic matrix.

(h) A steep rhyolite dyke (RHY) with flow banded margins is cut by a late stage dolerite (DOL). This dolerite has irregular margins. The wall rock is bedded sandstone and pebble breccia of GGF M1. Rock bolts are approximately 40 cm long (5,163 E, 18,437.5 N, 250 level).

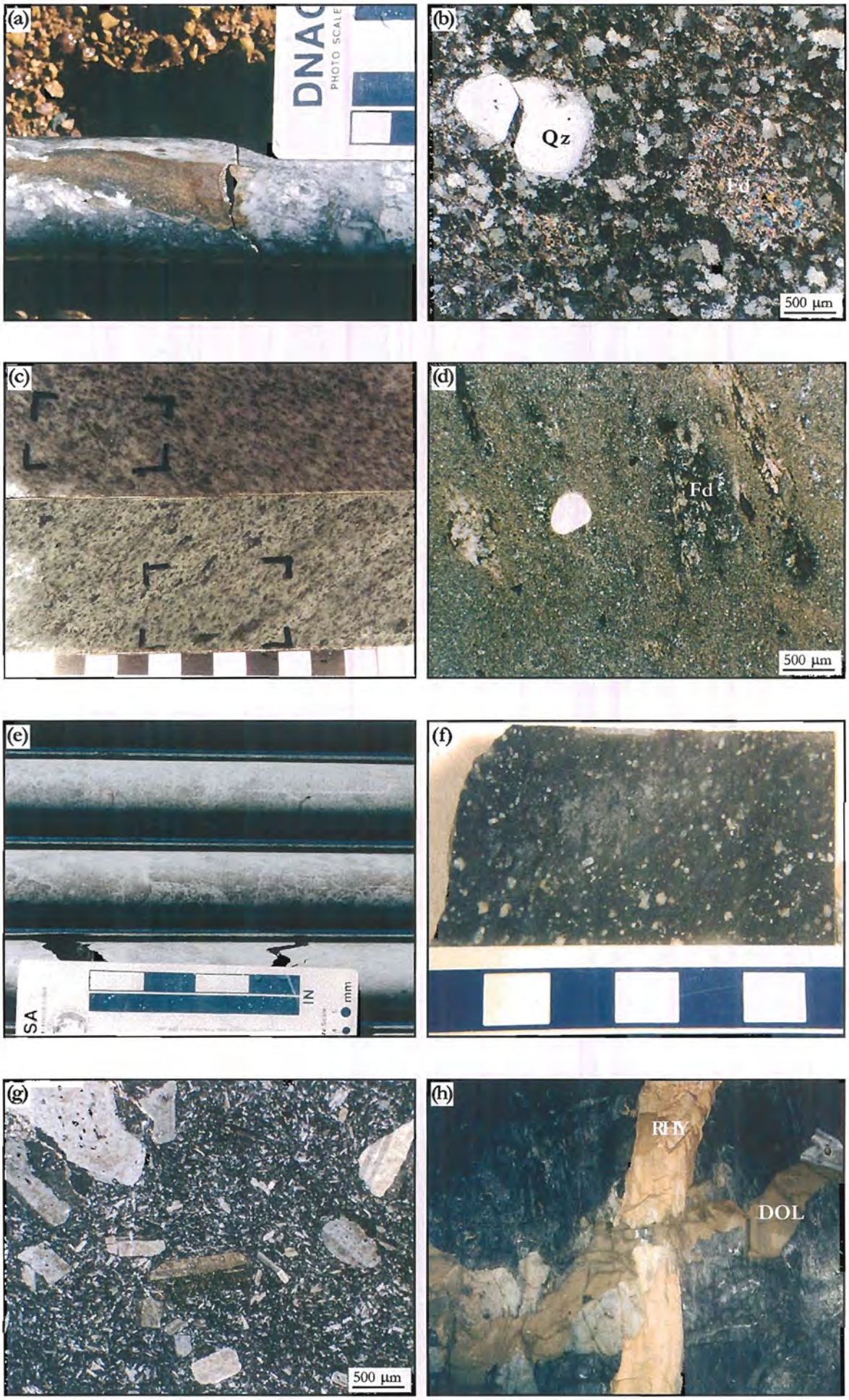
(a)
(b)
Qz
Fd
500 µm
(c)
(d)
Fd
500 µm
(e)
SA
IN
mm
(f)
(g)
500 µm
(h)
RHY
DOL

population (up to 3% modal) also occurs within RD2 and is less than 1 mm in size. Both of these quartz phenocryst populations have quartz overgrowths and rare recrystallisation to megaquartz. All feldspar phenocrysts within RD2 near Gossan Hill are altered to chlorite, carbonate and muscovite, but frequently retain their original tabular morphologies (Fig. 3.15b). The groundmass of RD2 is also intensely altered to muscovite, quartz, carbonate and chlorite, and has a strongly developed cleavage (Fig. 3.15b). Amygdules in RD2 are up to 5 mm and have rounded shapes, filled by carbonate, quartz and lesser chlorite. The distribution of amygdules throughout the RD2 is erratic, but tends to occur in its uppermost parts.

3.4.2 SCF M2: rhyodacite breccia facies

Rhyodacite breccia facies occurs within and overlying massive rhyodacite and is characterised by quartz, feldspar-phyric rhyodacite clasts in a quartz, feldspar-rich matrix. These breccias vary from monomict to polymict and have a discontinuous and lensoidal occurrence and are best developed to the south of the DAC3 intrusion between 18,050 N and 18,300 N (Fig. 3.14). This occurrence is coincident with the thickest development of RD2 and massive sulphide. Monomict rhyodacite breccia units are clast supported with a closed framework and vary from less than 5 m up to 15 m thick (Figs. 3.14 and 3.16). These breccia units have angular to subangular clasts up to 20 cm in size with commonly jigsaw fit textures.

Polymict rhyodacite breccia is rare, containing clasts of silicified sandstone, siltstone, massive pyrite and quartz-rich tuffaceous breccia and sandstone clasts in addition to rhyodacite clasts. This polymict rhyodacite breccia is poorly sorted, lacks grading and has angular to subrounded clasts up to 10 cm in size in a closed framework. The groundmass is quartz, feldspar-phyric. Sandstone and siltstone clasts form less than 10 to 15% of the polymict rhyodacite breccia, some of which have soft sediment deformation textures. The matrix of polymict rhyodacite breccia contains up to 5% disseminated pyrite.

3.4.3 Rhyodacite facies interpretation

Rhyodacite breccia facies predominantly overlies RD2 forming an upper breccia facies. The angular, jigsaw fit textures in this breccia facies support its occurrence as an upper breccia facies of the underlying massive coherent rhyodacite. The lower contact of RD2 is weakly discordant and erosional, with a basal breccia that represents the incorporation of underlying lithified and unlithified sediment of GGF M6 to basal parts of the flow. Polymict breccia occurs within and at the base of RD2 and represents the intercalation of underlying sediment to the rhyodacite lava during its emplacement. These observations support an extrusive origin for RD2. Although RD2 has a weakly discordant lower contact, it is broadly conformable to the underlying GGF. Clifford (1992) interpreted rhyodacite to have formed from high rates of effusive rhyodacite volcanism that produced sheet flows with kilometre-scale lateral extents. At Gossan Hill, the lateral continuity of RD2 is only interrupted where it is intruded by DAC3 dacite

The thickest development of the rhyodacite breccia facies occurs adjacent to the southern margin of the DAC3 intrusion. Polymict rhyodacite breccia facies in this

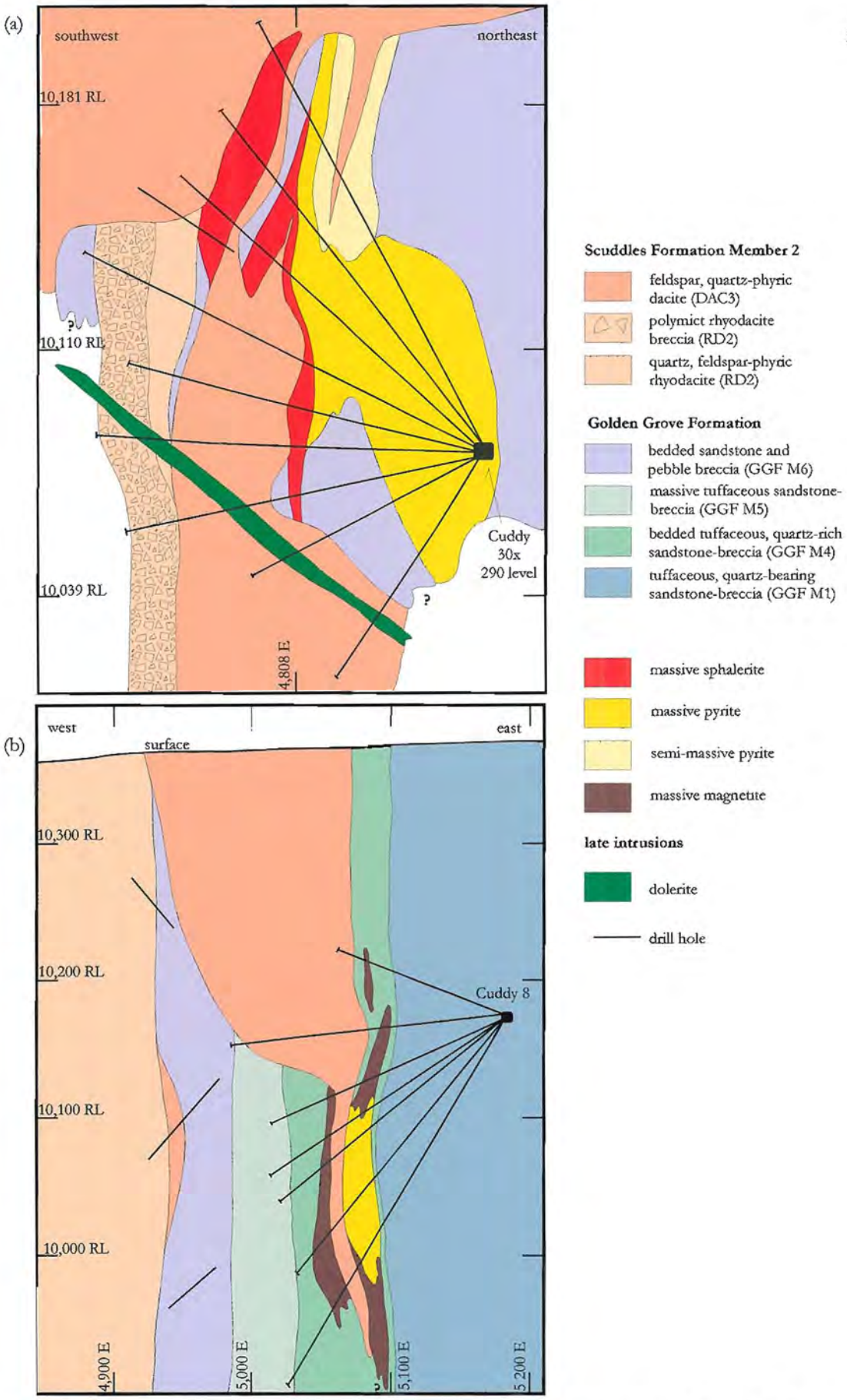

Figure 3.16: Cross sections through the Gossan Hill deposit. (a) Transform section (045 trend) in the central mineralised area. Massive sphalerite-pyrite is intruded by DAC3 dacite, and RD2 has an overlying breccia facies. Due to complex geometry in this area, the section is a 10 m window with an origin at 18,293.5 N, 4,847 E bearing 045. (b) East-west section (25 m window) along 18,720 N through massive pyrite and magnetite in GGF M4. A 'V' shaped DAC3 dacite intrusion cuts mineralisation, GGF M4 to M6 and RD2. Mine grid in metres.

locality indicate incorporation of debris from the underlying or adjacent sediment strata, including massive sulphides. Massive sulphide clasts in polymict rhyodacite breccia facies were derived from the erosion of underlying massive sulphides during rhyodacite emplacement, indicating massive sulphides were at or near the seafloor during RD2 emplacement. The extrusion of RD2 at Gossan Hill, resulted in the burial of the GGF and massive sulphides.

3.4.4 SCF M2: dacite (DAC3)

At Gossan Hill, DAC3 dacite represents the uppermost part of SCF M2. DAC3 dacite is a massive grey, feldspar, quartz-phyric unit (Fig. 3.15c) with sharp, intrusive and discordant to conformable contacts to underlying RD2 and rhyodacite breccia facies and the GGF (Fig. 3.16). At Gossan Hill, the DAC3 intrusion is oblique to bedding in the GGF and has sharp, chilled margins with local contact metamorphism of adjacent sediments. Rarely, the margins of the DAC3 intrusion are flow banded (over <10 cm) or contain clasts of sediment. In the central mineralised area of Gossan Hill (18,300 N to 18,750 N), DAC3 forms a 'V' shaped intrusion that disrupts the continuity of the GGF and RD2 from north to south (Fig. 3.16). This 'V' shaped DAC3 intrusion is narrow (<5 m) in lower members of the GGF and up to 350 m wide in the upper GGF M6 and RD2 (Fig. 3.16b).

Quartz phenocrysts in DAC3 are rounded to euhedral, are less than 1 mm in size (Fig. 3.15d) and form less than 2% modal. These phenocrysts commonly have embayed margins and are recrystallised to megaquartz. Feldspar phenocrysts are altered to mosaics of carbonate, muscovite and chlorite (Fig. 3.15d) and rarely have relict feldspar cores. Despite intense alteration, feldspar phenocrysts commonly retain their primary tabular morphology and form up to 30% modal, ranging in size from less than 300 μm to 4 mm. These altered feldspars phenocrysts have a strong alignment parallel to S3 cleavage with wrapping of cleavage or grain rotation indicated by pressure shadows. Large (up to 10 mm) subrounded patches of chlorite occur in DAC3 and contain relict cores of twinned plagioclase. These chlorite altered patches reflect feldspar glomeroaggregates that are altered to chlorite, carbonate and muscovite. The matrix of DAC3 is a fine-grained, relatively homogeneous muscovite altered quartz-feldspar mosaic.

3.4.5 SCF M2: dacite breccia facies

The dacite breccia facies are massive, monomict, poorly sorted and clast supported. Dacite breccia clasts and matrix are feldspar, quartz-phyric containing quartz phenocrysts less than 1 mm in size (Fig. 3.15e). Clasts range in size up 20 cm, have angular to subangular shapes with jigsaw fit textures and sharp curviplanar clast margins. Both clast and matrix of the dacite breccia facies are strongly altered to muscovite, carbonate and chlorite. Rare exotic lithic clasts of bedded silicified sandstone are also observed.

Dacite breccia facies overlies or occurs within DAC3, having sharp to gradational contacts with massive DAC3 dacite. The true thickness of breccia overlying DAC3 is difficult to estimate because of limited drilling. The main occurrence of dacite breccia is south of 18,200 N where it has a discontinuous and lensoidal occurrence.

3.4.6 Dacite facies interpretation

The occurrence of intercalated and overlying monomict breccia facies to massive DAC3, indicates that DAC3 was an extrusive lava. Curviplanar clasts with jigsaw fit textures are typical of hyaloclastite deposits related to lava extrusion in a subaqueous environment (Cas and Wright, 1988). Nonetheless, the geometry of DAC3 at Gossan Hill is consistent with a dome-like body that overlies its discordant 'V'-shaped volcanic feeder. Therefore DAC3 and related breccia facies at Gossan Hill formed as an intrusive-extrusive lava dome. As indicated by intrusive contacts, DAC3 dacite post-dates deposition of the GGF, massive sulphide, massive magnetite and the extrusion of RD2 rhyodacite.

Facies variations and thickness changes are observed in the GGF (M2 to M6 inclusive) and RD2 across this DAC3 intrusion. The DAC3 feeder structure is interpreted to occupy the site of pre-existing synvolcanic structure. Smaller lensoidal DAC3 intrusions occur north and south of mineralised area at Gossan Hill and have similar stratigraphic and facies associations. Regionally, Clifford (1992) recognises multiple sites of dome-like dacite intrusions within SCF M2, all of which have limited lateral extent. The occurrence of DAC3 as sills within GGF M5 (Section 3.3.4) reflect synvolcanic dacite intrusion.

3.5 Intrusions

Three late stage intrusions are identified at Gossan Hill. These intrusions post date deposition of the GGF and SCF and in order of intrusion are (1) porphyritic dacite dykes, (2) dolerite dykes and sills, and (3) rhyolite dykes. These intrusions are discussed below.

3.5.1 Dacite porphyries

Dark grey feldspar-porphyritic dacites intrude the GGF and SCF and have a minor occurrence at Gossan Hill. These dacite intrusions are narrow (<8 m thick), steep sided dykes that have sharp chilled margins (<30 cm thick). Dacite intrusions are plagioclase porphyritic (Fig. 3.15f) and contain minor quartz. Plagioclase phenocrysts (Fig. 3.15g) are euhedral and form up to 30% modal with a grain size of less than 1.5 mm. These phenocrysts commonly have reacted grain margins with minor carbonate and muscovite alteration. Quartz phenocrysts are small (<800 μm), weakly embayed and form less than 2% modal. The matrix of porphyritic dacite is a fine-grained (<50 μm) plagioclase-quartz mosaic.

3.5.2 Dolerite

Three phases of dolerite intrusion are identified at Gossan Hill and each phase differs in timing and structural orientation (Section 4.5). The two earliest phases of dolerite are widespread and have similar associations, except where earlier coarse-grained dolerite (<2 mm grain size) intrudes fine-grained dolerite (<0.3 mm grain size). The earliest coarse-grained dolerites are flat lying sills that are up to 50 m thick (Fig. 3.11a). These are intruded by fine-grained dolerite, which form parallel sided, narrow (<6 m thick) dykes that cut strata obliquely. Comparatively, late stage dolerite intrusions have a minor

occurrence at Gossan Hill and cuts both earlier coarse- and fine-grained dolerite as well as rhyolite intrusions (Section 3.5.3) (Fig. 3.15h).

Dolerite intrusions have fine-grained, chilled intrusive margins that are generally less than 30 cm wide. The margins of dolerite intrusions vary from sharp and planar to undulose and irregular or faulted. Rare clasts of wall rock, up to 20 cm in size, occur within dolerite along its margin. All dolerites have a similar mineralogy of clinopyroxene and plagioclase. Carbonate and chlorite alteration is strong and pervasive within the earlier dolerites, which also contain scattered epidote, clinozoisite, spinel and magnetite.

3.5.3 Rhyolite

Rhyolite intrusions are narrow (<5 m) fine-grained, aphyric to weakly feldspar, quartz-phyric parallel sided dykes. These rhyolites intrude the GGF at Gossan Hill, but are themselves intruded by Phase 3 dolerite (Fig. 3.15h). Rhyolite dykes are steeply dipping and parallel the dip of the GGF (Section 4.8). These dykes have sharp and planar to locally irregular contacts, often with fine-grained flow banded margins (Fig. 3.15h).

In GGF M1, rafts (<3 m) and fragments (<30 cm) of wall rock are common within rhyolite dykes and the long axis of wall rock fragments parallel the dyke margin. Based upon the lithology and jigsaw-fit textures between the wall rock and the incorporated rafts and fragments within rhyolite, these clasts were derived from the adjacent strata. Stratigraphic disruption by rhyolite dykes is minor.

3.6 Geometry and distribution of the GGF

Stratigraphic members of the GGF and SCF form a laterally extensive layered stratigraphy with a strike continuance in excess of 25 km. The facies architecture at the Gossan Hill deposit has many similarities to the regional architecture proposed by Clifford (1992). The regional continuance of the GGF is disrupted by cross cutting intrusions of the SCF and displacement along late brittle faults. Additionally, GGF M2, GGF M3 and SCF M1 have a lensoidal and discontinuous occurrence. In view of these constraints, proposed transport and depositional processes for volcaniclastic and epiclastic facies of the GGF, must account for large volume transport of detritus, and include depositional processes capable of producing a laterally continuous, layered stratigraphic succession.

3.7 Deposition of the Golden Grove Formation

The depositional processes for the GGF are assessed in the following sections by comparison and contrast of physical attributes within the different members of this formation (*e.g.*, crystal enrichment, grading, bedding and lithic morphology and abundance). In addition, the context of mineralisation within the GGF is also examined to evaluate the stratigraphic timing of mineralisation and the depositional environment associated with its formation.

3.7.1 Mechanisms of emplacement

The volcano-sedimentary environment for deposition of the Gossan Hill Group is a deep, subaqueous setting (Clifford, 1992). Within the GGF, a subaqueous depositional environment is supported by the abundant sedimentary characteristics of the sequence, including stratification and grading. Normal grading within this strata indicates the influence of gravitational depositional processes and consequently, tuffaceous debris must have been water saturated. The absence of welded textures and gas pipe structures throughout the sequence also indicates a cold state of emplacement. As mudstone facies do not occur within the GGF, this succession was deposited by successive sedimentation events, which lacked significant quiescent periods for mudstone accumulation.

Transport and deposition of the GGF took place by mass flows (Clifford, 1992). Mass flow processes can account for the transfer of large volumes of material from their source to their depositional sites (Cas and Wright, 1988; McPhie *et al.*, 1993), which is a critical aspect in view of the 28 km strike continuance of the GGF. Mass flow transport processes proposed for the Golden Grove Domain involve large volume and laterally extensive depositional events. Flux and supply of detritus to these mass flows would also require a large volume source area.

Each stratigraphic member within the GGF has distinct lithological characteristics such as bedding, grain size, volcanic quartz and clast-matrix abundances. These differences not only reflect differences in the source, but also variations in the processes by which they were deposited. GGF M1, M3, M4 and M5 predominately consist of tuffaceous material, whilst GGF M2 and M6 have a mixed epiclastic source with lesser tuffaceous material. GGF M1 is a tuffaceous sequence dominated by pumiceous lithic clasts and quartz. GGF M1 varies from bedded to massive breccia and sandstone, and has normal grading, reverse grading, slump folding, conformable and unconformable contacts, crystal-rich sandstone and shard-rich sandstone. Within the GGF M1 sequence, the transition from a bedded basal sequence to a more massive top, represents a change in sediment flux and depositional style. GGF M4 is a fine-grained bedded tuffaceous quartz crystal-rich sequence. The abundance of angular quartz and shard fragments within GGF M4 reflects a quartz-porphyritic pyroclastic source. Volcanic quartz enrichment of up to 15% modal within some beds indicates crystal enrichment resultant from transportation and depositional processes. GGF M5 differs from these above mentioned tuffaceous members as it is massive, with rare bedding and consists dominantly of moderately sorted shard and pumiceous detritus with minor quartz. Due to the absence of bedding and grading within GGF M5, its deposition likely represents a rapid large volume event.

Volcanic quartz is an important mapping tool within the GGF due to its resistance to alteration. Volcanic quartz throughout the GGF generally have minor embayment textures, however, some quartz-rich beds of GGF M4 have strong quartz embayment (*e.g.*, Fig. 3.7d). Where observed, quartz embayment has microcrystalline quartz overgrowths. The history of quartz within the GGF appears to reflect strong embayment prior to the effects of alteration that caused overgrowths. Nonetheless, embayment and resorption textures may also be associated with alteration as observed by Allen (1988) at

Benambra.

Factors affecting crystal concentrations are (1) the degree of magma crystallinity, (2) physical fractionation and sorting processes associated with pyroclastic eruption and transportation processes, and (3) epiclastic reworking resulting in localised enrichment of crystals (Cas and Wright, 1988). The abundance of euhedral and angular quartz grains in GGF M4 and to a lesser extent GGF M1, indicates quartz liberation and fracture during explosive volcanism. Normal grading and crystal enrichment of quartz in some beds within GGF M4 likely indicative of epiclastic reworking during transport.

As epiclastic processes commonly introduce exotic lithic components, tuffaceous members of the GGF (M1, M3, M4 and M5) have not undergone substantial epiclastic reworking due to their homogeneous pumiceous lithic clast population. Tuffaceous pebble breccia beds throughout these members also have moderately sorted pumiceous fragments in a fine-grained matrix. The matrix to these pumiceous lithic clasts is a closely packed tuffaceous matrix that consisted of shards and pumice shreds. Pumiceous lithic clasts vary from tabular to blocky and angular, some of which have evidence of *in situ* fracture. The brittle nature of cold glass could result in size refinement during transportation due to fragmentation resulting from cohesion and grain interaction.

In view of these constraints, the deposition of tuffaceous strata within the GGF is likely to have resulted from successive water-supported volcaniclastic mass flows. Turbulent, high density mega-turbidites, which lead to laterally extensive deposits (McPhie *et al.*, 1993), are consistent with observations made in the GGF at Gossan Hill. A multiple felsic source for tuffaceous materials is indicated by differences in the quartz and lithic clast constituents between the tuffaceous members.

By contrast, GGF M2 and M6 are bedded epiclastic sequences of siltstone, sandstone and breccia with a multiple provenance. Clifford (1992) interprets these members to represent background sedimentation from low volume turbidite mass flows. As exemplified by the interbedded GGF M5-M6 contact, the deposition of epiclastic strata was interrupted by pulses of tuffaceous mass flows. The proportion of tuffaceous material within epiclastic strata is commonly masked by intense, texturally destructive alteration. Nonetheless, based on alteration textures, this study suggests that these members contain a significant proportion of tuffaceous material. GGF M2 represents small volume epiclastic-tuffaceous deposits, which mark a time break between two separate episodes of tuffaceous sedimentation (*i.e.*, GGF M1 and M4). Within GGF M6, breccia beds contain clasts with similar lithologies and alteration to underlying strata, indicating their local derivation by slumping and erosion. The role of water settling, particularly suspended ash and shards from tuffaceous mass flows, may have a contributed to the tuffaceous components of these thinly bedded sequences.

3.7.2 A question of hiatus: When and how many?

A hiatus is a break or interruption in the continuity of a stratigraphic sequence where the interval separating stratigraphic depositional events is not necessarily quantified (Bates and Jackson, 1987). The occurrence of hiatus is relevant to seafloor ore forming

processes as quiescent periods are required for the accumulation of seafloor sulphides (Morton *et al.*, 1991; Kerr and Gibson, 1993). In the GGF sedimentation breaks are denoted by lithofacies changes, but as each of the members of the GGF represent successive depositional episodes, they do not necessarily indicate hiatus. At Gossan Hill, sedimentation hiatus is indicated by (1) lenses of sulphide-bearing breccia near the base of GGF M4, and (2) multiple hydrothermal chert-lithic units within the upper parts of GGF M6. In the first case, sulphide-bearing breccia within GGF M4 indicate a quiescence period associated with sulphide deposition prior to the erosion of sulphides and altered strata that formed these breccias. In the second case, hydrothermal chert beds associated with massive sulphide deposition, formed between the low volume pulses of sedimentation, which separate them in GGF M6. From these occurrences, periods of massive sulphide deposition can be ascribed to hiatus at the onset of GGF M4 deposition and as multiple sedimentation hiatus during GGF M6.

3.7.3 Devitrification state of the tuffaceous strata

Natural glass is chemically unstable (Marshall, 1961; Friedman and Long, 1984). This chemical instability accommodates two dominant processes; devitrification and alteration. Devitrification or the transition of glass to crystalline matter, involves the development of spherulites, micropoikilitic quartz and quartz-alkali feldspar intergrowths. The mechanisms and products of these devitrification processes are not well understood (Lofgren, 1971a;b). In felsic rocks at the Benambra VHMS deposit, devitrification is interpreted to involve the recrystallisation of glass into fibrous and massive quartzo-feldspathic aggregates (Allen, 1988). Experimental studies on glassy rhyolite (Lofgren, 1971b) define the rate of devitrification in glass to vary according to temperature. Glass which is cooler (<300°C) takes longer to devitrify than glass which is hot (>300°C) (Lofgren, 1971b). Allen (1988) used this conclusion to imply that glass at relatively lower temperatures is likely to hydrate and alter rather than devitrify, due to the longer residence time necessary for the latter.

The deep subaqueous depositional setting of the GGF would have been conducive to the hydration and alteration of glass, assuming that tuffaceous detritus was glassy at the time of emplacement. In order to review the devitrification state of the GGF, three boundary conditions for the tuffaceous strata at Gossan Hill are recognised. These are (1) the erupted tuffaceous material was glassy, (2) tuffaceous material was cold at emplacement, and (3) tuffaceous material now consists entirely of quartz and chlorite. The preservation of volcanic textures within the GGF is strongly correlated to the degree of quartz alteration, with rare preservation in chlorite alteration.

Tuffaceous volcaniclastics of GGF M1, M4, M5, and some beds within GGF M6, consist of altered tube pumice, vesicular pumice, pumice shreds and glass shards. In these members, preserved textural evidence of devitrification occurs as quartz-replaced spherulites, microlites and interlocking rod textures after quartzo-feldspathic mosaics. The rarity of these devitrification textures suggests minor devitrification of glass occurred. The timing of this devitrification was prior to, during or after deposition of

tuffaceous strata in the GGF. The limited occurrence of altered devitrification textures reflects either the dominantly glassy state of the tuffaceous matter after emplacement or poor textural preservation of devitrification textures by alteration minerals. The former is favoured due to generally good preservation of glassy volcanic textures throughout tuffaceous strata of the GGF.

In the GGF at Gossan Hill, alteration of tuffaceous material has resulted in a pervasive to domainal quartz-chlorite alteration. Clifford (1992) interprets domainal quartz-chlorite alteration textures within GGF M1 to reflect differential devitrification states that resulted in later domainal alteration. However, poor textural preservation within chlorite alteration makes this interpretation equivocal. It is entirely possible that domainal alteration textures may also reflect different hydration states or diagenetic alteration of glassy constituents within the tuffaceous strata.

Although chlorite altered domains have a weak flattening parallel to cleavage due to competency contrasts during deformation (Chapter 4), volcanic textures throughout tuffaceous strata of the GGF lack flattening and compaction textures. These glassy volcanic textures in the GGF contrast markedly with diagenetically flattened and compacted pumice textures in the footwall of the Rosebery deposit (McPhie and Allen, 1992). In order to prevent diagenetic compaction processes, tuffaceous strata in the GGF must have been indurated prior to lithification. Induration of the GGF could have occurred by devitrification, diagenetic alteration and/or hydrothermal alteration processes.

3.7.4 Diagenetic alteration

The alteration of glass involves the hydration of glass to form alteration products such as clay or zeolite (Walton, 1975; Dimroth and Lichtblau, 1979; Hodder *et al.*, 1990; Capaccioni and Coniglio, 1995). Diagenetic alteration products are commonly derived directly from the volcanic glass and are not necessarily associated with changes in texture (Quantin *et al.*, 1988). Furthermore, clay and zeolite are common diagenetic alteration products of pumiceous and glassy strata hosting VHMS mineralisation (Iijima, 1974). Within felsic volcaniclastics of the Kuroko district, the alteration of glass to zeolite or clay is associated with diagenetic compaction. However differential alteration of glass to zeolites (*e.g.*, saponite) within these volcaniclastics, is largely controlled by temperature (Utada, 1991). Diagenetic alteration can result in the induration of the glassy precursor, simultaneously preserving primary volcanic textures. Therefore, domainal quartz-chlorite alteration textures within the GGF at Gossan hill could reflect different diagenetic alteration products of volcanic glass.

3.7.5 Textural preservation: Diagenetic or hydrothermal alteration?

It is not possible to quantify the degree of devitrification or the extent and development of diagenetic alteration that occurred in the GGF at Gossan Hill. Irrespectively, the GGF has widespread textural preservation of tuffaceous components. Complete devitrification of volcanic glass results in textural destruction (Marshall, 1961; McPhie *et al.*, 1993) and therefore considered unlikely to have occurred in the GGF. Diagenetic

alteration and partial devitrification of glass instead, can preserve primary volcanic textures (Lofgren, 1971a; Quantin *et al.*, 1988).

Considering the Archean age of the GGF and its proximity to massive sulphide mineralisation at Gossan Hill, textural preservation of this succession is remarkable. Nonetheless, complete textural destruction occurs within mineralisation and intense hydrothermal alteration. Moreover, Clifford (1992) identified this textural preservation within the GGF and alteration to quartz-chlorite to be a regional phenomenon. Therefore, any mechanism proposed for textural preservation of tuffaceous strata at Gossan Hill must invoke a regionally extensive mechanism. Based upon the absence of compaction textures within the GGF, textural preservation and induration must have occurred rapidly and soon after or during emplacement. The processes associated with textural preservation of the GGF relate to its alteration and are investigated in Chapter 7.

3.7.6 Porosity and permeability

The initial permeability and porosity of pumiceous breccia and sandstone of the GGF was very high, as indicated by abundant tube and vesicular pumice and the clast supported framework of breccia lithologies. By contrast, shard-rich sandstone and siltstone, consisting of closely packed arrays of shards and pumiceous shreds, may have had variably high to low permeability and porosity contrasts depending on the physical properties of discrete beds. Contrasts between primary permeability and porosity properties within strata of the GGF were likely factors controlling migrating hydrothermal fluids. The presence of carbonate-quartz filled cavities in breccia (*e.g.*, Fig. 3.6a) indicates primary pore space and intra-clast porosity, which would have also contributed to an initially high porosity and permeability of the glassy GGF volcaniclastic succession.

3.8 Summary

- The GGF is a laterally extensive (> 28 km), layered volcano-sedimentary succession that hosts massive sulphide mineralisation at Gossan Hill. This formation is divided into six members (GGF M1 to M6), which consist of tuffaceous volcaniclastics and lesser mixed provenance, tuffaceous-bearing epiclastics.
- The SCF overlies the GGF and forms the hangingwall to massive sulphide mineralisation. The lower parts of the SCF consist of an extrusive rhyodacite lava (RD2) overlain by an intrusive-extrusive dacite lava dome (DAC3). Both of these lavas have associated autoclastic breccia facies. DAC3 dacite intrudes the GGF and RD2 rhyodacite and overlies its volcanic feeder.
- Tuffaceous volcaniclastics of the GGF (GGF M1, M3, M4 and M5) vary from massive breccia (pebble to granule) to bedded breccia, sandstone and siltstone. These units are generally characterised by well-preserved tube pumice, vesicular pumice, pumiceous shreds and shards and volcanic quartz. Volcanic quartz is distinctive within each tuffaceous member of the GGF due to characteristic variations in size, abundance and morphology.

- Deposition of the tuffaceous strata in the GGF occurred by successive large volume subaqueous high density turbidite mass flows. Tuffaceous volcaniclastics were emplaced cold and consisted of moderately to well sorted, relatively homogeneous pumiceous lithic clast populations and fine-grained sand and ash. Mass flow transport resulted in minor modification of juvenile tuffaceous material.
- Epiclastic-tuffaceous strata within the GGF (M2 and M6) have a polymict lithic clast population indicating multiple sources. These bedded epiclastic-tuffaceous sequences represent subaqueous, low volume turbidites and suspension settling deposits, typical of background sedimentation. Textural evidence supports a greater tuffaceous component to these members than previously identified.
- The GGF is altered to quartz and chlorite, but alteration has resulted in generally good textural preservation. The absence of diagenetic compaction textures indicates the sequence was indurated soon after emplacement.
- Stratigraphic thickness variations (on a scale of metres) occur within GGF M2, M3 and M6. Thickest development of this strata coincides with the location massive sulphide-magnetite mineralisation, with a changes in thickness across the discordant SCF M2 DAC3 dacite volcanic feeder structure.
- The occurrence of massive sulphide-bearing breccia in GGF M4 and hydrothermal chert beds within the M1 Marker of GGF M6 represent sedimentation hiatus and paleoseafloor sites of hydrothermal activity. Chert in the M1 Marker at Gossan Hill indicates multiple seafloor positions during accumulation of GGF M6.
- Synvolcanic structural control is indicated by changes in thickness of the GGF (M2, M3 and M6) across the DAC3 volcanic feeder. This dacite intruded the site of a former synvolcanic structure (growth fault), the later which influenced thickness variation in lithofacies of the GGF.

Chapter 4

Structure and metamorphism

4.1 Introduction

Previous interpretations of the structural and metamorphic history for the Golden Grove Domain differ amongst authors (Frater 1978; 1983a;b; Ashley, 1983; Archibald, 1990; Watkins and Hickman, 1990a; Clifford, 1992). Watkins and Hickman (1990a) compiled a regional structural framework for the Murchison Province and identified four main phases of deformation affecting the Golden Grove Domain. Table 4.1 summarises the salient regional structural features identified by previous workers. A comparison of these structural studies highlights the inconsistencies of previous interpretations between the number, style and timing of recognised deformational events that affected the Golden Grove Domain, particularly near the sites of mineralisation at Gossan Hill and Scuddles.

Initial structural investigations at Gossan Hill (Frater, 1978; 1983a;b) failed to recognise the importance of faulting. Subsequent work, which resolved lithological and facies associations of the volcanic succession (Clifford, 1992), indicated that the Golden Grove Domain was more structurally disrupted than previously identified and that many inferred syndepositional facies thickness variations resulted from fault related structural modifications of a layered stratigraphic package.

4.2 Aims

The structural investigations of this study used newly available underground exposures at Gossan Hill to reassess structural deformation and metamorphism. Assessment of the structural history was confined to the Gossan Hill area and comparisons, where possible, were made to other structural features and studies of the Golden Grove Domain. A major objective of this study was to identify primary structural controls on lthe ithofacies and massive sulphide at the Gossan Hill deposit, as well as the effects of superimposed structural modifications.

4.3 Synvolcanic structures

The recognition of synvolcanic structures is a prime objective in the exploration for VHMS deposits. Synvolcanic structures provide the focus for large volumes of mineralising-hydrothermal fluids on their ascent to the seafloor and also represent primary litho-stratigraphic controls, as well as conduits for successive volcanic activity (Setterfield *et al.*, 1995). Synvolcanic structures are reported from both modern and

Table 4.1: Summary of structural interpretation by previous workers in the Golden Grove Domain. Watkins and Hickman (1990a) proposed a regional structural framework for the Murchison Province and identified five deformational events. The D5 deformation only affects the Minjar Range Domain and is not included in this summary. Structural elements identified in other studies by Frater (1978), Archibald (1990) and Clifford (1992) are presented in the context of the structural framework of Watkins and Hickman (1990a).

Regional Framework Watkins and Hickman (1990a)		**D1: horizontal structures**	**D2: east-west folds north-south compression**	**D3: north-south folds east-west compression**	**D4: shear zones & faults east-west compression**
Summary		Recumbent folding and thrusting	Tight, upright east-west folds	Tight to isoclinal north-south folds	Faulting and shearing with north-trends: considered late D3
Timing*		2.92 Ga	2.69-2.68 Ga	2.69-2.68 Ga	2.64-2.62 Ga
Watkins and Hickman (1990a)	**Fabric**	bedding parallel foliation in limbs of regional isoclinal F1 folds	weakly developed & obscured by D3 and D4	intense penetrative fabric parallel to F3 axial plane	sub-vertical and anastomosing fabrics; S-C fabrics near shear zones
	Faulting	horizontal thrusting	N/R	N/R	N-NNE and NE-NW faults and shear zones, generally with dextral movement
	Folding	long wavelength isoclinal to recumbent folds (Luke Creek Group)	upright folds, vertical axial planes and horizontal fold axes (common in BIF)	D2 fold modification and N-NE to N-NW tight to isoclinal folds with vertical axial planes : DOMINANT STRUCTURE OF THE MURCHISON PROVINCE	F3 folds attenuated in D4 shear zones and folds
Archibald (1990)	**Fabric**	near bedding parallel schistosity	N/R	strong foliation (200-220°), moderate greenschist metamorphism and flattening of clasts	N/R
	Faulting	N/R	N/R	shear zones parallel to axial F3 fold surface with dextral strike slip	minor faults post-dating S3 schistosity
	Folding	N/R	early folding	mesoscopic folds, shallow to steep which contribute to local thickening: F1/F2 interference folds not identified	N/R
Frater (1978)	**Fabric**	N/R	N/R	close spaced, steeply dipping F3 axial planar cleavage	crenulation cleavage
	Faulting	N/R	N/R	NE-E faults (060-080°) steeply dipping and south block east (sinistral) movement	N-NE steep faults with east block south (dextral) displacement
	Folding	N/R	axial plane: 132°/78° SW plunging 40° NW	axial plane: 180°/80°W plunging 52° N	N/R
Clifford (1992)	**Fabric**	N/R	weak east-west cleavage in the Thundelarra Group	steeply dipping, F3 axial planar strong schistosity in all groups and intrusives	N/R
	Faulting	N/R	N/R	sub-horizontal faults intruded by dacite and dolerite: pre- to syn- NW D3 folding	north and east trending conjugate faults with dextral and sinistral displacement and intense quartz veining
	Folding	equivocal mesoscopic folds which may also be interpreted as soft sediment deformation	N/R	mesoscopic tight, upright steeply plunging NW trending folds	N/R

* sources are Watkins and Hickman (1990a) and Pidgeon and Wilde (1990), N/R structural element not recognised

ancient settings, where they are associated with active volcanism during periods of extension (Kappel and Franklin, 1989; Ben-Avraham and Zoback, 1992). Synvolcanic controls to the localisation and distribution of massive sulphide and alteration are reported from the Thalanga (Hill, 1996) and Hellyer (Downs, 1993) VHMS deposits. A key criterion to the identification of such structures is the recognition of abrupt facies changes or rapid thickness variations caused by contemporaneous volcano-sedimentary processes and faulting (Setterfield *et al.*, 1995; Berry and Keele, 1997). As a result of continued volcanism, structural activity and overprinting by successive deformational and metamorphic processes, the recognition of synvolcanic structures is largely equivocal, with the sites of these structures commonly occupied by later volcanic intrusions (Setterfield *et al.*, 1995).

A potential synvolcanic structure was identified at Gossan Hill based on a number of geological constraints. Such constraints include stratigraphic thickness variations, the localisation and asymmetry of alteration, massive sulphide and massive magnetite adjacent to the inferred structure, and a facies change due to the intrusion of a large dacite body along the structure. These features are discussed below.

4.3.1 Geological constraints

The Golden Grove Domain consists of a layered, north-south striking strata with a lateral continuation of 28 km. Small scale (mm to m) syndepositional normal faults are commonly observed throughout the strata and indicate structural activity during sedimentation. Larger scale syndepositional structures are also evident from facies analysis. At Gossan Hill, the strike continuity of the Golden Grove Formation (GGF) is interrupted by a dacite dome (DAC3; Clifford 1992) cognate with the overlying Scuddles Formation. This DAC3 dacite discordantly intrudes GGF M4 to GGF M6 and the hangingwall rhyodacite (RD2), forming a 'V' shaped wedge (Fig. 4.1). This intrusion is narrowest in GGF M4 (<2 m) and widest in GGF M6 and RD2 (>100 m) proximal to its inferred extrusion site (Fig. 4.1). The thickness of GGF M6 changes across this DAC3 dacite and is thickest on its southern side. Rhyodacite breccia facies overlying rhyodacite (RD2) is only observed on the southern side of the DAC3 dacite intrusion (Chapter 3). Rhyodacite breccia facies, which contains lithic clasts of rhyodacite and less commonly bedded sediment and massive sulphide, represents talus breccia formed during rhyodacite extrusion (Chapter 3).

The distribution of chemical facies and alteration adjacent to the dacite intrusive also supports the potential location of a synvolcanic structure. The thickest development of massive magnetite, massive sulphide, sulphide veins and intense wall rock alteration is located on the southern margin of the DAC3 dacite intrusion. The asymmetry of these chemical facies adjacent to DAC3 dacite is illustrated in Figure 4.1, with the thickness of massive sulphide, massive magnetite and the alteration intensity decreasing with distance away from DAC3 to the south. A sulphide stringer-silicification zone is also developed in GGF M5 adjacent to the dacite, connecting the Zn- and Cu-rich sulphide zones. Underlying the thickest development of massive sphalerite is a massive pyrite zone coincident with the southern margin of DAC3 in GGF M6. Archibald (1990) attributed

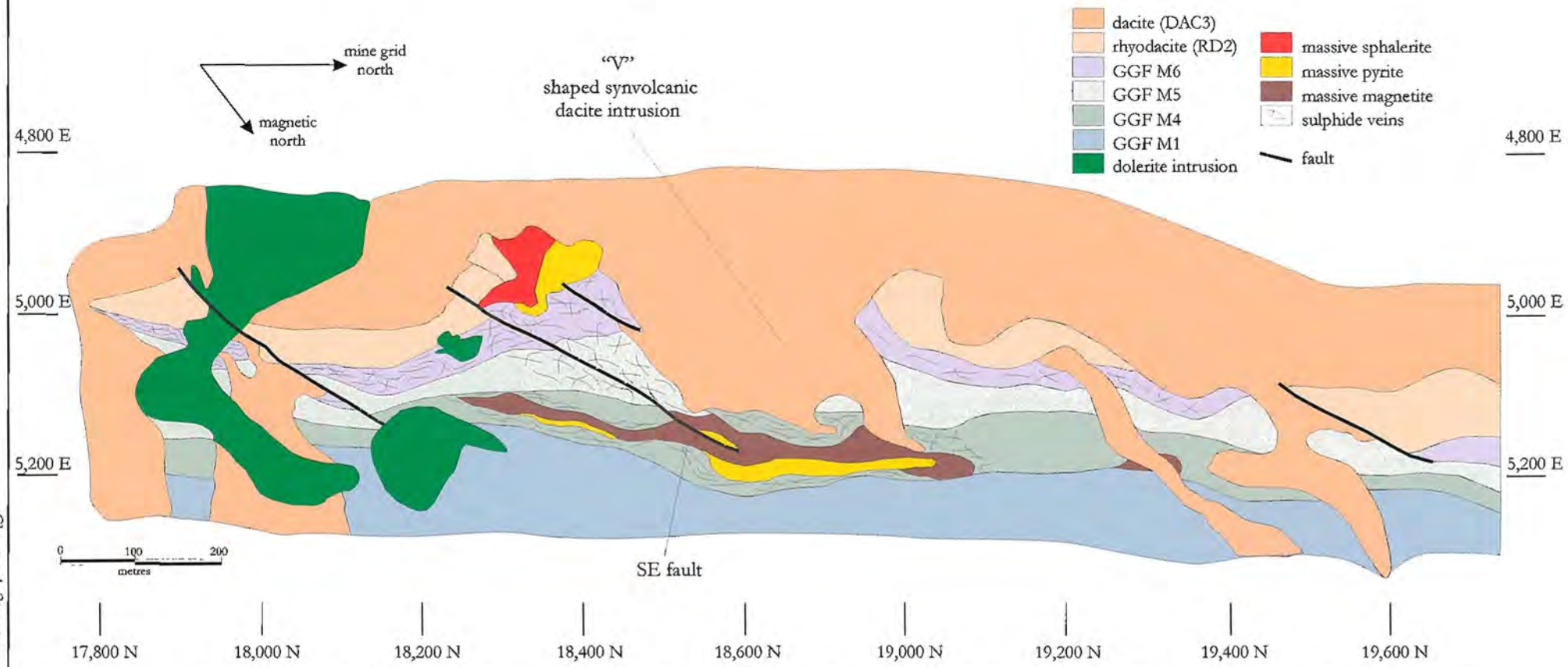

Figure 4.1: Composite level plan at 10,100 R.L. (250 m below surface) through Gossan Hill. The layered stratigraphy is north-south striking and a synvolcanic dacite (DAC3) cuts across stratigraphy forming a 'V' shaped intrusion at 18,800 N. Massive magnetite and massive pyrite are hosted by GGF M4 and massive pyrite-sphalerite by GGF M6 adjacent to this DAC3 intrusion. A well developed stringer zone also cuts stratigraphy in this area. Massive sulphide, massive magnetite and the alteration zones lens out to the south and, on the northern side of the dacite, weak stringer veining is present. The greatest stratigraphic thickness change occurs in GGF M6 from south to north across the DAC3 dacite, with the thickest development of GGF M6 at the site of massive sulphides on the southern side of the DAC3 dacite. This interpretation is compiled from transform east-west and plan interpretation work completed from the diamond drill hole database. Mine grid in metres.

the thickening of the Zn-rich massive sulphides in GGF M6 to folding associated with late brittle faulting. However, although some rotation of bedding is observed (Section 4.4), the thickening of GGF M6 could be partially attributed to shortening associated with dacite emplacement. On the northern side of the DAC3 dacite intrusion, sulphides are weakly developed in GGF M4 and GGF M6 as stringer veins, with massive sulphide absent.

These observations support the interpretation that DAC3 dacite represents the former site of a synvolcanic structure. The south side (down thrown block) was mineralised and the north side (up thrown block) was altered and weakly mineralised. It is proposed that the DAC3 dacite, which intrudes the host sequence and hangingwall rhyodacite, was extruded on to the seafloor along a growth structure. The absence of sulphides within the dacite indicates that this volcanism post-dates mineralisation. Moreover, the wedge shape of the dacite intrusion demonstrates that the original growth structure was subvertical in dip, with a north-south strike orientation.

Computer modelling of lithological boundary surfaces by MZC geologists using VULCAN software enabled the geometry and thickness variations of the stratigraphic units to be examined. Changes in the slope of the lithological contact for GGF M4-M1 and GGF M6-RD2 between the northern and southern sides of the DAC3 intrusion are observed (Fig. 4.2). A change in slope of the GGF M4-M1 lithological contact suggests potential rotation on the synvolcanic structure after deposition of GGF M1, but before GGF M4 deposition. Limited thickness variations in GGF M4 and GGF M5 indicate that minor reactivation, if any, occurred on the synvolcanic structure during the deposition of these units. The thickness variation in GGF M6 likely reflects structural activity at a time coincident with GGF M6 deposition and mineralisation. Smaller dacite intrusions north of the main intrusion (19,300 N, Fig. 4.2) may also represent synvolcanic structures. Thickness variations across these smaller dacites are not identified due to poorly constrained stratigraphic information in these areas, however, minor mineralisation and alteration adjacent to these sites support the inference that smaller dacite bodies may have also intruded pre-existing synvolcanic structures.

4.3.2 Synvolcanic structures at the Scuddles deposit

Evidence for synvolcanic fault structures are present at Scuddles and, due to its close proximity to Gossan Hill, is a comparable analogue. Review of geological modelling of the Scuddles deposit, generated using VULCAN software by MZC geologists, indicate that Scuddles has a similar lithological-structural framework to Gossan Hill. Figure 4.3 is a long section projection of stratigraphic and mineralised surfaces at the Scuddles deposit. A dacite intrusion (DAC3, Clifford, 1992) cuts across the layered stratigraphy at the southern end of the Scuddles deposit, intruding the Golden Grove Formation and the hangingwall DAC1 dacite. The thickest development and highest grades of massive sulphide abut this DAC3 dacite intrusion. Limited drilling on the southern side of the DAC3 dacite, indicates weak sulphide veining.

The orientation of the DAC3 dacite intrusions between the Scuddles and Gossan Hill

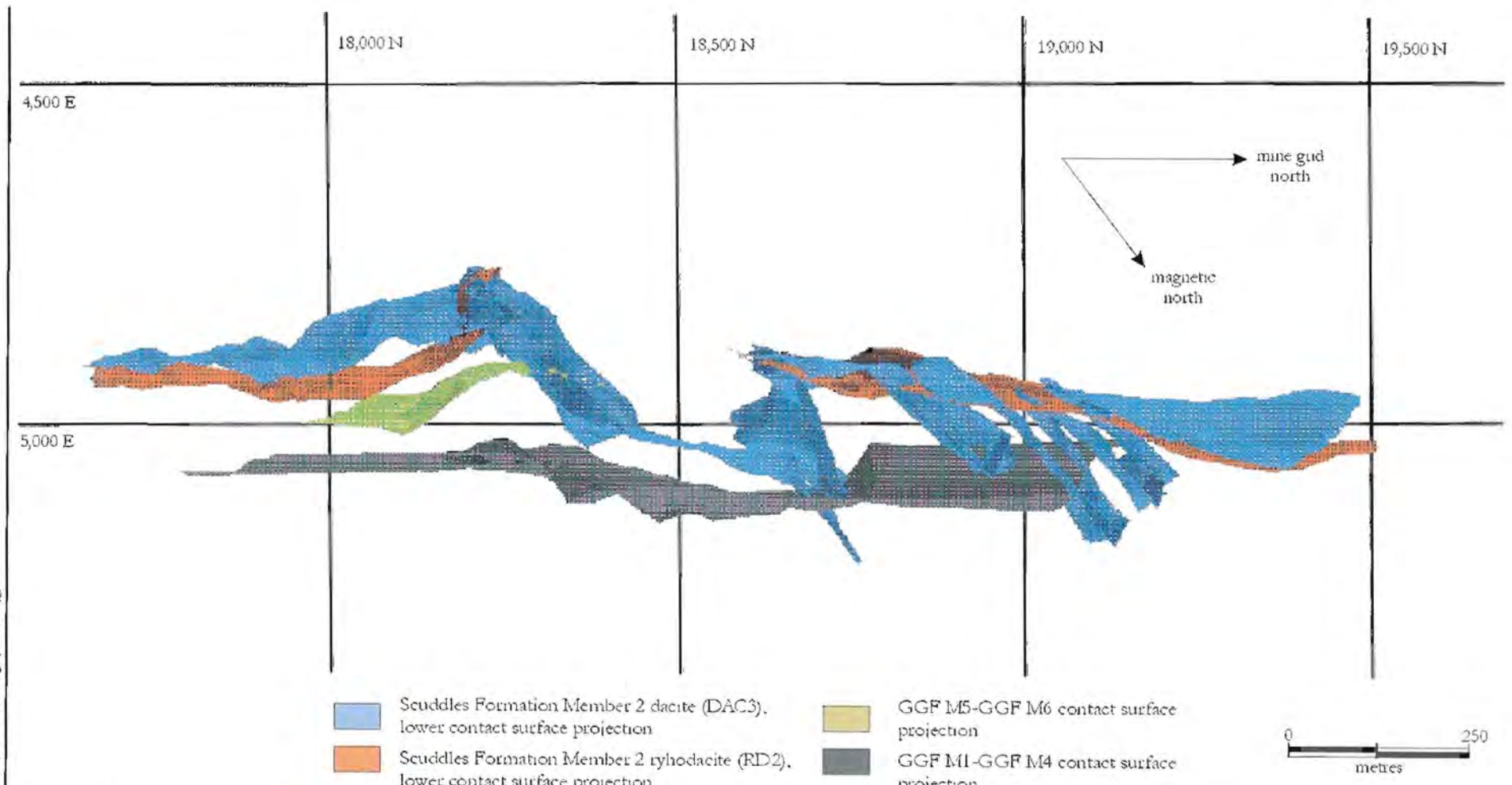

Figure 4.2: Longitudinal north-south projection of stratigraphic surfaces from the Gossan Hill VHMS deposit, with surfaces rotated to the horizontal. The three dimensional projection was generated using VULCAN software by MZC geologists. The image shows the footwall surface of the Scuddles Formation dacite (DAC3) in blue, as a 'V' shaped unit that cuts the Golden Grove Formation and the hangingwall rhyodacite (RD2). The dacite is interpreted to occupy the site of a former synvolcanic structure. The contact between GGF M1 and GGF M4 has a change in slope across the DAC3 intrusion suggesting synvolcanic activity on the structure prior to the deposition of GGF M4.

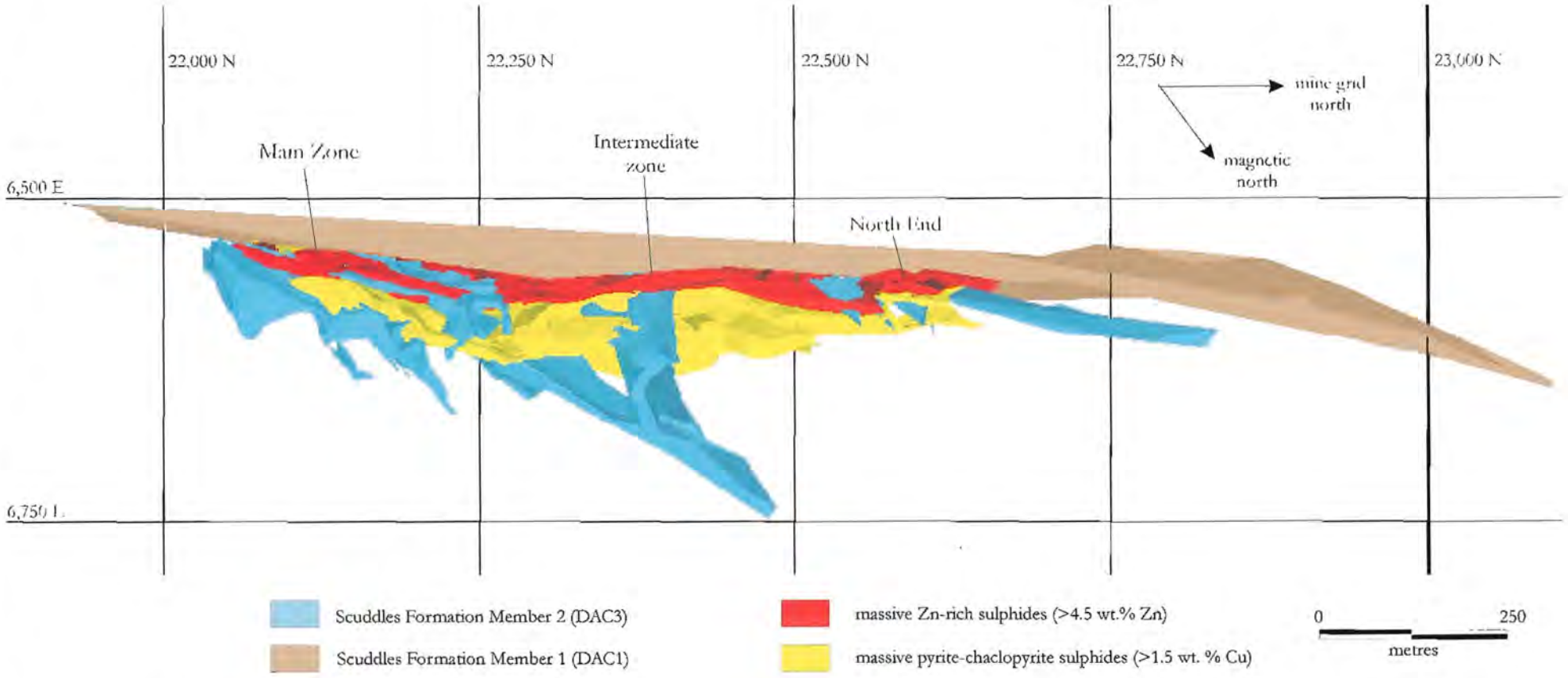

Figure 4.3: Longitudinal north-south projection through the Scuddles VHMS deposit with the stratigraphic surfaces rotated to horizontal. The model was generated using VULCAN software by MZC geologists from the underground diamond drill hole database. The dacite DAC3 (blue) is an elongate body that intrudes the Golden Grove Formation and the hangingwall DAC1 unit. Massive sulphides abut the DAC3 dacite on its northern margin and are coincident to the thickest development and highest grades of Cu and Zn. Massive sulphides underlie the hangingwall dacite DAC1 and thins to the north. The DAC3 dacite is interpreted to represent the site of a former synvolcanic structure. Smaller dacite intrusions at 22,350 N and at 22,600 N may also represent the sites of former synvolcanic structures and coincide with thickened zones of massive sulphide, known as the Intermediate Zone and the North End respectively.

deposits are similar (*c.f.* Figs. 4.2 and 4.3). No inference can be made on stratigraphic thickness changes at Scuddles from this modelling due to the limited data on the southern side of the DAC3 dacite intrusion. Facies work by Clifford (1992) however, identified a potential lateral thickness change in GGF M6 at the Scuddles deposit. In addition, Clifford (1992) also identified a fracture system with a steep 80° north pitch and inferred this structure to influence the thickness of massive sulphide and GGF M6. This DAC3 intrusion at Scuddles is interpreted to have similar structural and facies associations to that identified at Gossan Hill, and used a syndepositional structure, after the formation of massive sulphides, to its site of extrusion. Smaller, antithetic and synthetic DAC3 dacite bodies cut massive sulphide at the Intermediate Zone (22,350 N) and the North End (22,600 N) respectively, and are coincident with zones of increased thickness of massive sulphide (Fig. 4.3). These smaller dacite intrusions probably also used synvolcanic mineralising structures.

4.3.3 Gossan Hill and Scuddles: a structural model

Frater (1978) and Ashley *et al.* (1988) proposed structural models where sulphide mineralisation was localised by basin bounding fault structures. However, Clifford (1992) argued that such models were inconsistent with the observed lateral continuity of the layered stratigraphic package in the Golden Grove Domain, since the same basins that controlled the formation of mineralisation would have also controlled the localisation of the stratigraphic units. Clifford (1992) proposed a mechanism where syndepositional differential subsidence occurred in response to active growth structures. This mechanism would result in small scale topographic lows due to subsidence, rather than large scale scarp faults, thereby causing localised thickness variations consistent with the layered regional stratigraphy. Further observations in this thesis, including the presence of small-scale thickness variations and localised breccia due to local topographic depressions, also support Clifford's (1992) model.

The Gossan Hill and Scuddles deposits have similar relationships between stratigraphy, massive sulphide and structure. Based on these relationships, the DAC3 dacite bodies at both deposits are inferred to occupy synvolcanic structural sites. Although the orientation of the DAC3 dacites is similar, the orientation of massive sulphide zones, which abut the DAC3 dacite intrusions, differ. Massive sulphides and magnetite at Gossan Hill are thickest in the north adjacent to the dacite and lens out to the south (Fig. 4.1). At Scuddles, massive sulphide abut the dacite in the south, thinning and lensing out to the north (Fig. 4.3). A simple normal fault or graben model can not explain the different orientation of these mineralised zones. The structural model proposed to resolve these differences is a rotational block model as illustrated in Figure 4.4. A non-horizontal extensional regime, which induces rotational movement along synvolcanic growth structures, would generate local structural lows in opposing directions. Sulphide mineralisation forming in these structural lows explain the opposing trends of the mineralised zones between the Scuddles and Gossan Hill deposits. The rotational movement and resultant offset along these growth structures was small (10's m), due to the small scale thickness changes observed in GGF M6 and rhyodacite (RD2) across the

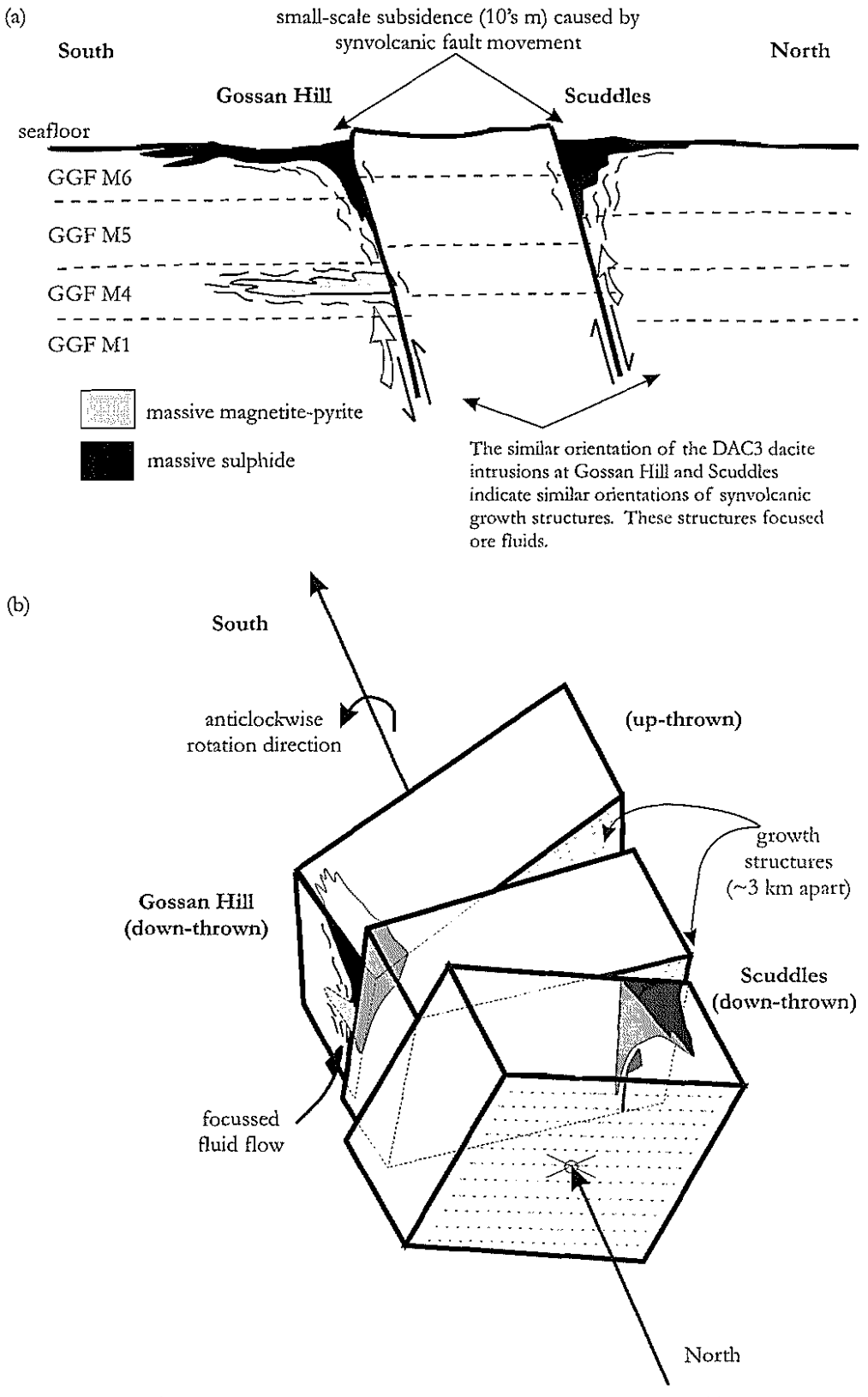

Figure 4.4: (a) Projected north-south schematic section through Gossan Hill and Scuddles. Massive sulphide at Scuddles is thickest in the south and lenses out to the north, whilst massive sulphide and magnetite at Gossan Hill are thickest in the north and lens out to the south. The dacite intrusions (DAC3) of the Scuddles Formation (SCF M2), are interpreted to represent the sites of subparallel synvolcanic structures along which mineralising fluids were focused. To explain the differences in the orientation of massive sulphides between Scuddles and Gossan Hill, as well as the similar orientation of the synvolcanic structures, a rotational block model (b) is proposed. (b) The rotational movement on synvolcanic structures results in locally developed structural lows, where the two deposits are sited. Rotational movement along these synvolcanic structures created local structural lows in which sulphide mineralisation was deposited, causing the opposing directions of the two deposits.

DAC3 intrusion at Gossan Hill. This rotational model is further supported by the change in the slope of the GGF M4-M1 surface across the DAC3 dacite intrusion (Fig. 4.2).

4.4 Bedding

Bedding at Gossan Hill strikes northwest to north-northwest, faces west and is subvertical to steeply west dipping (Fig. 4.5a). These trends are consistent throughout the entire Golden Grove Domain (Watkins and Hickman, 1990a; Clifford, 1992). Local variations in the strike and dip of bedding are interpreted to be the result of sedimentary structures including; cross bedding, slumping, syndepositional faulting and erosional contacts with mantled bedding. Irregularities in the strike and dip of bedding result principally from undulatory erosional surfaces and their mantling by overlying depositional units (*c.f.* Section 3.3.1). Syn-sedimentary slump folds are observed in GGF M1 (Fig. 4.6a) and are exposed at surface (18,450 N, 5,180 E). Cleavage clearly post-dates these intraformational folds, intersecting the bedding at an oblique angle. Intraformational slump folds reflect local instability of the sandstone and pebble breccia during deposition. Quartz-muscovite-chlorite alteration banding in GVF M4 is also subparallel to bedding (Fig. 4.5b), is cut by cleavage and likely reflects bedding in the sandstone.

Archibald (1990) interpreted a major second generation (F2) synformal fold at C zone (~18,400 N, Fig. 4.1) on the basis of form surfaces and vergence, as well as F1 folds in surface exposures of GGF M1. The results of this study illustrate that bedding is not folded with consistent upward facing in normal and reverse graded sediments that negates a folded stratigraphy (Fig. 4.5a). Archibald's (1990) F1 folds are interpreted here to be slump folds. Some local rotation of bedding is, however, noted in GGF M6 adjacent to massive sulphide and the hangingwall DAC3 intrusion.

4.5 Dolerite intrusions

Dolerite dykes and sills are volumetrically insignificant in the Gossan Hill mineralised zone. These dykes are less than 5 m wide, steeply dipping and discordant with chilled intrusive contacts. Margins may be undulose or sheared, but are generally planar, continuous and intrusive. Three phases of dolerite intrusion were identified in underground exposure. The earliest phase dips between 60° to 83° northeast-southwest and strikes 130° to 180° (Fig. 4.5c). A weakly developed spaced cleavage is developed in the muscovite-altered chill margins and is an indication of intrusion prior to penetrative deformation. The second phase of dolerite dykes intrudes the first phase and is fine-grained with well-developed chilled margins. Limited measurements on this dolerite dyke indicate a dip of 60° to 80° northeast to southeast and strike of 020° to 162° (Fig. 4.5c). A weakly developed cleavage through this dolerite is also an indication of intrusion prior to penetrative deformation.

The third dolerite intrusive phase postdates the first and second phases, as well as the rhyolite intrusions. This third dolerite phase has highly irregular contacts dipping between 55° to 80° south to southeast, striking mainly at 020° (Fig. 4.5d). Thickness of

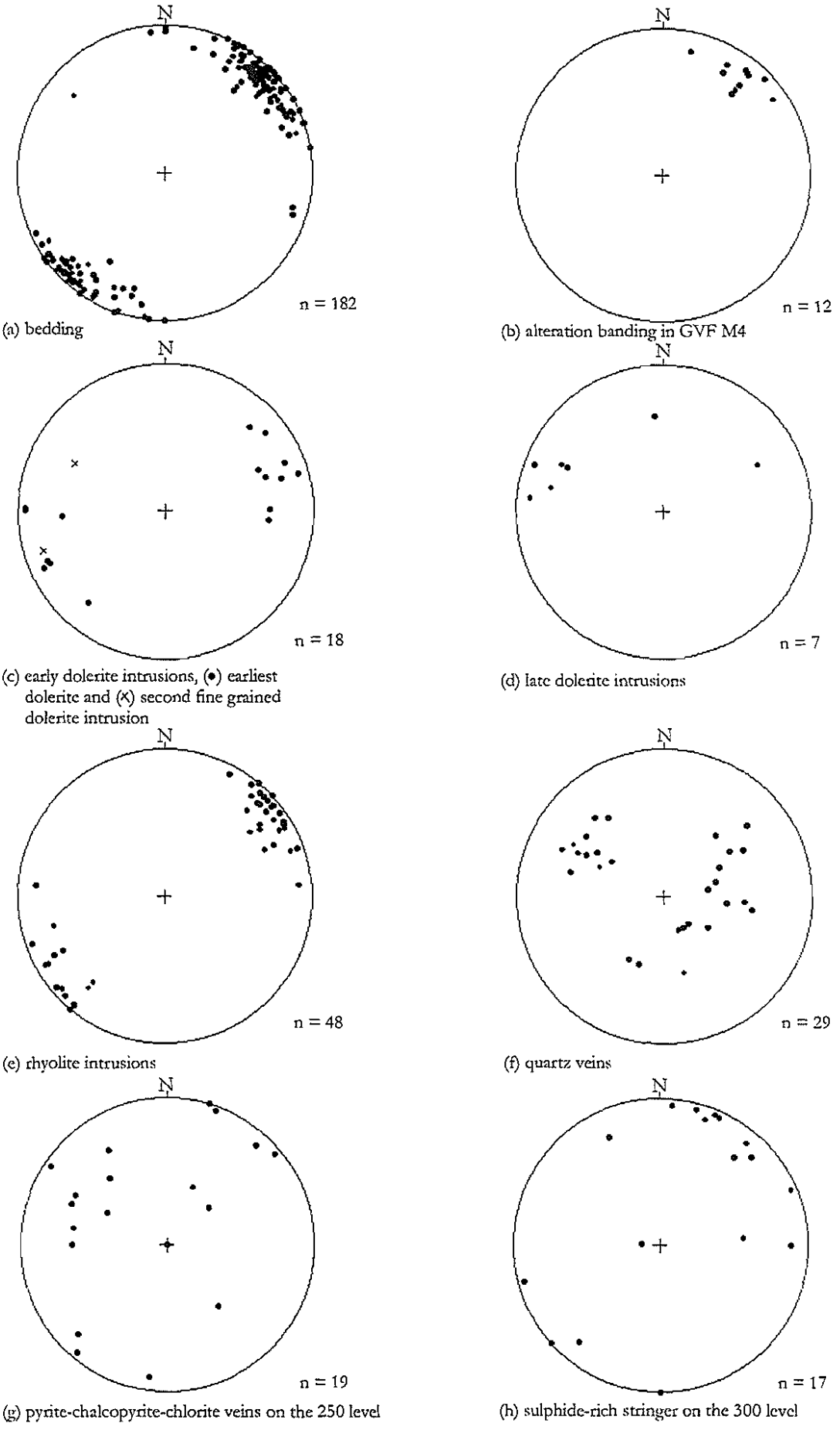

(a) bedding

(b) alteration banding in GVF M4

(c) early dolerite intrusions, (•) earliest dolerite and (×) second fine grained dolerite intrusion

(d) late dolerite intrusions

(e) rhyolite intrusions

(f) quartz veins

(g) pyrite-chalcopyrite-chlorite veins on the 250 level

(h) sulphide-rich stringer on the 300 level

Figure 4.5: Equal area stereonet projections of (a) poles to bedding (GVF M4 and GGF M1 to M6 inclusive), (b) poles to quartz-muscovite-chlorite alteration banding in GVF M4, (c) poles to early dolerite intrusions, (d) poles to late dolerite intrusions, (e) poles to rhyolite intrusions, (f) poles to early quartz veins in intensely silicified GGF M4 indicating two conjugate vein orientations and (g-h) poles to sulphide veins in mineralisation of GGF M4, GGF M5 and GGF M6 from the 250 and 300 level respectively.

Figure 4.6

(a) Slump folding (arrows) of a sandstone bed within a sequence of thinly bedded sandstone and pebble breccia of GGF M1. Intensely silicified sandstone beds have white siliceous haloes along the bed margins (Cuddy #4, 5,185 E, 18,677 N).

(b) Planar continuous southeast fault in silicified breccia and sandstone of GGF M1. The banded antitaxial fault vein is filled by quartz, carbonate, chlorite and wall rock fragments. Adjacent quartz-carbonate veins parallel the fault plane and are discontinuous. Rock bolts are 40 cm long (Cuddy #7, 5,184 E, 18,543 N).

(c) Quartz-chlorite striations on a southeast fault surface. The fault is in a pebble breccia of GGF M1. Quartz-chlorite striations have two orientations, both of which indicate reverse movement. The first reverse movement is steeper at 75° and the second at 50° (Cuddy #6, 5,185 E, 18,604 E).

(d) Sharp intrusive contact between a late stage rhyolite intrusion and massive breccia of GGF M1. The rhyolite has pervasive muscovite alteration and contains a spaced cleavage. Cleavage is also strongly developed in GGF M1 breccia adjacent to this rhyolite intrusion. A small discontinuous southeast fault offsets the rhyolite margin and has a dextral sense of displacement. Quartz, carbonate and chlorite in fill the fault vein. Rock bolts are 40 cm long (300 level, 5,075 E, 18,235 N).

(e) Southeast oriented, carbonate-quartz filled antitaxial fault zone in massive dolerite. A halo of chlorite-muscovite alteration envelops the fault zone. Cleavage, which is well developed in the alteration halo around the fault, is wrapped into the fault and indicates reverse movement (Cuddy #3, 5,194 E, 18,716 N).

(f) Sheared contact between massive quartz altered breccia and sandstone of GGF M1 and magnetite-pyrite-chlorite altered units of GGF M4. This contact has an intense cleavage within chlorite altered GGF M4. Sulphide veins in GGF M4 are subparallel the direction of shearing. Discontinuous quartz-carbonate veins occur in GGF M1 adjacent to the fault and reflect brittle deformation in the silicified breccia. Rock bolts are 40 cm long (300 level, 5,027 E, 18,243 N).

(a)

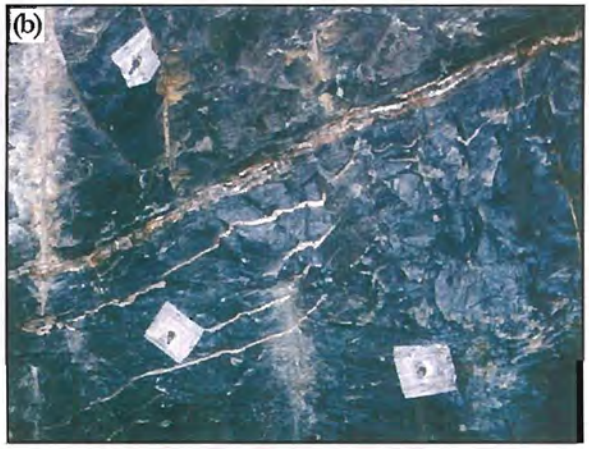
(b)

(c)
CM
IN
DNAG

(d)
07
130

(e)

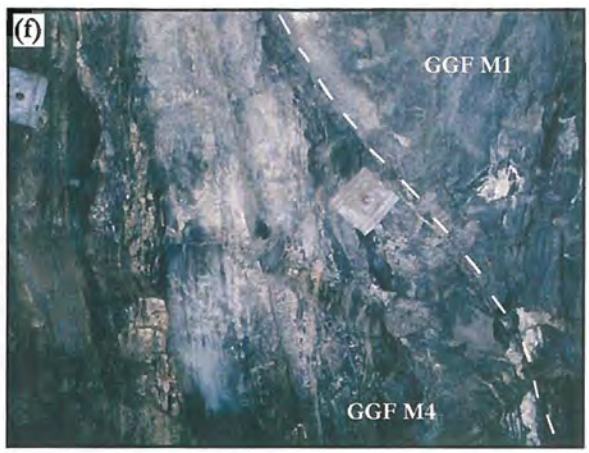
(f)
GGF M1
GGF M4

the late stage dolerite varies between 0.1 to 3 m. The absence of a cleavage in this dolerite supports a late stage intrusion, possibly analogous to the Proterozoic dolerites observed elsewhere in the Warriedar Fold Belt (Watkins and Hickman, 1990a).

Flat lying dolerites at Gossan Hill are interpreted from drill hole data to be less than 50 m thick and occur close to surface in the south of Gossan Hill where they occur at the base of weathering. The timing and orientation of these flat lying dolerites is not constrained, but may have a similar timing to the first and/or second phase of dolerite intrusions due to cleavage within chilled margins.

4.6 Rhyolite intrusions

Rhyolites intrude all members of the GGF but are intruded by late stage dolerite (Section 4.5). Rhyolite intrusions are subparallel to bedding and form narrow, steeply dipping to subvertical dykes with margins ranging from sharp and planar to locally sheared and veined. These dykes are frequently 1 to 5 m wide, but range down to less than 30 cm. Rhyolites strike 130° to 185°, dipping between 65° and 90° southwest to northeast and often have flow banded margins (<20 cm wide) (Fig. 4.5e). Cleavage is poorly developed within these rhyolite intrusions but where present, is spaced and weakly developed in the muscovite altered, flow banded margins.

4.7 Faults

All faults observed at Gossan Hill are late brittle structures with small displacements (generally less than 2 m). Two main movement directions are identified from quartz-chlorite-carbonate striations on fault surfaces. These movements are reverse and dextral wrench, with the wrench displacement commonly overprinting earlier reverse displacement. Faults are subdivided below into four groups according to the orientation of fault surfaces, namely; southeast, east, north and southwest.

4.7.1 Southeast faults

The southeast fault orientations are the most common faults recorded underground. All stratigraphic units including GGF M1, M4, M5, GVF M4, dolerite and rhyolite intrusions, and magnetite-copper mineralisation host these southeast striking faults. In many cases, these faults define the contact between two units (*e.g.*, GGF M1 and dolerite) and are less than 20 cm wide with banded antitaxial vein and wall rock fragment infill (Fig. 4.6b). Fault veins are muscovite-chlorite or chlorite-quartz-carbonate-pyrite with muscovite altered sheared rock fragments. Wall rocks to the faults are locally sheared indicating strong brittle deformation adjacent to the fault. Southeast striking faults dip steeply and are subparallel to both bedding and cleavage (Fig. 4.7a), although most faults generally have a shallower dip than bedding (*c.f.* Figs. 4.5a and 4.7a). Chlorite shear zones parallel to bedding occur as narrow zones between more competent beds and are included as part of the southeast fault group. Movement on fault planes, as indicated by striations (Figs. 4.6c and 4.7b) and offset strata (Fig. 4.6d), is commonly reverse (with minor dextral or sinistral components) and may be overprinted by wrench and/or and reverse movements (Fig. 4.7c). The most common ordering of fault movement, indicated from overprinting

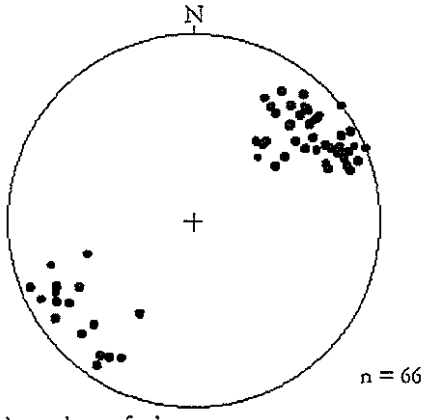

(a) southeast faults

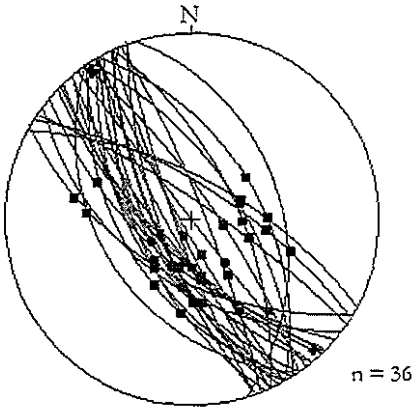

(b) southeast fault striations
(■) reverse, (•) dip slip, (+) dextral

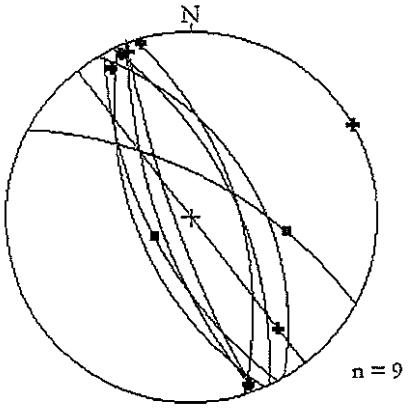

(c) southeast faults, overprinting striations
(■) reverse, (+) dextral

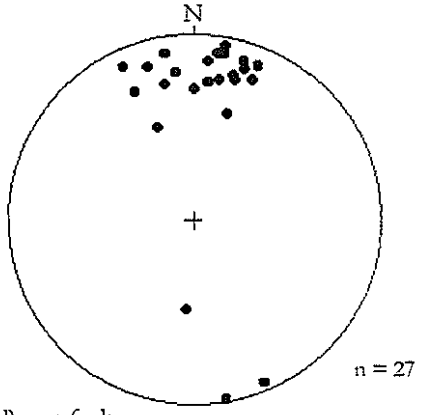

(d) east faults

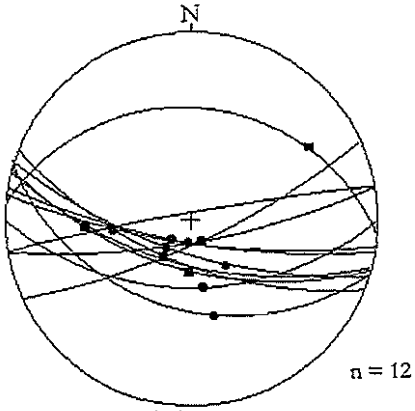

(f) east faults striations
(■) reverse, (•) dip slip

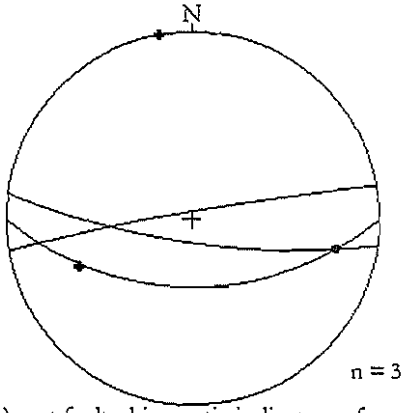

(e) east faults, kinematic indicators of second reactivations (+) dextral

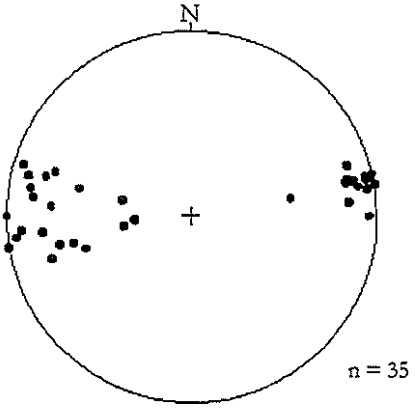

(g) north-south faults

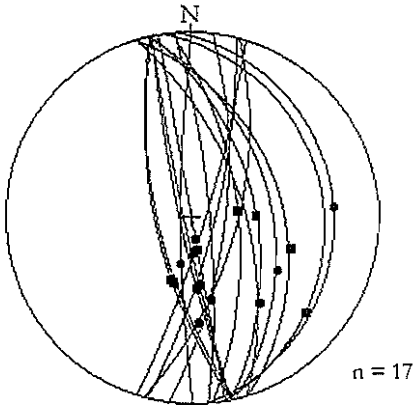

(h) striations on north-south directed faults
(■) reverse, (•) dip slip

Figure 4.7: Equal area stereonet projections of (a) poles to all southeast faults measured, (b) striations on southeast faults, (c) overprinting striations on southeast faults, (d) poles to all measured east faults, (e) striations on east faults, (f) overprinting striation movement indicators on east faults (g) poles to all measured north-south faults and (h) striations on north-south faults.

striations, is earlier reverse followed by dextral wrench. Cleavage and bedding drag is observed in these faults indicating cleavage formation prior to or synchronous with fault movements. Cleavage drag (Fig. 4.6e) record reverse and dextral fault movements that post-date cleavage formation.

A southeast striking 1.5 m shear zone (Fig. 4.6f) offsets the contact between GGF M1 and M4 on the 300 level. This fault zone marks the contact between the unmineralised GGF M1 footwall and magnetite-Cu mineralisation. GGF M1 is intensely quartz altered and GGF M4 is intensely chlorite-carbonate-pyrite altered. Adjacent to this faulted contact, the orientation of sulphide-carbonate veins in GGF M4 parallels the direction of shearing. Extensional quartz veins are developed adjacent to this structure across the direction of shear and consist of chalcopyrite-pyrite-quartz extensional veins (Fig. 4.8a). Quartz veins occur on the eastern side of the fault in GGF M1. Kinematic indicators recorded two deformation events; (1) an early dip slip event, and (2) a later dextral wrench. The magnitude of displacement is not known, but geological constraints from drilling indicate it is a few metres.

A zone of brittle deformation at the stratigraphic contact between the GGF M1 and GVF M4 is illustrated in Figure 4.9. The contact plane is marked by a southeast striking fault, although north-south, east and southwest faults also occur in this locality, as well as abundant veins with similar orientations to the faults. The main fault group present is the southeast striking fault group. The area represents a zone of brittle faulting in competent GVF M4 units, which offset the GGF M1-GVF M4 contact by an estimated 50 m (Fig. 4.9).

Rhyolite intrusions commonly have southeast-southwest striking faulted contacts. In some cases, shearing parallel to the faults is parallel to the muscovite-altered rhyolite flow banded margins and is denoted by a locally intense foliation. The offset of rhyolite margins indicates reverse displacement, generally less than 1 m. Carbonate-quartz veins parallel to the fault are also offset and indicate that reverse movement post-dates fault and vein propagation.

Within massive pyrite-magnetite in GGF M4 a southeast fault has a 122° strike, dipping 55° to 75° north. This fault is up to 1 m wide, with a quartz-carbonate-chlorite-wall rock and magnetite-pyrite-pyrrhotite filled antitaxial vein and a sheeted planar fault trace (Fig. 4.8b). Strong adjacent zones of shearing are present in the chlorite-magnetite-sulphide altered host. Cleavage drag into the fault indicates movement after/or synchronous with cleavage formation, with both chlorite-quartz striations and cleavage drag indicating reverse movement. Overprinting striations associated with a later wrench movement are developed upon earlier striations associated with reverse movement. This fault has strong cleavage in the adjacent intensely chloritised wall rock and offsets the magnetite-pyrite zones (*c.f.* Fig. 4.1).

4.7.2 East faults

East striking faults are observed within GGF M1, M4, M5 and massive pyrite and dolerite intrusions. These faults have planar fault traces and are less than 40 cm wide

Figure 4.8

(a) Faulted contact between massive pyrite-magnetite-chlorite and tuffaceous breccia in GGF M1 footwall. Subhorizontal extensional chalcopyrite-rich veins penetrate from the sulphide zone into the silicified footwall zone. These veins are extensional veins associated with a southeast adjacent fault and the local remobilisation of sulphides into fractures (300 level, 5,034 E, 18,248 N).

(b) Planar southeast fault and sheared zone within intense chlorite alteration of sandstone in GGF M4. The fault has a 50 cm quartz-carbonate vein and contains sheared chloritic altered wall rock. Both reverse and dextral movement striations were observed along this fault. Rock bolts are 40 cm long (300level, 4,974 E, 18,490 E).

(c) Undulose, discontinuous white quartz veins in an intensely silicified GGF M4 siltstone. These quartz veins form subparallel sets of veins that are truncated against a larger pyrite-chalcopyrite-chlorite stringer vein. Rock bolts are 40 cm long (250 level, 5,103 E, 18,457 N).

(d) Pyrite-chalcopyrite-chlorite stringer veins hosted by intensely silicified sandstone of GGF M4. The stringer veins form a regular pattern of wide continuous veins, with abundant small (<10 mm) pyrite-chalcopyrite-chlorite veins in the wall rock. Early quartz veins (top left) are narrow, undulose and discontinuous, but have similar orientations to some of the pyrite-chalcopyrite-chlorite veins. Rock bolts are 40 cm long (250 level, 5,103 E, 18,465 N, *c.f.* Fig. 3.8).

(e) Subparallel adjacent pyrite-chlorite veins in an intensely chlorite altered bedded sandstone of GGF M4. The pyrite-chlorite veins are subparallel to bedding and cleavage (250 level, 5,109 E, 18,440 N).

(a)

(b)

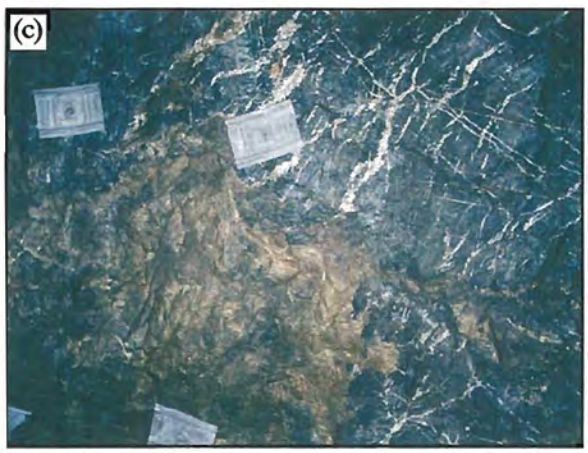
(c)

(d)

(e)

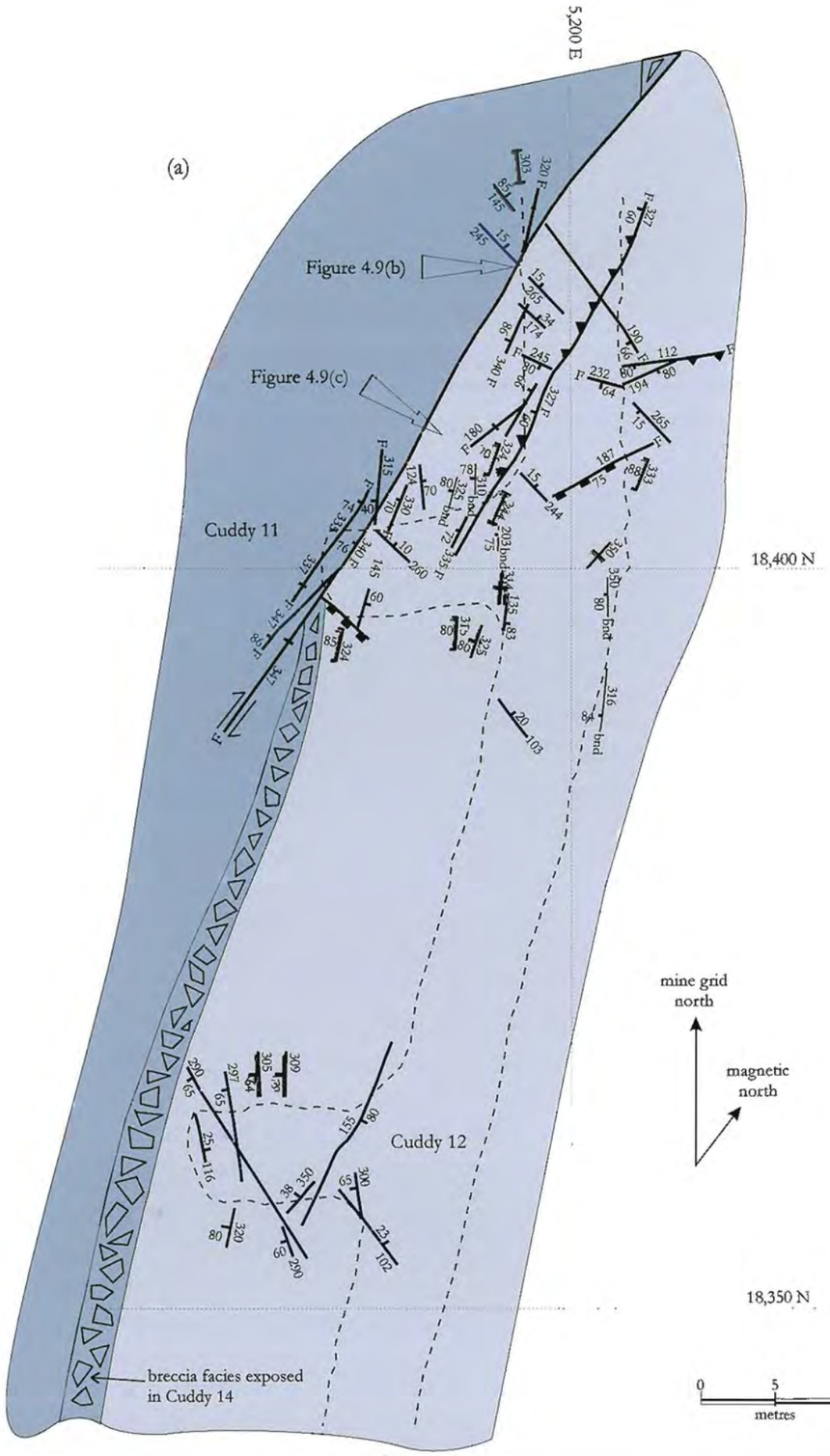

GGF M1, bedded sandstone and breccia

GGF M1, coarse-grained breccia

GVF M4, sandstone

bedding, dip and strike

bedding, vertical and strike

cleavage, dip and strike

bnd alteration banding in Member GV4

cleavage, vertical and strike

quartz-carbonate-chlorite veins dip and strike

F fault, dip and strike

F normal fault

F reverse fault

decline outline

Figure 4.9: (a) A zone of brittle deformation at the contact between GVF M4 and GGF M1 is exposed in Cuddy 11. The southern side of the contact is strongly faulted by an array of southeast faults and offset by a dextral wrench component of approximately 50. The southern side of the faulted contact is an array of southeast faults, as well as east, north-south and southwest faults. Abundant quartz-carbonate and carbonate-quartz-chlorite veins with similar orientations to the faults are present and are interpreted to be associated fault development. Away from the fault contact, GVF M4 in Cuddy 12 hosts abundant quartz-carbonate-chlorite syntaxial and antitaxial veins. Alteration banding is strongly developed in GVF M4 in this area, with the alteration predating faulting, veining and cleavage. The veining in Cuddy 12 and the veining and faulting in Cuddy 11 reflect brittle deformation in competent footwall lithologies with faulting developed proximal to the lithological boundary. (b) The faulted contact between GVF M4 and GGF M1 in Cuddy 11. Subhorizontal, planar quartz-carbonate veins offset by late dextral movement on the fault. (c) Flat lying, sheeted east-west quartz-carbonate veins in Cuddy 11. Location of (b) and (c) are indicated in (a).

with banded quartz, carbonate, chlorite and wall rocks fragment infill. The dips of east striking faults vary between 40° south to subvertical (Fig. 4.7d) and have at least two movements. Kinematic indicators on fault planes predominantly record dip slip movement and less commonly reverse movement (Fig. 4.7e). Overprinting striations, where present, indicate a dextral reactivation sense to east faults that had earlier dip slip movement (Fig. 4.7f). Small-scale (<1 m) dextral displacement is also confirmed by the offset of dolerite margins. East oriented faults rarely have cleavage drag and movement is interpreted to be small (less than a few metres).

4.7.3 North-south faults

North-south striking faults (Fig. 4.7g) cut across all stratigraphic units from GVF M4 to GGF M6, as well as dolerite and rhyolite intrusions, and have similar orientations to the early dolerite intrusions. North-south faults often form the contact between intrusive phases and the host rock. These faults have planar, sheeted fault planes with antitaxial, banded vein fill. Fault veins are between 0.2 to 20 cm wide and consist of quartz, carbonate, chlorite and wall rock, with minor pyrite and muscovite. Some faults have muscovite-chlorite halos forming up to 20 cm zones that envelop the fault. Alteration halos can form strongly foliated envelopes, with foliation parallel to the fault plane. Kinematic indicators record reverse and dip slip fault fibres, with the most common fault movement being pure reverse (Fig. 4.7h). Cleavage drag is observed at some north-south faults that have reverse kinematic indicators. Indicators of secondary fault reactivation are rare and indicate secondary dextral wrench movement along fault planes that have earlier reverse kinematic indicators (Fig. 4.10a). Associated quartz-carbonate veins form sheeted flat lying veins (Section 4.8). The timing of north-south faults is similar to that of the southeast faults, with the faults pre- to syn-cleavage formation and last movement on the fault planes post-dating cleavage development.

4.7.4 Southwest faults

Southwest striking faults occur within GGF M1, GVF M4 and dolerite intrusions. These faults have planar traces, dips that vary from between 46° southeast to subvertical (Fig. 4.10b) and are the least abundant fault type recorded. Southwest faults are zones between 1.5 to 20 cm wide, with banded and antitaxial fault veins of quartz, carbonate, muscovite, wall rock and minor pyrite. Kinematic fault movement indicators recognised include normal dip slip and reverse movements (Fig. 4.10c). At least two fault movements are indicated, but the timing relation between these movements could not be established due to the absence of overprinting kinematic fibres. Associated veins are filled with quartz, carbonate and chlorite, with banded, discontinuous or sigmoidal vein forms.

4.8 Veins

Vein groups were divided into six types on the basis of orientation. The earliest veins identified at Gossan Hill are quartz veins (Section 4.8.1) that are cut by sulphide-rich stringer veins (Section 4.8.2). In addition, four groups of quartz, carbonate, chlorite veins associated with late brittle deformation are identified. These four vein groups are

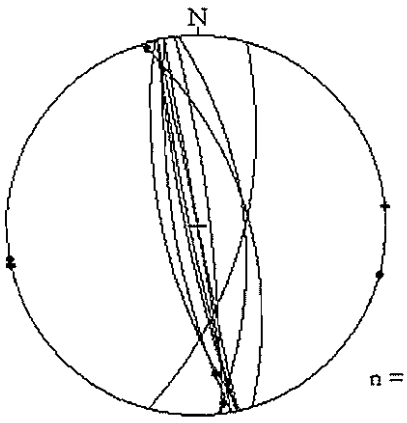

(a) north-south faults, overprinting second striations (+) dextral

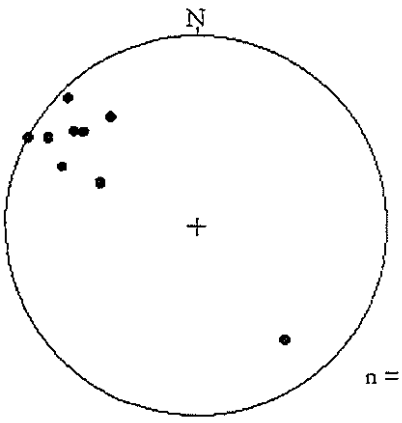

(b) southwest faults

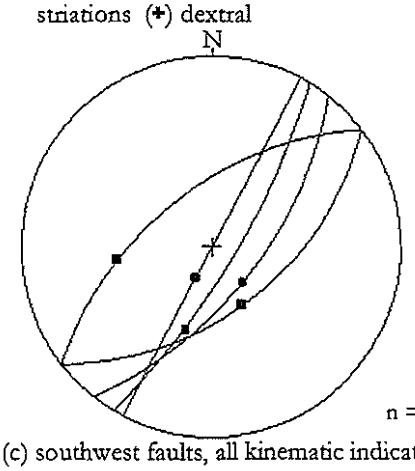

(c) southwest faults, all kinematic indicators (■) reverse, (•) dip slip

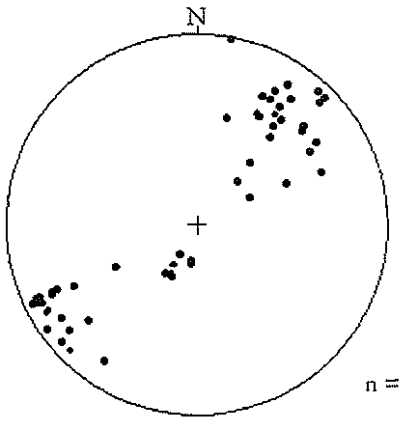

(d) southeast veins

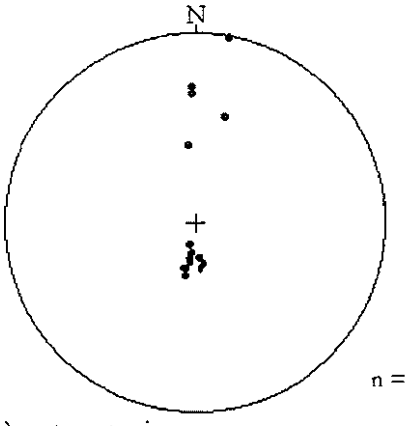

(e) east-west veins

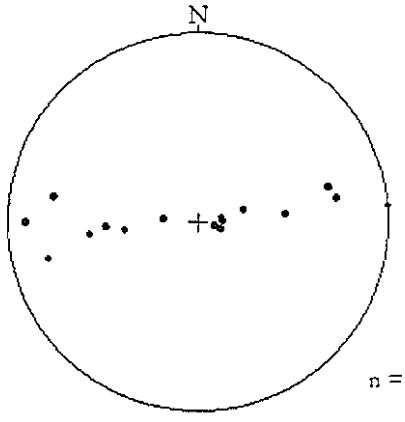

(f) north-south veins

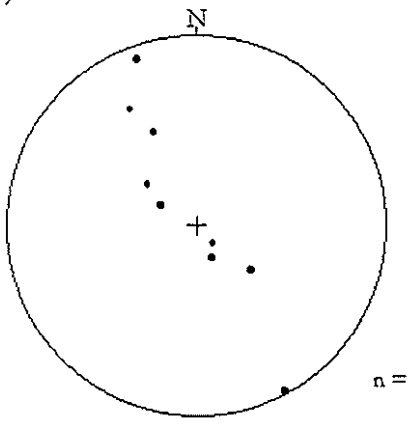

(g) southwest veins

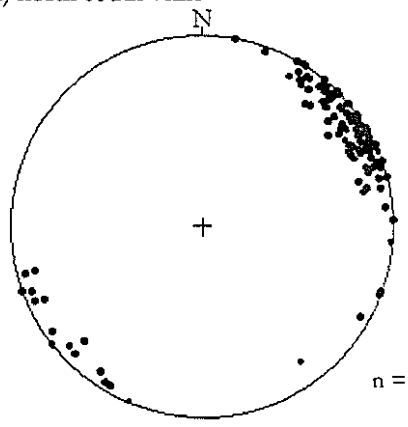

(h) cleavage (S3)

Figure 4.10: Equal area stereonet projections of (a) overprinting striations on north-south faults, (b) poles to southwest faults (c) all striation movement indicators on southwest faults (d-g) poles to late brittle quartz-carbonate-chlorite veins with, (d) poles to southeast veins, (e) poles to east-west veins, (f) poles to north-south veins, (g) poles to southwest veins and (e) poles to S3 cleavage planes.

characterised by southeast, east-west, north-south, and southwest vein orientations, which are identical to the orientation of faults previously discussed.

4.8.1 Pre-mineralising quartz veins

Quartz veins exposed underground on the 250 level are hosted by intensely silicified GGF M4 volcaniclastics within a sulphide stringer zone. The exposure of these quartz veins is limited to a 60 m wide zone underlying massive pyrite-magnetite mineralisation, and are not identified elsewhere. Quartz veins range in thickness from 1 to 4 cm and vary from sheeted, continuous to undulose and discontinuous veins that are infilled by white quartz (Fig. 4.8c). Some quartz veins host minor chlorite, chalcopyrite and pyrite. Two conjugate quartz vein orientations are recognised (Figs. 4.5f and 4.11). These two vein sets form arrays of subparallel or stepped veins with a southeast (139° to 189°) or southwest (195° to 247°) strike and dips of 25° to 63° southwest and 40° to 65° southeast respectively. The quartz veins reflect brittle deformation of the wall rock, indicating that GGF M4 was competent at the time of quartz vein formation. Quartz veins are absent from adjacent zones of chlorite alteration within GGF M4 (Fig. 4.11).

Quartz veins are truncated and transected by sulphide stringer veins (Figs. 4.8c and 4.11). This indicates that quartz veins formed prior to the sulphide veins and preceded massive sulphide formation within GGF M4. Early quartz veins therefore, represent pre-mineralising veins that formed during a period of north-south extension.

4.8.2 Sulphide veins

Sulphide stringer veins overly and underlie massive sulphide in GGF M4, M5 and M6. These stringer veins are generally pyrite-rich and have variable continuity, width, orientation and host associations. Silicified wall rock fragments may be found within some sulphide veins, indicating antitaxial vein formation. In some occurrences, sulphide veins can have strong fracture control, forming consistently orientated subparallel vein sets (Figs. 4.8d and 4.11). However, the orientation of sulphide veins varies between zones of mineralisation and alteration. This section reviews the orientation of sulphide veins and examines potential structural control to these mineralising conduits. The occurrence and distribution of sulphide veins is further evaluated in Chapter 5.

Sulphide veins on the 250 level consist of pyrite, chalcopyrite and chlorite and have some similar vein orientations to the early quartz veins (*c.f.* Figs. 4.5g and 4.5f), whilst some veins parallel bedding (*c.f.* Figs. 4.5g and 4.5a). Sulphide veins on the 300 level have stronger bedding control than veins from the 250 level, with veins mostly parallel to bedding (Figs. 4.5h and 4.8e). The orientation of sulphide veins from the 250 and 300 level indicates that sulphide veins had strong control from pre-existing fractures in the host rock, represented by early white quartz veins, as well as lithological control by bedding planes. The absence of early quartz vein trends from sulphide vein orientations on the 300 level reflects stronger bedding control to sulphide veins. The limited distribution of early quartz veins within GGF M4 also indicates their limited influence during sulphide vein formation.

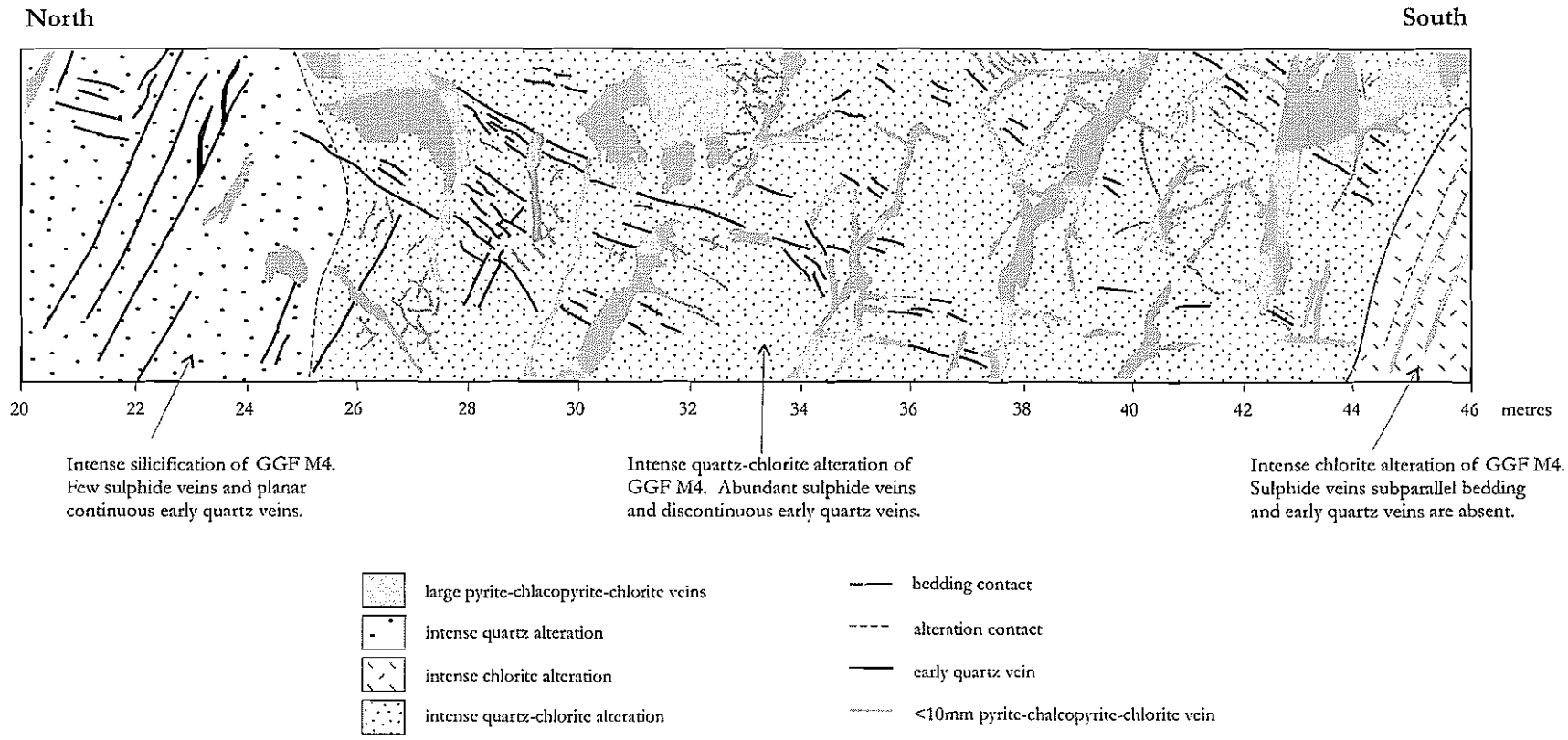

Figure 4.11: Underground wall mapping from the 250 level. Pervasive intense quartz altered sandstone-siltstone of GGF M4 host early quartz veins, as well as sulphide veins. Early quartz veins form subparallel, sheeted to discontinuous veins. Sulphide veins cut across early quartz vein, with some sulphide veins paralleling the early quartz veins. At 44 metres a conformable alteration boundary from quartz to intense chlorite alteration occurs. This contact marks the transition of sulphide veins to bedding-parallel orientations and the absence of early quartz veins from intense chlorite alteration. Vertical scale = horizontal scale.

4.8.3 Southeast veins

Southeast striking veins are the most abundant veins occurring within GVF M4, GGF M1, GGF M4 and dolerite intrusions. Southeast veins are less than 3 cm wide, syntaxial to antitaxial veins filled with white quartz-carbonate or carbonate-quartz-chlorite-pyrite. The vein style is typically planar and sheeted, frequently with stepped subparallel veins. The dip of this vein group varies from shallow (<20°) to subvertical (Fig. 4.10d). Southeast veins parallel and are spatially associated with the southeast fault group, where these veins formed as extensional veins, commonly having extensional fibre fill.

Quartz-carbonate veins parallel and cut across the contact margins of the early dolerite intrusions, indicating post-dolerite vein formation. Dextral offset of these veins at the margins of dolerite indicates that movement on southeast faults occurred after vein formation. Similar observations are made in southeast veins adjacent to the rhyolite intrusions, with veins having reverse offset and crenulation due to cleavage (Section 4.9). Alteration halos enveloping southeast veins include quartz, muscovite-quartz and chlorite halos that penetrate up to 40 cm into the wall rock (Fig. 4.12a). Southeast veins also parallel the alteration banding in GVF M4 (Fig. 4.12b). The orientation of the southeast veins is generally shallower than bedding and subparallel cleavage and the orientation of rhyolite intrusions. Veins may be offset by movement on southeast faults and displaced or crenulated by the penetrative cleavage.

4.8.4 East-west veins

East-west striking veins occur within GVF M4, GGF M1, GGF M4 and dolerite and rhyolite intrusions. Vein contain quartz-carbonate fill and are up to 4 cm wide. Veins are generally planar and continuous, but may also be sigmoidal or stepped. East-west veins vary from shallow (10° to 30°) to steeply dipping veins (40° to 60°) (Fig. 4.10e). Steeper east-west veins have cleavage related deformation, including crenulation and displacement in the plane of cleavage (refer Section 4.9.1). East-west veins cut across the southeast fault (Fig. 4.12c) and north-south fault groups, and are commonly offset by reverse displacement on these faults. Vein formation was most likely synchronous to these fault groups.

4.8.5 North-south veins

North-south striking veins are less than 10 cm wide and have banded quartz-carbonate or carbonate-chlorite vein fill. They occur in GGF M1 and GVF M4 as well as dolerite and rhyolite intrusions. The style of vein is sheeted to discontinuous and sigmoidal. The dip of north-south veins varies from shallow (10°) to subvertical (Fig. 4.10f). North-south veins parallel the orientation of dolerite intrusions and north-south faults, but cut across some southeast faults. Where associated with southeast faults, veins form flat lying stepped, subparallel extension veins. Chlorite and muscovite-quartz halos less than 10 cm wide commonly envelop these veins. Reverse offset of north-south veins across southeast faults is consistent with reverse striation movement indicators (<30 cm) on southeast faults. The reverse offset of north-south veins indicates vein formation synchronous to, or earlier than, fault formation.

Figure 4.12

(a) A planar carbonate-quartz-pyrite southeast vein within sandstone of GGF M1. The vein has an asymmetric, 3 cm quartz alteration halo. Minor undulations in the planar trace of the vein are the effect of a high angle anastomosing cleavage in the wall rock and vein (250 level, 5,120 E, 18,436 N).

(b) A continuous, planar carbonate-chlorite vein that has a well-developed quartz-muscovite alteration halo. The halo forms a narrow envelope around the vein. This southeast oriented vein occurs in GVF M4 sandstone and parallels quartz-muscovite-chlorite alteration banding within the sandstone (Cuddy #13, 5,176 E, 18,320 N).

(c) Southeast fault within quartz-chlorite altered thinly bedded sandstone and breccia of GGF M1. The fault trace is planar and the fault vein is carbonate-quartz. Subhorizontal, discontinuous east-west quartz filled tension veins are associated with the fault and cut across the fault plane. Rock bolts are 40 cm long (300 level, 5,102 E, 18,248 N).

(d) Stepped planar quartz-carbonate filled southwest vein in massive sandstone of GGF M5 (300 level, 4,993 E, 18,242 N).

(e) Pervasive intense quartz alteration of a pumiceous pebble breccia from GGF M1. Relict lithic clasts have variable chlorite or quartz alteration, and the pebble breccia contains a spaced anastomosing cleavage that wraps lithic fragments. Chlorite altered lithic clasts host a continuous cleavage and have weak flattening parallel to the plane of cleavage (250 level, 5,140 E, 18,438 N).

(f) Thinly bedded fine-grained sandstone from GGF M1. Beds have differential intense quartz-chlorite or chlorite alteration corresponding to alternating light and dark grey bands respectively. The chlorite-altered beds contain a well-developed, closely spaced penetrative cleavage. In more competent quartz-altered beds cleavage is absent or a weakly developed, spaced cleavage is present. The angle between cleavage and bedding is oblique (Pump Access Cuddy 190 level, 5,217 E, 18,866 N).

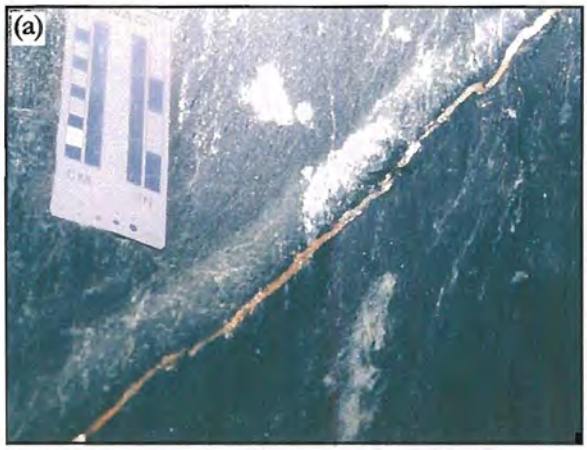
(a)

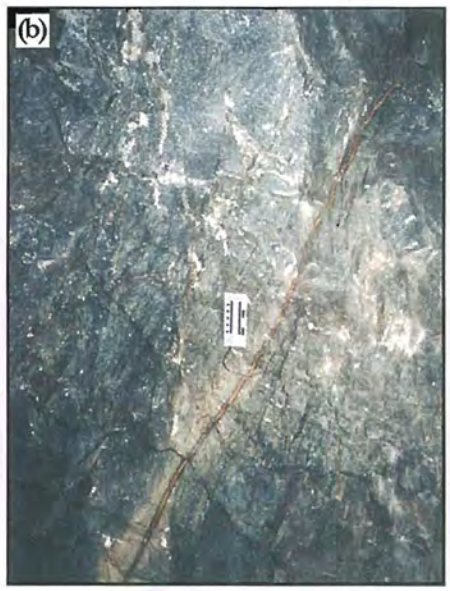
(b)

(c)
S

(d)

(e)
IN
mm

(f)
CM

4.8.6 Southwest veins

Southwest striking veins occur in GVF M4, GGF M1, GGF M4, GGF M5, and massive pyrite-magnetite-pyrite-chalcopyrite . The dip of southwest veins varies from shallow (10°) to subvertical (Fig. 4.10g). These veins have quartz-carbonate-pyrite-chalcopyrite fill with rare euhedral tourmaline (<500 μm in size). Southwest veins are less than 15 cm wide and have banded to fibrous extensional vein fill. Southwest veins vary from planar, sheeted veins to narrow, discontinuous veins and some form stepped veins adjacent to southeast faults (*e.g.*, Fig. 4.12d). These veins are also crenulated by cleavage and offset by late fault movement.

4.9 Cleavage

Previous workers at Gossan Hill (Frater, 1978; Ashley 1988; Watkins and Hickman, 1990a) identified a spaced S2 cleavage that formed a bedding parallel fabric. The results of this study agree with those of Clifford (1992) and Potter (1991), and did not identify S2 fabric, but a single anastomosing S3 cleavage. The S3 penetrative cleavage at Gossan Hill strikes northwest to north-northwest and is oblique to and anticlockwise of bedding, with a steep 75° west to subvertical dip (Fig. 4.10h). This S3 cleavage has a consistent orientation parallel to the subvertical axial surface of the megascopic anticline, with the Golden Grove Domain located on its western limb.

At Gossan Hill, the cleavage intensity varies amongst volcano-sedimentary lithofacies and alteration types. In intensely silicified pebble breccia (*e.g.*, GGF M1), the cleavage is anastomosing, undulose and spaced (Fig. 4.12e), with chlorite altered lithic clasts having a weak flattening in the plane of cleavage. Within the chlorite-quartz altered fine-grained, thinly bedded sediments, cleavage forms a spaced, continuous cleavage preferentially developed in chlorite altered beds (Fig. 4.12f). Intensely chlorite altered volcaniclastics have a closely spaced cleavage that imparts a schistosity. The hangingwall rhyodacite (RD2) and dacite (DAC3) units show a well-developed cleavage, defined by the alignment of muscovite and elongation of chlorite-carbonate altered feldspars. Cleavage is also weakly developed in rhyolite and dolerite intrusions, indicating cleavage formation post-dates emplacement of these intrusions.

The angle between bedding and cleavage is oblique and usually less than 20°. In intensely chlorite altered wall rocks, the angle between bedding and cleavage is less than 10°, reflecting ductile deformation and the possible rotation of bedding with respect to cleavage. Examples of such cases are bedding parallel sulphide veins that also parallel cleavage (Figs. 4.13a and 4.8e). Some intensely quartz altered rocks do not have a penetrative cleavage and where sulphide veins are hosted by intensely quartz altered wall rock, preferential development of cleavage within the sulphide-chlorite vein is observed. In addition, massive sulphide and stringer veins have a spaced penetrative cleavage indicating that mineralisation pre-dated cleavage.

The contact between massive quartz sandstone and massive pyrite-chlorite in GGF M4 has local remobilisation of pyrite along cleavage planes, which cause local irregularities in this contact (Fig. 4.13b). Within massive magnetite, cracking patterns in magnetite are

Figure 4.13

(a) Adjacent subparallel pyrite-chlorite-chalcopyrite stringer veins. A strongly developed cleavage is present in the intensely chlorite altered GGF M4 host. The orientation of the sulphide veins parallels bedding in GGF M4 and the orientation of the penetrative cleavage. Rock bolts are 40 cm long (250 level, 5,103 E, 18,887 N).

(b) Contact between quartz-chlorite altered massive quartz sandstone of GGF M4 and massive pyrite-chalcopyrite. The contact is sharp and planar, but locally irregular due to remobilisation of pyrite and chalcopyrite along cleavage planes (250 level, 5,109 E, 18,440 N).

(c) Discontinuous, undulose small extensional fractures in massive magnetite (Mgt). These fractures are perpendicular to cleavage and are filled by fibrous talc (sample 97U069).

(d) As for (c) under crossed nicols

(e) Deformation of apatite (Ap) in a sulphide, chlorite altered sandstone of GGF M4. Apatite crystals have chlorite-sulphide pressure shadows and cleavage parallel slip planes (arrow). Cleavage parallel slip displaces the margin of the apatite grain in a sinistral sense (sample 97U058).

(f) As for (e) under crossed nicols

(g) Cleavage wraps around a recrystallised and fractured pyrite grain (Py). The cleavage is well-developed in the fine-grained chlorite matrix. The pyrite grain has chlorite and sulphide (chalcopyrite-pyrite) filled pressure shadows. The occurrence of chalcopyrite in these pressure shadows indicates the local remobilisation of chalcopyrite during deformation (sample 97U025).

(h) As for (g) under plane polarised light

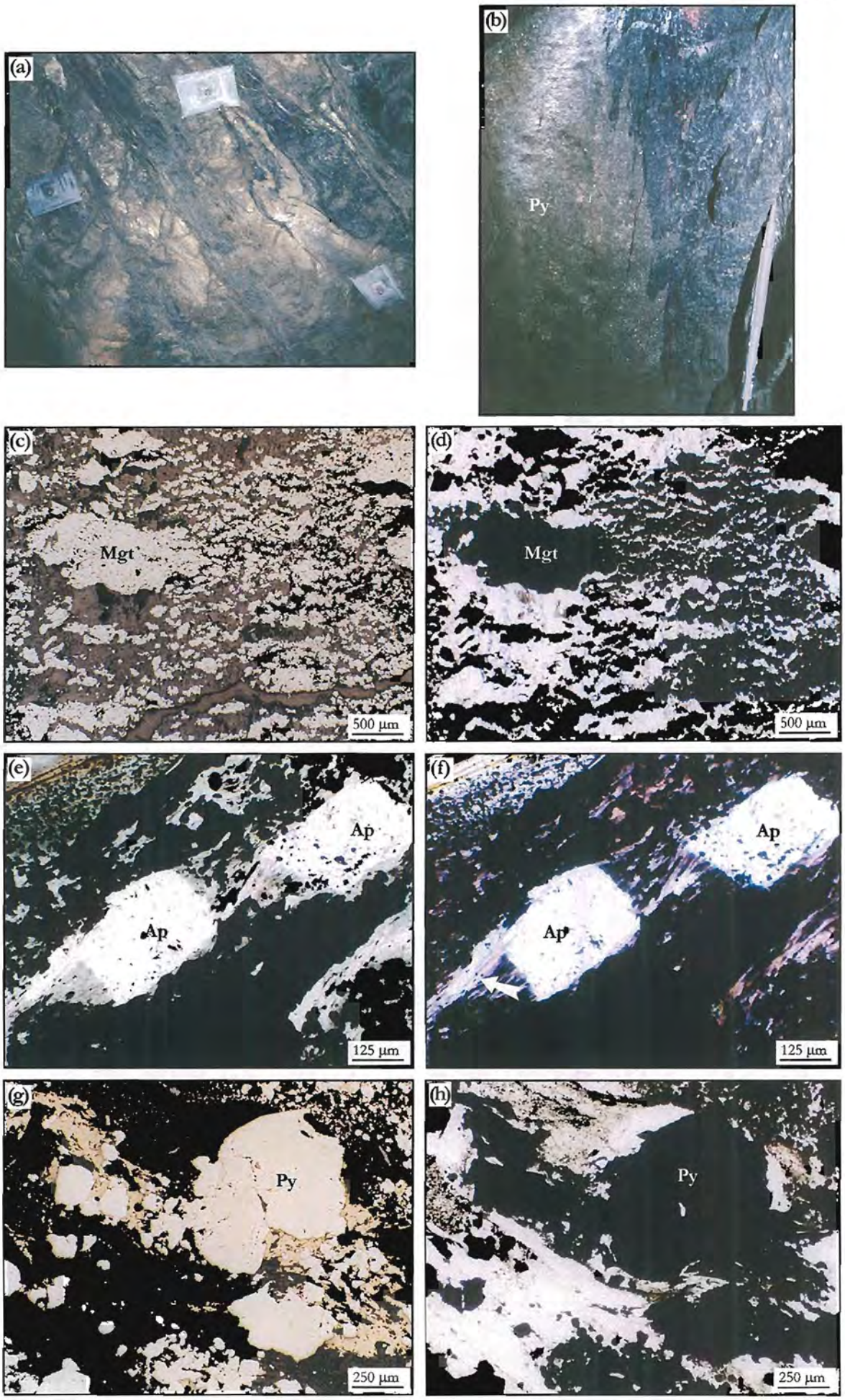
(a)
(b)
Py
(c)
Mgt
500 µm
(d)
Mgt
500 µm
(e)
Ap
Ap
125 µm
(f)
Ap
Ap
125 µm
(g)
Py
250 µm
(h)
Py
250 µm

perpendicular to cleavage and are infilled by talc extensional fibres that parallel cleavage (Figs. 4.13c and 4.13d). Volcanic quartz, siliceous nodules and pyrite grains have cleavage wrapping around them, resulting in augen textures with pressure shadows. Displacement or slip parallel to cleavage planes is observed in areas with strong to intense cleavage development (Figs. 4.13e and 4.13f). Pressure shadows around volcanic quartz, coarse-grained pyrite (Figs. 4.13g and 4.13h) and apatite grains on oriented samples indicate reverse or dextral senses of rotation. In such cases, the cleavage wraps around the more competent grains and demonstrates a post-mineralising cleavage. Pressure shadows have variable mineralogies with fine- and coarse-grained fibrous arrays of quartz, carbonate and chlorite, with less common chalcopyrite and pyrrhotite (Figs. 4.13g and 4.13h). Rounded zones of massive magnetite in massive pyrite have cleavage wrapping (Fig. 4.14a). It is therefore concluded that the remobilisation of sulphides, including pyrite, chalcopyrite and pyrrhotite occurred during cleavage formation, but that magnetite behaved more competently and preferentially underwent brittle deformation.

4.9.1 Folded veins

Stringer sulphide-carbonate-chlorite veins and late stage quartz-carbonate-chlorite veins often have locally crenulated, disrupted and folded textures. As previously discussed (Section 4.8), sulphide veins are associated with the formation of massive sulphides, whilst the quartz-carbonate-chlorite veins formed during brittle deformation after mineralisation. The crenulation, disruption and folding of both vein types is the result of deformation induced during penetrative cleavage development and substantiates the formation of these vein prior to regional penetrative deformation. In general, veins that are folded at Gossan Hill are veins that have a high angle between the vein orientation and the plane of cleavage (Fig. 4.15). Veins subparallel to cleavage and bedding are not folded, but commonly have necking and boudinage deformation structures (Section 4.10.2, Fig. 4.15).

Folded sulphide veins occur within intensely chlorite or chlorite-quartz altered lithofacies. Fold morphologies are tight and upright, with a wavelength less than 30 cm (Fig. 4. 14b). The fold hinges are subhorizontal and cleavage is convergent and axial planar. Stacked, parallel, subhorizontal sulphide veins have similar folding within adjacent veins (Fig. 4.14c).

Folded, late stage quartz-carbonate-chlorite veins are frequently disrupted or crenulated by the cleavage, having fracture and offset parallel to cleavage (Figs. 4.14d and 4.14e) that reflect superimposed brittle deformation. Micro-quartz-carbonate veins are also folded with quartz having undulose extinction (Fig. 4.14e). Folded quartz-carbonate-chlorite veins commonly have open, upright fold forms and small wavelengths (<5 cm), with cleavage axial planar (Fig. 4. 14f). This folding is attributed to shortening in response to cleavage development. Intensely silicified and competent units of GGF M1 have veins that are more disrupted by brittle deformation than by ductile folding. Therefore, competency differences of the host rocks and the angle between the vein and cleavage (Fig. 4.15) are the major controls of folded vein morphologies.

Figure 4.14

(a) A zone of massive magnetite (Mgt) within massive pyrite-chalcopyrite-chlorite (Py-Cpy). The cleavage is well-developed in the massive sulphide and wraps around the more competent massive magnetite zone (250 level, 5,108 E, 18,493 N).

(b) Folded pyrite-pyrrhotite-carbonate vein in intensely chlorite-quartz altered sandstone of GGF M5. The folds are upright and have a wavelength of 10 cm, with smaller folds (less than 3 cm) on the limbs. The cleavage is axial planar to the subhorizontal sulphide vein. The folding in the vein reflects ductile deformation parallel to the plane of cleavage, within a chlorite-rich rock (300 level, 4,974 E, 18,244 N).

(c) Stacked folded pyrite-pyrrhotite-carbonate veins from intensely chlorite-quartz altered sandstone of GGF M5. The pyrite-rich veins are subparallel, flat lying veins that are folded by an axial planar cleavage as explained in (b). In this case the subparallel pyrite-pyrrhotite-carbonate veins have similar folding in each of the veins, which substantiate cleavage-related deformation. The veins have attenuation and pinch and swell, which is associated with minor displacement along the plane of cleavage (300 level, 4,973 E, 18,245 N).

(d) A micro-quartz vein cuts across a fine-grained, intensely quartz altered formerly glassy and shard rich, quartz-bearing sandstone of GGF M5 (sample 97U007).

(e) As for (d) under crossed nicols highlighting the undulose extinction pattern and fracture of quartz within the folded microvein. A small fault, delineated by fine-grained muscovite, shears one limb of the microvein.

(f) A planar, sheeted carbonate-quartz southeast oriented vein with in an intensely quartz altered, pebble breccia of GGF Ml. Small-scale irregularities in the vein trace include small displacements (<1 cm), crenulation and weak folding. These deformational features are axial planar to folding and parallel cleavage (250 level, 5,146 E, 18,438 N).

(g) Carbonate-quartz boudins along the contact between massive quartz-bearing sandstone of GGF M4 and a rhyolite intrusion. Shearing parallel to this contact also parallels the boudinage structures of the carbonate-quartz vein. The boudins are asymmetric, but the direction of movement on the shear zones is not clear. Note also the crenulated carbonate-quartz vein in the massive sandstone (left), with crenulation parallel to shearing along the contact margin (250 level, 5,110 E, 18,437 N).

(a)
Mgt
Py-Cpy

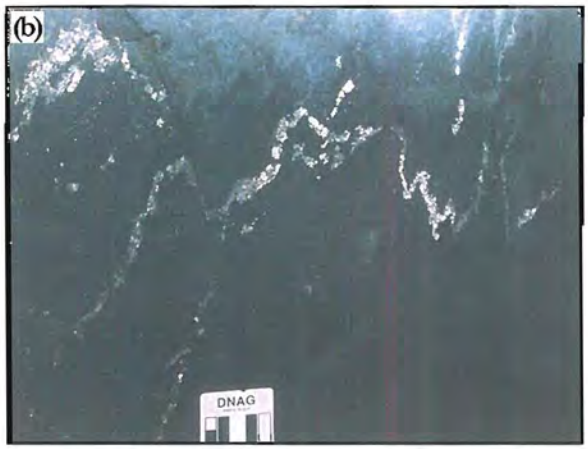
(b)
DNAG

(c)

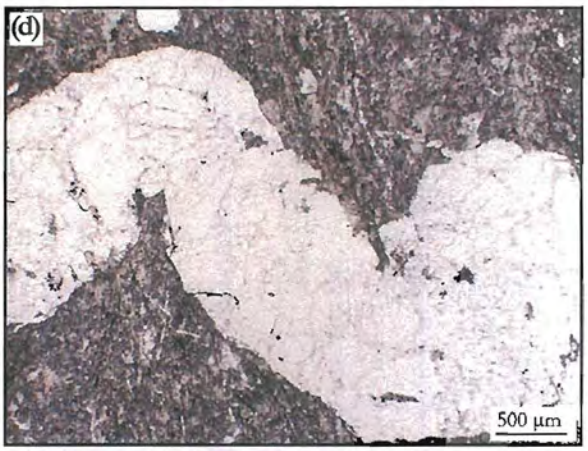
(d)
500 µm

(e)
500 µm

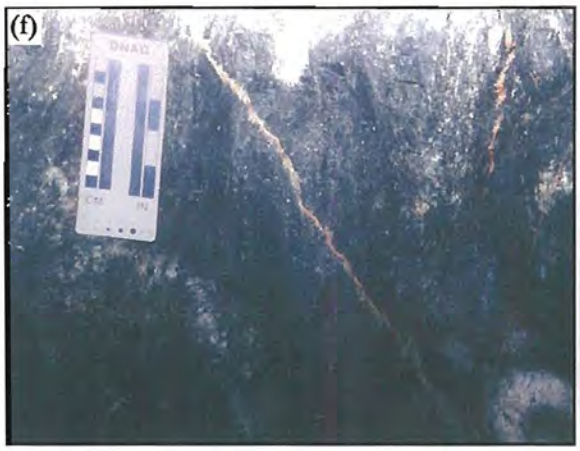
(f)

(g)

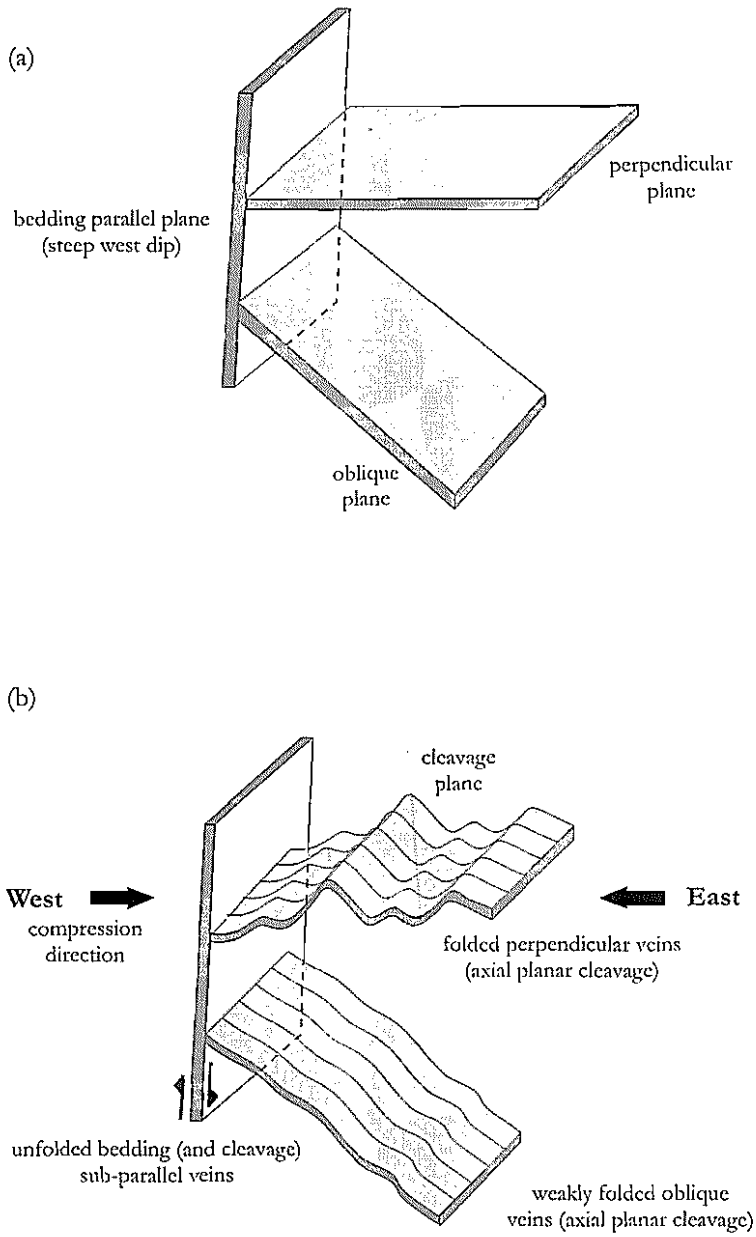

Figure 4.15: Schematic illustration of the deformation of sulphide-rich stringer veins and late brittle quartz-carbonate veins at Gossan Hill. (a) Illustration of the different orientations of veins prior to D3 deformation, with veins sub-parallel, perpendicular or oblique to bedding. (b) The D3 regional penetrative deformation is an east-west compression event defined by Watkins and Hickman (1990a). This event results crenulation, disruption and folding of veins that are perpendicular, or at a high angle to bedding. Veins that are oblique to bedding may have weak disruption or folding. Veins that are subparallel to bedding, are also subparallel to cleavage and do not have folded vein forms but may however, have strong cleavage or boudinage structures.

4.9.2 Boudinage structures

Boudinage structures are observed in carbonate-quartz veins and are common within sulphide veins. Boudinage of carbonate-quartz veins at the margin of a rhyolite intrusion (Fig. 4.14g) are associated with shearing parallel to the rhyolite margin and reverse movement along this margin. Massive sulphide veins within intensely chlorite altered wall rock commonly show necking and boudinage (Fig. 4.16a). In these examples, cleavage is intensely developed in adjacent chlorite wall rock, and wraps around the more competent sulphide zones. These boudins reflect competency differences between chlorite- and sulphide-rich assemblages and coincide with zones of strong cleavage. In sulphide-carbonate-rich veins, necking of veins is a common feature (Fig. 4.16b). These veins are hosted by a chlorite matrix and form locally discontinuous veins that parallel cleavage and commonly have extensional fractures perpendicular to cleavage that are infilled by carbonate, chlorite or talc.

4.10 Metamorphism

The Golden Grove Domain has a prograde metamorphic assemblage typical of the biotite zone of the greenschist facies (Ashley *et al.*, 1988; Clifford, 1992). At Gossan Hill, the metamorphic assemblage of the GGF consists of quartz, chlorite, muscovite, carbonate, rutile and ilmenite, which is consistent with this interpretation. Near and within chemical facies at Gossan Hill, metamorphic minerals also include minor chloritoid, talc, andalusite, epidote, actinolite, sulphide and magnetite. Each of the members of the GGF have different metamorphic minerals and mineral abundances, as indicated in Table 4.2. In contrast to the regional metamorphic assemblage as defined by Clifford (1992) and Watkins and Hickman (1990a), biotite has not been observed within the GGF or dacite and rhyodacite of the Scuddles Formation overlying the Gossan Hill deposit. Metamorphic minerals at the Gossan Hill deposit are discussed below.

4.10.1 Chlorite

Chlorite is an abundant mineral in the host rocks at Gossan Hill. It forms the matrix in sulphide-rich zones where it represents an intense hydrothermal alteration of volcaniclastic precursors. The distribution and composition of chlorite are addressed in Chapter 7. In strongly cleaved zones, chlorite is fine-grained (<50 μm) and delineates an anastomosing to intense planar cleavage (Fig. 4.16c). Cleavage delineated by chlorite commonly wraps around more competent grains. Chlorite in pressure shadows is best developed around large pyrite grains (Fig. 4.16d) and is fibrous or forms subhedral coarse-grained (<300 μm) interleaved mosaics. Within massive sulphide and sulphide veins, chlorite is commonly coarse-grained (>100 μm) interstitial to sulphide grains and consists of fibrous to decussate chlorite that overprints the S3 cleavage.

4.10.2 Muscovite

All fine-grained (<50 μm) white mica is referred to as muscovite and no attempt has been made to differentiate between muscovite and paragonite. Muscovite occurs in the matrix throughout the Golden Grove and Scuddles Formations, but is most abundant in the

Figure 4.16

(a) Boudinaged adjacent pyrite-chalcopyrite veins in massive sulphide from GGF M4. Between adjacent sulphide veins are zones of intense chlorite altered wall rock, that are strongly cleaved. The boudinaged sulphide veins have extensional fractures across the cleavage, which are filled by chlorite and quartz. The necking of these sulphide veins also parallel the direction of cleavage. Rock bolts are 40 cm long (250 level, 5,107 E, 18,489 N).

(b) Intensely chlorite altered sandstone in GGF M4 containing abundant, discontinuous pyrite-pyrrhotite-carbonate-magnetite veins. The veins parallel cleavage and have well-developed necking structures and extensional fractures perpendicular to cleavage (250 level, 5,075 E, 18,492 N).

(c) Photomicrograph of a stretched pyrite-pyrrhotite-carbonate-magnetite vein from (b). The sulphide-carbonate vein is hosted by fine-grained chlorite that contains disseminated rutile and ilmenite. The vein is parallel to cleavage, as defined by alignment of chlorite. Subparallel sets of undulose fractures perpendicular to cleavage are extensional fractures that are in filled by quartz (sample 97U049).

(d) Coarse-grained chlorite pressure shadow around large, euhedral pyrite grains (Py) within a fine-grained chlorite matrix (sample 762040).

(e) Pervasive, fine-grained muscovite alteration of massive dacite. Fine-grained, poorly formed muscovite and carbonate occurs through the matrix of this dacite and defines the S3 cleavage. The alteration of feldspar phenocrysts (Fd) is an intense carbonate-muscovite-chlorite alteration (sample 769074).

(f) Fractured magnetite grains (Mgt) from massive magnetite in GGF M4. Fractures are planar to undulatory and filled by fibrous talc (sample769060).

(g) Decussate textures of talc within chalcopyrite-pyrite (opaques) and chlorite (sample 769152).

(h) Disseminated grains of ilmenite and rutile within a fine-grained chlorite matrix (Chl) (sample 769264).

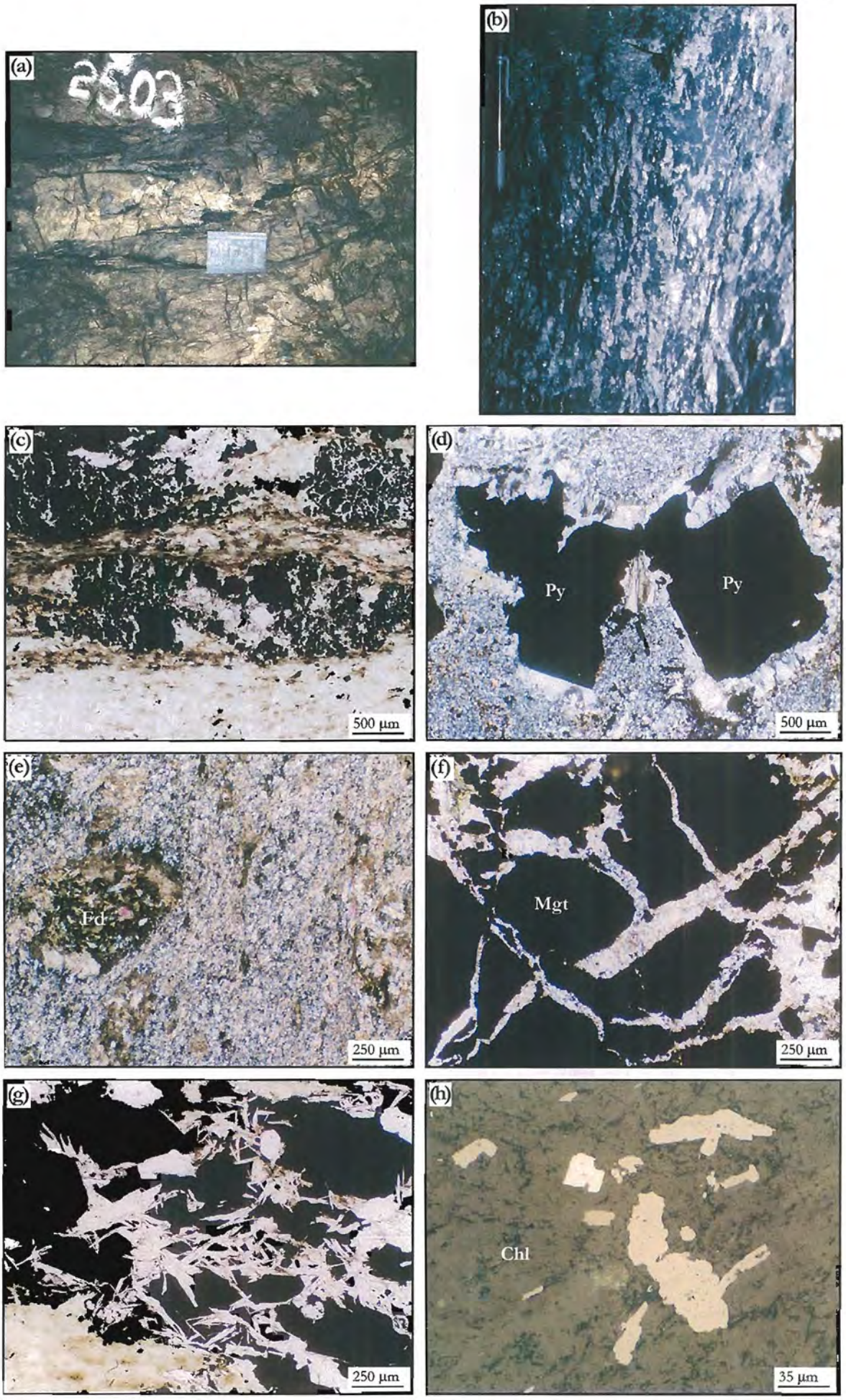
(a)
(b)
(c)
500 µm
(d)
Py
Py
500 µm
(e)
Pd
250 µm
(f)
Mgt
250 µm
(g)
250 µm
(h)
Chl
35 µm

Table 4.2: Stratigraphic distribution and relative abundance of metamorphic minerals at Gossan Hill. Minor minerals form less than 5% modal.

Stratigraphy	major minerals	minor minerals
Scuddles Formation Member 2		
dacite (DAC3)	muscovite, carbonate, chlorite	epidote, chloritoid
rhyodacite (RD2)	muscovite, carbonate, chlorite	epidote
Golden Grove Formation		
GGF M6	quartz, chlorite, carbonate, sulphides, magnetite	ilmenite, rutile, andalusite, chloritoid, muscovite, talc, actinolite
GGF M5	chlorite, quartz,	muscovite, carbonate
GGF M4	chlorite, quartz, carbonate, sulphides, magnetite, talc	ilmenite, rutile, chloritoid, muscovite, actinolite, andalusite
GGF M1	quartz, chlorite	muscovite, ilmenite, rutile
Gossan Valley Formation		
GVF M4	muscovite, quartz, chlorite	ilmenite, rutile
Late intrusions		
dacite porphyry	albite	muscovite, chlorite, carbonate
dolerite	chlorite, epidote, sphene	dinozoisite
rhyolite	muscovite	

latter (Table 4.2). Within Members of the Golden Grove Formation, muscovite is generally minor and occurs as disseminated grains in a quartz-chlorite alteration. Muscovite commonly forms small (<20 μm) acicular grains whose alignment delineate the penetrative cleavage. The rhyodacite and dacite units of the Scuddles Formation have abundant muscovite (>20%), which are fine-grained (<50 μm) and also define cleavage by alignment (Fig. 4.16e). In the massive dacite (DAC3), relict feldspar morphologies are delineated by coarse-grained muscovite (>100 μm), carbonate and chlorite. Fibrous muscovite is also common within massive sulphides, where it forms grains less than 200 μm that cut across the cleavage.

4.10.3 Talc

Talc is abundant in magnetite-rich zones (up to 40%) and is less abundant in massive sulphide. In massive magnetite, the magnetite grains are strongly fractured having subparallel sets of undulatory, discontinuous, extensional fractures that are commonly infilled by aligned, fine-grained fibrous talc parallel to cleavage. In these extensional sites, talc fibres range from planar to curviplanar (Fig. 4.16f) and record heterogeneous extension.

In massive sulphide, talc forms fine-grained (<100 μm), fibrous grains in association with muscovite, which may be aligned and delineate cleavage. Talc also forms coarse-grained (up to 350 μm), radiating, decussate mosaics in massive sulphide and stringer veins and sulphide-chlorite alteration. Coarse-grained talc infills interstices between sulphide grains and aggregates (Fig. 4.16g) or occurs adjacent to sulphides within chlorite. Decussate talc cut across the S3 penetrative cleavage.

4.10.4 Carbonate

Carbonate ranges in composition from calcite, ankerite to siderite and has a widespread distribution throughout the Scuddles Formation (calcite) and massive magnetite and sulphide (ankerite to siderite). The occurrence, distribution composition of carbonate alteration is discussed in Chapter 7. Undulose extinction and deformation textures exist in some carbonate grains, however euhedral grains (up to 1 mm) that lie across a chlorite defined cleavage, indicate widespread recrystallisation of carbonate during metamorphism.

4.10.5 Epidote and clinozoisite

Subhedral to euhedral epidote grains, less than 0.2 mm in size, are dispersed through late dolerite intrusions and the hangingwall DAC3 dacite. Some dolerite intrusions have strong epidote alteration, with epidote forming up to 15% modal. Massive dacite contains minor epidote (<2%) within intensely muscovite-carbonate-chlorite altered feldspars. Minor clinozoisite was also identified within altered feldspar. Rare epidote (<1% modal) was identified in massive sphalerite, occurring as rounded, scattered, subhedral grains less than 20 μm in size.

4.10.6 Sphene

Sphene has a minor occurrence in the Scuddles Formation DAC3 dacite (<1%) and in epidote altered dolerite intrusions (<5%). Sphene occurs as scattered grains less than 200 μm in size.

4.10.7 Ilmenite-rutile

Ilmenite and rutile abundances range from minor (<3%) to accessory (<1%) and occur as disseminated grains throughout the Golden Grove Formation. Their textural forms vary from acicular, lath-shaped to blebby-shaped grains (Fig. 4.16h) that are poorly formed, skeletal or spongy. Ilmenite and rutile grains are commonly small (<100 μm in size), but can form aggregates up to 300 μm. Ilmenite and rutile are most abundant in intense chlorite alteration, but and also interstitial to magnetite and sulphide within massive magnetite and sulphide. Ilmenite and rutile grains may be aligned parallel to cleavage or form grains that lie across the cleavage.

4.10.8 Chloritoid

Chloritoid is a minor mineral (<5%) and is present within GGF M4, GGF M6 and DAC3 dacite. In GGF M4 and GGF M6, chloritoid occurs within intense chlorite (±sulphide) alteration. Chloritoid forms isolated euhedral grains or interpenetrating, radiating to interlocking 'bow tie' (Bearley, 1988) aggregates (Figs. 4.17a and 4.17b). Chloritoid grain sizes rarely exceed 2 mm and chloritoid may be aligned parallel to cleavage or occur as dispersed grains that lie across cleavage (Fig. 4.17c). Evidence of brittle deformation in chloritoid includes grain dislocation structures, foliated crystals and crystals with chlorite (±pyrrhotite) replaced ragged margins. Radiating aggregates of chloritoid in chlorite often have magnetite and pyrrhotite rims that infill cleavage and fracture spaces within the chloritoid grains. The resulting texture is a 'pseudo-dendritic' array of irregular

Figure 4.17

(a) 'Bow tie' morphologies characteristic of chloritoid within an intensely chlorite and pyrite (Py) altered rock at Gossan Hill. The chlorite matrix is fine-grained, and both this matrix and the chloritoid grains contain small scattered grains of ilmenite and rutile (disseminated opaques) (sample 762040).

(b) As for (a) under crossed polarised light. This view also highlights the well-formed chlorite pressure shadows around pyrite (Py) (sample 762040)

(c) Variably oriented chloritoid grains in massive dacite. The chloritoid grains cut the cleavage, which is defined by pervasive muscovite alteration in the dacite groundmass. Chloritoid grains also cross the boundaries between chlorite-altered feldspars (Fd) and altered matrix (sample 760214).

(d) Chloritoid with pyrrhotite and magnetite replacement along its cleavage planes. A fine-grained chlorite matrix hosts the chloritoid. The pyrrhotite and magnetite replacement imparts a 'dendritic' appearance to the chloritoid grain (sample 762040).

(e) Intense chlorite alteration of a sandstone from GGF M4. The chlorite groundmass of this rock contains large, scattered, blocky and segmented andalusite porphyroblasts. Scale in cm (sample 760466)

(f) Andalusite porphyroblast within a fine-grained chlorite matrix. Fine-grained ilmenite and rutile sieve the chlorite matrix and andalusite grain. This porphyroblast consists of adjacent blocky segments, which is consistent with the two glide planes of andalusite. The central parts of the andalusite porphyroblast are intergrown with chloritoid and quartz (sample 762040).

(g) As for (f) under crossed nicols highlighting the intergrowth of quartz-chlorite with andalusite in the central parts of the andalusite porphyroblast and internal zonation within some of the blocky segments.

(h) As for (f) and (g) under reflected light. Magnetite, pyrite, pyrrhotite rim each of the blocky segments of the andalusite porphyroblast.

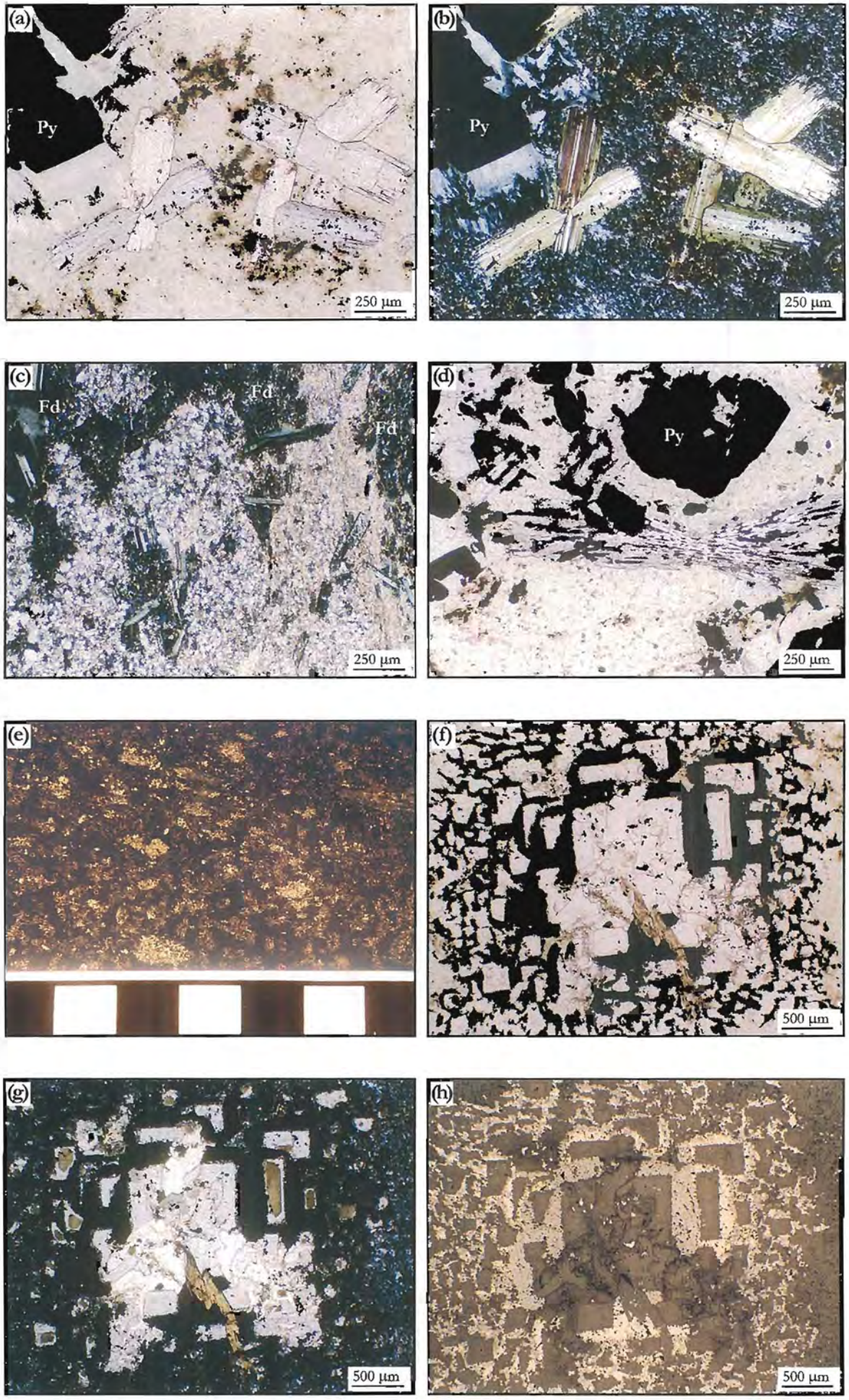
(a)
Py
250 µm
(b)
Py
250 µm
(c)
Fd
Fd
Fd
250 µm
(d)
Py
250 µm
(e)
(f)
500 µm
(g)
500 µm
(h)
500 µm

pyrrhotite-magnetite grains in chloritoid, where the 'dendritic' appearance is inherited from the original orientation of chloritoid grains (Fig. 4.17d). Chloritoid also occurs in pressure shadows around large blocky grains of pyrite or andalusite. Chloritoid and andalusite intergrowths (Fig. 4.17d) indicate the similar timing of these minerals.

4.10.9 Andalusite

Large, well-formed, prismatic, variably altered laths of andalusite are present within the intense chlorite alteration associated with massive sulphide at Gossan Hill (Fig. 4.17e). Andalusite is restricted in occurrence to GGF M4 and GGF M6 and in some beds forms up to 30% modal. Andalusite has a patchy dispersed occurrence below and adjacent to massive pyrite where it is commonly associated with chloritoid, pyrrhotite and magnetite. Andalusite forms euhedral, isolated tabular laths that have straight extinction and a grain size of up to 4 mm. Laths have variable orientations within the cleaved groundmass and generally lie across the cleavage. Rarely, andalusite grains are aligned parallel to cleavage with poorly defined chlorite-chloritoid pressure shadows around these grains.

Andalusite laths generally consist of blocky to tabular, jigsaw-fit pieces, each which may have internal symmetric zonation (Figs. 4.17f and 4.17g). Irregular, pyrrhotite-sphalerite-magnetite-pyrite rims (Fig. 4.17h) enclose the andalusite laths, including the blocky pieces of which they are comprised. These sulphide-magnetite rims can be up to 2 mm wide. Blocky equant fragments and sulphide-magnetite rims retain the original tabular morphology of the andalusite porphyroblasts, with sulphide-magnetite rims separated from andalusite by a micron-sized rim of chlorite.

4.10.10 Actinolite

Rare actinolite (<1%) was observed in massive sulphide and sulphide-chlorite alteration of GGF M4 and GGF M6. Actinolite grains are up to 500 μm in length and have bladed, acicular forms.

4.10.11 Discussion

The metamorphic mineral assemblage has its greatest mineralogical variation in members of the GGF that host the massive sulphide and magnetite. Chlorite, muscovite and talc consist of fine- (<100 μm) and coarse-grained phases. In these cases, the finer-grained minerals define the penetrative cleavage by their alignment and likely formed during the penetrative deformation. In the case of talc, which commonly infills fractures in magnetite, curviplanar fibrous grains delineate inhomogeneous stress during the penetrative deformation. However, decussate, coarse-grained chlorite, muscovite and talc cut across the cleavage and formed after penetrative deformation, which indicates peak metamorphism post-dated penetrative deformation.

The association of ilmenite and rutile to the cleavage indicates that its formation pre- and post-dated penetrative deformation. Ilmenite and rutile grains that cut cleavage indicate that some of these grains may be metamorphic in origin. Similarly, the presence of deformed and altered chloritoid, in addition to pristine chloritoid reflects at least two phases of chloritoid formation, namely pre- and post-penetrative deformation. The

occurrence of chloritoid is commonly correlated with regionally metamorphosed rocks (Ribbe, 1982; Deer *et al.*, 1992), but and is also reported to occur within hydrothermal alteration related to massive sulphide mineralisation (Franklin *et al.*, 1975; Morton and Nebel, 1984). In the later occurrence, chloritoid is a metamorphic mineral whose occurrence correlates specifically to the original high Al and Fe contents of host rock. At the Mattabi massive sulphide deposit, andalusite and chloritoid occur in footwall alteration and are metamorphic products of an earlier hydrothermal clay alteration (Franklin *et al.*, 1975; Morton and Franklin, 1987). Moreover, studies of the formation and stability of chloritoid, indicate its formation has a strong dependence on the bulk composition of the original host rock (LaTour, 1980). Chloritoid will form in units whose bulk compositions are (1) comparatively high in Al_2O_3, (2) low in Na_2O, K_2O and CaO, and (3) have high FeO/(FeO+MgO) ratios. At Gossan Hill the occurrence of chloritoid-andalusite within intense Fe-rich chlorite alteration (Chapter 7) is consistent with its metamorphic origin in units containing high Al and Fe.

Andalusite is a metamorphic orthosilicate mineral that forms at moderate to low temperatures, typically within contact metamorphic aureoles of igneous intrusions (Deer *et al.*, 1992; Mange and Maurer, 1992). Deformation in andalusite is common via gliding parallel to the (001) and the (100) cleavage directions (Deer *et al.*, 1992; Ribbe, 1982). Andalusite at Gossan Hill has a blocky segmentation consistent with this style of deformation, with optically continuous extinction angles between adjacent blocky segments. The extinction zonation observed in blocky andalusite segments is not caused by major compositional variation (*c.f.* Appendix A2.1), but may reflect thermal *in situ* modification during metamorphism.

At Gossan Hill, intergrowths between andalusite, chloritoid and quartz, all of which have sulphide-magnetite rims, are interpreted to reflect the metamorphic reaction of Fe-rich chlorite to form andalusite. For example:

2 quartz + 5 Fe-chloritoid + amesite = daphnite + 4 Mg-chloritoid + 2 andalusite + H_2O

The equilibration between sulphide and magnetite may have also been constrained by metamorphic reactions during andalusite formation. For example:

5 pyrite + 4 daphnite = 4 andalusite + 5 magnetite + 8 quartz + 10 pyrrhotite +16 H_2O

The reaction of Fe-rich silicate assemblages to andalusite and sulphide-magnetite may be responsible for the blocky crystal disaggregation and the sulphide-magnetite rims formed around the blocky andalusite segments.

Textural relationships indicate that andalusite formed during peak metamorphism, synchronous to the formation of chloritoid and quartz. Andalusite has reacted grain boundaries to chlorite and replacement of chlorite by sulphide-magnetite. The formation of andalusite during peak metamorphism occurred after penetrative deformation, as inferred from the rarity of pressure shadows and cleavage related deformation in andalusite. The restricted occurrence of andalusite (±chloritoid) to specific beds within GGF M4 and GGF M6, reflect the specific Fe-rich composition of these beds due to

intense Fe-rich chlorite hydrothermal alteration of formerly glassy, pumiceous volcaniclastics.

4.10.12 Timing of peak metamorphism

Coarse-grained chlorite, muscovite and talc decussate textures overprint the S3 regional penetrative cleavage and support the recrystallisation of these minerals after the formation of S3. Equilibrium textures between chloritoid, andalusite and quartz support the synchronous formation of these minerals and cut across S3 cleavage. The blocky segmentation of andalusite grains is attributed to metamorphic reactions of chlorite forming andalusite, chloritoid, quartz, magnetite and sulphides along preferred deformation planes within andalusite. These textural associations indicate that peak metamorphism post-dated the regional penetrative cleavage. This conclusion is consistent with the timing of regional metamorphism proposed by Watkins and Hickman (1990a).

4.10.13 Temperature indicator minerals

The temperature of peak metamorphism for a chlorite-chloritoid-andalusite-quartz-rutile mineral assemblage was calculated using the THERMOCALC program (Version 2.4) of Powell and Holland (1990), assuming H_2O saturated conditions. Activity data for chloritoid and chlorite were calculated using microprobe analysis listed in Appendix A2.2. These calculations suggest that peak metamorphic temperatures reached 452±4°C at 1 kbar, consistent with the greenschist facies mineral assemblage observed at Gossan Hill. As this metamorphic mineral assemblage does not constrain pressure the pressure is assumed to be relatively low (<1 kbar) with a pressure sensitivity of 20°C/kbar. Recalculated temperatures using different Fe-chlorite determined for chlorite at Gossan Hill yield negligible changes in the metamorphic temperature estimate.

4.11 Summary of deformation and metamorphism at Gossan Hill

Gossan Hill has undergone multiple phases of deformation that include early pre- to syn-mineralising and post-mineralising events, the later which include penetrative deformation and metamorphism. The attributes and characteristics of these events are summarised below.

- A synvolcanic growth fault controlling and localising mineralisation at Gossan Hill is inferred from changes in the thickness of GGF M6 and rhyodacite breccia facies, as well as the asymmetry of massive and stringer veins and intense alteration. A DAC3 dacite intrusion of the hangingwall Scuddles Formation occupies the site of this synvolcanic structure. Rotational block movement along this synvolcanic structure is inferred from a change in the slope of the GGF M4-M1 lithological surface and opposing trends of the massive sulphide zones between the Gossan Hill and Scuddles deposits. Comparable stratigraphic and structural frameworks between the Gossan Hill and Scuddles deposits reflect similar structural controls to the distribution of lithofacies, mineralisation and alteration.
- Early silicification of GGF M4 is inferred from the presence of pre-mineralising

quartz veins formed by brittle deformation of this strata prior to massive sulphide deposition. Sulphide stringer veins overprint early quartz veins, with quartz vein formation attributed to early deformation in north-south extension regime.

- Sulphide veins formed along pre-existing fractures (early quartz veins) and bedding plane conduits. The orientation of sulphide veins was largely controlled by bedding as observed by their common bedding-parallel orientations. Deformation of these veins has involved some rotation to bedding and cleavage parallel orientations due to ductile chlorite host rocks.
- No evidence of D1 or D2 is observed at Gossan Hill.
- Intrusion of late stage dolerite occurred along a north-south orientations. Late stage rhyolite intrusions have a north-south or northwest-southeast orientation. Emplacement of these intrusions likely occurred along pre-existing fractures and faults developed during D3 and D4 deformation.
- A period of brittle deformation pre-dating or synchronous with the regional (D3) deformational event is indicated. Four groups of faults and veins are identified to have formed during this stage and are oriented southeast-northwest, east-west, north-south, southwest-northeast. Faults have similar characteristics, including associated veins and displacement directions. In general, the observed displacement on all faults post-dates vein formation and the most common movement directions are reverse overprinted by dextral wrench. Refraction of some faults to bedding parallel directions is also observed. North-south and southeast veins parallel faults with the same orientation, and are interpreted as coeval. East-west and southwest veins generally form shallow to subhorizontal veins adjacent to faults, with flat lying extensional veins reflecting strong vertical extensional associated with this phase of faulting. The best preserved evidence of deformation prior to D3 (and S3) are the subhorizontal, quartz-carbonate veins that are disrupted, crenulated or folded by S3. It is possible that the dolerites may have intruded north-south faults and that the rhyolites intruded the southeast faults. This requires these structures to pre-date the regional D3 deformation.
- The regional penetrative deformation (D3) is associated with mesoscopic, northwest-southeast folding and an axial planar cleavage that forms the dominant fabric at Gossan Hill. Penetrative deformation is interpreted to result during regional east-west compression (Watkins and Hickman, 1990a). At Gossan Hill, cleavage results in a closely spaced and planar to anastomosing fabric. The patterns of cleavage development, and its effect on altered and mineralised zones, reflect both brittle and ductile deformation, dependant on the alteration style and lithofacies type. Chlorite zones have ductile deformation with boudinage and necking structures and folded veins. Brittle structures include extensional fractures, generally in sulphide-magnetite zones, disrupted veins and displacement in the plane of cleavage. Where veins are disrupted or folded, cleavage is an axial planar fabric.
- Continued east-west compression (D4) resulted in activation and re-activating of

fault planes, which have a reverse and dextral wrench sense of movement respectively. The D4 deformation is considered to be associated with brittle faulting and veining with widespread re-activation of pre-existing D3 structures.

- A metamorphic mineral assemblage of chlorite, muscovite, talc, carbonate, epidote, ilmenite, rutile, chloritoid and andalusite overprints S3 and represents peak metamorphism after penetrative deformation. The peak metamorphic temperature is estimated to be 452±4°C at 1 kbar, which is consistent with greenschist facies metamorphism.

4.12 Regional considerations and exploration ramifications

The geology of the Gossan Hill-Scuddles area is given in Figure 2.8. Mesoscopic faults include the Racecourse, Cullens, Luisini and Flying Hi fault zones, which have a north-south trend. This set of laterally continuous parallel fractures is regionally extensive (*c.f.* Fig. 2.7) and defined by geophysical lineaments and stratigraphy offsets. Horizontal displacement along faults range from less than 100 m up to 750 m, as in the case of the Racecourse Fault (Fig. 2.8). Offset along these faults is consistently dextral. These structures are late brittle features that have the same orientation to the north-south fault set identified at Gossan Hill. North-south fault development is considered to have occurred prior to the regional D3 deformation event, with the dextral movement on these regional faults associated with D4 deformation, offsetting strata, the granite margin and the Minjar Range Group (Fig. 2.7).

Regionally, dolerite intrusions parallel the north-south faults. Strong fracture control to the dolerite intrusion event is evident from these patterns with the dolerites most likely utilising north-south fault systems. East-west faults are also a common feature in the regional geology. These structures have dextral offset and are interpreted to be offset by north-south structures during late stage movement.

In exploration terms, all of the above mentioned structures are late brittle structures and unrelated to sites of mineralisation. The orientation of synvolcanic structures controlling mineralisation at Gossan Hill and Scuddles is determined by the orientation of the dacite intrusions that occupy the synvolcanic fracture sites. DAC3 dacite intrusions have a north-south orientation similar to the late brittle structures, which makes their identification difficult. However, the recognition of sites where the Scuddles Formation cuts across the Golden Grove Formation is one criterion by which these synvolcanic structures could be identified.

Chapter 5

Sulphide and magnetite mineralisation

5.1 Introduction

At Gossan Hill, massive sulphide and massive magnetite are hosted within a thick sequence of bedded felsic tuffaceous volcaniclastics of the Golden Grove Formation (GGF). Facies investigations indicate that massive sulphides have an upper and a lower stratigraphic association, and these two zones are separated by up to 150 m of volcaniclastics. The upper and lower massive sulphide zones occur within GGF M6 and GGF M4 respectively. Sulphides within GGF M4 are Cu-rich, whilst sulphides in GGF M6 are Zn-Cu-rich. In addition to massive bodies, sulphides occurs in numerous veins that are Fe-, Cu- or Zn-rich. A Cu-Fe-rich stringer zone connects the upper and lower massive sulphide zones. In total, sulphides occur through an estimated stratigraphic thickness of 250 m. Massive magnetite is also present, but only occurs in the lower stratigraphic association of GGF M4, where it is adjacent to massive sulphide and stringer veins.

The stratigraphic separation of massive sulphide zones, as observed at Gossan Hill, is not uncommon in VHMS deposits. For example, East Thalanga in the Mount Windsor Volcanic Belt, Queensland, has two ore positions that appear to have formed from the same mineralising system (Hill, 1996). The Balcooma deposit, northern Queensland, is another example of multiple ore lenses, with each lens having a different stratigraphic occurrence and a Zn-Cu or Cu-rich sulphide assemblage (Huston, 1988). However, in contrast to Thalanga, the Balcooma deposit was formed from separate mineralising systems (Huston, 1988). Many Canadian Archean VHMS deposits are also characterised by at least two or more, stratigraphically separate or 'stacked' sulphide lenses (Sangster, 1972; Barrett *et al.*, 1992). These deposits include Mobrum (Barrett *et al.*, 1992), Ansil and Corbet (Knuckey and Watkins, 1982; Barrett *et al.*, 1993; Galley *et al.*, 1995), Millenbach (Knuckey *et al.*, 1982; Kalogeropoulos and Scott, 1989; Kerr and Gibson, 1993) and Mattabi (Franklin *et al.*, 1975; Morton *et al.*, 1991). VHMS deposits may also consist of multiple sulphide lenses that lack substantial stratigraphic separation (*e.g.*, Rosebery, Huston, 1988; Lees *et al.*, 1990; Large, 1992, and Que River, Large *et al.*, 1989).

Frater (1978) interpreted the mutual occurrence of sulphide and magnetite at Gossan Hill as the result of multiple (at least two) periods of sulphide formation, with the co-deposition of magnetite during the early phases of sulphide formation. Conversely, Clifford (1992) interpreted Gossan Hill to have formed from a single, long-lived

deposition of magnetite during the early phases of sulphide formation. Conversely, Clifford (1992) interpreted Gossan Hill to have formed from a single, long-lived hydrothermal system. These contrasting interpretations at Gossan Hill highlight the complexity of this deposit and set the scene for this chapter, which aims to:

- define the geometry and distribution of massive sulphide, massive magnetite and stringer veins with respect to the volcaniclastic succession and synvolcanic structures;
- establish the relative timing between the upper and lower massive sulphide zones, stringer veins and massive magnetite;
- constrain the relative duration of sulphide and magnetite formation at Gossan Hill, and assess its development as a single or multi-phase hydrothermal system;
- assess the significance of massive magnetite at Gossan Hill;
- examine evidence for exhalation versus replacement at Gossan Hill;
- compare and contrast observations at Gossan Hill with the nearby Scuddles deposit.

5.2 Ore types

Three main ore types occur at Gossan Hill, *viz* massive sphalerite, massive pyrite and massive magnetite. The term massive sulphide in this thesis is reserved for abundances greater than 50 wt.% (*i.e.*, massive sphalerite has >50 wt.% sphalerite). Massive sphalerite only occurs in GGF M6, whilst massive pyrite occurs in both GGF M6 and GGF M4. Massive magnetite (>50 wt.% magnetite) only occurs in the lower ore zone in GGF M4.

At Gossan Hill, a deep weathering profile extends from surface to depths of up to 100 m. This weathering has resulted in gossanous massive sulphide and massive magnetite and caused chalcophile element dispersion in the pisolitic laterite near the surface (Smith and Pedrix, 1983). Two supergene enrichment zones occur in the gossanous outcrop of the primary ore. These are an Au-oxide zone overlying massive pyrite-sphalerite in GGF M6 and a Cu-supergene zone overlying massive pyrite-chalcopyrite-magnetite in GGF M4. Although the weathered sulphide zones are an important resource (Table 5.1), this study is focussed on the primary ore.

The hypogene and supergene mineralogy of massive sulphide and massive magnetite is given in Table 5.2, with tonnage and grade data listed in Table 5.1. Unoxidised massive sulphide generally consists of sphalerite, pyrite, chalcopyrite and pyrrhotite, with massive magnetite consisting mainly of magnetite. Gangue minerals are chlorite and quartz in massive sulphide, and chlorite and carbonate in massive magnetite. MZC geologists have quantified the volume of massive magnetite at 5.56 million cubic metres with an average specific gravity of 4.3 (S. Johansen, *pers. comm.*). Therefore massive magnetite (*i.e.*, >50 wt.% magnetite) at Gossan Hill forms an estimated 12 Mt.

5.3 Terminology

Underground access to the central and northern parts of the Gossan Hill deposit (18,240 N to 18,780 N) was developed during the recently completed feasibility study. As part of

Table 5.1: Results from the 1994-1997 feasibility study which upgraded the estimated resource of Gossan Hill to 7.0 Mt. @ 3.4% Cu and 2.2 Mt. @ 11.3% Zn with 1.5 g/t Au and 102 g/t Ag for the primary mineralised zones and 5.3 Mt. @ 1.5% Cu and 2.0 Mt. @ 2.2 g/t Au and 86 g/t Ag for the oxide-supergene mineralised zones. Tonnage and grades are from the 1997 Normandy shareholders report.

	Tonnes (Mt)	Zn (%)	Cu (%)	Pb (%)	Ag (g/t)	Au (g/t)
Zn (indicated)	1.2	10.3	0.3	1	89	1.5
Zn (inferred)	1.03	12.5	0.3	1.2	117	1.4
Cu (indicated)	5.23	0.3	3.5	-	13	0.4
Cu (inferred)	1.8	0.3	3.3	-	19	0.4
Cu-supergene	5.27	-	1.5	-	-	-
Au-oxide	2.01	-	-	-	86	2.2

Table 5.2: Mineralogy of massive sphalerite, massive pyrite and massive magnetite listing the major, minor, accessory, gangue and supergene minerals. The supergene minerals occur in the weathered upper 100 metres overlying the primary mineral zones and are compiled from Frater (1978).

	Major	Minor	Accessory	Gangue	Supergene
massive sphalerite	sphalerite, pyrite, pyrrhotite	galena, magnetite arsenopyrite, tetrahedrite-tennantite, chalcopyrite, bismuthinite	electrum, native silver, cassiterite	quartz, chlorite, carbonate, muscovite, talc, rutile, ilmenite, epidote	marcasite, pyrrhotite, pyrite, goethite, chalcocite, Fe-oxides, electrum
massive pyrite	pyrite, chalcopyrite, pyrrhotite	magnetite, marcasite	sphalerite	chlorite, quartz, carbonate, apatite, talc, muscovite, chloritoid, andalusite, ilmenite, rutile	marcasite, chalcocite, malachite, cuprite covellite, Fe-oxides, goethite, pyrrhotite
massive magnetite	magnetite	pyrite, pyrrhotite, chalcopyrite, marcasite		carbonate, talc, chlorite, quartz, muscovite, ilmenite, rutile	maghemite, hematite

this feasibility study, drilling was undertaken by MZC on 40-m-spaced, east-west sections. However, due to time constraints, underground exposure and diamond drill results of the 1994-1997 feasibility study were only reviewed in the last year of this study. As a result, much of the work presented in this study was completed on the earlier generations of drilling from the surface. Due to the strong deviation of these surface drill holes, interpretations were carried out on a series of transform sections oriented 30° east of mine grid north. Where possible, these sections were reverted to east-west sections and integrated with recent drill results. As the recent feasibility study did not extend to the southern reaches of Gossan Hill (*i.e.*, 17,770 N to 18,220 N), drill sections in these areas are presented as transform sections. The recent exploration has highlighted significant differences to the geometry of the Gossan Hill deposit from that described by Frater (1978), Ashley *et al.* (1988) and Clifford (1992).

In order to distinguish between the different areas of mineralisation at Gossan Hill, the terminology of 'lens' and 'panel' was used by MZC geologists to differentiate massive sulphides in GGF M4 from massive sulphides in GGF M6 respectively (*e.g.*, Scott, 1991). This mine-based terminology is not implemented here due to its potential genetic connotations. In place, all occurrences of massive sulphide and massive magnetite are ubiquitously referred to as 'zones'. Additionally, the upper Zn-rich stratigraphic association was previously cited as the 'hangingwall chert' and the lower Cu-rich stratigraphic association as the 'main mineralised zone' (Frater, 1978; Ashley, 1983; Ashley *et al.*, 1988; Whitford and Ashley, 1992). Both of these terminologies have also been abandoned.

5.4 Mineralisation in GGF M6: The upper stratigraphic association

GGF M6 contains massive sphalerite, massive pyrite and sulphide veins, all of which occur within the upper bedded sandstone to pebble breccia sequence (Section 3.3.5, Fig. 5.1). However, sulphide veins also occur in the lower thickly bedded parts of GGF M6. In GGF M6, massive sulphides are laterally continuous over the 630 m between 17,700 N to 18,330 N. Flat lying dolerite sills in the southern and central areas of the deposit, interrupt the continuity of massive sulphide. The southern-most occurrence of massive sulphide is referred to as 'A' zone and the central area as 'C' zone (18,200 N to ~18,330 N) (Fig. 5.1). Sulphides terminate in the south at 17,650 N, where a thinly developed stringer vein zone is intruded by DAC3 dacite (Fig. 5.1). From the south at A zone to the north at C zone, a gradual thickening of massive sulphide and veins is observed. At C zone, massive sulphides abut a DAC3 dacite intrusion (Fig. 5.1). North of this DAC3 dacite, mineralisation was weakly developed in GGF M6, and consists predominantly of sulphide veins with minor massive sulphide; this zone is discontinuous northwards and is referred to as 'D' zone (Fig. 5.1). The geometry and association of massive sulphide and sulphide veins within GGF M6 are discussed in the following sections.

5.4.1 Geometry and distribution

Massive sphalerite is laterally continuous between 17,700 N and 18,330 N, whilst massive pyrite is best developed at C zone between 18,220 N and 18,330 N. Massive pyrite at C zone underlies massive sphalerite. Narrow zones of massive pyrite (<5 m intervals) occur south of C zone within massive sphalerite, but are discontinuous and lensoidal. The massive sphalerite is conformable to bedding (~310°) with a steep west to subvertical dip, however, massive pyrite at C zone cuts across bedding.

In the south at A zone, massive sphalerite thins to less than 5 m and has an underlying 5 to 10 m wide stringer zone (Fig. 5.2). Mineralisation at A zone does not outcrop, with massive sulphides having a down dip extent in excess of 200 m. Dolerite intrudes the GGF and massive sulphide, but does not significantly offset the strata or massive sulphide (Fig. 5.2). At A zone, massive sphalerite is conformable to bedded sandstone and pebble breccia in GGF M6, whilst stringer veins are stratabound. The southward thinning of massive sphalerite and sulphide veins toward A zone is coincident with the southward thinning of GGF M6 (Chapter 3).

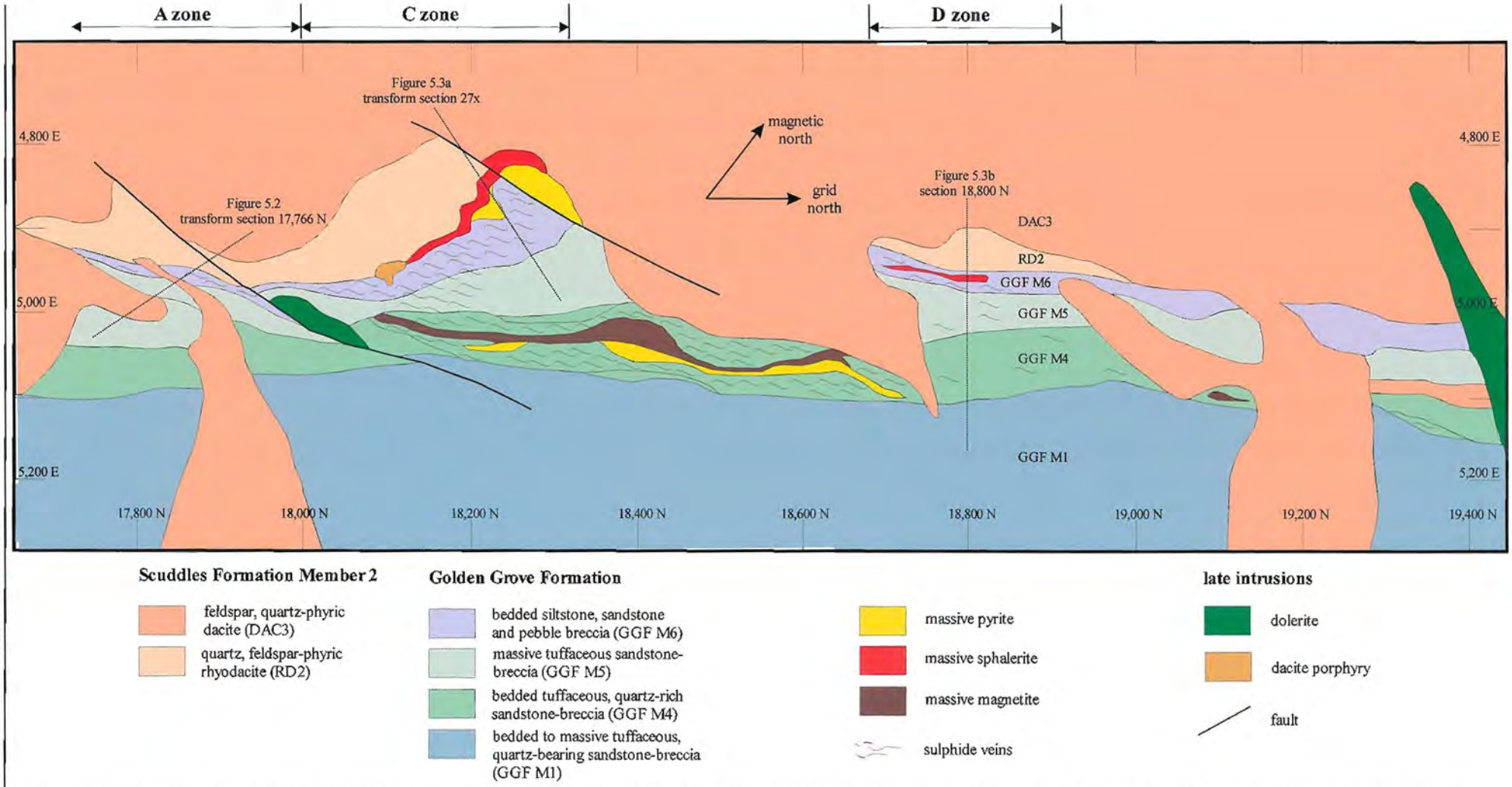

Figure 5.1: Plan projection at 10,200 m RL of the Gossan Hill VHMS deposit (~150 m below surface; 50 m window). Massive sphalerite and pyrite occur in GGF M6, whilst massive pyrite and magnetite occur in GGF M4. Zones of massive sulphide and massive magnetite are enveloped by sulphide veins. The DAC3 dacite of the Scuddles Formation Member 2 intrudes the GGF as well as RD2 rhyodacite of the same member. Massive sulphide, stringer veins and massive magnetite occur on the southern side of a DAC3 dacite intrusion. Mine grid in metres.

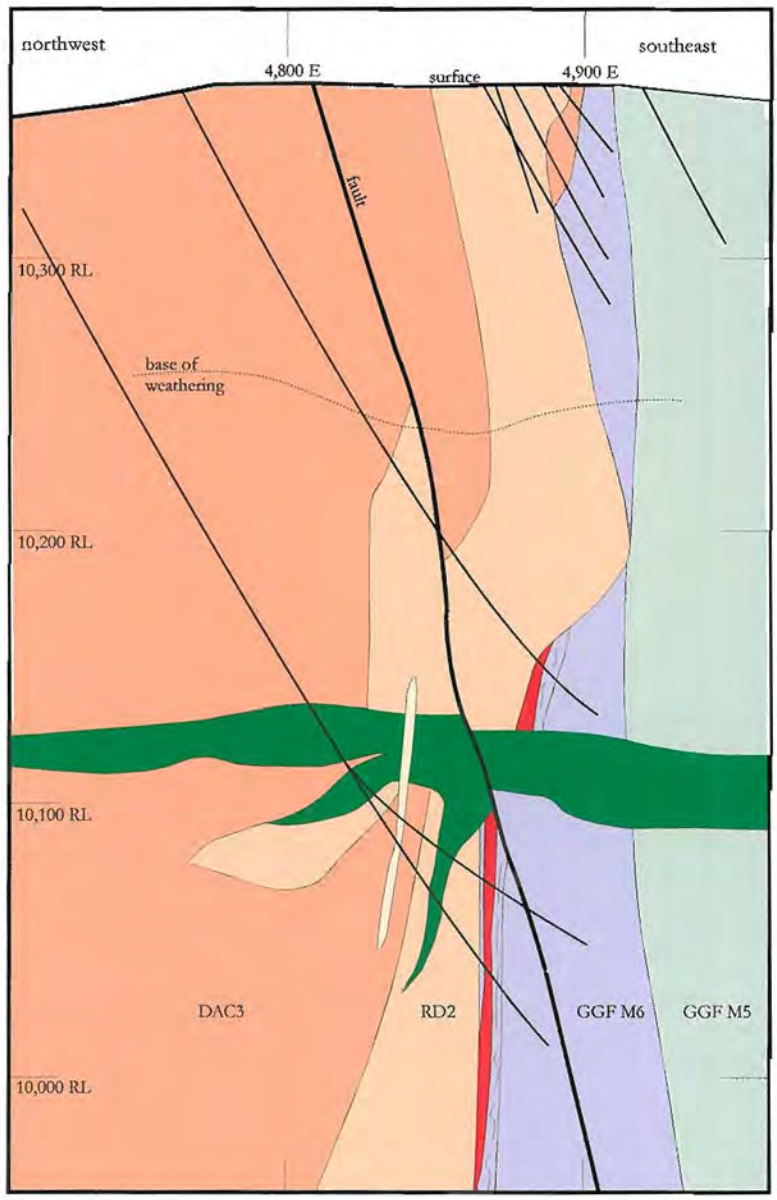

Figure 5.2: Section in the south of Gossan Hill at A zone along transform section 17,766 N (refer Fig. 5.1 for location). A flat lying dolerite intrudes the Golden Grove and Scuddles Formations. Massive sphalerite forms a narrow zone (~5 m thick) and is underlain by a narrow semi-conformable zone of sphalerite-rich veins within GGF M6. A late brittle fault cuts the sequence with minor displacement.

Between A and C zone, massive sphalerite is broadly conformable to GGF M6, but the width of massive sulphide and stringer zone varies. Narrower zones of massive sphalerite are enclosed by thicker developments of veining, and conversely, wider massive sphalerite zones have narrow adjacent zones of veins. Between A and C zone, massive sulphides are Zn-rich in the uppermost parts and increasingly pyrite-chalcopyrite-rich in lower parts toward C zone. The geometry of massive sulphide between A and C zone is complicated by late dolerite and porphyritic dacite intrusions, as well as minor displacement along brittle faults.

C zone represents the thickest development of massive sulphides with up to 45 m of massive sphalerite overlying up to 60 m of massive pyrite. C zone also has overlying and underlying sulphide-rich stringer veins (Fig. 5.3a). The geometry of C zone is stratabound with a subvertical dip. Massive sulphide is not continuous from C zone across the DAC3 dacite to the northern D zone. D zone consists of weakly developed, discontinuous, stratabound stringer sulphides, with minor massive sulphides less than 6 m thick (Fig. 5.3b).

5.4.2 Upper contacts

Massive sphalerite is commonly overlain by conformable, silicified, sulphide-veined, bedded strata or by massive rhyodacite breccia facies (Fig. 5.4). At C zone, massive sphalerite has sharp, discordant contacts against DAC3 dacite, which itself has fine-grained chilled margins. Where overlain by polymict rhyodacite breccia, the upper contact of massive sphalerite is sharp and locally undulose, due to erosional basal contacts of the breccia. The rhyodacite breccia occupies a narrow zone (up to 5 m), that locally contains sulphide clasts (Fig. 5.4b) and disseminated sulphides in the breccia matrix. This sulphide clast-bearing rhyodacite breccia forms an erosional basal breccia to unmineralised massive rhyodacite (RD2) (Fig. 5.4b).

In other places, massive sulphide has sharp to gradational, conformable to disconformable and erosional, upper contacts to unmineralised, silicified, bedded sandstone-siltstone and pebble breccia (Fig. 5.4d). These upper contacts between massive sphalerite and unmineralised sandstone-breccia vary from sharp or gradational (<10 cm wide), and have tens of metres of unmineralised, bedded strata overlying massive sphalerite (*e.g.*, Fig. 5.4d). M1 Marker chert-lithic horizons commonly occur in these overlying bedded sequences and in some places are themselves veined by pyrite. Elsewhere, massive sulphides have gradational contacts (<2 m) to pyrite-sphalerite veined bedded sandstone and siltstone (Fig. 5.4a), or are faulted (Fig. 5.4c). At C zone, the upper contact of massive sphalerite is gradational to a sulphide-veined (sphalerite-pyrite veins) sandstone-siltstone and pebble breccia sequence. Within these gradational veined contacts, the intensity and abundance of stringer veins decreases away from massive sulphides towards unmineralised bedded sediments. In the north at D zone, sulphide veins occur in bedded sandstone-siltstone, which are interbedded with unmineralised pebble breccia (Fig. 5.4e). The upper contact of the stringer veins at D zone is sharp and conformable (Fig. 5.4e).

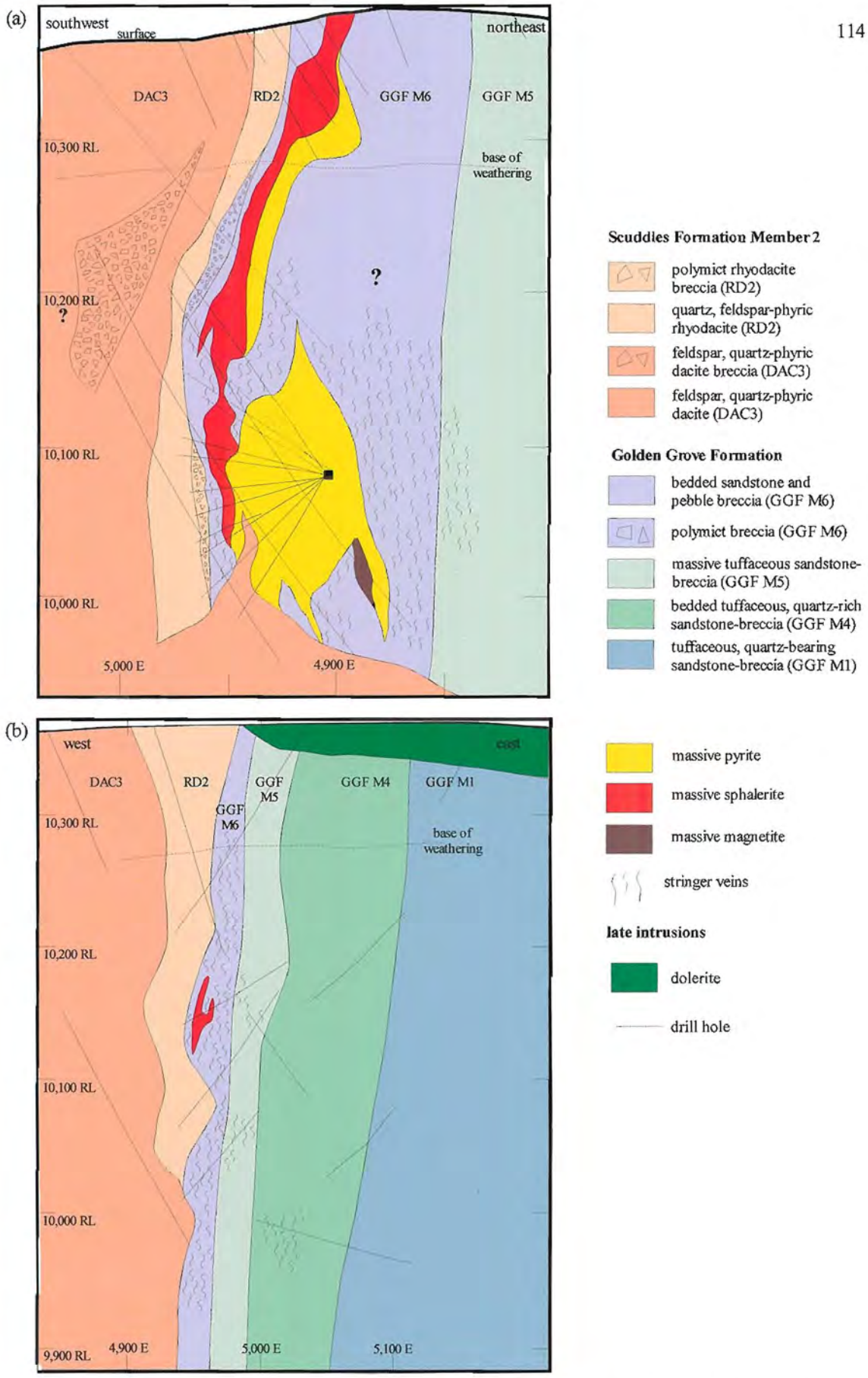

Figure 5.3: Sections through the upper ore zone. (a) Transform section through C zone (Cuddy 27x, 10 m window) illustrating the distribution of massive sphalerite, massive pyrite and stringer veins in GGF M6. (b) East-west section 18,800 N (25 m window) in the north of Gossan Hill at D zone. Massive sphalerite is thinly developed and enveloped by a stringer zone in GGF M6. Mine grid in metres.

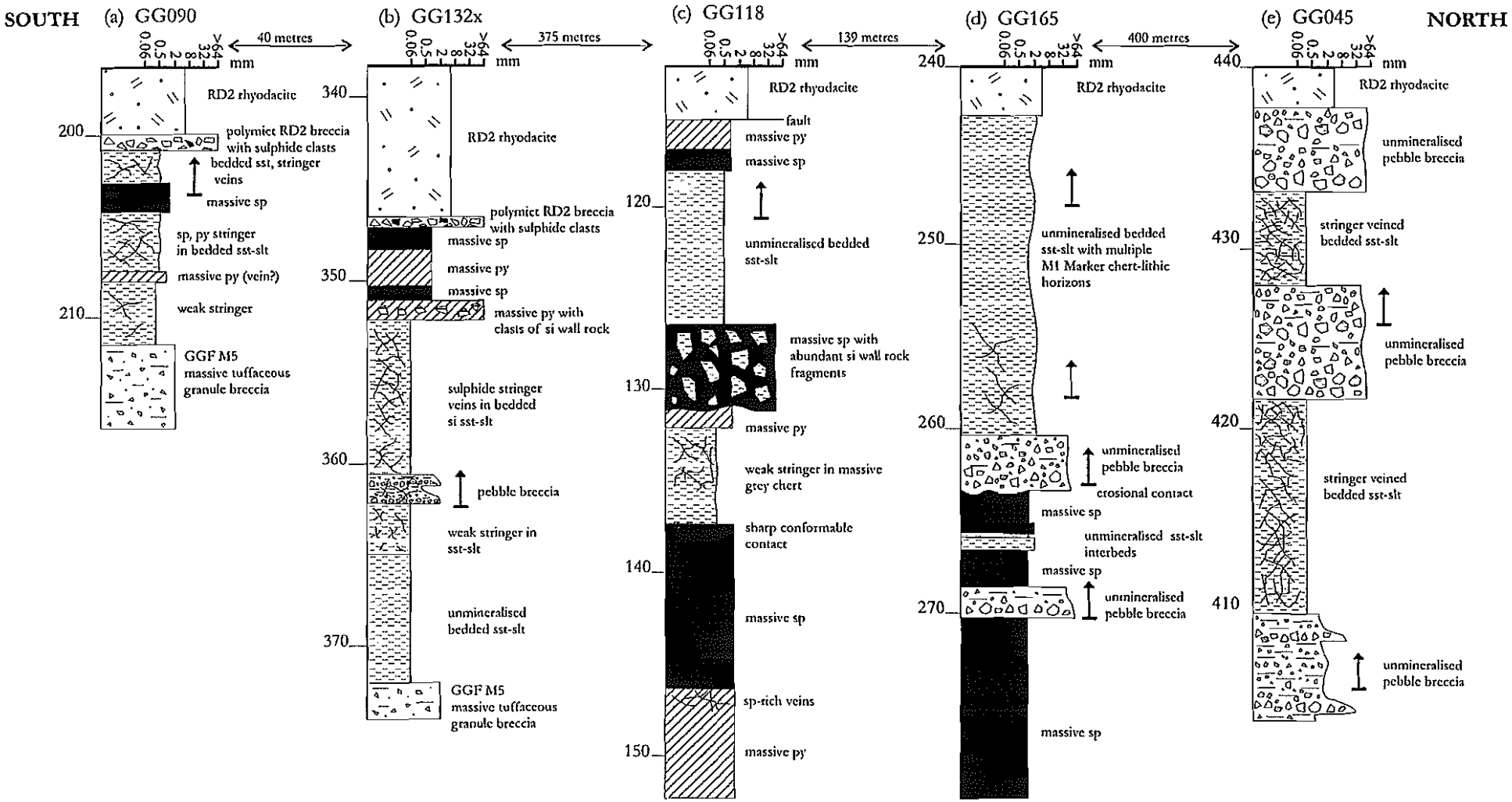

Figure 5.4: Simplified graphic logs of drill holes through the upper contact of massive sulphide at Gossan Hill from south to north. (a) GG090 (transform section 17,729 N) south of A zone, (b) GG132x (transform section 17,766 N) at A zone, (c) GG118 (transform section 18,141 N), (d) GG165 at C zone and (e) GG045 at D zone. Vertical distances down hole in metres and horizontal scale measures grain size. All lithologies are in GGF M6 unless otherwise specified. Up directions indicate facing from graded beds. Abbreviations used are py = pyrite, slt = silststone, si = quartz alteration, sp = sphalerite, sst = sandstone.

In summary, narrow intervals of thinly bedded sandstone-siltstone and pebble breccia generally overly massive sphalerite. Overlying sediments may be veined by sulphides and represent gradational upper contacts, or be conformable and free of sulphide veins. In the south at A zone, massive sphalerite is generally overlain by polymict rhyodacite breccia facies that contains massive sulphide clasts.

5.4.3 Lower contacts

The lower contact between massive sulphide and veined wall rock is gradational to sharp. At A zone, massive sulphide has a 10 mm wide sharp contact with intensely silicified bedded wall rock that contains sulphide veins. The basal contact of stringer veins in this location is gradational over 5 m to unmineralised bedded strata. The basal contact of this stringer zone has decreasing intensity and vein widths away from massive sphalerite. In the south of Gossan Hill, the width of the underlying stringer vein zone approximates the width of GGF M6 and is conformable to the lower contact of GGF M6 and GGF M5 (Fig. 5.4a). Northwards from A zone, the lower contact of massive sphalerite to underlying veined wall rock is sharp, and bedded sandstone and siltstone (*e.g.*, Fig. 5.4b) host sulphide veins. In all occurrences, the intensity of veining decreases away from massive sulphide and represents gradational lower massive sulphide contacts.

Stringer veins are weakly developed in GGF M5, and the stringer zone is increasingly discordant northwards towards C zone. At C zone, the lower contact from massive sphalerite to massive pyrite is gradational, varying from 0.2 to 5 m in width and involves increasing pyrite, pyrrhotite and/or magnetite with depth (Fig. 5.5a). This gradational contact is not only characterised by a mineralogical change, but also by the occurrence of sphalerite veins in massive pyrite (*e.g.*, Fig. 5.5a at 330 m). Near the lower massive sphalerite contact, there are narrow sphalerite-rich zones (<2 m) (Fig. 5.5b at 315 m).

The lower contact of massive pyrite against the stringer zone is also gradational, except where faulted. Gradational contacts of massive pyrite vary from centimetres to metres in thickness (Fig. 5.5a), and contain abundant relict wall rock, particularly where pyrite-rich veins coalesce to form semi-massive pyrite. In underground exposure, the lower contact of stringer mineralisation is gradational over a distance of decimetres (Appendix A3.1a and A3.1b). The size and intensity of stringer veins decreases away from massive pyrite, and the stringer zone is discordant across the lower contact of GGF M6 (Appendix A3.1a and A3.1b).

In summary, the lower contact of massive sphalerite grades to either massive pyrite at C zone or to a zone containing sulphide veins. The intensity of stringer veins generally decreases away from the massive sulphide. At C zone, massive sphalerite has gradational lower contacts to massive pyrite, which grades into a stringer vein zone. Stringer mineralisation is stratabound to semi-conformable within GGF M6 in the south, but is increasingly discordant to GGF M6 towards C zone. The distribution of the stringer zone is further evaluated in Section 5.4.6.

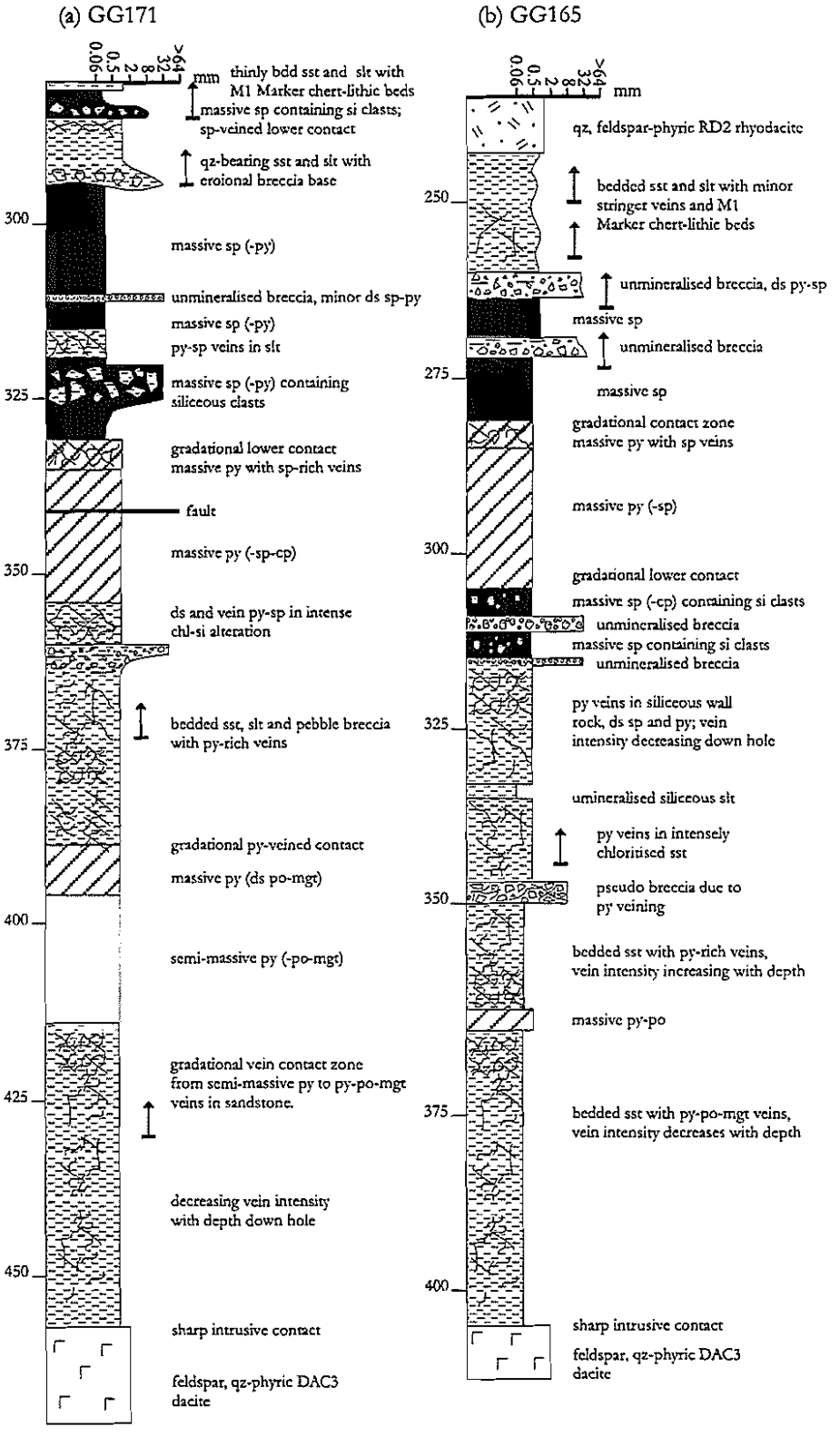

Figure 5.5: Simplified graphic logs through massive sphalerite, massive pyrite and stringer veining in the upper ore zone (GGF M6) at C zone from drill holes (a) GG171 and (b) GG165. Massive sphalerite overlies massive pyrite and has gradational lower contacts. Massive pyrite interdigitates with sulphide-rich stringer veins. Massive pyrite and sphalerite contain intervals of unmineralised bedded sandstone and pebble breccia that may have breccia textures due to sulphide replacement of the silicified wall rock. Both drill holes GG165 and GG171 have pyrite-pyrrhotite-magnetite in their lower parts and sphalerite-pyrite in their upper parts. Distance down hole is in metres. Arrows indicate facing in graded beds. Abbreviations used are ds = disseminated, chl = chlorite alteration, cp = chalcopyrite, mgt = magnetite, po = pyrrhotite, py = pyrite, qz = quartz, slt = siltstone, si = quartz alteration, sp = sphalerite, sst = sandstone.

Figure 5.6

(a) Orange, fine-grained massive sphalerite containing finely disseminated pyrite. Minor quartz and chlorite occur interstitial to sphalerite and pyrite. The sample is from the upper parts of C zone. Scale in cm (sample 762091).

(b) Dark red, coarse-grained, annealed sphalerite. Pyrite and galena occur interstitial to sphalerite. The gangue is quartz. The sample has a crude banding and is from the south of Gossan Hill at A zone. Scale in cm (sample 760222).

(c) Massive fine-grained pyrite underlying massive sphalerite from the 300 level. Massive pyrite is weakly banded, and contains abundant disseminated pyrrhotite and magnetite. The gangue is chlorite. Weakly developed fractures in massive pyrite are filled with pyrrhotite, chlorite and quartz. Scale in cm (sample 97U052).

(d) Coalescing subhedral and irregular shaped pyrite aggregates forming massive coarse-grained pyrite in chlorite. Fine-grained magnetite and pyrrhotite in ill fractured pyrite aggregates. Underground exposure on the 300 level. Scale in cm (sample 97U053).

(e) Grey, intensely silicified wall rock in GGF M6 cut by narrow, millimetre-wide planar, discontinuous pyrite-chlorite and chlorite veins. Pyrite-chlorite veins cut chlorite veins. Subparallel chlorite bands in the silicified wall rock delineate relict bedding in the altered sandstone. A 'pseudo' breccia texture is superimposed on the wall rock by the sulphide-chlorite veins. Scale is in cm (4,814 E, 18,259 N, 10,179 RL, GG96/182 at 110.3 metres).

(f) Sulphide- and carbonate-rich veins cutting massive, intensely silicified sandstone in GGF M6. Stringer veins form a stockwork with pyrite-rich veins cutting the carbonate-rich veins. The pyrite veins have irregular thickness and are discontinuous. Carbonate-rich veins are narrower and more continuous. Underground exposure on the 300 level (4,896 E, 18,254 N, 10,050 RL).

(g) Irregular sphalerite-rich vein grading to a pyrite-rich vein in GGF M6 at C zone. The sphalerite-rich vein contains sphalerite, pyrite and quartz and has bleached silicified halos in the adjacent wall rock. Chlorite±sulphide micro-veins produce an apparent breccia texture to the precursor sandstone, and these veins also have grey, bleached millimetre-wide haloes caused by silicification. Scale in cm (4,815 E, 18,260 N, 10,180 RL, G96/182 at 111.2 metres).

(h) *In situ* brecciation of a thinly bedded sandstone-siltstone interval in GGF M6. Banding in the wall rock 'pseudo clasts' are subparallel bands of differing chlorite-quartz alteration. Some pseudo clasts are chert due to intense silicification. The margins of all pseudo clasts, particularly adjacent to the chlorite±pyrite veins, have millimetre-sized quartz haloes. Scale in cm (4,813 E, 18,261 N, 10,170 RL, G96/182 at 101.0 metres).

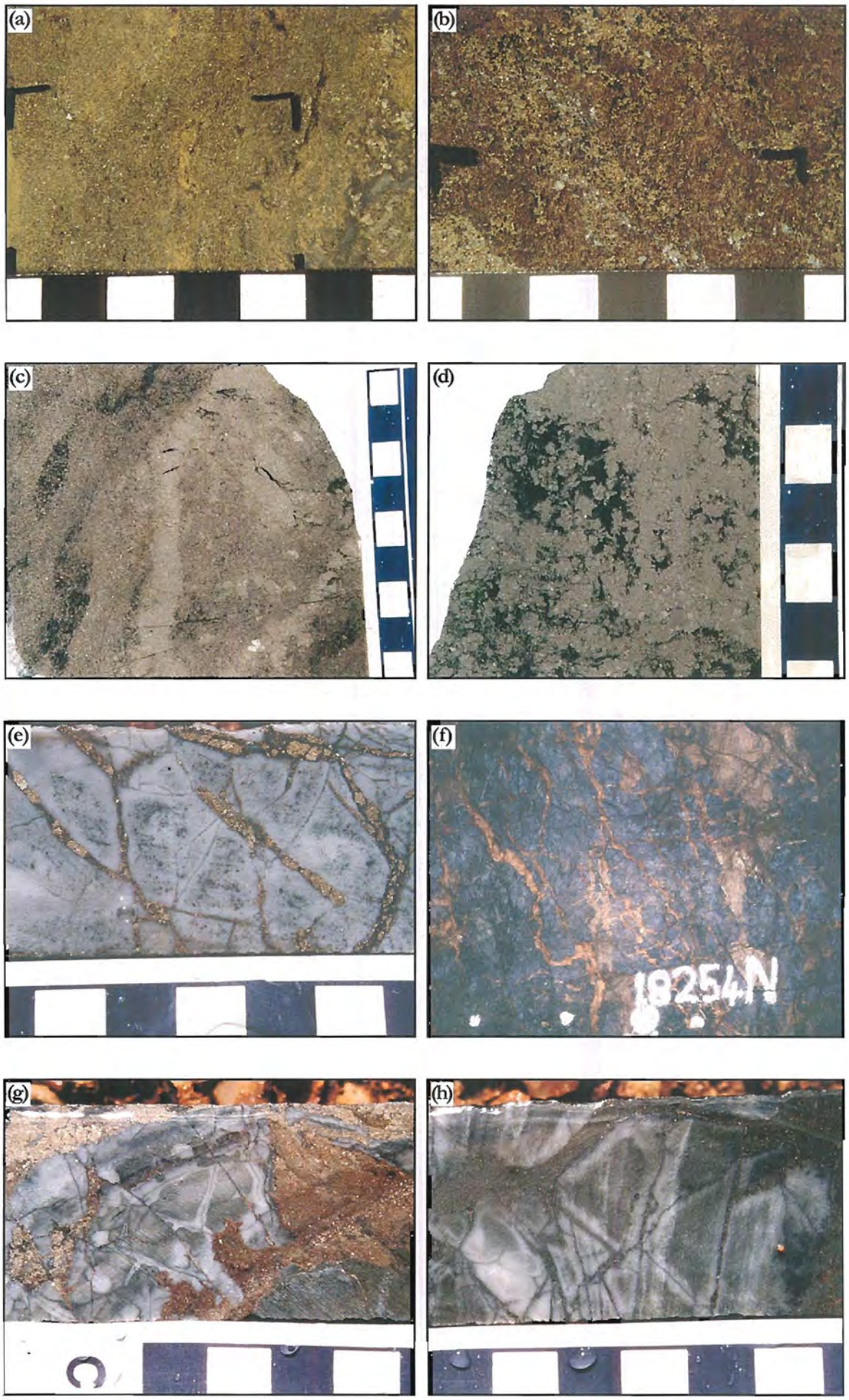
(a)
(b)
(c)
(d)
(e)
(f)
18254N
(g)
(h)

5.4.4 Massive sphalerite

Massive sphalerite consists mainly of sphalerite, with variable proportions of pyrite, galena, quartz and chlorite (Fig. 5.6a). In the south of Gossan Hill, massive sphalerite contains scattered pyrite grains and can have irregular narrow intervals of massive pyrite. The semi-continuous stratiform occurrence of massive sphalerite is due to lensing and interdigitation of massive sphalerite with sphalerite-rich stringer veins. Magnetite occurs as rare disseminations within massive sphalerite south of C zone. At C zone, both magnetite and pyrrhotite are common, particularly where there is abundant pyrite in massive sphalerite. Massive sphalerite can be fine- or coarse-grained (>200 μm), with galena typically occurring in coarse-grained sphalerite (Fig. 5.6b). The colour of sphalerite is variable, from lighter, honey-coloured sphalerite in the upper parts of massive sphalerite, to darker, red or brown sphalerite in the lower or coarse-grained parts of massive sphalerite. Both fine- and coarse-grained sphalerite are intermixed in massive sphalerite, with sphalerite adjacent to DAC3 dacite generally coarse-grained and annealed. Banded massive sphalerite is rare but does occur near the contact of massive sphalerite with DAC3 dacite. This banding consists of millimetre to centimetre wide sphalerite-rich and pyrite-rich bands parallel to the contact.

5.4.5 Massive pyrite

Massive pyrite occurs as narrow intervals within massive sphalerite. For example, massive pyrite at A zone occurs as a narrow, 2 m wide layer within massive sphalerite and also as a 1 m zone underlying massive sphalerite (Fig. 5.4b at 350 m). The latter occurrence is probably a pyrite-rich vein because it has sharp contacts with silicified wall rock, and it contains wall rock clasts. Massive pyrite generally consists of fine-grained (<0.5 mm) pyrite with interstitial quartz-chlorite gangue. At C zone, massive pyrite consists of closely packed euhedral to subhedral pyrite that is fine- (<0.5 mm) to coarse-grained (<5 mm) (Figs. 5.6c and 5.6d respectively). Massive pyrite commonly contains abundant interstitial chalcopyrite, pyrrhotite and magnetite.

5.4.6 Stringer veins

Stringer veins overlie, underlie and interdigitate with massive sulphides in GGF M6. Commonly, the contacts between massive sulphide and stringer mineralisation are gradational, but are locally sharp and conformable. Stringer veins are absent from adjacent or overlying hangingwall lavas of Scuddles Formation. Stringer veins are however, intensely developed in sediments adjacent to massive sulphide, generally with a decreasing intensity (both in abundance and width) away from the massive sulphide. Sulphide stringer veins are less intensely developed at A zone where they form a semi-conformable zone within GGF M6 (Section 5.4.3). At C zone, stringer veins are intensely developed, forming a stockwork that cuts across stratigraphy, as illustrated in Appendices A3.1a and A3.1b.

Stringer veins are hosted by quartz and/or chlorite altered, bedded sandstone-siltstone and pebble breccia of GGF M6. The veins generally have sharp margins against intensely silicified or quartz-chlorite altered wall rock. Veins are typically sulphide-rich with either

pyrite or sphalerite as the major sulphide, and vein mineralogy is given in Section 5.9. The width of the veins can be less than 1 mm or as wide as 5 m (Appendix A3.1b). Laterally continuous sulphide veins tend to be planar and either parallel or weakly discordant to bedding (Appendices A3.1a and A3.1b, Section 4.8.2). Veins that cut across bedding at a high angle may also be planar, but are generally discontinuous, and pinch and swell. Both planar and discontinuous veins form anastomosing stockwork zones below and within wall rock in massive sulphide. Figure 5.6e illustrates millimetre wide, pyrite-rich veins that are planar, discontinuous and randomly oriented through an intensely silicified wall rock of GGF M6. In this example, sulphide veins have superimposed a breccia texture on the siliceous wall rock. A larger-scale example of similar vein-wall rock textures is given in Figure 5.6f. Silicification of the host rock extends several millimetres either side of the sulphide veins, bleaching the rock (Fig. 5.6g). Furthermore, sulphide-rich veins cut fine, less than 1 mm wide veins of chlorite (Fig. 5.6g). The interconnected array of sulphide and chlorite veins result in a 'pseudo' brecciation texture of a thinly bedded sandstone-siltstone host rock (Fig. 5.6h). Within the 'pseudo' breccia clasts, banding, relict after bedding, often has different orientations and jigsaw fit textures (Figs. 5.6h and 5.7a), indicating that sulphide and chlorite veining caused local rotation and disruption of the host rock. Chlorite and sulphide veins represent fractures and indicate strong fracturing of the rock prior to or during vein formation. Fracture processes resulted in local disruption of the host and the development of *in situ* breccia textures. To accommodate such a brittle deformation as inferred from these widespread fractures, the rock must have been indurated prior to fracturing.

Many sulphide veins are parallel to bedding in GGF M6 (Chapter 4). The larger sulphide veins tend to parallel bedding and occur between beds of sandstone and pebble breccia. In these examples, the vein walls are sharp to gradational, with the latter having disseminated sulphides in adjacent beds or smaller, millimetre-sized, radiating sulphide veins penetrating the adjacent wall rock (Fig. 5.7c). Similar trends are also observed in narrower sulphide veins (<20 mm) that parallel bedding in sandstone-siltstone intervals (Figs. 5.7b and 5.7d). These veins have sharp or gradational (<1 mm) margins, pinch and swell, and there is disseminated sulphide in the wall rock. The abundance of bedding parallel veins in the stringer zone indicates that bedding planes acted as planes of weakness during vein formation.

At the Scuddles deposit, stringer mineralisation underlies massive sphalerite and massive pyrite. The sulphide veins differ from their counterparts at Gossan Hill, with the pyrite-chalcopyrite-rich stockwork in GGF M6 at Scuddles lacking evidence of bedding control (Fig. 5.7e). The Scuddles stringer veins are hosted by intensely quartz-chlorite altered wall rock of GGF M6, and appear to be entirely fracture controlled.

5.4.7 Indicators of relict wall rock

Within stringer zones, relict, altered, wall rock fragments are common. The increasing intensity of stringer veining towards massive sulphide is associated with a decrease in the

Figure 5.7

(a) Sphalerite-rich veins in intensely silicified wall rock. Sphalerite veins form centimetre to millimetre-sized networks, which result in a pseudo breccia texture. *In situ* disaggregation textures are observed, with minor clast rotation inferred from changes in the orientation of the banding (after bedding) in the silicified clasts. Scale in cm (4,823 E, 18,264 N, 10,183 RL, G96/182 at 122.7 metres).

(b) Sphalerite-rich veining in a bedded sequence of sandstone and siltstone of GGF M6. The bedded interval is intensely silicified and sphalerite veins are both discordant and parallel to bedding. Discordant veins form centimetre-wide irregular veins that have relict wall rock clasts within the vein. Conformable veins are narrower, millimetre-wide veins that are continuous and have sharp to gradational vein margins (photo provided courtesy of Bruce Gemmell).

(c) Larger conformable pyrite-rich vein in thinly bedded, quartz-chlorite altered sandstone and siltstone of GGF M6. The vein has conformable sharp margins to adjacent sediment. Radiating, discordant, centimetre- to millimetre-wide pyrite-rich veins occur in the adjacent wall rock, and are discontinuous away from the main conformable pyrite-rich vein (4,894 E, 18,239 N, 10,050 RL, Cuddy 25x on the 300 level).

(d) Sub-parallel pyrite-carbonate stringer veins in bedded sandstone and granule breccia of GGF M6, near its contact to GGF M5. Veins are conformable to bedding and are planar. These continuous veins have sharp margins to the chlorite-quartz-altered wall rock. Narrow millimetre-sized, discontinuous and discordant pyrite-carbonate-rich veins emanate outward from the wider conformable veins (4,971 E, 18, 244N, 10,050 RL, 300 level access drive).

(e) Stringer veining underlying massive sulphide at the Scuddles deposit. Pyrite-chalcopyrite stringer veins occur in pervasive intense quartz-chlorite altered sandstone of GGF M6. The anastomosing pyrite-chalcopyrite veins form a stockwork and show no preferred orientation to bedding. The crenulation textures and small-scale folding in many of these veins is axial planar to the penetrative cleavage. Rock bolts are 40 cm long (underground exposure on the 470 level).

(f) A metre-sized zone of intensely silicified, thinly bedded sandstone occurs within massive pyrite. The contact between massive pyrite and the sandstone clast are sharp to gradational. Within the silicified clast, pyrite veining is conformable to bedding, but these veins are discontinuous and planar (4,929 E, 18,244 N, 10,050 RL, underground exposure on the 300 level access drive).

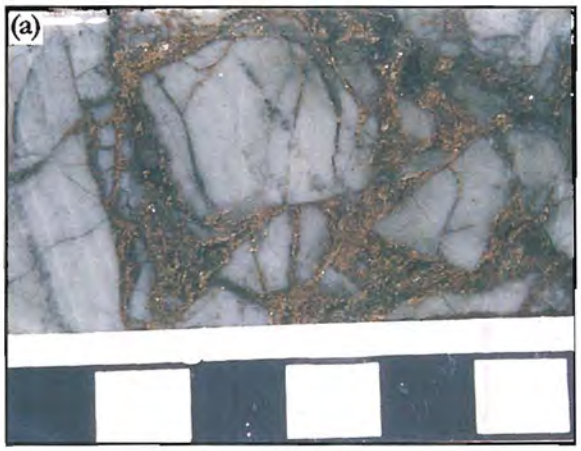
(a)

(b)

(c)

(d)

(e)

(f)

size and abundance of visible relict wall rock fragments. At Gossan Hill, it is not uncommon for fragments of grey, unmineralised, intensely quartz altered rock to occur within both massive pyrite and massive sphalerite (Figs. 5.4c, 5.7f and Appendices A3.1a and A3.1b). These clasts of relict wall rock occur throughout massive sulphide and vary in size up to 2 m, but are generally less than 5 cm with subrounded to subangular forms and sharp margins. Some wall rock clasts have banding, possibly relict of bedding, whilst others consist of massive chert with no relict textures due to intense silicification. The two possible origins for wall rock clasts are (1) relict wall rock due to replacement and veining, or (2) clasts incorporated in massive sulphide during reworking. There is little evidence to support reworked massive sulphides, due to the existence of gradational ore contacts, and the absence of sedimentary or breccia textures within massive sulphides. These observations support a replacement and veining origin for the chert clasts.

Unmineralised beds or bedded intervals of sandstone-siltstone and pebble breccia occur throughout the massive sulphides and contain minor disseminated sulphide or sulphide veins. Unmineralised beds can form single beds (from <0.1 to 50 cm), bedded intervals (<4 m wide) (Fig. 5.4d) or massive grey chert. The contacts between massive sulphide and unmineralised beds vary from sharp to gradational (<10 cm). It is likely that some of these intervals are large wall rock fragments, as observed in Figure 5.7f, but they could also represent unmineralised, bedded intervals in the massive sulphide. At C zone, discrete horizons of sandstone and pebble breccia occur within massive sphalerite (Figs. 5.5a and 5.5b), and include clast supported pebble breccia with only minor disseminated sulphide. The unmineralised, more finely grained bedded sequences in massive sulphides locally host minor disseminated pyrite.

5.4.8 Porosity and permeability controls of the wall rock

The contacts between massive sulphide and unmineralised pebble breccia or bedded sandstone intervals are commonly gradational. These gradational contacts are up to 10 cm wide, with decreasing sulphide contents away from the massive sulphide. An example of a gradational replacement contact between massive sphalerite and a pebble breccia is given in Figure 5.8a. In this pebble breccia, massive sulphide forms the matrix to unmineralised, silicified clasts, and the clast margins have contacts varying from gradational (millimetres wide) to sharp against the massive sulphide. By contrast, some pebble breccia units in massive sulphide contain only minor disseminated sulphide (pyrite and sphalerite) in the matrix. Similarly, beds of sandstone within massive sphalerite may contain minor disseminated sulphide (Fig. 5.8b), whilst nearby sandstone is strongly veined by sulphides.

The difference in the abundance and occurrence of sulphides within and between bedded breccia and sandstone-siltstone beds and intervals, probably results from primary permeability contrasts in the volcaniclastic sequence. Permeability control on the distribution of sulphides on a bed-scale could be induced by either (1) a primary permeability (lithological), or (2) permeability modified by hydrothermal alteration (*i.e.*, different permeability for quartz and chlorite altered rocks). Similarly, the distribution of

Figure 5.8

(a) Gradational contact between massive sphalerite and a pebble breccia in GGF M6 at C zone. Sphalerite and lesser pyrite form the matrix to silicified clasts in the pebble breccia. The pebble breccia is polymict having silicified lithic clasts (cream) and chlorite-quartz altered lithic clasts (grey). Scale in inches (sample 762093).

(b) Diffuse pyrite vein in a granule breccia bed within bedded sandstone-breccia of GGF M6. Pyrite occurs as disseminations through the chlorite-quartz altered granule breccia, whilst in adjacent quartz-chlorite altered sandstone, pyrite forms planar discontinuous narrow veins. Scale in cm (4,820 E, 18,265 N, 10,067 RL, GG96/184 at 42.5 m).

(c) Massive magnetite (dark grey) has sharp conformable contacts with chlorite-talc altered sandstone-siltstone in GGF M4. The bedded sandstone intervals contain disseminated magnetite. Magnetite is also veined by diffuse pyrite-pyrrhotite veins and carbonate-quartz veins (~ 5,051 E, 18,640 N, 10,113 RL, GG162 between 311 to 315 m).

(d) Sharp contact between massive magnetite-carbonate (Mgt) (oxidised to brown colour) and fine-grained massive DAC3 dacite (DAC)(5,009 E, 18,429 N, 9,980 RL, GG038 at 454.3 metres).

(e) Sharp contact of massive magnetite with massive pyrite-chalcopyrite. Some magnetite can be seen in the massive pyrite and the contact consists of a narrow interval of chloritised sandstone. This contact is conformable and its context is illustrated in mapping given in Appendix 5.2. Rock bolts are 40 cm long (5,089 E, 18,486 N, 10,100 RL, underground exposure on the 250 level).

(f) Massive magnetite containing abundant interstitial carbonate. Magnetite forms fine- and coarse-grained aggregates in a chlorite-altered sandstone of GGF M4. Magnetite aggregates locally coalesce, whilst both chlorite and magnetite host a spaced undulatory cleavage (S3). Scale in cm (sample 97U10).

(g) Nodular massive magnetite containing large (1-2 mm) subrounded magnetite grains and aggregates. The matrix consists of carbonate and minor talc, chalcopyrite and pyrrhotite. Carbonate and talc fill fractures in the magnetite. Scale in cm (sample 769320).

(h) Massive magnetite with angular to sub-rounded patches of intensely quartz-chlorite altered sandstone. Volcanic quartz is rare in these relict wall rock patches. The contacts between the enclosing massive magnetite and the wall rock are gradational to sharp. Massive magnetite in this has a fine-grained granular texture. Scale in cm (sample 762007).

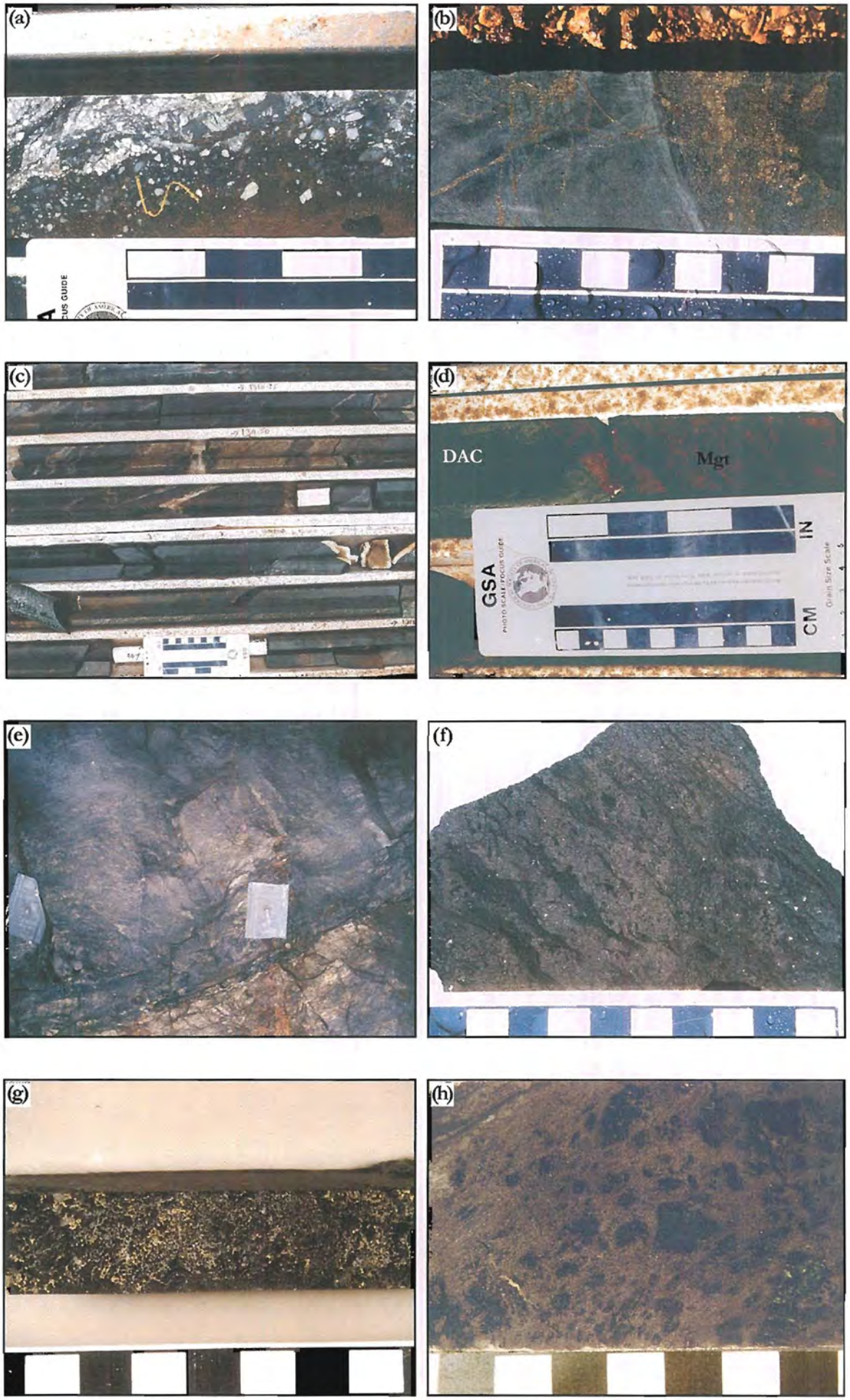
(a)
(b)
(c)
(d)
DAC
Mgt
GSA
IN
CM
(e)
(f)
(g)
(h)

stringer vein mineralisation is the direct result of available pathways used by circulating hydrothermal fluids. In the case of Gossan Hill, these were primarily controlled by bedding planes and fractures (Section 5.4.6).

The inhomogeneous distribution of stringer veins through the strata at Gossan Hill may result from the bulk impermeability of the host sequence, as exemplified by the absence of fluid pathways in beds or bedded intervals that lack stringer veins. Additionally, the presence of siliceous wall rock clasts in massive sulphide (Section 5.4.7) is evidence of wall rock permeability to the pervading mineralising-hydrothermal solutions. Intense silicification during sulphide formation caused the incomplete replacement of permeable strata resulting in relict wall rock fragments in massive sulphide. Moreover, siliceous alteration accompanying sulphide formation may have locally indurated the strata and limited conduits for circulating mineralising fluids. Resulting fluid overpressuring of the pile induced hydraulic fracturing, which served to increase permeability and available conduits. Initiation of these fractures was likely have been controlled by differential competency contrasts within the host sequence, as evidenced by differing styles and abundances of veins between beds.

5.4.9 Discussion

Massive sulphide within GGF M6 occurs in the upper bedded sandstone-siltstone and pebble breccia sequence. These sulphides consist of massive sphalerite, massive pyrite and stringer veins. Massive sphalerite is laterally continuous (630 m) and generally overlies massive pyrite. Both massive sphalerite and massive pyrite interfinger with sulphide veining, which underlies, overlies and occurs within the massive sulphides. Bedded sandstone, siltstone and pebble breccia sequences overlie massive sulphides. Locally these overlying sedimentary sequences contain chert-lithic horizons of the M1 Marker and are veined by sulphides.

Stringer veins are most intensely developed adjacent to massive sulphide and decrease in intensity with distance away from massive sulphide. Stringer veins below massive sulphide form an anastomosing stockwork. At Gossan Hill, the thickness of massive sulphide increases northwards from A zone and is accompanied by an increase in the width of underlying stringer stockwork. Massive sulphides attain their greatest thickness on the southern side of a discordant DAC3 dacite at C zone. At this location, a core of massive pyrite is developed below massive sphalerite, and both pyrite and stringer veins are discordant to stratigraphy.

The morphology of massive sphalerite is sheet-like and broadly conformable, whilst at C zone, massive pyrite is mound-like and disconformable. The thickening of massive sulphides to the north is associated with the transition from semi-conformable to discordant mineralisation. Massive sulphides are not continuous across the DAC3 dacite, and north of this dacite is a narrow zone of stringer veining with minor massive sulphide, known as D zone. The change in thickness of massive sulphide across the DAC3 dacite coincides with the inferred location of a synvolcanic structure that is now occupied by DAC3 dacite. Massive sulphides and stringer veins do not occur in the DAC3 dacite,

which together with its chilled margins, indicate the dacite is younger than massive sulphide.

The form, occurrence and distribution of the sulphide veins indicate strong fracture and bedding control. Fracture controlled veins may have resulted from hydraulic brecciation of the wall rock, involving brittle deformation of an indurated wall rock. Evidence of relict wall rock is ubiquitous throughout massive sulphide and stringer zones in GGF M6. Many stringer veins have bleached wall rock margins that resulted from intense silicification during sulphide vein formation. Silicification is texturally destructive and has commonly modified the adjacent wall rocks to grey chert. Stringer veins and the abundance of relict wall rock, as well as unmineralised bedded intervals within massive sulphides and stringer zones, indicate that the dominant mechanism of sulphide formation was by replacement.

Clasts of chert within massive sulphide represent incomplete sulphide replacement of intensely silicified, impermeable relict wall rock fragments in an originally permeable strata. Massive sulphides that contain relict wall rock, probably reflect anastomosing stringer zones that had near-complete wall rock replacement. Overlying stringer veins intercalated with unmineralised sandstone-breccia to massive sulphides could reflect synchronous volcaniclastic sedimentation during sulphide formation. The presence of multiple M1 Marker chert-lithic horizons in GGF M6 (Chapter 3) supports multiple seafloor positions throughout this sequence associated with a changing seafloor position during sulphide formation. At some stage, the formation of massive sulphides within GGF M6 may have taken place at the seafloor, but was buried by continued sedimentation.

5.5 Massive magnetite

Massive magnetite is hosted by thinly bedded, quartz-rich tuffaceous sandstone and granule breccia of GGF M4. Massive magnetite consists primarily of magnetite, but also contains disseminations and veins of chalcopyrite, pyrrhotite and pyrite. Massive magnetite has a strike of 650 m and is spatially associated with massive pyrite and stringer veins in the lower massive sulphide zone (Section 5.6). Massive magnetite forms two main zones between 18,230 N to 18,470 N and 18,440 N to 18,720 N, and two smaller zones, one each in the south (18,110 N to 18,175 N) and north (18,680 N to 18,760 N) of Gossan Hill (Fig. 5.9). Laterally, these four massive magnetite zones form a semi-continuous interval between 18,110 N to 18,760 N (Fig. 5.9), and are interconnected by disseminated or vein magnetite. Furthermore, small lensoidal zones of massive magnetite within GGF M4 occur to the north of Gossan Hill at 19,100 N and 19,300 N (Fig. 5.1).

Each of the four massive magnetite zones also include narrow zones (generally <1 m) of altered sediments, and up to 10 m of semi-massive magnetite (30-50% magnetite). The intercalated occurrences of semi-massive magnetite and altered wall rock within massive magnetite are discussed in Section 5.5.4.

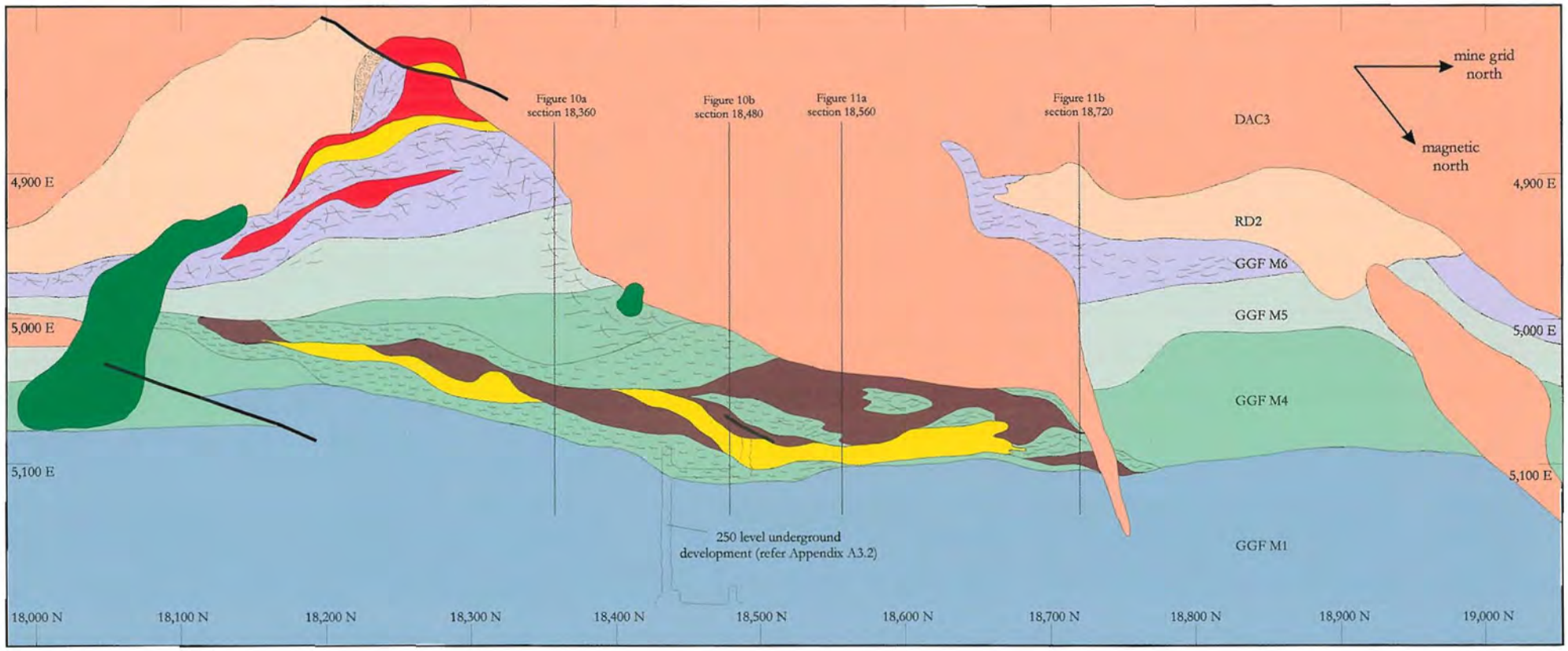

Figure 5.9: Level plan at 10,150 RL (200 m below surface) of the central and northern area of Gossan Hill. Massive pyrite, massive magnetite and stringer veins occur in GGF M4. Both massive sulphide and massive magnetite thin to the south and grade in to stringer vein zones. Massive sulphides in both ore zones are enveloped by a semiconformable stringer vein zones. Stringer veins massive magnetite and massive sulphides in GGF M4 and GGF M6 thin to the south. The upper and lower ore zones are connected by a discordant stringer zone through GGF M5. This stringer zone is best developed adjacent to the DAC3 dacite, which intrudes GGF M1 to GGF M6, the hangingwall RD2 rhyodacite and sulphide and magnetite. Refer to Figure 5.1 for legend. Mine grid in metres.

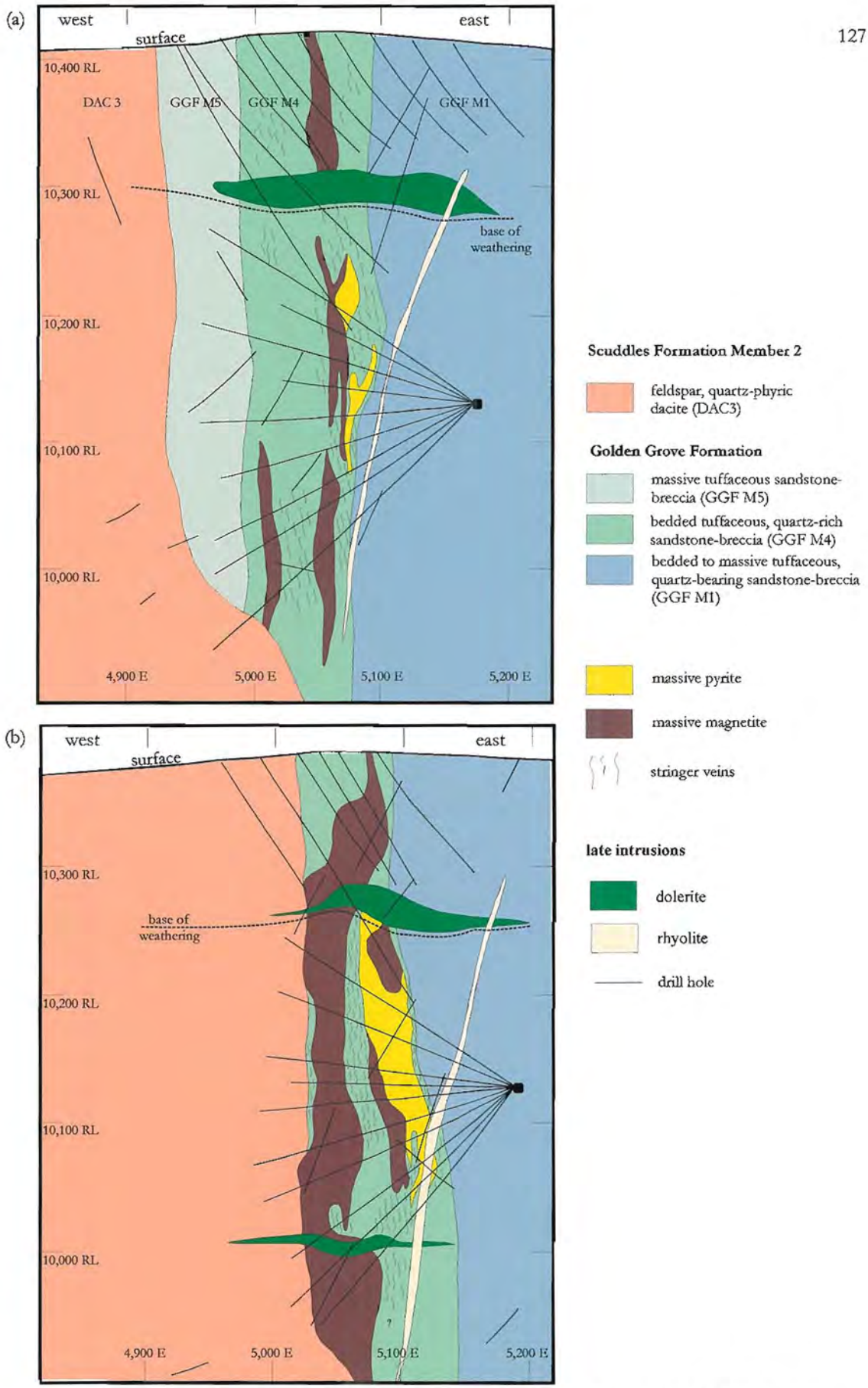

Figure 5.10: East-west sections of the lower ore zone at Gossan Hill. (a) Section 18,360 N (20 m window) consists of podiform zones of massive magnetite in GGF M4. Massive pyrite is discontinuous and underlies massive magnetite. Weak sulphide veining occurs in the host rock. (b) East-west section 18,480 N (20 m window) has thicker development of massive magnetite in the upper zone, with massive pyrite discordant to the lower massive magnetite zone. Stringer veins occur between massive pyrite and massive magnetite. The upper contact of massive magnetite and GGF M4 is intruded by DAC3 dacite. Mine grid in metres.

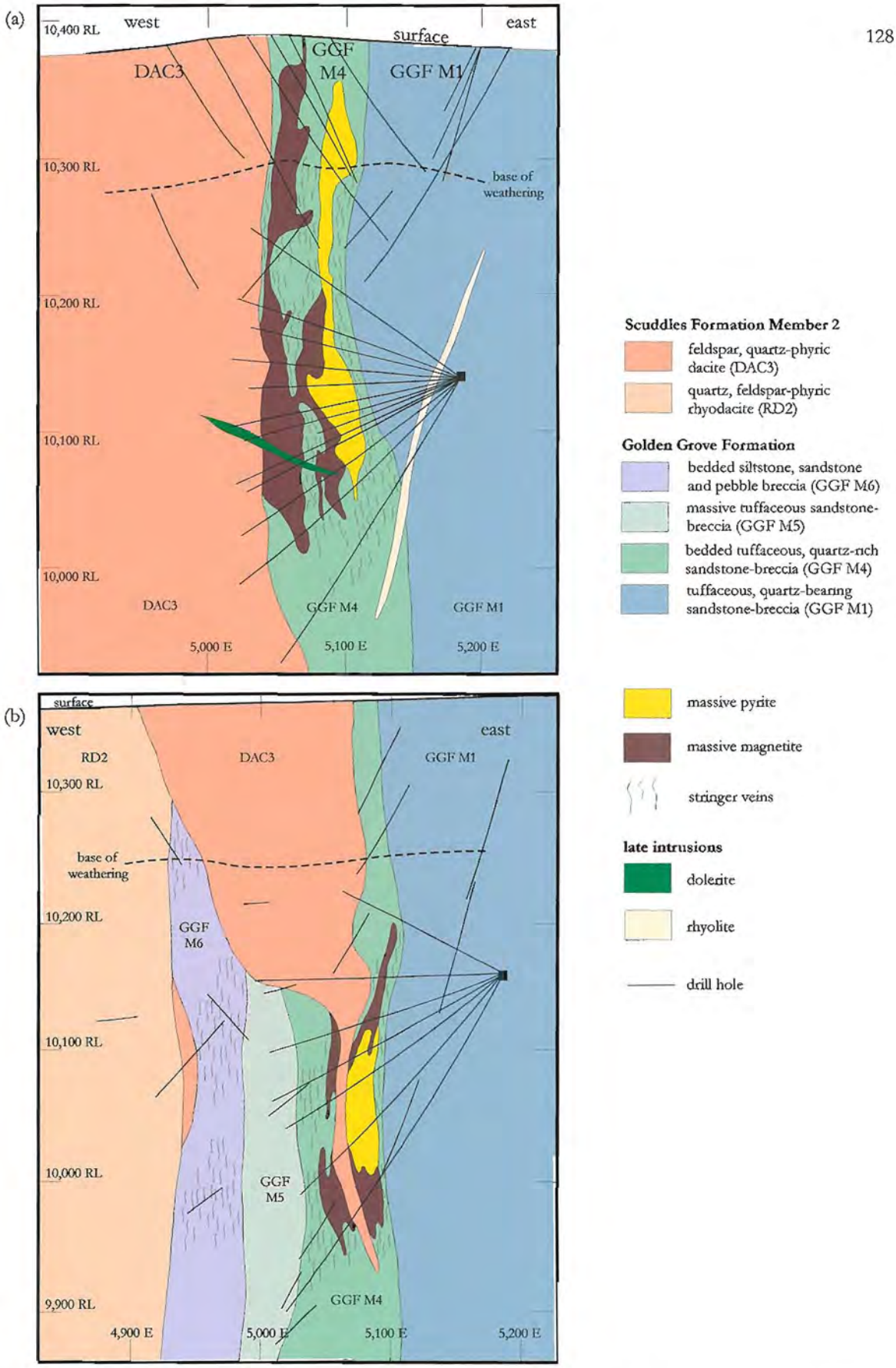

Figure 5.11: East-west cross sections through the lower ore zone in GGF M4. (a) East-west section 18,560 N (20 m window) in the central part of massive sulphide and massive magnetite. The upper and lower massive magnetite zones coalsece. Massive pyrite is a continuous zone below and discordant to massive magnetite. Sulphide veins envelops both magnetite and pyrite. DAC3 dacite intrudes massive magnetite and GGF M4. (b) East-west section 18,720 N (20 m window). Massive magnetite and massive pyrite form narrow zones in GGF M4 and are intruded by DAC3 dacite. Stringer veins occurs in GGF M4 and GGF M6 (D zone).

5.5.1 Distribution and geometry

Massive magnetite forms semi-conformable zones within GGF M4 that have a subvertical dip and a strike subparallel to bedding (~310°). Figures 5.10 and 5.11 are successive east-west cross sections from south to north through massive magnetite in GGF M4. Within this member, massive magnetite occupies two stratigraphic levels (Figs. 5.10a and 5.10b). These stratigraphic levels are poorly constrained due to the absence of marker horizons within the volcaniclastics. These two zones of massive magnetite form an upper magnetite horizon, at a stratigraphic distance of at least 10 m below the GGF M4-M5 contact, and a lower magnetite horizon at 5 to 15 m above the lower GGF M1-M4 contact (Figs. 5.10 and 5.11). Therefore, massive magnetite does not coincide with the stratigraphic contacts of the tuffaceous member in which it is hosted.

In the south, the upper and lower massive magnetite zones are separated by up to 40 m of bedded, quartz-rich sandstone (Fig. 5.10a). However, in the north where massive magnetite is more thickly developed, the upper and lower magnetite zones coalesce (Fig. 5.11a). In this area, massive magnetite is intruded by the DAC3 dacite, but north of this dacite (>18,700 N), massive magnetite is absent from GGF M4 (Fig. 5.9). A gradual thickening of massive magnetite from south to north is observed, with massive magnetite attaining its maximum thickness of 40 m adjacent to the southern margin of the discordant DAC3 dacite (Fig. 5.9 at 18,560 N).

Both the upper and lower massive magnetite zones are discontinuous down dip (Figs. 5.10 and 5.11), with massive magnetite transitional to semi-massive or stringer magnetite. Transitional contacts may also occur between magnetite and massive sulphide or sulphide stringer veins. The maximum down dip extent of massive magnetite is 500 m, which coincides with its thickest development (Fig. 5.10b).

5.5.2 Upper contacts

The upper contacts of massive magnetite are locally with bedded quartz-rich sandstone, massive feldspar, quartz-phyric DAC3 dacite or rarely with massive pyrite. Most commonly, massive magnetite is overlain by bedded sandstone, and these contacts are gradational from 10 cm to 10 m through semi-massive magnetite to disseminated magnetite in quartz-rich sandstone. The gradational contacts represent decreasing magnetite contents with increasing distance from massive magnetite (Figs. 5.12a and 5.12c), and correspond to an increase in the abundance of relict volcanic textures, such as volcanic quartz and bedding (Fig. 5.12c). Within these gradational contacts, however, the contact between semi-massive magnetite and massive magnetite is locally sharp and conformable (Fig. 5.12c). Less commonly, the upper contacts of massive magnetite are semi-conformable and sharp against magnetite-veined, quartz-rich, bedded sandstone (Figs. 5.12b and 5.8c).

Between 18,510 N and 18,650 N, massive magnetite has a sharp upper contact with DAC3 dacite (Fig. 5.9). Adjacent to this contact, massive dacite is fine-grained (feldspars <0.5 mm) with a weakly developed chilled intrusive margin (Figs. 5.8d and 5.12d). DAC3 dacite is discordant to both bedding in GGF M4 and to massive magnetite. This

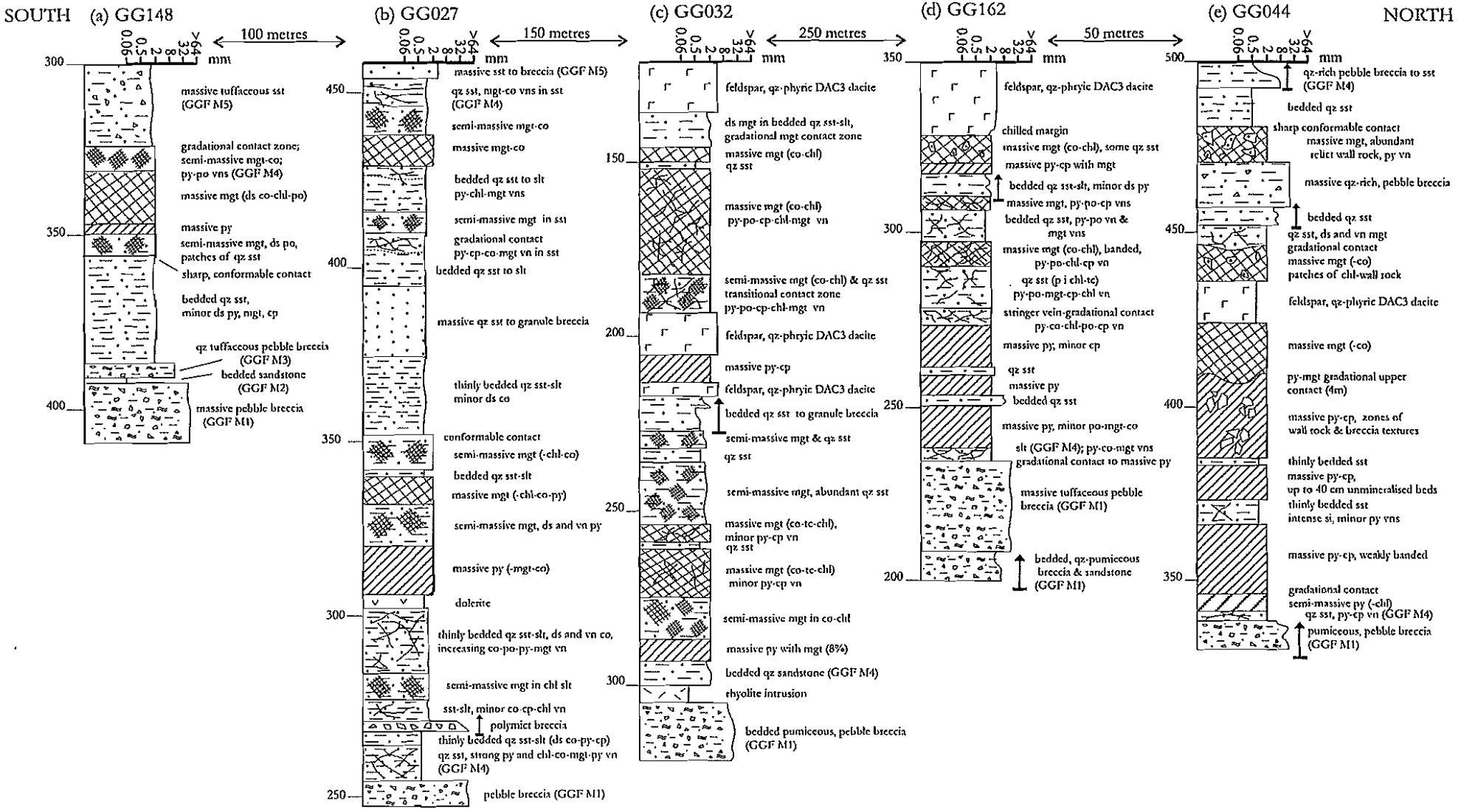

Figure 5.12: Simplified graphic logs of drill holes through massive magnetite, massive pyrite and stringer veins in GGF M4 (a) GG148 (transform section 18,187 N), (b) GG027 (transform section 18,288 N), (c) GG032 (transform section 18,438 N), (d) GG162 (transform section 18,688 N) and (e) GG044 (transform section 18,738 N). Vertical distances are down hole distances in metres. Facies are in GGF M4 unless otherwise specified. Up directions indicate facing from graded beds. Abreviations used are chl = chlorite, cp = chalcopyrite, co = carbonate, ds = disseminated, mgt = magnetite, py = pyrite, si = siliceous alteration, slt = siltstone, sst = sandstone, tc = talc, vn = vein.

contact is in part, sheared. The stratigraphically lower massive magnetite zone may have an upper contact with massive pyrite, as observed in underground development (Fig. 5.8e and Appendix A3.2). In this case, the contact varies from sharp to irregular, and can be both parallel and discordant to bedding.

5.5.3 Lower contacts

In all cases, the lower contact of massive magnetite is gradational and grades through semi-massive magnetite to either bedded quartz-rich sandstone, massive pyrite or a sulphide stringer zone. This gradational contact occurs over a stratigraphic interval of 0.1 to 5 m and is generally discordant. Commonly, semi-massive magnetite contacts are accompanied by a gradual increase in pyrrhotite as the altered wall rock is approached. Gradational or transitional contacts from massive magnetite to semi-massive magnetite and disseminated magnetite reflect the decreasing proportions of magnetite (Fig. 5.12a). The contact between semi-massive magnetite and underlying sandstone may also be sharp and conformable (Fig. 5.12a). Quartz-rich sandstone underlying massive magnetite commonly contains finely disseminated (<5% modal) magnetite.

The lower stratigraphic magnetite zone also contains intervals of semi-massive magnetite, as well as zones of pyrite-pyrrhotite-carbonate (±magnetite) veins (Fig. 5.12d). Contacts between massive magnetite and massive pyrite are gradational (Appendix A3.2), with decreasing proportions of magnetite and increasing proportions of pyrite-pyrrhotite away from massive magnetite. In these contact zones, pyrite within magnetite occurs as disseminations that are interstitial to the magnetite or as pyrite-rich veins.

5.5.4 Massive magnetite

Massive magnetite has a wide variety of textures including massive interlocking aggregates of magnetite, fine-grained, disseminated magnetite and banded magnetite-carbonate. Massive magnetite contains magnetite, carbonate (ankerite to siderite), chlorite, talc and minor quartz, and other accessory phases are listed in Table 5.2. Magnetite aggregates form irregularly shaped patches that have cleavage or cracking patterns due to deformation (Section 4.13 and Fig. 5.8f). These magnetite aggregates have interstitial carbonate, chlorite and talc, which also infill fractures in magnetite (Fig. 5.8g). Massive magnetite zones that consist of finely disseminated magnetite tend to have a homogeneous appearance, whereas magnetite aggregates have an inhomogeneous texture. Banded magnetite is rare at Gossan Hill and consists of millimetre-sized, alternating, monominerallic bands of magnetite and carbonate, which are disrupted and discontinuous. Within any massive magnetite zone, all three of these textures can be intermixed. Textural studies in Chapter 6 detail the characteristics and variation in massive magnetite. Disseminated and vein pyrrhotite and chalcopyrite occur throughout massive magnetite, but are most common at the margins of massive magnetite, particularly where it is adjacent to massive pyrite. Massive magnetite may also be free of disseminated and vein sulphides.

Within massive magnetite, narrow zones of 0.3 to less than 1 m of chlorite-altered sandstone occur. These narrow zones may be bedded sandstone intervals or single beds

that have sharp conformable contacts to the enclosing massive magnetite. Sandstone beds or bedded intervals can contain sulphide or magnetite veins or may be free of both magnetite and sulphide (Fig. 5.12d). Unusual siliceous nodular alteration textures (Chapter 7) and volcanic quartz occur in these unmineralised sandstone interbeds (Fig 5.12c). Elsewhere, massive magnetite may contain irregular shaped patches of quartz-chlorite altered wall rock (Fig. 5.8h) that contains relict volcanic quartz.

5.5.5 Discussion

Massive magnetite forms two sheet-like zones, each having semi-conformable to discordant upper and lower contacts within GGF M4. Laterally, these two massive magnetite zones are semi-continuous over a distance of 650 m and consist of four bodies interconnected by disseminated and vein magnetite. The two stratigraphic levels of massive magnetite do not coincide with stratigraphic contacts, but are stratabound within the host rocks of GGF M4. From south to north massive magnetite thickens, and attains a maximum thickness of 40 m where the upper and lower magnetite zones coalesce (18,450 N to 18,650 N). This anastomosing massive magnetite zone is interpreted to represent a focal area for the fluids responsible for magnetite formation. This area is also coincident with the southern margin of the DAC3 dacite intrusion, which is interpreted to occupy a synvolcanic feeder site.

Massive magnetite has a distinct mineralogical association with carbonate (ankerite to siderite), chlorite and talc gangue. In strongly fractured zones, carbonate, chlorite and talc fill tensional structures in magnetite, indicating their local redistribution during deformation.

Zones of semi-massive, disseminated and vein magnetite envelop massive magnetite and represent gradational upper and lower contacts. These transitional contacts between massive magnetite and altered, bedded, quartz-rich sandstone indicate a replacement origin of the magnetite in GGF M4. Bedded, quartz-rich sandstone intervals within massive magnetite can have sharp, conformable contacts. Beds or bedded intervals enveloped by massive magnetite may represent horizons that were less permeable to the magnetite-forming fluids. Massive magnetite is generally associated with complete textural destruction of the host rock, however, massive magnetite also incorporates semi-massive magnetite that has less intense wall rock alteration to magnetite, carbonate and chlorite. In many cases these horizons contain 'windows' of relict wall rock, which despite intense alteration, contain relict volcanic textures or volcanic quartz. These 'windows' indicate incomplete magnetite replacement of a tuffaceous quartz sandstone precursor. The differential permeability of the bedded GGF M4 sequence could have strongly contributed to the observed interfingering of wall rock, massive magnetite and semi-massive magnetite zones.

The separation between the upper and lower massive magnetite zones could represent multiple periods of massive magnetite deposition near the seafloor or permeability/ porosity and chemically controlled sub-seafloor replacement. Interrupted massive magnetite formation by ongoing sedimentation would result in the migration of the

seafloor concurrent to magnetite deposition. Alternatively, all magnetite deposition may have formed completely by replacement of GGF M4 strata, with its distribution controlled by permeability and chemical contrasts. Both mechanisms account for the gradational contacts in massive magnetite. It is now necessary to establish the context, timing and association between massive magnetite and adjacent massive pyrite and sulphide stringer zones, prior to evaluating these possible origins.

5.6 Mineralisation in GGF M4: The lower stratigraphic association

Massive sulphide in the lower stratigraphic association is massive pyrite and generally Cu-rich. Massive pyrite is hosted by bedded, tuffaceous, quartz-rich sandstone to granule breccia of GGF M4. Its mineralogy consists of pyrite and pyrrhotite, with variable proportions of chalcopyrite and magnetite in a chlorite and quartz matrix (Table 5.2). This section describes the distribution of massive pyrite and its relationship to massive magnetite.

5.6.1 Distribution and geometry

The geometry of massive pyrite in GGF M4 is podiform with discontinuous zones that interfinger with zones of sulphide veins and massive magnetite. These massive pyrite zones have subvertical dips and broadly conformable strikes (~310°), but are locally discordant. Massive pyrite occurs in the lower 30 to 40 m of GGF M4 (Figs. 5.10 and 5.11), and at least 5 to 10 m above the GGF M1-M4 stratigraphic contact. Massive pyrite attains a maximum thickness of 25 m in the north between 18,450 N and 18,650 N (Fig. 5.9), coinciding with the thickest development of massive magnetite (Fig. 5.11a). In this lower ore association, two main zones of massive pyrite are observed; one to the south between 18,160 N to 18,350 N (190 m strike) and the second in the north between 18,450 N to 18,680 N (270 m strike) (Fig. 5.9). There is a discontinuity of 50 m between the two zones (Fig. 5.9), showing that massive pyrite is not as laterally extensive or continuous as massive magnetite.

North of 18,650 N, near the DAC3 dacite intrusion, massive pyrite thins northwards into sulphide stringer. Similarly, the southernmost extension of massive pyrite thins to less than 2 m before grading into massive magnetite and sulphide stringer veins (Fig. 5.9). Massive pyrite juxtaposes the lower stratigraphic zone of massive magnetite (Figs. 5.10 and 5.11), with massive pyrite occurring adjacent to or below massive magnetite. The contact between massive pyrite and massive magnetite varies from conformable to discordant. Discordant contacts occur where massive pyrite is thickest and cuts across massive magnetite (Fig. 5.10b). Massive pyrite interdigitates with massive magnetite (Fig. 5.11a), both along strike and down dip, and massive pyrite can be transitional to massive magnetite (Fig. 5.11b). Massive pyrite can also form separate, isolated narrow zones (Figs. 5.10a and 5.11a).

5.6.2 Upper contacts

The upper contacts of massive pyrite are gradational over 1 to 10 m to massive magnetite, altered bedded sandstone or sulphide-veined sandstone. Graded upper

Figure 5.13

(a) Massive magnetite with abundant pyrite-chalcopyrite (±pyrrhotite) veins. These veins vary from wide (centimetres) to narrow (millimetres) and are generally discontinuous with planar to undulatory contacts. These textures are typical in pyrite-magnetite contact zones (5,094 E, 18,492 N, 10,100 RL, underground exposure on the 250 level).

(b) Massive pyrite with a blebby to nodular texture in an intense chlorite-quartz gangue. The pyrite grains are coarse-grained (up to 1-2 mm) to fine-grained (<0.5 mm) and locally coalesce to form aggregates. Chalcopyrite and pyrrhotite occur around pyrite grain margins and in fractures. Scale in cm (sample 97U038).

(c) Massive banded pyrite-chalcopyrite. Bands are up to 1 cm-wide and consist of coarse-grained pyrite (1-2 mm) and fine-grained pyrite (<0.5 mm) with interstitial chlorite. The fine-grained pyrite bands have abundant chlorite and a well-developed cleavage. The coarser pyrite bands contain chalcopyrite in fractures and around pyrite grains. Scale in cm (sample 97U028).

(d) Parallel pyrite-chlorite stringer veins in a fine-grained, intensely chlorite altered wall rock of GGF M4. These veins anastomose and form semi-massive pyrite. Pyrite veins are greater than 2 mm wide, continuous to discontinuous and locally anastomosing bands. The resultant mineral banding in these veins is parallel to bedding. Pyrite is fine-grained (<0.1 mm) and cleavage is well developed in the chlorite between the veins. Scale in cm (sample 97U037).

(e) Conformable pyrite-chalcopyrite vein in an intensely silicified, bedded sandstone, siltstone and breccia sequence close to the base of GGF M4. The wall rock also hosts minor discontinuous veinlets and disseminations of pyrite and chalcopyrite (5,107 E, 18,431 N, 10,100 RL, 250 level access drive).

(f) Stockwork stringer veins underlying massive pyrite in GGF M4, consisting of discontinuous and irregular veins of pyrite-chalcopyrite-chlorite. The wall rock is intensely silicified, however some relict banding (-bedding?) is preserved. Scale in cm (sample 97U031).

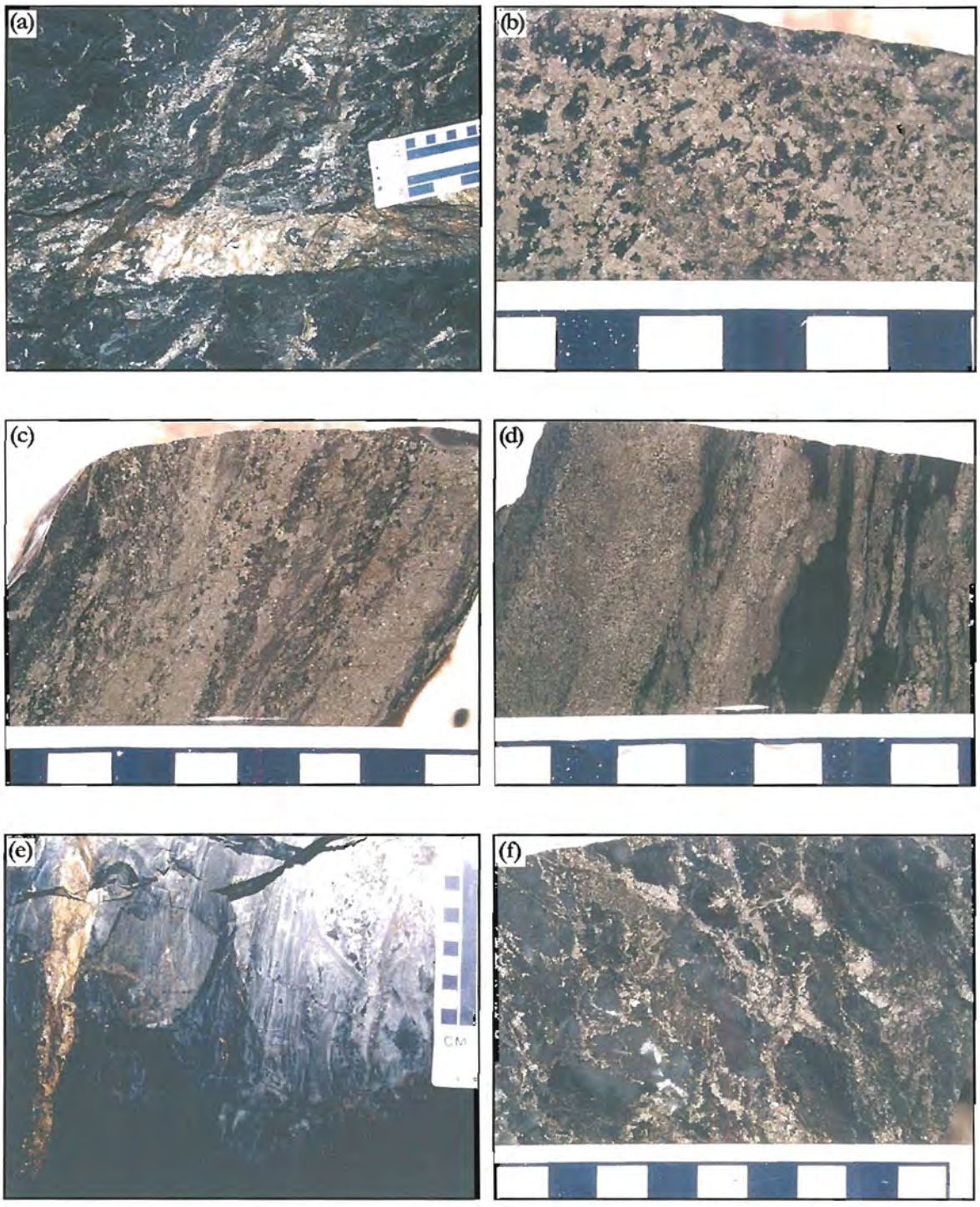
(a)
(b)
(c)
(d)
(e)
(f)
CM

contacts to overlying massive magnetite are denoted by the gradual increase of magnetite in massive pyrite towards massive magnetite. These gradational contacts form a 1 to 5 m wide massive pyrite-magnetite transitional zone (Figs. 5.12c, 5.12e and Appendix A3.2). Within these pyrite-magnetite transitional zones, pyrite occurs as disseminations and veins (Fig. 5.13a), and pyrrhotite and chalcopyrite are locally abundant.

The upper contact between massive pyrite and the bedded sandstone is also gradational over a distance of up to 10 m (Fig. 5.12b). Within this interval, sulphide veins and disseminated pyrite within the wall rock decrease in abundance away from massive pyrite. Increasing volcanic textures and volcanic quartz in the wall rock also coincides with the decrease in sulphide abundance. Although sulphide veins in the wall rock form part of the transitional upper contact of massive pyrite, the contact between massive pyrite and stringer veins can be sharp and conformable, as observed in underground exposure (Appendix A3.2).

DAC3 dacite intrudes massive pyrite; it has a sharp contact with pyrite and fine-grained, chilled margins. This contact is locally sheared and commonly chalcopyrite is abundant in the adjacent massive pyrite.

5.6.3 Lower contacts

The lower contact of massive pyrite lies at 5 to 10 m above the GGF M1-M4 stratigraphic contact. The narrow interval between massive pyrite and GGF M1 consists of bedded, quartz-rich sandstone that contains abundant sulphide in veins and as disseminations. In this narrow zone, the intensity of stringer veins increases toward massive pyrite, representing a gradational lower contact to massive pyrite (Appendix A3.2).

The lower contact of the stringer zone is sharp and occurs at the lower stratigraphic contact of GGF M4 (Fig. 5.12e). Underground exposure (Appendix A3.2) reveals that intense pyrite-chalcopyrite stringer veining is stratabound to GGF M4, which forms an anastomosing 10 m wide stockwork zone, with sharp, conformable contacts against overlying massive pyrite. Massive pyrite may be chalcopyrite-rich near its lower contact. The lower contact of massive pyrite is rarely sharp and conformable against unmineralised bedded sediments that lack stringer mineralisation.

GGF M1, and GGF M2 and M3, where present, do not host massive sulphide or stringer veins, and contain less than 1% disseminated pyrite. The lower boundary of the massive pyrite and the stringer zone is sharp and conformable to the lithofacies change between GGF M4 and GGF M1, or GGF M2-M3 where present.

5.6.4 Massive pyrite

Massive pyrite in GGF M4 has a wide textural variation and includes fine-grained (<0.5 mm) subhedral to euhedral pyrite as well as large blocky to rounded coarse-grained pyrite (>0.5 mm) that range up to 5 mm in size. Fine-grained massive pyrite has a homogeneous texture, whilst more coarsely grained massive pyrite has a blebby, inhomogeneous texture (Fig. 5.13b). Irrespective of its textural variation, massive pyrite

consists of closely packed pyrite grains, typically with interstitial quartz and chlorite (Fig. 5.13b).

Chalcopyrite is common interstitial to pyrite, occurring at grain margins and along fractures. Disseminated magnetite and pyrrhotite is also common in massive pyrite. Pyrrhotite has a similar occurrence to chalcopyrite and is locally associated with magnetite, particularly within the transitional contact zones between massive pyrite and massive magnetite. Banding in massive pyrite is common and is denoted by adjacent bands of texturally different pyrite and chlorite (Fig. 5.13c). This banding is commonly subparallel to veins that are themselves subparallel to bedding. Additionally, pyrite-chalcopyrite-rich veins have banding, which generally parallels the vein walls. This banding is well developed where veins coalesce to form massive pyrite (Fig. 5.13d).

Within massive pyrite, intervals up to 4 m of massive to semi-massive chalcopyrite may occur. These chalcopyrite zones have 10 cm wide, gradational contacts against massive pyrite. Additionally, massive pyrite also contains up to 15 cm wide beds of unmineralised, quartz-rich sandstone (Figs. 5.12d and 5.12e). Less commonly, up to 10 m wide, bedded intervals of intensely chloritised sandstone-siltstone occur (Fig. 5.12e). The contacts of these unmineralised beds or bedded intervals are sharp and generally conformable. Although rounded zones of silicified wall rock are not observed in the massive pyrite of GGF M4, clasts of chlorite-altered wall rock and massive magnetite occur (Chapter 4, Fig. 4.14a and Appendix A3.2).

5.6.5 Stringer veins

Sulphide-rich stringer veins form a large portion of the mineralised zone in GGF M4, and occur throughout the bedded sequence. Sulphide veins adjacent to massive pyrite are pyrite-chalcopyrite-chlorite-quartz veins, however, away from massive pyrite, sulphide veins have a more variable mineral content with differing abundances of pyrite, chalcopyrite, pyrrhotite, magnetite, carbonate, chlorite, quartz and talc. The relationships of these different sulphide veins are discussed in Section 5.9.

Sulphide veins are spatially related to massive pyrite in GGF M4, and form an envelope around massive pyrite. The most intense stringer veining occurs adjacent to massive pyrite, but the distribution of these stringer veins is more widespread than that of massive pyrite. The gradational contacts of stringer veins to massive pyrite reflect the intensity of anastomosing sulphide veins, which locally coalesce to form massive pyrite (Appendix A3.2). The distribution and intensity of sulphide stringer veins is variable, forming discontinuous zones that interdigitate with unmineralised sandstone. In stringer mineralisation underlying massive pyrite, two pebble breccia beds containing sulphide clasts have been identified (Section 3.3.3). These pebble breccia units have sharp, locally undulose contacts with sulphide-veined sandstone of GGF M4.

Massive pyrite is discordant and grades in to massive magnetite due to decreasing sulphide veins in massive magnetite. Sulphide stringer veins not only occur in both the lower and upper massive magnetite zones, but also in the wall rock between them (Figs. 5.10b and 5.11a). They also occur throughout, and overlying, the upper massive

magnetite zone. Stringer zones therefore form discordant to semi-conformable zones within GGF M4, despite the observation that many sulphide veins are parallel to bedding. Where massive magnetite and massive pyrite attain their thickest development between 18,430 N and 18,650 N (Fig. 5.9), sulphide veins form a stockwork. North and south of this stockwork, sulphide veins are generally less intensely developed and envelops massive pyrite, thinning in width as massive pyrite thins, or grading laterally from massive pyrite to stringer mineralisation along strike.

The alteration of the GGF M4 wall rock has been altered to quartz and chlorite, and these alteration types are associated with different stringer vein forms. Intense silicification is associated with veins below massive pyrite in the basal parts of GGF M4, and sulphide veins hosted by silicified wall rock have sharp vein margins, resembling the style and form of stringer veins associated with massive sulphides and silicified wall rock in GGF M6. However, sulphide veins in GGF M4 differ from veins in GGF M6 as they rarely contain sphalerite. Nonetheless, veins in GGF M4 have similar vein forms, and fracture and bedding control to veins in GGF M6. In GGF M4, sulphide veins may form millimetre- to metre-sized veins that have variable continuity. In general, veins parallel to bedding tend to form thicker veins (<3 m) and are laterally more continuous (*e.g.*, Fig 5.13e). Cross cutting veins range up to 1 m in width, but tend to be narrower (<10 cm), with more irregular and discontinuous forms. Structural investigations (Chapter 4) indicate that the orientation of stringer veins underlying massive pyrite in GGF M4 are parallel to bedding and the orientation of pre-mineralisation quartz veins (Section 4.8). Therefore, many sulphide veins within silicified wall rock in GGF M4 have strong structural control. However, a large portion of veins are narrow and discontinuous networks with veins having irregular (Fig 5.13f) to planar (Figs. 5.14a, 5.14b and 5.14c) forms.

In silicified wall rock, sulphide veins have sharp margins that vary from planar to irregular. Disseminated pyrite and chalcopyrite also occur in the wall rock interstitial to these veins (Figs. 5.13e and 5.13f). Stringer veins also have sulphide mineral banding parallel to the vein walls and contain relict wall rock fragments (Fig. 5.14a). Pseudo breccia textures are observed between sulphide veins and the silicified wall rock, with *in situ* modification of wall rock (Fig. 5.14b). These textures are analogous to those described in Section 5.4.6, and the intense silicification of the wall rock, produced chert with relict bedding. Due to the preservation of these bedding features, *in situ* textures such as rotation of 'pseudo-clasts' and jigsaw fit are indicated.

Chlorite alteration of the wall rock in GGF M4 has been more widespread, and chlorite-altered rocks contain sulphide veins with different characteristics. These veins are more disseminated and conformable to weakly discordant or laterally continuous to discontinuous (Fig. 5.14d). Some vein margins are sharp, but others are gradational to disseminated sulphide in the adjacent wall rock. Discontinuous veins vary in width and commonly pinch, swell and coalesce (Fig. 5.14e). Veins in chlorite altered wall rocks commonly consist of pyrrhotite, pyrite, chalcopyrite, carbonate and chlorite.

Figure 5.14

(a) Pyrite-chalcopyrite-chlorite vein with sharp margins in intense pervasive quartz-chlorite altered sandstone and breccia of GGF M4. A 1 cm fragment of relict wall rock (chert) occurs in this vein. Scale in cm (sample 97U030).

(b) Intense pervasive quartz alteration in GGF M4. Pyrite-chalcopyrite-chlorite veins cut the altered wall rock. The wall rock is strongly fractured and narrow fractures are in filled by chlorite. Quartz-chlorite alteration zoning in the wall rock fragments is observed, from outer chlorite-quartz alteration rims to inner bleached cores of intensely quartz altered rock. Scale in cm (sample 97U034).

(c) Grey intensely quartz-chlorite altered thinly bedded (<4 mm) sandstone-siltstone in GGF M4. Differential quartz-chlorite alteration in the wall rock results in light and darker coloured beds. Pyrite-chalcopyrite veins are discontinuous and vary from conformable to cross cutting veins. Scale in cm (sample 97U030).

(d) Contact between massive pyrite and pyrite-pyrrhotite-rich stringer mineralisation. Massive pyrite contains abundant magnetite. Pyrite-pyrrhotite stringer mineralisation forms an irregular network of discontinuous, undulatory veins in a chlorite matrix (5,038 E, 18,498N, 10,100 RL, 250 level).

(e) Blebby pyrite-pyrrhotite-carbonate-magnetite-chlorite veins in intensely chlorite-altered and cleaved sandstone of GGF M4. The blebby pyrite veins consist of pyrite aggregates with interstitial carbonate-magnetite-pyrrhotite and chlorite. This style of pyrite vein forms locally discontinuous, conformable veins in the wall rock. Some of the pyrite is strongly fractured with carbonate-pyrrhotite-chalcopyrite in fill. Scale in cm (sample 97U036).

(f) Massive chalcopyrite with minor disseminated magnetite, pyrrhotite and pyrite. Scale in cm (sample 769036).

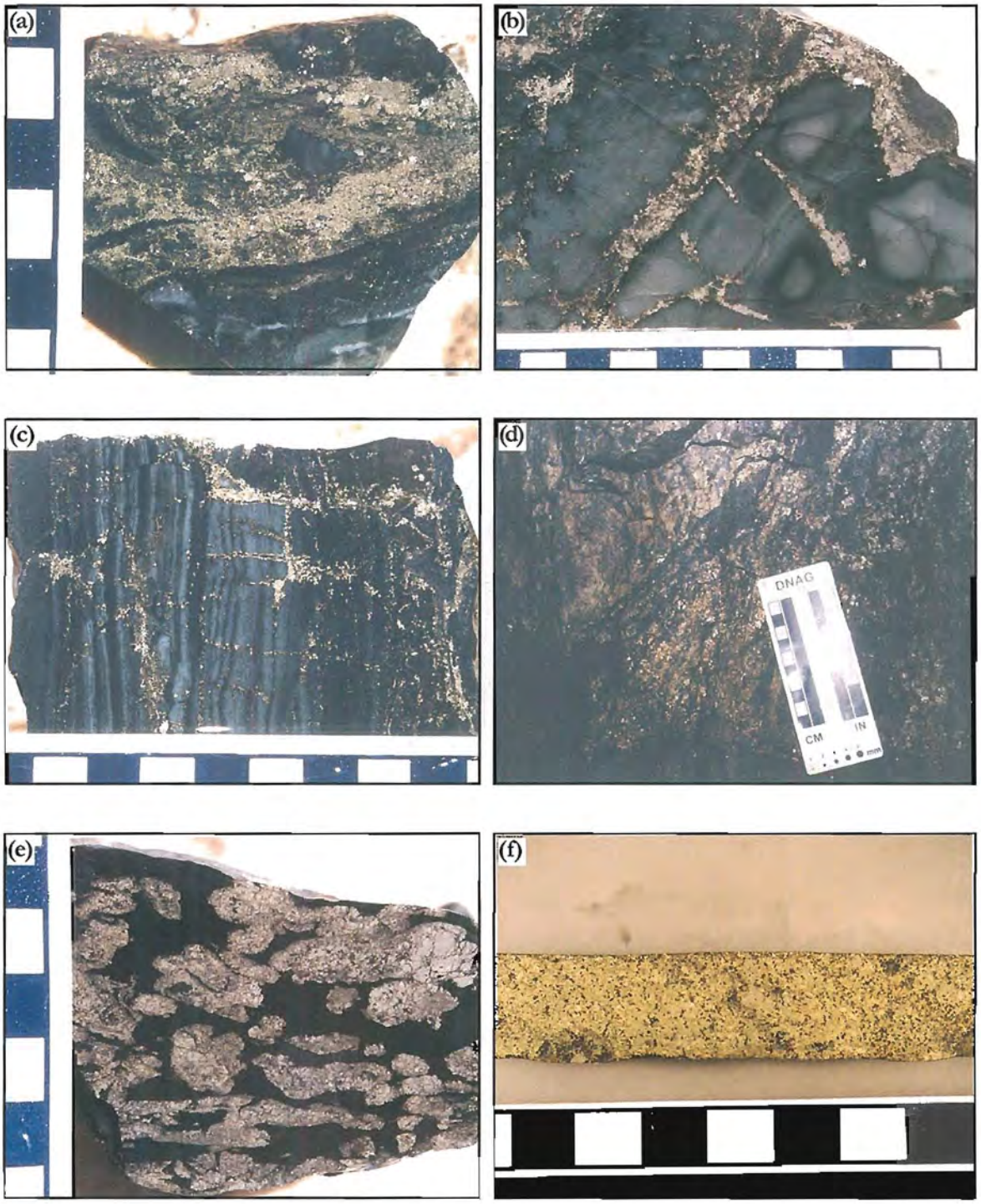
(a)
(b)
(c)
(d)
DNAG
CM
IN
mm
(e)
(f)

5.6.6 Discussion

Massive pyrite has gradational upper and lower contacts against sulphide-rich veins, which form a stringer envelope. Within the GGF M4 sequence, massive pyrite is both conformable and discordant, and contains beds or bedded intervals of unmineralised sandstone. Sulphide veins occur throughout the upper and lower massive magnetite zone and the host rocks of GGF M4. Sulphide veins decrease in intensity away from massive pyrite. Additionally, massive pyrite is discordant against the stratigraphically lower massive magnetite zone, with magnetite having gradational and veined contacts. These attributes mean that massive pyrite must have originated by replacement of the pre-existing sandstone-massive magnetite assemblages. That is, massive pyrite overprints and post-dates massive magnetite. However, the rare occurrence of sulphide clasts in polymict breccias in the pyrite stringer zone at the base of GGF M4 (Chapter 3), is inconsistent with the interpretation that the massive pyrite formed entirely by replacement. Pyrite clasts in these polymict breccias were probably derived locally, with breccia deposition at the seafloor. As the polymict breccia beds are only observed near the base of GGF M4, this occurrence indicates at least one seafloor position associated with pyrite formation, and also that some pyrite pre-dated the formation of massive magnetite.

The thickest development of massive pyrite and sulphide stringer veins occur where massive magnetite is thickest between 18,430 N and 18,650 N. This area is considered to have formed a mineralising feeder zone during the sulphide hydrothermal system, as well as a focal area during massive magnetite formation. It is only in this feeder zone that massive pyrite is discordant to massive magnetite. In addition, the area between 18,430 N to 18,650 N is also the site where DAC3 dacite intrudes the volcaniclastic pile and the mineralised zones. As DAC3 dacite does not contain sulphide or magnetite and has chilled intrusive contacts to both the wall rock and mineralisation, its intrusion post-dated the formation of massive magnetite, massive sulphide and sulphide veins.

The tuffaceous footwall sequence of GGF M1 is unmineralised. A strong permeability control on the distribution of mineralisation is indicated by its occurrence immediately above the GGF M1-M4 contact. Additional evidence of permeability control on massive pyrite and massive magnetite is also revealed by their semi-conformable distributions within the strata of GGF M4. Massive magnetite occurs as two semi-conformable to discordant zones. Massive pyrite generally underlies massive magnetite, suggestive that massive magnetite may have influenced the distribution of massive pyrite. Sulphide veins exhibit widespread structural control by their orientations and distributions. The occurrence of stringer mineralisation throughout GGF M4 suggests its formation at least after the completed deposition of GGF M4.

Geological constraints indicate that massive magnetite and massive pyrite did not form synchronously. Sulphide stringer mineralisation formed synchronously with massive pyrite, due to the enveloping distribution of veins. Ruxton (1986) described the entire lower sulphide zone at Gossan Hill as a large Cu-rich stockwork zone. Notably, sulphide veins do not cut across massive pyrite. Massive pyrite and sulphide veins formed after

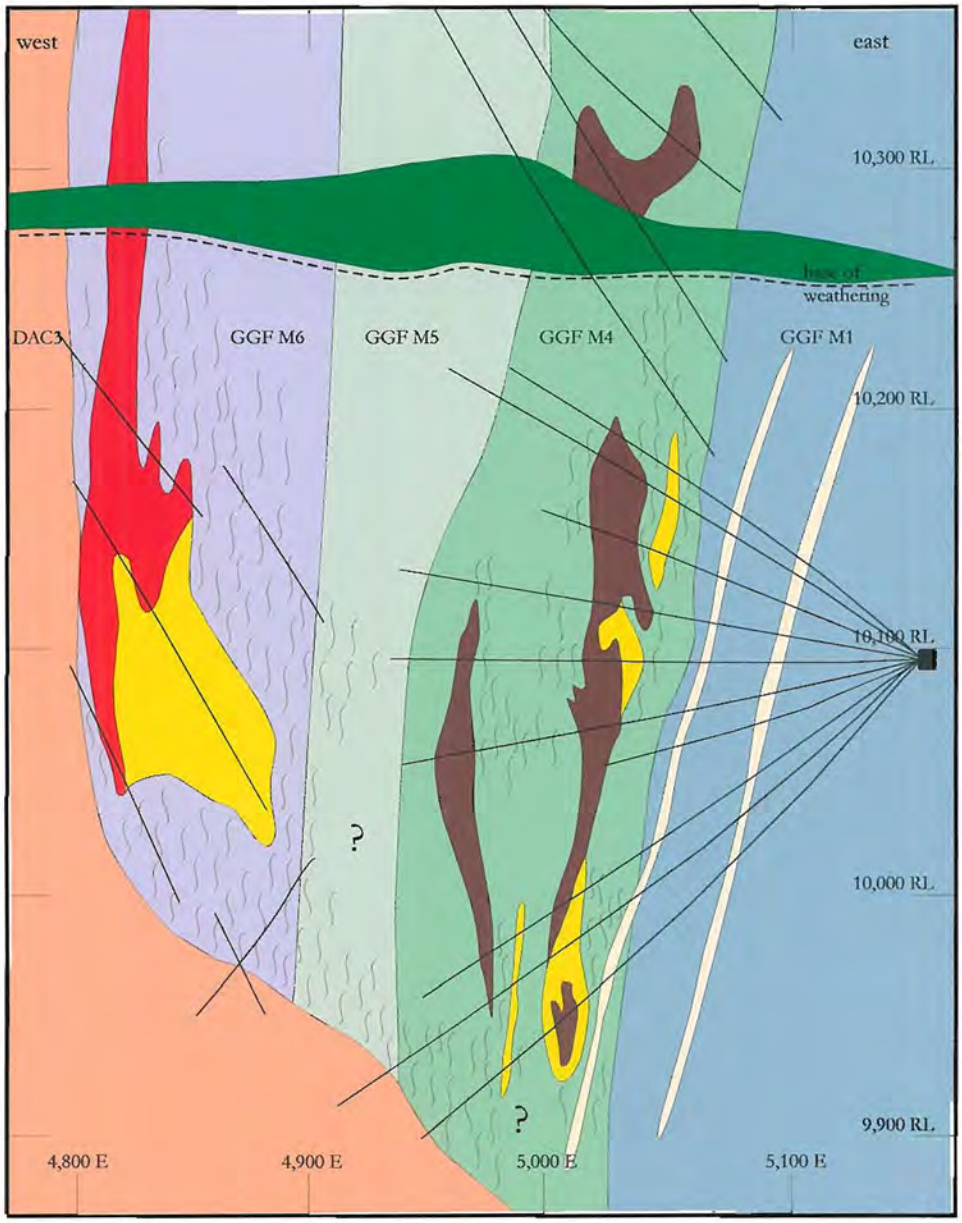

Figure 5.15: East-west section 18,280 N (20 m window) illustrating the relationship between massive sphalerite and massive pyrite in GGF M6 to massive pyrite and massive magnetite in GGF M4. A zone of stringer veins envelopes massive sulphide in GGF M6, and is well developed adjacent to massive dacite at depth below the massive pyrite. Stringer veins in GGF M4 have an erratic distribution and are best developed adjacent to massive pyrite and DAC3 dacite. Mine grid in metres.

massive magnetite due to the cross cutting associations. However, the juxtaposition between massive magnetite and massive pyrite and stringer veins, indicate that hydrothermal fluids likely used the same conduit. Nonetheless, the relative duration of sulphide deposition is unclear due to evidence that indicates some pyrite deposition prior to the onset of magnetite formation. With the above criteria, the association between the upper and lower massive sulphide zones is reviewed.

5.7 The relationship of the lower and upper massive sulphide zones

GGF M5 stratigraphically separates massive sulphides and stringer veins that occur in GGF M6 and GGF M4. GGF M5 is a massive, tuffaceous granule breccia to sandstone, which does not contain massive sulphide. South of 18,100 N, GGF M5 contains minor disseminated pyrite (<1%) however, north of 18,100 N, GGF M5 hosts sulphide stringer veins. Stringer veins in GGF M5 are most intensely developed adjacent to the discordant DAC3 dacite (Fig. 5.9 at ~18,350 N). Where these sulphide veins occur, GGF M5 is intensely silicified.

A discordant sulphide-rich stringer zone connects the lower and upper sulphide mineralised zones. The morphology of this stringer zone is not well constrained by drilling, but is observed underground (Appendix A3.1b) and illustrated in Figure 5.15. This discordant stringer mineralisation is best developed on the southern side of, and adjacent to, DAC3 dacite (Figs. 5.1, 5.9 and 5.15). The stringer zone has a broad, asymmetric shape and the intensity of stringer veins decreases away from DAC3 dacite and massive sulphide at C zone mineralisation in GGF M5 and GGF M6. The mineralogy of sulphide veins within GGF M5 is similar to those in GGF M4, with veins containing pyrite, pyrrhotite, magnetite, carbonate, chlorite, and quartz. Importantly, veins in GGF M5 contain minor to trace amounts of sphalerite. These veins however, do not have preferred orientations, which may partially reflect the absence of bedding in the massive homogeneous GGF M5 sequence.

5.8 The distribution of chalcopyrite

Chalcopyrite occurs in the lower and upper massive sulphide zones, within massive pyrite and sulphide veins. Upper and lower zones of chalcopyrite enrichment are common in deposits that have stratigraphically separated ore lenses (Huston, 1988). At Gossan Hill, chalcopyrite occurs in the upper ore zone as disseminations within massive pyrite and in sulphide veins, and to a lesser extent within massive sphalerite. However, massive pyrite and massive sphalerite may also be barren of chalcopyrite.

Massive pyrite and sulphide veins of GGF M4 also contain chalcopyrite, but its distribution is comparatively erratic, and podiform to lensoidal. The most common occurrence of chalcopyrite is within stringer veins. Chalcopyrite is also scattered through massive magnetite and the GGF M4 wall rock. Disseminated chalcopyrite in the wall rock occurs near pyrite- and pyrrhotite-rich veins, which also contain chalcopyrite. In this lower ore zone, massive chalcopyrite occurs as irregular discontinuous zones up to 2 m wide in massive pyrite. These zones of massive chalcopyrite (Fig. 5.14f) generally

form near the contact of massive pyrite and massive magnetite, or between massive pyrite and dacite.

5.9 Mineralogy and association of the stringer veins

Many VHMS deposits have stockwork zones below massive sulphides (Sangster, 1972; Gemmell and Large, 1992; Large, 1992) and in some occurrences, extensive stockwork zones form the bulk of the orebody (*e.g.*, Mount Lyell, Large, 1992). In these occurrences, stockwork zones represent epigenetic mineralisation that may be associated with syngenetic mineralisation at, or proximal to, an inferred seafloor position (Lydon, 1984; Large, 1992). Stringer veins represent conduits whereby focussed hydrothermal fluids transgressed the wall rock. Stockwork zones can be used to delineate hydrothermal feeder flow paths and to define the paragenesis of the mineralising hydrothermal fluids by means of vein ordering (*e.g.*, Gemmell and Large, 1992). Additionally, the form and style of the stringer veins can highlight the degree of interaction between the wall rock and the hydrothermal fluids.

This section details vein form, mineralogy and paragenesis to establish the relative timing of mineralogically distinct veins and their association to massive sulphides and massive magnetite. The lower and upper massive sulphide zones grade from a Cu-rich assemblage in the lower ore zone, to a Zn-Cu-rich association in the upper ore zone. In both stratigraphic occurrences, sulphide veins form a large part of this assemblage and have similar metal zonation patterns. Magnetite veins associated with massive magnetite do not generally contain Cu- or Zn-rich minerals. Sulphide veins at Gossan Hill form a stockwork that coalesces to form massive sulphide, and includes both sulphide-bearing and sulphide-rich veins.

Table 5.3: Description of the seven major vein types at Gossan Hill. Each vein type has a distinct mineralogy, with both diffuse to sharp veins in each vein type. Type I is associated with early pre-mineralisation deformation and Type VI is associated with post-mineralising deformation (refer Chapter 4). Vein Types II to V are associated with formation of massive magnetite and sulphide mineralisation. The column 'host' refers to members of the Golden Grove Formation and bracketed numbers indicate that the vein type is weakly developed or of a minor occurrence in that stratigraphic member.

Vein Type	Mineralogy	Form	Host
I	quartz	well-formed	M4
II	chlorite-carbonate	well-formed, diffuse	M4, M5, (M6)
III	magnetite-carbonate (-chlorite)	well-formed, diffuse	M4
IV	pyrite-chlorite (-carbonate-pyrrhotite)	well-formed, diffuse	M4, M6
V (A)	pyrite-pyrrhotite-chalcopyrite-carbonate-chlorite-magnetite	well-formed, diffuse	M4, M6, (M5)
V (B)	pyrite-sphalerite (-chlorite-quartz)	well-formed, diffuse	M4, M6, (M5)
VI	quartz-carbonate-chlorite	well-formed, banded	M1, M2/3, M4, M5, M6, SC2, dolerite, rhyolite

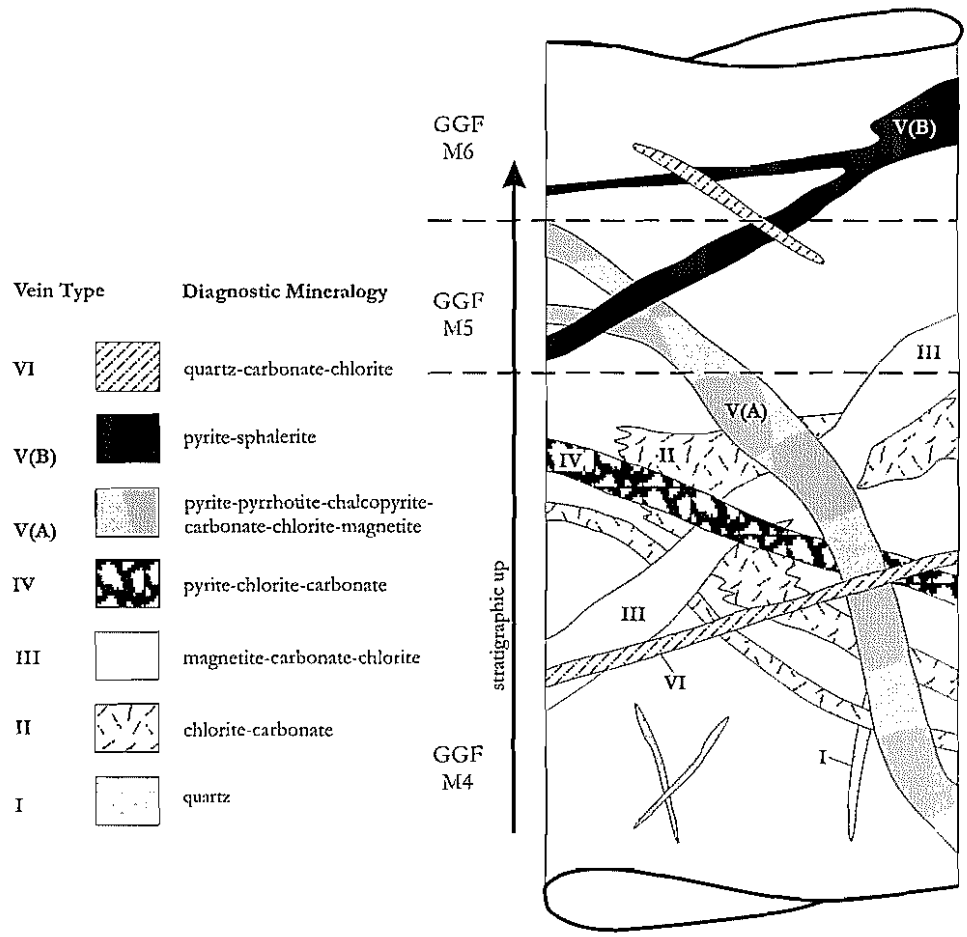

Figure 5.16: Paragenetic scheme of stringer veins at Gossan Hill. Based on mineralogy and cross cutting relationships, seven vein types are identified. Vein Type I and VI are associated with early and late stage deformation respectively. Type II veins are chlorite-rich, whilst Type III veins are magnetite-rich and form stringer veins adjacent to massive magnetite in GGF M4. Vein Types IV and V are associated with massive pyrite, massive sphalerite throughout GGF M4, GGF M5 and GGF M6, and cut across magnetite and chlorite veins.

5.9.1 Vein form

The two end-member vein forms recognised at Gossan Hill are (1) diffuse veins, and (2) sharp veins. Diffuse veins are commonly irregular with poorly defined margins, which grade over millimetres or centimetres to altered wall rock. These veins are diagnostic of replacement because of their gradational contacts, and enclosed and interdigitating relict wall rock. Diffuse veins tend to have wide mineral variation and indicate poorly constrained fluid pathways, with the gradational margins due to fluid interaction with the wall rock. These veins tend to occur in chlorite-altered rocks. In comparison, sharp veins have sharply defined margins and tend to occur in silicified rocks. They are generally pyrite-chalcopyrite- or pyrite-sphalerite-rich. Sharp veins can form wide (metres) to wispy, thin (millimetres) irregular to planar veins. The sharp margins of these veins indicate constrained and focussed fluid conduits, with the minerals of the veins formed in isolation of the wall rock, potentially as dilational fill. The formation of either diffuse or sharp veins at Gossan Hill may be related to available pathways through the host sequence that developed in response to competency and permeability contrasts, and fluid pressure.

5.9.2 Vein mineralogy

Based on mineralogy, form, the association between the wall rock and alteration, as well as cross cutting relationships, seven vein types (Types I to VI) have been identified at Gossan Hill (Fig. 5.16). The mineralogy of each vein Type I to VI is described in Table 5.3, with vein Type V subdivided into (A) or (B) veins according to mineral contents.

5.9.3 Type I

Type I veins are quartz veins, which are only identified in GGF M4 below massive pyrite. These veins are described in structural studies (Section 4.8.1) and are cross cut by pyrite-chalcopyrite-rich veins of Type V(A).

5.9.4 Type II

Chlorite-carbonate veins (Type II) vary from sharp to diffuse and occur throughout GGF M4, GGF M5 and GGF M6, in either quartz or chlorite altered rocks (Fig. 5.17a). They are generally free of magnetite and sulphide but contain disseminated carbonate. Well-formed chlorite veins can be centimetre- or millimetre wide, wispy, undulose to planar veins in silicified wall rock (GGF M5 and GGF M6). Diffuse chlorite veins are generally associated with chlorite-altered wall rock in GGF M4. Chlorite-carbonate veins may occur as single veins or anastomosing zones, which grade to intense, pervasive, chlorite-altered wall rock. Chlorite-carbonate veins are most abundant in GGF M4, and may be conformable or discordant to bedding. Texturally, chlorite in these veins forms an interlocking mosaic, whereas carbonate occurs as disseminated subhedral grains or grain aggregates.

5.9.5 Type III

Type III veins are magnetite-carbonate veins that have variable chlorite contents. Accessory minerals include pyrrhotite and talc. Within these veins, the abundances of

Figure 5.17

(a) Type II chlorite vein in pervasive chlorite altered GGF M4 sandstone. The vein has sharp margins and consists entirely of dark green chlorite. Narrow ribbon veins of carbonate cut across the vein and the chloritised wall rock (sample 769276).

(b) Intense pervasive chlorite-altered fine-grained siltstone in GGF M4. Fine-grained disseminated magnetite forms irregular diffuse veins (Type III) through the chloritised wall rock. The magnetite in these veins has a relatively homogeneous granular form. Ribbon carbonate veins cut across the chlorite wall rock and magnetite veins. Scale in cm (sample 769245).

(c) Type III massive magnetite vein consisting of granular magnetite with carbonate in as intensely chlorite altered sandstone of GGF M4. Minor pyrrhotite and chalcopyrite occur as disseminations in the vein. This Type III magnetite vein has sharp margins. Scale in cm (sample 769160).

(d) Massive magnetite with a cross cutting pyrite-chlorite vein (Type IV). Massive magnetite contains irregular patches of chlorite-carbonate altered wall rock (GGF M4). The pyrite-chlorite vein contains coarse-grained pyrite in chlorite and has sharp margins. Minor pyrite is disseminated in magnetite adjacent to the vein (sample 769060).

(e) Pyrite-chalcopyrite-pyrrhotite vein of Type V(A). The vein has sharp margins and is hosted in intensely quartz altered wall rock of GGF M6 (sample 769291).

(f) A pyrrhotite-pyrite-magnetite-chalcopyrite-carbonate-chlroite-quartz vein (TypeV(A)) in intensely silicified wall rock of GGF M5. The vein has sharp planar margins. Scale in cm (sample 769113).

(g) Stringer veins in a grey, intensely silicified wall rock. Narrow, planar to irregular chlorite veins occur in the chert and imposes a breccia appearance to the chert. Two sulphide veins cut the wall rock and chlorite veins, with all veins having sharp margins. The pyrrhotite-pyrite-magnetite-carbonate-chlorite vein (Type V(A)) is cut by a later pyrite-sphalerite vein (Type V(B)). Scale in cm (sample 769209).

(h) Type V(B) sphalerite-pyrite vein from D zone. The vein has a pyrite-sphalerite outer zone and an inner coarser-grained sphalerite zone. The wall rock is intensely chlorite-quartz altered sandstone in GGF M6. Scale in cm (sample 769344).

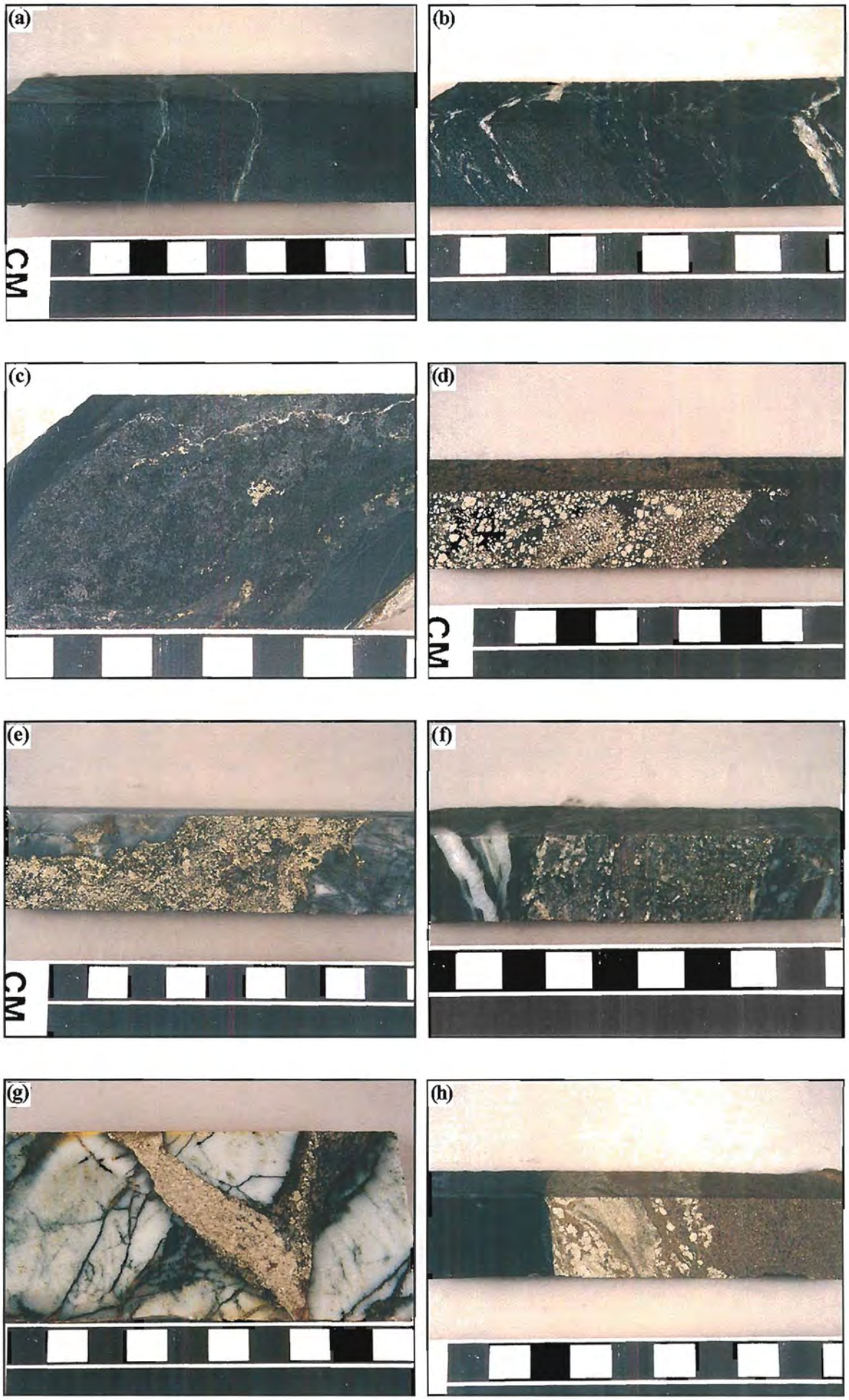
(a)
CM
(b)
(c)
(d)
CM
(e)
CM
(f)
(g)
(h)

magnetite or carbonate is variable. Veins have diffuse forms, generally lacking sharp margins and interdigitate with the wall rock (Fig. 5.17b). Relict volcanic textures in magnetite-carbonate veins include irregular zones of silicified tube pumice, shard textures, ilmenite-rutile and volcanic quartz. Rarely Type III veins have sharp margins (Fig. 5.17c). Type III veins only occur in GGF M4 near zones of massive magnetite and are interpreted to be have formed during massive magnetite development. Magnetite in these veins is generally fine-grained and granular. Type III veins cut chlorite veins (Type II) as well as chlorite altered wall rock.

5.9.6 Type IV

Type IV veins are typically rich in pyrite and chlorite, but may also contain minor carbonate, pyrrhotite and talc. In general, these veins are sharp (Fig. 5.17d) with locally irregular or diffuse margins that occur as disseminations of pyrite proximal to the vein. Type IV veins are characterised by coarse-grained pyrite (>1 mm) that is subhedral and fractured. Chlorite (-carbonate) occurs interstitial to pyrite grains, as does minor disseminated pyrrhotite and talc. Pyrite-chlorite veins cut massive magnetite, magnetite veins and disseminated magnetite in the chlorite-altered wall rock of GGF M4. Type IV veins predominantly occur in GGF M4 and less commonly in GGF M6 below massive pyrite.

5.9.7 Type V

Vein Type V are sulphide-rich, being either pyrite-pyrrhotite-chalcopyrite-rich (Type V(A)) or pyrite-sphalerite-rich (Type V(B)). Both vein types make up the majority of veins in stringer zones adjacent to massive sulphide, with Type V(B) consistently cutting Type V(A). Pyrite-sphalerite veins are associated with massive sphalerite and pyrite in GGF M6, and pyrite-pyrrhotite-chalcopyrite-rich veins with massive pyrite in GGF M6 and GGF M4. The minerals and their relative abundances within in these veins are variable. For example pyrite-sphalerite veins (Type V(B)) can be pyrite-rich or sphalerite-rich. Type V veins are observed to cut massive magnetite and pyrite-chlorite Type IV veins. The timing of Type V(A) and Type V(B) veins is determined at C zone where sphalerite-rich veins cut pyrite-chalcopyrite veins adjacent to massive sphalerite (Fig. 5.4c).

Type V(A): pyrite-pyrrhotite-chalcopyrite-rich veins

The majority of sulphide veins at Gossan Hill fit in to this category, with Type V (A) veins occurring in GGF M4, GGF M5 and GGF M6. This vein type has the most diverse mineralogy and greatest variation in the relative mineral abundances of all veins at Gossan Hill. Veins vary from chalcopyrite-rich to chalcopyrite-bearing and are typically either pyrite-dominant (Fig. 5.17e) or pyrrhotite-dominant (Fig. 5.17f). Pyrite-chalcopyrite veins are generally contain interstitial chlorite and quartz, whilst pyrrhotite-rich veins have a more diverse mineralogy that includes carbonate, chlorite, magnetite and talc. Notably, pyrrhotite-rich veins are carbonate-rich. Pyrite-chalcopyrite-chlorite veins form a stockwork underlying massive pyrite in GGF M4, whilst away from massive pyrite in GGF M4, pyrrhotite-carbonate veins tend to have a more widespread

distribution. Sphalerite, where present, is in minor to accessory proportions within Type V(A) veins in GGF M5 and GGF M6. Magnetite is a major to minor mineral (<20% modal) and forms disseminated, idiomorphic grains sieved by sulphide. The association between pyrite-pyrrhotite-chalcopyrite veins and massive sulphide in GGF M4 and GGF M6 indicate that they formed with massive sulphides.

Type V(B): pyrite-sphalerite-rich veins

Major minerals in vein Type V(B) are pyrite, sphalerite, chlorite and quartz. Sphalerite or pyrite may form minor to major constituents within a chlorite and/or quartz matrix (Figs. 5.17g and 5.17h). Pyrite-sphalerite veins underlie and overlie massive sphalerite in GGF M6. Veins can be centimetres to metres in width, have sharp margins and generally occur in silicified wall rock. Veins are either conformable or discordant to bedding and are often associated with modified wall rock textures (Section 5.4.6). Adjacent to massive pyrite or massive sphalerite, veins locally coalesce to form intense stringer that grades in to massive sulphide. Examples of this are best developed at C zone. Both chlorite and quartz occur interstitial to sulphides within these veins and have major to minor proportions. Chlorite is generally associated with pyrite-rich veins, whilst quartz is common in sphalerite-rich veins.

5.9.8 Type VI

Type VI veins are quartz-carbonate-chlorite veins that are associated with late stage, post-mineralising, brittle deformation (Chapter 4, Section 4.8). Quartz is generally the major constituent of these veins, but banded, antitaxial, quartz-carbonate-chlorite veins also occur. Type VI veins cut all other veins including massive sulphide and massive magnetite.

5.9.9 Summary

The seven different vein types at Gossan Hill are summarised schematically in Figure 5.16. Veins in this classification are mineralogically and texturally constrained by the occurrence of the major minerals and cross cutting relationships. Vein Types I and VI are associated with early and late deformation respectively and are not related to the formation of massive sulphide or massive magnetite.

Vein Types II to V represent veining developed during formation of massive magnetite and sulphide mineralisation at Gossan Hill. Veins that are chlorite- and magnetite-rich (Types II and III) are associated with massive magnetite formation. The sulphide rich veins are Types IV and V, however type IV is not widely distributed. Sulphide-rich veins of Type V have the greatest mineralogical variation and their formation is associated with the main mineralising stage at Gossan Hill. Type V veins form two sub-vein types. Pyrite-sphalerite veins of Type V(B), cut pyrite-pyrrhotite-chalcopyrite Type V(A) veins. Type V(B) veins are spatially associated with massive sphalerite (GGF M6), whilst Type V(A) veins are associated with massive pyrite (GGF M4 and GGF M6) and form discordant stringer stockwork. Type V stringer veins were synchronously developed with massive sulphide and form a stringer envelope and stockwork.

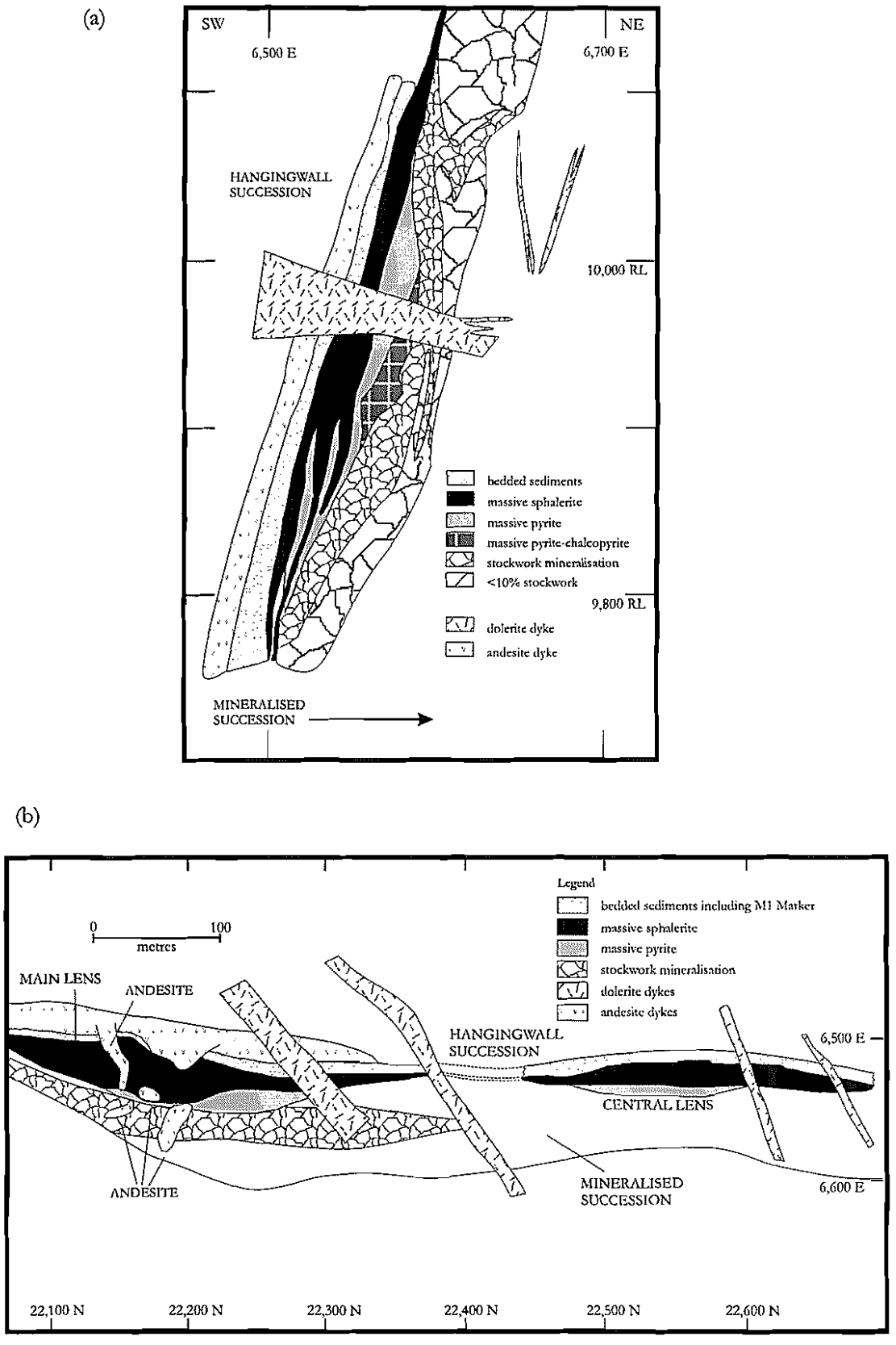

Figure 5.18: Cross section and plan through the Scuddles VHMS deposit (after Mill *et al.*, 1990). (a) East-west cross section (22,240 N) through the main lens of massive sulphide at Scuddles. An extensive stockwork system underlies massive sulphide. (b) Plan projection (10,000 RL). Massive sulphide is broadly conformably to bedding, with stockwork veining below the massive sulphides.

5.10 Mineralisation at the Scuddles deposit

The geology of the Scuddles VHMS deposit, 4 km north of Gossan Hill, is illustrated in Figure 5.18. Despite its proximity to Gossan Hill, the Scuddles deposit does not have mineralisation in the lower stratigraphic ore zone (GGF M4). Massive magnetite and massive pyrite-chalcopyrite do not occur in the quartz-rich sandstone below Scuddles, and only rare occurrences of stringer veins are observed. Massive sphalerite, massive pyrite and sulphide stockwork are restricted in occurrence to GGF M6, with stringer veining identified in GGF M5. Despite these differences, the Scuddles deposit has an analogous setting to mineralisation in the upper stratigraphic association at Gossan Hill.

Scuddles has a strike length of 600 m, with massive sulphides attaining a maximum thickness of 50 m (Mill *et al.*, 1990; Barley, 1992). The morphology of Scuddles is a stratiform, sheet-like development of massive sulphide, overlying a discordant, epigenetic stringer zone (Ford, 1992). Metal zonation grades from a Zn-rich upper zone (massive sphalerite) to a Cu-rich lower zone (massive pyrite and stringer veins), with Cu-rich stringer zone discordant in GGF M6 and GGF M5. Chalcopyrite is abundant in stringer veins and massive pyrite, the latter of which is also discordant to massive sphalerite (Ford, 1992). Magnetite is observed within the massive sulphides at Scuddles and occurs as idiomorphic disseminations (Ashley *et al.*, 1988; Mill, 1990). The Scuddles deposit and Zn-Cu-rich sulphide in GGF M6 at Gossan Hill therefore, have similar aspect ratios, asymmetry, morphology, mineralogy and metal zonation.

Other similarities between Scuddles and Gossan Hill include the occurrence of the M1 Marker chert-lithic horizons. At Scuddles, the M1 Marker overlies massive sphalerite, but can also occur within massive sphalerite. The M1 Marker at Scuddles consists of laminated quartz-chlorite-carbonate, magnetite-bearing iron formation and is the result of exhalative chemical precipitation (Ashley *et al.*, 1988). Current interpretations postulate an exhalative origin for the mineralisation at Scuddles based on its geometry and mineral assemblage. The lower Cu-Fe massive sulphide and stringer zone are considered to have formed immediately below the seafloor, occupying an extensive feeder system (Ashley *et al.*, 1988). Observed polymict sulphide clast-bearing breccia and breccia ore at Scuddles are consistent with a seafloor position.

The broad structural setting of the Scuddles deposit was discussed in Chapter 4 (Section 4.3.2). A syn-volcanic structure was identified at the southern end of the massive sulphide, adjacent to a DAC3 dacite and the thickest accumulation of massive sulphide and stringer mineralisation. At Scuddles, a DAC3 dacite intrusion also occupies a former synvolcanic hydrothermal feeder structure.

The geological setting at Scuddles is similar to that identified at Gossan Hill in the upper stratigraphic association. In a regional context, massive sulphide formation in the Golden Grove Domain can be correlated to the upper parts of GGF M6. Minor zones of massive magnetite do however, occur elsewhere in the GGF south of Gossan Hill.

5.11 Discussion

Massive sulphide bodies at the Gossan Hill deposit occur in different stratigraphic horizons and have a zonation from a Cu-rich lower sulphide zone to an upper Zn-Cu-rich sulphide zone. This metal zonation pattern is typical of Cu-Zn VHMS deposits (Large, 1977; 1992; Lydon 1984; Franklin *et al.*, 1981) and is discussed in Chapter 10. Mineralisation at Gossan Hill, in both the upper and lower stratigraphic associations formed sheet-like zones that are both conformable and discordant to the host lithology. Massive sulphide and stringer mineralisation in GGF M4 forms an asymmetric, stratabound zone. Mineralisation in GGF M6 forms a continuous sheet of massive sulphide and stringer that is also asymmetric, but varies from stratabound to discordant, with an extensive underlying stockwork zone. The gradational upper and lower contacts of these sulphide zones suggest they formed by replacement.

At C zone, massive sulphides attain their greatest thickness and massive pyrite and stringer stockwork are developed below massive sphalerite. At this locality, interbedded M1 Marker chert-lithic units, thought to represent hydrothermally precipitated horizons, overlie and interfinger with the massive sulphides. C zone is a mound-shaped zone, which may have formed at or near the seafloor. The presence of stringer mineralisation in overlying bedded strata, as well as the intercalated unmineralised beds within massive sulphide, are evidence of sedimentation ongoing with massive sulphide formation. Repetition of M1 chert-lithic horizons throughout the GGF M6 bedded sequence support this interpretation. Notably, sulphate minerals and breccia ore are not observed at Gossan Hill, with sulphide banding generally occurring in stringer veins or zones of anastomosing sulphide veins. The absence of breccia ores is consistent with sub-seafloor sulphide formation. Nonetheless, massive sulphide clasts in polymict breccia at the base of the hangingwall rhyodacite indicate its near seafloor position. Additionally, the southward thinning of the massive sulphide and stringer mineralisation away from C zone reflects increasing distance from the hydrothermal feeder, and lateral fluid migration. Bedding parallel sulphide veins support this interpretation.

The massive pyrite and massive magnetite bodies in GGF M4 are thickest in the north, below the thickest development of massive sphalerite-pyrite in GGF M6. Massive magnetite has two stratigraphic positions within GGF M4, near the base and top. Relative to massive magnetite, massive pyrite occurs below and is discordant to the lower magnetite zone. Sulphide stringer that formed synchronously to massive pyrite, envelops massive pyrite, with vein intensity decreasing away from massive pyrite.

Discordant stockwork veins connects the upper and lower massive sulphide zones. This stockwork coincides with the maximum thickness in massive magnetite, and massive pyrite in GGF M4 and M6. Sulphide stockwork cuts the upper and lower massive magnetite zones, strata of GGF M4, GGF M5 and GGF M6, indicating that stockwork formation post-dated their deposition. However, the occurrence of polymict, sulphide clast-bearing breccia near the base of GGF M4, indicates an earlier seafloor position associated with some pyrite deposition. Therefore sulphide deposition may have

commenced as early as the onset of sedimentation depositing GGF M4. Nonetheless, the main sulphide event post-dated the deposition of GGF M4, GGF M5 and part of GGF M6, as well as massive magnetite.

Massive magnetite formation must have occurred between these two sulphide events and its stratabound occurrence within GGF M4 indicates that it was later than the deposition of GGF M4. The two stratigraphic levels of massive magnetite within GGF M4 probably indicate preferential replacement along more permeably horizons in GGF M4. The juxtaposition of massive magnetite and massive pyrite in GGF M4, suggests that hydrothermal fluids responsible for massive magnetite and the upper and lower massive sulphide zones used the same conduit.

The asymmetry and thickness variations of the massive sulphides in GGF M4 and GGF M6 and massive magnetite in GGF M4 indicates that hydrothermal fluids were focussed along a synvolcanic structure. The DAC3 dacite in the hangingwall post-dates massive sulphide and massive magnetite formation, and occupies the site of a former synvolcanic structure (Chapter 3). Frater (1978; 1985a) suggested massive sphalerite in GGF M6 may have been partially removed during dacite intrusion. However, DAC3 dacite contacts are not disruptive and no clasts of sulphide or sediment within this dacite are present to support Frater's (1978; 1985a) conclusion. The thickest development of massive sulphide in GGF M4 and GGF M6, massive magnetite and discordant stringer lie adjacent to the discordant DAC3 dacite. Southwards from the DAC3 dacite, the thickness of massive sulphide and massive magnetite decreases, likely due to the increased distance from the hydrothermal feeder. North of the dacite intrusion, mineralisation is weakly and sporadically developed as stringer mineralisation in GGF M6. Therefore hydrothermal fluid circulation associated with massive magnetite and mineralisation must have been restricted to the southern side of the inferred feeder structure that is now occupied by dacite.

Based on observations presented in this chapter, the formation of the Gossan Hill VHMS deposit is proposed as an evolving hydrothermal system that spanned a significant stratigraphic interval and had multiple phases (at least two) of sulphide formation. An early, small volume, massive sulphide event is proposed at the time equivalent to the onset of tuffaceous sedimentation in GGF M4. The absence of mineralisation in GGF M1 reflects its impermeability to mineralising fluids throughout the duration of the system.

The main massive sulphide event is correlated with the upper parts of GGF M6, post-dating massive magnetite formation and deposition of GGF M5 and part of GGF M6. This period of massive sulphide formation is correlated regionally to the Scuddles VHMS deposit. Massive sulphides in GGF M4 are interpreted to have formed during this stage, due to cross cutting associations with massive magnetite and stratigraphy. Massive pyrite and extensive peripheral stringer mineralisation were also formed at this time. Synchronous to the development of massive and vein sulphides in GGF M4, was the development of stockwork adjacent to the feeder zone in GGF M5 and GGF M6, as well

as massive pyrite and massive sphalerite near the seafloor and overlying its central feeder. The feeder structure is now represented by a DAC3 dacite intrusion of the Scuddles Formation. Sulphide mineralisation is absent from the Scuddles Formation and thus the hydrothermal system must have waned prior to the onset of proximal felsic volcanism.

The Gossan Hill VHMS deposit is considered to represent an intermittent VHMS system that was repeatedly buried by turbiditic mass flow sedimentation. Burial by sedimentation may have resulted in diffusing fluid discharge, forcing lateral migration of hydrothermal fluids, until conduits could be established by hydraulic fracturing. The promotion of lateral hydrothermal discharge allows advective, convective or conductive cooling of the ore fluid and consequent sub-surface precipitation of sulphides (Lydon, 1988). Also, the effect of sedimentary superposition could have promoted the mixing of hydrothermal fluids with entrained seawater or pore water.

Hydrothermal precipitates may decrease the permeability of the VHMS system by the constriction of existing channel ways (Lydon, 1984). The creation of new fluid channels by either hydraulic, seismic or tectonic fracturing of the wall rock, initiates the growth of the system with continued repetition of these processes for as long the duration of high temperature hydrothermal flow (Lydon, 1988). Excellent evidence of hydraulic fracture is present at Gossan Hill in sulphide veins and resultant pseudo breccia wall rock textures, which include jigsaw fit and clast rotation. Stockwork zones at Gossan Hill therefore represent a hydrothermal breccia pipe, formed by repeated and concomitant episodes of hydraulic fracturing and precipitation of hydrothermal minerals in fractures as well as hydrothermal alteration or modification of the wall rock. The volume expansion required by dilatant hydraulic fracturing in VHMS systems can be accommodated by the upward displacement of the fragmented rocks of the breccia pipe (Lydon 1988), and account for the gradational or discordant lower sulphide contacts.

5.12 Summary

- The Gossan Hill deposit has two ore horizons that are stratigraphically separated by 150 m. Tuffaceous strata in GGF M4 and tuffaceous-epiclastic strata in GGF M6 host the lower and upper ore zones respectively. The strike of mineralisation is conformable. Metal zonation varies from a Cu-rich in the lower ore zone to Cu-Zn-rich in the upper ore zone;
- Massive sphalerite and massive pyrite in GGF M6 have gradational contacts to stringer mineralisation above and below massive sulphides. Massive sphalerite forms an asymmetric sheet that thins to the south and attains it greatest thickness adjacent to DAC3 dacite. Massive sulphides may have been partially exposed during formation. This interpretation is based on the occurrence of hydrothermal chert-lithic horizons and clasts of massive sulphides in overlying rhyodacite breccia facies. A near seafloor position is invoked for the formation of massive sulphides in GGF M6;
- In GGF M6, massive sulphides and stringer mineralisation interfinger with

unmineralised bedded stratigraphy. This results from a changing seafloor position, due to ongoing sedimentation during sulphide accumulation;

- Massive magnetite has gradational upper and lower contacts, but also contains abundant wall rock. Massive magnetite formed by replacement of GGF M4, along two more permeable zones within the tuffaceous volcaniclastic sequence;
- Cu-rich massive pyrite in GGF M4 forms a discontinuous sheet that is gradational to stringer stockwork. The bulk of massive pyrite and stringer mineralisation in GGF M4 is discordant to and cuts across massive magnetite and strata, indicating that much of this mineralisation post-dated massive magnetite deposition. Nonetheless, sulphide clast-bearing breccia at the base of GGF M4 indicate minor sulphide deposition predated massive magnetite and a former seafloor position during the early stages of sulphide deposition at Gossan Hill;
- Stringer sulphide mineralisation forms an envelope to massive pyrite in GGF M4. A stockwork, which is discordant to GGF M5 and GGF M6, connects the lower and upper massive sulphide zones and envelopes massive pyrite and massive sphalerite. The extensive development of stringer mineralisation at Gossan Hill indicates mineralisation is *in situ* and has not been transported;
- The thickest development of massive magnetite and massive pyrite in GGF M4 is adjacent to a DAC3 dacite. The juxtaposition of these zones highlight use of the same feeder by hydrothermal fluids responsible for massive magnetite and sulphide mineralisation. Massive magnetite, massive pyrite and stringer mineralisation in GGF M4 have asymmetric geometry and thin to the south away from their inferred feeder;
- North of the DAC3 dacite, minor sulphide and stringer occur. Mineralising fluids were therefore focussed to the south of this feeder, potentially within a structural low. This synvolcanic feeder structure controlled the localisation of hydrothermal-mineralising fluids and is now occupied by DAC3 dacite;
- Sulphide veins have widespread evidence of structural control, which includes hydraulic induced fracture and bedding;
- The similarities between Gossan Hill and Scuddles indicate that the main ore forming event in the Golden Grove Domain occurred during deposition of GGF M6. Only minor sulphides at Gossan Hill are earlier occurring at the onset of GGF M4 deposition and prior to massive magnetite formation;
- Mineralisation does not occur in the footwall GGF M1, but is stratabound above the lower contact of GGF M4. The footwall must therefore have been sealed and impermeable to mineralising hydrothermal fluids, which may have promoted focussed hydrothermal flow along the synvolcanic feeder;
- The Gossan Hill hydrothermal system was an evolving system that had an early minor and a later, major sulphide stage, which were separated by an interval of tuffaceous and epiclastic sedimentation, during which time massive magnetite formed.

Chapter 6

Ore minerals and their textures

6.1 Introduction

This chapter addresses the mineralogy of the sulphide and magnetite zones at Gossan Hill. The minerals in massive magnetite, massive sulphide and sulphide veins were summarised in Chapter 5 (Table 5.2, Section 5.9) and consist of pyrite, sphalerite, chalcopyrite and pyrrhotite, with sphalerite mainly restricted to the upper ore zone. Although magnetite is the main mineral in massive magnetite, it also occurs as disseminated grains in massive and sulphide veins. Gangue minerals in massive sulphide, sulphide veins and massive magnetite are principally chlorite, quartz and ankerite-siderite.

Detailed mineralogy and textural work was completed on the Gossan Hill deposit by Frater (1978; 1985a;b). Frater (1978) documented the primary and replacement sulphide textures in ore, as well as deformation, recrystallisation and remobilisation textures. Frater (1978) concluded that most sulphides had evidence of recrystallisation and/or remobilisation, which prevented the establishment of a primary paragenesis. The principal objective of this chapter was to confirm the relative paragenetic timing of magnetite in massive magnetite and sulphides, and to integrate the results of Frater (1978) with observations and compositional data generated in this study.

6.2 Sphalerite

Sphalerite occurs as (1) massive sphalerite, (2) disseminated sphalerite, and (3) vein-hosted sphalerite. Sphalerite is a major component of the upper ore zone, where it is commonly associated with pyrite, chalcopyrite, galena, tetrahedrite, arsenopyrite, magnetite, electrum, cobaltite, cassiterite and native silver.

Sphalerite varies in colour from pale orange, honey-yellow to dark red-brown and has a grain size of less than 400 μm. Massive sphalerite consists of polycrystalline sphalerite (Fig. 6.1a) and contains minor interstitial quartz or chlorite. Rare evidence of growth zonation occurs as rounded chalcopyrite inclusions (<20 μm) in sphalerite (Figs. 6.1b and 6.1c). Polycrystalline sphalerite commonly has twinned and equant grains with grain junctions that approximate 120°. Sphalerite grains interstitial to megaquartz commonly form cuspate, angular to 'Y' shaped grains, and matrix quartz is commonly sieved by rounded, micron-sized inclusions of sphalerite. Banding in massive sphalerite is rare and

Figure 6.1

(a) Honey-red polycrystalline sphalerite (Sp) with minor interstitial quartz (Qz) and pyrite (opaque) (sample 760222).

(b) Interlocking sphalerite grains that contain rounded, scattered inclusions of chalcopyrite (opaque) hosted by megaquartz (Qz). A colour variation is observed from the centre of some sphalerite grains (red) to the outer parts of the grains (orange-brown) (sample 769291).

(c) Polycrystalline sphalerite (Sp), with minor pyrite (Py) and chalcopyrite in a euhedral chlorite matrix (Chl). Chalcopyrite occurs as fine-grained inclusions that are scattered through the sphalerite grains and along sphalerite grain margins (Sample 769291).

(d) Fine-grained sphalerite in a chlorite matrix. Chlorite consists of interlocking euhedral grains that have interstitial sphalerite. Grain size changes in chlorite and sphalerite define tabular to irregular patches, which represent chlorite-sphalerite pseudomorphs (sample 760348).

(e) Histogram showing the distribution of FeS in sphalerite from massive sphalerite, sphalerite-pyrite veins (Type V(B)) and chlorite-magnetite-pyrrhotite-sphalerite veins (Type V(A)) at the Gossan Hill deposit.

(f) ZnS *versus* FeS in sphalerite from massive sphalerite, sphalerite-pyrite veins (Type V(B)) and chlorite-magnetite-pyrrhotite-sphalerite veins (Type V(A)). Note: A and C refer to A zone in the south of Gossan Hill, and C zone in the central parts of the deposit respectively.

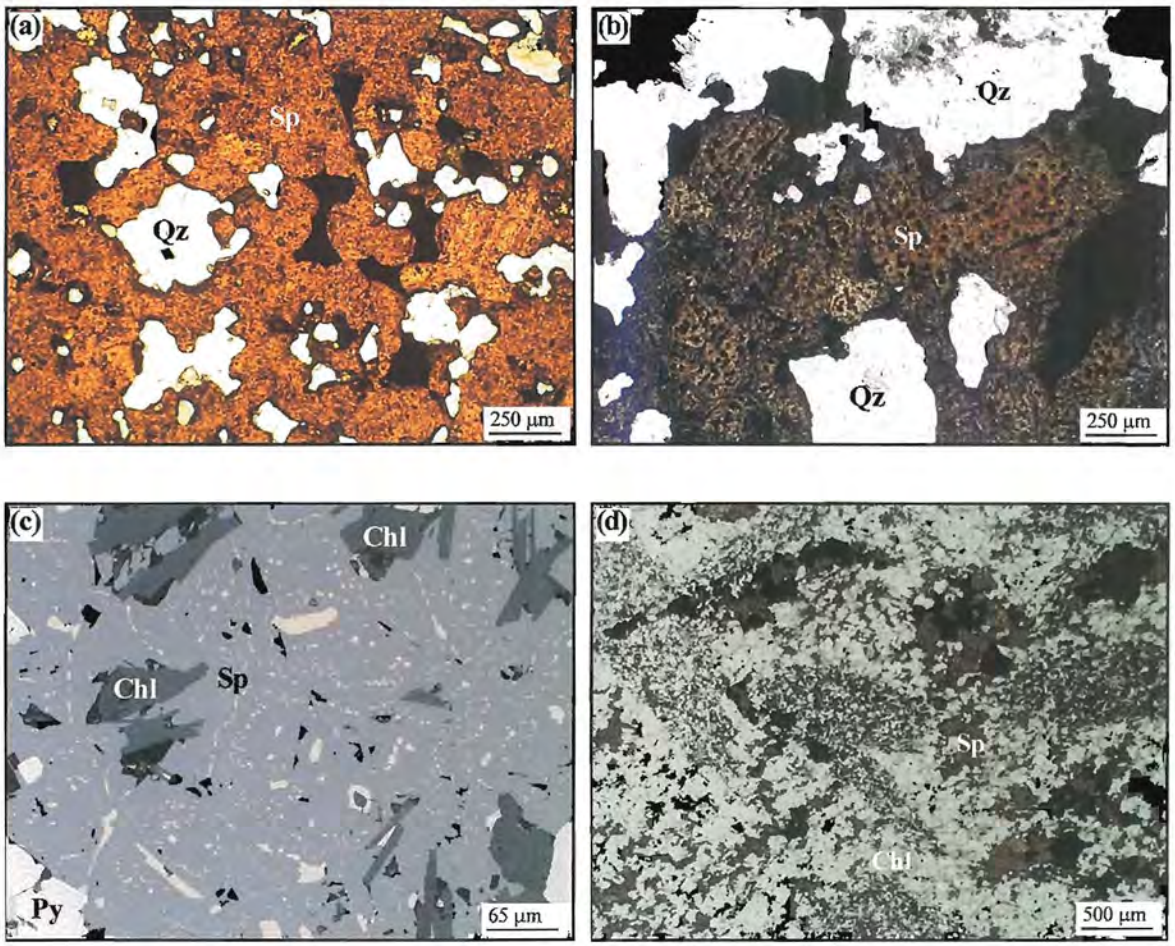
(a)
Sp
Qz
250 µm
(b)
Qz
Sp
Qz
250 µm
(c)
Chl
Chl
Sp
Py
65 µm
(d)
Sp
Chl
500 µm

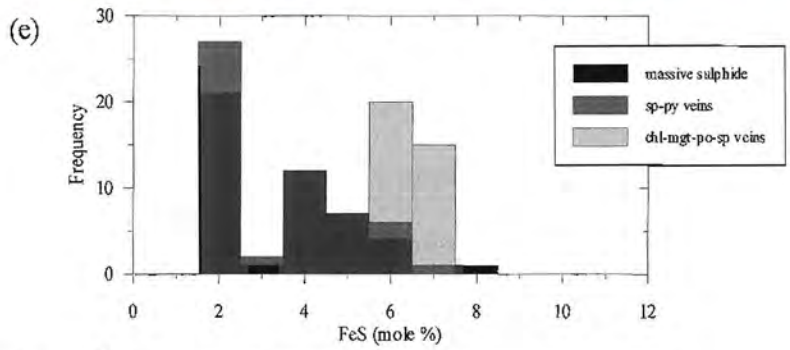
(e)
Frequency
FeS (mole %)
massive sulphide
sp-py veins
chl-mgt-po-sp veins

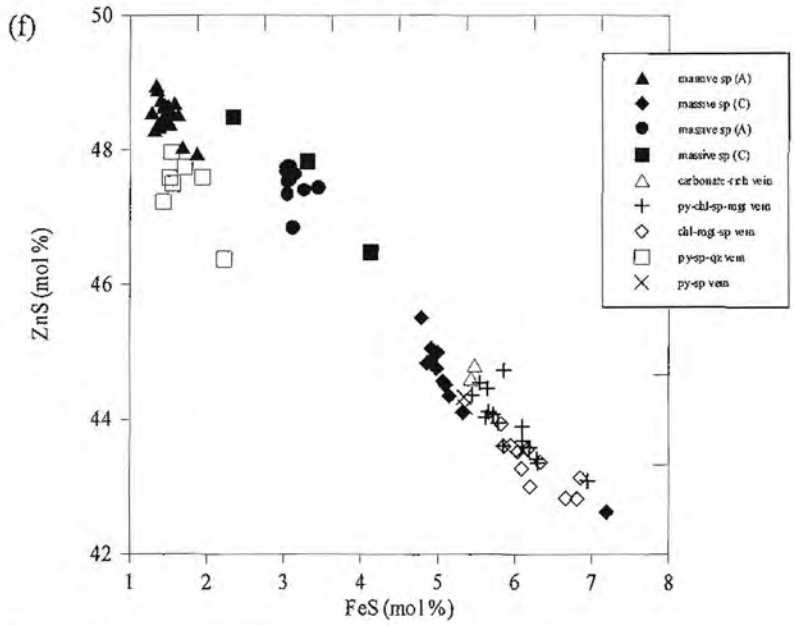
(f)
ZnS (mol %)
FeS (mol %)
massive sp (A)
massive sp (C)
massive sp (A)
massive sp (C)
carbonate-rich vein
py-chl-sp-mgt vein
chl-mgt-sp vein
py-sp-qz vein
py-sp vein

occurs in sphalerite veins. In these cases, alternating polycrystalline sphalerite and pyrite bands are less than 5 mm wide and have gradational margins to adjacent bands.

Disseminated sphalerite (<5% modal) occurs as scattered grains in intensely quartz- or chlorite-altered volcaniclastics, or within massive pyrite in the upper ore zone. Disseminated sphalerite forms gradational margins to massive sphalerite zones and haloes around Type V(B) sphalerite veins, and typically consists of irregular to rounded grains that have variable sizes (<100 μm) (Fig 6.1d). Finely disseminated (micron-sized) sphalerite locally imparts a red-orange colour to the wall rock or quartz grains that they sieve. In chlorite altered wall rocks in GGF M6, sphalerite is typically dark red to brown colour and has angular shapes due to its occurrence in euhedral chlorite (Fig. 6.1d). Rare, poorly defined tabular sphalerite-chlorite pseudomorphic textures (<2 mm in size) are defined by changes in the sphalerite and chlorite grain size (Fig 6.1d).

Within stringer veins, sphalerite is a major (>30%, sphalerite-pyrite Type V(B) veins) to minor (<5%, pyrite-pyrrhotite-chalcopyrite-rich Type V(A) veins in GGF M5) mineral. Sphalerite in Type V(B) veins has similar textures to massive sphalerite. Sphalerite in Type V(A) veins is dark brown and occurs as scattered, irregular, anhedral grains interstitial to pyrite, pyrrhotite and chlorite.

6.2.1 Recrystallisation and deformation of sphalerite

At Gossan Hill, sphalerite lacks microfractures, deformation twins and slip and kink bands (Frater, 1978; 1985a;b). Instead, equant polygonal grains and less commonly annealed grains in polycrystalline sphalerite are consistent with recrystallisation. 'Mature' annealed textures, such as those observed at Thalanga (Hill, 1996), are not present. Furthermore, sphalerite inclusions in megaquartz and *vice versa* indicate the similar timing of quartz and sphalerite recrystallisation. The ductile deformation of sphalerite is also inferred from preferentially aligned fabrics, minor bending of growth twins and lattice dislocations (Frater, 1978).

Rounded chalcopyrite inclusions and 'chalcopyrite disease' (Barton and Bethke, 1987) is rare in sphalerite at Gossan Hill . The lack of chalcopyrite disease in sphalerite at Gossan Hill, likely reflects the segregation of chalcopyrite to grain and twin boundaries during remobilisation and recrystallisation.

The occurrence of sphalerite in pressure shadows and as fracture fill in pyrite supports the local remobilisation of sphalerite during or after penetrative deformation. Furthermore, decussate textures between chlorite in sphalerite are equilibrium textures that lack impingement. This suggests that the remobilisation of sphalerite occurred during or after peak metamorphism and is consistent with the conclusions of Frater (1985b), who argued synkinematic sphalerite recrystallisation and remobilisation.

6.2.2 Composition of sphalerite

Sphalerite (and all other mineral) compositions were determined using a Cameca SX50 electron microprobe at the University of Tasmania. Sphalerite was analysed for S, Fe Mn, Cu, Zn, Ag, Hg, Bi and Se; these results are given in Appendix A4.1 and summarised in

Table 6.1. Of these elements, Mn, Cu, Ag, Hg and Se were below detection (Appendix A4.1). The Bi content of sphalerite ranges up to 0.5 wt.%, but is also generally below detection (Appendix A4.1).

The FeS content of sphalerite ranges from 1.3 to 7.2 mole % (average of 3.9 mole %) (Table 6.1, Figs. 6.1e and 6.1f). Sphalerite has a linear correlation between FeS and ZnS, the latter which ranges from 42.6 to 49.0 mole % (average of 46 mole %) (Fig. 6.1f). Sphalerite in massive sphalerite and Type V(B) veins have similar FeS contents, which span the complete range of FeS values in sphalerite at Gossan Hill (Table 6.1). At the south end of the Gossan Hill deposit (A zone), massive sphalerite has the lowest FeS contents (highest ZnS contents; Table 6.1). Average sphalerite FeS values (Table 6.1) indicate that massive sphalerite and Type V(B) veins have lower FeS contents than sphalerite in Type V(A) veins (Fig. 6.1e and Table 6.1). In comparison, Type V(A) veins contain sphalerite with the highest FeS contents (Fig. 6.1f). Therefore, a vertical and lateral zonation in sphalerite composition is inferred through the upper ore zone at Gossan Hill. The FeS contents of sphalerite increase with depth through the upper ore zone as ZnS contents decrease. Increasing FeS contents (decreasing ZnS) also occur laterally from A to C zone.

The FeS content of sphalerite can be used to infer the relative temperature of sphalerite formation. Sphalerite with low FeS contents (pale coloured sphalerite) forms at relatively low temperatures from oxidising solutions (Urabe, 1974; Hannington and Scott, 1989; Ames *et al.*, 1993). Hannington *et al.* (in press) use the FeS content of sphalerite in some Archean Canadian VHMS deposits to differentiate between high temperature Zn-Cu-rich (high FeS) and low temperature Zn-rich (low FeS) sulphide mineralisation. Nonetheless,

Table 6.1: Summary of the FeS and ZnS contents of sphalerite within the upper ore zone at Gossan Hill (expressed as mole %). Results are reported in Appendix A4.1. A and C refer to A zone in the south of Gossan Hill and C zone near the inferred feeder zone respectively.

Rock Type	n*	FeS (min)	FeS (max)	FeS (mean)	ZnS (mean)
Massive sphalerite					
A, orange, fine-grained sphalerite-chlorite	21	1.3	1.9	1.5	48.5
A, dark red-brown, coarse-grained sphalerite-quartz	11	3	3.5	3.1	47.5
C, dark red, coarse-grained sphalerite-quartz	11	4.8	7.2	5.2	44.6
C, honey-red, fine-grained sphalerite-quartz	3	2.3	4.2	3.3	47.6
Stringer veins					
A, Type V(B) quartz-sphalerite-pyrite vein	7	1.4	2.2	1.7	47.4
C, Type V(B) pyrite-sphalerite vein	3	5.3	6.1	5.6	44
A, Type V(A) carbonate-rich with minor sphalerite	2	5.4	5.5	5.5	44.7
C, Type V(A) pyrite-magnetite-sphalerite-chlorite vein	15	5.5	6.9	5.9	43.9
C, Type V(A) chlorite-magnetite-sphalerite vein	11	5.8	6.9	6.3	43.3
Overall					
All	84	1.3	7.2	3.9	46
Massive sphalerite	46	1.3	7.2	2.9	47.2
Type V(B) sphalerite-pyrite veins	10	1.4	6.1	2.9	46.4
Type V(A) pyrite-chlorite-carbonate-magnetite-sphalerite veins	28	5.4	7	6	43.7

* indicates number of analysis

actively forming seafloor hydrothermal deposits have FeS contents with wide variation in FeS contents, some of which range up to 44 mole % FeS (Peter and Scott, 1988; Scott, 1983; Hekinian *et al.*, 1980). However, Hill (1996) inferred uniformly high sphalerite FeS contents at Thalanga (8 to 12 mole %) to relate to sphalerite-pyrite recrystallisation and re-equilibration during peak metamorphism.

The trend of increasing sphalerite FeS contents with depth and proximity to C zone at Gossan Hill could indicate (1) primary compositional variation in sphalerite related to temperature gradients, or (2) the imprint of recrystallisation processes. It is suggested here that both (1) and (2) have caused the present distribution of FeS in sphalerite at Gossan Hill. Preserved FeS ratios in sphalerite are inferred in the upper parts of massive sphalerite from A to C zone where the principal matrix mineral is quartz. Textural evidence of sphalerite remobilisation and recrystallisation is present in Type V(A) veins and the deeper parts of the upper ore zone (Section 6.2.1), which may have caused the re-equilibration of sphalerite with chlorite, ankerite-siderite and pyrrhotite in these zones. Therefore, the increase in the FeS contents of sphalerite from A to C zone likely represents a thermal gradient, with sphalerite at A zone forming at lower temperatures more distally from the interpreted hydrothermal feeder at C zone.

6.3 Pyrite

Pyrite is the most abundant sulphide mineral in the Gossan Hill deposit. Pyrite occurs (1) in massive pyrite of the upper and lower ore zones, (2) as a major constituent of sulphide veins (Types IV, V(A) and V(B)), and (3) as disseminated grains in altered wall rock adjacent to massive pyrite and sulphide veins.

Pyrite has two main textural types; (1) inclusion-poor pyrite (Fig. 6.2a), and (2) inclusion-rich pyrite (Fig. 6.2b). Inclusion-poor pyrite consists of adjacent euhedral to subhedral grains, which coalesce to form large patches. Inclusion-rich pyrite typically forms large irregular shaped patches (<3 mm) of aggregated, anhedral pyrite that is sieved by micron-sized inclusions of chlorite, carbonate, quartz, chalcopyrite, pyrrhotite and sphalerite. The abundance of these inclusions gives the pyrite a spongy appearance.

6.3.1 Pyrite in massive sphalerite

Pyrite in massive sphalerite occurs as disseminated grains (<2 mm) or massive aggregates up to 10 mm in size within polycrystalline sphalerite (Fig. 6.2a) and quartz. Both disseminated and aggregated pyrite commonly consist of euhedral grains that are generally inclusion-poor (Fig. 6.2a). Nonetheless, minor scattered, rounded inclusions of sphalerite (<100 μm), galena (<50 μm) and chalcopyrite (<50 μm) are observed within pyrite grains. Rare embayed grains in sphalerite indicate the local replacement of pyrite by sphalerite. Inclusion-rich pyrite is uncommon in massive sphalerite, but where present, form rims up to 2 mm wide around inclusion-poor euhedral pyrites. This relationship suggests the later formation of inclusion-rich pyrite. Inclusion-rich pyrites also form tabular, lath-shaped (<2 mm) aggregates. As these are unusual structures for pyrite, they are interpreted to be pseudomorphs.

Figure 6.2

(a) Euhedral, inclusion-poor pyrite grains in a sphalerite matrix. The adjacent pyrite grains form massive pyrite. Upper ore zone at Gossan Hill (sample 760419).

(b) Irregular-shaped pyrite aggregate. Pyrite is inclusion-rich and hosted by a quartz matrix (grey). Lower ore zone at Gossan Hill (sample 769424).

(c) Skeletal pyrite in a sphalerite matrix. Sample from the upper ore zone at Gossan Hill (sample 760461).

(d) Colloform pyrite with interstitial chalcopyrite and sphalerite. Upper ore zone at Gossan Hill (sample 760426).

(e) Massive pyrite from the lower ore zone. This pyrite consists of densely packed pyrite grains that are inclusion-rich and inclusion-poor (euhedral). Chalcopyrite occurs between the pyrite grains and as inclusions in the inclusion-rich anhedral pyrite (sample 97U041).

(f) Concentric zonation in fine-grained pyrite within massive pyrite-sphalerite of the upper ore zone (sample 769344).

(g) Zoned euhedral pyrite grains in a chlorite matrix (grey). The zonation in these pyrites is defined by micron-sized inclusions of chlorite and quartz. Note in some pyrites the zonation is truncated at the pyrite grain margins. Upper ore zone (sample 762055).

(h) Skeletal pyrite within massive magnetite (grey). Lower ore zone (sample 762054).

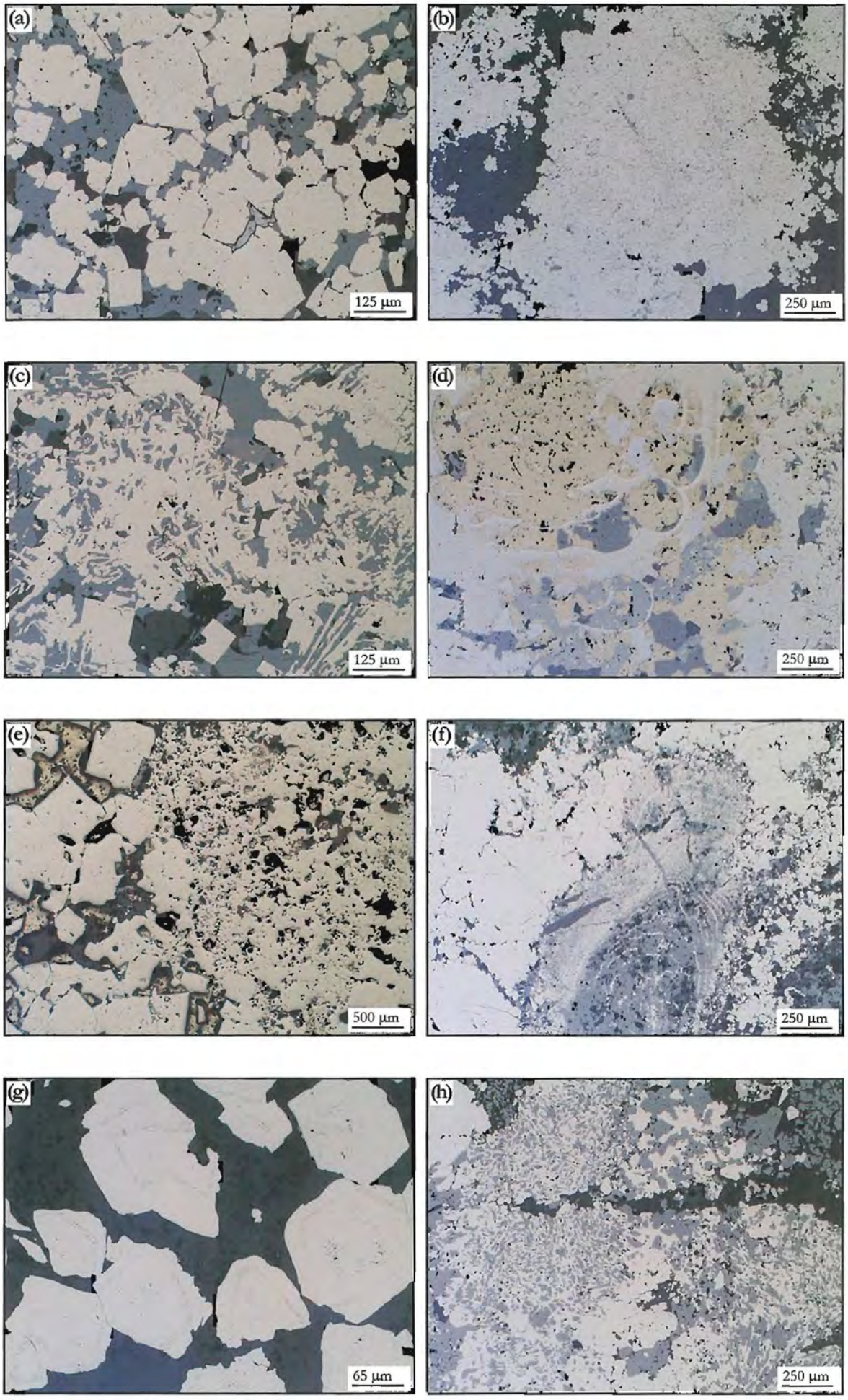
(a)
125 µm
(b)
250 µm
(c)
125 µm
(d)
250 µm
(e)
500 µm
(f)
250 µm
(g)
65 µm
(h)
250 µm

Skeletal pyrite grains (<4 mm in size) in massive sphalerite are common (Fig. 6.2c). These pyrites have skeletal fishbone to cross-shaped textures with interstices filled by sphalerite and lesser chalcopyrite. Skeletal pyrites locally forms overgrowths around euhedral pyrite grains or are intergrown with anhedral inclusion-rich pyrite. Skeletal pyrite is a common textural form to pyrite (*e.g.*, Graham *et al.*, 1988; Paradis *et al.*, 1988; Hannington *et al.*, in press) and suggest the replacement of pyrite by sphalerite.

Rare colloform pyrite occurs in massive sphalerite (Fig. 6.2d). Colloform pyrite consists of rhythmic, curviplanar bands of pyrite, with bands less than 250 μm wide. Colloform pyrites consist of inclusion-poor and inclusion-rich pyrite that is intergrown with sphalerite, chalcopyrite and arsenopyrite (Fig. 6.2d). Frater (1978) interpreted colloform pyrite as rarely preserved evidence of primary sulphide textures at Gossan Hill.

6.3.2 Massive pyrite (GGF M4 and GGF M6)

Pyrite in massive pyrite of the lower (GGF M4) and upper (GGF M6) ore zones have similar textures. In the upper ore zone massive pyrite consists of adjacent euhedral to subhedral pyrite (<1 mm) with lesser inclusion-rich pyrite in a quartz matrix (Fig. 6.2e). Aggregates of these pyrites range up to 10 mm in size. In the lower ore zone, pyrite in massive pyrite consists mainly of inclusion-rich pyrite with minor inclusion-poor pyrite. The latter has a similar grain size (<800 μm) compared to euhedral pyrites the upper ore zone. The matrix of massive pyrite in the lower ore zone is quartz, chlorite and chalcopyrite. Minor rounded inclusions of chalcopyrite (<50 μm in size) are common in euhedral pyrites of both ore zones. However, inclusions of galena in the euhedral pyrite of the upper ore zone are absent from the euhedral pyrite of the lower ore zone. In both ore zones, inclusion poor, euhedral pyrites have polygonal grain shapes typical of metamorphic recrystallisation (*c.f.* Hannington *et al.*, in press). Rare pyrite atoll textures and embayment to chalcopyrite were observed and suggest local replacement of pyrite by chalcopyrite.

Inclusion-rich pyrite in the upper ore zone contains abundant inclusions (<20 um) of quartz, chlorite, chalcopyrite and galena. Inclusion-rich pyrites form rims around euhedral pyrite grains and aggregates, some of which define concentric zonation in pyrite (Fig 6.2f). In some cases, crude banding in pyrite is defined by the grain sizes of the inclusions in the pyrite. In massive pyrite of the lower ore zone, inclusion-rich pyrite is abundant and forms irregular shaped aggregates up to 4 mm in size within a chlorite or chalcopyrite matrix. Inclusions within these pyrites are chlorite, carbonate, magnetite, rutile-ilmenite or quartz. Due to the abundance of these inclusions, inclusion-rich pyrites are weakly anisotropic. Moreover, inclusion-rich pyrite may cement scattered euhedral pyrite grains.

Zones of micron-sized inclusions form symmetric rims within pyrite and define a zonation. Textural modification of pyrite can be inferred by the truncation of these zones along the pyrite grain margins (*e.g.*, Fig. 6.2g). MacLean and Fleet (1989) interpret truncated growth zonation in pyrite to result from chemical redistribution of pyrite that retains some primary internal zonation.

Within the gradational contact between massive pyrite and massive magnetite, pyrite grains are euhedral to subhedral (<4 mm) and intergrown with marcasite. These pyrite grains do not have the spongy textures typical of inclusion-rich pyrite, but contain abundant scattered inclusions of rounded (<30 μm), elongate (<150 μm) to acicular (<400 μm) magnetite grains (Fig. 6.2h). The abundance of magnetite inclusions within euhedral pyrites imparts a skeletal texture to the pyrite grains. Furthermore, some granular magnetite grains are enclosed by euhedral pyrite, whilst some pyrite grains are free of magnetite inclusions. The abundance of magnetite inclusions in pyrite, and the encasement of magnetite grains by pyrite, support the replacement and overgrowth of magnetite by pyrite.

6.3.3 Pyrite in stringer veins

Type V(B) veins (pyrite-sphalerite) typically consist of large (<10 mm), anhedral and spongy inclusion-rich pyrite. These pyrites contain abundant inclusions (<10 μm) of chlorite, quartz, chalcopyrite and galena. Crude banding in Type V(B) veins result in bands of inclusion-rich pyrite that parallels the vein margin.

Type V(A) veins (pyrite-chalcopyrite-pyrrhotite-magnetite-chlorite-carbonate) contain euhedral inclusion-poor and anhedral inclusion-rich pyrite. Euhedral pyrite (<4 mm) commonly occurs in Type V(A) veins that are chalcopyrite-rich, but these grains have inclusion-rich pyrite rims. Inclusion-rich pyrite rims have rounded inclusions (<20 μm) of galena and sphalerite. Magnetite grains within Type V(A) veins are euhedral and are sieved by rounded to euhedral inclusions (<50 μm) of pyrite.

Type IV (pyrite-chlorite) veins have euhedral to subhedral inclusion-poor pyrite grains in a chlorite matrix. Pyrite grains are up to 3 mm in size and the grain margins of pyrite are weakly embayed by the chlorite matrix.

6.3.4 Disseminated pyrite (GGF M4 and GGF M6)

Disseminated pyrite (<20% modal) is common in altered beds and bedded intervals within and adjacent to massive pyrite and sulphide veins in the upper and lower ore zones. Finely disseminated pyrite appears to parallel sedimentary layering in sandstone and siltstone and imparts a dark grey colour to the host rock. Disseminated pyrite typically occurs in chlorite altered wall rocks and is euhedral to rounded, inclusion-poor, and up to 5 mm in size. These pyrite grains typically have embayed and ragged margins to the chlorite in the matrix, commonly with chlorite inclusion-rich (<40 μm) rims. Alternating bands of inclusion-rich and inclusion-poor pyrite around a central euhedral pyrite grain define zonation in large composite pyrite grains. Marcasite intergrowths in euhedral pyrite are also observed.

Radiating skeletal textures are common in disseminated pyrite grains at Gossan Hill (Fig. 6.3a). Large, rounded pyrite grains (up to 10 mm across) commonly have concentric banding, with numerous alternating bands (up to 10 bands <500 μm wide) of skeletal pyrite and anhedral inclusion-rich pyrite. Skeletal pyrite bands contain elongate grains that radiate outwards from the centre of the pyrite grain (perpendicular to the banding

Figure 6.3

(a) Skeletal pyrite in massive pyrite from the upper ore zone. This composite pyrite grain has a subhedral, inclusion-poor pyrite core and multiple rims of skeletal pyrite. The skeletal pyrite grains are oriented perpendicular to the orientation of the rims (sample 760383).

(b) Pyrite breccia. Inclusion-poor pyrite is veined and hosted by chalcopyrite. Lower ore zone at Gossan Hill (sample 769030).

(c) Euhedral magnetite containing scattered chalcopyrite inclusions in massive inclusion-poor pyrite from the lower ore zone (sample 762010)

(d) Pyrite grains hosted by chalcopyrite in massive pyrite-chalcopyrite from the lower ore zone (sample 760290).

(e) Chalcopyrite in the lower ore zone that contains euhedral chlorite grains (sample 769152).

(f) Anhedral, polycrystalline pyrrhotite with scattered subhedral magnetite and quartz in the lower ore zone (sample 769235).

(g) Euhedral magnetite grains hosted by polycrystalline sphalerite in the upper ore zone. The magnetite grains contain scattered sphalerite inclusions (sample 760461).

(h) Euhedral magnetite in the upper ore zone, which contains abundant inclusions of pyrite. These magnetite grains occur throughout massive pyrite (inclusion-rich and inclusion-poor pyrite) of the upper ore zone (sample 760461).

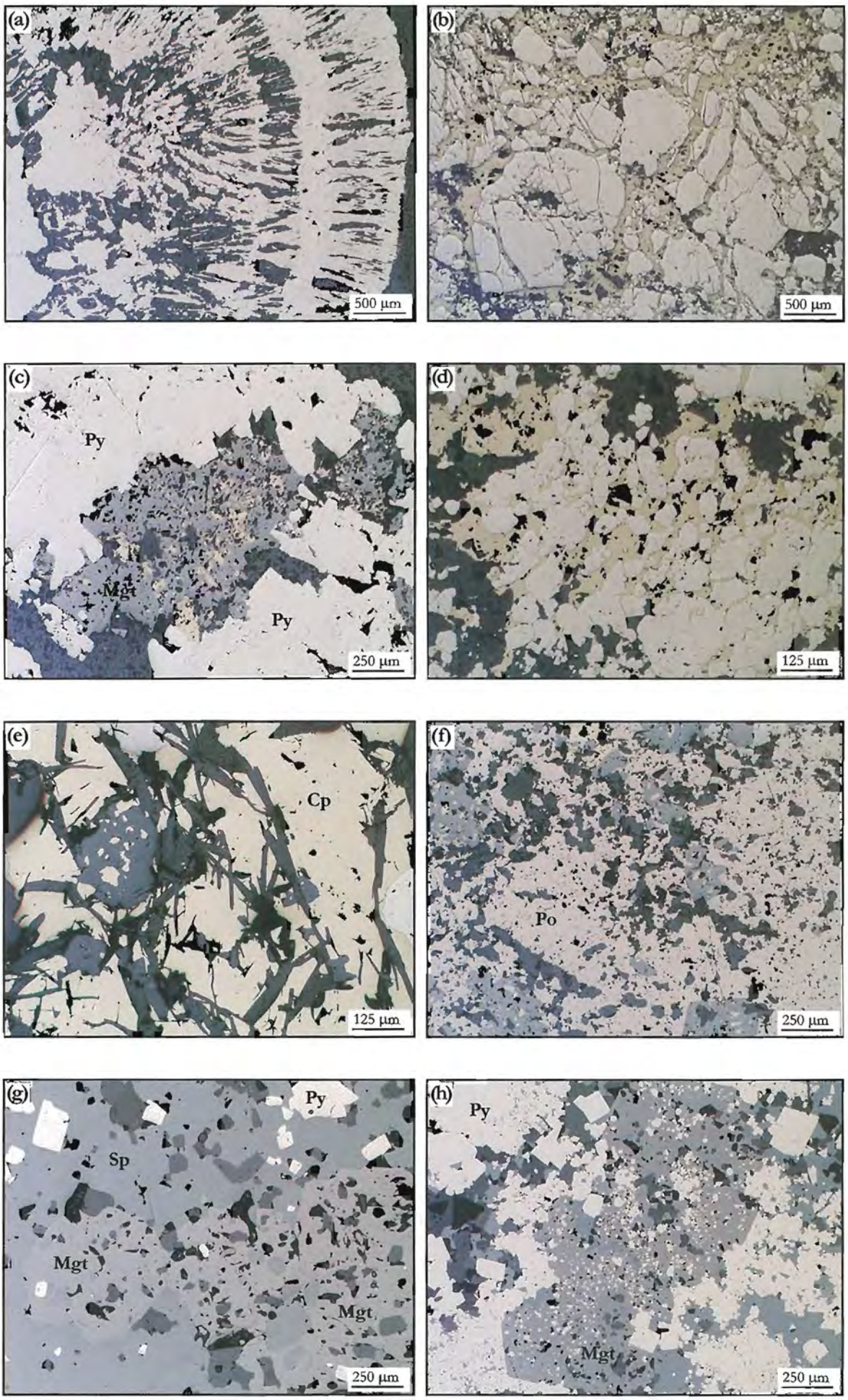
(a)
500 µm
(b)
500 µm
(c)
Py
Mgt
Py
250 µm
(d)
125 µm
(e)
Cp
125 µm
(f)
Po
250 µm
(g)
Py
Sp
Mgt
Mgt
250 µm
(h)
Py
Mgt
250 µm

direction) (Fig. 6.3a). Skeletal pyrite is a typical texture formed during the rapid deposition of pyrite (Ramdohr, 1969; Craig and Vokes, 1992).

Large scattered euhedral pyrite grains are common in beds that contain andalusite and chloritoid. Pyrite also forms rims around the blocky segments of andalusite porphyroblasts (Chapter 4). This pyrite contains abundant (<40 μm size) inclusions of chlorite, magnetite and pyrrhotite. Pyrite rims around andalusite formed during peak metamorphism (Chapter 4).

6.3.5 Deformation textures

Throughout the Gossan Hill deposit, all textural types of pyrite have undergone deformation. Deformation is typically manifested as fractured pyrite grains or aggregates, some of which have *in situ* breccia textures (Fig. 6.3b). Fractures in pyrite vary from undulose cracking patterns across cleavage to discontinuous planar fractures. The distribution of fractures within pyrite is not homogeneous, with some grains lacking fractures and others extensively fractured. In massive sphalerite, sphalerite, chalcopyrite, galena, chlorite and quartz typically fill fractures in pyrite. In massive pyrite (GGF M4 and GGF M6), chalcopyrite, pyrrhotite and chlorite commonly fills fractures in pyrite. Undulose cracking patterns locally contain a fibrous fill of chlorite and quartz. Folded Type V(A) veins have an axial planar cleavage (defined by chlorite), whilst pyrite in the veins has undulating extensional fractures perpendicular to cleavage.

Disseminated pyrite grains in chlorite generally lack fractures, and instead have pressure shadows and cleavage wrapping. These structures indicate the local rotation of pyrite grains. Pressure shadows consist of coarse-grained chlorite (<200 μm), fibrous quartz and less commonly, pyrrhotite, chalcopyrite and chloritoid.

6.3.6 Marcasite

Minor marcasite was observed in massive pyrite of the lower ore zone. Marcasite occurs in magnetite- and pyrrhotite-rich zones within massive pyrite. Marcasite forms euhedral to subhedral grains up to 60 μm that are commonly hosted by euhedral, inclusion-poor pyrite.

6.3.7 Composition of pyrite

Pyrite was analysed for Co, Ni, Zn, As, Ag, Se and Pb (Appendix A4.2). Minor compositional variation in pyrite was observed at Gossan Hill, with pyrite having near stoichiometric Fe and S ratios (Appendix A4.2). Impurities detected in the upper ore zone were Co (up to 1.0 wt.%), Zn (up to 1.2 wt.% Zn), As (up to 1.9 wt.%), Ag (up to 0.4 wt.%) and Pb (up to 4.9 wt.%). However, in view of the inclusion-rich nature of many pyrites, it is likely that elevated Zn and Pb represent an electron beam overlap with fine-grained sphalerite and galena inclusions. Pyrite in the lower ore zone contained elevated Co (up to 3.0 wt.%), As (up to 1.0 wt.%) and Pb (up to 2.4 wt.%) (Appendix A4.2). As cobaltite, arsenopyrite and galena inclusions were rare in the lower ore zone, the impurities are considered to be stoichiometric substitutions in pyrite.

6.3.8 Discussion

Pyrite has two major textural forms, which are (1) euhedral to subhedral, inclusion-poor pyrite, and (2) anhedral, inclusion-rich pyrite. The relative timing of these pyrites is inclusion-poor pyrite followed by inclusion-rich pyrite as indicated by common inclusion-rich overgrowths around euhedral pyrite. There is little evidence of pyrite recrystallisation as shown by the lack of annealed textures in pyrite. However, dense inclusion-rich, anhedral pyrite at Kidd Creek is interpreted to represent recrystallised pyrite aggregates that have porous or cellular structures (Hannington *et al.*, in press). It is therefore possible, that inclusion-rich anhedral pyrites represent recrystallised pyrites. In support of this argument, is the presence of truncated zonation in pyrite and decussate chlorite and pyrite intergrowths in the lower ore zone, which infer some pyrite recrystallisation synchronous with peak metamorphism. The occurrence of ubiquitous deformation structures in both major textural forms of pyrite, indicates that recrystallisation, where it occurred, was synchronous with or post-dated penetrative deformation. Due to the preservation of these brittle deformation fabrics in pyrite, pyrite recrystallisation did not cause pyrite remobilisation. Furthermore, these relationships support formation of most pyrite prior to deformation and metamorphism. However, pyrite-pyrrhotite-magnetite reaction rims on andalusite porphyroblasts indicate that some pyrite formed during peak metamorphism (refer Appendix A2.2).

6.4 Chalcopyrite

The three main occurrences of chalcopyrite at Gossan Hill are (1) within massive pyrite (GGF M4 and GGF M6), (2) a minor to major constituent of Type V(A) sulphide veins, and (3) disseminations in the wall rock of the lower ore zone and massive magnetite adjacent to massive pyrite and sulphide veins. In these occurrences, chalcopyrite forms (1) polycrystalline anhedral aggregates, (2) scattered irregular grains, (3) a fracture fill in pyrite and magnetite, or (4) inclusions in pyrite, magnetite, pyrrhotite and rarely sphalerite. In the lower ore zone, massive pyrite locally grades into narrow intervals of massive chalcopyrite, particularly near the margins of massive pyrite zones.

Within massive sphalerite and Type (VB) veins, chalcopyrite forms less than 5% modal and occurs as rounded to irregular shaped grains typically along the grain boundaries of polycrystalline sphalerite and less commonly as inclusions (<100 μm) within sphalerite. Chalcopyrite inclusions (<50 μm) also sieve inclusion-rich pyrite and euhedral magnetite in massive sphalerite (Fig. 6.3c) and infill interstices in skeletal pyrite. In colloform pyrite, chalcopyrite occurs between the curviplanar pyrite bands.

In massive chalcopyrite (>50% chalcopyrite), polycrystalline aggregates of chalcopyrite contain scattered euhedral pyrite and anhedral pyrrhotite grains in an apatite, chlorite carbonate matrix. Massive pyrite (GGF M4 and GGF M6) and Type V(A) veins can have minor (<2% modal) to major (>2% modal) amounts of chalcopyrite. Chalcopyrite commonly forms an anhedral polycrystalline interlocking matrix to pyrite, pyrrhotite, magnetite, quartz and chlorite within massive pyrite (Fig. 6.3d). In massive pyrite, chalcopyrite inclusions (<50 μm) sieve inclusion-rich pyrite and occur as scattered

inclusions in euhedral inclusion-poor pyrite and euhedral magnetite (Fig. 6.3c). Fractured pyrite grains and aggregates commonly have fractures infilled by chalcopyrite, without impingement of pyrite margins. Chalcopyrite also occurs in pressure shadows around disseminated euhedral pyrite grains.

Carbonate grains that occur as scattered grains in massive pyrite commonly contain abundant inclusions of chalcopyrite. Chalcopyrite in the massive pyrite forms small rounded inclusions (<30 μm) in quartz or occurs as 'V' shaped grains (<200 μm) at the junctions of euhedral quartz. Decussate chlorite commonly contains angular, irregularly shaped chalcopyrite grains between fibrous chlorite (Fig. 6.3e). Disseminated chalcopyrite in silicified wall rock of the lower ore zone occurs as rounded grains (<100 μm) within microcrystalline quartz mosaics.

The composition of chalcopyrite at Gossan Hill is near stoichiometric (Appendix A4.3). Minor amounts of Zn (up to 0.6 wt.%) and Bi (up to 0.5 wt.%) were identified in chalcopyrite within massive sphalerite of the upper ore zone.

6.4.1 Discussion

The lack of deformation textures in chalcopyrite led Frater (1978; 1985b) to conclude that it had undergone recrystallisation during deformation and metamorphism. Moreover, chalcopyrite can be remobilised at temperatures as low as 200°C (Kelly and Clark, 1975). The widespread occurrence of chalcopyrite filling fractures in pyrite at Gossan Hill supports extensive, but localised, remobilisation during deformation. This interpretation is consistent with the occurrence of chalcopyrite in pressure shadows around pyrite grains. Furthermore, decussate chlorite with interstitial chalcopyrite indicates that the recrystallisation and remobilisation occurred during peak metamorphism.

The lack of impingement textures between chalcopyrite and pyrite indicates that chalcopyrite formed a ductile matrix during the brittle deformation of pyrite. Furthermore, inclusions of chalcopyrite in inclusion-rich pyrite and pyrrhotite suggests some chalcopyrite incorporation to pyrite during remobilisation and recrystallisation.

6.5 Pyrrhotite

Pyrrhotite occurs in massive pyrite and Type V(A) stringer veins in the upper and lower ore zones. In the upper ore zone, the abundance of pyrrhotite increases with depth, whilst pyrrhotite is ubiquitous throughout the lower sulphide zone. Pyrrhotite in massive pyrite and Type V(A) veins forms scattered, irregular shaped grains or polycrystalline aggregates. Pyrrhotite is typically associated with pyrite and magnetite (Fig. 6.3f). In fractured pyrite grains and aggregates, pyrrhotite fills fractures, where it forms anhedral grains along pyrite and magnetite grain margins. Rounded pyrrhotite inclusions are common in pyrite and magnetite. However, pyrrhotite itself commonly contains rounded inclusions of chalcopyrite, chlorite and quartz. Within pyrrhotite-rich Type V(A) veins, pyrrhotite forms rare lath-shaped grains up to 200 μm long. In carbonate gangue in the lower ore zone, embayed carbonate grains are enclosed and sieved by pyrrhotite, suggesting pyrrhotite replacement. Pyrrhotite also occurs along the margins of andalusite

porphyroblasts, and as elongate anhedral grains that parallel the cleavage of chloritoid (Chapter 4). Electron microprobe analyses of pyrrhotite are given in Appendix A4.4.

6.5.1 Discussion

Pyrrhotite grains are typically anhedral. The local remobilisation of pyrrhotite is indicated by its occurrence as a fracture fill of pyrite and the lack of deformation textures within it. The abundance of chalcopyrite inclusions in some anhedral pyrrhotite grains, suggests a similar timing of remobilisation for these two minerals. The occurrence of pyrrhotite as intergrowths with chloritoid and as rims around andalusite indicates that some pyrrhotite formed during peak metamorphism (Chapter 4).

6.6 Magnetite

Magnetite is a major mineral in the Gossan Hill deposit where it forms a minor to major constituent of massive sulphide and Type V(A) sulphide veins, and is the principal constituent of massive magnetite. The textural characteristics of magnetite grains differ between magnetite disseminated in sulphide from that in massive magnetite.

6.6.1 Disseminated magnetite in sulphide

Within massive sulphide and Type V(A) sulphide veins of the lower and upper ore zones, magnetite occurs as disseminated, euhedral to subhedral grains up to 600 μm in size. This type of magnetite does not form massive magnetite. Euhedral magnetite is a major constituent (<20 % modal) in massive pyrite in GGF M6 and GGF M4. Magnetite occurs as scattered grains in sulphide or grain aggregates up to 3 mm in size, and is typically hosted by pyrite, chalcopyrite and pyrrhotite, and less commonly, sphalerite (Fig. 6.3g). Commonly, euhedral magnetite grains contain rounded inclusions (up to 250 μm in size, but generally <50 μm) of pyrite, chalcopyrite, pyrrhotite, sphalerite, arsenopyrite, chlorite and quartz (Fig. 6.3h). At the Scuddles deposit, Ruxton (1986) identified widespread euhedral magnetite in massive sphalerite and the M1 Marker. However, despite the common occurrence of euhedral magnetite in massive sphalerite at Gossan Hill, it is absent from M1 Marker.

6.6.2 Magnetite in massive magnetite

Magnetite in the massive magnetite of the lower ore zone (GGF M4) is characterised by anhedral magnetite with granular, inclusion-rich (spongy) and skeletal forms. Less commonly lath-shaped to banded magnetite textures are observed. These textures make magnetite in the massive magnetite texturally distinct from the euhedral magnetite in sulphide. Granular, inclusion-rich, skeletal and lath-shaped magnetite locally occurs within a single sample. These texturally different magnetite types locally coalesce and form large aggregates up to 10 mm in size.

Granular magnetite

Granular magnetite is the most common textural form of magnetite and consists of equant subhedral to anhedral magnetite (<300 μm) in a chlorite, carbonate and quartz matrix (Figs. 6.4a and 6.4b). This type of magnetite forms the massive magnetite and

occurs in Type III veins. Sulphides are absent from granular magnetite. The consistent sizing of magnetite grains gives a relatively homogeneous texture to the massive magnetite (Fig. 6.4b). Granular magnetite may also form irregular to blocky shaped patches (<10 mm) that are intermixed with other textural forms of magnetite or the altered host rock.

Inclusion-rich and skeletal magnetite

Inclusion-rich and skeletal magnetite grains (Figs. 6.4c and 6.4d) are anhedral and have irregular shapes. They typically contain abundant angular to irregular inclusions of chlorite and carbonate, which impart a spongy to skeletal texture to the magnetite. Other minor matrix constituents are microcrystalline quartz and talc. In all cases inclusion-rich and skeletal magnetite grains are free of sulphide. Inclusion-rich and skeletal magnetite form scattered composite aggregates of magnetite. Skeletal magnetite also rims granular magnetite grains, with these rims less than 100 μm wide. Skeletal magnetite commonly occurs throughout granular massive magnetite, but can also form large (up to 3 cm) composite clusters. These clusters or aggregates skeletal magnetite have irregular to blocky and tabular shapes consisting of dense arrays of skeletal magnetite in a carbonate matrix.

Skeletal magnetite grains may have rounded to rhomb shaped outlines, but consist of disseminated, irregularly distributed blebs of magnetite in carbonate (Fig. 6.4d). It is likely that the rhomb shape of some skeletal magnetite is inherited from euhedral carbonate, suggesting partial replacement of carbonate by magnetite.

Lath-shaped magnetite

At Gossan Hill, lath-shaped magnetite is rare and consists of inclusion-rich, spongy magnetite that forms acicular, platy to tabular grains up to 300 μm in size (Fig. 6.4c). These laths have variably orientations, are hosted in a carbonate, chlorite, talc or quartz matrix, and may locally coalesce to form radiating to 'boxwork' textures (Fig. 6.4e).

Banded textures

Banded magnetite is rare in the massive magnetite and consists of granular to skeletal magnetite and, less commonly, lath-shaped magnetite that form alternating bands with carbonate or quartz. Magnetite bands vary from 40 μm to 2 mm in width and have locally undulose subparallel alignment (Figs. 6.4f and 6.4g). Carbonate bands between magnetite consist of interlocking subhedral carbonate that are sieved by rounded inclusions of magnetite. Some magnetite bands contain lath-shaped magnetite grains, which are up to 1 mm and oriented perpendicular to banding. The margins of magnetite bands with carbonate bands vary from sharp to gradational. Where present, magnetite bands are less than 3 cm, and laterally discontinuous. These discontinuous magnetite bands typically interdigitate with massive granular or skeletal magnetite in the massive magnetite.

Figure 6.4

(a) Massive magnetite consisting of fine-grained granular magnetite. This type of magnetite has a homogeneous texture. Scale in cm (sample 769125).

(b) Photomicrograph of granular magnetite from massive magnetite. The magnetite grains are hosted by chlorite (sample 769325).

(c) Photomicrograph of massive magnetite containing irregular-shaped magnetite grains with skeletal magnetite rims. The matrix in this sample is carbonate (ankerite-siderite) (sample 769319).

(d) Skeletal magnetite grains in massive magnetite, some of which rim around and form inclusions within carbonate (ankerite-siderite) grains (sample 769319).

(e) Lath-shaped magnetite in massive magnetite. The laths form an interlocking array of variably oriented magnetite grains in a carbonate (ankerite-siderite) matrix (sample 769159).

(f) Hand specimen of massive magnetite with abundant carbonate. Rare banding in massive magnetite (arrows) consist of alternating magnetite and carbonate (ankerite-siderite) bands. Scale in cm (sample 769325).

(g) Photomicrograph of banded magnetite showing bands of magnetite alternating with carbonate. Some of the bands are discontinuous and undulatory (sample 769325).

(h) Fractured inclusion-rich magnetite grains in a carbonate-talc matrix from massive magnetite (sample 769128).

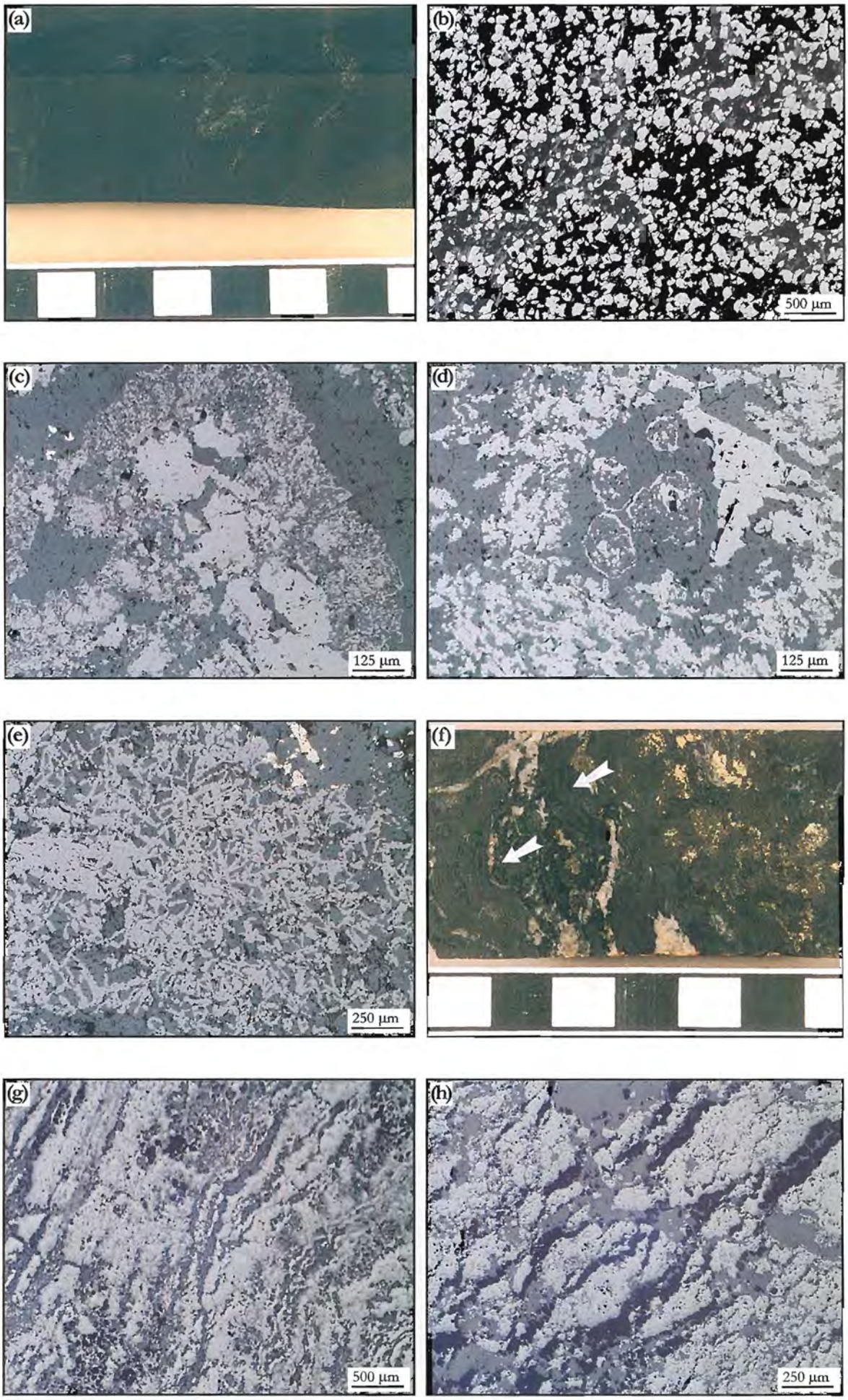
(a)
(b)
500 µm
(c)
125 µm
(d)
125 µm
(e)
250 µm
(f)
(g)
500 µm
(h)
250 µm

6.6.3 Deformation textures

Massive magnetite is highly fractured, with fractures less than 2 mm wide and filled by subhedral carbonate and talc. These irregularly oriented fractures impart an *in situ* jigsaw fit brecciation texture to massive magnetite (Fig. 6.4g). Deformation textures also include an undulose 'cracking pattern' that consists of subparallel sets of narrow (<0.5 mm) fractures through the massive magnetite. These fracture sets are oriented across the cleavage and are infilled by carbonate or fibrous talc, chlorite and/or quartz (Chapter 4).

6.6.4 Discussion

One of the key observations of this research is the different textures of magnetite observed in massive and vein sulphide from magnetite in the massive magnetite. Magnetite in sulphide is euhedral, and typically sieved by sulphide inclusions (pyrite, chalcopyrite, pyrrhotite and sphalerite). Sulphide inclusions likely result from the encapsulation of sulphide during euhedral magnetite formation, and indicate the synchronous timing between euhedral magnetite and sulphide.

Anhedral, granular to skeletal magnetite in the massive magnetite lacks sulphide inclusions, but contains abundant carbonate and chlorite. Carbonate and chlorite occur as inclusions, enclosed grains and as intergrowths with skeletal magnetite. Although these associations indicate a similar timing of precipitation between magnetite, chlorite and carbonate, carbonate fracture fill suggests local remobilisation and recrystallisation of carbonate during deformation and metamorphism.

Granular magnetite is a common textural form and is typical of magnetite formed by slow, unimpeded growth (Ramdohr, 1969). Its widespread occurrence in massive magnetite at Gossan Hill is interpreted to represent a primary hydrothermal precipitate. In comparison, skeletal and inclusion-rich magnetite are characteristic of rapidly deposited magnetite (Ramdohr, 1969). Frater (1978) interpreted the composite aggregates of granular and skeletal magnetite in the massive magnetite to be syndepositional magnetite breccia. However, due to the interdigitating association between all textural types magnetite (excluding euhedral magnetite) with altered tuffaceous host rocks of GGF M4, no evidence was observed to support Frater's (1978) conclusion. Instead, these observations are consistent with the formation of magnetite in massive magnetite by replacement. Moreover, it is possible that the irregular to blocky aggregates of granular and/or skeletal magnetite within the massive magnetite were inherited during the replacement of the granule breccia host rock of GGF M4. Irregularities in the magnetite textures may therefore have been controlled by original heterogeneity in the volcaniclastics.

Lath-shaped, acicular and bladed magnetite are uncharacteristic textural forms (Ramdohr, 1969; Picot and Johan, 1982). These textures are, however, common to hematite (*e.g.*, Ramdohr, 1969; Craig and Vaughan, 1981). Using this comparison, Frater (1978) inferred a large part of massive magnetite at Gossan Hill to result from the thermal metamorphism of a hematite-Fe-oxide precursor assemblage to magnetite. Based on

similar magnetite textures in the Tennant Creek deposits, Large (1974) also inferred magnetite to have pseudomorphed hematite. However, unlike Tennant Creek, massive magnetite (and massive sulphide) at Gossan Hill does not contain hematite. The absence of hematite could result from (1) the complete replacement of hematite by magnetite, or (2) the initial absence of hematite during magnetite and sulphide formation. In the latter case, lath-shaped magnetite grains may have also resulted as pseudomorphs of another unknown mineral phase (*e.g.*, pyrrhotite, Koski *et al.*, 1988; Goodfellow and Blaise, 1988) or pseudomorphs of lithics (*e.g.*, pumice shreds and shards). Moreover, spherulitic and bladed magnetite in the Warrego deposit at Tennant Creek, were interpreted by Wedekind (1990) to have formed during the direct, and extremely rapid, precipitation of magnetite into uncharacteristic shapes. In view of these points, it is possible that lath-shaped magnetite at Gossan Hill may be primary hydrothermal precipitates.

6.7 Ilmenite and rutile

Ilmenite and rutile are accessory minerals (<2% modal) in massive sulphide and massive magnetite, and also occur as scattered grains throughout the GGF. Ilmenite-rutile grains were not observed however in the sulphide veins. Typically ilmenite and rutile have poorly-formed, skeletal and spongy grains but may be euhedral tabular, acicular, and blebby shapes with a grain size up to 200 μm (Fig. 6.5a). In massive sulphide and magnetite, ilmenite and rutile occur as encapsulated grains in inclusion-rich anhedral pyrite and skeletal magnetite aggregates in massive magnetite respectively.

The composition of ilmenite and rutile is given in Appendix A4.6. Ilmenite and rutile have end member compositions containing minor Mn (<1.1 wt.%) and Mg (<0.6 wt.%) (Appendix A4.6). There is a zonation of ilmenite-rutile in the GGF, from rutile in GGF M1, to rutile and ilmenite in GGF M4 and ilmenite in GGF M5 and GGF M6. Exsolution textures between ilmenite and rutile occur in GGF M4 with cores of rutile enclosed by anhedral ilmenite. Commonly, rutile cores have a lath-shape and exsolution textures with outer ilmenite envelopes.

6.7.1 Discussion

Ilmenite and rutile are common accessory minerals in many VHMS deposits (*e.g.*, Huston 1988), with the source of Ti invoked to be locally derived from primary Ti-bearing minerals during hydrothermal alteration (Jiang *et al.*, 1996). Moreover, Hutchinson and Searle (1971) identified syngenetic exhalative mineralisation to be depleted in Ti, whilst epigenetic stringer mineralisation retained Ti from the footwall lithology. Huston (1988) identified Ti-rich staurolite alteration in below massive sulphides at the Balcooma deposit, whilst Ti-poor staurolite occurred in syngenetic mineralisation. Huston (1988) used the Ti contents of staurolite to infer the seafloor location during sulphide mineralisation.

At Gossan Hill, ilmenite and rutile are considered to be metamorphic products (Chapter 4). However, the encapsulation of ilmenite-rutile grains in pyrite and magnetite may indicate that some ilmenite-rutile formed prior to, or synchronous with, massive magnetite and massive sulphide formation. In this scenario, Ti may have been sourced

Figure 6.5

(a) Irregular composite grain of ilmenite and rutile (Ilm-Ru) within chlorite of GGF M4 (sample 762050).

(b) Scattered galena (Ga) within massive sphalerite (Sp) of the upper ore zone (sample 760362).

(c) Massive interlocking sphalerite (Sp) in the upper ore zone containing anhedral chalcopyrite (Cp) and tetrahedrite (Tet) grains. Euhedral arsenopyrite (Asp) grains are scattered through chalcopyrite, tetrahedrite and sphalerite (sample 769059).

(d) Native silver grains (Ag) from a pyrite vein in the upper ore zone (sample 760350).

(e) Electrum (El) hosted by skeletal pyrite (Py) in massive sphalerite from the upper ore zone (sample 760461).

(f) Electrum (El) hosted by skeletal pyrite grains (Py) in massive sphalerite from the upper ore zone. Skeletal pyrite also contains irregular grains of galena and pyrrhotite (sample 760461).

(g) Euhedral arsenopyrite grains (Asp) hosted by massive, polycrystalline sphalerite (Sp) in the upper ore zone (sample 760461).

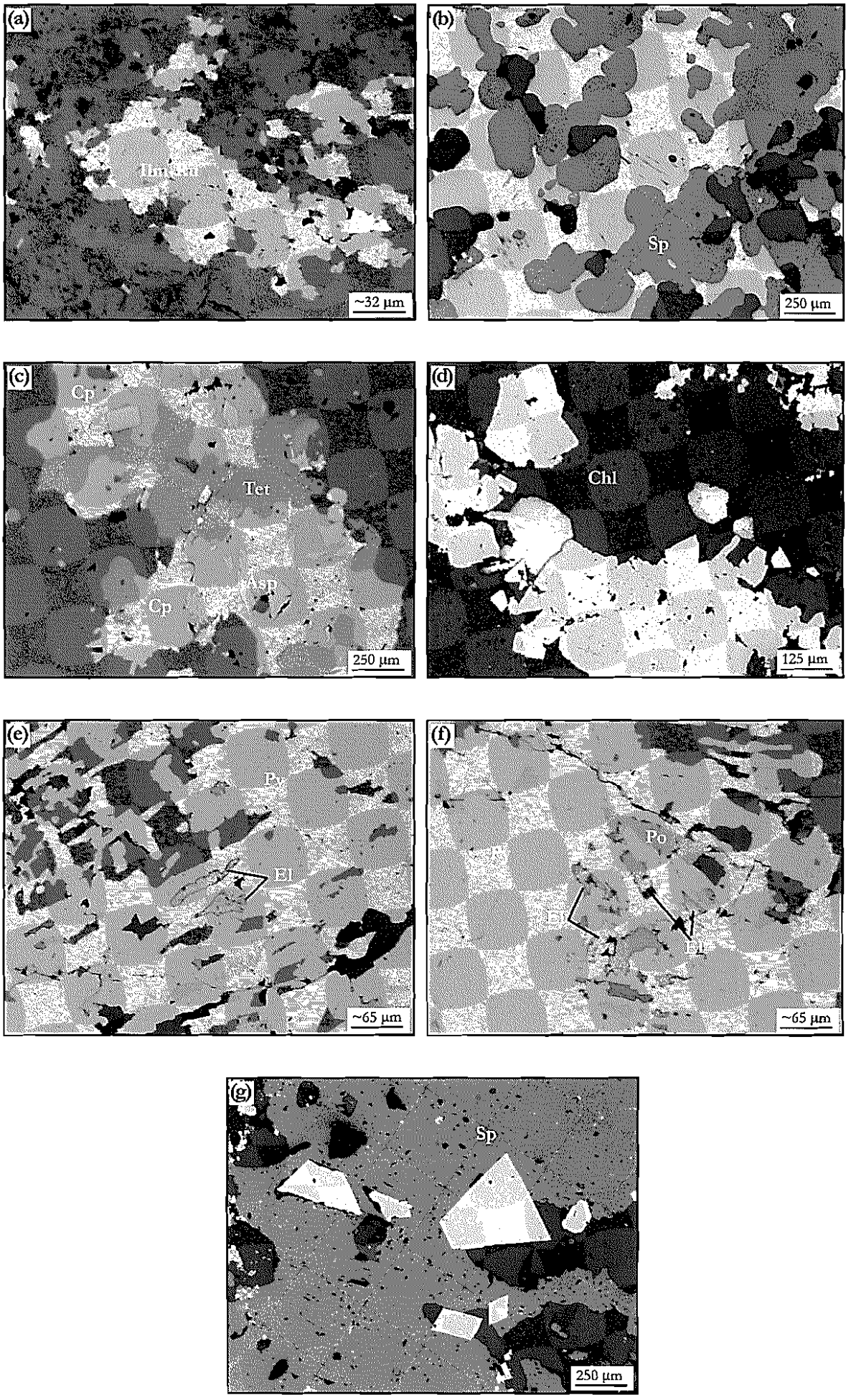
(a)
Ilm
~32 µm
(b)
Sp
250 µm
(c)
Cp
Tet
Sp
Cp
250 µm
(d)
Chl
125 µm
(e)
Py
El
~65 µm
(f)
Po
El
El
~65 µm
(g)
Sp
250 µm

locally from the host tuffaceous volcaniclastics, which were replaced by the sulphide and magnetite.

6.8 Galena

Galena has a minor (up to 5% modal) to accessory (<1% modal) occurrence in massive sphalerite and massive pyrite of the upper ore zone. Galena also occurs as rare inclusions in pyrite within massive pyrite of the lower ore zone and Type V(A) veins. Within massive sphalerite, galena occurs as anhedral, coarse-grained, polycrystalline aggregates (<2 mm) interstitial to, and along grain boundaries of sphalerite (Fig. 6.5b). Galena is also a common inclusion within inclusion-rich pyrite and also fills skeletal and radial structures in pyrite. Galena inclusions in pyrite are typically rounded and up to 50 μm in size. Fractures through pyrite in the upper ore zone are also commonly filled by galena. Compositionally, galena has low concentrations of Ag (<0.5 wt.%) and Bi (<1.0 wt.%) (Appendix A4.7).

6.9 Tetrahedrite

At Gossan Hill, tetrahedrite in massive sphalerite is associated with galena and arsenopyrite. Tetrahedrite occurs as (1) irregular shaped grains (<500 μm) in sphalerite adjacent to scattered euhedral arsenopyrite (Fig. 6.5c), (2) narrow rims (<30 μm) along the margins of galena, or (3) as inclusions (<30 μm) within galena that also contain arsenopyrite. Electron microprobe analysis of tetrahedrite (Appendix A4.8) indicate that it is argentiferous with a Ag content that ranges up to 29.0 wt.%. This elevated concentration of Ag in tetrahedrite contrasts with low Ag values observed in galena (Section 6.8), indicating that the main residence of Ag at Gossan Hill is within tetrahedrite.

6.10 Native silver

Native silver is rare and was observed as free grains in Type V(B) pyrite veins overlying massive sphalerite at the southern end of Gossan Hill. Native silver occurs as rounded to irregular shaped grains up to 200 μm in pyrite, quartz and chlorite veins. Native silver contains 94.0 to 99.8 wt.% Ag, with Au contents up to 0.6 wt.% (Appendix A4.9).

6.11 Electrum

Rare electrum was observed in massive sphalerite of the upper ore zone at Gossan Hill. Electrum grains (70 μm in size) are hosted by skeletal, inclusion-rich pyrite (Figs. 6.5e and 6.5f), which are hosted within polycrystalline sphalerite. Electrum grains are irregular and elongate to rounded grains (Figs. 6.5e and 6.5f). Electrum was also observed in euhedral pyrite within massive pyrite of the lower ore zone. In this case, electrum occurred as rounded to subrounded grains up to 50 μm.

As the composition of electrum was the subject of work by Everett (1990), only a few electrum grains were analysed in this study. The composition of electrum is given in Appendix A4.10 and illustrated by the fineness (1000* Au/(Au+Ag)) plot in Figure 6.6. The average fineness of electrum in massive sphalerite in the upper ore zone is 341,

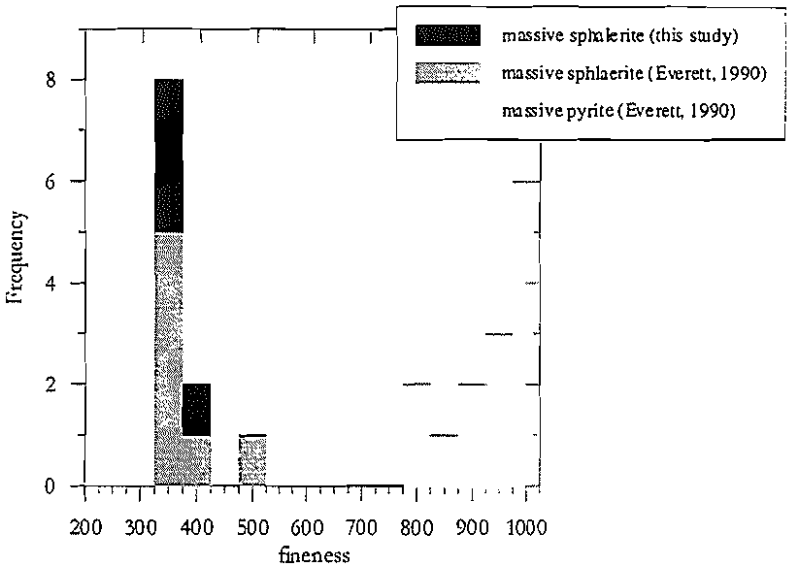

Figure 6.6: Electrum fineness (100*Au/(Au+Ag)) at the Gossan Hill deposit. Electrum grains have a bimodal fineness distribution. Electrum fineness in massive sphalerite of the upper ore zone (GGF M6) is lower than the fineness of electrum in the lower ore zone (GGF M4).

which is lower than electrum in massive pyrite of the lower ore zone (range of 941 to 994; Everett, 1990). These results indicate that electrum in the upper ore zone is enriched in Ag compared with electrum in the lower ore zone.

6.12 Cobaltite

Cobaltite occurs as disseminated euhedral grains (<250 μm) in massive sphalerite of the upper ore zone. At Gossan Hill, cobaltite has Fe contents that range from 2.1 to 6.2 wt.% (Appendix A4.11), which correspond to a ranges in As of 40.1 to 45.3 wt.% and Co from 30.5 to 34.1 wt.%. Such compositional variations are common to cobaltite (Ramdohr, 1980).

6.13 Arsenopyrite

Arsenopyrite is a common accessory mineral of massive sphalerite and massive pyrite in the upper ore zone. Arsenopyrite occurs as scattered euhedral grains in polycrystalline sphalerite, where it is commonly associated with, and hosted by, pyrite, galena and tetrahedrite (Fig. 6.5g). Arsenopyrite typically forms euhedral grains that range up to 600 μm.

Arsenopyrite was analysed by electron microprobe and the results are given in Appendix A4.12. The As content of arsenopyrite varies from 34.1 to 47.5 wt.% (average of 43.5 wt.%), Fe ranges from 34.0 to 38.7 wt.% (average of 35.1 wt.%) and S ranges from 18.7 to 30.4 wt.%. Minor elements in arsenopyrite include Co (up to 0.6 wt.%), Cu (up to 2.1 wt.%) and Zn (up to 0.8 wt.%) (Appendix A4.12).

6.14 Gangue mineralogy and textures

Gangue minerals in massive and vein sulphide are chlorite, quartz, carbonate, talc and apatite. Gangue minerals in massive magnetite are similar, and include, in order of abundance, carbonate, chlorite, talc and quartz. Furthermore, all of these minerals occur as alteration minerals of the host rocks (Chapter 7).

6.14.1 Quartz

Quartz in massive and vein sulphide is typically megaquartz, which forms grains up to 0.5 mm in size (Fig. 6.7a). Quartz is most abundant in the upper ore zone where it forms the matrix to sphalerite and pyrite in massive sphalerite and massive pyrite. In massive sphalerite, megaquartz occurs as equant, rounded grains that locally contain rounded inclusions of sphalerite. Quartz also occurs in pressure shadows around disseminated pyrite grains and infills fractures in pyrite. In both of these cases, quartz is typically fibrous. In massive magnetite, quartz is minor, but where present it forms a microcrystalline mosaic interstitial to magnetite (Fig. 6.7b).

6.14.2 Chlorite

Chlorite is the main gangue mineral in sulphide veins and massive sulphide in the lower ore zone. Typically, chlorite occurs as fine-grained (<50 μm) to coarse-grained interlocking mosaics (Fig. 6.7c), but can also form euhedral, fibrous and decussate mosaics (refer Chapter 4). Large, euhedral interpenetrating chlorite grains are common in sulphide veins hosted by siliceous host rocks (Fig. 6.7d).

6.14.3 Carbonate

In massive and vein sulphide, carbonate occurs as scattered subhedral grains or an interlocking anhedral matrix (Fig. 6.7e). Carbonate grains are generally less than 250 μm and contain abundant inclusions of chalcopyrite and pyrite. Carbonate grains in contact with chalcopyrite are embayed, suggesting replacement of carbonate by chalcopyrite.

In massive magnetite, carbonate (ankerite to siderite; Chapter 7) typically forms the matrix and consists of interlocking anhedral to euhedral grains less than 1 mm (Fig. 6.7f). Carbonate is commonly sieved by inclusions of magnetite, which support synchronous formation of magnetite and carbonate. However, embayed and atoll carbonate associated with magnetite, indicates partial replacement of carbonate by magnetite. Fractures in massive magnetite are commonly infilled by euhedral to subhedral carbonate, which suggests the local remobilisation of carbonate during deformation.

6.14.4 Talc

Talc is minor and occurs as scattered grains in chlorite or as euhedral decussate grains in the matrix of massive and vein sulphide (Chapter 4). In massive magnetite, talc occurs as fine-grained (<100 μm) patches in chlorite and also as fibrous grains that infill fractures in massive magnetite.

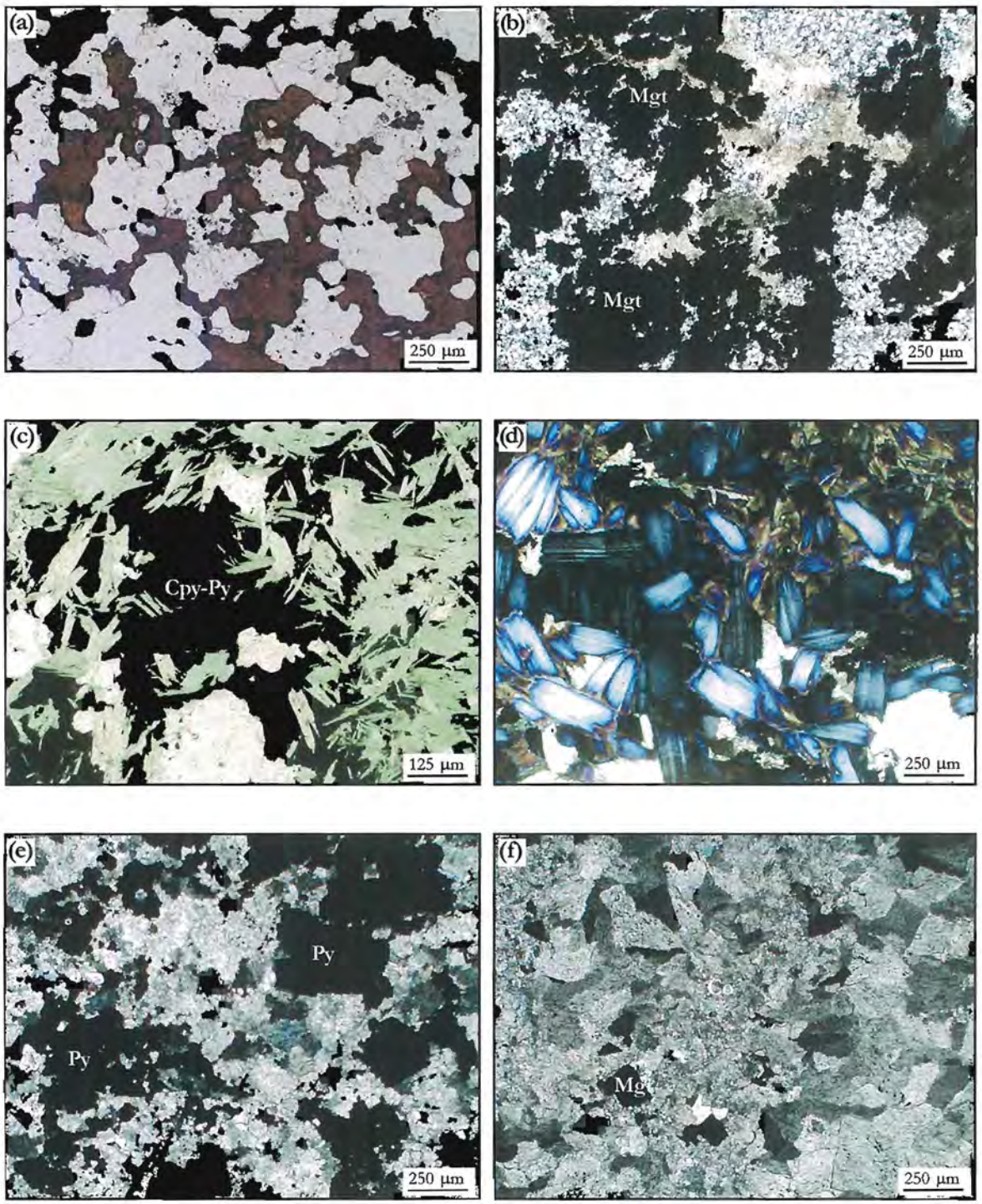

Figure 6.7: (a) Sphalerite in a megaquartz matrix of the upper ore zone. Quartz grains are polygonal and contain scattered inclusions of sphlaerite (sample 760222). (b) Microcrystalline quartz mosaic hosting irregular-shaped magnetite grains (Mgt). The matrix also contains anhedral, fine-grained carbonate (ankerite-siderite) (sample 769318). (c) Chalcopyrite and pyrite grains (Cpy-Py) in an interlocking euhedral chlorite matrix (sample 769228). (d) Large euhedral chlorite grains within a Type V(A) vein (sample 769209). (e) Pyrite (Py) in an interlocking subhedral to anhedral carbonate (ankerite-siderite) matrix in the upper ore zone (sample 760369). (f) Magnetite (Mgt) grains in an interlocking, euhedral carbonate (Co) matrix from massive magnetite of the lower ore zone (sample 769233).

6.14.5 Apatite

Apatite only occurs in massive sulphide in the lower ore zone where it forms disseminated euhedral grains less than 200 μm. Apatite occurs in the quartz or chlorite of the massive sulphide.

6.15 Discussion and summary

At Gossan Hill, rare colloform pyrite in the upper ore zone is one of the few primary sulphide ore textures preserved. The general lack of these textures suggests that deformation and metamorphism, particularly in the more ductile minerals, have extensively modified the sulphides. The modification of sulphide textures is further substantiated by fractured pyrite, which has fractures infilled by chalcopyrite, sphalerite, galena and pyrrhotite in both the upper and lower ore zones.

Polycrystalline, equant sphalerite, characteristic of sphalerite recrystallisation, occurs in massive sphalerite of the upper ore zone. Equilibrium sphalerite-chlorite and sphalerite-quartz textures indicate that these minerals had similar recrystallisation histories. Sphalerite has lower FeS (higher ZnS) contents in the upper parts of massive sphalerite and at A zone. This trend is, in part, interpreted to be a primary compositional zonation related to the temperatures of sphalerite deposition. Lower FeS contents of sphalerite likely formed at lower temperatures proximal to the seafloor, and laterally away from the main vent zone at C zone. Some sphalerite-chlorite re-equilibration may have occurred towards the base of the upper ore zone, where the FeS contents in sphalerite are higher.

Pyrite in massive pyrite (GGF M6 and GGF M4) has two distinct textural types; (1) inclusion-poor, euhedral pyrite, and (2) inclusion-rich anhedral pyrite. Euhedral pyrite is the main type in the upper ore zone, whilst inclusion-rich pyrite is abundant in the lower ore zone. Inclusion-rich pyrite post-dates euhedral pyrite, as inferred from overgrowth relationships. Furthermore, it is possible that inclusion-rich pyrite is the product of pyrite recrystallisation. Nonetheless, both inclusion-rich and inclusion-poor pyrite in massive sulphide have similar deformation textures, which are developed as grain fracture with sulphide fill. In comparison, disseminated pyrite in chlorite-altered wall rocks lack fracture, but have well developed pressure shadows. Disseminated pyrites are typically euhedral, inclusion-poor grains, which suggest their recrystallisation during deformation and/or metamorphism.

Skeletal pyrite is common in disseminated pyrite of the wall rock adjacent to or within massive sulphide and sulphide veins. These textures of pyrite are characteristic of rapidly deposited pyrite (Section 6.3). Radial pyrite grains that have concentric zonation defined by texturally different pyrite, are interpreted to represent nucleation textures, and support the replacement of the wall rock by pyrite.

Chalcopyrite, galena and pyrrhotite lack deformation textures and typically occur interstitial to pyrite in massive sulphide of the lower and upper ore zones. These minerals occur as inclusions in pyrite and as fracture fill. The distribution of these minerals in massive and vein sulphides at Gossan Hill likely relates to the strength and

ductility of these minerals. As such, these sulphides reach their brittle-ductile transition boundaries at lower temperatures and pressure than pyrite and magnetite (Clark and Kelly, 1973, Cox *et al.*, 1981, Marshall and Gilligan 1987), and will tend to remobilised and recrystallise rather than deform.

The construction of a sulphide-magnetite paragenesis at Gossan Hill has not been possible, due to the widespread recrystallisation and remobilisation of sulphides. However, the local replacement of sphalerite by pyrite is inferred in the upper ore zone by skeletal pyrite textures. Furthermore, similar skeletal textures exist between pyrite and magnetite in the gradational contact zones between massive magnetite and massive pyrite. These textures suggest the local replacement of magnetite by pyrite. Moreover, the distinct textural differences of magnetite in massive magnetite from that in sulphide, is consistent with their separate stages of formation. Magnetite in sulphide is euhedral and typically sieved by sulphide inclusions. These attributes support the synchronous formation of this magnetite during sulphide mineralisation. In comparison, magnetite in massive magnetite lacks sulphide and has distinct granular to skeletal textures. In addition, magnetite in massive magnetite is considered to have formed as a primary precipitate that replaced the GGF M4 volcaniclastic wall rock, rather than the product of a thermally metamorphosed Fe-oxide, hematite rock. The textural variation of magnetite in the massive magnetite may also have been contributed to by the inhomogeneity of the volcaniclastics, which it replaced.

Chapter 7

Alteration mineralogy, distribution and timing

7.1 Introduction

The Golden Grove Formation (GGF) has a regionally extensive, intense quartz-chlorite alteration assemblage (Clifford, 1992). Volcanic quartz is the only relict primary mineral phase in the GGF after alteration and metamorphism. At Gossan Hill, the mineralogical variation and alteration intensity increase towards massive magnetite and sulphide mineralisation, where local alteration envelopes occur. This chapter reviews the alteration in the GGF and the hangingwall Scuddles Formation at Gossan Hill with the following aims:

- to delineate the distribution, zonation and mineral compositions of the alteration at Gossan Hill and;
- to propose a relative paragenetic ordering for the development of alteration, and explore the genetic link between alteration and mineralisation.

7.2 Alteration mineralogy

Four dominant alteration types are identified at Gossan Hill. These are (1) siliceous, (2) chlorite, (3) carbonate, and (4) muscovite alteration. Minor alteration minerals include talc, magnetite, pyrite, pyrrhotite, apatite and chloritoid, all of which occur in chlorite alteration. Regional alteration in the GGF and local conformable alteration adjacent to massive magnetite and sulphide at Gossan Hill, indicate strong lithofacies control on the distribution of the main alteration types. The associations between alteration, mineralisation and stratigraphy are listed in Table 7.1.

Overprinting relations between the alteration types indicate that Gossan Hill has experienced multiple alteration events. However, not all of this alteration is associated with mineralisation. The sequence of alteration events is (1) regional quartz-chlorite (± muscovite) alteration of the GGF, (2) chlorite, carbonate, magnetite, talc alteration associated with massive magnetite, (3) chlorite, pyrite, pyrrhotite, apatite, chloritoid alteration associated with massive sulphide in the lower ore zone and a siliceous alteration in the upper ore zone, and (4) muscovite, carbonate with minor quartz and chlorite alteration in the hangingwall.

Table 7.1: Alteration mineralogy of stratigraphic members in the GGF and Scuddles Formation near mineralisation at Gossan Hill. The major alteration minerals are quartz and chlorite, with minor minerals induding carbonate, talc, pyrite, pyrrhotite, apatite and chloritoid. Relative variations in the proportion of these alteration minerals occur adjacent to, or within, massive magnetite, massive sulphide and sulphide vein mineralisation, but reflect broadly conformable alteration.

Strata	Major Minerals	Minor Minerals	Associated Mineralisation
SC2 (DAC3 dacite)	muscovite, carbonate, quartz	chlorite	disseminated pyrite
SC2 (RD2 rhyodacite)	muscovite, quartz, carbonate	chlorite	disseminated pyrite
M1 Marker-chert	quartz, carbonate	chlorite	disseminate pyrite, magnetite
M1 Marker-lithic	chlorite, carbonate	ilmenite	disseminated pyrite, magnetite
GGF M6	quartz	chlorite, carbonate, ilmenite	massive sphalerite, massive pyrite, stringer veins
GGF M5	quartz	chlorite, ilmenite, muscovite	stringer veins
	quartz, carbonate	chlorite, ilmenite	stringer veins
GGF M4	quartz, chlorite	carbonate, muscovite	disseminated pyrite, stringer veins
	carbonate, chlorite	talc, quartz	massive magnetite
	chlorite, carbonate, magnetite, talc, pyrite, pyrrhotite	apatite, chloritoid, andalusite, rutile, ilmenite, muscovite	massive magnetite, massive sulphide, stringer veins
GGF M1	quartz, chlorite	muscovite, rutile	none

7.3 Regional alteration

Away from massive magnetite and sulphide mineralisation at Gossan Hill, quartz-chlorite (± muscovite) alteration is ubiquitous in the tuffaceous and epiclastic strata of the GGF. Clifford (1992) documents this alteration to be a regional alteration of the GGF that occurs throughout the Golden Grove Domain. Except for volcanic quartz grains, tuffaceous and epiclastic strata are entirely altered to quartz and chlorite, but contain well-preserved glassy volcanic textures (*e.g.*, Fig. 7.1a). Muscovite is minor and forms scattered grains (<50 μm). Although mineralogically simple, this ubiquitous quartz-chlorite alteration is an intense, pervasive alteration that is useful to constrain processes of textural preservation and the relative timing of hydrothermal alteration events at Gossan Hill.

In the GGF, the alteration of pumice and shard-rich tuffaceous strata to quartz has preserved many volcanic textures including tube striations, vesicle structures and grain outlines (*e.g.*, Fig. 7.1a). Cuspate quartz-altered fragments hosted by chlorite represent quartz-replaced, partially preserved bubble wall junctions and shards (Fig. 7.1b). The chlorite in regional quartz-chlorite alteration is typically fine-grained (<20 μm) and alters the finer ash- to sand-sized matrix of tuffaceous pebble breccia and sandstone in the GGF. The differential chlorite or quartz alteration commonly highlights volcanic textures, as observed where chlorite parallels quartz-replaced tube striation structures (Fig. 7.1c) and forms rims to quartz-filled vesicles (Fig. 7.1d). Nonetheless, textural preservation in the

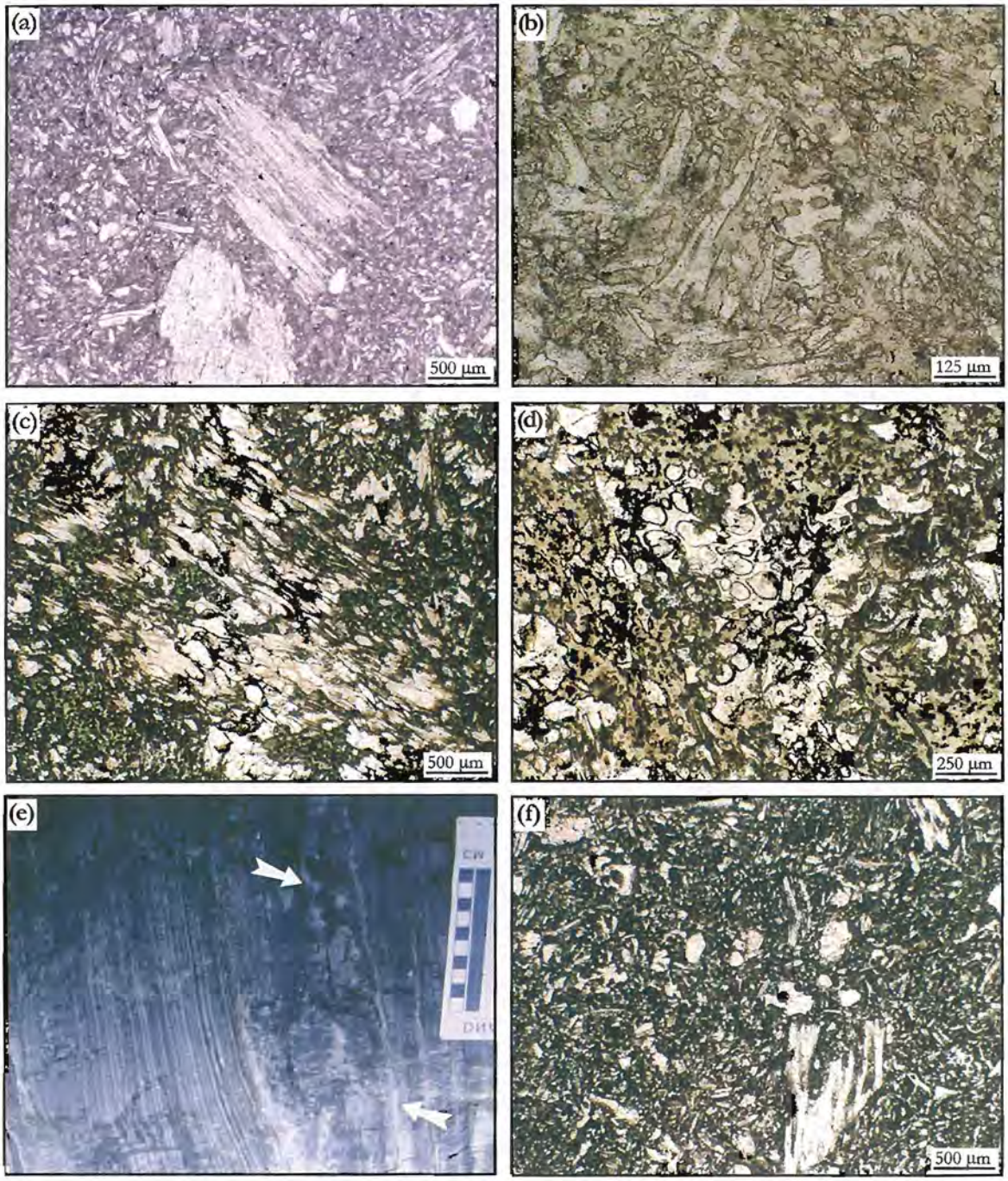

Figure 7.1: (a) Photomicrograph of quartz-replaced pumice in a shard-rich matrix from a sandstone within GGF M4. Delicate tube striations and grain outlines are preserved by intense quartz alteration (sample 769214). (b) Chlorite alteration of tube pumice. Chlorite alteration parallels tube striations within the pumiceous lithic clasts and obscures the primary volcanic texture (sample 769076). (c) Chlorite-altered sandstone of GGF M5 with intense fine-grained chlorite alteration of the matrix. The matrix contains quartz-replaced cuspate to curviplanar shards and bubble wall junctions (sample 97U006). (d) Partially chlorite altered vesicular pumice lithic clasts in a chlorite matrix. Vesicles within the pumice are preserved by narrow rims of chlorite around the vesicle margins, whilst the vesicles are hosted within and in filled by quartz (sample 769331). (e) Millimetre-scale laminae of differentially quartz and quartz-chlorite altered beds in a thinly bedded sandstone of GGF M1. The alteration is conformable and narrow fluted textures are observed along the contacts with coarser-grained beds (arrows)(300 level). (f) Well-preserved fine-grained tuffaceous sandstone of GGF M5 consisting of quartz-replaced tube and vesicular pumice lithic clasts in a shard-rich matrix consisting of cuspate to curviplanar quartz-replaced shards and bubble wall junctions. Minor chlorite-quartz alteration occurs in the groundmass (sample 769218).

(Fig. 7.1c) and forms rims to quartz-filled vesicles (Fig. 7.1d). Nonetheless, textural preservation in the GGF relates to the degree of quartz alteration, whilst chlorite alteration is associated with textural destruction.

7.3.1 Alteration of the footwall (GGF M1)

In the footwall GGF M1, alteration textures vary according to changes in lithofacies grain size (Fig. 7.2a). Within the pebble breccia facies, the distribution of quartz-chlorite alteration forms a domainal alteration that reflects and enhances the coarse-grained brecciated nature of the primary lithofacies (Fig. 7.2b). This domainal quartz-chlorite alteration occurs as irregularly shaped, interlocking patches of quartz or chlorite alteration that, in turn, reflect differential quartz or chlorite alteration of lithic clasts and matrix in the pebble breccia (Figs. 7.2c and 7.2d). Chlorite domains vary from blocky to tabular patches up to 5 cm in size, often with sharp, curviplanar to cuspate margins that highlight the original morphology of the pumiceous lithic clasts (Fig. 7.2b). The shape and size of chlorite domains vary according to the size and shape of lithic clasts between beds. Fine-grained (<20 μm), interlocking chlorite domains may also reflect chlorite alteration of the matrix.

Quartz alteration of silicified pebble breccia beds consists of interlocking megaquartz and microcrystalline quartz mosaics. Quartz altered pumiceous lithic clasts and shards commonly have poorly defined grain margins. A common feature in GGF M1 is a white siliceous rim or halo of microcrystalline quartz around lithic clasts (Fig. 7.2b). Quartz alteration in the pebble breccia facies of GGF M1 is more widely developed than chlorite alteration and quartz is a pervasive intense alteration of the matrix and lithic clasts. Volcanic quartz throughout GGF M1 retains its original morphology, often having micron-sized overgrowths of microcrystalline quartz (Fig 7.2c).

Bedded sandstone sequences in GGF M1 generally have a homogeneous banded to laminated quartz-chlorite alteration, which parallels bedding (Fig. 7.1e). The alteration of sandstone within GGF M1 reflects relatively homogeneous quartz alteration of fine-grained tuffaceous beds that contain disseminated chlorite. Colour contrasts between sandstone beds reflect relative changes in the abundance of chlorite and quartz (Fig. 7.1e). Intensely silicified beds contain minor disseminated chlorite and are light grey, whilst darker grey-green beds have higher proportions of disseminated fine-grained chlorite. In some occurrences, alternating bands of quartz and/or chlorite alteration form a laminar (mm-sized) alteration, where laminae of white quartz alteration parallel bed contacts and form fluted alteration textures (Fig. 7.1d). The laminated differential quartz-chlorite alteration of sandstone beds reflects bed-specific conformable alteration.

7.3.2 Alteration of the host rocks (GGF M4, GGF M5 and GGF M6)

Away from mineralisation at Gossan Hill, the alteration of the host rocks GGF M4, GGF M5 and the lower part of GGF M6, is similar to the quartz-chlorite alteration of the footwall (GGF M1). However, this host rock alteration is relatively homogeneous and lacks a domainal appearance. The transition from domainal alteration in GGF M1 to homogeneous alteration in the host rocks is conformable to the lower contact of GGF

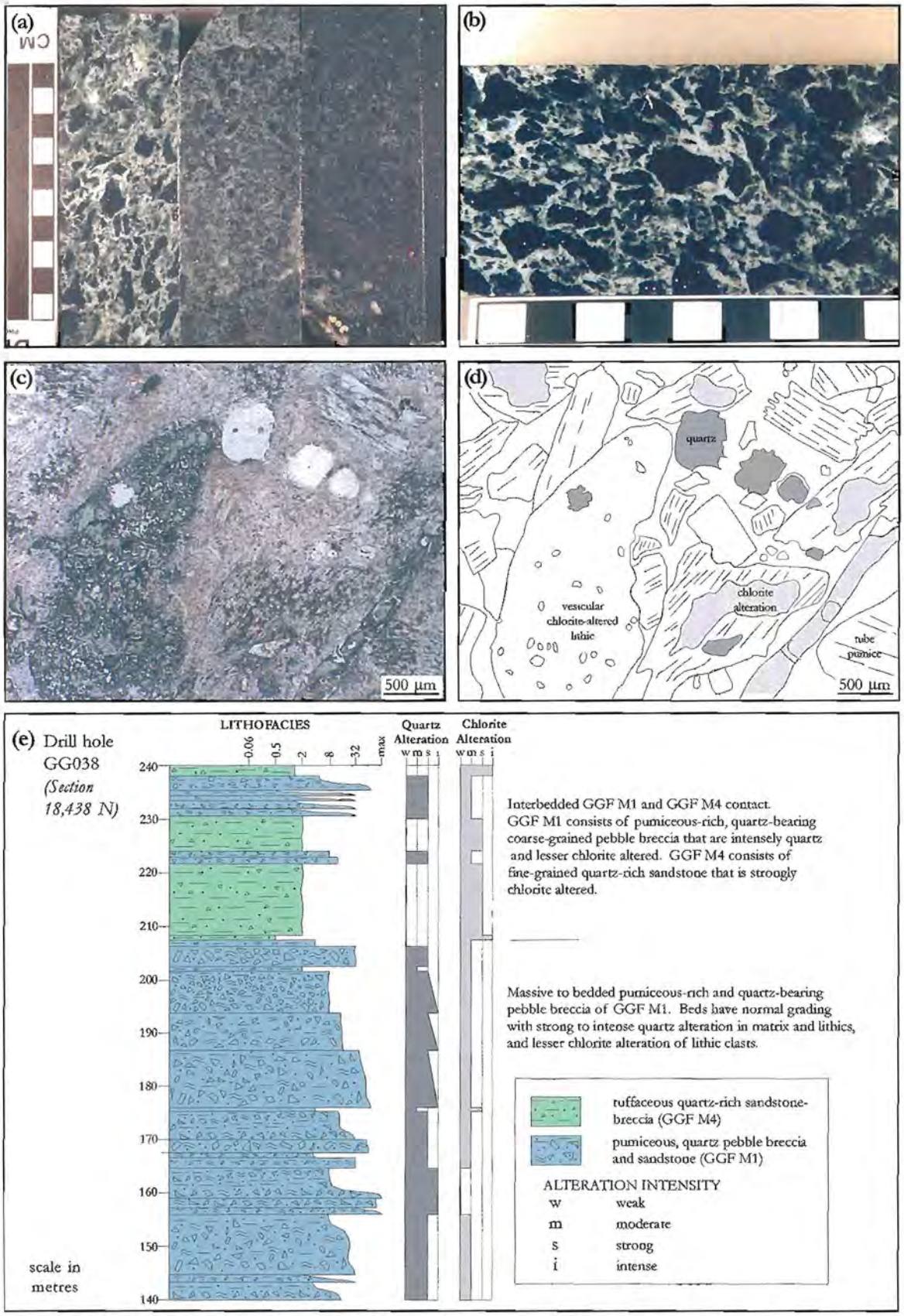

Figure 7.2: Footwall alteration in GGF M1. (a) Quartz-chlorite alteration textures in pebble breccia and coarse-grained sandstone facies. Different facies have different alteration textures. Pebble breccia have domainal quartz-chlorite whereas sandstone has homogeneous quartz-chlorite alteration (samples 769146, 769142, 769143). (b) Quartz and chlorite alteration in a pebble breccia. Lithic clasts have preferential quartz-chlorite alteration. The matrix is intensely quartz altered (sample 769146). Scale in cm. (c) Photomicrograph of (b) with domainal chlorite and quartz alteration of lithic clasts. (d) Interpretation of (c). (e) Intensity distribution of quartz and chlorite alteration in lithofacies the footwall GGF M1. Quartz and/or chlorite alteration is conformable on a bed-scale. A transition from quartz-chlorite to chlorite alteration occurs at the GGF M1-M4 contact.

M4 and reflects the lithofacies change from pebble breccia in the footwall to sandstone-siltstone in the host strata (Fig. 7.2e). The regional alteration of GGF M4, GGF M5 and GGF M6 is principally quartz, with complete quartz alteration of formerly glassy pumiceous shreds and shards that results in excellent textural preservation (Figs. 7.1a and 7.1f). This quartz alteration consists of microcrystalline quartz and megaquartz. Chlorite tends to occur as minor disseminations interstitial to quartz in the finer, ash-sized matrix of the host rocks (Fig. 7.1f). Volcanic quartz within the host strata retains its primary morphology and commonly has micron-thick overgrowths of quartz around grain margins or along fractures.

The upper bedded parts of GGF M6, overlying and interdigitating with sulphide mineralisation, have conformable alteration that varies between adjacent beds. The alteration of sandstone-siltstone beds in GGF M6 varies from quartz, to quartz-chlorite, to chlorite to carbonate alteration (Fig. 7.3).

Fine-grained sandstone and siltstone in GGF M6 tend to have intense quartz alteration with minor disseminated chlorite. In bedded sandstone-siltstone, grey to green colour contrast between beds reflect stratabound alteration. Light grey beds have intense silicification and consist entirely of microcrystalline quartz, whilst green-coloured beds have higher proportions of disseminated chlorite in quartz alteration. Conformable quartz or quartz-chlorite alteration of thinly bedded, fine-grained sandstone-siltstone is represented by millimetre-wide parallel laminae that mimic and preserve sedimentary layering. As no primary grain size variations are observed, some laminae may result from alteration-induced laminae parallel to sedimentary layering (Fig. 7.3e).

Pebble breccia and coarse-grained sandstone beds in the upper parts of GGF M6 are less intensely silicified than thinly bedded sandstone-siltstone beds. Pebble breccia beds also tend to have alteration textures that reflect the primary lithofacies and are chlorite, quartz and/or carbonate altered. Chlorite spotted textures (Figs. 7.3a and 7.3b) arise from the differential chlorite alteration of the lithic clasts within a microcrystalline quartz matrix. The shape of chlorite 'spots' reflects lithic clasts with cuspate margins (Fig. 7.3b). Tuffaceous pebble breccia and sandstone beds in GGF M6 have preferential, stratabound carbonate alteration (Figs. 7.3c and 7.3d). Mottled, fine-grained (<100 μm) carbonate (ankerite to calcite) forms the matrix of the breccia and also pseudomorphs graded lithic clasts that have cuspate to curviplanar margins. Polymict pebble breccia beds in GGF M6 have intensely silicified lithic clasts hosted by a chlorite matrix. In summary, the upper parts of GGF M6 have conformable alteration that is bed specific between quartz, chlorite or carbonate alteration and indicates strong lithofacies control on the distribution of alteration.

7.3.3 Nodular siliceous alteration

At Gossan Hill, a nodular siliceous alteration texture occurs within GGF M4 and GGF M5. This texture is useful in identifying lithofacies within zones of intense chlorite alteration as well as constraining the relative timing of alteration. Siliceous nodules have a scattered and patchy distribution (Fig. 7.4a) with gradational to sharp margins against

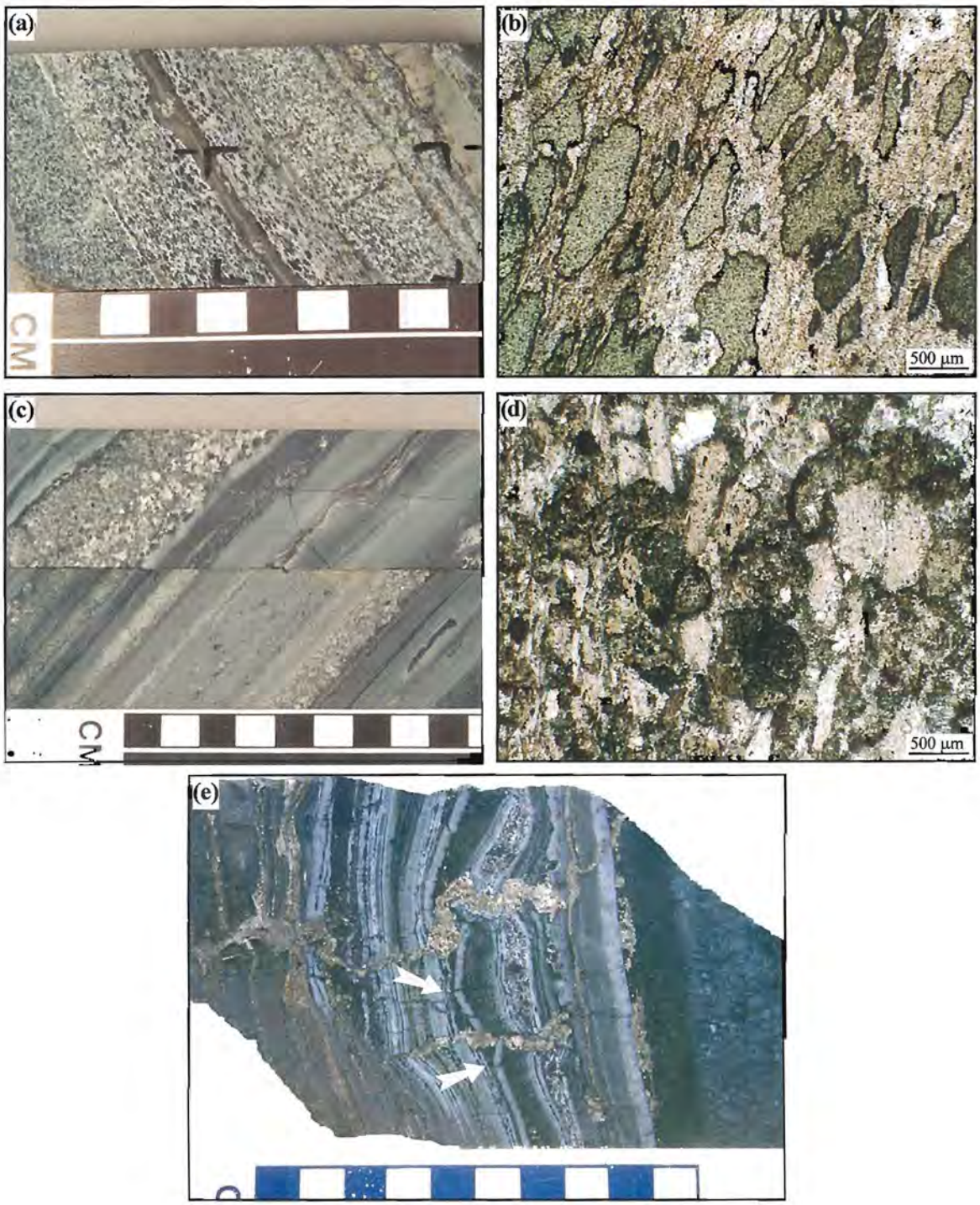

Figure 7.3: Alteration in GGF M6 sandstone-silstone and breccia overlying massive sulphide at Gossan Hill. (a) Chlorite spotted alteration. Chlorite spots are hosted in an intensely silicified matrix. Chlorite spots have different sizes between beds in the thinly bedded sandstone sequence (sample 760346). (b) Photomicrograph of chlorite spots, consisting of irregular shaped chlorite patches with cuspate margins. These spots consist of fine-grained chlorite in a matrix of microcrystalline quartz (sample 760346). (c) Thinly bedded sandstone and pebble breccia sequence within GGF M6. Alteration is bed-specific and coarser-grained pebble breccia beds are carbonate altered, whilst finer-grained sandstone beds are quartz altered (samples 769308 and 769309). (d) Photomicrograph of carbonate alteration in a pebble breccia bed in (c). Carbonate replaces lithic clasts and the matrix (sample 769309). (e) Banded conformable alteration of a thinly bedded sandstone-siltstone sequence within GGF M6. Beds have preferential siliceous alteration (light grey), as well as chlorite-quartz (grey), chlorite spotted alteration and chlorite (grey-green). Some fractured siliceous beds are observed (arrows) (sample 97U056). Scale in cm.

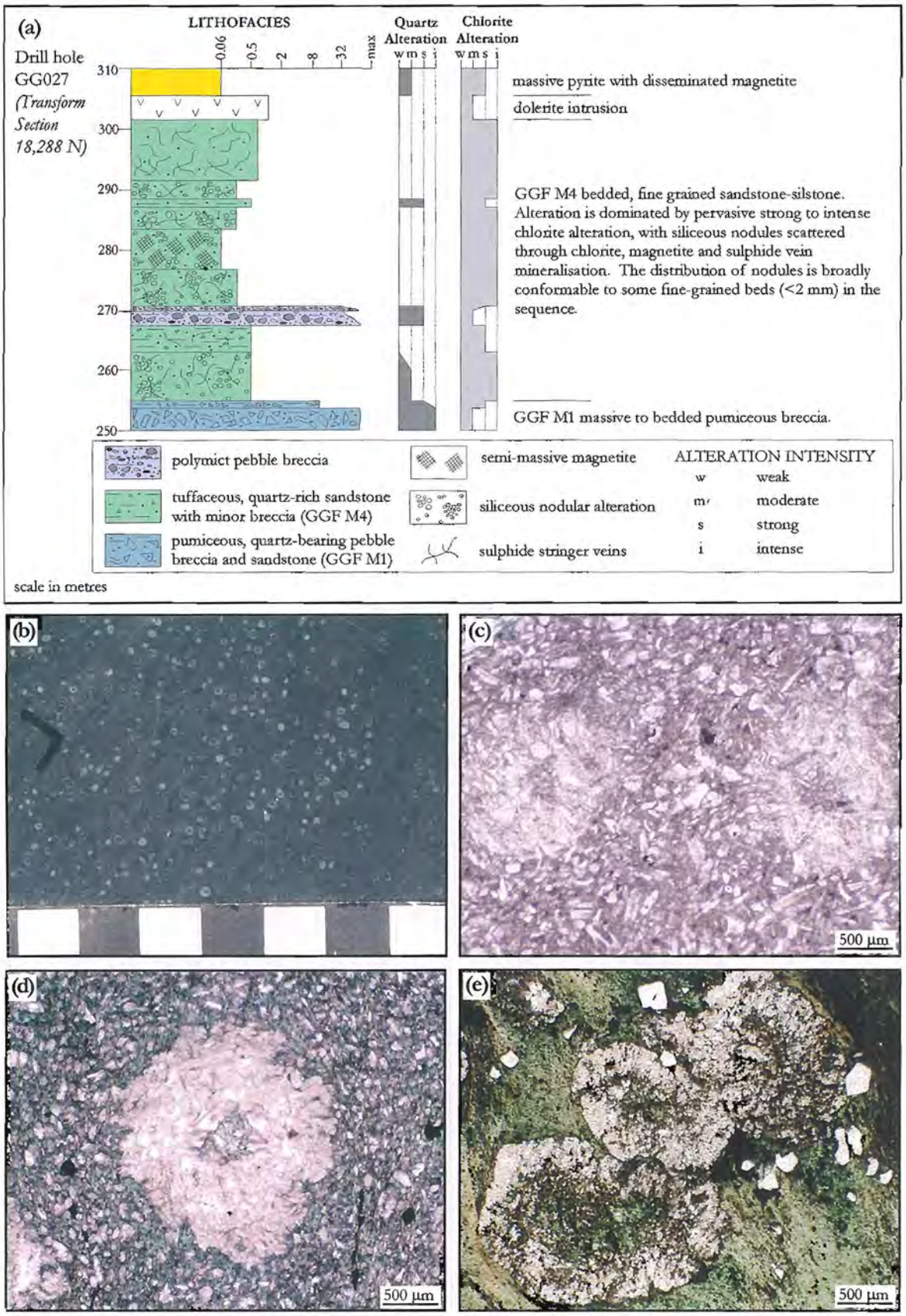

Figure 7.4: Nodular siliceous alteration. (a) Lithofacies diagram showing the distribution of siliceous nodules in GGF M4. (b) Scattered siliceous nodules in a quartz-chlorite altered sandstone of GGF M4. Scale in cm (sample 760499). (c) Photomicrograph of siliceous nodules in a shard-rich sandstone of GGF M4. Volcanic textures are preserved within and outside of the nodular texture (sample 769214). (d) Siliceous nodules in strong chlorite alteration. Volcanic textures are observed within the nodule, but poorly preserved outside of the nodule. The siliceous nodule has a chlorite-altered pumiceous lithic clast in its centre (sample 760499). (e) Siliceous nodules in chlorite. The matrix is completely altered to chlorite (sample 769267).

the quartz-chlorite altered wall rock. In hand specimen, the siliceous nodules are milky green to white. These nodules have rounded, ovate to hourglass shapes and are less than 8 mm in size (Fig. 7.4b).

The siliceous nodules principally consist of interlocking microcrystalline quartz mosaics that contain disseminated fine-grained (<50 μm) chlorite (Fig. 7.4b). Chlorite occurs interstitial to quartz, but may also form concentric rims or cores to the nodules (Fig. 7.4c). The intense nodular-shaped quartz alteration preserves relict volcanic textures, which include pumiceous lithic clasts, bubble wall junctions and shards. These textures are consistent with the volcanic textures observed in the wall rock (Fig. 7.4c). Occasionally, volcanic quartz or a lithic fragment is present in the centre of these nodular structures (Fig. 7.4d), forming a core to the quartz ±chlorite outer zones.

Siliceous nodules commonly occur in intense chlorite alteration adjacent to and within massive magnetite and sulphide mineralisation in GGF M4 (Fig. 7.4e). These siliceous nodules may contain preserved tuffaceous volcanic textures and have deformation structures that include quartz filled fractures, cleavage wrapping, boudinage and pressure shadows (Fig 7.4e). In adjacent wall rock, intense chlorite alteration lacks relict volcanic textures (Fig. 7.4e). This association indicates that the siliceous nodules formed as a quartz (±chlorite) alteration of a tuffaceous lithology, which predated the texturally destructive effects of intense chlorite alteration outside of the nodular siliceous alteration. The similar textures and mineralogy between siliceous nodules and regional quartz-chlorite alteration, is consistent with their synchronous formation.

7.3.4 Textural preservation: A discussion

Tuffaceous components of the GGF are ubiquitously altered to a quartz-chlorite (± muscovite) assemblage. This regionally extensive alteration has resulted in the widespread preservation of delicate pumice and shard textures. The replacement of formerly glassy volcanic components by quartz preferentially preserves volcanic textures, whilst chlorite alteration results in textural destruction. However, the occurrence of both quartz and chlorite alteration enhances many textural attributes in the volcaniclastic protolith, reflecting variations in the primary volcanic facies.

Although quartz-chlorite alteration is ubiquitous throughout the GGF, it has resulted in different alteration textures between members of the succession. The conformable distribution of quartz-chlorite alteration textures indicate a strong primary lithofacies control. In the footwall (GGF M1) the distinctive domainal distribution of quartz-chlorite alteration reflects preferential quartz or chlorite alteration of matrix and lithic clasts in coarse-grained pebble breccia facies. This preferential alteration of matrix and clasts to chlorite or quartz may have developed due to a primary compositional or intra-grain permeability control. The common occurrence of chlorite along and outward from tube striations and vesicular structures in pumice, suggest that chlorite developed as a porosity fill. By contrast, the relatively homogeneous quartz-chlorite alteration of host succession (GGF M4, GGF M5 and lower part of GGF M6) reflects alteration of well-sorted, fine-grained (sand to ash) lithofacies. In bedded sandstone within GGF M4, the

differential quartz and chlorite alteration of beds indicates bed-specific permeability control for the distribution of alteration. The general absence of coarse-grained pebble breccia lithic clasts from GGF M4 and GGF M5 suggests that the grain size of the volcaniclastic protolith was a major control on the distribution of quartz-chlorite alteration. This inference is consistent with the broad upward fining of the GGF succession, which correlates to the upward decrease in the abundance of chlorite. The intensity of quartz alteration, which increases upwards, may reflect a cooling gradient of fluids from which silica was a deposited as quartz.

Diagenetic-related hydrothermal alteration of modern vitric and pumiceous sands result in the alteration of glass and feldspar to palagonite, smectite and zeolite (Iijima, 1974; Tazaki and Fyfe, 1992). These alteration products, which result from the interaction of circulating pore water with volcanic glass, form inward from grain margins and permeability structures (Tazaki and Fyfe, 1992). The distribution of chlorite along and outward from tube striations in lithic clasts of GGF M1 are textures consistent with diagenetic alteration of glass along permeability structures. The alteration products of glass however, depend on its composition. Rhyolite glass preferentially alters to clay-zeolite and more Mg-rich glass of intermediate composition preferentially undergoes dissolution (Marsaglia and Tazaki, 1992). Hydrothermal experiments on rhyolitic glass (200°C) indicate that it reacts as a Na-K ion exchanger and that it alters preferentially to clay/zeolite rather than undergoing recrystallisation (Suresh *et al.*, 1980; Marsaglia and Tazaki, 1992). Primary rhyodacitic (refer Chapter 8) volcanic glass in the GGF may therefore, have undergone initial and partial alteration to clay-zeolite. However, if this alteration occurred, it was overprinted by chlorite alteration formed during hydrothermal alteration or metamorphism.

Surface coatings of clay/zeolite minerals along permeability structures and grain margins of tuffaceous material can contribute to their textural preservation during later alteration (*e.g.*, Iijima, 1974; Walton, 1975; Dimroth and Lichtblau, 1979; DiMarco and Lowe, 1989; Hassler and Simonson, 1989). This mechanism is proposed at Gossan Hill due to the excellent textural preservation of tube striations, vesicle and shard structures despite their alteration and replacement by continuous interlocking arrays of microcrystalline quartz and megaquartz.

7.3.5 Laminar alteration

Bed-specific conformable quartz and/or chlorite occur within thinly bedded parts of the GGF (*i.e.*, GGF M1, GGF M4 and the upper parts of GGF M6). The colour variations between these beds reflect the different proportions of quartz or chlorite alteration within them. Alteration boundaries coincide with bedding contacts. Bed conformable alteration reflects the preferential alteration of lithofacies to quartz-chlorite alteration mixtures, and may relate to primary permeability and porosity contrasts between the beds in the sequence. Laminar alteration parallel to bedding contacts has likely resulted from localised fluid migration parallel and outwards from bedding contacts. Conformable differential quartz-chlorite alteration of beds within thinly bedded strata must have

resulted from lateral pervasive fluid channelling. Preferential alteration to quartz and/or chlorite alteration either resulted from compositionally different beds or the permeability contrasts in the sequence.

The bed-scale alteration observed in the upper parts of GGF M6 involves carbonate, in addition to chlorite and quartz alteration. The bed-specific alteration patterns in this part of the strata may relate to its inferred near seafloor position during mineralisation. Seafloor oxidation processes, in addition to hydrothermal-mineralising processes, may have contributed to alteration. The alteration in the upper parts of GGF M6 is similar to alteration described in the Key Tuffite host rocks of the Mattagami deposit, Canada. The altered Key Tuffite formed at the seafloor by contemporaneous sedimentation and exhalative sulphide and chert deposition (Roberts, 1975; Liaght and MacLean, 1992).

7.3.6 Timing constraints and origin of nodular alteration

Preserved volcanic textures within and outside of siliceous nodules indicate the synchronous development of nodular siliceous alteration during regional quartz-chlorite alteration. Siliceous nodules formed from the alteration and replacement of glassy detritus by megaquartz and microcrystalline quartz. Their scattered distribution in GGF M4 and GGF M5 indicates that these nodules formed sporadically within finer-grained sand- to ash-sized tuffaceous strata, commonly around a sand-sized lithic core. The rounded shapes typical of siliceous nodular alteration at Gossan Hill, are a natural habit for silica that nucleates in a highly permeable and porous environment by outwards replacement (Knauth, 1994). Siliceous nodules at Gossan Hill developed as nucleation structures which infilled primary porosity. Further evidence of quartz nucleation textures exists in GGF M1 where siliceous haloes commonly envelop pumiceous lithic clasts. These textures indicate that the nucleation of quartz during regional quartz-chlorite alteration was a widespread process.

Siliceous nodules in intense chlorite alteration zones adjacent to and within massive magnetite and massive sulphide mineralisation denote the resilience of siliceous nodules to the effects of later alteration and mineralisation. Siliceous nodules have preserved volcanic textures, whilst the host rock is completely replaced by chlorite. Therefore, nodular siliceous alteration must have formed prior to the intense chlorite alteration event. Due to the fine-grained interlocking meshwork of microcrystalline quartz within the siliceous nodules, these nodules formed impermeable zones to the effects of later chlorite alteration.

7.3.7 Timing of regional quartz-chlorite alteration in the GGF

The ubiquitous quartz-chlorite alteration of the GGF is a regional background alteration. This alteration transformed an originally glassy, tuffaceous felsic volcaniclastic succession to quartz, with lesser chlorite, and minor muscovite assemblage. The replacement of felsic volcanic glass in the succession took place either by diffusion or replacement processes and was a major metasomatic event (refer Chapter 8). Regional quartz-chlorite alteration caused preservation of lithofacies and volcanic textures. The lack of compaction textures in the GGF (Chapter 3) indicates that quartz-chlorite alteration took

place prior to diagenetic compaction. Furthermore, the preservation of volcanic textures within intense hydrothermal alteration and mineralised zones at Gossan Hill indicates that quartz-chlorite alteration developed prior to massive magnetite and sulphide mineralisation.

Regionally extensive silicification of volcaniclastic strata is known in other Archean greenstone belts. These occurrences indicate the widespread replacement of volcaniclastics by quartz in the Archean (Lowe and Knauth, 1977; DiMarco and Lowe, 1989). For example, the Archean Onverwacht Group in South Africa consists of a 10 km thick sequence that is replaced by quartz (Lowe and Knauth, 1977; DeWit *et al.*, 1982; Paris *et al.*, 1985). The Panorama sandstone in the Pilbara Craton, Western Australia, is another example a tuffaceous volcano-sedimentary succession that has near complete replacement by quartz (DiMarco and Lowe, 1989). In both of these examples, the silicification event took place synchronous with or shortly after deposition. Silicification led to widespread textural preservation of the strata and to alteration-induced lithification and cementation, which in turn, prevented further alteration, compaction and minimised the effects of metamorphism.

The origin of regional-scale siliceous alteration in Archean volcaniclastic sequences is enigmatic, but it is suggested to result from synvolcanic diagenetic-hydrothermal alteration (DiMarco and Lowe, 1989). Furthermore, the siliceous alteration within Archean greenstone sequences is commonly associated with volcaniclastic rocks, which in interpreted to reflect higher water-rock interactions caused by magmatic heat sources (DeWit *et al.*, 1982; Gibson *et al.*, 1983). Nonetheless, intense siliceous alteration is also observed in coherent Archean rocks. Gibson *et al.* (1983) interpret the regionally silicified andesite in the Amulet Formation, Noranda, to result from the interaction of circulating seawater within an originally permeable andesite during synvolcanic activity. Similarly, regional silicification in Archean volcaniclastic sequences is interpreted to result by the circulation of coeval seawater through originally permeable rocks during low temperature rock-water interactions (Spooner and Fyfe, 1973; DeWit *et al.*, 1982; Gibson *et al.*, 1983; Barley and Groves, 1984). As quartz is inert below 300°C (Hoagland and Elders, 1978), DiMarco and Lowe (1989) constrain the temperature of silicification in the Panorama sandstone to temperatures less than 300°C based on the presence of stable volcanic quartz.

Many Archean volcano-sedimentary sequences are silicified to a degree unknown in younger rocks (Knauth, 1978; 1994). The phenomenon of Archean silicification has been attributed to an inferred warmer climatic temperature and silica saturated seawater in the Archean environment, rather than the exclusive result of hydrothermal activity (Paris *et al.*, 1985; Garrels, 1987; Knauth, 1994). Other possible sources of silica may include silica derived from volcanic glass and biologic silica (Knauth, 1994). The later type is known to be an important source of silica in modern sea-floor massive sulphide systems (Haymon and Kastner, 1981; Williams *et al.*, 1985; Williams and Crerar, 1985; Hesse, 1988). However, the nature of the primary Archean silica precipitates remain poorly understood (Knauth, 1994).

Background regional quartz-chlorite alteration of the GGF is therefore not unusual for an Archean volcaniclastic succession. Moreover, its alteration may have been promoted by the high abundance of uncompacted glassy pumice within the tuffaceous succession, due to the chemical instability of volcanic glass and the high surface area and permeability of pumice (Fiske, 1969; Williams *et al.*, 1985).

The timing of quartz-chlorite alteration in the GGF pre-dates diagenetic compaction as well as hydrothermal alteration related to the formation of massive magnetite and massive sulphides. Furthermore, the absence of feldspar in the GGF (Chapter 3) supports the alteration of tuffaceous material prior to devitrification. Therefore, regional quartz-chlorite alteration must have developed soon after, or synchronous with, mass flow emplacement and prior to magnetite and sulphide mineralisation.

Early quartz-chlorite alteration of the GGF caused the differential reduction in permeability and porosity of the succession by quartz and chlorite (after clay-zeolite?) replacement and cementation. The decreased porosity and permeability effectively sealed much of the GGF to the extent that much of the sequence became impermeable to subsequent mineralising hydrothermal alteration. This sealing and induration of the strata are consistent with the simple alteration assemblage, as induration prevented the development of more complex mineral assemblages that characterise hydrothermal alteration and greenschist facies metamorphism. Further support is gained from brittle fracture of siliceous beds that are mantled by overlying beds (Fig. 7.3e) and pre-mineralisation quartz veins in GGF M4 (Chapter 4). In both cases early induration and siliceous alteration accommodated brittle deformation. Additionally, it is likely that the induration of the GGF significantly contributed to the focussing of later hydrothermal-mineralising fluids along fracture-induced permeability structures at Gossan Hill (Chapter 5).

7.4 Local siliceous alteration

An asymmetric, discordant to semiconformable, localised siliceous alteration envelopes and hosts massive and vein sulphides in the upper ore zone and its underlying discordant vein stockwork (Figs. 7.5a and 7.5b). Away from massive sulphide, this intense siliceous alteration grades into regional quartz-chlorite alteration (Fig. 7.5b). A narrow zone of banded siliceous alteration also occurs in GGF M4, below massive pyrite within underlying stringer stockwork. This narrow minor zone of intense siliceous alteration occurs above the GGF M1-GGF M4 stratigraphic contact, and grades into intense chlorite alteration (Section 7.5). Siliceous alteration at the base of GGF M4 has similar textures to the local siliceous alteration observed in GGF M6.

Intense local siliceous alteration renders the wall rock a chert. These rocks consist of interlocking mosaics of microcrystalline quartz and lack relict volcanic textures (Figs. 7.5c and 7.5d). Alteration banding within chert is common and parallels bedding, reflecting intense quartz alteration of thinly bedded sandstone-siltstone beds (Fig. 7.5c). The banding is delineated by small grain size changes within the quartz alteration and often, by minor disseminations of chlorite and/or sulphide. Within GGF M5, siliceous

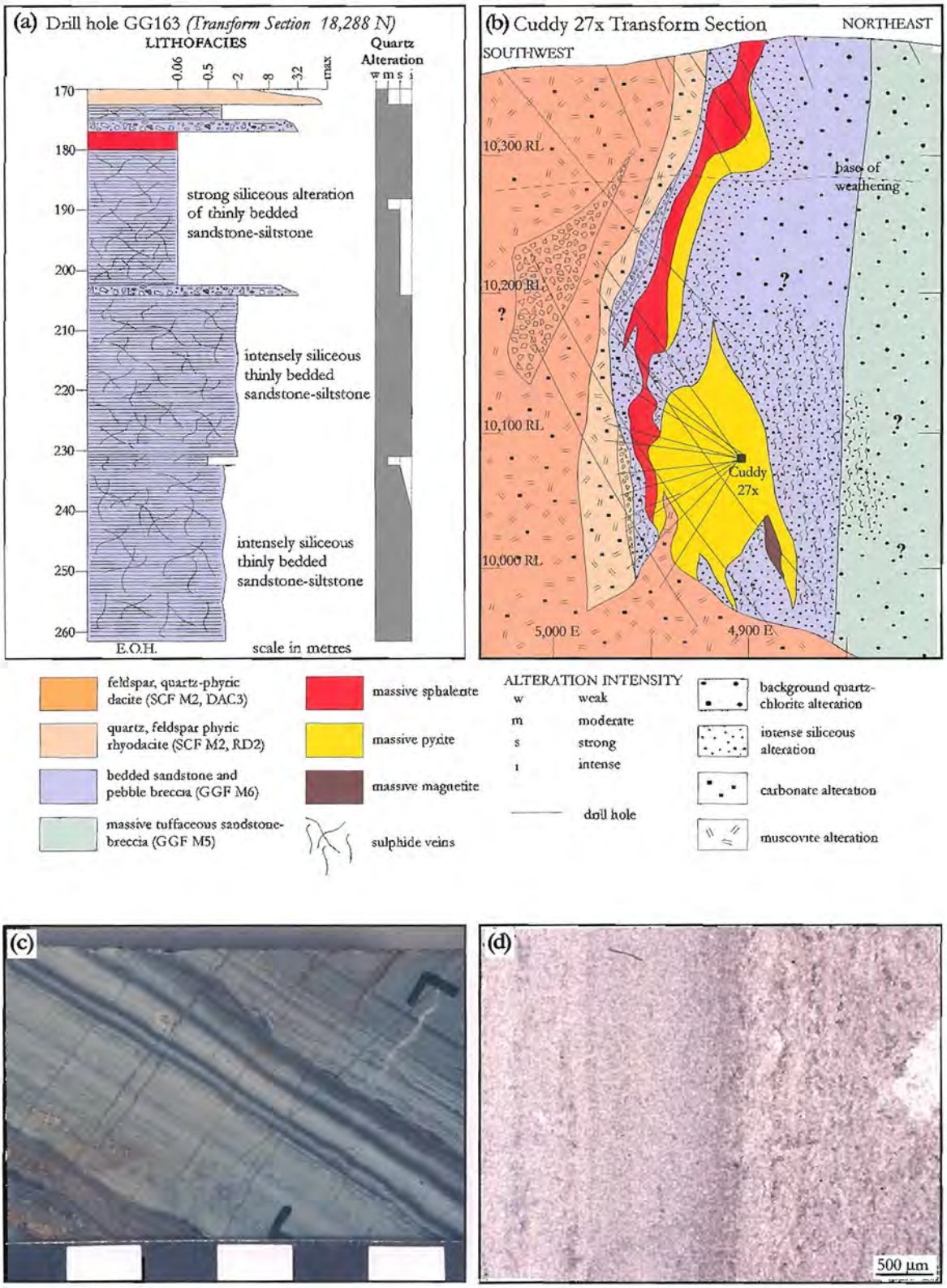

Figure 7.5: Intense siliceous alteration. (a) Lithofacies diagram illustrating the distribution of intense siliceous alteration through thinly bedded strata of GGF M6 underlying and overlying massive sulphide mineralisation. (b) Transform section (along Cuddy 27x) through C zone at Gossan Hill. Intense siliceous alteration forms an alteration envelop to massive sphalerite and massive pyrite in the upper ore zone. (c) Intense siliceous alteration of a thinly bedded sandstone (sample 760495). Sedimentary layering is preserved. Scale in cm. (d) Photomicrograph of (c). Thinly bedded sandstone-siltstone that consists of microcrystalline quartz. Banding parallel to bedding is delineated by grain size changes and minor variations in the abundance of quartz and chlorite.

alteration results in massive chert that reflects the massive lithology of the tuffaceous precursor. Chert that hosts sulphide veins commonly hasbleached quartz haloes that parallel vein margins (Chapter 5).

7.4.1 Timing of local siliceous alteration

Intense silicification is a common alteration of footwall and host rocks proximal to many VHMS deposits (*e.g.*, Gibson *et al.*, 1983; Gemmell and Large, 1992; Skirrow and Franklin, 1994; Lentz and Goodfellow, 1996). Generally, silicification processes in VHMS deposits are associated with high temperature mineralising fluids, with intense quartz alteration occurring in the hotter parts of the mineralising system, reflecting silica enrichment in the feeder (*e.g.*, Hellyer, Gemmell and Large, 1992; New Brunswick No. 12, Lentz and Goodfellow, 1996). At Gossan Hill, intense siliceous alteration represents the fine-grained quartz replacement of the wall rock. This process caused textural destruction, except for locally preserved sedimentary layering. The host association of local intense siliceous alteration with massive and stockwork sulphides at Gossan Hill, is an indication of their similar genesis. Furthermore, the bleached siliceous vein haloes associated with sulphide veins indicate that this siliceous alteration was synchronous with sulphide mineralisation. The spatial distribution of intense siliceous alteration may also have been limited by the relative impermeability of the wall rock, due to earlier regional quartz-chlorite alteration (Section 7.3.8). Therefore, the localised siliceous alteration at Gossan Hill is attributed to proximal hydrothermal alteration during the formation of massive sulphide mineralisation in the upper ore zone.

7.5 Local chlorite alteration

A zone of intense chlorite alteration envelops massive magnetite and massive sulphide in the lower ore zone at Gossan Hill. Within the lower ore zone, chlorite is also a major gangue constituent of massive magnetite, massive sulphide and sulphide veins. This intense chlorite alteration occurs in GGF M4 and forms a narrow, broadly stratabound to stratiform envelope to the massive magnetite, massive sulphide and stringer vein zones (Figs. 7.6a and 7.6b). The intensity of chlorite alteration in GGF M4 increases proximal to stringer veins, massive magnetite and sulphide mineralisation, with sulphide stringer veins commonly having diffuse chlorite alteration haloes. Within the chlorite alteration zone, chlorite forms modally up to 90%, and hosts minor pyrite, pyrrhotite, chalcopyrite, carbonate, magnetite, talc, quartz, apatite, ilmenite, rutile, muscovite, chloritoid and andalusite. Chlorite occurs as fine-grained (<50 μm) interlocking meshworks (Figs. 7.6c and 7.6d) that lack relict volcanic textures, but commonly contain scattered volcanic quartz grains (Fig. 7.6d).

The intensity of alteration within the chlorite envelope commonly varies between adjacent sandstone, siltstone and granule breccia beds in the strata. Irregular patches and beds of quartz-chlorite altered tuffaceous sandstone-siltstone and siliceous nodular alteration occur within intense chlorite alteration (Section 7.3.4). Volcanic quartz grains in GGF M4 chlorite alteration are well-preserved, but commonly have embayment and fracture. Furthermore, 'ghost' clasts of megaquartz-chlorite often occur within intense

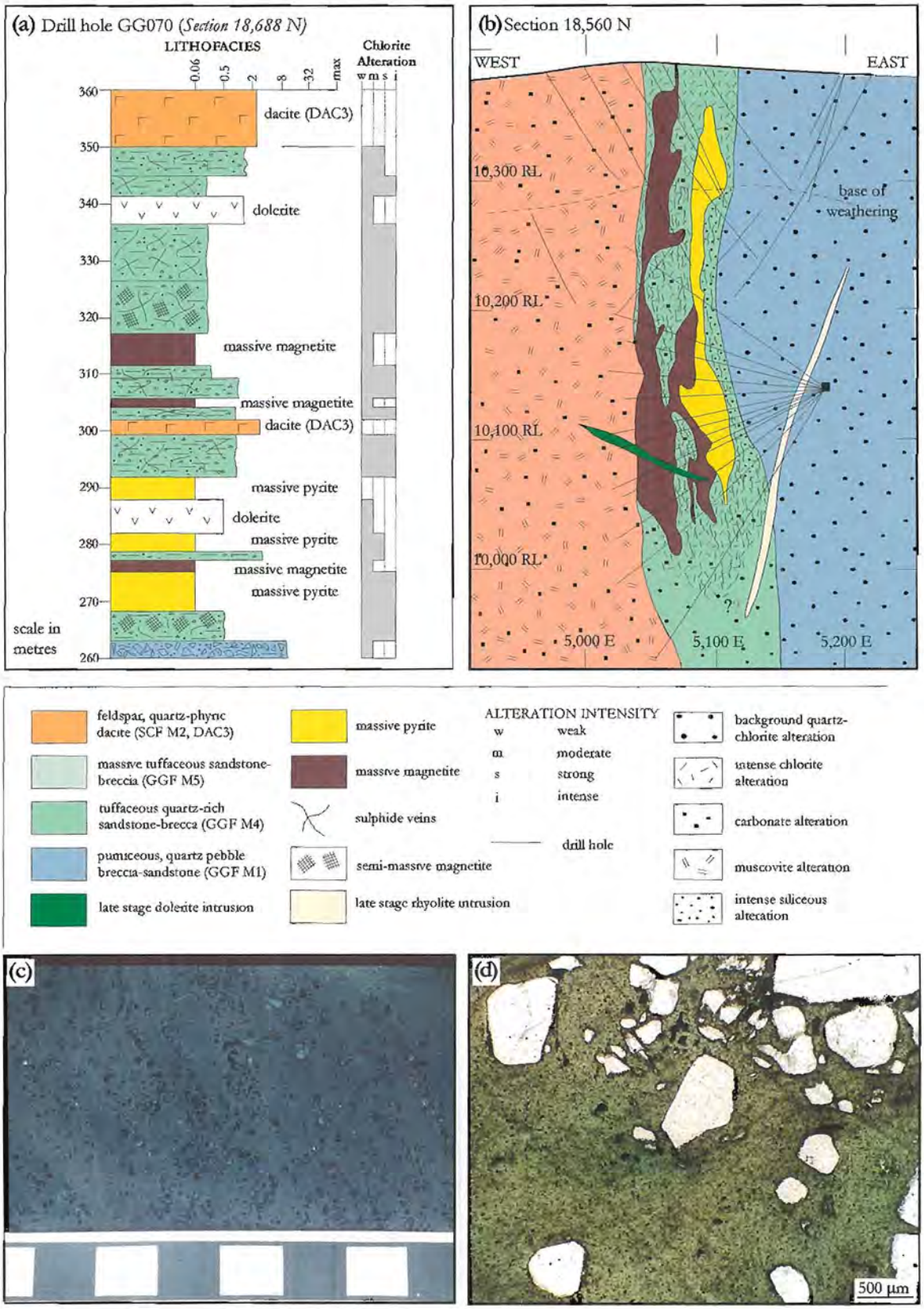

Figure 7.6: Intense chlorite alteration. (a) Lithofacies diagram illustrating the distribution of intense chlorite alteration within GGF M4 adjacent to massive magnetite, massive sulphide and sulphide vein mineralisation. (b) East-west cross section through the lower ore zone at Gossan Hill indicating the distribution of alteration. Intense chlorite alteration forms an envelop to the massive magnetite, massive sulphide and sulphide veins. (c) Intense chlorite alteration of a quartz-rich sandstone in GGF M4. Scale in cm (sample 760357). (d) Photomicrograph of quartz-rich sandstone in (c), with chlorite alteration consiting of fine-grained chlorite hosting well-preserved volcanic quartz grains and finely disseminated ilmenite-rutile (opaques) (sample 760357).

7.5.1 Composition of chlorite

The composition of chlorite is known to vary between and within hydrothermal alteration associated with VHMS deposits (Franklin *et al.*, 1981; Urabe *et al.*, 1983). Canadian Archean Noranda-type deposits typically have Mg-rich chlorite whereas Mattabi-type deposits have Fe-rich chlorite (Morton and Franklin, 1987). A solid solution series exists between these two chlorite end members with the compositional change reflecting the limited substitution of Al for Si and more abundant substitution of Mg for Fe in chlorite (Hey, 1954). The classification of Hey (1954) is used at Gossan Hill to define the variation in chlorite compositions.

Electron microprobe analysis of chlorite at Gossan Hill are listed in Appendix A5.1 and summarised in Table 7.2. Chlorite at Gossan Hill is principally Fe-rich, varying from psudoethuringite, ripidolite to pynochlorite compositions (Fig. 7.7). A broad positive trend between Si/Al and Fe*/(Fe*+Mg) indicates both Al-Si and Fe-Mg substitution (Fig. 7.7). This positive correlation reflects a broad enrichment of Fe in chlorite upwards through the GGF (Fig. 7.7), with chlorite having Fe*/(Fe*+Mg) ratios that vary from 0.54 in the footwall (GGF M1) to 0.78 in GGF M6. The composition of chlorite at the Scuddles deposit also has a similar distribution, with a broad trend of increasing Fe in chlorite up sequence (Ashley *et al.*, 1988; Potter, 1991). At Scuddles, the Fe*/(Fe*+Mg) ratios vary from 0.55 to 0.45 in the footwall, up to 0.65 in the hangingwall (Ashley *et al.*, 1988; Potter, 1991).

Morton and Franklin (1987) suggested that differences in the composition of chlorite relate principally to the relative amount of cold unreacted seawater drawn down into the discharge zone. Morton and Franklin (1987) interpret Mg-rich chlorite in the Noranda-type deposits to have formed from a greater contribution of unreacted seawater during mineralisation. An alternative source of Mg in Mg-rich chlorites could also relate to

Table 7.2: Average chlorite compositions from alteration and mineralisation at Gossan Hill. Data from Appendix A5.1.

Stratigraphic Member	n	SiO_2 (wt.%)	Al_2O_3 (wt.%)	MgO (wt.%)	MnO (wt.%)	FeO* (wt.%)	H_2O (wt.%)	Fe#	Mg#
GGF M6									
sphalerite-chlorite	12	22.4	23.6	7.8	0.2	35	11	0.72	0.28
sulphide veins	22	23.1	23.68	12.4	0.3	28.7	11.2	0.57	0.43
GGF M5									
carbonate nodular alteration	3	28.5	21.9	22.3	0.1	16.2	12.2	0.29	0.71
GGF M4									
intense chlorite alteration	22	24.8	19.7	14.3	0.1	28.5	11	0.53	0.47
quartz sandstone	19	24.5	20.2	14.1	0.1	28.4	11	0.53	0.47
siliceous nodular alteration	3	25.4	18.7	13.7	0	30.2	11.1	0.55	0.45
chlorite-andalusite	12	22.3	22.3	6.1	0.2	37.6	10.7	0.78	0.22
chlorite-apatite	16	23.3	20.9	9.2	0.2	34	10.8	0.68	0.32
GGF M1									
pumiceous breccia	9	24	23.2	13.1	0.1	27.8	11.3	0.54	0.46
Overall	118	24.7	22.6	12.1	0.2	32.1	11.5	0.63	0.41

* indicates total iron, Mg# = Mg/(Mg+Fe*), Fe# = Fe*/(Fe*+Mg), n = number of analysis

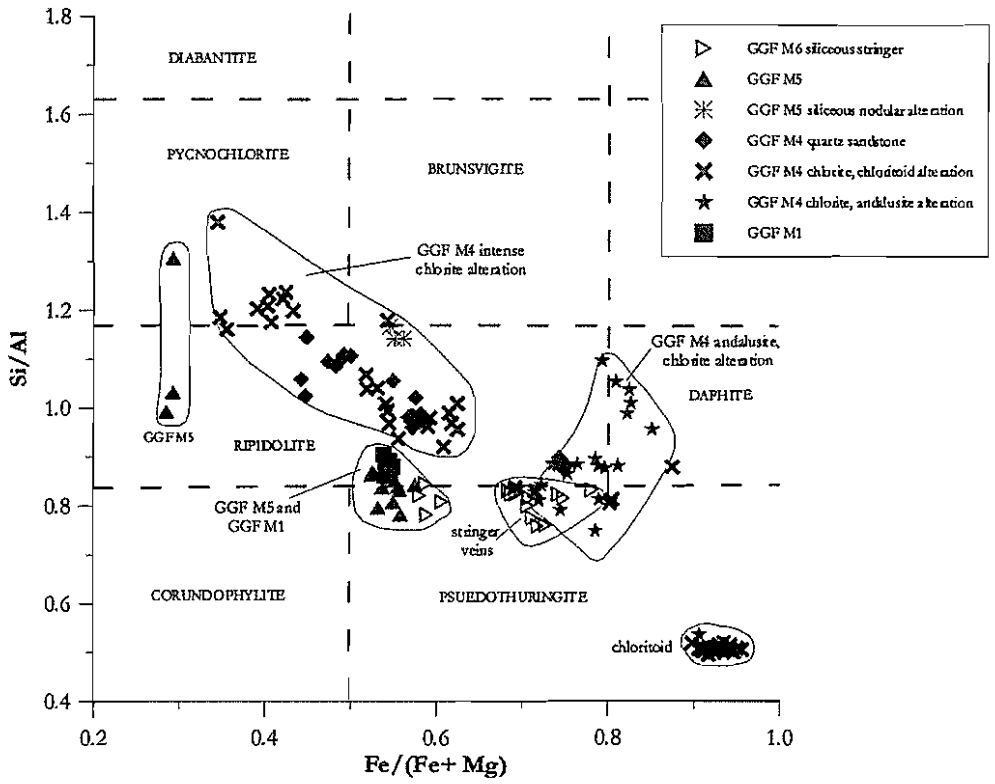

Figure 7.7: The composition of chlorite at Gossan Hill according to the classification of Hey (1954). Samples include chlorite in altered wall rock, massive sulphide and sulphide vein mineralisation. A broad positive correlation exists between Si/Al and Fe/(Fe+Mg). This correlation reflects a gradual, but non-systematic, enrichment of Fe into chlorite from the hangingwall to the footwall.

underlying Mg-rich mafic footwall rocks in these deposits (Morton and Franklin, 1987). At Gossan Hill, the occurrence of Fe-rich chlorite as an alteration zone and the major gangue mineral in massive magnetite and massive sulphide in the lower ore zone is consistent with its formation in an Fe-rich mineralising system.

7.5.2 Timing of localised chlorite alteration

The occurrence of an intense chlorite alteration envelope to the massive magnetite, massive sulphide and stringer veins in GGF M4 indicates the genetic association of this alteration with the mineralisation. This association is further substantiated by the presence of chlorite haloes around sulphide veins and, the occurrence of chlorite as a major gangue within massive magnetite, massive sulphide and sulphide veins. Therefore, chlorite alteration in GGF M4 likely formed during the massive magnetite and sulphide mineralisation at Gossan Hill. Moreover, chlorite associated with massive magnetite is texturally and compositionally indistinguishable from the chlorite associated with sulphide mineralisation.

Localised intense chlorite alteration formed by the alteration and replacement of tuffaceous strata in GGF M4. This is indicated by the presence of relict patches and beds of tuffaceous sandstone in which, with intense chlorite alteration overprints earlier regional quartz-chlorite alteration. The differential chlorite alteration between beds invokes localised permeability/porosity controls on its distribution. Moreover, the stratabound

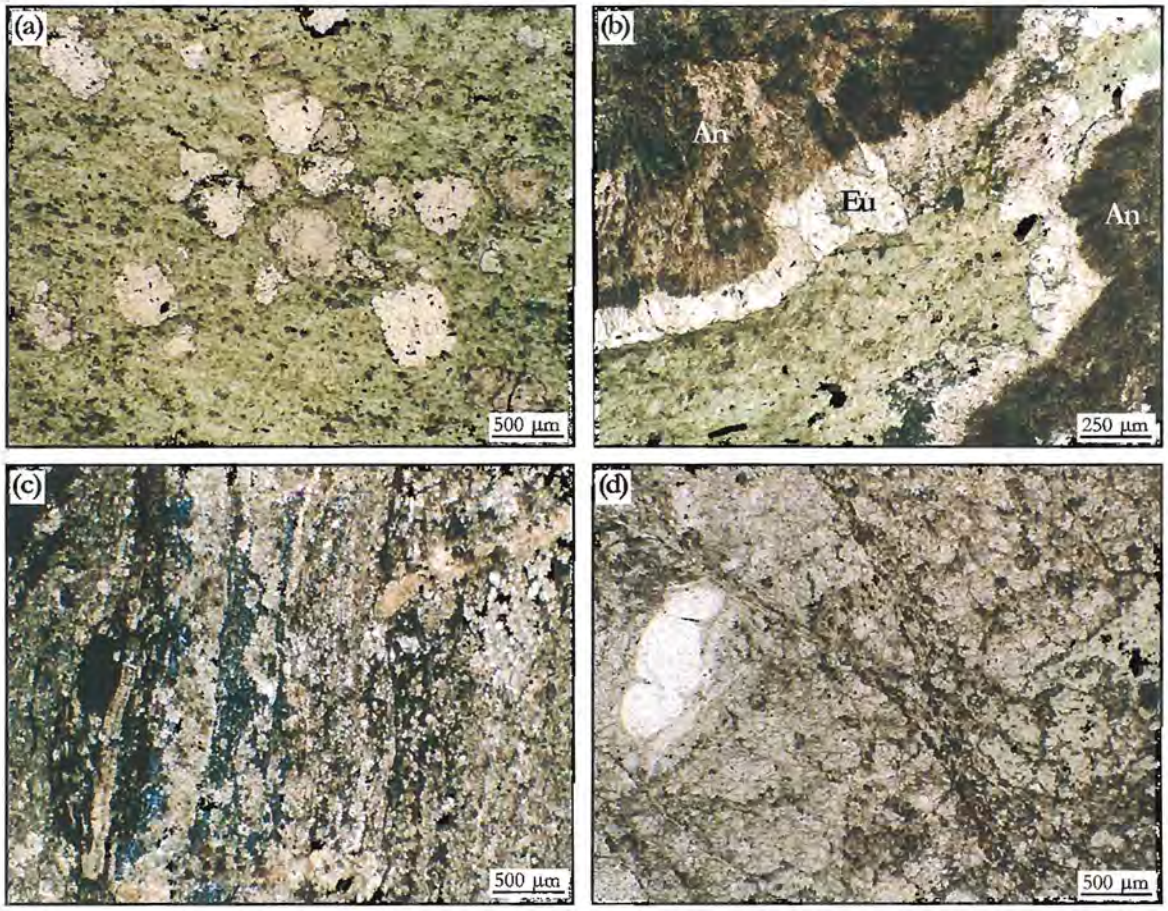

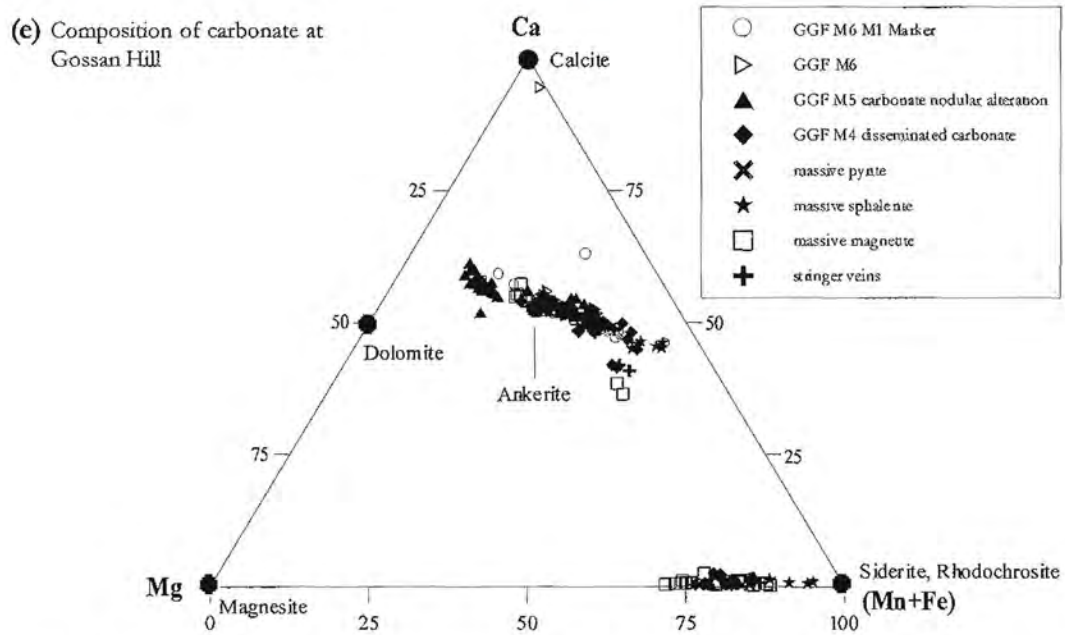

Figure 7.8: Carbonate alteration textures and composition. (a) Scattered euhedral to subhedral carbonate grains in fine-grained intense chlorite alteration of GGF M4 (sample 769083). (b) Zoned carbonate patches in intense chlorite alteration of GGF M4. Carbonate varies from poorly formed, anhedral fine-grained inner zones (An) that are overgrown by well-formed euhedral carbonate grains (Eu) (sample769083). (c) Banded carbonate with minor chlorite in the M1 Marker from GGF M6 (sample 760490). (d) Pervasive and disseminated fine-grained carbonate alteration of the groundmass within a massive rhyodacite lava (RD2) of the Scuddles Formation (sample 769304). (e) Composition of carbonate at Gossan Hill. Carbonates vary from ankerite to siderite, with ankerite the principal carbonate phase in the GGF. Data from Appendix A5.2.

occurrence of intense chlorite alteration indicates a lateral lithofacies control, with chlorite development concentrated in the immediate magnetite-sulphide ore-forming environment.

Adjacent to massive magnetite and sulphide mineralisation in GGF M4, replacement of quartz-chlorite altered strata by chlorite results in the destruction of relict volcanic textures. The abundant relict volcanic quartz lying within the intensely chlorite altered strata has textures that range from blocky relatively unreacted grains to strongly reacted embayed grains. Embayment of the volcanic quartz grains within chlorite alteration implies that intense chlorite alteration formed from hydrothermal fluids with temperatures in excess of 300°C (DiMarco and Lowe, 1989; Hoagland and Elders, 1978). Therefore, intense chlorite alteration within the lower ore zone is likely to represent a high temperature alteration stage, during the formation of massive magnetite and massive sulphide.

7.6 Carbonate alteration

Carbonate is a major gangue phase in the massive magnetite, massive sulphide and sulphide veins at Gossan Hill (Chapter 6). However, carbonate does not form an alteration zone, but occurs as disseminations throughout the intense chlorite alteration of the lower ore zone. Carbonate also occurs as a nodular alteration within GGF M5, as a bed-specific alteration in the upper parts of GGF M6, and as a pervasive intense alteration of rhyodacite and dacite in the hangingwall Scuddles Formation.

7.6.1 Distribution and textures

Within the lower ore zone, carbonate varies from ankerite to siderite (Section 7.6.2) and occurs as disseminations through the chlorite alteration (Fig. 7.8). The distribution of carbonate is erratic having intense development within and adjacent to massive magnetite, massive sulphide and sulphide veins. Carbonates form rhombs up to 1 mm (Fig. 7.8a), irregular anhedral grains, anastomosing zones with concentrically zoned grains (Fig. 7.8b) and patches of anhedral carbonate within chlorite. Carbonate grains also contain inclusions of magnetite, chalcopyrite and chlorite.

To the south of Gossan Hill, a nodular carbonate alteration occurs in GGF M5 (Figs. 7.9a and 7.9b), which varies from isolated, scattered zones or banded coalescing aggregates in quartz-chlorite altered GGF M5 (Fig. 7.9c). Carbonate nodules are up to 8 mm in size, having rounded shapes with irregular gradational margins. These carbonate textures resemble siliceous nodular alteration (Section 7.3.4) however they consist of carbonate and lack volcanic textures. Carbonate within the nodules is anhedral, fine-grained and has a dolomitic ankerite composition (refer Fig. 7.8e).

In tuffaceous pebble breccia beds of the uppermost parts of GGF M6 carbonate forms a layered alteration (refer Figs. 7.3c and 7.3d). Carbonate altered beds have sharp conformable contacts with adjacent quartz-chlorite beds and consist of poorly-formed, anhedral and interlocking grains that pseudomorph lithics and alter the matrix (Figs. 7.3c and 7.3d). Bands and laminae of carbonate also occur in lithic beds of the M1 Marker (Fig. 7.8c), where rhythmic carbonate bands less than 300 μm wide occur with chlorite or quartz bands.

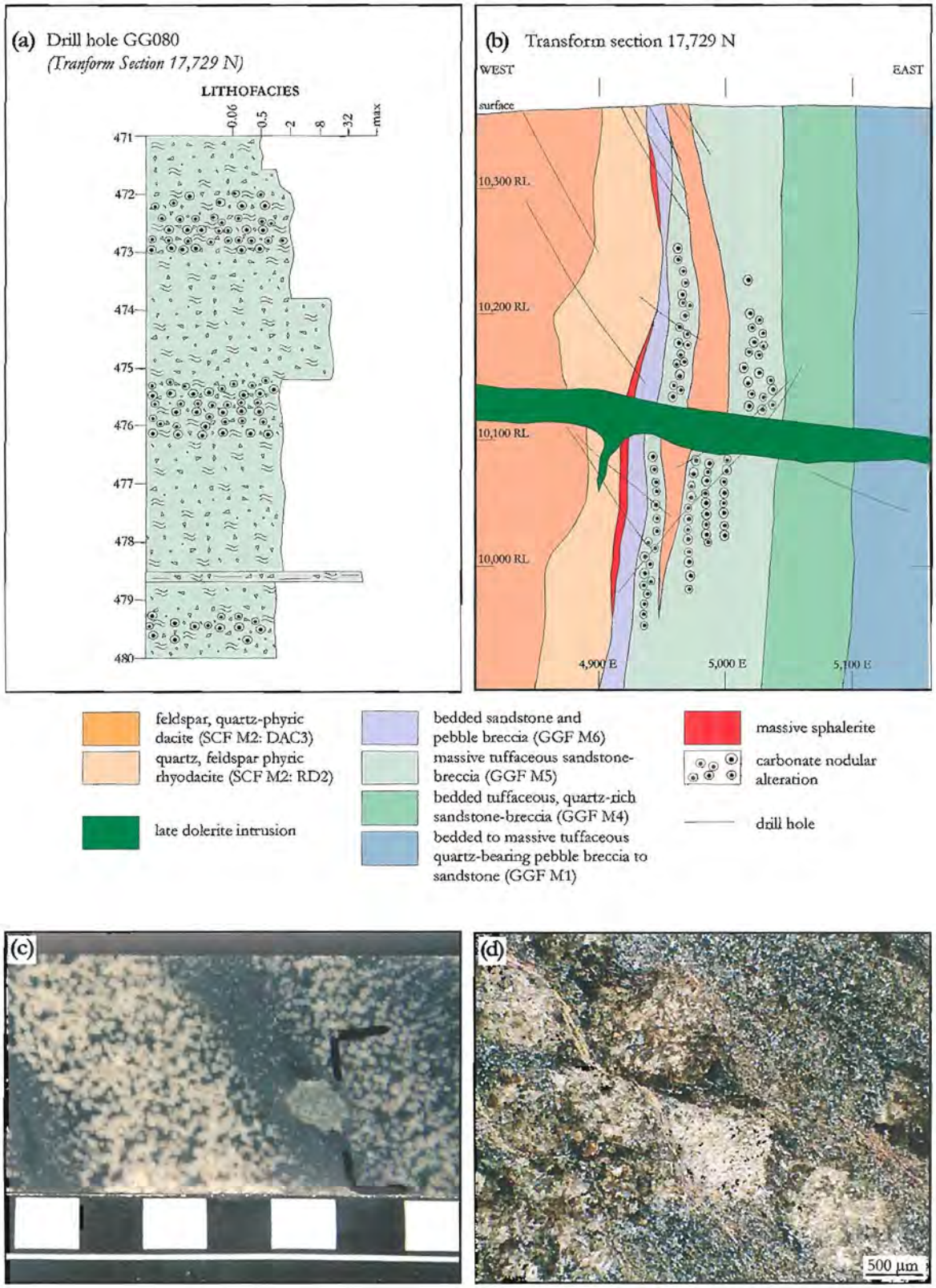

Figure 7.9: Carbonate nodular alteration within GGF M5 to the south of Gossan Hill. (a) Lithofacies diagram illustrating the semiconformable and scattered occurrence of the carbonate nodular alteration within massive sandstone of GGF M5. (b) Transform section 17,729 N at Gossan Hill showing the distribution of nodular carbonate alteration within GGF M5 below the massive sphalerite and GGF M6. (c) Planar, broadly banded zones of nodular carbonate alteration in a massive quartz-chlorite altered sandstone of GGF M5. The nodules are rounded and locally anastomose and coalsece (sample 760251). Scale in cm. (d) Photomicrograph of carbonate nodules in (c). Nodules consist of anhedral, fine-grained carbonate in a carbonate and muscovite altered matrix (sample 760251).

Carbonate is widely developed within rhyodacite and dacite of the Scuddles Formation. Strong pervasive carbonate alteration occurs through the groundmass (Fig. 7.8d) and relict feldspar phenocrysts. In the dacite groundmass, carbonate consists of small (<50 μm) anhedral grains, whilst in altered feldspar phenocrysts carbonate is subhedral and up to 200 μm in size. The carbonate alteration of the rhyodacite is similar to the dacite, but carbonate also infills amygdules in the rhyodacite.

7.6.2 Composition of carbonate

Carbonate electron microprobe analyses (Appendix A5.2) vary in composition from ankerite to siderite (Fig. 7.8e and Table 7.3). Iron-rich carbonates (range of 28.8 to 67.3 wt.% $FeCO_3$, Table 7.3) are the main carbonate in the intense chlorite (±carbonate) alteration envelope of the lower ore zone. Carbonates that form nodules in GGF M5 are ankeritic, but tend to have low Fe contents (average of 13.1 wt.% $FeCO_3$) and are more Ca-Mg-enriched dolomitic compositions (Fig. 7.8f). Lower Fe CO_3 concentrations in carbonate are also present in the carbonate alteration of pebble breccias within GGF M6 and the M1 Marker (Fig. 7.8f). Mn-bearing carbonates (up to 16.5 wt.% $MnCO_3$, Table 7.3) occur within massive sulphide and sulphide veins of the upper ore zone and indicate some Mn enrichment to Zn-rich mineralisation. Overall, the composition of carbonate at Gossan Hill varies from Fe-rich in the lower ore zone and in massive sulphide, with lower Fe carbonates in the carbonate alteration of the uppermost parts of GGF M6 and the hangingwall.

7.6.3 Timing of carbonate alteration

The occurrence of ankerite-siderite as a major gangue in massive magnetite, massive sulphide and stringer veins, together with its occurrence within the intense chlorite

Table 7.3: Average carbonate compositions at Gossan Hill. Data from Appendix A5.2.

Stratigraphic Member	n	$MgCO_3$ (wt.%)	$CaCO_3$ (wt.%)	$MnCO_3$ (wt.%)	$FeCO_3$ (wt.%)
GGF M6					
M1 Marker chert	18	19.8	50.4	3.8	25.2
sandstone and breccia	29	19.1	54.2	3.1	23. 5
GGF M5					
carbonate nodular alteration	37	33	52.9	1.6	13.1
GGF M4					
chlorite-carbonate alteration	49	26.2	23	2.8	49.9
GGF M4 massive magnetite					
massive magnetite	27	29.2	41	0.6	30.6
GGF M4, M5 and M6: stringer veins					
pyrite-sphalerite-pyrrhotite-magnetite carbonate veins	11	21.3	31.7	16.16	31.6
chlorite-magnetite-carbonate veins	8	22	23.1	1.5	55.6
carbonate-sulphide veins	20	24.6	51.3	0.9	23.6
pyrite-chlorite-carbonate veins	6	20.6	49	3.2	28.8
GGF M4 and M6: massive sulphide					
massive sphalerite in GGF M6	12	12.7	29	16.5	44.3
massive pyrite in GGF M4	8	27.2	0.7	6.7	67.3

n = number of analysis

alteration envelope of the lower ore zone, support the synchronous formation of carbonate with ore formation. The Fe-rich composition of carbonate in the lower ore zone is consistent with the Fe-rich nature of mineralisation and Fe-rich chlorite alteration. Texturally and compositionally, the ankerite-siderite formed during massive magnetite is indistinguishable from the carbonates in sulphide mineralisation.

Nodular carbonates are a common alteration feature of many VHMS deposits (*e.g.*, Scuddles, Ashley *et al.*, 1988; Hellyer, Gemmell and Large, 1992; Bradley, 1997; Hercules and Rosebery, Khin Zaw, 1991; Thalanga, Hill, 1996). This alteration texture is common to footwall alteration, often forming discrete zones peripheral to sulphide mineralisation (*e.g.*, Bradley, 1997). At Gossan Hill, nodular carbonate alteration occurs in the footwall of the upper ore zone, as a replacement texture of a tuffaceous protolith overprinting earlier quartz-chlorite alteration. The limited distribution of nodular carbonate alteration to the southern margin of massive sulphide reflects its development as a peripheral alteration to massive sulphide mineralisation. Carbonate alteration in GGF M6 and the M1 Marker is minor and conformable. The dolomitic ankerite compositions of nodular carbonate alteration in GGF M5 suggest formation from a more seawater-dominated source.

Carbonate alteration in the Scuddles Formation varies from a strong to intense, pervasive alteration of the groundmass and feldspar phenocrysts. The intensity of this alteration decreases with distance into the hangingwall. Although the compositions of carbonate in this alteration were not determined by microprobe analysis, reaction with dilute HCl_{aq} acid indicates they are calcite. The ubiquitous occurrence of carbonate alteration within rhyodacite and dacite overlying the massive sulphide mineralisation indicates that it was developed as a hydrothermal alteration product, after emplacement of the hangingwall.

7.7 Muscovite alteration

Muscovite within the GGF is a minor to accessory mineral that occurs as disseminated grains in regional quartz-chlorite alteration and in the intense chlorite alteration surrounding the lower ore zone in GGF M4. Muscovite is generally absent from intense siliceous alteration in the upper ore zone and stringer stockwork. Where present, muscovite forms finely disseminated grains (<20 μm) that may be aligned to define cleavage. Nonetheless, muscovite is a major alteration phase within rhyodacite and dacite of the Scuddles Formation. Abundant muscovite commonly imparts a bleached, cream-grey colour to these volcanic rocks and forms in excess of 20% modal (Fig. 7.10a). Muscovite is fibrous, fine-grained (<50 μm) and occurs throughout the groundmass where it is commonly aligned and defines cleavage (Fig. 7.10b). Muscovite also occurs as an alteration of feldspar phenocrysts, where it tends to be coarser-grained (<100 μm). Muscovite from Gossan Hill was not analysed in this study.

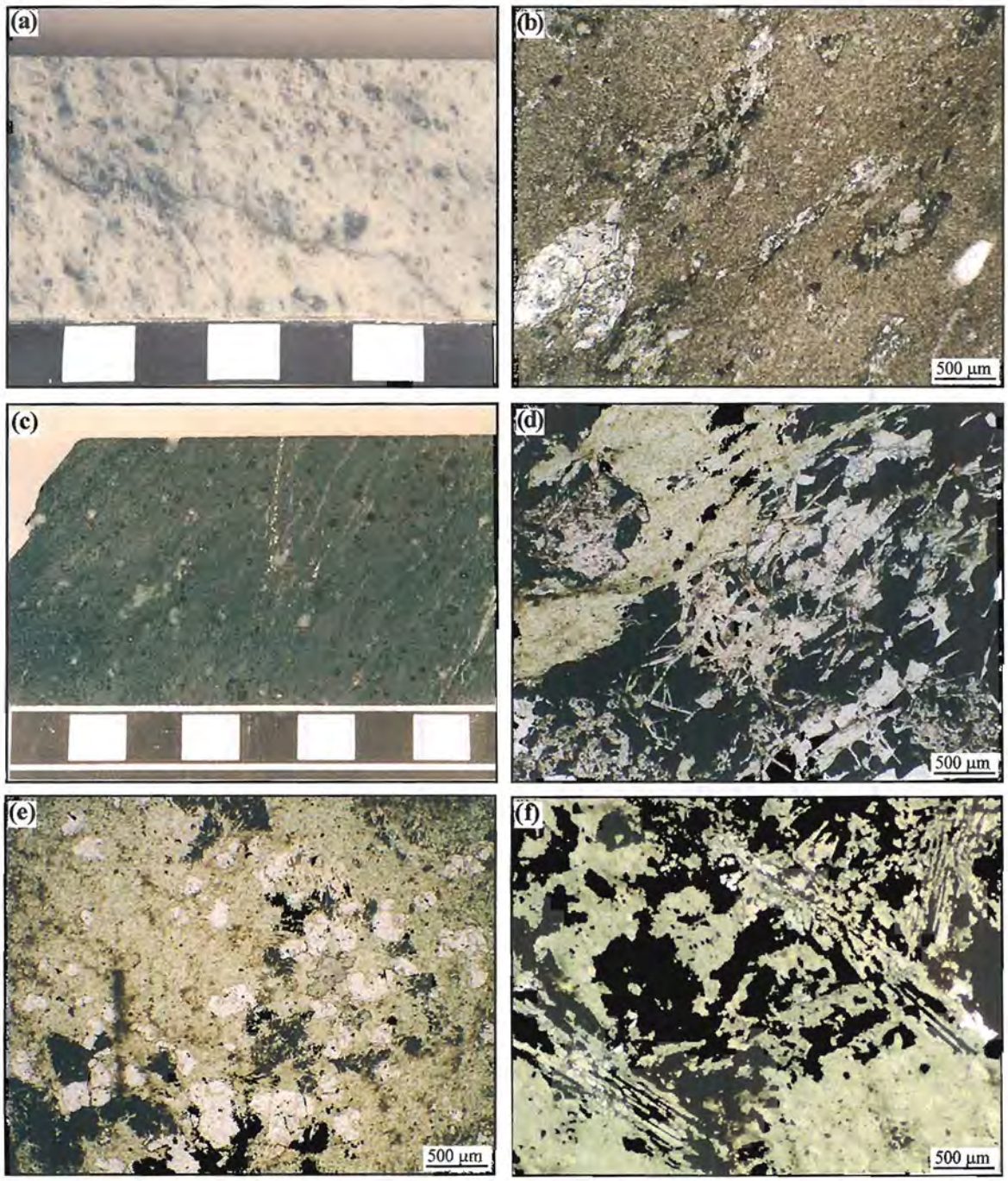

Figure 7.10: (a) Muscovite-carbonate alteration of a massive quartz-phyric rhyodacite lava in the hangingwall Scuddles Formation Member 2 (sample 760214). Scale in cm. (b) Photomicrograph of fine-grained pervasive muscovite alteration of the groundmass within a feldspar, quartz-phyric dacite of the Scuddles Formation Member 2 (sample 760207). Muscovite is aligned and defines cleavage, whilst feldspar phenocrysts are altered to carbonate-chlorite. (c) Pervasive talc-chlorite alteration hosting disseminated pyrite and chalcopyrite (opaques) in the lower ore zone (sample 769174). Scale in cm. (d) Photomicrograph of acicular talc and fine-grained chlorite hosting sulphides (opaques)(sample 769152). (e) Photomicrograph of disseminated subhedral apatite grains in a chlorite matrix with disseminated sulphides in GGF M4 (sample 769228). (f) Photomicrograph of chloritoid alteration in fine-grained chlorite of GGF M4. The chloritoid is partially replaced along cleavage planes by pyrrhotite and magnetite (opaques) (sample 762039).

7.8 Minor alteration minerals

7.8.1 Talc

Talc occurs within the local intense chlorite±carbonate alteration envelope of the lower ore zone. Talc is generally fine-grained (<50 μm) and consists of acicular grains in chlorite and sulphide (Figs. 7.10c and 7.10d). Talc is also a common gangue constituent of the massive magnetite and massive sulphide. No compositional data was obtained for talc.

7.8.2 Apatite

Apatite forms a minor alteration mineral within the intense chlorite±carbonate alteration envelope of the lower ore zone. Apatite occurs as disseminated euhedral grains (Figs. 7.10d and 7.10e) that are commonly deformed, as indicated by cleavage wrapping, cleavage slip and pressure solution shadows. Apatite grains are up to 0.4 mm in size and may form up to 2% modal. Apatite commonly occurs within disseminated sulphide (pyrite-pyrrhotite-chalcopyrite)-chlorite alteration, which suggests an origin related to sulphide forming processes. Electron microprobe analysis of apatite indicates elevated F levels (4.8 to 6.2 wt.%, Appendix A5.3).

7.8.3 Chloritoid and andalusite

Although chloritoid and andalusite are metamorphic minerals (Chapter 4), their presence at Gossan Hill reflects hydrothermal alteration in the GGF. Andalusite is often intergrown with chloritoid (Chapter 4), and these minerals principally occur in intense chlorite alteration of the lower ore zone. Their distribution is erratic, but andalusite and chloritoid are generally confined to discrete beds in the lower alteration envelope. Chloritoid forms large euhedral radiating laths up to 1 mm in size that are hosted within fine-grained chlorite. Chloritoid is commonly corroded and partially replaced along cleavage planes by mixtures of chlorite, pyrrhotite and pyrite (Fig. 7.10f). Electron microprobe analysis of chloritoid (Appendix A5.4) indicates it has a relatively homogeneous composition (Fig. 7.7). Chloritoid and andalusite in alteration associated with VHMS deposits represent the metamorphic products of aluminous hydrothermal alteration, which in turn, reflect strong acid leaching of the wall rock (Franklin *et al.*, 1975; Hannington *et al.*, 1997).

7.9 Alteration zonation

Within VHMS deposits, the distribution of hydrothermal alteration in fragmental rocks is commonly extensive and diffuse, compared with alteration in coherent rock types (Franklin *et al.*, 1981; Morton and Franklin, 1987). In fragmental lithologies, the alteration below massive sulphides is often developed as semiconformable alteration zones. This alteration distribution can be related to the physical control of lithofacies on the fluids responsible for alteration-mineralisation. The volcaniclastic, pumice-rich nature of the GGF at Gossan Hill would have had initially, a high porosity and permeability, and differential permeability/ porosity contrasts between sandstone-siltstone in the GGF may have locally controlled the migration of circulating fluids. Furthermore, the initial presence of volcanic glass in the GGF, would have been an unstable and reactive medium. These characteristics mean that lithofacies were a significant control on the distribution and styles of alteration at Gossan

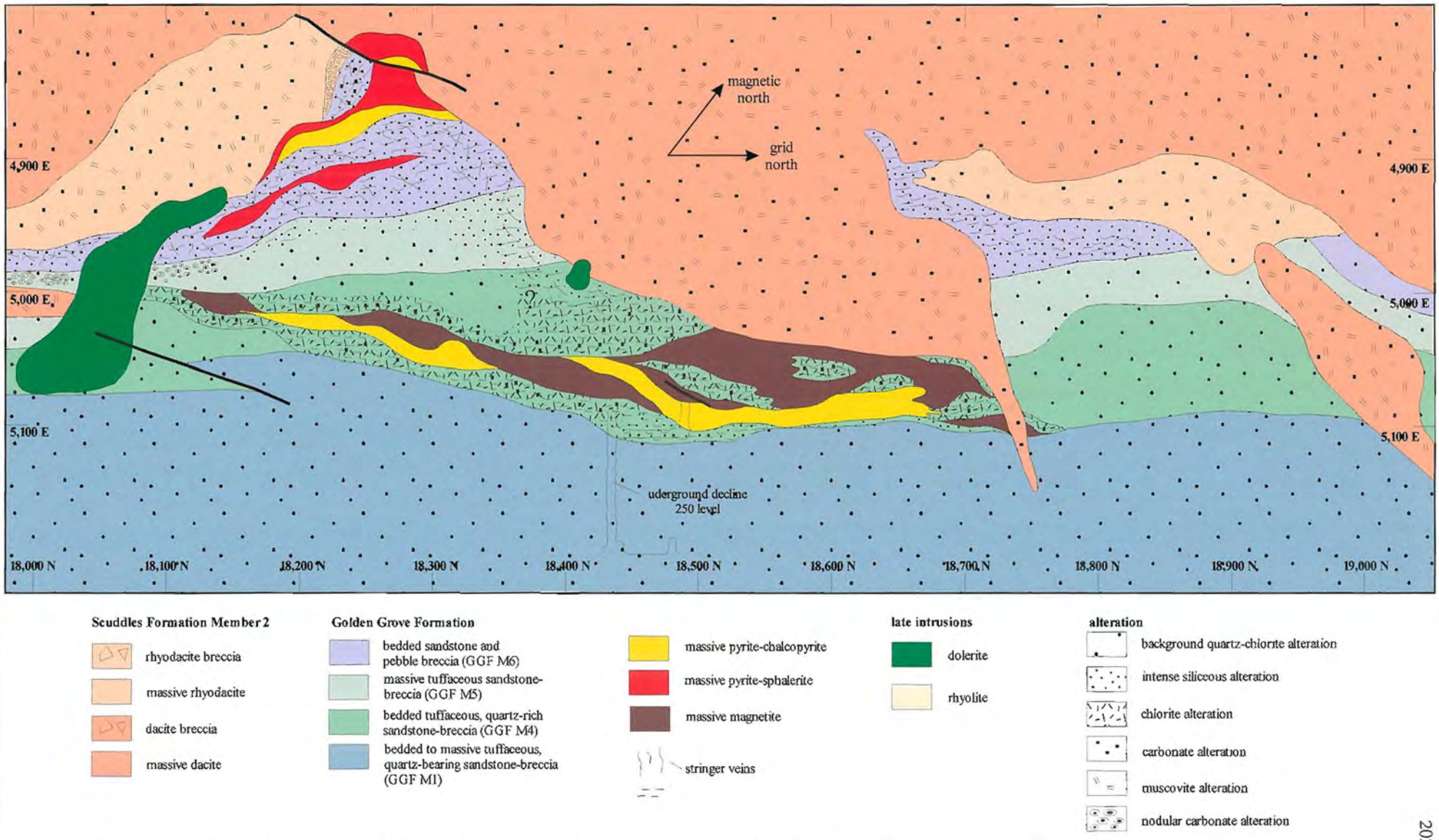

Figure 7.11: Level plan 10,150 R.L (200 m below surface) illustrating the distribution of alteration over the central and northern areas of Gossan Hill.

Hill.

Ubiquitous early quartz-chlorite alteration occurred soon after, or during, emplacement of the GGF. This regional alteration of the GGF, replaced volcanic glass by differential quartz and chlorite alteration. The distribution of quartz and chlorite differs between and within lithofacies, generating texturally distinct, but mineralogically similar, semiconformable alteration zones that correspond to discrete members of the GGF. Moreover differential quartz-chlorite alteration between beds in all members reflects local permeability/porosity contrasts. Substantial chemical and mineralogical modification of the GGF occurred during early quartz-chlorite alteration. This modification caused induration of the tuffaceous succession and sealed much of the succession to the effects of subsequent hydrothermal alteration and metamorphic re-adjustment.

At Gossan Hill, the localised zones of intense hydrothermal alteration overprint earlier quartz-chlorite alteration. The hydrothermal alteration zones are (1) a chlorite-rich alteration in the lower ore zone, and (2) a siliceous alteration in the stockwork and upper ore zone. These intense hydrothermal alteration zones form tightly constrained alteration envelopes around massive magnetite and massive sulphide mineralisation (Figure 7.11).

Intense chlorite alteration in the lower ore zone contains carbonate, pyrite, pyrrhotite, magnetite, apatite, chloritoid and andalusite, and envelopes massive magnetite, massive sulphide and sulphide vein mineralisation. This chlorite alteration zone is semiconformable and stratabound to GGF M4. Although intense chlorite alteration in the lower ore zone is semiconformable and laterally continuous over the strike of massive magnetite and massive sulphide in GGF M4, it has the same lateral distribution as sulphide vein mineralisation. The width of chlorite alteration is generally less than 30 m away from ore, extending to the outer margins of sulphide vein mineralisation. The contact between chlorite alteration envelop and the regional quartz-chlorite alteration is gradational and characterised by decreasing proportions of chlorite and the absence of sulphide veins (Fig. 7.11). The occurrence of massive magnetite and massive sulphide within chlorite indicates that chlorite alteration likely formed during both massive magnetite and sulphide stages. Intense chlorite alteration of the quartz-chlorite altered protolith in the lower ore zone probably developed at, and outwards from, magnetite and sulphide vein/permeability conduits. Furthermore, the restricted distribution of intense chlorite alteration reflects the relative impermeability of the wall rock away from the central conduit or feeder to mineralisation.

Localised intense siliceous alteration occurs as a narrow, asymmetric envelope to the discordant stockwork connecting the lower and upper ore zones. It also forms a semiconformable alteration envelope to the upper ore zone (Fig. 7.11). Intense siliceous alteration hosts sulphide vein mineralisation and has gradational contacts to quartz-chlorite alteration outwards from the central feeder. A narrow zone of siliceous alteration also occurs at the base of GGF M4 below the massive sulphide. At the base of GGF M4, siliceous alteration hosts sulphide veins and is laterally discontinuous.

Carbonate, occurring as a disseminated alteration within the chlorite alteration envelope, is

best developed adjacent to massive magnetite and within massive magnetite, massive sulphide and sulphide veins (Fig. 7.11). Nodular carbonate alteration within GGF M5 is a localised alteration that occurs at southern end of Gossan Hill below the massive sulphide mineralisation. Pervasive muscovite-carbonate alteration of the hangingwall rhyodacite occurs over the strike of mineralisation at Gossan Hill (Fig. 7.11). Carbonate and muscovite alteration of the groundmass and feldspar phenocrysts characterise this alteration. The intensity of carbonate and muscovite alteration decreases with distance into the hangingwall and extends at least 200 to 300 m. The upper limit of this alteration is not constrained due to limited drilling information.

7.9.1 Alteration zonation at the Scuddles deposit

The alteration mineralogy and distribution at the Scuddles deposit were investigated by Ashley *et al.* (1988) and Clifford (1992). The distribution of alteration at Scuddles is illustrated in Figure 7.12. Ubiquitous quartz-chlorite (±muscovite) alteration of the GGF is defined throughout the footwall and host rocks to mineralisation. Massive sulphide at Scuddles is underlain and enveloped by zones of intense siliceous alteration as well as intense chlorite-carbonate-talc-sulphide alteration. However, the distribution of these zones and their association to massive sulphide mineralisation is poorly constrained. A zone of muscovite alteration extends over 200 m into the hangingwall volcanics (DAC1 and DAC3), however the upper and lateral extent of this alteration is also poorly defined.

7.10 Alteration paragenesis

At Gossan Hill, the alteration mineralogy is relatively simple and forms both broad semiconformable and localised stratabound alteration zones. The relative timing of alteration is given in Figure 7.13. The earliest alteration identified is quartz with a lesser chlorite and muscovite (after clay and zeolite?) assemblage, associated with a regional-scale pervasive silicification of the GGF. The duration of this hydrothermal event is unconstrained but may have been synchronous with depositional stages of the GGF, up until the onset of hydrothermal alteration associated with massive sulphide formation. Quartz-chlorite alteration affected the entire GGF throughout the Golden Grove Domain and resulted in the mass replacement of glassy tuffaceous constituents by quartz and chlorite. As clay-zeolite are common alteration products of glass (Iijima, 1974; Quantin *et al.*, 1988), chlorite in the GGF may have had a clay-zeolite precursor, which was transformed to chlorite either during successive hydrothermal alteration or during greenschist metamorphism. All other alteration assemblages overprint this early alteration.

Regional quartz-chlorite alteration of the GGF was a ground preparation event, which indurated and reduced the permeability and porosity of the succession. Subsequent hydrothermal fluids were focussed along a synvolcanic feeder, near the site of the DAC3 dacite intrusion, and through fracture induced permeability structures. The wall rock adjacent to massive sulphide and sulphide veins was locally silicified by hot, silica saturated mineralising fluids. This localised silicification is semiconformable to massive sulphide in the upper ore zone and discordant in the stringer stockwork.

Intense chlorite alteration that envelopes the massive sulphide, massive magnetite and

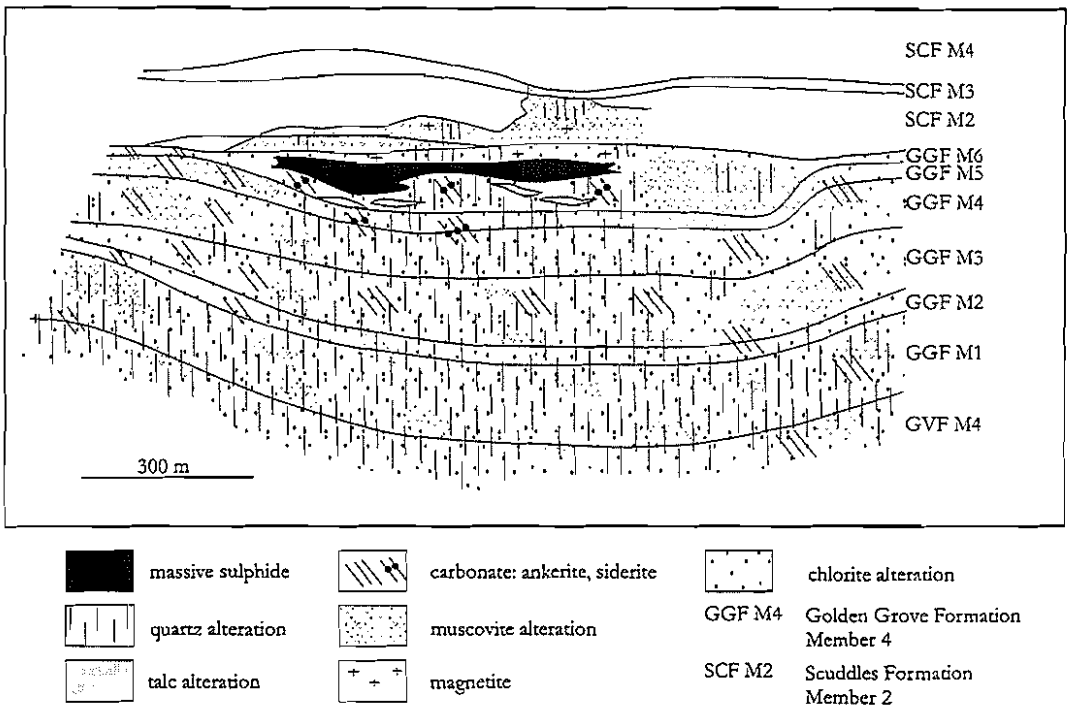

Figure 7.12: Schematic representation of the stratigraphy, massive sulphide and alteration at the Scuddles deposit (from Clifford, 1992).

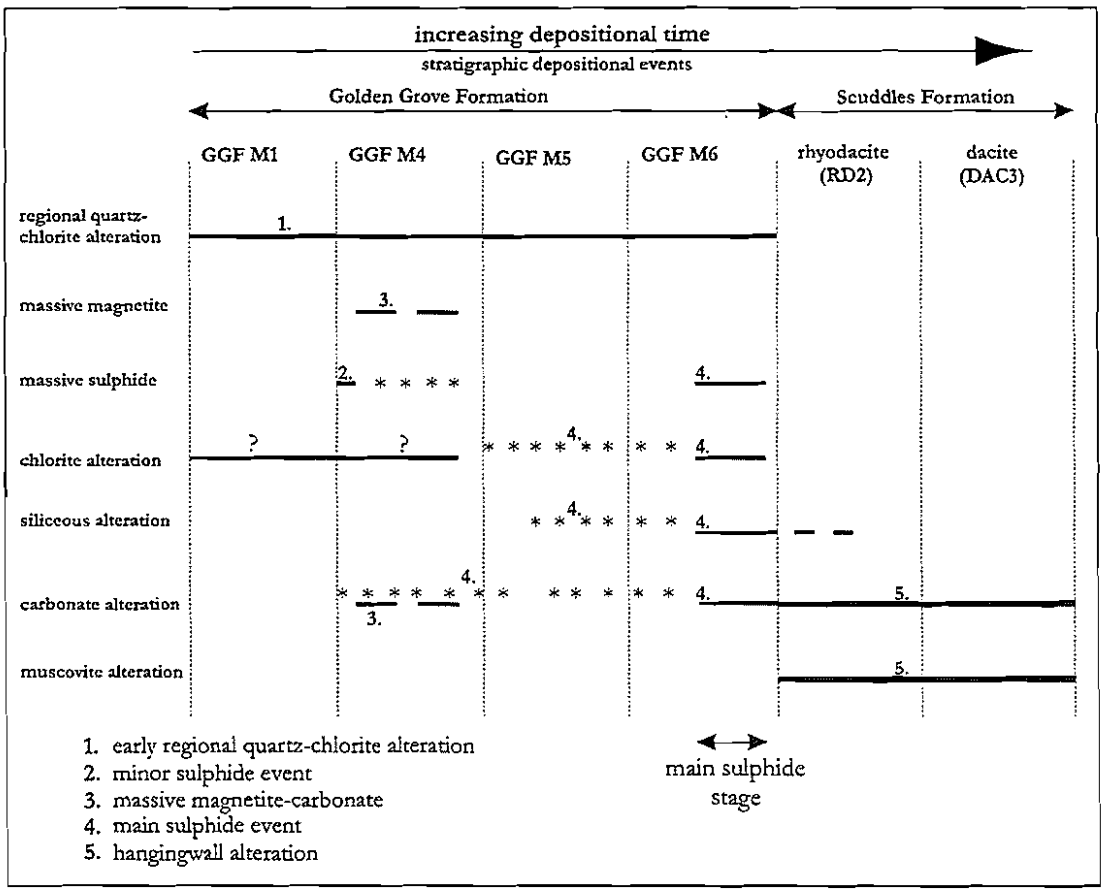

Figure 7.13: Relative timing of alteration with respect to the deposition of stratigraphic members that host massive sulphide and massive magnetite at Gossan Hill. Solid lines indicate contemporaneous alteration with sedimentation whereas * indicates later alteration and replacement by hydrothermal processes associated with ore formation in GGF M6. Early quartz-chlorite alteration is overprinted by later alteration associated with the formation of massive magnetite and massive sulphide.

stringer veins in GGF M4, overprints the early quartz-chlorite alteration of the GGF. Textural support for this timing relationship comes from nodular siliceous alteration in chlorite. Intense chlorite alteration formed synchronously with massive magnetite, massive sulphide and stringer vein mineralisation. Therefore, chloritisation in the lower ore zone represents hydrothermal alteration associated with the deeper, Cu-enriched parts of mineralisation at Gossan Hill.

Carbonate alteration has a spatial and genetic association to both massive magnetite and massive sulphide, where it occurs as an alteration and gangue mineral. Carbonate occurs within the intense chlorite alteration that envelopes the lower ore zone and is considered to have formed during both massive magnetite and massive sulphide stages. The nodular carbonate within GGF M5 occurs below massive sulphide at the southern end of Gossan Hill and likely represents a more distal alteration formed during sulphide mineralisation in the upper ore zone. Carbonate within GGF M6 generally overlies massive sulphides and forms a bed-specific alteration of breccia and sandstone. The association of carbonate alteration with M1 Marker chert, suggest a near sea floor alteration associated with lower temperatures. Carbonate alteration in the hangingwall dacite and rhyodacite is pervasive and ubiquitous, representing hydrothermal alteration continued during burial and waning of the hydrothermal system at Gossan Hill.

In the Scuddles Formation, muscovite is a major alteration mineral that is strongly developed in rhyodacite, but decreases in abundance away from mineralisation. Muscovite alteration is associated with carbonate and minor chlorite-quartz alteration of the hangingwall volcanics, all of which are considered to have formed during hangingwall alteration, after burial of the Gossan Hill deposit.

7.11 Synthesis

- Four major alteration zones are identified at Gossan Hill; (1) regional quartz-chlorite ± muscovite alteration, (2) chlorite, carbonate, magnetite, talc, pyrite, pyrrhotite alteration in the lower ore zone, (3) intense siliceous alteration in the stockwork and upper ore zone, and (4) muscovite, carbonate alteration in the hangingwall.
- Quartz-chlorite ± muscovite alteration is a ubiquitous early alteration that is regionally extensive and resulted in the near complete quartz-chlorite replacement of the GGF. This alteration preserved glassy volcanic textures, led to induration and reduced permeability of the succession such that subsequent hydrothermal alteration and mineralising events were locally controlled by the relative impermeability of the succession.
- A localised intense envelope of chlorite ±carbonate alteration occurs around the lower ore zone and overprints regional quartz-chlorite alteration. Minor alteration minerals also include talc, magnetite, pyrite, pyrrhotite, apatite, chloritoid and andalusite. Chlorite and carbonate are both Fe-rich, and carbonates vary from ankerite to siderite. The formation of this semiconformable alteration occurred as a culmination of localised hydrothermal alteration related to the formation of massive magnetite,

massive sulphide and sulphide veins. Its distribution as reflects strong lithofacies control and the relative impermeability of the wall rock resultant from earlier quartz-chlorite alteration.

- Intense siliceous alteration forms an envelope around discordant mineralisation in the stockwork, and a semiconformable alteration to the upper ore zone. Intense siliceous alteration led to textural destruction of relict volcanic textures. Towards the top of GGF M6, intense siliceous alteration gives way to a bedded alteration. Beds in this thinly bedded sequence have differential quartz, chlorite and carbonate alteration.
- Hydrothermal alteration in the hangingwall consists of muscovite and carbonate with minor chlorite and quartz. This alteration is ubiquitous in rhyodacite and dacite, but decreases in intensity with distance into the hangingwall (at least 200 to 300 m). Hangingwall alteration was developed during or after emplacement of the hangingwall lavas, and formed as a result of burial and waning of the hydrothermal system at Gossan Hill.

Chapter 8

Lithogeochemistry

8.1 Introduction

This chapter describes the lithogeochemistry of the strata hosting the Gossan Hill deposit, including the footwall (GGF M1), host rocks (GGF M4, M5 and M6) and the hangingwall volcanics (SCF M2). Emphasis is given to the alteration geochemistry of these rocks due to the lack of unaltered lithologies at Gossan Hill and in the Golden Grove Domain.

8.2 Aims

Immobile element geochemistry is used to define the primary geochemical characteristics of the lithofacies at Gossan Hill, particularly in view of their widespread, intense alteration (Chapter 7). The application of immobile element geochemistry at Gossan Hill assesses the homogeneity and compositional variation of the Golden Grove Formation (GGF). The alteration geochemistry examines the distribution of elements considered to be mobile in an ore-forming environment, in order characterise alteration depletion and enrichment trends related to mineralisation.

8.3 Previous geochemical investigations

The lithogeochemistry of the GGF has been an integral part of regional exploration programs by the Normandy Group, and is the focus of many company reports (*e.g.*, Radford, 1992). Clifford (1992) investigated regional geochemical trends within the Gossan Hill Group, concentrating largely on primary compositional variation in the succession. Likewise, the nearby Scuddles deposit has been the subject of numerous geochemical studies including those of Ashley (1983), Potter, (1991), Ashley *et al.* (1988) and Whitford and Ashley (1992). Frater (1978) recognised a number of geochemical trends in the rocks surrounding the Gossan Hill deposit. These trends, however, had little stratigraphic control due to an unresolved stratigraphy at this time. This study has the benefit of stratigraphic orientation (Chapter 3; Clifford, 1992), which was unavailable to past researchers.

8.4 Sample details

A total of 88 samples from unweathered drill core were selected for geochemical analyses. This suite of samples is representative of the least altered and altered strata

within the GGF M1 to GGF M6 inclusive, and the hangingwall SCF M2. Samples were selected to incorporate both a lateral (strike) and a section (cross strike) database from which the geochemical variation at the Gossan Hill deposit was investigated. Sample locations are illustrated in Figure 8.1. The location of drill holes, together with the steep dip and stratigraphic separation of upper and lower ore zones, precluded investigation of the entire stratigraphy along a single section. Some samples of the M1 Marker (GGF M6) at the Scuddles deposit were also analysed in order to compare their geochemistry with similar units at the Gossan Hill deposit. The breakdown of geochemical samples used in this thesis is given in Table 8.1.

Table 8.1: List of geochemical samples analysed at Gossan Hill. Note: n indicates number of samples

Strata	Least altered samples	n	Altered samples	n
SCF M2 (DAC3)	feldspar, quartz-phyric dacite	12		
SCF M2 (RD2)	quartz, feldspar-phyric rhyodacite	10		
GGF M6	sandstone and polymict breccia	7	intense siliceous alteration	2
	tuffaceous sandstone	3	intense chlorite alteration	3
	M1 Marker	3		
GGF M5	tuffaceous sandstone	3	nodular carbonate alteration	4
GGF M4	tuffaceous sandstone and breccia	8	intense chlorite alteration	3
			nodular siliceous alteration	2
			magnetite-chlorite alteration	2
			andalusite-chloritoid-chlorite	3
GGF M1	tuffaceous pebble breccia	10		
porphyritic dacite	feldspar-phyric dacite	2		
dolerite		2		

8.4.1 Analytical techniques

Major and trace element whole rock analyses were carried out using the X-ray fluorescence facility at the School of Earth Sciences, University of Tasmania. Rock samples were initially crushed using a steel jaw crusher to produce fragments less than 3 cm. These fragments were then hand picked, and ground in a tungsten-carbide ring mill for 3 minutes to produce a rock powder (<200 μm). Approximately 1 gram of each sample was ignited initially at 500°C for four hours (due to the high sulphide contents), and then at 1000°C overnight. Volatile loss on ignition (LOI) was determined by weighing samples before and after ignition.

Major elements were determined as oxides SiO_2, TiO_2, Al_2O_3, FeO (all iron as FeO), MnO, MgO, CaO, Na_2O_3, K_2O, P_2O_5 and S, using fused disks. Trace elements La, Ce, Nd, Nb, Zr, Sr, Cr, Ba, Sc, V, Sn, Cu, Pb, Zn, Ni, Y and Rb were determined using pressed powder pills. Both major and trace element determinations were carried out on a Phillips 1410 automated XRF under the guidance of Phil Robinson (Analyst), using standard procedures outlined by Norrish and Chappell (1977). Trace elements Ag, As, Bi, Mo, Cd, Sb, Cs, Tl, Th, U were analysed by Analabs (Perth) using ICP-MS.

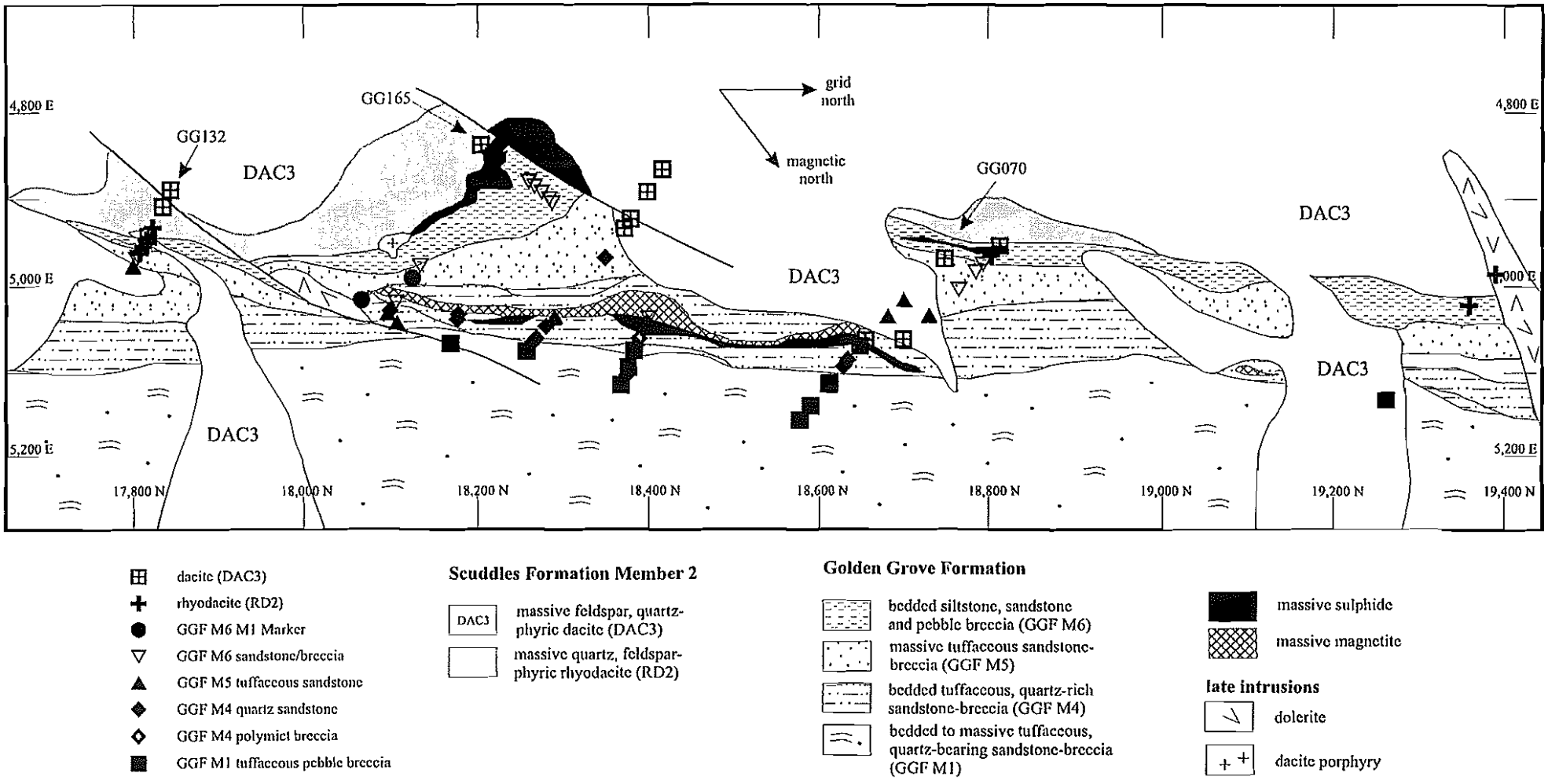

Figure 8.1: Plan projection at 10,200 metres R.L. (~150 m below surface) through the Gossan Hill deposit. The location of the geochemical samples analysed in this study is projected. The samples were collected from drill holes along the strike of the deposit. The three main intercepts sampled were GG132 at 17,800 N in the south, GG165 at C zone (18,300 N) and GG070 through massive magnetite and Cu-rich sulphides (~18,600 N). Mine grid in metres.

8.5 Immobile element characterisation

Immobile elements were used to determine the primary composition of the rocks at Gossan Hill. In general, the suite of elements demonstrated to remain immobile under greenschist facies metamorphism and hydrothermal alteration are; Ti, Zr, Y, Nb, Ga, P, REE, V, Cr, Sc, Hf Ta and Th (Winchester and Floyd, 1977). Furthermore, Ashley *et al.* (1988) and Whitford and Ashley (1992) demonstrated that Ti, V, Zr, Nb and Y remain immobile in alteration at the Scuddles deposit. At Gossan Hill, only those samples considered least altered are reviewed in this section (Appendix A6.1) and variation in immobile elements is tabulated in Table 8.2.

Table 8.2: Ranges in the immobile elements of the least altered rocks from the Gossan Hill deposit. Note: n = number of analyses, bx = breccia, sst = sandstone. Data listed in Appendix A6.1.

	SCF M2 (DAC3)	SCF M2 (RD2)	GGF M6 (bx & sst)	GGF M6 (tuffaceous sst)	GGF M5	GGF M4 (bx)	GGF M4 (tuffaceous sst)	GGF M1
n	11	10	7	3	7	2	6	10
TiO_2 (wt.%)	0.35-0.53	0.33-0.48	0.07-0.35	0.13-0.68	0.22-0.36	0.13-0.81	0.17-0.57	0.19-0.51
Al_2O_3 (wt.%)	13.5-14.8	10.5-15.4	1.3-13.0	5.4-12.4	9.3-11.4	5.07-16.4	6.9-18.1	4.9-15.2
Zr (ppm)	145-166	234-337	10-304	83-131	221-321	135-137	179-472	98-189
Nb (ppm)	4.1-6.5	88-13	bd-10.7	3.2-5.5	7.5-12.0	3.8-4.8	7.0-16.2	3.4-7.6
Y (ppm)	10-14	35-107	2-59	15-26	48-71	27-34	42-64	12-50
V (ppm)	49-86	21-35	2-92	6-209	bd-4	bd-242	bd-13	3-103
Cr (ppm)	27-89	16-13	3-65	4-88	2-3	2-42	2-4	2-104

The linear correlation of high field strength elements (HFSE) reflects the preservation of primary element ratios due to their immobility (*e.g.*, Whitford, *et al.*, 1992; MacLean and Barrett, 1993). At Gossan Hill Nb, Zr and Y are immobile, as demonstrated in Figure 8.2 by constant Y/Nb and Nb/Zr ratios that project through the origin. The DAC3 dacite, late dacite intrusions and GGF M1 all have lower Y, Nb and Zr values than the RD2 rhyodacite, GGF M4 and GGF M5 (Fig. 8.2). The wide variation of the Y/Nb and Nb/Zr ratios in breccia and sandstone of GGF M6, reflects their polymict lithology. Whitford and Ashley (1992) also identified variations in Zr/Nb ratios at the Scuddles deposit, with the 'Mineralised Horizon' having lower Zr/Nb ratios than the footwall or hangingwall. This trend is not observed at Gossan Hill due to the similar geochemistry of the DAC3 dacite and GGF M1, as well as overlap with GGF M6.

Although Al and Ti are considered immobile (Whitford *et al.*, 1989), in zones of extreme hydrothermal alteration proximal to volcanogenic mineralisation, these element have been demonstrated to be slightly mobile (Larson, 1984; Wynne and Strong, 1984). At Gossan Hill, Al_2O_3 and TiO_2 (Fig. 8.3) have a positive linear correlation, with clustered data for DAC3, RD2, GGF M1 and GGF M5, with higher Al_2O_3 and TiO_2 values broadly correlated to the uppermost members of the GGF. Dolerite intrusions do not lie on this linear trend, but have higher TiO_2 consistent with a mafic composition. The host members GGF M4 and GGF M6 have the widest spread in TiO_2 and Al_2O_3 values (Fig. 8.3) with some samples deviating from the main linear trend. This scatter in TiO_2 and

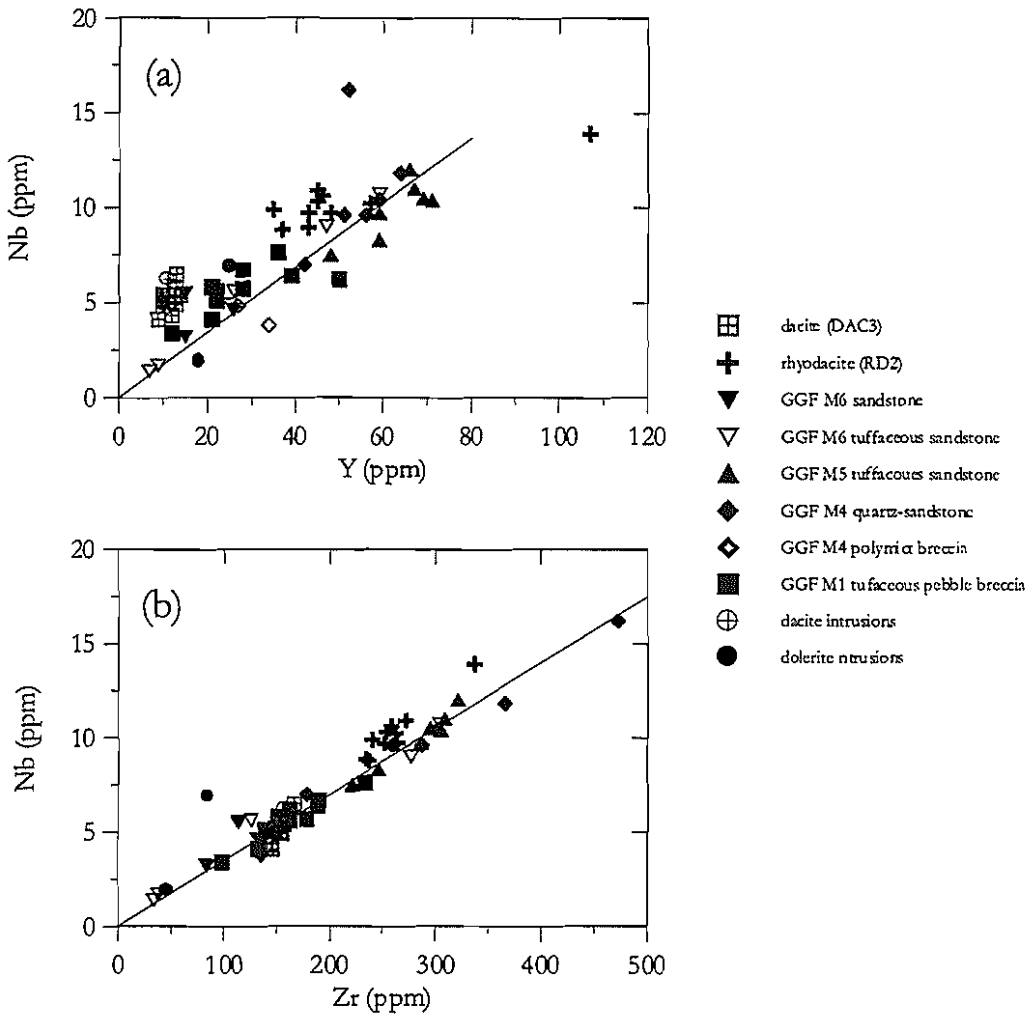

Figure 8.2: (a) Y *versus* Nb and (b) Zr *versus* Nb. The positive linear correlation in (a) and (b) indicate that primary Y/Nb and Zr/Nb ratios have been preserved. Plotted values are volatile free normalised. Raw data in Appendix A6.1.

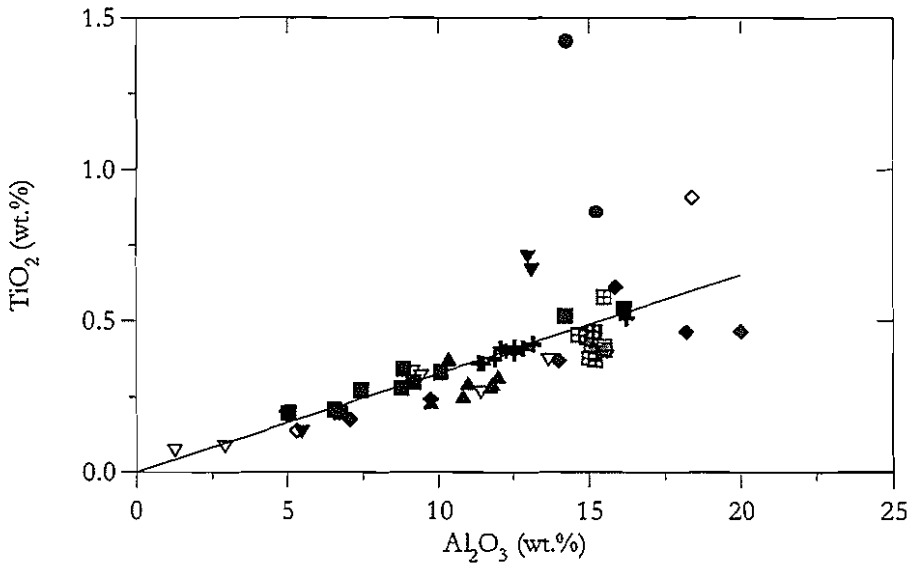

Figure 8.3: Al_2O_3 *versus* TiO_2 illustrating a broad positive linear correlation that indicates the preservation of primary ratios between these elements. Some variation off the linear trend is noted and may indicate that Al and Ti had limited mobility, particularly within GGF M4 and GGF M6. Plotted values are volatile free normalised. Symbols as in Figure 8.2.

Al_2O_3 values is interpreted to represent the local mobility of Al and Ti near sites of mineralisation. Petrographic evidence for the local mobility of Al_2O_3 is present in intense phyllosilicate altered zones (chlorite and chloritoid), that contain andalusite, and also as scattered ilmenite and rutile, which are common accessory minerals in intense chlorite alteration of the GGF. Moreover, GGF M6 commonly has low levels of TiO_2 and Al_2O_3, which may be caused by intense silicification, that lead to the localised leaching of Ti and Al.

Regional studies by Clifford (1992) on the GGF concur with results of this study. Clifford (1992) interpreted the localised mobility of Al as a result of intense hydrothermal alteration. Moreover, GGF M4 and GGF M6 host massive sulphide and, therefore, an initially constant TiO_2/Al_2O_3 ratio may have been partially modified by the local mobility of Al and Ti under extreme hydrothermal alteration related to mineralisation. However, the compositional clustering of data in other SCF and GGF stratigraphic members is an indication that TiO_2/Al_2O_3 ratios were not substantially modified away from massive sulphide.

Winchester and Floyd (1977) devised an immobile element discrimination diagram that characterises different rock types and their magmatic affinity, based on the assumption that the relative abundance of immobile trace elements are a function of magmatic differentiation. This diagram uses Zr/TiO_2 ratios as a differentiation index and Nb/Y ratios as an alkalinity index, and the least altered Gossan Hill samples (Appendix A6.1) are shown in Figure 8.4. With the exception of the late dolerite intrusions, most of the Gossan Hill samples lie within the rhyodacite-dacite field. The hangingwall dacite (DAC3) and rhyodacite (RD2) each form a distinct cluster, as do GGF M1, GGF M5 and GGF M4 (sandstone). The remainder samples (GGF M4 breccia, GGF M6 sandstone and breccia) have a range in composition, which indicates a primary variation likely due to their polymict lithology. Whitford and Ashley (1992) obtained similar results for the GGF at the Scuddles deposit. Both the GGF and SCF have a calc-alkaline geochemistry.

Whitford and Ashley (1992) identified a negative correlation between Zr and TiO_2 at Scuddles, however, this trend is absent from the Gossan Hill sample suite (Fig. 8.5). The Zr/TiO_2 ratios of DAC3 and RD2 have geochemically distinct clusters, with the late porphyritic dacite intrusions geochemically indistinct from the DAC3 dacite. Stratigraphically, the Ti/Zr ratio is constant in the SCF (Fig. 8.6), with a ratio of 10 for RD2 and 20 for DAC3. The Ti/Zr ratio increases up to 70 in the GGF, with elevated ratios correlated to massive sulphide in GGF M6 (Fig. 8.6). These rare high Ti/Zr ratios are likely related to the locally remobilisation of TiO_2 near massive sulphide (Fig. 8.6).

8.5.1 Immobile element geochemistry summary

At Gossan Hill, Nb, Y and Zr have evidence of immobility, whereas Ti and Al are considered to have locally remobilised near sites of massive sulphide. Immobile elements distinguish the hangingwall rhyodacite (RD2) from dacite (DAC3), with DAC3 having a composition that is transitional from dacite to andesite. The tuffaceous members of the GGF (GGF M1, GGF M4 and GGF M5) are rhyodacitic in composition, with each

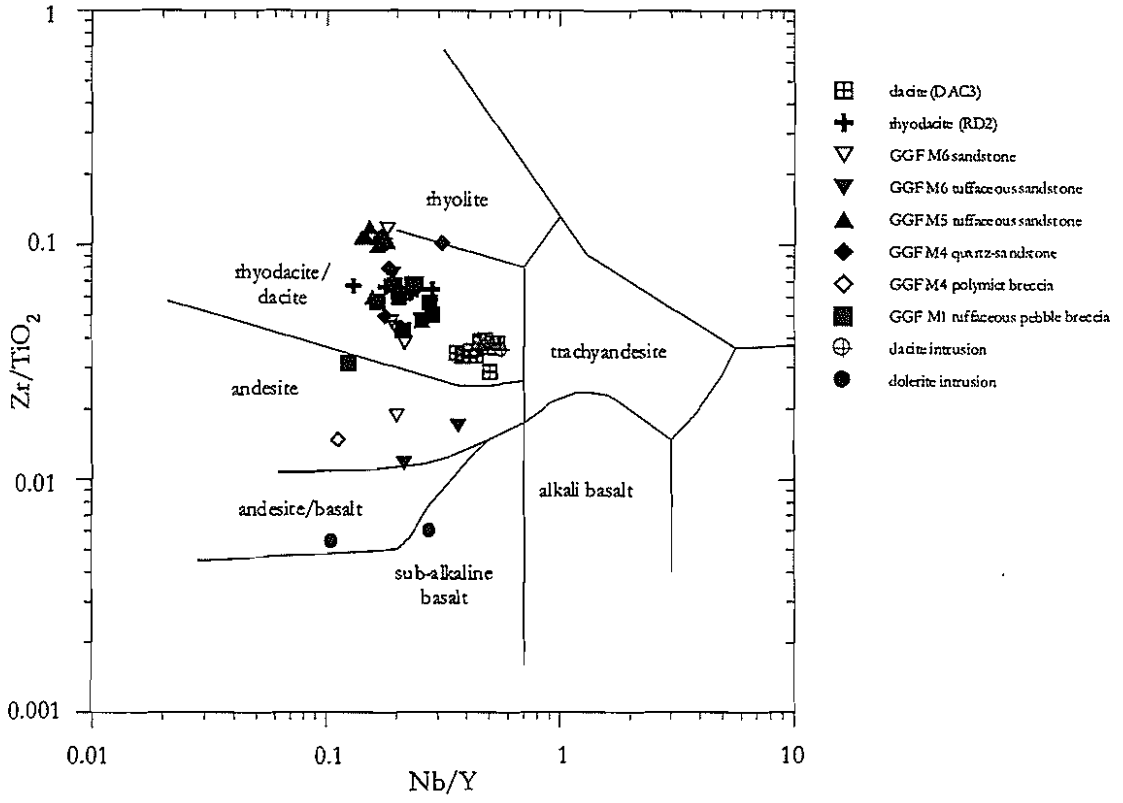

Figure 8.4: Nb/Y *versus* Zr/TiO_2 discrimination diagram after Winchester and Floyd (1977), illustrating the composition of the lithologies in the GGF and the SCF at Gossan Hill. The hangingwall rhyodacite (RD2) and dacite (DAC3) have narrow compositional variations. GGF M6 has a wide range of compositions. Data used is normalised to volatile free contents.

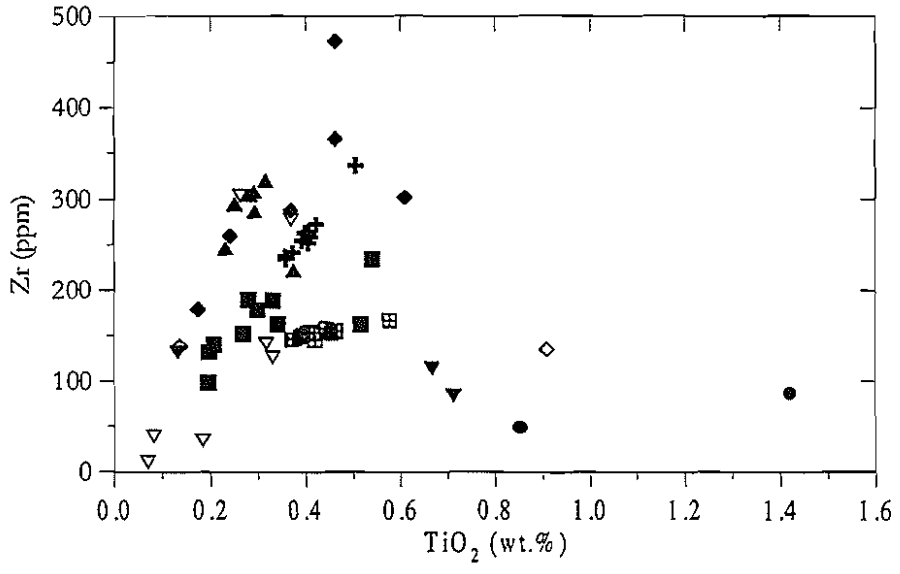

Figure 8.5: TiO_2 *versus* Zr illustrating the scatter of the data points. Scatter in TiO_2 is observed in GGF M6 and GGF M4 and is attributed to the mobility of TiO_2, as indicated by the disseminated occurrence of ilmenite-rutile througout these members. Symbols as in Figure 8.4. Data used is normalised to volatile free contents.

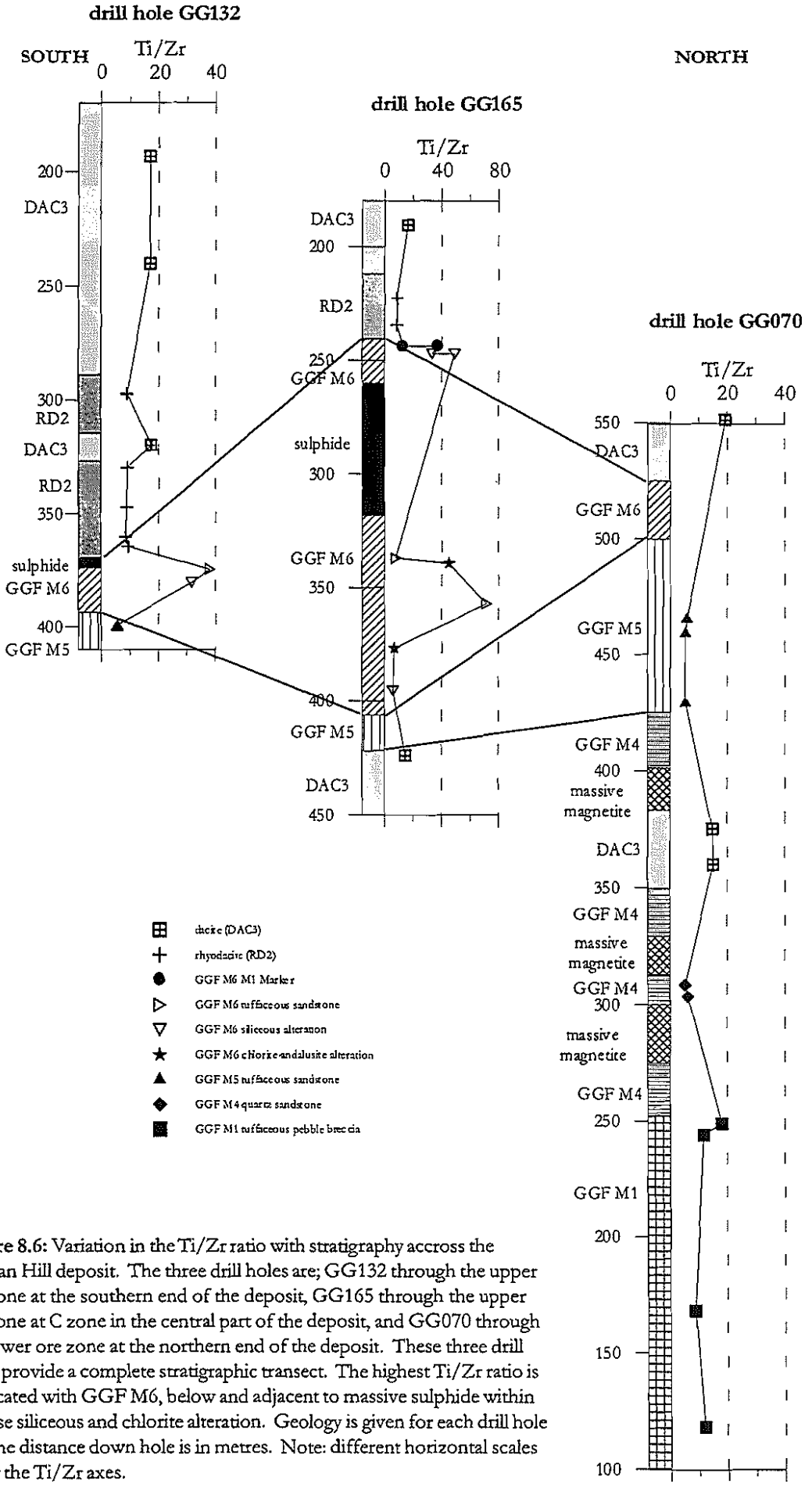

Figure 8.6: Variation in the Ti/Zr ratio with stratigraphy accross the Gossan Hill deposit. The three drill holes are; GG132 through the upper ore zone at the southern end of the deposit, GG165 through the upper ore zone at C zone in the central part of the deposit, and GG070 through the lower ore zone at the northern end of the deposit. These three drill holes provide a complete stratigraphic transect. The highest Ti/Zr ratio is assoicated with GGF M6, below and adjacent to massive sulphide within intense siliceous and chlorite alteration. Geology is given for each drill hole and the distance down hole is in metres. Note: different horizontal scales along the Ti/Zr axes.

having similar Nb/Y ratios. The similarity in Nb/Y ratios indicates that tuffaceous strata of the GGF are relatively homogeneous in composition. The scatter of Zr/TiO_2 in GGF M4 (breccia) and GGFM6 (sandstone and breccia) reflect compositional variation from andesite to rhyolite, which likely results from their polymict source.

8.6 Alteration geochemistry

Multiple hydrothermal stages are recognised at Gossan Hill (Chapter 7), and the whole rock geochemistry represents the bulk superposition of these chemical changes on the original composition of the rock. Alteration geochemistry in this chapter reviews the relative enrichment and depletion of mobile elements in the strata and alteration surrounding Gossan Hill. Samples used in this section include least altered (Appendix A6.1) and altered samples (Appendix A6.2).

8.6.1 Major element variations

Within hydrothermal alteration at greenschist facies metamorphism, the major oxides SiO_2, FeO, MgO, MnO, CaO, Na_2O and K_2O are mobile. As detailed in Chapter 7, the GGF has widespread replacement by quartz and chlorite during its alteration. Alteration minerals in the GGF comprise at least 80%, and up to 100% of the rocks. Although alteration is ubiquitous in the GGF, the distribution of the alteration minerals can be heterogeneous on a bed-scale. This means that the alteration is difficult to characterise geochemically.

The alteration surrounding the Gossan Hill deposit is characterised by changes in the relative abundance of quartz and chlorite. This alteration is strongly reflected by the whole rock SiO_2 and FeO contents of the GGF (Fig. 8.7a). A negative linear correlation between SiO_2 and FeO (Fig. 8.7a) not only highlights the wide variation in SiO_2 and FeO contents, but also that elevated SiO_2 corresponds to low FeO and *vice versa.* This linear trend (Fig. 8.7a) is interpreted in Figure 8.7b to delineate footwall (GGF M1) and host rock (GGF M4, GGF M5 and GGF M6) alteration, by changes in the relative abundances of quartz and chlorite. In comparison, the SiO_2 and FeO contents of the hangingwall rhyodacite and dacite are different from those of the GGF, and form a cluster separated from the main linear trend (Fig. 8.7b). Therefore, the alteration geochemistry of the SCF and the GGF are different.

The footwall GGF M1 and host rocks of GGF M6 are the most intensely silicified rocks (Figs. 8.7a), with SiO_2 levels ranging up to 86 wt.%. The intense chlorite alteration typical of alteration in GGF M4 contains high FeO (>20 wt.%) and low SiO_2 (<55 wt.%). However, intense Fe-rich alteration adjacent to massive sulphide and magnetite within GGF M4, deviates from the SiO_2-FeO linear trend, due to elevated FeO caused by disseminated sulphide and magnetite in the alteration (Fig. 8.7b). The average composition of chlorite (Chapter 7) is also plotted in Figure 8.7b for comparison. The compositional variation of chlorite is mainly in FeO and MgO and defines a subvertical trend (Fig. 8.7b). This chlorite trend defines a broad, but progressive FeO enrichment in chlorite from the hangingwall to the footwall. The apparent antithetic trend in chlorite composition with respect to the negative SiO_2-FeO trend is consistent with the low FeO

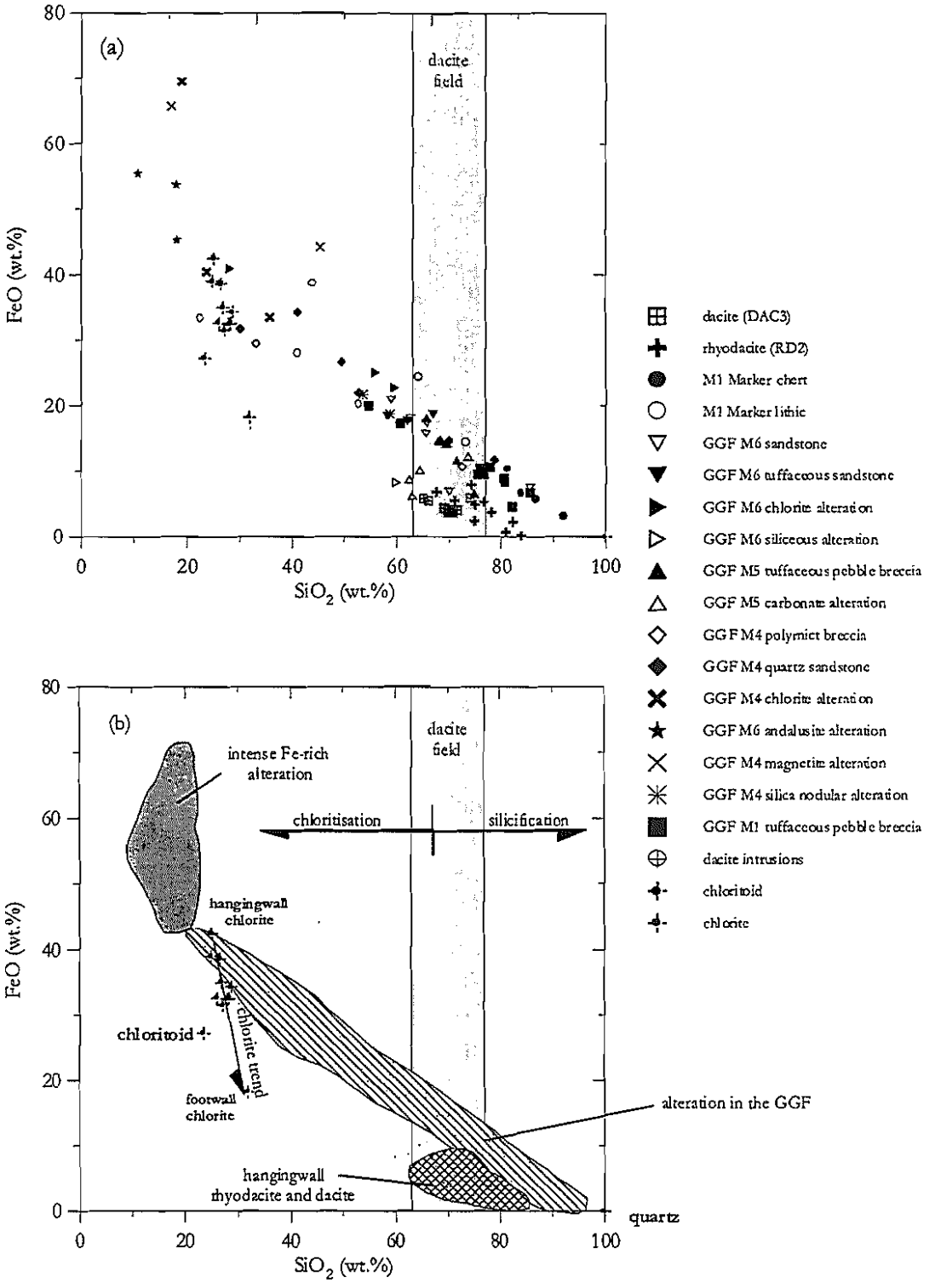

Figure 8.7: (a) SiO_2 *versus* FeO illustrating the distribution of SiO_2 and FeO in least altered and altered samples at Gossan Hill. Data normalised to volatile free contents. (b) Interpretation of (a). Samples in the GGF (M1, M4, M5 and M6) define a negative linear trend that reflects the relative proportions of FeO in chlorite and SiO_2 in quartz and chlorite. The compositions of chorite from Gossan Hill are also plotted and define a trend (arrow). The hangingwall SCF volcanics have little variation in SiO_2 and FeO and define a field that lies below the main linear trend in the GGF. Intense FeO enrichment occurs in some samples from GGF M4 due to disseminated sulphide and magnetite in these samples, as lie above the main SiO_2-FeO linear trend of the GGF.

contents in the footwall GGF M1. In addition, the lack of chlorite in the hangingwall is consistent with the relatively constant FeO contents of these rocks. Moreover, siliceous alteration is minor in the hangingwall, with the higher SiO_2 contents of rhyodacite with respect to dacite consistent with a primary compositional variation.

Whole rock MgO values in the sample suite range from 0.05 to 15.9 wt.% and the compositional variation of chlorite and carbonate is plotted for comparison in Figure 8.8a. The SiO_2 and MgO contents of RD2, DAC3, GGF M1, GGF M6 and GGF M5 are negatively correlated (Fig. 8.8a). This negative trend reflects a change from MgO-bearing chlorite in GGF M4 (high whole rock MgO) to more Fe-rich chlorite (low whole rock MgO) toward the hangingwall. High whole rock MgO content is therefore, associated with intense chlorite alteration in GGF M4 and carbonate alteration (*e.g.*, GGF M5). The MgO content in carbonate ranges up to 17.5 wt.% and approximates the upper range of whole rock MgO values. Nonetheless, the composition of chlorite and its abundance is likely the main controlling factor for the negative MgO-SiO_2 trend. Moreover, rocks that have high SiO_2 contents (>55 wt.%) have minor chlorite-carbonate alteration, which is indicated by low whole rock MgO contents (*c.f.* Figs. 8.7 and 8.8a).

At Gossan Hill, the GGF and SCF have MnO values generally less than 0.4 wt.% (Fig. 8.8b), but range up to 1.02 wt.%. The MnO contents of these rocks do not correlate with SiO_2. Instead elevated MnO contents occur within the chlorite-carbonate altered beds of the M1 Marker in GGF M6. The MnO content of chlorite and carbonate (plotted on Figure 8.8b) have a narrow range for chlorite (0.02 to 0.29 wt.%) and a higher range for carbonate (0.7 to 12.7 wt.%). This suggests that the main MnO contribution is due to carbonate alteration.

A positive whole rock FeO and MgO correlation (Fig. 8.8c) suggests that the abundance and composition of chlorite is a major control on the geochemistry of the GGF. Whole rock analyses in Figure 8.8c have a broad linear FeO-MgO trend through the origin, indicating a relatively constant FeO-MgO ratio. Samples that have high FeO contents due to disseminated sulphide and magnetite, deviate from this linear trend. Similarly, samples with high MgO above this linear trend are carbonate (high Mg) altered. The hangingwall rhyodacite and dacite have low MgO and FeO levels and plot near the origin (Fig. 8.8c). The composition of chlorite (plotted in Fig. 8.8c) has a linear decrease in MgO that correlated with increasing FeO (Fig. 8.8d). This change in chlorite composition represents the transition from the footwall to the hangingwall, with rocks along this trend intensely chlorite altered.

Carbonate compositions are transitional from Mg-rich carbonate in the hangingwall to relative Fe-rich carbonate in GGF M4 (Fig. 8.8c). Alteration proximal to mineralisation in the GGF is therefore characterised by increasing FeO and MgO whole rock contents toward mineralisation as a result of chlorite-carbonate alteration. This alteration in turn corresponds to a decreasing SiO_2 trend with increasing FeO and MgO, as a result of compositional changes in chlorite and to a lesser extent, carbonates. This interpretation is illustrated in Fig. 8.8d.

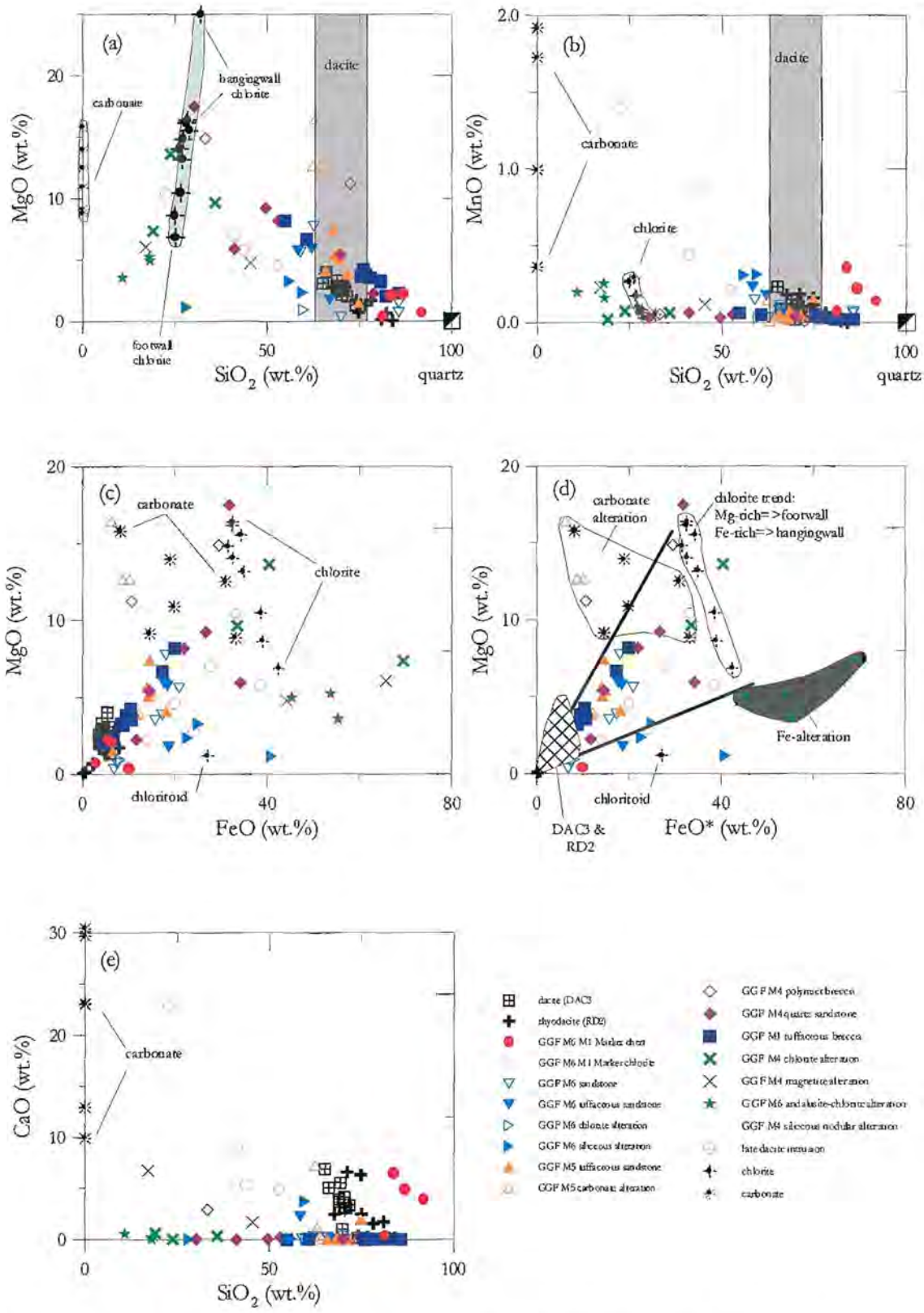

Figure 8.8: Whole rock analyses of least altered and altered samples from Gossan Hill, illustrating the distribution of MgO, MnO and CaO. The distribution of these elements reflects the relative abundances of chlorite and carbonate in alteration. (a) Negative correlation between MgO and SiO_2, with the range in MgO values similar to the range in chlorite compositions, (b) SiO_2 *versus* MnO illustrating the generally low MnO values in the whole rock data, but elevated MnO in carbonate and carbonate-altered samples, (c) FeO *versus* MgO showing a positive correlation of whole rock data, (d) interpretation of (c) with chlorite and carbonate composition fields indicated, and (e) SiO_2 *versus* CaO illustrating the generally low whole rock CaO contents of rocks in the GGF, with elevated CaO in the rhyodacite (RD2) and dacite (DAC3) of the hangingwall SCF.

Whole rock CaO ranges up to 6.37 wt.% (Fig. 8.8e). Higher CaO values occur in GGF M4 and are associated with magnetite alteration. High CaO also occurs in the hangingwall dacite and rhyodacite and chert and chlorite beds in the M1 Marker. The dacite has higher CaO contents than the rhyodacite. The variation in CaO whole rock values reflects the dominance of calcite alteration in the hangingwall and scattered ankerite through alteration in the GGF (Chapter 7). However, the widespread depletion in CaO contents of the GGF also reflects the absence of feldspar in this formation.

At the Scuddles deposit, Ashley (1983) defined a geochemical alteration trend within the GGF, based on the mobility of FeO, MgO and (K_2O+Na_2O). The alteration trend at Scuddles was defined by FeO enrichment towards ore, however, at Gossan Hill, this trend is absent (Fig. 8.9). Figure 8.9 demonstrates the widespread depletion in Na_2O and K_2O within the GGF at Gossan Hill, with strong relative enrichment in FeO. Only two rhyodacite analysis have higher Na_2O+K_2O relative to FeO and MgO (Fig. 8.9), which are caused by elevated SiO_2 due to siliceous alteration, rather than high Na_2O and K_2O contents in rhyodacite. In addition, the alteration trend defined by Ashley (1983) at Scuddles depicts a gradual, but intense enrichment in FeO towards the massive sulphide (Fig. 8.9). This trend is not present in the geochemistry of the GGF at Gossan Hill, with these samples having uniform, intense depletion in Na_2O and K_2O, and relative enrichment in FeO. Therefore, Figure 8.9, indicates that the GGF at Gossan Hill has a relatively uniform alteration characterised by Fe-enrichment and intense Na_2O and K_2O depletion. Moreover, this style of alteration is not present in the hangingwall volcanics.

Many alteration geochemical studies of VHMS deposits use alteration indices to characterise the intensity and style of alteration. Examples include the Ishikawa Index (Ishikawa *et al.*, 1976), the chlorite index (Large *et al.*, 1996) and the Mn-carbonate index (Large *et al.*, 1996). Alteration indices use element ratios to highlight the relative depletion and enrichment of whole rock oxides within hydrothermal alteration surrounding VHMS deposits. The indices cited above specifically use Na_2O and K_2O in the index, as alteration in many VHMS deposits commonly contain feldspar and muscovite. Typically, alteration surrounding massive sulphides is associated with feldspar destruction (Na_2O depletion) and muscovite alteration (K_2O enrichment) (*e.g.*, the Kuroko deposits in Date *et al.*, 1983).

Feldspar and muscovite are common minerals of the hangingwall SCF, however, the GGF lacks feldspar and contains scattered, but minor muscovite alteration. Therefore, the application of the Ishikawa, chlorite and Mn-carbonate indices is limited, due to the use of Na_2O and K_2O within these indices. To characterise alteration at Gossan Hill, an index that does not incorporate Na_2O and K_2O in the discriminant must be used, and in place, elements that are compatible within the main alteration minerals, chlorite and carbonate, can be used.

The index used in this study is termed the chlorite-carbonate index (CCI) and is defined as:

$$\text{chlorite-carbonate index (CCI)} = \frac{100(0.5FeO+MgO)}{(0.5FeO+MgO+2CaO+2MnO)}$$

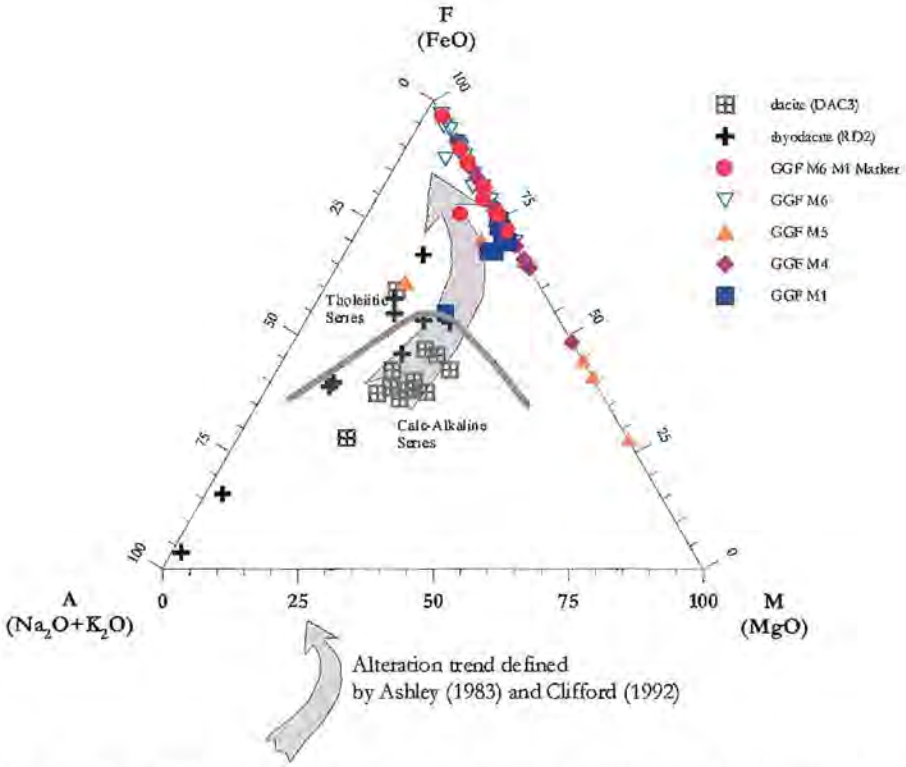

Figure 8.9: The AFM (Na_2O+K_2O-FeO-MgO) diagram used by Ashely (1983) and Clifford (1992) to infer alteration trends at the Scuddles deposit. Gossan Hill analyses have depletion in Na_2O+K_2O, and intense FeO enrichment. The alteration trend defined by Ashley (1983) (arrow) is not applicable to the altered GGF at Gossan Hill. Instead, intense FeO enrichment is indicated. The calc-alkaline and tholeiitic series trend is defined from Irvine and Baragar (1971). Note: only the lithology of samples is indicated in this plot for simplification.

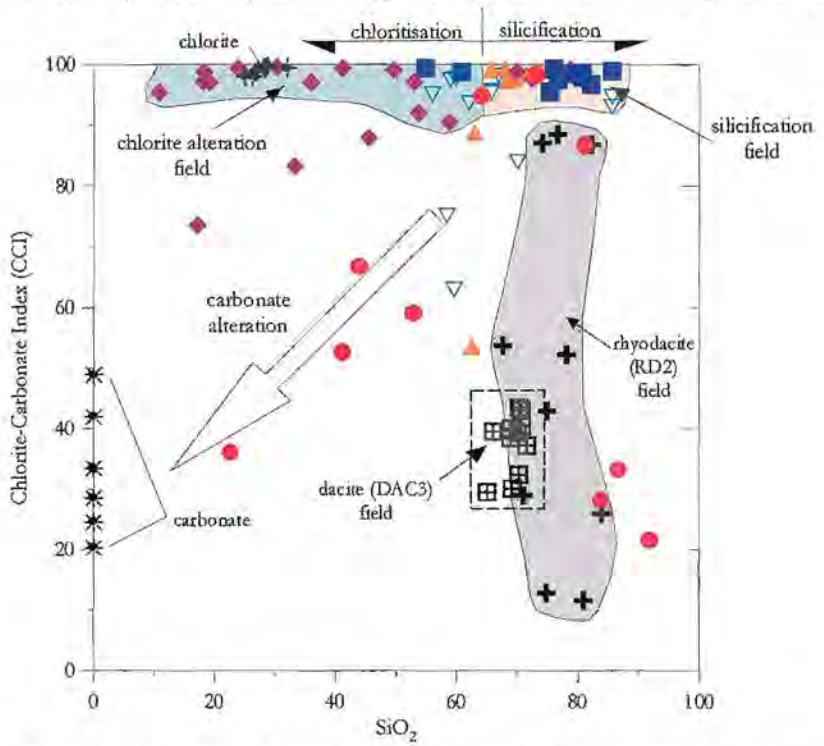

Figure 8.10: Distribution of the chlorite-carbonate index (CCI) *versus* SiO_2 at Gossan Hill. The CCI is defined as 100(0.5FeO+MgO)/(0.5FeO+MgO+2CaO+2MnO). This index does not use K_2O and Na_2O in the discriminant due to intense depletion of these elements throughout the GGF. The CCI uses elements in the main alteration minerals to indicate alteration trends at Gossan Hill. Silicification and chloritisation in the GGF have high CCI indices (>90) and SiO_2 contents that are greater than 60 wt.% and less than 60 wt.% respectively. Carbonate alteration in the GGF and the hangingwall SCF have a range in CCI values between 10 to 90. In general, the hangingwall SCF has higher SiO_2 contents than carbonate alteration in the GGF. Dacite (DAC3) has a more tightly constrained field in both CCI and SiO_2 than rhyodacite (RD2), indicating that the rhyodacite has relatively stronger carbonate alteration than the dacite. Legend and symbols as given in Figure 8.9.

As SiO_2 has major abundances in the whole rock geochemistry of the GGF at Gossan Hill, it is not used in the CCI. Figure 8.10 illustrates SiO_2 *versus* CCI, which differentiates between alteration in the hangingwall (SCF M2) and chlorite-carbonate alteration of the GGF. Within the hangingwall, alteration is less intense in DAC3 than in RD2, due to the higher spread in RD2 data (Fig. 8.10). Carbonate alteration is represented by intermediate CCI ratios (20-80), whilst chlorite alteration is represented by high CCI ratios (>80). The composition of chlorite and carbonate minerals at Gossan Hill is also plotted in Figure 8.10 for comparison.

8.6.2 Down hole variations

The geochemistry of three drill holes (GG132, GG165 and GG070) was investigated to examine stratigraphic alteration trends. Drill hole GG132 is an intercept through the southern end of Gossan Hill (17,766 N), GG165 intersects massive Zn-rich sulphides at C zone and GG070 intersects Cu-rich massive sulphide and massive magnetite (18,688 N). Although these drill holes only intersect part of the stratigraphy, they provide a complete stratigraphic transect through alteration, massive sulphide and massive magnetite of the Gossan Hill deposit.

Drill hole GG132 (Fig. 8.11) intersects the hangingwall DAC3 dacite and RD2 rhyodacite, as well as GGF M6 and GGF M5. The distribution of major elements through this sequence is characterised by decreases in SiO_2, and strong enrichment in FeO, MgO and MnO contents toward the massive sulphides in GGF M6. The CaO levels become weakly elevated adjacent to the hangingwall-GGF contact, whilst Na_2O and K_2O are intensely depleted through the GGF.

Drill hole GG165 (Fig. 8.12) intersects the SC2 volcanics and cuts a thick sequence of massive sulphide in GGF M6, terminating in the DAC3 dacite (Chapter 3). GG165 has similar major element variations to GG132, with a decrease in SiO_2 and increase in FeO, MgO, MnO and CaO proximal to the hangingwall-GGF contact. The DAC3 dacite at the base of the drill hole has similar major element abundances to DAC3 dacite in the hangingwall. Altered GGF M6 underlying massive sulphide has variable, elevated SiO_2, which corresponds to high, but variable FeO contents. MgO, MnO, CaO, Na_2O and K_2O have ubiquitous depletion in GGF M6 and GGF M5, with Na_2O levels below detection.

Drill hole GG070 (Fig. 8.13) intersects DAC3 dacite, the GGF from GGF M5 to GGF M1 and massive sulphide and magnetite within GGF M4. The footwall GGF M1 has constant SiO_2 contents, but slight increases in FeO, MgO and MnO towards the GGF M4 contact and massive sulphide and magnetite. GGF M1 is depleted in CaO, Na_2O and K_2O. GGF M4 has similar major element distributions to GGF M1, with the exception of a marked depletion in SiO_2 and enrichment in FeO, which reflects the increased abundance of chlorite in GGF M4. GGF M5 has relatively constant SiO_2, MgO and CaO, with slight increases in MnO and FeO with distance from underlying GGF M4. The dacite intrusion in GG070 has similar major element contents to those in GG132 and GG165.

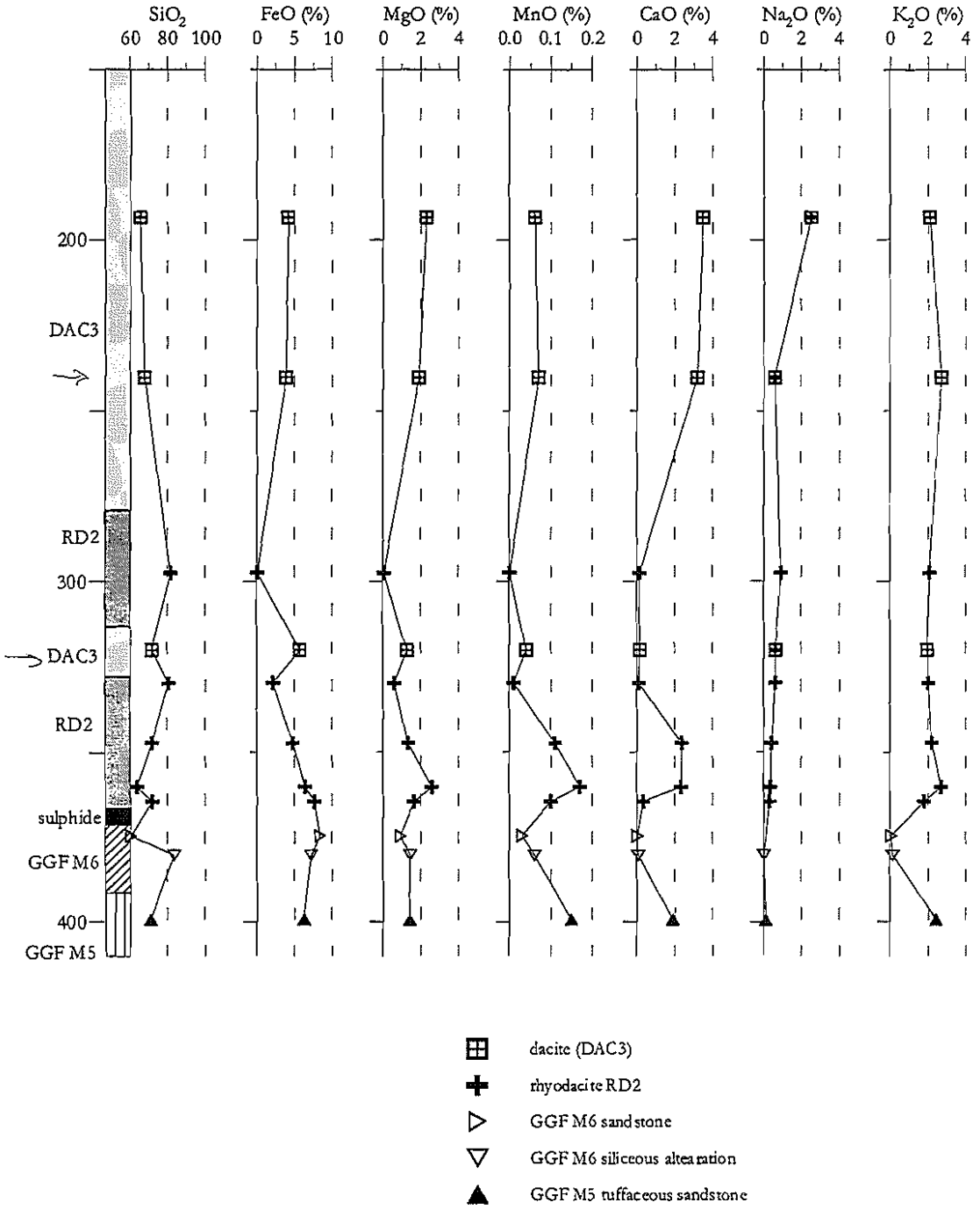

Figure 8.11: Down hole variation of major element data along GG132 at the southern end of the Gossan Hill deposit.

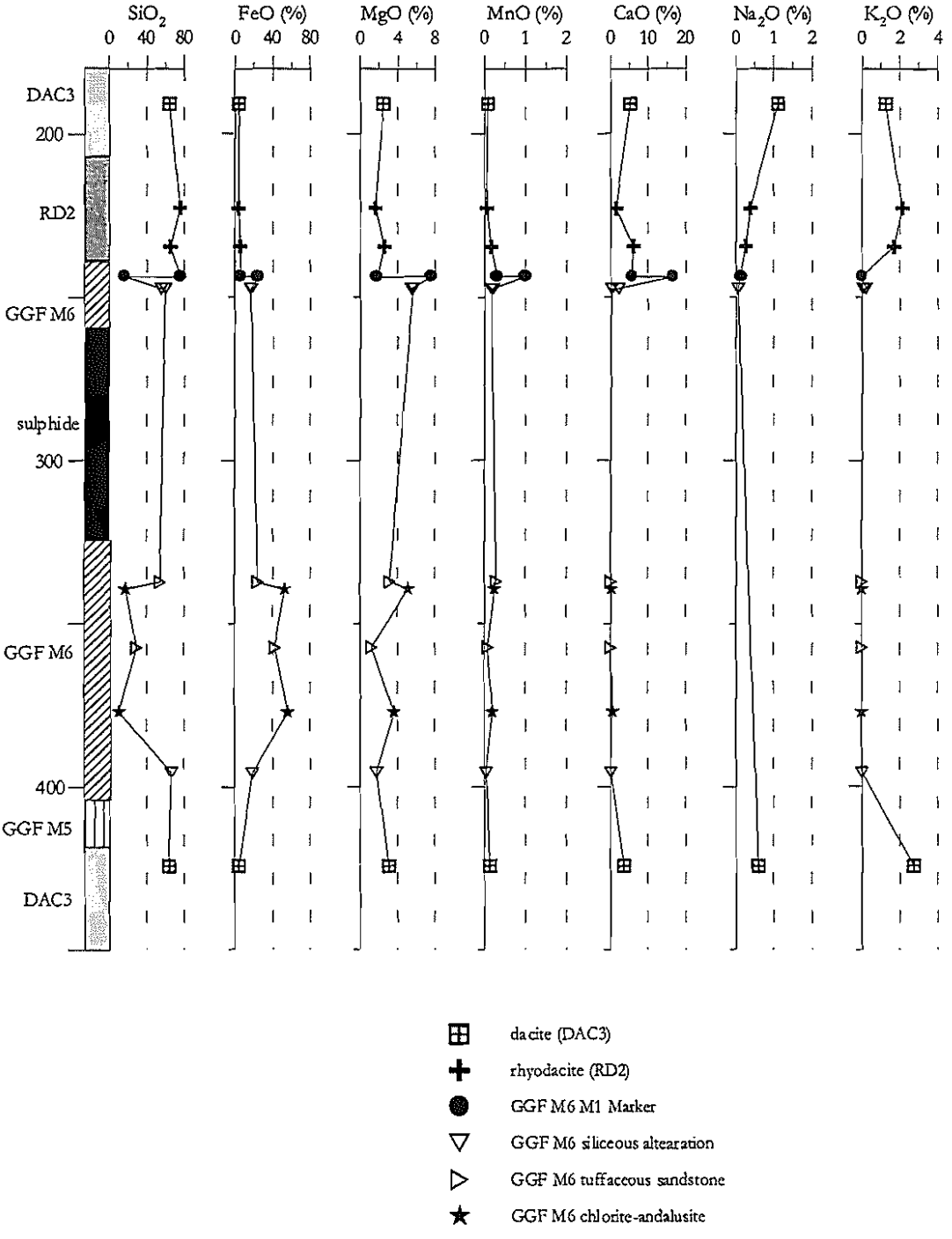

Figure 8.12: Down hole variation of major element data along GG165 through the central parts of the upper ore zone (C zone) at the Gossan Hill deposit.

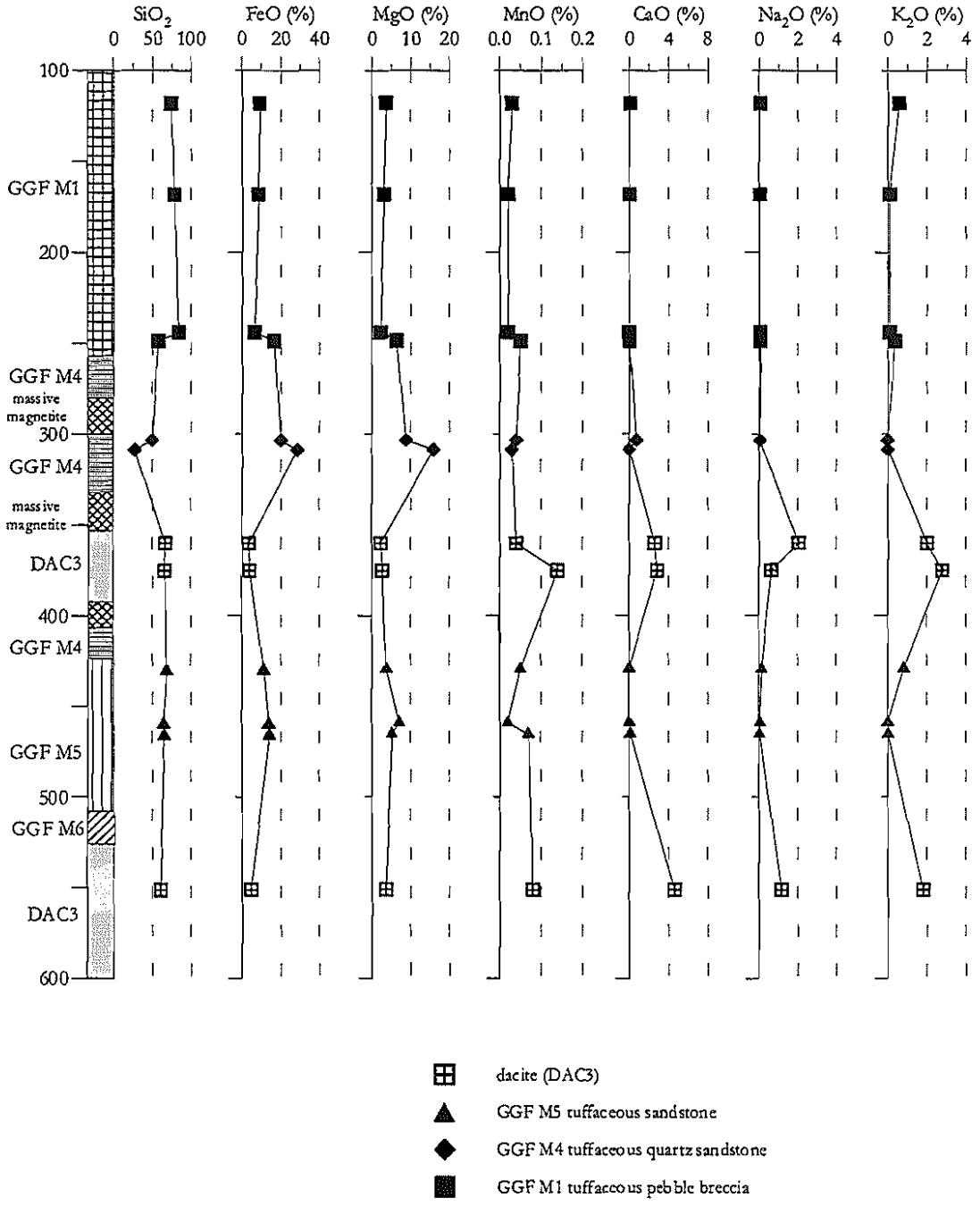

Figure 8.13: Down hole variation of major element data along GG070 through Cu-rich stringer veins and massive magnetite in GGF M4 at the northern end of the Gossan Hill deposit. Values below detection are not plotted.

8.6.3 Summary of major element geochemistry

Major element geochemical patterns at Gossan Hill reflect the distribution of the alteration minerals quartz, chlorite and carbonate. Changes in the relative proportion of these minerals and their composition affect the major element geochemistry. Widespread depletion in Na_2O and K_2O is observed throughout the GGF, and reflects the absence of feldspar in this formation and minor muscovite alteration. The correlation between SiO_2, FeO, MgO and, to a lesser extent, MnO, is due to intense quartz and chlorite alteration. In addition, the correlation between FeO and MgO is largely the result of changes in chlorite composition from Mg-bearing chlorite in the footwall to Fe-rich chlorite in the hangingwall. Carbonate alteration also contributes to this variation, with siderite-ankerite in GGF M4 and more calcic carbonates in GGF M5, GGF M6 and SCF M2. The SiO_2 contents are elevated in GGF M6, GGF M5 and GGF M1, which results from widespread siliceous alteration. The higher SiO_2 contents in these units contrast with the lower SiO_2 contents in GGF M4, due to the predominance of chlorite alteration in GGF M4.

Alteration adjacent to massive sulphide and massive is characterised by high FeO contents due to disseminated sulphide, magnetite and Fe-rich chlorite. Hangingwall volcanics (SCF M2) have lower FeO contents, with gradual MgO and MnO enrichment proximal to the contact with the GGF. This trend reflects the absence of chlorite in hangingwall (SCF M2) and the dominance of calcite-muscovite alteration, as characterised by elevated CaO and K_2O contents. Decreasing Na_2O from the SCF toward the GGF reflects the destruction of feldspar by this alteration.

8.6.4 Trace element variations

The trace elements Sr, Ba, Sn, Cu, Pb, Zn, Ni, and Rb were analysed by XRF, and are tabulated in Appendix A6.1 and A6.2. The Ba contents are highest in the hangingwall SCF M2 (Fig. 8.14a), with average contents of 420 ppm and 295 ppm for dacite and rhyodacite respectively. Moreover, late porphyritic dacite intrusions have the highest concentrations of Ba (up to 1288 ppm) (Fig. 8.14a). Elevated Ba in the hangingwall SCF M2 is also associated with elevated Sr and Rb (*c.f.* Figs. 8.14a and 8.14b). In turn, elevated Sr corresponds to elevated CaO values (Fig. 8.14c). The elevated Ba, Sr and Rb contents of the hangingwall volcanics likely reflect the presence of these elements in feldspar. In comparison the GGF has low Ba, Sr and Rb contents (Figs. 8.14a and 8.14b). Minor Ba, Sr and Rb enrichment is, however, observed in GGF M1 where Ba, Sr and Rb range up to 246 ppm, 42 ppm and 31 ppm respectively.

The association between Cu, Zn, Pb, Ni and Sn at Gossan Hill is illustrated in Figure 8.14. The average Zn content of massive sulphide in GGF M6 is 12 wt.%, however the adjacent siliceous alteration has Zn levels of up to 850 ppm. Similarly, Cu-rich massive sulphides in GGF M4 have an average Cu grade of 2 wt.% and up to 612 ppm in the adjacent chlorite alteration zone (Fig. 8.14d). Cu and Zn (Fig. 8.14d) have elevated values throughout GGF M6, whilst elsewhere, Cu is below 100 ppm and Zn below 1000 ppm. GGF M4 has higher Zn contents than Cu, despite its host relation to Cu-rich

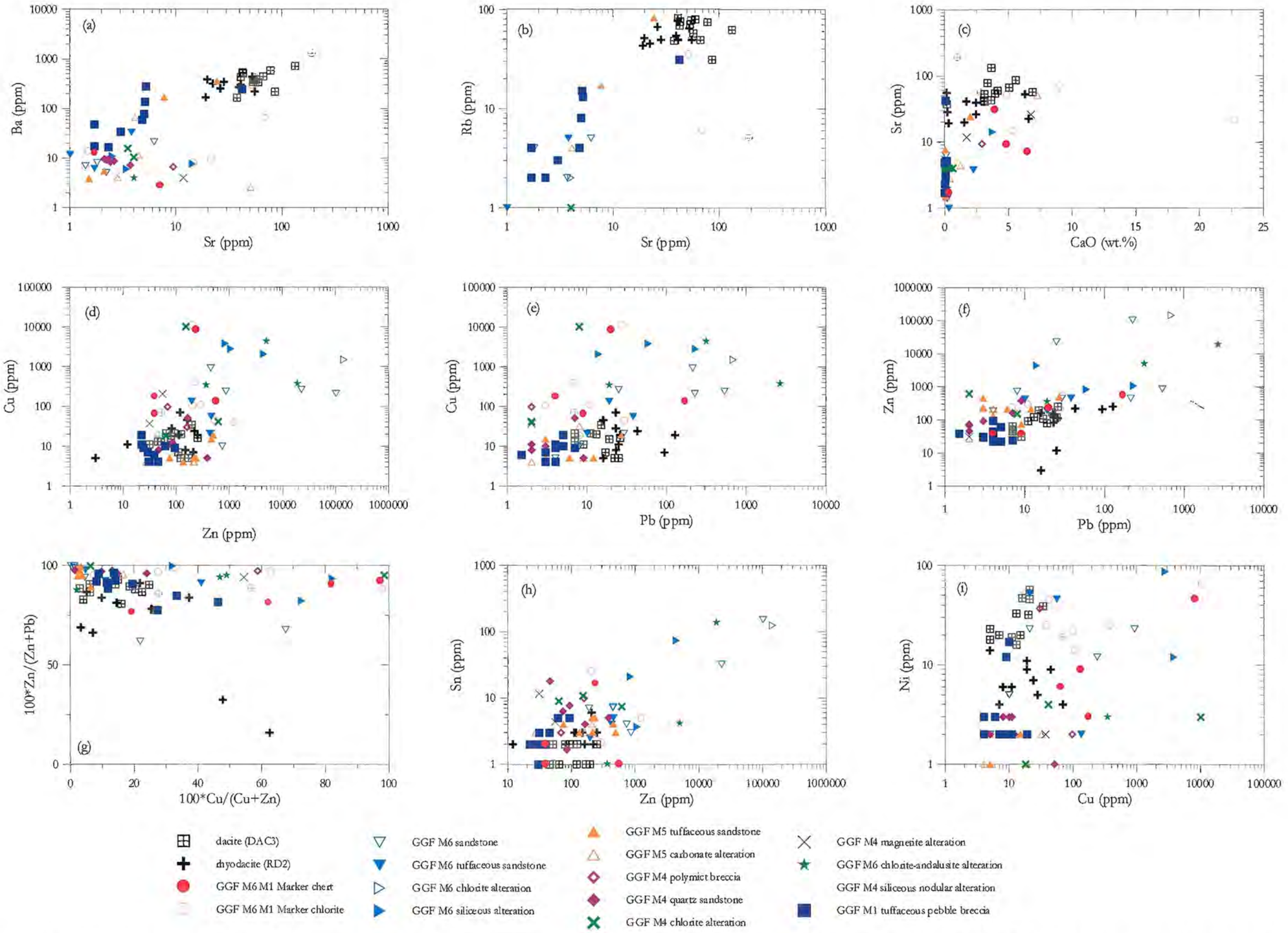

Figure 8.14: Variation diagrams of trace element XRF data. The samples include altered and least altered samples from the GGF and the SCF at Gossan Hill. (a) Sr *versus* Ba, (b) Sr *versus* Rb, (c) CaO *versus* Sr, (d) Zn *versus* Cu, (e) Pb *versus* Cu, (f) Pb *versus* Zn, (g) Cu ratio (100Cu/(Cu+Zn)) *versus* Zn ratio (100Zn/(Zn+Pb), (h) Zn *versus* Sn, and (i) Cu *versus* Ni. Values below detection are not plotted. Note: elevated Sr and Ba values in rhyodacite (RD2) and dacite (DAC3) (8.14a), elevated Sr and Rb values in rhyodacite (RD2) and dacite (DAC3) (8.14b), high CaO and Sr values in rhyodacite (RD2) and dacite (8.14c), high Zn, Pb and Cu values in GGF M6 (8.14d, 8.14e and 8.14f), the variation of Cu and Zn ratios in the GGF and SCF (8.14g), high Sn, Ni and Cu values in GGF M6 (8.14h and 8.14i).

mineralisation (Fig. 8.14d). The distribution of Pb (Figs. 8.14e and 8.14f) is similar to Zn, with high Pb (up to 688 ppm) within for GGF M6, and less than 30 ppm elsewhere in the GGF. The lowest Pb values (<8 ppm) occur within the footwall GGF M1 and within chlorite alteration of GGF M4. At Gossan Hill, the zinc ratio (100*Zn/(Zn+Pb)) in altered rocks generally has values above 75, except for two samples of RD2 rhyodacite (Fig. 8.14g). This indicates the higher levels of Zn relative to Pb throughout the GGF (Fig. 8.14g). Comparatively, the copper ratio (100*Cu/(Cu+Zn)) has a wide spread (0 to 100). Unmineralised altered wall rocks typically have a copper ratio of less than 50, due to the higher Zn contents relative to Cu (*e.g.,* Fig 8.14d). In addition, high Zn contents correspond to high Sn and Ni in GGF M6 (Figs. 8.14h and 8.14i respectively).

8.6.5 Down hole variation of trace elements

Ba, Sr and Rb decrease down hole (GG132, Fig. 8.15) through the hangingwall SCF (over 150 m) toward to the GGF contact and massive sulphide. In the GGF M6, Sn is correlated to elevated Zn, Pb, Cu and Zn ratios. Rhyodacite and dacite have low Zn and Cu contents, but have a slight increase in Pb content proximal to the GGF contact (over 50 m. GG165 (Fig. 8.16) has decreasing Sr, Rb and Ba in the hangingwall volcanics near the GGF contact. Sn has low values throughout drill hole GG165, with the exception of a single anomalous sample in GGF M6, underlying massive sulphide. This sample also has anomalous Zn, Pb and Cu. Massive sulphide and alteration through GGF M4 (Fig. 8.17) has general trace element depletion, as does the footwall GGF M1. However, minor elevated values of Zn and Sn occur in some samples from GGF M4.

8.6.6 Trace element summary

Ba, Sr and Rb contents are highest in the hangingwall SCF M2 and likely trace elements in feldspar. Decreasing trends in these elements proximal to the GGF contact likely result from feldspar alteration. Ba, Sr and Rb have consistently low values throughout the GGF. The highest Cu and Zn values in altered samples occurs within GGF M6, below massive sulphide, whilst GGF M4 has scattered anomalous Zn values (up to 1000 ppm) relative to Cu (100 ppm). The highest Pb contents are correlated to the highest Zn contents in GGF M6, with the footwall GGF M1 having the lowest abundance in Pb of samples from the GGF.

8.7 ICPMS data

The trace elements Ag, As, Bi, Mo, Cd, Sb, Cs, Tl, Th and U were analysed by ICP-MS. This suite of elements was investigated as part of the CODES AMIRA P439 project (Final Report, May 1998) in order to evaluate low level anomalism in alteration adjacent to VHMS deposits.

The results from ICP-MS analyses are given in Appendices A6.1 and A6.2. Of the elements analysed, Tl is universally below detection at Gossan Hill, whilst Bi, Cd and As are also generally below detection, but have a few scattered values. The Th/U ratio is relatively constant throughout the GGF (average of 4), with some lower values within intense chlorite-andalusite altered zones below C zone (Fig 8.18a). The Sb levels in the

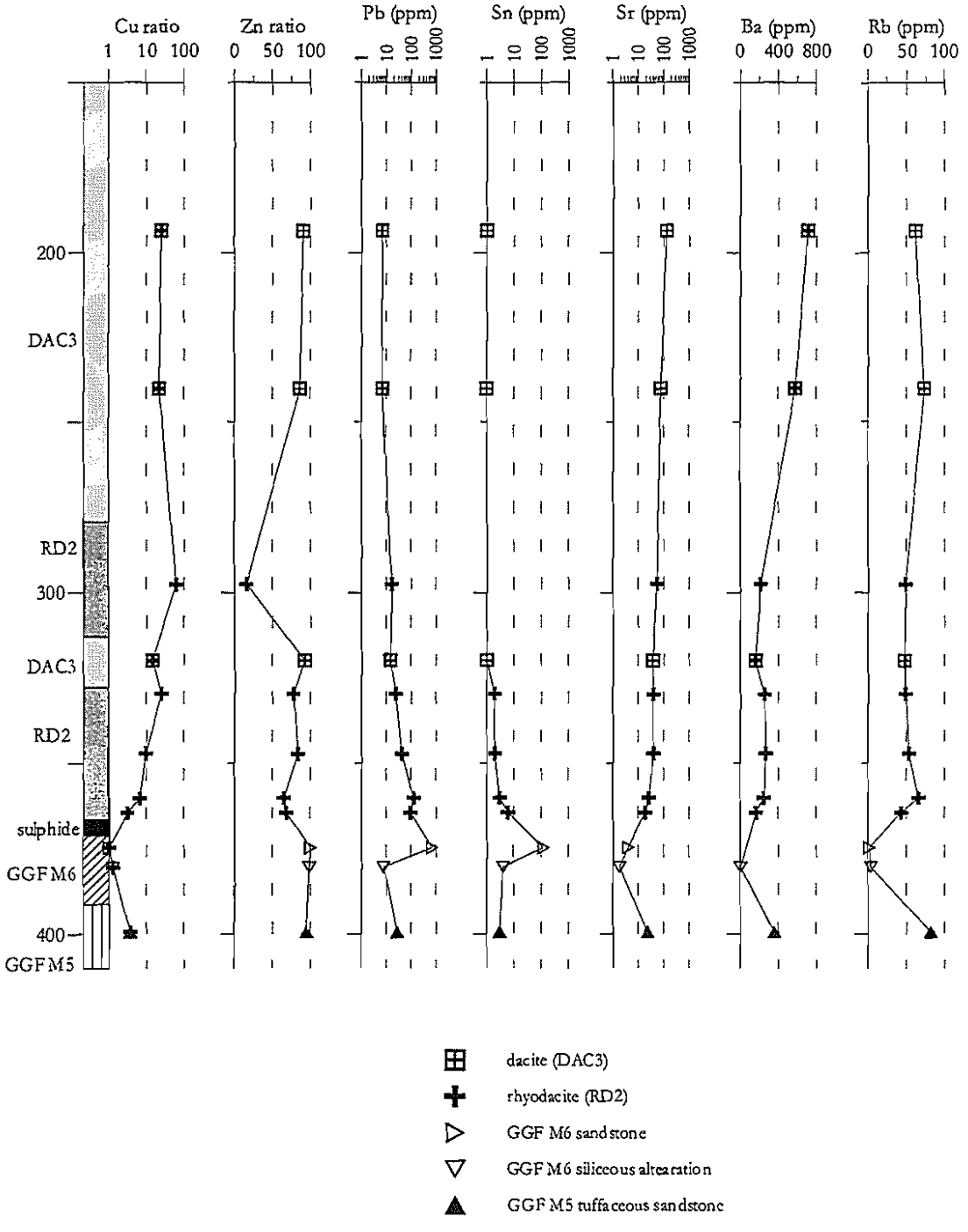

Figure 8.15: Down hole variation of XRF trace element data along GG132 at the southern end of the Gossan Hill deposit.

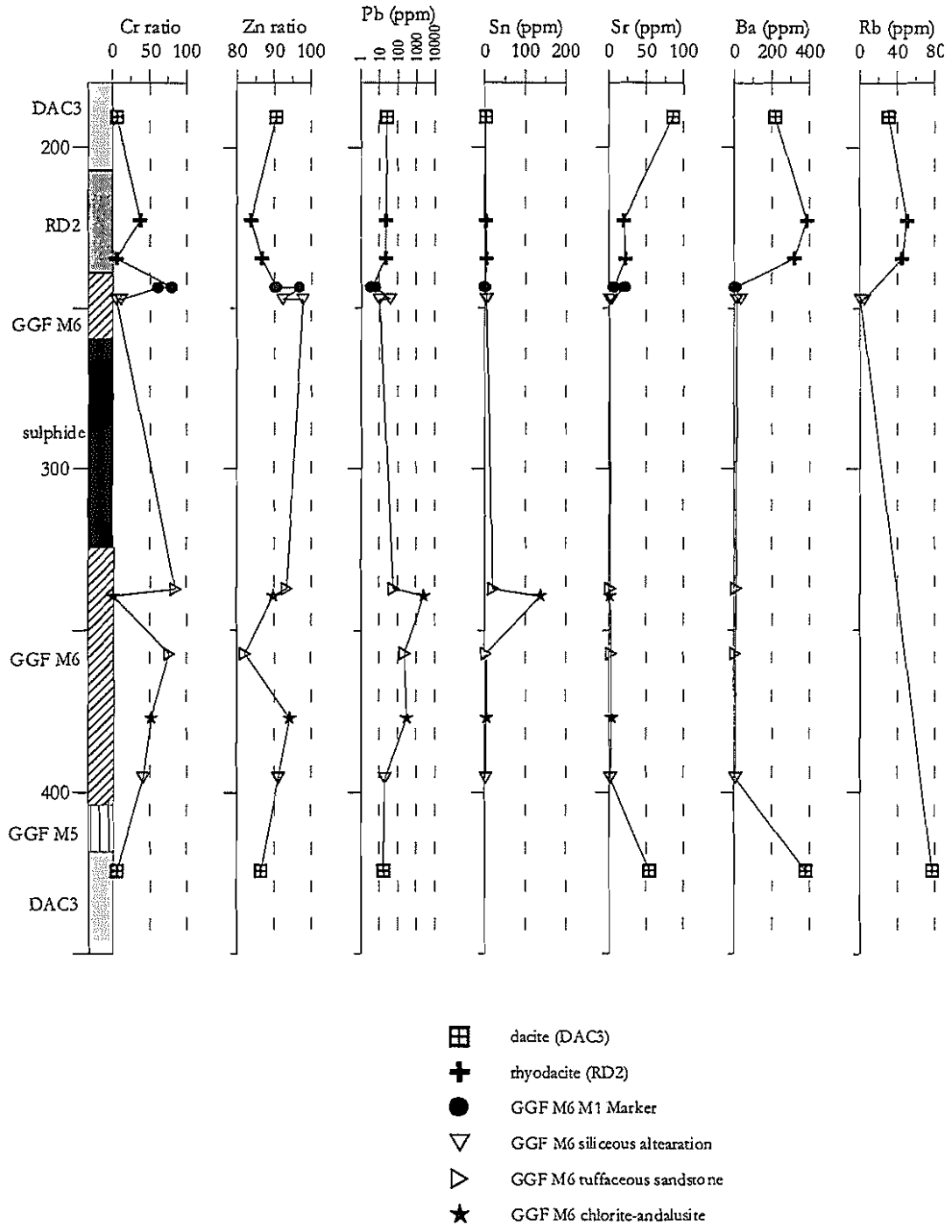

Figure 8.16: Down hole variation of XRF trace element data along GG165 through the central parts of the upper ore zone (C zone) at the Gossan Hill deposit.

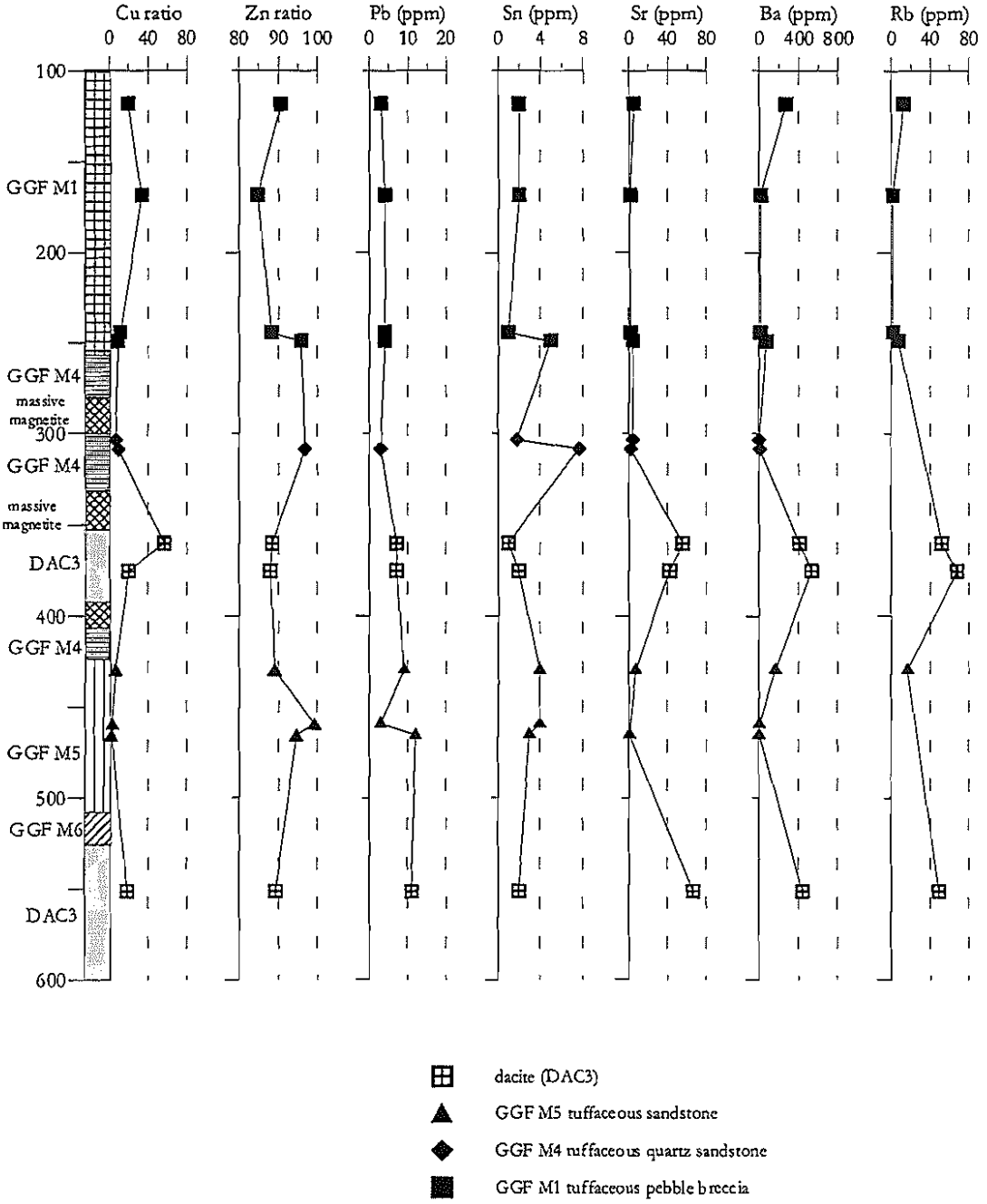

Figure 8.17: Down hole variation of XRF trace element data along GG070 through Cu-rich stringer veins and massive magnetite in GGF M4 at the northern end of the Gossan Hill deposit. Values below detection are not plotted.

rocks at Gossan Hill are generally above background (1ppm for modern arc rocks; Stoltz, 1997) and up to 13.9 ppm in GGF M6 (Fig. 8.18b). The highest Mo contents occur in GGF M1 (up to 42.9 ppm) and GGF M4 (up to 6.3 ppm)(Fig. 8.18c). Elevated Ag (up to 33.8 ppm) also occurs in GGF M6 (Fig. 8.18d), as does As (up to 5040 ppm) in the silicified lithologies of GGF M6 (Fig. 8.18e). Bi (Fig. 8.18f) has its highest values in GGF M6 (up to 10.2 ppm) and in the chlorite alteration of GGF M4 (up to 11.3 ppm). The most elevated Cd values (up to 473 ppm) occur in siliceous alteration of GGF M6 (Fig. 8.18g), whilst Cs (Fig. 8.18h) is generally low (<1.9 ppm) through the sample suite, having its highest values in GGF M5 (up to 0.7 ppm) and SCF M2 (up to 1.9 ppm).

Correlation matrix calculations between the ICPMS and XRF trace element suite at Gossan Hill indicate a number of strong inter-element associations. Bivariate plots of correlated elements are given in Figure 8.19. Positive correlation exists between Bi, Sb and As (Figs.8.19a, 8.19b and 8.19c), which reflects the enrichment of these elements in siliceous alteration in GGF M6. Furthermore, Bi also has a positive correlation with Cu (Fig. 8.19d) and Zn (Fig. 8.19e) in GGF M6, which indicates its close association to sulphide. Moreover, Cd has a positive correlation with Sn (Fig. 8.19f), Zn (Fig. 8.19g) and Ag (Fig. 8.19h) in GGF M6, and a positive correlation is observed between Ag and Cu in GGF M6.

8.7.1 Down hole variation

Down hole ICP-MS trace element variations are illustrated in Figure 8.20 (GG132), Figure 8.21 (GG165) and Figure 8.22 (GG070). Th/U values are constant through all drill intercepts. Gradual anomalism of Sb and As in the SCF M2 hangingwall rhyodacite exists towards the GGF contact (Fig. 8.20). However, Cs decreases towards to this contact (Figs. 8.20 and 8.21). Mo levels in the SCF hangingwall rhyodacite have elevated values (Fig. 8.20). GGF M6 proximal to massive sulphides has elevated levels of Sb, Mo Ag and As (Figs. 8.20 and 8.21). The footwall GGF M1 (Fig. 8.23) has localised enrichment in Cs, Sb and Cd within 30 m of the footwall contact, whilst relatively high Mo is observed throughout GGF M1. Alteration associated with massive sulphide-magnetite (GGF M4) has variable but generally low levels of Ag, As, Sb, Cs and Cd.

8.7.2 Discussion

The ICPMS trace element suite have their highest values of Bi, As, Sb, Cu, Zn, Sn and Ag in siliceous alteration of GGF M6, which hosts Zn-rich massive sulphides. All of these elements have positive inter-element correlation. The higher levels of these trace elements is consistent with the more diverse ore mineralogy of the upper ore zone in GGF M6 (*e.g.*, arsenopyrite, tetrahedrite and native silver; Chapter 6). In comparison, alteration in GGF M4 that hosts Cu-rich sulphides and massive magnetite has generally low levels of the ICPMS trace elements suite. Therefore, a different trace element associated exists between the upper (GGF M6) and lower (GGF M4) ore zones at Gossan Hill. The footwall GGF M1, also has low levels of the elements analysed by ICPMS, with the exception of scattered higher Mo values in quartz-chlorite alteration.

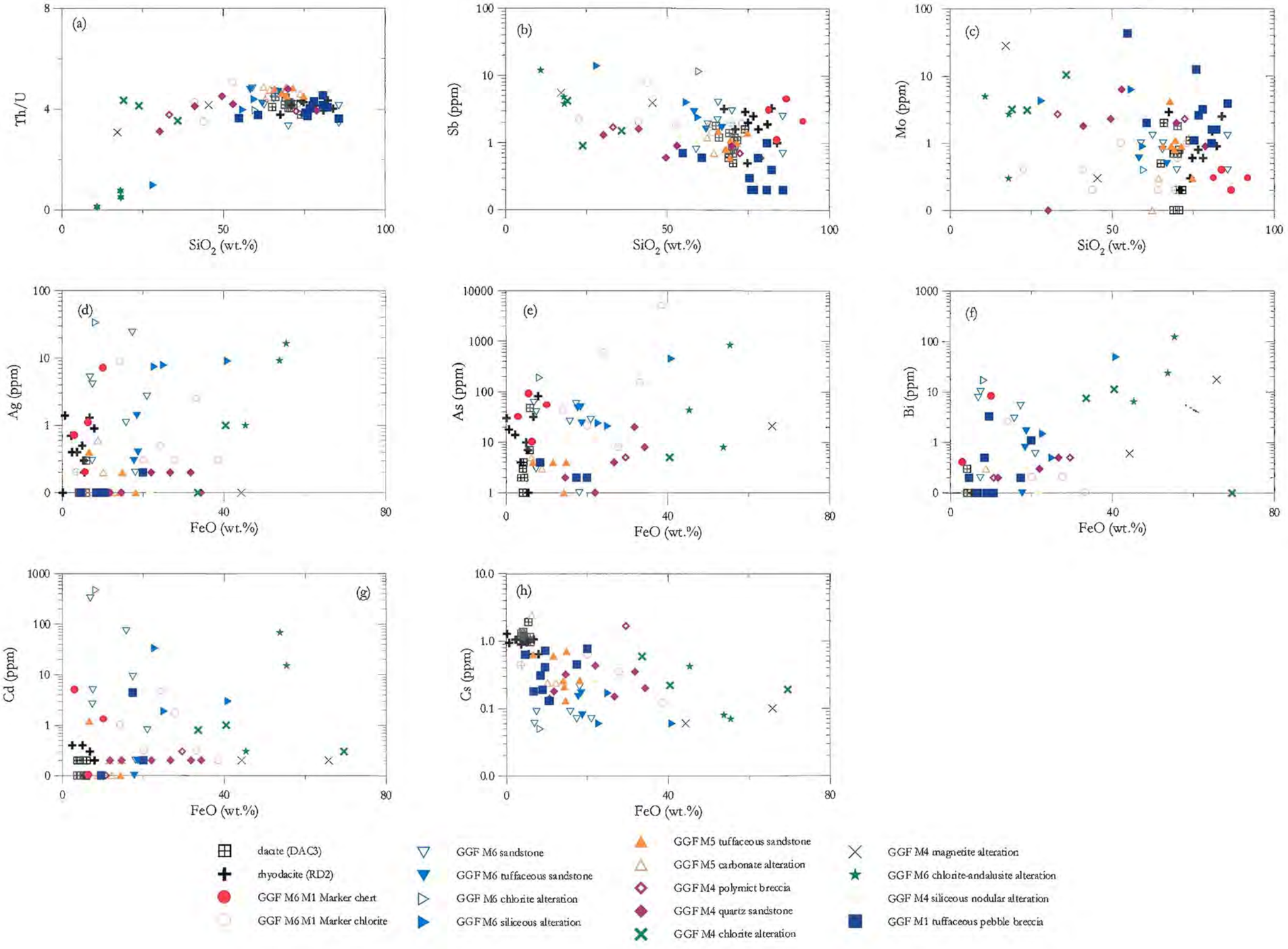

Figure 8.18: Variation diagrams of ICPMS trace element data against whole rock SiO_2 and FeO for the Gossan Hill sample suite. (a) SiO_2 *versus* Th/U, (b) SiO_2 *versus* Sb, (c) SiO_2 *versus* Mo, (d) FeO *versus* Ag, (e) FeO *versus* As, (f) FeO *versus* Bi, (g) FeO *versus* Cd, and (h) FeO *versus* Cs. Values below detection are not plotted. Note: relatively constant Th/U ratios (8.18a) and the highest Sb, Ag, As, Bi and Cd contents occur GGF M6 (8.18b, 8.18d, 8.18e, 8.18f and 8.18g).

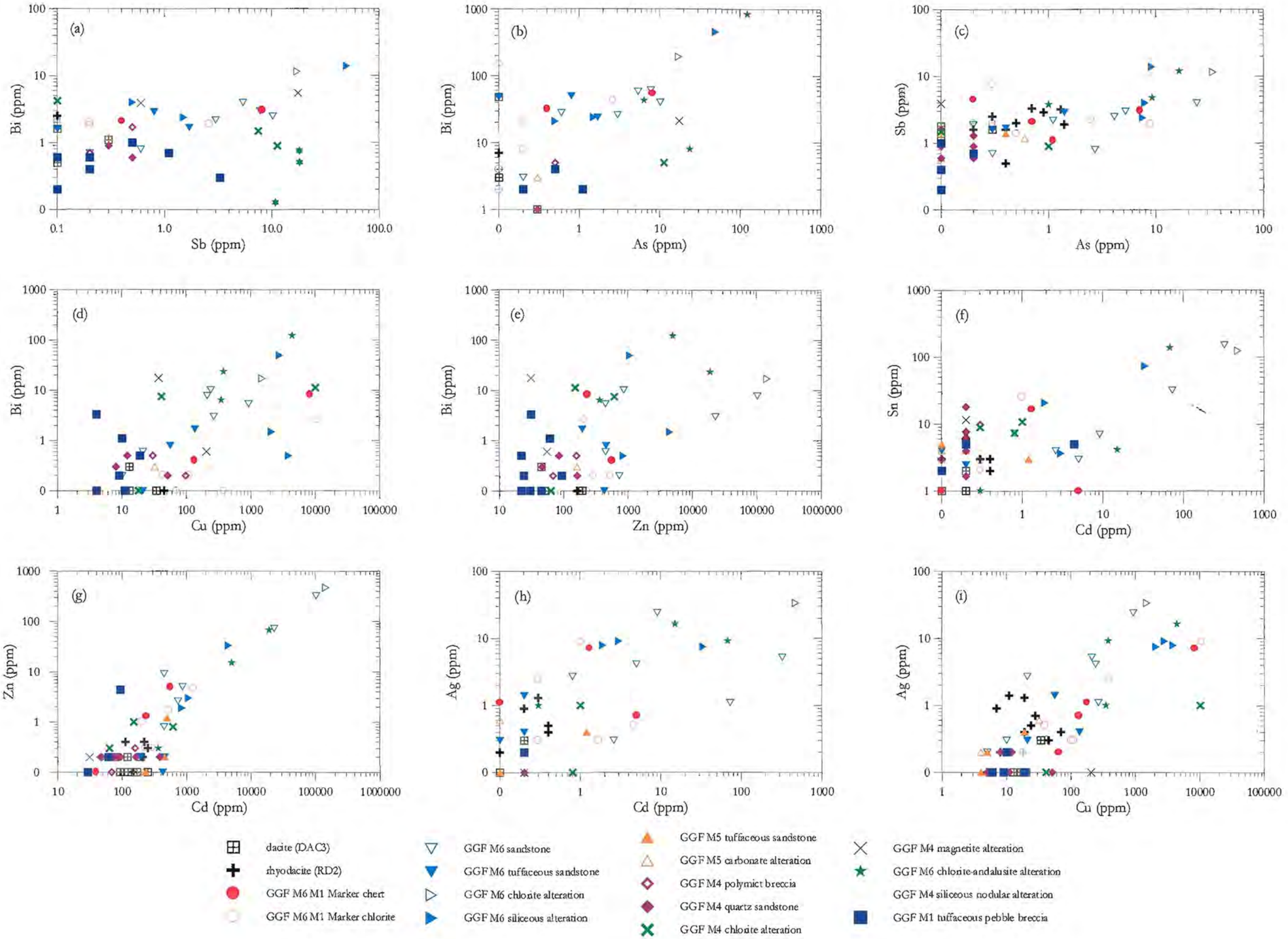

Figure 8.19: Inter-element correlation plots between ICPMS and XRF trace element data. (a) Sb *vs.* Bi, (b) As *versus* Bi, (c) As *versus* Sb, (d) Cu *versus* Bi, (e) Zn *versus* Bi, (f) Cd *versus* Sn, (g) Cd *versus* Zn, (h) Cd *versus* Ag, and (i) Cu *versus* Ag. Values below detection are not plotted. Note: positive correlation between Sb and Bi (8.19a) and As, Sb and Bi (8.19b and 8.19c), the highest values of Bi, Cu, Zn, Sn and Cd occur in GGF M6 (8.19d, 8.18e, and 8.18f, and a positive correlation between Ag and Cu with the highest values occurring in GGF M6 (8.19i).

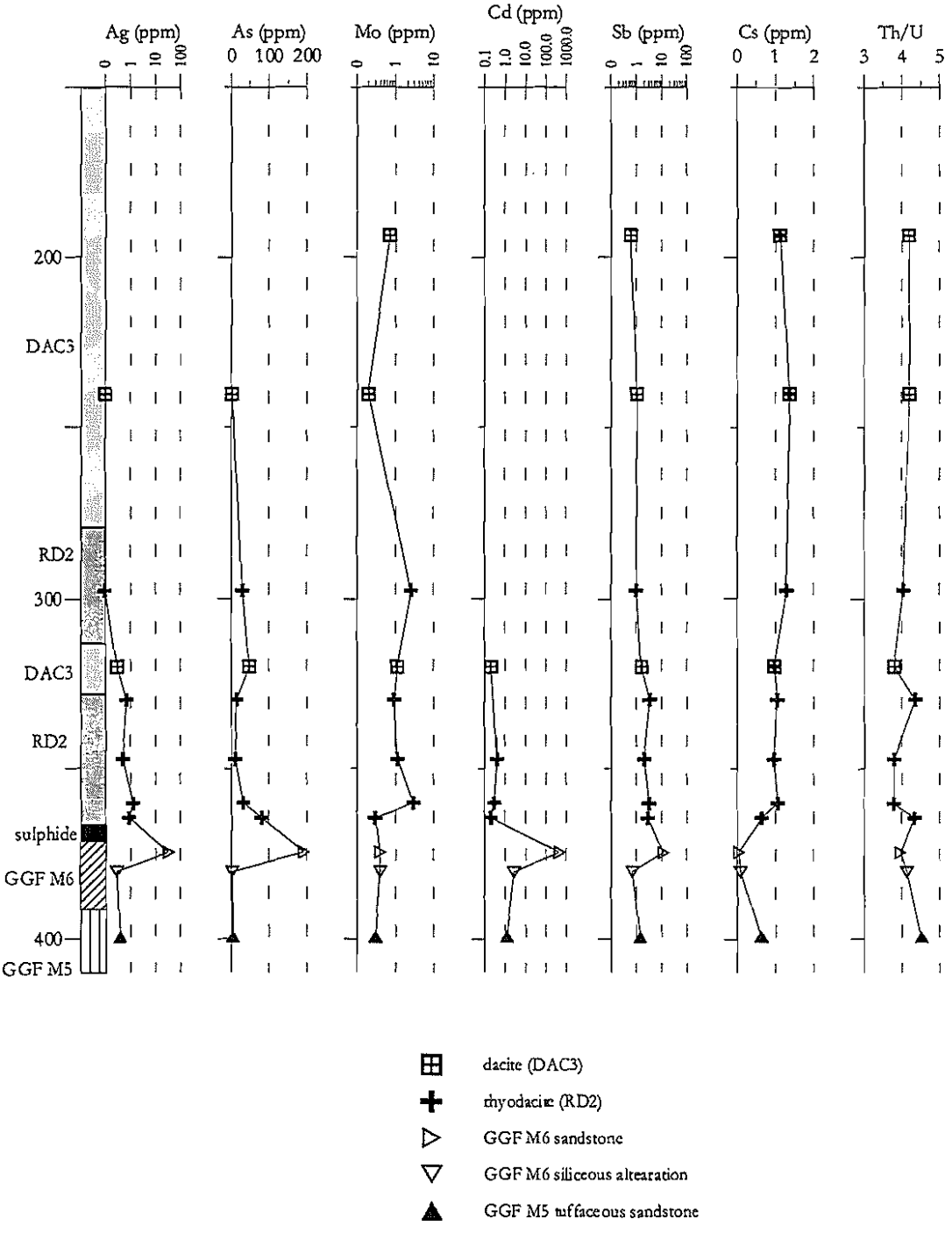

Figure 8.20: Down hole variation in ICPMS trace element data along GG132 at the southern end of the Gossan Hill deposit.

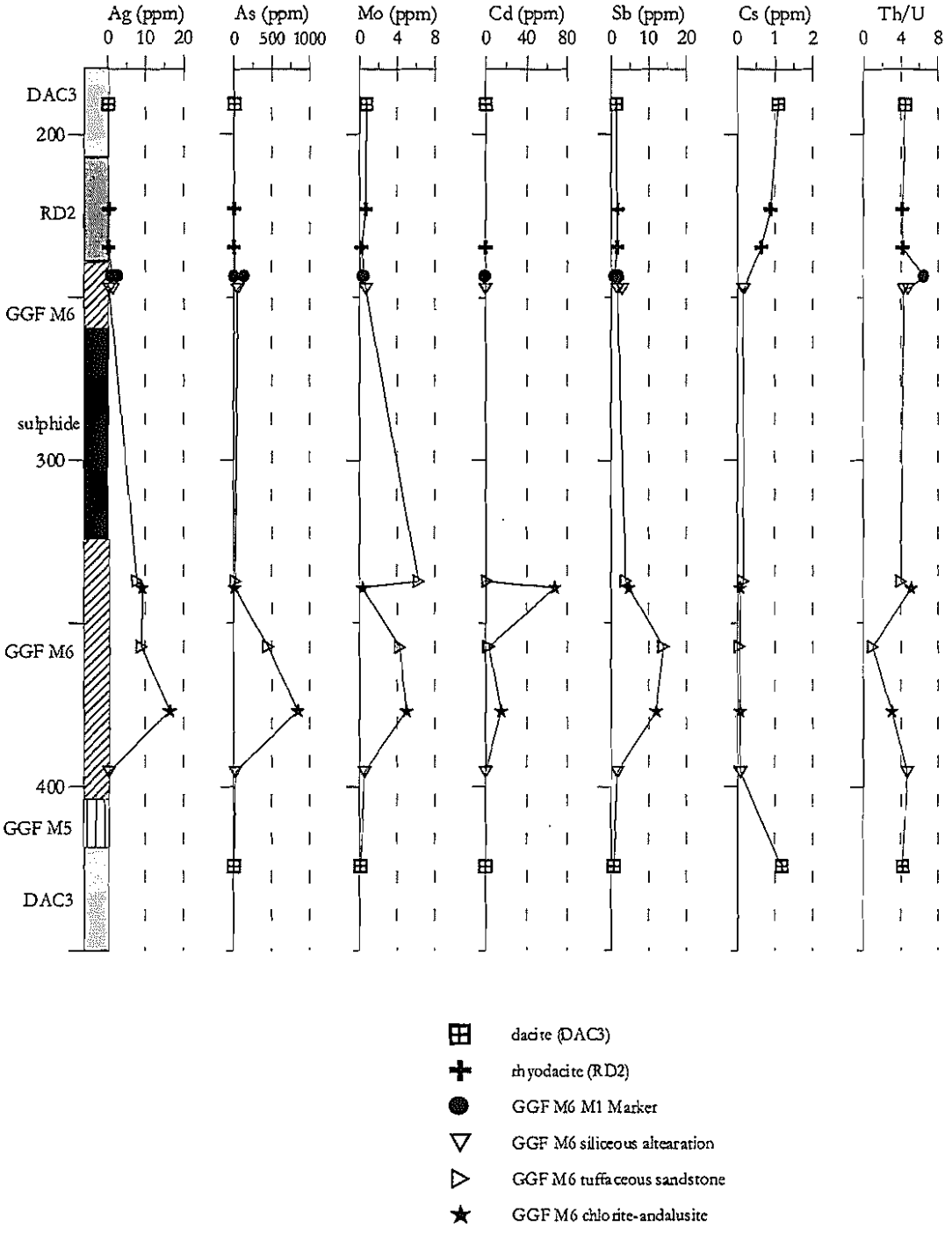

Figure 8.21: Down hole variation in ICPMS trace element data along GG165 through the central parts of the upper ore zone (C zone) at the Gossan Hill deposit.

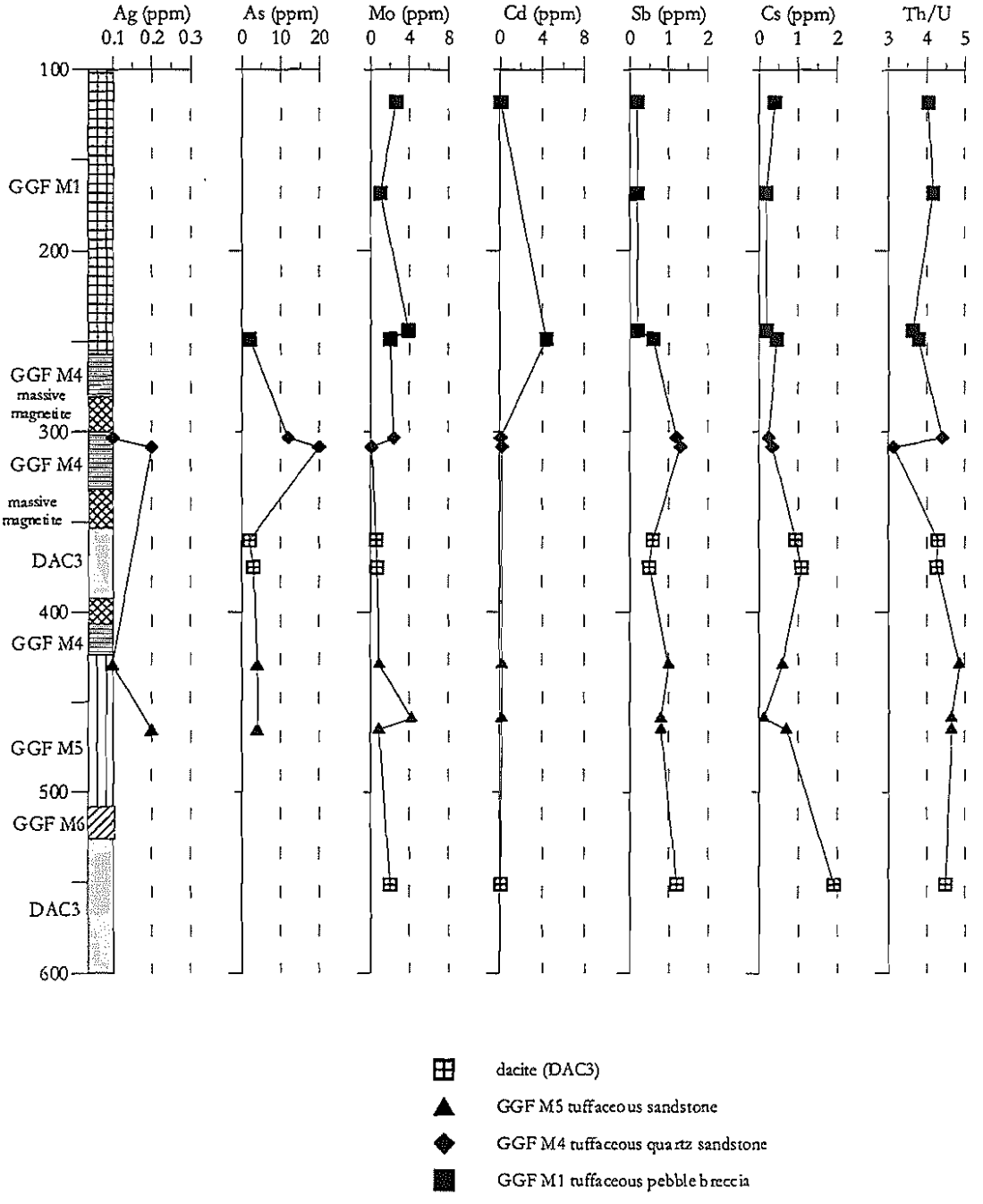

Figure 8.22: Down hole variation in ICPMS trace element data along GG070 through Cu-rich stringer veins and massive magnetite in GGF M4 at the northern end of the Gossan Hill deposit. Values below detection are not plotted.

8.8 The M1 Marker

The M1 Marker (Section 3.3.6) is significant as a stratigraphic marker horizon, and as an indication of proximity to massive sulphide. Chert beds in the M1 Marker are interpreted to represent siliceous beds derived from the mineralising fluids mixing with seawater (*e.g.*, Ashley *et al.*, 1988). Chert beds in the M1 Marker are interbedded with chlorite beds that likely represent altered siltstone beds. Similar interbedded chert-lithic horizons are described at the Kuroko deposits (Kalogeropolous and Scott, 1983; 1989), the New Brunswick deposit (Peter and Goodfellow, 1996) and the Thalanga deposit (Duhig *et al.*, 1992; Doyle, 1996). This section aims to characterise the M1 Marker and investigate its hydrothermal origin using whole rock geochemistry. Three M1 Marker samples from Gossan Hill and 2 from Scuddles were analysed (Appendix A6.2). Chert and chlorite beds in these samples were analysed separately.

Peter and Goodfellow (1996) use immobile elements (*i.e.* Ti, Al, Zr, P, Cr) to differentiate between detrital and hydrothermal sources. The immobile element abundances within the M1 Marker are plotted in Figure 8.23, and the chert and chlorite beds (for both Gossan Hill and Scuddles) have distinct geochemical differences. Chert beds have TiO_2 and Al_2O_3 contents that are near, or below detection levels (Fig. 8.23a). However, the chlorite beds in the M1 Marker at Scuddles are enriched in Al_2O_3 with respect to those at Gossan Hill. Similar relationships also exist between TiO_2 and Zr (Fig. 8.23b), where low Zr contents occur in chert (<10 ppm), compared with the chlorite beds (up to 228 ppm). P_2O_5 contents in the chert are also low (<0.01 ppm), and higher in chlorite beds. Moreover, chlorite beds in the M1 Marker at Scuddles have higher P_2O_5 contents than at Gossan Hill (Fig. 8.23d). The distribution of Zr (Fig. 8.23d) is similar to P_2O_5, with chert having low Zr, and higher levels in the chlorite beds. The Cr contents of chert is low (<25 ppm), compared with higher levels (up to 1520 ppm) in chlorite beds (Fig. 8.23e). Therefore, the lithic and chert bands of the M1 Marker have very different immobile element contents. However, based on these immobile elements, no distinction can be made between chert and chlorite beds in the M1 Marker at either the Gossan Hill or Scuddles deposits.

Figure 8.24 illustrates distinct major oxide element differences between the chert and chlorite beds in the M1 Marker at Scuddles and Gossan Hill. However, both the chert and chlorite beds are similar between the two deposits (Fig. 8.24). The distribution of mobile major and trace elements in the M1 Marker is illustrated in Figure 8.25. FeO and SiO_2 (Fig. 8.25a) have a negative linear correlation similar to the trend throughout the GGF (*c.f.* Fig 8.7). This correlation indicates that chlorite beds in the M1 Marker at Gossan Hill and Scuddles have lower SiO_2 (22 to 73 wt.%) than the chert (81 to 91 wt.%). FeO in chert ranges up to 10.1 wt.%, whilst FeO in the chlorite bands ranges from 13 to 43 wt.%. The high FeO content of chlorite beds is attributed to intense chlorite alteration, as well as the scattered distribution of pyrite and magnetite. The high SiO_2 content of the chert beds is consistent with their microcrystalline quartz mineralogy. On the basis of FeO and SiO_2, both the chlorite and chert bands are indistinguishable between the two deposits.

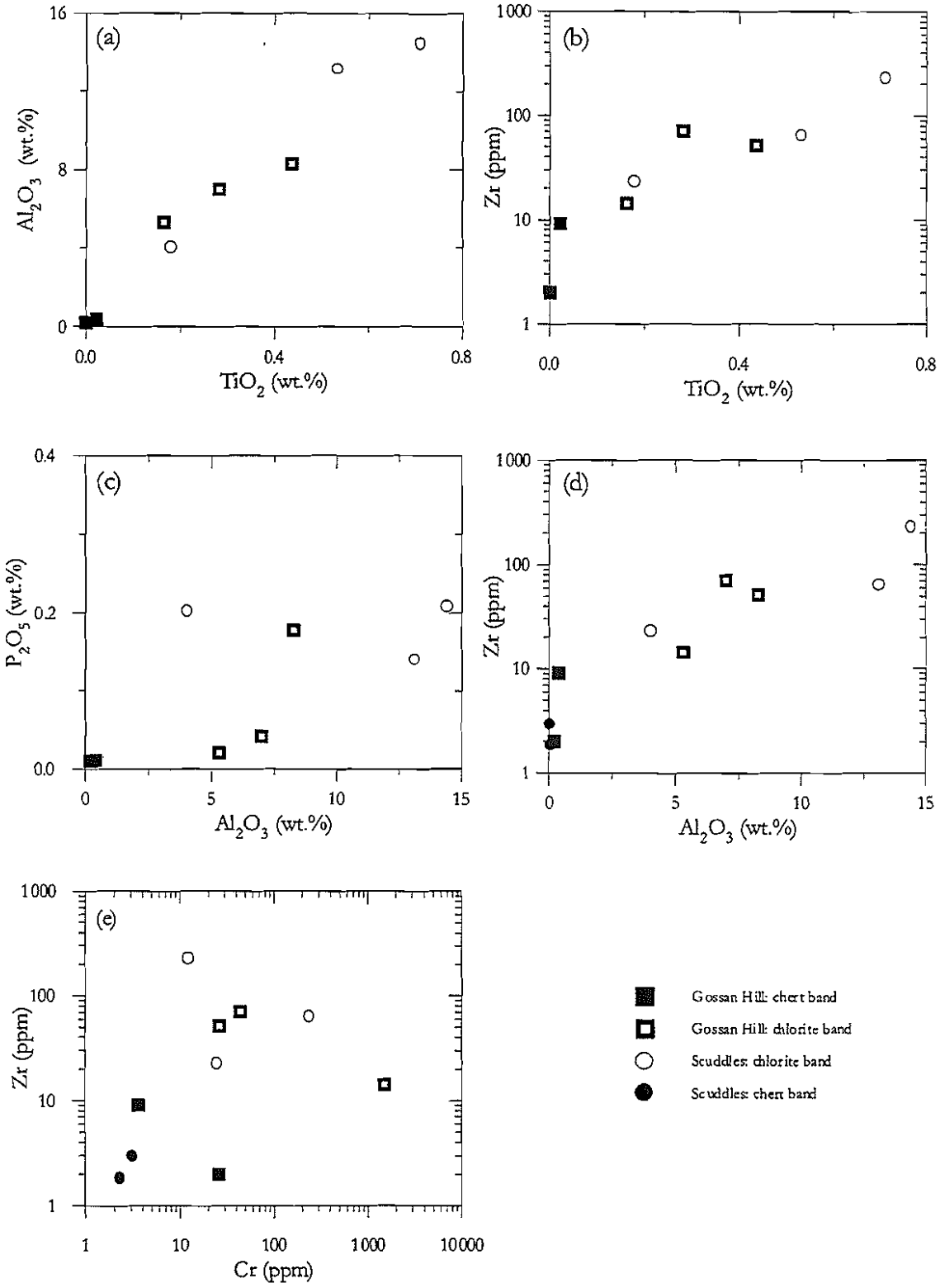

Figure 8.23: Immobile element variation of chert and chlorite bands in the M1 Marker at the Gossan Hill (square) and Scuddles (circle) deposits. (a) TiO_2 *versus* Al_2O_3, (b) TiO_2 *versus* Zr, (c) Al_2O_3 *versus* P_2O_5, (d) Al_2O_3 *versus* Zr, and (e) Cr *versus* Zr. Note: values below detection are not plotted and values for the Scuddles M1 Marker chert beds in (a), (b) and (c) are below detection limits.

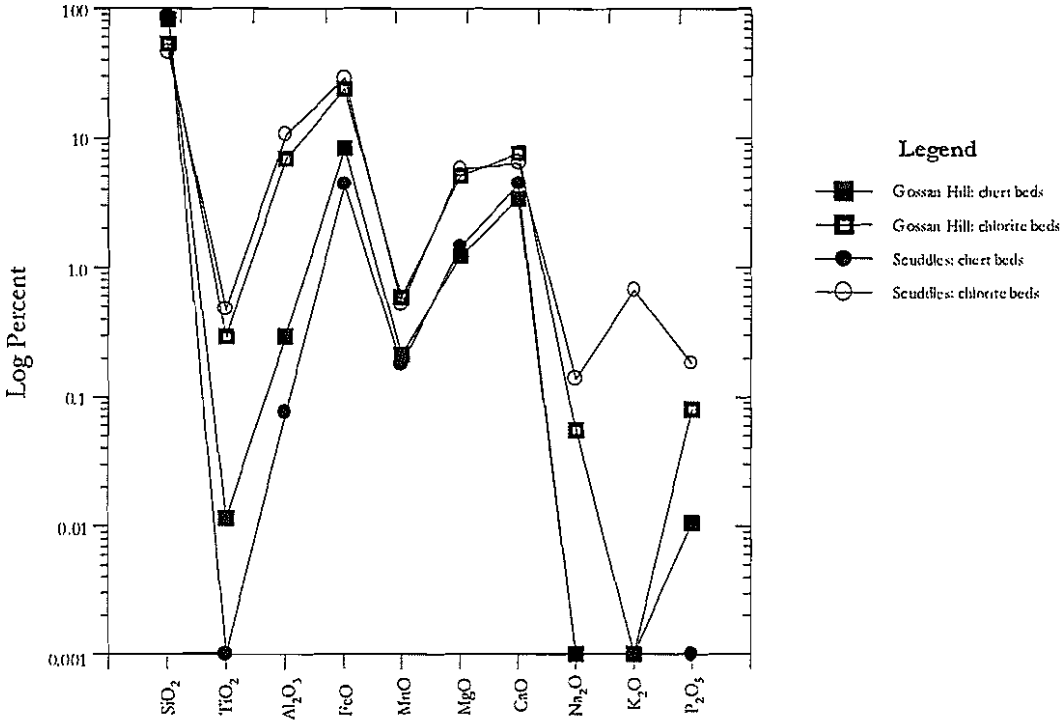

Figure 8.24: Major element spider diagram of average values in chert and chlorite beds from the M1 Marker at Gossan Hill and Scuddles. Data from Appendix A6.2.

MgO contents of chert beds are less than 0.21 wt.% for both Gossan Hill and Scuddles. However, chlorite beds have MgO contents that vary from 0.1 to 10 wt.%. A positive correlation between FeO and MgO (Fig. 8.25b) and FeO and MnO contents (Fig. 8.25c) exists where chert beds have low MgO (<2.1 wt.%) and low MnO (<0.2 wt.%) contents. In comparison, the MgO and MnO content of chlorite bands is higher (2.2 to 10.4 wt.% MgO and 0.21 to 4.8 wt.% MnO). The variations in FeO, MgO and MnO contents of the chlorite beds likely reflect local differences in the abundance and composition of chlorite in the M1 Marker between the two deposits. CaO contents (Fig. 8.25d) vary between the chert and chlorite bands ranging from 0.4 to 22.7 wt.%. This range reflects carbonate alteration, which is also likely to contribute to variation in the MnO and MgO contents.

Irregular distributions of Sr, Zn, Ag, Cu and Cd occur between chlorite and chert bands (Figs. 8.25e-i). However, chert beds tend to have lower Zn (Fig. 8.25e), Sr (Fig. 8.25f), Ag (Fig. 8.25g) and Cu (Fig. 8.25h) than the chlorite beds. Cd and Zn (Fig. 8.25i) are positively correlated, but do not discriminate between the chert and chlorite beds. Other trace elements, not shown in Figure 8.25 are below detection in the chert and chlorite beds (Appendix A6.2). These elements include Na_2O, K_2O, La, Ce, Nd, Nb, Ba, Sc, Sn, Rb, Bi, Mo, Cs, Tl, Th and U.

8.8.1 Discussion

The elements Ti, Al, Zr and Cr are considered relatively immobile under hydrothermal conditions and their source is likely to be detrital (*e.g.*, Peter and Goodfellow, 1996). Aluminosilicate minerals consist mainly of Si, Ti, Al, Mg, Zr, and Cr and support a

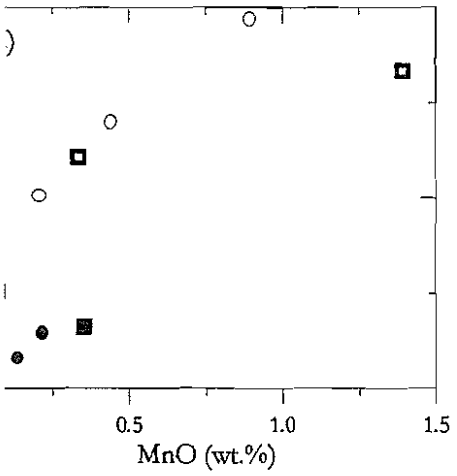

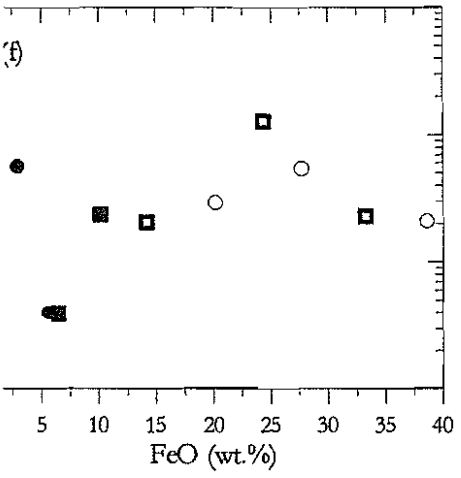

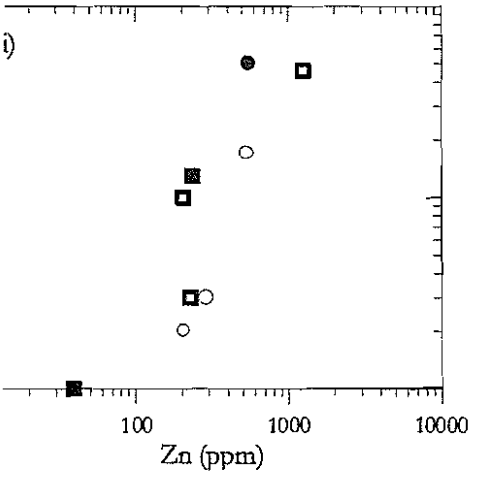

) SiO_2 *versus* FeO, (b) MgO *versus* FeO, (c) MnO *versus* FeO, (d) CaO
otted.

detrital origin for the M1 Marker chlorite beds due to their high immobile element contents. The fine-grained, thinly bedded and laminated sedimentary attributes of the M1 Marker also support some sandstone/siltstone detrital contribution. Nonetheless, some hydrothermal contribution to these chlorite beds can be argued. In hydrothermal systems, the elements Fe, Mn, Pb, Zn, Cd, Ca, Sr, Ba, P are mobile and may occur in hydrothermal precipitates (iron oxide, chlorite, carbonate, quartz and sulphide). The abundance of immobile elements (reflecting a detrital origin) (Fig. 8.23) in chlorite bands and the lack of immobile elements in chert bands, reflect a lithic *versus* hydrothermal origin. It is clear from mobile elements (Fig. 8.25) however, that both chert and chlorite bands have some degree of hydrothermal contribution, although the hydrothermal contribution in the chert bands is interpreted to be greater.

Previous authors use Al-Fe-Mn discrimination diagrams to define the extent of hydrothermal contribution in "exhalative" hydrothermal cherts. Al-Fe-Mn diagrams discriminate hydrothermal (Mn and Fe) from detrital (Al) sources. This scheme has been successfully applied to modern seafloor sulphide deposits, as well as to ancient VHMS deposits (*e.g.*, Duhig et al., 1992; Doyle, 1996; Herzig *et al.*, 1988 and Peter and Goodfellow, 1996). Samples from the M1 Marker are plotted on an Al-Fe-Mn diagram in Figure 8.26. Chert bands from the M1 Marker at Gossan Hill and Scuddles have relative Fe enrichment and low levels of Mn and Al, whilst the chlorite bands have higher Al, Mn and lower Fe (Fig. 8.26). Therefore, both chlorite and chert bands have a significant hydrothermal component.

Adachi *et al.* (1986) report that the source of silica in hydrothermal cherts may originate from volcanogenic sources or precipitates from emanating hydrothermal solutions. Examples of modern hydrothermal cherts (*e.g.*, Adachi *et al.*, 1986; Herzig *et al.*, 1988) indicate that the hydrothermal silica precipitate is amorphous. Therefore, it is possible that the chert beds in the M1 Marker may have had an amorphous silica precursor, but

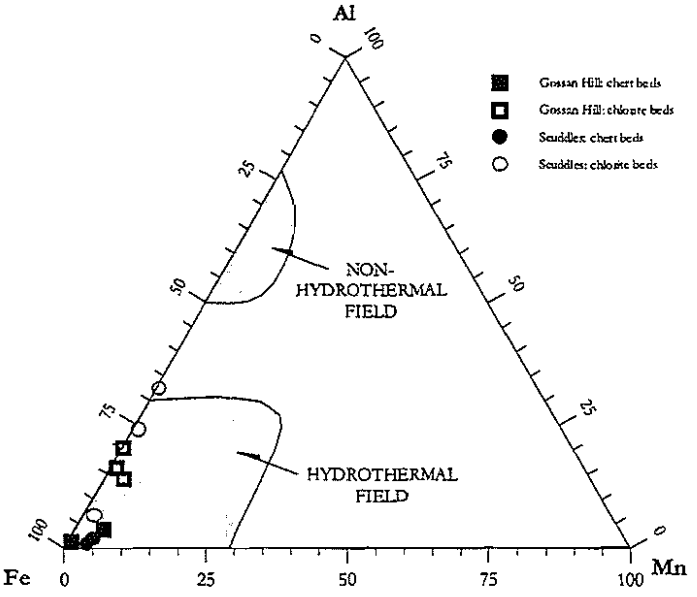

Figure 8.26: Al-Fe-Mn ternary plot of chert and chlorite beds from the M1 Marker at Gossan Hill and Scuddles. The composition of the chert and chlorite beds lie within the hydrothermal field of Adachi *et al.* (1986) indicating that they have a significant hydrothermal component.

now consist of fine-grained microcrystalline quartz mosaics.

The geochemistry of the chert and chlorite beds in the M1 Marker is different. Chlorite beds were probably derived during fine-grained sedimentation synchronous with the hydrothermal activity responsible for the formation of the chert beds. Chert beds were likely formed during periods of low sedimentation (hiatus?), as hydrothermal precipitates composed of silica, minor pyrite and magnetite. The layered sedimentary structure of the M1 Marker indicates its formation was cyclic, with alternating hydrothermal chert precipitation and sedimentation. Hydrothermal pulses responsible for the formation of chert beds in the M1 Marker are the most likely cause of hydrothermal alteration of the interbedded chlorite beds. This hydrothermal modification of chlorite beds resulted in higher FeO, MgO, MnO and CaO contents due to alteration.

No geochemical differences have been identified between the M1 Marker at the Gossan Hill and Scuddles deposits. Minor variations in immobile elements within chlorite beds may reflect variation in the lithic source. Therefore, the composition and stratigraphic position of the M1 Marker is similar at both deposits.

8.8.2 Summary

The thinly layered M1 Marker formed from pulses of hydrothermal activity at the seafloor, synchronous with the formation of massive sulphide. The composition and stratigraphic position of chert and chlorite beds that form the M1 Marker at Gossan Hill and Scuddles, are similar and support a common origin. The hydrothermal contribution in the chert beds is greater than that in the chlorite beds. High Al_2O_3, TiO_2, Zr, Cr in chlorite beds is evidence of a detrital contribution, which is absent from chert. The passage of hydrothermal fluids, responsible for the formation of chert beds, likely altered the chlorite beds and contributed to their hydrothermal signature. The FeO contents of the chlorite beds reflect chlorite and carbonate alteration. The M1 Marker at both Scuddles and Gossan Hill represent units formed by mechanisms and processes directly related to the formation of massive sulphides.

8.9 Discussion

The geochemistry of the GGF at Gossan Hill reflects intense metasomatic alteration of the entire volcaniclastic succession, particularly near sites of massive sulphide and magnetite. The geochemistry of the GGF is strongly related to the distribution of alteration minerals within it (*c.f.* Chapter 7) define broad semiconformable alteration. In comparison, the hangingwall volcanics of the SCF are less altered and are mineralogically and geochemically distinct from the GGF. In the GGF and SCF, immobile elements are distinct for each stratigraphic member, whereas mobile elements in the GGF are principally affected by changes in the abundance of quartz and chlorite.

8.9.1 Geochemistry of the hangingwall (SCF M2)

The RD2 rhyodacite and DAC3 dacite have muscovite, calcite and minor chlorite alteration of the groundmass and feldspar phenocrysts, which increases in intensity towards the GGF contact. Elevated Ba, Sr, and Rb contents in dacite and rhyodacite are

related to the occurrence of feldspar within these lavas. The decrease of Ba, Sr and Rb contents, particularly in massive rhyodacite over the 200 m proximal to the GGF contact, is likely related to the increased intensity of alteration and the destruction of feldspar proximal to the GGF contact.

Rhyodacite and dacite lack high FeO contents, but have a weak FeO, MgO and MnO enrichment towards the GGF contact. This enrichment only occurs within 100 m of the hangingwall contact, and reflects increased abundances of carbonate and sulphide near this contact. Hangingwall alteration is characterised by minor quartz and chlorite (SiO_2 and FeO values are lower than the GGF) and the presence of calcite and muscovite (high CaO and K_2O respectively). Metal contents in the hangingwall are low and trace element variation in Cs, As and Sb is minor, with slight depletion in Cs and enrichment in As and Sb adjacent to the GGF contact. The geochemical characteristics of the hangingwall rhyodacite and dacite alteration are given in Table 8.3.

Table 8.3: Geochemical characteristics of alteration at Gossan Hill.

HANGINGWALL ALTERATION (SCF M2)			
Lithology:	dacite	feldspar, quartz	
	rhyodacite	quartz, feldspar	
Alteration:	carbonate, sericite, quartz, ±chlorite, ±pyrite, ±sphalerite		
Geochemistry:	**Depletion**	strong, ubiquitous	Na_2O, K_2O
	Depletion	<200m from GGF contact	Sr, Ba, (Rb), Cs, SiO_2
	Enrichment	<100 m from GGF contact	FeO, MgO, MnO, As, Sb, CaO
HOST SEQUENCE (GGF M6)			
Lithology:	tuffaceous and polymict siltstone-sandstone-breccia		
Alteration:	quartz, ±chlorite, ±carbonate, ±sphalerite, ±pyrite, ±magnetite, ±ilmenite		
Geochemistry:	**Depletion**	strong and ubiquitous	Na_2O, K_2O
	Enrichment	sporadic distribution	Cd, As, Pb, Fe, Zn, Ag, Bi, Sb, Sn
	Enrichment	strong to intense	SiO_2, ±(FeO, MgO, CaO, MnO)
HOST SEQUENCE (GGF M5)			
Lithology:	tuffaceous sandstone consisting of quartz and altered pumice and shards		
Alteration:	quartz, chlorite, ±carbonate, ±pyrite, ±ilmenite, ±rutile		
Geochemistry:	**Depletion**	strong and ubiquitous	Na_2O, K_2O
	Depletion	strong	CaO
	Enrichment	weak anomalism	Pb, Zn, ±Rb, ±Sr, ±Cs, ±Sb
	Enrichment	pervasive strong	SiO_2, FeO, MgO, MnO
	Enrichment	sporadic	CaO
HOST SEQUENCE (GGF M4)			
Lithology:	tuffaceous sandstone to pebble breccia consisting of altered quartz, pumice and shards		
Alteration:	quartz, chlorite, ±carbonate, ±pyrite, ±magnetite ±chloritoid, ±apatite, ±andalusite, ±pyrrhotite, ±talc, ±rutile, ±ilmenite		
Geochemistry:	**Depletion**	strong and ubiquitous	Na_2O, K_2O
	Depletion	strong	CaO
	Enrichment	weak anomalism	TiO_2, MnO, Al_2O_3, ±Zn, ±Pb, ±Mo, ±Bi, ±Sb
	Enrichment	pervasive strong to intense	SiO_2, FeO, MgO, ±CaO, ±Cu
FOOTWALL ALTERATION (GGF M1)			
Lithology:	pumiceous pebble breccia consisting of quartz and altered pumice and shards		
Alteration:	quartz, chlorite, ±pyrite, ±rutile		
Geochemistry:	**Depletion**	strong and ubiquitous	Na_2O, K_2O, CaO
	Enrichment	weak anomalism	TiO_2, MnO, Mo, Cs
	Enrichment	pervasive strong to intense	SiO_2, FeO, MgO

8.9.2 Geochemistry of the host sequence (GGF M4, M5 and M6)

Based on immobile element compositions, GGF M4 and GGF M5 have relatively homogeneous rhyodacite compositions. Nonetheless, GGF M6 and breccia in GGF M4 have a wide range in immobile elements that indicate a heterogeneous composition. Throughout the GGF host sequence, Na_2O and K_2O are depleted, due to the general absence of muscovite (K_2O depletion) and lack of feldspar (Na_2O depletion) within this sequence (Table 8.3). Intense quartz-chlorite alteration is defined by a correlation between the major oxides SiO_2, FeO, MgO and, to a lesser extent, MnO. A strong positive correlation between FeO and MgO locally relates to changes in the composition of chlorite from MgO-bearing in GGF M4 to FeO-rich in GGF M6. Erratic CaO contents in GGF M4, GGF M5 and GGF M6 reflect patchy carbonate (mainly ankerite) alteration. The highest FeO values in the host sequence occur in alteration adjacent to massive sulphide and massive magnetite in GGF M4, whereas SiO_2 enrichment in GGF M5 and GGF M6 is caused by intense silicification.

The geochemistry of GGF M4 is characterised by intense enrichment in FeO, MgO and MnO, with sporadic CaO and depletion in SiO_2, CaO, K_2O and Na_2O. Enrichment in FeO, MgO and MnO reflect the higher abundance of chlorite in alteration within GGF M4, particularly near massive sulphide and magnetite. Enrichment in MgO and FeO contents is common in alteration below massive sulphides (*e.g.*, Larson, 1984).

Trace element compositions (XRF and ICP-MS) of the host sequence are highest in siliceous alteration within GGF M6 adjacent to massive sulphide. High values of Bi, As, Sb, Cu, Zn, Pb, Sn, Cd and Ag, all with positive inter-element correlation, are observed in the siliceous alteration (Table 8.3). The anomalism of these elements is consistent with the occurrence of the elements in ore minerals of the upper ore zone (Chapter 6). In comparison, rocks in GGF M4 and GGF M5 have low levels of these elements.

8.9.3 Geochemistry of the footwall (GGF M1)

The footwall GGF M1 has a relatively homogeneous rhyodacite immobile element composition. The footwall is ubiquitously depleted in Na_2O and K_2O, reflecting the lack of feldspar and muscovite within it (Table 8.3). Extreme Na_2O and K_2O depletion not only occurs at Gossan Hill, but is also a regional characteristic of the GGF (Clifford, 1992). Cerling *et al.* (1985) report that the low temperature alteration of siliceous volcanic glass can involve considerable exchange of hydrogen for Na^+ and/or K^+ ions. Therefore, Na^+ may have been leached from volcanic glass during early alteration. CaO contents are low throughout GGF M1 and are related to the absence of carbonate in the footwall. Trace elements throughout GGF M1 are also depleted, with a few high Mo values in the footwall.

The major elements in the footwall GGF M1 are SiO_2 and FeO, and reflect its alteration to quartz and chlorite (Table 8.3). Intense silicification of this package is indicated by high SiO_2values. The addition of SiO_2 *via* silicification processes is commonly associated with VHMS deposits (*e.g.*, Skirrow and Franklin, 1994; Galley, 1983; Klemd *et al.*, 1989). At Gossan Hill the timing of the footwall silicification is related to an early regional

event prior to local silicification stages during massive sulphide formation (Chapter 7). Geochemically, these two silicification stages are distinguished by trace element contents, with scattered Mo values in regional quartz-chlorite alteration and enrichment in Bi, As, Sb, Cu, Zn, Pb, Sn, Cd and Ag in local silicification proximal to massive sulphide (*i.e.* GGF M6).

8.9.4 Review of geochemical characteristics of the Scuddles deposit

Geochemical studies by Ashley (1983) and Whitford and Ashley (1992) at the Scuddles deposit characterised the geochemistry of alteration. Anomalous depletion in Na_2O and K_2O was also identified throughout the GGF at Scuddles. The geochemistry of the GGF host sequence at Scuddles had SiO_2 contents that were inversely related to MgO, FeO and MnO contents. The enrichment in SiO_2 increased toward the top of the GGF, with MgO, FeO and MnO enrichment in the stratigraphically lower parts of the host sequence. Elevated MgO, FeO and MnO were associated with disseminated sulphide and stringer veins. Ashley (1983) summarised these geochemical trends to be the result of an initial Na and K depletion, followed by progressive Mg-Fe enrichment, and ultimate enrichment in Fe due to the hydrothermal alteration associated with formation of the Scuddles deposit.

Trace elements Zn, Pb, Ag, Sn and F are enriched towards the top of mineralisation (Ashley, 1983). Additionally, Cd, In, Pb, Ag, Hg, Co, As, Bi and Sn are also high in GGF M6 at Scuddles but lack ubiquitous elevated contents and are unreliable indicators of mineralisation (Radford, 1992). Lower parts of mineralisation at Scuddles are characterised by high Cu, W, Se, Mo and P_2O_5, where as the footwall has sporadic levels of Mo. P_2O_5 is locally concentrated in Cu-rich stringer mineralisation at the base of mineralisation and reflects the local occurrence of apatite (Ashley, 1983). The geochemical results of alteration at the Scuddles deposit are summarised in Table 8.4 and are similar to those identified at Gossan Hill (Table 8.3).

Table 8.4: Geochemical characteristics of alteration and strata at the Scuddles deposit (after Ashley 1983).

HANGINGWALL ALTERATION (SCF M1 and SCF M2)			
Lithology:	dacite (SCF M1)	consisting of feldspar, quartz	
	dacite (SCF M2)	consisting of feldspar, quartz	
Alteration:	carbonate, muscovite quartz, ±chlorite, ±pyrite		
Geochemistry:	**Depletion**	strong peripheral to sulphides	Na_2O, CaO, Sr
HOST SEQUENCE (Mineralised Horizon = GGF M6)			
Lithology:	polymict and tuffaceous siltstone-sandstone-breccia		
Alteration:	quartz, ±chlorite, ±carbonate, ±sphalerite, ±pyrite		
Geochemistry:	**Enrichment**	lower parts of sequence	Cu, Fe, Mg, As, Co
	Enrichment	Zn-rich zones	Zn, Fe, Pb, Ag, Mn, As, Sb, Co
	Enrichment	ubiquitous	MnO
FOOTWALL ALTERATION (GGF M5)			
Lithology:	pumiceous pebble breccia consisting of quartz, pumice and shards		
Alteration:	quartz, chlorite, ±pyrite, ±rutile ±ilmenite		
Geochemistry:	**Depletion**	strong and ubiquitous	Na_2O, CaO, Sr
	Enrichment	progressive to upper contact	Fe, Zn, Cu, Pb, As, S, Mg, Mn, Co

8.10 Conclusions

- Immobile elements ratios indicate that the GGF and SCF lithologies all have rhyodacite compositions. Homogeneity of the tuffaceous GGF volcaniclastics GGF M1, GGF M5 and, to a lesser extent, GGF M4, is reflected by similar immobile element ratios (Ti/Zr, Nb/Y) for each member. GGF M6 have a wide range of ratios and indicate heterogeneity due to the polymict nature of this member. The local mobility of TiO_2 and Al_2O_3 proximal to mineralisation was also identified.
- The footwall (GGF M1), GGF M5 and GGF M6 are strongly SiO_2 enriched, reflecting the general depletion of other major elements. Silicification of the GGF caused extensive leaching of Na_2O and K_2O from volcanic glass in the succession.
- GGF M4 has FeO, MgO and MnO enrichment caused by intense chlorite alteration.
- A positive correlation between SiO_2 and FeO in the GGF indicates the dominance of quartz and chlorite alteration throughout the succession. Inter-element correlation between FeO and MgO results from changes in the composition and abundance of chlorite.
- Blanket Na and K depletion precludes the application of alteration indices to characterise the alteration at Gossan Hill.
- Within GGF M6, Cd, As, Pb, Fe, Zn, Ag, Bi, Sb and Sn are anomalous in siliceous alteration proximal to massive sulphides. Elsewhere the GGF lacks a distinctive trace element signature.
- Geochemical alteration in the hangingwall volcanics is defined by K_2O and CaO enrichment, reflecting muscovite and calcite alteration. The geochemical signature of hangingwall alteration is different from trends identified in the GGF.
- Chert beds in the M1 Marker have a geochemistry consistent with their origin as a hydrothermal precipitate. Chlorite beds in the M1 Marker have a mixed immobile and mobile element geochemistry, and likely represent hydrothermally modified lithic-rich beds.

Chapter 9

Metal zonation

9.1 Introduction

The metal zonation of VHMS deposits has proved useful in understanding the genesis of these deposits. It is widely recognised that VHMS deposits display a metal zonation that ranges from a central Fe to Fe-Cu rich core, passing upwards and outwards to zones of Cu-Pb-Zn metal enrichment and finally to zones of Pb-Zn-Ba metal enrichment (Large, 1977; 1992; Eldridge *et al.*, 1983; Kuroda, 1983; Khin Zaw, 1989; McArthur and Dronseika, 1990; Hill, 1996). These metal zonation patterns are used to infer physiochemical conditions and temperatures of metal deposition as well as metal transport mechanisms and potential feeder sites to the deposits (*e.g.*, Large, 1977; 1992; Solomon and Walshe, 1979; Ohmoto *et al.*, 1983; Gemmell and Large, 1992). Despite well-constrained zonation models for mound deposits, the metal zonation of sheet and blanket-type deposits are somewhat more complex (Huston, 1988; Large, 1992). This complexity arises from a less focussed hydrothermal system and the probability of multiple feeder sites as proposed by Huston (1988).

The observed metal zonation of mound deposits reflects the final stage in their evolution. The classical zonation patterns described by Eldridge *et al.* (1983), result either from continual hydrothermal modification and overprint during sulphide formation, or from multiple episodes of hydrothermal activity. Both of these result in mound-building and zone refining processes. This is exemplified in stacked VHMS deposits where the cumulative metal zonation patterns reflect, (1) multiple hydrothermal-mineralising events, and (2) hydrothermal overprint of lower deposits by the hydrothermal systems forming the overlying sulphide deposits (*e.g.*, Knuckey *et al.*, 1982a; Huston, 1990; Huston *et al.*, 1995).

Large (1992) defines three different types of VHMS deposits based on metal contents; (1) Cu deposits, (2) Cu-Zn deposits, and (3) Zn-Pb-Cu deposits. Of these three types, the Zn-Pb-Cu association is the most common deposit type in Australia. Metal zonation within deposits of the Cu-type, such as Mount Morgan and Mount Lyell is generally poor, whilst Cu-Zn and Zn-Pb-Cu deposits have well-developed metal zonation (Large, 1992). Cu-Zn deposits, are the main deposit type within Late Archean rocks (Sangster, 1972). Principally, these Archean deposits differ from Proterozoic deposits in their relatively low abundance of Pb and the general absence of Ba and sulphate minerals (*e.g.*, Sangster,

1972; Franklin *et al.*, 1975; Frater, 1978; Knuckey *et al.*, 1982a;b; Barrett *et al.*, 1991; Mill *et al.*, 1990; Barrett *et al.*, 1991; 1992; 1993).

The aims of this metal zonation study at Gossan Hill are to:

- identify the gross zonation patterns within the deposit;
- examine the metal associations within the different mineralised zones and to compare them with the gross zonation patterns;
- define potential feeder zones from metal concentrations.

9.2 Previous work

Frater (1978) identified a bimodal Cu and Zn metal association at Gossan Hill, which consists of three distinct signatures.

(1) Zn-Pb-rich (sphalerite, galena, ±chalcopyrite, ±magnetite, ±pyrrhotite);

(2) Zn-Cu-rich (pyrite, sphalerite, chalcopyrite, magnetite, pyrrhotite);

(3) Cu-rich (pyrite, chalcopyrite, magnetite, ±pyrrhotite).

The metal zonation of the Gossan Hill deposit was broadly defined by Frater (1978) to have a Cu-rich centre that passes vertically upward to a Zn-Cu association underlying a Zn-Pb association. The transition between the Zn-Cu and Zn-Pb zones is gradual, however the relationship between the Cu- and Zn-Cu associations has not been defined. The spatial association between the sulphide and magnetite zones (Chapter 5), concluded that a large part of the Cu-rich mineralisation in the lower and upper ore zones consists of stringer veins. It is therefore possible to review the metal zonation within and between Zn-Cu and Zn-Pb sulphides in the upper ore zone (GGF M6) with the Cu-rich sulphides of the lower ore zone (GGF M4).

Frater (1978) identified a highly variable correlation between the distribution of sulphide and magnetite. Similar patterns between the 1% and 2% Cu contours in the lower ore zone at Gossan Hill, indicate that the main Cu concentration occurs near the base of massive sulphides, approximately 200 m below surface (Frater, 1978). It was only in this location that Frater (1978) noted a high correlation between Cu and magnetite. This correlation will prove significant later in this chapter for the identification of a hydrothermal feeder (Section 9.7.2).

9.1 Methods

In this thesis, assay data is used to investigate metal zonation. The assays represent split diamond drill core, from 0.2 to 2 m intervals (average of 1 m), routinely assayed by MZC and limited in this study to drill holes generated in the 1994-1997 feasibility study. MZC routinely analyse for Cu, Pb, Zn, Ag, Co, Au, Fe and specific gravity. Contoured metal diagrams use MZC assay data from which the elements, Cu, Pb, Zn, Ag, Au, Fe and specific gravity, were contoured. Although this database also included Co, these values are generally below detection. Zn and Cu ratios were not contoured due to the low values of Pb and Zn outside of the upper ore zone that result in a wide spread of these

ratios, which make them spurious. The southern limit of drilling in the 1994-1997 feasibility study is approximately 18,200 N. Therefore the southern parts of the upper ore zone are not included in this metal zonation study. In addition, the weathered upper 100 m of Gossan Hill were excluded from this investigation.

Metal contours in this thesis were generated on the contouring program SURFER (v. 6.2). Due to the close spacing of data points within the mineralised zone, a method of linear kriging was used. In all cases, a 5 m grid interval was used and the specification for each east-west section, as well as the plan and north-south long projections, are given in Appendix A7.1.

The variation of the Zn and Cu ratios was investigated along two sections; one from the lower ore zone in GGF M4 (composite of sections 18,560 N and 18,480 N) and the other a composite section through the upper ore zone in GGF M6 (18,300 N). Drill holes along these sections are listed in Appendix A7.2. Analyses in each ore zone were subdivided on the basis of ore type following the criteria described in Appendix A7.3.

9.2 Metal contours

Contoured diagrams give a visual and spatial guide to the concentrations and correlation between metals. Contoured diagrams were generated over the mineralised zone at Gossan Hill (Figs. 9.1 to 9.7). Each of these diagrams has four east-west sections, a plan projection along 10,150 RL and a composite long section through 5,000 E in order to illustrate the three dimensional variation of each metal.

9.2.1 Results

Metal contours over the mineralised zone at Gossan Hill (Figs. 9.1 to 9.7) illustrate the Zn, Pb, Ag, Au association in massive sphalerite of the upper ore zone and Cu-Fe enrichment in massive pyrite and stringer mineralisation of the lower ore zone. Cu enrichment also occurs in discordant stringer mineralisation between the upper and lower ore zones, as well as in massive pyrite underlying massive sphalerite. Massive magnetite has high Fe contents and does not contain significant base metals. The distribution of metals in the ore zones defines a gradual enrichment from a high grade, Cu-Fe rich base, upwards to Cu-Zn, to a Zn-Pb-Ag and Au zone at the top of ore.

The distribution of Cu at Gossan Hill (Fig. 9.1) is dissimilar to that of Pb (Fig. 9.2), Zn (Fig. 9.3) and Ag (Fig. 9.4), but in part, similar to Au (Fig. 9.5), and weakly with Fe (Fig. 9.6) and specific gravity (Fig. 9.7). The spatial correlation of Cu and Au is best developed in the lower ore zone between 18,500 N and 18,700N, where Cu has its highest concentrations in massive pyrite (Fig. 9.1). Cu in this lower ore zone forms a broad zone that plunges northwards. A lower grade Cu zone also occurs in the upper ore zone within massive pyrite and below massive sphalerite (Fig. 9.1). The lower and upper ore zones are weakly interconnected by a series of regions anomalous in Cu, which reflect the residence of Cu in sulphide veins. It is also notable that massive magnetite in the lower ore zone (dashed black lines in Fig. 9.1) only contains scattered anomalous Cu values.

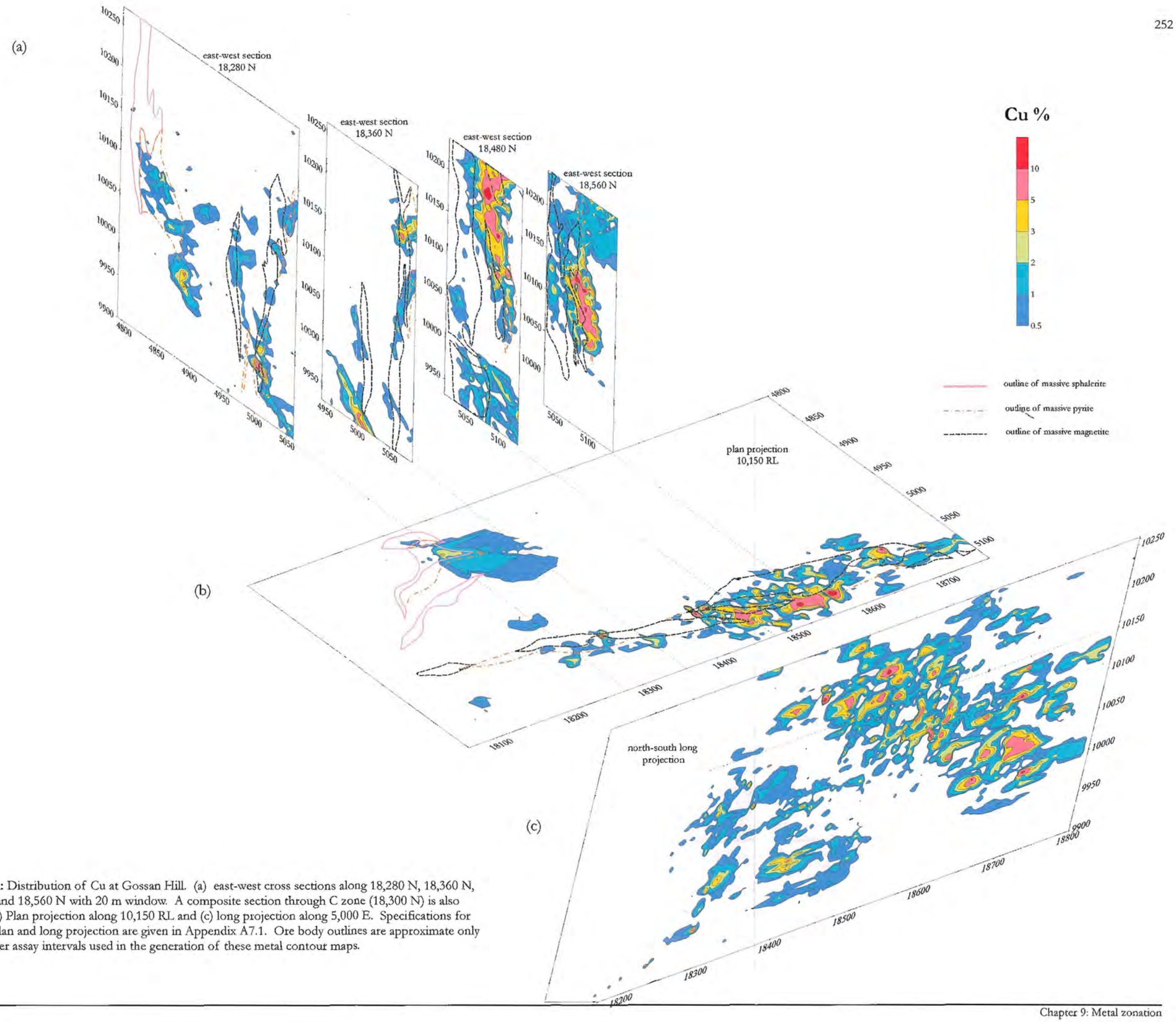

Figure 9.1: Distribution of Cu at Gossan Hill. (a) east-west cross sections along 18,280 N, 18,360 N, 18,480 N and 18,560 N with 20 m window. A composite section through C zone (18,300 N) is also shown. (b) Plan projection along 10,150 RL and (c) long projection along 5,000 E. Specifications for sections, plan and long projection are given in Appendix A7.1. Ore body outlines are approximate only due to wider assay intervals used in the generation of these metal contour maps.

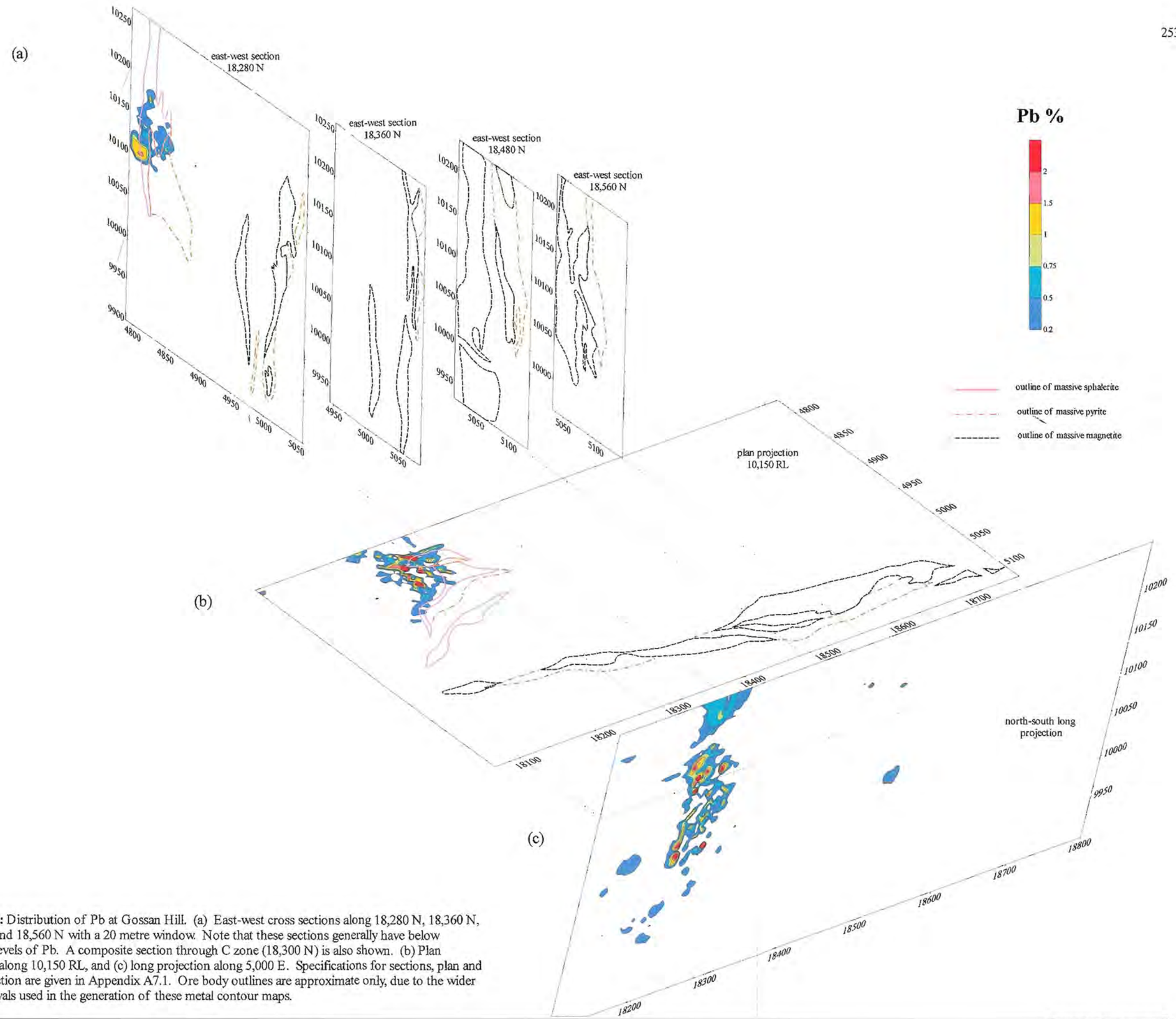

Figure 9.2: Distribution of Pb at Gossan Hill. (a) East-west cross sections along 18,280 N, 18,360 N, 18,480 N and 18,560 N with a 20 metre window. Note that these sections generally have below detection levels of Pb. A composite section through C zone (18,300 N) is also shown. (b) Plan projection along 10,150 RL, and (c) long projection along 5,000 E. Specifications for sections, plan and long projection are given in Appendix A7.1. Ore body outlines are approximate only, due to the wider assay intervals used in the generation of these metal contour maps.

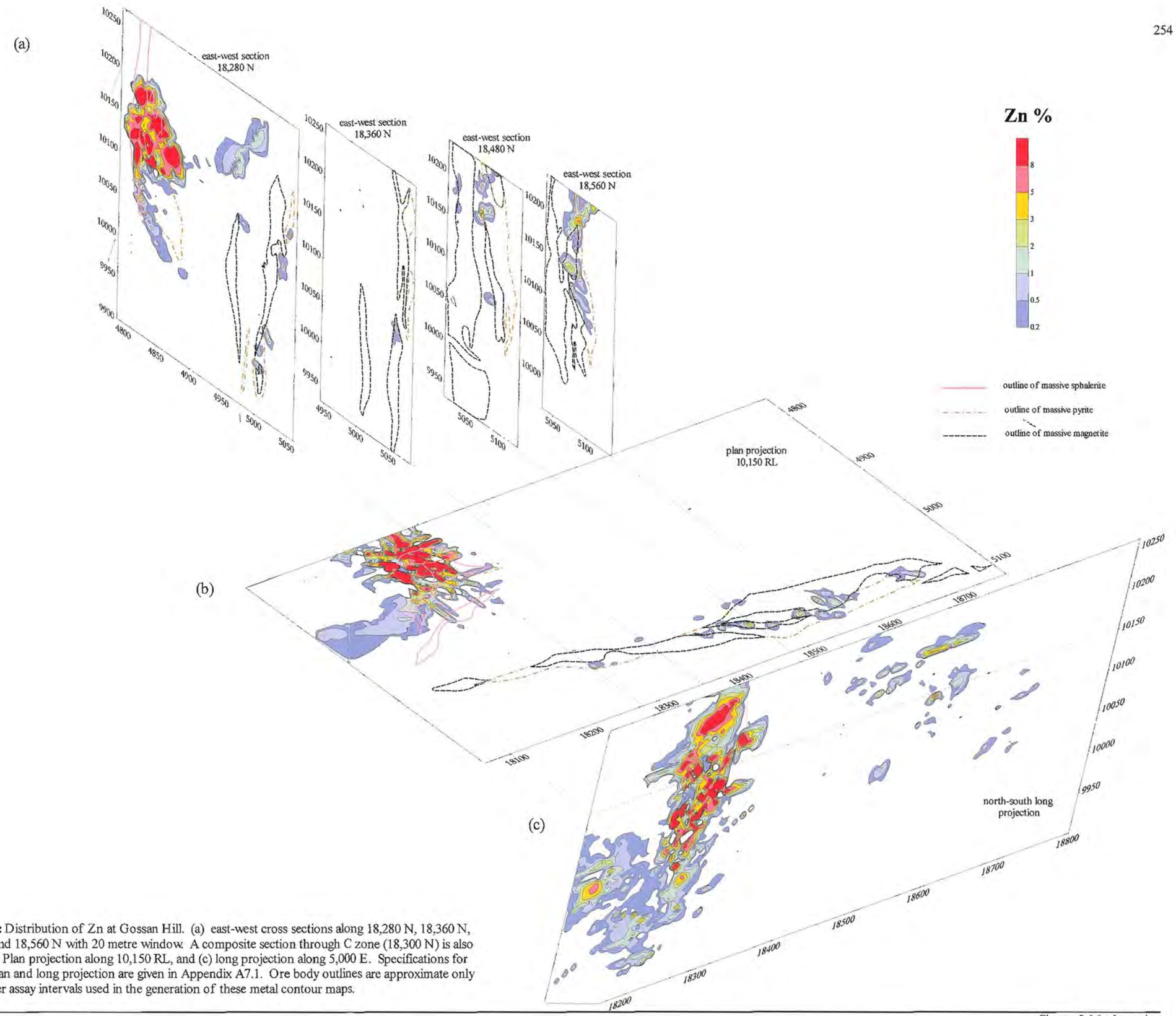

Figure 9.3: Distribution of Zn at Gossan Hill. (a) east-west cross sections along 18,280 N, 18,360 N, 18,480 N and 18,560 N with 20 metre window. A composite section through C zone (18,300 N) is also shown. (b) Plan projection along 10,150 RL, and (c) long projection along 5,000 E. Specifications for sections, plan and long projection are given in Appendix A7.1. Ore body outlines are approximate only due to wider assay intervals used in the generation of these metal contour maps.

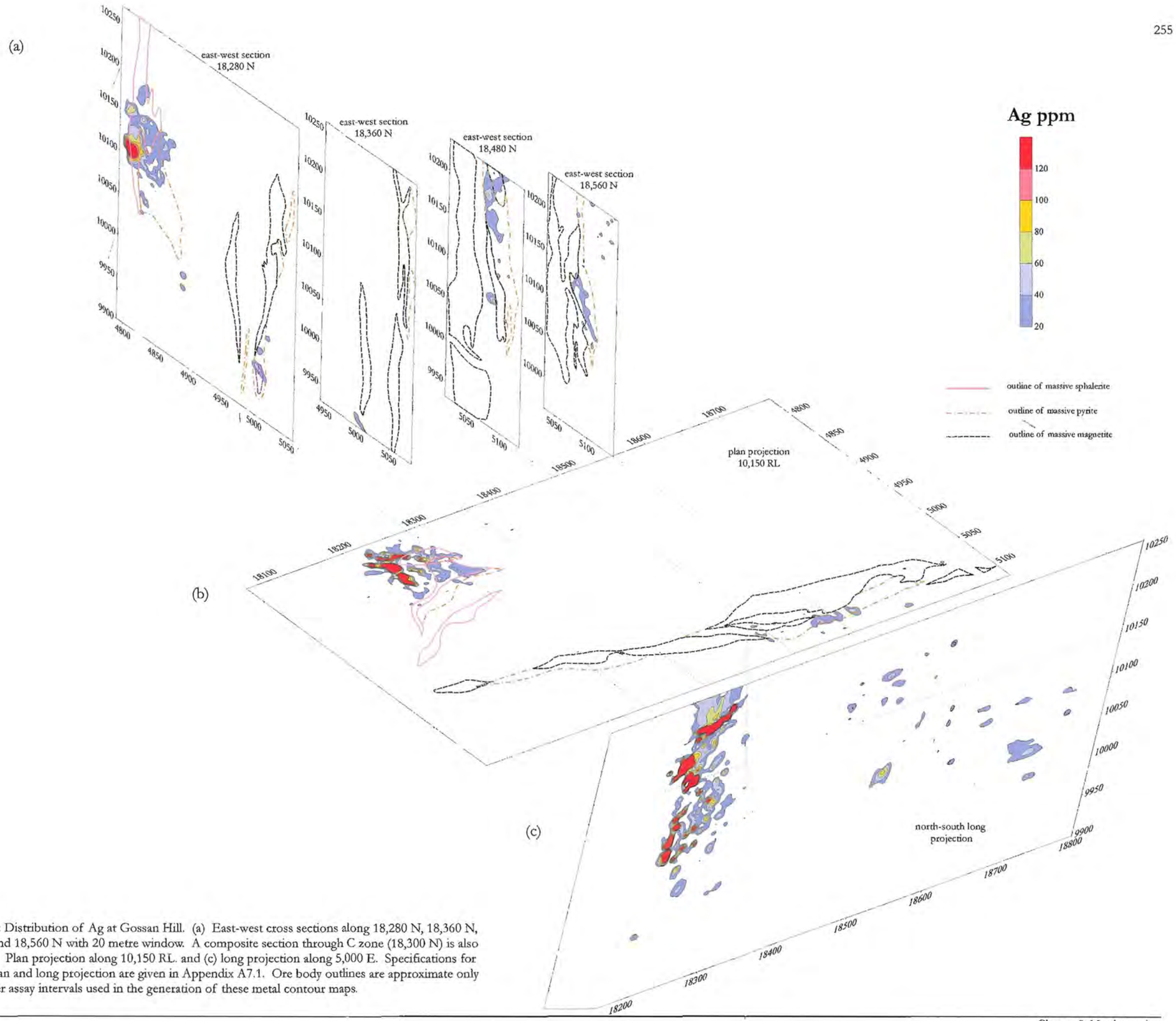

Figure 9.4: Distribution of Ag at Gossan Hill. (a) East-west cross sections along 18,280 N, 18,360 N, 18,480 N and 18,560 N with 20 metre window. A composite section through C zone (18,300 N) is also shown. (b) Plan projection along 10,150 RL. and (c) long projection along 5,000 E. Specifications for sections, plan and long projection are given in Appendix A7.1. Ore body outlines are approximate only due to wider assay intervals used in the generation of these metal contour maps.

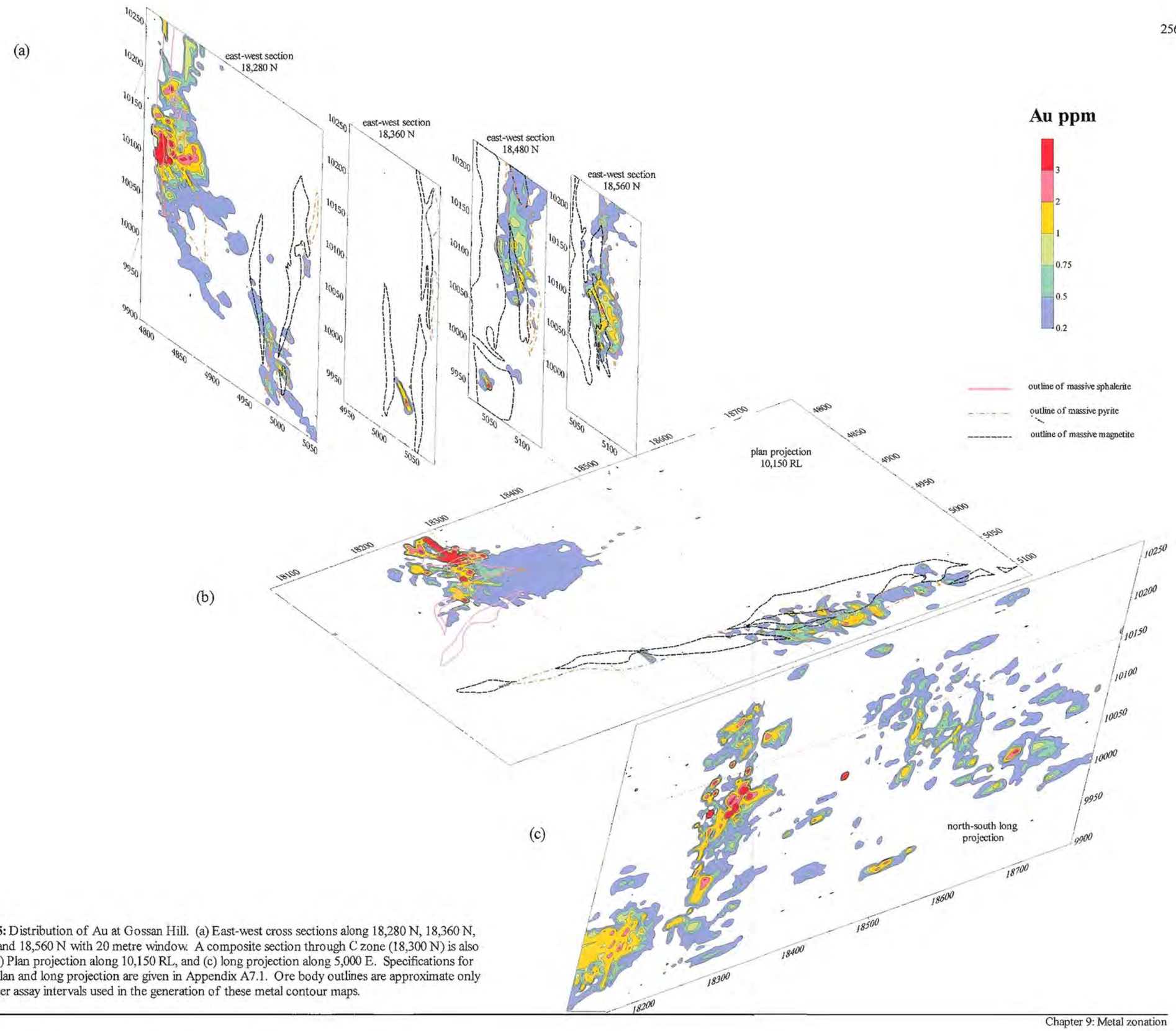

Figure 9.5: Distribution of Au at Gossan Hill. (a) East-west cross sections along 18,280 N, 18,360 N, 18,480 N and 18,560 N with 20 metre window. A composite section through C zone (18,300 N) is also shown. (b) Plan projection along 10,150 RL, and (c) long projection along 5,000 E. Specifications for sections, plan and long projection are given in Appendix A7.1. Ore body outlines are approximate only due to wider assay intervals used in the generation of these metal contour maps.

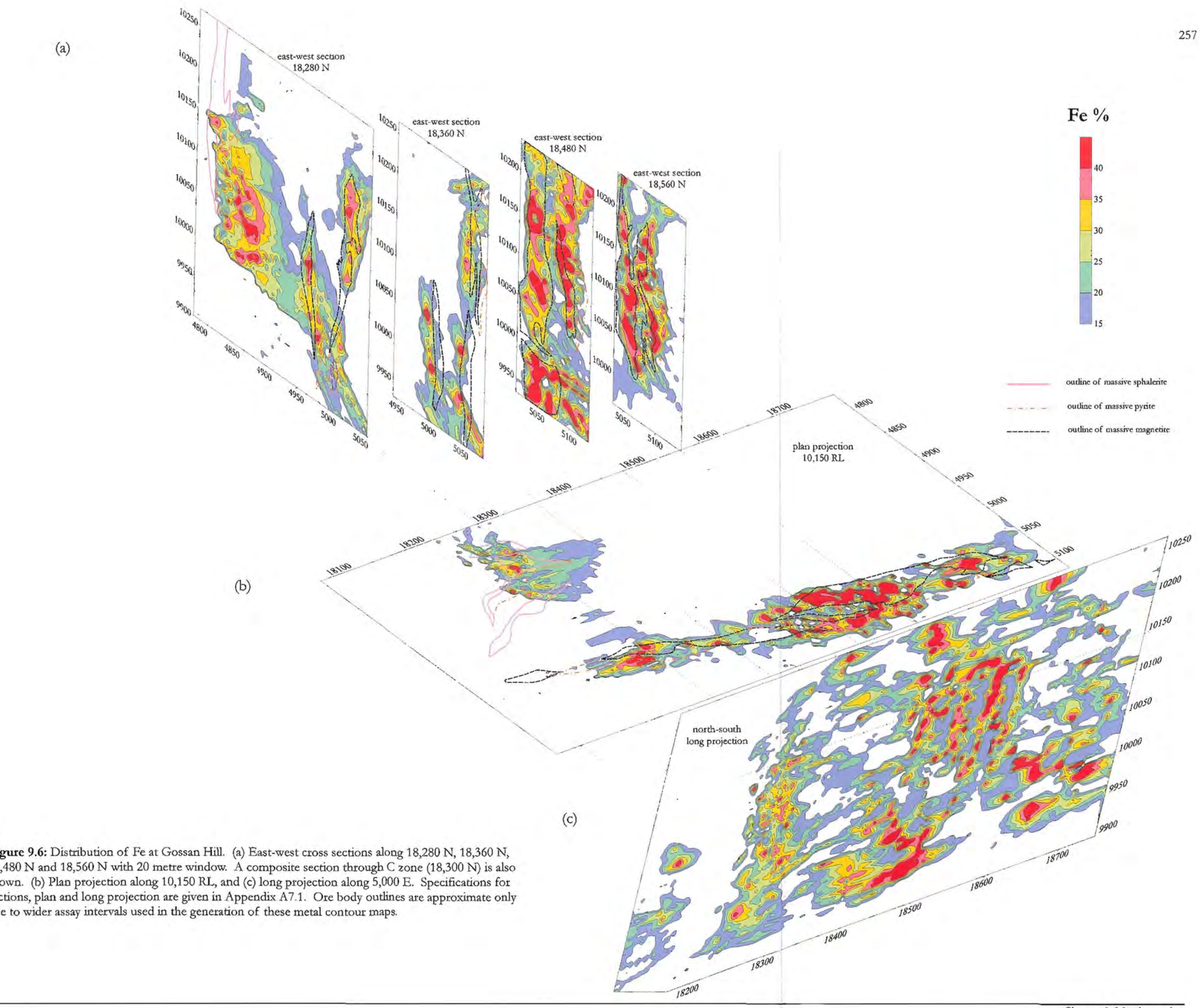

Figure 9.6: Distribution of Fe at Gossan Hill. (a) East-west cross sections along 18,280 N, 18,360 N, 18,480 N and 18,560 N with 20 metre window. A composite section through C zone (18,300 N) is also shown. (b) Plan projection along 10,150 RL, and (c) long projection along 5,000 E. Specifications for sections, plan and long projection are given in Appendix A7.1. Ore body outlines are approximate only due to wider assay intervals used in the generation of these metal contour maps.

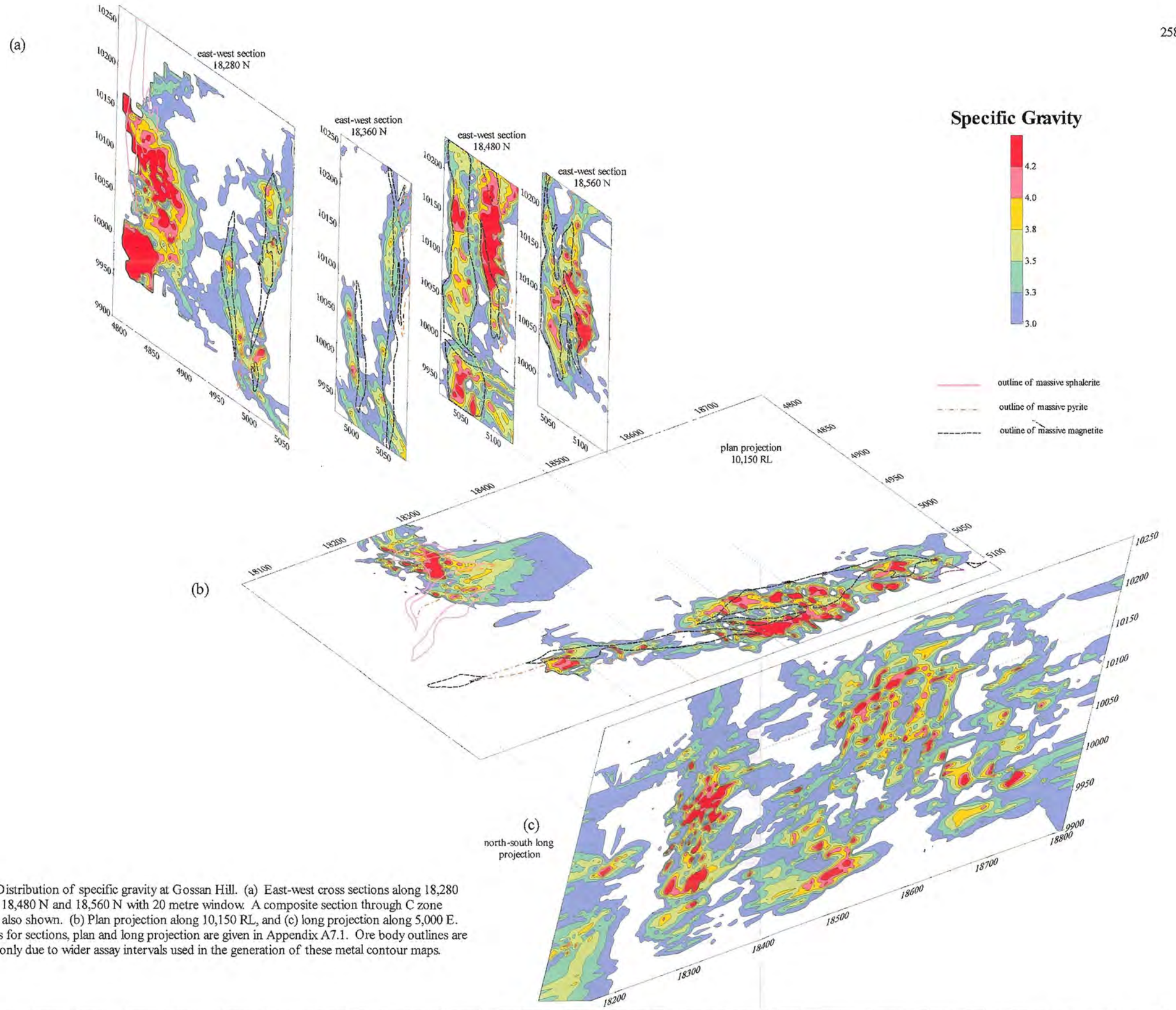

Figure 9.7: Distribution of specific gravity at Gossan Hill. (a) East-west cross sections along 18,280 N, 18,360 N, 18,480 N and 18,560 N with 20 metre window. A composite section through C zone (18,300 N) is also shown. (b) Plan projection along 10,150 RL, and (c) long projection along 5,000 E. Specifications for sections, plan and long projection are given in Appendix A7.1. Ore body outlines are approximate only due to wider assay intervals used in the generation of these metal contour maps.

The distribution of Pb, Zn, Ag and Au (Figs. 9.2 to 9.5) correlates well. The highest values of each of these metals occur in the upper ore zone within massive sphalerite. The lower ore zone has scattered low level Zn and Ag, with Pb absent from this zone (Fig. 9.2). The distribution of Pb and Ag is generally localised to the upper ore zone in massive sphalerite, with Zn and Au having more widely distributed concentrations. Moreover, Au (Fig. 9.5) is more widely distributed than Zn, and the highest concentrations of Au coincide with the highest concentrations of Zn, Pb and Ag in the upper ore zone. Low level Au values (<2 ppm) are also associated with the highest concentrations of Cu (Fig. 9.5c) and Au forms a broad zone of scattered interconnected anomalies with a similar northward plunge to that of Cu. Therefore, Au is associated with Zn in the upper ore zone, and Cu in the lower ore zone. The Pb, Zn, Ag and Au contours in the upper ore zone are steep and indicate sharp contacts between high grade massive sulphides and the enclosing rock, particularly to the west against the hangingwall. The anomalous zone of Zn, Ag, Pb and Au has a subvertical plunge (*e.g.* Fig. 9.3) and is laterally continuous towards the south (*e.g.*, Figs. 9.3b and 9.3c).

The distribution of Fe and specific gravity at Gossan Hill relates to the high density of these rocks due to high concentrations of Fe in magnetite and sulphide. Fe contours (Fig. 9.6) provide the best guide to the distribution of massive sulphide, massive magnetite and stringer zones, irrespective of their metal concentrations. Iron in the lower ore zone maps out the two interconnected, subvertical massive magnetite lenses (Fig. 9.6a; 18,480 N and 18,560 N), with the highest Fe concentrations (>35 %) located in the central area between 18,500 N and 18,600 N (Fig. 9.6b). These high Fe values coincide with both massive sulphide and massive magnetite. Within the lower ore zone, the contour gradients are steep indicating sharp contacts of magnetite and sulphide against less Fe-enriched wall rock, which is the hangingwall dacite to the west. The upper ore zone has comparatively lower concentrations in Fe and delineates zones of massive sulphide. The distribution of Fe in the upper ore zone highlights a broad anomalous Fe zone corresponding to the stringer stockwork that interconnects the upper and lower ore zones (Fig. 9.6a; 18,280 N). Specific gravity has a very similar distribution to Fe, with the highest values occurring in massive magnetite and massive sulphide (Fig. 9.7). In the Fe and specific gravity contour diagrams (Figs. 9.6 and 9.7), the lower ore zone plunges to the north, whilst the upper ore zone has a subvertical plunge.

9.3 Zn and Cu ratio values

In Phanerozoic VHMS deposits, the Zn ratio (100*Zn/(Zn+Pb)) varies from 60 to 90 (Huston and Large, 1987). However, average Zn ratio values differ (1) between deposits, and (2) between ore types within a single deposit. These variations reflect differences in the depositional temperature and salinity of the metal-bearing ore fluids (Huston and Large, 1987). High Zn ratios within Late Archean VHMS deposits reflect low Pb contents in these deposits. The Cu ratio (100*Cu/(Cu+Zn)) has also been used to constrain physiochemical conditions of ore formation, however these values tend to be more variable than Zn ratio values (*e.g.*, Sangster, 1972; Knuckey *et al.*, 1982a). At Gossan Hill, the variation in the Cu and Zn ratios identify a primary bimodal metal

distribution within and between the lower and upper ore zones.

9.3.1 The upper ore zone

Zn and Cu ratios within the upper ore zone are illustrated in Figures 9.8a and 9.8b. The variation in these ratios between ore types is given in Appendix A7.4. The upper ore zone is characterised by high Zn ratios that are skewed toward values of 100 (Fig. 9.8a). This trend is significantly different from the distribution of the Zn ratio in Phanerozoic deposits, but is typical of Late Archean VHMS deposits due to low Pb abundances in these systems (Huston and Large, 1987). The mean Zn ratio in the upper ore zone at Gossan Hill is 84.0, but it varies from 14 to 100 and has a high standard deviation (13.5). This indicates a wide variation in the relative proportions of Zn and Pb. A mean Zn ratio of 84.0 at Gossan Hill is higher than observed within most Australian VHMS deposits, but is comparable to Zn ratios in the Waterloo deposit (Huston *et al.*, 1995) and the Canadian Archean deposits (Table 9.1). Skewed Zn ratio distributions are also observed in each ore type within GGF M6 (Appendix A7.4), with mean values varying from 81.1 to 92.0 and high standard deviations varying from 10.7 to 13.7.

At Gossan Hill, the Zn ratio increases from a mean of 82.2 in the altered wall rock, to 81.1 in massive pyrite, to 86.5 in stringer veining, and 92.0 in massive sphalerite (Appendix A7.4). These values reflect an increase in the Zn ratio stratigraphically upwards and correspond to the highest Zn ratios within high grade Zn-Pb sulphides in the uppermost parts of the upper ore zone. Notably, the highest standard deviation of

Table 9.1: Grades, tonnage, base metal values and Cu and Zn ratios of various Australian Proterozoic VHMS deposits and both Australian and Archean Cu-Zn VHMS deposits. Note due to low Pb contents in Canadian Archean deposits, Pb is not reported.

Deposit Type	Deposit	Tonnage (Mt.)	Pb %	Zn %	Cu %	Zn ratio	Cu Ratio	Reference*
Australian	Rosebery	19.4	5	15.2	0.74	76.4	4.6	1
Proterozoic	Hercules	2.57	5.2	16.7	0.42	76.3	2.5	1
Zn-Pb-Cu	Hellyer	15	7	13	0.4	65	3	1
VHMS deposits	Que River	3.5	7	12.5	0.35	64.1	2.7	1
	Thalanga	6.4	3.9	12.3	2.2	75.9	15.2	2
	Waterloo	0.37	2.8	19.7	3.8	87.6	16.2	2
Australian	Scuddles	26.2	0.5	6.9	1.2	93.2	14.8	1
Archean Cu-Zn	Gossan Hill**	2.2	1.1	11.4	0.3	91.2	2.6	
VHMS deposits	Gossan Hill#	7.1	-	0.3	3.4	-	91.9	
	Teutonic Bore	2.2	0.9	11.1	3.5	92.5	24	1
Canadian	Millenbach	> 3.0	-	4.5	3.5	-	43.8	3
Archean Cu-Zn	Detour	2.7	-	2	2.9	-	59.2	3
VHMS deposits	Geco	26	-	4.01	1.97	-	32.9	4
	Corbet	2.9	-	2	2.9	-	59.2	5
	Mobrun	10.4	-	5.43	0.76	-	12.3	6
	Mattabi	12.8	0.84	7.6	0.91	90	10.76	7
	Mattagami	20	-	10.5	0.7	-	6.3	8

*1. Large, 1992, 2. Berry *et al* (1992), 3. Knuckey *et al* (1982a), 4. Friesen *et al* (1982), 5. Knuckey and Watkins (1982), 6. Barrett et al. (1991), 7. Franklin et al. (1975), 8. Roberts (1975).

**upper ore zone at Gossan Hill, # lower ore zone at Gossan Hill

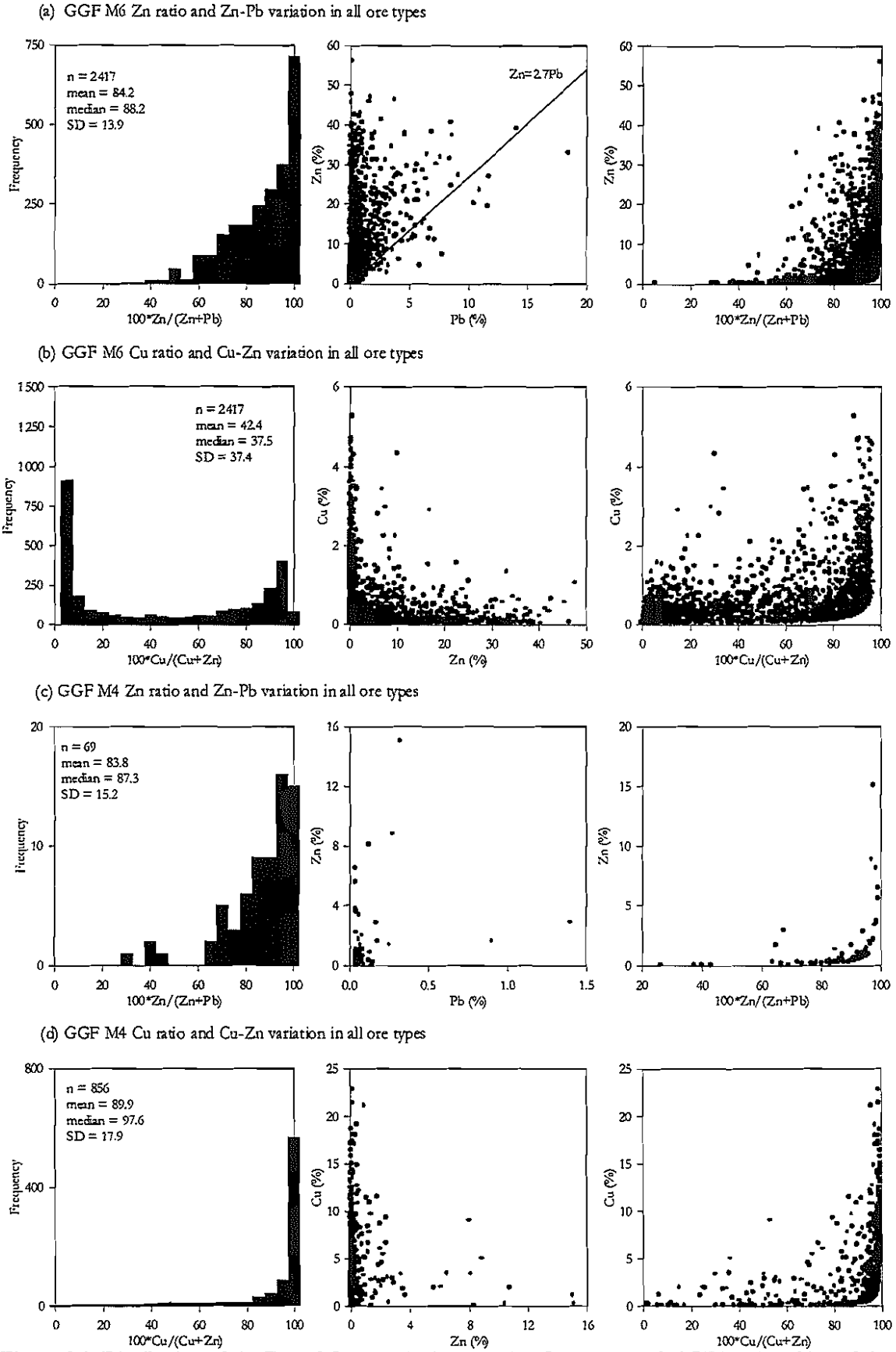

Figure 9.8: Distribution of the Zn and Cu ratios in the upper Zn-Cu ore zone of GGF M6 (a and b) and the lower Cu-rich ore zone of GGF M4 (c and d). (a) Zn ratio and Zn-Pb variation in all ore types within GGF M6, (b) Cu ratio and Zn-Cu variation of all ore types within GGF M6, (c) Zn ratio and Zn-Pb variation of all ore types within GGF M4, and (d) Cu ratio and Cu-Zn variation of all ore types within GGF M4. Data used is from composite section 18,300 N (GGF M6) and east-west sections 18,480 N and 18,560 N (GGF M4). Drill holes used are listed in Appendix A7.2. SD = standard deviation. Cu, Pb, Zn values <0.02% are not plotted.

13.7 occurs within stringer veining and reflects the mineralogical variation of these sulphide veins.

The Pb and Zn contents of the upper ore zone have a weak correlation (Fig. 9.8a; Appendix A7.4). This contrasts with Phanerozoic deposits, where these metals have a generally well defined linear distribution (*e.g.*, Huston and Large, 1987; Hill, 1996). The magnitude of Zn enrichment in the upper ore zone at Gossan Hill, is however, similar to Phanerozoic VHMS deposits (Huston and Large, 1987; Khin Zaw, 1989; Hill, 1996), whilst the magnitude of Pb enrichment is significantly less at Gossan Hill. At Rosebery, the sulphide ore lies above the line Zn=1.5Pb (Zn ratio of 60.0), whilst at Gossan Hill this lower cut off is Zn = 2.7Pb (Zn ratio of 73.0) (Fig. 9.8a) due to lower Pb contents. The weak correlation between Zn and Pb, together with the low abundances of Pb, result in generally higher and more variable Zn ratios than that observed within Phanerozoic deposits. The causes for the poor correlation of Zn and Pb may result from undersaturation of Pb in the ore solutions, as well as variations in temperature and salinity (Huston and Large, 1987).

The Cu ratio in the upper ore zone ranges from 0 to 100 (Fig. 9.8b) and has a mean Cu ratio of 37.9 with a very high standard deviation (37.8). The variation of Cu ratios between ore types (Appendix A7.4) highlights dominantly low values (< 20) in massive sphalerite, stringer mineralisation and wall rock. The distribution of Cu ratios in these ore types is skewed towards values of zero. The spread in the Cu ratio within massive pyrite (0 to 100; Appendix A7.4) indicates that this ore type has the most variable Cu and Zn contents, with high Zn corresponding to low Cu and *vice versa*. Zn and Cu contents of ore types within this upper ore zone generally lack correlation (Fig. 9.8b and Appendix A7.4). Good correlation between Cu and the Cu ratio in massive sphalerite (Appendix A7.4) reflects decreased Zn and increased Cu contents within massive sphalerite towards the footwall (Section 9.4.1). Despite this correlation in massive sphalerite, the Cu ratio in the upper ore zone lacks a systematic stratigraphic variation between ore types, which likely indicates differing physiochemical conditions under which Cu and Zn were transported and deposited.

9.3.2 The lower ore zone

Zn ratios in the lower ore zone differ markedly from values within the upper ore zone (Fig. 9.8c). The lower ore zone has lower Zn ratios (mean of 63.9) and a higher standard deviation (15.8). The spread of Zn ratio values in this lower ore zone reflects low Pb contents (generally less than 0.2 wt. %) (Fig. 9.8c). This trend is observed within each of the different ore types within the lower ore zone (Appendix A7.5), where Zn is generally less than 4 wt.% and has no correlation with Pb (Fig. 9.8c). The Zn ratio of the lower ore zone is therefore complicated by the low Pb and Zn levels, which result in variable Zn ratios.

The Cu ratio within the lower ore zone has a skewed distribution towards values of 100 with a mean of 87.0 (Fig. 9.8d) and a high standard deviation (19.3). Consistently high Cu ratios are observed within each ore type of the lower ore zone (Appendix A7.5e to

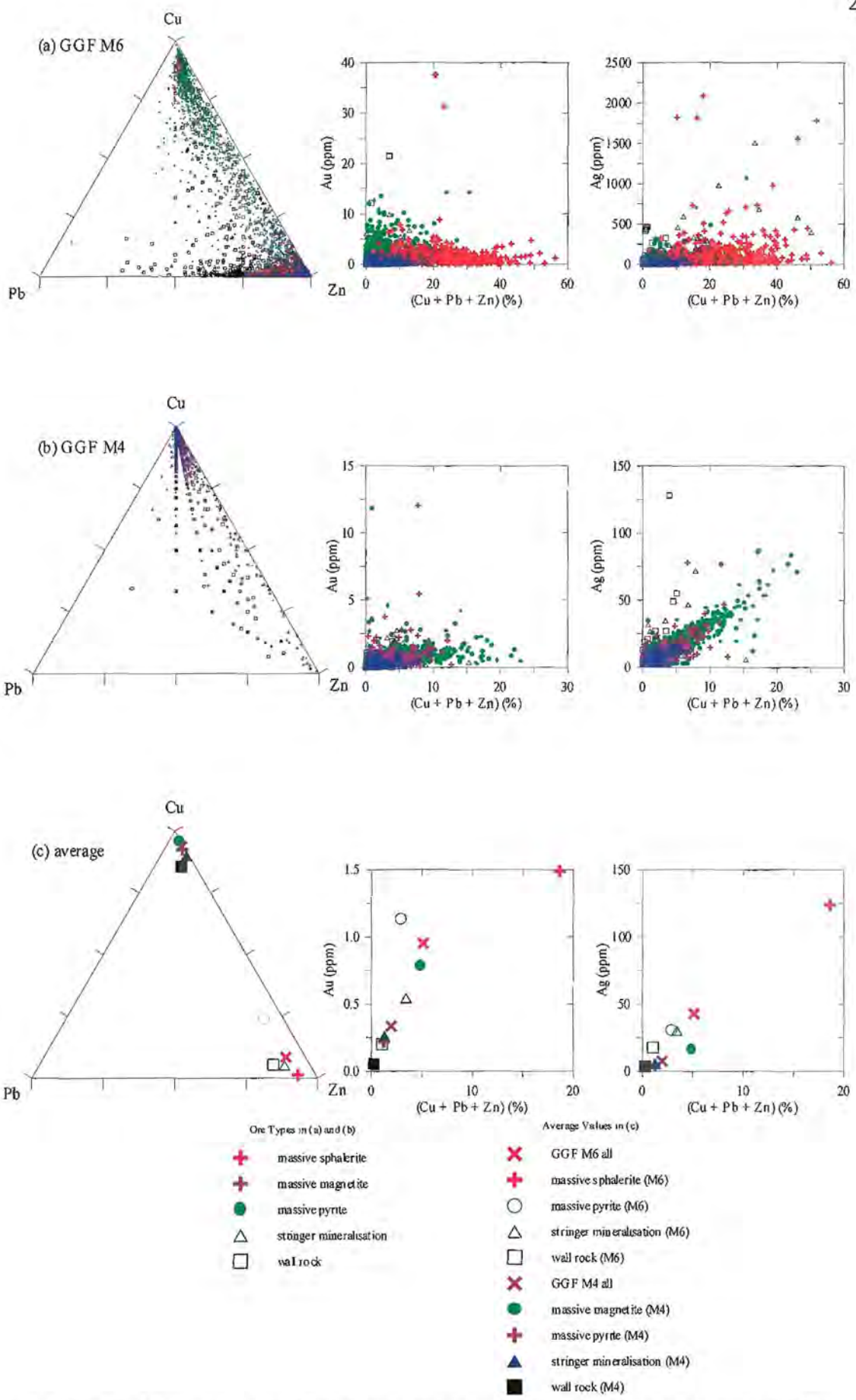

Figure 9.9: Cu-Pb-Zn ternary diagram for (a) the upper ore zone in GGF M6, (b) the lower ore zone in GGF M4 and (c) average metal values in each ore type from the lower and upper ore zones. Assay values derived from composite section 18,300 N for (a), and sections 18,480 N and 18,560 N for (b). Drill holes used are listed in Appendix A7.2.

A7.5g) and indicate the dominance of Cu over Zn. The skewed distribution of Cu ratios in the lower ore zone (Fig. 9.8d) reflect high Cu concentrations that have low, but scattered Zn and the lack of a correlation between Cu and Zn. The application of the Cu ratio and Zn ratio is of limited use in the lower ore zone due to low levels of Zn and Pb in this zone.

9.4 Metal associations

Scatter and ternary diagrams are useful in assessing the degree of inter-element correlation between metals. For Gossan Hill, the total base metal contents (Cu+Pb+Zn), the stratigraphic variation of metals and their inter-element correlation are illustrated in Figures 9.9 to 9.13. These plots were generated from MZC assay data along composite section 10,300 N for the upper ore zone and east-west sections 18,480 N and 18,560N for the lower ore zone. The data were also subdivided into massive sphalerite, pyrite and magnetite and wall rock according to specifications listed in Appendix A7.2.

At Gossan Hill, the total base metal content (Cu+Pb+Zn) differs between the upper and lower ore zones (Fig. 9.9). The upper ore zone has higher total metal contents (<58 wt.%) than the lower ore zone (<25 wt.%) (Fig. 9.9). On a ternary Cu-Pb-Zn diagram, the upper ore zone is characterised by scattered data along the Cu-Zn join, with some Pb enrichment indicated by data along the Zn-Pb join (Fig. 9.9a). From this diagram, the wide scatter in Cu-Zn values indicates a large variation in the relative proportions of Cu and Zn between ore types and wall rock. In the upper ore zone, samples with lower Cu+Pb+Zn values are more enriched in Au, whilst Ag has the opposite trend (Fig. 9.9a). Comparatively, the lower ore zone has strong enrichment in Cu relative to Pb and Zn (Fig. 9.9b) and Au does not correlate with Cu+Pb+Zn, but Ag does correlate with total base metal contents. The average values for both ore zones (Fig. 9.9c) highlight the bimodal Cu-Zn metal association at Gossan Hill with Zn enrichment in the upper ore zone and Cu enrichment in the lower ore zone. The average values of Au and Ag in both ore zones have broad positive correlation to Cu+Pb+Zn with highest values of Au and Ag occurring in the upper ore zone (Fig. 9.9c).

A bimodal Cu-Zn metal distribution is typical of Late Archean VHMS deposits (Large, 1992). Sangster (1972) noted that the distribution of total metals is strongly influence by the abundance of Zn in these deposits. This results from the high magnitude of Zn concentration in ore, relative to that of Cu. For example, at Gossan Hill the proportion of Zn may vary from 3 to 30 wt.% between the upper and lower ore zones, whilst Cu may vary from 1 to 5 wt.% respectively. The change in Zn and Cu concentrations is an order of magnitude for Zn, but only 5-fold for Cu. Therefore the positive correlation between Ag, Au and the total metal contents are broadly reflecting the changes in Zn concentrations and indicate their association to the highest concentrations of Zn.

9.4.1 Variation in metals with stratigraphy

Two examples of the variation in metals with stratigraphy are given in Figure 9.10. In the upper ore zone, the highest concentrations of Zn, Pb, Ag, Au, Cu and Fe occur in the uppermost massive sulphides, which have a sharp hangingwall contact with sandstone in

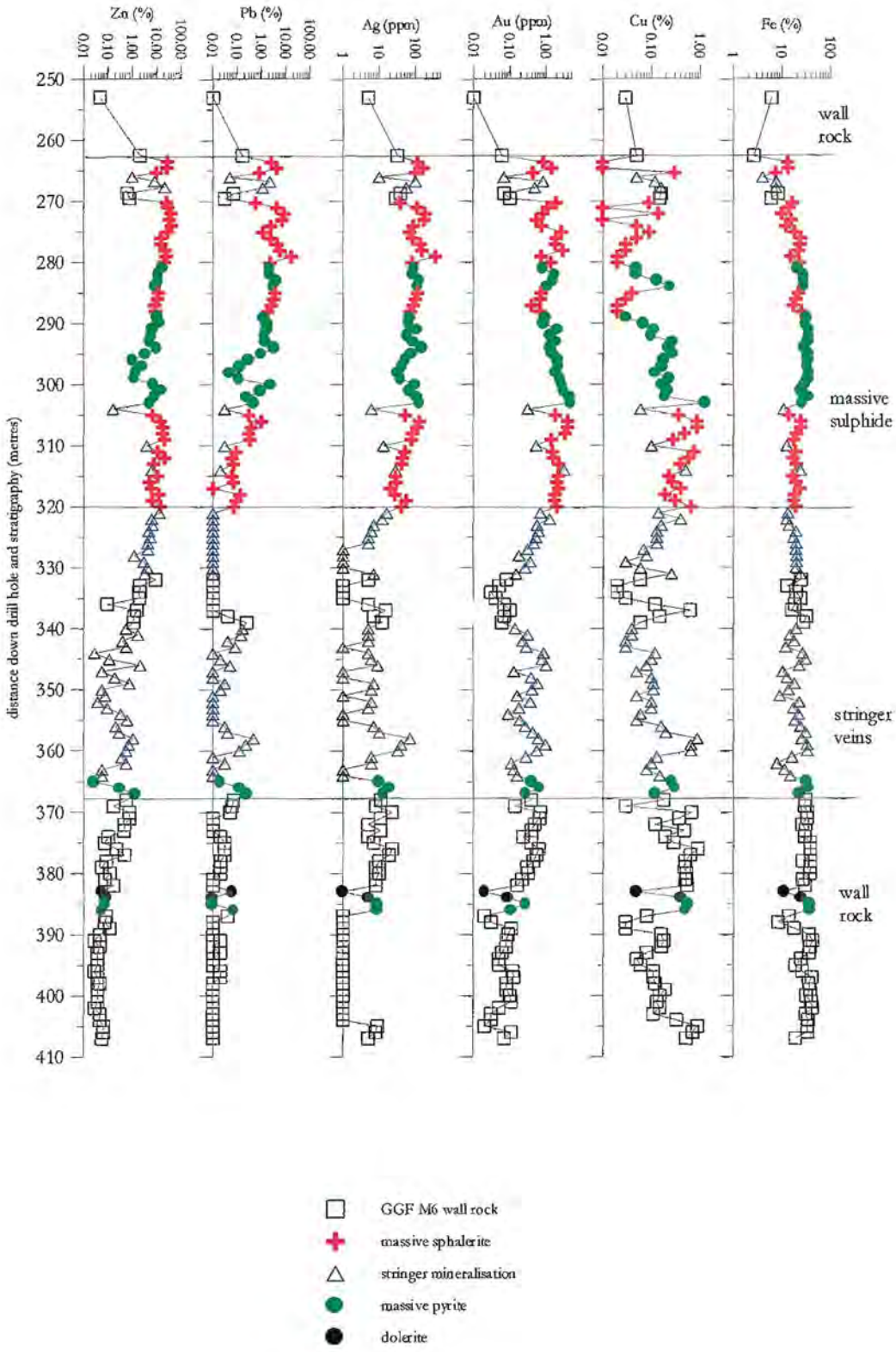

Figure 9.10a: Stratigraphic variation of metals in the upper ore zone through GGF M6 at C zone, including massive sphalerite, massive pyrite and sulphide veins. Data compiled from assay values along drill hole GG165.

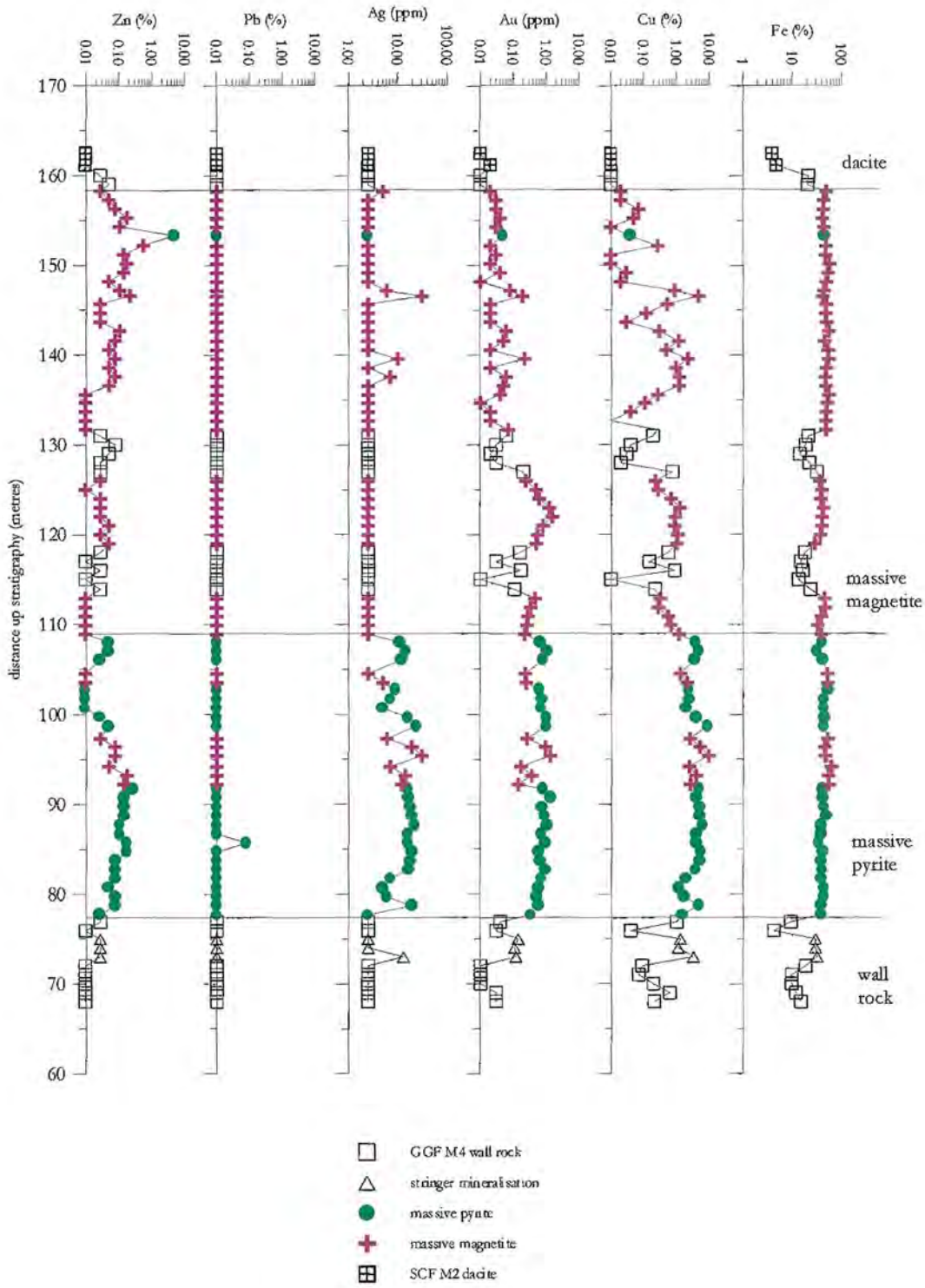

Figure 9.10b: Stratigraphic variation of metals in the lower ore zone through GGF M4, along east-west section 18,480 N through massive pyrite, massive magnetite and the wall rock. Data compiled from assay values along drill hole G96/54.

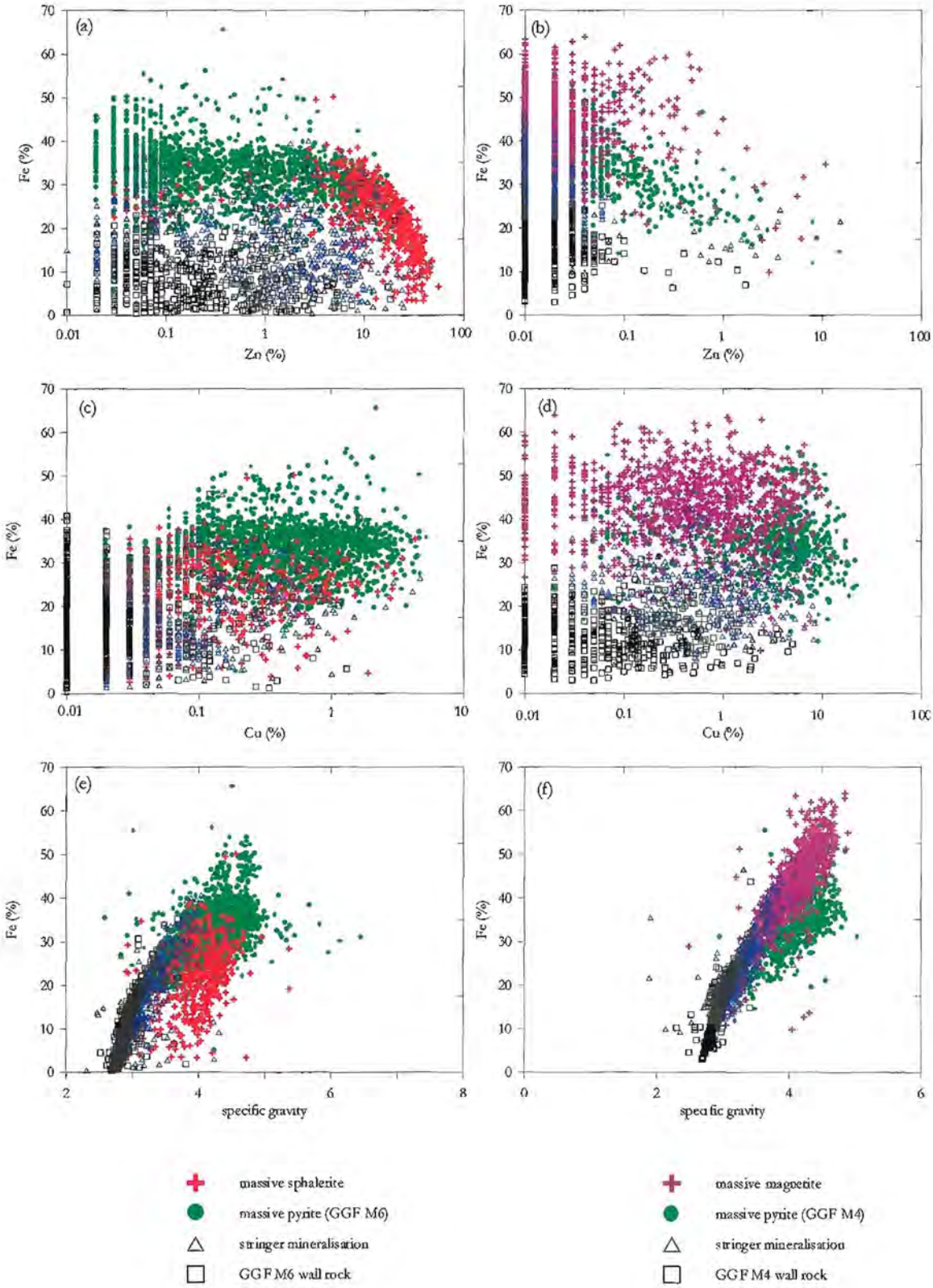

Figure 9.11: Scatter diagrams illustrating the association between Fe and the main ore metals. Fe *versus* Zn within (a) GGF M6 and (b) GGF M4. Fe *versus* Cu within (c) GGF M6 and (d) GGF M4. Fe *versus* specific gravity within (e) GGF M6 and (f) GGF M4. Source of data is composite section 18,300 N for GGF M6 and east-west sections 18,480 N and 18,560 N for GGF M4. Drill holes used for each section are listed in Appendix A7.2.

GGF M6 (Fig. 9.10a). Within this sulphide zone, the levels of Zn, Pb, Ag, Au and Fe decrease with depth. Cu concentrations in the upper ore zone do not vary systematically with depth and Cu has a spiky distribution both within massive sulphide and underlying stringer mineralisation and wall rock. This erratic Cu distribution is typical of vein controlled mineralisation.

The lower ore zone (Fig. 9.10b) has depleted Pb and Ag within massive magnetite, but some Ag anomalism within massive pyrite underlying massive magnetite. Massive magnetite has spiky, erratic concentrations of Zn, Cu and Au associated with sulphide veins within magnetite. Massive pyrite contains elevated Cu, Zn Ag and Au, which also occur in the underlying stringer. Gold and Cu have similar patterns (Fig. 9.10b) in this lower ore zone, with a broad increase in their concentrations toward the footwall, attaining their highest concentrations in the lowest parts of massive pyrite. Nonetheless, Fe has high concentrations throughout massive magnetite and massive pyrite.

9.4.2 Inter-element associations

The main difference between the upper and lower ore zones is not only in the relative abundances of Zn and Cu, but also in the abundance of Fe. The lower ore zone is more enriched in Fe (<65 wt.%) than the upper ore zone (<50 wt.%) due to the high abundance of magnetite in the former (Fig. 9.11). In the upper ore zone, both massive sphalerite and pyrite have higher Zn and Fe than stringer mineralisation and wall rock (Fig. 9.11a). Stringer stockwork has a range in Zn and Fe, which reflects sulphide vein mineralisation. The Zn content within the lower ore zone is an order of magnitude lower (Fig. 9.11b) and the highest Zn concentrations occur in massive pyrite.

In both ore zones Cu primarily occurs in massive pyrite and the magnitude of Cu enrichment is similar in both the lower and upper ore associations. The Cu-Fe scatter diagrams indicate that Cu concentrations in the upper ore zone are highest in massive sphalerite and massive pyrite but have a wide variation (Fig. 9.11c and 9.11d). The Cu content of massive pyrite is not ubiquitous and massive pyrite may be relatively barren of Cu. However, in the lower ore zone Cu has its highest concentrations in massive pyrite, whereas massive magnetite and stringer veins have variable Cu concentrations. These scattered, variable Cu values reflect Cu concentrated within sulphide veins. The specific gravity of rocks in both ore zones (Fig. 9.11d and 9.11f) correlates to the proportion of Fe within them, with massive magnetite and pyrite having the highest specific gravity.

9.4.3 Gold

The association between Au, Ag and base metals is presented as a series of log normal scatter plots for the upper and lower ore zones (Figs. 9.12 and 9.13). Gold has two associations within VHMS deposits, which are; (1) a Pb-Zn-Ag-Au association, and (2) a Cu-Au association (Huston, 1988; Large *et al.*, 1989; Huston *et al.*, 1992). As previously identified (Section 9.4.1), Au at Gossan Hill has its highest concentrations (up to 40 ppm) in massive sulphides of the upper ore zone (both massive sphalerite and pyrite), but varies to less than 0.01 ppm (detection limit) in massive pyrite, stringer mineralisation and wall rock (Fig. 9.12a). In the upper ore zone, Au correlates best with Zn, and weakly

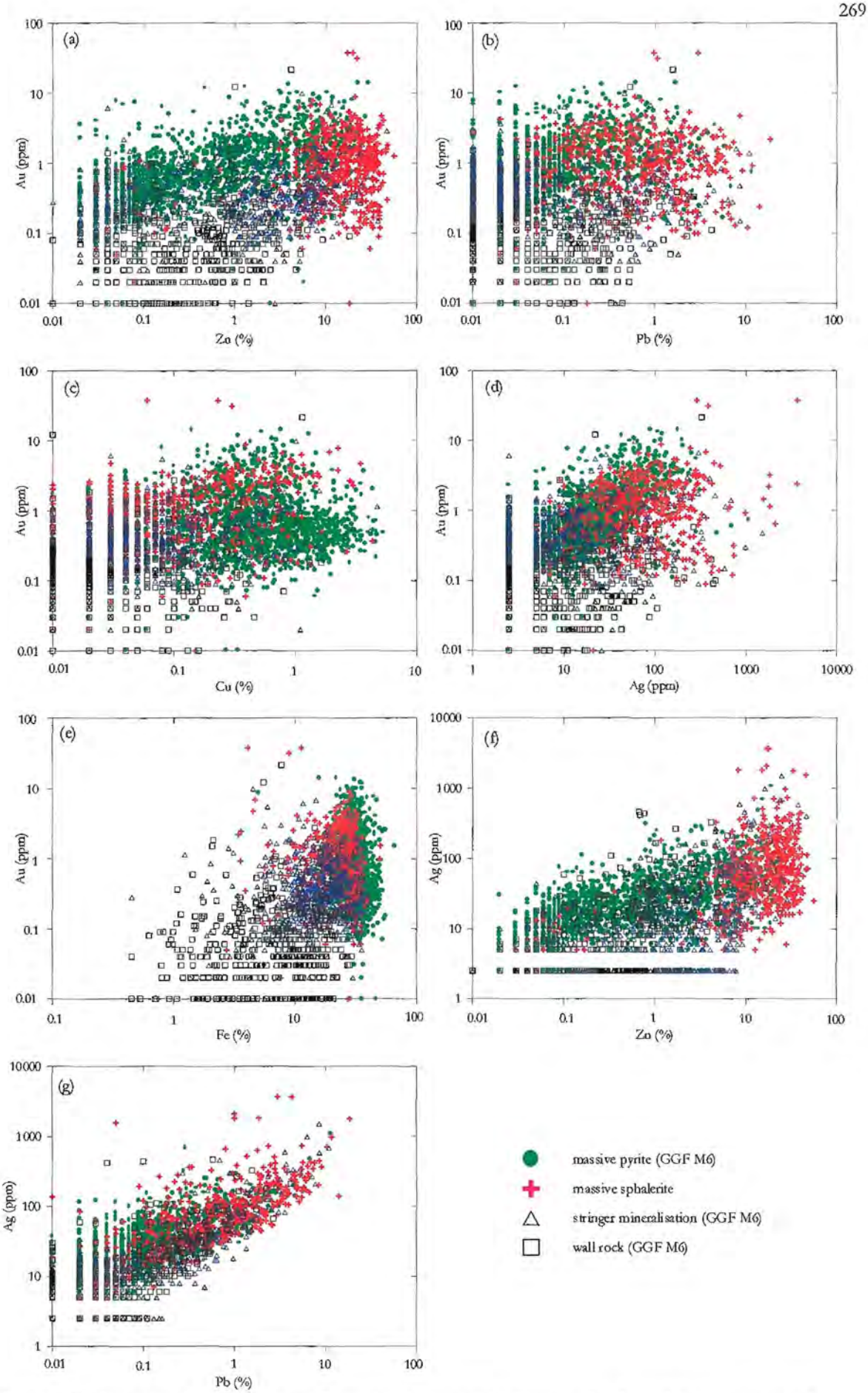

Figure 9.12: Log normal scatter diagrams illustrating the association between Au, Ag and the main ore metals within the upper ore zone of GGF M6 at Gossan Hill. Source of data is composite section 18,300 N and drill holes used are listed in Appendix A7.2. Values below detection limits are not plotted.

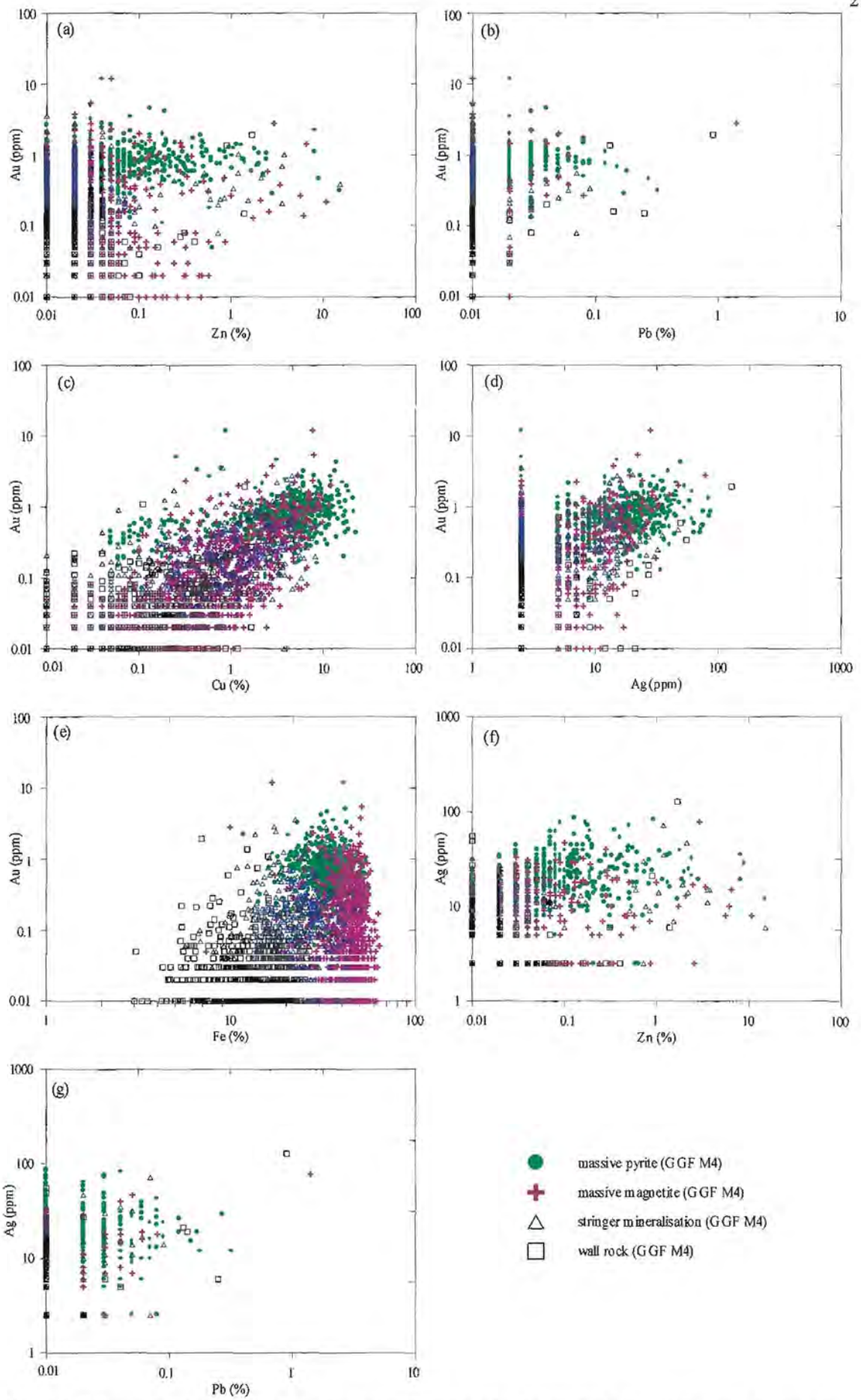

Figure 9.13: Log normal scatter diagrams illustrating the association between Au, Ag and the main ore metals within the lower ore zone of GGF M4 at Gossan Hill. Sources of data are east-west cross sections 18,480 N and 18,560 N. Drill holes used are listed in Appendix A7.2. Values below detection limits are not plotted.

with Pb (Fig. 9.12b) and Ag (Fig. 9.12c). Within massive pyrite, stringer mineralisation and the wall rock, there is a wide scatter in Au and Zn (Fig. 9.12a), as there is in Pb and Ag concentrations. Not only do the highest Au contents occur with the highest Zn concentrations in the upper ore zone, but they also correlate with the highest concentrations in Ag and Pb. A weak positive correlation is also observed between Au and Cu (Fig. 9.12c) and a strong correlation between Au and Fe (Fig. 9.12e). This indicates that the highest Au grades correlate with high Fe in the form of massive pyrite. Moreover, Figure 9.12a indicates the lack of a zone refining Au-Zn rich zone from Gossan Hill, such as seen at the Que River, Hellyer and Rosebery deposits (Large *et al.*, 1990).

Within the lower ore zone Au (Fig. 9.13) is positively correlated with Cu (Fig. 9.13c) and Ag (Fig. 9.13d) within massive pyrite and to a lesser extent, within massive magnetite. Within this lower ore zone, massive pyrite has the highest concentrations in Zn (Fig. 9.13a), Au, Ag, Pb (Fig. 9.13b) and Cu. Lower metal values generally occur in stringer mineralisation and the wall rock. The magnitude of Au enrichment within the lower ore zone is generally less than that observed in the upper ore zone (*c.f.*, Figs. 9.12a and 9.13a). Au also has a correlation with Fe in the lower ore zone with high Au and Fe in massive pyrite (Fig. 9.13e).

9.4.4 Silver

Silver has a good positive correlation with Au, Zn and Pb in the upper ore zone (Fig. 9.12), with the highest concentrations of these metals occurring within massive sphalerite and massive pyrite. Stringer mineralisation and the wall rock have generally lower, but scattered Ag values (*e.g.*, Fig. 9.12d). Within the lower ore zone, Ag and Au (Fig. 9.13d) are well correlated with the highest values of both in massive pyrite. However, Ag does not correlate well with Zn (Fig. 9.13f) or Pb (Fig.9.13g) in the lower ore zone and the concentrations of Ag are an order of magnitude lower than values of the upper ore zone.

9.5 Discussion

Metal zonation patterns at the Gossan Hill deposit are schematically illustrated in Figure 9.14, and resemble typical zonation patterns of Archean VHMS deposits (*e.g.*, Knuckey *et al.*, 1982a). At the Gossan Hill deposit, the gross zonation of metals from footwall to hangingwall consists of a lower Cu-Fe (± Au) zone that grades upwards to a Fe (±Cu) zone (Fig. 9.14). This Fe (±Cu) zone interconnects the lower and upper ore zones. The upper ore zone grades from a Cu-Zn-Fe base to a high grade Zn-Pb-Ag-Au (±Cu) top (Fig. 9.14). The unusual characteristics of Gossan Hill deposit are; (1) its high concentration of Fe due to the presence of magnetite in the lower ore zone, (2) volumetrically more Cu-Fe mineralisation than Zn-Pb-Ag-Au, and (3) the dominance of broad zones of scattered interconnected anomalous metal concentrations rather than massive zones. This latter attribute results from the widespread distribution of stringer veins in the Gossan Hill deposit.

The upper ore zone consists of a broadly stratiform zone of Pb-Zn-Ag-Au (±Cu) enrichment that grades downwards to a discordant Cu-Zn (±Ag, ±Au) association (Fig.

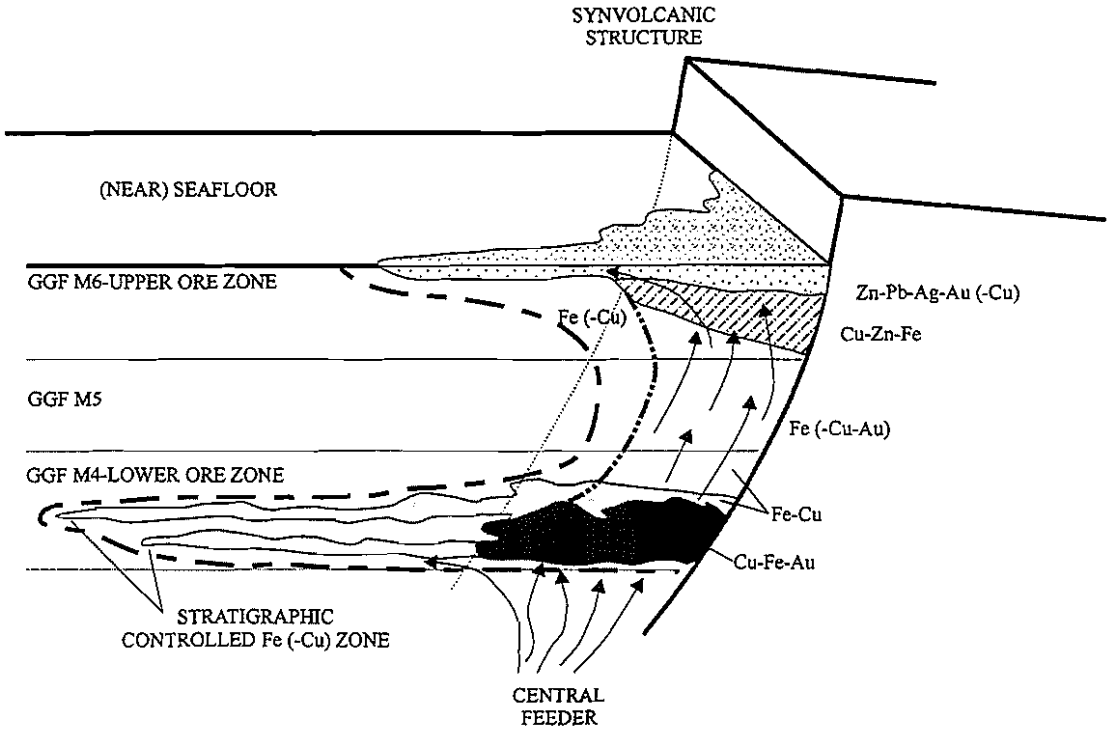

Figure 9.14: Schematic illustration of metal zonation at Gossan Hill. The lower ore zone has enrichment in Fe-Cu-Au with the main concentration of Cu-Au occurring below massive magnetite at the base of mineralisation. A broad feeder zone, enriched in Fe and containing Fe-Cu-Au (-Zn) joins the upper and lower ore zones. The upper ore zone has metal zonation from a Cu-Zn-Fe zone upwards to a high grade Zn-Pb-Ag-Au zone.

9.14). In this upper ore zone, Pb, Zn, Ag and Au attain their highest concentrations and have a strong positive inter-element correlation. The Zn ratio in the upper ore zone at Gossan Hill works well, where a greater proportion of Zn with respect to Pb results in high Zn ratios typical of Archean VHMS deposits. There is a systematic decrease in the Zn ratio through the upper ore zone with depth, due to decreasing Zn contents. This trend also indicates that the Zn ratio has not been significantly modified during deformation. Copper ratios in the upper ore zone tend to have a spread in values that make its application limited and which, reflect a poor correlation between Cu and Zn. Copper in this upper ore zone is generally contained within massive pyrite, although massive pyrite may also be barren of Cu.

In the lower ore zone, the metal associations are relatively simple and consist of Cu, Au and Fe. Here, Zn, Ag and Pb are generally absent, however Zn and Ag may occur in very low concentrations within massive pyrite. As Cu and Zn do not correlate in the lower ore zone due to the general absence of Zn, the Cu ratio is not applicable. Moreover, the ubiquitous low levels of Pb in the lower ore zone mean that the Zn ratio is also not applicable. Within the lower ore zone there is an association between Cu and Au, however the concentration of Au is significantly less than that observed in the upper ore zone. Both Cu and Au form broad interconnected zones with scattered anomalous values. Iron and Cu also have a poor correlation within this lower zone, due to the bimodal occurrence of Fe in both massive sulphide and massive magnetite.

9.5.1 Magnetite-sulphide (Cu-Fe) association of the lower ore zone

A complex spatial association has been established between massive magnetite and massive pyrite in the lower ore zone (Chapter 5). This is supported by the abundance of sulphide veining in magnetite and the overprint of massive magnetite by sulphides, which indicates their formation from two different hydrothermal stages (Chapter 5). Within the lower ore zone Cu does not have a positive correlation with Fe, as massive magnetite contains a wide variation in Cu contents, which is associated with the sulphide veining of magnetite. Spatially, the zones of highest Fe enrichment interdigitate with Cu, but the highest Cu concentrations generally underlie the high Fe magnetite zones. This Cu-Fe zone is best developed between 18,450 N and 18,600 N at the north of Gossan Hill. South of 18,450 N, Cu concentrations decrease to scattered anomalous values, whilst Fe forms an asymmetric laterally continuous zone.

9.5.2 Location of feeder zones

The Cu contours indicate that the highest Cu-Au enrichment occurs in the interval between 18,450 N to 18,600 N in the lower ore zone. Laterally away from this zone, Cu enrichment becomes scattered. This scatter is associated with the transition from massive to stringer vein sulphides. The Cu-Au enriched interval (18,450 N to 18,600 N) also coincides with the highest Fe values associated with massive magnetite, the latter forming an asymmetric zone that thins laterally to the south. The northern Cu-Au-Fe concentration (18,450 N to 18,600 N; *e.g.*, Figs. 9.1, 9.5 and 9.6) represents a feeder site, where hydrothermal fluids were focussed and the hottest part of the mineralising

system. The Cu-Au-Fe feeder plunges to the north (~65°) with the highest Cu-Au grades along this trend. Outward from this feeder Cu-Au contents decrease, whist Fe is laterally continuous. The north plunge of the Cu-Au-Fe feeder zone parallels the plunge of the hangingwall dacite, which is interpreted to occupy the site of a former synvolcanic structure. The elongate north-south asymmetry of high Fe contents and to a lesser extent Cu, indicates a strong stratigraphic control to the lateral distribution of Fe. The lower grade of the Cu-Au envelop that encloses the high grade Cu-Au central zone is laterally less extensive than the distribution of Fe and related to stringer sulphides.

Spatially, the upper ore zone has different characteristics and inter-element associations than the lower ore zone. This is reflected by the correlation between Pb, Zn, Ag, Au and a subvertical plunge to the ore zone. The difference in plunge orientation between the upper and lower ore zone is a reflection of the strong structural control on the lower ore zone and strong stratigraphic control on the upper ore zone. An association between Pb, Zn, Ag, Au in the upper ore zone is consistent with lower temperature fluids, probably due to its deposition near the seafloor.

The upper and lower ore zones are interconnected by anomalous Fe and scattered Cu, Au, and to a lesser extent, Ag and Zn, which occur within stringer vein mineralisation. Near the surface the north plunging Cu-Au-Fe feeder intersects the subvertical plunging Pb-Zn-Ag-Au (±Cu) zone. This indicates that the upper ore zone overlies its feeder zone as illustrated in Figure 9.14. The distribution of Fe best illustrates the connection between the upper and lower sulphide zones. This Fe zone contains minor base and precious metals, which include scattered values of Cu, Au, Ag and Zn.

9.5.3 Metal zonation at Scuddles

Metal zonation at the Scuddles deposit is described by Ashley *et al.* (1988), Large *et al.* (1989) and Mill *et al.* (1990). The main metals in the Scuddles deposit are Fe, Zn, Cu and Pb, which contrasts with the Gossan Hill deposit due to the relatively lower volume of Zn-rich mineralisation in the latter (Ashley *et al.*, 1988). The average Cu/Zn values for the Scuddles resource is ~1:7, however, a large variation exists between the sulphide zones. Within the Scuddles deposit, Zn concentrations are highest in the thickest parts of the massive sulphide, and the distributions of Pb and Ag closely follow that of Zn. This zone forms a stratiform sheet of massive sulphide that is underlain by a discordant massive pyrite and stringer zone (Ford, 1992). Although Cu broadly follows the patterns of Zn in the upper stratiform sulphide sheet, the highest Cu concentrations straddle the lower boundary with massive pyrite and stringer stockwork, which underlies the Zn and occur within massive pyrite and stringer veins. Therefore, Scuddles has a zone with high Zn (Ag-Pb) and low Cu that is discordant to an underlying zone of high Cu and low Zn-Pb-Ag.

Large *et al.* (1989) report that the Scuddles deposit has significant Au (average of 0.9 ppm) and a complex association between the Au and base metals. Gold occurs throughout the Zn-Cu-rich sulphide mineralisation, but is depleted in the underlying Cu-rich stringer. Nonetheless, the highest Au grades do not correspond to the highest Zn

grades at the stratigraphic top of the Scuddles deposit. Instead, high Au occurs as a zone in the centre of the deposit and coincides with the transition of Zn-Cu-rich massive sulphide to stringer mineralisation (Large *et al.*, 1989; Ford, 1992). A positive linear correlation exists between Au and Cu at Scuddles, however no correlation exists between Au and Zn in the massive sphalerite ore (Large *et al.*, 1989).

The metal zonation at the Scuddles deposit, from footwall to hangingwall, consists of a central zone of Cu-Au-Fe that grades upward to Cu-Au-Fe-Zn and outwards to Zn-Pb-Ag (±Cu). This zonation is equivalent to the upper ore zone at Gossan Hill, and to which, the Scuddles VHMS deposit is stratigraphically correlated. The main differences between these two deposits are that the Scuddles deposits has (1) a higher volume of Zn-rich sulphides, (2) the absence of a lower ore position in GGF M4, and (3) the lack of a Zn-Pb-Ag-Au correlation in Zn-rich ore.

9.6 Summary

- Metal zonation at Gossan Hill grades from a Cu-Au-Fe enriched lower ore zone in GGF M4 to a Cu-Zn association in the upper ore zone, which passes upwards and laterally to a Pb-Zn-Ag-Au (±Cu) association.
- A broad zone of Fe, which contains scattered Cu, Au and Zn, interconnects the upper and lower ore zones at Gossan Hill.
- The highest Cu-Fe concentrations occur in the lower ore zone, which has a northward plunge. The highest Cu grades occur at the base of massive sulphide in this zone. The north plunging Cu-Fe zone is inferred to form a feeder zone.
- The subvertical plunge of the Pb-Zn-Ag-Au (±Cu) upper ore zone is consistent with strong stratigraphic control due to its formation near the paleo-seafloor.
- Gold has two associations at Gossan Hill; (1) a high grade Pb-Zn-Ag-Au (±Cu) association in the upper ore zone, and (2) a lower grade Cu-Au association in the lower ore zone.
- Metal zonation at the Scuddles deposit resembles metal patterns and associations in the upper ore zone Gossan Hill, however the volume of Zn-rich ore is greater at Scuddles than at Gossan Hill. Other differences between the deposits include the low Au contents in the Zn-Pb-Ag-rich ore and the absence of a lower ore zone at the Scuddles deposit.

Chapter 10

Sulphur isotopes

10.1 Introduction

Sulphur isotopes can be used to constrain the source, variation and evolution of sulphur in VHMS deposits (Ohmoto, 1972; Rye and Ohmoto, 1974; Ohmoto and Rye, 1979; Franklin *et al.*, 1981). The fractionation of sulphur is not singularly controlled by temperature, but also by oxidation-reduction, which include the activity of oxygen and sulphur, pH and the type of sulphur species in the system (Ohmoto and Rye, 1979; Ohmoto *et al.*, 1983; Watanabe and Sakai, 1983). Sulphur isotopes can be used to constrain these physicochemical parameters during the ore formation.

In VHMS deposits, the three main sources of sulphur are (1) sulphur in seawater, (2) magmatic sulphur, and (3) leached volcanic rock sulphur; the latter which is isotopically indistinguishable from magmatic sulphur (Ohmoto and Rye, 1979; Ohmoto *et al.*, 1983; Ohmoto and Goldhaber, 1997). Moreover, three hypotheses are proposed for the origin of reduced sulphur (H_2S) in these deposits. Reduced sulphur can originate from (1) partial to complete inorganic reduction of seawater sulphur combined with dissolution of rock sulphur (Sasaki, 1970; Ohmoto *et al.*, 1983; Solomon *et al.*, 1988), (2) derivation of reduced sulphur from a deep seated magmatic source (Ishihara and Sasaki, 1978), and (3) biogenic reduction of seawater sulphate (Sangster, 1968).

The sulphur isotope compositions of Phanerozoic VHMS deposits are broadly correlated to the isotopic composition of coeval seawater (Sangster, 1968; Claypool *et al.*, 1980; Ohmoto, 1996). The chemistry of Archean seawater is however, controversial and poorly constrained, with sulphur isotopes values in Archean VHMS deposits generally close to 0‰ (Ryznar *et al.*, 1967; Seccombe, 1977; Strauss, 1986; Cameron and Hattori, 1987; Ohmoto, 1996).

Previous sulphur isotope studies at Gossan Hill identified a significant sulphur isotope variation with a range of 6.9‰ (Seccombe and Frater, 1981), with samples analysed mainly from the lower ore zone. The sulphur isotope study in this thesis investigates (1) the sulphur isotope variation through the Zn-Cu and Cu-rich ore zones, (2) potential stratigraphic variation, and (3) the source of sulphur and degree of isotope equilibrium during ore formation at Gossan Hill.

10.2 Methods

Sulphur isotope measurements were made on a VG Isogas Sira II mass spectrometer in the Central Science Laboratory at the University of Tasmania. All results are reported in standard notation relative to the Canon Diablo Troilite (CDT). This study used both conventional and microanalytical techniques to determine the sulphur isotope compositions of primary, unweathered sulphides. The sulphides analysed were pyrite, sphalerite, chalcopyrite, galena and pyrrhotite.

Samples analysed by conventional sulphur isotope methods used drilled and hand picked sulphide separates. These separates were combusted with excess Cu_2O to produce SO_2, according to the methodology of Fritz *et al.* (1974) and Robinson and Kusakabe (1975). Samples were selected using polished sections to avoid contamination by fine-grained sulphide intergrowths. Replicate analysis of internal standards determined a reproducibility of 0.2‰ at 1σ precision.

Microanalytical sulphur isotope determinations used a Nd:YAG laser ablation microprobe in the Central Science Laboratory at the University of Tasmania. The operational procedures of this facility are documented by Huston *et al.* (1992a; 1995b). Rock chips, 150 μm thick, were polished using 1 μm diamond paste to reduce the isotopic fractionation caused by rough surfaces. Ablated polished rock chips yielded crater sites that varied in diameter from 90 to 150 μm and the current of ablation initiation depended on the sulphide species (Table 10.1). Results were corrected for laboratory dependent fractionation factors (Table 10.1; Huston *et al.*, 1995b) and standardised to the CDT. Precision factors for this laser ablation facility vary between sulphide species (Table 10.1) and average 0.4‰ (1σ precision).

Conventional isotope measurements were made to determine the variation and distribution of sulphur isotope compositions at Gossan Hill. To achieve this, conventional analyses were completed on samples from 5 diamond drill holes through the upper and lower ore zones in GGF M6 and GGF M4 respectively. Microanalytical techniques investigated intra- and inter-grain $\delta^{34}S$ variations, mainly in zoned pyrite. In total, 132 sulphur isotope measurements were made; 91 by conventional analyses that included 56 analyses from the upper Zn-Cu ore zone and 35 analyses from the lower Cu-rich ore zone.

Table 10.1: Analytical details of sulphide minerals from Gossan Hill, analysed by laser ablation. Fractionation factors (*) and analytical uncertainties (#) are from Huston *et al.* (1995b).

Mineral	Current (ampere)	Ablation Crater (μm)	Fractionation Factor* (‰)	Uncertainty# (1σ) (‰)
pyrite	32 - 34	90 - 150	5.75	0.41
sphalerite	31.5 - 34	100 - 150	2.85	0.39
galena	26	100	4.32	0.57
chalcopyrite	29 - 31	130 - 150	4.45	0.44
pyrrhotite	30 - 32	100 - 150	4.12	0.31

10.3 Results

Sulphur isotope results from Gossan Hill are illustrated in Figure 10.1a and listed in Appendix A8.1. The overall variation in $\delta^{34}S$ values is 12.6‰, which range from -4.8 to 7.8‰, and have an average of 2.1 ± 1.6‰ (Fig. 10.1a, Table 10.2). Pyrite $\delta^{34}S$ values range from -1.0 to 7.8‰ (mean of 2.1‰), whilst sphalerite ranges from 1.2 to 5.1‰ (mean of 2.9‰), chalcopyrite ranges from -0.3 to 3.1‰ (mean of 1.5‰), galena ranges from 0.0 to 1.2‰ (mean of 0.6‰) and pyrrhotite ranges from -4.8 to 5.0‰ (mean of 0.7‰) (Fig. 10.1a). The widest variation in $\delta^{34}S$ values is observed in pyrite and pyrrhotite. Average $\delta^{34}S$ values for sphalerite are generally heavier than pyrite.

10.3.1 Isotopic differences between the upper and lower ore zones

The upper Zn-Cu ore zone in GGF M6 has a wider range of $\delta^{34}S$ values and a higher mean than the lower Cu-rich ore zone in GGF M4 (Figs. 10.1b and 10.1c, Table 10.2). This is typified by the $\delta^{34}S$ values of pyrite, which range from -1.0 to 7.8‰ (mean of 2.3‰) in the upper ore zone and 0.5 to 3.5‰ (mean of 1.8‰) in the lower ore zone. These results also indicate that the greatest $\delta^{34}S$ variation at Gossan Hill occurs in the upper Zn-Cu ore zone. Previously published sulphur isotope data from Gossan Hill (Fig. 10.1d) was biased towards $\delta^{34}S$ sulphide compositions of the lower Cu-rich ore zone and has similar distributions to results from GGF M4 (*c.f.* Fig. 10.1c).

10.3.2 Isotopic differences between ore types

The three ore types at Gossan Hill are massive sphalerite, massive pyrite and stringer mineralisation; the distribution of sulphur isotope values for each ore type is illustrated in Figure 10.2 and tabulated in Table 10.2. Massive magnetite only occurs in the lower ore zone (GGF M4) and does not contain paragenetically coeval sulphide, but is commonly veined by sulphides.

In GGF M6, the range of $\delta^{34}S$ values in massive sphalerite and massive pyrite are similar (Figs. 10.2a and 10.2b, Table 10.2) with mean values of 2.7 and 2.8‰ respectively. Within massive sphalerite, pyrite has $\delta^{34}S$ values varying from 0.6 to 6.1‰ (mean of 2.8‰) and

Table 10.2: Maximum, minimum and mean $\delta^{34}S$ values for ore types within GGF M6 and GGF M4 at Gossan Hill. Ore types are massive sphalerite (MSS), massive pyrite (MPY), stringer mineralisation (STZ) and sulphides in the wall rock (WR).

Stratigraphy	Ore Type	n*	$\delta^{34}S$ Minimum (‰)	$\delta^{34}S$ Maximum (‰)	$\delta^{34}S$ Mean (‰)	Standard Deviation (‰)
All sulphides		132	-4.8	7.8	2.1	1.6
GGF M6	all	84	-4.8	7.8	2.4	1.7
	MSS	39	0	6.1	2.7	1.3
	MPY	13	-1	7.8	2.8	2.1
	STZ	18	-4.8	4.1	2	2.1
	WR	17	-0.3	3.8	1.8	1.1
GGF M4	all	39	-1.6	3.4	1.6	0.9
	MPY	9	0.5	3.4	1.8	1
	STZ	28	-1.6	3	1.5	0.9
	WR	2	1.4	1.6	1.5	0.2

* n indicates number of analyses

(a) Overall sulphide variation at Gossan Hill

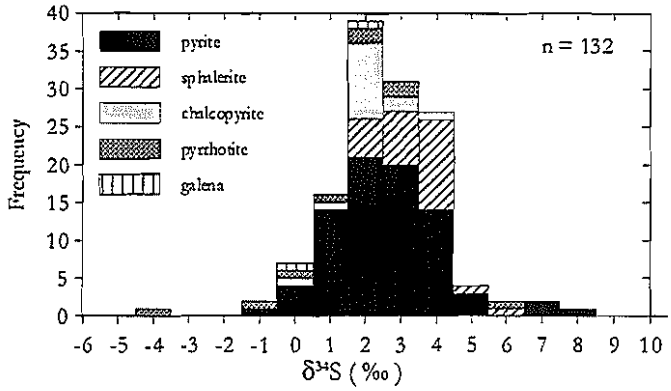

(b) GGF M6 - the upper Zn-Cu ore zone

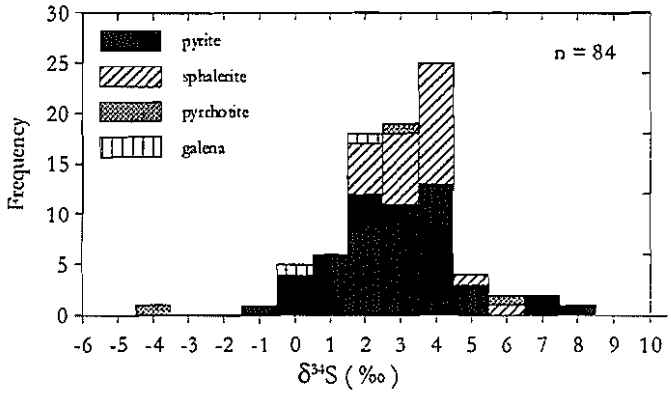

(c) GGF M4 - the lower Cu-rich ore zone

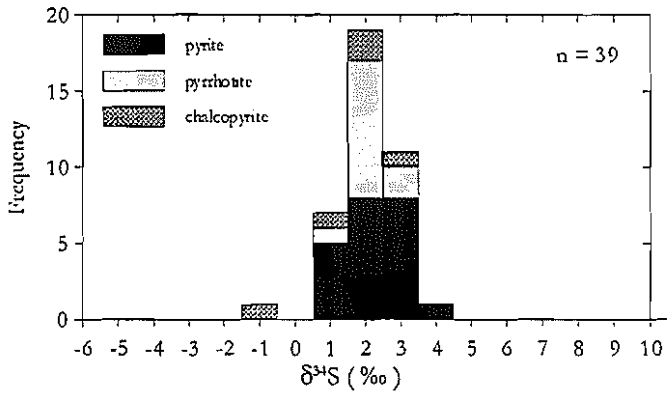

(d) Seccombe and Frater (1981)

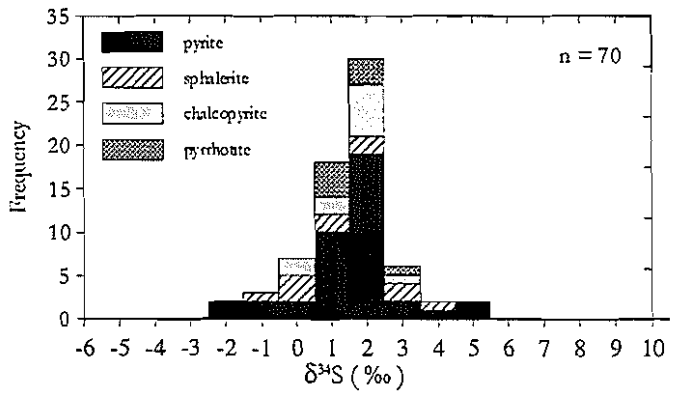

Figure 10.1: Sulphur isotope variation at the Gossan Hill deposit. (a) Overall variation in $\delta^{34}S$ values at Gossan Hill (this study), (b) $\delta^{34}S$ values in the upper Zn-Cu ore zone of GGF M6, (c) $\delta^{34}S$ values in the lower Cu-rich ore zone of GGF M4, and (d) previously published sulphur isotope data from Gossan Hill by Seccombe and Frater (1981).

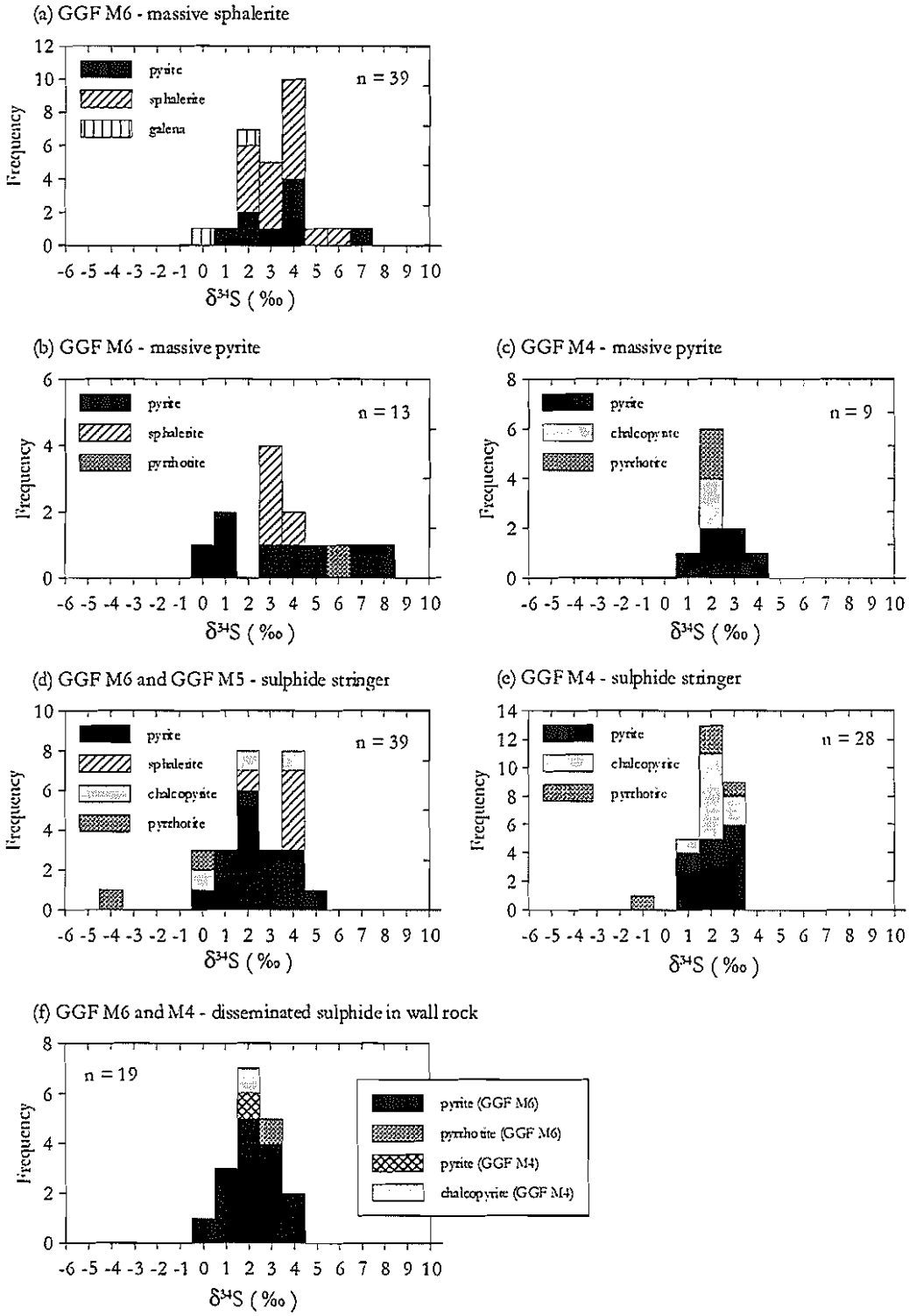

Figure 10.2: Sulphur isotope variation in the different stratigraphic ore types at Gossan Hill. (a) Massive sphalerite in GGF M6, (b) massive pyrite in GGF M6, (c) massive pyrite in GGF M4, (d) sulphide stringer vein mineralisation in GGF M6 and GGF M5, (e) sulphide stringer mineralisation in GGF M4, and (f) disseminated sulphide in the GGF M6 and GGF M4 wall rock.

$\delta^{34}S$ values of sphalerite from 1.5 to 5.1‰ (mean of 2.9‰). In the massive pyrite, pyrite has $\delta^{34}S$ ranging from -1.0 to 7.8‰ with a mean of 2.6‰. Stringer mineralisation in GGF M6 and GGF M5 (Fig. 10.2d) contain slightly lighter isotope values than massive sulphides in GGF M6, ranging from 0.0 to 4.1‰ (mean of 2.0‰), with the exception of a single pyrrhotite $\delta^{34}S$ value at -4.8‰. The range of $\delta^{34}S$ values in GGF M6 and GGF M5 stringer mineralisation is narrower than the range in overlying massive sulphides.

In GGF M4, massive pyrite has a narrow range in $\delta^{34}S$ values from 0.5 to 3.4‰ (mean of 1.8‰) (Fig. 10.2c). Associated stringer mineralisation in GGF M4 has a range of $\delta^{34}S$ values from -1.6 to 3.0‰ (mean of 1.5‰) (Fig. 10.2e). The range and average $\delta^{34}S$ values in stringer mineralisation are therefore similar to massive sulphides in GGF M4 (Fig. 10.2c).

Pyrite disseminated in the wall rock adjacent to massive sulphide in GGF M6 and GGF M4 (Fig. 10.2f) has similar $\delta^{34}S$ values with a range from -0.3 to 3.8‰ (mean of 1.7‰). These $\delta^{34}S$ values for pyrite in the wall rock compare closely with $\delta^{34}S$ values in massive pyrite and stringer mineralisation in GGF M4 (Figs. 10.2c, 10.2e and 10.2f). Sulphur isotope variation between the different ore types at Gossan Hill confirms that the greatest variation and heaviest $\delta^{34}S$ values occur in the upper Zn-Cu ore zone (Fig. 10.1b).

10.3.3 Isotopic differences between sulphide veins

At Gossan Hill, a large proportion of the mineralisation occurs in veins. Three paragenetically different sulphide vein stages are identified: (1) Type IV (pyrite-chlorite), (2) Type V(A) (pyrite-chalcopyrite-pyrrhotite-carbonate-magnetite-chlorite), and (3) Type V(B) (pyrite-sphalerite-chlorite-quartz) veins. Sulphur isotope analysis of sulphides within each of these veins is illustrated in Figure 10.3 and summarised in Table 10.3.

Type IV veins have a narrow variation in $\delta^{34}S$ values from 0.6 to 3.0‰ (mean of 1.7‰) (Fig. 10.3a), which is similar to massive pyrite in GGF M4 (*c.f.* Fig. 10.2c). Type V(A) veins have $\delta^{34}S$ values that range from -4.8 to 3.6‰ (mean of 1.3‰) (Fig. 10.3b), whilst Type V(B) veins range from 0.8 to 4.1‰ (mean of 2.7‰) (Fig. 10.3c). As expected, Type V(B) veins are isotopically similar to massive sphalerite (Fig. 10.2a), as these veins grade into

Table 10.3: Minimum, maximum and average $\delta^{34}S$ values for Type IV, Type V(A) and Type V(B) sulphide veins at Gossan Hill.

Vein Type	Mineral	n*	$\delta^{34}S$ Minimum (‰)	$\delta^{34}S$ Maximum (‰)	$\delta^{34}S$ Mean (‰)	Standard Deviation (‰)
IV	pyrite	7	0.6	3	1.7	0.8
V(A)	overall	39	-4.8	3.6	1.3	1.4
	pyrite	19	-0.2	3.6	1.6	0.9
	sphalerite*	1	-	3.2	-	-
	pyrrhotite	7	-4.8	2.2	-0.2	2.4
	chalcopyrite	12	-0.3	3.1	1.4	0.8
V(B)	overall	12	0.8	4.1	2.7	1.1
	pyrite	7	0.8	4.1	2.6	1.2
	sphalerite	5	1.2	3.6	2.8	1

* indicates number of analysis

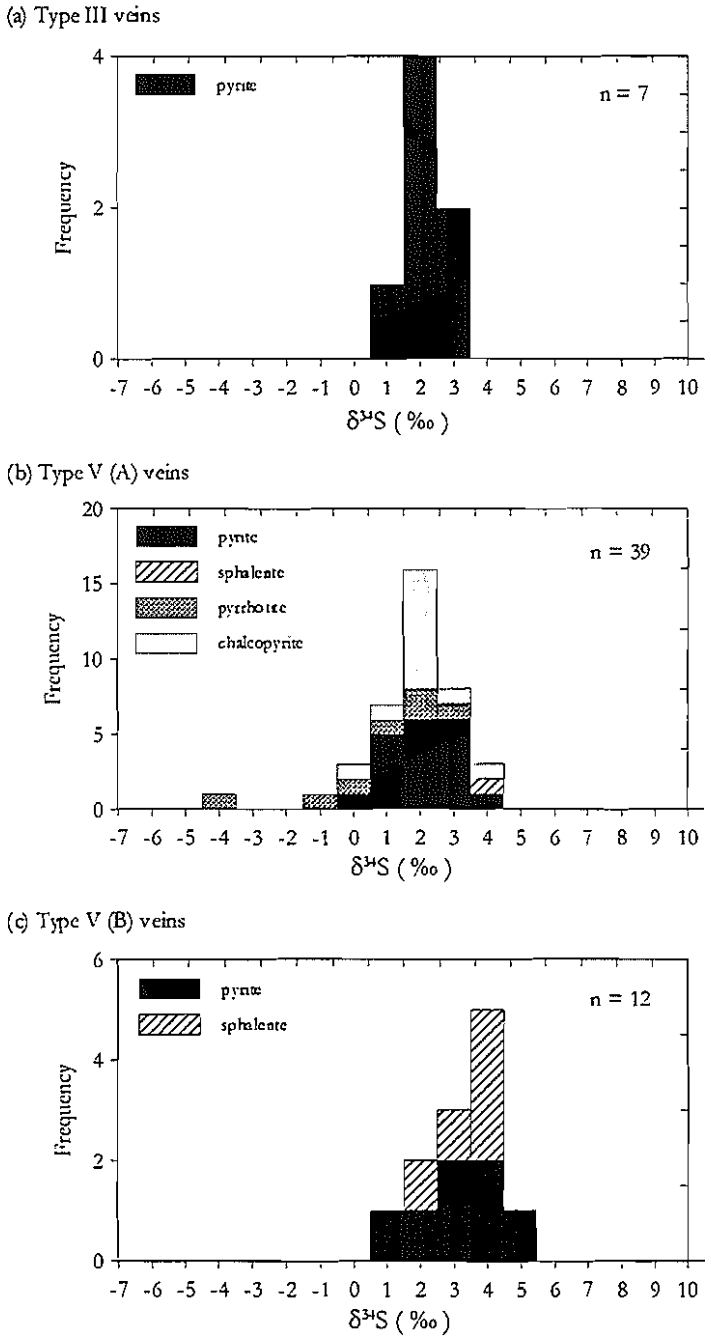

Figure 10.3: Sulphur isotope variation of sulphides in each of the paragenetically different vein types at Gossan Hill. (a) Type IV pyrite-chlorite veins, (b) Type V(A) pyrite-pyrrhotite-chalcopyrite-magnetite-sphalerite-carbonate-chlorite veins, and (c) Type V(B) pyrite-sphalerite-chlorite-quartz veins.

massive sphalerite and have heavier average $\delta^{34}S$ values than other vein types. The widest range of $\delta^{34}S$ values occurs in Type V(A) veins, with the greatest $\delta^{34}S$ variation occurring in pyrrhotite (Fig. 10.3b). Within vein Type V(A), the $\delta^{34}S$ values between co-existing sulphide species indicate widespread isotopic disequilibrium (Appendix A8.1). However, limited evidence of isotopic equilibrium between pyrite-sphalerite occurs in Type V(B) veins.

The $\delta^{34}S$ signature of each vein type at Gossan Hill is slightly different, but the ranges and means of the $\delta^{34}S$ values in each vein type resemble the ore type to which it is genetically related. Type IV veins only occur in GGF M4, Type V(A) veins envelop the lower ore zone and connect it to the upper ore zone, whilst Type V(B) veins envelop massive sphalerite and pyrite in GGF M6. The distribution of $\delta^{34}S$ values between these different veins types indicates increasingly heavier $\delta^{34}S$ values in paragenetically later sulphide veins (*i.e.*, Type V(B)).

10.3.4 Spatial variation of $\delta^{34}S$ values

Variation of $\delta^{34}S$ measurements along diamond drill core are illustrated in Figure 10.4, with drill holes arranged from south to north over the mineralised area at Gossan Hill. Three drill holes (GG132, GG134 and GG165) intersect Zn-Cu massive sulphide in the upper ore zone from A zone (GG132) northward to C zone (GG165) (Figs. 10.4a, 10.4b and 10.4c). Sulphur isotope variation through the central part of the Cu-rich lower ore zone in GGF M4 is given along drill hole GG070 (Fig. 10.4d), whilst $\delta^{34}S$ values at the northern end of Gossan Hill (D zone) are given along GG045 (Fig. 10.4e).

In the upper Zn-Cu ore zone, $\delta^{34}S$ values have the widest variation at A zone in the south of Gossan Hill, with a range of 8.1‰ from -0.3 to 7.8‰ (mean of 3.5‰) (Fig. 10.4a). No systematic variation in $\delta^{34}S$ values with depth is observed along GG132 at A zone, and the range of 8.1‰ is from pyrite grains in a single sample at 371.1 metres (Fig. 10.4a). Between A and C zone the range in $\delta^{34}S$ values along GG134 is 4.6‰ from 0.0 to 4.5‰ (mean of 2.6‰) (Fig. 10.4b). A broad increase in the $\delta^{34}S$ values with depth of ~1.2‰ is observed (Fig. 10.4b). At C zone, the range in $\delta^{34}S$ values along drill hole GG165 is 5.1‰ from -1.0 to 4.0‰ (mean of 2.3‰), excluding a single pyrrhotite $\delta^{34}S$ value at -4.8‰ (Fig. 10.4c). A broad systematic decrease in the $\delta^{34}S$ values along GG165 is observed, with an overall change of ~3‰ from the base to the top of sulphides at C zone (Fig. 10.4c).

Drill hole GG070 through Cu-rich sulphides in GGF M4 (Fig. 10.4d) has a narrow range in $\delta^{34}S$ values of 3.6‰ from -0.5 to 3.1‰ (mean of 1.4‰). This narrow variation in $\delta^{34}S$ values includes sulphides within massive pyrite, stringer veins and sulphide veins in massive magnetite (Fig. 10.4). Consistent $\delta^{34}S$ values are also observed in Cu-rich stringer mineralisation along drill hole GG045 (Fig. 104e).

The variation of $\delta^{34}S$ values within massive sulphides has a decreasing range and mean with depth. In the upper ore zone, $\delta^{34}S$ values also have decreasing isotopic variation from A zone to C zone, indicating lateral variation, with the widest range in $\delta^{34}S$ values occurring away from the hydrothermal feeder area (*i.e.*, at A zone, GG132 in Fig. 10.4a). However, throughout the Cu-rich lower ore zone, $\delta^{34}S$ values have a relatively narrow range with

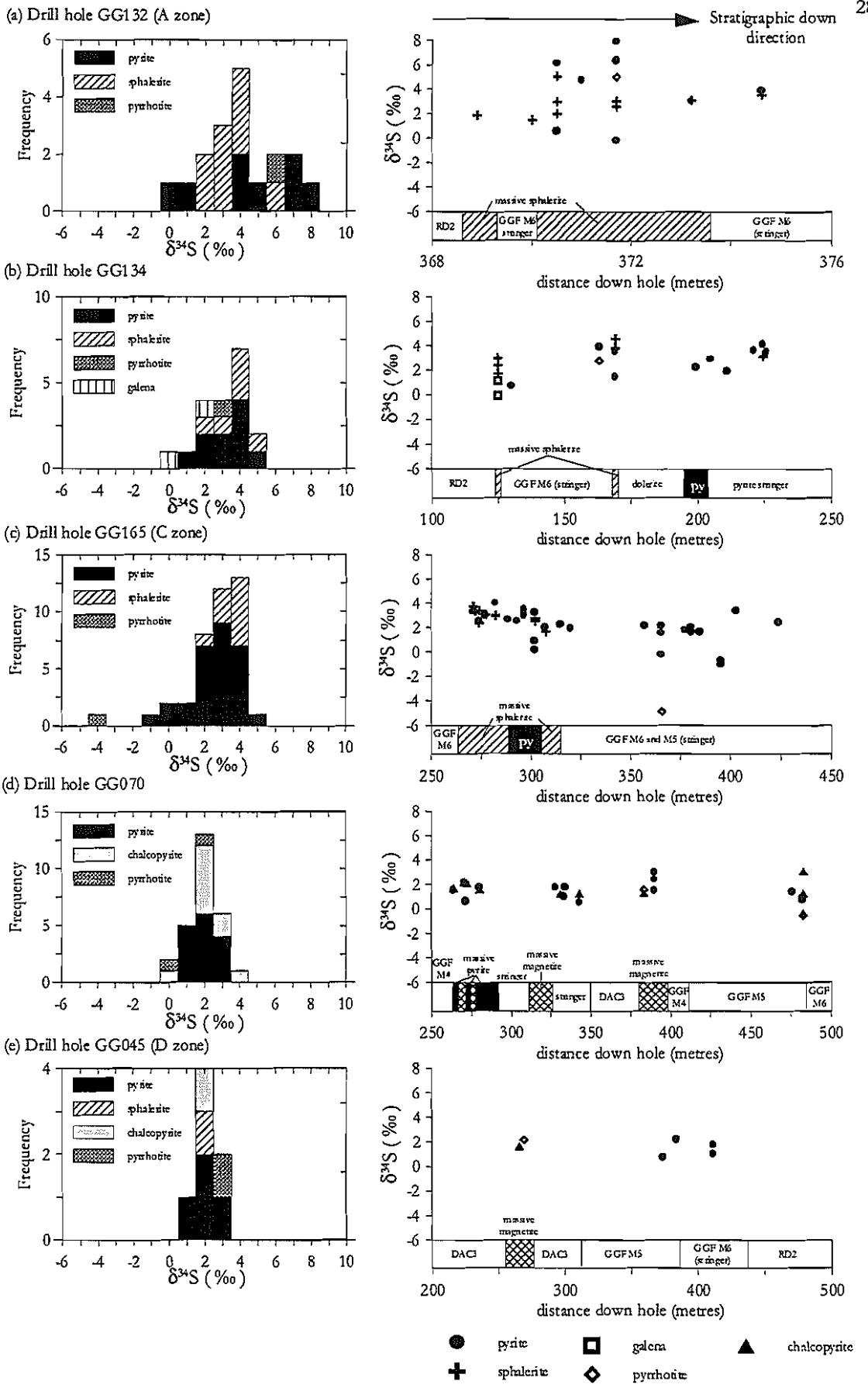

Figure 10.4: Spatial distribution of sulphur isotope values along drill holes through Gossan Hill. These drill holes are ordered from south to north through the deposit and are: (a) GG132 through GGF M6 in the south at A zone, (b) GG134 in GGF M6 between A and C zones, (c) GG165 through GGf M6 and M5 at C zone, (d) GG070 through massive sulphide and magnetite in GGF M4, and (f) GG045 through the northern end of Gossan Hill at D zone. Simplified geological logs and frequency distribution diagrams for each drill hole are also given.

lower average values than Zn-Cu sulphides in the upper ore zone. The stratigraphic distribution of $\delta^{34}S$ values indicates greater sulphur isotope homogeneity proximal to the inferred feeder zone, represented by drill holes GG165 and GG070 (Figs. 10.4c and d). The overall systematic stratigraphic variation of $\delta^{34}S$ values at Gossan Hill (Fig. 10.5) indicates an increase in $\delta^{34}S$ values of approximately 1.5‰ from the base of Cu-rich lower ore zone to the top of Zn-rich sulphide mineralisation.

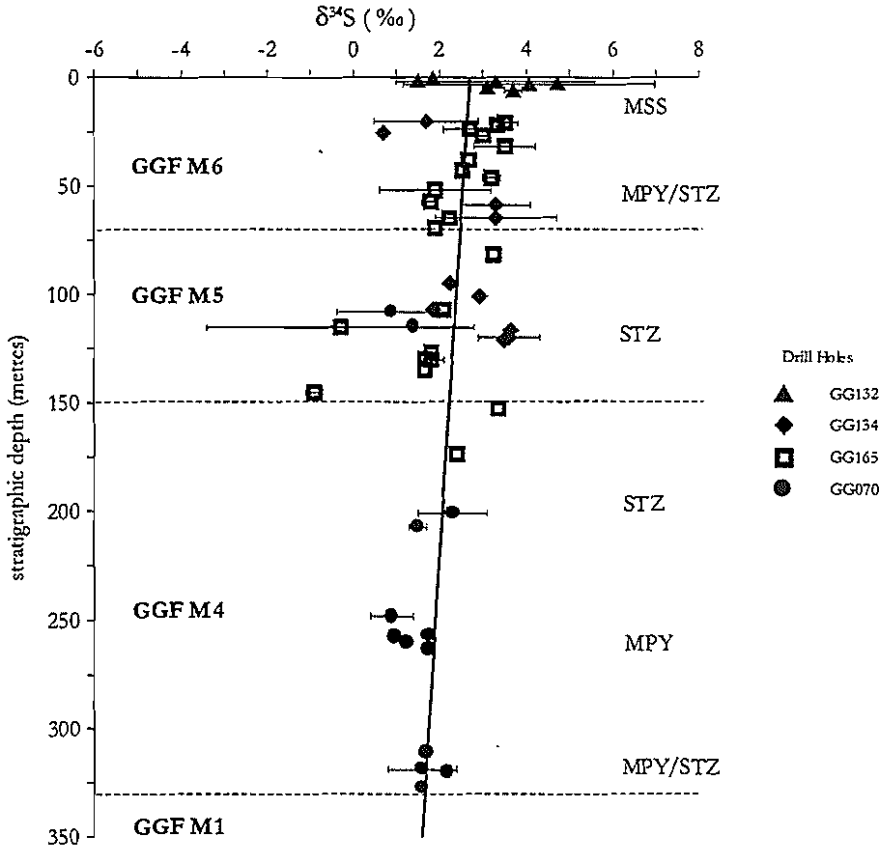

Figure 10.5: Stratigraphic vairation of $\delta^{34}S$ compositions at Gossan Hill. Standard deviation of mean $\delta^{34}S$ values for each sample shown as error bars. The diagram is constructed from four drill hole intercepts; GG132, GG134 and GG165 through massive sulphide in GGF M6 and GGF M5, and GG070 through mineralisation in GGF M4. A broad systematic increase from lighter to heavier $\delta^{34}S$ values of approximately 1.2‰ occurs from the lower ore zone in GGF M4 to the top of the upper ore zone in GGF M6. Data listed in Appendix A8.1. MSS = massive sphalerite, MPY = massive pyrite, STZ = sulphide stringer veins.

10.3.5 Intra-grain $\delta^{34}S$ variation in pyrite

Laser ablation sulphur isotope determinations on zoned pyrite grains examined the $\delta^{34}S$ variation within these texturally distinct pyrites. Results from this investigation are given in Appendix A8.1 and illustrated in Figure 10.6. The greatest range in $\delta^{34}S$ values within a single pyrite grain is 2.0‰ (Fig. 10.6) from an isotopically lighter inner core ($\delta^{34}S$ value of -0.3‰) through successive rims of pyrite, with the heaviest $\delta^{34}S$ values occurring in the outer pyrite rim ($\delta^{34}S$ value of 1.6‰). This zonation in zoned pyrite mirrors the overall

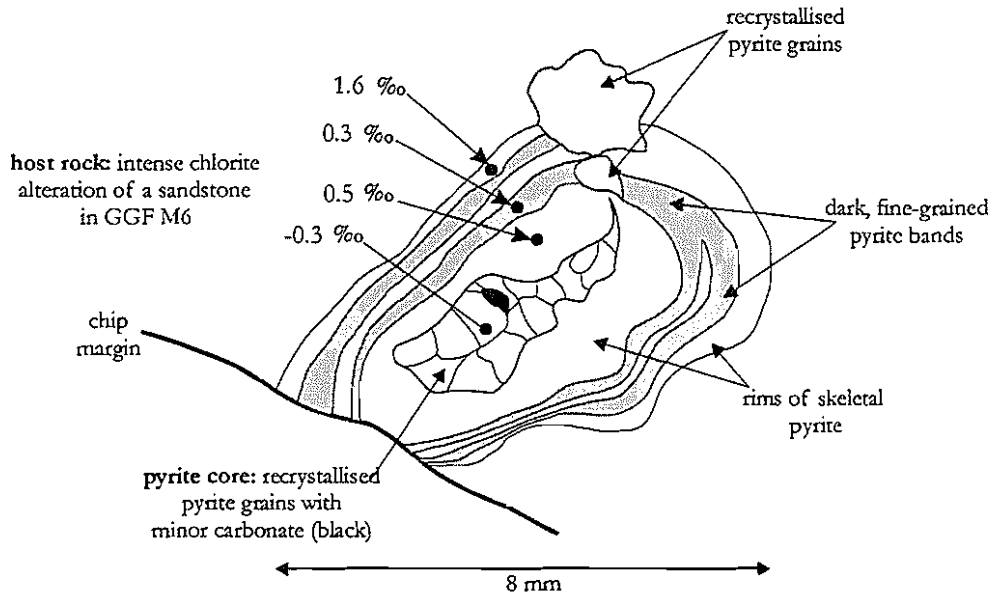

Figure 10.6: Intra-grain sulphur isotope laser ablation traverse across a concentrically zones pyrite grain (sample 760383) from disseminated pyrite in the wall rock of a GGF M6 sandstone. The pyrite grain consists of an inner recrystallised pyrite core that is concentrically encolsed by alternating bands of fine-grained pyrite and skeletal pyrite. The outer rims of this zones pyrite grain have heavier $\delta^{34}S$ values than $\delta^{34}S$ values in the pyrite core.

trend of $\delta^{34}S$ values, with progressively heavier pyrite in the outermost pyrite rims.

In massive sphalerite, sphalerite grains within a single sample have $\delta^{34}S$ values that differ by less than 0.7‰ (Appendix A8.1). This variation is less than the variation observed in texturally zoned pyrite grains. At A zone in massive sphalerite, $\delta^{34}S$ values of pyrite within a single sample have the widest variation of 8.1‰ (refer Fig. 10.4a).

10.4 Discussion

The sulphur isotope composition of sulphides at Gossan Hill has an overall variation in their $\delta^{34}S$ values of 8.8‰ (excluding a single $\delta^{34}S$ value of -4.8‰ in pyrrhotite). This variation is wider than previously reported at Gossan Hill (Seccombe and Frater, 1981) and comparable in magnitude to the sulphur isotope variation in many Phanerozoic deposits (*e.g.*, Balcooma in Huston, 1988; Thalanga in Hill, 1996; Hercules in Khin Zaw, 1991; Hellyer in Gemmell and Large, 1992). However, average $\delta^{34}S$ values in sulphides at Gossan Hill (2.1 ± 1.7‰) are significantly lower than the mean $\delta^{34}S$ values in most Phanerozoic deposits, but typical of Archean VHMS deposits (Section 10.4.3). This narrow range in sulphur isotope composition indicates a broadly uniform sulphur source during sulphide formation at Gossan Hill. Nonetheless, a small magnitude systematic increase in the $\delta^{34}S$ values of sulphide toward the top of ore at Gossan Hill, indicates a change in the sulphur isotope signature of mineralisation with proximity to the seafloor.

10.4.1 Phanerozoic VHMS deposits

In Phanerozoic VHMS deposits, the sulphur isotope variability is broadly related to the seawater sulphate evolution curve (Claypool *et al.*, 1980). The $\delta^{34}S$ values of sulphides in Phanerozoic deposits are positive and lie between 0‰ and the $\delta^{34}S$ value of contemporaneous seawater, generally with a difference of ~15‰ (Sangster, 1978; Claypool

et al., 1980; Franklin *et al.*, 1981). Sulphate minerals in these deposits are typically isotopically heavier than sulphides (Fig. 10.7) and are compositionally related to, but generally different from, the $\delta^{34}S$ values of contemporaneous seawater (Ohmoto and Rye, 1979; Claypool *et al.*, 1980; Franklin *et al.*, 1981; Ohmoto, 1996).

Biogenic reduction of sulphur in Phanerozoic VHMS deposits is considered to be a minor process, due to the observed narrow range in sulphide $\delta^{34}S$ values (Ohmoto and Rye, 1979; Ohmoto, 1996). The favoured interpretation of the sulphur isotope variation in Phanerozoic deposits is the leaching of rock sulphur combined with the inorganic reduction of seawater sulphate during hydrothermal fluid circulation through the underlying rocks (Green *et al.*, 1981; Ohmoto *et al.*, 1983; Ohmoto, 1996; Ohmoto and

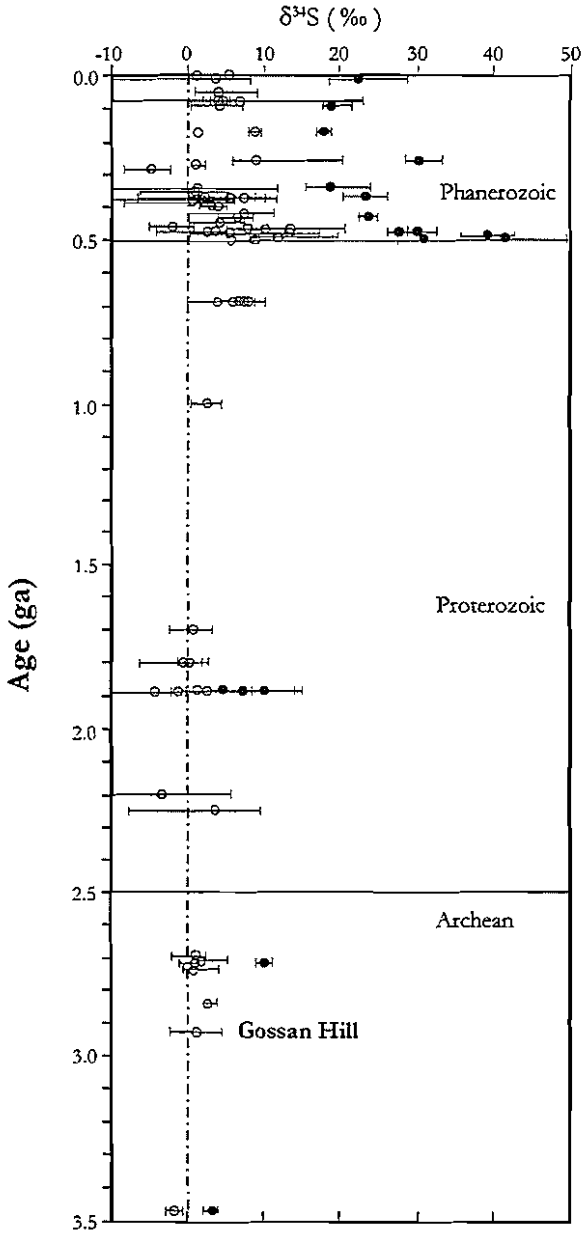

Figure 10.7: Changes in the $\delta^{34}S$ values of VHMS deposits over time, from the Early Archean to modern, currently forming sulphide deposits. Open circles and lines indicate the mean and range of sulphide minerals (excluding galena) respectively. Closed circles and line indicate the mean and range in sulphate minerals respectively (after Huston, 1997).

Goldhaber, 1997). The formation of sulphate in the upper parts of many Phanerozoic deposits (*e.g.*, Rosebery in Green *et al.*, 1981; Hellyer in Sharpe, 1991) is attributed to oxidised sulphur (SO_4^{2-}) either derived from ambient seawater or carried in the upwelling ore fluids (Ohmoto, 1996).

10.4.2 The Archean perspective

Sulphide $\delta^{34}S$ values in Archean VHMS deposits typically have narrow ranges with values that range between 0‰ and 2‰ (Ryznar *et al.*, 1967; Coomer and Schwartz, 1974; Seccombe, 1977; Franklin *et al.*, 1981; Cameron and Hattori, 1987; Huston, 1997; Ohmoto and Goldhaber, 1997). The narrow variation in $\delta^{34}S$ values of Archean VHMS deposits is principally the result of fractionation trends between co-existing sulphide minerals. However, small magnitude systematic variation in the $\delta^{34}S$ values with ore type are noted in some deposits (*e.g.*, Ryznar *et al.*, 1967; Coomer and Schwartz, 1974).

Archean VHMS deposits generally lack sulphate minerals, which is used to infer fundamentally different sulphur sources or environments of sulphide deposition during the Archean (Large, 1977; Lambert *et al.*, 1978; Huston, 1997). In Early Archean rocks associated with VHMS mineralisation, barite is reported at North Pole (Western Australia) and Barberton (South Africa), and this barite is thought to have formed by the replacement of gypsum (Lambert *et al.*, 1978). The $\delta^{34}S$ values of these barites (~3.7‰) is used to estimate the $\delta^{34}S$ values of Archean seawater as being between 2 and 3‰ (Lambert *et al.*, 1978; Ohmoto and Felder, 1987; Ohmoto, 1992; 1996; Ohmoto *et al.*, 1993; Bowins and Crocket, 1994).

The paucity of sulphate in Archean rocks is attributed to the composition of coeval seawater and a general lack of sulphate in Archean seawater (Eastoe *et al.*, 1990; Eastoe and Gustin, 1996). The narrow range of sulphide $\delta^{34}S$ values is interpreted to reflect widespread anoxia and generally reducing ocean environments in the Archean (Large, 1977; Lambert *et al.*, 1978; Cameron and Hattori, 1987; Huston, 1997), such that little fractionation occurred between igneous H_2S and dissolved aqueous H_2S. In comparison, sulphate-free Phanerozoic deposits are interpreted to result from reduced fluids where sulphate formed a minor component of the ore fluid (*e.g.*, Balcooma in Huston, 1988).

In the Archean, oxidising conditions may have prevailed in localised basins that had different degrees of oxidation or shallow-water environments such as those inferred at North Pole (*e.g.*, Lambert *et al.*, 1978; Hattori *et al.*, 1983). The layered ocean model preferred by these authors, envisaged that anoxic bottom waters lay below more oxidised surficial sulphate-bearing waters, with sulphate-free deposits forming in the deeper-water anoxic layer and sulphate-bearing deposits forming in the upper oxidised waters (Eastoe and Gustin, 1996). This model reflects the restricted availability of oxygen in marine basins in the Archean, particularly in deeper water (Lambert *et al.*, 1978; Cameron and Hattori, 1987).

Ohmoto (1996) presented an alternative hypothesis in which, Precambrian seawater containing significant dissolved sulphate and the Phanerozoic process of sulphate reduction, applied throughout geological time. Ohmoto (1996) inferred that, like

Phanerozoic sulphate, Proterozoic seawater sulphate varied between 10 and 30‰, but Archean seawater sulphate had relatively constant $\delta^{34}S$ values of 2 to 3‰. Huston (1997) considers this model unlikely due to the differences in the magnitude and range of sulphide $\delta^{34}S$ values between the Phanerozoic, Proterozoic and Archean deposits, which suggests that the same processes across the geological eras did not occur.

10.4.3 Interpretation of $\delta^{34}S$ values in Archean VHMS deposits

Ohmoto (1996) argues for two reduced sulphur sources in Archean VHMS deposits. These are (1) magmatic or rock sulphur ($\delta^{34}S = 0$) and (2) seawater sulphur ($\delta^{34}S = \sim 2‰$), which resulted in $\delta^{34}S$ values of sulphide between 0‰ and contemporaneous seawater with relatively little variation.

As Archean VHMS deposits have a narrow range of $\delta^{34}S$ values, widespread inorganic sulphate reduction in the ore fluids is considered unlikely (Donnelly *et al.*, 1977; Hattori *et al.*, 1983; Ohmoto, 1996; Huston, 1997). Huston (1997) argued that partial inorganic reduction of Archean seawater sulphate ($\delta^{34}S$ of ~2‰) would produce ore fluids with sulphide $\delta^{34}S$ values between -10 and -25‰, which is inconsistent with observed $\delta^{34}S$ values of ~0‰. Nonetheless, a sulphur contribution by Archean seawater cannot be eliminated, due to inferred similar $\delta^{34}S$ values for dissolved sulphur in Archean seawater and meteoric fluids (*e.g.*, Lambert, 1978). To produce an Archean ore fluid with sulphide $\delta^{34}S$ values of ~0‰, Huston (1997) proposed a high contribution (67%) of dissolved rock sulphur ($\delta^{34}S$ ~0 to 5‰) and a limited contribution (33%) of reduced Archean seawater sulphate ($\delta^{34}S = -10‰$) to form a VHMS deposit with $\delta^{34}S$ of ~0‰. Based on these parameters, the role of inorganic reduction of seawater sulphate, if it occurred at all, was a minor source of sulphur in Archean ore forming fluids (Huston, 1997; Ohmoto, 1996). Additionally, the low sulphur content of reduced Archean seawater could also explain its minor contribution to ore forming fluids (Section 10.4.2).

The near 0‰ sulphur isotope signature of Archean VHMS deposits has also been attributed to reduced sulphur entirely evolved from (1) a magmatic source, (2) a dissolved rock sulphur source, or (3) a combination of (1) and (2) (Sangster, 1978; Lambert *et al.*, 1978; Skyring and Donnelly, 1982; Eastoe *et al.*, 1990; Bowins and Crocket, 1994; Huston, 1997). In all cases, oxidised sulphur (SO_4^{2-}) is interpreted as a minor component of the ore fluid with no significant oxidation of the ore fluid upon exhalation (Lambert *et al.*, 1978), as supported by the absence of sulphate. However, the $\delta^{34}S$ variation in Archean deposits is too small to have been produced entirely by a magmatic sulphur source (Ohmoto and Rye, 1979; Ohmoto, 1986; Ohmoto and Goldhaber, 1997). Sangster (1978) and Skyring and Donnelly (1982) proposed an alternative oxidised sulphur source in Archean seawater (SO_2) to explain the significantly positive $\delta^{34}S$ values in some sulphide minerals.

Biogenic sulphate reduction was not considered to be a major process in the formation of VHMS deposits prior to 2.4 Ga. (Lambert *et al.*, 1978; Strauss, 1986; 1989; Huston, 1997). The ranges and variation of $\delta^{34}S$ values due to biogenically reduced sulphur are generally large (Ohmoto and Rye, 1979), which is inconsistent with the narrow variation in Archean VHMS deposits. Minor evidence of biogenic reduction of sulphate is, however, found in

some Archean banded iron formations (*e.g.*, Lambert *et al.*, 1978; Skyring and Donnelly, 1982; Bowins and Crocket, 1994). The widespread absence of sulphate reducing bacteria in the Archean is also used to infer global anaerobic conditions that inhibited the oxidation of sulphur (Hattori *et al.*, 1983).

In summary, the sulphur isotope systematics of Archean VHMS deposits are contentious due to varied interpretations of the Archean environment and its chemistry. It has been predicted that in the reducing Archean environment, the main sulphur contribution in VHMS deposits was from an igneous rock sulphur source (*e.g.*, Bowins and Crocket, 1994; Huston, 1997). The role of Archean seawater sulphur in the ore fluids is thought to be minor, either due to limited sulphur in seawater or a limited oxidised sulphur (SO_4^{2-} or SO_2) reservoir (Skyring and Donnelly, 1982; Strauss, 1989). The sulphur isotope systematics of Archean deposits therefore differs significantly from those of Phanerozoic deposits (*c.f.* Section 10.4.1).

The results of this sulphur isotope study at Gossan Hill support the inference that Archean seawater was not significantly oxidising, due to the absence of sulphate minerals and the generally low $\delta^{34}S$ values (average of ~2.1 ± 1.6‰) of Gossan Hill sulphides. However, rare $\delta^{34}S$ values up to 7.8‰ could indicate that a limited reservoir of oxidised sulphur was present in Archean seawater, as these values are significantly heavier than the estimated $\delta^{34}S$ values for contemporaneous seawater (~2 to 3‰).

10.4.4 Variation in $\delta^{34}S$ values

Systematic variation in $\delta^{34}S$ values is common in many VHMS deposits of both of Phanerozoic and Archean ages. Phanerozoic examples include the Heath Steele deposit, New Brunswick, where $\delta^{34}S$ values decrease from footwall to hangingwall (Lusk and Crocket, 1969), whilst at Rosebery, Hellyer, Waterloo, Agincourt and Thalanga, the $\delta^{34}S$ values increase from footwall to hangingwall (Green *et al.*, 1981; Gemmell and Large, 1992; Huston *et al.*, 1995a; Hill, 1996). Archean examples of systematic variation include the Quemont deposit, Noranda where $\delta^{34}S$ values delineate a small, but broad enrichment with depth (Ryznar *et al.*, 1967). Systematic variation of $\delta^{34}S$ values also occurs in the Millenbach deposit, Noranda, with an upward and outward increase in $\delta^{34}S$ values from 1.2 ± 3‰ in the lower Cu rich zones, to higher $\delta^{34}S$ values (up to 3.8‰) in the upper Zn-rich zones (Coomer and Schwartz, 1974).

At Gossan Hill, systematic stratigraphic variation in the $\delta^{34}S$ values of sulphide reflects a progressive, small trend to heavier $\delta^{34}S$ values upward through ore (Section 10.3.4). The magnitude of this enrichment is ~1.2‰, from average $\delta^{34}S$ values of 1.6‰ in the lower Cu-rich zone to 2.8‰ in the upper Zn-Cu zone (Table 10.2). Not only are the heaviest $\delta^{34}S$ values recorded in the upper Zn-Cu zone, but the widest variations in $\delta^{34}S$ values also occur in the upper ore zone (variation of 7.8‰). In the lower Cu-rich zone, the variation of $\delta^{34}S$ values is markedly less (<3‰).

The systematic variation of $\delta^{34}S$ values with ore type and stratigraphy has several possible interpretations. Increasing $\delta^{34}S$ values with depth are inferred to reflect changes in the fO_2 and pH conditions of the ore fluids in the later stages of sulphide formation rather than

variation in the source of sulphur (Rye and Ohmoto, 1974; Kajiwara, 1971). Decreasing $\delta^{34}S$ values in sulphides with depth are considered to indicate progressive mixing of the hydrothermal fluids with reduced seawater sulphate or leaching of igneous sulphur (Green *et al.*, 1981; Gemmell and Large, 1992; Hill, 1996) or a decrease in the igneous sulphur content of the hydrothermal fluids (Solomon *et al.*, 1988).

10.4.5 Geothermometry

Between sulphide species, isotopic equilibrium is illustrated by the $\delta^{34}S$ values of pyrite > sphalerite > chalcopyrite > galena (Rye and Ohmoto, 1974). The difference between the $\delta^{34}S$ values of co-existing sulphide minerals can be used to estimate the temperature of formation assuming isotopic equilibrium between species and that no isotopic exchange between the sulphide minerals occurred after deposition (Ohmoto and Rye, 1979). Geothermometry estimates are based on the temperature dependence of fractionation between sulphide (and/or sulphate) species under equilibrium conditions, with the differences in $\delta^{34}S$ values of the co-existing sulphide pairs used to estimate temperatures of deposition (Ohmoto and Rye, 1979; Ohmoto and Goldhaber, 1997). Additionally, greenschist to upper amphibolite facies metamorphism will not significantly reset the sulphur isotope values, however re-equilibration of sulphur isotopes occurs above upper amphibolite facies (Ohmoto and Rye, 1979; Crowe, 1994).

At Gossan Hill, sulphide $\delta^{34}S$ values commonly deviate from the pyrite > sphalerite > chalcopyrite > galena fractionation pattern, indicating widespread isotopic disequilibrium. However, rare compliance with this fractionation trend (Appendix A8.1) indicates localised isotopic equilibrium conditions. A contributing problem is the small difference in the $\delta^{34}S$ values between the sulphide pairs, which is often within the analytical precision of the conventional or laser ablation sulphur isotope technique. Only sulphide pairs having equilibrium fractionation patterns, with differences greater than the analytical uncertainty were used to estimate temperatures.

Sixteen sulphide-sulphide pairs in this study, have evidence of isotopic and textural equilibrium. These co-existing sulphide pairs were sphalerite-galena, pyrite-chalcopyrite, pyrite-pyrrhotite and pyrite-sphalerite. Temperatures for each sulphide pair were calculated using the equations of Ohmoto and Rye (1979) and temperature estimates are given in Appendix A8.1 and illustrated in Figure 10.8. These temperature estimates range from -2°C to 911°C with sulphide pair temperatures greater than 450°C and less than 100°C considered geologically unreasonable for sulphide deposition in a VHMS system (*e.g.*, Large, 1992). Moreover, temperatures greater than 450°C exceed the estimated peak greenschist facies metamorphic temperature for Gossan Hill (Chapter 4).

Seven sulphide pair temperature estimates yield temperatures of between 227°C and 362°C (Fig. 10.8), for pyrite-chalcopyrite (361°C), sphalerite-galena (354°C and 362°C), pyrite-pyrrhotite (227°C and 255°C) and pyrite-sphalerite (269°C and 283°C) sulphide pairs (Appendix A8.1). These temperatures are comparable, but slightly hotter than expected temperature ranges for Zn-rich and Cu-rich mineralisation of 175-235°C and 270-250°C respectively (Large, 1992). Additionally, these temperatures are significantly lower than the

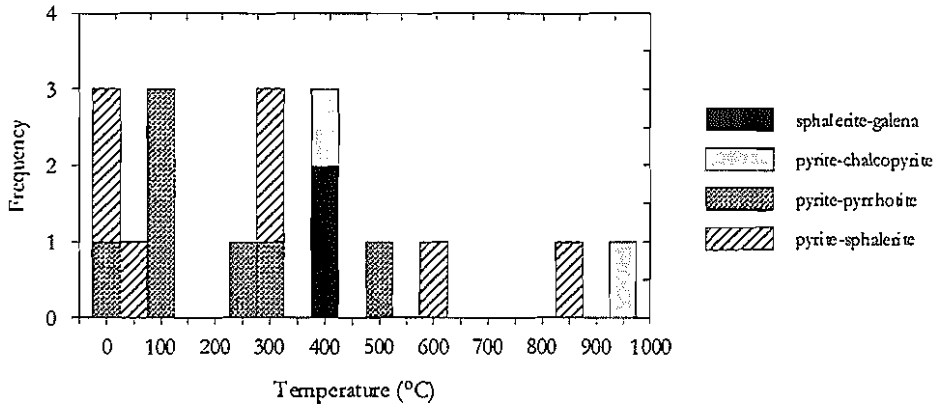

Figure 10.8: Frequency histogram of calculated temperatures from sulphide-sulphide pairs at the Gossan Hill deposit. Data listed in Appendix A8.1

estimated metamorphic temperatures at Gossan Hill (450°C), suggesting that the $\delta^{34}S$ values for some sulphides may not have been significantly affected by metamorphism. These sulphide pair geothermometers occur in veins or in massive sphalerite may have been isolated from the effects of metamorphism by the siliceous alteration in the wall rock. However, due to the overall wide range in temperatures (-2°C to 911°C), these temperature estimates are considered to be unreliable.

10.4.6 Gossan Hill sulphur isotope model

The distribution and variation in $\delta^{34}S$ values for sulphides at Gossan Hill is schematically illustrated in Figure 10.9. The distribution of $\delta^{34}S$ values at Gossan Hill is characterised by an isotopically homogeneous lower Cu-rich ore zone including massive pyrite, stringer mineralisation and sulphides in the wall rock of GGF M4. Progressive enrichment in $\delta^{34}S$ values is observed stratigraphically upwards to Zn-rich mineralisation in the upper ore zone of GGF M6. The small magnitude of this enrichment (*i.e.*, ~1.2‰) likely reflects the similar isotopic signatures of the end-member sulphur sources, which are (1) Archean seawater (~2 to 3‰), (2) leached igneous rock sulphur (~0‰), and (3) magmatic sulphur (~0‰).

Increasing $\delta^{34}S$ values in sulphide at Gossan Hill are interpreted to reflect the progressive mixing trend between two sulphur-bearing fluids. Upwelling hydrothermal fluids carrying reduced sulphur are interpreted to principally contain leached igneous rock sulphur with a minor contribution from a magmatic sulphur source. The similar $\delta^{34}S$ values between the wall rock sulphides (GGF M4 and GGF M6) and massive sulphides in the lower Cu-rich ore zone (Figure 10.9) indicate the uniformity of this leached rock sulphur-magmatic sulphur source. Furthermore, the homogeneous sulphur isotope composition in the lower ore zone supports its formation by sub-seafloor replacement (Chapter 5), which prevented the mixing of upwelling hydrothermal fluids with seawater.

The upper Zn-Cu ore zone at Gossan Hill has the heaviest and greatest variation in sulphide $\delta^{34}S$ values. The increase in $\delta^{34}S$ values toward massive sphalerite at Gossan Hill reflects the mixing of upwelling ore fluids with seawater. As Gossan Hill is interpreted to have formed largely by sub-seafloor replacement processes (Chapter 5), it is unlikely that

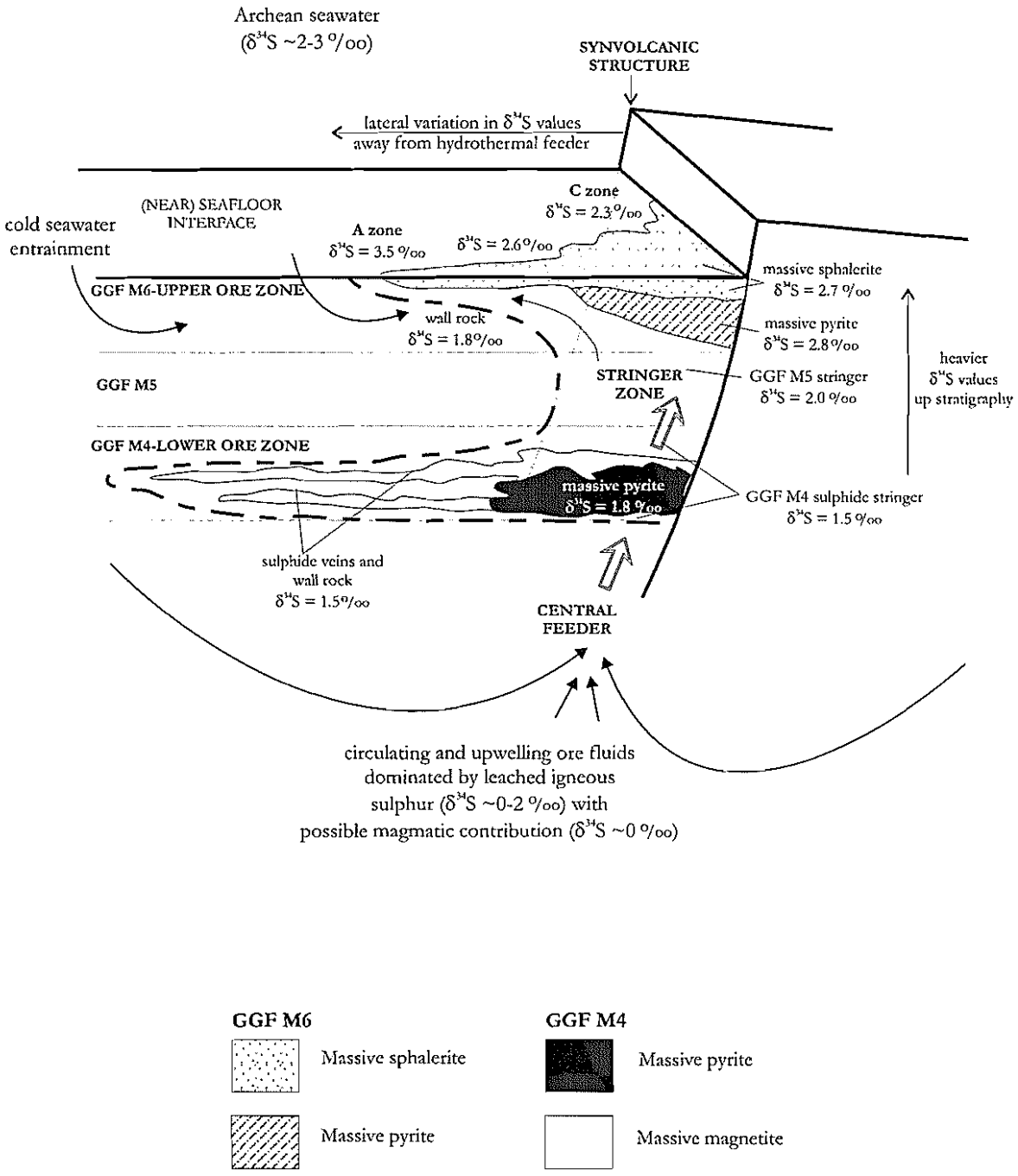

Figure 10.9: Schematic illustration of the variation in sulphide $\delta^{34}S$ values with stratigraphy and ore type at Gossan Hill. A slight stratigraphic enrichment in sulphide $\delta^{34}S$ values occurs from the lower Cu-rich ore zone in GGF M4 to the upper Zn-Cu ore zone in GGF M6. Within massive sphalerite at the top of Gossan Hill, sulphur isotope variation is greatest and occurs laterally away from the central feeder, with an increase in the $\delta^{34}S$ values of pyrite and sphalerite from C to A zone. The sulphur isotope model predicts circulation of ore fluids within the rock column that leached igneous rock sulphur, with minor magmatic sulphur contribution. The $\delta^{34}S$ variation at the top of the pile is associated with proximity of the massive sulphides to the seafloor, due to progressive mixing with locally entrained seawater.

hydrothermal fluids mixed freely with seawater, but possibly with entrained seawater in seawater saturated volcaniclastics. The variation of sulphide $\delta^{34}S$ values at the top of Gossan Hill in massive sphalerite, is consistent with upwelling hydrothermal fluids dominated by leached igneous rock sulphur and minor magmatic sulphur, progressively mixing with entrained reduced and relatively sulphate deficient Archean seawater proximal to the seafloor. The mixing of upwelling ore fluids with entrained and relatively reduced Archean seawater, led to increased variation in $\delta^{34}S$ sulphide values. This increased variation likely resulted from the oxidation-reduction state of coeval Archean seawater, which may have contained minor amounts of oxidised sulphur that caused values as high as 7.8‰. Moreover, the widest variation in sulphide $\delta^{34}S$ values occurs at A zone due to its greater distance from the central feeder and main upflow zone, where a greater sulphur contribution from coeval seawater was possible.

10.5 Summary

- The overall variation in sulphur isotope compositions for sulphides at Gossan Hill is 12.6‰, with an average of 2.1 ± 1.7‰.
- A systematic stratigraphic variation of sulphide $\delta^{34}S$ values is observed at Gossan Hill, with an increase of ~1.2‰ from the footwall to the hangingwall. Although small, this variation is considered significant in view of the narrow range for $\delta^{34}S$ values in Archean deposits. Increased $\delta^{34}S$ values towards the upper ore zone at Gossan Hill are also accompanied by an increased range in $\delta^{34}S$ values, with the greatest variation occurring in massive sphalerite of the upper ore zone.
- Hydrothermal fluids responsible for Cu-rich sulphides in the lower ore zone at Gossan Hill, including massive sulphide and stringer veins, have mean $\delta^{34}S$ values of 1.6‰ and a narrow range (-1.6 to 3.4‰). This data indicates a relatively uniform reduced sulphur source that is dominated by leached igneous rock sulphur with a possible magmatic sulphur contribution.
- The $\delta^{34}S$ values of sulphides within massive magnetite (either as disseminations or veins) do not differ from $\delta^{34}S$ values of sulphides in massive pyrite and stinger veins in GGF M4.
- Heavier average $\delta^{34}S$ values (2.8‰) and a wider sulphur isotope range (-4.8 to 7.8‰) in Zn-Cu mineralisation of the upper ore zone (GGF M6) is explained by hydrothermal fluid mixing near the seafloor. Upwelling hydrothermal fluids, dominated by leached igneous rock sulphur, mixed with entrained relatively sulphur-deficient seawater ($\delta^{34}S$ values of 2 to 3‰). The increased variability in $\delta^{34}S$ values southwards away from the central feeder (C zone), is also attributed to this mixing mechanism, with a greater proportion of seawater mixing occurring away from the feeder and central upflow zone.
- Limited evidence of isotopic equilibrium is observed between sulphides at Gossan Hill. The $\delta^{34}S$ values of sulphide-sulphide mineral pairs in isotopic equilibrium yield temperature estimates that vary from between -2°C to 911°C.

Chapter 11

Oxygen, hydrogen and carbon isotopes

11.1 Introduction

The application of oxygen, hydrogen and carbon isotopes to hydrothermal ore deposits can define and constrain geochemical parameters of ore formation (*e.g.*, Taylor 1974; 1979; Ohmoto and Rye, 1979; Ohmoto, 1996; Ohmoto and Goldhaber, 1997). These parameters include the nature, isotopic composition and origin of ore fluids, temperature of formation, oxidation-reduction state and fluid-rock interaction variables (*e.g.*, Taylor, 1974; 1979; Ohmoto and Rye, 1979; Cathles, 1983; Nesbitt *et al.*, 1984). Examples of stable isotope studies on VHMS deposits include the Rosebery deposit (Khin Zaw and Large, 1992), the Kuroko deposits (Green *et al.*, 1983; Pisutha-Arnond and Ohmoto, 1983) and currently forming seafloor analogues (Peter, 1986).

Whole rock and mineral silicate oxygen isotopes studies of Archean VHMS deposits are widely reported (*e.g.*, Costa *et al.*, 1983; Barrett *et al.*, 1992; Huston *et al.*, 1995). In the Noranda area, Canada, wholerock oxygen isotopes define vectors to massive sulphide mineralisation by defining patterns that are attributed to the progressive oxygen isotope depletion or enrichment resultant from the circulation of hydrothermal fluids (MacLean and Hoy, 1991; Barrett *et al.*, 1993; Cathles, 1993; Hoy, 1993; Paradis *et al.*, 1993). By contrast studies of hydrogen and carbon-oxygen isotopes in Archean VHMS deposits are few, but are common in Archean lode Au deposits (*e.g.*, Golding *et al.*, 1988; Karhu *et al.*, 1993). The limited application of hydrogen and carbon-oxygen isotopes to Archean VHMS deposits reflects the generally deformed and metamorphosed occurrence of this deposit type (Sangster, 1972; Franklin *et al.*, 1981) and the susceptibility of carbon-oxygen and hydrogen isotopes to resetting by metamorphic events (Rye and Ohmoto, 1974; Taylor, 1974; 1979; Ohmoto and Rye, 1979).

Gossan Hill has had a long complex history that encompasses two major hydrothermal stages, four deformation events and peak metamorphism at temperatures of 454 ± 4°C (Chapter 4). This study is the first to investigate oxygen, hydrogen and carbon isotopes at Gossan Hill and is directed at identifying isotopic differences between the two main hydrothermal events (*i.e.*, massive magnetite *versus* massive sulphide). The aims were to:

- distinguish physicochemical differences in the massive magnetite and massive sulphide ore forming environments (*i.e.*, constrain a single or multiple formational fluids);
- establish formation temperatures and ore fluid compositions for massive magnetite and

massive sulphide using oxygen isotope mineral pair geothermometry and;

- assess the effect of metamorphism on the isotope composition of minerals.

11.2 Methods

Oxygen isotopes on chlorite, magnetite and whole rock samples, and hydrogen isotopes on chlorite were analysed at the Centre for Isotope Research, CSIRO, Sydney. Magnetite and chlorite mineral separates were hand picked, with contamination reduced by magnetic separation and microscopic grain checking. Impurities in chlorite due to carbonate intergrowths were eliminated using a Na acetate digestion (Brewster, 1980; Jackson, 1956). Whole rock oxygen isotopes were completed on powdered rock. All oxygen isotope analyses were determined using the method of Clayton and Mayeda (1963). The c gas was analysed on a Finnigan 252 mass spectrometer with an accuracy of ± 0.2‰. Hydrogen isotopes were determined using the method of Bigeleisen *et al.* (1952) with an accuracy of ± 1‰. All analyses are reported relative to standard mean ocean water (SMOW).

Carbon and oxygen isotopes on ankerite were completed at the Central Science Laboratory, University of Tasmania, according to the method of McCrea (1950), using a Finnigan Isogas 2000 mass spectrometer. Carbonate was separated from hand samples using a fine diamond drill. All samples were reacted with phosphoric acid at 25°C for 24 hours and results are expressed relative to the Peedee Formation Belemnite (PDB) for carbon and SMOW for oxygen.

11.3 Results

The results of oxygen, hydrogen and carbon isotope analyses at Gossan Hill are given in Appendix A9.1. In total, 19 oxygen isotope analysis were completed on magnetite (8), chlorite (8), and whole rock samples (3), together with 8 hydrogen isotopes (chlorite) and 21 carbon-oxygen isotopes on carbonate.

11.3.1 Oxygen isotope composition of magnetite

Magnetite that was analysed included magnetite from massive magnetite (GGF M4) and magnetite disseminated within massive sulphide (GGF M4 and M6) (Appendix A9.1). The overall variation of $\delta^{18}O$ values for magnetite are 3.9 to -3.7‰ (Fig. 11.1a), with a mean of 0.5 ± 3.1‰ (Table 11.1). Magnetite in massive magnetite tends to have lighter $\delta^{18}O$ compositions (-0.3 to -3.7‰; mean of -2.6 ± 2.0‰; n=3) than magnetite in massive sulphide (-1.0 to 3.9‰; mean of 2.3 ± 2.0‰; n=5).

Table 11.1: Oxygen isotope composition of magnetite at Gossan Hill. All values are relative to SMOW.

	n*	Min (‰)	Max (‰)	Mean (‰)	SD# (‰)
Magnetite (all)	8	-3.7	3.9	0.5	3.1
Massive magnetite (GGF M4)	3	-3.7	-0.3	-2.6	2
Sulphide-hosted magnetite (GGF M4 and M6)	5	-1	3.9	2.3	2

* indicates number of analyses, # standard deviation

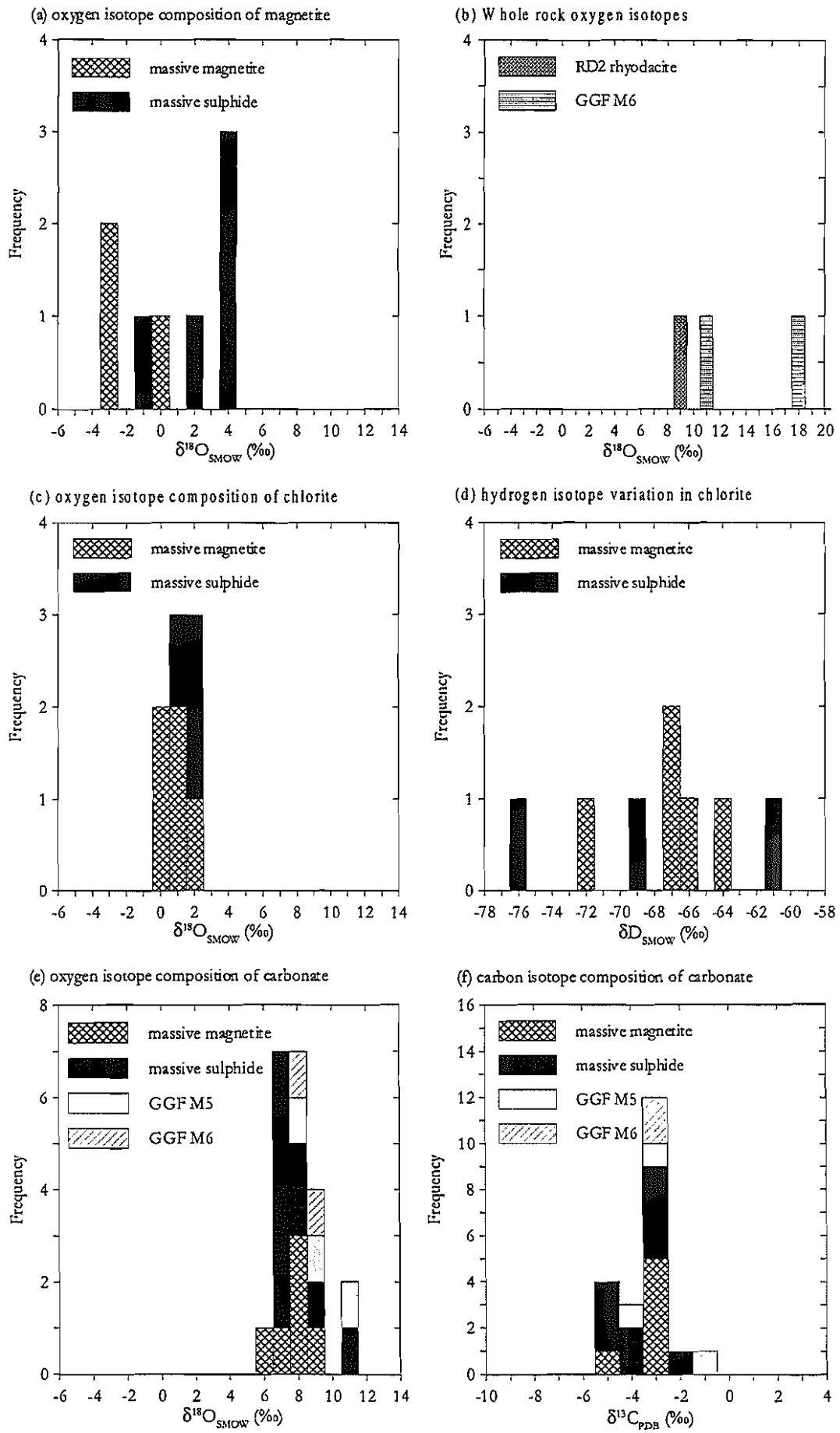

Figure 11.1: Isotope composition of minerals at Gossan Hill. (a) Oxygen isotope variation of magnetite, (b) whole rock oxygen isotope variation, (c) oxygen isotope variation in chlorite, (d) hydrogen isotope variation in chlorite, (e) oxygen isotope variation in carbonate, and (f) carbon isotope variation in carbonate.

11.3.2 Whole rock oxygen isotopes

Whole rock oxygen isotopes were a minor component of this study, with 3 determinations made on geologically diverse samples. These samples were rhyodacite in the hangingwall (RD2; $\delta^{18}O$ of 8.7‰), intensely silicified sandstone in stockwork mineralisation of GGF M6 ($\delta^{18}O$ of 17.4‰) and chert from the M1 Marker at the top of GGF M6 ($\delta^{18}O$ of 10.2‰) (Fig. 11.1b). These limited analyses indicate that wide whole rock oxygen isotope variation exists at Gossan Hill, but is not discussed further.

11.3.3 Oxygen isotope composition of chlorite

The oxygen isotope compositions of chlorite at Gossan Hill have a narrow range of $\delta^{18}O$ values from -0.7 to 2.0‰ with a mean of 0.6 ± 1.0‰ (Appendix A9.1 and Fig. 11.1c). Chlorite alteration hosting magnetite and sulphide in GGF M4 have $\delta^{18}O$ values between -0.7 and 1.9‰ (mean of 0.3 ± 1.1‰) (Table 11.2). The $\delta^{18}O$ values of chlorite in sulphide veins of GGF M6 vary from 0.1 to 2.0‰ with a mean of 1.1 ± 1.0‰ (Table 11.2). Although the range of $\delta^{18}O$ values for chlorite in both these occurrences is similar, chlorite in GGF M4, has slightly lighter $\delta^{18}O$ values than chlorite in GGF M6.

11.3.4 Hydrogen isotope composition of chlorite

The δD values of chlorite range from -61.9 to -76.0‰ with a mean of -68.3 ± 4.4‰ (Fig. 11.1d and Table 11.2). Chlorite alteration in GGF M4 has a narrower range of δD values from -64.9 to -72.6‰ (mean of -67.8 ± 2.9‰) compared to chlorite in sulphide veins of GGF M6, which ranges from -61.9 to -76.0‰ (mean of -69.1 ± 7.1‰) (Table 11.2). The variation in δD values of chlorite indicates that chlorite in GGF M4 is isotopically more homogeneous than chlorite in GGF M6.

Table 11.2: Variation in the oxygen ($\delta^{18}O$) and hydrogen (δD) isotope composition of chlorite at Gossan Hill. All analysis relative to SMOW.

	n*	$\delta^{18}O$ (‰)				δD (‰)			
		Min	Max	Mean	SD#	Min	Max	Mean	SD#
All	8	-0.7	2	0.6	1	-76	-61.9	-68.3	4.4
GGF M6	3	0.1	2	1.1	1	-76	-61.9	-69.1	7.1
GGF M4	5	-0.7	1.9	0.3	1.1	-72.6	-64.9	-67.8	2.9

* indicates number of analysis; # standard deviation

11.3.5 Oxygen isotope composition of carbonate

The isotopic compositions of 21 carbonates from Gossan Hill were determined and results are given in Appendix A9.1. Of these samples, 6 are from massive magnetite (GGF M4), 10 from massive sulphide and stringer mineralisation (GGF M4), 3 from carbonate nodular alteration (GGF M5) and 2 from carbonate alteration in GGF M6. At Gossan Hill, carbonates have $\delta^{18}O$ values that vary from 5.9 to 10.7‰ with a mean of 7.7 ± 1.2‰ (Fig. 11.1e and Table 11.3). Carbonates in GGF M4 have $\delta^{18}O$ values between 5.8 and 8.8‰ (mean of 7.3 ± 1.0‰) for massive magnetite and $\delta^{18}O$ values from 6.5 to 10.1‰ (mean of 7.4 ±1.1‰) for massive sulphide. Nodular carbonate alteration in GGF M5 has the widest variation of $\delta^{18}O$ values at Gossan Hill varying from 7.9 to 10.7‰ (mean of 9.1 ± 1.5‰). In GGF M6, carbonate alteration has $\delta^{18}O$ values of 8.0 to 9.0‰ (mean of 8.5 ± 0.7‰),

Table 11.3: Carbon and oxygen isotope results of carbonate in massive sulphide, massive magnetite and carbonate alteration in GGF M5 and GGF M6 at Gossan Hill.

	n*	$\delta^{13}C_{PDB}$ (‰)				$\delta^{18}O_{SMOW}$ (‰)			
		Max	Min	Mean	SD#	Min	Max	Mean	SD#
All	21	-1.4	-5.7	-3.9	1.1	5.6	10.7	7.7	1.2
GGF M6	2	-3.3	-3.6	-3.4	0.3	8	9	8.5	0.7
GGF M5	3	-1.5	-4.9	-3.4	1.8	7.9	10.7	9.1	1.5
GGF M4 (sulphide)	10	-2.3	-5.7	-4.1	1.1	6.5	10.1	7.4	1.1
GGF M4 (massive magnetite)	6	-3.2	-5.4	-4	0.7	5.6	8.8	7.3	1

* indicates number of analysis, # indicates standard deviation

which includes carbonate in the M1 Marker ($\delta^{18}O$ value of 9.0‰). Based on these data, the $\delta^{18}O$ values of carbonate in massive magnetite and massive sulphide in GGF M4 are isotopically indistinguishable, while the $\delta^{18}O$ values of carbonate trend to heavier values towards the top of ore (*i.e.*, GGF M5 and GGF M6).

11.3.6 Carbon isotope composition of carbonate

The overall variation in $\delta^{13}C$ values of carbonate is narrow, ranging from -1.4 to -5.7‰ (mean of -3.9 ± 1.1‰) (Fig. 11.1f and Table 11.3). Carbonates in GGF M4 have $\delta^{13}C$ values from -3.2 to -5.4‰ (mean of -4.0 ± 0.7‰) in massive magnetite and from -2.3 to -5.7‰ (mean of -4.1 ± 1.1‰) in massive sulphide, indicating that these two mineralisation types are isotopically indistinguishable. The $\delta^{13}C$ values of nodular carbonate alteration (GGF M5) range from -4.9 to -1.4‰ (mean of -3.4 ±1.8‰) and in GGF M6 carbonate has relatively homogeneous $\delta^{13}C$ values of -3.6 to -3.3‰ (mean of -3.4 ± 0.3‰) (Fig 11.1f and Table 11.3). A broad trend to slightly heavier $\delta^{13}C$ values occurs up stratigraphy.

11.4 Oxygen isotope mineral pair geothermometry

The fractionation of oxygen isotope values between coexisting mineral pairs is dependent on temperature and can be used as a geothermometer (Taylor, 1974) assuming; (1) the exchange reactions reached equilibrium, (2) the oxygen isotope compositions were not subsequently altered by water-rock interaction or metamorphism, and (3) the temperature dependence of fractionation factors is known from experimental and theoretical calculations (Ohmoto and Rye, 1979; Taylor, 1979; 1974). Oxygen isotope geothermometry was applied at Gossan Hill on mineral pairs from massive magnetite (GGF M4; 3 analysis) and Type V(A) sulphide veins (GGF M4; 2 analysis) (Appendix A9.1 and Table 11.4) to constrain the temperature and isotopic composition of these events. The mineral pairs investigated were magnetite-chlorite, magnetite-carbonate and carbonate-chlorite (Table 11.4).

Oxygen isotope fractionation factors for magnetite are reported for high temperature (500 to 800°C; Bottinga and Javoy, 1973) and low temperature (<400°C; Blattner *et al.*, 1983; Becker and Clayton, 1976) systems. The latter were used in this thesis to estimate formation temperatures. For chlorite and carbonate, the equilibrium oxygen isotope

Table 11.4: Results of oxygen isotope fractionations ($\Delta_{a\text{-}b}$) for mineral pairs with calculated temperatures and fluid compositions. All oxygen isotope values are relative to SMOW.

Sample	Mineral	$\delta^{18}O$ (‰)	Mineral Pair	$\Delta_{a\text{-}b}$ (‰)	T°C	$\delta^{18}O_{fluid}$ (‰)	Reference*
760374**	magnetite	3.9	mgt-chl	1.9	-100	1	1
	chlorite	2					2
760432**	magnetite	3.4	mag-chl	2.1	-100	0.5	1
	chlorite	1.3					2
769137#	chlorite	-0.7	ank-chl	9.4	222	-2.8	2
	ankerite	8.7					3
769325#	magnetite	-0.3	ank-mgt	7.6	535	2.9	1
	ankerite	7.3					3
769327#	magnetite	-3.6	mgt-chl	-5.5	-87	-5.7	1
	chlorite	1.9	ank-chl	5.8	466	2.5	2
	ankerite	7.7	ank-mgt	11.3	n.s.	n.s.	3

*oxygen isotope fractionation equation parameters for; (1) magnetite from Blattner *et al.* (1983), (2) chlorite from Savin and Lee (1988), and (3) ankerite from Fisher and Land (1986)

mgt = magnetite, chl = chlorite, ank = ankerite

massive magnetite GGF M4, ** Type V(A) sulphide vein GGF M4, n.s. = no solution

fractionation factors are dependent on mineral composition (*e.g.*, Longstaffe, 1989; Savin and Lee, 1988; Field and Fifarek, 1985). Due to Fe-rich chlorite and carbonate at Gossan Hill (Chapter 7), the equilibrium equations for Fe-rich chlorite (Savin and Lee, 1988) and ankerite (Fisher and Land, 1986) were used in geothermometer calculations.

The geothermometry results yield a range of formational temperatures from -100° to 535°C. Different temperature estimates within a single sample (769327; Table 11.4) and negative temperature estimates in geologically similar samples (760374 and 760432; Table 11.4), indicate that isotopic equilibrium was not attained or preserved between these minerals. Due to textural evidence of equilibrium between magnetite, chlorite and carbonate, it is possible that some later oxygen isotope exchange occurred between these minerals. Isotopic exchange may have occurred during the overprint of massive magnetite by sulphide, or during peak greenschist metamorphism. As magnetite in both sulphide and massive magnetite yields unlikely temperature estimates, isotopic exchange during metamorphism is is considered most likely. Similar conclusions regarding oxygen isotopic disequilibrium due to metamorphic resetting are reported from VHMS deposits in the Noranda district (Paradis *et al.*, 1993; MacLean and Hoy, 1991).

The mineral pair temperature estimates for ankerite-chlorite are 466° and 222°C (Table 11.4). A temperature of 466°C is consistent with the temperature estimate of peak metamorphism (454 ± 4°C) at Gossan Hill, suggestive that carbonate and chlorite were re-equilibrated with a metamorphic fluid. This suggestion is also supported by evidence of textural recrystallisation of these minerals (Chapter 7). Under the assumption of metamorphic re-equilibration, the $\delta^{18}O_{H2O}$ of the metamorphic fluid is ~2.5‰ (Table 11.4).

The resetting of $\delta^{18}O$ values in carbonate and chlorite is common (Savin and Lee, 1988; Ohmoto, 1986; Valley, 1986; Ohmoto and Rye, 1979; Taylor 1979), and it is considered less likely that the $\delta^{18}O$ values of magnetite have been reset. Assuming the $\delta^{18}O$ values of

magnetite at Gossan Hill are primary, their $\delta^{18}O$ values can be integrated with experimental data to constrain the composition of hydrothermal fluids. The isotope partition coefficient function for magnetite-H_2O ($1000\ln\alpha \approx \delta^{18}O_{magnetite}-\delta^{18}O_{H2O}$) has negative values (Becker and Clayton, 1976) and therefore, the $\delta^{18}O_{H2O}$ must be greater than the $\delta^{18}O_{magnetite}$ value in an equilibrium system. Using this constraint, the broad isotopic differences between fluids forming magnetite in massive magnetite and massive sulphide may be determined.

The massive magnetite has generally lighter $\delta^{18}O$ values (mean of -2.6 ‰) than magnetite in sulphide (mean of 2.4‰). This suggests that the $\delta^{18}O_{H2O}$ values of the formation fluids differed between the massive magnetite and massive sulphide events, as the $\delta^{18}O_{H2O}$ value of the fluid must be greater than these observed values. This suggests that the $\delta^{18}O_{H2O}$ value of the fluid forming the massive sulphide was isotopically heavier than that forming massive magnetite, with the magnitude of this difference strongly dependent on temperature.

The influence of temperature on the magnitude of the $\delta^{18}O_{H2O}$ values required in both massive magnetite and sulphide is illustrated in Table 11.5, assuming the average $\delta^{18}O$ values for magnetite. In the experimentally determined magnetite fractionation curve, the maximum oxygen isotope partition coefficient function is ~10‰ (Becker and Clayton, 1976). To attain temperatures in the range of 175 to 350°C, typical of massive sulphide formation (Large, 1992), the $\Delta_{magnetite-H2O}$ must approach 7 to 10‰ (Table 11.5), whilst smaller differences are required for lower temperatures. If massive magnetite was deposited at lower temperatures (*e.g.*, <200°C) relative to massive sulphide, then the $\delta^{18}O_{H2O}$ must have become isotopically heavier during the transition from massive magnetite to massive sulphide formation. Based on the equilibrium fractionation of magnetite, the ore fluids forming magnetite in both massive magnetite and massive sulphide must have had isotopically heavier values than the observed $\delta^{18}O_{magnetite}$ values. In view of the likely temperature range of 175-350°C, the $\delta^{18}O$ of the fluids is constrained to

Table 11.5: Calculated temperature ranges of magnetite formation for a given range of $\delta^{18}O_{H2O}$ values of a fluid. The constraints on the fractionation partition coefficient ($1000\ln\alpha$) limit the possible range of values as $\delta^{18}O_{H2O}$, which must be greater than the $\delta^{18}O_{magnetite}$ with a difference of less than ~10‰. Average oxygen isotope compositions for magnetite in massive magnetite and massive sulphide are used (refer Table 11.3).

Massive magnetite		Massive sulphide		$\Delta_{magnetite-H2O}$	T (°C)
$\delta^{18}O_{magnetite}$ (‰)	$\delta^{18}O_{H2O}$ (‰)	$\delta^{18}O_{magnetite}$ (‰)	$\delta^{18}O_{H2O}$ (‰)	(‰)	
-2.6	-2	2.4	3	-0.6	-43
-2.6	-1	2.4	4	-1.6	-24
-2.6	0	2.4	5	-2.6	-5
-2.6	1	2.4	6	-3.6	15
-2.6	2	2.4	7	-4.6	38
-2.6	3	2.4	8	-5.6	63
-2.6	4	2.4	9	-6.6	91
-2.6	5	2.4	10	-7.6	126
-2.6	6	2.4	11	-8.6	171
-2.6	7	2.4	12	-9.6	271
-2.6	8	2.4	13	-10.6	no solution

6-8‰ for the magnetite stage and 11-13‰ for the sulphide stage. This effectively rules out a seawater dominated fluid source for sulphides ($\delta^{18}O_{H2O}$ ~0‰) as proposed at the Kuroko deposits (Pisutha-Arnond and Ohmoto, 1983), assuming that the composition of modern seawater has prevailed through Earth history.

11.5 Oxygen and hydrogen variation in chlorite

The oxygen and hydrogen isotope variation in chlorite at Gossan Hill is illustrated in Figure 11.2a, with chlorite in sulphide veins (GGF M6) indistinguishable from chlorite alteration in GGF M4. The preservation of primary δD values in phyllosilicate minerals during later geological events is problematic, because oxygen isotopic exchange is common at temperatures above 400°C (Savin and Lee, 1988; Taylor, 1974). The δD and $\delta^{18}O$ values of chlorite at Gossan Hill are close to the expected composition δD and $\delta^{18}O$ values of known metamorphic chlorites (Fig. 11.2b). Isotopic variation from the typical metamorphic chlorite compositions arises from the initial isotopic composition of the chlorite (or its clay precursor) prior to isotope exchange with a metamorphic fluid (Longstaffe, 1989). It is therefore likely that the δD and $\delta^{18}O$ values of chlorite at Gossan Hill were reset during greenschist metamorphism, which is consistent with geothermometry results (Section 11.4; Chapter 4).

11.6 Isotopic variation in carbonate

Oxidised carbon in carbonate can originate from (1) degassing of CO_2-rich magmatic sources, (2) oxidation of organic carbonaceous material or inorganic methane, (3) dissolution of sedimentary carbonate, and (4) dissolution of igneous carbonate (Ohmoto, 1972; 1986; Ohmoto and Rye, 1979). Three types of carbonate are likely at Gossan Hill. These are; (1) primary carbonate associated with the deposition of volcanic and volcaniclastic strata, (2) hydrothermal carbonate associated with massive magnetite, and (3) hydrothermal carbonate associated with massive sulphide. Due to overprinting hydrothermal events, primary carbonate in the host sequence likely exchanged isotopically with hydrothermal fluids and hydrothermal carbonate in massive magnetite may also have re-equilibrated during the later sulphide forming fluids. Furthermore, recrystallisation of all of these carbonates also occurred during metamorphism and their $\delta^{18}O$ values were at least partially reset (Section 11.4).

The carbonates analysed from Gossan Hill are ankerite in composition and their $\delta^{18}O$ and $\delta^{13}C$ variation is given in Figure 11.3a. The ankerite has a relatively narrow $\delta^{18}O$ (7.7 ± 1.2‰) and $\delta^{13}C$ (–3.9 ± 1.1‰) variation suggesting a relatively homogeneous source. Moreover, the isotopic composition of the ankerite is similar in both the massive magnetite and the massive sulphide (Fig 11.3a). A weak positive variation in the $\delta^{13}C$ values of carbonate may result from; (1) carbonate deposition along temperature gradients, (2) mixing between carbonate sources, (3) decarbonation due to metamorphism, and (4) decreasing CO_2/CH_4 ratios (Taylor, 1974; Ohmoto and Rye, 1979; Pisutha-Arnond and Ohmoto, 1983). Each of these aspects is discussed in the following sections.

(a) Variation of oxygen and hydrogen isotopes in chlorite.

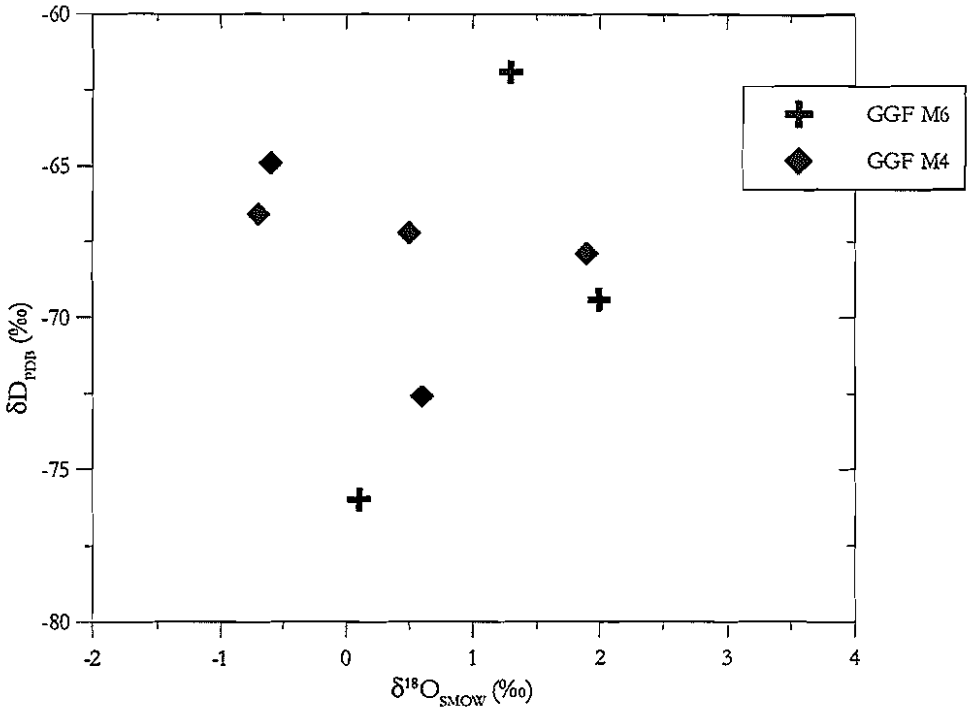

(b) Comparison of the isotopic composition of chlorite, with the known fluid compositions.

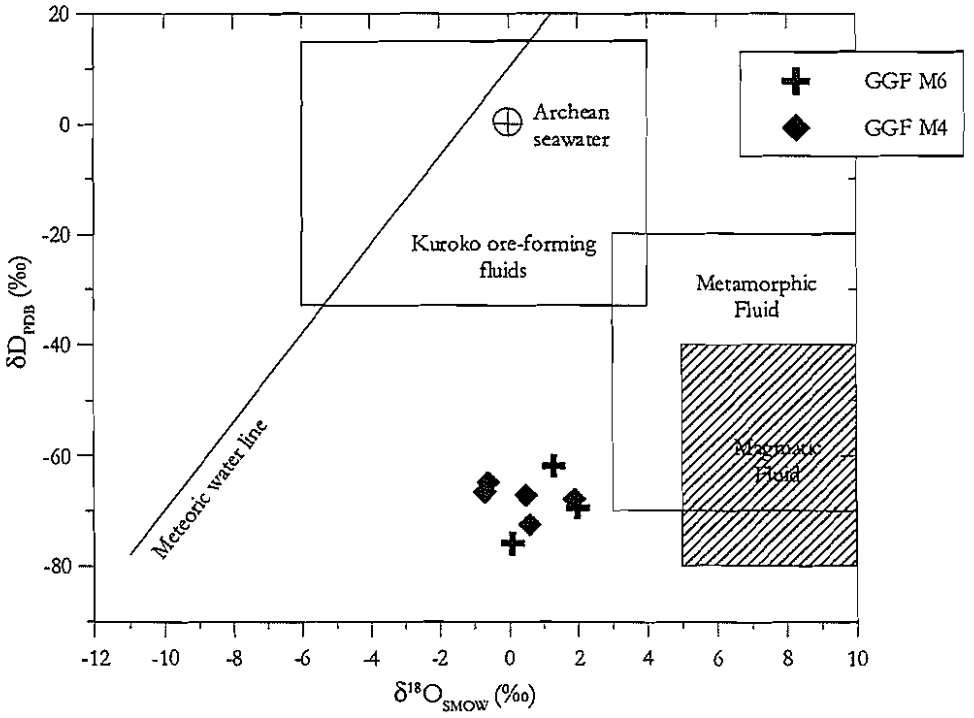

Figure 11.2: (a) Oxygen-hydrogen isotope variation of chlorite at Gossan Hill, and (b) oxygen-hydrogen composition of chlorite relative to the know isotopic composition of meteoric water, Archean seawater, magmatic water and metamorphic water (from Taylor, 1974; Ohmoto, 1986; Sheppard, 1986) and the Kuroko ore-forming fluids (from Pisutha-Arnond and Ohmoto, 1983).

(a) Carbon-oxygen isotopic variation in carbonate.

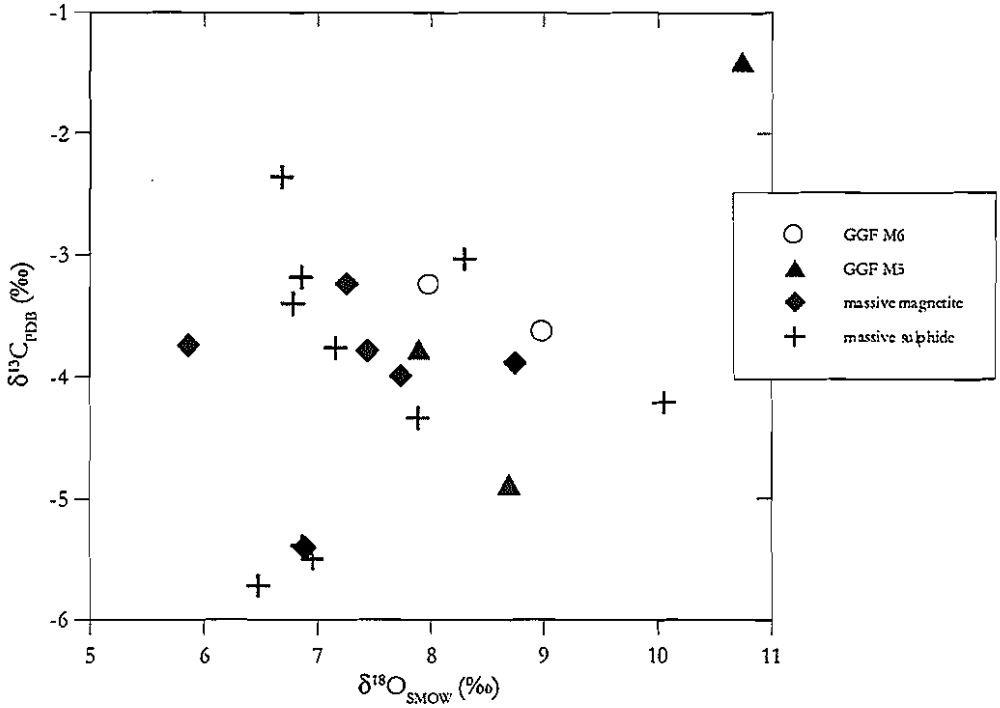

(b) Carbon-oxygen isotope variation at Gossan Hill with known fluid compositions.

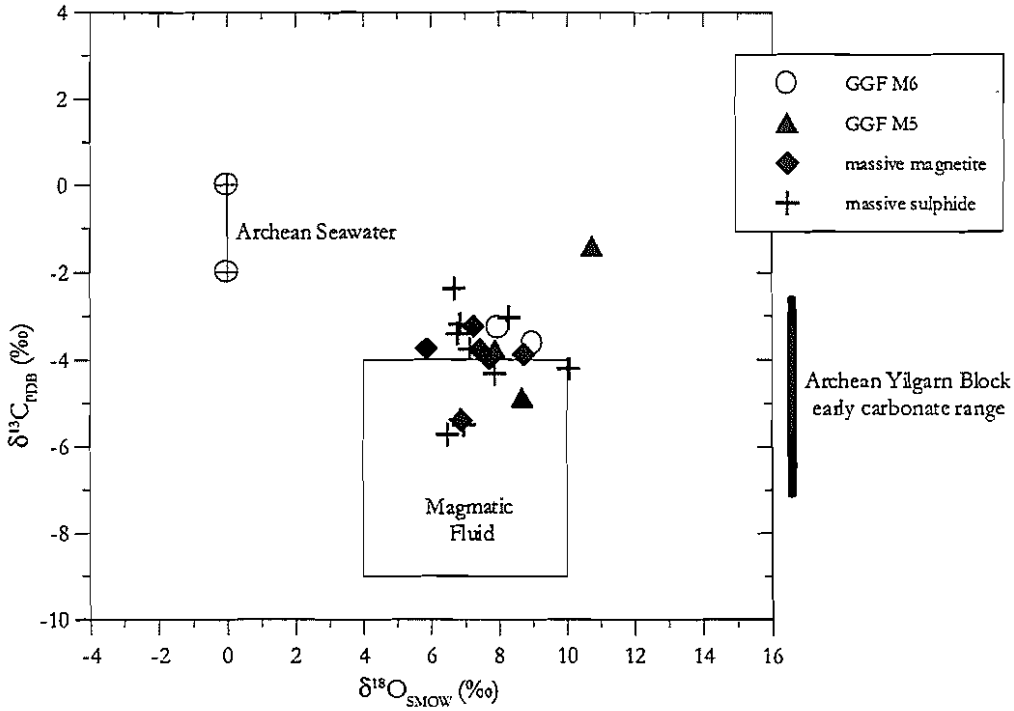

Figure 11.3: (a) Carbon-oxygen isotope composition of carbonate at Gossan Hill, and (b) comparison of carbon-oxygen isotope values at Gossan Hill with magmatic fluids (after Ohmoto and Rye, 1979) and Archean seawater (Viejer, 1990; Schidlowski, 1983). Note: the Gossan Hill data overlaps with the carbon isotope composition of early hydrothermal carbonate in the Archean Yilgarn Block ($\delta^{18}O$ values not supplied) (Grove and Barley, 1987).

11.6.1 VHMS deposits

Irrespective of age, VHMS deposits generally contain carbonates that have a narrow range in $\delta^{13}C$ values between 0 and -5 ‰ (MacLean and Hoy, 1991; Khin Zaw and Large, 1992; Huston, 1997). This $\delta^{13}C$ variation is interpreted to reflect H_2O-rich and CO_2-poor ore fluids consistent with a dissolved bicarbonate seawater source (Ohmoto and Rye, 1979 Pisutha-Arnond and Ohmoto, 1983; Valley, 1986; Huston, 1997). The associated range of $\delta^{18}O$ in carbonates from VHMS deposits is considerably wider (7 to 20‰; Huston, 1997) and typically lighter than that of coeval marine carbonate (25 to 35‰; Taylor and Sheppard, 1986). These observed $\delta^{13}C$ and $\delta^{18}O$ variations in VHMS deposits are interpreted to be primarily temperature induced, with narrower variation of the $\delta^{13}C$ values expected for the temperature range of 100 to 300°C (Ohmoto and Rye, 1979; Huston, 1997). The range in $\delta^{13}C$ and $\delta^{18}O$ values at Gossan Hill is consistent with the reported variation in other VHMS deposits.

11.6.2 Temperature gradients

The temperature dependent fractionation of carbonate can produce increasing $\delta^{13}C$ and $\delta^{18}O$ values due to depositional temperature gradients (O'Neil *et al.*, 1969; Ohmoto and Rye, 1979; Golding and Wilson, 1983). The Rosebery deposit, Tasmania, has a positive correlation between the $\delta^{13}C$ and $\delta^{18}O$ values attributed to decreasing temperatures towards the upper parts of the massive sulphide (Khin Zaw and Large, 1992). Furthermore, the tight cluster of isotope data at Rosebery reflects limited late isotopic overprint despite evidence of high temperature (>300°C) Devonian granite-related metasomatism (Khin Zaw and Large, 1992).

Equilibrium fractionation data for dolomite and ankerite (Ohmoto and Rye, 1979; Fisher and Land, 1986) indicate that the greatest fractionation in $\delta^{13}C$ occurs toward lower temperatures. From these fractionation curves, an absolute change in $\delta^{13}C$ values of ankerite at Gossan Hill of 4.3‰ should correspond to a ~10‰ fractionation in $\delta^{18}O$ values, however the observed variation is only 4.9‰. This data indicates that a single-stage temperature variation model cannot singularly explain the variation in $\delta^{13}C$ and $\delta^{18}O$ values at Gossan Hill.

11.6.3 Isotopic constraints on Archean seawater

The isotopic composition of contemporaneous seawater is important as the ore fluids in VHMS deposits are thought to be dominated by modified contemporaneous seawater, having a modified seawater isotopic signature (*e.g.*, Pisutha-Arnond and Ohmoto, 1983; Ohmoto, 1996; Huston, 1997). Barley and Groves (1987) consider VHMS deposits in the Archean Yilgarn to be seawater-derived, with a lesser component derived from the leaching of carbonate in volcanics. The $\delta^{18}O$ values of Archean seawater have remained unchanged to the present-day, having a composition of ~0‰ (Schidlowski *et al.*, 1983; Veizer *et al.*, 1990). The estimated $\delta^{13}C$ composition is also thought to have been ~0‰, although it is also argued that the $\delta^{13}C$ composition of Archean seawater varied to lighter compositions (-2 to -5‰) due to stratified basinal waters (Spooner *et al.*, 1974; Veizer, 1985; Beukes *et al.*, 1990). This range of $\delta^{13}C$ values for Archean seawater (0 to -5‰)

means that carbonates at Gossan Hill may have had $\delta^{13}C$ compositions similar to their contemporaneous seawater, whereas $\delta^{18}O$ values at Gossan Hill were heavier than modern seawater.

11.6.4 Archean Au deposits

Carbonate isotope systematics of many Archean Au deposits in Western Australia (*e.g.*, Golding *et al.*, 1988; 1990) and the Canadian Archean (*e.g.*, Kontak *et al.*, 1988) have similar ranges in $\delta^{13}C$ values to those observed at Gossan Hill. Two major sources of carbon and oxygen in Archean Au deposit carbonates are considered likely. These are (1) derivation from a mantle or granitic source, and (2) from decarbonation or dissolution of carbonates and silicates during metamorphism (Golding *et al.*, 1988).

In Archean systems, low temperature seafloor alteration produces carbonate with $\delta^{13}C$ values close to the inferred value of Archean seawater (0 to -2‰) (Donnelly *et al.*, 1977; Golding *et al.*, 1988; Barley and Groves, 1987). Fault controlled regional alteration associated with carbonate formation, has carbonate with $\delta^{13}C$ values between -2.0 and -6.0‰ and these carbonates are isotopically similar to carbonate associated with Au mineralisation in the Yilgarn, Western Australia (Donnelly *et al.*, 1977; Golding *et al.*, 1988; 1990; McNaughton *et al.*, 1990). A magmatic derivation for fault-controlled and Au-related carbonate is the favoured model, due to the absence of coupled $\delta^{13}C$ and $\delta^{18}O$ depletion indicative of partial metamorphic decarbonation (Ohmoto and Rye, 1979; Valley, 1986; Golding *et al.*, 1988; Kerrich, 1990). Nonetheless, CO_2 contribution by metamorphic fluids cannot be ruled out because high temperature dissolution can produce CO_2 that is isotopically similar to the original carbonate (Ohmoto and Rye, 1979; Kerrich, 1987).

11.6.5 Organic contributions–examples from Archean BIF deposits

The $\delta^{13}C$ values of carbonates at Gossan Hill do not support a major oxidised carbon contribution from organic carbonaceous material, or the dominance of CH_4 in the system (*c.f.*, Ohmoto and Rye, 1979; Strauss, 1986; Karhu *et al.*, 1993). Organic dervied carbon sources generally result in carbonates with very light $\delta^{13}C$ values as observed in some Archean Au deposits (Hattu schist belt, Finland in Karhu *et al.*, 1993) and Archean BIF (*e.g.*, Sherman, Ontario in Bowins and Crocket, 1994; Canadian Shield in Thode and Goodwin, 1983).

In the Yilgarn Block, the $\delta^{13}C$ of kerogen has values ranging from -46 to -15‰ (Donnelly *et al.*, 1977; McNaughton *et al.*, 1990;), which is typical of maturated organic detritus from sedimentary rocks of all ages (Ohmoto and Rye, 1979). The mixing of oxidised carbonate from an organic carbonaceous source with an inorganic oxidised carbon source (seawater) can lead to variation in $\delta^{13}C$ values between the two end member $\delta^{13}C$ compositions. This phenomenon is interpreted to have occurred in sulphidic sediments from the Canadian Shield (Strauss, 1986) and in the Temagami Archean BIF, Ontario, evidenced by a wide variation of carbonate $\delta^{13}C$ values (Bowins and Crocket, 1994). In these occurrences, bacterial processes were active in the reducing environment, giving rise to carbonate isotopic compositions distinctly lighter than the inferred value of Archean seawater

(Schidlowski *et al.*, 1983; Veizer *et al.*, 1990). Accompanying evidence for a carbonaceous contribution occurs as graphitic sediments (Bowins and Crocket, 1984; Strauss, 1986;). At Gossan Hill, the narrow range of $\delta^{13}C$ values is inconsistent with derivation from an oxidised carbonaceous source which is supported by the absence of graphitic sediments in the volcaniclastic strata.

11.6.6 Metamorphic effects

Complete metamorphic homogenisation results in isotopically similar isotope signatures between mineral phases (Valley, 1986). Complete metamorphic homogenisation is not observed at Gossan Hill due to variations in the $\delta^{18}O$ composition between carbonate, chlorite and magnetite. Coupled depletion in $\delta^{18}O$ and $\delta^{13}C$ occurs in partial metamorphic decarbonation (Sheppard and Schwartz, 1970; Taylor 1979; Valley, 1986). Due to the absence of a positive correlation between $\delta^{18}O$ and $\delta^{13}C$ values in carbonates at Gossan Hill (Fig. 11.3a), this process probably did not occur at Gossan Hill. Hydrothermal carbonates typically retain their $\delta^{13}C$ values (Ohmoto and Rye, 1979), whereas changes of $\delta^{18}O$ in carbonate to lower values are common due to their susceptibility to oxygen isotope exchange (O'Neil, 1987).

11.6.7 Discussion

The isotopic evolution of carbonate minerals at Gossan Hill is complex due to multiple hydrothermal events and a metamorphic event. It is unlikely that the current carbonate isotopic compositions are entirely primary, but are now hydrothermally or metamorphically modified values. The $\delta^{18}O$ isotopes of ankerites reflect modified values due to equilibration with a metamorphic fluid (Section 11.4).

The $\delta^{13}C$ values at Gossan Hill are similar to values reported in early Archean carbonates in the Yilgarn Block (Barley and Groves, 1987; Fig. 11.3b). This range in $\delta^{15}C$ values also overlaps with the composition of typical magmatic fluids (Fig. 11.3b), possibly indicating a magmatic contribution to the hydrothermal events. Although a contribution from an oxidised carbonaceous source cannot be ruled out, it is considered unlikely due to the narrow variation in $\delta^{13}C$ values at Gossan Hill and the absence of carbonaceous sediments in the volcanic strata. The $\delta^{13}C$ values at Gossan Hill do not constrain the source of carbon in ore fluids or differentiate the fluid responsible for its formation.

11.7 Summary

- The oxygen isotope composition of magnetite varies from 3.9 to -3.7 ‰ (average of 0.5 ‰) with lighter isotope values in massive magnetite compared to magnetite in massive sulphide.
- Oxygen and hydrogen isotopes of chlorite have a narrow variation from $\delta^{18}O$ of -0.7 to 2 ‰ and δD of -61.0 to -76.0 ‰ and are consistent with metamorphic fluid equilibration.
- Oxygen isotope geothermometry between co-existing carbonate and chlorite pairs yield geologically unreasonable formation temperatures, consistent with isotopic resetting during metamorphism.

- Oxygen isotope magnetite geothermometry suggests that the composition of magnetite was unchanged during metamorphism. The systematics of magnetite fractionation constrain the $\delta^{18}O_{H2O}$ compositions of the formation fluid from 6 to 13‰ for magnetite and sulphide fluids. These values are inconsistent with the inferred $\delta^{18}O_{H2O}$ composition of seawater, but are consistent with direct input from a rock-buffered fluid or a direct magmatic contribution.
- Carbonate oxygen-carbon isotope values at Gossan Hill vary from 5.9 to 10.7‰ and -1.4 to -5.7‰ respectively. The oxygen isotope values of carbonate were reset during metamorphism, while the carbon isotope values are probably unchanged. The variation of $\delta^{13}C$ values at Gossan Hill is typical for early Archean carbonate in the Yilgarn Block, but does not define a fluid source.

Chapter 12

The genesis of the Gossan Hill deposit

12.1 Introduction

Gossan Hill is one of the largest economic Archean Cu-Zn VHMS deposits in Australia. Despite its classification as a VHMS deposit, Gossan Hill has many differences when compared to typical VHMS models. Nonetheless, Gossan Hill has similarities to some Canadian Archean VHMS deposits (*c.f.* Sangster, 1972; Franklin *et al.*, 1981; Large, 1992) and therefore, comparison with these deposits is useful to constrain the processes and chemical conditions which led to ore genesis. This chapter synthesises the geological constraints on ore formation at the Gossan Hill deposit and presents a genetic model. This genetic model also accounts for the geological differences between the Gossan Hill and the nearby Scuddles deposit. Diagnostic geological criteria developed in this study at Gossan Hill facilitate exploration vectors to the recognition of similar resources elsewhere in the Golden Grove Domain, with potential application to other areas of the Yilgarn Craton.

12.1.1 VHMS deposits: Definition, classifications and styles

VHMS deposits, defined as stratabound to stratiform massive sulphides overlying a zone of discordant sulphide veining within hydrothermally altered rock (Franklin *et al.*, 1981; Lydon, 1988; Franklin, 1993), represent the accumulation of sulphides precipitated in a subaqueous environment from hydrothermal solutions at or near the seafloor (Lydon, 1984). Stringer veins and stockwork mineralisation represent near seafloor channel ways of the hydrothermal system (Lydon, 1984; 1988). Several classification schemes are used including; volcanic host-rock lithology (Sangster and Scott, 1976; Morton and Franklin, 1987), host rock composition (Barrie and Hannington, 1997) and tectonic setting (Sawkins, 1976; Zlotnik-Khotkevitch, 1993), deposit morphology (Large, 1992), alteration mineral assemblages (Sillitoe *et al.*, 1996) and metal contents (Solomon, 1976; Franklin *et al.*, 1981; Large, 1992). In particular, the non-genetic metal content classification of Solomon (1976) distinguishes the Cu-Zn-rich nature of Archean VHMS deposits from Phanerozoic VHMS deposits that are typically Zn-Pb-Cu- or Cu-rich (Sangster, 1972; Sangster and Scott, 1976; Franklin *et al.*, 1981).

The characteristics and variation of VHMS deposit styles are diverse and have been summarised by Large (1992), Franklin *et al.* (1981), Sangster (1972), Ohmoto (1996) and Lydon (1984; 1988). The major styles of VHMS deposits in Australia are summarised in

Figure 12.1. This diversity in style (Fig. 12.1) reflects many deposit-scale variables such as (1) lithology, (2) permeability and geochemical contrasts, (3) the nature of mineralising conduits, (4) the degree of hydrothermal fluid-rock interaction, and (5) the chemistry of ore fluids and coeval seawater. All these factors contribute to variations in the morphology, the distribution and nature of hydrothermal alteration within a single deposit (*e.g.*, Morton and Franklin, 1987).

Mound-type deposits (*e.g.*, Hellyer, Gemmell and Large, 1992; Kuroko deposits, Ohmoto *et al.*, 1983; Ohmoto, 1996; Noranda deposits, Morton and Franklin, 1987) are mound-shaped stratiform massive sulphide zones overlying a central feeder (Figs. 12.1a and 12.2). The Cu-rich base and the feeder zone represent the hottest parts of the mineralising system, with mineral and metal zonation reflecting fluid cooling gradients caused by their interaction with seawater (Ohmoto *et al.*, 1983). Narrow feeder zones below mound deposits form as structurally focussed vent zones due to fluid constrainment by the relative impermeability of coherent volcanic footwall lithologies (*e.g.*, Eldridge *et al.*, 1983; Gemmell and Large, 1992). The growth of mound deposits, as illustrated in Figure 12.2, is *via* progressive construction during cyclic waxing and waning periods of sulphide deposition, associated with gradual upward and outward increases in temperature and zone refining processes (Ohmoto *et al.*, 1983; Lydon, 1988; Large, 1992).

Sheet-type deposits (*e.g.*, Rosebery, Green *et al.*, 1981; Huston, 1988; Thalanga, Hill, 1996; Mattabi, Franklin *et al.*, 1981) have sheet-like massive sulphide lenses that typically overly broad alteration and feeder zones (Fig. 12.1d). Their morphology is likely due to fragmental footwall lithologies (Morton and Franklin, 1987). Wide footwall alteration zones that lack sharp mineralogical boundaries result principally from ore fluids that are poorly focussed through the relatively permeable footwall lithology (Morton and Franklin, 1987). Moreover, episodes of massive sulphide deposition interrupted by strata building events tend to form stacked deposits (Fig. 12.1g) such as Que River, Tasmania (Fig. 12.1g), Waterloo and Agincourt, Queensland (Huston *et al.*, 1995a) and Millenbach, Canada (Sangster, 1972 Knuckey *et al.*, 1982a). Stacked deposits have stratigraphically separate lenses of massive sulphide that are interconnected by stringer veining. In most cases, the lower lenses of stacked deposits tend to be Cu-rich due to zone refining and hydrothermal overprint (Large *et al.*, 1988).

According to the examples above, the Gossan Hill deposit is hybrid between the end member mound, sheet and stacked deposit styles. The upper ore zone of Gossan Hill has affinities that resemble the mound style. This is due to the presence of discordant massive pyrite underlain by a tightly constrained feeder zone. In addition, the upper ore zone is also transitional upwards to sheet-like massive sphalerite (Chapter 5). The sheet-like development of massive sphalerite at Gossan Hill is consistent with its fragmental footwall lithology, however, the distribution of related hydrothermal alteration is constrained to the feeder and thereby, dissimilar to the Mattabi-classification of Morton and Franklin (1987). Furthermore, the stratigraphic separation of the Zn-Cu and Cu-rich ore zones at Gossan Hill could be interpreted as a stacked mineralising system.

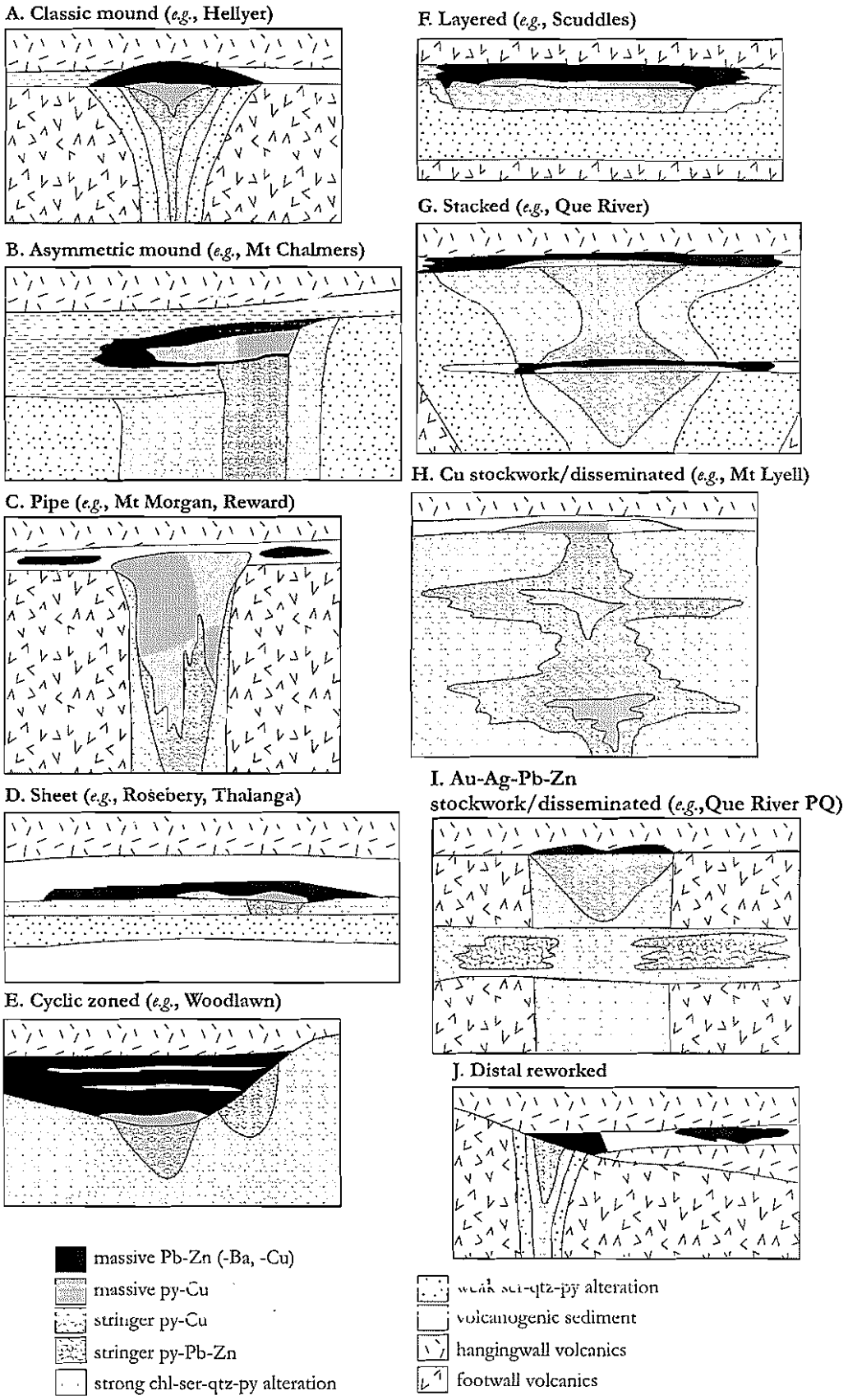

Figure 12.1: Schematic representation of the ten major styles of VHMS deposits in Australia (from Large, 1992).

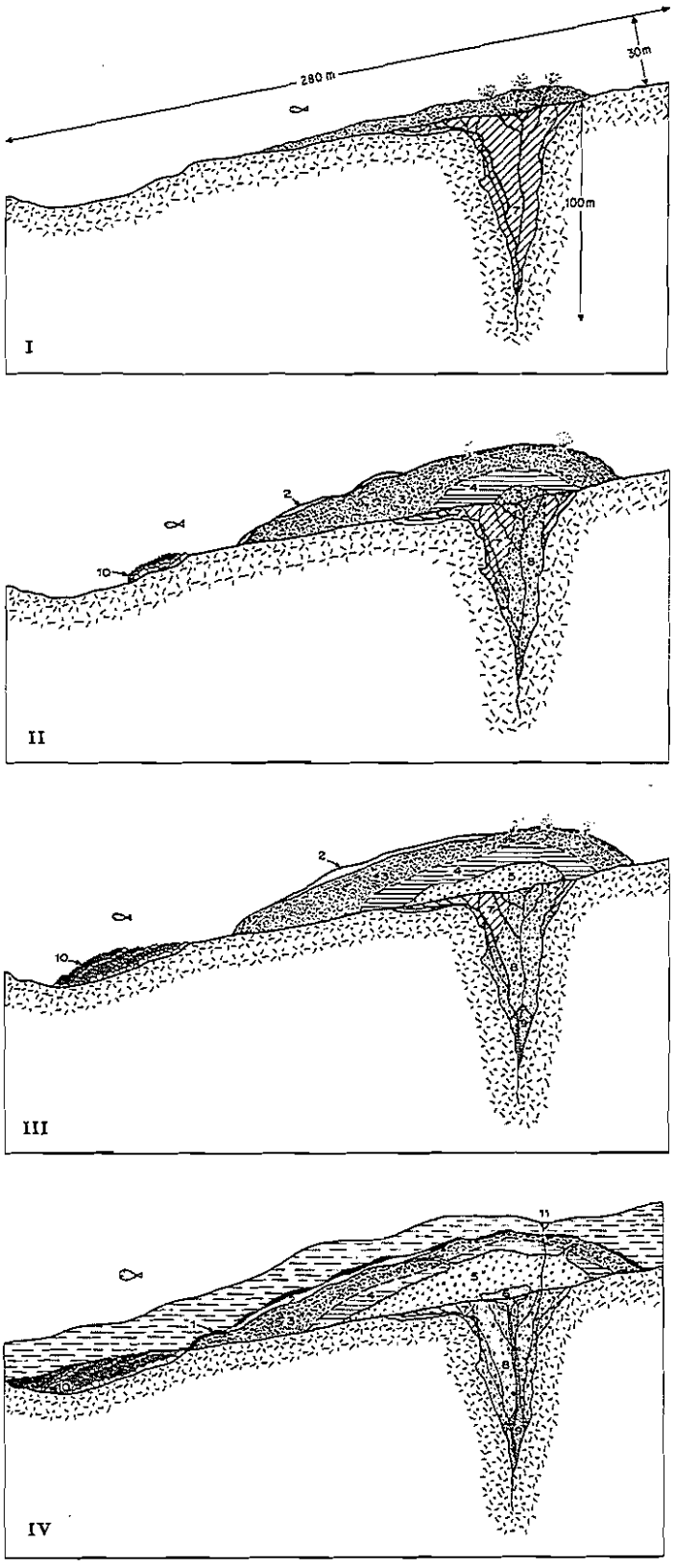

Figure 12.2: Diagram illustrating the development of an ideal Kuroko orebody from Eldridge *et al.* (1983). 1. tetsusekiei or chert-hematite layer, 2. barite ore, 3. massive black ore (sp+py+ga+ba), 4. massive semi-black ore (sp+py+cpy), 5. massive cpy+py, 6. massive pyrite, 7. massive sp+py+ga+qz, 8. siliceous yellow ore (cpy+py+qz), 9. py+qz, 10. transported fragmental ore, 11. late stage sulphide veins.

12.1.2 Differences between Archean and Phanerozoic VHMS deposits

Magnetite and hematite are common non-sulphide metallic minerals in VHMS deposits (Lydon, 1984). However, many Phanerozoic deposits lack magnetite and hematite, or these minerals form minor constituents of ore (*e.g.*, Hellyer in McArthur, 1996; Rosebery in Green *et al.*, 1981 and Waterloo and Agincourt in Huston *et al.*, 1995a). In contrast, many Late Archean deposits have magnetite as a major constituent of ore, whereas hematite is absent (*e.g.*, Mattabi, Franklin *et al.*, 1975; Mattagami, Roberts, 1975; Orchan, Large, 1977; Millenbach, Knuckey *et al.*, 1982a; Corbet, Knuckey and Watkins, 1982b; Scuddles, Mill *et al.*, 1990b; Ansil, Galley *et al.*, 1995). In these Archean deposits, magnetite and pyrrhotite are typically concentrated at the base of the ore within massive sulphide and underlying stringer veins (Large, 1977; Franklin, 1993). In the Canadian Archean VHMS deposits, few constraints on the origin and timing of magnetite are provided in the literature. At the Ansil deposit, the timing of magnetite is contentious and is postulated as a late post-sulphide hydrothermal stage (Galley *et al.*, 1995). In this case, the formation of magnetite is part of a calc-silicate skarn alteration overprint below the orebody that replaced significant volumes of sulphide (~0,3 Mt) (Galley *et al.*, 1995). Although Barrett *et al.* (1991) also favour magnetite replacement processes at the Ansil deposit, they suggest that some magnetite also formed during sulphide mineralisation because Cu-rich zones cut magnetite-rich zones.

Despite mineralogical differences between Archean and Phanerozoic VHMS deposits, Ohmoto (1996) argues that the formation of these deposits throughout geological time has involved similar geological processes. The Cu-Zn Archean deposits are also characterised by low Pb contents, which is attributed to the low Pb contents of underlying volcanics (Lambert and Groves, 1981). However, the lack of sulphate, together with the abundant magnetite, pyrrhotite and Fe-rich chlorite alteration in Archean VHMS ores can partially be explained by chemical variations in the Archean environment (Large, 1977; Ohmoto, 1996) (Section 12.3).

12.2 The Gossan Hill deposit

Massive sulphide at the Gossan Hill deposit is syngenetic with the deposition of the host Golden Grove Formation (GGF). Geologic evidence supports the genesis of Gossan Hill from multiple hydrothermal-mineralising stages in an evolving system. This system had a strong stratigraphic, structural and geochemical control on the distribution and localisation of alteration, massive magnetite and massive sulphide.

12.2.1 Depositional environment

The Golden Grove Domain consists of a layered, laterally continuous (28 km) stratigraphic succession of calcalkaline volcanics and tholeiitic basalt sequences. The Gossan Hill deposit occurs within the GGF of the Gossan Hill Group, which is dated at ~3.0 Ga (Wang *et al.*, 1998). The six members of the GGF (M1 to M6) consist of rhyodacitic, massive to bedded, quartz-poor to quartz-rich, tuffaceous volcaniclastics with lesser bedded epiclastics. Only four members of the GGF occur at Gossan Hill (GGF M1, GGF M4, GGF M5 and GGF M6; Fig. 12.3) and the total thickness of the

strata approximates 500 m (Fig. 12.3). At Gossan Hill, massive and vein sulphide spans the stratigraphic interval from the middle of the GGF (M4) to the top (M6) of the succession (Fig. 12.3).

Tuffaceous facies in the GGF (GGF M1, M4, M5 and part of M6) represent re-deposited pyroclastic products emplaced *via* successive episodes of high-density turbidite mass flows (Clifford, 1992; Fig. 12.4). Tuffaceous facies consist of altered pumice lithics, shards and volcanic quartz detritus. The absence of feldspar and devitrification, diagenetic compaction and welding textures, indicate that the tuffaceous detritus was glassy and cold at the time of emplacement. Bedding and normal grading support the deposition of tuffaceous strata from water saturated mass flows in a deep submarine environment. Epiclastic strata (GGF M2 and part of M6) consists mostly of polymict sandstone, siltstone and breccia, but also contain interbedded tuffaceous sandstone and siltstone. Interbedded tuffaceous units result from the suspension settling of fine-grained tuffaceous material during deposition. These sediments therefore, reflect background epiclastic sedimentation occurring between tuffaceous sedimentation. The increased abundance of epiclastic facies towards the top of the GGF, records the waning of tuffaceous deposition, whilst the absence of GGF M2 and GGF M3 at Gossan Hill (Fig. 12.3) reflect a depositional hiatus. Syngenetic sulphide within the volcaniclastic sequence at Gossan Hill indicates that the mineralisation formed during sedimentation, in the absence of proximal volcanism.

The coherent massive lavas and domes present in the hangingwall Scuddles Formation (SCF) represent the onset of regionally extensive proximal volcanism, after deposition of the GGF. Regionally extensive sheet flows in the SCF are characterised at Gossan Hill by the rhyodacite member (SCF M2; RD2). The upper parts of the SCF reflect a transition to localised dome volcanism. At Gossan Hill an intrusive-extrusive dacite dome (DAC3) intrudes the GGF. The volcanic feeder zone of this dacite dome is interpreted to occupy the site of a former synvolcanic structure.

12.2.2 Deformation and metamorphism

Elements of D1 and D2 regional deformation are not observed at Gossan Hill. The earliest recognised deformation event at Gossan Hill is D3. D3 is developed as a north-south penetrative fabric (S3) that is associated with regional scale folding and minor faulting. Faults developed during D3 were reactivated during D4. These faults have minor displacement (metres) and contemporaneous quartz-chlorite-carbonate brittle veins. The timing of D3 and D4 post-dates massive sulphide, massive magnetite and hydrothermal alteration. This relationship is evidenced by:

(1) A ubiquitous S3 cleavage throughout massive magnetite and massive pyrite. S3 results in brittle deformation cracking patterns and the infill of fractures by carbonate, chlorite and sulphide.

(2) A penetrative S3 cleavage weakly developed in siliceous alteration and intensely developed in chlorite altered wall rock. In the later boudinage and necking structures, as well as axial planar cleavage folding of sulphide veins are common.

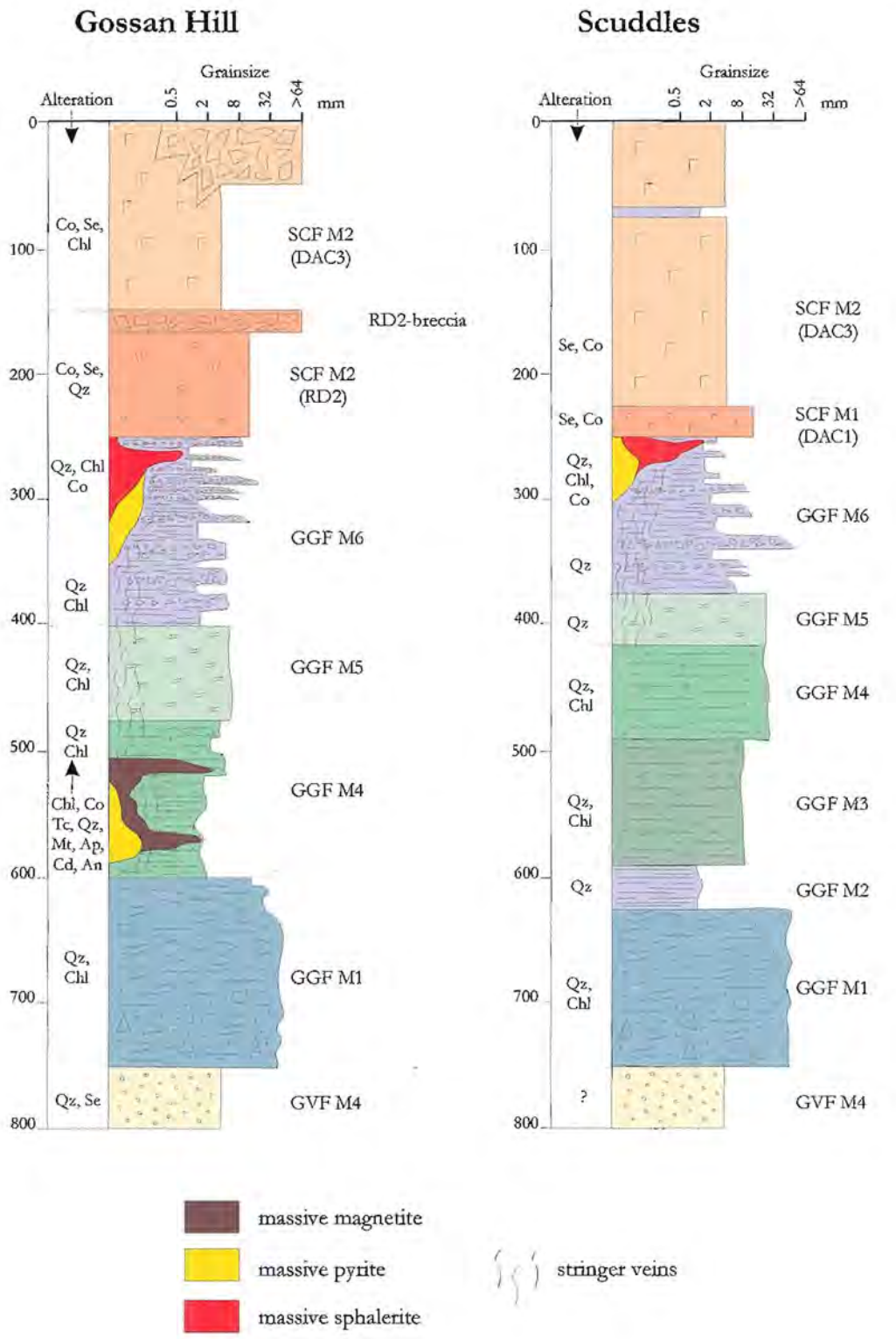

Figure 12.3: Stratigraphy and facies variation of the Golden Grove Formation (GGF) at the Gossan Hill and Scuddles deposits. Note thickness variations of each member of the GGF between the two deposits (*e.g.*, GGF M4 and GGF M5). Note also that GGF M2 and GGF M3 are present at Scuddles, but generally absent from strata at Gossan Hill. The main alteration minerals are listed to the left of each graphic log. Vertical scale represents true thickness in metres. Abbreviations: Co = carbonate, Se = muscovite, Qz = quartz, Chl = chlorite, Tc = talc, Mt = magnetite, Ap = apatite, Cd = chloritoid, An = andalusite, GGF = Golden Grove Formation, GVF = Gossan Valley Formation, SCF = Scuddles Formation.

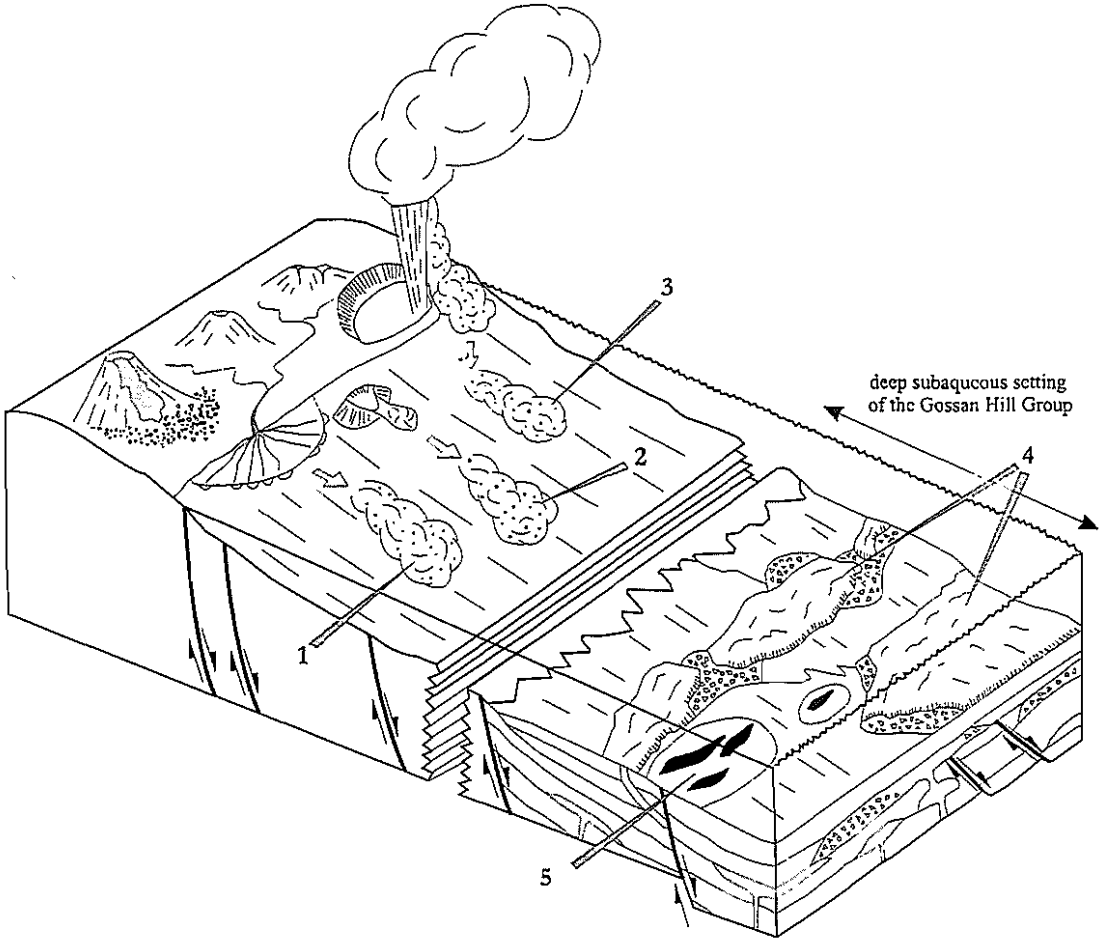

Figure 12.4: Schematic representation of the depositional setting of the Gossan Hill Group (from Clifford, 1992). The numbers indicate the emplacement of stratigraphic components occurred by:

1 subaqueous mass-flow of tuffaceous sediments derived from a variably eroded andesitic volcanic terrain;

2 subaqueous mass-flow of sediments derived from rapidly degraded shallow marine silicic tuff ring/cone;

3 subaqueous mass-flow of sediments derived from the flow transformation of silicic pyroclastic flows;

4 subaqueous effusive volcanism producing lavas and associated autoclastic facies and

5 chemical facies (massive sulphide/massive magnetite) precipitated from concentrated hydrothermal discharge focused by syndepositional structures.

(3) Faulting and quartz-carbonate-chlorite veining in wall rocks, massive sulphide and massive magnetite.

Peak metamorphism (up to greenschist facies) occurred synchronous to or post-D4 and overprints S3 and D4 faults. This metamorphism led to extensive recrystallisation of chlorite, carbonate, talc and sulphide minerals. At Gossan Hill, the typical metamorphic mineral assemblage consists of quartz, chlorite, carbonate and muscovite, with minor chloritoid, andalusite, talc, epidote, rutile and ilmenite. As the metamorphic and hydrothermal mineral assemblages are similar, metamorphism did not cause major chemical changes. The minor occurrence of muscovite and the absence of biotite throughout the GGF at Gossan Hill indicates that the metamorphic reactions were governed by pre-existing alteration assemblages. The absence of biotite at Gossan Hill likely reflects early and widespread alkali depletion of the GGF. Andalusite-chloritoid-chlorite-quartz metamorphic assemblages developed in some parts of the strata due to the low alkali and high Al_2O_3 contents of the wall rocks. Equilibrium between andalusite, chloritoid, chlorite and quartz yield a peak metamorphic temperature estimate of 454 ± 4°C at 1 kbar (Chapter 4).

12.2.3 Synvolcanic structural control on the siting of mineralisation

The lateral continuity and thickness variations of the GGF members favour the presence of a synvolcanic growth fault. This growth fault led to differential subsidence. Several lines of evidence support the presence of a synvolcanic structure at Gossan Hill.

(1) Thickness variations (10's metres) in GGF M6 and the breccia facies of RD2.

(2) A change in slope of the GGF M1-M4 contact surface, reflecting synvolcanic activity prior to deposition of GGF M4.

(3) Asymmetry of the massive magnetite and massive sulphide zones. Thickest development of each occurs adjacent to the south side of the structure and reflects the location of the hydrothermal feeder in a structural low.

(4) Minor mineralisation north of the growth structure reflecting a structural high.

(5) Asymmetry of the stringer stockwork and hydrothermal alteration envelop connecting the upper and lower ore zones.

(6) Metal zonation from a Cu-Fe (Au) base upwards towards a Zn-Cu top. This trend defines the hydrothermal feeder zone and the hottest part of the system on the south side of the structure.

(7) The presence of a volcanic feeder to a dacite dome, which occupies the synvolcanic structure.

At Gossan Hill, hydrothermal fluids forming both magnetite and sulphides were structurally focussed along the same conduit. As indicated by the slope change in the GGF M1-M4 contact surface, the initiation of this focussing structure took place at the onset of GGF M4. The constant thickness of GGF M5, but thickness variation of GGF M6 indicates that structural reactivation took place during the deposition of GGF M6.

An early set of quartz veins in GGF M4 are paralleled and overprinted by sulphide stringer veins. This relationship indicates that the indurated host underwent brittle fracturing during synvolcanic structural activity. The synvolcanic structure was also used as a volcanic feeder for proximal dacite volcanism, as denoted by the intrusion of dacite along the structure. The orientation of the dacite feeder (as well as the Cu-Fe±Au enrichment beside it), indicates that the structure plunges 65° north. Synvolcanic structural control is also observed at the Scuddles deposit (Chapter 4). At Scuddles, massive sulphides are located north of its feeder zone, but the dacite has a similar orientation, which support a rotational movement along these structures (Chapter 4).

12.2.4 Replacement *versus* seafloor deposition

It is widely accepted that VHMS deposits form by both seafloor exhalative processes and sub-seafloor replacement processes (*e.g.*, Eldridge *et al.*, 1983; Lydon, 1988; Humphris *et al.*, 1995). For example, Barton (1978) and Ohmoto *et al.* (1983) interpreted the Kuroko deposits to have formed from cyclic systems, with waxing and waning periods associated with exhalation and replacement. Similar observations are also made in modern seafloor sulphide deposits (*e.g.*, Gallinatti, 1984; Humphris *et al.*, 1995). Replacement is genetically related to the formation of syngenetic mineralisation and occurs in the substrate below and within previously exhaled sulphides. The distinction between exhalative and replacement mineralisation is therefore highly contentious.

Lithofacies provide the best criteria by which replacement and exhalation processes can be distinguished. Replacement processes may be inferred from, (1) the presence of relict grains, clasts and relict strata within sulphides, (2) the impregnation of a lithology by sulphides, (3) the discordance of sulphides to lithofacies, and (4) gradational contacts. Criteria for exhalative sulphide can include, (1) sulphide breccia ore facies, (2) sulphide clasts in overlying units, (3) chimney fragments, (4) hydrothermal chert or chert-iron facies (*e.g.*, Doyle, 1997; Hill, 1996; Peter and Goodfellow, 1996; Kalogeropoulous and Scott, 1983), (5) open space primary sulphide textures (Eldridge *et al.*, 1983), and (6) bedded sulphide facies.

At Gossan Hill, evidence supporting the exhalative deposition of massive sulphides is manifested as clasts of massive sulphide in wall rock breccia facies. Sulphide clast-bearing breccia facies occur at the base of GGF M4 and at the base of the hangingwall rhyodacite. The stratigraphic contexts of these breccia facies indicate that there were multiple phases of seafloor sulphide deposition. These phases were separated by significant intervals of sedimentation. Nonetheless, massive sulphide at Gossan Hill, lack mineral banding and breccia ore which typify exhalative massive sulphides deposits (*e.g.*, Ohmoto *et al.*, 1983). In addition, conformable chert beds within the M1 Marker were formed as exhalative hydrothermal precipitates and occur throughout GGF M6. The number of these chert beds indicates multiple seafloor positions during GGF M6 deposition. Preservation by burial is likely a result of continued sedimentation during hydrothermal activity.

Despite limited evidence for exhalation, there is widespread evidence for the replacement

origin of the massive sulphide and massive magnetite at Gossan Hill (Chapter 5). This is evidenced by (1) gradational hangingwall contacts for massive magnetite and sulphide, (2) sulphide veining in sediment overlying massive sulphide, and (3) large rafts or bedded intervals of altered unmineralised wall rock within the massive sulphide and magnetite. Partial replacement of sandstone and polymict breccia by sulphides is also observed in GGF M6 and indicates that sulphide replacement occurred preferentially along more permeable horizons in the strata. Widespread replacement of lithological units is also supported by textural evidence such as common radial nucleation structures in pyrite. Furthermore, the wide distribution of stringer veins throughout the feeder and upper and lower ore zones indicate that a large part of sulphide mineralisation formed by fracture and fill processes. Although evidence exists to support ore formation at Gossan Hill by both exhalation and replacement processes, the dominant mechanism for ore formation was sub-seafloor replacement.

12.2.5 The role of sedimentation

Studies of the sediment filled axial valley on the Juan de Fuca Ridge conclude that rapid sedimentation can be conducive to the formation of large hydrothermal mineral deposits (Davis *et al.*, 1987). Furthermore, sulphide deposition concurrent with sedimentation is manifested by the presence of highly altered sediment layers in sulphide (Davis *et al.*, 1987; Krasnov, 1994). In both cases, sediment cover thermally insulates the underlying strata by reducing the extent of conductive heat loss. Sediment insulation inhibits groundwater recharge and promotes long-lived hydrothermal discharge (Davis *et al.*, 1987). The low permeability of sediments may also prevent heat loss through widespread ventilated groundwater convection. In this case, sulphide precipitation is promoted by the mixing of ambient pore water in the sediments (Davis *et al.*, 1987). The substrate created in this process is efficient for the sub-surface precipitation of minerals, whilst synchronous sedimentation protects hydrothermal deposits from the corrosive effects of seawater (Davis *et al.*, 1987).

Pervasive hydrothermal circulation during volcaniclastic sedimentation is also documented in the magnetite-rich ferruginous jasper horizons of the Bleida basin of Morocco (Leblanc and Billaud, 1990). This long-lived Fe-rich hydrothermal system has formed multiple mineralised horizons due to burial by ongoing turbidite sedimentation. Pulses of hydrothermal activity are also accelerated by subsidence induced hydrothermal flow due to sediment dewatering (LeBlanc and Billaud, 1990). Studies of modern hydrothermal systems have shown the effect of sediment cover on the active vent sites as defocusing mechanisms to hydrothermal fluids in addition to promoting silica precipitation (Tivey and Delaney, 1986). Furthermore, constraining hydrothermal fluid escape by a low-permeability crust such as sediments, may lead to increased fluid circulation within the mound, that results in an upward migration of isotherms and the replacement of previous precipitates by higher temperature mineral assemblages (Lydon, 1988).

The environment of ore formation at Gossan Hill can be correlated with low volume

turbidite and suspension settling that led to the deposition of GGF M6. This sedimentation reflects background sedimentation that followed a period of high volume, mass flow emplacement of GGF M1 to GGF M5. The continuity of successive sedimentation events depositing GGF M1 to GGF M5 is inferred from their relatively homogeneous geochemistry. Low volume epiclastic sedimentation of GGF M6 was simultaneous with the formation of massive sulphide. This conclusion is supported by (1) evidence of sulphide replacement, (2) soft sediment deformation between veins and strata, and (3) by the occurrence of unmineralised beds or bedded intervals within massive sulphide. Ongoing sedimentation and a changing seafloor position during sulphide accumulation led to the diffusion and lateral focus of hydrothermal fluids through the strata, which promoted sulphide deposition by replacement processes.

12.2.6 Timing and formation of massive magnetite

Massive magnetite at Gossan Hill occurs as two continuous, sheet-like stratabound zones that discordantly interfinger adjacent to their synvolcanic feeder. Massive magnetite within GGF M4 was formed by selective replacement of strata. Widespread evidence of replacement is manifested as complex, interdigitating, gradational upper and lower contacts between massive magnetite and wall rocks, with massive magnetite commonly containing patches, beds and bedded intervals of altered tuffaceous sandstone. Sheet-like massive magnetite zones at Gossan Hill reflect the preferential replacement of more permeable strata in GGF M4, in particular the shard-rich and volcanic quartz crystal-poor lithologies. The gradual southward thinning of massive magnetite sheets reflect the strong stratigraphic control on these replacement processes. Nonetheless, the overall asymmetry and discordance of massive magnetite to the host rocks indicates structural control by proximity to the hydrothermal feeder zone.

At Gossan Hill, massive magnetite contains magnetite, carbonate, chlorite, quartz and talc, but lacks sulphides. This mineralogy resembles iron formation that overly VHMS deposits (Lydon, 1984), as well as banded iron formations (BIF). In general, iron formations overlying massive sulphides can be magnetite-rich or magnetite-poor, and represent the products of low temperature hydrothermal processes (Lydon, 1988; Duhig *et al.*, 1992; Hill, 1996; Doyle, 1997). Iron formations represent the precipitation of Fe-oxides from hydrothermal solutions forming massive sulphide at or near the seafloor (Hill, 1996; Duhig *et al.*, 1992).

The massive magnetite at Gossan Hill differs in occurrence, distribution and mineralogy from typical iron formations due to its lack of quartz, and the abundance Fe-rich carbonate and chlorite with the magnetite. Furthermore, massive magnetite at Gossan Hill is also dissimilar to Archean Agloma-type BIF deposits (*c.f.* Groves *et al.*, 1987; Watkins and Hickman, 1990a). For example, massive magnetite at Gossan Hill lacks many characteristics common to BIF including; (1) the absence of layering, (2) mineralogical banding, (3) hematite, (4) interlayered chert, (5) carbonate facies, (6) sulphide facies, (7) organic carbonaceous matter, and (8) a continuous strike (>1 km) extent (*c.f.* Vielreicher *et al.*, 1994; Eichler, 1976; Gross, 1991; Isley, 1995). Therefore,

massive magnetite at Gossan Hill is a unique chemical facies for a VHMS deposit.

The mineralogy of massive magnetite represents a primary mineral assemblage rather than the result hydrothermally metamorphosed seafloor weathering products. Evidence supporting magnetite as a primary hydrothermal mineral phase in include, (1) its occurrence within the relatively homogeneous tuffaceous sequence of GGF M4 indicating a lack of significant sedimentation breaks for seafloor weathering to have occurred, (2) the absence of mineralogical banding typical of ironstone formation at the seafloor, (3) the absence of hematite and pyrrhotite, and (4) the textural predominance of granular magnetite. This interpretation contrasts with that of Frater (1978; 1983a; 1985a) who interpreted the massive magnetite to have formed by the thermal metamorphism of a primary hematite-goethite assemblage into magnetite. Similar thermal metamorphic processes have been invoked for massive magnetite at the Tennant Creek deposits (Wedekind *et al.*, 1994; Large, 1975). At Gossan Hill, Frater (1985a; 1983a) concluded that the Fe-oxide zones were formed at shallow depths within the volcaniclastic pile. According to this model, Gossan Hill developed as two exhalative sulphide stages separated by an intermediate stage of oxidised hydrothermal exhalation and seafloor weathering. Although lath-shaped and boxwork magnetite are observed in the massive magnetite, their occurrence is rare. These textures suggest that magnetite pseudomorphed a pre-existing mineral, which is inferred to be hematite by Frater (1978), but alternatively may have been pyrrhotite (*c.f.* Middle Valley, Krasnov, 1994).

At Gossan Hill, massive magnetite pre-dates massive sulphide, and massive magnetite is consistently veined and in places replaced by sulphide. Gradational and veined contacts between massive magnetite and massive sulphide represent the overprint of magnetite by sulphides. Furthermore, textural evidence supports that massive magnetite was formed earlier as indicated by magnetite grains in massive magnetite that lack sulphide inclusions. In comparison, magnetite grains that precipitated with the massive sulphides are riddled with sulphide inclusions.

12.2.7 Timing and formation of massive sulphide

Two periods of sulphide deposition took place at Gossan Hill. The first stage is evidenced at the base of GGF M4 as polymict, pyrite-clast bearing breccia lenses. This early sulphide stage was a small-scale localised pyrite-rich episode. The second and main sulphide stage, forming massive sulphides and stringer mineralisation, occurred after the formation of massive magnetite and is correlated with sedimentation of GGF M6. The discordant relationship of massive pyrite to massive magnetite in the lower ore zone, together with the widespread stringer stockwork connecting the lower and upper ore zones supports this conclusion. Despite their stratigraphic separation, there is no evidence to support the development of the upper and lower sulphide zones as a stacked system due to repeated seafloor hydrothermal episodes. Strong structural localisation of massive sulphide and stockwork is exemplified by its thickest development adjacent to the feeder zone. Moreover, adjacent zones of massive magnetite and massive sulphide in the lower ore zone indicate that both formed from hydrothermal fluids using the same

feeder zone.

Massive sulphides in the upper ore zone formed during contemporaneous sulphide precipitation and sedimentation. As such, GGF M6 is a 'favourable horizon' as supported by the localtion of massive sulphides at the Scuddles deposit in GGF M6. The lower sulphide zone in GGF M4 at Gossan Hill was formed by veining and replacement processes. The Cu-rich replacement style of mineralisation in the lower ore zone formed from hot fluids at depths of at least 250 m below the inferred seafloor position (*i.e.*, upper parts of GGF M6). Sulphide deposition was promoted at the base of the massive magnetite and locally formed a discordant massive replacement zone adjacent to the feeder.

12.2.8 Ground preparation and hydrothermal alteration

A number of alteration stages are identified at Gossan Hill (Chapter 7). The timing of alteration is as follows:

(1) syndepositional regional quartz-chlorite alteration of the footwall and host succession;

(2) Fe-chlorite, magnetite, ankerite-siderite, talc, quartz alteration in GGF M4 associated with massive magnetite;

(3) Fe-chlorite, pyrite, pyrrhotite, chalcopyrite, quartz, ankerite-siderite, talc, apatite alteration associated with the lower ore zone (GGF M4) and quartz (±chlorite, ±ankerite-siderite, ±pyrite, ±sphalerite) associated with the upper ore zone (GFF M6);

(4) muscovite, carbonate, chlorite, quartz alteration of the hangingwall Scuddles Formation.

At Gossan Hill and throughout the GGF, the preservation of delicate shard and tube pumice textures indicates alteration of volcanic glass soon after emplacement and prior to diagenetic compaction, devitrification and the destructive effects of hydrothermal alteration. The initially permeable and porous GGF tuffaceous succession allowed for the circulation of fluids and associated alteration. Volcanic glass was differentially replaced by quartz and chlorite, and may have had intermediate alteration products such as Fe-oxide coatings and clay-smectite. This alteration contributed to the excellent textural preservation of primary volcanic textures. The preservation of volcanic textures within the massive magnetite and massive sulphide (*e.g.*, siliceous nodules) confirms that quartz-chlorite alteration occurred prior to the main hydrothermal-mineralising stages. Furthermore, the effect of the quartz-chlorite alteration served to control and localise the later hydrothermal fluids by indurating and reducing the permeability of the host rock succession.

Although ubiquitous throughout the GGF, the early replacement of strata by quartz-chlorite alteration was not necessarily homogeneous in style. Beds within bedded strata, such as GGF M4 and parts of GGF M1, have different bedding specific alteration, and are variably quartz and/or chlorite altered. The variable alteration distribution not only

indicates that the alteration formed from lateral fluid circulation, but likely also by different primary permeability and porosity contrasts between beds in the strata. However, the homogeneous quartz-chlorite alteration of GGF M5 is attributed to the massive and relatively homogeneous nature of the protolith.

Hydrothermal alteration associated with the massive magnetite and massive sulphide in the lower ore zone forms a narrow envelop (<10 m). The mineralogical similarity of this alteration in both massive magnetite and massive sulphide suggests its contemporaneous formation with both mineralisation types. This alteration consists of Fe-chlorite, magnetite, pyrite-pyrrhotite, ankerite-siderite, talc and apatite, with minor quartz. Disseminated magnetite has textures similar to the magnetite in massive magnetite. The limited distribution of the alteration envelope in the lower ore zone reflects its confinement to the immediate ore-forming environment. This may have been caused by permeability reduction due to earlier quartz-chlorite alteration of the volcaniclastics.

Intense quartz alteration surrounds sulphide stringer and the upper ore zone in GGF M5 and GGF M6 respectively. This silicification resulted in the replacement of the wall rock by fine-grained mosaics of microcrystalline quartz, and destroyed volcanic textures. The intensity of silicification away from massive sulphides decreases and sulphide veins commonly have siliceous halos that formed synchronously with the veins. Nonetheless, alteration of thinly bedded GGF M6 overlying massive sulphides has differential quartz, chlorite and carbonate alteration, which is bed specific. This alteration may be cumulative from the combined effects of seafloor weathering and low temperature hydrothermal alteration.

The limited lateral distribution of hydrothermal alteration associated with massive magnetite and massive sulphide at Gossan Hill contrasts markedly with the generalised distribution patterns of hydrothermal alteration in fragmental footwall lithologies (*e.g.*, Mattabi-type, Morton and Franklin, 1987). The narrow envelopes of hydrothermal alteration at Gossan Hill are more typical of alteration distributions in coherent footwall lithologies. This pattern is explained by the induration and reduction in permeability of the footwall, prior to mineralisation and during the early regional alteration event. The modification of the primary physical properties of the GGF caused permeability-porosity contrasts analogous to coherent lavas. This ground preparation event restricted the formation of hydrothermal alteration and mineralisation to the immediate upflow zone.

Hydrothermal alteration in lavas of the hangingwall Scuddles Formation occurred above the Gossan Hill deposit. Alteration in the hangingwall resulted in feldspar destruction and pervasive groundmass alteration to a carbonate and muscovite, and lesser chlorite and quartz mineralogy. This alteration represents the waning of the hydrothermal system after emplacement of the hangingwall. Although this alteration is not widespread (less than 150 m above the hangingwall contact), its distribution is poorly constrained by drilling.

12.2.9 Geochemical constraints on alteration at Gossan Hill

Based on immobile element geochemistry the GGF has a rhyodacitic composition (Chapter 8). Extensive metasomatism of the GGF during alteration involved the replacement of volcanic glass by quartz and chlorite. This process resulted in extensive alkali depletion. The depletion in Na_2O, K_2O and CaO also reflect the absence of feldspar and the minor occurrence of muscovite in the GGF. Replacement of volcanic glass led to increased abundances of FeO, MgO, MnO and SiO_2 due to chloritisation and silicification processes. In particular, elevated FeO and MgO are associated with chlorite alteration proximal to mineralisation, and the former by disseminated sulphide and magnetite. The geochemistry of alteration at Gossan Hill is inconsistent with observed footwall alteration in Canadian Archean VHMS deposits, which is characterised by Na_2O depletion and K_2O, MgO and FeO* enrichment (Lydon, 1984; Franklin *et al.*, 1981). However, widespread zones of silicification and chloritisation are commonly associated with the Canadian Archean VHMS deposits (Franklin *et al.*, 1981).

The alteration geochemistry of the lower ore zone reflects its alteration mineralogy. This is characterised by strong enrichment in FeO, MgO and to a lesser extent MnO and CaO, due to the presence of Fe-rich chlorite, Fe-carbonates, pyrite, pyrrhotite and magnetite. The Fe-rich composition of chlorite and carbonate is typical of Archean deposits (Franklin *et al.*, 1981). Intense siliceous alteration in the feeder and the upper ore zone, is delineated by high SiO_2 contents with sporadic enrichment in FeO due to variable chlorite, sulphide and carbonate contents. Trace element enrichment in Ag, As, Pb, Zn, Sn, Co occur and are locally related to sulphides in alteration. Chert beds in the M1 Marker are classified as hydrothermal precipitates based on low immobile element contents (Chapter 8). These chert bands consist mainly of SiO_2 due to a high content of quartz, but also contain variable CaO, FeO and MnO due to common scattered carbonate, chlorite and pyrite. Geochemistry of the hangingwall Scuddles Formation has locally strong Na_2O depletion due to the destruction of feldspar and K_2O and CaO enrichment due to muscovite and carbonate alteration.

12.3 Archean environments

It is widely argued that present day atmospheric and hydrospheric conditions differ from those that prevailed during the Archean (*e.g.*, Cloud, 1976; Veizer *et al.*, 1989; Krupp *et al.*, 1994). These arguments are partly based on (1) the widespread occurrence of BIF deposits, and (2) stable isotope systematics. Prior to ~2.2 Ga, higher geothermal gradients are suggested based on the cooling of the Earth and its relatively thin crust during this time (Myer, 1981; Ohmoto, 1994). Global heat flows are estimated to have been 2 to 3 times higher than the present day for the period 2.7-1.8 Ga (Lambert, 1976). This higher heat flow is suggested to have caused a significant increase in ocean temperatures. Estimates of Archean ocean bottom temperatures vary from ~30°C, based on sulphur isotope characteristics of biogenic pyrites in sedimentary rocks (Ohmoto and Felder, 1987), up to temperatures of ~80°C, based on oxygen isotopes of Archean cherts and phosphates (Karhu and Epstein, 1986).

The geochemistry of the Archean oceans is poorly constrained. Estimates of oxygen contents (pO_2) in Archean seawater vary by as much as eleven orders of magnitude. All estimates are however, lower than the present day values (Kasting *et al.*, 1992). The lower pO_2 contents, together with widespread BIF deposition during the Archean, suggest generally higher concentrations of Fe^{2+} and CO_2 in Archean seawater. Estimates of Fe^{2+} concentrations range from between 1 to 20 ppm, to as high as 400 ppm (Mel'nick, 1973; Ewers, 1980; Holland, 1984). Additionally, it is also assumed that Si^{2+} was abundant in Archean seawater (*e.g.*, Knauth, 1994; Krupp *et al.*, 1994; Isley, 1995). These fundamentally different chemical attributes of Archean seawater must have facilitated the transport of Fe^{2+} and Si^{2+} in solution, since an anoxygenous seawater environment prevents the fixation of Fe^{2+}. Therefore, Archean oceans may have been a potential source of Fe^{2+} (Eichler, 1976). Moreover, the absence of sulphate in the Late Archean rock record is also used to infer a widespread lack of oxidized sulphur in Archean waters (Lambert and Groves, 1981).

12.4 Geochemical constraints

Important geochemical constraints in resolving the genesis of VHMS deposits lie with the origin and geochemistry of ore fluids, including the origin of metals and geochemical controls on metal transport and precipitation. Much of the current understanding regarding the origin or ore fluids and metals is qualitative with fluid inclusion studies proving the best means of quantitative determination of ore fluid geochemistry. At Gossan Hill, fluid inclusion studies were not possible due to strong recrystallisation of the ore zones. Nonetheless, some geochemical constraint can be made by analogy with geochemical constraints determined at similar deposit types.

12.4.1 Ore fluid origins

Ohmoto (1996) argues that ore fluids in VHMS systems evolve by the continuous interaction of seawater with volcanic rock, without a magmatic contribution. A major seawater component in VHMS ore fluids is suggested by similarities in the salinity, δD, $\delta^{18}O$ and $\delta^{34}S_{SO4}$ values of the ore fluids with those of contemporaneous seawater (Ohmoto and Rye, 1974; Green *et al.*, 1981; Pisutha-Arnond and Ohmoto, 1983; Khin Zaw and Large, 1992; Ohmoto, 1996). Deep convective circulation of seawater through volcanic rock modifies the seawater and alters the volcanic rock by leaching processes (*e.g.* Spooner and Fyfe, 1973; Pisutha-Arnond and Ohmoto, 1983). These rock-water interactions and exchange reactions transform the seawater-dominated fluids to ore forming fluids (Ohmoto, 1996). Any magmatic contribution to these ore fluids may be obscured by the inherited sulphur isotope signatures from the volcanic rock (*e.g.*, Li and Manuel, 1994). Furthermore, the sulphur isotope systematics of the Archean have similar signatures of seawater, volcanic rock sulphur and magmatic sulphur.

12.4.2 Source of Metals

In VHMS deposits, two metal sources are postulated; (1) derivation from the leaching of volcanic rocks (Ohmoto and Rye, 1974, Solomon, 1976; Large, 1977; Solomon, 1981; Ohmoto, 1996), and (2) contribution from magmatic volatiles (Henley and Thornley,

1979; Stanton, 1985; 1990). No direct evidence of either contribution has been established. Solomon (1976) and Stoltz and Large (1992) propose that lithologies from the Mount Read Volcanics, Tasmania are a potential metal source for the VHMS deposits observed in this belt, with metals leached during extensive seawater convection. This is suggested on the basis of rock volume and potential metal reservoir calculations (Stoltz and Large, 1992), which could account for the known metal enrichment in this belt. Furthermore, Ohmoto (1996) identified strong metal depletion in host rocks to the Kuroko deposits. The leaching hypothesis argues that progressive water-rock interaction of convecting seawater with volcanic rock, resulted in modification of the fluids by increased salinity, lower $f O_2$ and the decrease in pH, which in turn, enable the fluids to leach metal (Hutchinson, 1982).

Advocates of magmatic sources argue that the genetic link between VHMS deposits and fractionated calcalkaline volcanism is an indication of the strong relationship between the ore-forming processes and the fractionation and volatile release that occurs during magmatic evolution (Stanton, 1985). However, it is also widely argued that metals were cumulatively sourced from a combination of both magmatic volatiles and seawater leaching (Stanton, 1990). Sawkins (1986) and Stanton (1985) argue that only small volumes of magmatic solutions, containing high concentrations of metals, mix with large volumes of seawater in the upper parts of the volcanic succession. Less soluble metals may therefore be sourced from magmatic contribution (*e.g.*, Cu, Bi, Sn, Mo and Te), whilst more soluble metals may be derived from seawater (*e.g.*, Zn, Pb, Ba, Ag, As, Sb, Hg) (Huston *et al.*, 1995a).

The observed replacement and chemical modification of the GGF at Gossan Hill and throughout the Golden Grove Domain is an indication of extensive seawater leaching and alteration. Such voluminous leaching may have contributed to metal enrichment in the hydrothermal fluids that formed massive sulphide deposits in this belt. However, as this study was focussed on Gossan Hill, all geochemical samples were proximal to the deposit and a regional background study would be necessary to substantiate this hypothesis of widespread metal depletion in the GGF succession. Nonetheless, a magmatic contribution to the ore fluids forming Gossan Hill cannot be dismissed. A magmatic contribution is partly supported by the $\delta^{13}C$ isotope values of carbonate (-1.4 to 5.7‰), $\delta^{34}S$ values of sulphides (average of 2.1 ± 1.7‰), high concentrations of Cu in ore and the timing of massive sulphide formation prior to the onset of proximal felsic volcanism. In addition, minor occurrences of apatite in sulphide-related alteration at Gossan Hill may also support a magmatic contribution. For example, in the Kiruna magnetite-apatite ores, both magmatic (Nystrom and Henriquez, 1994; Ferenczi, 1994) and leaching (Parak, 1985) hypothesis are proposed as sources for phosphorus and Fe. If a magmatic contribution did occur at Gossan Hill, its amount must have been minor compared with the volume of seawater fluids required to leach and replace the entire GGF prior to massive sulphide mineralisation.

12.4.3 Temperatures of formation

Sulphur isotope geothermometry at Gossan Hill yield equivocal temperatures of sulphide formation (Chapter 10). Oxygen isotopes give broad formation temperatures of between 150°C and 350°C (Chapter 11) at Gossan Hill and suggest similar formation temperatures for both massive sulphide and magnetite. Further temperature controls can also be inferred from metal zonation patterns and the metal solubility data as described below.

The chemical transport and deposition of metals in VHMS systems is largely dependant on the solubility of metals in solution (Large, 1992). Typical temperature models for the evolution of VHMS deposits involves early low temperature stages, which evolve to higher temperature stages (*e.g.*, Ohmoto *et al.*, 1983; Pisutha-Arnond and Ohmoto, 1983; Large, 1992). The transport of significant quantities of Cu and Au as chloride complexes in solution requires hydrothermal fluid temperatures in excess of 300°C (Huston and Large, 1989; Ohmoto *et al.*, 1983; Large, 1992). Lead and Zn can be transported in solution at lower temperatures due to their lower solubilities (>175°C; Large, 1992). Therefore, metal zonation patterns indicate hydrothermal temperature regimes related to ore precipitation with; basal pyrite-chalcopyrite-Au forming above 350°C, pyrite-chalcopyrite between 300°C to 350°C, low grade Pb-Zn-Ag between 235°C to 300°C and high grade Pb-Zn-Ag-Au at temperatures between 175°C to 235°C (Large, 1992).

At Gossan Hill, the lower sulphide ore zone consists of pyrite-chalcopyrite with sporadic enrichments of Au, suggesting formational temperatures of 300°C to 350°C. The upper ore zone has pyrite-chalcopyrite zone grading upwards to a high-grade sphalerite zone that contains elevated concentrations of Ag and Au. This zonation in the upper ore zone indicates a gradual decrease in temperature from 300°C at its base to 175°C at its top and is consistent with the cooling of ore fluids by increased mixing with seawater towards the upper parts of the orebody. The occurrence of Au in the upper Zn-rich zone at Gossan Hill could suggest Au transport at lower temperatures as bisulphide complexes (Hannington and Scott, 1989; Huston and Large, 1989).

12.4.4 Characteristics of Fe

Iron solubility is dependant on salinity, temperature, pressure, pH, fO_2 and fS_2 (Barnes, 1979; Davidson, 1992; Williams, 1994). The transport of Fe as chloride complexes occurs at temperatures above 200°C and the precipitation of iron is caused by cooling (Hemley *et al.*, 1992). At lower temperatures, Fe is mainly transported as Fe^{2+} (Barnes, 1979), although Fe is more soluble in solutions where reducing conditions, elevated temperatures and elevated salinity prevail (Maynard, 1983; Williams, 1994). At low temperatures less than 50°C), Fe is also soluble in alkaline fluids, but its transport in modern seawater as Fe^{2+} is limited by the high fO_2 and low CO_2 content of modern seawater (Garrels, 1987; Davidson, 1992).

By definition, VHMS deposits are Fe-rich systems, with the Fe in Phanerozoic deposits typically in sulphides and, to a lesser extent, in alteration mineral phases (Hutchinson, 1982). In Archean VHMS deposits, magnetite and Fe-rich alteration minerals (*i.e.*,

chlorite and carbonate) together with sulphides, are abundant. Nonetheless, Archean VHMS deposits do not necessarily require an additional Fe-source to account for the presence of iron oxides, as these systems are naturally Fe-rich. Instead, a different distribution of Fe is observed, which can be principally related to the chemistry of the ore forming fluids, which in turn, controls the partitioning of Fe to the different minerals in the system (Section 12.4.5).

The source of Fe in VHMS systems has similar origins and controversies as the source of metals discussed in Section 12.4.2. Leaching hypothesis are advocated in other magnetite-rich mineral deposits such as Tennant Creek and BIF deposits (*e.g.*, Wedekind *et al.*, 1989; Castro, 1994; Isley, 1995). However, in Agloma-type BIF deposits potential sources of Fe include Archean seawater (Eichler, 1976; Isley, 1995), weathering of continental crust (Krupp *et al.*, 1994) and sub seafloor hydrothermal processes (Eichler, 1976; Castro, 1994; Isley, 1995). In these deposits, isotopic and geochemical evidence support a hydrothermal origin to Fe and Si in BIF (Isley, 1995).

12.4.5 Sulphur and oxygen activity

Typical VHMS ore fluids are geochemically characterised by; pH = 4, NaCl = 1 m, $aH_2S = 10^{-3}$ and $SO_4^{2-}/H_2S = 10^{-1}$, with the temperatures of various metal zones dependant on variations in pH, salinity and fO_2 of the fluid (Large, 1992). The presence of pyrrhotite and magnetite, and the absence of barite in many Archean VHMS deposits result from specific physicochemical conditions of the ore forming fluids (Large, 1977; 1992; Ohmoto, 1996). Large (1977; 1992) interprets abundant magnetite and pyrrhotite in Archean systems to reflect lower fO_2 and aH_2S levels in ore fluids compared with the Paleozoic systems. Values of fO_2 at 10^{-42} atmosphere (at 300°C) and aH_2S at 10^{-3}, in equilibrium with pyrite-magnetite-pyrrhotite, are estimated to account for pyrrhotite-magnetite rich ore in Archean deposits including ore at Scuddles and Gossan Hill (Figs. 12.5 and 12.6) (Large, 1977; 1992). These values are lower than those of Paleozoic deposits (fO_2 at 10^{-35} atmosphere and aH_2S of $10^{-2.5}$ in equilibrium with pyrite; Large, 1977). Furthermore, the lower fO_2 and aH_2S values in Archean ore fluids are interpreted to reflect lower fO_2 values in Archean seawater, and the dominance of reduced sedimentary-volcanic packages in the Archean crust (Large, 1977).

Sulphur and oxygen deficient ore forming fluids are suggested for a number of other magnetite-rich deposits. Pyrrhotite and magnetite-rich sulphides from Middle Valley, Juan de Fuca Ridge formed from ore fluids containing low fO_2 and low aH_2S (Krasnov, 1994). The Proterozoic stratiform magnetite-Cu-Au Starra deposit is also interpreted to have formed during exhalation of low aH_2S fluids during high temperature output (250°C to 380°C) (Davidson, 1992). Davidson (1992) explains the hematite-magnetite assemblage at Starra to have formed from the expulsion of an oxidised version of an H_2S-deficient VHMS ore fluid, into an oxidised marine basin. However at Gossan Hill, the absence of hematite supports low fO_2 values in the ore fluids.

High temperature, reducing (low fO_2) and sulphur-poor fluids can therefore account for the abundance of magnetite and pyrrhotite in Archean VHMS deposits. Magnetite and

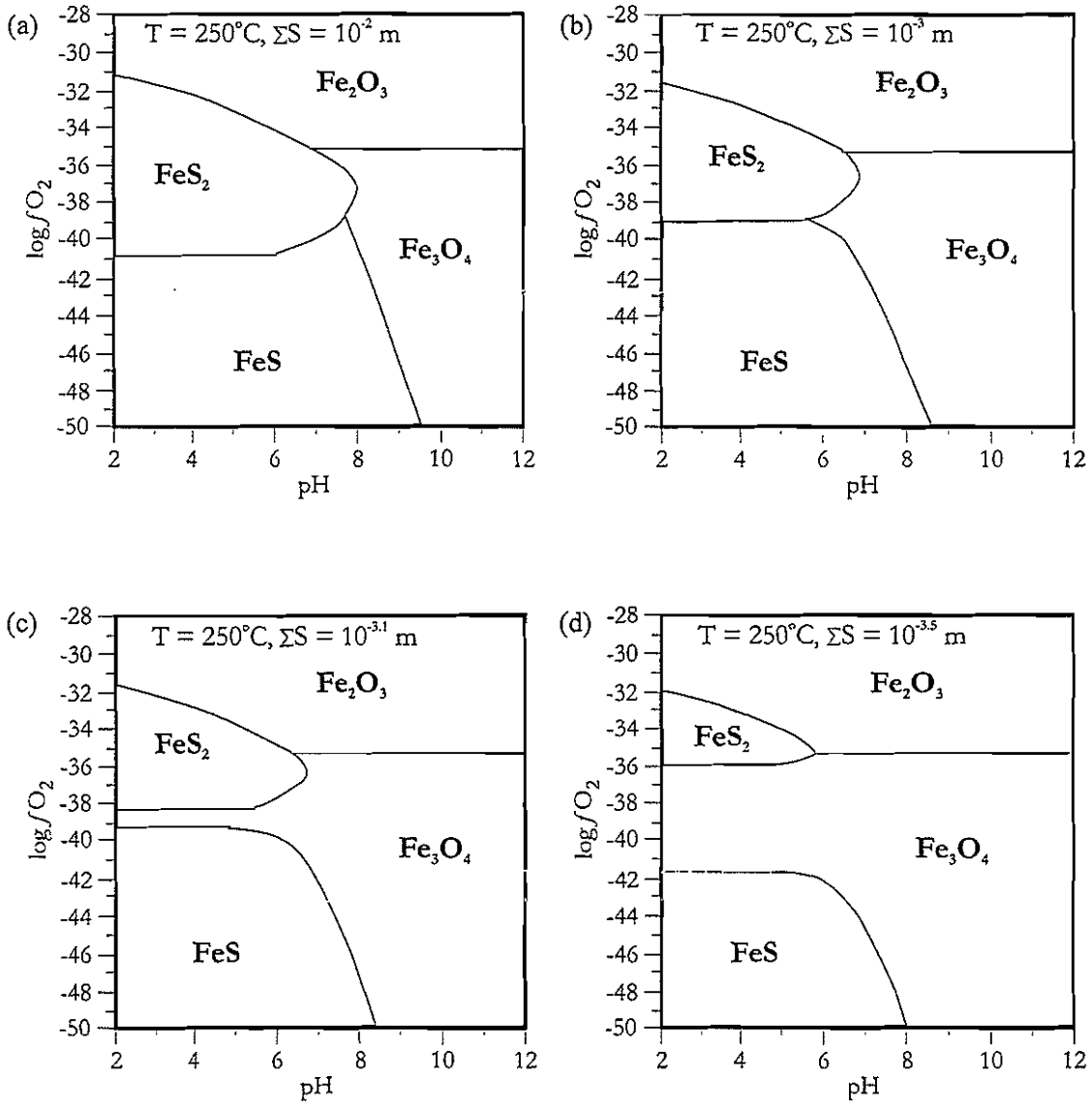

Figure 12.5: Stability fields of Fe-S-O minerals in f O_2-pH space at 250°C for four different values of total dissolved sulphur in a hydrothermal fluid: $\Sigma S = 10^{-2}$, 10^{-3}, $10^{-3.1}$, and $10^{-3.5}$molal, assuming NaCl is 1 molal. The activity diagrams (a-d) illustrate the opening of an Fe_3O_4 incursion field between the FeS_2 and FeS fields as proposed by Large (1977), which is caused by a decrease in the total sulphur content of the hydrothermal fluid. The boundary lines between the Fe-S-O minerals have been calculated from equilibria constants in Barton and Skinner (1979) and Johnson *et al.* (1992), and the distribution of species was undertaken using an unpublished spreadsheet developed by Dr. David Cooke at the Centre for Ore Deposit Research.

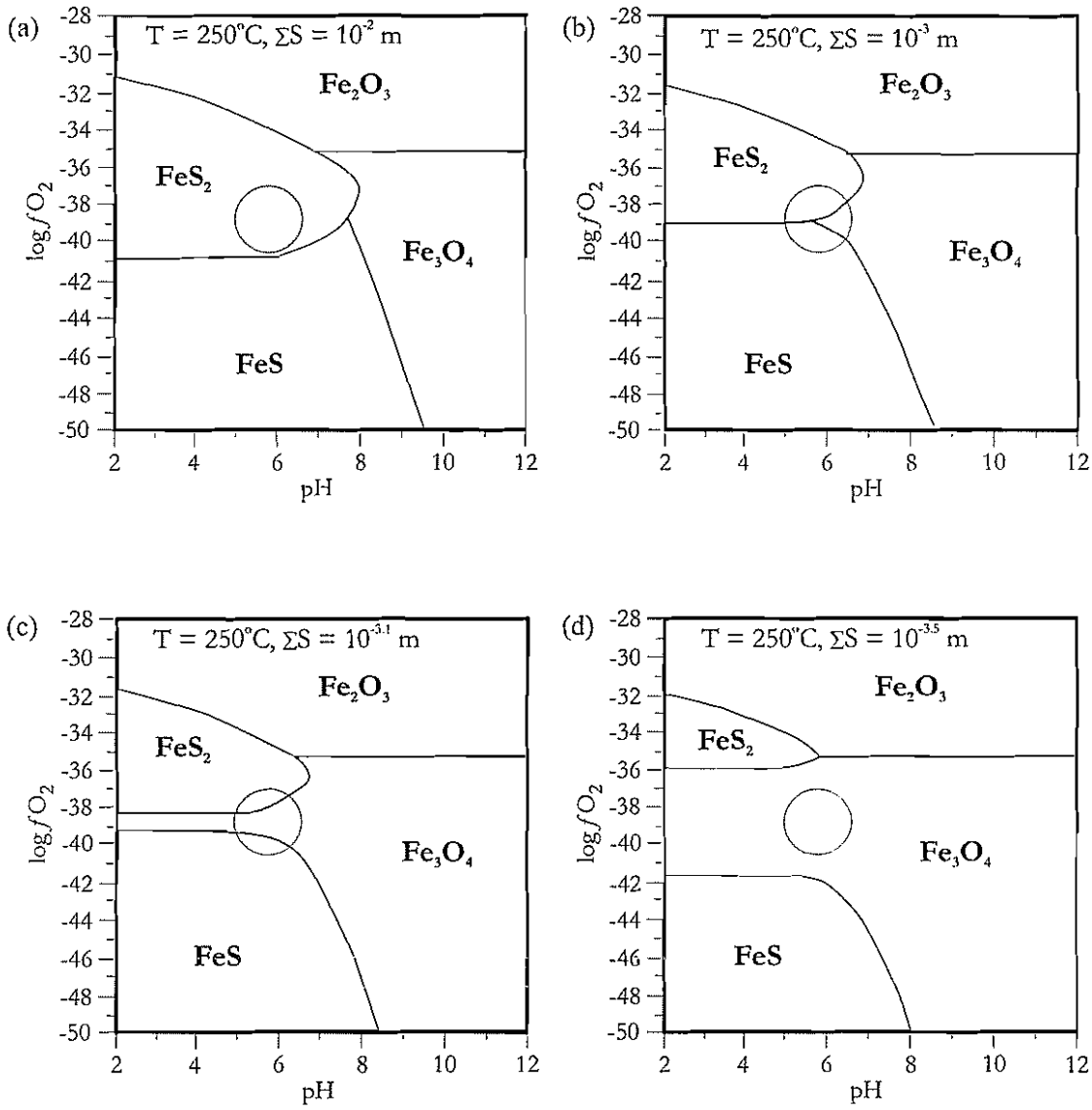

Figure 12.6: Stability fields of Fe-S-O minerals in $f\ O_2$-pH space at 250°C as described in Figure 12.5. A possible field for the hydrothermal solutions forming the Gossan Hill deposit is indicated (grey ellipse) at different values of total dissolved sulphur in a hydrothermal fluid: $\Sigma S = 10^{-2}$, 10^{-3}, $10^{-3.1}$, and $10^{-3.5}$ molal, assuming NaCl is 1 molal. Massive sulphides at Gossan Hill are proposed to have formed from fluids with higher ΣS values: *i.e.*, 10^{-2}, 10^{-3} and $10^{-3.1}$ molal in (a), (b) and (c). However, massive magnetite at Gossan Hill is proposed to have formed from similar hydrothermal solutions that contained lower ΣS values in the hydrothermal fluid and which, occupied the magnetite incursion field between pyrite and pyrrhotite: *i.e.*, $10^{-3.5}$ in (d). Note: the boundary lines between the Fe-S-O minerals have been calculated from equilibria constants in Barton and Skinner (1979) and Johnson *et al.* (1992), and the distribution of species was undertaken using an unpublished spreadsheet developed by Dr. David Cooke at the Centre for Ore Deposit Research.

pyrrhotite in massive sulphides at Gossan Hill can be explained by the field indicated in Figure 12.6 (circle). Nonetheless, different constraints are necessary for magnetite that is not in equilibrium with sulphide. This is represented at Gossan Hill by the presence of genetically earlier massive magnetite that is devoid of co-depositional sulphide. Using the geochemical model of Large (1977), a prolonged period of magnetite deposition is possible from sustained high temperature (>300°C), sulphur deficient ($aH_2S = 10^{-3.5}$), reducing fluids ($fO_2 < 10^{-40}$ atmosphere), with other physicochemical characteristics (*i.e.*, pH, salinity) similar to more typical VHMS ore fluids. Ore fluids with these geochemical characteristics can widen the magnetite stability field, which develops as an incursion between the pyrite and pyrrhotite stability fields as illustrated in Figures 12.5 and 12.6. Fluid evolution from magnetite (Fig. 12.6d) to sulphide (pyrite-pyrrhotite) (Fig. 12.6a to 12.6c) forming ore fluids in equilibrium with magnetite, therefore require redox changes by increasing fO_2 and aH_2S values within the fluids. At Gossan Hill, sustained high temperature during this redox transition is indicated on the basis of the Cu-Au-Fe metal content of the lower ore zone, which suggests temperatures were in excess of 350°C.

12.4.6 Chemical control on formation of the lower sulphide zone

The precipitation of ore minerals from solution result from physicochemical changes in pH, boiling, mixing, unmixing, cooling, oxidation and reduction (Barnes, 1979; Pisutha-Arnond and Ohmoto, 1983; Lydon, 1988; Khin Zaw *et al.*, 1994). In the case of the Tennant Creek deposits, massive ironstones host genetically later Au-Cu-Bi mineralisation (Wedekind *et al.*, 1989; Rattenbury, 1992; Huston *et al.*, 1993; Ferenczi, 1994). The formation of earlier ironstone bodies at Tennant Creek, provided a chemical trap for later sulphide mineralisation, with sulphide precipitation induced by chemical interaction between the sulphide ore fluids and the ironstones (Wedekind, 1990; Ferenczi, 1994; Khin Zaw *et al.*, 1994). This mechanism of chemical buffering results in ore fluid redox changes that promote sulphide deposition. Similar mechanisms of Au-sulphide mineralisation have also been suggested in BIF (*e.g.*, Vielreicher *et al.*, 1994; Groves *et al.*, 1987).

A mechanism of chemical buffering, which induced redox changes is suggested for the location and formation of the lower sulphide ore zone at Gossan Hill. The lower ore zone formed by replacement of massive magnetite and the GGF M4 wall rock. Pre-existing massive magnetite in GGF M4, provided a chemical trap to later upwelling sulphide-bearing hydrothermal ore fluids. The interaction of these fluids with massive magnetite resulted in redox changes of the ore solutions due to more oxidised fluids interacting with reducing massive magnetite zones. Widespread sulphide veining in massive magnetite indicates extensive fluid-rock interaction. These redox changes led to the precipitation of sulphides in the substrate from high temperature solutions at the lower contact of, and discordantly through massive magnetite.

12.5 Gossan Hill: A genetic model

As outlined in the preceding sections, the timing and distribution of massive magnetite, sulphide mineralisation and alteration are relatively well constrained. The Gossan Hill

deposit formed from a evolving hydrothermal-mineralising system. Six alteration-mineralising stages are identified at Gossan Hill and illustrated in Figures 12.7 to 12.12. In order these stages are:

(1) Initiation of the system with minor sulphide exhalation and alteration;

(2) Sedimentation and regionally extensive alteration;

(3) Replacement of GGF M4 at Gossan Hill by massive magnetite;

(4) Structural re-activation and evolution to a sulphide-forming system;

(5) Major stage of sulphide deposition;

(6) burial and waning of the hydrothermal-mineralising system.

12.5.1 Stage I: Initiation

The hydrothermal system at Gossan Hill (Fig. 12.7) began during or soon after the deposition of GGF M1, but prior to the onset of GGF M4. Although epiclastic sediments of GGF M2 indicate background sedimentation, the lack of both GGF M2 and GGF M3 in the Gossan Hill area indicates a sedimentation hiatus, possibly as a result of a local topographic high. During this sedimentation hiatus, minor pyrite-rich sulphides formed at the seafloor, but were locally eroded and re-deposited as small talus breccia lenses of polymict pyrite-clast bearing breccia at the base of GGF M4.

Fluids convecting through the pile were Archean seawater (refer Fig. 12.7 for chemical characteristics) and were locally focussed upward along a synvolcanic structure at Gossan Hill. The higher geothermal gradient and seawater bottom temperatures during the Archean (Section 12.3) may have initiated shallow fluid convection, where GGF M1 formed a regional aquifer. Circulating fluids through the highly permeable and porous footwall (GGF M1), reacted with volcanic glass in the succession. This led to the alteration and alkalis leaching from chemically unstable volcanic glass. The alteration of volcanic glass may also have included hydration, Fe-oxide grain surface coatings as well as partial clay-smectite, chlorite and quartz replacement, all of which contributed to the preservation of volcanic textures. Initiation during Stage I was a low temperature event (<200°C) where Fe and Si were sourced from Archean seawater, whilst sulphur may have been locally leached from the volcanics.

12.5.2 Stage II: Ground preparation

Ground preparation by early quartz-chlorite alteration at Gossan Hill (Fig. 12.8) is part of a regional event that caused substantial chemical modification and induration of the GGF. This alteration occurred synchronous with, or soon after, the successive episodes of tuffaceous sedimentation, which included a large part of the GGF (GGF M4 to the lower parts of GGF M6). Strata building stages involved regional-scale, voluminous mass-flows episodes that later waned to a low volume epiclastic and suspension sedimentation regime (upper part of GGF M6). Inactive synvolcanic structures, as denoted by the constant thickness of GGF M5, were buried. Moreover, the high permeability, porosity and abundance of volcanic glass in the tuffaceous strata were susceptible to alteration from convecting fluids.

STAGE I : INITIATION

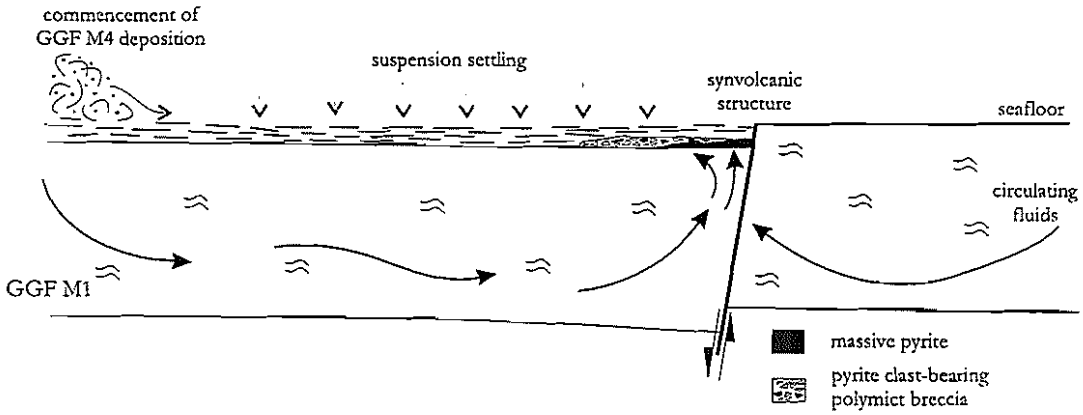

DEPOSITIONAL ENVIRONMENT: Mass-flows depositing coarse-grained pumice-rich breccia and sandstone of GGF M1 and fine-grained sandstone-siltstone of GGF M4.

- Highly permeable/porous sequence and chemically unstable due to abundant volcanic glass.
- Depositional hiatus (absence of GGF M2 and M3) reflecting regional topographic high.
- Commencement of GGF M4 deposition by mass flow and suspension settling; fine-grained crystal- and shard-rich sandstone-siltstone.

STRUCTURE: Initiation of growth structure having small-scale displacement (metres) causing differential subsidence.

HYDROTHERMAL FLUIDS: Low temperature fluids (<200°C) dominated by Archean seawater. Characteristics of Archean seawater:

- elevated bottom water temperatures (~30°C to 80°C)
- oxygen poor (low fO_2)
- reducing
- Si, Ca, Fe and CO_2 bearing

sulphur and sulphate deficient

FLUID CIRCULATION: Shallow convective circulation with GGF M1 forming an aquifer due to highly permeable lithologies. Fluid temperatures increase with convective circulation and the higher Archean geothermal gradient. Reaction of convecting fluids with volcanic glass result in:

- LEACHING: alkalis from volcanic glass (*i.e.* Na, K, Ca depletion) and,

DEPOSITING: hydration of glass, Fe-oxide coatings, alteration of volcanic glass to clay-smectite, chlorite, quartz (*i.e.* Fe, Mg, Si addition)

MINERALISATION: Minor pyrite-rich sulphide deposited at the seafloor and locally reworked to small polymict breccia lenses (<1 m wide).

- SULPHUR SOURCE: minor reduced sulphur leached from wall rocks.

ALTERATION: Local silicification proximal to seafloor

REGIONAL ASPECTS: Regional-scale strata depositional events and alteration. Development of synvolcanic structures cause local differential subsidence and thickness changes in GGF M2 and M3. Minor development of M1 Marker hydrothermal cherts elsewhere at this stratigraphic level. Mineralisation is not recorded elsewhere.

SCUDDLES: Absence of synvolcanic structure and mineralisation. Thick development of GGF M2 and M3 indicating lack of a deposition hiatus. No M1 Marker hydrothermal cherts recorded at this stratigraphic level.

SUMMARY: Initiation of extensive, regional alteration and localised small-scale, near-vent pyrite dominated reworked sulphide mineralisation at Gossan Hill. No evidence for this stage at Scuddles.

Figure 12.7: Stratigraphic, structural and geochemical characterisation of hydrothermal initiation during Stage I in the genesis of the Gossan Hill deposit.

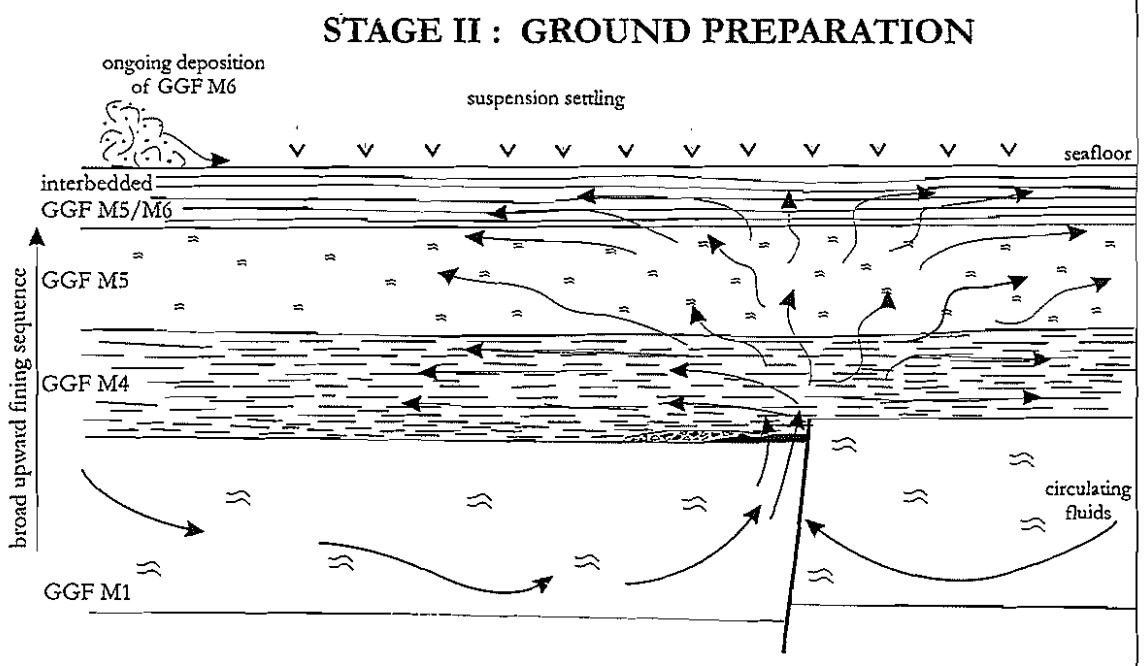

DEPOSITIONAL ENVIRONMENT: Periods of tuffaceous strata building (M4 to part of M6) as a result of successive mass-flows. Strata consists of pumiceous shreds, lithics, shards and volcanic quartz.

- Highly permeable/porous sequence and chemically unstable due to abundant volcanic glass.
- The basal interbedded section of GGF M5/M6 indicates the waning of tuffaceous mass flow episodes, giving way to low volume turbidite and suspension settling that form the upper parts of GGF M6.

STRUCTURE: Sedimentation led to burial of pre-existing synvolcanic structure, accounting for the constant thickness of GGF M5. The absence of a structural conduit in the upper strata limits convective fluid circulation.

HYDROTHERMAL FLUIDS: Continued low temperature (<200°C) convection of Archean seawater (refer Stage I). Re-establishement of convective circulation after host rock deposition. Part of a regional convection system leading to the chemical modification of seawater to hydrothermal fluids.

FLUID CIRCULATION: Shallow convective circulation. GGF M1 forms the principal aquifer. Fluid circulation is structurally focused in the lower stratigraphy, but transgressive to diffuse in the upper strata. Differential permeability of bedded strata causes widespread lateral fluid migration.

- LEACHING: alkalis from volcanic glass (*i.e.* Na, K, Ca depletion)
- DEPOSITING: hydration of glass, Fe-oxide coatings clay-smectite, chlorite, quartz (*i.e.* Fe, Mg, Si addition).

MINERALISATION: None

ALTERATION: Pervasive, intense siliceous-chlorite alteration resulting in widespread preservation of volcanic textures. Differential permeability in GGF M4 leads to preferential alteration of bedded strata. Silicification is more homogeneous the upper massive parts of the GGF (GGF M5 and GGF M6) reflecting increased deposition of Si due to cooling circulating fluids proximal to the seafloor.

REGIONAL ASPECTS: Regionally extensive quartz-chlorite alteration of the Golden Grove Formation throughout the Golden Grove Domain. Regional preservation of volcanic textures.

SCUDDLES: Intense siliceous-chlorite alteration and metasomatism of the strata as part of a regional alteration system.

SUMMARY: Extensive metasomatism characterised by alkali depletion and mass-replacement of volcanic glass by quartz-chlorite, due to diffuse fluid circulation of Archean seawater.

Figure 12.8: Stratigraphic, structural and geochemical characterisation of a regionally extensive silicification event during Stage II in the genesis of the Gossan Hill deposit.

STAGE III : MASSIVE MAGNETITE

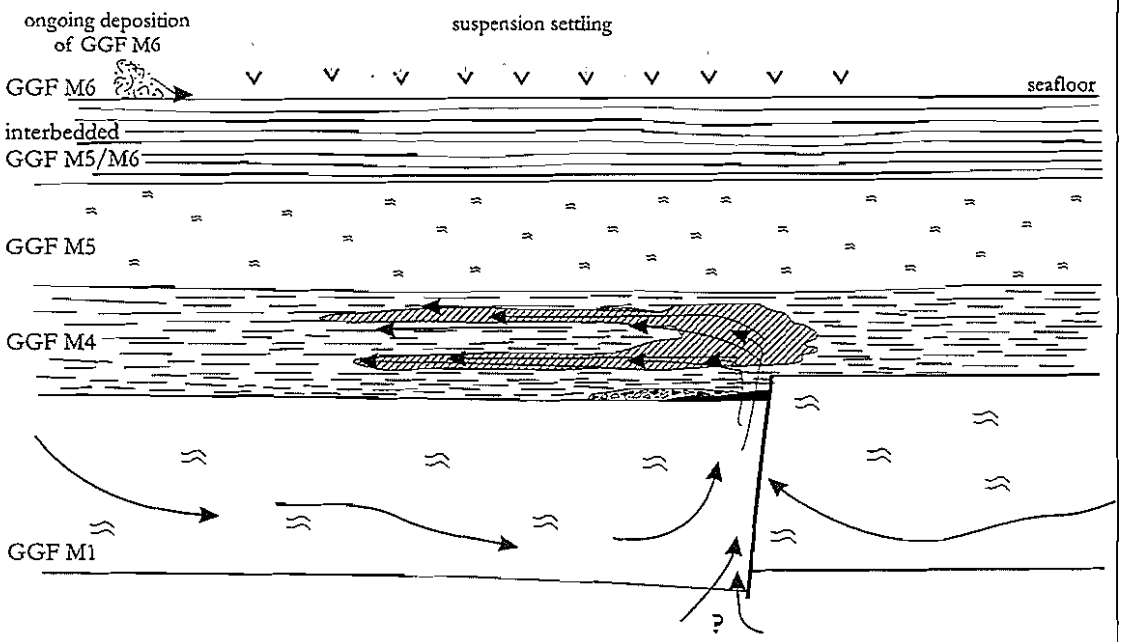

DEPOSITIONAL ENVIRONMENT: Minor, thinly bedded, sedimentation of GGF M6 by low volume turbidity currents and suspension settling. Period of relative quiescence.

STRUCTURE: No structural activity.

HYDROTHERMAL FLUIDS: Modified Archean seawater, with modification attributed to continued convection associated with heating and leaching of volcanic rocks. Hydrothermal fluid characterised by:

- temperatures greater than 300°C
- reducing, low oxygen contents (low fO_2)
- high Fe and CO_2 contents
- low sulphur contents (low aH_2S)

FLUID CIRCULATION: Structurally focused in lower strata by buried synvolcanic structure. Due to previous alteration during Stage II, GGF M5 and GGF M6 are indurated and impermeable. Fluids were focused laterally through differentially chlorite-quartz altered GGF M4.

- LEACHING: possibly metals ?
- DEPOSITING: magnetite, Fe-chlorite, Fe-carbonate, talc, minor quartz (*i.e.* Fe, Ca, Mg, Mn and Si addition)

MINERALISATION: Formation of massive magnetite (stippled) by subsurface replacement and veining, above and outward from structural feeder. Stratiform magnetite zone form by differential replacement along more permeable horizons in GGF M4. Strong structural and stratigraphic control.

- IRON SOURCE: leaching of wall rocks with possible contributions from Archean seawater.

ALTERATION: Disseminated magnetite, Fe-chlorite, Fe-carbonate and talc alteration as an envelop to the massive magnetite.

REGIONAL ASPECTS: Not regionally widespread. Only minor magnetite is recorded at this stratigraphic location elsewhere in district.

SCUDDLES: Massive magnetite absent possibly due to lack of synvolcanic structural conduit.

SUMMARY: Major episode of massive magnetite formation at Gossan Hill due to heated reduced, Fe-rich and sulphur deficient hydrothermal fluids with stratigraphic structural control on the localisation of magnetite replacement.

Figure 12.9: Stratigraphic, structural and geochemical characterisation of the formation of massive magnetite in Stage III of the genesis of the Gossan Hill deposit.

STAGE IV: SYNVOLCANIC STRUCTURE REACTIVATION AND SULPHIDE INITIATION

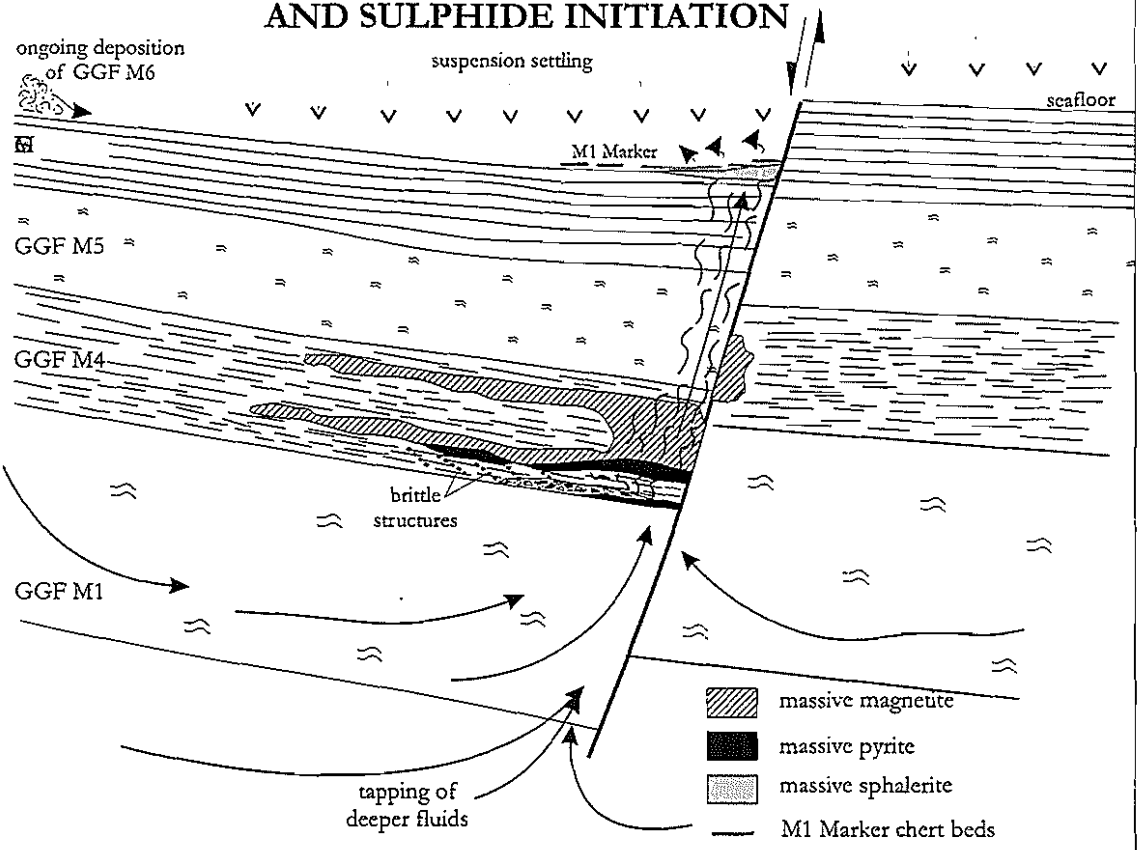

DEPOSITIONAL ENVIRONMENT: Minor, thinly bedded, sedimentation of GGF M6 by low volume turbidity currents and suspension settling.

STRUCTURE: Reactivation of synvolcanic structure causing differential subsidence and creating a structural low at Gossan Hill. Reactivation re-opens the structural conduit causing brittle deformation of silicified wall rock in GGF M4 and taps deeper circulating fluids.

HYDROTHERMAL FLUIDS: More typical VHMS fluids dominated by modified Archean seawater with higher reduced sulphur contents due to the contribution by deeper fluids with a rocks sulphur source and possible minor contribution from magmatic source. Hydrothermal fluid characterised by:

- high temperature 300°C to >350°C fluids
- reducing, low oxygen contents (low fO_2)
- high Fe, Si, CO_2 rich, high metals (Cu-Zn) contents
- higher sulphur contents (high aH_2S)

FLUID CIRCULATION: Structurally controlled conduit where the precipitation of sulphides in the subsurface is due to fluid redox changes induced by fluid interaction with massive magnetite. Fluid temperatures decrease towards the seafloor by mixing with cold seawater.

MINERALISATION: Sulphides deposited in the mineralising conduit. **Lower ore zone:** py-cpy-po-mgt. **Upper ore zone and stringer:** py-cpy-po-mgt below sp-py.

ALTERATION: Narrow envelop of chlorite-sulphide around the lower ore zone with quartz (chlorite-carbonate) surrounding the upper ore zone and stockwork.

REGIONAL ASPECTS: Numerous uneconomic sulphide occurrences in the GGF M6 favourable horizon, including M1 Marker cherts.

SCUDDLES: Synvolcanic structural activation forming a mineralising conduit for hydrothermal fluids. Localisation of mineralisation to the upper ore zone with exhalation indicated by thick M1 Marker.

SUMMARY: Reactivation of synvolcanic structure led to increased reduced sulphur contents of fluids and formation of sulphides. Structurally controlled conduit with subsurface replacement of magnetite in the lower ore zone and localised exhalation in the upper ore zone.

Figure 12.10: Stratigraphic, structural and geochemical characterisation of the initiation of sulphide deposition during Stage IV of the genesis of the Gossan Hill deposit.

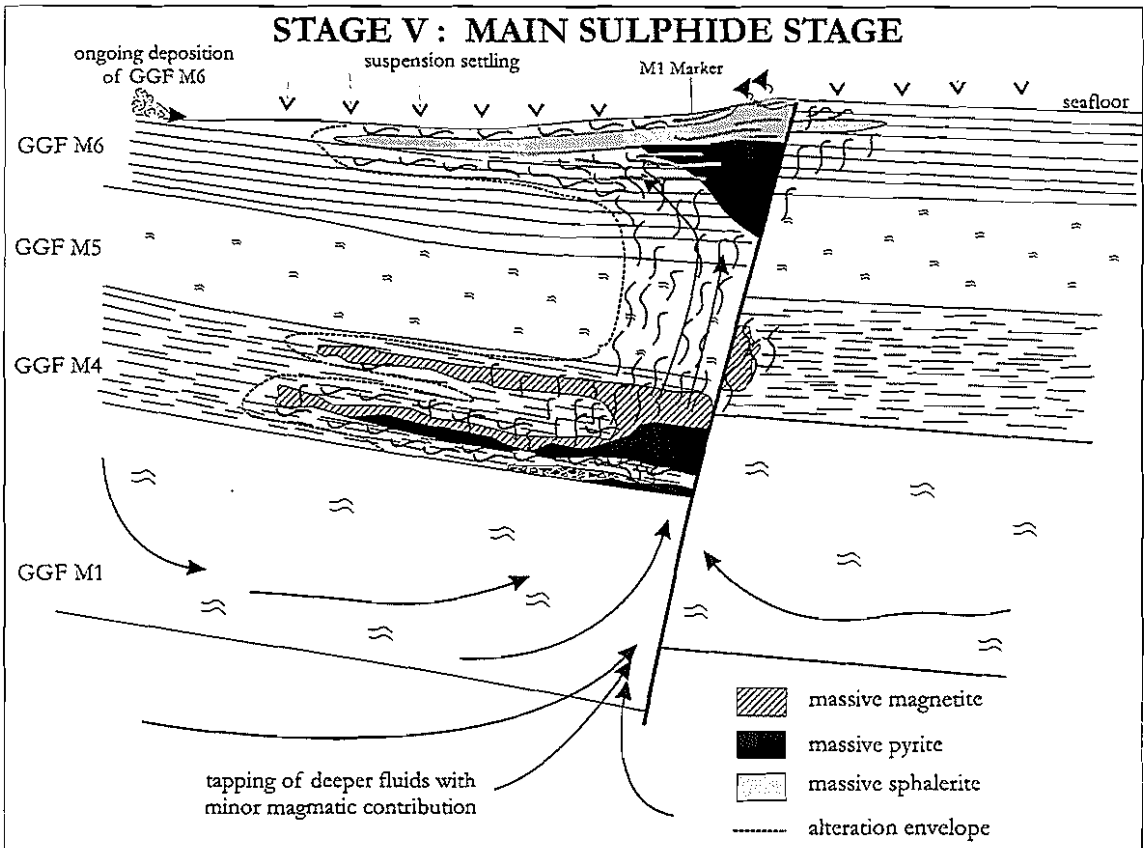

DEPOSITIONAL ENVIRONMENT: Ongoing sedimentation of GGF M6 with infill of structural low, repeated shallow burial of sulphides and M1 Marker by sediments.

STRUCTURE: Development of mineralising feeder parallel to synvolcanic structure.

HYDROTHERMAL FLUIDS: Typical Archean VHMS fluids dominated by modified Archean seawater. Tapping of deeper circulating fluids, possibly with a minor magmatic contribution. Hydrothermal fluid characterised by:

- high temperature 300°C to >350°C fluids
- reducing, low oxygen contents (low fO_2)
- high Fe, Si, CO_2-rich, high metals (Cu-Zn) contents
- higher sulphur contents (high aH_2S)

FLUID CIRCULATION: Main upflow zone reflects a structural and permeability controlled conduit. Sulphides precipitate in the substrate of the lower ore zone due to chemical entrapment by massive magnetite. Upwelling fluids cool with proximity to seafloor by mixing with entrained seawater. Later local lateral fluid migration due to permeability contrasts and bedding parallel veining.

MINERALISATION: Sulphides were deposited in and outward from the mineralising conduit largely by veining and replacement processes. **Lower ore zone:** stratiform to discordant sheet and vein enveloped of py-cpy-po-mgt. **Upper ore zone and stringer:** stringer stockwork and massive pyrite zone consisting of py-cpy-po-mgt below a sheet of sp-py. Metal zonation reflects sustained high temperature sulphide mineralisation in the lower ore zone (Cu-Fe-Au) and cooling of fluids upward (Cu-Fe) to the seafloor (Zn-Ag-Au).

ALTERATION: Narrow envelopes of hydrothermal alteration with chlorite-sulphide-carbonate-apatite in the lower ore zone and quartz-chlorite-carbonate in the upper ore zone and stockwork. Alteration mineral zonation reflects the cooling gradient of the fluids.

REGIONAL ASPECTS: Two major known deposits at Gossan Hill and Scuddles. Only minor sulphide mineralisation elsewhere (*i.e.*, regional prospects).

SCUDDLES: Major event involvingstrong structural control and lack of ore in the lower ore zone reflecting the absence of earlier magnetite. More extensive stockwork and larger accumulation of sulphide in upper ore zone.

SUMMARY: A main sulphide mineralising event with structurally focused feeder zones. Sulphide deposition was dominated by sub-seafloor veining and replacement.

Figure 12.11: Stratigraphic, structural and geochemical characterisation of the main sulphide stage during Stage V of the genesis of the Gossan Hill deposit.

STAGE VI : BURIAL

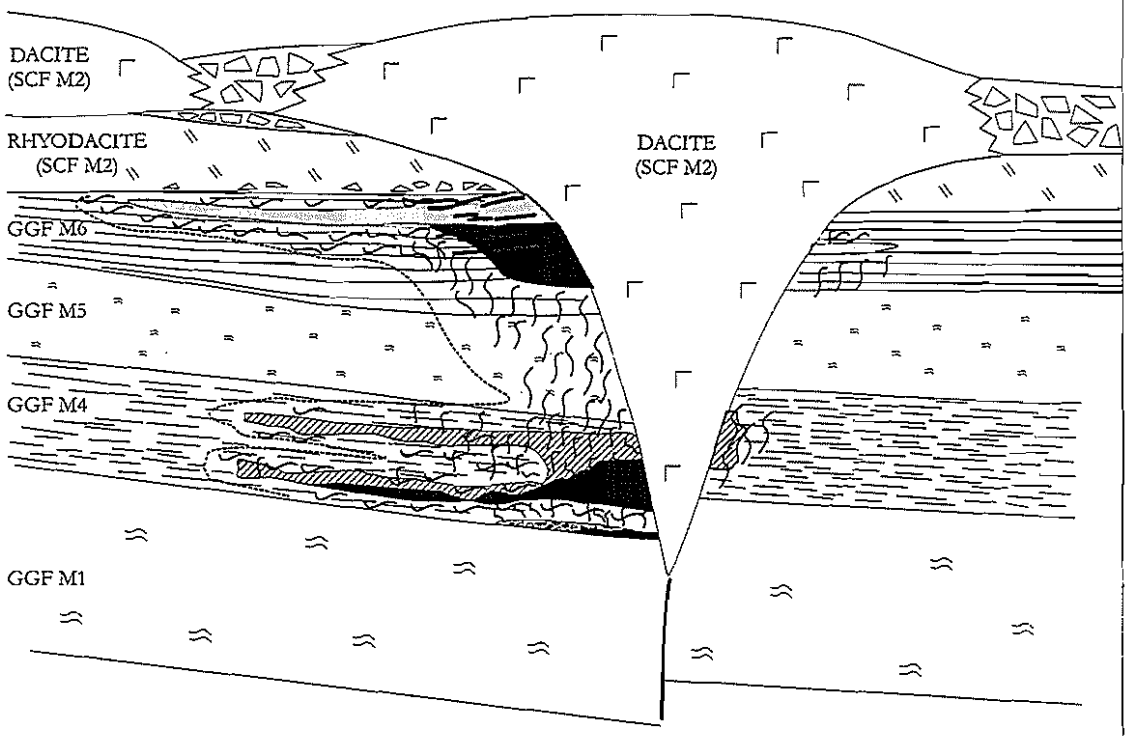

DEPOSITIONAL ENVIRONMENT: Burial of sulphides by massive felsic lavas of the Scuddles Formation (SCF M2):

Rhyodacite: extrusion as sheet-like flows with erosional polymict bases that contain sulphide clasts and autoclastic upper facies.

Dacite: intrusion-extrusion of dacite dome along the mineralising conduit with autoclastic facies in upper extrusive parts.

STRUCTURE: None

HYDROTHERMAL FLUIDS: Termination of convective circulation due to plugging of synvolcanic structures.

MINERALISATION: No significant sulphide deposition. Thermal recrystallisation and remobilisation of sulphides were caused by the intrusion of dacite.

ALTERATION: Limited near-vent alteration of rhyodacite and dacite volcanics. Alteration of feldspar and pervasive carbonate-muscovite groundmass alteration.

REGIONAL ASPECTS: Widespread felsic volcanism, abundant dacite dome structures.

SCUDDLES: Same as for Gossan Hill.

SUMMARY: Burial of the Golden Grove Formation and massive sulphides by proximal volcanis of the Scuddles Formation. Minor hydrothermal alteration and sulphide recrystallisation. Shut down of the mineralising system.

Figure 12.12: Stratigraphic, structural and geochemical characterisation of the burial and waning of the Gossan Hill mineralising system during Stage VI in the genesis of the Gossan Hill deposit.

Convective circulation was re-established after strata building and involved Archean seawater fluids similar to those in Stage I. Fluid convection occurred on a regional scale with GGF M1 as the principal aquifer. The absence of a structural conduit in the upper strata limited fluid circulation, with the buried synvolcanic structure locally focussing fluids in the lower strata. As a result, homogeneous quartz-chlorite alteration occurred in the massive GGF M5, whilst in bedded strata (*i.e.*, GGF M4 and M6) fluids were focussed laterally along beds and bed contacts resulting in differential bedding parallel quartz-chlorite alteration of the more permeable parts of the sequence.

Early alteration during Stage II involved widespread alkali depletion from volcanic glass and its replacement by quartz, chlorite and possibly clay-smectite minerals. Volcanic quartz was stable during this alteration. The effect of this alteration caused extensive preservation of volcanic textures and resulted in the differential reduction of the primary permeability and porosity of the succession. Some beds and members of the GGF (*e.g.* GGF M5) were indurated and rendered impermeable to subsequent hydrothermal-mineralising stages. Similar to Stage I, this alteration was low temperature (<200°C) with Si and Fe likely derived from Archean seawater. The extensive leaching of alkalis from the volcanic glass gradually resulted in the modification of the circulating fluid, possibly to more saline compositions. Continued convective circulation also resulted in a gradual fluid temperature increase, marking the modification and transition of Archean seawater dominated fluids to hydrothermal fluids of Stage III.

12.5.3 Stage III: Massive magnetite

Formation of massive magnetite during Stage III (Fig. 12.9) represents the evolution of Stage II by continued convective circulation, progressive fluid heating and modification *via* leaching processes within the volcanic pile. During Stage III, structural inactivity and general sedimentation quiescence prevailed. Continued convective fluid circulation, driven by higher Archean geothermal gradients, heated fluids to temperatures greater than 300°C. Convective circulation of fluids may have related to developing magma chambers at depth that later sourced the hangingwall Scuddles Formation volcanics. The compositional modification of circulating fluids resulted from the leaching of Ca, K and Na and possibly Pb and Zn from volcanic glass.

At Gossan Hill, hydrothermal fluids were focussed upwards through the base of the GGF along the buried synvolcanic structure. Fluid dispersion to the upper strata occurred only above this structure. The development of impermeable aquasols during earlier low temperature alteration (*e.g.*, GGF M5 in Stage II) prevented the upward movement of hydrothermal fluids. Massive magnetite formed in the substrate at the transition zone above the structural feeder where fluids moved laterally along more permeable horizons in GGF M4. The precipitation of massive magnetite within GGF M4 took place by the replacement of permeable shard-rich (crystal-poor) facies, with the development of two stratiform massive magnetite zones. A discordant zone of massive magnetite formed above the mineralising conduit with localised envelopes of disseminated magnetite, Fe-rich carbonate, Fe-rich chlorite and minor quartz alteration accompanying massive

magnetite formation.

The principal oxide mineral formed during Stage III was magnetite due to the high temperature, low $f\ O_2$, reducing and sulphur deficient composition of the hydrothermal fluids. This fluid composition prevented the precipitation of hematite and sulphides. Abundant magnetite and Fe-rich carbonate (ankerite to siderite) indicates the fluids were Fe- and CO_2-rich. These hydrothermal fluids were similar to ore fluids that formed massive sulphide, except that they lacked significant reduced sulphur (low aH_2S) to form sulphide, and occur within the magnetite incursion field of Large (1977) (Figs. 12.5 and 12.6). Hydrothermal fluids of Stage III may have also been metal-bearing, but if so, their low sulphur contents prevented the deposition of metal as sulphides. A potential source of O_2, necessary for magnetite precipitation, could have been derived from earlier clay-smectite alteration products of volcanic glass. Clay-smectite minerals facilitate O_2 storage as adsorbed and constitutional water due to their expandable structures, which is lost on heating (Deer *et al.*, 1992).

12.5.4 Stage IV: Synvolcanic structure re-activation and sulphide initiation

Stage IV marks the evolution of the hydrothermal system from a Fe- to a Fe-S system. This transition resulted from the re-activation of the synvolcanic structure at Gossan Hill (Fig. 12.10). Synvolcanic structural activity during this stage is inferred from the thickness changes in GGF M6, and is also inferred at Scuddles, where a synvolcanic structure was initiated. At Gossan Hill, structural re-activation tapped deeper, hotter, sulphur- and metal-bearing fluids which were focussed upwards along the re-opened synvolcanic mineralising conduit. These fluids, characterised as typical Archean VHMS ore fluids (*i.e.*, hot ~350°C, acidic, metal-bearing, H_2S-rich with low $f\ O_2$) initiated the precipitation of sulphides at Gossan Hill. The development of a feeder zone reflects the main upflow zone, which was confined by the relative impermeability of the wall rock due to earlier alteration. Constrained ore fluids initiated fracture-vein fill, as well as differential replacement of the wall rock in the feeder.

Focussed, upwelling hydrothermal fluids encountered massive magnetite, which acted as a physical and chemical barrier. Massive magnetite formed a chemical trap to these upwelling hydrothermal fluids and caused the precipitation of sulphides in the lower ore zone. Due to its sub-seafloor location, hydrothermal fluids did not cool by mixing with seawater, but maintained their high temperature and precipitated sulphide by redox changes. A pyrite-chalcopyrite ±pyrrhotite ±magnetite ±electrum assemblage, with a relatively homogeneous sulphur isotopic composition, resulted.

Near the seafloor, upwelling hydrothermal fluids cooled by mixing with entrained seawater. This process formed a sheet-like, sphalerite-rich zone, overlying a discordant pyrite-sphalerite-chalcopyrite zone in the mineralising conduit. Local exhalation of fluids precipitated M1 Marker hydrothermal chert bands. However, continued low volume sedimentation of GGF M6 caused the progressive burial of these sulphides and exhalative cherts. Episodes of seafloor exhalation and low volume sedimentation resulted in an upward migrating seafloor position, with repeated burial of sulphides

promoting lateral fluid dispersion and the deposition of sulphides by sub-seafloor replacement and veining.

12.5.5 Stage V: The main sulphide event

Progressive growth and development of the lower and upper sulphide zones (Fig. 12.11) resulted from continued hydrothermal activity in Stage V. Pyrite-chalcopyrite-rich mineralisation in the lower ore zone was accumulated by sub-seafloor replacement and veining processes. These sulphides occur below and are discordant to massive magnetite near the mineralising conduit. The mineralising conduit focussed fluids to the upper sulphide zone, the conduit tightly constrained by the impermeable wall rock. In the stockwork, mineralising vein conduits developed mainly by hydrofracture processes. The upper ore zone developed as a mound-like body adjacent to, and overlying, its feeder zone. Metal zonation in the upper ore zone reflects a cooling gradient for the hydrothermal fluids approaching the seafloor due to mixing with entrained seawater. The hydrothermal ore fluids may have had a minor magmatic contribution as inferred from the occurrence of apatite in alteration and the lighter sulphur isotopic signature of the sulphides in the lower ore zone (average $\delta^{34}S$ of 1.5‰). Magmatic contribution to the hydrothermal fluids could reflect active magma chambers at depth, which were responsible for overlying proximal effusive volcanism of the Scuddles Formation.

Sedimentation, by low volume turbidity currents and suspension settling filled in the structural low adjacent to the synvolcanic structure. Mound-like massive sulphides formed by replacement processes adjacent to, and overlying, the mineralising conduit. These sulphides developed as a central discordant core of massive pyrite-chalcopyrite overlying stringer mineralisation and below a stratiform sheet-like massive sphalerite zone. The stratiform development of massive sphalerite, may reflect an earlier seafloor position, which continued to grow by stratigraphically controlled replacement after burial, as indicated by intercalated and overlying sediments. Some exhalation of mineralising fluids resulted in the formation of the M1 Marker chert beds through the bedded sequence of GGF M6, due to sporadic periods of exhalation followed by sedimentation and burial. Sulphide replacement of sediments, together with repeated episodes of fracture and vein fill in the feeder and the upper ore zone may have contributed to the thickening of GGF M6 adjacent to the feeder. The main processes of sulphide precipitation took place by sub-seafloor veining and the replacement of strata.

The asymmetric funnel shape of the feeder reflects the confinement of sulphide mineralisation to the main vent area. This confinement arose from the reduced permeability of the wall rock due to earlier alteration. As a result, hydrothermal alteration accompanying sulphide mineralisation was also restricted in its distribution. In the hotter Cu-rich lower ore zone, alteration developed as narrow envelope. This alteration consists of Fe-rich chlorite, sulphides and minor apatite. In the discordant feeder and the upper ore zone, an envelope of intense silicification surrounds the sulphides, whilst in sediments overlying the upper ore zone alteration is bed specific and varies from quartz, chlorite to carbonate.

12.5.6 Stage VI: Burial and waning

Waning of the hydrothermal-mineralising system during Stage VI at Gossan Hill (Fig. 12.12) was induced by proximal volcanism, which disrupted and buried the system. Regionally extensive volcanism used synvolcanic structures as volcanic feeders for the extrusion of lava. At Gossan Hill, the extrusion of a rhyodacite lava (RD2) caused minor erosion of the sedimentary substrate, including the upper ore zone, where it was proximal to the seafloor. The rhyodacite extrusion was followed by the intrusion-extrusion of a dacite dome (DAC3) along the synvolcanic feeder structure. This dacite dome was, in turn, buried by continued proximal felsic volcanic products of the upper parts of the Scuddles Formation. The burial of massive sulphides prevented their erosion and corrosion by seafloor weathering and caused the waning of the hydrothermal system. Localised hydrothermal alteration of the overlying hangingwall lavas occurred during this stage.

12.6 Gossan Hill and Scuddles: Contrasting deposits

The depositional events leading to emplacement of the GGF were ubiquitous throughout the Golden Grove Domain. This is indicated by the regionally continuous and layered stratigraphic sequence of the GGF. Similarly, the early alteration during Stages I and II was also ubiquitous in the GGF, as seen by the widespread preservation of volcanic textures in lithologies at the Scuddles deposit. Nonetheless, stratigraphic differences between the two deposits do exist as thickness variations in some stratigraphic members (refer Figure 12.3). While Gossan Hill lacks GGF M2 and M3, these members are present at Scuddles indicating continued sedimentation rather than hiatus. Despite this difference, the thickness of the GGF is approximately the same at both deposits (*i.e.*, 500 m; Fig. 12.3). Early alteration and metasomatism of the GGF at Scuddles caused reduced permeability and preservation of volcanic textures in the succession, just like at Gossan Hill.

The main difference between the Gossan Hill and Scuddles deposits is the absence of massive magnetite in the later. Despite this, stratigraphic, structural, mineralogical and geochemical similarities exist between the two deposits. Massive sulphides at Scuddles are located in the same stratigraphic horizon (GGF M6) as the upper ore zone at Gossan Hill. The absence of massive magnetite from Scuddles may reflect a lack of structural conduits during Stage III. However, the initiation of synvolcanic growth structures at Scuddles led to the onset of sulphide mineralisation (Stage IV), without the deposition of massive magnetite (Stage III).

A similar structural-stratigraphic framework exists between the Gossan Hill and Scuddles deposits, with both having local thickening and asymmetry of GGF M6, massive sulphides and alteration, as well as intrusive dacite volcanic feeders. However, multiple hydrothermal-mineralising feeder conduits at Scuddles are supported by (1) multiple volcanic dacite feeders, (2) the greater lateral strike extent of ore (~650 m; Mill *et al.*, 1990b), and (3) the local thickening of massive sulphide at Main Lens, Intermediate Lens and the North Lens. The formation of Scuddles may therefore be likened to the

coalesced mound model of Huston (1988).

Sulphide formation at Scuddles (Stages IV and V) took place near and at the seafloor. Replacement and veining processes in the substrate, accompanied by quartz-chlorite alteration, occurred throughout GGF M5 and GGF M6. The absence of a lower sulphide ore zone at Scuddles reflects the absence of massive magnetite as a chemical barrier against upwelling fluids and, as a consequence the precipitation of sulphide did not occur in the deeper substrate. Sulphide accumulation was restricted entirely to the upper ore zone of GGF M6.

Hydrothermal-mineralising fluids at Scuddles and Gossan Hill are considered similar due to the similar alteration, metal zonation and mineralogy. Associations between lithofacies and massive sulphide ore at Scuddles suggest that exhalation had a greater role than at Gossan Hill. The thick development of M1 Marker bedded chert-lithic horizons (<6 m), massive sulphide breccia ore, banded ore and lenses of polymict sulphide-clast bearing talus breccia onlapping massive sulphides supports a seafloor mineralising system at Scuddles. Periods of sedimentation during sulphide formation are supported by M1 Marker horizons within the orebody (*i.e.*, the inter-ore marker of Ashley *et al.*, 1988). Furthermore, lower sedimentation rates at Scuddles may have promoted seafloor sulphide precipitation over replacement processes that dominated Gossan Hill.

The waning of the hydrothermal system at Scuddles is likened to Gossan Hill Stage VI, resulting from burial due to the extrusion of coherent volcanic hangingwall lavas. Dacite dome volcanism at Scuddles (DAC1 and DAC3) used pre-existing synvolcanic structures. Such with volcanic feeders intrude along synvolcanic structures at Main Lens and at Intermediate Lens. Hydrothermal alteration of the hangingwall volcanics occurred during waning of the mineralising system in a similar style to that observed at Gossan Hill.

12.7 Exploration ramifications

Key geological aspects at Gossan Hill can be applied to the exploration for similar resources in the Golden Grove Domain, with potential application to volcaniclastic sequences in greenstone belts elsewhere in the Archean Yilgarn Craton of Western Australia. Although GGF M6 is a favourable horizon hosting mineralisation at both Gossan Hill and Scuddles, the occurrence of minor massive sulphides within GGF M1-M4 at Gossan Hill means that the entire stratigraphic interval GGF M2 to GGF M6 is prospective for VHMS mineralisation. This stratigraphic interval corresponds to the duration of hydrothermal activity in the GGF. Due to the relative impermeability of GGF strata by early alteration, alteration related to mineralisation is confined to the immediate ore-forming environment. As a result, trace and whole rock geochemistry in the GGF do not yield laterally extensive vectors towards mineralisation. Despite the presence of hangingwall alteration, further work is necessary to establish its distribution and lateral extent.

A number of geological criteria provide constraints to the potential recognition of a

VHMS ore-forming environment within the GGF.

(1) The recognition of hydrothermal chert bands (M1 Marker) in the GGF, which represent hydrothermal precipitates formed from processes related to mineralisation. Lithic-chert M1 Marker intervals are developed at Gossan Hill and Scuddles, however their occurrences away from mineralisation is not well constrained;

(2) The identification of thickness variations (10's m) in members of the GGF. Sulphide mineralisation can be correlated with the thickening of the strata, particularly in GGF M6, but potentially also in the stratigraphic interval of GGF M2 to GGF M6.

(3) The location of volcanic feeder structures below dacite domes, which occupy relict synvolcanic structures that controlled the localisation of mineralisation and alteration. Feeder structures at Gossan Hill and Scuddles have a similar orientation of 050° (mine grid) with a plunge of 65° north.

(4) Geophysical delineation of anomalous magnetite concentrations. This technique has been extensively applied in the Golden Grove Domain and contributed to the discovery of Scuddles. However, the application of this technique may be limited by the presence of low magnetite contents in some sulphide, considering the wide spectrum of variation in magnetite contents between the Scuddles and Gossan Hill deposits.

Chapter 13

Conclusions

The main conclusions of this thesis on the Gossan Hill VHMS deposit are listed below.

(1) The Gossan Hill deposit is located in the discrete tectonostratigraphic Golden Grove Domain. The layered and laterally extensive (28 km) stratigraphy of the Golden Grove Domain is a coherent succession of felsic to mafic volcaniclastic and volcanic rocks that were deposited in a deep subaqueous environment. The rocks hosting the Gossan Hill deposit are dated at ~3.0 Ga and have calcalkaline affinities consistent with formation in an arc-related environment. No coeval granitoid magmatism is identified. Subvertical strata in the Golden Grove Domain lie on the western limb of a north plunging F3 anticline.

(2) Massive sulphide and magnetite at the Gossan Hill deposit lie within the Golden Grove Formation volcaniclastic succession. The formation has six members that consist of re-deposited tuffaceous volcaniclastics and lesser mixed provenance, tuffaceous-bearing epiclastics. Massive coherent lavas of the Scuddles Formation overly the Golden Grove Formation and form the hangingwall to massive sulphide.

(3) At Gossan Hill, tuffaceous strata of the Golden Grove Formation (GGF M1, M3, M4, M5 and part of M6) are an upward fining succession of pebble breccia to sandstone-siltstone that consist of volcanic quartz and altered pumiceous lithics, shreds, shards and ash. Tuffaceous strata were emplaced by successive large volume, cold, water saturated, high density turbidite mass flow episodes of distally sourced pyroclastic material. Minor reworking during transportation is inferred from a relatively homogenous immobile element (rhyodacite) signature.

(4) Epiclastic strata at Gossan Hill (GGF M2 and upper parts of GGF M6) consist of thinly bedded, polymict pebble breccia and sandstone-siltstone, interbedded with tuffaceous shard- to ash-rich sandstone-siltstone. These strata were deposited from low volume turbidity currents synchronous with the suspension settling of fine-grained tuffaceous material. Mixed provenance epiclastic-tuffaceous strata record the waning of tuffaceous sedimentation and were associated with periods of relative sedimentation quiescence.

(5) The hangingwall Scuddles Formation at Gossan Hill, consists of a sheet-like rhyodacite at its base, which is overlain and intruded by a dacite dome. These coherent volcanic units record the onset of proximal volcanism. Polymict, sulphide

clast-bearing breccia at the base of the rhyodacite is derived from erosion of the substrate during extrusion and indicates the proximity of massive sulphides to the seafloor. Dacite forms an intrusive-extrusive dome that overlies its volcanic feeder and intrudes rhyodacite and the Golden Grove Formation. Chilled contacts support dacite intrusion post-mineralisation.

(6) The regional deformation events D1 and D2 are not observed at Gossan Hill. Deformation at Gossan Hill (D3 and D4) is manifested as a spaced penetrative cleavage, boudinage, faulting and veining developed during east-west compression. Massive magnetite and massive sulphide at Gossan Hill have the same generations of deformation as the host rocks. Peak greenschist facies metamorphism (454 ± 4°C at 1 kbar based on andalusite-chloritoid-chlorite-quartz equilibrium) was synchronous with D4 deformation and resulted in the widespread recrystallisation of sulphides at Gossan Hill.

(7) The Gossan Hill deposit consists of two ores zones that are stratigraphically separated by 150 m of tuffaceous and epiclastic strata. The lower sulphide ore zone is hosted by bedded, tuffaceous sandstone-siltstone of GGF M4. The upper ore zone is hosted by epiclastic-tuffaceous pebble breccia and sandstone-siltstone of GGF M6. The upper ore zone occurs below, but within 10 m of the upper contact of GGF M6. Sulphide veins form a stockwork feeder zone that interconnects the lower and upper ore zones.

(8) Large zones of massive magnetite (12 Mt) are present in the lower sulphide ore zone of GGF M4. Massive magnetite consists of fine-grained magnetite in an ankerite-siderite, Fe-chlorite, talc and lesser quartz matrix. Massive magnetite forms an asymmetric zone that is discordant above its feeder, but thins southwards into two semi-continuous stratabound sheets. Common interdigitating and bedded intervals of tuffaceous strata occur within massive magnetite. Massive magnetite also has gradational to veined upper and lower contacts. These relationships are consistent with the formation of massive magnetite by sub-seafloor replacement processes along permeable horizons in the tuffaceous strata of GGF M4, laterally outwards from the feeder.

(9) Massive sulphides in the lower ore zone (GGF M4) consist of pyrite, chalcopyrite, pyrrhotite and magnetite in an Fe-rich chlorite, ankerite-siderite, talc, quartz and minor apatite matrix. Cu-rich sulphide veins envelop and grade laterally in to Cu-rich massive sulphide. The massive sulphides are thickest below, but discordant to the thickest parts of the massive magnetite. Massive sulphide and its sulphide vein envelop are stratabound and thin southwards. Veined upper and lower contacts to massive sulphides in the lower ore zone indicate formation mainly by fracture fill and replacement processes. However, small (<1 m wide) lensoidal, polymict, pyrite-clast bearing breccia beds occur near the base of GGF M4 and below massive sulphide. These breccia beds support a paleoseafloor and potential hiatus during which, minor pyrite was formed.

(10) Massive sulphides in the upper ore zone consist of pyrite, sphalerite, pyrrhotite, chalcopyrite and magnetite with minor galena, tetrahedrite and arsenopyrite in a quartz, chlorite and carbonate matrix. The upper sulphide ore zone overlies the asymmetric, discordant stockwork that connects the upper and lower ore zones. Stockwork mineralisation grades upward to a discordant, mound-shaped zone of massive pyrite, which in turn, grades upwards and laterally into a sheet of massive sphalerite. Sphalerite-pyrite vein mineralisation envelops massive sphalerite and both are asymmetric and thin to the south. Gradational and veined upper and lower contacts of massive sphalerite to epiclastic strata of GGF M6 support that sphalerite formed by replacement and veining, with its stratabound distribution indicative of strong stratigraphic control.

(11) Interconnecting and enveloping the massive sulphides are sulphide veins which suggest the synchronous formation of the upper and lower sulphide ore zones. Sulphide replacement was a dominant process as indicated by (1) incomplete replacement of pebble breccia and sandstone-siltstone in the upper and lower ore zones, (2) common intercalated sulphide-free beds in the massive sulphide, and (3) clasts of relict wall rock in massive sulphide. These attributes also suggest that the distribution of sulphide replacement was locally controlled by permeability and porosity contrasts within the host rock succession. Sub-seafloor replacement processes are further supported by a lack of sulphide breccia ore and mineral banding in massive sulphide. However, exhalation processes did occur, as inferred from hydrothermal chert beds in the M1 Marker within the upper parts of GGF M6. These cherts suggest that minor exhalation was ongoing with formation of the upper sulphide ore zone. Continued sedimentation forming GGF M6 buried the exhalative layers, which were subsequently cut by sulphide veins. Therefore, the main sulphide stage at Gossan Hill was syndepositional with tuffaceous-epiclastic sedimentation depositing GGF M6.

(12) Evidence for synvolcanic structural control at Gossan Hill is (1) thickness changes in members of the GGF (GGF M6 and rhyodacite breccia facies), (2) a slope change of the GGF M1-M4 contact surface, (3) thickness changes in massive magnetite, massive sulphide, sulphide vein mineralisation and hydrothermal alteration envelops, and (4) asymmetry of massive magnetite, massive sulphide, sulphide vein mineralisation and hydrothermal alteration envelops. This synvolcanic growth fault had at least two stages of structural activity during the deposition of the GGF. Furthermore, this structure formed the conduit for hydrothermal fluids during massive magnetite and sulphide mineralisation, and also for later dacite dome volcanism. The thickest development of massive magnetite, massive sulphide, sulphide vein mineralisation and hydrothermal alteration are located adjacent to the inferred synvolcanic structure and thin southwards away from the conduit.

(13) Massive magnetite pre-dates massive sulphide and sulphide veins. This is indicated by the replacement of magnetite by sulphide, sulphide veining of massive magnetite and by massive sulphide that cross cuts massive magnetite. Massive magnetite and

sulphide mineralisation formed during two separate stages. This is supported by texturally different magnetite in massive magnetite (typically granular to skeletal and lacking sulphide) to magnetite in massive and vein sulphide (typically euhedral and sieved by sulphide inclusions).

(14) An early, regional, quartz-chlorite alteration of the GGF preserved tuffaceous volcanic textures by the replacement of pumice and shards by quartz and chlorite. This alteration occurred prior to diagenetic compaction and mineralisation at Gossan Hill. Induration, caused by regional quartz-chlorite alteration, reduced the permeability of the succession and sealed much of the succession to texturally destructive effects of hydrothermal alteration, mineralisation and metamorphism. It is likely that regional quartz-chlorite alteration contributed significantly to the focussing of later hydrothermal fluids to available structural conduits.

(15) Zones of intense hydrothermal alteration envelop massive magnetite, massive sulphide and stockwork mineralisation. These local alteration envelops overprint regional quartz-chlorite alteration. In the lower ore zone, a narrow zone of Fe-rich chlorite alteration surrounds massive magnetite and massive sulphide. This alteration also contains scattered ankerite-siderite, pyrite, pyrrhotite, magnetite and apatite. Alteration related to massive magnetite is indistinguishable from that associated with massive and vein sulphides. The upper ore zone and its underlying stockwork have an intense quartz alteration envelop. Carbonate-muscovite (±chlorite, ±quartz) alteration occurs throughout the hangingwall Scuddles Formation rhyodacite and dacite.

(16) A positive correlation of FeO* and SiO_2 in the GGF reflects regional quartz-chlorite alteration, as well as local chlorite and siliceous hydrothermal alteration that surrounds mineralisation at Gossan Hill. This geochemistry reflects the widespread depletion in alkalis, which likely occurred by the alteration of volcanic glass. This is confirmed by the absence of feldspar and minor occurrence of muscovite in the GGF. Localised Fe-chlorite and ankerite-siderite alteration surrounding the lower ore zone has intense FeO*, MgO and MnO enrichment. The upper ore zone is characterised by intense enrichment in SiO_2 with sporadic trace element enrichment of Cd, As, Pb, Fe, Zn, Ag, Bi, Sb and Sn. Alteration in the hangingwall is characterised by enrichment in K_2O and CaO and depletion in Na_2O, which corresponds to pervasive muscovite and carbonate alteration.

(17) Metal zonation at Gossan Hill grades from Cu-Fe (±Au) in the lower ore zone to Zn-Cu-rich at the base of the upper ore zone. The upper ore zone grades upwards and laterally from Zn-Cu to Zn-Ag-Au (±Cu, ±Pb)-rich sulphides. Sulphide veins in the discordant stockwork connecting the two ore zones form a zone of scattered Fe-Cu ±Au, ±Zn. Massive magnetite in the lower ore zone lacks base metals and has sheet-like Fe-rich zones. The highest concentrations of Cu-Fe occur at the base of the lower ore zone and define a north plunging feeder. In the upper ore zone Zn-Ag-Au (±Cu, ±Pb) enrichment indicates a strong stratigraphic control to mineralisation.

(18) Overall, sulphur isotope values on sulphides at Gossan Hill vary from -4.8 to 7.8‰ (average of 2.1 ± 1.7‰). These $\delta^{34}S$ values have a systematic stratigraphic increase from the base to the top of sulphide mineralisation, suggest the progressive mixing of upwelling ore fluids with entrained seawater. The heaviest and greatest range of $\delta^{34}S$ values occurs toward the top of the upper ore zone in massive sphalerite (δ^{34}Spyrite -1.0 to 7.8‰; average of 2.3‰). In the lower ore zone, $\delta^{34}S$ values have a relatively homogeneous composition (δ^{34}Spyrite 0.5 to 3.5‰; average of 1.8‰) that reflect a relatively homogeneous rock sulphur source and/or possible magmatic contribution.

(19) The $\delta^{18}O$ composition of magnetite in massive magnetite has lighter $\delta^{18}O$ than values for magnetite disseminated in the massive sulphide. Based on the fractionation systematics for magnetite, the $\delta^{18}O_{H2O}$ fluid compositions must be heavier than the $\delta^{18}O$ of magnetite, which at Gossan Hill, broadly constrain $\delta^{18}O_{H2O}$ from 6‰ to 13‰. It is, therefore, unlikely that these ore fluids were pure seawater, but have values consistent with the rock buffering of circulating fluids and/or direct magmatic contribution.

(20) The Gossan Hill deposit formed in an evolving hydrothermal system, which corresponds to approximately 500 m of tuffaceous and epiclastic sedimentation. Six stages are envisaged in the formation of Gossan Hill.

(1) Initiation of a synvolcanic structure and regional seawater convection that caused extensive metasomatism and alteration of the GGF.

(2) Continued sedimentation, seawater circulation and metasomatism associated with the gradual heating of circulating fluids.

(3) Formation of massive magnetite by subsurface replacement from high temperature, sulphur-deficient fluids above a synvolcanic conduit.

(4) Reactivation of the synvolcanic structure, tapping deeper, hot, sulphur-and metal-bearing fluids, which caused subsurface sulphide replacement of massive magnetite and near seafloor sulphide deposition higher in the stratigraphy by exhalation and replacement.

(5) Continued sulphide mineralisation.

(6) Burial of the hydrothermal system by proximal volcanism.

(21) Hydrothermal fluids forming both massive magnetite and massive sulphide are inferred to have similar chemical attributes. These are high temperature (300° to 350°C), reducing, slightly acidic, low fO_2 compositions. The principal difference of the ore fluid that formed massive magnetite from that which formed massive sulphide, was its lower H_2S content. Massive magnetite likely formed from fluids with low H_2S contents, which evolved to H_2S-bearing during sulphide mineralisation. The increase in the H_2S content of fluids during sulphide mineralisation is attributed to the tapping of deeper, potentially magmatic, sulphur-bearing fluids during synvolcanic structural reactivation. The sub-seafloor precipitation of sulphide in the lower ore zone was caused by chemical entrapment due to pre-existing massive

magnetite. A potential heat source driving convection at Gossan Hill may have been shallow magma chambers associated with later emplacement of the hangingwall Scuddles Formation.

(22) The nearby Scuddles deposit has similar stratigraphic, structural and geochemical characteristics to the upper ore zone at Gossan Hill. However, the Scuddles deposit lacks massive magnetite and a lower sulphide ore zone as seen at Gossan Hill. The formation of Scuddles occurred from a single, structurally focussed, sulphide mineralising stage at or near the seafloor at a time equivalent to the formation of the upper ore zone at Gossan Hill.

(23) Geological constraints on the genesis the Gossan Hill deposit can be applied to the exploration for similar resources. Potential criteria for exploration include the identification of volcanic-sedimentary thickness variations, the recognition of synvolcanic feeders sites as dacite domes and hydrothermal chert beds. All these features have potential use as indicators of sulphide mineralising processes.

References

Adachi, M., Yamamoto, K. and Sugisaki, R., 1986. Hydrothermal chert and associated siliceous rocks from the northern Pacific: Their geological significance as indication of ocean ridge activity. *Sedimentary Geology*, v. 47, p. 125-148.

Allen, R.L., 1988. False pyroclastic textures in altered silicic lavas, with implications for volcanic-associated mineralisation. *Economic Geology*, v. 83, p. 1424-1446.

Ames, D.E., Franklin, J.M. and Hannington, M.D., 1983. Mineralogy and geochemistry of active and inactive chimney and massive sulfides, Middle Valley, northern Juan de Fuca Ridge: An evolving hydrothermal system. *The Canadian Mineralogist*, v. 31, p. 997-1024.

Archibald, N.J., Bettenay, L.F., Bickle, M.J. and Groves, D.I., 1981. Evolution of the Archean crust in the Eastern Goldfields Province of the Yilgarn Block, Western Australia *in Glover, J. E. and Groves, D. I., (Eds.)*, Archean Geology. *Geological Society of Australia special publication*, Perth, v. 7, p. 491-504.

Archibald, N.J., 1990. Tectonic framework of Golden Grove area, Warriedar Fold Belt, Yalgoo Region, Western Australia: Comparative structural studies at Gossan Hill and Scuddles. Internal MZC report by Port Mineral and Mining Services.

Arriens, P.A., 1971. The Archean geochronology of Australia *in Glover, J. E., (Ed.)*, Symposium on Archean rocks. *Geological Society of Australia special publication*, Perth, v. 3, p. 11-23.

Ashley, P.M., 1983. Geochemistry and wallrock alteration phenomena at the Scuddles deposit, Golden Grove district, Western Australia, with application to volcanogenic massive sulphide exploration. Regional Studies Group, Minerals Department, ESSO Australia Limited.

Ashley, P.M., 1984. Wallrock alteration at the Scuddles volcanogenic massive sulphide deposit, Golden Grove district, Western Australia. *Geoscience in the development of natural resources, 7th AGC, Geological Society of Australia, Abstracts*, v. 12, p. 39-40.

Ashley, P.M., Dudley, R.J., Lesh, R.H., Marr, J.M. and Ryall, A.W., 1988. The Scuddles Cu-Zn prospect, an Archean volcanogenic massive sulfide deposit, Golden Grove district, Western Australia. *Economic Geology*, v. 83, p. 918-951.

Ayres, L.D. and Corfu, F., 1991. Stacking of disparite volcanic and sedimentary units by thrusting in the Archean Favourable Lake greenstone belt, central Canada. *Precambrian Research*, v. 50, p. 221-238.

Barley, M.D. and Groves, D.I., 1984. Constraints on mineralization of the Warrawoona Group. *University of Western Australia, Geological Department University Extension Publication*, v. 9, p. 54-67.

Barley, M.D. and Groves, D.I., 1987. Hydrothermal alteration of Archaean supracrustal sequences in the central Norseman-Wiluna Belt, Western Australia: A brief review *in Ho, S.E. and Groves, D. I., (Eds.)*, Recent advances in understanding Precambrian Gold deposits. *Geology Department and University Extension, University of Western Australia*, Perth, v. 11, p. 51-56.

Barley, M.E. and Groves, D.I., 1990. Deciphering the tectonic evolution of Archaean

greenstone belts: The importance of contrasting histories to the distribution of mineralization in the Yilgarn Craton, Western Australia. *Precambrian Research*, v. 46, p. 3-20.

Barley, M.E., 1992. A review of Archean volcanic-hosted massive sulfide and sulphate mineralisation in Western Australia. *Economic Geology*, v. 87, p. 855-872.

Barley, M.E., Groves, D.I. and Blake, T.S., 1992. Archaean metal deposits related to tectonics: Evidence from Western Australia *in Glover, J. E. and Ho, S. E., (Eds.)*, The Archaean: Terrains, processes and metallogeny. *University of Western Australia*, Perth, v. 22, p. 307-324.

Barnes, H.L., 1979. Solubilities of ore minerals *in Barnes, H. L., (Ed.)*, Geochemistry of hydrothermal ore deposits. Wiley Interscience, New York, v. 798.

Barrett, T.J., Cattalani, S., Chartrand, F. and Jones, P., 1991. Massive sulfide deposits of the Noranda area, Quebec. II. The Aldermac mine. *Canadian Journal of Earth Sciences*, v. 28, p. 1301-1327.

Barrett, T.J., Cattalani, S., Hoy, L., Riopel, J. and LaFleur, P.J., 1992. Massive sulfide deposits of the Noranda area, Quebec. IV. The Mobrun mine. *Canadian Journal of Earth Sciences*, v. 29, p. 1349-1374.

Barrett, T.J., Cattalani, S. and MacLean, W.H., 1993. Volcanic lithogeochemistry and alteration at the Delbridge massive sulfide deposit, Noranda, Quebec. *Journal of Geochemical Exploration*, v. 48, p. 135-173.

Barrett, T.J., MacLean, W.H., Cattalani, S. and Hoy, L., 1993. Massive sulphide deposits of the Noranda Area, Quebec. V. The Corbett Mine. *Canadian Journal of Earth Sciences*, v. 30, p. 1934-1954.

Barrie, C.T. and Hannington, M.D., 1997. Classification of VMS deposits based on host rock compositions *in Barrie, C. T. and Hannington, M. D., (Eds.)*, Volcanic associated massive sulfide deposits: Processes and examples in modern and ancient settings. *Gelogical Association of Canada shortcourse*, Ottawa, p. 1-12.

Barton, P.B.J., 1978. Some ore textures involving sphalerite from the Furutobe Mine, Akita Prefecture, Japan. *Economic Geology*, v. 28, p. 293-200.

Barton, P.B., Jr., and Bethke, P.M., 1987. Chalcopyrite disease in sphalerite: Pathology and epidomiology. *American Mineralogist*, v. 72, p. 451-467.

Barton, P.B., and Skinner, B.J., 1979. Sulfide mineral stability *in Barnes, H. L. (Ed.)*, Geochemistry of hydrothermal ore deposits, second edition, New York, Wiley and Sons, p. 278-403.

Bates, R.L. and Jackson, J.A., 1987. Glossary of geology. American Geological Institute, Virginia, 788 p.

Baxter, J.L., 1974. Murgoo, Western Australia. 1:250,000 geological series with explanatory notes. *Western Australia Geological Survey*, Perth.

Baxter, J.L., 1982. Stratigraphic and structural setting of the Warriedar Fold Belt *in Baxter, J. L., (Ed.)*, Archean geology of the southern Murchison: Excursion Guide. *Geological Society of Australia.*

Baxter, J.L. and Lipple, S.L., 1985. Perenjori, Western Australia. 1:250,000 geological series with explanatory notes. *Geological Survey of Western Australia*, Perth.

Bearley, A.J., 1988. Chloritoid from low-grade pelitic rocks in North Wales. *Mineralogical Magazine*, v. 52, p. 394-396.

Becker, R.H. and Clayton, R.N., 1976. Oxygen isotope study of a Precambrian banded iron-formation, Hamersley Range, Western Australia. *Geochemica et Cosmochimica Acta*, v. 40, p. 1153-1165.

Ben-Avraham, Z. and Zoback, M.D., 1992. Transform-normal extension and asymmetric

basins: An alternative to pull-apart models. *Geology*, v. 20, p. 423-426.

Berry, R.F., Huston, D.L., Stolz, A.J., Hill, A.P., Beams, S.D., Kuronen, U. and Taube, A., 1992. Stratigraphy, structure, and volcanic hosted mineralization of the Mount Windsor subprovince, north Queensland, Australia. *Economic Geology*, v. 87, p. 739-762.

Berry, R.F. and Keele, R.A., 1997. Cambrian tectonics and mineralisation in western Tasmania. *Mining Geology Conference*, Launceston 10-14, p. 13-16.

Beukes, N.J., Klein, C., Kaufmann, A.J. and Hayes, J.M., 1990. Carbonate petrography, kerogen distribution and carbon and oxygen isotope variations in an early Proterozoic transition from limestone to iron-formation deposition, Transvaal Supergroup. *Economic Geology*, v. 85, p. 663-690.

Bigeleisen, J., Perlman, M.L. and Prosser, H.C., 1952. Conversion of hydrogenic materials to hydrogen for isotopic analysis. *Analytical Chemistry*, v. 24, p. 1356.

Binns, R.A. and Scott, S.D., 1993. Actively forming polymetallic sulfide deposits associated with felsic volcanic rocks in the eastern Manus back-arc basin, Papua New Guinea. *Economic Geology*, v. 88, p. 2226-2236.

Blattner, P., Braithwaite, W.R. and Glover, R.B., 1983. New evidence on magnetite oxygen isotope geothermometers at 175° and 112°C in Wairakei steam pipelines (New Zealand). *Chemical Geology (Isotope Geoscience)*, v. 1, p. 195-204.

Bottinga, Y. and Javoy, M., 1973. Comments on oxygen isotope geothermometry. *Earth and Planetary Science Letters*, v. 20, p. 250-265.

Bowins, R.J. and Crocket, J.H., 1994. Sulfur and carbon isotopes in Archean banded iron formations: Implications for sulfur sources. *Chemical Geology (Isotope Geoscience Section)*, v. 111, p. 307-323.

Boyd, G. and Frankcombe, K.F., 1994. Geophysical responses over the Scuddles VMS deposit *in Dentith, M. C., Frankcombe, K. F., Ho, S. E., Shepherd, J. M., Groves, D. I. and Trench, A., (Eds.)*, Geophysical signatures of Western Australian mineral deposits. *Australian Society of Exploration Geophysics special publication*, Perth, v. 7, p. 133-144.

Bradley, A., 1997. The geology and genesis of the chlorite-carbonate alteration in the footwall of the Hellyer VHMS deposit. *Unpub. B.Sc. Hons. Thesis*, University of Tasmania.

Brewster, G.R., 1980. Effect of chemical pretreatment on x-ray powder diffraction characteristics of clay minerals derived from volcanic ash. *Clays and Clay Minerals*, v. 28, p. 303-310.

Browning, P., Groves, D.I., Blockley, J.G. and Rosman, K.J.R., 1987. Lead isotope constraints on the age and source of gold mineralization in the Archean Yilgarn Block, Western Australia. *Economic Geology*, v. 82, p. 971-986.

Cameron, E.M. and Hattori, K., 1987. Archean sulphur cycle: Evidence from sulphate minerals and isotopically fractionated sulphides in Superior Province, Canada. *Chemical Geology (Isotope Geoscience Section)*, v. 65, p. 341-358.

Capaccioni, B. and Coniglio, S., 1995. Varicolored and vesiculated tuffs from La Fossa volcano, Vulcano Island (Aeolian Archipelago, Italy): Evidence of syndepositional alteration processes. *Bulletin of Volcanology*, v. 57, p. 61-70.

Card, K.D., 1990. A review of the Superior Province of the Canadian Shield, a product of Archean accretion. *Precambrian Research*, v. 48, p. 99-156.

Carey, S.N. and Sigurdsson, H., 1984. A model of volcanogenic sedimentation in marginal basins *in Kokelaar, B. P. and Howells, M. F., (Eds.)*, Marginal Basin Geology: Volcanic and associated sedimentary and tectonic processes in modern and ancient marginal basins. *Geological Society special publication*, v. 16, p. 37-58.

Cas, R.A.F. and Wright, J.V., 1988. Volcanic successions modern and ancient: A geological

approach to processes, products and successions. Allen and Unwin, Sydney, 528 p.

Castro, L.O., 1994. Genesis of banded iron formations. *Economic Geology*, v. 89, p. 1384-1397.

Cathles, L.M., Guber, A.L., Lenagh, T.C. and Dudas, F.O., 1983. Kuroko-type massive sulfide deposits of Japan: Products of an aborted island-arc rift. *Economic Geology Monograph*, v. 5, p. 96-114.

Cathles, L.M., 1983. An analysis of the hydrothermal system responsible for massive sulfide deposition in the Hokuroku Basin of Japan. *Economic Geology Monograph*, v. 5, p. 439-487.

Cathles, L.M., 1993. Oxygen isotope alteration in the Noranda mining district, Abitibi Greenstone Belt, Quebec. *Economic Geology*, v. 88, p. 1483-1511.

Cerling, T.E., Brown, F.H. and Bownam, J.R., 1985. Low-temperature alteration of volcanic glass: Hydration, Na, K, $\delta^{18}O$ and Ar mobility. *Chemical Geology*, v. 52, p. 281-293.

Clark, B.R. and Kelly, W.C., 1973. Sulphide deformation studies, I. Experimental deformation of pyrrhotite to 2000 bars and 500°C. *Economic Geology*, v. 68, p. 332-352.

Claypool, G.E., Holser, W.T., Kaplan, I.R., Sakai, H. and Zak, I., 1980. The age curves of sulfur and oxygen isotopes in marine sulfate and their mutual interpretation. *Chemical Geology*, v. 28, p. 199-260.

Clayton, R.N. and Mayeda, T.K., 1963. The use of bromine pentafluoride in the extraction of oxygen from oxides and silicates for isotopic analysis. *Geochemica et Cosmochima Acta*, v. 27, p. 43-52.

Clifford, B., MacMahon, M. and Sheppy, N., 1990. Geological setting of the Scuddles and Gossan Hill Archean volcanogenic massive sulphide deposits at Golden Grove *in Ho, S. E., Glover, J. E., Myers, J. S. and Muhling, J. R., (Eds.)*, Third international Archean symposium. *Geology Department and University Extension, University of Western Australia*, Perth, v. 21, p. 19-201.

Clifford, B.A., 1992. Facies and palaeoenvironment analysis of the Archean volcanic-sedimentary succession hosting the Golden Grove Cu-Zn massive sulphide deposits, Western Australia. *Unpub. Ph.D. Thesis*, Monash University.

Cloud, P., 1976. The begining of biospheric evolution and their biogeochemical conseqeunces. *Paleobiology*, v. 2, p. 351-387.

Coomer, P.G. and Schwarcz, H.P., 1974. Sulfur isotopic study of a massive, volcanogenic Archaean sulfide ore deposit. *Geological Society of America, Abstracts with Programs*, v. 6, p. 693-694.

Costa, U.R., Barnett, R.L. and Kerrich, R., 1983. The Mattagmi Lake mine Archean Zn-Cu sulfide deposit, Quebec: Hydrothermal coprecipitation of talc and sulfides in a sea floor brine pool-evidence from geochemistry, $^{18}O/^{16}O$ and mineral chemistry. *Economic Geology*, v. 78, p. 1144-1203.

Cox, S.F., Etheridge, M.A. and Hobbs, B.E., 1981. The experimental ductile deformation of polycrystalline and single crystal pyrite. *Economic Geology*, v. 76, p. 2105-2117.

Craig, J.R. and Vaughan, D.J., 1981. Ore microscopy and ore petrography. Wiley Interscience, New York, 409 p.

Craig, J.R. and Vokes, F.M., 1992. Ore mineralogy of the Appalachian-Caledonian stratabound sulfide deposit. *Ore Geology Reviews*, v. 7, p. 77-123.

Crowe, D.E., 1994. Preservation of original hydrothermal $\delta^{34}S$ values in greenschist to upper amphibolite volcanogenic massive sulphide deposits. *Geology*, v. 22, p. 873-876.

Date, J., Watanabe, Y. and Saeki, Y., 1983. Zonal alteration around the Fukazawa Kuroko deposits, Akita Prefecture, Northern Japan. *Economic Geology Monograph*, v. 5, p. 365-386.

Davidson, G.J., 1992. Hydrothermal geochemistry and ore genesis of sea-floor volcanogenic copper-bearing oxide ores. *Economic Geology*, v. 87, p. 889-912.

Davis, E.E., Goodfellow, W.D., Bornhold, B.D., Adshead, J., Blaise, B., Villinger, H. and

Le Cheminant, G.M., 1987. Massive sulfides in a sedimented rift valley, northern Juan de Fuca Ridge. *Earth and Planetary Science Letters*, v. 82, p. 49-61.

de la Hunty, L.E., 1973. Cue, Western Australia. 1:250,000 geological series with explanatory notes. *Western Australia Geological Survey*, Perth.

de Laeter, J.R., Libby, W.G. and Trendall, A.F., 1981. The older Precambrian geochronology of Western Australia *in Glover, J. E. and Groves, D. I., (Eds.)*, Archean Geology. *Geological Society of Australia*, Perth, v. 7, p. 145-157.

Deer, W.A., Howie, R.A. and Zussman, J., 1992. An introduction to rock-forming minerals. Longman, Hong Kong, 696 p.

DeWit, M.J., Hart, R., Martin, A. and Abbott, P., 1982. Archean abiogenic and probably biogenic structures associated with mineralized hydrothermal vent systems and regional metasomatism, with implications for greenstone belt structures. *Economic Geology*, v. 77, p. 1783-1802.

DiMarco, M.J. and Lowe, D.R., 1989. Petrography and provenance of silicified early Archaean volcaniclastic sandstones, eastern Pilbara Block, Western Australia. *Sedimentology*, v. 36, p. 821-836.

Dimroth, E. and Lichtblau, P., 1979. Metamorphic evolution of Archean hyaloclastites, Noranda area, Quebec, Canada. Part I: Comparison of Archean and Cenozoic sea-floor metamorphism. *Canadian Journal of Earth Sciences*, v. 16, p. 1315-1340.

Dolye, M., 1996. Volcanic influences in the formation of iron oxide-silica deposits in a volcanogenic-massive sulfide terrain, Mount Windsor Volcanic belt, Queensland. *AMIRA Project P439*, October 1996, p. 87-142.

Donnelly, T.H., Lambert, I.B., Oehler, D.Z., Hallberg, J.A., Hudson, D.R., Smith, J.W., Bavinton, O.A. and Golding, L., 1977. A reconnaissance study of stable isotope ratios in Archaean Rocks from the Yilgarn Block, Western Australia. *Journal of the Geological Society of Australia*, v. 24, p. 409-420.

Downs, R.C., 1993. Syndepositional fault controls on the Hellyer volcanic-hosted massive sulphide deposit. *Unpub. M.Sc. Thesis*, University of Tasmania.

Doyle, M.G., 1997. A Cambro-Ordovician submarine volcanic succession hosting massive sulfide mineralisation: Mount Windsor Subprovince, Queensland. *Unpub. Ph.D. Thesis*, University of Tasmania.

Dudley, R.J., Ashley, P.M., Ryall, A.W. and May, E.R., 1984. Scuddles: An Archaean-aged volcanogenic massive sulphide deposit, Golden Grove, Western Australia. *Geological Society of Australia, Abstracts*, v. 12, p. 153-154.

Duhig, N.C., Stoltz, J., Davidson, G.J. and Large, R.R., 1992. Cambrian microbial and silica gel textures in silica iron exhalites from the Mount Windsor volcanic belt, Australia: Their petrography, chemistry, and origin. *Economic Geology*, v. 87, p. 764-784.

Eastoe, C.J., Gustin, M.S., Hurlbut, D.F. and Orr, R.L., 1990. Sulfur isotopes in Early Proterozoic volcanogenic massive sulfide deposits: New data from Arizona and implications for ocean chemistry. *Precambrian Research*, v. 46, p. 353-364.

Eastoe, C.J. and Gustin, M.M., 1996. Volcanogenic massive sulfide deposits and anoxia in the Phanerozoic oceans. *Ore Geology Reviews*, v. 10, p. 179-197.

Eichler, J., 1976. Origin of the Precambrian banded iron-formations *in Wolf, K. H., (Ed.)*, Handbook of strata-bound and stratiform ore deposits. II. Regional studies and specific deposits, Au, U, Fe, Mn, Hg, Sb, W and P deposits. Elsevier Scientific Publishing Company, Amsterdam, v. 7, p. 157-201.

Eldridge, C.S., Barton, P.B. and Ohmoto, H., 1983. Mineral textures and their bearing on formation of the Kuroko orebodies. *Economic Geology Monograph*, v. 5, p. 241-281.

Elias, M., 1982. Belele, Western Australia. 1:250,000 geological series with explanatory notes. *Western Australia Geological Survey*, Perth.

Everett, C.E., 1990. The siting and timing of gold mineralization, and its relation to base-metals in the Gossan Hill volcanogenic massive sulfide deposit of the Murchison Province. *Unpub. B.Sc. Hons. Thesis*, University of Western Australia, 110 p.

Ewers, W.E., 1980. Chemical conditions for the precipitation of banded iron-formations *in Trudinger, P. A., Walter, M. R. and Ralph, M. J., (Eds.)*, Biogeochemistry of Ancient and Modern Environments. Springer-Verlag, New York, p. 83-92.

Ferenczi, P.A., 1994. Are Tennant Creek style ironstone-related gold-copper-bismuth deposits unique? A review of available data and a comparison with possible analogous deposits *in Hallenstein, C. P., (Ed.)*, Australian mining looks north: Challenges and choices, *Australasian Institute of Mining and Metallurgy*, Darwin, p. 171-177.

Field, C.W. and Fifarek, R.H., 1985. Light stable-isotope systematics in the epithermal environment *in Berger, B. R. and Bethke, P. M., (Eds.)*, Geology and geochemistry of epithermal systems. *Society of Economic Geologists, reviews in economic geology*, v. 2, p. 99-128.

Fisher, R.V., 1965. Settling velocity of glass shards. *Deep Sea Research*, v. 12, p. 345-353.

Fisher, R.V., 1984. Submarine volcaniclastic rocks *in Kokelaar, B. P. and Howells, M. F., (Eds.)*, Marginal basin geology: Volcanic and associated sedimentary and tectonic processes in modern and ancient marginal basins. *Geological Society special publication*, v. 16, p. 5-27.

Fisher, R.S. and Land, L.S., 1986. Diagenetic history of Eocence Wilcox sandstones, south-central Texas. *Geochimica et Cosmochimica Acta*, v. 50, p. 551-561.

Fiske, R.S., 1969. Recognition and significance of pumice in marine pyroclastic rocks. *Geological Society of America Bulletin*, v. 80, p. 1-8.

Fletcher, I.R., Libby, W.G. and Rosman, K.J.R., 1994. Sm-Nd model ages of granitoid rocks in the Yilgarn Craton. *Geological Survey of Western Australia Report*, v. 37, p. 61-73.

Floyd, P.A. and Winchester, J.A., 1978. Identification and discrimination of altered and metamorphosed volcanic rocks using immobile elements. *Chemical Geology*, v. 21, p. 291-306.

Ford, R.M., 1992. Evidence for the syngenetic copper mineralization at the Scuddles Cu-Zn volcanogenic massive sulphide deposit of the Murchison Province, Western Australia. *Unpub. B.Sc. Hons. Thesis*, University of Western Australia.

Franklin, J.M., Kasarda, J. and Poulsen, K.H., 1975. Petrology and chemistry of the alteration zone of the Mattabi massive sulfide deposit. *Economic Geology*, v. 70, p. 63-73.

Franklin, J.M., Lydon, J.W. and Sangster, D.F., 1981. Volcanic-associated massive sulfide deposits. *Economic Geology, 75th Anniversary Volume*, p. 485-627.

Franklin, J.M., 1993. Volcanic-associated massive sulphide deposits *in Kirkham, R. V., Sinclair, W. D., Thorpe, R. I. and Duke, J. M., (Eds.)*, Mineral deposit modelling. *Geological Association of Canada Special paper*, v. 40, p. 315-334.

Frater, K.M., 1978. The Golden Grove copper-zinc deposit, Western Australia: An Archean exhalative, volcanogenic occurrence. *Unpub. Ph.D. Thesis*, University of Newcastle.

Frater, K.M., 1983a. Geology of the Golden Grove prospect, Western Australia: A volcanogenic massive sulfide-magnetite deposit. *Economic Geology*, v. 78, p. 875-919.

Frater, K.M., 1983b. Effects of metasomatism and development of quartz 'eyes' in intrusive and extrusive rocks at Golden Grove Cu-Zn deposit, Western Australia. *Transactions of the Institute of Mining and Metallurgy*, v. 92, p. B121-B131.

Frater, K.M., 1985a. Mineralisation at the Golden Grove Cu-Zn deposit, Western Australia. I: Premetamorphic textures of the opaque minerals. *Canadian Journal of Earth Sciences*, v. 22, p. 1-14.

Frater, K.M., 1985b. Mineralization at the Golden Grove Cu-Zn deposit, Western Australia. II: Deformation texture of the opaque minerals. *Canadian Journal of Earth Sciences*, v. 22, p. 15-26.

Friedman, I. and Long, W., 1984. Volcanic glasses, their origins and alteration processes. *Journal of Non-Crystalline Solids*, v. 67, p. 127-133.

Friesen, R.G., Pierce, G.A. and Weeks, R.M., 1982. Geology of the Geco base metal deposit *in Hutchinson, R.W., Spence, C. D. and Franklin, J. M., (Eds.)*, Precambrian sulphide deposits. *Geological Association of Canada*, v. 25, p. 343-363.

Fritz, P., Drimmie, R.J. and Nowocki, V.K., 1974. Preparation of sulfur dioxide for mass spectrometer analyses by combustion of sulfides with copper oxide. *Analytical Chemistry*, v. 46, p. 164-166.

Galley, A.G., 1983. Characteristics of semi-conformable alteration zones associated with volcanogenic massive sulphide districts. *Journal of Geochemical Exploration*, v. 48, p. 175-200.

Galley, A.G., Watkinson, D.H., Jonasson, I.R. and Riverin, G., 1995. The subsea-floor formation of volcanic-hosted massive sulfide: Evidence from the Ansil Deposit, Rouyn-Noranda, Canada. *Economic Geology*, v. 90, p. 2006-2017.

Gallinatti, B.C., 1984. Initiation and collapse of active circulation in a hydrothermal system at the mid-Atlantic Ridge, 23°N. *Journal of Geophysical Research*, v. 89, p. 3275-3289.

Garrels, R.M., 1987. A model for the deposition of microbanded Precambrian iron-formations. *American Journal of Science*, v. 287, p. 91-106.

Gee, R.D., Baxter, J.L., Wilde, S.A. and Williams, I.R., 1981. Crustal development in the Archaean Yilgarn Block, Western Australia *in Glover, J. E. and Groves, D. I., (Eds.)*, Archean Geology. *Geological Society of Australia*, Perth, v. 7, p. 43-56.

Gemmell, J.B. and Large, R.R., 1992. Stringer system and alteration zones underlying the Hellyer volcanic-hosted massive sulfide deposit, Tasmania, Australia. *Economic Geology*, v. 87, p. 620-649.

Gibson, H.L., Watkinson, D.H. and Comba, C.D.A., 1983. Silicification: Hydrothermal alteration in an Archean geothermal system within the Amulet Rhyolite Formation, Noranda, Quebec. *Economic Geology*, v. 78, p. 954-971.

Giles, C.W., 1981. Archaean calc-alkaline volcanism in the Eastern Goldfields Province, Western Australia *in Glover, J. E. and Groves, D. I., (Eds.)*, Archean Geology. *Geological Society of Australia*, Perth, v. 7, p. 275-286.

Gimeno, D., 1994. Genesis of crystal-rich epiclastic rocks from subaqueous silicic lava domes: role of thermal shock on quartz phenocrysts. *Sedimentary Geology*, v. 90, p. 33-47.

Golding, S.D. and Wilson, A.F., 1983. Geochemical and stable isotope studies of the No. 4 lode, Kalgoorlie, Western Australia. *Economic Geology*, v. 78, p. 438-450.

Golding, S.D., McNaughton, N.J., Turner, J.V., Barley, M.E., Groves, D.I., Ho, S.E. and Rock, N.M.S., 1988. Fluid sources and circulation paths for Archaean gold deposits: Constraints from carbon and oxygen isotope studies *in Goode, A. D. T. and Bosma, L. I. (Eds.)*, Bicentennial Gold 88, extended abstracts oral programme, *Geological Society of Australia*, Melbourne, v. 22, p. 217-224.

Golding, S.D., Barley, M.E., Cassidy, K.F., Groves, D.I., Ho, S.E., Hronsky, J.M.A., McNaughton, N.J., Sang, J.H. and Turner, J.V., 1990. Oxygen and hydrogen isotopes *in Ho, S. E., Groves, D. I. and Bennett, J. M., (Eds.)*, Gold deposits of the Archaean Yilgarn Block, Western Australia: Nature, genesis and exploration guides. *Geological Department and University Extension, University of Western Australia, Perth*, v. 20, p. 252-258.

Goodfellow, W.D. and Blaise, B., 1988. Sulfide formation and hydrothermal alteration of hemipelagic sediment in Middle Valley, northern Juan de Fuca Ridge. *Canadian Mineralogist*, v. 26, p. 675-696.

Graham, U.M., Bluth, G.J. and Ohmoto, H., 1988. Sulfide-sulfate chimneys on the East Pacific Rise, 11° and 13°N latitudes. Part I: Mineralogy and paragenesis. *Canadian Mineralogist*, v. 26, p. 487-504.

Green, G.R., Solomon, M. and Walshe, J.L., 1981. The formation of the volcanic-hosted massive sulfide ore deposit at Rosebery, Tasmania. *Economic Geology*, v. 76, p. 304-338.

Green, G.R., Ohmoto, H. and Date, J., 1983. Whole-rock oxygen isotope distribution in the Fukazawa-Kosaka area, Hokuroku district, Japan, and its potential application to mineral exploration. *Economic Geology Monograph*, v. 5, p. 395-411.

Gross, G.A., 1991. Genetic concepts for iron-formation and associated metalliferous sediments. *Economic Geology Mongraph*, v. 8, p. 51-81.

Groves, D.I. and Batt, W.D., 1984. Spatial and temporal variations of Archaean metallogenic associations in terms of evolution of granitoid-greenstone terrains with particular emphasis on the Western Australian shield *in Kroner, A., Manso, G. N. and Goodwin, A. M., (Eds.)*, Archaean geochemistry: The origin and evolution of the Archaean continental crust. Springer-Verlag, Berlin, p. 73-98.

Groves, D.I., Phillips, G.N., Falconer, L.J., Houstoun, S.M., Ho, S.E., Browning, P., Dahl, N. and McNaughton, N.J., 1987. Evidence for an epigenetic origin for BIF-hosted gold deposits in greenstone belts of the Yilgarn Block, Western Australia *in Ho, S. E. and Groves, D. I., (Eds.)*, Recent advances in understanding Precambrian gold deposits. *University of Western Australia, Perth*, v. 11, p. 167-179.

Hallberg, J.A., Johnston, C. and Bye, S.M., 1976. The Archaean Marda Igneous Complex, Western Australia. *Precambrian Research*, v. 3, p. 111-136.

Hallberg, J.A. and Wilson, P., 1983. Relative timing of intrusion in the Eucalyptus area, northeastern Yilgarn Block, Western Australia. *Journal of the Geological Society of Australia*, v. 30, p. 383-392.

Hallberg, J.A. and Giles, C.W., 1986. Archaean felsic volcanism in the northeastern Yilgarn Block, Western Australia. *Australian Journal of Earth Sciences*, v. 33, p. 413-427.

Hannington, M.D. and Scott, S.D., 1989. Sulfidation equilibria as guides to gold mineralisation in volcanogenic massive sulfides: Evidence from sulfide mineralogy and the composition of sphalerite. *Economic Geology*, v. 84, p. 1978-1995.

Hannington, M.D., Poulsen, K.H., Thompson, J.F.H. and Sillitoe, R.H., 1997. Volcanogenic gold and epithermal-style mineralization in the VMS environment. *in Barrie, C. T. and Hannington, M. D., (Eds.)*, Volcanic-associated massive sulfide deposits: Processes and examples in modern and ancient settings. *Geological Association of Canada shortcourse manual*, Ottawa, p. 183-214.

Hannington, M.D., Bleeker, W. and Kjarsgaard, I., in press. Sulfide mineralogy, geochemistry, and ore genesis of the Kidd Creek deposit: Part I. North, central, and south orebodies. *Economic Geology*.

Harris, M.F., Ashley, P.M., Dudley, R.J., Lesh, R.H., Marr, J.M. and Ryall, A.W., 1982. The Gossan Hill and Scuddles volcanogenic massive sulphide deposits of Golden Grove, Western Australia *in Baxter, J. L., (Ed.)*, Archean geology of the southern Murchison: Excursion guide. *Geological Society of Western Australia*, Perth, p. 41-73.

Hassler, S.W. and Simonson, B.M., 1989. Deposition and alteration of volcaniclastic strata in two large, early, Proterozoic iron-formations in Canada. *Canadian Journal of Earth Sciences*, v. 26, p. 1574-1585.

Hattori, K., Finley, A.F. and Krouse, H.R., 1983. Sulfur isotope abundances in Aphebian clastic rocks: Implications for the coeval atmosphere. *Nature*, v. 302, p. 323-326.

Haymon, R.M. and MacDonald, K.C., 1985. The geology of deep-sea hot springs. *American Scientist*, v. 73, p. 441-449.

Heiken, G. and Wohletz, K., 1991. Fragmentation processes in explosive volcanic eruptions *in Fisher, R. V. and Smith, G. A., (Eds.)*, Sedimentation in volcanic settings. *SEPM special publication*, v. 45, p. 19-26.

Hekinian, R., Fevrier, M., Bischoff, J.L., Picot, P. and Shanks, W.C., 1980. Sulfide deposits from the East Pacific Rise near 21°N. *Science*, v. 207, p. 1433-1444.

Hemley, J.J., Cygan, G.L., Fein, J.B., Robinson, G.R. and D'Angelo, W.M., 1992. Hydrothermal ore-forming processes in the light of studies in rock-buffered systems. I: Iron-copper-zinc-lead sulfide solubility relations. *Economic Geology*, v. 87, p. 1-22.

Henley, R.W. and Thornley, P., 1979. Some geothermal aspects of polymetallic massive sulfide formation. *Economic Geology*, v. 74, p. 1600-1612.

Herzig, P.M., Becker, K.P., Stoffers, P., Backer, H. and Blum, N., 1988. Hydrothermal silica chimney fields in the Galapagos spreading centre at 86° West. *Earth and Planetary Science Letters*, v. 89, p. 261-272.

Hesse, R., 1988. Silica diagenesis: Origin of inorganic and replacement chert. *in McIlreath, I. and Morrow, D., (Eds.)*, Diagenesis. *Geological Association of Canada*, v. 4, p. 253-275.

Hesse, R., 1989. Origin of chert: Diagenesis of biogenic siliceous sediments. *Geoscience Canada*, v. 15, p. 171-192.

Hey, M.H., 1954. A new review of the chlorites. *The Mineralogical Magazine*, v. 30, p. 277-292.

Hill, A.P., 1996. Structure, volcanic setting, hydrothermal alteration and genesis of the Thalanga massive sulphide deposit. *Unpub. Ph.D. Thesis*, University of Tasmania.

Hoagland, J.R. and Elders, W.A., 1978. Hydrothermal mineralogy and isotope geochemistry of Cierro Prieto geothermal field, Mexico, 1. Hydrothermal mineral zonation. *Geothermal Resource Council Transactions*, v. 2, p. 283-286.

Hodder, A.P.W., Green B.E. and Lowe, D.J., 1990. A two-stage model for the formation of clay minerals from tephra-derived volcanic glass. *Clay Minerals*, v. 25, p. 313-327.

Holland, H.D., 1984. The chemical evolution of the Atmosphere and the oceans. Princeton University Press, Princeton, 582 p.

Hoy, L.D., 1993. Regional evolution of hydrothermal fluids in the Noranda district, Quebec: Evidence from $\delta^{18}O$ values from volcanogenic massive sulfide deposits. *Economic Geology*, v. 88, p. 1526-1541.

Humphris, S.E, Herzig, P.M, Miller, D.J., *et al.*, 1996. Drilling an active hydrothermal system on a sediment-free slow spreading ridge, ocean drilling program Leg 158. *Proceedings of the Ocean Drilling Program Initial Reports*, v. 158, College Station (Ocean Drilling Program).

Huston, D.L. and Large, R.R., 1987. Genetic and exploration significance of the zinc ratio (100Zn/(Zn+Pb)) in massive sulfide systems. *Economic Geology*, v. 82, p. 1521-1539.

Huston, D.L., 1988. Aspects of the geology of massive sulfide deposits from the Balcooma district, northern Queensland and Rosebery, Tasmania: Implications for ore genesis. *Unpub. Ph.D. Thesis*, University of Tasmania.

Huston, D.L. and Large, R.R., 1989. A chemical model for the concentration of gold in volcanogenic massive sulphide deposits. *Ore Geology Reviews*, v. 4, p. 171-200.

Huston, D.L., 1990. The stratigraphic and structural setting of the Balcooma volcanogenic massive sulphide lenses, northern Queensland. *Australian Journal of Earth Sciences*, v. 37, p. 423-440.

Huston, D.L., Bottrill, R.S., Creelman, R.A., Khin Zaw, Ramsden, A.R. and Rand, S., 1992. Geologic and geochemical controls on the mineralogy and grain size of gold-bearing phases in eastern Australian volcanogenic massive sulfide deposits. *Economic Geology*, v. 87, p. 785-811.

Huston, D.L., Power, M. and Large, R.R., 1992a. Laser ablation of sulphur isotope analysis at the University of Tasmania: Preliminary results from a new technique with research and exploration applications. *Bulletin of the Geological Survey of Tasmania*, v. 70, p. 93-95.

Huston, D.L., Bolger, C. and Cozens, G., 1993. A comparison of mineral deposits at the Gecko and White Devil deposits: implications for ore genesis in the Tennant Creek district, Northern Territory, Australia. *Economic Geology*, v. 88, p. 1198-1225.

Huston, D.L., Kuronen, U. and Stolz, J., 1995a. Waterloo and Agincourt prospects, northern Queensland: Contrasting styles of mineralization within the same volcanogenic hydrothermal system. *Australian Journal of Earth Sciences*, v. 42, p. 203-221.

Huston, D.L., Power, M., Gemmell, J.B. and Large, R.R., 1995b. Design, calibration and geological application of the first operational Australian laser ablation sulphur isotope microprobe. *Australian Journal of Earth Sciences*, v. 42, p. 549-555.

Huston, D.L., Taylor, B.E., Bleeker, W., Stewart, B., Cook, R. and Koopman, E.R., 1995c. Isotope mapping around the Kidd Creek deposit, Onatrio: Application to exploration and comparison with other geochemical indicators. *Exploration Mining Journal*, v. 4, p. 175-185.

Huston, D.L., 1997. Stable isotopes and their significance for understanding the genesis of volcanic-hosted massive sulfide deposits: A review *in Barrie, C. T. and Hannington, M. D., (Eds.)*, Volcanic-associated massive sulfide deposits: Processes and example in modern and ancient settings shortcourse. *Geological Association of Canada shortcourse manual*, Ottawa, p. 157-181.

Hutchinson, R.W. and Searle, D.L., 1971. Stratabound pyrite deposits in Cyprus and relations to other sulfide ores. *Society of Mining Geology of Japan, special issue*, v. 3, p. 198-205.

Hutchinson, R.W., 1982. Syn-depositional hydrothermal processes and Precambrian sulfide deposits *in Hutchinson, R. W., Spence, C. D. and Franklin, J. M., (Eds.)*, Precambrian sulphide deposits. *Geological Association of Canada special paper*, v. 25, p. 761-791.

Iijima, A., 1974. Clay and zeolitic alteration zones surrounding Kuroko deposits in the Hokuroku district, northern Akita, as submarine hydrothermal-diagenetic alteration products. *Mining Geology special issue*, v. 6, p. 267-289.

Irvine, T.N. and Baragar, W.R., 1971. A guide to the chemical classification of the common volcanic rocks. *Canadian Journal of Earth Sciences*, v. 8, p. 523-548.

Ishihara, S. and Sasaki, A., 1978. Sulfur of Kuroko deposits-a deep seated origin. *Mining Geology*, v. 28, p. 361-367.

Ishikawa, Y., Sawaguchi, T., Iwaya, S. and Horiachi, M., 1976. Delineation of prospecting targets for Kuroko deposits based on modes of volcanism underlying dacite and alteration halos. *Mining Geology*, v. 26, p. 105-117 (in Japanese with English abstract).

Isley, A.E., 1995. Hydrothermal plumes and the delivery of iron to banded iron formations. *Journal of Geology*, v. 103, p. 169-185.

Jackson, M.L., 1956. Dispersion of soil minerals: Removal of chemical cements and development of electrostatic charge *in Jackson, M. L., (Ed.)*, Soil chemical analysis. University of Wisconsin, Wisconsin, p. 31-36.

Jiang, S.Y. and Palmer, M.R., 1996. Mn-rich ilmenite for the Sullivan Pb-Zn-Ag deposit, British Columbia. *The Canadian Mineralogist*, v. 34, p. 29-36.

Johnson, J.W., Oelkers, E.H. and Helgeson, H.C., 1992. SUPCRT92: A software package for calculating the standard molal thermodynamic properties of minerals, gases, aqueous species and reaction from 1 to 5000 bars and 0°C to 1000°C. *Computers and Geosciences* , v. 18, p. 899-947.

Kajiwara, Y., 1971. Sulfur isotope study of the Kuroko-ores of the Shankanai No. 1 deposits, Akita Prefecture, Japan. *Geochemical Journal*, v. 4, p. 157-181.

Kalogeropoulos, S.I. and Scott, S.D., 1983. Mineralogy and geochemistry of tuffaceous

exhalites (Tetsusekiei) of the Fukazawa Mine, Hokuroku district, Japan *in Ohmoto, H. and Skinner, B. J., (Eds.)*, The Kuroko and related volcanogenic massive sulphide deposits. *Economic Geology Monograph*, v. 5, p. 412-432.

Kalogeropoulos, S.I. and Scott, S.D., 1989. Mineralogy and geochemistry of an Archean tuffaceous exhalite: The Main Contact Tuff, Millenbach mine area, Noranda, Quebec. *Canadian Journal of Earth Sciences*, v. 26, p. 88-105.

Kappel, E.S. and Franklin, J.M., 1989. Relationships between geologic development of ridge crests and sulfide deposits in the northeast Pacific Ocean. *Economic Geology*, v. 84, p. 485-505.

Karhu, J. and Epstein, S., 1986. The implication of the oxygen isotope records in coexisting cherts and phosphates. *Geochemica et Cosmochimica Acta*, v. 50, p. 1745-1756.

Karhu, J.A., Nurmi, P.A. and O'Brien, H.E., 1993. Carbon and oxygen isotope ratios of hydrothermal carbonates associated with gold mineralization in the late Archean Hattu schist belt, Ilomantsi, eastern Finland *in Nurmi, P. A. and Sorjonen-Ward, P., (Eds.)*, Geological development, gold mienralization and exploration methods in the Late Archean Hattu schist belt, Ilomantsi, eastern Finland. *Geological Survey of Finland special paper*, v. 17, p. 307-316.

Kasting, J.F., Holland, H.D. and Kump, L.R., 1992. Atmospheric evolution: The rise of oxygen *in Schopf, J. W. and Klein, C., (Eds.)*, The Proterozoic biosphere: a multidisciplinary study. Cambridge University Press, New York, p. 159-164.

Kelly, W.C. and Clark, B.R., 1975. Sulphide deformation studies: III. Experimental deformation of chalcopyrite to 2000 bars and 500°C. *Economic Geology*, v. 70, p. 431-453.

Kerr, D.J. and Gibson, H.L., 1993. A comparison of the Horne volcanogenic massive sulfide deposit and intracauldron deposits of the Mine Sequence, Noranda, Quebec. *Economic Geology*, v. 88, p. 1419-1442.

Kerrich, R., 1987. The stable isotope geochemistry of Au-Ag vein deposits in metamorphic rocks *in Kyser, T. K., (Ed.)*, Shortcourse in stable isotope geochemistry of low temperature fluids. *Mineralogical Association of Canada*, Saskatoon, v. 13, p. 287-336.

Kerrich, R., 1990. Carbon-isotope systematics of Archean Au-Ag vein deposits in the Superior Province. *Canadian Journal of Earth Sciences*, v. 27, p. 40-56.

Khin Zaw, 1991. The effect of Devonian metamorphism on the mineralogy and geochemistry of the Cambrian VMS deposits in the Rosebery-Hercules district, western Tasmania. *Unpub. Ph.D. Thesis*, University of Tasmania.

Khin Zaw and Large, R.R., 1992. The precious metal-rich South Hercules mineralization, western Tasmania: A possible subsea-floor replacement volcanic-hosted massive sulfide deposit. *Economic Geology*, v. 87, p. 931-952.

Khin Zaw, Huston, D.L., Large, R.R., Mernagh, T. and Hoffman, C.F., 1994. Microthermometry and geochemistry of fluid inclusions from the Tennant Creek gold-copper deposits: Implications for ore deposition and exploration. *Mineralium Depsosita*, v. 29, p. 288-300.

Klemd, R., Maiden, K.J., Okrusch, M. and Richter, P., 1989. Geochemistry of the Matchless metamorphosed massive sulfide deposit, south west Africa/Namibia: Wall-rock alteration during submarine ore-forming processes. *Economic Geology*, v. 84, p. 603-617.

Knauth, P.L. and Lowe, D.R., 1978. Oxygen isotope geochemistry of cherts from the Onverwact Group (3.4 billion years), Transvaal, South Africa, with implications for secular variations in the isotopic composition of cherts. *Earth and Planetary Science Letters*, v. 41, p. 209-222.

Knauth, L.P., 1994. Petrogenesis of chert *in P.J. Heaney, P. T., Prewitt, C. T. and Gibbs, G.V., (Eds.)*, Silica: Physical behaviour, geochemistry and materials applications. *Mineralogical Society of America reviews in mineralogy*, v. 29, p. 233-258.

Knuckey, M.J., Comba, C.D.A. and Riverin, G., 1982a. Structure, metal zoning and alteration at the Millenbach deposit, Noranda, Quebec *in Hutchinson, R. W., Spence, C. D. and Franklin, J. M.,*

(Eds.), Precambrian sulphide deposits. *Geological Association of Canada*, v. 25, p. 255-295.

Knuckey, M.J. and Watkins, J.J., 1982b. The geology of the Corbet massive sulphide deposit Noranda district, Quebec, Canada *in Hutchinson, R. W., Spence, C. D. and Franklin, J. M., (Eds.)*, Precambrian sulphide deposits. *Geological Association of Canada*, v. 25, p. 297-319.

Kontak, D.J., Smith, P.K., Kerrich, R. and King, R.W., 1988. Distribution of carbonate $\delta^{13}C$ and $^{87}Sr/^{86}Sr$ in gold deposits of the Meguma terrane, Nova Scotia and Superior Province, Canada: implication for C and Sr source reservoirs *in Goode, A. D. T. and Bosma, L. I., (Eds.)*, Bicentennial gold 88, extended abstracts oral programme. *Geological Society of Australia*, Melbourne, v. 22, p. 225-229.

Koski, R.A., Shanks III, W.C., Bohrson, W.A. and Oscarson, R.L., 1988. The composition of massive sulfide deposits from the sediment-covered floor of Escanaba Trough, Gorda Ridge: Implications for depositional processes. *Canadian Mineralogist*, v. 26, p. 655-673.

Krasnov, S., Stepanova, T. and Stepanov, M., 1994. Chemical composition and formation of a massive sulfide deposit, Middle Valley, northern Juan De Fuca Ridge (Site 856). *Proceedings of the Ocean Drilling Program scientific results*, v. 139, p. 353-372.

Krupp, R., Oberthur, T. and Hirdes, W., 1994. The Early Precambrian atmosphere and hydrosphere: Thermodynamic constrains from mineral deposits. *Economic Geology*, v. 89, p. 1581-1598.

Kuroda, H., 1983. Geologic characteristics and formation environments of the Furutobe and Matsuki Kuroko deposits, Akita Prefecture, northeast Japan. *Economic Geology Monograph*, v. 5, p. 149-166.

Lambert, R.J., 1976. Archean thermal regimes, crustal and upper mantle temperatures, and a progressive evolutionary model for the earth *in Windley, B. F., (Ed.)*, The early history of the Earth. Wiley, New York, p. 363-376.

Lambert, I.B., Donnelly, T.H., Dunlop, J.S.P. and Groves, D.I., 1978. Stable isotopic compositions of early Archaean sulphate deposits of probable evaporitic and volcanogenic origins. *Nature*, v. 276, p. 808-811.

Lambert, I.B., 1978. Sulphur isotope investigation of Archean mineralisation and some implications concerning geobiochemical evolution *in Glover, J. E. and Groves, D. I., (Eds.)*, Archean cherty metasediments: Their sedimentology, micopalaeontology, biogeochemistry and significance to mineralisation. *Publications of Geology Department and Extension Service, University of Western Australia*, Perth, v. 2, p. 45-56.

Lambert, I.B. and Groves, D.I., 1982. Early earth evolution and metallogeny *in Wolf, K. H., (Ed.)*, Handbook of strata-bound and stratiform ore deposits. Elsevier, Amsterdam, v. 8, p. 378-425.

Large, R.R., 1974. Hydrothermal mineral zonation at the Juno mine, Tennant Creek goldfield, central Australia. *Economic Geology*, v. 69, p. 1183.

Large, R.R., 1975. Zonation of hydrothermal minerals at the Juno Mine, Tennant Creek Goldfield, Central Australia. *Economic Geology*, v. 70, p. 1387-1413.

Large, R.R., 1977. Chemical evolution and zonation of massive sulfide deposits in volcanic terrains. *Economic Geology*, v. 72, p. 549-572.

Large, R.R., Huston, D.L., McGoldrick, P.J., Ruxton, P.A. and McArthur, 1988. Gold distribution and genesis in Australian volcanogenic massive sulfide deposits, and significance for gold transport models. *AMIRA Project 84/P2*, University of Tasmania.

Large, R., Huston, D., McGoldrick, P., McArthur, G., Wallace, D., Carswell, J., Purvis, G., Creelman, R. and Ramsden, A., 1990. Gold in western Tasmania *in Glasson, K.R. and Rattigan, J.H. (Eds.)*, Geological aspects of the discovery of some important mineral deposits in Australia. Australasian Institute of Mining and Metallurgy Monograph, v. 17., p. 71-81.

Large, R.R., 1992. Australian volcanic-hosted massive sulfide deposits: Features, styles, and genetic models. *Economic Geology*, v. 87, p. 471-510.

Large, R.R., Stolz, A.J. and Duhig, N., 1996. Preliminary assessment of MRV geochemical database in terms of possible vectors. *AMIRA Project P439*, May 1996, p. 197-209.

Larson, P.B., 1984. Geochemistry of the alteration pipe at the Bruce Cu-Zn volcanogenic massive sulphide deposit, Arizona. *Economic Geology*, v. 79, p. 1880-1896.

LaTour, T.E., Kerrich, R., Hodder, R.W. and Barnett, R.L., 1980. Chloritoid stability in very iron-rich altered pillow lavas. *Contributions to Mineralogy and Petrology*, v. 74, p. 165-173.

Leblanc, M. and Billaud, P., 1990. Zoned and recurrent deposition of Na-Mg-Fe-Si exhalites and Cu-Fe sulfides along syndsedimentary faults (Bleida, Morocco). *Economic Geology*, v. 85, p. 1759-1769.

Lees, T., Khin Zaw, Large, R.R. and Huston, D.L., 1990. Rosebery and Hercules copper-lead-zinc-deposits *in Hughes, F. E., (Ed.)*, Geology and mineral deposits of Australia and Papua New Guinea. *Australasian Institute of Mining and Metallurgy*, Melbourne, v. 1, p. 1241-1247.

Lentz, D.R. and Goodfellow, W.D., 1996. Intense silicification of footwall sedimentary rocks in the stockwork alteration zone beneath the Brunswick No. 12 massive sulphide deposit, Bathurst, New Brunswick. *Canadian Journal of Earth Sciences*, v. 33, p. 284-302.

Li, B. and Manuel, O.K., 1994. A noble gas technique for the identification of mantle and crustal materials and its application to the Kuroko deposits. *Geochemical Journal*, v. 28, p. 47-69.

Liaghat, S. and MacLean, W.H., 1992. The Key Tuffite, Mattagami mining district: Origin of the tuff components and mass changes. *Exploration Mining Geology*, v. 1, p. 197-207.

Lipple, S.L., Baxter, J.L. and Marston, R.J., 1983. Ninghan, Western Australia. 1:250,000 series explanatory notes. *Western Australia Geological Survey*, Perth.

Lofgren, G., 1971a. Spherulitic textures in glassy and crystalline rocks. *Journal of Geophysical Research*, v. 76, p. 5635-5648.

Lofgren, G., 1971b. Experimentally produced devitrification textures in natural rhyolitic glass. *Geological Society of America Bulletin*, v. 82, p. 111-124.

Longstaffe, F.J., 1989. Stable isotopes as tracers in clastic diagenesis *in Hutcheon, I. E., (Ed.)*, Burial diagenesis. *Mineralogical Association of Canada*, Montreal, v. 15, p. 201-277.

Lowe, D.R. and Knauth, L.P., 1977. Sedimentology of the Onverwacht Group (3.4 Billion Years), Transvaal, South Africa, and its bearing on the characteristics and evolution of the early earth. *Journal of Geology*, v. 85, p. 699-723.

Lowe, D.R., 1982. Sediment gravity flows: II. Depositional models with special reference to the deposits of high-density turbidity currents. *Journal of Sedimentary Petrology*, v. 52, p. 279-297.

Ludden, J. and Hubert, C., 1986. Geological evolution of the Late Archean Abitibi greenstone belt of Canada. *Geology*, v. 14, p. 707-711.

Lusk, J. and Crocket, J.H., 1969. Sulfur isotope fractionation in coexisting sulfides from the Heath Steele B-1 orebody, New Brunswick, Canada. *Economic Geology*, v. 64, p. 147-155.

Lydon, J.W., 1984. Ore deposit models No. 8. Volcanogenic massive sulfide deposits part 1: A descriptive model. *Geoscience Canada*, v. 11, p. 195-202.

Lydon, J.W., 1988. Ore deposit models No. 14. Volcanogenic massive sulfide deposits part 2: Genetic models. *Geoscience Canada*, v. 15, p. 43-67.

MacLean, P.J. and Fleet, M.E., 1989. Detrital pyrite in the Witwatersrand gold fields of South Africa: Evidence from truncated growth banding. *Economic Geology*, v. 84, p. 2008-2011.

MacLean, W.H. and Hoy, L.D., 1991. Geochemistry of hydrothermally altered rocks at the Horne Mine, Noranda, Quebec. *Economic Geology*, v. 86, p. 506-528.

MacLean, W.H. and Barrett, T.J., 1993. Lithogeochemical techniques using immobile elements. *Journal of Geochemical Exploration*, v. 48, p. 109-133.

Mange, M.A. and Maurer, H.F.W., 1992. Heavy minerals in colour. Chapman and Hall, Melbourne, 145 p.

Marchig, V., Rosch, H., Lalou, C., Brichet, E. and Oudin, E., 1988. Mineralogical zonation and radiochronological relations in a large sulphide chimney from the East Pacific Rise at 18°25'S. *The Canadian Mineralogist*, v. 26, p. 541-544.

Marsaglia, K.M. and Tazaki, K., 1992. Diagenetic trends in Leg 126 sandstones. *Proceedings of the Ocean Drilling Program scientific results*, v. 126, p. 125-138.

Marshall, R.R., 1961. Devitrification of natural glass. *Geological Society of America Bulletin*, v. 72, p. 1493-1520.

Marshall, B. and Gilligan, L.B., 1987. An introduction to remobilization: Information from ore-body geometry and experimental considerations. *Ore Geology Reviews*, v. 2, p. 87-131.

Maynard, J.B., 1983. Geochemistry of sedimentary ore deposits. Springer-Verlag, Berlin, 322 p.

McArthur, G.J., 1996. Textural evolution of the Hellyer massive sulphide deposit. *Unpub. Ph.D. Thesis*, University of Tasmania.

McCrea, J.M., 1950. The isotope chemistry of carbonates and a paleotemperature scale. *Journal of Chemical Physics*, v. 18, p. 849-857.

McNaughton, N.J., Barley, M.E., Cassidy, K.F., Golding, S.D., Groves, D.I., Ho, S.E., Hronsky, J.M.A., J.H., S. and Turner, J.V., 1990. Carbon isotope studies *in Ho, S. E., Groves, D. I. and Bennett, J. M., (Eds.)*, Gold deposits of the Archaean Yilgarn Block, Western Australia: Nature, genesis and exploration guides. *Geological Department and University Extension, University of Western Australia*, Perth, v. 20, p. 246-251.

McPhie, J. and Allen, R.L., 1992. Facies architecture of mineralised submarine volcanic sequences, Cambrian Mount Read Volcanics, western Tasmania. *Economic Geology*, v. 87, p. 587-596.

McPhie, J., Doyle, M. and Allen, R., 1993. Volcanic textures: A guide to the interpretation of textures in volcanic rocks. *Centre for Ore Deposits and Exploration Studies*, University of Tasmania, 198 p.

Mel'nik, Y.P., 1982. Precambrian banded iron-formation. Elsevier, Amsterdam, 310 p.

Mill, J.H.A., 1990. The Scuddles base metal deposit: An exploration case history *in Glasson, K. R. and Rattigan, J. H., (Eds.)*, Geological aspects of the discovery of some important mineral deposits in Australia. *Australian Institute of Mining and Metallurgy Monograph*, v. 17, p. 211-218.

Mill, J.A., Clifford, B.A., Dudley, R.J. and Ruxton, P.A., 1990. Scuddles Zn-Cu deposit at Golden Grove *in Hughes, F. E., (Ed.)*, Geology of mineral deposits of Australia and Papua New Guinea. *Australian Institute of Mining and Metallurgy*, Melbourne, v. 2, p. 583-590.

Morton, R.L. and Nebel, M.L., 1984. Hydrothermal alteration of felsic volcanic rocks at the Helen Siderite Deposit, Wawa, Ontario. *Economic Geology*, v. 79, p. 1319-1333.

Morton, R.L. and Franklin, J.M., 1987. Two fold classification of Archean volcanic associated massive sulfide deposits. *Economic Geology*, v. 82, p. 1057-1063.

Morton, R.L., Walker, J.S., Hudak, G.J. and Franklin, J.M., 1991. The early development of an Archean submarine Caldera complex with emphasis on the Mattabi massive sulphide deposit. *Economic Geology*, v. 86, p. 1002-1011.

Mueller, A.G., Campbell, I.H., Schiotte, L., Sevigny, J.H. and Layer, P.W., 1996. Constraints on the age of granitoid emplacement, metamorphism, gold mineralization, and subsequent cooling of the Archean greenstone terrane at Big Bell, Western Australia. *Economic Geology*, v. 91, p. 896-915.

Myers, J.S. and Watkins, K.P., 1985. Origin of granite-greenstone patterns, Yilgarn Block, Western Australia. *Geology*, v. 13, p. 778-780.

Myers, J.S., 1988. Early Archaean Narryer Gneiss Complex, Yilgarn Craton, Western Australia. *Precambrian Research*, v. 38, p. 297-308.

Myers, J.S., 1990. Precambrian tectonic evolution of part of Gondwana, SW Australia. *Geology*, v. 18, p. 537-540.

Myers, J.S., 1992. Tectonic evolution of the Yilgarn Craton, Western Australia *in Glover, J. E. and Ho, S. E., (Eds.)*, The Archaean: Terrains, processes and metallogeny. *University of Western Australia special publication*, Perth, v. 22, p. 265-273.

Myers, J.S., 1995. The generation and assembly of an Archaean supercontinent: Evidence from the Yilgarn Craton, Western Australia *in Coward, M. P. and Ries, A. C., (Eds.)*, Early Precambrian Processes. *Geological Society of Australia special publication*, Perth, v. 95, p. 143-154.

Nelson, D.R., Swager, C.P., Ahmat, A.L., Morris, P.A., Smithies, R.H., Witt, W.K. and Wyche, S., 1994. Shrimp U-Pb zircon dating of Archaean greenstones from the Eastern Goldfields. *Geological Society of Australia, Abstracts*, v. 37, p. 313-314.

Nesbitt, B.E., Longstaffe, F.J., Shaw, D.R. and Muehlenbachs, K., 1984. Oxygen isotope geochemistry of the Sullivan massive sulfide deposit, Kimberly, British Columbia. *Economic Geology*, v. 79, p. 933-946.

Nisbet, E.G. and Fowler, C.M.R., 1983. Model for Archean plate tectonics. *Geology*, v. 11, p. 376-379.

Norrish, K. and Chappell, B.W., 1977. X-ray fluorescence spectrography *in Zussman, J. I., (Ed.)*, Physical methods in determinative mineralogy. Academic Press, p. 161-214.

Nystrom, J.O. and Henriquez, F., 1994. Magmatic features of iron ores of the Kiruna type in Chile and Sweden: Ore textures and magnetite geochemistry. *Economic Geology*, v. 89, p. 820-839.

O'Neil, J.R., Calyton, R.N. and Mayeda, T.K., 1969. Oxygen isotope fractionation in divalent metal carbonates. *Journal of Chemical Physics*, v. 51, p. 5547-5558.

O'Neil, J.R., 1987. Preservation of H, C, and O isotopic ratios in the low temperature environment *in Kyser, T. K, (Ed.)*, Shortcourse handbook of stable isotope geochemistry of low temperature processes. *Mineralogical Association of Canada*, v. 13, p. 85-128.

Ohmoto, H., 1972. Systematic of sulfur and carbon isotopes in hydrothermal ore deposits. *Economic Geology*, v. 67, p. 551-578.

Ohmoto, H. and Rye, R.O., 1974. Hydrogen and oxygen isotopic compositions of fluid inclusions in the Kuroko deposits, Japan. *Economic Geology*, v. 69, p. 947-953.

Ohmoto, H. and Rye, R.O., 1979. Isotopes of sulfur and carbon *in Barnes, H. L., (Ed.)*, Geochemistry of hydrothermal ore deposits. John Wiley and Sons, New York, v. 1, p. 509-567.

Ohmoto, H., Mizukami, M., Drummond, S.E., Eldridge, C.S., Pisutha-Arnond, V. and Lenagh, T.C., 1983. Chemical processes of Kuroko formation. *Economic Geology Monograph*, v. 5, p. 570-604.

Ohmoto, H., 1986. Stable isotope geochemistry of ore deposits *in Valley, J. W., Taylor, J., H.P. and O'Neil, J. R., (Eds.)*, Stable isotopes in high temperature geological processes. *Mineralogical Society of America reviews in mineralogy*, v. 16, p. 491-560.

Ohmoto, H. and Felder, R.P., 1987. Bacterial activity in the warmer, sulphate-bearing Archaean oceans. *Nature*, v. 328, p. 244-246.

Ohmoto, H., 1992. Biogeochemistry of sulfur and the mechanisms of sulfide-sulfate mineralization in Archean oceans *in M. Schidlowski, Golubic, S., Kimberley, M. M., McKirdy, D. M. and Trudinger, P. A., (Eds.)*, Early organic evolution implications for mineral and energy resources. Springer-Verlag, Berlin, v. 1, p. 378-397.

Ohmoto, H., 1994. Submarine hydrothermal systems: From Kuroko to banded iron formations. Geoscience Australia 1994 and beyond, 12th AGC, *University of Western Australia*, Perth, v. 37, p. 324.

Ohmoto, H., 1996. Formation of volcanogenic massive sulfide deposits: The Kuroko perspective. *Ore Geology Reviews*, v. 10, p. 135-177.

Ohmoto, H. and Goldhaber, M.B., 1997. Sulfur and carbon isotopes *in Barnes, H. L., (Ed.)*, Geochemistry of hydrothermal ore deposits. John Wiley and Sons, v. 1, third edition, p. 517-611.

Paradis, S., Jonasson, I.R. and Le Cheminant, G.M., 1988. Two zinc-rich chimneys from the Plume Site, southern Juan de Fuca Ridge. *Canadian Mineralogist*, v. 26, p. 637-654.

Paradis, S., Taylor, B.E., Watkinson, D.H. and Jonasson, I.R., 1993. Oxygen isotope zonation and alteration in the northern Noranda district, Quebec: Evidence for hydrothermal fluid flow. *Economic Geology*, v. 88, p. 1512-1525.

Parak, T., 1985. Phosphorus in different types of ore, sulfides in the iron deposits, and the type and origin of ores at Kiruna. *Economic Geology*, v. 80, p. 646-665.

Paris, I., Stainstreet, I.G. and Hughes, M.J., 1985. Cherts of the Barberton Greenstone Belt interpreted as products of submarine exhalative activity. *Journal of Geology*, v. 93, p. 111-129.

Peter, J.M., 1986. Genesis of hydrothermal vent deposits in the southern trough of Guaymas Basin, Gulf of California: A mineralogical and geochemical study. *Unpub. M.Sc. Thesis*, University of Toronto, 180 p.

Peter, J.M. and Scott, S.D., 1988. Mineralogy, composition, and fluid-inclusion microthermometry of seafloor hydrothermal deposits in the southern trough of Guaymas Basin, Gulf of California. *Canadian Mineralogist*, v. 26, p. 567-587.

Peter, J.M. and Goodfellow, W.D., 1996. Mineralogy, bulk and rare earth element geochemistry of massive sulphide-associated hydrothermal sediments of the Brunswick Horizon, Bathurst Mining Camp, New Brunswick. *Canadian Journal of Earth Sciences*, v. 33, p. 252-283.

Picot, P. and Johan, Z., 1982. Atlas of ore minerals. Elsevier, 49-249 p.

Pidgeon, R.T. and Wilde, S.A., 1990. The distribution of 3.0 Ga and 2.7 Ga volcanic episodes in the Yilgarn Craton of Western Australia. *Precambrian Research*, v. 48, p. 309-325.

Pidgeon, R.T., Furfaro, D. and Clifford, B.A., 1994. Investigation of the age and rate of deposition of part of the Gossan Hill Group, Golden Grove using conventional single grain zircon U-Pb geochronology. *Geological Society of Australia, Abstracts*, v. 37, p. 346.

Pisutha-Arnond, V. and Ohmoto, H., 1983. Thermal history, and chemical and isotopic compositions of the ore-forming fluids responsible for the Kuroko massive sulfide deposits in the Hokuroku district of Japan. *Economic Geology Monograph*, v. 5, p. 523-558.

Pitt, J., 1990. The Gossan Hill deposit *in Glasson, K. R. and Rattigan, J. H., (Eds.)*, Geological aspects of the discovery of some important mineral deposits in Australia. *Australasian Institute of Mining and Metallurgy Monograph*, v. 17, p. 103-106.

Potter, B.K., 1991. Chemical and physical effects of wall rock alteration around volcanogenic massive sulphide deposits. *Unpub. B.Sc. Hons. Thesis*, University of Western Australia.

Powell, R. and Holland, T.J.B., 1990. An enlarged and updated internally consistent thermodynamic data set with uncertainties and correlations: The system K_2O-Na_2O-MgO-MnO-FeO-Fe_2O_3-Al_2O_3-TiO_2-SiO_2-C-H_2-O_2. *Journal of Metamorphic Geology*, v. 8, p. 89-124.

Quantin, P., Gautheyrou, J. and Lorenzoni, P., 1988. Halloysite formation through in situ weathering of volcanic glass from trachytic pumices, Vico's Volcano, Italy. *Clay Minerals*, v. 23, p. 423-437.

Radford, 1992. Golden Grove and Scuddles lithogeochemistry. *Normandy internal memorandum*, 44 p.

Ramdohr, P., 1969. The ore minerals and their intergrowths. Pergamon Press, Oxford, London, first edition, 1174 p.

Ramdohr, P., 1980. The ore minerals and their intergrowths. Pergamon Press, Oxford, London, third edition 1205 p.

Rattenbury, M.S., 1992. Stratigraphic and structural controls on ironstone mineralization in the Tennant Creek goldfield, Northern Territory, Australia. *Australian Journal of Earth Sciences*, v. 39, p. 591-602.

Ribbe, P.H., 1982. Staurolite *in Ribbe, P. H., (Ed.)*, Orthosilicates. *Reviews in Mineralogy*, v. 5, p. 171-188.

Roberts, R.G., 1975. The geological setting of the Mattagami Lake Mine, Quebec: A volcanogenic massive sulfide deposit. *Economic Geology*, v. 70, p. 115-129.

Robinson, B.W. and Kusakabe, M., 1975. Quantitative preparation of SO_2 for $^{34}S/^{32}S$ analyses from sulfides by combustion with cuperous oxide. *Analytical Chemistry*, v. 47, p. 1179-1181.

Robinson, S.H. and Belford, S.M., 1991. The Scuddles massive sulphide discovery: An exploration case history. *Exploration Geophysics*, v. 22, p. 315-320.

Ruxton, P., 1986. Controls of Au and Ag grades in volcanogenic sulphide deposits: Scuddles and Teutonic Bore. *AMIRA Final Report 84/P2*, University of Tasmania, p. 72-83.

Ruxton, P., 1986. Controls of Au and Ag grades in volcanogenic sulphide deposits: Teutonic Bore. *AMIRA Final* Report 84/P2, University of Tasmania, p. 72-83.

Rye, R.O. and Ohmoto, H., 1974. Sulfur and carbon isotopes and ore genesis: A review. *Economic Geology*, v. 69, p. 826-842.

Ryznar, G., Campbell, F.A. and Krouse, H.R., 1967. Sulfur isotopes and the origin of the Quemont ore body. *Economic Geology*, v. 62, p. 664-678.

Sangster, D.F., 1968. Relative sulphur isotope abundances of ancient seas and stratabound sulphide deposits. *Geological Association of Canada Proceedings*, v. 17, p. 79-91.

Sangster, D.F., 1972. Precambrian volcanogenic massive sulphide deposits in Canada: A review. *Geological Survey of Canada*, v. 77-22, p. 1-44.

Sangster, D.F. and Scott, S.D., 1976. Precambrian stratabound massive Cu-Zn-Pb sulfide ores of North America *in Wolf, K. H., (Ed.)*, Handbook of strata-bound and stratiform ore deposits. Elsevier, Amsterdam, v. 2, p. 129-222.

Sangster, D.F., 1978. Exhalites associated with Archean volcanogenic massive sulphide deposits *in Glover, J. E. and Groves, D. I., (Eds.)*, Archean cherty metasediments: their sedimentology, micropalaeontology, biogeochemistry, and significance to mineralisation. *Geology Department and Extension, University of Western Australia*, Perth, v. 2, p. 70-81.

Saskai, A., 1970. Seawater sulfate as a possible determinant for sulfur isotopic compositions of some strata-bound sulfide ores. *Geochemical Journal*, v. 4, p. 41-51.

Savin, S.M. and Lee, M., 1988. Isotopic studies of phyllosilicates *in Bailey, S. W., (Ed.)*, Hydrous phyllosilicates. *Mineralogical Society of America reviews in mineralogy*, v. 19, p. 189-223.

Sawkins, F.J., 1986. Some thoughts on the genesis of Kuroko-type deposits. Geology in the real world- the Kingsley Dunham volume. *London Institute of Mining and Metallurgy*, p. 387-394.

Schidlowski, M.R., Hayes, J.M. and Kaplan, I.R., 1983. Isotopic inferences of ancient biochemistries: Carbon, sulfur, hydrogen and nitrogen *in Schopf, J. W., (Ed.)*, Earth's earliest biosphere: its origin and evolution. Princeton University Press, Princeton, p. 149-186.

Schiotte, I. and Campbell, I.H., 1996. Chronology of the Mount Magnet granite-greenstone terrain, Yilgarn Craton. Western Australia: Implications for field based predictions of the relative timing of granitoid emplacement. *Precambrian Research*, v. 78, p. 237-260.

Scott, S.D., 1983. Chemical behaviour of sphalerite and arsenopyrite in hydrothermal and metamorphic environments. *Mineralogical Magazine*, v. 47, p. 427-435.

Scott, A.K., 1991. Resource estimate for the Gossan Hill copper deposit. Murchison zinc company.

Seccombe, P.K., 1977. Sulphur isotope and trace metal composition of stratiform sulphides as an ore guide in the Canadian Shield. *Journal of Geochemical Exploration*, v. 8, p. 117-137.

Seccombe, P.K. and Frater, K.M., 1981. A preliminary study of sulphur isotopes and ore genesis at the Golden Grove copper deposit Western Australia *in Glover, J. E. and Groves, D. I., (Eds.)*, Archean Geology: Second International Symposium. *Geological Society of Australia special publication*, Perth, v. 7, p. 421-428.

Setterfield, T.N., Hodder, R.W., Gibson, H.L. and Watkins, J.J., 1995. The McDougall-Despina fault set, Noranda, Quebec: Evidence for fault-controlled volcanism and hydrothermal fluid flow. *Exploration Mining Geology*, v. 4, p. 381-393.

Shackleton, R.M., 1995. Tectonic evolution of greenstone belts *in Coward, M. P. and Ries, A. C., (Eds.)*, Early Precambrian processes. *Geological Society special publication*, v. 95, p. 53-65.

Sharpe, R., 1991. The distribution, mineralogy and paragenesis of the Hellyer baritic and siliceous caps. *Unpub. B.Sc. Hons. Thesis*, University of Tasmania.

Sheppard, S.M.F. and Schwarcz, H.P., 1970. Fractionation of carbon and oxygen isotopes and magnesium between coexisting metamorphic calcite and dolomite. *Contributions to Mineralogy and Petrology*, v. 26, p. 161-198.

Sheppy, N.R. and Clifford, B.A., 1991. Golden Grove Joint Venture review of exploration at Golden Grove 1971-1990: Suggested future strategies. MZC internal report.

Sheppy, N.R., Verbeddk, P. and MacMahon, M.M., 1992. Murchison Zinc Company, Golden Grove Joint Venture annual exploration report. MZC internal report.

Sillitoe, R.H., Hannington, M.D. and Thompson, J.F.H., 1996. High sulfidation deposits in the volcanogenic massive sulfide environment. *Economic Geology*, v. 91, p. 204-212.

Skirrow, R.G. and Franklin, J.M., 1994. Silicification and metal leaching in semiconformable alteration beneath the Chisel Lake massive sulfide deposit, Snow Lake, Manitoba. *Economic Geology*, v. 89, p. 31-50.

Skyring, G.W. and Donnelly, T.H., 1982. Precambrian sulfur isotopes and a possible role for sulfite in the evolution of biological sulfate reduction. *Precambrian Research*, v. 17, p. 41-61.

Smith, R.E., Frater, K.M. and Moeskops, P.G., 1980. Golden Grove Cu-Zn deposit, Yilgarn Block, Western Australia *in Butt, C. R. M. and Smith, R. E., (Eds.)*, Conceptual models in exploration geochemistry. *Journal of Geochemical Exploration*, v. 12, p. 195-199.

Smith, R.E. and Pedrix, J.L., 1983. Pisolitic laterite geochemistry in the Golden Grove massive sulphide district, Western Australia. *Journal of Geochemical Exploration*, v. 18, p. 131-164.

Solomon, M., 1976. "Volcanic" massive sulphide deposits and their host rocks-a review and an explanation *in Wolf, K A., (Ed.)*, Handbook of strata-bound and stratiform ore deposits, II. Regional studies and specific deposits. Elsevier, Amsterdam, p. 21-50.

Solomon, M. and Walshe, J.L., 1979. The formation of massive sulfide deposits on the sea floor. *Economic Geology*, p. 797-813.

Solomon, M., 1981. An introduction to the geology and metallic mineral resources of Tasmania. *Economic Geology*, v. 76, p. 194-208.

Solomon, M., Eastoe, C.J., Walshe, J.L. and Green, G.R., 1988. Mineral deposits and sulfur isotope abundances in the Mount Read volcanics between Que River and Mount Darwin, Tasmania. *Economic Geology*, v. 83, p. 1307-1328.

Spooner, E.T.C. and Fyfe, W.S., 1973. Sub sea-floor metamorphism, heat and mass transfer. *Contributions to Mineralogy and Petrology*, v. 42, p. 287-304.

Spooner, E.T.C., Beckinsale, R.D., Fyfe, W.S. and Smewing, J.D., 1974. $\delta^{18}O$ enriched ophilitic metabasic rocks from E. Liguria (Italy), Pindos (Greece) and Troodos (Cyprus). *Contributions to Mineralogy and Petrology*, v. 47, p. 41-62.

Stanton, R.L., 1985. Stratiform ores and geological processes. *Royal Society of New South Wales*, v. 118, p. 77-100.

Stanton, R.L., 1990. Magmatic evolution and the ore type-lava type affiliations of volcanic exhalative ores. *Australasian Institute of Mining and Metallurgy Monograph*, v. 15, p. 101-107.

Stolz, A.J. and Large, R.R., 1992. Evaluation of the source rock control on precious metal grades in volcanic-hosted massive sulfide deposits from western Tasmania. *Economic Geology*, v. 87, p. 720-738.

Stolz, A.J., Large, R.R. and Duhig, N., 1996. Progress report on the utilisation of the Mount Read Volcanics database. *AMIRA Project P439*, May 1996, p. 181-196.

Strauss, H., 1986. Carbon and sulfur isotopes in Precambrian sediments from the Canadian Shield. *Geochemica et Cosmochimica Acta*, v. 50, p. 2653-2662.

Strauss, H., 1989. Carbon and sulfur isotope data for carbonaceous metasediments from the Kidd Creek massive sulfide deposit and vicinity, Timmins, Ontario. *Economic Geology*, v. 84, p. 959-962.

Suresh, N.K., Bancroft, G.M., Fyfe, W.S. and Brown, J.D., 1980. Leaching behaviour of rhyolite glass. *Nature*, v. 284, p. 435-437.

Taylor, H.P.J., 1974. The application of oxygen and hydrogen isotope studies to problems of hydrothermal alteration and ore deposition. *Economic Geology*, v. 69, p. 843-883.

Taylor, H.P., 1979. Oxygen and hydrogen isotope relationships in hydrothermal mineral deposits *in Barnes, H. L., (Ed.)*, Geochemistry of hydrothermal ore deposits. John Wiley and Sons, New York, v. 1, p. 236-277.

Taylor, H.P. and Sheppard, S.M.F., 1986. Igneous rocks: I. Processes of isotopic fractionarion and isotope systematics *in J.W. Valley, Taylor, H. P. and O'Neil, J. R., (Eds.)*, Stable isotope processes in high temperature geological processes. *Mineralogical Society of America reviews in mineralogy*, v. 16, p. 227-271.

Tazaki, K. and Fyfe, W.S., 1992. Diagenetic and hydrothermal mineral alteration observed in Izu-Bonin deep-sea sediments, Leg 126. *Proceedings of the Ocean Drilling Program, Scientific Results*, v. 126, p. 101-112.

Thode, H.G. and Goodwin, A.M., 1983. Further sulfur and carbon isotope studies of Late Archean iron-formations of the Canadian Shield and the rise of sulfate reducing bacteria. *Precambrian Research*, v. 20, p. 337-356.

Thurston, P.C. and Chivers, K.M., 1990. Secular variation in greenstone sequence development emphasising the Superior Province, Canada. *Precambrian Research*, v. 46, p. 21-58.

Tivey, M.K. and Delaney, J.R., 1986. Growth of large sulfide structure on the Endeavour Segment of the Juan de Fuca Ridge. *Earth and Planetary Science Letters*, v. 77, p. 303-317.

Urabe, T., 1974. Iron content of sphalerite coexisting with pyrite from some Kuroko deposits. *Society Mining Geologists Japan Special Issue*, v. 6, p. 377-384.

Urabe, T., Scott, S.D. and Hattori, H.D., 1983. A comparison of footwall-rock alteration and geothermal systems beneath some Japanese and Canadian volcanogenic massive sulfide deposits. *Economic Geology Monograph*, v. 5, p. 345-364.

Utada, M., 1991. Zeolitization in the Neogene formations of Japan. *Episodes*, v. 14, p. 242-245.

Vaasjoki, M., 1984. Geochronological and genetic implications of lead isotopic data from the Archaean massive sulphide deposits at Golden Grove, Teutonic Bore and Salt Creek, Western Australia. *Geological Society of Australia, Abstracts*, v. 12, p. 522.

Valley, J.W., 1986. Stable isotope geochemistry of metamorphic rocks *in Valley, J.W., Taylor, H. P. and O'Neil, J. R., (Eds.)*, Stable isotopes in high temperature geological processes. *Mineralogical Society of America reviews in mineralogy*, v. 16, p. 445-489.

Veilreicher, R.M., Groves, D.I., Ridley, J.R. and McNaughton, N.J., 1994. A replacement origin for the BIF-hosted gold deposit at Mt. Morgan, Yilgarn Block, W.A. *Ore geology Reviews*, v. 9, p. 325-347.

Veizer, J., 1985. Carbonates and ancient oceans: isotopic and chemical record on time scales of 10^7 and 10^9 years *in Sundquist, E. T. and Broecker, W. S., (Eds.)*, The carbon cycle and atmospheric CO_2: Natural variations Archean to present. *AGU Geophysical Monograph*, Washington, v. 32, p. 595-601.

Veizer, J., Clayton, R.N., Hinton, R.W., vonBrunn, V., Mason, T.R., Buck, S.G. and Hoefs, J., 1990. Geochemistry of Precambrian carbonates. 3. Shelf seas and non-marine environments of the Archean. *Geochemica et Cosmochima Acta*, v. 54, p. 2717-2729.

Viezer, J., Hoefs, J., Ridler, R.H., Jensen, L.S. and Lowe, D.R., 1989. Geochemistry of Precambrian carbonates: I. Archean hydrothermal systems. *Geochimica et Cosmochimica Acta*, v. 53, p. 845-857.

Walton, A.W., 1975. Zeolitic diagenesis in Oligocene volcanic sediments, Trans-Pecos Texas. *Geological Society of America Bulletin*, v. 86, p. 615-624.

Wang, L.G., McNaughton, N.J. and Groves, D.I., 1993. An overview of the relationship between granitoid intrusions and gold mineralisation in the Archaean Murchison Province, Western Australia. *Mineralium Deposita*, v. 28, p. 482-494.

Wang, O., Campbell, I.H. and Schiotte, L., 1996. Age constraints on the supracrustal sequence in the Murchison Province, Yilgarn Block: a new insight from the SHRIMP zircon dating. *Geological Society of Australia, Abstracts*, v. 41, p. 458.

Wang, Q., Schiotte, L. and Campbell, I.H., 1998. Geochronology of supracrustal rocks from the Golden Grove area, Murchison Province, Yilgarn Craton, Western Australia. *Australian Journal of Earth Sciences*, v. 45, p. 571-577.

Watanabe, M. and Sakai, H., 1983. Stable isotope geochemistry of sulfates from the Neogene ore deposits in the Green Tuff regions, Japan. *Economic Geology Monograph*, v. 8, p. 282-291.

Watkins, K.P. and Tyler, I.M., 1985. Structural and stratigraphic relationships in the Archaean granite-greenstone terrain around Cue, Western Australia. *Western Australia Geological Survey Report*, v. 14, p. 46-56.

Watkins, K.P., Tyler, I.M. and Hickman, A.H., 1987. Cue, Western Australia. 1:250,000 geological series with explanatory notes. *Western Australia Geological Survey*, Perth.

Watkins, K.P. and Ahmat, A.L., 1988. Murchison Province metamorphic facies. 1:500,000 metamorphic facies sheet with explanatory notes. *Western Australia Geological Survey*, Perth.

Watkins, K.P. and Hickman, A.H., 1990a. Geological evolution and mineralization of the Murchison Province, Western Australia. *Geological Survey of Western Australia Bulletin*, v. 137, p. 0-267.

Watkins, K.P. and Hickman, A.H., 1990b. Geology of the Murchison Province granite-greenstone terrain, Western Australia *in Ho, S. E., Glover, J. E., Myers, J. S. and Muhling, J. R., (Eds.)*, Third International Archean Symposium: excursion guidebook. *Geology Department and University Extension, University of Western Australia*, Perth, v. 21, p. 147-171.

Watkins, K.P., Fletcher, I.R. and deLaeter, J.R., 1991. Crustal evolution of Archaean granitoids in the Murchison Province, Western Australia. *Precambrian Research*, v. 50, p. 311-336.

Wedekind, M.R., Large, R.R. and Williams, B.T., 1989. Controls on high-grade gold mineralization at Tennant Creek, Northern Territory, Australia. *Economic Geology Monograph*, v. 6, p. 168-179.

Wedekind, M.R., 1990. Geology and geochemistry of the Warrego Au-Cu-Bi mine, Tennant Creek, Northern Territory, Australia. *Unpub. Ph.D. Thesis*, University of Tasmania, 380 p.

Wedekind, M.R., Large, R.L. and Williams, B.T., 1994. Controls on high-grade gold mineralization at Tennant Creek, Northern Territory, Australia. *Economic Geology*, v. 89, p. 168-179.

Whitford, D.J., McPherson, W.P.A. and Wallace, D.B., 1989. Geochemistry of the host rocks of the volcanogenic massive sulfide deposit at Que River, Tasmania. *Economic Geology*, v. 84, p. 1-21.

Whitford, D.J. and Ashley, P.M., 1992. The Scuddles volcanic-hosted massive sulfide deposit, Western Australia: geochemistry of the host rocks and evaluation of lithogeochemistry for exploration. *Economic Geology*, v. 87, p. 873-888.

Wiedenbeck, M. and Watkins, K.P., 1993. A time scale for granitoid emplacement in the Archean Murchison Province, Western Australia, by single zircon geochronology. *Precambrian Research*, v. 61, p. 1-26.

Williams, L.A. and Crerar, D.A., 1985. Silica diagenesis, II. General mechanisms. *Journal of Sedimentary Petrology*, v. 55, p. 312-321.

Williams, L.A., Parks, G.A. and Crerar, D.A., 1985. Silica diagenesis, I. Solubility controls. *Journal of Sedimentary Petrology*, v. 55, p. 301-311.

Williams, P.J., 1994. Iron mobility during synmetamorphic alteration in the Selwyn Range area, NW Queensland: Implications for the origin of ironstone-hosted Au-Cu deposits. *Mineralium Deposita*, v. 29, p. 250-260.

Winchester, J.A. and Floyd, P.A., 1977. Geochemical discrimination of different magma series and their differentiation products using immobile elements. *Chemical Geology*, v. 20, p. 325-343.

Wynne, P.J. and Strong, D.F., 1984. The Strickland prospect of southwestern Newfoundland: A lithogeochemical study of metamorphosed and deformed volcanogenic massive sulphides. *Economic Geology*, v. 79, p. 1620-1642.

Zaleski, E. and Peterson, V.L., 1995. Depositional setting and deformation of massive sulfide deposits, iron-formation and associated alteration in the Manitouwadge Greenstone Belt, Superior Province, Canada. *Economic Geology*, v. 90, p. 2244-2261.

Zlotnik-Khotkevitch, A.G., Mirlin, E.G., Elyanova, E.A., Shirai, E.P., Ageyeva, S.T., Mironov, Y.V., Zorina, Y.G. and Kuznetsov, A.G., 1993. Comparative classification of formational settings of modern and ancient sulfide ores. *Resource Geology special issue*, v. 17, p. 16-168.

Appendices

Appendix A1.1: List of drill holes logged (1:250 scale)

GG064	G96/071	GG132	G96/11
GG027	GG045	GG080	G96/046
GG138	GG165	GG090	G96/192
GG042	GG161	GG103	GG179
GG33	GG153	GG131	G96/180
GG038	GG173	GG132X	GG180
GG157	GG171	GG130	G96/183
GG032	GG163	GG135X	G96/184
GG162	GG160	GG132	G96/182
GG070	GG045	GG101	G96/178
GG141	GG139	GG099	
GG045	GG044	GG127	
GG139	GG148	GG134	
GG048	GG118	GG136	
GG095			

Note: Core logging examples of drill holes GG064 and GG134 are given
Detailed logs of the remainder drill holes logged can be obtained by contacting the author.

Summary of logging codes

Intensity	**Colour**	**Distribution**	**Minerals**
w = weak	bn = brown	ds = disseminated	co = carbonate
m = moderate	cm = cream	mas = massive	cpy = chalcopyrite
s = strong	gn = green	tr = trace	chl = chlorite
i = intense	gy = grey	vnd = veined	fd = feldspar
	rd = red		mgt = magnetite
	yw = yellow		po = pyrrhotite
	wh = white		py = pyrite
			qtz = quartz
			se = muscovite
			si = siliceous

FROM FOOTWALL TO HANGINGWALL

GOS AN HILL PROJECT

ENTERED TO MINE / MEC GEOL UPDATED.

TRANSFORM SECTION 13288 | Cu Lens | GEO Rob | DATE 7/9/95 | PAGE 1/13 | BHID GG064

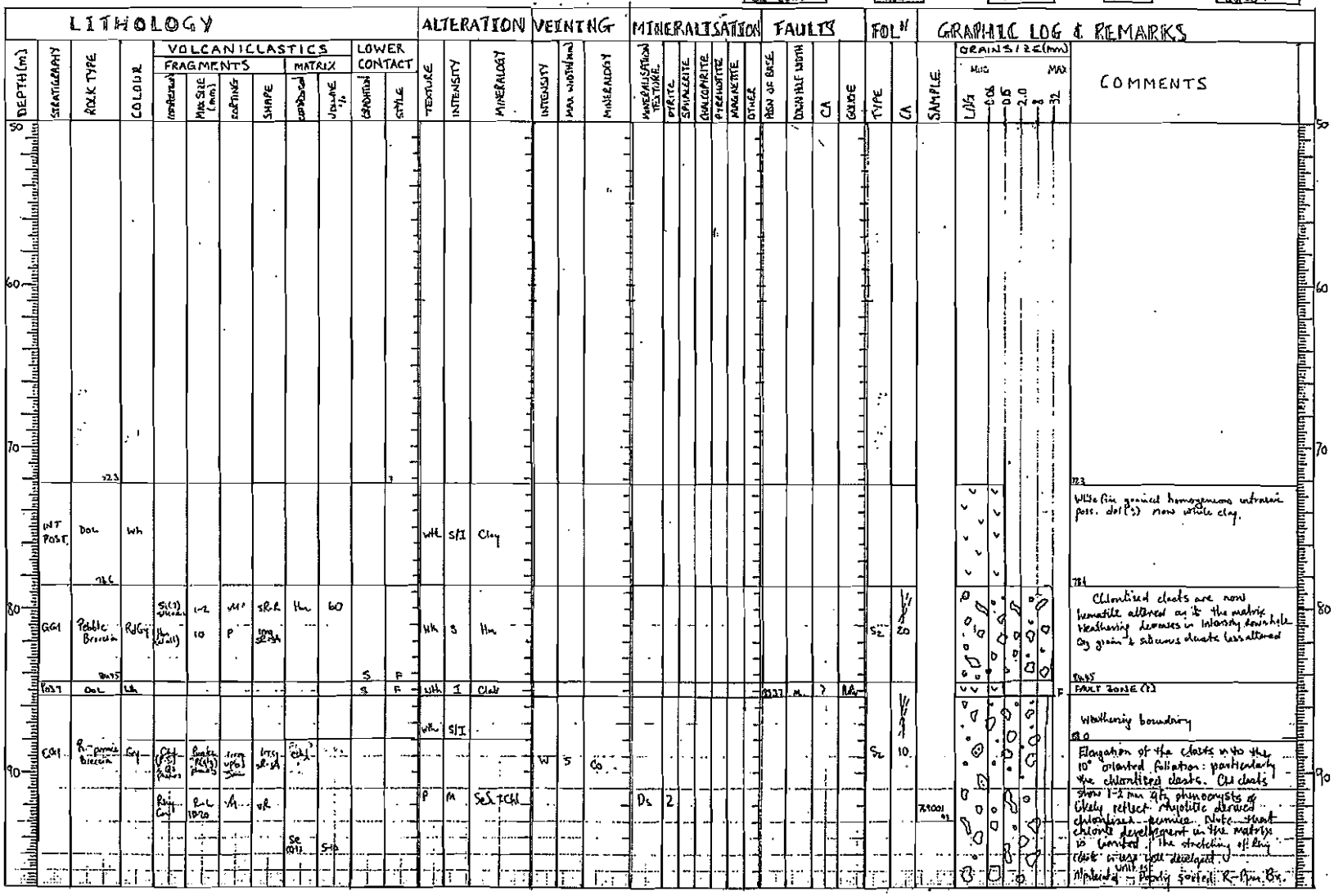

GOSSAN HILL PROJECT

TRANSFORM 18289 | Cu Lens | GEO Rob | DATE 9/9/95 | PAGE 2/13 | BHID GG064

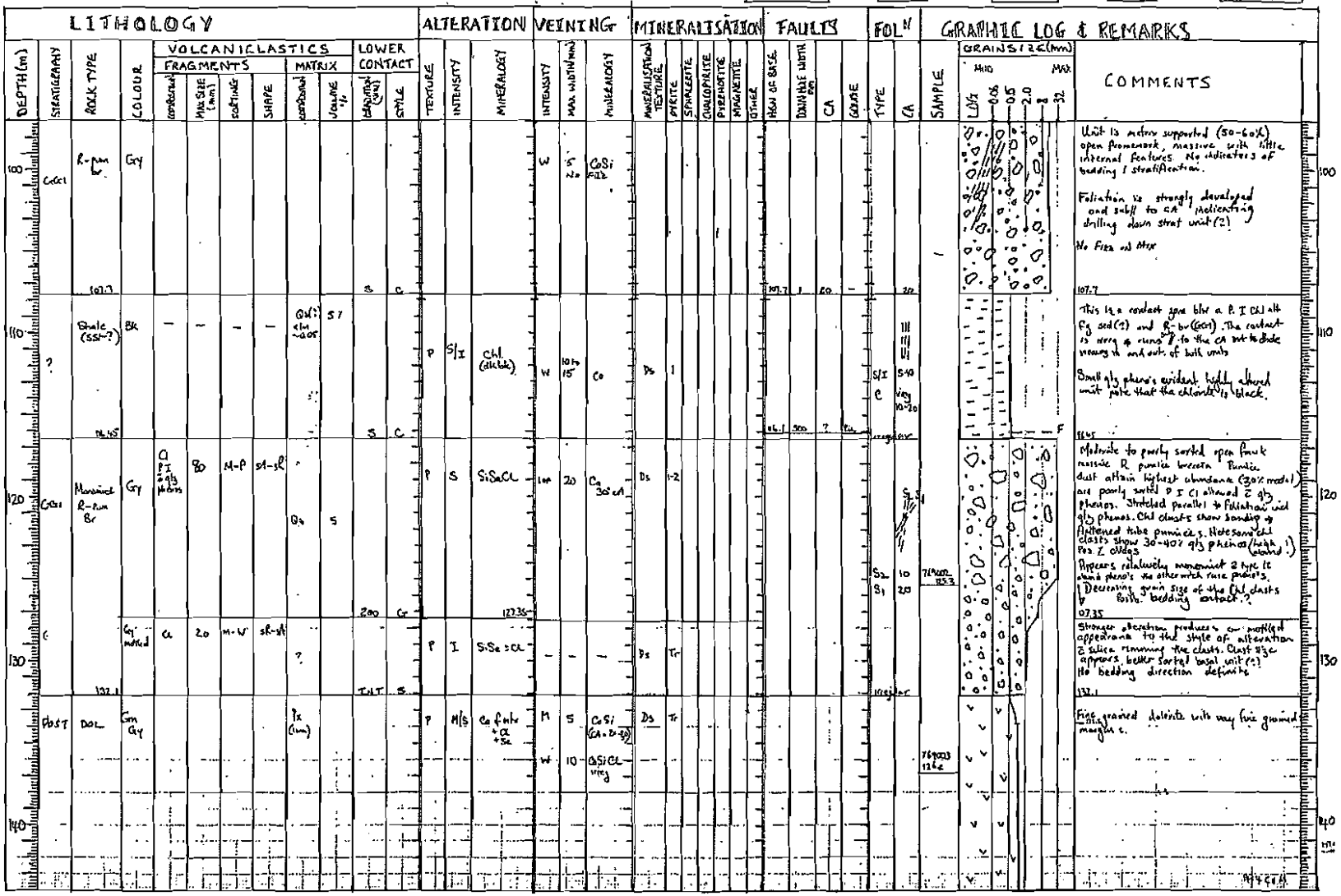

GOSSAN HILL PROJECT

TRANSFORM SECTION 18288 | CuLens | GEO Rob | DATE 10/9/95 | PAGE 4/13 | BHID GG064

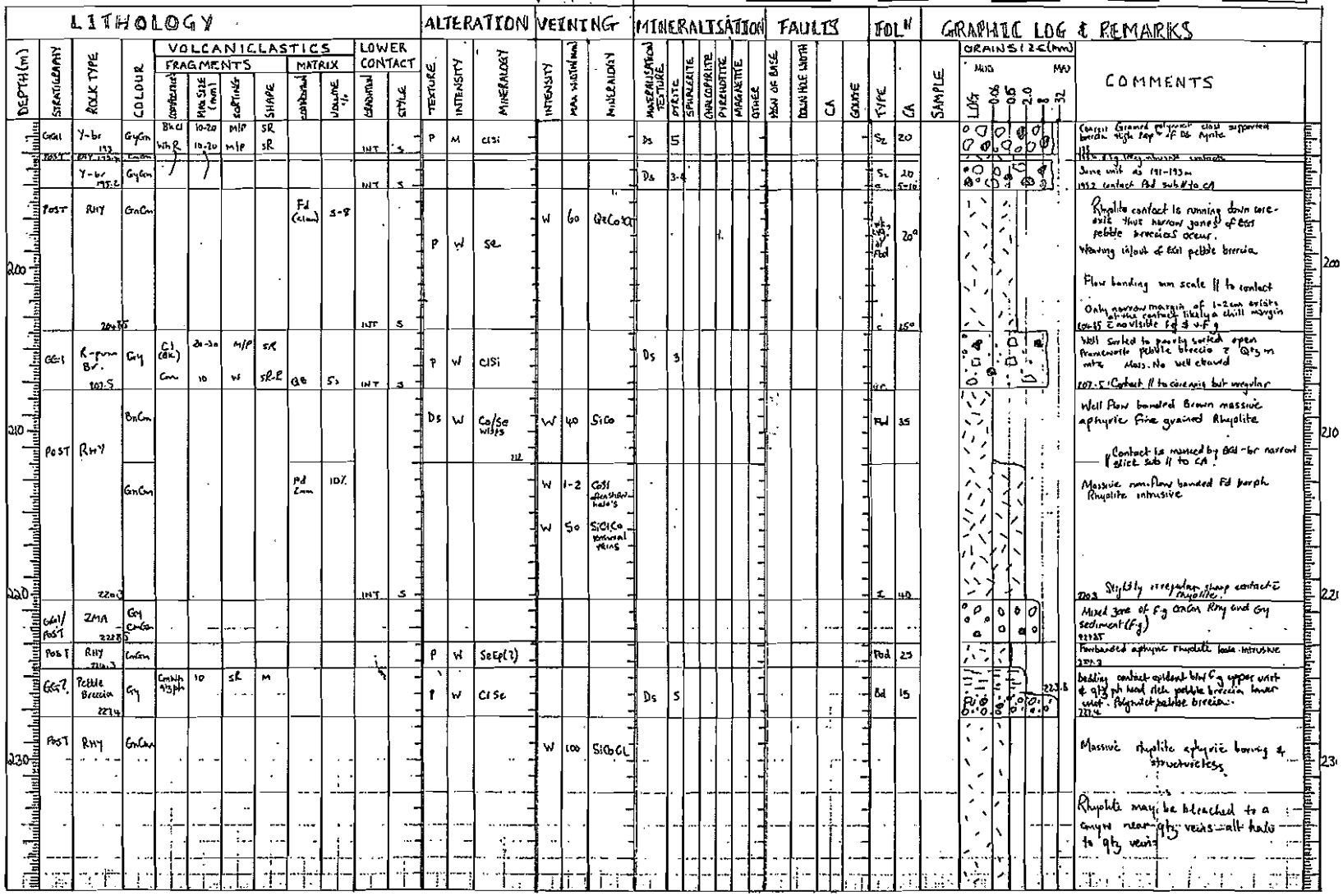

GOSSAN HILL PROJECT

Transform Section 18288 | Ca Lens | GEO Rob | DATE 10/9/95 | PAGE 5/15 | BHID GG0644

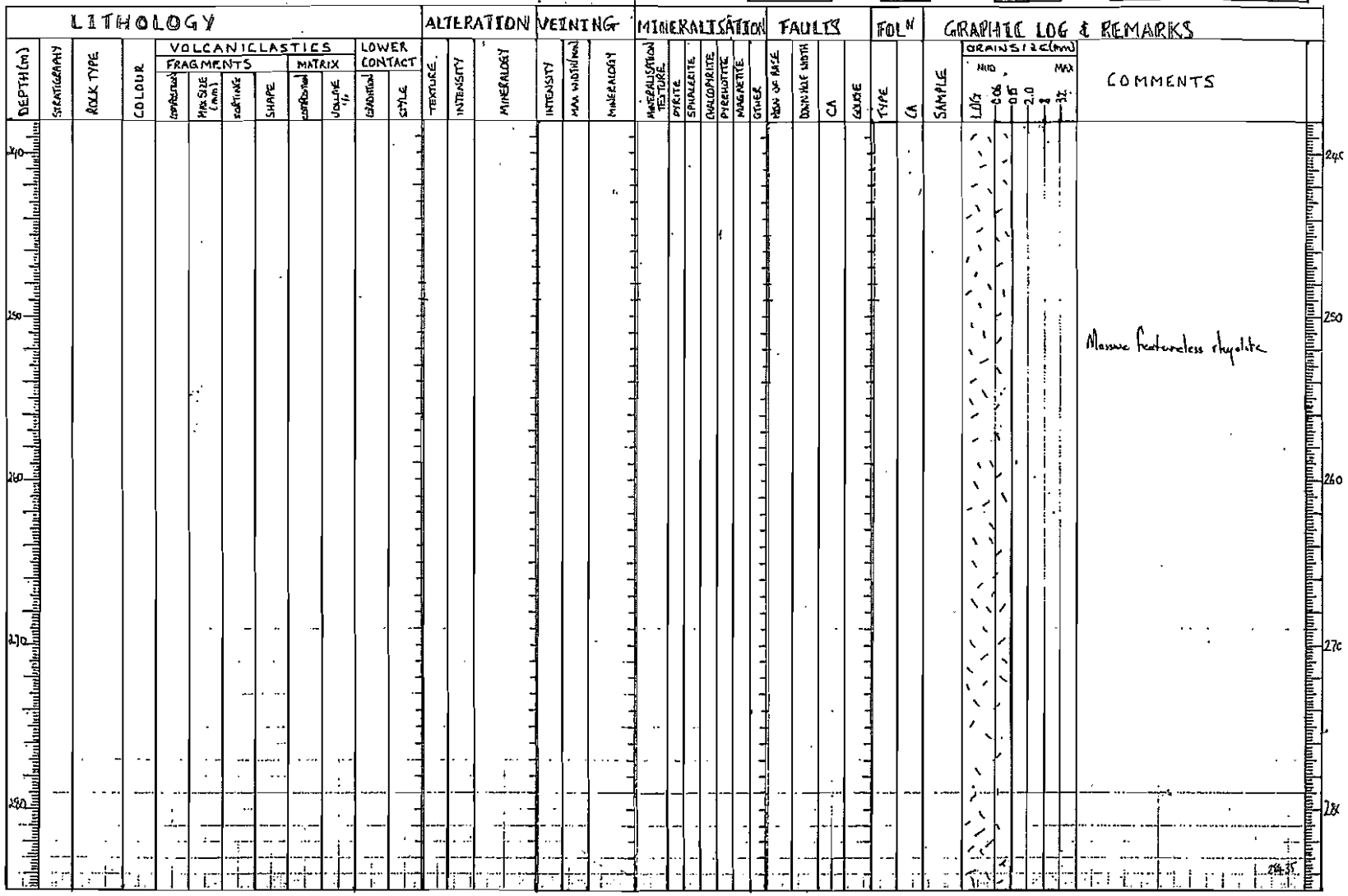

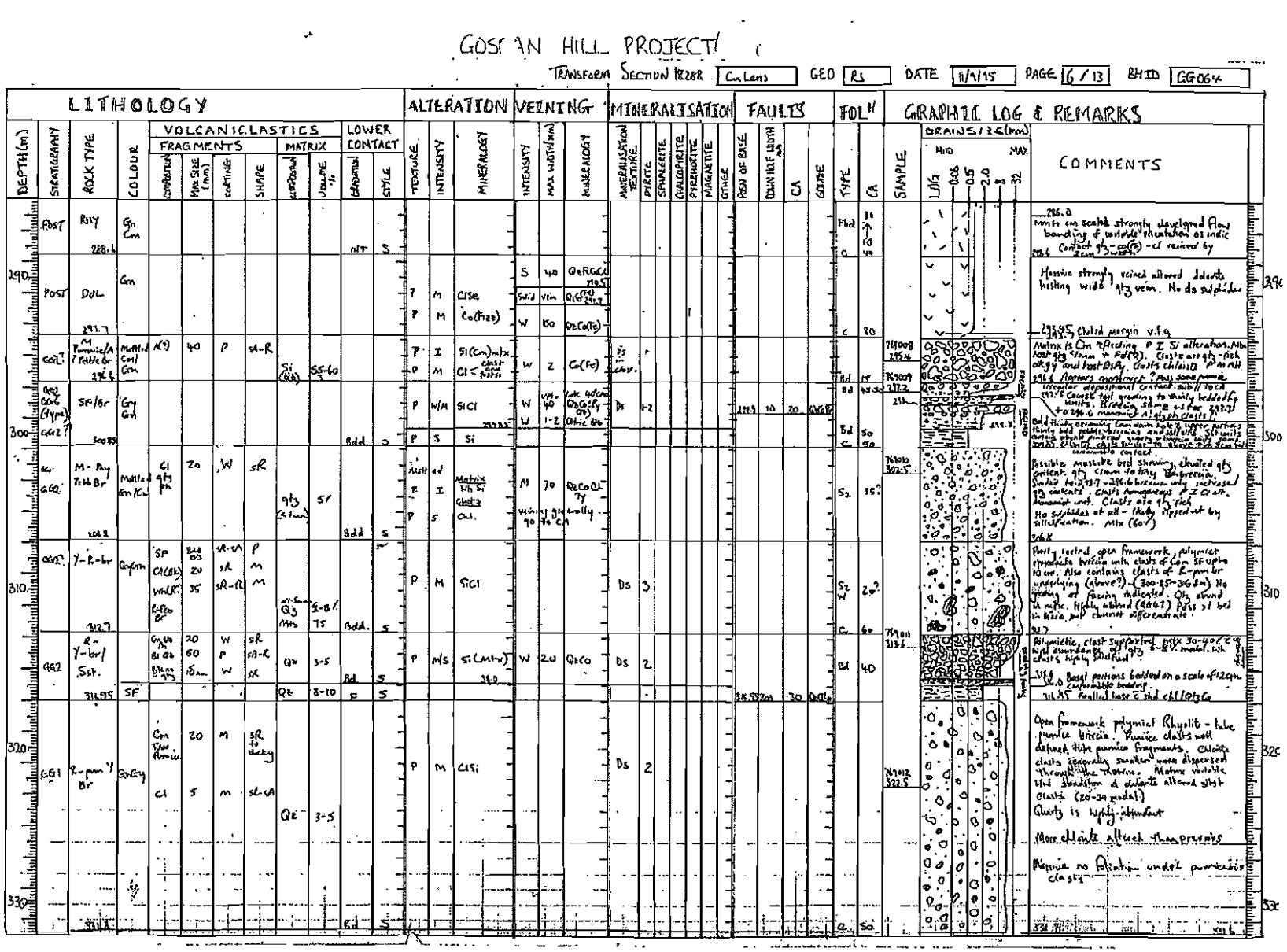
GOSSAN HILL PROJECT
TRANSFORM SECTION 12288
Cu Lens
GEO RS
DATE 11/9/15
PAGE 6 / 13
BHID GG064
LITHOLOGY
ALTERATION
VEINING
MINERALISATION
FAULTS
FOL'N
GRAPHIC LOG & REMARKS
DEPTH (m)
STRATIGRAPHY
ROCK TYPE
COLOUR
VOLCANICLASTICS
FRAGMENTS
MATRIX
LOWER CONTACT
TEXTURE
INTENSITY
MINERALOGY
MAX WIDTH (mm)
MINERALISATION TEXTURE
PYRITE
SPHALERITE
CHALCOPYRITE
PYRRHOTITE
MAGNETITE
GANGUE
SAMPLE
GRAINSIZE (mm)
COMMENTS

GOSSAN HILL PROJECT

Transform Section 12520N | C. Lewis | GEO: Rob | DATE: 11/9/95 | PAGE: 6/13 | BHID: GG064

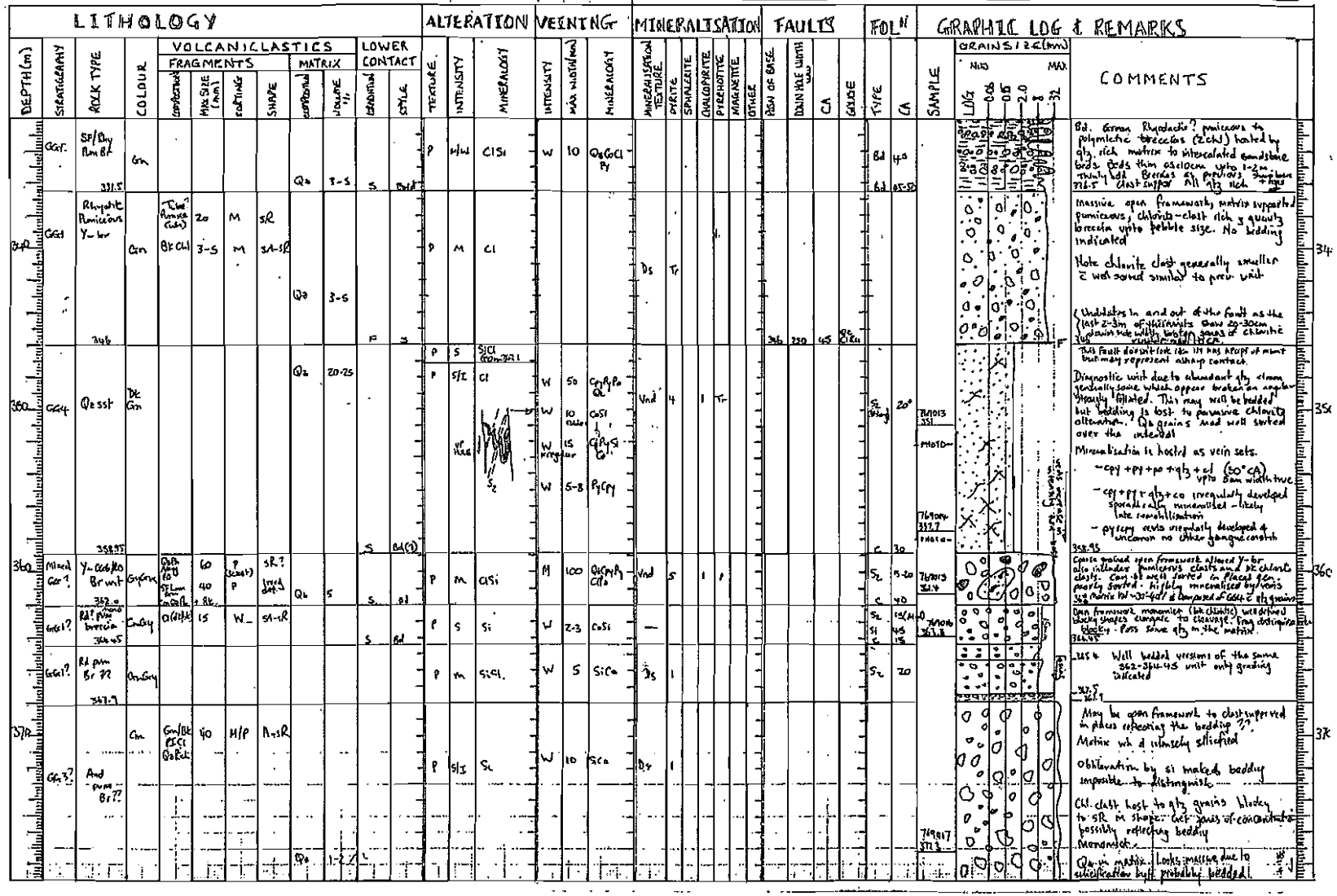

GOSSAN HILL PROJECT

TRANSFORM SECTION 182XXN | Cu Lens | GEO: Rob | DATE: 12/9/15 | PAGE: 7/13 | BHID: GG064

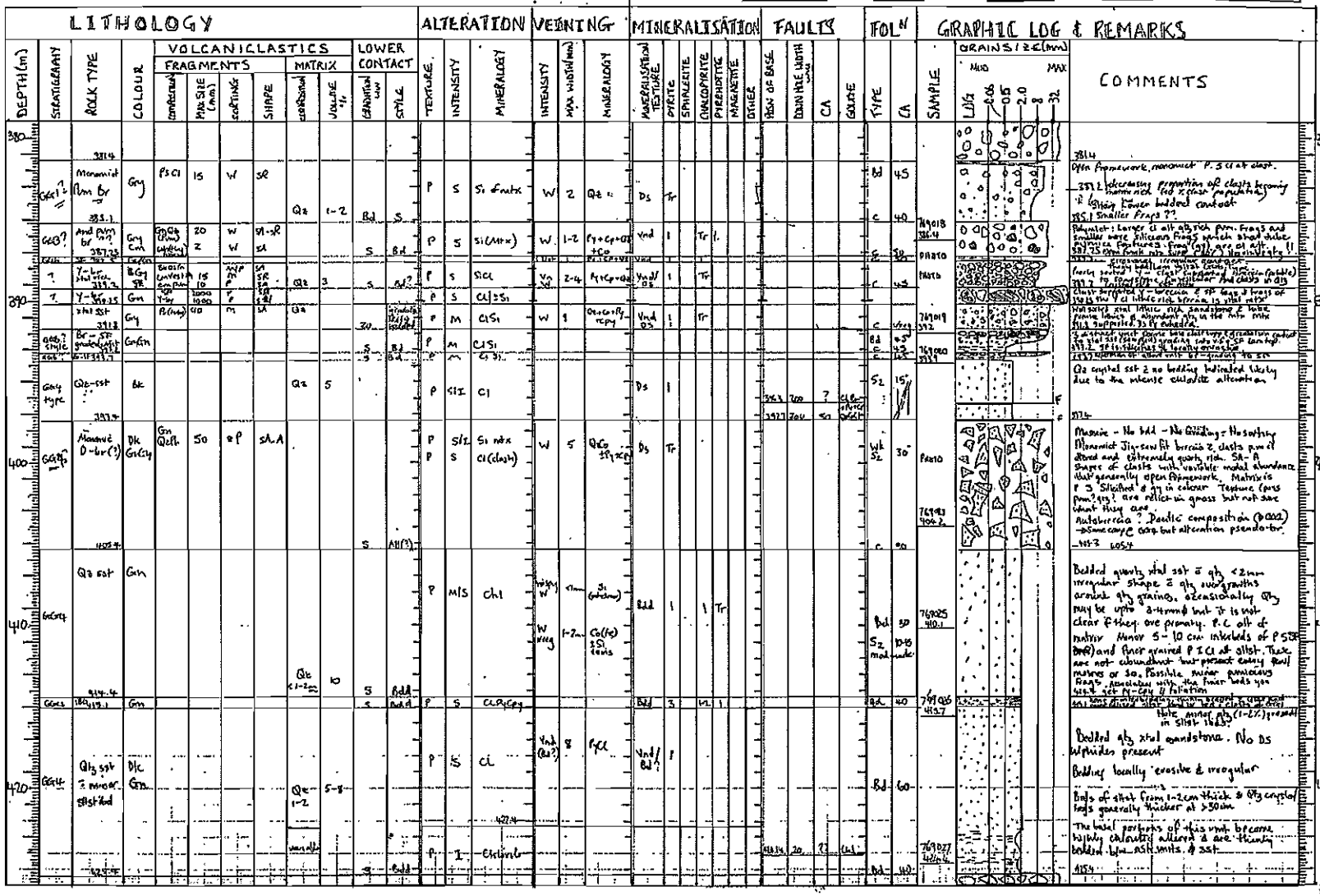

GOS AN HILL PROJECT

TRANSFORM SECTION 18288 | Ga Lens | GEO Rob | DATE 10/9/15 | PAGE 3/13 | RHID GG064

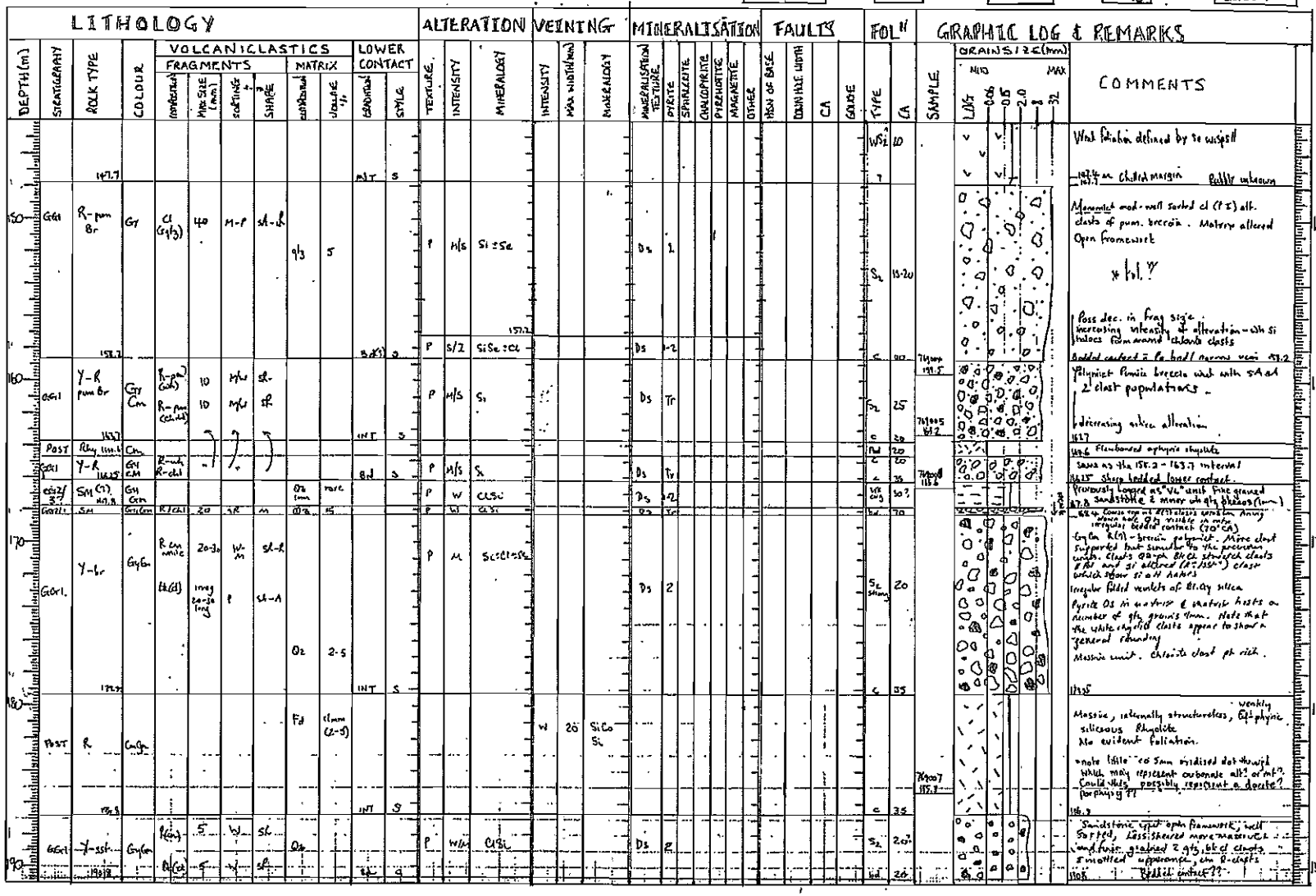

GOSSAN HILL PROJECT

TRANSFORM SECTION 182.88N | Cu Lens | GEO: Rob | DATE: 13/1/95 | PAGE: 8/13 | BHID: GG064

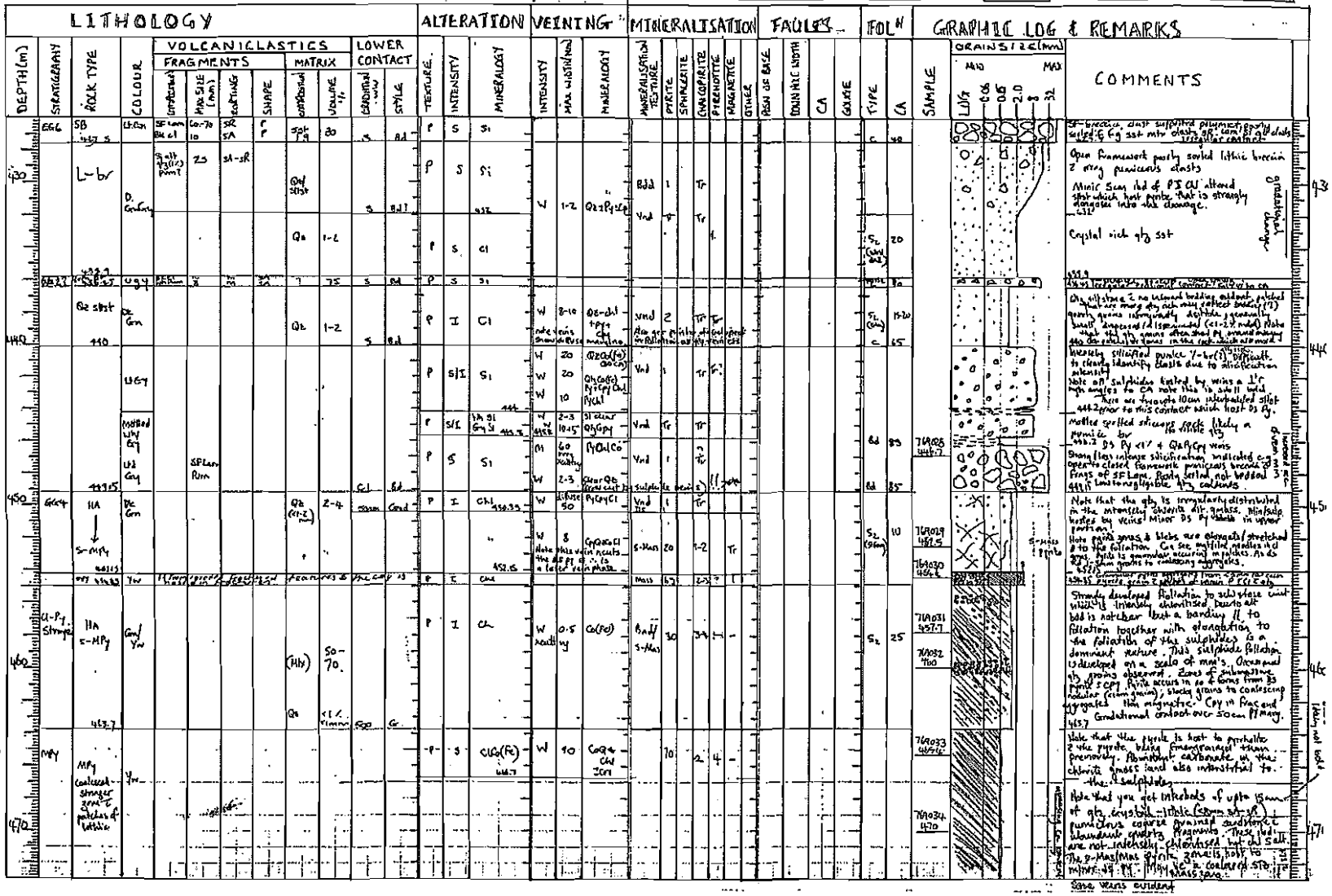

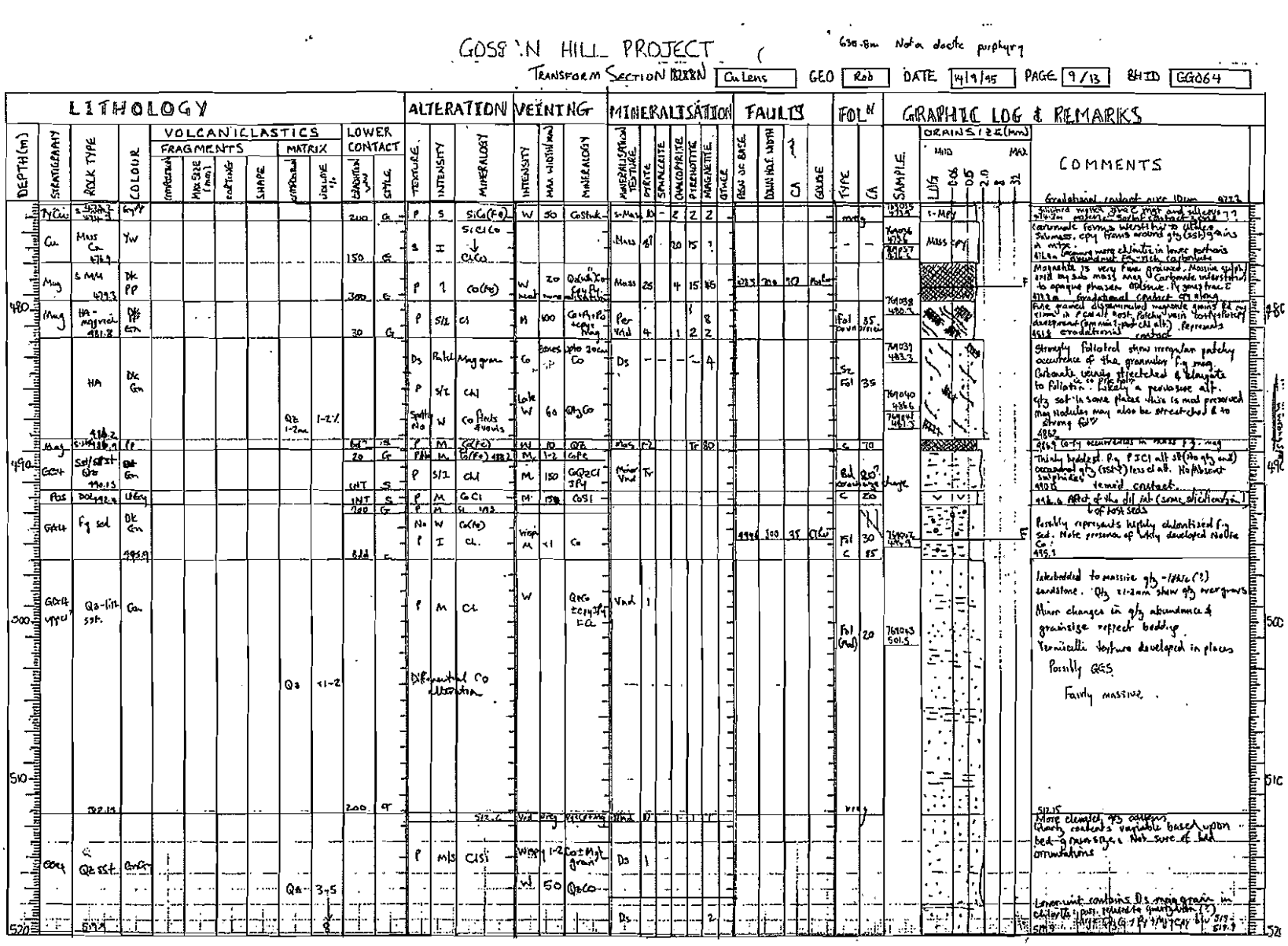
GOSSAN HILL PROJECT
TRANSFORM SECTION
Culens
Rob
4/9/95
9/13
GG064
LITHOLOGY
ALTERATION
VEINING
MINERALISATION
FAULTS
FOL^N
GRAPHIC LOG & REMARKS
VOLCANICLASTICS
FRAGMENTS
MATRIX
LOWER CONTACT
COMMENTS
DEPTH(m)
STRATIGRAPHY
ROCK TYPE
COLOUR
SAMPLE
480
490
500
510
520

GOSPAN HILL PROJECT

TRANSFORM SECTION 18288N | Cu LENS | GEO: Rob | DATE: 4/9/95 | PAGE: 10/13 | RHID: GG064

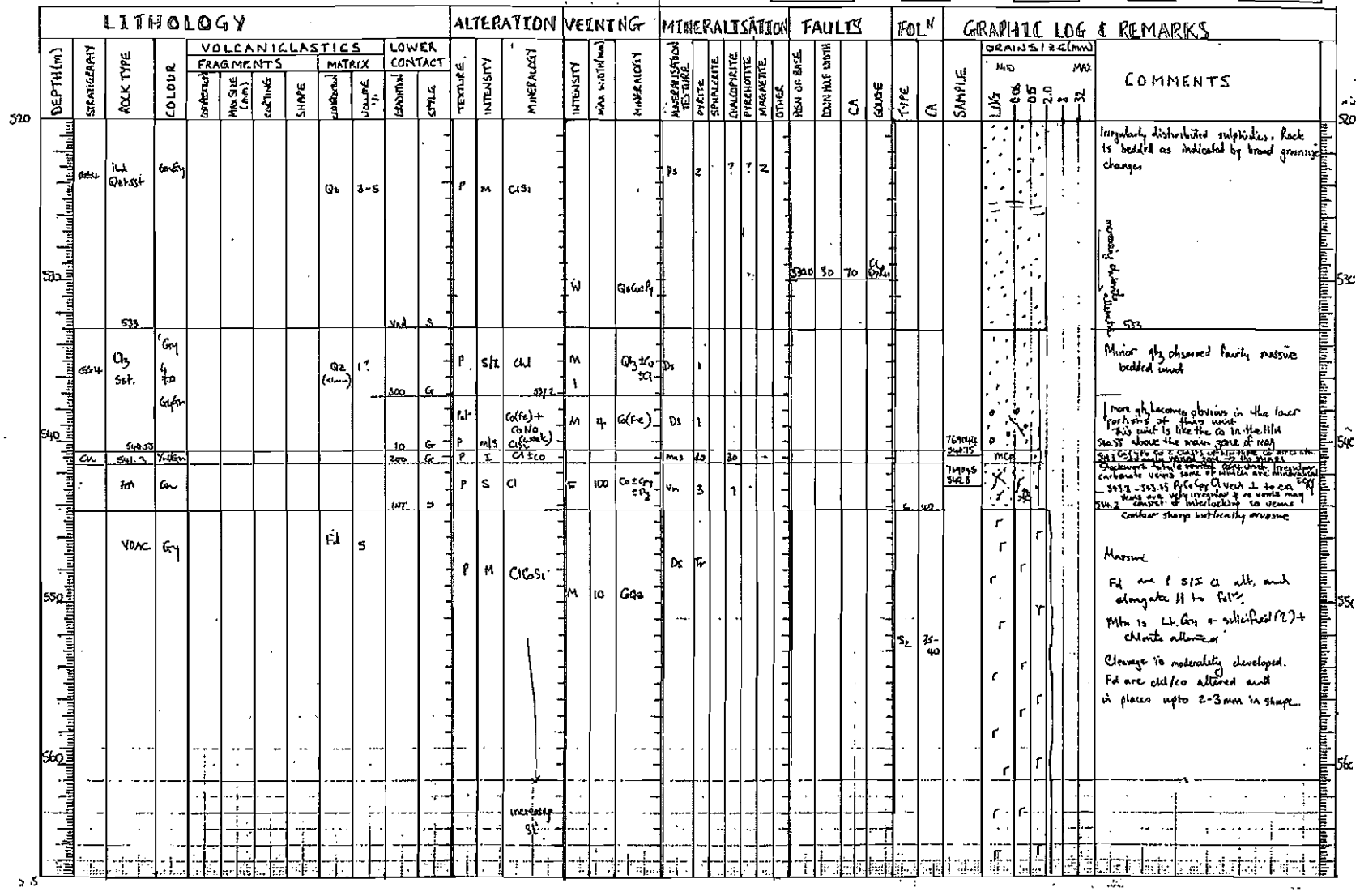

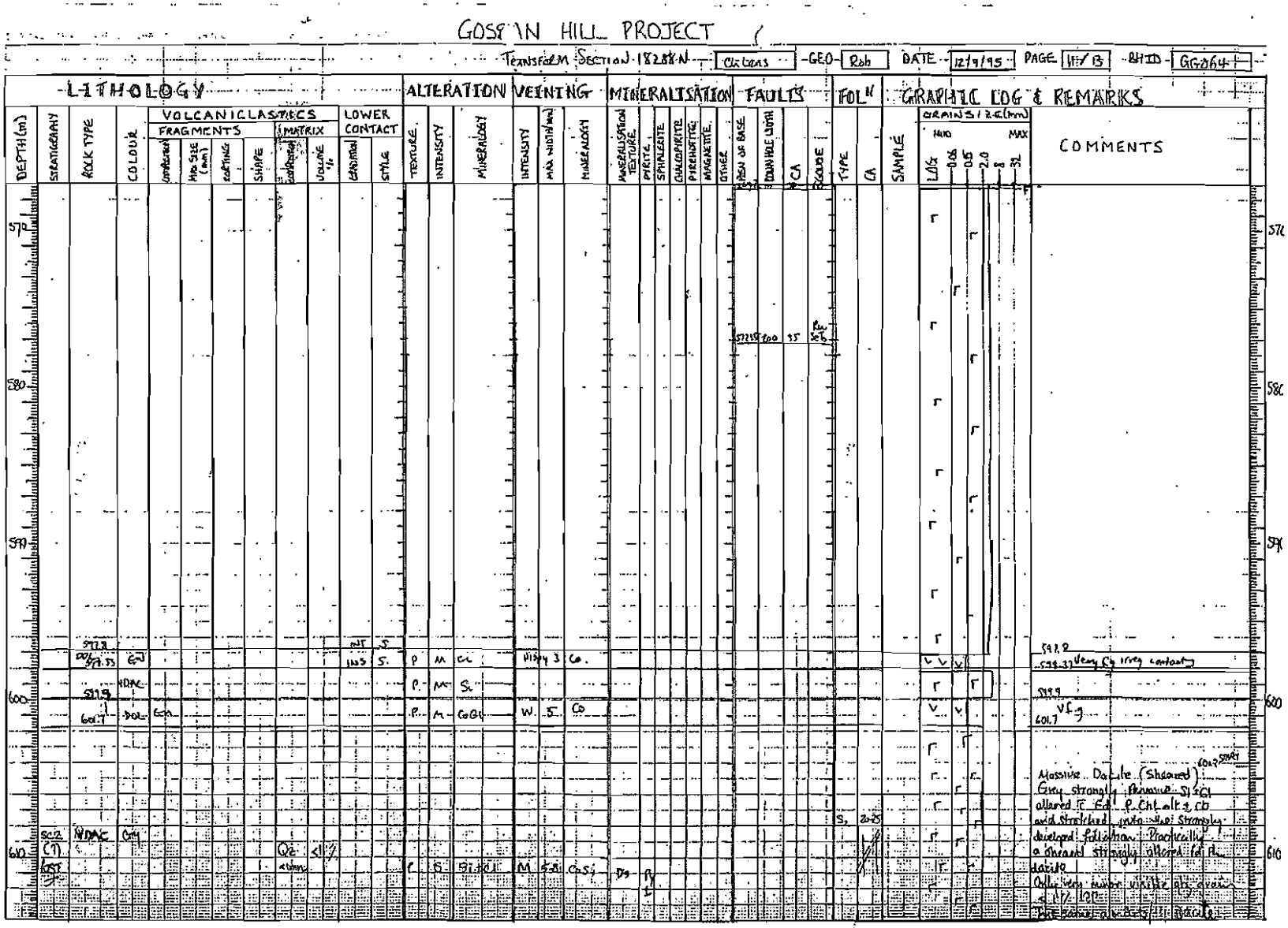
GOSSAN HILL PROJECT
Transform Section 18288N
GEO - Rob
DATE - 12/9/95
PAGE - 11 / 13
BHID - GG264
LITHOLOGY
ALTERATION
VEINING
MINERALISATION
FAULTS
FOLN
GRAPHIC LOG & REMARKS
VOLCANICLASTICS
FRAGMENTS
MATRIX
LOWER CONTACT
DEPTH (m)
ROCK TYPE
COLOUR
COMMENTS
Massive Dacite (Sheared)
Grey strongly foliated Sil Chl
altered & fol. P. Chl alt & Cb
and Strk/dip, vein vein strongly
developed foliation. Practically
a sheared strongly altered fol di...
dacite
Occ inch wide visible pyrite
veins
The base of the ...

GOSSAN HILL PROJECT

Transform Section 18288N | Cu Lens | GEO: Rob | DATE: 12/9/95 | PAGE: 12/13 | BHID: GG064

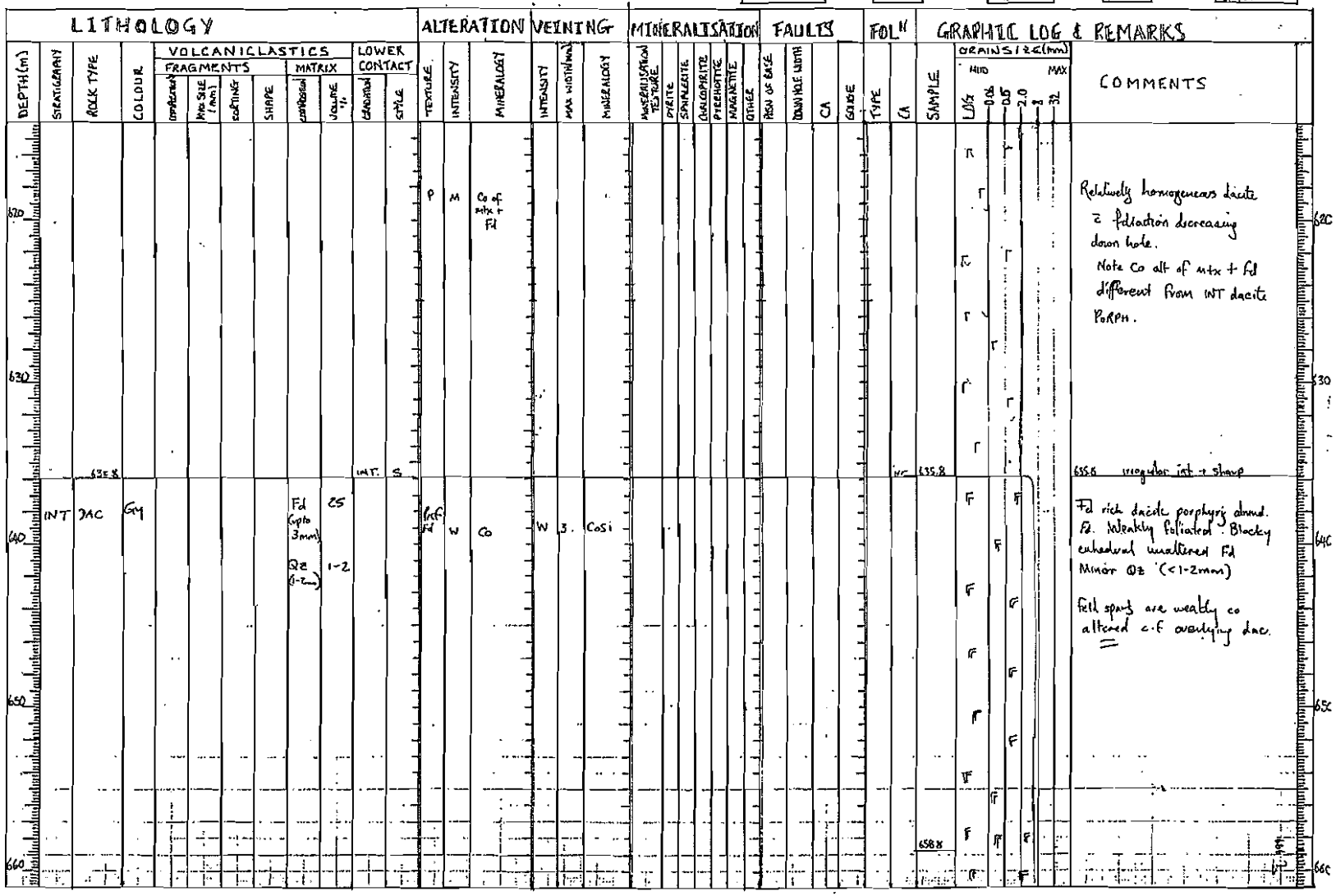

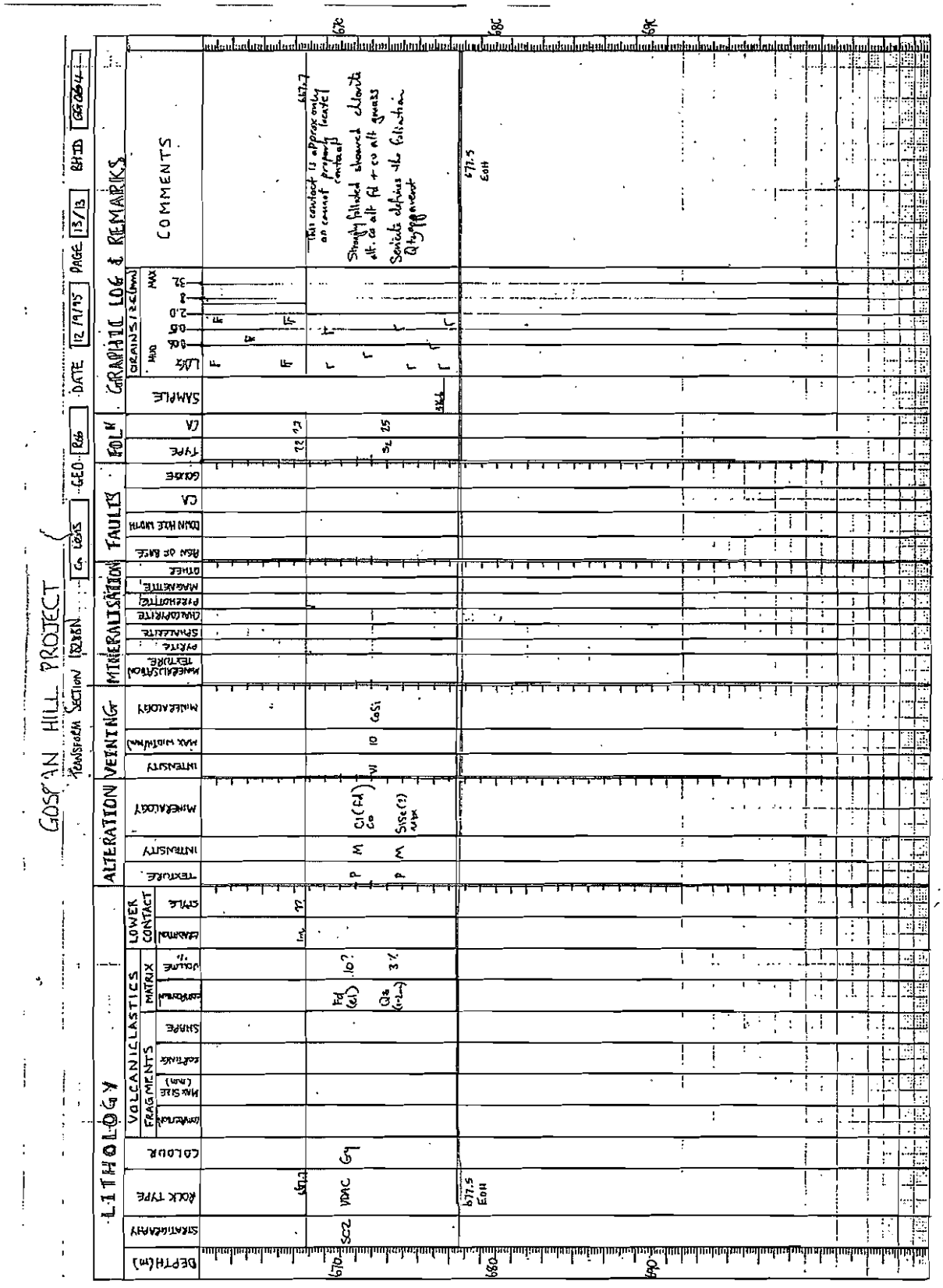
GOSPAN HILL PROJECT
TRANSVERSE SECTION 10300N
Co. LOGS
GEO. RBB
DATE 12/9/95
PAGE 13/13
BHID GG0644
LITHOLOGY
ALTERATION
VEINING
MINERALISATION
FAULTS
FOL'N
SAMPLE
GRAPHIC LOG & REMARKS
COMMENTS
DEPTH(m)
STRATIGRAPHY
ROCK TYPE
COLOUR
VOLCANICLASTICS
FRAGMENTS
MATRIX
LOWER CONTACT
TEXTURE
INTENSITY
MINERALOGY
MAX WIDTH(m)
MINERALISATION TEXTURE
PYRITE
SPHALERITE
CHALCOPYRITE
PYRRHOTITE
MAGNETITE
OTHER
BASE OF BASE
DOWN HOLE WIDTH
CA
GOUGE
TYPE
CA
SAMPLE
DRAINS/RECOMM
COMMENTS
671.5
EOH

LITHOLOGY
ALTERATION
VEINING
MINERALISATION
FAULTS
FOL
GRAPHIC LOG & REMARKS
COMMENTS
LAY SAM HILL PROJECT
TRANSFORM SECTION 18095
PANEL B
GEO RS
DATE 13/11/94
PAGE 1/6
BHID GG134
DEPTH(m)
LITHOLOGY
ROCK TYPE
COLOUR
VOLCANICLASTICS
FRAGMENTS
MATRIX
LOWER CONTACT
ALTERATION
INTENSITY
MINERALOGY
VEINING
INTENSITY
MINERALISATION
FAULTS
SAMPLE
GRAPHIC LOG
COMMENTS

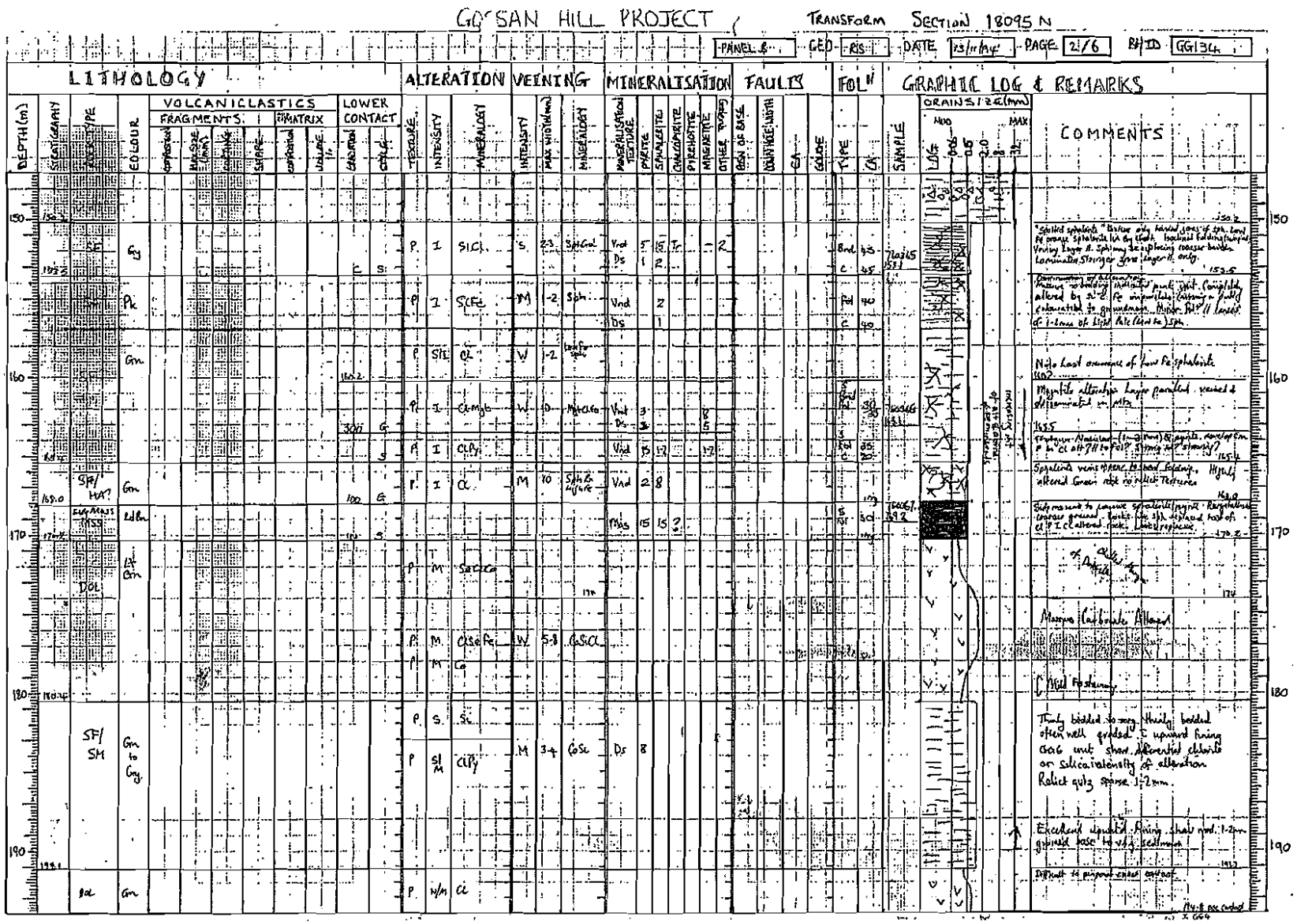
GC SAN HILL PROJECT
TRANSFORM SECTION 18095 N
PANEL 8
GEO RIS
DATE 13/11/96
PAGE 2/6
BH ID GG134
LITHOLOGY
ALTERATION
VEINING
MINERALISATION
FAULTS
FOL^N
GRAPHIC LOG & REMARKS
DEPTH (m)
VOLCANICLASTICS
FRAGMENTS
MATRIX
LOWER CONTACT
COLOUR
TEXTURE
INTENSITY
MINERALOGY
SAMPLE
GRAINSIZE (mm)
COMMENTS

GILT SAN HILL PROJECT
TRANSFORM
SECTION 18095 N
DATE 19/11/94
PAGE 3/6
BHID GGH34
GEO RS
PANEL 16
LITHOLOGY
ALTERATION
VEINING
MINERALISATION
FAULTS
EOL
GRAPHIC LOG & REMARKS
SAMPLE
COMMENTS
DEPTH(m)
VOLCANICLASTICS
MATRIX
LOWER CONTACT
FRAGMENTS
ROCK TYPE
COLOUR
TEXTURE
INTENSITY
MINERALOGY
MINERALISATION
PYRITE
SPHALERITE
CHALCOPYRITE
PYRRHOTITE
MAGNETITE
OTHER
DISTANCE (MM)
AZ
DIP
TYPE
LOG
GRAINSIZE (mm)

GLENSAH HILL PROJECT
TRANSORA SECTION
PANEL 16
GEO: RS
DATE: 14/11/94
PAGE 4/16
BHID GG1134
LITHOLOGY
ALTERATION VEINING
MINERALISATION FAULTS
GRAPHIC LOG & REMARKS
COMMENTS
SAMPLE
DEPTH (m)
STRATIGRAPHY
ROCK TYPE
COLOUR
VOLCANICLASTICS
FRAGMENTS
MATRIX
LOWER CONTACT
TEXTURE
INTENSITY
MINERALOGY
VEINING
MINERALISATION TEXTURE
ARSENOPYRITE
SPHALERITE
CHALCOPYRITE
PYRRHOTITE
MAGNETITE
OTHER
BOU de BASE
BOU MOE Horn
CA
GLYME
FOLIATION
GRAINSIZE (mm)
LOG
MAX
MIN
150
160
170
180

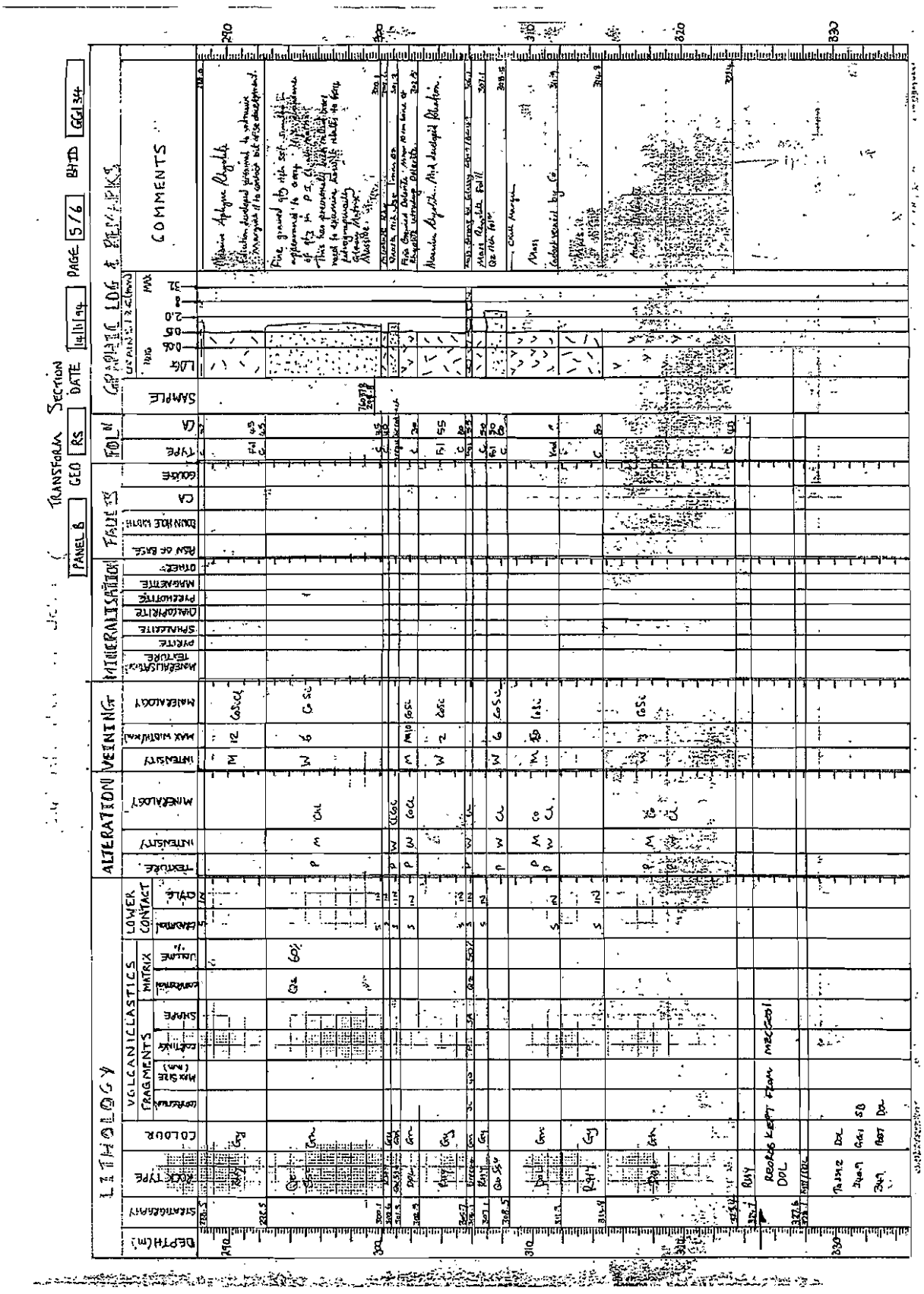
TRANSFORM Section
PANEL B
GEO RS
DATE 14/10/94
PAGE 5/6
BHID GGd34
LITHOLOGY
ALTERATION
VEINING
MINERALISATION
FAULTS
FOLIA
SAMPLE
GEOTECHNICAL LOG & REMARKS
COMMENTS
DEPTH (m)
STRATIGRAPHY
ROCK TYPE
COLOUR
VOLCANICLASTICS
FRAGMENTS
MATRIX
LOWER CONTACT
TEXTURE
INTENSITY
MINERALOGY
MAX WIDTH (mm)
MINERALISATION TEXTURE
PYRITE
SPHALERITE
CHALCOPYRITE
PYRRHOTITE
MAGNETITE
OTHER?
REM OF BASE
DOWN HOLE WIDTH
CA
GOUGE
TYPE
CA
Log
SAMPLE
COMMENTS

Appendix A1.2: Rock catalogue

UTas catalogue	Field#	Rock name	Rock description	Lithostratigraphy	DDH	Depth	North	East	RL
138578	760206	dacite	grey fspr qz phyric lava, weak chl si alteration	Mb2 Scuddles Fm	GG132	193.4	17843.2	4829.7	10187.7
138579	760207	dacite	msve grey fspr qz phyric lava, strong chl si alteration	Mb2 Scuddles Fm	GG132	240.2	17834.2	4853.0	10148.2
138580	760208	dolerite	msve green aphyric strong chl alteration	Proterozoic intrusion	GG132	263.7	17829.5	4864.8	10128.4
138581	760209	rhyodacite	msve qz fspr phyric lava, weak si alteration	Mb2 Scuddles Fm	GG132	280.3	17826.1	4873.2	10114.5
138582	760210	dolerite	green msve intrusion, strong chl calcite alteration	Proterozoic intrusion	GG132	288.0	17824.5	4877.1	10108.0
138583	760211	rhyodacite	cream qz fspr phyric lava	Mb2 Scuddles Fm	GG132	297.5	17822.5	4881.9	10100.1
138584	760212	dacite	grey fspr qz phyric lava, weak chl si alteration	Mb2 Scuddles Fm	GG132	305.9	17820.7	4886.2	10093.1
138585	760214	dacite	grey msve fspr qz phyric lava, weak chl si alteration	Mb2 Scuddles Fm	GG132	319.9	17817.7	4893.4	10081.5
138586	760215	rhyodacite	grey msve qz fspr phyric lava, weak chl alteration	Mb2 Scuddles Fm	GG132	329.7	17815.5	4898.5	10073.4
138587	760217	rhyodacite	grey msve qz fspr phyric lava, weak ser alteration	Mb2 Scuddles Fm	GG132	347.2	17811.7	4907.8	10059.1
138588	760218	rhyodacite	grey msve qz phyric vesicular lava	Mb2 Scuddles Fm	GG132	360.2	17808.8	4914.7	10048.5
138589	760219	rhyodacite	grey msve qz phyric vesicular lava,ser altered	Mb2 Scuddles Fm	GG132	364.5	17807.8	4917.1	10045.0
138590	760222	sphalerite	msve recrystallised with silic wall rock clasts	Mb6 Golden Grove Fm	GG132	368.9	17806.7	4919.4	10041.4
138591	760224	sphalerite	msve contact between mas sph and chert wall rock	Mb6 Golden Grove Fm	GG132	370.0	17806.5	4920.0	10040.5
138592	760225	sphalerite	msve recrystallised sph mas with silic chert clasts	Mb6 Golden Grove Fm	GG132	370.5	17806.4	4920.3	10040.1
138593	760226	pyrite	msve fine grained pyrite	Mb6 Golden Grove Fm	GG132	371.0	17806.3	4920.6	10039.7
138594	760227	pyrite	msve minor dissem magnetite	Mb6 Golden Grove Fm	GG132	371.7	17806.1	4920.9	10039.2
138595	760228	sphalerite	msve minor dissem py	Mb6 Golden Grove Fm	GG132	373.2	17805.8	4921.8	10037.9
138596	760230	sandstone	intense silic alteration	Mb6 Golden Grove Fm	GG132	374.6	17805.5	4922.5	10036.8
138597	760231	siltstone	bedded bx and siltstone, strong silic alteration	Mb6 Golden Grove Fm	GG132	380.4	17804.1	4925.6	10032.1
138598	760233	sandstone	grey tuffaceous, intense silic alteration	Mb5 Golden Grove Fm	GG132	399.3	17799.8	4935.8	10016.8
138599	760236	rhyodacite	grey msve qz fspr phyric lava, patchy ser alteration	Mb2 Scuddles Fm	GG132x	324.7	17811.0	4899.5	10082.2
138600	760241	sandstone	stringer minn intense silic alteration	Mb6 Golden Grove Fm	GG132x	355.8	17796.4	4921.5	10065.9
138601	760251	sandstone	bedded dissem sph	Mb5 Golden Grove Fm	GG090	218.6	17756.7	4948.0	10178.4
138602	760253	sandstone	tuffaceous, ankerite nodular alteration	Mb5 Golden Grove Fm	GG090	242.8	17745.8	4962.9	10162.8
138603	760254	rhyodacite	grey msve qz phyric lava	Mb2 Scuddles Fm	GG101	124.9	17748.6	4932.9	10261.3
138604	760264	rhyodacite	bx with dissem py and sph	Mb2 Scuddles Fm	GG131	204.7	17791.2	4904.2	10186.6
138605	760273	sandstone	bedded pumiceous intense silic alteration	Mb6 Golden Grove Fm	GG080	466.8	17842.1	4918.0	9926.1
138606	760290	dacite	msve fspr qz phyric pervasive ser alteration	Mb2 Scuddles Fm	GG080	531.0	17829.0	4949.4	9871.6
138607	760293	sandstone	qz rich tuffaceous bedded intense silic alteration	Mb6 Golden Grove Fm	GG080	545.8	17825.9	4956.8	9859.2
138608	760304	dacite	msve fspr qz phyric hyaloclastite bx	Mb2 Scuddles Fm	GG103	204.6	17772.6	5071.0	10176.9
138609	760308	breccia	tuffaceous qz bearing bedded intense silic alteration	Mb4 Golden Grove Fm	GG103	249.2	17777.8	5048.6	10138.7
138610	760323	rhyodacite	msve grey qz fspr phyric lava strong ser alteration	Mb2 Scuddles Fm	GG135X	336.7	17896.4	4904.6	10075.3

Appendix A1.2: Rock catalogue

UTas catalogue	Field#	Rock name	Rock description	Lithostratigraphy	DDH	Depth	North	East	RL
138611	760336	sandstone	msve intense silicification py veins	Mb6 Golden Grove Fm	GG130	200.8	18186.9	4923.8	10199.2
138612	760342	sandstone	tuffaceous dissem sph	Mb6 Golden Grove Fm	GG118	124.4	18186.6	4928.3	10268.4
138613	760343	sandstone	stringer minn dissem sph in intense silic alteration	Mb6 Golden Grove Fm	GG118	126.2	18186.5	4929.3	10266.9
138614	760346	sandstone	stringer py minn intense silic alteration	Mb6 Golden Grove Fm	GG118	133.9	18186.1	4933.6	10260.5
138615	760348	siltstone	dissem sph	Mb6 Golden Grove Fm	GG118	137.9	18185.9	4935.8	10257.2
138616	760350	chert	stringer minn py vein in intense silic alteration	Mb6 Golden Grove Fm	GG118	148.0	18185.5	4941.5	10248.8
138617	760352	sandstone	stringer minn magnetite veins intense chl si alteration	Mb6 Golden Grove Fm	GG118	161.9	18184.8	4949.3	10237.3
138618	760356	sandstone	qz rich dissem magnetite and po	Mb4 Golden Grove Fm	GG118	250.5	18178.4	5002.7	10167.1
138619	760357	sandstone	qz rich tuffaceous	Mb4 Golden Grove Fm	GG118	262.1	18177.2	5010.2	10158.3
138620	760361	chert	stringer minn dissem sph in intense silic alteration	Mb6 Golden Grove Fm	GG134	113.4	18138.5	4926.8	10279.0
138621	760362	sphalerite	msve dissem py chlaocpyrite and galena	Mb6 Golden Grove Fm	GG134	124.6	18135.5	4932.6	10269.9
138622	760364	breccia	polymict msve	Mb6 Golden Grove Fm	GG134	130.1	18134.0	4935.4	10265.4
138623	760366	sandstone	M1 Marker bedded chert and chlorite sandstone	Mb6 Golden Grove Fm	GG134	163.1	18124.9	4952.7	10238.8
138624	760367	sphalerite	msve crse grained dissem py	Mb6 Golden Grove Fm	GG134	169.2	18123.2	4955.9	10233.9
138625	760368	pyrite	msve nodular py with dissem magnetite	Mb6 Golden Grove Fm	GG134	199.3	18114.1	4972.1	10210.3
138626	760369	magnetite	msve abundant ankerite and dissem py	Mb4 Golden Grove Fm	GG134	202.7	18113.0	4973.9	10207.6
138627	760370	pyrite	msve fine grained with dissem magnetite	Mb6 Golden Grove Fm	GG134	205.2	18112.2	4975.3	10205.7
138628	760371	sandstone	intense chl alteration dissem magnetite pyrrhotite	Mb6 Golden Grove Fm	GG134	211.4	18110.2	4978.7	10200.9
138629	760372	pyrite	msve dissem magnetite and ankerite	Mb6 Golden Grove Fm	GG134	221.1	18107.1	4984.0	10193.4
138630	760373	sandstone	stringer minn intense chl alteration py chl veins	Mb6 Golden Grove Fm	GG134	224.6	18105.9	4985.9	10190.7
138631	760374	chert	stringer minn py magnetite veins silic alteration	Mb6 Golden Grove Fm	GG134	225.7	18105.6	4986.5	10189.8
138632	760375	sandstone	qx rich tuffaceous	Mb4 Golden Grove Fm	GG134	245.2	18099.1	4997.1	10174.8
138633	760376	sandstone	qz rich tuffaceous	Mb4 Golden Grove Fm	GG134	253.0	18096.4	5001.3	10168.8
138634	760380	siltstone	thinly bedded strong chl alteration dissem py	Mb6 Golden Grove Fm	GG136	122.0	18190.2	4931.6	10263.0
138635	760381	chert	stringer minn sph veins intense silic	Mb6 Golden Grove Fm	GG136	125.4	18190.1	4932.3	10259.6
138636	760383	sandstone	intense chl alteration dissem py magnetite	Mb6 Golden Grove Fm	GG136	138.7	18189.6	4934.8	10246.6
138637	760384	pyrite	msve low iron sph dissem py	Mb6 Golden Grove Fm	GG136	142.5	18189.4	4935.6	10242.9
138638	760386	sphalerite	msve dissem py	Mb6 Golden Grove Fm	GG127	97.9	18115.9	4959.8	10301.9
138639	760389	sandstone	msve tuffaceous intense chl ankerite alteration	Mb5 Golden Grove Fm	GG127	114.0	18114.5	4970.5	10289.7
138640	760392	sandstone	stringer minn cpy ankerite py pyrrhotite vein	Mb6 Golden Grove Fm	GG127	125.7	18113.2	4978.1	10281.1
138641	760400	magnetite	msve crse grained dissem py	Mb4 Golden Grove Fm	GG127	141.3	18111.5	4988.6	10269.7
138642	760410	sandstone	tuffaceous ankerite nodular alteration	Mb5 Golden Grove Fm	GG127	179.0	18107.3	5014.4	10242.6
138643	760411	sandstone	tuffaceous ankerite nodular alteration	Mb5 Golden Grove Fm	GG127	179.4	18107.3	5014.7	10242.3

Appendix A1.2: Rock catalogue

UTas catalogue	Field#	Rock name	Rock description	Lithostratigraphy	DDH	Depth	North	East	RL
138644	760414	sphalerite	msve upper contact with intense silic sandstone	Mb6 Golden Grove Fm	GG165	263.4	18231.8	4792.8	10127.9
138645	760417	sphalerite	msve fine grained	Mb6 Golden Grove Fm	GG165	271.0	18234.6	4795.5	10121.3
138646	760418	sphalerite	msve crse grained recrystallised sph	Mb6 Golden Grove Fm	GG165	272.2	18235.1	4795.9	10120.3
138647	760419	sphalerite	msve banded dissem py	Mb6 Golden Grove Fm	GG165	273.9	18235.7	4796.5	10118.8
138648	760420	sphalerite	msve banded sph and py	Mb6 Golden Grove Fm	GG165	277.0	18236.9	4797.6	10116.2
138649	760421	pyrite	msve minor dissem sph in fine grained py	Mb6 Golden Grove Fm	GG165	282.0	18238.7	4799.3	10111.9
138650	760423	pyrite	msve fine grained with dissem py	Mb6 Golden Grove Fm	GG165	288.2	18241.1	4801.5	10106.6
138651	760424	pyrite	msve crse grained chl gangue	Mb6 Golden Grove Fm	GG165	293.2	18242.9	4803.2	10102.3
138652	760425	pyrite	msve crse grained	Mb6 Golden Grove Fm	GG165	296.4	18244.1	4804.4	10099.5
138653	760426	pyrite	msve crse grained veined by sph	Mb6 Golden Grove Fm	GG165	302.0	18246.3	4806.3	10094.7
138654	760428	sphalerite	msve dissem py and cpy	Mb6 Golden Grove Fm	GG165	307.4	18248.3	4808.2	10090.1
138655	760430	sandstone	tuffaceous intense chl silic alteration	Mb6 Golden Grove Fm	GG165	314.9	18251.1	4810.8	10083.7
138656	760431	chert	stringer minn intense silic alteration with py veins	Mb6 Golden Grove Fm	GG165	319.6	18252.9	4812.5	10079.6
138657	760432	sandstone	stringer minn sph, magnetite, pyrrhotite, chl veins	Mb6 Golden Grove Fm	GG165	331.6	18257.4	4816.7	10069.4
138658	760433	sandstone	intense chl alteration	Mb6 Golden Grove Fm	GG165	337.1	18259.5	4818.7	10064.6
138659	760434	sandstone	intense chl dissem andalusite, chloritoid, magnetite	Mb6 Golden Grove Fm	GG165	339.3	18260.3	4819.4	10062.8
138660	760435	chert	stringer minn intense silic alteration py veins	Mb6 Golden Grove Fm	GG165	348.3	18263.7	4822.7	10055.1
138661	760436	sandstone	stringer minn intense chl py pyrrhotite veins	Mb6 Golden Grove Fm	GG165	357.2	18267.0	4825.9	10047.5
138662	760438	chert	stringer minn intense silic alteration py chl veins	Mb6 Golden Grove Fm	GG165	365.5	18270.1	4828.9	10040.4
138663	760440	sandstone	stringer minn dissem py pyrrhotite magnetite	Mb6 Golden Grove Fm	GG165	377.0	18274.3	4833.2	10030.6
138664	760441	sandstone	intense chl dissem andalusite, chloritoid, magnetite	Mb6 Golden Grove Fm	GG165	379.9	18275.4	4834.3	10028.1
138665	760442	pyrite	msve crse grained py	Mb6 Golden Grove Fm	GG165	380.3	18275.6	4834.4	10027.8
138666	760443	sandstone	stringer minn intense chl dissem py magnetite pyrrhotite veins	Mb6 Golden Grove Fm	GG165	385.0	18277.3	4836.2	10023.8
138667	760444	pyrite	msve crse grained	Mb6 Golden Grove Fm	GG165	395.6	18281.2	4840.2	10014.8
138668	760445	sandstone	tuffaceous dissem py	Mb6 Golden Grove Fm	GG165	402.9	18283.9	4842.9	10008.6
138669	760446	sandstone	stringer minn dissem py magnetite chl alteration	Mb6 Golden Grove Fm	GG165	424.2	18291.8	4851.1	9990.6
138670	760447	dacite	grey fspr qz phyric lava strong calcite alteration	Mb2 Scuddles Fm	GG165	424.2	18291.7	4851.1	9990.6
138671	760449	rhyodacite	peperitic margin of qz fd phyric lava	Mb2 Scuddles Fm	GG160	136.7	18217.4	4789.8	10241.1
138672	760451	rhyodacite	peperitic margin of qz fd phyric lava	Mb2 Scuddles Fm	GG160	146.4	18220.7	4792.8	10232.5
138673	760455	sphalerite	msve dissem sph py in intense silic alteration	Mb6 Golden Grove Fm	GG160	233.3	18251.7	4819.5	10155.8
138674	760459	pyrite	msve with dissem magnetite chl	Mb6 Golden Grove Fm	GG160	260.2	18261.5	4827.5	10132.0
138675	760461	pyrite	msve minor dissem sph magnetite	Mb6 Golden Grove Fm	GG160	277.6	18267.8	4832.7	10116.7
138676	760463	pyrite	msve abundant dissem magnetite	Mb6 Golden Grove Fm	GG160	305.5	18278.0	4841.0	10092.1

Appendix A1.2: Rock catalogue

UTas catalogue	Field#	Rock name	Rock description	Lithostratigraphy	DDH	Depth	North	East	RL
138677	760464	pyrite	msve crse grained intense chl alteration	Mb6 Golden Grove Fm	GG160	320.6	18283.4	4845.5	10078.7
138678	760465	sandstone	intense chl dissem andalusite, chloritoid, magnetite	Mb6 Golden Grove Fm	GG160	332.1	18287.6	4848.9	10068.6
138679	760466	sandstone	intense chl dissem andalusite, chloritoid, magnetite	Mb6 Golden Grove Fm	GG160	334.2	18288.4	4849.6	10066.7
138680	760472	sandstone	msve tuffaceous intense chl alteration dissem py	Mb6 Golden Grove Fm	GG163	176.0	18235.8	4826.6	10228.8
138681	760473	sandstone	intense chl dissem andalusite, chloritoid, magnetite	Mb6 Golden Grove Fm	GG163	188.7	18241.8	4832.6	10219.4
138682	760474	sandstone	tuffaceous intense silic alteration dissem py	Mb6 Golden Grove Fm	GG163	195.9	18245.2	4836.0	10214.0
138683	760475	sandstone	tuffaceous intense silic alteration dissem sph	Mb6 Golden Grove Fm	GG163	201.0	18247.6	4838.4	10210.2
138684	760479	sandstone	qz rich with strong silic chl alteration	Mb6 Golden Grove Fm	GG163	216.3	18254.9	4845.6	10198.9
138685	760480	sandstone	tuffaceous strong chl silic alteration dissem py	Mb6 Golden Grove Fm	GG163	234.1	18263.3	4854.0	10185.6
138686	760486	dacite	grey fspr qz phyric lava	Mb2 Scuddles Fm	GG165	190.7	18204.9	4768.1	10190.7
138687	760487	rhyodacite	qz fspr phyric amygdaloidal lava pervasive calcite	Mb2 Scuddles Fm	GG165	222.7	18216.7	4778.8	10162.9
138688	760488	rhyodacite	qz fspr phyric amygdaloidal lava pervasive calcite	Mb2 Scuddles Fm	GG165	234.5	18221.0	4782.8	10152.8
138689	760489	sandstone	M1 Marker bedded chert chlorite intervals	Mb6 Golden Grove Fm	GG165	243.0	18224.2	4785.1	10145.4
138690	760490	sandstone	M1 Marker bedded chert chlorite intervals	Mb6 Golden Grove Fm	GG165	243.7	18224.4	4785.9	10144.8
138691	760491	sandstone	msve tuffaceous intense silic chl alteration	Mb6 Golden Grove Fm	GG165	247.3	18225.8	4787.2	10141.7
138692	760492	dolerite	medium grained pervasive strong chl alteration	Proterozoic intrusion	GG148	137.7	18192.6	4880.1	10248.9
138693	760495	chert	stringer minn py veins intense silic alteration	Mb6 Golden Grove Fm	GG148	194.7	18189.7	4913.5	10202.8
138694	760499	sandstone	green tuffaceous intense silic chl alteration	Mb5 Golden Grove Fm	GG148	219.7	18188.1	4928.7	10183.0
138695	760500	sandstone	stringer minn intense chl veins of py magnetite cpy	Mb5 Golden Grove Fm	GG148	235.4	18187.0	4938.3	10170.7
138696	762004	sandstone	qz poor tuffaceous strong chl silic alteration	Mb5 Golden Grove Fm	GG148	291.7	18182.3	4973.7	10127.2
138697	762005	sandstone	qz rich tuffaceous strong chl silic alteration	Mb4 Golden Grove Fm	GG148	317.7	18179.7	4990.3	10107.3
138698	762006	sandstone	stringer minn ankerite vein cutting py pyrrhotite vein	Mb4 Golden Grove Fm	GG148	324.4	18178.9	4994.6	10102.2
138699	762007	magnetite	msve relict patches of silic altered wall rock	Mb4 Golden Grove Fm	GG148	332.1	18178.0	5000.0	10096.0
138700	762009	magnetite	msve dissem py cpy and pyrrhotite	Mb5 Golden Grove Fm	GG148	341.1	18177.1	5005.3	10089.6
138701	762010	pyrite	msve crse grained in intense chl gangue	Mb4 Golden Grove Fm	GG148	348.3	18176.2	5010.0	10084.1
138702	762014	sandstone	qz rich intense chl alteration dissem py magnetite	Mb4 Golden Grove Fm	GG148	371.9	18173.2	5025.2	10066.3
138703	762016	sandstone	tuffaceous intense chl alteration	Mb3 Golden Grove Fm	GG148	391.0	18170.7	5037.5	10051.9
138704	762018	breccia	qz rich tuffaceous intense mottled chl silic alteration	Mb1 Golden Grove Fm	GG148	400.7	18169.3	5043.8	10044.7
138705	762019	dacite	fspr qz phyric msve hyaloclastite bx	Mb2 Scuddles Fm	GG171	201.0	18180.3	4784.6	10180.1
138706	762027	sphalerite	msve crse grained recrystallised with dissem py	Mb6 Golden Grove Fm	GG171	297.2	18216.8	4816.4	10096.3
138707	762029	sphalerite	msve crse grained recrystallised with qz	Mb6 Golden Grove Fm	GG171	308.5	18221.3	4820.4	10086.7
138708	762030	sphalerite	msve low iron fine grained with dissem py	Mb6 Golden Grove Fm	GG171	319.0	18225.5	4824.2	10077.9
138709	762031	sphalerite	stringer minn sph py veins in intense silic alteration	Mb6 Golden Grove Fm	GG171	322.7	18227.0	4825.6	10074.8

Appendix A1.2: Rock catalogue

UTas catalogue	Field#	Rock name	Rock description	Lithostratigraphy	DDH	Depth	North	East	RL
138710	762034	pyrite	msve intense silic altered wall rock with py veins	Mb6 Golden Grove Fm	GG171	354.6	18240.2	4837.4	10048.3
138711	762039	sandstone	intense chl dissem andalusite, chloritoid, magnetite	Mb6 Golden Grove Fm	GG171	388.5	18254.5	4850.3	10020.4
138712	762040	sandstone	intense chl dissem andalusite, chloritoid, magnetite	Mb6 Golden Grove Fm	GG171	392.8	18256.3	4852.0	10016.9
138713	762050	sandstone	intense chl dissem andalusite, chloritoid, magnetite	Mb6 Golden Grove Fm	GG173	327.9	18256.1	4852.3	10081.0
138714	762052	pyrite	msve minor dissem sph magnetite	Mb6 Golden Grove Fm	GG173	355.1	18268.2	4862.4	10058.8
138715	762053	sandstone	intense chl dissem andalusite, chloritoid, magnetite	Mb4 Golden Grove Fm	GG173	373.8	18276.5	4869.6	10043.7
138716	762054	magnetite	msve minor dissem crse grained py	Mb4 Golden Grove Fm	GG173	377.0	18277.9	4870.9	10041.1
138717	762055	sandstone	intense chl dissem andalusite, chloritoid, magnetite	Mb4 Golden Grove Fm	GG173	396.9	18286.8	4878.9	10025.3
138718	762057	sandstone	tuffaceous intense chl alteration	Mb5 Golden Grove Fm	GG173	434.0	18303.7	4894.8	9996.3
138719	762059	sphalerite	msve recrystallised high iron dissem py arsenopyrite	Mb6 Golden Grove Fm	GG099	119.0	18073.7	4954.0	10283.2
138720	762063	sandstone	intense silic and chl spotted alteration dissem py	Mb6 Golden Grove Fm	GG099	150.7	18067.6	4976.9	10262.2
138721	762064	sandstone	M1 Marker bedded chert chlorite intervals	Mb6 Golden Grove Fm	GG099	157.8	18066.3	4928.1	10257.5
138722	762065	pyrite	msve crse grained dissem magnetite and ankerite	Mb6 Golden Grove Fm	GG099	169.6	18063.8	4990.8	10249.9
138723	762078	pyrite	msve crse grained dissem cpy	Mb4 Golden Grove Fm	GG044	390.6	18695.7	5075.3	10018.3
138724	762084	sandstone	qz bearing crse grained strong chl alteration	Mb4 Golden Grove Fm	GG044	500.0	18737.1	5023.9	9931.4
138725	762085	sandstone	qz rich tuffaceous dissem py	Mb4 Golden Grove Fm	GG044	533.3	18753.0	5005.5	9908.5
138726	762091	sphalerite	msve low iron sph sericite silica gangue	Mb6 Golden Grove Fm	GG161	277.8	18218.0	4867.0	10117.0
138727	762092	breccia	polymict dissem sph	Mb6 Golden Grove Fm	GG161	282.5	18219.2	4869.2	10112.5
138728	762093	sphalerite	msve replacement of a polymict bx	Mb6 Golden Grove Fm	GG161	284.7	18220.0	4870.0	10111.0
138729	762094	sandstone	thinly bedded tuffaceous	Mb6 Golden Grove Fm	GG161	289.5	18221.1	4871.7	10106.9
138730	769009	breccia	qz poor tuffaceous patchy chl silic alteration	Mb1 Golden Grove Fm	GG064	297.2	18234.3	5052.1	10122.5
138731	769018	sandstone	bedded tuffaceous	Mb2 Golden Grove Fm	GG064	387.5	18254.7	5029.7	10038.7
138732	769021	sandstone	qz rich strong chl silic alteration	Mb4 Golden Grove Fm	GG064	404.2	18260.0	5024.9	10022.4
138733	769030	pyrite	msve crse grained py	Mb4 Golden Grove Fm	GG064	454.4	18276.3	5010.1	9927.2
138734	769036	chalcopyrite	msve minor dissem pyrrhotite	Mb4 Golden Grove Fm	GG064	475.6	18284.0	5003.0	9958.0
138735	769049	breccia	tuffaceous qz bearing pat silici chl alteration	Mb1 Golden Grove Fm	GG027	251.9	18257.5	5055.2	10168.9
138736	769050	sandstone	intense silic alteration veined by chl and ankerite	Mb4 Golden Grove Fm	GG027	259.4	18259.2	5052.2	10162.2
138737	769053	siltstone	pervasive intense chl alteration	Mb4 Golden Grove Fm	GG027	287.3	18266.2	5040.7	10137.8
138738	769054	magnetite	msve hosts cross cutting py vein	Mb4 Golden Grove Fm	GG027	288.6	18266.5	5040.1	10136.6
138739	769056	breccia	pervasive intense chl ankerite alteration	Mb4 Golden Grove Fm	GG027	296.7	18268.7	5036.8	10129.6
138740	769057	pyrite	msve minor dissem ankerite and magnetite	Mb4 Golden Grove Fm	GG027	307.9	18271.8	5032.1	10119.9
138741	769058	pyrite	msve minor dissem magnetite	Mb4 Golden Grove Fm	GG027	313.6	18273.4	5029.7	10115.0
138742	769060	magnetite	msve fine grained with cross cutting py vein	Mb4 Golden Grove Fm	GG027	327.1	18277.0	5024.0	10103.0

Appendix A1.2: Rock catalogue

UTas catalogue	Field#	Rock name	Rock description	Lithostratigraphy	DDH	Depth	North	East	RL
138743	769061	siltstone	intense chl alteration	Mb4 Golden Grove Fm	GG027	336.7	18280.2	5020.1	10095.1
138744	769065	sandstone	massive tuffaceous qz poor	Mb5 Golden Grove Fm	GG027	364.5	18288.9	5008.5	10071.4
138745	769066	sandstone	tuffaceous intense chl and nodular ankerite alteration	Mb5 Golden Grove Fm	GG027	369.5	18290.4	5006.3	10067.2
138746	769072	sandstone	qz rich thinly bedded tuffaceous	Mb4 Golden Grove Fm	GG027	517.3	18349.2	4924.0	9961.0
138747	769073	dacite	grey fspr qz phyric lava	Mb2 Scuddles Fm	GG027	571.0	18372.1	4883.6	9934.3
138748	769074	dacite	grey fspr qz phyric lava	Mb2 Scuddles Fm	GG027	587.7	18379.4	4870.0	9927.8
138749	769075	dacite	grey fspr qz phyric lava	Mb2 Scuddles Fm	GG027	630.9	18398.6	4833.8	9914.3
138750	769076	dacite	fd porphyritic intrusion	Proterozoic intrusion	GG027	667.5	18415.6	4802.6	9905.6
138751	769077	magnetite	msve minor dissem py	Mb4 Golden Grove Fm	GG027	680.4	18264.4	5043.6	10143.8
138752	769078	sandstone	qz poor tuffaceous intense chl silic alteration	Mb5 Golden Grove Fm	GG138	286.3	18302.2	4952.1	10115.9
138753	769080	magnetite	msve dissem ankerite and chl	Mb4 Golden Grove Fm	GG138	312.8	18292.7	4961.3	10092.9
138754	769083	siltstone	intense chl alteration with dissem ankerite and py	Mb4 Golden Grove Fm	GG138	328.0	18287.1	4966.5	10079.8
138755	769088	sandstone	qz rich tuffaceous intense silic alteration	Mb1 Golden Grove Fm	GG088	206.5	18372.3	5092.2	10198.3
138756	769089	sandstone	qz rich intense chl alteration	Mb4 Golden Grove Fm	GG038	218.3	18374.3	5088.4	10187.3
138757	769091	sandstone	qz rich tuffaceous dissem carbonate alteration	Mb4 Golden Grove Fm	GG038	236.4	18377.7	5082.8	10170.5
138758	769093	sandstone	cross cutting py ankerite vein in intense chl alteration	Mb4 Golden Grove Fm	GG038	257.2	18382.2	5076.2	10151.3
138759	769095	sandstone	qz rich tuffaceous intense chl alteration	Mb4 Golden Grove Fm	GG038	275.1	18386.2	5070.5	10134.8
138760	769100	magnetite	msve chl gangue	Mb4 Golden Grove Fm	GG038	311.5	18394.6	5058.5	10101.4
138761	769105	sandstone	qz poor tuffaceous intense chl silic alteration	Mb5 Golden Grove Fm	GG038	424.9	18422.4	5018.6	9999.0
138762	769113	chert	stringer minn py magnetite cpy ankerite chl veins	Mb5 Golden Grove Fm	GG042	422.6	18349.0	4898.0	10086.0
138763	769115	chert	stringer min py ankerite chl vein	Mb5 Golden Grove Fm	GG042	408.3	18432.7	4907.5	10094.6
138764	769121	sandstone	qz poor tuffaceous strong chl alteration	Mb4 Golden Grove Fm	GG042	369.3	18235.2	4933.5	10117.8
138765	769125	magnetite	msve fine grained with py ankerite chl gangue	Mb4 Golden Grove Fm	GG032	153.5	18425.6	5013.1	10248.1
138766	769127	magnetite	msve fine grained with cpy ankerite py vein	Mb4 Golden Grove Fm	GG032	177.0	18419.3	5023.7	10228.1
138767	769128	magnetite	msve crse grained with dissem talc ankerite and chl	Mb4 Golden Grove Fm	GG032	188.5	18416.3	5028.9	10218.4
138768	769134	pyrite	msve dissem ankerite and magnetite	Mb4 Golden Grove Fm	GG032	290.6	18390.6	5081.1	10134.5
138769	769137	sandstone	intense silic alteration with ankerite chl vein	Mb4 Golden Grove Fm	GG033	352.9	18293.0	4969.3	10102.8
138770	769142	breccia	qz bearing tuffaceous intense silic chl alteration	Mb1 Golden Grove Fm	GG157	109.6	18367.5	5101.8	10300.1
138771	769143	breccia	qz bearing tuffaceous intense silic chl alteration	Mb1 Golden Grove Fm	GG157	121.0	18369.7	5096.1	10290.4
138772	769144	dolerite	crse grained strong chl alteration	Proterozoic intrusion	GG157	137.5	18372.6	5087.6	10276.6
138773	769145	dolerite	fine grained strong chl alteration	Proterozoic intrusion	GG157	142.6	18373.5	5084.9	10272.4
138774	769146	breccia	qz bearing tuffaceous intense silic chl alteration	Mb1 Golden Grove Fm	GG157	157.1	18376.1	5077.2	10260.3
138775	769148	breccia	quartz bearing tuffaceous intense silic alteration	Mb1 Golden Grove Fm	GG157	198.6	18383.6	5054.3	10226.6

Appendix A1.2: Rock catalogue

UTas catalogue	Field#	Rock name	Rock description	Lithostratigraphy	DDH	Depth	North	East	RL
138776	769149	carbonate	msve recrystallised fine grained interlocking	Mb4 Golden Grove Fm	GG157	208.9	18385.5	5048.9	10218.3
138777	769150	sandstone	qz rich tuffaceous dissem ankerite magnetite	Mb4 Golden Grove Fm	GG157	211.7	18386.1	5046.9	10216.0
138778	769151	sandstone	intense chl alteration ankerite py cpy magnetite vein	Mb4 Golden Grove Fm	GG157	269.8	18397.9	5014.2	10169.5
138779	769152	sandstone	intense chl alteration ankerite py cpy magnetite vein	Mb4 Golden Grove Fm	GG157	219.9	18387.7	5042.3	10209.4
138780	769153	sandstone	intense chl alteration ankerite py cpy magnetite vein	Mb4 Golden Grove Fm	GG157	222.8	18388.2	5040.7	10207.1
138781	769155	breccia	tuffaceous qz bearing pat silici chl alteration	Mb4 Golden Grove Fm	GG157	228.6	18389.4	5037.4	10202.5
138782	769156	magnetite	msve dissem ankerite chl and cpy	Mb4 Golden Grove Fm	GG157	235.4	18390.8	5033.6	10197.0
138783	769159	magnetite	msve dissem ankerite chl and cpy	Mb4 Golden Grove Fm	GG157	262.7	18396.4	5018.2	10175.2
138784	769160	sandstone	intense chl alteration magnetite chl vein	Mb4 Golden Grove Fm	GG157	266.8	18397.0	5016.0	10172.0
138785	769162	sandstone	pervasive strong chl alteration	Mb6 Golden Grove Fm	GG157	279.4	18400.0	5008.8	10161.8
138786	769163	magnetite	msve dissem carbonate	Mb4 Golden Grove Fm	GG157	285.5	18401.3	5005.4	10156.9
138787	769165	breccia	qz bearing tuffaceous intense silic chl alteration	Mb1 Golden Grove Fm	GG162	188.7	18605.6	5112.9	10216.2
138788	769166	breccia	qz bearing tuffaceous intense silic chl alteration	Mb1 Golden Grove Fm	GG162	200.0	18609.0	5108.4	10206.6
138789	769170	pyrite	msve fine grained	Mb4 Golden Grove Fm	GG162	246.8	18622.4	5086.7	10167.2
138790	769174	sandstone	qz rich intense chl alteration dissem py magnetite	Mb4 Golden Grove Fm	GG162	285.4	18632.8	5066.9	10135.7
138791	769175	sandstone	qz rich intense chl silic alteration	Mb4 Golden Grove Fm	GG162	287.6	18633.4	5065.7	10133.9
138792	769185	pyrite	msve minor dissem cpy	Mb4 Golden Grove Fm	GG162	335.6	18644.8	5038.2	10096.3
138793	769201	sandstone	qz rich tuffaceous intense chl silic alteration	Mb4 Golden Grove Fm	GG064	404.2	18850.5	4945.3	10218.9
138794	769209	sandstone	intense silic alteration py, magnetite chl vein	Mb5 Golden Grove Fm	GG139	223.8	18834.0	4976.0	10173.0
138795	769214	sandstone	qz rich tuffaceous intense chl alteration	Mb4 Golden Grove Fm	GG139	261.2	18821.4	4996.9	10144.0
138796	769217	sandstone	qz rich intense chl alteration py rich sulphide veins	Mb4 Golden Grove Fm	GG139	288.9	18811.5	5010.9	10122.9
138797	769218	sandstone	qz rich intense silic alteration	Mb4 Golden Grove Fm	GG139	293.7	18809.8	5013.5	10119.2
138798	769220	siltstone	qz rich tuffaceous intense chl silic alteration	Mb4 Golden Grove Fm	GG139	328.2	18797.3	5032.8	10093.5
138799	769225	breccia	qz rich tuffaceous patchy silici chl alteration	Mb1 Golden Grove Fm	GG048	244.9	18477.9	5095.3	10171.9
138800	769228	sandstone	intense chl dissem andalusite, chloritoid, magnetite	Mb6 Golden Grove Fm	GG048	256.7	18481.1	5089.4	10162.2
138801	769232	magnetite	msve dissem and veined ankerite	Mb4 Golden Grove Fm	GG048	294.3	18491.4	5057.9	10131.1
138802	769233	magnetite	msve veined by py pyrrhotite cpy carbonate veins	Mb4 Golden Grove Fm	GG048	298.2	18492.4	5068.9	10127.9
138803	769235	magnetite	msve veined by py pyrrhotite cpy carbonate veins	Mb4 Golden Grove Fm	GG048	312.8	18498.9	5057.1	10108.5
138804	769236	magnetite	msve dissem ankerite cross cutting py chl vein	Mb4 Golden Grove Fm	GG048	316.7	18497.5	5059.7	10112.7
138805	769238	breccia	tuffaceous qz bearing pat silici chl alteration	Mb4 Golden Grove Fm	GG048	328.6	18500.9	5053.6	10103.1
138806	769243	sandstone	intense chl with cross cutting py chl vein	Mb4 Golden Grove Fm	GG048	350.5	18507.6	5041.5	10086.0
138807	769244	magnetite	msve dissem carbonate chl and talc	Mb4 Golden Grove Fm	GG048	354.4	18508.8	5039.4	10083.0
138808	769245	sandstone	intense chl alteration dissem magnetite carbonate	Mb4 Golden Grove Fm	GG048	358.7	18510.0	5037.0	10080.0

Appendix A1.2: Rock catalogue

UTas catalogue	Field#	Rock name	Rock description	Lithostratigraphy	DDH	Depth	North	East	RL
138809	769249	sandstone	intense chl tuffaceous dissem magnetite carbonate	Mb4 Golden Grove Fm	GG048	393.8	18521.9	5015.4	10054.7
138810	769254	breccia	qz rich tuffaceous intense chl alteration	Mb1 Golden Grove Fm	GG070	118.0	18576.2	5152.0	10273.7
138811	769255	breccia	qz bearing tuffaceous intense silic chl alteration	Mb1 Golden Grove Fm	GG070	168.1	18588.6	5131.8	10229.5
138812	769258	breccia	qz bearing tuffaceous intense silic chl alteration	Mb1 Golden Grove Fm	GG070	244.0	18609.9	5101.1	10163.5
138813	769259	breccia	tuffaceous qz bearing pat silici chl alteration	Mb1 Golden Grove Fm	GG070	248.8	18611.2	5099.1	10159.3
138814	769260	pyrite	msve minor dissem cpy	Mb4 Golden Grove Fm	GG070	263.7	18615.6	5092.9	10146.5
138815	769263	sandstone	intense chl alteration dissem magnetite carbonate	Mb4 Golden Grove Fm	GG070	270.4	18617.5	5090.1	10140.7
138816	769264	sandstone	intense chl alteration dissem magnetite carbonate	Mb4 Golden Grove Fm	GG070	271.9	18618.0	5089.5	10139.4
138817	769265	sandstone	contain magnetite cpy and py veins	Mb4 Golden Grove Fm	GG070	280.0	18620.4	5086.0	10132.5
138818	769266	sandstone	qz rich tuffaceous intense chl alteration	Mb4 Golden Grove Fm	GG070	294.4	18624.7	5079.7	10120.3
138819	769267	sandstone	qz rich tuffaceous intense chl alteration	Mb4 Golden Grove Fm	GG070	303.4	18627.6	5075.7	10112.8
138820	769269	sandstone	qz rich tuffaceous intense chl alteration	Mb4 Golden Grove Fm	GG070	308.5	18629.2	5073.4	10108.5
138821	769271	magnetite	msve dissem carbonate and crse grained py	Mb4 Golden Grove Fm	GG070	327.7	18635.5	5064.4	10092.8
138822	769272	sandstone	intense chl alteration veined by talc py magnetite	Mb4 Golden Grove Fm	GG070	330.6	18636.5	5063.0	10090.4
138823	769273	sandstone	intense chl alteration veined by talc py magnetite	Mb4 Golden Grove Fm	GG070	333.3	18637.4	5061.7	10088.3
138824	769274	sandstone	intense chl alteration veined by py chl	Mb4 Golden Grove Fm	GG070	333.6	18637.5	5061.5	10088.0
138825	769275	sandstone	intense chl alteration veined by talc py magnetite	Mb4 Golden Grove Fm	GG070	342.7	18640.6	5057.1	10080.7
138826	769276	sandstone	intense chl alteration	Mb4 Golden Grove Fm	GG070	346.0	18642.0	5056.0	10078.0
138827	769277	sandstone	qz rich tuffaceous intense chl alteration	Mb4 Golden Grove Fm	GG070	347.0	18642.1	5054.9	10077.3
138828	769278	dacite	grey fspr qz phyric lava calcite alteration	Mb2 Scuddles Fm	GG070	360.1	18646.9	5048.2	10067.2
138829	769279	dacite	grey fspr qz phyric lava calcite alteration	Mb2 Scuddles Fm	GG070	375.2	18653.2	5039.6	10056.4
138830	769280	magnetite	msve veined by py pyrrhotite chl carbonate veins	Mb4 Golden Grove Fm	GG070	383.3	18656.8	5034.8	10051.0
138831	769281	magnetite	msve veined by chl py veins	Mb4 Golden Grove Fm	GG070	389.7	18659.7	5030.8	10046.9
138832	769286	sandstone	tuffaceous qz poor intense chl silic alteration	Mb5 Golden Grove Fm	GG070	429.1	18679.1	5005.8	10023.5
138833	769288	sandstone	tuffaceous qz poor intense chl silic alteration	Mb5 Golden Grove Fm	GG070	465.2	18698.0	4982.4	10003.6
138834	769289	sandstone	intense chl alt dissem py pyrrhotite magnetite	Mb4 Golden Grove Fm	GG070	475.8	18703.7	4975.4	9998.0
138835	769290	sandstone	intense chl alt dissem py pyrrhotite magnetite	Mb5 Golden Grove Fm	GG070	482.7	18707.5	4970.8	9994.5
138836	769291	chert	intense silic alteation py pyrrhotite veins	Mb6 Golden Grove Fm	GG070	496.3	18715.0	4962.0	9988.0
138837	769294	rhyodacite	msve qz fspr phyric lava	Mb2 Scuddles Fm	GG070	551.2	18745.8	4924.8	9961.4
138838	769302	rhyodacite	msve qz fspr phyric lava	Mb2 Scuddles Fm	GG095	295.3	19386.7	4946.4	10070.2
138839	769303	rhyodacite	msve qz fspr phyric lava	Mb2 Scuddles Fm	GG095	378.4	19356.1	4990.1	10007.0
138840	769304	rhyodacite	msve qz fspr phyric lava	Mb2 Scuddles Fm	GG095	409.3	19341.9	5009.2	9987.3
138841	769308	sandstone	pumiceous bedded intense silic chl alteration	Mb6 Golden Grove Fm	GG095	448.3	19323.7	5034.0	9963.3

Appendix A1.2: Rock catalogue

UTas catalogue	Field#	Rock name	Rock description	Lithostratigraphy	DDH	Depth	North	East	RL
138842	769309	sandstone	pumiceous bedded intense silic chl alteration	Mb6 Golden Grove Fm	GG095	455.3	19320.4	5038.5	9959.1
138843	769318	magnetite	msve crse grained dissem ankerite	Mb4 Golden Grove Fm	GG095	536.8	19281.0	5091.9	9911.8
138844	769319	magnetite	msve banded crse grained dissem ankerite	Mb4 Golden Grove Fm	GG095	537.2	19280.8	5092.2	9911.5
138845	769320	magnetite	msve banded crse grained dissem ankerite	Mb4 Golden Grove Fm	GG095	539.4	19280.0	5093.0	9910.0
138846	769321	magnetite	msve dissem carbonate py chl veined	Mb4 Golden Grove Fm	GG095	548.0	19275.5	5099.4	9905.5
138847	769325a	breccia	tuffaceous qz bearing pat silici chl alteration	Mb1 Golden Grove Fm	GG095	582.6	19258.5	5122.5	9886.2
138848	769325b	magnetite	msve dissem ankerite banded	Mb4 Golden Grove Fm	GG045	255.0	18678.8	5058.9	10169.5
138849	769326	magnetite	msve dissem carbonate py chl veined	Mb4 Golden Grove Fm	GG045	265.9	18684.8	5052.0	10164.7
138850	769327	sandstone	intense chl alteration tuffaceous	Mb4 Golden Grove Fm	GG045	269.3	18686.8	5049.7	10163.2
138851	769328	dacite	fspr qz phy lava pervasive calcite alteration	Mb2 Scuddles Fm	GG045	286.2	18697.2	5038.1	10156.7
138852	769331	sandstone	gmassive tuffaceous qz poor intense silic alteration	Mb5 Golden Grove Fm	GG045	333.0	18727.8	5004.5	10145.8
138853	769334	sandstone	intense silic alteration py chl vein	Mb5 Golden Grove Fm	GG045	374.1	18755.7	4974.8	10140.4
138854	769335	sandstone	intense silic alteration py chl vein	Mb4 Golden Grove Fm	GG045	378.2	18758.5	4971.8	10140.0
138855	769336	breccia	bedded qz poor sandstone intense silic chl alteration	Mb6 Golden Grove Fm	GG045	384.0	18762.3	4967.5	10139.6
138856	769340	sandstone	intense silic alteration py chl veins	Mb6 Golden Grove Fm	GG045	411.9	18779.9	4945.9	10138.1
138857	769341	breccia	bedded tuffaceous intense silic alteration	Mb6 Golden Grove Fm	GG045	415.2	18782.0	4943.3	10138.1
138858	769343	breccia	bedded dissem sph	Mb6 Golden Grove Fm	GG045	428.6	18790.2	4932.8	10138.0
138859	769344	sandstone	intense silic alteration py carbonate veins	Mb6 Golden Grove Fm	GG045	431.8	18792.0	4930.0	10138.0
138860	769345	breccia	plymict msve	Mb6 Golden Grove Fm	GG045	435.6	18794.5	4927.2	10138.1
138861	769346	rhyodacite	qz fspr phyric lava pervsvie calcite ser alteration	Mb2 Scuddles Fm	GG045	443.8	18799.6	4920.8	10138.4
138862	769347	rhyodacite	qz fspr phyric lava pervsvie calcite ser alteration	Mb2 Scuddles Fm	GG045	460.4	18809.8	4907.7	10138.9
138863	973017	rhyodacite	qz fspr phyric lava pervsvie calcite ser alteration	Mb2 Scuddles Fm	G96/184	89.0	18230.7	4784.6	10061.1
138864	97U004	sandstone	qz rich pervasive intense chl ser alteration	Mb4 Gossan Valley Fm			18864.5	5216.5	10225.0
138865	97U005	sandstone	thinly bedded qz rich tuffaceous intense silic chl	Mb1 Golden Grove Fm			18863.8	5212.8	10225.0
138866	97U006	breccia	qz rich tuffaceous intense silic chl alteration	Mb1 Golden Grove Fm			18862.7	5191.6	10225.0
138867	97U007	sandstone	bedded qz rich tuffaceous intense silic chl alteration	Mb1 Golden Grove Fm			18857.4	5207.1	10225.0
138868	97U012	breccia	qz bearing tuffaceous intense silic chl alteration	Mb1 Golden Grove Fm			18763.4	5192.2	10200.0
138869	97U013	breccia	bedded qz bearing tuffaceous patchy chl silic	Mb1 Golden Grove Fm			18720.8	5184.7	10187.5
138870	97U014	sandstone	tuffaceous qz bearing intense chl silic alteration	Mb1 Golden Grove Fm			18712.2	5204.1	10187.5
138871	97U020	sandstone	bedded qz rich tuffaceous intense silic chl alteration	Mb1 Golden Grove Fm			18437.4	5150.2	10100.0
138872	97U021	breccia	msve qz rich tuffaceous intense silic chl alteration	Mb1 Golden Grove Fm			18437.3	5138.5	10100.0
138873	97U024	breccia	msve qz rich tuffaceous intense silic chl alteration	Mb1 Golden Grove Fm			18437.6	5126.8	10100.0
138874	97U025	pyrite	msve fine grained with abundant chl	Mb4 Golden Grove Fm			18440.3	5108.8	10100.0

Appendix A1.2: Rock catalogue

UTas catalogue	Field#	Rock name	Rock description	Lithostratigraphy	DDH	Depth	North	East	RL
138875	97U027	sandstone	qz rich tuffaceous intense chl alteration	Mb4 Golden Grove Fm			18439.4	5109.5	10100.0
138876	97U028	pyrite	msve fine grained dissem cpy	Mb4 Golden Grove Fm			18445.0	5109.0	10100.0
138877	97U030	sandstone	intense silic alteration with py cpy veins	Mb4 Golden Grove Fm			18436.0	5108.0	10100.0
138878	97U031	sandstone	qz rich intense chl alteration py veined	Mb4 Golden Grove Fm			18440.0	5101.0	10100.0
138879	97U034	sandstone	stringer minn py cpy chl vein	Mb4 Golden Grove Fm			18444.0	5103.0	10100.0
138880	97U036	sandstone	qz rich with py chl veins	Mb4 Golden Grove Fm			18477.0	5103.0	10100.0
138881	97U037	magnetite	msve cross cut by py carbnate pyrrhotite veins	Mb4 Golden Grove Fm			18460.0	5103.0	10100.0
138882	97U038	pyrite	msve crse grained dissem cpy	Mb4 Golden Grove Fm			18439.0	5091.0	10100.0
138883	97U041	magnetite	msve fine grained dissem carbonate silic alteration	Mb4 Golden Grove Fm			18492.5	5107.2	10100.0
138884	97U043	magnetite	msve dissem ankerite	Mb4 Golden Grove Fm			18490.2	5068.6	10100.0
138885	97U046	sandstone	qz rich tuffaceous intense chl ser alteration	Mb4 Gossan Valley Fm			18390.5	5201.0	10092.0
138886	97U047	breccia	thinly bedded qz rich tuffaceous intense silic chl	Mb1 Golden Grove Fm			18323.5	5165.2	10076.0
138887	97U049	breccia	bedded qz rich tuffaceous intense silic chl alteration	Mb1 Golden Grove Fm			18283.6	5165.1	10068.0
138888	97U050	sandstone	qz rich tuffaceous intense chl alteration	Mb1 Golden Grove Fm			18283.7	5109.8	10068.0
138889	97U052	pyrite	msve fine grained	Mb6 Golden Grove Fm			18293.0	4851.0	10050.0
138890	97U053	pyrite	msve crse grained	Mb6 Golden Grove Fm			18267.0	4874.0	10050.0
138891	97U056	sandstone	intense silic alteration with chlorite spots	Mb6 Golden Grove Fm			18237.6	4885.4	10050.0
138892	97U058	sandstone	M1 Marker bedded chert and chlorite	Mb4 Golden Grove Fm			18231.4	4886.5	10050.0
138893	97U062	sandstone	intense chl alteration with folded py veins	Mb6 Golden Grove Fm			18245.0	4969.8	10050.0
138894	97U063	sandstone	tuffaceous qz bearing pat silici chl alteration	Mb6 Golden Grove Fm			18236.7	4977.4	10050.0
138895	97U066	sandstone	tuffaceous qz bearing pat silici chl alteration	Mb5 Golden Grove Fm			18243.4	5047.3	10050.0
138896	97U069	magnetite	msve fine grained banded carbonate magnetite	Mb4 Golden Grove Fm			18243.5	5021.9	10050.0
138897	97U075	breccia	tuffaceous qz bearing pat silici chl alteration	Mb1 Golden Grove Fm			18237.0	5053.2	10050.0
138898	97U076	sandstone	qz beargin bedded tuffaceous intense silic chl	Mb1 Golden Grove Fm			18523.1	5185.8	10108.0
138899	97U078	breccia	tuffaceous qz bearing pat silici chl alteration	Mb1 Golden Grove Fm			18603.0	5185.8	10124.0

Appendix A2.1: Electron microprobe analysis of andalusite

Sample	760466	760466	760466	760466	760466	760466	760466	760466	760466	760466	760466	760466	769228	769228	769228	769228
Position	GGF M6	GGF M6	GGF M6	GGF M6	GGF M6	GGF M6	GGF M6	GGF M6	GGF M6	GGF M6	GGF M6	GGF M6	GGF M6	GGF M6	GGF M6	GGF M6
Zone	C	C	C	C	C	C	C	C	C	C	C	C	18,538 N	18,538 N	18,538 N	18,538 N
Matrix	chlorite	chlorite	chlorite	chlorite	chlorite	chlorite	chlorite	chlorite	chlorite	chlorite	chlorite	chlorite	chlorite	chlorite	chlorite	chlorite
Description	zoned blocky segment	zoned blocky segment	zoned blocky segment	zoned blocky segment	zoned blocky segment	zoned blocky segment	zoned blocky segment	zoned blocky segment	zoned blocky segment	zoned blocky segment	zoned blocky segment	large lath	large lath	large lath	large lath	large lath
Analysis	core	core	rim	rim 1/3	core 2/3	rim 3/3	rim 1/3	core 2/3	rim 3/3	core	rim					
SO_3	0.04	0.00	0.07	0.04	0.04	0.00	0.09	0.03	0.01	0.00	0.02	0.00	0.11	0.07	0.13	0.00
P_2O_5	0.03	0.02	0.00	0.00	0.00	0.00	0.04	0.00	0.06	0.05	0.00	0.00	0.05	0.00	0.00	0.00
SiO_2	36.23	36.31	36.20	36.28	36.49	36.11	35.97	36.12	36.46	36.14	36.24	36.23	35.96	35.74	36.00	35.97
TiO_2	0.00	0.01	0.03	0.00	0.00	0.01	0.00	0.02	0.00	0.00	0.01	0.01	0.04	0.07	0.00	0.02
Al_2O_3	62.26	61.10	61.43	60.44	60.46	60.80	61.19	61.28	60.95	61.51	59.90	60.69	61.84	62.68	61.97	61.56
Cr_2O_3	0.02	0.00	0.00	0.00	0.01	0.00	0.00	0.00	0.03	0.05	0.03	0.00	0.00	0.00	0.00	0.00
MgO	0.01	0.11	0.08	0.06	0.00	0.04	0.05	0.02	0.03	0.00	0.20	0.14	0.00	0.00	0.00	0.00
CaO	0.03	0.02	0.01	0.00	0.01	0.00	0.00	0.03	0.00	0.04	0.00	0.00	0.01	0.00	0.02	0.03
MnO	0.00	0.00	0.01	0.01	0.02	0.06	0.04	0.05	0.07	0.01	0.00	0.00	0.00	0.01	0.02	0.00
FeO	0.61	1.40	1.07	1.24	0.59	0.67	0.78	1.00	0.53	0.85	2.71	1.07	0.66	0.62	0.75	0.78
NiO	0.09	0.01	0.01	0.00	0.00	0.01	0.00	0.00	0.00	0.03	0.05	0.00	0.00	0.01	0.02	0.02
Na_2O	0.01	0.02	0.00	0.00	0.00	0.01	0.00	0.01	0.01	0.00	0.02	0.01	0.05	0.02	0.02	0.02
K_2O	0.00	0.00	0.00	0.00	0.00	0.00	0.00	0.00	0.01	0.00	0.00	0.00	0.01	0.02	0.00	0.00
Total	99.33	99.00	98.91	98.07	97.62	97.71	98.16	98.56	98.16	98.68	99.18	98.15	98.72	99.22	98.94	98.41

All iron as Fe^{2+}

Appendix A2.2: Temperature and pressure calculations of peak metamorphism

THERMOCALC version 2.4 by Powell and Holland (1990)

Sample description: Intensely chlorite altered volcaniclastic from GGF M4 (762040). Large (up to 5 mm) euhedral pyrite grains scattered in a chlorite matrix with disseminated ilmenite and rutile (<0.1 mm) and andalusite (up to 8 mm). Andalusite grains have and pyrrhotite-magnetite-chlorite-sphalerite rims. Mineral compositions were determined using a Cameca SX50 electron microprobe at the University of Tasmania.

oxide (wt. %)	chlorite	chloritoid
WO_3	0.00	0.00
SiO_2	21.44	23.69
TiO_2	0.06	0.02
SnO_2	0.01	0.00
Al_2O_3	23.00	39.85
MgO	6.98	1.17
CaO	0.01	0.02
MnO	0.29	0.39
FeO	36.42	27.26
CuO	0.00	0.04
ZnO	0.04	0.03
Na_2O	0.04	0.00
K_2O	0.02	0.00
F	0.00	0.03
Cl	0.02	0.00
Total	88.33	92.50

Activity data (assuming ideal activities)

	Mg chloritoid	Fe chloritoid	clinozoisite	daphnite	amesite	rutile	ilmenite	andalusite
a	0.0699	0.8670	0.0004	0.0725	0.0016	1.00	1.00	1.00
sd (a)/a	0.2595	0.0500	0.9449	0.3059	0.5535	0.00	0.00	0.00

Possible metamorphic reactions:

1) rutile + Fe-chloritoid = andalusite + ilmenite +H_2O
2) 5Fe-chloritoid + clinozoisite = daphnite + 5Mg-chloritoid
3) 2quartz + Mg-chloritoid + amesite = clinozoisite + 2andalusite + H_2O
4) 2quartz + 5Fe-chloritoid + amesite = daphnite + 4Mg-chloritoid + 2andalusite + H_2O
5) 5amesite + 5Fe-chloritoid = 10quartz + 10andalusite +daphnite +4clinozoinsite + $5H_2O$
6) 5rutile +5Mg-chloritoid + daphnite = clinozoisite + 5andalusite + 5ilmenite + $5H_2O$
7) clinozoisite + Fe-chloritoid +andalusite + rutile = 2quartz + ilmenite + Mg-chloritoid 4 amesite
8) clinozoisite + 2Fe-chloritoid + 2rutile = 2quartz + 2ilmenite + Mg-chloritoid + amesite +H_2O
9) daphnite + 4Mg-chloritoid + 5rutile = 2quartz + 5ilmenite + 3andalusite + amesite + $4H_2O$
10) 5rutile + 5andalusite + daphnite + 4clinozoisite = 5amensite + 5ilmenite + l0quartz
11) 4clinozoisite + daphnite + 5Fe-chloritoid + 10rutile = 10quartz + 10ilmenite + 5amesite + $5H_2O$
12) 3clinozoisite + 2daphite + 5Mg-chloritoid + 10rutile = 10quartz + 10ilmenite + 5amesite +$5H_2O$

Calculations at P = 3.0 Kbar (for $x(H_2O) = 1.0$)

	T (P)	sd (T)	a	sd (a)	b	c	ln_K	sd (ln_K)
1.	538	97	239.01	2.65	-0.31203	1.419	1.472	4.685
2.	372	2655	-43.77	3.76	0.00424	0.272	7.503	1.653
3.	461	157	-160.96	10.89	0.21336	-17.128	9.115	4.944
4.	508	72	41.58	2.45	-0.04736	2.905	-2.053	0.365

Average Temperatures (for $x(H_2O) = 1.0$)

P	1.0	2.0	3.04	4.0	5.0
av. T	452	474	495	514	532
sd	4	5	5	5	6
f	0.6	0.4	0.5	0.8	1.1

Appendix A3.1: Underground mapping of the 300 level

The diagram below illustrates the format of this appendix, which is presented in four sheets. Appendix A3.1a to A3.1d are compiled mapping and structural data collected from the 290 decline (Appendix A3.1d), through the footwall and massive sulphide and mangetite in GGF M4 (Appendix A3.1b and A3.1c) and massive sulphide in GGF M6 (Appendix A3.1a). Appendices A3.1a and A3.1b indicate the discordant nature of stringer sulphide veining below massive pyrite in GGF M6.

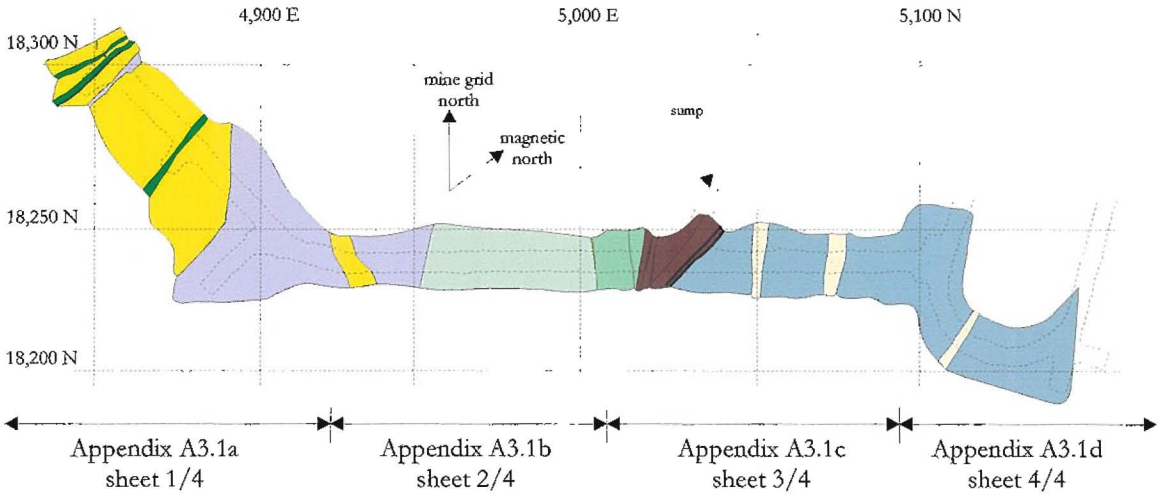

Legend

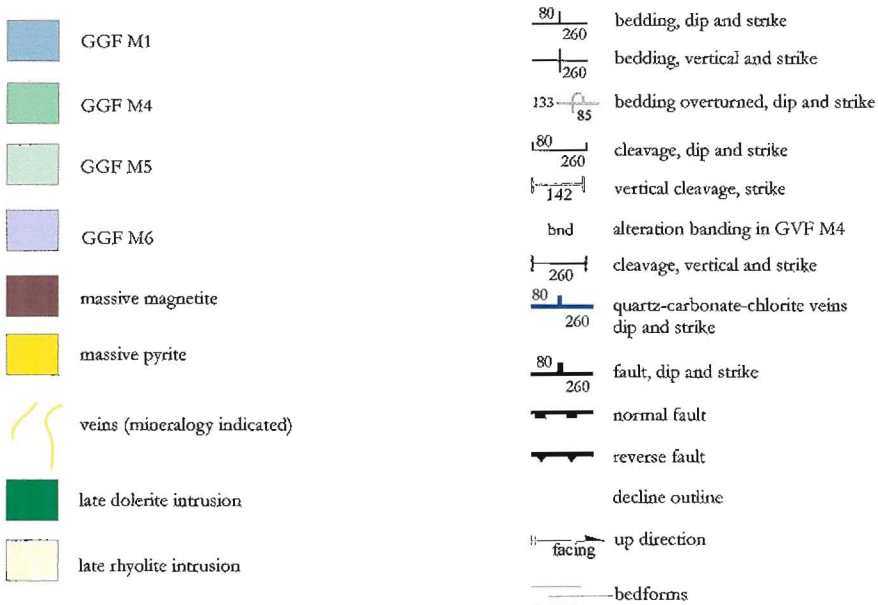

Abbreviations:

py = pyrite, sp = sphalerite, po = pyrrhotite, cpy = chalcopyrite, mgt = magnetite, co = carbonate, chl = chlorite, si = silica alteration, qz = quartz, ds = disseminated, bx = breccia, pb = pebble, bnd = banding, vn = vein, i = intense, s = strong, p = pervasive and ibd = interbedded

Appendix A3.1a: 300 level underground mapping (sheet 1/4)

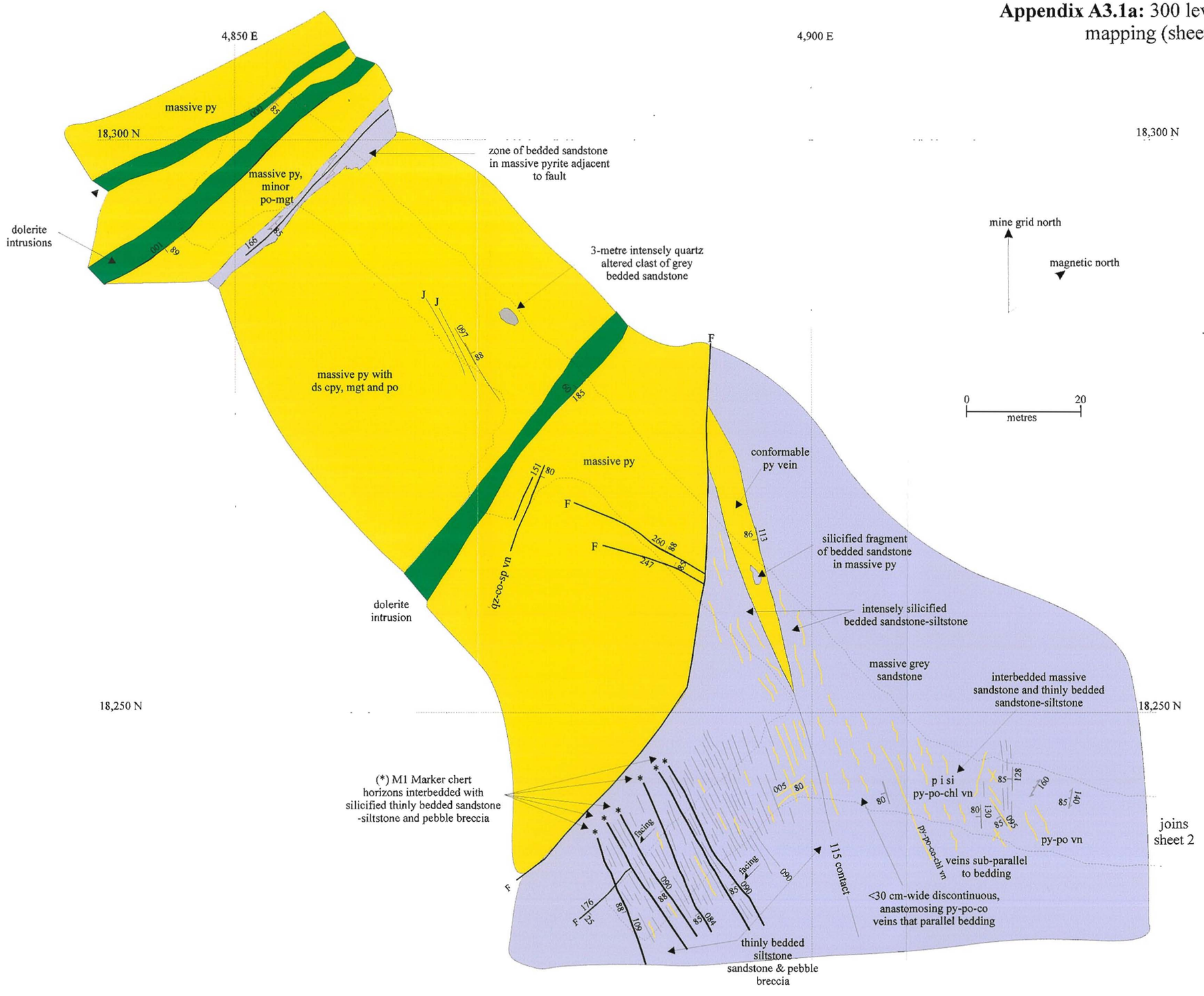

Appendix A3.1b: 300 level underground mapping (sheet 2/ 4)

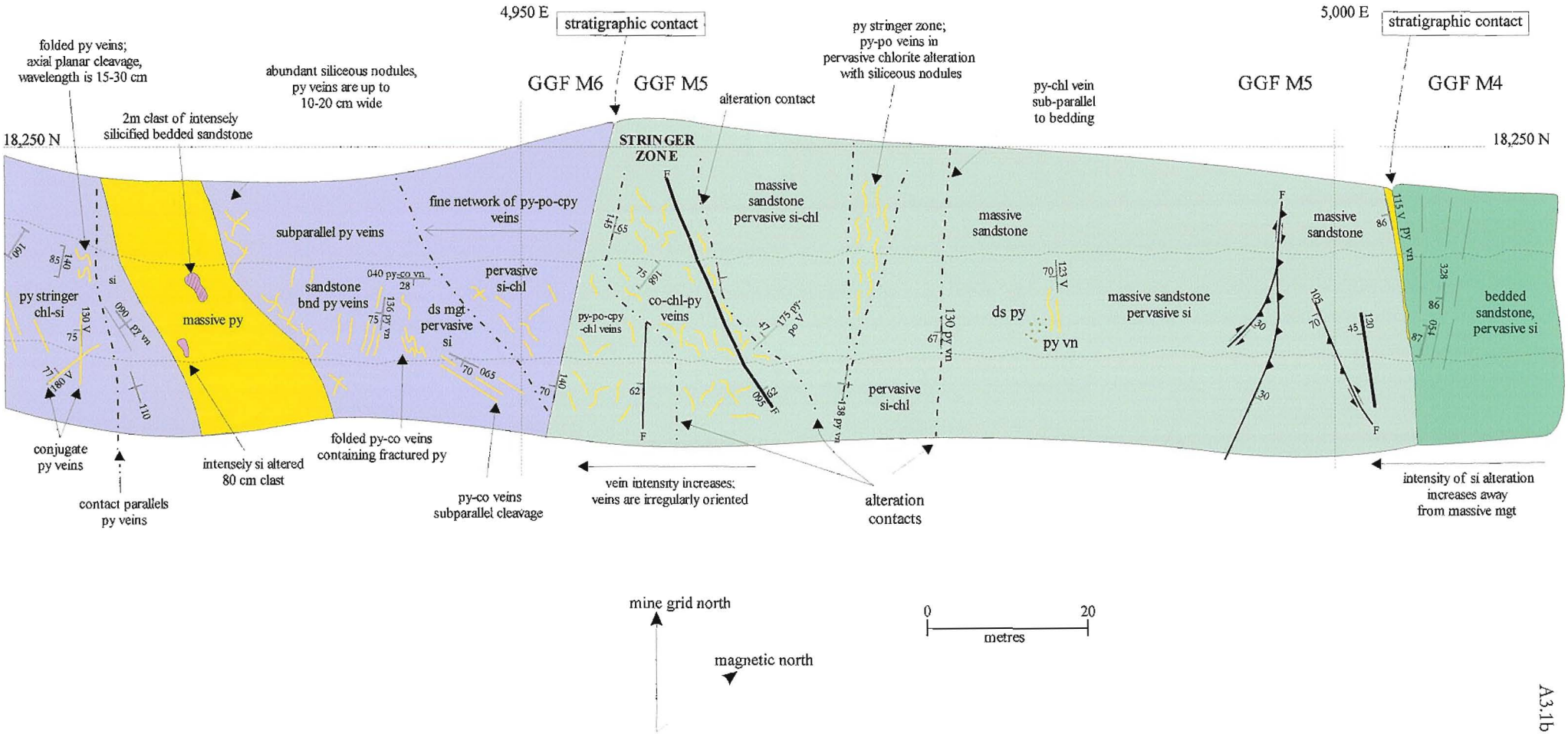

A3.1b

Appendix A3.1c: 300 level underground mapping (sheet 3/4)

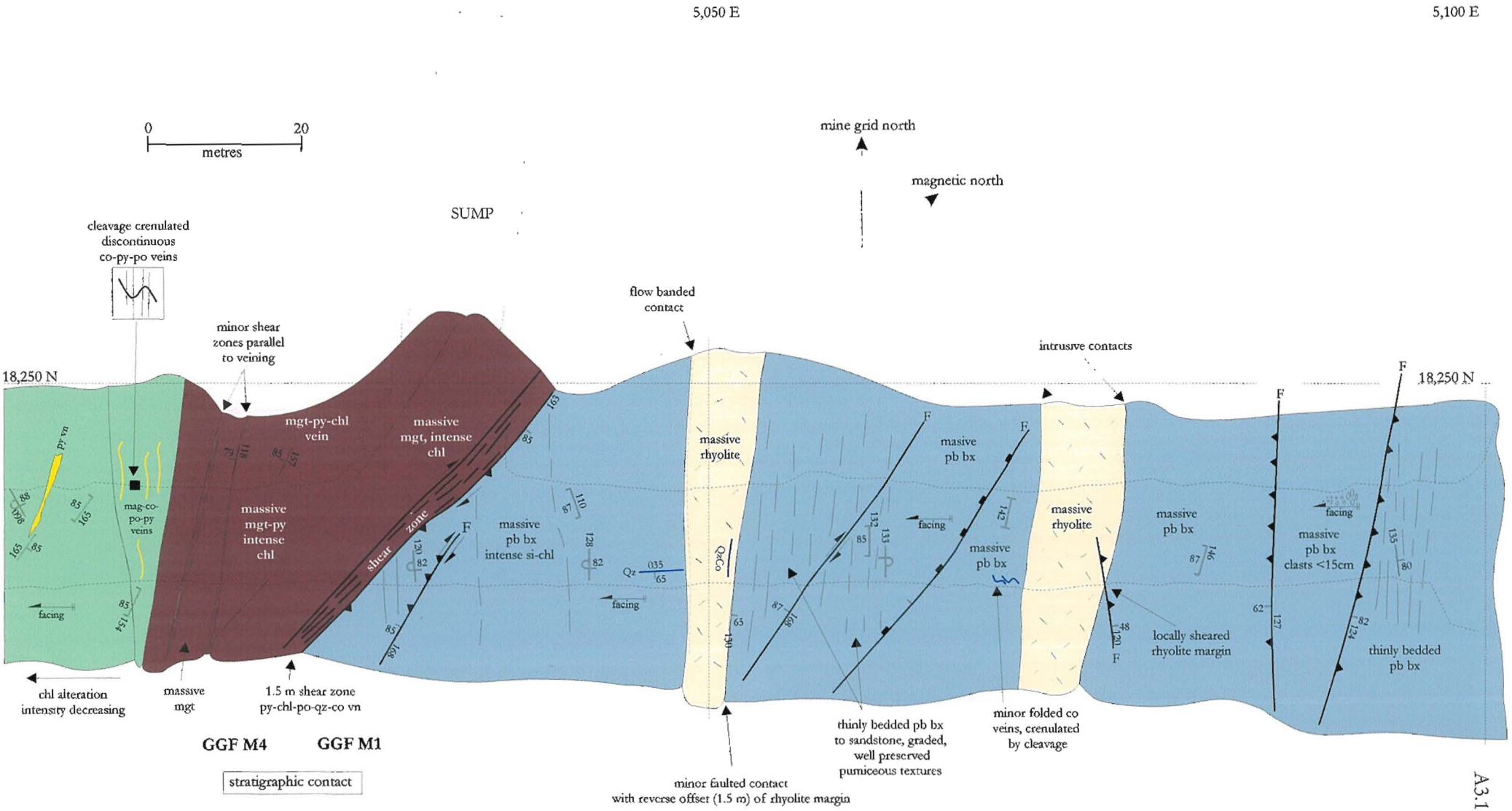

A3.1c

Appendix A3.1d: 300 level underground mapping (sheet 4/ 4)

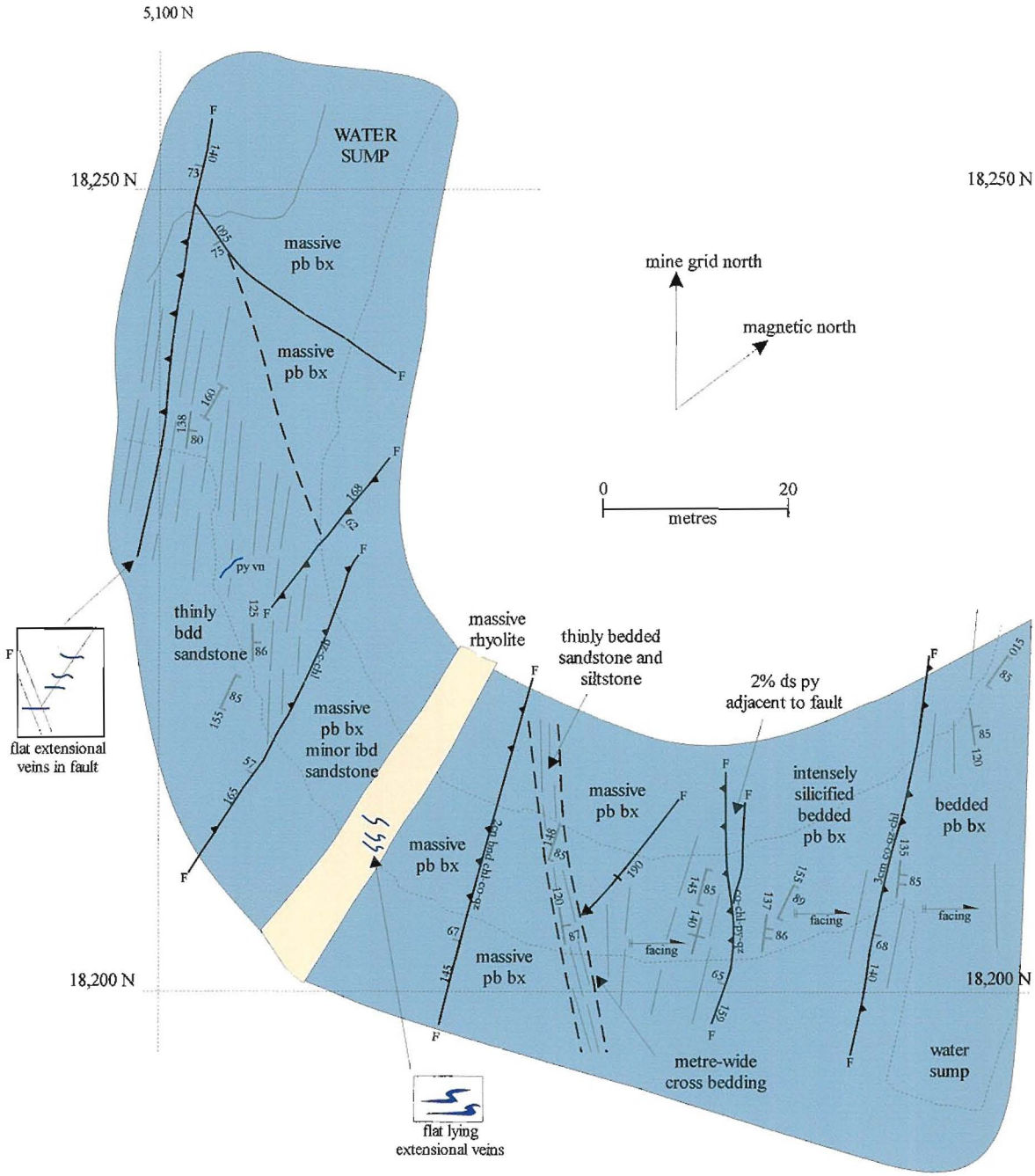

Appendix A3.2: Underground mapping of the 250 level

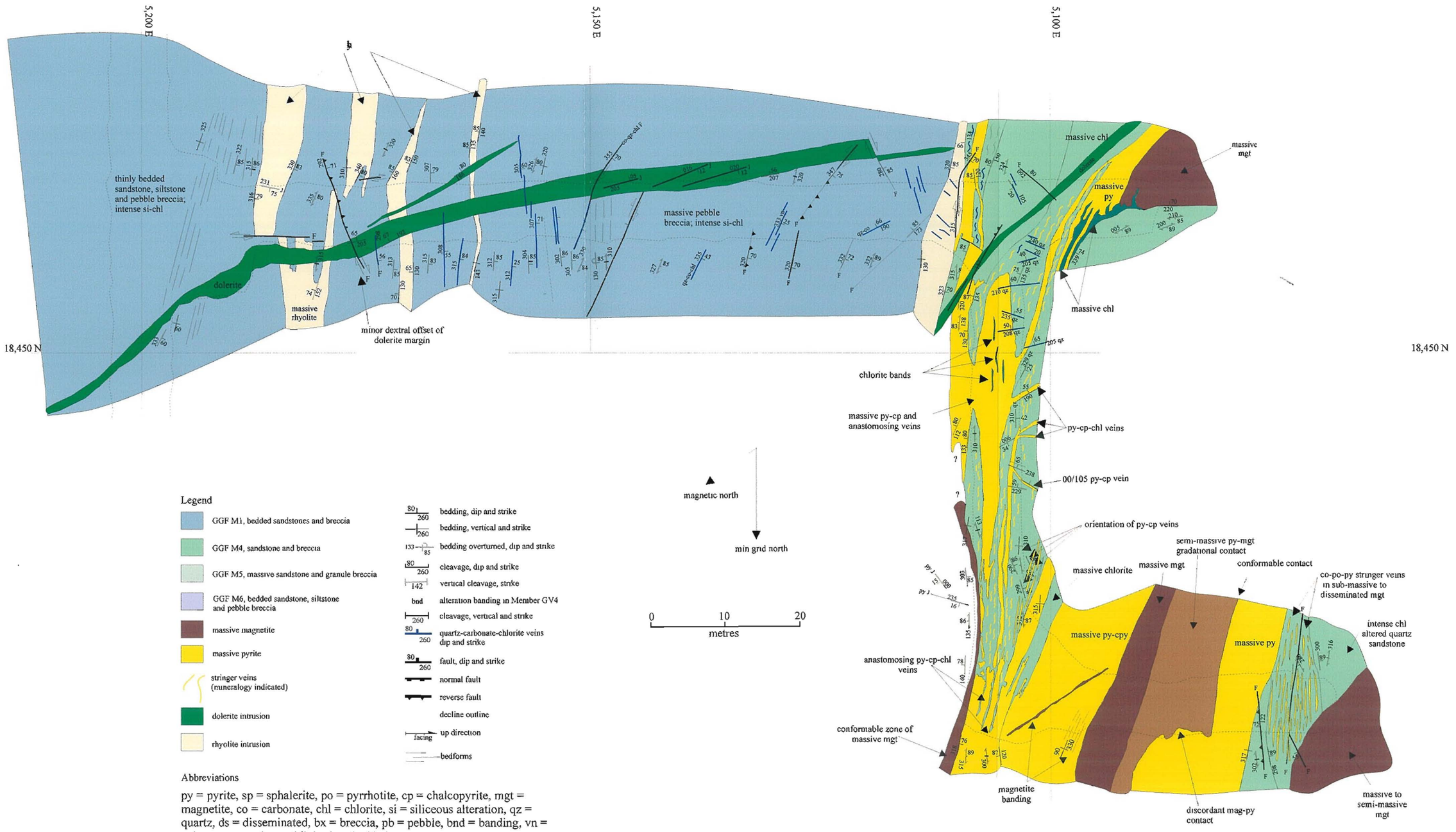

Legend

- GGF M1, bedded sandstones and breccia
- GGF M4, sandstone and breccia
- GGF M5, massive sandstone and granule breccia
- GGF M6, bedded sandstone, siltstone and pebble breccia
- massive magnetite
- massive pyrite
- stringer veins (mineralogy indicated)
- dolerite intrusion
- rhyolite intrusion

- bedding, dip and strike
- bedding, vertical and strike
- bedding overturned, dip and strike
- cleavage, dip and strike
- vertical cleavage, strike
- bnd — alteration banding in Member GV4
- cleavage, vertical and strike
- quartz-carbonate-chlorite veins dip and strike
- fault, dip and strike
- normal fault
- reverse fault
- decline outline
- facing — up direction
- bedforms

Abbreviations

py = pyrite, sp = sphalerite, po = pyrrhotite, cp = chalcopyrite, mgt = magnetite, co = carbonate, chl = chlorite, si = siliceous alteration, qz = quartz, ds = disseminated, bx = breccia, pb = pebble, bnd = banding, vn = vein, p = pervasive and ibd = interbedded

Appendix A4.1: Electron microprobe analysis of sphalerite

Sample No.	760384	760384	760384	760384	760384	760384	760384	760384	760384	760384	760384	760384	760384	760384	760384	760384	760384	760384	760384	760384	760384
North	18189.4	18189.4	18189.4	18189.4	18189.4	18189.4	18189.4	18189.4	18189.4	18189.4	18189.4	18189.4	18189.4	18189.4	18189.4	18189.4	18189.4	18189.4	18189.4	18189.4	18189.4
East	4935.6	4935.6	4935.6	4935.6	4935.6	4935.6	4935.6	4935.6	4935.6	4935.6	4935.6	4935.6	4935.6	4935.6	4935.6	4935.6	4935.6	4935.6	4935.6	4935.6	4935.6
R.L.	10242.9	10242.9	10242.9	10242.9	10242.9	10242.9	10242.9	10242.9	10242.9	10242.9	10242.9	10242.9	10242.9	10242.9	10242.9	10242.9	10242.9	10242.9	10242.9	10242.9	10242.9
drill hole	GG 136	GG 136	GG 136	GG 136	GG 136	GG 136	GG 136	GG 136	GG 136	GG 136	GG 136	GG 136	GG 136	GG 136	GG 136	GG 136	GG 136	GG 136	GG 136	GG 136	GG 136
metre	142.5	142.5	142.5	142.5	142.5	142.5	142.5	142.5	142.5	142.5	142.5	142.5	142.5	142.5	142.5	142.5	142.5	142.5	142.5	142.5	142.5
zone	A	A	A	A	A	A	A	A	A	A	A	A	A	A	A	A	A	A	A	A	A
host rock	sp-chl	sp-chl	sp-chl	sp-chl	sp-chl	sp-chl	sp-chl	sp-chl	sp-chl	sp-chl	sp-chl	sp-chl	sp-chl	sp-chl	sp-chl	sp-chl	sp-chl	sp-chl	sp-chl	sp-chl	sp-chl
sp host	chl	chl	chl	chl	chl	chl	chl	chl	chl	chl	chl	chl	chl	chl	chl	chl	chl	chl	chl	chl	chl
sp colour	pale or	pale or	pale or	pale or	pale or	pale or	pale or	pale or	pale or	pale or	pale or	pale or	pale or	pale or	pale or	pale or	pale or	pale or	pale or	pale or	pale or
sp texture	massive	massive	massive	massive	massive	massive	massive	massive	massive	massive	massive	massive	massive	massive	massive	massive	massive	massive	massive	massive	massive
label	sphaler	sphaler	sphaler	sphaler	sphaler	sphaler	sphaler	sphaler	sphaler	sphaler	sphaler	sphaler	sphaler	sphaler	sphaler	sphaler	sphaler	sphaler	sphaler	sphaler	sphaler
S	32.69	32.95	32.87	32.96	32.82	33.28	32.88	33.60	32.75	32.93	32.87	32.77	33.10	33.26	33.11	32.93	33.26	33.13	33.22	32.79	32.89
Mn	0.01	0.00	0.01	0.00	0.00	0.02	0.00	0.00	0.01	0.03	0.00	0.01	0.00	0.01	0.02	0.00	0.01	0.01	0.02	0.01	0.02
Fe	1.60	1.56	1.67	1.69	1.66	1.76	1.87	1.96	1.81	1.67	1.72	1.54	1.66	1.68	2.15	1.47	1.52	1.57	1.58	1.75	1.55
Cu	0.00	0.03	0.00	0.00	0.00	0.03	0.00	0.00	0.00	0.01	0.00	0.00	0.00	0.02	0.00	0.01	0.05	0.02	0.00	0.01	0.00
Zn	65.24	66.05	65.16	65.08	65.31	65.58	65.31	65.50	65.45	65.61	65.51	65.86	65.12	65.80	64.52	65.01	65.07	64.96	65.25	65.03	64.63
Ag	0.04	0.00	0.00	0.05	0.00	0.00	0.01	0.00	0.00	0.00	0.04	0.00	0.00	0.02	0.00	0.00	0.01	0.00	0.05	0.02	0.03
Hg	0.15	0.00	0.31	0.15	0.00	0.00	0.17	0.04	0.13	0.27	0.20	0.09	0.00	0.00	0.00	0.00	0.00	0.00	0.15	0.00	0.15
Se	0.03	0.00	0.00	0.05	0.00	0.00	0.00	0.03	0.00	0.05	0.00	0.00	0.00	0.00	0.00	0.00	0.00	0.00	0.00	0.00	0.00
Sb																					
As																					
Bi																					
Total	99.76	100.59	100.02	99.98	99.79	100.67	100.24	101.13	100.15	100.57	100.34	100.27	99.88	100.79	99.80	99.42	99.92	99.69	100.27	99.61	99.27

Abbreviations: sp = sphalerite, chl = chlorite, py =pyrite, qz = quartz, asp = arsenopyrite, cp = chalcopyrite, tet = tetrahedrite, co = carboante, mgt = magnetite, or = orange, br = brown

Appendix A4.1: Electron microprobe analysis of sphalerite *(continued)*

Sample No.	760461	760461	760461	760461	760461	760461	760461	760461	760461	760461	760461	762059	762059	762059	762059	762059	762059	762059	762059	762059
North	18267.8	18267.8	18267.8	18267.8	18267.8	18267.8	18267.8	18267.8	18267.8	18267.8	18267.8	18073.7	18073.7	18073.7	18073.7	18073.7	18073.7	18073.7	18073.7	18073.7
East	4832.7	4832.7	4832.7	4832.7	4832.7	4832.7	4832.7	4832.7	4832.7	4832.7	4832.7	4954.0	4954.0	4954.0	4954.0	4954.0	4954.0	4954.0	4954.0	4954.0
R.L.	10116.7	10116.7	10116.7	10116.7	10116.7	10116.7	10116.7	10116.7	10116.7	10116.7	10116.7	10283.2	10283.2	10283.2	10283.2	10283.2	10283.2	10283.2	10283.2	10283.2
drill hole	GG160	GG160	GG160	GG160	GG160	GG160	GG160	GG160	GG160	GG160	GG160	GG099	GG099	GG099	GG099	GG099	GG099	GG099	GG099	GG099
metre	277.6	277.6	277.6	277.6	277.6	277.6	277.6	277.6	277.6	277.6	277.6	119.0	119.0	119.0	119.0	119.0	119.0	119.0	119.0	119.0
zone	C	C	C	C	C	C	C	C	C	C	C	A	A	A	A	A	A	A	A	A
host rock	sp-py-qz	sp-py-qz	sp-py-qz	sp-py-qz	sp-py-qz	sp-py-qz	sp-py-qz	sp-py-qz	sp-py-qz	sp-py-qz	sp-py-qz	sp	sp	sp	sp	sp	sp	sp	sp	sp
sp host	py-qz	py-qz	py	py	py	py	py-qz	qz	qz	py	py	asp-qz	asp-qz	asp-qz	cp-qz	cp-qz	py-qz	py-qz	qz-py-cp	asp-cp-tet
sp colour	dark red	dark red	dark red	dark red	dark red	dark red	dark red	dark red	dark red	dark red	dark red	red-br	red-br	red-br	red-br	red-br	red-br	red-br	red-br	red-br
sp texture	massive	massive	massive	massive	massive	massive	massive	massive	massive	massive	massive	massive	massive	massive	massive	massive	massive	massive	massive	massive
label	tetra	tetra	tetra	tetra	tetra	tetra	tetra	tetra	tetra	tetra	tetra	tetra	tetra	tetra	tetra	tetra	tetra	tetra	tetra	tetra
S	33.31	33.46	33.46	33.66	33.84	33.07	33.50	33.66	33.42	33.32	33.29	31.95	32.30	32.22	32.19	32.29	32.91	32.32	31.82	31.62
Mn																				
Fe	5.60	5.74	5.70	5.66	5.85	5.77	5.88	6.18	5.95	5.88	8.35	3.44	3.47	3.53	3.50	3.46	3.58	3.74	3.91	3.53
Cu	0.00	0.04	0.02	0.02	0.03	0.04	0.02	0.00	0.04	0.00	0.07	0.02	0.01	0.00	0.00	0.00	0.05	0.00	0.06	0.09
Zn	62.33	61.53	61.02	61.21	61.49	60.74	60.52	59.86	59.90	60.03	57.87	63.18	63.39	63.80	63.25	62.84	62.94	63.38	62.75	62.53
Ag	0.00	0.00	0.02	0.07	0.00	0.01	0.04	0.00	0.00	0.02	0.07	0.00	0.00	0.06	0.00	0.04	0.00	0.06	0.04	0.00
Hg																				
Se																				
Sb	0.01	0.01	0.00	0.00	0.00	0.00	0.01	0.01	0.01	0.00	0.01	0.00	0.00	0.00	0.00	0.01	0.00	0.00	0.00	0.00
As	0.00	0.00	0.00	0.00	0.00	0.05	0.00	0.00	0.00	0.00	0.01	0.00	0.04	0.00	0.00	0.00	0.00	0.01	0.00	0.00
Bi	0.49	0.17	0.24	0.00	0.09	0.00	0.14	0.00	0.10	0.00	0.36	0.00	0.09	0.00	0.12	0.00	0.38	0.00	0.00	0.14
Total	101.74	100.95	100.45	100.62	101.30	99.67	100.09	99.71	99.42	99.25	100.02	98.59	99.30	99.61	99.05	98.64	99.86	99.52	98.57	97.91

Abbreviations: sp = sphalerite, chl = chlorite, py =pyrite, qz = quartz, asp = arsenopyrite, cp = chalcopyrite, tet = tetrahedrite, co = carboante, mgt = magnetite, or = orange, br = brown

Appendix A4.1: Electron microprobe analysis of sphalerite *(continued)*

Sample No.	760426	760426	760426	762057	762057	762031	762031	762031	762031	762031	762031	762031	762031	762031	762031	762031	762031	762031	762031	762031
North	18246.3	18246.3	18246.3	18303.7	18303.7	18227.0	18227.0	18227.0	18227.0	18227.0	18227.0	18227.0	18227.0	18227.0	18227.0	18227.0	18227.0	18227.0	18227.0	18227.0
East	4806.3	4806.3	4806.3	4894.8	4894.8	4825.6	4825.6	4825.6	4825.6	4825.6	4825.6	4825.6	4825.6	4825.6	4825.6	4825.6	4825.6	4825.6	4825.6	4825.6
R.L.	10094.7	10094.7	10094.7	9996.3	9996.3	10074.8	10074.8	10074.8	10074.8	10074.8	10074.8	10074.8	10074.8	10074.8	10074.8	10074.8	10074.8	10074.8	10074.8	10074.8
drill hole	GG165	GG165	GG165	GG173	GG173	GG171	GG171	GG171	GG171	GG171	GG171	GG171	GG171	GG171	GG171	GG171	GG171	GG171	GG171	GG171
metre	302.0	302.0	302.0	434.0	434.0	322.7	322.7	322.7	322.7	322.7	322.7	322.7	322.7	322.7	322.7	322.7	322.7	322.7	322.7	322.7
zone	C	C	C	A	A	C	C	C	C	C	C	C	C	C	C	C	C	C	C	C
host rock	sp-py	sp-py	sp-py	co	co	stringer	stringer	stringer	stringer	stringer	stringer	stringer	stringer	stringer	stringer	stringer	stringer	stringer	stringer	stringer
sp host	py	py	py	co-chl	co-chl	py-mgt-chl	py-mgt-chl	py-mgt-chl	py-chl	py-chl	py-mgt	py-mgt	py-mgt	py-mgt	py-mgt	py-mgt	py-qz	py-qz	py-chl	py-chl
sp colour	or-red	or-red	or-red	red	red	red	red	red	red	red	red	red	red	red	red	red	red	red	red	red
sp texture	massive	massive	massive	vein	vein	vein	vein	vein	vein	vein	vein	vein	vein	vein	vein	vein	vein	vein	vein	vein
label	tetra	tetra	tetra	tetra	tetra	tetra	tetra	tetra	tetra	tetra	tetra	tetra	tetra	tetra	tetra	tetra	tetra	tetra	tetra	tetra
S	31.76	32.15	31.95	32.68	32.85	33.56	33.31	33.25	33.12	32.83	33.25	33.49	33.76	33.56	33.47	33.63	33.26	33.57	32.71	33.42
Mn																				
Fe	3.75	4.69	2.65	6.30	6.25	6.73	6.55	8.06	6.43	7.00	6.61	7.08	7.27	6.55	6.77	7.34	6.56	6.35	6.78	7.30
Cu	0.09	0.03	0.07	0.20	0.25	0.00	0.08	0.02	0.03	0.08	0.06	0.01	0.07	0.04	0.06	0.08	0.03	0.03	0.07	0.12
Zn	63.48	61.73	64.34	60.29	60.11	59.86	59.72	58.49	60.40	58.93	59.64	59.38	59.88	59.91	59.02	59.33	60.46	60.56	60.56	58.79
Ag	0.00	0.03	0.00	0.01	0.06	0.00	0.00	0.00	0.03	0.02	0.00	0.00	0.00	0.02	0.05	0.09	0.00	0.00	0.00	0.00
Hg																				
Se																				
Sb	0.00	0.00	0.00	0.02	0.02	0.00	0.00	0.00	0.00	0.01	0.01	0.00	0.00	0.01	0.00	0.00	0.00	0.00	0.01	0.00
As	0.00	0.00	0.00	0.00	0.00	0.00	0.00	0.00	0.00	0.00	0.00	0.00	0.07	0.00	0.06	0.00	0.00	0.03	0.00	0.02
Bi	0.00	0.00	0.08	0.16	0.08	0.15	0.00	0.00	0.28	0.33	0.20	0.00	0.15	0.00	0.00	0.09	0.00	0.00	0.45	0.00
Total	99.08	98.62	99.09	99.65	99.61	100.31	99.66	99.82	100.29	99.19	99.77	99.95	101.20	100.08	99.43	100.56	100.31	100.54	100.57	99.65

Abbreviations: sp = sphalerite, chl = chlorite, py =pyrite, qz = quartz, asp = arsenopyrite, cp = chalcopyrite, tet = tetrahedrite, co = carboante, mgt = magnetite, or = orange, br = brown

Appendix A4.1: Electron microprobe analysis of sphalerite *(continued)*

Sample No.	760432	760432	760432	760432	760432	760432	760432	760432	760432	760432	760432	760350	760350	760350	760350	760350	760350	762055	762055	762055
North	18257.4	18257.4	18257.4	18257.4	18257.4	18257.4	18257.4	18257.4	18257.4	18257.4	18257.4	18185.5	18185.5	18185.5	18185.5	18185.5	18185.5	18286.8	18286.8	18286.8
East	4816.7	4816.7	4816.7	4816.7	4816.7	4816.7	4816.7	4816.7	4816.7	4816.7	4816.7	4941.5	4941.5	4941.5	4941.5	4941.5	4941.5	4878.9	4878.9	4878.9
R.L.	10069.4	10069.4	10069.4	10069.4	10069.4	10069.4	10069.4	10069.4	10069.4	10069.4	10069.4	10248.8	10248.8	10248.8	10248.8	10248.8	10248.8	10025.3	10025.3	10025.3
drill hole	GG165	GG165	GG165	GG165	GG165	GG165	GG165	GG165	GG165	GG165	GG165	GG118	GG118	GG118	GG118	GG118	GG118	GG171	GG171	GG171
metre	331.6	331.6	331.6	331.6	331.6	331.6	331.6	331.6	331.6	331.6	331.6	148.0	148.0	148.0	148.0	148.0	148.0	396.9	396.9	396.9
zone	C	C	C	C	C	C	C	C	C	C	C	A	A	A	A	A	A	C	C	C
host rock	chl	chl	chl	chl	chl	chl	chl	chl	chl	chl	chl	stringer	stringer	stringer	stringer	stringer	stringer	chl-py	chl-py	chl-py
sp host	co-mgt-chl	co-mgt-chl	chl	mgt	chl	mgt	mgt	sp	sp	mgt-co-chl	mgt-co-chl	chl-py	chl-py	chl-py	chl-py	chl-py	chl-py	chl	chl	py
sp colour	or-red	or-red	or-red	or-red	or-red	or-red	or-red	or-red	or-red	or-red	or-red	or-red	or-red	or-red	or-red	or-red	or-red	dark red	dark red	dark red
sp texture	vein	vein	vein	vein	vein	vein	vein	vein	vein	vein	vein	vein	vein	vein	vein	vein	vein	vein	vein	vein
label	tetra	tetra	tetra	tetra	tetra	tetra	tetra	tetra	tetra	tetra	tetra	tetra	tetra	tetra	tetra	tetra	tetra	tetra	tetra	tetra
S	33.17	33.46	33.49	33.64	33.27	33.55	33.33	33.19	33.42	33.26	33.27	33.34	33.23	33.22	33.06	33.78	33.29	33.55	33.72	33.78
Mn																				
Fe	7.64	7.12	6.89	7.19	6.72	7.05	6.97	7.94	7.35	7.84	6.72	2.25	1.97	1.77	1.77	2.56	1.73	7.10	6.24	6.25
Cu	0.06	0.08	0.05	0.02	0.03	0.05	0.07	0.06	0.06	0.04	0.04	0.29	0.16	0.23	0.29	0.23	0.10	0.04	0.05	0.00
Zn	57.44	57.81	59.13	59.43	59.35	58.55	58.73	58.49	58.83	57.70	58.56	64.59	64.33	64.63	63.25	62.41	63.61	59.19	60.27	60.68
Ag	0.00	0.00	0.03	0.00	0.00	0.00	0.03	0.03	0.05	0.00	0.00	0.07	0.13	0.04	0.07	0.12	0.01	0.00	0.00	0.00
Hg																				
Se																				
Sb	0.01	0.01	0.06	0.01	0.00	0.02	0.00	0.02	0.00	0.02	0.00	0.01	0.00	0.02	0.03	0.00	0.02	0.00	0.00	0.00
As	0.00	0.00	0.00	0.00	0.00	0.00	0.00	0.00	0.00	0.00	0.00	0.06	0.05	0.00	0.00	0.00	0.00	0.00	0.04	0.00
Bi	0.10	0.00	0.00	0.00	0.00	0.15	0.00	0.19	0.03	0.00	0.02	0.30	0.18	0.09	0.19	0.00	0.09	0.05	0.00	0.00
Total	98.42	98.48	99.64	100.29	99.37	99.38	99.14	99.92	99.74	98.87	98.60	100.91	100.04	99.99	98.66	99.10	98.85	99.92	100.32	100.72

Abbreviations: sp = sphalerite, chl = chlorite, py =pyrite, qz = quartz, asp = arsenopyrite, cp = chalcopyrite, tet = tetrahedrite, co = carboante, mgt = magnetite, or = orange, br = brown

Appendix A4.2: Electron microprobe analysis of pyrite

Sample	762053	762053	762053	762053	762053	762053	762053	762053	762053	762053	762053	762053	762053	762053	762053	762053	762053	760384	760384	760384	760384
North	18276.5	18276.5	18276.5	18276.5	18276.5	18276.5	18276.5	18276.5	18276.5	18276.5	18276.5	18276.5	18276.5	18276.5	18276.5	18276.5	18276.5	18189.4	18189.4	18189.4	18189.4
East	4869.6	4869.6	4869.6	4869.6	4869.6	4869.6	4869.6	4869.6	4869.6	4869.6	4869.6	4869.6	4869.6	4869.6	4869.6	4869.6	4869.6	4935.6	4935.6	4935.6	4935.6
R.L.	10043.7	10043.7	10043.7	10043.7	10043.7	10043.7	10043.7	10043.7	10043.7	10043.7	10043.7	10043.7	10043.7	10043.7	10043.7	10043.7	10043.7	10242.9	10242.9	10242.9	10242.9
drill hole	GG173	GG173	GG173	GG173	GG173	GG173	GG173	GG173	GG173	GG173	GG173	GG173	GG173	GG173	GG173	GG173	GG173	GG136	GG136	GG136	GG136
metre	373.8	373.8	373.8	373.8	373.8	373.8	373.8	373.8	373.8	373.8	373.8	373.8	373.8	373.8	373.8	373.8	373.8	142.5	142.5	142.5	142.5
zone	C	C	C	C	C	C	C	C	C	C	C	C	C	C	C	C	C	B	B	B	B
host	chl-and	chl-and	chl-and	chl-and	chl-and	chl-and	chl-and	chl-and	chl-and	chl-and	chl-and	chl-and	chl-and	chl-and	chl-and	chl-and	chl-and	sp-chl	sp-chl	sp-chl	sp-chl
py host	chl	chl	chl	and	and	and	and	and	and	and	and	and	and	and	and	and	chl	chl	chl	chl	chl-sp
py form	eu	eu	eu	eu	eu	eu	eu	eu	eu	eu	eu	mas	mas	mas	mas	mas	eu	eu	eu	eu	eu
py type	ds	ds	ds	ds	ds	ds	ds	ds	ds	ds	ds	rim	rim	rim	rim	rim	ds	ds	ds	ds	ds
label	pyrite	pyrite	pyrite	pyrite	pyrite	pyrite	pyrite	pyrite	pyrite	pyrite	pyrite	pyrite	pyrite	pyrite	pyrite	pyrite	pyrite	pyrite	pyrite	pyrite	pyrite
S	51.87	51.88	51.77	52.23	51.72	52.73	51.97	52.50	52.10	52.42	52.68	52.43	52.23	51.99	52.67	52.74	53.02	53.21	53.25	53.26	52.98
Fe	47.47	47.83	47.62	47.51	48.06	47.86	47.74	47.72	47.49	47.84	48.10	47.87	48.00	47.42	47.62	47.64	46.66	45.73	45.79	45.26	46.21
Co	0.00	0.00	0.01	0.00	0.03	0.03	0.01	0.00	0.00	0.00	0.01	0.00	0.00	0.19	0.00	0.00	0.98	0.00	0.00	0.00	0.00
Ni	0.02	0.00	0.00	0.02	0.00	0.00	0.02	0.00	0.00	0.00	0.00	0.00	0.00	0.11	0.00	0.02	0.01	0.00	0.00	0.02	0.02
Zn	0.00	0.00	0.00	0.04	0.04	0.01	0.02	0.01	0.00	0.02	0.01	0.04	0.00	0.00	0.02	0.00	0.00	0.06	0.00	0.46	0.47
As	0.00	0.00	0.00	0.00	0.11	0.00	0.00	0.00	0.00	0.00	0.00	0.00	0.00	0.55	0.05	0.00	0.00	0.00	0.00	0.00	0.00
Ag	0.00	0.00	0.01	0.00	0.00	0.04	0.06	0.01	0.03	0.00	0.00	0.00	0.04	0.00	0.03	0.00	0.02	0.00	0.00	0.00	0.00
Se	0.00	0.01	0.00	0.00	0.00	0.00	0.00	0.00	0.01	0.01	0.02	0.01	0.01	0.02	0.00	0.00	0.00	0.00	0.00	0.00	0.00
Pb	0.09	0.16	0.17	0.12	0.16	0.11	0.13	0.06	0.16	0.18	0.16	0.10	0.18	0.09	0.11	0.08	0.11	0.12	0.14	0.18	0.18
Total	99.45	99.88	99.58	99.92	100.12	100.78	99.95	100.30	99.79	100.47	100.98	100.45	100.46	100.37	100.50	100.48	100.80	99.12	99.18	99.18	99.86

Abbreviations: and = andalusite, bnd = banded, chl = chlorite, cfm = colloform, co = carbonate, cp = chalcopyrite, def = deformed, ds = disseminated, eu = euhedral, mas = massive, no = nodular, py = pyrite, qz = quartz, skel = skeletal, sp = sphalerite, spg = spongy, vn = vein

Appendix A4.2: Electron microprobe analysis of pyrite *(continued)*

Sample	760384	760384	760384	760384	760384	760384	760384	760461	760461	760461	760461	760461	760461	760461	760461	760461	760461	760461	760461	760461	760461	760461
North	18189.4	18189.4	18189.4	18189.4	18189.4	18189.4	18189.4	18267.8	18267.8	18267.8	18267.8	18267.8	18267.8	18267.8	18267.8	18267.8	18267.8	18267.8	18267.8	18267.8	18267.8	18267.8
East	4935.6	4935.6	4935.6	4935.6	4935.6	4935.6	4935.6	4832.7	4832.7	4832.7	4832.7	4832.7	4832.7	4832.7	4832.7	4832.7	4832.7	4832.7	4832.7	4832.7	4832.7	4832.7
R.L.	10242.9	10242.9	10242.9	10242.9	10242.9	10242.9	10242.9	10116.7	10116.7	10116.7	10116.7	10116.7	10116.7	10116.7	10116.7	10116.7	10116.7	10116.7	10116.7	10116.7	10116.7	10116.7
drill hole	GG136	GG136	GG136	GG136	GG136	GG136	GG136	GG160	GG160	GG160	GG160	GG160	GG160	GG160	GG160	GG160	GG160	GG160	GG160	GG160	GG160	GG160
metre	142.5	142.5	142.5	142.5	142.5	142.5	142.5	277.6	277.6	277.6	277.6	277.6	277.6	277.6	277.6	277.6	277.6	277.6	277.6	277.6	277.6	277.6
zone	B	B	B	B	B	B	B	C	C	C	C	C	C	C	C	C	C	C	C	C	C	C
host	sp-chl	sp-chl	sp-chl	sp-chl	sp-chl	sp-chl	sp-chl	sp-py	sp-py	sp-py	sp-py	sp-py	sp-py	sp-py	sp-py	sp-py	sp-py	sp-py	sp-py	sp-py	sp-py	sp-py
py host	chl-sp	chl-sp	chl-sp	chl-sp	chl-sp	chl-sp	chl-sp	sp	sp	sp	sp	sp	sp	sp	sp	sp	sp	sp	sp	sp	sp	sp
py form	eu	eu	eu	eu	eu	eu	eu	eu	eu	skel	spg	spg	eu	eu	spg	spg	eu	eu	skel	skel	eu	eu
py type	ds	ds	ds	ds	ds	ds	ds	core	rim	mas	mas	mas	mas	mas	mas	mas	rim	core	mas	mas	mas	ds
label	pyrite	pyrite	pyrite	pyrite	pyrite	pyrite	pyrite	pyrite	pyrite	pyrite	pyrite	pyrite	pyrite	pyrite	pyrite	pyrite	pyrite	pyrite	pyrite	pyrite	pyrite	pyrite
S	52.97	53.46	53.25	53.35	53.83	53.67	53.49	52.07	52.49	52.04	51.46	51.75	52.72	52.82	51.83	53.21	53.03	52.84	51.51	51.73	52.50	52.70
Fe	45.92	45.96	46.00	45.81	46.04	46.74	46.61	46.06	46.12	45.95	46.16	46.49	46.50	46.47	46.38	46.16	46.60	46.29	45.98	45.35	46.46	46.10
Co	0.00	0.01	0.00	0.03	0.00	0.00	0.00	0.02	0.02	0.02	0.00	0.00	0.00	0.00	0.02	0.01	0.00	0.00	0.03	0.00	0.02	0.02
Ni	0.02	0.00	0.00	0.01	0.02	0.02	0.01	0.01	0.00	0.01	0.02	0.00	0.02	0.00	0.02	0.00	0.01	0.00	0.02	0.00	0.00	0.01
Zn	0.27	0.90	0.28	1.20	0.25	0.05	0.27	0.00	0.09	0.02	0.19	0.01	0.00	0.07	0.05	0.37	0.06	0.17	0.02	0.10	0.12	0.22
As	0.00	0.00	0.07	0.00	0.00	0.01	0.02	0.05	0.00	0.00	0.00	0.00	0.01	0.00	0.00	0.00	0.04	0.00	0.00	0.00	0.05	0.00
Ag	0.04	0.02	0.00	0.02	0.02	0.02	0.02	0.00	0.00	0.00	0.00	0.05	0.00	0.02	0.01	0.02	0.00	0.00	0.00	0.00	0.00	0.00
Se	0.00	0.00	0.01	0.01	0.00	0.01	0.00	0.00	0.00	0.00	0.01	0.02	0.00	0.00	0.00	0.02	0.00	0.00	0.01	0.03	0.01	0.00
Pb	0.14	0.12	0.19	0.14	0.00	0.07	0.15	0.12	0.04	0.01	0.19	0.00	0.08	0.20	0.00	0.12	0.10	0.18	0.16	1.01	0.35	0.13
Total	99.36	100.47	99.80	100.57	100.16	100.59	100.57	98.33	98.76	98.06	98.03	98.32	99.34	99.58	98.29	99.91	99.83	99.47	97.72	98.21	99.52	99.17

Abbreviations: and = andalusite, bnd = banded, chl = chlorite, cfm = colloform, co = carbonate, cp = chalcopyrite, def = deformed, ds = disseminated, eu = euhedral, mas = massive, no = nodular, py = pyrite, qz = quartz, skel = skeletal, sp = sphalerite, spg = spongy, vn = vein

Appendix A4.2: Electron microprobe analysis of pyrite *(continued)*

Sample	760461	760461	760461	760461	760461	760461	760461	760480	760480	760480	760480	760480	760480	760480	760480	760480	760480	760480	760480	760480	760480
North	18267.8	18267.8	18267.8	18267.8	18267.8	18267.8	18267.8	18263.3	18263.3	18263.3	18263.3	18263.3	18263.3	18263.3	18263.3	18263.3	18263.3	18263.3	18263.3	18263.3	18263.3
East	4832.7	4832.7	4832.7	4832.7	4832.7	4832.7	4832.7	4854.0	4854.0	4854.0	4854.0	4854.0	4854.0	4854.0	4854.0	4854.0	4854.0	4854.0	4854.0	4854.0	4854.0
R.L.	10116.7	10116.7	10116.7	10116.7	10116.7	10116.7	10116.7	10185.6	10185.6	10185.6	10185.6	10185.6	10185.6	10185.6	10185.6	10185.6	10185.6	10185.6	10185.6	10185.6	10185.6
drill hole	GG160	GG160	GG160	GG160	GG160	GG160	GG160	GG163	GG163	GG163	GG163	GG163	GG163	GG163	GG163	GG163	GG163	GG163	GG163	GG163	GG163
metre	277.6	277.6	277.6	277.6	277.6	277.6	277.6	234.1	234.1	234.1	234.1	234.1	234.1	234.1	234.1	234.1	234.1	234.1	234.1	234.1	234.1
zone	C	C	C	C	C	C	C	C	C	C	C	C	C	C	C	C	C	C	C	C	C
host	sp-py	sp-py	sp-py	sp-py	sp-py	sp-py	sp-py	py-chl	py-chl	py-chl	py-chl	py-chl	py-chl	py-chl	py-chl	py-chl	py-chl	py-chl	py-chl	py-chl	py-chl
py host	sp	sp	sp	sp	sp	sp	sp	chl	chl	chl	chl	chl	chl	chl	chl	chl	chl	chl	chl	chl	chl
py form	eu	eu	eu	eu	eu	eu	eu	eu	eu	eu	eu	spg	spg	spg	eu	eu	eu	eu	blocky	blocky	blocky
py type	mas	mas	mas	mas	mas	mas	mas	rim	core	rim	mas	rim	core	rim	ds	ds	ds	ds	rim 1/10	2/10	3/10
label	pyrite	pyrite	pyrite	pyrite	pyrite	pyrite	pyrite	pyrite	pyrite	pyrite	pyrite	pyrite	pyrite	pyrite	pyrite	pyrite	pyrite	pyrite	pyrite	pyrite	pyrite
S	51.88	51.99	52.82	52.48	52.79	52.30	52.29	52.90	52.78	52.67	52.47	51.80	52.33	52.74	52.19	52.94	52.60	52.59	52.78	52.96	52.89
Fe	45.70	46.81	46.11	47.07	47.15	46.09	46.09	45.11	45.69	45.09	45.22	45.19	45.52	45.51	45.56	45.69	45.44	45.61	45.46	45.36	46.03
Co	0.00	0.00	0.00	0.01	0.00	0.01	0.00	0.00	0.00	0.00	0.00	0.00	0.00	0.00	0.00	0.02	0.00	0.00	0.00	0.03	0.00
Ni	0.00	0.00	0.00	0.01	0.00	0.00	0.01	0.02	0.00	0.00	0.00	0.00	0.02	0.01	0.02	0.00	0.00	0.00	0.00	0.00	0.00
Zn	0.00	0.07	0.06	0.20	0.17	0.02	0.06	0.03	0.01	0.02	0.00	0.00	0.00	0.01	0.00	0.01	0.00	0.00	0.00	0.00	0.00
As	0.00	0.00	0.00	0.00	0.00	0.00	0.00	0.00	0.00	0.00	0.00	0.00	0.00	0.00	0.00	0.00	0.00	0.00	0.00	0.00	0.00
Ag	0.00	0.00	0.01	0.00	0.01	0.01	0.03	0.01	0.00	0.01	0.00	0.01	0.00	0.00	0.00	0.03	0.02	0.00	0.02	0.02	0.00
Se	0.01	0.02	0.00	0.00	0.02	0.00	0.00	0.00	0.00	0.00	0.00	0.00	0.00	0.03	0.00	0.00	0.00	0.00	0.00	0.01	0.00
Pb	0.11	0.15	0.11	0.01	0.15	0.25	0.11	0.09	0.00	0.00	0.21	0.14	0.23	0.14	0.02	0.02	0.12	0.15	0.16	0.04	0.06
Total	97.70	99.04	99.10	99.76	100.29	98.69	98.59	98.15	98.48	97.79	97.90	97.15	98.10	98.44	97.79	98.71	98.18	98.35	98.42	98.43	98.98

Abbreviations: and = andalusite, bnd = banded, chl = chlorite, cfm = colloform, co = carbonate, cp = chalcopyrite, def = deformed, ds = disseminated, eu = euhedral, mas = massive, no = nodular, py = pyrite, qz = quartz, skel = skeletal, sp = sphalerite, spg = spongy, vn = vein

Appendix A4.2: Electron microprobe analysis of pyrite *(continued)*

Sample	760480	760480	760480	760480	760480	760480	760480	760480	760480	760350	760350	760350	760350	760350	760350	760350	760350	760350	760350	760350	762055	762055
North	18263.3	18263.3	18263.3	18263.3	18263.3	18263.3	18263.3	18263.3	18263.3	18185.5	18185.5	18185.5	18185.5	18185.5	18185.5	18185.5	18185.5	18185.5	18185.5	18185.5	18286.8	18286.8
East	4854.0	4854.0	4854.0	4854.0	4854.0	4854.0	4854.0	4854.0	4854.0	4941.5	4941.5	4941.5	4941.5	4941.5	4941.5	4941.5	4941.5	4941.5	4941.5	4941.5	4878.9	4878.9
R.L.	10185.6	10185.6	10185.6	10185.6	10185.6	10185.6	10185.6	10185.6	10185.6	10248.8	10248.8	10248.8	10248.8	10248.8	10248.8	10248.8	10248.8	10248.8	10248.8	10248.8	10025.3	10025.3
drill hole	drill hole	drill hole	drill hole	drill hole	drill hole	drill hole	drill hole	drill hole	drill hole	GG118	GG118	GG118	GG118	GG118	GG118	GG118	GG118	GG118	GG118	GG118	GG173	GG173
metre	metre	metre	metre	metre	metre	metre	metre	metre	metre	148	148	148	148	148	148	148	148	148	148	148	396.9	396.9
zone	C	C	C	C	C	C	C	C	C	B	B	B	B	B	B	B	B	B	B	B	C	C
host	py-chl	py-chl	py-chl	py-chl	py-chl	py-chl	py-chl	py-chl	py-chl	py	py	py	py	py	py	py	py	py	py	py	py-chl	py-chl
py host	chl	chl	chl	chl	chl	chl	chl	chl	chl	chl	chl	chl	chl	chl	chl	chl	chl	chl	chl	chl	chl	chl
py form	blocky	blocky	blocky	blocky	blocky	blocky	blocky	blocky	blocky	eu	eu	eu	eu	eu	eu	eu	eu	eu	eu	eu	eu	eu
py type	5/10	6/10	7/10	8/10	9/10	10/10	def	def	def	vn	vn	vn	vn	vn	vn	vn	vn	vn	vn	vn	core	rim
label	pyrite	pyrite	pyrite	pyrite	pyrite	pyrite	pyrite	pyrite	pyrite	pyrite	pyrite	pyrite	pyrite	pyrite	pyrite	pyrite	pyrite	pyrite	pyrite	pyrite	pyrite	pyrite
S	52.79	52.52	52.48	51.35	51.93	52.56	52.61	52.53	52.05	52.45	51.92	52.67	52.33	52.57	52.41	52.82	52.24	52.52	52.46	52.02	50.17	50.58
Fe	46.26	45.58	45.86	45.48	45.82	46.29	45.60	45.32	45.62	45.54	45.40	45.91	46.13	45.74	46.20	46.21	45.79	45.95	46.33	45.92	46.94	46.57
Co	0.00	0.00	0.00	0.00	0.00	0.00	0.00	0.02	0.00	0.00	0.01	0.01	0.00	0.00	0.00	0.00	0.00	0.00	0.00	0.00	0.02	0.00
Ni	0.00	0.02	0.02	0.00	0.01	0.00	0.02	0.00	0.01	0.00	0.01	0.01	0.02	0.03	0.01	0.00	0.01	0.01	0.00	0.01	0.00	0.00
Zn	0.03	0.00	0.00	0.00	0.06	0.05	0.00	0.01	0.00	0.01	0.00	0.00	0.04	0.07	0.09	0.00	0.00	0.01	0.13	0.02	0.01	0.00
As	0.00	0.00	0.00	0.00	0.00	0.00	0.00	0.00	0.00	0.00	0.06	0.00	0.01	0.10	0.00	0.00	0.00	0.00	0.01	0.00	0.00	0.00
Ag	0.00	0.05	0.01	0.00	0.02	0.00	0.00	0.03	0.00	0.02	0.04	0.02	0.01	0.00	0.00	0.00	0.00	0.04	0.01	0.07	0.02	0.01
Sc	0.00	0.00	0.00	0.00	0.00	0.00	0.00	0.00	0.02	0.01	0.01	0.02	0.02	0.00	0.00	0.01	0.01	0.00	0.00	0.00	0.03	0.02
Pb	0.21	0.16	0.31	0.23	0.09	0.10	0.05	0.23	0.03	0.49	0.67	0.14	0.11	0.24	0.19	0.12	0.15	0.01	0.09	0.74	0.00	0.00
Total	99.29	98.32	98.69	97.06	97.93	98.99	98.28	98.14	97.73	98.51	98.12	98.76	98.66	98.74	98.90	99.16	98.21	98.54	99.03	98.77	97.19	97.18

Abbreviations: and = andalusite, bnd = banded, chl = chlorite, cfm = colloform, co = carbonate, cp = chalcopyrite, def = deformed, ds = disseminated, eu = euhedral, mas = massive, no = nodular, py = pyrite, qz = quartz, skel = skeletal, sp = sphalerite, spg = spongy, vn = vein

Appendix A4.2: Electron microprobe analysis of pyrite *(continued)*

Sample	762055	762059	762059	762059	762059	762059	762059	762059	760426	760426	760426	760426	760426	760426	760426	760426	760426	760426	760426	760411	760411	760411
North	18286.8	18073.7	18073.7	18073.7	18073.7	18073.7	18073.7	18073.7	18246.3	18246.3	18246.3	18246.3	18246.3	18246.3	18246.3	18246.3	18246.3	18246.3	18246.3	18107.3	18107.3	18107.3
East	4878.9	4954.0	4954.0	4954.0	4954.0	4954.0	4954.0	4954.0	4806.3	4806.3	4806.3	4806.3	4806.3	4806.3	4806.3	4806.3	4806.3	4806.3	4806.3	5014.7	5014.7	5014.7
R.L.	10025.3	10283.2	10283.2	10283.2	10283.2	10283.2	10283.2	10283.2	10094.7	10094.7	10094.7	10094.7	10094.7	10094.7	10094.7	10094.7	10094.7	10094.7	10094.7	10242.3	10242.3	10242.3
drill hole	GG173	GG099	GG099	GG099	GG099	GG099	GG099	GG099	GG165	GG165	GG165	GG165	GG165	GG165	GG165	GG165	GG165	GG165	GG165	GG127	GG127	GG127
metre	396.9	119	119	119	119	119	119	119	302	302	302	302	302	302	302	302	302	302	302	179.4	179.4	179.4
zone	C	B	B	B	B	B	B	B	C	C	C	C	C	C	C	C	C	C	C	B	B	B
host	py-chl	mas sp	mas sp	mas sp	mas sp	mas sp	mas sp	mas sp	mas sp	mas sp	mas sp	mas sp	mas sp	mas sp	mas sp	mas sp	mas sp	mas sp	mas sp	no co	no co	no co
py host	chl-sp	sp-qz	sp-qz	qz	qz	qz	qz	qz	sp	sp	sp	sp	sp	sp	sp	cp-tet	cp-tet	sp	sp	co-chl	co-chl	co-chl
py form	mas	spg	spg	spg	spg	spg	mas	mas	spg	spg	spg	eu	eu	eu	eu	cfm	cfm	eu	eu	eu	eu	eu
py type	def	ds	ds	mas	mas	ds	def	def	mas	mas	mas	mas	core	mid	rim	bnd	bnd	mas	mas	core	rim	ds
label	pyrite	pyrite	pyrite	pyrite	pyrite	pyrite	pyrite	pyrite	pyrite	pyrite	pyrite	pyrite	pyrite	pyrite	pyrite	pyrite	pyrite	pyrite	pyrite	pyrite	pyrite	pyrite
S	50.31	51.57	51.28	51.05	51.94	51.23	48.93	51.33	51.39	51.02	51.19	51.84	51.09	50.92	51.22	50.41	50.23	51.65	50.99	53.44	53.49	53.45
Fe	46.62	46.03	45.74	46.07	46.28	46.05	44.39	46.70	46.32	46.17	46.16	45.64	46.08	46.26	46.26	46.12	45.57	46.38	46.49	46.91	46.67	46.89
Co	0.05	0.08	0.12	0.02	0.02	0.00	0.09	0.00	0.01	0.08	0.08	0.35	0.00	0.00	0.00	0.01	0.08	0.07	0.07	0.02	0.04	0.01
Ni	0.00	0.01	0.00	0.01	0.03	0.00	0.07	0.01	0.00	0.00	0.01	0.00	0.02	0.00	0.04	0.02	0.00	0.01	0.00	0.00	0.01	0.00
Zn	0.02	0.00	0.05	0.04	0.03	0.00	0.00	0.01	0.29	0.04	0.09	0.81	0.00	0.00	0.01	0.00	0.02	0.00	0.02	0.04	0.01	0.03
As	0.00	0.16	0.19	0.05	0.04	0.04	1.89	0.03	0.04	0.05	0.11	0.21	0.04	0.01	0.05	0.21	0.13	0.03	0.07	0.15	0.06	0.17
Ag	0.00	0.00	0.01	0.02	0.00	0.03	0.11	0.00	0.00	0.00	0.00	0.00	0.00	0.00	0.02	0.02	0.42	0.00	0.00	0.00	0.00	0.01
Se	0.00	0.00	0.02	0.01	0.00	0.04	0.02	0.02	0.00	0.01	0.00	0.00	0.00	0.00	0.00	0.00	0.01	0.00	0.00	0.01	0.01	0.01
Pb	0.17	0.52	0.91	0.11	0.04	0.07	4.90	0.15	0.19	0.15	0.25	0.54	0.00	0.07	0.08	0.61	0.30	0.00	0.03	0.04	0.00	0.26
Total	97.17	98.38	98.32	97.39	98.37	97.45	100.40	98.24	98.24	97.51	97.89	99.39	97.23	97.26	97.68	97.39	96.76	98.15	97.67	100.60	100.27	100.82

Abbreviations: and = andalusite, bnd = banded, chl = chlorite, cfm = colloform, co = carbonate, cp = chalcopyrite, def = deformed, ds = disseminated, eu = euhedral, mas = massive, no = nodular, py = pyrite, qz = quartz, skel = skeletal, sp = sphalerite, spg = spongy, vn = vein

Appendix A4.2: Electron microprobe analysis of pyrite *(continued)*

Sample	760411	760411	760411	760411	760411	760411	762057	762057	762057	762031	762031	762031	762031	762031	762031	762031	762031	762031	762031	762031	769121	769121
North	18107.3	18107.3	18107.3	18107.3	18107.3	18107.3	18303.7	18303.7	18303.7	18227.0	18227.0	18227.0	18227.0	18227.0	18227.0	18227.0	18227.0	18227.0	18227.0	18227.0	18325.2	18325.2
East	5014.7	5014.7	5014.7	5014.7	5014.7	5014.7	4894.8	4894.8	4894.8	4825.6	4825.6	4825.6	4825.6	4825.6	4825.6	4825.6	4825.6	4825.6	4825.6	4825.6	4933.5	4933.5
R.L.	10242.3	10242.3	10242.3	10242.3	10242.3	10242.3	9996.3	9996.3	9996.3	10074.8	10074.8	10074.8	10074.8	10074.8	10074.8	10074.8	10074.8	10074.8	10074.8	10074.8	10117.8	10117.8
drill hole	GG127	GG127	GG127	GG127	GG127	GG127	GG173	GG173	GG173	GG171	GG171	GG171	GG171	GG171	GG171	GG171	GG171	GG171	GG171	GG171	GG042	GG042
metre	179.4	179.4	179.4	179.4	179.4	179.4	434	434	434	322.7	322.7	322.7	322.7	322.7	322.7	322.7	322.7	322.7	322.7	322.7	369.3	369.3
zone	B	B	B	B	B	B	B	B	B	C	C	C	C	C	C	C	C	C	C	C	18288	18288
host	no co	no co	no co	no co	no co	no co	no co	no co	no co	sp vn	sp vn	sp vn	sp vn	sp vn	sp vn	sp vn	sp vn	sp vn	sp vn	sp vn	sst	sst
py host	co-chl	co-chl	co	co	co	co	co	co	co	sp	sp	sp	sp	chl-sp	sp	sp	qz-sp	sp	sp	sp	chl-qz	chl-qz
py form	eu	eu	spg	skel	eu	eu	eu	eu	eu	eu	eu	eu	eu	spg	eu	eu	spg	spg	eu	skel	skel	skel
py type	ds	ds	ds	ds	ds	ds	ds	ds	ds	core	rim	ds	ds	ds	ds	ds	ds	mas	eu	ds	ds	core
label	pyrite	pyrite	pyrite	pyrite	pyrite	pyrite	pyrite	pyrite	pyrite	pyrite	pyrite	pyrite	pyrite	pyrite	pyrite	pyrite	pyrite	pyrite	pyrite	pyrite	pyrite	pyrite
S	53.54	51.46	53.45	53.35	52.96	52.73	39.46	39.39	39.37	53.71	52.74	53.12	53.27	53.71	53.01	53.53	53.12	52.94	53.11	53.68	53.892	53.921
Fe	46.33	45.33	46.63	47.02	46.80	46.73	58.63	58.51	59.63	46.55	46.53	46.61	46.62	46.20	45.98	46.38	47.10	46.66	46.32	46.58	46.551	45.708
Co	0.02	0.00	0.02	0.07	0.00	0.03	0.05	0.31	0.22	0.00	0.01	0.07	0.07	0.05	0.23	0.00	0.00	0.03	0.11	0.00	0.292	1.128
Ni	0.00	0.00	0.00	0.00	0.00	0.00	0.00	0.01	0.01	0.00	0.01	0.01	0.00	0.01	0.00	0.01	0.00	0.00	0.00	0.01	0	0.005
Zn	0.00	0.00	0.01	0.00	0.00	0.00	0.01	0.00	0.04	0.36	0.56	0.60	0.22	0.41	0.51	0.61	0.11	0.09	0.52	0.48	0	0.005
As	0.11	0.14	0.06	0.07	0.13	0.18	0.06	0.06	0.06	0.05	0.44	0.10	0.02	0.11	0.26	0.04	0.03	0.08	0.15	0.06	0.07	0.21
Ag	0.04	0.05	0.00	0.01	0.00	0.01	0.02	0.00	0.00	0.03	0.03	0.00	0.01	0.00	0.00	0.03	0.02	0.04	0.04	0.01	0	0.009
Se	0.02	0.00	0.02	0.01	0.00	0.01	0.03	0.03	0.02	0.00	0.00	0.00	0.01	0.00	0.01	0.00	0.01	0.00	0.01	0.03	0.013	0.015
Pb	0.04	0.31	0.00	0.26	0.24	0.25	0.00	0.12	0.05	0.03	1.10	0.00	0.00	0.09	0.60	0.00	0.00	0.00	0.36	0.06	0.2264	0.4084
Total	100.11	97.29	100.19	100.79	100.14	99.95	98.26	98.42	99.39	100.74	101.41	100.50	100.23	100.58	100.59	100.61	100.39	99.83	100.61	100.88	101.04	101.41

Abbreviations: and = andalusite, bnd = banded, chl = chlorite, cfm = colloform, co = carbonate, cp = chalcopyrite, def = deformed, ds = disseminated, eu = euhedral, mas = massive, no = nodular, py = pyrite, qz = quartz, skel = skeletal, sp = sphalerite, spg = spongy, vn = vein

Appendix A4.3: Electron microprobe analysis of chalcopyrite

Sample	760461	762059	762059	762059	762059	762059	762059	762059	762059	760426	760426	760426	760411	762057	762057	762057	762057	762057	762057	762057	762057	762057
North	18267.8	18073.7	18073.7	18073.7	18073.7	18073.7	18073.7	18073.7	18073.7	18246.3	18246.3	18246.3	18107.3	18303.7	18303.7	18303.7	18303.7	18303.7	18303.7	18303.7	18303.7	18303.7
East	4832.7	4954.0	4954.0	4954.0	4954.0	4954.0	4954.0	4954.0	4954.0	4806.3	4806.3	4806.3	5014.7	4894.8	4894.8	4894.8	4894.8	4894.8	4894.8	4894.8	4894.8	4894.8
R.L.	10116.7	10283.2	10283.2	10283.2	10283.2	10283.2	10283.2	10283.2	10283.2	10094.7	10094.7	10094.7	10242.3	9996.3	9996.3	9996.3	9996.3	9996.3	9996.3	9996.3	9996.3	9996.3
drill hole	GG160	GG099	GG099	GG099	GG099	GG099	GG099	GG099	GG099	GG165	GG165	GG165	GG127	GG173	GG173	GG173	GG173	GG173	GG173	GG173	GG173	GG173
metre	277.6	119	119	119	119	119	119	119	119	302	302	302	179.4	434	434	434	434	434	434	434	434	434
zone	C	A	A	A	A	A	A	A	A	C	C	C	A	A	A	A	A	A	A	A	A	A
host	sp-py	mas sp	mas sp	mas sp	mas sp	mas sp	mas sp	mas sp	mas sp	sp-py	sp-py	sp-py	no co	no co	no co	no co	no co	no co	no co	no co	no co	no co
cp host	py-sp	sp	sp	py	tet-py	sp-tet	sp-tet	py	py	py	py	py	py	chl	chl	chl	co-py	co-sp	co-sp	co-sp	co-sp	co-sp
cp form	incl	poly	poly	rim	incl	incl	incl	fracture	fracture	incl	incl	fracture	incl	poly	poly	poly	poly	poly	poly	poly	poly	poly
label	tetra	tetra	tetra	tetra	tetra	tetra	tetra	tetra	tetra	tetra	tetra	tetra	tetra	tetra	tetra	tetra	tetra	tetra	tetra	tetra	tetra	tetra
S	34.74	33.90	33.36	33.28	33.79	33.07	32.95	33.21	32.98	33.00	33.02	33.28	34.49	34.02	34.25	34.01	34.19	33.86	34.07	34.10	34.40	34.21
Fe	31.92	31.43	31.30	31.83	31.74	31.47	31.51	31.65	31.99	32.07	32.01	32.18	31.22	31.60	31.46	31.54	31.23	31.36	31.78	31.75	31.77	31.84
Cu	33.87	34.55	34.29	34.17	34.29	34.42	35.01	34.68	34.49	34.14	34.81	34.47	34.57	34.33	34.76	34.74	34.58	34.62	34.56	34.75	34.69	34.59
Zn	0.05	0.04	0.00	0.05	0.01	0.12	0.03	0.00	0.06	0.01	0.04	0.00	0.00	0.03	0.05	0.04	0.00	0.00	0.00	0.07	0.02	0.04
As	0.00	0.00	0.09	0.00	0.00	0.00	0.00	0.01	0.00	0.04	0.00	0.00	0.00	0.00	0.00	0.00	0.00	0.00	0.00	0.00	0.00	0.00
Ag	0.01	0.01	0.00	0.03	0.03	0.01	0.03	0.00	0.00	0.02	0.00	0.00	0.01	0.00	0.00	0.09	0.04	0.02	0.05	0.00	0.01	0.00
Sb	0.00	0.02	0.02	0.00	0.00	0.01	0.00	0.00	0.02	0.01	0.00	0.00	0.04	0.01	0.02	0.00	0.03	0.00	0.00	0.00	0.00	0.00
Bi	0.00	0.00	0.48	0.14	0.17	0.08	0.44	0.00	0.18	0.00	0.02	0.00	0.00	0.00	0.00	0.04	0.15	0.00	0.00	0.15	0.03	0.00
Total	100.59	99.96	99.54	99.50	100.04	99.18	99.96	99.54	99.71	99.28	99.90	99.93	100.33	99.99	100.54	100.46	100.21	99.85	100.47	100.82	100.92	100.69

Abbreviations used are : bx = breccia, chl = chlorite, co = carbonate,incl = inclusion, mas = massive, no = nodular, py = pyrite, poly = polycrystalline, qz = quartz, sp = sphalerite, tet = tetrahedrite

Appendix A4.4: Electron microprobe analysis of pyrrhotite

Sample	762053	762053	762053	762053	762053	762053	760466	760466	760432	760432	760432	760432	760432	769121	769121	769121	769121	769121
North	18276.5	18276.5	18276.5	18276.5	18276.5	18276.5	18288.4	18288.4	18257.4	18257.4	18257.4	18257.4	18257.4	18325.2	18325.2	18325.2	18325.2	18325.2
East	4869.6	4869.6	4869.6	4869.6	4869.6	4869.6	4849.6	4849.6	4816.7	4816.7	4816.7	4816.7	4816.7	4933.5	4933.5	4933.5	4933.5	4933.5
R.L.	10043.7	10043.7	10043.7	10043.7	10043.7	10043.7	10066.7	10066.7	10069.4	10069.4	10069.4	10069.4	10069.4	10117.8	10117.8	10117.8	10117.8	10117.8
drill hole	GG173	GG173	GG173	GG173	GG173	GG173	GG160	GG160	GG165	GG165	GG165	GG165	GG165	GG042	GG042	GG042	GG042	GG042
metre	373.8	373.8	373.8	373.8	373.8	373.8	334.2	334.2	331.6	331.6	331.6	331.6	331.6	369.30	369.30	369.30	369.30	369.30
zone	C	C	C	C	C	C	C	C	C	C	C	C	C					
host	chl-and	chl-and	chl-and	chl-and	chl-and	chl-and	chl-and	chl-and	co-sp vn	co-sp vn	co-sp vn	co-sp vn	co-sp vn	pum sst	pum sst	pum sst	pum sst	pum sst
po host	and	and	and	and	and	and	and	and	sp-mgt	chl	chl	chl	chl	qz	qz	co	co	co
po form	rim	rim	rim	rim	rim	rim	rim	rim	ds	ds	poly	incl	poly	ds	ds	ds	ds	ds
label	pyrite	pyrite	pyrite	pyrite	pyrite	pyrite	pyrite	pyrite	pyrite	pyrite	pyrite	pyrite	pyrite	pyrite	pyrite	pyrite	pyrite	pyrite
S	37.28	37.50	37.77	37.61	37.59	37.45	37.43	37.68	39.49	39.52	38.90	37.24	39.19	38.82	39.09	38.09	38.09	38.43
Fe	61.31	61.61	61.18	61.30	61.06	61.02	61.04	60.55	59.37	60.23	59.86	59.67	59.42	60.66	60.60	60.26	60.22	60.58
Co	0.08	0.07	0.08	0.08	0.06	0.07	0.11	0.16	0.00	0.01	0.00	0.02	0.02	0.06	0.06	0.05	0.07	0.15
Ni	0.00	0.00	0.00	0.00	0.00	0.01	0.01	0.00	0.02	0.03	0.06	0.00	0.06	0.00	0.01	0.00	0.00	0.00
Zn	0.00	0.05	0.00	0.02	0.00	0.00	0.00	0.00	0.00	0.00	0.06	0.00	0.01	0.00	0.04	0.01	0.00	0.01
As	0.00	0.00	0.00	0.00	0.00	0.00	0.00	0.00	0.06	0.08	0.07	0.05	0.06	0.09	0.04	0.07	0.06	0.03
Ag	0.01	0.06	0.01	0.00	0.00	0.00	0.01	0.05	0.03	0.00	0.01	0.03	0.03	0.00	0.00	0.00	0.05	0.00
Sc	0.00	0.00	0.01	0.01	0.01	0.01	0.01	0.01	0.00	0.02	0.00	0.00	0.00	0.00	0.00	0.00	0.01	0.01
Pb	0.11	0.19	0.11	0.11	0.08	0.10	0.07	0.16	0.12	0.00	0.00	0.00	0.00	0.13	0.00	0.07	0.19	0.00
Total	98.79	99.48	99.16	99.13	98.80	98.66	98.68	98.61	99.09	99.88	98.94	97.01	98.79	99.78	99.84	98.56	98.68	99.22

Abbreviations used: and = andalusite, chl = chlorite, co = carbonate, ds = disseminated, incl = inclusion, mgt = magnetite, po = pyrrhotite, poly = polycrystalline, pum = pumiceous, qz = quartz, sp = sphalerite, sst = sandstone, vn = vein

Appendix A4.5: Electron microprobe analysis of magnetite

Sample	760432	760432	760432	760432	760432	760432	760432	760432	760432	760432	769174	769174	769174	769174	769174	769174
North	18257.4	18257.4	18257.4	18257.4	18257.4	18257.4	18257.4	18257.4	18257.4	18257.4	18632.8	18632.8	18632.8	18632.8	18632.8	18632.8
East	4816.7	4816.7	4816.7	4816.7	4816.7	4816.7	4816.7	4816.7	4816.7	4816.7	5066.9	5066.9	5066.9	5066.9	5066.9	5066.9
R.L.	10069.4	10069.4	10069.4	10069.4	10069.4	10069.4	10069.4	10069.4	10069.4	10069.4	10135.7	10135.7	10135.7	10135.7	10135.7	10135.7
drill hole	GG165	GG165	GG165	GG165	GG165	GG165	GG165	GG165	GG165	GG165	GG162	GG162	GG162	GG162	GG162	GG162
metres	331.6	331.6	331.6	331.6	331.6	331.6	331.6	331.6	331.6	331.6	285.4	285.4	285.4	285.4	285.4	285.4
zone	C	C	C	C	C	C	C	C	C	C	Cu	Cu	Cu	Cu	Cu	Cu
host rock	V(Λ) vein	V(Λ) vein	V(Λ) vein	V(Λ) vein	V(Λ) vein	V(Λ) vein	V(Λ) vein	V(Λ) vein	V(Λ) vein	V(Λ) vein	altered GGF M4	altered GGF M4	altered GGF M4	altered GGF M4	altered GGF M4	altered GGF M4
mgt host	sp-co-chl	chl	chl	chl	chl	chl	chl	chl-co	chl-co	chl-co	chl-qz	chl-qz	chl-qz	chl-qz	chl-qz	chl-qz
mgt texture	eu	eu	eu	eu	eu	eu	eu	eu	eu	eu	granular	granular	granular	granular	granular	granular
MgO	0.00	0.00	0.01	0.00	0.11	0.00	0.00	0.01	0.00	0.00	0.09	0.00	0.01	0.16	0.02	0.01
Al_2O_3	0.08	0.04	0.04	0.04	0.06	0.04	0.00	0.13	0.15	0.06	0.17	0.01	0.02	0.29	0.05	0.02
TiO_2	0.02	0.06	0.11	0.04	0.02	0.03	0.01	0.04	0.05	0.05	0.03	0.11	0.02	0.07	0.04	0.08
V_2O_5	0.01	0.08	0.12	0.06	0.10	0.03	0.06	0.00	0.00	0.04	0.00	0.00	0.04	0.00	0.03	0.01
Cr_2O_3	0.01	0.02	0.01	0.05	0.02	0.01	0.01	0.00	0.00	0.06	0.02	0.00	0.00	0.04	0.02	0.00
MnO	0.00	0.00	0.05	0.00	0.01	0.00	0.05	0.06	0.00	0.06	0.01	0.05	0.00	0.00	0.00	0.01
FeO	31.45	31.39	31.52	31.46	30.28	31.32	31.40	31.44	31.42	31.51	31.17	31.59	31.56	31.34	31.49	31.54
ZnO	0.12	0.00	0.05	0.02	0.03	0.03	0.22	0.24	0.08	0.18	0.03	0.00	0.03	0.01	0.00	0.00
Fe_2O_3	69.70	69.45	69.67	69.64	67.56	69.42	69.83	69.68	69.43	69.80	69.25	69.87	70.08	69.52	69.81	69.81
Total	101.38	101.03	101.58	101.30	98.18	100.88	101.58	101.60	101.13	101.75	100.76	101.63	101.76	101.42	101.46	101.48

Abbreviations: chl = chlorite, co = carbonate, eu = euhedral, qz = quartz, sp = sphalerite

Appendix A4.5: Electron microprobe analysis of magnetite *(continued)*

Sample	769174	769174	769174	769174	769174	769174	769174	769174	769174	769175	769175	769175	769175	769175	769175
North	18632.8	18632.8	18632.8	18632.8	18632.8	18632.8	18632.8	18632.8	18632.8	18633.4	18633.4	18633.4	18633.4	18633.4	18633.4
East	5066.9	5066.9	5066.9	5066.9	5066.9	5066.9	5066.9	5066.9	5066.9	5065.7	5065.7	5065.7	5065.7	5065.7	5065.7
R.L.	10135.7	10135.7	10135.7	10135.7	10135.7	10135.7	10135.7	10135.7	10135.7	10133.9	10133.9	10133.9	10133.9	10133.9	10133.9
drill hole	GG162	GG162	GG162	GG162	GG162	GG162	GG162	GG162	GG162	GG162	GG162	GG162	GG162	GG162	GG162
metres	285.4	285.4	285.4	285.4	285.4	285.4	285.4	285.4	285.4	287.6	287.6	287.6	287.6	287.6	287.6
zone	Cu	Cu	Cu	Cu	Cu	Cu	Cu	Cu	Cu	Cu	Cu	Cu	Cu	Cu	Cu
host rock	altered GGF M4	altered GGF M4	altered GGF M4	altered GGF M4	altered GGF M4	altered GGF M4	altered GGF M4	altered GGF M4	altered GGF M4	altered GGF M4	altered GGF M4	altered GGF M4	altered GGF M4	altered GGF M4	altered GGF M4
mgt host	chl-qz	chl-qz	chl-qz	chl-qz	chl-qz	chl-qz	chl-qz	chl-qz	chl-qz	chl-qz	chl-qz	chl-qz	chl-qz	chl-qz	chl-qz
mgt texture	granular	granular	granular	granular	granular	granular	granular	granular	granular	granular	granular	granular	granular	granular	granular
MgO	0.01	0.03	0.00	0.02	0.00	0.00	0.00	0.00	0.00	0.00	0.01	0.02	0.00	0.02	0.06
Al_2O_3	0.09	0.06	0.00	0.03	0.02	0.07	0.06	0.02	0.01	0.04	0.00	0.00	0.03	0.04	0.23
TiO_2	0.09	0.21	0.02	0.04	0.05	0.02	0.17	0.38	0.01	0.03	0.04	0.03	0.06	0.05	0.05
V_2O_5	0.04	0.00	0.05	0.04	0.00	0.00	0.06	0.00	0.00	0.06	0.07	0.01	0.01	0.00	0.00
Cr_2O_3	0.03	0.00	0.00	0.00	0.00	0.00	0.03	0.00	0.00	0.00	0.00	0.02	0.00	0.02	0.00
MnO	0.00	0.03	0.02	0.00	0.00	0.04	0.00	0.00	0.00	0.06	0.00	0.02	0.00	0.00	0.01
FeO	31.57	31.40	31.25	31.53	31.48	31.25	31.58	31.75	31.38	30.52	31.79	31.55	31.47	31.60	31.23
ZnO	0.08	0.02	0.06	0.00	0.00	0.00	0.07	0.01	0.04	0.00	0.00	0.05	0.00	0.17	0.00
Fe_2O_3	69.67	69.03	69.44	70.00	69.76	69.34	69.41	69.00	69.70	67.81	70.52	70.08	69.65	70.03	69.11
Total	101.57	100.79	100.85	101.66	101.30	100.72	101.36	101.17	101.13	98.52	102.42	101.77	101.22	101.92	100.68

Abbreviations: chl = chlorite, co = carbonate, eu = euhedral, qz = quartz, sp = sphalerite

Appendix A4.6: Electron microprobe analysis of ilmenite and rutile

Sample	769174	769174	769174	769174	769174	769174	769175	769175	769175	769175	769091	769091	769091	769091	769091	769091	769091	769091	769091	769091
North	18632.8	18632.8	18632.8	18632.8	18632.8	18632.8	18633.4	18633.4	18633.4	18633.4	18377.7	18377.7	18377.7	18377.7	18377.7	18377.7	18377.7	18377.7	18377.7	18377.7
East	5066.9	5066.9	5066.9	5066.9	5066.9	5066.9	5065.7	5065.7	5065.7	5065.7	5082.8	5082.8	5082.8	5082.8	5082.8	5082.8	5082.8	5082.8	5082.8	5082.8
R.L.	10135.7	10135.7	10135.7	10135.7	10135.7	10135.7	10133.9	10133.9	10133.9	10133.9	10170.5	10170.5	10170.5	10170.5	10170.5	10170.5	10170.5	10170.5	10170.5	10170.5
drill hole	GG162	GG162	GG162	GG162	GG162	GG162	GG162	GG162	GG162	GG162	GG038	GG038	GG038	GG038	GG038	GG038	GG038	GG038	GG038	GG038
metres	285.4	285.4	285.4	285.4	285.4	285.4	287.6	287.6	287.6	287.6	236.4	236.4	236.4	236.4	236.4	236.4	236.4	236.4	236.4	236.4
zone	Cu	Cu	Cu	Cu	Cu	Cu	Cu	Cu	Cu	Cu	Cu	Cu	Cu	Cu	Cu	Cu	Cu	Cu	Cu	Cu
host rock	altered GGF M4	altered GGF M4	altered GGF M4	altered GGF M4	altered GGF M4	altered GGF M4	altered GGF M4	altered GGF M4	altered GGF M4	altered GGF M4	altered GGF M4	altered GGF M4	altered GGF M4	altered GGF M4	altered GGF M4	altered GGF M4	altered GGF M4	altered GGF M4	altered GGF M4	altered GGF M4
ilm host	chl-qz	chl-qz	chl-qz	mgt	chl	chl-qz	chl-qz	chl-qz	mgt	chl	chl	chl	chl	chl	chl	chl	chl	chl	chl	chl
ilm texture	spg	spg	spg	spg	spg	spg	spg	spg	spg	spg	spg	spg	spg	spg	spg lath	spg lath	spg	spg	spg lath	spg lath
MgO	0.22	0.03	0.02	0.03	0.04	0.01	0.05	0.01	0.00	0.01	0.16	0.00	0.04	0.03	0.11	0.02	0.05	0.01	0.03	0.13
Al_2O_3	0.00	0.00	0.00	0.00	0.00	0.00	0.00	0.00	0.00	0.00	0.00	0.00	0.00	0.00	0.00	0.00	0.00	0.00	0.00	0.17
TiO_2	49.93	49.51	49.78	50.53	49.61	49.88	49.93	50.12	49.27	49.66	49.71	50.04	51.06	51.21	50.16	51.45	51.43	50.57	50.62	63.01
Cr_2O_3	0.00	0.00	0.00	0.00	0.01	0.00	0.02	0.01	0.00	0.00	0.00	0.03	0.00	0.00	0.03	0.02	0.00	0.00	0.01	0.00
MnO	0.57	0.51	0.52	0.55	0.54	0.56	0.78	0.81	0.77	0.74	0.93	0.90	0.93	0.89	0.90	0.91	0.87	0.91	0.87	0.69
FeO	43.93	43.95	44.21	44.82	43.99	44.27	44.04	44.23	43.52	43.89	43.46	44.10	44.91	45.10	44.02	45.32	45.27	44.55	44.60	35.12
Fe_2O_3	3.60	4.41	3.87	2.72	4.17	3.55	3.69	3.70	4.67	4.32	3.70	3.87	2.39	1.54	3.18	1.16	1.63	2.86	2.65	0.00
SiO_2	1.13	0.16	0.11	0.08	0.06	0.06	0.05	0.00	0.00	0.00	0.34	0.05	0.04	0.02	0.31	0.10	0.08	0.05	0.04	0.34
Total	99.38	98.55	98.49	98.74	98.42	98.32	98.55	98.89	98.24	98.61	98.31	98.99	99.37	98.78	98.69	98.99	99.33	98.94	98.82	99.46

Abbreviations: chl = chlorite, mgt = magnetite, qz = quartz, spg = spongy texture

Appendix A4.7: Electron microprobe analysis of galena

Sample	762059	762059	762059	762059	762059
North	18073.7	18073.7	18073.7	18073.7	18073.7
East	4953.9	4953.9	4953.9	4953.9	4953.9
R.L.	10283.2	10283.2	10283.2	10283.2	10283.2
drill hole	GG099	GG099	GG099	GG099	GG099
metres	119.0	119.0	119.0	119.0	119.0
zone	B	B	B	B	B
host rock	mas sp	mas sp	mas sp	mas sp	mas sp
ga host	spg py	spg py-cp	spg py-cp	sp-qz	sp-qz
S	13.50	13.26	13.38	13.31	13.44
Ag	0.28	0.33	0.50	0.35	0.25
Pb	84.97	81.98	84.66	83.43	83.26
Bi	0.59	0.96	0.26	0.61	0.45
Se	0.00	0.00	0.00	0.00	0.02
Total	99.33	96.52	98.79	97.70	97.42

Appendix A4.8: Electron Microprobe analysis of tetrahedrite

Sample	762059	762059	762059	762059	762059	760426	760426	762059
North	18073.1	18073.1	18073.1	18073.1	18073.1	18246.3	18246.3	18073.1
East	4953.9	4953.9	4953.9	4953.9	4953.9	4806.3	4806.3	4953.9
R.L.	10283.2	10283.2	10283.2	10283.2	10283.2	10094.7	10094.7	10283.2
drill hole	GG099	GG099	GG099	GG099	GG099	GG099	GG099	GG099
metres	119.0	119.0	119.0	119.0	119.0	119.0	119.0	119.0
zone	B	B	B	B	B	C	C	B
host rock	mas sp	mas sp	mas sp	mas sp	mas sp	mas sp	mas sp	mas sp
tet host	cp	cp	cp-sp	cp-sp	cp-py	cp-py	cp-py	sph
S	27.69	20.04	20.17	20.15	25.87	21.53	21.40	21.34
Fe	0.24	5.01	4.82	5.07	3.60	5.35	5.17	5.32
Cu	43.52	17.81	17.68	17.46	40.04	23.67	23.55	17.70
Zn	0.28	1.49	1.58	1.34	0.33	1.50	1.51	1.43
As	1.26	0.39	0.53	0.48	8.24	0.63	0.23	0.50
Ag	0.28	28.64	28.17	29.00	9.78	20.35	20.79	28.23
Sb	26.24	25.39	25.23	25.70	0.96	25.92	26.73	25.36
Bi	0.00	0.11	0.15	0.00	0.00	0.00	0.32	0.32
Total	99.51	98.87	98.32	99.18	88.81	98.94	99.70	100.20

Abbreviations: cp = chalcopyrite, mas = massive, sp = sphalerite

Appendix A4.9: Electron microprobe analysis of native silver

Sample	760350	760350	760350	760350	760350	760350	760350	760350	760350	760350
North	18185.5	18185.5	18185.5	18185.5	18185.5	18185.5	18185.5	18185.5	18185.5	18185.5
East	4941.9	4941.9	4941.9	4941.9	4941.9	4941.9	4941.9	4941.9	4941.9	4941.9
R.L.	10248.8	10248.8	10248.8	10248.8	10248.8	10248.8	10248.8	10248.8	10248.8	10248.8
drill hole	GG118	GG118	GG118	GG118	GG118	GG118	GG118	GG118	GG118	GG118
metre	148.0	148.0	148.0	148.0	148.0	148.0	148.0	148.0	148.0	148.0
zone	B	B	B	B	B	B	B	B	B	B
host rock	py-qz vein	py-qz vein	py-qz vein	py-qz vein	py-qz vein	py-qz vein	py-qz vein	py-qz vein	py-qz vein	py-qz vein
Ag host	py	py	py	py	py-qz	py-qz	py-qz	py-qz	py-qz	py-qz
Ag	97.77	98.87	98.36	97.86	99.62	98.99	97.84	98.84	99.25	99.27
Au	0.00	0.00	0.11	0.00	0.12	0.02	0.00	0.00	0.01	0.00
Hg	0.00	0.01	0.00	0.00	0.00	0.00	0.00	0.00	0.00	0.06
Total	97.77	98.87	98.47	97.86	99.74	99.01	97.84	98.85	99.27	99.32
Fineness	0.00	0.00	1.13	0.00	1.19	0.21	0.00	0.04	0.12	0.00

Abbreviations: py = pyrite, qz = quartz
Fineness = 100*(Au/(Au+Ag)

Appendix A4.10: Electron microprobe analysis of electrum

Sample	760461	760461	760461	760461
North	18267.8	18267.8	18267.8	18267.8
East	4832.7	4832.7	4832.7	4832.7
R.L.	10116.7	10116.7	10116.7	10116.7
drill hole	GG160	GG160	GG160	GG160
metre	277.6	277.6	277.6	277.6
zone	C	C	C	C
host rock	mas sp-py	mas sp-py	mas sp-py	mas sp-py
Au host	py	py	py	py
Ag	66.12	65.47	64.88	63.98
Au	31.71	33.73	34.52	34.98
Hg	0.03	0.22	0.17	0.05
Total	97.85	99.42	99.57	99.01
Fineness	324.11	339.98	347.30	353.48

Abbreviations: mas = massive, py = pyrite, qz = quartz
Fineness = 100*(Au/(Au+Ag)

Appendix A4.11: Electron microprobe analysis of cobaltite

Sample	762059	762059	769121	769121	769121	769121	769121	769121	769121	769121	769121	769121	769121	769121	769121	769121	769121	769121	769121
North	18307.8	18307.8	18325.2	18325.2	18325.2	18325.2	18325.2	18325.2	18325.2	18325.2	18325.2	18325.2	18325.2	18325.2	18325.2	18325.2	18325.2	18325.2	18325.2
East	4953.9	4953.9	4933.5	4933.5	4933.5	4933.5	4933.5	4933.5	4933.5	4933.5	4933.5	4933.5	4933.5	4933.5	4933.5	4933.5	4933.5	4933.5	4933.5
R.L.	9989.5	9989.5	10117.8	10117.8	10117.8	10117.8	10117.8	10117.8	10117.8	10117.8	10117.8	10117.8	10117.8	10117.8	10117.8	10117.8	10117.8	10117.8	10117.8
drill hole	GG099	GG099	GG042	GG042	GG042	GG042	GG042	GG042	GG042	GG042	GG042	GG042	GG042	GG042	GG042	GG042	GG042	GG042	GG042
metres	119.0	119.0	369.3	369.3	369.3	369.3	369.3	369.3	369.3	369.3	369.3	369.3	369.3	369.3	369.3	369.3	369.3	369.3	369.3
zone	B	B	Cu	Cu	Cu	Cu	Cu	Cu	Cu	Cu	Cu	Cu	Cu	Cu	Cu	Cu	Cu	Cu	Cu
host rock	mas sp	mas sp	chl sst	chl sst	chl sst	chl sst	chl sst	chl sst	chl sst	chl sst	chl sst	chl sst	chl sst	chl sst	chl sst	chl sst	chl sst	chl sst	chl sst
cobaltite host	sph-qz	sph	chl-qz	chl-qz	chl-qz	chl-qz	chl-qz	co	co	co	co	co	co	co	co	co	co	co	co
texture	eu	eu	eu	eu	eu	eu	eu	eu	eu	eu	eu	eu	eu	eu	eu	eu	eu	eu	eu
S	20.67	20.32	19.38	21.56	22.68	20.09	21.15	21.91	22.27	22.19	19.31	19.61	19.59	22.01	21.09	22.02	20.36	20.23	22.08
Fe	3.85	3.51	2.32	4.78	6.15	2.48	4.81	5.18	4.41	4.63	2.69	2.56	2.74	5.03	3.21	4.94	2.25	2.12	4.00
Co	30.47	30.82	33.74	31.80	30.57	33.47	32.23	31.54	32.79	32.53	33.31	34.15	33.37	31.52	33.14	32.22	33.90	33.77	32.33
As	45.31	44.44	45.06	41.87	40.11	43.94	42.21	41.26	41.09	41.02	45.18	45.05	44.66	41.35	42.51	41.13	43.67	43.86	41.62
Ag	0.00	0.00	0.02	0.00	0.00	0.01	0.05	0.04	0.00	0.00	0.00	0.00	0.01	0.03	0.00	0.01	0.00	0.01	0.00
Bi	0.00	0.00	0.00	0.00	0.00	0.00	0.00	0.00	0.00	0.00	0.00	0.00	0.00	0.00	0.00	0.00	0.00	0.00	0.00
Sb	0.00	0.00	0.01	0.00	0.02	0.03	0.01	0.00	0.01	0.02	0.00	0.00	0.00	0.00	0.00	0.01	0.02	0.00	0.00
Mn	0.00	0.00	0.00	0.01	0.00	0.03	0.02	0.00	0.01	0.01	0.03	0.00	0.01	0.01	0.03	0.06	0.01	0.01	0.05
Cu	0.00	0.00	0.02	0.02	0.00	0.00	0.00	0.01	0.02	0.00	0.00	0.01	0.01	0.02	0.00	0.01	0.03	0.01	0.05
Total	100.30	99.09	100.55	100.04	99.53	100.05	100.47	99.93	100.60	100.39	100.52	101.38	100.38	99.97	99.97	100.39	100.23	100.01	100.13

Abbreviations: mas = massive, sp = sphalerite, chl = chlorite, qz = quartz, sst = sandstone, co = carbonate, eu = euhedral

Appendix A4.12: Electron microprobe analysis of arsenopyrite

Sample No.	762059	762059	762059	762059	762059	762059	760426	760426	760426	760426	760426	760426	760426	760426	760222	760222	760222	760222	760222	760222
North	18307.8	18307.8	18307.8	18307.8	18307.8	18307.8	18246.3	18246.3	18246.3	18246.3	18246.3	18246.3	18246.3	18246.3	17806.8	17806.8	17806.8	17806.8	17806.8	17806.8
East	4898.6	4898.6	4898.6	4898.6	4898.6	4898.6	4806.3	4806.3	4806.3	4806.3	4806.3	4806.3	4806.3	4806.3	4919.4	4919.4	4919.4	4919.4	4919.4	4919.4
R.L	9989.5	9989.5	9989.5	9989.5	9989.5	9989.5	10094.7	10094.7	10094.7	10094.7	10094.7	10094.7	10094.7	10094.7	10041.4	10041.4	10041.4	10041.4	10041.4	10041.4
drill hole	GG099	GG099	GG099	GG099	GG099	GG099	GG165	GG165	GG165	GG165	GG165	GG165	GG165	GG165	GG132	GG132	GG132	GG132	GG132	GG132
metre	119.0	119.0	119.0	119.0	119.0	119.0	302.0	302.0	302.0	302.0	302.0	302.0	302.0	30.2	368.9	368.9	368.9	368.9	368.9	368.9
zone	B	B	B	B	B	B	C	C	C	C	C	C	C	C	A	A	A	A	A	A
host rock	mas sp	mas sp	mas sp	mas sp	mas sp	mas sp	mas sp-py	mas sp-py	mas sp-py	mas sp-py	mas sp-py	mas sp-py	mas sp-py	mas sp-py	mas sp-py	mas sp-py	mas sp-py	mas sp-py	mas sp-py	mas sp-py
asp host texture	sp eu	sp-qz eu	sp-qz eu	sp-qz eu	sp-qz eu	sp-qz eu	cp eu	cp eu	cp eu	py-cp eu	py-cp eu	py-cp eu	tet eu	tet eu	sp-qz eu	sp-qz eu	sp-qz eu	sp-qz eu	sp-qz eu	sp-qz eu
S	19.77	20.39	20.04	20.29	19.49	20.13	20.86	20.34	20.06	20.37	30.39	20.14	18.66	18.79	21.98	21.51	21.56	21.37	21.18	21.38
Fe	35.64	35.82	35.45	35.51	35.37	35.63	35.90	35.65	35.62	35.74	38.67	35.56	34.42	34.75	34.90	34.99	34.78	34.82	34.97	34.96
Co															0.13	0.04	0.00	0.04	0.07	0.00
Cu	0.04	0.03	0.03	0.05	0.02	0.05	0.09	0.10	0.32	0.12	0.08	0.16	2.11	0.52	0.02	0.04	0.04	0.01	0.00	0.00
Zn															0.01	0.05	0.00	0.00	0.01	0.02
As	45.49	45.09	45.59	45.33	46.02	45.49	44.26	45.17	45.62	44.92	34.06	45.63	47.52	47.31	42.35	42.77	43.10	43.16	43.07	42.90
Se	0.17	0.15	0.15	0.17	0.12	0.15	0.16	0.15	0.14	0.15	0.10	0.14	0.18	0.16	0.07	0.03	0.09	0.03	0.10	0.02
Ag	0.00	0.02	0.00	0.00	0.00	0.02	0.00	0.00	0.00	0.00	0.00	0.00	0.05	0.05	0.03	0.00	0.05	0.00	0.00	0.00
Cd															0.00	0.00	0.04	0.00	0.04	0.03
Sb															0.04	0.02	0.00	0.00	0.00	0.00
Au	0.00	0.00	0.01	0.00	0.00	0.00	0.02	0.00	0.00	0.00	0.00	0.00	0.12	0.06	0.12	0.00	0.01	0.11	0.00	0.14
Bi															0.00	0.00	0.00	0.00	0.00	0.00
Total	101.11	101.49	101.27	101.35	101.01	101.47	101.28	101.41	101.76	101.30	103.29	101.62	103.06	101.64	99.67	99.46	99.68	99.55	99.44	99.45

Abbreviations: mas = massive, sp = sphalerite, cp = chalcopyrite, eu = euhedral, py = pyrite, tet = tetrahedrite, qz = quartz

Note: blank cells indicate element not analysed

Appendix A4.12: Electron microprobe analysis of arsenopyrite *(continued)*

Sample No.	760222	762059	762059	762059	762059	762059	762059	762059	762059	762059	762059
North	17806.8	18307.8	18307.8	18307.8	18307.8	18307.8	18307.8	18307.8	18307.8	18307.8	18307.8
East	4919.4	4898.6	4898.6	4898.6	4898.6	4898.6	4898.6	4898.6	4898.6	4898.6	4898.6
R.L	10041.4	9989.5	9989.5	9989.5	9989.5	9989.5	9989.5	9989.5	9989.5	9989.5	9989.5
drill hole	GG132	GG099	GG099	GG099	GG099	GG099	GG099	GG099	GG099	GG099	GG099
metre	368.9	119.0	119.0	119.0	119.0	119.0	119.0	119.0	119.0	119.0	119.0
zone	A	B	B	B	B	B	B	B	B	B	B
host rock	mas sp-py	mas sp-py	mas sp-py	mas sp-py	mas sp-py	mas sp-py	mas sp-py	mas sp-py	mas sp-py	mas sp-py	mas sp-py
asp host texture	sp-qz eu	sp-qz eu	sp-qz eu	sp-qz eu	sp-qz eu	sp-qz eu	sp-qz eu	sp-qz eu	sp-qz eu	sp-qz eu	sp-qz eu
S	21.68	21.74	22.14	21.25	21.38	21.93	21.75	21.02	21.81	21.53	22.05
Fe	34.49	34.82	34.28	35.03	34.79	35.38	34.66	34.26	34.29	34.04	34.26
Co	0.13	0.01	0.57	0.00	0.00	0.04	0.00	0.08	0.15	0.34	0.30
Cu	0.00	0.03	0.05	0.00	0.01	0.00	0.01	0.03	0.00	0.04	0.01
Zn	0.00	0.05	0.00	0.00	0.00	0.02	0.00	0.08	0.78	0.05	0.37
As	42.38	41.95	41.27	42.70	42.72	41.79	42.13	43.11	42.40	42.32	41.74
Se	0.10	0.02	0.14	0.07	0.00	0.10	0.03	0.02	0.08	0.12	0.07
Ag	0.00	0.00	0.00	0.00	0.00	0.00	0.00	0.00	0.00	0.14	0.09
Cd	0.00	0.05	0.00	0.00	0.00	0.00	0.00	0.02	0.00	0.00	0.00
Sb	0.00	0.00	0.02	0.03	0.00	0.00	0.00	0.05	0.00	0.00	0.00
Au	0.17	0.18	0.00	0.00	0.00	0.09	0.07	0.00	0.08	0.00	0.07
Bi	0.00	0.00	0.00	0.00	0.00	0.00	0.00	0.00	0.00	0.00	0.00
Total	98.95	98.86	98.47	99.09	98.90	99.35	98.66	98.68	99.62	98.57	98.97

Abbreviations: mas = massive, sp = sphalerite, cp = chalcopyrite, eu = euhedral, py = pyrite, tet = tetrahedrite, qz = quartz

Note: blank cells indicate element not analysed

Appendix A5.1: Electron microprobe analysis of chlorite

Sample	Description	Strata	Associated minerals	Character	Analysis	WO_3	SiO_2	TiO_2	SnO_2	Al_2O_3	MgO	CaO	MnO	FeO*	CuO	ZnO	Na_2O	K_2O	H_2O	F	Cl	Total	Mg#
760357	intense chlorite alteration of sandstone	GGF M4	chl, qz, mgt	intlck gmas	1	0.00	22.00	0.02	0.02	21.16	6.92	0.00	0.10	37.61	0.00	0.00	0.02	0.01	10.56	0.00	0.03	98.45	0.25
760357	intense chlorite alteration of sandstone	GGF M4	chl, qz, mgt	intlck gmas	2	0.00	22.26	0.06	0.00	21.59	7.08	0.00	0.08	37.58	0.00	0.00	0.03	0.03	10.69	0.00	0.04	99.45	0.25
760357	intense chlorite alteration of sandstone	GGF M4	chl, qz, mgt	intlck gmas	3	0.00	22.25	0.09	0.00	21.02	7.24	0.00	0.04	37.57	0.01	0.07	0.00	0.00	10.63	0.00	0.02	98.93	0.26
760384	massive sp, chl	GGF M6	chl, sp	fibrous	1	0.11	22.91	0.03	0.38	23.64	8.45	0.01	0.30	33.26	0.00	0.81	0.00	0.00	11.03	0.11	0.00	101.04	0.31
760384	massive sp, chl	GGF M6	chl, sp	fibrous	2	0.00	22.87	0.01	0.21	23.21	8.54	0.00	0.27	34.44	0.29	0.71	0.03	0.00	11.07	0.04	0.01	101.70	0.31
760384	massive sp, chl	GGF M6	chl, sp	fibrous	3	0.00	22.41	0.06	0.21	23.32	8.12	0.02	0.23	35.27	0.00	0.24	0.02	0.00	10.99	0.00	0.00	100.89	0.29
760384	massive sp, chl	GGF M6	chl, sp	fibrous	1	0.09	21.80	0.02	0.31	24.36	7.48	0.03	0.22	35.61	0.24	0.97	0.01	0.01	11.06	0.00	0.00	102.21	0.27
760384	massive sp, chl	GGF M6	chl, sp	fibrous	2	0.00	22.29	0.05	0.14	23.69	8.15	0.00	0.19	35.04	0.00	0.42	0.00	0.01	10.98	0.07	0.01	101.04	0.29
760384	massive sp, chl	GGF M6	chl, sp	fibrous	3	0.00	22.50	0.05	0.21	23.21	7.06	0.00	0.22	36.35	0.00	0.29	0.01	0.00	10.91	0.05	0.01	100.87	0.26
760384	massive sp, chl	GGF M6	chl, sp	fibrous	1/2rim	0.00	22.73	0.02	0.10	23.43	8.48	0.00	0.31	34.17	0.00	0.40	0.01	0.00	11.02	0.03	0.00	100.70	0.31
760384	massive sp, chl	GGF M6	chl, sp	fibrous	2/2core	0.17	22.45	0.08	0.00	23.37	6.87	0.01	0.28	36.61	0.00	0.46	0.01	0.00	10.91	0.10	0.00	101.32	0.25
760384	massive sp, chl	GGF M6	sp	fibrous	3	0.00	22.89	0.01	0.00	23.41	8.68	0.00	0.05	33.60	0.00	0.97	0.01	0.00	11.04	0.02	0.00	100.68	0.32
760384	massive sp, chl	GGF M6	chl, sp	fibrous	1	0.00	22.01	0.04	0.00	24.13	7.79	0.01	0.17	34.42	0.29	0.23	0.00	0.00	10.94	0.00	0.00	100.03	0.29
760384	massive sp, chl	GGF M6	chl, sp	fibrous	2	0.00	22.24	0.04	0.03	22.68	5.85	0.00	0.37	37.45	0.00	0.41	0.01	0.01	10.74	0.00	0.00	99.83	0.22
760384	massive sp, chl	GGF M6	chl, sp	fibrous	3	0.00	21.67	0.00	0.00	24.27	7.51	0.02	0.22	34.20	0.10	0.63	0.01	0.00	10.86	0.00	0.01	99.50	0.28
760411	co nodular alteration	GGF M5	co	fibrous	1	0.00	26.99	0.05	0.20	22.19	22.78	0.04	0.04	16.79	0.00	0.12	0.01	0.01	12.08	0.10	0.01	101.40	0.71
760411	co nodular alteration	GGF M5	co	fibrous	2	0.00	31.68	0.04	0.00	20.58	21.21	0.07	0.06	15.66	0.04	0.07	0.01	0.00	12.32	0.16	0.01	101.91	0.71
760411	co nodular alteration	GGF M5	co	fibrous	3	0.00	26.74	0.02	0.00	22.86	22.80	0.01	0.05	16.20	0.00	0.01	0.01	0.00	12.08	0.09	0.00	100.86	0.72
760432	stringer vein: mgt, co, po, cp, chl	GGF M6	chl, sp	fibrous	1	0.00	23.16	0.03	0.02	21.78	10.63	0.00	0.48	31.81	0.00	0.30	0.01	0.00	10.94	0.05	0.00	99.21	0.37
760432	stringer vein: mgt, co, po, cp, chl	GGF M6	chl, sp	fibrous	2	0.00	22.27	0.02	0.02	23.95	11.47	0.04	0.51	28.88	0.01	0.09	0.01	0.00	11.01	0.04	0.01	98.31	0.41
760432	stringer vein: mgt, co, po, cp, chl	GGF M6	chl, sp	fibrous	1	0.00	22.63	0.05	0.01	23.47	11.90	0.00	0.52	29.07	0.00	0.00	0.02	0.00	11.08	0.00	0.01	98.77	0.42
760432	stringer vein: mgt, co, po, cp, chl	GGF M6	chl, sp	fibrous	2	0.00	22.45	0.01	0.01	23.77	11.67	0.00	0.35	30.11	0.00	0.00	0.00	0.00	11.09	0.06	0.00	99.52	0.41
760432	stringer vein: mgt, co, po, cp, chl	GGF M6	chl, sp	fibrous	1	0.00	22.17	0.01	0.00	23.48	11.06	0.03	0.47	30.51	0.00	0.03	0.01	0.03	10.98	0.02	0.00	98.80	0.39
760432	stringer vein: mgt, co, po, cp, chl	GGF M6	chl, sp	fibrous	1	0.00	22.26	0.05	0.00	23.41	11.08	0.00	0.55	30.41	0.00	0.13	0.00	0.00	10.93	0.14	0.06	99.00	0.39
760432	stringer vein: mgt, co, po, cp, chl	GGF M6	chl, sp	fibrous	2	0.00	22.72	0.07	0.00	23.51	11.83	0.04	0.61	29.08	0.01	0.05	0.02	0.00	11.06	0.10	0.00	99.08	0.42
760432	stringer vein: mgt, co, po, cp, chl	GGF M6	chl, sp	fibrous	1	0.00	22.13	0.00	0.04	24.06	11.42	0.03	0.51	29.10	0.00	0.08	0.01	0.02	10.99	0.09	0.00	98.47	0.41
760432	stringer vein: mgt, co, po, cp, chl	GGF M6	chl, sp	fibrous	2	0.00	22.97	0.07	0.07	23.11	11.48	0.01	0.46	29.10	0.07	0.06	0.04	0.01	11.04	0.00	0.03	98.52	0.41
760466	intense chl, ad alteration	GGF M4	chl	fibrous	1	0.07	22.49	0.04	0.10	23.47	5.63	0.03	0.15	37.83	0.00	0.07	0.01	0.00	10.87	0.00	0.02	100.78	0.21
760466	intense chl, ad alteration	GGF M4	chl	fibrous	2	0.00	24.94	0.02	0.00	19.29	5.64	0.07	0.21	38.78	0.00	0.00	0.03	0.07	10.69	0.04	0.05	99.83	0.21

Abbreviations: ad = andalusite, ap = apatite, asp = arsenopyrite, cd = chloritoid, chl = chlorite, co = carbonate, cp = chalcopyrite, ilm = ilmenite, mgt = magnetite, po = pyrrhotite, qz = quartz, ru = rutile, sp = sphalerite
py = pyrite, gmass = groundmass, intlck = interlocking, wfmd = well formed, f.g. = fine grained, c.g. = goarse grained, rep = replacing, itg = intergrown
* all iron as Fe^{2+}, Mg# = Mg/(Mg+Fe)

Appendix A5.1: Electron microprobe analysis of chlorite *(continued)*

Sample	Description	Strata	Associated minerals	Character	Analysis	WO_3	SiO_2	TiO_2	SnO_2	Al_2O_3	MgO	CaO	MnO	FeO*	CuO	ZnO	Na_2O	K_2O	H_2O	F	Cl	Total	Mg#
760473	intense chl, cd alteration	GGF M4	chl, cd, sp	intlck gmas	1	0.00	21.65	0.07	0.00	22.60	5.23	0.00	0.27	38.58	0.00	0.12	0.02	0.03	10.60	0.00	0.00	99.17	0.19
760473	intense chl, cd alteration	GGF M4	chl, cd	intlck gmas	2	0.00	22.31	0.00	0.05	22.66	8.32	0.00	0.19	33.44	0.00	0.52	0.01	0.00	10.76	0.00	0.01	98.25	0.31
760473	intense chl, cd alteration	GGF M4	chl, cd	intlck gmas	1	0.00	22.21	0.08	0.02	22.73	7.81	0.01	0.15	35.07	0.01	0.20	0.04	0.00	10.78	0.04	0.01	99.17	0.28
760473	intense chl, cd alteration	GGF M4	chl, cd	wfmd lath	2	0.00	21.99	0.00	0.02	21.24	3.31	0.03	0.24	41.40	0.16	0.14	0.00	0.00	10.39	0.04	0.02	98.97	0.12
760473	intense chl, cd alteration	GGF M4	chl, cd	intlck gmas	1	0.00	21.57	0.10	0.00	22.75	5.30	0.02	0.13	38.53	0.00	0.21	0.01	0.01	10.61	0.00	0.00	99.23	0.20
762040	intense chl, ad alteration	GGF M4	chl, cd, ad, po	intlck gmas	1	0.00	22.55	0.06	0.00	22.73	7.58	0.00	0.27	35.32	0.00	0.06	0.01	0.00	10.80	0.07	0.00	99.45	0.28
762040	intense chl, ad alteration	GGF M4	cd, chl	f.g. gmas	1	0.00	21.44	0.06	0.01	23.00	6.98	0.01	0.29	36.42	0.00	0.04	0.04	0.02	10.69	0.00	0.02	99.01	0.25
762040	intense chl, ad alteration	GGF M4	cd, chl	f.g. gmas	2	0.00	22.32	0.03	0.03	22.64	8.37	0.01	0.24	34.45	0.00	0.02	0.00	0.00	10.81	0.00	0.01	98.91	0.30
762040	intense chl, ad alteration	GGF M4	cd, chl, py	c.g. gmas	1	0.00	21.94	0.01	0.02	22.98	7.78	0.01	0.26	35.67	0.05	0.09	0.00	0.00	10.80	0.03	0.01	99.65	0.28
762040	intense chl, ad alteration	GGF M4	py, po, chl	intlck gmas	1	0.00	18.16	0.00	0.10	28.75	2.30	0.02	0.28	39.56	0.04	0.08	0.00	0.00	10.63	0.00	0.01	99.92	0.09
762040	intense chl, ad alteration	GGF M4	py, po, chl	intlck gmas	1	0.00	22.53	0.08	0.00	23.11	7.78	0.02	0.32	34.71	0.02	0.01	0.02	0.02	10.87	0.01	0.00	99.48	0.29
762040	intense chl, ad alteration	GGF M4	chl, cd, ad, po	wfmd lath	3	0.00	24.41	0.04	0.04	19.65	5.29	0.01	0.22	40.17	0.00	0.00	0.00	0.09	10.73	0.00	0.04	100.69	0.19
762057	stringer vein: co-chl	GGF M5	co	fibrous	1	0.00	23.25	0.05	0.00	23.53	12.75	0.00	0.07	28.34	0.02	0.05	0.01	0.01	11.19	0.06	0.01	99.36	0.45
762057	stringer vein: co-chl	GGF M5	co	fibrous	2	0.00	23.30	0.07	0.20	23.25	13.08	0.00	0.02	28.61	0.00	0.00	0.03	0.03	11.25	0.02	0.02	99.87	0.45
762057	stringer vein: co-chl	GGF M5	co	fibrous	3	0.00	23.27	0.05	0.00	23.75	12.99	0.00	0.06	29.01	0.00	0.00	0.00	0.00	11.30	0.05	0.02	100.50	0.44
762057	stringer vein: co-chl	GGF M5	co	fibrous	4	0.00	24.18	0.04	0.00	23.24	13.20	0.01	0.11	27.95	0.00	0.04	0.06	0.03	11.33	0.08	0.01	100.28	0.46
762057	stringer vein: co-chl	GGF M5	co	fibrous	1	0.00	23.59	0.07	0.03	23.33	13.37	0.01	0.11	27.81	0.12	0.09	0.02	0.00	11.31	0.00	0.02	99.88	0.46
762057	stringer vein: co-chl	GGF M5	co	fibrous	2	0.00	23.79	0.05	0.13	23.41	13.69	0.00	0.10	26.89	0.01	0.01	0.03	0.00	11.28	0.09	0.03	99.50	0.48
762057	stringer vein: co-chl	GGF M5	co	fibrous	3	0.00	23.62	0.04	0.03	23.96	13.54	0.01	0.03	27.92	0.13	0.00	0.01	0.02	11.42	0.01	0.00	100.72	0.46
762057	stringer vein: co-chl	GGF M5	co	fibrous	4	0.00	24.31	0.05	0.00	23.74	13.34	0.03	0.08	26.35	0.00	0.04	0.10	0.04	11.34	0.06	0.05	99.52	0.47
762057	stringer vein: co-chl	GGF M5	co	fibrous	1	0.00	22.84	0.02	0.00	24.82	12.45	0.01	0.18	27.99	0.29	0.12	0.02	0.00	11.31	0.00	0.01	100.07	0.44
762057	stringer vein: co-chl	GGF M5	co	fibrous	2	0.00	23.14	0.00	0.00	23.32	11.90	0.01	0.06	28.70	0.29	0.06	0.00	0.01	11.10	0.00	0.02	98.62	0.43
762057	stringer vein: co-chl	GGF M5	co	fibrous	1/2core	0.00	22.91	0.04	0.07	24.10	12.93	0.03	0.14	28.09	0.15	0.00	0.01	0.00	11.26	0.04	0.00	99.76	0.45
762057	stringer vein: co-chl	GGF M5	co	fibrous	2/2rim	0.00	23.14	0.00	0.00	24.70	13.22	0.03	0.13	26.77	0.16	0.06	0.00	0.01	11.31	0.05	0.02	99.61	0.47
769091	strongly chl altered qz sandstone	GGF M4	chl, mgt, ilm	f.g. gmas	1	0.00	23.83	0.04	0.03	20.60	12.71	0.02	0.01	30.20	0.03	0.03	0.00	0.01	10.89	0.23	0.01	98.65	0.43
769091	strongly chl altered qz sandstone	GGF M4	chl, mgt, ilm	f.g. gmas	2	0.00	23.80	0.05	0.02	20.80	12.20	0.00	0.00	30.74	0.10	0.00	0.01	0.00	10.97	0.07	0.00	98.75	0.41
769091	strongly chl altered qz sandstone	GGF M4	chl, mgt, ilm	c.g. lath	1	0.00	24.67	0.12	0.00	19.86	13.68	0.02	0.08	29.78	0.00	0.06	0.04	0.01	11.06	0.17	0.00	99.54	0.45
769091	strongly chl altered qz sandstone	GGF M4	chl, mgt, ilm	f.g. gmas	2	0.00	23.89	0.02	0.00	21.13	12.62	0.02	0.00	30.13	0.06	0.00	0.01	0.02	11.07	0.00	0.00	98.97	0.43
769091	strongly chl altered qz sandstone	GGF M4	chl, mgt, ilm	f.g. gmas	1	0.00	23.92	0.07	0.00	20.91	12.31	0.00	0.11	30.33	0.05	0.01	0.01	0.01	10.92	0.22	0.02	98.88	0.42

Abbreviations: ad = andalusite, ap = apatite, asp = arsenopyrite, cd = chloritoid, chl = chlorite, co = carbonate, cp = chalcopyrite, ilm = ilmenite, mgt = magnetite, po = pyrrhotite, qz = quartz, ru = rutile, sp = sphalerite
py = pyrite, gmass = groundmass, intlck = interlocking, wfmd = well formed, f.g. = fine grained, c.g. = goarse grained, rep = replacing, itg = intergrown
* all iron as Fe^{2+}, Mg# = Mg/(Mg+Fe)

Appendix A5.1: Electron microprobe analysis of chlorite *(continued)*

Sample	Description	Strata	Associated minerals	Character	Analysis	WO_3	SiO_2	TiO_2	SnO_2	Al_2O_3	MgO	CaO	MnO	FeO*	CuO	ZnO	Na_2O	K_2O	H_2O	F	Cl	Total	Mg#
769091	strongly chl altered qz sandstone	GGF M4	chl, mgt, ilm	f.g. gmas	2	0.00	23.90	0.09	0.03	20.87	12.60	0.00	0.09	29.93	0.01	0.00	0.02	0.02	11.01	0.05	0.00	98.60	0.43
769091	strongly chl altered qz sandstone	GGF M4	chl, mgt, ilm	c.g. fibrous	1	0.00	24.63	0.04	0.01	20.49	12.23	0.04	0.07	29.70	0.03	0.00	0.00	0.02	10.87	0.34	0.00	98.47	0.42
769091	strongly chl altered qz sandstone	GGF M4	chl, mgt, ilm	f.g. gmas	2	0.00	24.00	0.11	0.05	20.74	12.58	0.04	0.00	30.19	0.00	0.00	0.04	0.03	10.92	0.26	0.01	98.97	0.43
769091	strongly chl altered qz sandstone	GGF M4	chl, mgt, ilm	f.g. gmas	1	0.00	23.91	0.01	0.00	20.64	12.70	0.00	0.08	30.21	0.00	0.00	0.00	0.00	10.97	0.08	0.01	98.61	0.43
769091	strongly chl altered qz sandstone	GGF M4	chl, mgt, ilm	f.g. gmas	2	0.00	24.00	0.08	0.00	20.77	12.73	0.02	0.16	29.81	0.00	0.00	0.03	0.01	10.99	0.11	0.01	98.72	0.43
769091	strongly chl altered qz sandstone	GGF M4	chl, mgt, ilm	f.g. gmas	1	0.00	23.98	0.07	0.00	20.62	12.42	0.01	0.11	30.91	0.00	0.04	0.03	0.02	11.05	0.01	0.00	99.26	0.42
769121	intensely chl altered qz sandstone	GGF M4	chl, mgt, ilm	gmas	1	0.00	23.57	0.06	0.00	20.94	10.96	0.04	0.04	32.68	0.00	0.00	0.01	0.01	10.97	0.00	0.00	99.28	0.37
769121	intensely chl altered qz sandstone	GGF M4	chl, po, asp	c.g. fibrous	2	0.00	23.71	0.07	0.00	20.93	11.82	0.01	0.07	30.44	0.00	0.08	0.00	0.01	10.93	0.00	0.03	98.10	0.41
769121	intensely chl altered qz sandstone	GGF M4	chl, mgt, ilm	f.g. gmas	1	0.00	23.32	0.09	0.00	20.45	11.31	0.02	0.06	32.73	0.00	0.09	0.00	0.00	10.90	0.00	0.02	99.00	0.38
769121	intensely chl altered qz sandstone	GGF M4	chl, mgt, ilm	f.g. gmas	1	0.00	23.59	0.00	0.04	19.86	11.02	0.00	0.09	32.81	0.00	0.03	0.01	0.00	10.73	0.18	0.01	98.37	0.37
769121	intensely chl altered qz sandstone	GGF M4	chl, mgt, ilm	c.g. gmas	2	0.00	23.97	0.04	0.05	20.78	12.08	0.05	0.20	31.44	0.00	0.02	0.01	0.00	11.01	0.11	0.06	99.81	0.41
769121	intensely chl altered qz sandstone	GGF M4	chl, mgt, ilm	gmas	1	0.00	23.82	0.07	0.00	20.44	11.31	0.00	0.03	32.31	0.00	0.00	0.02	0.01	10.93	0.03	0.00	98.97	0.38
769121	intensely chl altered qz sandstone	GGF M4	chl, mgt, ilm	gmas	1	0.00	23.12	0.03	0.04	21.34	11.40	0.01	0.03	31.72	0.00	0.11	0.00	0.00	10.90	0.07	0.02	98.78	0.39
769121	intensely chl altered qz sandstone	GGF M4	chl, mgt, ilm	gmas	1	0.00	22.09	0.11	0.01	21.16	7.25	0.00	0.01	37.69	0.00	0.03	0.03	0.02	10.63	0.00	0.02	99.05	0.26
769121	intensely chl altered qz sandstone	GGF M4	chl, mgt, ilm	gmas	1	0.00	25.44	0.02	0.03	18.33	14.00	0.04	0.07	29.69	0.01	0.00	0.03	0.01	11.06	0.00	0.03	98.77	0.46
769146	pumiceous breccia	GGF M1	chl, qz, ru	intlck gmas	1	0.00	24.25	0.01	0.00	22.77	13.32	0.02	0.08	27.67	0.01	0.02	0.02	0.00	11.26	0.08	0.03	99.54	0.46
769146	pumiceous breccia	GGF M1	chl, qz, ru	intlck gmas	2	0.00	24.15	0.05	0.00	23.19	13.05	0.01	0.03	27.88	0.00	0.11	0.06	0.05	11.33	0.00	0.03	99.93	0.45
769146	pumiceous breccia	GGF M1	chl, qz, ru	intlck gmas	1	0.00	23.82	0.06	0.00	23.07	12.87	0.06	0.10	27.01	0.00	0.06	0.03	0.02	11.11	0.14	0.00	98.36	0.46
769146	pumiceous breccia	GGF M1	chl, qz, ru	intlck gmas	2	0.00	23.97	0.07	0.00	22.84	12.99	0.07	0.08	27.81	0.01	0.00	0.04	0.02	11.16	0.16	0.05	99.27	0.45
769146	pumiceous breccia	GGF M1	chl, qz, ru	intlck gmas	1	0.00	24.02	0.00	0.06	23.23	13.20	0.02	0.10	28.00	0.00	0.04	0.02	0.03	11.31	0.07	0.02	100.12	0.46
769146	pumiceous breccia	GGF M1	chl, qz, ru	intlck gmas	2	0.00	24.02	0.08	0.00	23.49	13.08	0.00	0.09	28.05	0.00	0.00	0.00	0.03	11.36	0.01	0.04	100.24	0.45
769146	pumiceous breccia	GGF M1	chl, qz, ru	rep pumice	1	0.00	23.67	0.00	0.10	23.37	13.11	0.00	0.13	27.85	0.00	0.06	0.00	0.00	11.27	0.04	0.00	99.60	0.46
769146	pumiceous breccia	GGF M1	chl, qz, ru	rep pumice	1	0.00	24.14	0.00	0.00	23.32	13.23	0.01	0.09	28.02	0.04	0.11	0.06	0.03	11.33	0.11	0.01	100.50	0.46
769146	pumiceous breccia	GGF M1	chl, qz, ru	c.g. gmas	2	0.00	24.03	0.01	0.00	23.20	13.00	0.03	0.08	28.21	0.09	0.00	0.02	0.03	11.31	0.03	0.02	100.08	0.45
769174	chl, co altererd qz sandstone	GGF M4	chl, qz	f.g. itg qz	1	0.00	24.86	0.00	0.01	20.60	16.86	0.06	0.13	24.32	0.00	0.13	0.10	0.10	11.21	0.16	0.10	98.64	0.55
769174	chl, co altererd qz sandstone	GGF M4	chl, qz	f.g. itg qz	2	0.00	25.11	0.06	0.00	20.14	17.21	0.00	0.00	24.39	0.01	0.01	0.05	0.05	11.15	0.31	0.07	98.55	0.56
769174	chl, co altererd qz sandstone	GGF M4	chl, qz	f.g. itg qz	2	0.00	25.17	0.06	0.02	19.31	15.25	0.01	0.00	27.22	0.04	0.00	0.01	0.02	11.03	0.22	0.05	98.42	0.50
769174	chl, co altererd qz sandstone	GGF M4	chl, qz	f.g. itg qz	1	0.00	25.12	0.08	0.00	19.48	15.97	0.02	0.05	25.63	0.00	0.02	0.06	0.05	11.01	0.30	0.01	97.78	0.53
769174	chl, co altererd qz sandstone	GGF M4	chl, qz	f.g. itg qz	2	0.00	25.92	0.03	0.02	19.23	17.14	0.03	0.00	24.88	0.01	0.03	0.04	0.01	11.21	0.26	0.05	98.85	0.55

Abbreviations: ad = andalusite, ap = apatite, asp = arsenopyrite, cd = chloritoid, chl = chlorite, co = carbonate, cp = chalcopyrite, ilm = ilmenite, mgt = magnetite, po = pyrrhotite, qz = quartz, ru = rutile, sp = sphalerite
py = pyrite, gmass = groundmass, intlck = interlocking, wfmd = well formed, f.g. = fine grained, c.g. = goarse grained, rep = replacing, itg = intergrown
* all iron as Fe^{2+}, Mg# = Mg/(Mg+Fe)

Appendix A5.1: Electron microprobe analysis of chlorite *(continued)*

Sample	Description	Strata	Associated minerals	Character	Analysis	WO_3	SiO_2	TiO_2	SnO_2	Al_2O_3	MgO	CaO	MnO	FeO*	CuO	ZnO	Na_2O	K_2O	H_2O	F	Cl	Total	Mg#
769174	chl, co altererd qz sandstone	GGF M4	chl, qz	f.g. itg qz	1	0.00	25.13	0.06	0.00	19.33	15.61	0.01	0.06	26.94	0.03	0.00	0.02	0.01	11.10	0.13	0.06	98.47	0.51
769174	chl, co altererd qz sandstone	GGF M4	chl, qz	f.g. itg qz	1	0.00	25.27	0.05	0.00	19.35	15.74	0.03	0.10	27.21	0.01	0.01	0.00	0.02	11.12	0.23	0.02	99.15	0.51
769175	intensely chl altered qz sandstone	GGF M4	chl, mgt, ilm	f.g. gmas	1	0.00	26.65	0.10	0.00	18.49	18.17	0.00	0.11	23.55	0.00	0.02	0.01	0.00	11.22	0.36	0.00	98.68	0.58
769175	intensely chl altered qz sandstone	GGF M4	chl, mgt, ilm	f.g. gmas	2	0.00	26.23	0.03	0.02	18.05	18.93	0.02	0.11	22.98	0.08	0.00	0.00	0.02	11.12	0.40	0.03	98.02	0.59
769175	intensely chl altered qz sandstone	GGF M4	chl, mgt, ilm	f.g. gmas	1	0.00	26.42	0.05	0.00	18.63	19.50	0.00	0.00	22.34	0.03	0.02	0.00	0.02	11.24	0.43	0.03	98.72	0.61
769175	intensely chl altered qz sandstone	GGF M4	chl, mgt, ilm	f.g. gmas	2	0.00	26.39	0.11	0.03	18.70	17.85	0.00	0.09	24.30	0.04	0.05	0.00	0.00	11.26	0.29	0.00	99.11	0.57
769175	intensely chl altered qz sandstone	GGF M4	chl, mgt, ilm	f.g. gmas	1	0.00	26.33	0.08	0.04	18.49	18.82	0.01	0.12	22.69	0.05	0.00	0.01	0.02	11.19	0.35	0.03	98.21	0.60
769175	intensely chl altered qz sandstone	GGF M4	chl, mgt, ilm	c.g. fibrous	2	0.00	26.60	0.01	0.01	19.05	21.08	0.01	0.18	20.05	0.00	0.01	0.01	0.02	11.52	0.16	0.00	98.70	0.65
769175	intensely chl altered qz sandstone	GGF M4	chl, mgt, ilm	c.g. fibrous	3	0.00	28.58	0.04	0.00	17.57	20.89	0.02	0.00	19.60	0.00	0.03	0.02	0.00	11.46	0.36	0.03	98.60	0.66
769175	intensely chl altered qz sandstone	GGF M4	chl, mgt, ilm	f.g. gmas	1	0.00	26.22	0.03	0.02	18.93	18.49	0.01	0.05	22.68	0.01	0.06	0.02	0.00	11.21	0.31	0.00	98.04	0.59
769175	intensely chl altered qz sandstone	GGF M4	chl, mgt, ilm	f.g. gmas	2	0.00	26.66	0.01	0.00	19.49	20.38	0.00	0.05	20.07	0.00	0.08	0.00	0.02	11.39	0.36	0.04	98.55	0.64
769175	intensely chl altered qz sandstone	GGF M4	chl, mgt, ilm	f.g. gmas	1	0.00	26.64	0.03	0.00	18.28	18.14	0.00	0.04	23.86	0.01	0.00	0.02	0.04	11.18	0.38	0.01	98.64	0.58
769228	intense ap, ad, cd, chl alteration	GGF M4	ap, chl	wfmd gmas	1	0.00	23.12	0.03	0.00	19.42	4.79	0.04	0.15	40.88	0.40	0.00	0.00	0.00	10.49	0.00	0.00	99.32	0.17
769228	intense ap, ad, cd, chl alteration	GGF M4	ap, chl	f.g. gmas	2	0.00	22.26	0.01	0.00	21.84	6.87	0.06	0.21	37.47	0.01	0.00	0.00	0.02	10.67	0.04	0.04	99.48	0.25
769228	intense ap, ad, cd, chl alteration	GGF M4	ap, cd, chl	fibrous gmas	1	0.00	22.36	0.06	0.00	21.44	6.32	0.00	0.34	36.81	0.07	0.09	0.03	0.01	10.51	0.13	0.01	98.17	0.23
769228	intense ap, ad, cd, chl alteration	GGF M4	ap, cd, chl	fibrous gmas	2	0.00	22.49	0.00	0.00	21.65	5.09	0.01	0.18	39.20	0.00	0.00	0.03	0.00	10.59	0.03	0.02	99.28	0.19
769228	intense ap, ad, cd, chl alteration	GGF M4	ap, ad, chl,cd	fibrous gmas	1	0.00	21.78	2.40	0.02	19.32	3.99	0.00	0.07	40.95	0.00	0.04	0.03	0.01	10.42	0.00	0.01	99.03	0.15
769228	intense ap, ad, cd, chl alteration	GGF M4	ap, ad, chl,cd	fibrous gmas	2	0.00	22.39	0.04	0.02	21.20	5.83	0.02	0.19	38.18	0.09	0.01	0.01	0.03	10.55	0.00	0.05	98.59	0.21
769228	intense ap, ad, cd, chl alteration	GGF M4	ap, ad, chl,cd	fibrous gmas	1	0.00	22.12	0.06	0.00	21.42	5.50	0.03	0.22	38.59	0.04	0.12	0.01	0.00	10.54	0.00	0.01	98.65	0.20
769228	intense ap, ad, cd, chl alteration	GGF M4	ap, ad, chl,cd	c.g. fibrous	2	0.00	22.10	0.02	0.00	21.27	5.74	0.06	0.31	38.40	0.23	0.00	0.06	0.03	10.54	0.00	0.01	98.76	0.21
769228	intense ap, ad, cd, chl alteration	GGF M4	ap, ad, chl,cd	c.g. fibrous	3	0.00	22.70	0.05	0.00	21.76	7.31	0.00	0.35	36.46	0.04	0.00	0.02	0.01	10.74	0.05	0.04	99.51	0.26
769228	intense chl, ad alteration	GGF M4	cp	fibrous	2	0.00	20.56	0.07	0.03	23.30	5.69	0.00	0.35	37.20	0.18	0.02	0.00	0.00	10.41	0.13	0.06	98.00	0.21
769228	intense chl, ad alteration	GGF M4	cp	fibrous	3	0.00	22.89	0.03	0.01	18.72	4.84	0.01	0.15	40.73	0.31	0.00	0.01	0.02	10.33	0.00	0.01	98.06	0.17
769228	intense chl, ad alteration	GGF M4	chl, ad, ap, cd	fibrous	1	0.00	22.98	0.06	0.00	19.71	4.90	0.02	0.18	40.57	0.04	0.03	0.02	0.00	10.48	0.01	0.01	98.98	0.18
769238	intense chl and siliceous nodules	GGF M4	chl, qz, ru	gmas	2	0.00	25.37	0.06	0.00	18.48	13.81	0.02	0.06	29.66	0.00	0.00	0.01	0.01	10.97	0.16	0.02	98.62	0.45
769238	intense chl and siliceous nodules	GGF M4	chl, qz, ru	gmas	2	0.00	25.12	0.03	0.00	18.69	13.80	0.00	0.02	30.27	0.00	0.00	0.00	0.00	11.06	0.01	0.04	99.04	0.45
769238	intense chl and siliceous nodules	GGF M4	chl, qz, ru	gmas	1	0.00	25.57	0.06	0.06	19.02	13.42	0.00	0.00	30.74	0.02	0.04	0.00	0.01	11.15	0.07	0.03	100.18	0.44
769266	chl, ap alteration	GGF M4	chl, ap, qz	gmas	1	0.00	24.00	0.08	0.04	21.74	12.93	0.00	0.02	28.89	0.02	0.10	0.02	0.00	10.98	0.34	0.02	99.18	0.44
769266	chl, ap alteration	GGF M4	chl, ap, qz	gmas	2	0.00	24.47	0.09	0.03	20.60	13.41	0.01	0.13	28.18	0.08	0.08	0.01	0.02	11.07	0.01	0.02	98.20	0.46

Abbreviations: ad = andalusite, ap = apatite, asp = arsenopyrite, cd = chloritoid, chl = chlorite, co = carbonate, cp = chalcopyrite, ilm = ilmenite, mgt = magnetite, po = pyrrhotite, qz = quartz, ru = rutile, sp = sphalerite
py = pyrite, gmass = groundmass, intlck = interlocking, wfmd = well formed, f.g. = fine grained, c.g. = goarse grained, rep = replacing, itg = intergrown
* all iron as Fe^{2+}, Mg# = Mg/(Mg+Fe)

Appendix A5.1: Electron microprobe analysis of chlorite *(continued)*

Sample	Description	Strata	Associated minerals	Character	Analysis	WO_3	SiO_2	TiO_2	SnO_2	Al_2O_3	MgO	CaO	MnO	FeO*	CuO	ZnO	Na_2O	K_2O	H_2O	F	Cl	Total	Mg#
769266	chl, ap alteration	GGF M4	chl, ap, qz	c.g. gmas	1	0.00	24.79	0.02	0.00	20.26	14.15	0.02	0.01	27.24	0.07	0.17	0.00	0.00	10.99	0.22	0.02	97.94	0.48
769266	chl, ap alteration	GGF M4	chl, ap, qz	f.g. gmas	2	0.00	25.08	0.08	0.00	20.47	13.62	0.01	0.04	27.54	0.01	0.09	0.03	0.01	11.06	0.14	0.02	98.20	0.47
769266	chl, ap alteration	GGF M4	chl, ap, qz	c.g. gmas	2	0.00	24.35	0.07	0.02	21.35	13.52	0.02	0.14	28.94	0.00	0.14	0.02	0.01	11.10	0.29	0.00	99.97	0.45
769266	chl, ap alteration	GGF M4	chl, ap, qz	f.g. gmas	1	0.00	24.44	0.06	0.00	20.87	13.35	0.01	0.05	28.28	0.08	0.02	0.00	0.00	11.10	0.00	0.00	98.25	0.46
769266	chl, ap alteration	GGF M4	chl, ap, qz	f.g. gmas	2	0.00	25.05	0.06	0.03	19.91	14.47	0.03	0.07	27.75	0.00	0.10	0.00	0.00	11.11	0.11	0.01	98.68	0.48

Abbreviations: ad = andalusite, ap = apatite, asp = arsenopyrite, cd = chloritoid, chl = chlorite, co = carbonate, cp = chalcopyrite, ilm = ilmenite, mgt = magnetite, po = pyrrhotite, qz = quartz, ru = rutile, sp = sphalerite
py = pyrite, gmass = groundmass, intlck = interlocking, wfmd = well formed, f.g. = fine grained, c.g. = goarse grained, rep = replacing, itg = intergcown
* all iron as Fe^{2+}, Mg# = Mg/(Mg+Fe)

Appendix A5.2: Electron microprobe analyses of carbonate

Sample	Description	Strata	Associated minerals	Character	$MgCO_3$	$CaCO_3$	$MnCO_3$	$FeCO_3$	$ZnCO_3$	$SrCO_3$	$BaCO_3$	Total
760227	massive py, co	GGF M6	co, py	wfmd, intlck	16.14	47.56	20.87	17.79	0.00	0.00	0.01	102.78
760227	massive py, co	GGF M6	co, py	wfmd, intlck	14.15	48.20	16.60	22.26	0.06	0.00	0.00	101.29
760227	massive py, co	GGF M6	co, py	wfmd, intlck	14.89	47.54	19.08	19.88	0.13	0.00	0.03	101.58
760227	massive py, co	GGF M6	co, py	euhedral	8.49	50.03	9.27	34.23	0.03	0.02	0.00	102.19
760227	massive py, co	GGF M6	co, py	wfmd, intlck	13.21	49.34	7.56	31.95	0.51	0.11	0.03	102.82
760227	massive py, co	GGF M6	co, py	wfmd, intlck	10.53	49.49	7.39	35.57	0.44	0.01	0.01	103.45
760227	massive py, co	GGF M6	co, py	euhedral	9.43	49.29	9.43	34.55	0.29	0.02	0.00	103.04
760227	massive py, co	GGF M6	co, py	drusy, intlck	13.57	0.85	22.05	66.26	0.03	0.00	0.00	102.89
760227	massive py, co	GGF M6	co, py	wfmd, intlck	7.53	1.11	12.25	82.52	0.39	0.00	0.04	103.95
760227	massive py, co	GGF M6	co, sp	euhedral	17.55	1.61	29.39	53.51	0.00	0.00	0.00	102.25
760227	massive py, co	GGF M6	co, sp	drusy, intlck	9.24	0.74	15.65	78.22	0.00	0.00	0.00	103.93
760227	massive py, co	GGF M6	co, sp	drusy, intlck	17.38	1.63	28.06	54.99	0.77	0.00	0.01	102.85
760251	nodular co alteration	GGF M5	co, mus, qz	intlck	23.56	51.62	2.53	23.68	0.00	0.02	0.00	101.40
760251	nodular co alteration	GGF M5	co, mus, qz	intlck	24.60	53.10	3.82	23.69	0.03	0.00	0.00	105.24
760251	nodular co alteration	GGF M5	co, mus, qz	intlck	22.60	56.23	1.98	23.22	0.00	0.01	0.00	104.03
760251	nodular co alteration	GGF M5	co, mus, qz	intlck	21.52	56.18	3.70	22.20	0.00	0.00	0.00	103.60
760251	nodular co alteration	GGF M5	co, mus, qz	intlck	25.95	54.35	2.89	19.72	0.00	0.00	0.00	102.92
760251	nodular co alteration	GGF M5	co, mus, qz	intlck	20.60	55.48	2.80	24.79	0.03	0.00	0.00	103.70
760251	nodular co alteration	GGF M5	co, mus, qz	mas, drusy	26.69	54.98	1.91	20.60	0.00	0.02	0.00	104.20
760251	nodular co alteration	GGF M5	co, mus, qz	mas, drusy	27.27	55.71	1.25	19.30	0.03	0.00	0.03	103.59
760251	nodular co alteration	GGF M5	co, mus, qz	mas, drusy	29.99	55.24	1.36	16.54	0.00	0.00	0.00	103.13
760251	nodular co alteration	GGF M5	co, mus, qz	mas, drusy	27.45	55.20	1.32	19.57	0.05	0.00	0.00	103.58
760251	nodular co alteration	GGF M5	co, mus, qz	mas, drusy	26.46	53.85	3.90	19.79	0.10	0.00	0.00	104.09
760352	stringer vein: co, chl, mgt	GGF M4	co, po, chl	drusy, intlck	37.18	0.65	10.50	53.97	0.24	0.00	0.06	102.67
760352	stringer vein: co, chl, mgt	GGF M4	co, po, chl	drusy, intlck	22.19	0.30	3.11	77.02	0.05	0.00	0.04	102.85
760352	stringer vein: co, chl, mgt	GGF M4	po, chl	euhedral	38.42	0.62	10.71	53.15	0.00	0.00	0.02	103.03
760352	stringer vein: co, chl, mgt	GGF M4	po, chl	euhedral	30.37	0.43	3.90	68.12	0.00	0.00	0.03	102.88
760352	stringer vein: co, chl, mgt	GGF M4	po, co	drusy, intlck	31.15	2.72	0.28	68.02	0.13	0.00	0.00	102.35
760352	stringer vein: co, chl, mgt	GGF M4	po, co	drusy, intlck	36.63	1.15	4.14	60.73	0.03	0.00	0.03	102.87
760352	stringer vein: co, chl, mgt	GGF M4	co, po	drusy, intlck	34.86	0.77	6.41	59.93	0.00	0.00	0.04	102.56
760352	stringer vein: co, chl, mgt	GGF M4	co, po	drusy, intlck	38.52	0.61	8.34	55.52	0.10	0.00	0.03	103.37
760352	stringer vein: co, chl, mgt	GGF M4	co, chl	drusy, intlck	22.89	51.09	4.86	23.77	0.02	0.00	0.01	102.95
760352	stringer vein: co, chl, mgt	GGF M4	co, chl	drusy, intlck	27.75	51.76	3.80	18.80	0.00	0.02	0.00	102.29

Abbreviations: chl = chlorite, co = carbonate, cp = chalcopyrite, ilm = ilmenite, mus = muscovite, mgt = magnetite, po = pyrrhotite, py = pyrite, qz = quartz, sp = sphalerite
intlck = interlocking, iso = isolated, gmass = groundmass, mas = massive, wfmd = well-formed

Appendix A5.2: Electron microprobe analyses of carbonate *(continued)*

Sample	Description	Strata	Associated minerals	Character	$MgCO_3$	$CaCO_3$	$MnCO_3$	$FeCO_3$	$ZnCO_3$	$SrCO_3$	$BaCO_3$	Total
760352	stringer vein: co, chl, mgt	GGF M4	co	wfmd, intlck	27.08	52.12	4.60	19.22	0.00	0.05	0.03	103.11
760352	stringer vein: co, chl, mgt	GGF M4	co	wfmd, intlck	23.91	51.18	4.33	22.79	0.09	0.08	0.04	102.52
760352	stringer vein: co, chl, mgt	GGF M4	co	wfmd, intlck	29.01	51.11	4.29	16.93	0.12	0.06	0.00	101.53
760373	stringer vein: py, chl, cp	GGF M6	co, py, mgt	intlck, vein	19.49	42.31	4.66	34.69	0.01	0.00	0.00	101.41
760373	stringer vein: py, chl, cp	GGF M6	co, py, mgt	intlck, vein	20.87	43.37	3.16	34.20	0.00	0.03	0.01	101.98
760373	stringer vein: py, chl, cp	GGF M6	co	intlck, vein	19.73	53.55	0.62	28.01	0.02	0.04	0.00	102.64
760373	stringer vein: py, chl, cp	GGF M6	co	intlck, vein	19.61	52.73	0.61	28.38	0.00	0.00	0.06	102.14
760373	stringer vein: py, chl, cp	GGF M6	co, po, mgt	intlck, vein	21.56	50.89	4.12	24.92	0.00	0.00	0.03	101.60
760373	stringer vein: py, chl, cp	GGF M6	co, po, mgt	intlck, vein	22.27	51.04	5.80	22.64	0.00	0.00	0.00	101.87
760411	nodular co alteration	GGF M5	qz	drusy, gmas	37.24	51.99	0.81	10.29	0.01	0.05	0.01	100.38
760411	nodular co alteration	GGF M5	qz	drusy, gmas	35.12	51.17	0.96	11.53	0.01	0.08	0.00	98.87
760411	nodular co alteration	GGF M5	qz	drusy, gmas	36.19	52.73	2.88	8.25	0.04	0.00	0.00	100.09
760411	nodular co alteration	GGF M5	qz	drusy, gmas	35.39	50.69	1.70	9.73	0.03	0.00	0.01	97.54
760411	nodular co alteration	GGF M5	qz	drusy, gmas	35.35	52.43	0.95	11.25	0.02	0.09	0.00	100.09
760411	nodular co alteration	GGF M5	qz	drusy, gmas	35.09	51.09	0.95	11.62	0.04	0.08	0.06	98.93
760411	nodular co alteration	GGF M5	qz	drusy, gmas	36.95	51.77	1.03	10.31	0.00	0.04	0.00	100.09
760411	nodular co alteration	GGF M5	qz	drusy, gmas	35.36	51.60	0.88	12.22	0.03	0.02	0.00	100.10
760411	nodular co alteration	GGF M5	co	euhedral	36.00	53.39	1.81	8.84	0.00	0.00	0.05	100.09
760411	nodular co alteration	GGF M5	co	euhedral	35.85	51.73	1.16	9.87	0.00	0.03	0.00	98.64
760411	nodular co alteration	GGF M5	co	euhedral	34.64	53.49	3.46	8.49	0.00	0.00	0.02	100.09
760411	nodular co alteration	GGF M5	co	euhedral	36.95	51.85	1.72	8.77	0.00	0.00	0.02	99.31
760411	nodular co alteration	GGF M5	co	euhedral	36.56	52.31	0.76	10.39	0.03	0.04	0.01	100.09
760411	nodular co alteration	GGF M5	co	euhedral	36.52	50.90	0.80	10.33	0.04	0.05	0.00	98.62
760411	nodular co alteration	GGF M5	co	euhedral	38.47	52.40	1.07	8.12	0.00	0.04	0.00	100.09
760411	nodular co alteration	GGF M5	co	euhedral	37.28	51.83	0.93	8.38	0.00	0.01	0.01	98.43
760411	nodular co alteration	GGF M5	co	euhedral	35.85	55.50	0.76	6.91	0.07	0.02	0.02	99.12
760411	nodular co alteration	GGF M5	co	euhedral	38.07	53.26	0.77	7.12	0.00	0.03	0.00	99.25
760411	nodular co alteration	GGF M5	co	euhedral	38.74	45.93	0.91	11.31	0.07	0.02	0.01	96.99
760411	nodular co alteration	GGF M5	qz, co	euhedral	36.21	55.29	0.87	7.92	0.02	0.00	0.07	100.38
760411	nodular co alteration	GGF M5	qz, co	euhedral	36.02	53.48	1.82	8.00	0.03	0.03	0.01	99.39
760411	nodular co alteration	GGF M5	qz, co	euhedral	35.98	51.61	1.34	10.43	0.02	0.00	0.00	99.39
760411	nodular co alteration	GGF M5	qz, co	euhedral	37.00	54.74	0.79	7.48	0.00	0.03	0.05	100.09
760411	nodular co alteration	GGF M5	qz, co	euhedral	37.07	51.54	0.82	9.71	0.00	0.07	0.00	99.21

Abbreviations: chl = chlorite, co = carbonate, cp = chalcopyrite, ilm = ilmenite, mus = muscovite, mgt = magnetite, po = pyrrhotite, py = pyrite, qz = quartz, sp = sphalerite
intlck = interlocking, iso = isolated, gmass = groundmass, mas = massive, wfmd = well-formed

Appendix A5.2: Electron microprobe analyses of carbonate *(continued)*

Sample	Description	Strata	Associated minerals	Character	$MgCO_3$	$CaCO_3$	$MnCO_3$	$FeCO_3$	$ZnCO_3$	$SrCO_3$	$BaCO_3$	Total
760411	nodular co alteration	GGF M5	qz	intlck, gmas	35.33	51.34	0.94	12.89	0.05	0.00	0.03	100.59
760411	nodular co alteration	GGF M5	qz	intlck, gmas	35.97	52.08	1.18	10.50	0.00	0.04	0.00	99.78
760432	stringer vein: chl, mgt, co, cp, po, cp	GGF M4	sp	gmas, wfmd	21.41	49.60	11.45	19.14	0.39	0.00	0.00	101.99
760432	stringer vein: chl, mgt, co, cp, po, cp	GGF M4	sp	gmas, wfmd	21.03	49.82	11.48	18.77	0.24	0.00	0.03	101.38
760432	stringer vein: chl, mgt, co, cp, po, cp	GGF M4	mgt	inclusion	21.82	48.99	12.84	18.33	0.02	0.00	0.03	102.03
760432	stringer vein: chl, mgt, co, cp, po, cp	GGF M4	chl, mgt	iso	20.98	1.85	25.09	53.35	0.05	0.00	0.00	101.32
760432	stringer vein: chl, mgt, co, cp, po, cp	GGF M4	chl, mgt	iso	21.70	1.59	24.62	52.86	0.08	0.00	0.01	100.86
760432	stringer vein: chl, mgt, co, cp, po, cp	GGF M4	chl, mgt	intlck	21.61	48.74	11.47	18.64	0.05	0.00	0.01	100.53
760432	stringer vein: chl, mgt, co, cp, po, cp	GGF M4	chl, mgt	intlck	20.32	49.25	11.25	19.00	0.29	0.00	0.00	100.11
760432	stringer vein: chl, mgt, co, cp, po, cp	GGF M4	chl, mgt	intlck	21.18	1.19	23.91	54.22	0.31	0.00	0.03	100.84
760432	stringer vein: chl, mgt, co, cp, po, cp	GGF M4	chl, sp	intlck, wfmd	20.33	49.31	11.30	19.91	0.11	0.00	0.03	100.98
760432	stringer vein: chl, mgt, co, cp, po, cp	GGF M4	chl, sp	intlck, wfmd	19.87	0.75	22.41	56.57	0.31	0.00	0.02	99.93
760432	stringer vein: chl, mgt, co, cp, po, cp	GGF M4	chl, sp	intlck, wfmd	24.45	48.01	10.80	16.96	0.07	0.00	0.05	100.33
760490	M1 Marker bedded chert-chl	GGF M6	chl	euhedral	17.76	49.11	4.02	28.65	0.02	0.00	0.02	99.57
760490	M1 Marker bedded chert-chl	GGF M6	chl	euhedral	17.32	46.50	4.10	29.24	0.04	0.00	0.02	97.21
760490	M1 Marker bedded chert-chl	GGF M6	chl	euhedral	19.22	49.47	3.80	27.87	0.00	0.00	0.00	100.36
760490	M1 Marker bedded chert-chl	GGF M6	qz, co	intlck	19.64	49.97	4.29	26.80	0.01	0.00	0.00	100.70
760490	M1 Marker bedded chert-chl	GGF M6	chl	euhedral	7.77	47.71	3.85	38.05	0.00	0.00	0.00	97.38
760490	M1 Marker bedded chert-chl	GGF M6	qz, co	intlck	19.28	50.04	3.79	27.91	0.01	0.00	0.00	101.03
760490	M1 Marker bedded chert-chl	GGF M6	qz	drusy	18.70	49.54	4.30	28.46	0.06	0.00	0.03	101.08
760490	M1 Marker bedded chert-chl	GGF M6	chl, co	euhedral	19.71	50.15	4.13	27.07	0.00	0.00	0.00	101.06
760490	M1 Marker bedded chert-chl	GGF M6	chl, ilm	euhedral	30.77	53.49	3.93	11.26	0.04	0.00	0.00	99.49
760490	M1 Marker bedded chert-chl	GGF M6	chl, ilm	euhedral	16.36	48.30	4.22	30.12	0.00	0.00	0.07	99.06
760490	M1 Marker bedded chert-chl	GGF M6	chl, ilm	euhedral	31.64	54.07	3.26	8.95	0.00	0.00	0.01	97.92
760490	M1 Marker bedded chert-chl	GGF M6	chl, ilm	euhedral	30.40	50.92	3.48	13.00	0.03	0.00	0.06	97.90
760490	M1 Marker bedded chert-chl	GGF M6	co, chl	bdd, intlck	21.93	51.10	2.44	24.21	0.01	0.00	0.03	99.73
760490	M1 Marker bedded chert-chl	GGF M6	co, chl	bdd, intlck	16.85	47.35	4.26	28.12	0.00	0.00	0.00	96.58
760490	M1 Marker bedded chert-chl	GGF M6	co, chl	bdd, intlck	20.28	49.00	2.76	26.41	0.00	0.00	0.00	98.45
760490	M1 Marker bedded chert-chl	GGF M6	co, chl	bdd, intlck	19.48	48.33	3.18	27.82	0.00	0.00	0.04	98.84
760490	M1 Marker bedded chert-chl	GGF M6	co, chl	bdd, intlck	16.89	49.98	4.53	30.28	0.00	0.00	0.05	101.73
760490	M1 Marker bedded chert-chl	GGF M6	co, chl	bdd, intlck	13.05	62.95	3.25	20.03	0.05	0.00	0.04	99.38
762057	intense co alteration	GGF M5	chl, co	mas, wfmd	24.93	50.18	0.52	23.61	0.00	0.01	0.02	99.25
762057	intense co alteration	GGF M5	chl, co	mas, wfmd	25.30	51.69	0.39	24.05	0.00	0.03	0.00	101.46

Abbreviations: chl = chlorite, co = carbonate, cp = chalcopyrite, ilm = ilmenite, mus = muscovite, mgt = magnetite, po = pyrrhotite, py = pyrite, qz = quartz, sp = sphalerite
intlck = interlocking, iso = isolated, gmass = groundmass, mas = massive, wfmd = well-formed

Appendix A5.2: Electron microprobe analyses of carbonate *(continued)*

Sample	Description	Strata	Associated minerals	Character	$MgCO_3$	$CaCO_3$	$MnCO_3$	$FeCO_3$	$ZnCO_3$	$SrCO_3$	$BaCO_3$	Total
762057	intense co alteration	GGF M5	chl, co	mas, wfmd	28.62	51.19	0.59	19.75	0.02	0.02	0.01	100.20
762057	intense co alteration	GGF M5	chl, co	mas, wfmd	24.69	52.09	0.40	23.47	0.00	0.04	0.00	100.69
762057	intense co alteration	GGF M5	chl, co	mas, wfmd	24.01	50.73	0.19	25.23	0.00	0.04	0.00	100.20
762057	intense co alteration	GGF M5	chl, co	mas, wfmd	24.43	51.40	0.41	24.32	0.00	0.02	0.00	100.58
762057	intense co alteration	GGF M5	co	euhedral	28.16	52.64	0.50	19.37	0.02	0.01	0.00	100.70
762057	intense co alteration	GGF M5	co	euhedral	27.39	52.37	0.54	19.85	0.00	0.04	0.01	100.20
762057	intense co alteration	GGF M5	co	euhedral	27.84	52.42	0.63	19.56	0.00	0.03	0.03	100.50
762057	intense co alteration	GGF M5	co	euhedral	27.27	51.69	0.48	20.11	0.07	0.00	0.00	99.62
762057	intense co alteration	GGF M5	chl, co	mas, wfmd	22.70	51.47	0.24	26.10	0.00	0.04	0.01	100.55
762057	intense co alteration	GGF M5	chl, co	mas, wfmd	25.79	50.10	0.33	23.61	0.00	0.02	0.07	99.92
762057	intense co alteration	GGF M5	chl, co	mas, wfmd	24.88	51.06	2.58	22.09	0.03	0.00	0.00	100.64
762057	intense co alteration	GGF M5	co, chl	mas, wfmd	23.44	51.90	0.48	24.06	0.00	0.02	0.03	99.93
762057	intense co alteration	GGF M5	co, chl	mas, wfmd	23.47	51.57	0.69	24.40	0.05	0.04	0.00	100.21
762057	intense co alteration	GGF M5	co, chl	mas, wfmd	27.10	51.62	0.63	21.14	0.05	0.02	0.00	100.55
762057	intense co alteration	GGF M5	co, chl, sp	euhedral	21.32	50.39	1.99	27.40	0.02	0.02	0.01	101.15
762057	intense co alteration	GGF M5	co, chl, sp	euhedral	24.05	50.89	1.40	24.29	0.07	0.04	0.04	100.80
762057	intense co alteration	GGF M5	co, chl, sp	euhedral	16.96	49.67	2.22	31.16	0.01	0.00	0.00	100.01
762057	intense co alteration	GGF M5	co, chl, sp	gmas, wfmd	19.26	50.43	2.04	28.80	0.01	0.01	0.00	100.55
762065	massive py-co	GGF M6	co, py	wfmd, intlck	26.52	0.68	5.79	69.10	0.00	0.00	0.02	102.30
762065	massive py-co	GGF M6	co, py	wfmd, intlck	27.42	0.65	5.97	67.91	0.11	0.00	0.02	102.42
762065	massive py-co	GGF M6	co, py	wfmd, intlck	27.07	0.95	6.47	67.53	0.03	0.00	0.00	102.24
762065	massive py-co	GGF M6	co, py	wfmd, intlck	31.25	0.72	7.99	61.73	0.02	0.02	0.00	101.84
762065	massive py-co	GGF M6	co, py	wfmd, intlck	22.76	0.37	7.32	70.61	0.00	0.00	0.00	101.19
762065	massive py-co	GGF M6	co, cpy	wfmd, intlck	27.82	0.78	6.65	67.10	0.04	0.00	0.00	102.52
762065	massive py-co	GGF M6	co, cpy	wfmd, intlck	27.25	0.86	6.88	67.43	0.09	0.00	0.00	102.53
762065	massive py-co	GGF M6	co, cpy	wfmd, intlck	27.77	0.84	6.62	67.33	0.16	0.00	0.00	102.75
769056	co-chl altered qz sandstone	GGF M4	co, chl	euhedral	31.69	0.38	1.12	68.91	0.00	0.00	0.03	102.27
769056	co-chl altered qz sandstone	GGF M4	co, chl	euhedral	32.58	0.41	1.07	67.36	0.13	0.02	0.03	101.66
769056	co-chl altered qz sandstone	GGF M4	co, chl	euhedral	32.26	0.43	1.52	66.70	0.11	0.00	0.04	101.18
769056	co-chl altered qz sandstone	GGF M4	co, chl	intlck	31.41	50.81	0.17	17.00	0.00	0.01	0.00	101.21
769077	massive mgt-co	GGF M4	chl, mgt	euhedral	28.84	51.96	0.39	21.02	0.00	0.00	0.00	103.56
769077	massive mgt-co	GGF M4	co	intlck	24.70	1.10	0.57	74.74	0.04	0.00	0.01	101.49
769077	massive mgt-co	GGF M4	co	intlck	27.06	52.01	1.10	19.61	0.00	0.00	0.04	101.40

Abbreviations: chl = chlorite, co = carbonate, cp = chalcopyrite, ilm = ilmenite, mus = muscovite, mgt = magnetite, po = pyrrhotite, py = pyrite, qz = quartz, sp = sphalerite
intlck = interlocking, iso = isolated, gmass = groundmass, mas = massive, wfmd = well-formed

Appendix A5.2: Electron microprobe analyses of carbonate *(continued)*

Sample	Description	Strata	Associated minerals	Character	$MgCO_3$	$CaCO_3$	$MnCO_3$	$FeCO_3$	$ZnCO_3$	$SrCO_3$	$BaCO_3$	Total
769077	massive mgt-co	GGF M4	co, mgt	drusy, intlck	27.66	53.14	0.25	20.10	0.00	0.04	0.03	102.04
769077	massive mgt-co	GGF M4	co, mgt	drusy, intlck	27.26	1.07	0.37	72.93	0.00	0.00	0.03	101.76
769077	massive mgt-co	GGF M4	co, mgt	drusy, intlck	24.68	1.00	0.59	76.67	0.00	0.01	0.04	103.20
769077	massive mgt-co	GGF M4	co, mgt	drusy, intlck	30.06	0.77	0.26	70.54	0.00	0.00	0.04	101.86
769077	massive mgt-co	GGF M4	mgt, co	euhedral	24.96	52.00	2.54	21.30	0.11	0.00	0.00	101.02
769083	co, chl altered siltstone	GGF M4	chl	euhedral	26.14	0.66	1.43	72.68	0.00	0.00	0.01	102.17
769083	co, chl altered siltstone	GGF M4	chl	euhedral	25.69	1.40	2.96	72.32	0.00	0.00	0.00	102.48
769083	co, chl altered siltstone	GGF M4	chl	euhedral	26.58	1.00	1.39	72.60	0.00	0.00	0.02	101.79
769083	co, chl altered siltstone	GGF M4	chl	euhedral	25.69	0.54	1.64	73.04	0.00	0.00	0.00	102.78
769083	co, chl altered siltstone	GGF M4	chl	euhedral	27.52	0.52	0.94	72.91	0.07	0.00	0.00	102.13
769083	co, chl altered siltstone	GGF M4	chl	euhedral	26.44	1.07	2.41	72.59	0.16	0.00	0.05	102.75
769083	co, chl altered siltstone	GGF M4	chl	wfmd, vein	34.55	0.43	1.46	66.23	0.03	0.00	0.04	102.79
769083	co, chl altered siltstone	GGF M4	chl	wfmd, vein	25.74	0.85	2.43	72.78	0.03	0.01	0.00	102.20
769083	co, chl altered siltstone	GGF M4	chl	drusy, vein	28.87	2.74	0.46	69.40	0.09	0.00	0.00	101.72
769083	co, chl altered siltstone	GGF M4	chl	drusy, vein	25.92	0.88	3.43	71.59	0.26	0.00	0.01	102.22
769083	co, chl altered siltstone	GGF M4	chl	wfmd, vein	26.96	0.43	1.10	73.53	0.00	0.00	0.00	102.60
769083	co, chl altered siltstone	GGF M4	chl	drusy, vein	27.98	1.54	0.44	71.53	0.01	0.00	0.03	101.88
769083	co, chl altered siltstone	GGF M4	chl	drusy, vein	27.86	2.58	0.67	71.13	0.07	0.00	0.00	102.47
769083	co, chl altered siltstone	GGF M4	chl	drusy, intlck	25.51	0.51	2.25	73.99	0.00	0.00	0.06	102.46
769083	co, chl altered siltstone	GGF M4	chl	wfmd, intlck	26.97	0.35	1.42	73.86	0.00	0.00	0.01	102.73
769083	co, chl altered siltstone	GGF M4	chl	wfmd, intlck	28.26	0.46	0.86	72.68	0.00	0.00	0.00	102.39
769091	chl altered tuffaceous qz sandstone	GGF M4	chl, mgt, ilm	euhedral, ds	24.98	50.03	1.84	27.00	0.08	0.05	0.02	104.00
769091	chl altered tuffaceous qz sandstone	GGF M4	chl, mgt, ilm	euhedral, ds	25.63	49.79	1.74	27.31	0.00	0.04	0.03	104.55
769091	chl altered tuffaceous qz sandstone	GGF M4	chl, mgt, ilm	euhedral, ds	22.06	42.37	1.43	34.16	0.00	0.06	0.00	100.08
769091	chl altered tuffaceous qz sandstone	GGF M4	chl, mgt, ilm	euhedral, ds	21.44	42.05	1.61	34.97	0.02	0.00	0.00	100.08
769113	co, chl alteration in sandstone	GGF M4	co, chl	wfmd, intlck	13.97	51.00	3.49	33.69	0.11	0.00	0.01	102.32
769113	co, chl alteration in sandstone	GGF M4	co, chl	wfmd, intlck	19.74	51.73	2.27	28.14	0.13	0.01	0.00	102.04
769113	co, chl alteration in sandstone	GGF M4	co, chl	wfmd, intlck	23.49	53.54	0.50	25.03	0.04	0.06	0.00	102.73
769113	co, chl alteration in sandstone	GGF M4	co, py	drusy, intlck	21.98	50.95	3.99	24.93	0.06	0.00	0.00	101.94
769113	co, chl alteration in sandstone	GGF M4	co, py	drusy, intlck	21.19	50.69	4.12	25.64	0.08	0.02	0.00	101.80
769113	co, chl alteration in sandstone	GGF M4	co, py	drusy, intlck	18.67	51.53	3.02	28.45	0.00	0.00	0.08	101.86
769113	co, chl alteration in sandstone	GGF M4	co	drusy, intlck	20.33	52.65	0.54	27.99	0.00	0.04	0.02	101.72
769113	co, chl alteration in sandstone	GGF M4	co	wfmd, intlck	18.12	51.16	3.26	29.27	0.07	0.00	0.02	101.97

Abbreviations: chl = chlorite, co = carbonate, cp = chalcopyrite, ilm = ilmenite, mus = muscovite, mgt = magnetite, po = pyrrhotite, py = pyrite, qz = quartz, sp = sphalerite
intlck = interlocking, iso = isolated, gmass = groundmass, mas = massive, wfmd = well-formed

Appendix A5.2: Electron microprobe analyses of carbonate *(continued)*

Sample	Description	Strata	Associated minerals	Character	$MgCO_3$	$CaCO_3$	$MnCO_3$	$FeCO_3$	$ZnCO_3$	$SrCO_3$	$BaCO_3$	Total
769113	co, chl alteration in sandstone	GGF M4	co	drucy, intlck	21.74	51.49	0.79	27.38	0.00	0.00	0.05	101.92
769113	co, chl alteration in sandstone	GGF M4	chl, co	wfmd, vein	15.59	48.46	3.07	33.45	0.00	0.02	0.03	100.64
769113	co, chl alteration in sandstone	GGF M4	chl, co	wfmd, vein	14.94	46.83	3.41	35.45	0.00	0.00	0.00	100.65
769113	co, chl alteration in sandstone	GGF M4	chl, co	drusy, intlck	14.85	52.18	3.32	31.49	0.00	0.05	0.00	101.91
769163	massive mgt-co	GGF M4	co	wfmd, intlck	40.47	0.42	1.05	60.66	0.06	0.02	0.05	102.76
769163	massive mgt-co	GGF M4	co	wfmd, intlck	35.46	0.74	0.56	63.49	0.13	0.00	0.06	100.58
769163	massive mgt-co	GGF M4	co	drusy, intlck	30.07	55.17	0.08	16.09	0.11	0.02	0.00	101.72
769163	massive mgt-co	GGF M4	co	drusy, intlck	26.21	51.91	0.29	23.16	0.03	0.02	0.00	101.70
769163	massive mgt-co	GGF M4	mgt, co	wfmd	28.34	52.37	1.09	20.38	0.04	0.02	0.04	102.45
769163	massive mgt-co	GGF M4	mgt, co	wfmd	26.95	51.96	1.13	21.61	0.06	0.02	0.02	101.88
769163	massive mgt-co	GGF M4	mgt, co	wfmd	26.92	52.04	1.19	21.60	0.03	0.00	0.00	101.94
769163	massive mgt-co	GGF M4	co	drusy, intlck	28.19	52.44	0.41	20.86	0.00	0.00	0.00	101.92
769163	massive mgt-co	GGF M4	co	drusy, intlck	28.20	53.03	1.05	19.15	0.00	0.00	0.00	101.51
769163	massive mgt-co	GGF M4	co	drusy, intlck	27.81	52.68	1.11	20.28	0.00	0.03	0.06	102.09
769217	stringer vein: chl, mgt, co	GGF M4	chl, py, mgt	drusy, intlck	20.74	52.72	1.29	28.54	0.04	0.00	0.05	103.47
769217	stringer vein: chl, mgt, co	GGF M4	chl, py, mgt	drusy, intlck	24.07	37.68	2.18	38.06	0.16	0.00	0.00	102.32
769217	stringer vein: chl, mgt, co	GGF M4	chl, py, mgt	drusy, intlck	24.09	40.14	2.41	36.55	0.19	0.00	0.00	103.53
769217	stringer vein: chl, mgt, co	GGF M4	co, chl	euhedral	18.84	0.60	1.19	81.27	0.00	0.00	0.00	102.37
769217	stringer vein: chl, mgt, co	GGF M4	co, chl	euhedral	22.32	1.32	1.47	76.71	0.04	0.00	0.00	101.95
769217	stringer vein: chl, mgt, co	GGF M4	co, chl	euhedral	18.32	0.28	1.50	82.12	0.00	0.00	0.00	102.28
769217	stringer vein: chl, mgt, co	GGF M4	co, chl	euhedral	24.65	1.28	1.28	73.80	0.05	0.00	0.00	101.97
769217	stringer vein: chl, mgt, co	GGF M4	co, chl	intlck, mtx	22.67	50.35	0.46	27.58	0.17	0.00	0.01	101.35
769308	chl, co altered pumice breccia	GGF M6	co	mas, intlck	1.11	93.81	2.01	1.86	0.00	0.26	0.03	99.19
769308	chl, co altered pumice breccia	GGF M6	co	euhedral	1.18	93.97	2.15	1.82	0.05	0.11	0.01	99.36
769308	chl, co altered pumice breccia	GGF M6	co	mas, intlck	19.13	50.74	1.55	29.22	0.13	0.00	0.00	101.42
769308	chl, co altered pumice breccia	GGF M6	co	euhedral	19.00	54.20	2.46	26.85	0.00	0.00	0.00	102.61
769308	chl, co altered pumice breccia	GGF M6	co	mas, intlck	24.90	52.99	1.63	21.15	0.00	0.00	0.00	100.94
769308	chl, co altered pumice breccia	GGF M6	co	drusy, intlck	27.04	53.97	2.26	18.13	0.01	0.05	0.00	101.47
769308	chl, co altered pumice breccia	GGF M6	co	drusy, intlck	18.71	53.07	2.16	27.80	0.05	0.00	0.00	101.86
769308	chl, co altered pumice breccia	GGF M6	co	drusy, intlck	19.04	52.34	2.05	29.07	0.07	0.04	0.00	102.75
769308	chl, co altered pumice breccia	GGF M6	co	drusy, intlck	25.47	54.28	1.78	18.45	0.01	0.04	0.01	100.48
769308	chl, co altered pumice breccia	GGF M6	co	euhedral	23.38	51.91	2.54	24.21	0.00	0.00	0.06	102.16
769308	chl, co altered pumice breccia	GGF M6	co	wfmd	18.39	53.47	1.94	27.19	0.07	0.04	0.00	101.22

Abbreviations: chl = chlorite, co = carbonate, cp = chalcopyrite, ilm = ilmenite, mus = muscovite, mgt = magnetite, po = pyrrhotite, py = pyrite, qz = quartz, sp = sphalerite
intlck = interlocking, iso = isolated, gmass = groundmass, mas = massive, wfmd = well-formed

Appendix A5.2: Electron microprobe analyses of carbonate *(continued)*

Sample	Description	Strata	Associated minerals	Character	$MgCO_3$	$CaCO_3$	$MnCO_3$	$FeCO_3$	$ZnCO_3$	$SrCO_3$	$BaCO_3$	Total
769319	massive mgt-co	GGF M4	co, mgt	wfmd, intlck	32.41	52.08	0.20	16.01	0.04	0.01	0.01	101.67
769319	massive mgt-co	GGF M4	co, mgt	wfmd, intlck	36.79	53.51	0.05	10.43	0.05	0.00	0.00	101.25
769319	massive mgt-co	GGF M4	co, mgt	wfmd, intlck	32.17	53.50	0.19	16.36	0.00	0.01	0.00	102.41
769319	massive mgt-co	GGF M4	co, mgt	wfmd, intlck	27.67	52.55	0.16	21.04	0.00	0.02	0.00	102.68
769319	massive mgt-co	GGF M4	co, mgt	euhedral	25.66	52.16	0.20	23.82	0.00	0.06	0.06	102.07
769319	massive mgt-co	GGF M4	co, mgt	euhedral	27.27	51.85	0.20	21.21	0.05	0.06	0.03	100.83
769319	massive mgt-co	GGF M4	co, mgt	euhedral	31.02	52.22	0.43	17.62	0.14	0.00	0.04	102.39
769319	massive mgt-co	GGF M4	co, mgt	wfmd, intlck	31.15	52.38	0.15	16.66	0.02	0.00	0.00	100.50
769319	massive mgt-co	GGF M4	co, mgt	wfmd, intlck	30.73	52.15	0.16	18.41	0.15	0.01	0.03	101.71

Abbreviations: chl = chlorite, co = carbonate, cp = chalcopyrite, ilm = ilmenite, mus = muscovite, mgt = magnetite, po = pyrrhotite, py = pyrite, qz = quartz, sp = sphalerite
intlck = interlocking, iso = isolated, gmass = groundmass, mas = massive, wfmd = well-formed

Appendix A5.3: Electron microprobe analyses of apatite

Sample	Description	Strata	Associated minerals	Character	F	MgO	SiO_2	SrO	P_2O_5	Cl	CaO	BaO	FeO*	Total
769228	intense and, chl, cd, ap alteration	GGF M4	chl	euhedral, ds	5.72	0.00	0.03	0.00	41.77	0.00	54.73	0.00	0.17	102.41
769228	intense and, chl, cd, ap alteration	GGF M4	chl	euhedral, ds	6.12	0.00	0.04	0.00	41.59	0.01	54.43	0.00	0.39	102.58
769228	intense and, chl, cd, ap alteration	GGF M4	chl	euhedral, ds	4.28	0.71	3.26	0.01	36.23	0.04	46.94	0.00	7.77	99.23
769228	intense and, chl, cd, ap alteration	GGF M4	chl	euhedral, ds	5.24	0.00	0.00	0.00	41.83	0.02	55.01	0.00	0.12	102.21
769228	intense and, chl, cd, ap alteration	GGF M4	chl	euhedral, ds	6.05	0.00	0.03	0.00	41.94	0.05	54.41	0.00	0.08	102.56
769228	intense and, chl, cd, ap alteration	GGF M4	chl	euhedral, ds	6.18	0.10	1.11	0.01	40.26	0.03	52.83	0.01	2.08	102.61
769228	intense and, chl, cd, ap alteration	GGF M4	ad, chl	euhedral, ds	5.64	0.00	0.02	0.00	42.09	0.03	54.50	0.00	0.11	102.38
769228	intense and, chl, cd, ap alteration	GGF M4	chl	euhedral, ds	5.98	0.00	0.00	0.00	41.93	0.00	54.41	0.00	0.20	102.52
769228	intense and, chl, cd, ap alteration	GGF M4	chl	euhedral, ds	6.26	0.00	0.00	0.00	41.70	0.03	54.62	0.00	0.04	102.64
769266	stringer vein: chl, py, qz in sandstone	GGF M4	chl, qz, py	euhedral, ds	5.10	0.00	0.00	0.00	42.00	0.02	54.94	0.00	0.10	102.15
769266	stringer vein: chl, py, qz in sandstone	GGF M4	chl, qz, py	euhedral, ds	5.13	0.00	0.01	0.00	41.87	0.01	55.08	0.02	0.05	102.16
769266	stringer vein: chl, py, qz in sandstone	GGF M4	chl, qz, py	euhedral, ds	5.31	0.00	0.00	0.00	41.97	0.02	54.92	0.00	0.02	102.24
769266	stringer vein: chl, py, qz in sandstone	GGF M4	chl, qz, py	euhedral, ds	5.47	0.00	0.00	0.00	41.55	0.15	55.05	0.01	0.11	102.34
769266	stringer vein: chl, py, qz in sandstone	GGF M4	chl, qz, py	euhedral, ds	5.94	0.00	0.01	0.00	41.97	0.03	54.48	0.00	0.09	102.51
769266	stringer vein: chl, py, qz in sandstone	GGF M4	chl, qz, py	euhedral, ds	5.97	0.00	0.01	0.00	41.61	0.02	54.72	0.00	0.18	102.52
769266	stringer vein: chl, py, qz in sandstone	GGF M4	chl, qz, py	euhedral, ds	5.72	0.00	0.00	0.01	41.85	0.03	54.71	0.01	0.09	102.42
769266	stringer vein: chl, py, qz in sandstone	GGF M4	chl, qz, py	euhedral, ds	5.44	0.00	0.00	0.00	41.89	0.03	54.79	0.03	0.12	102.30
769266	stringer vein: chl, py, qz in sandstone	GGF M4	chl, qz, py	euhedral, ds	4.88	0.00	0.02	0.00	41.96	0.02	55.03	0.01	0.15	102.06
769266	stringer vein: chl, py, qz in sandstone	GGF M4	chl, qz, py	euhedral, ds	5.00	0.00	0.01	0.00	42.16	0.02	54.83	0.01	0.08	102.11
769266	stringer vein: chl, py, qz in sandstone	GGF M4	chl, qz, py	euhedral, ds	5.83	0.00	0.01	0.00	41.97	0.01	54.45	0.00	0.18	102.46
769266	stringer vein: chl, py, qz in sandstone	GGF M4	chl, qz, py	euhedral, ds	5.59	0.00	0.02	0.00	42.23	0.02	54.41	0.00	0.10	102.36
769266	stringer vein: chl, py, qz in sandstone	GGF M4	chl, qz, py	euhedral, ds	6.24	0.00	0.00	0.00	41.60	0.00	54.62	0.00	0.17	102.63
769266	stringer vein: chl, py, qz in sandstone	GGF M4	chl, qz, py	euhedral, ds	5.36	0.00	0.01	0.00	42.08	0.01	54.64	0.00	0.17	102.26
769266	stringer vein: chl, py, qz in sandstone	GGF M4	chl, qz, py	euhedral, ds	5.58	0.00	0.00	0.00	41.93	0.01	54.69	0.00	0.15	102.35
769266	stringer vein: chl, py, qz in sandstone	GGF M4	chl, qz, py	euhedral, ds	5.87	0.00	0.01	0.00	42.05	0.01	54.43	0.00	0.11	102.47
769266	stringer vein: chl, py, qz in sandstone	GGF M4	chl, qz, py	euhedral, ds	5.78	0.00	0.01	0.00	41.50	0.01	54.80	0.02	0.31	102.44

Abbreviations: ad = andalusite, ap = apatite, chl = chlorite, cd = chloritoid, py = pyrite, qz = quartz, ds = disseminated

all iron as Fe^{2+}

Appendix A5.4: Electron microprobe analyses of chloritoid

Sample	Description	Strata	Associated minerals	Character	SiO_2	TiO_2	SnO_2	Al_2O_3	MgO	CaO	MnO	FeO*	CuO	ZnO	Na_2O	K_2O	F	Cl	Total**
760473	intense cd, chl alteration	GGF M4	chl, cd, py, po	euhedral	23.34	0.00	0.00	38.94	1.08	0.00	0.47	27.39	0.00	0.12	0.03	0.00	0.00	0.00	91.36
760473	intense cd, chl alteration	GGF M4	chl, cd, py, po	euhedral	23.42	0.00	0.00	39.24	0.98	0.00	0.58	27.31	0.01	0.15	0.00	0.02	0.02	0.01	91.73
760473	intense cd, chl alteration	GGF M4	chl, cd, py, po	euhedral	23.37	0.00	0.01	39.30	0.96	0.00	0.59	27.95	0.00	0.17	0.01	0.01	0.00	0.00	92.38
760473	intense cd, chl alteration	GGF M4	chl, cd	euhedral	23.27	0.05	0.00	37.92	1.09	0.00	0.64	28.19	0.00	0.06	0.03	0.01	0.02	0.00	91.28
760473	intense cd, chl alteration	GGF M4	chl, cd	euhedral	23.71	0.00	0.00	39.09	0.94	0.00	0.58	27.53	0.03	0.16	0.02	0.02	0.08	0.00	92.16
760473	intense cd, chl alteration	GGF M4	chl, cd	euhedral	23.47	0.00	0.00	39.16	0.81	0.00	0.49	27.79	0.00	0.12	0.01	0.00	0.01	0.00	91.86
760473	intense cd, chl alteration	GGF M4	chl, cd	euhedral	23.51	0.01	0.00	39.85	0.88	0.00	0.53	27.51	0.03	0.06	0.00	0.01	0.00	0.02	92.41
760473	intense cd, chl alteration	GGF M4	chl, cd	euhedral	23.45	0.04	0.02	39.08	1.21	0.00	0.55	27.48	0.00	0.12	0.02	0.00	0.00	0.02	91.98
760473	intense cd, chl alteration	GGF M4	chl, cd	euhedral	23.53	0.00	0.00	39.44	1.02	0.00	0.46	27.42	0.00	0.13	0.00	0.00	0.00	0.00	92.01
760473	intense cd, chl alteration	GGF M4	chl, cd	euhedral	23.61	0.00	0.00	39.59	0.71	0.00	0.52	27.70	0.00	0.07	0.01	0.00	0.00	0.01	92.22
762040	intense ad, cd, chl alteration	GGF M4	chl, po, cd	euhedral	23.25	0.00	0.09	39.46	1.23	0.00	0.42	26.90	0.00	0.00	0.00	0.00	0.03	0.00	91.39
762040	intense ad, cd, chl alteration	GGF M4	chl, po, cd	euhedral	23.27	0.00	0.00	39.71	1.34	0.00	0.62	26.35	0.08	0.10	0.01	0.01	0.00	0.02	91.49
762040	intense ad, cd, chl alteration	GGF M4	chl, cd	intlck euhedral	23.83	0.06	0.04	40.20	1.47	0.00	0.59	27.00	0.00	0.04	0.04	0.01	0.00	0.00	93.27
762040	intense ad, cd, chl alteration	GGF M4	chl, cd	intlck euhedral	23.69	0.02	0.00	39.85	1.17	0.02	0.39	27.26	0.04	0.03	0.00	0.00	0.03	0.00	92.50
762040	intense ad, cd, chl alteration	GGF M4	chl, cd	intlck euhedral	23.70	0.00	0.00	39.69	1.33	0.00	0.60	27.54	0.01	0.07	0.00	0.00	0.02	0.03	92.99
762040	intense ad, cd, chl alteration	GGF M4	chl, cd	intlck euhedral	23.76	0.02	0.10	39.49	1.36	0.02	0.41	27.04	0.00	0.15	0.00	0.01	0.08	0.00	92.44
762040	intense ad, cd, chl alteration	GGF M4	chl, cd, po	relcit lath, po repl	23.95	0.00	0.02	39.97	1.45	0.00	0.58	26.55	0.00	0.15	0.00	0.00	0.00	0.00	92.66
762040	intense ad, cd, chl alteration	GGF M4	chl, cd, po	relcit lath, po repl	23.90	0.00	0.05	39.94	1.36	0.02	0.67	26.88	0.01	0.04	0.01	0.00	0.00	0.01	92.88
762040	intense ad, cd, chl alteration	GGF M4	chl, cd, po	euhedral	23.35	0.00	0.07	39.06	1.56	0.03	0.45	26.81	0.00	0.00	0.00	0.01	0.00	0.00	91.33
762040	intense ad, cd, chl alteration	GGF M4	chl, cd, po	euhedral	17.75	0.65	0.00	29.02	2.46	0.08	0.28	38.54	0.07	0.05	0.00	0.00	0.00	0.00	88.90
762040	intense ad, cd, chl alteration	GGF M4	chl, cd, po	euhedral	23.68	0.03	0.00	39.86	1.46	0.00	0.49	26.36	0.07	0.16	0.02	0.00	0.03	0.01	92.16
762040	intense ad, cd, chl alteration	GGF M4	chl, cd, py, po	subhedral	23.24	0.02	0.00	39.83	1.33	0.01	0.52	26.50	0.05	0.00	0.04	0.00	0.03	0.00	91.56
762040	intense ad, cd, chl alteration	GGF M4	chl, cd, py, po	relict lath, po repl	23.59	0.00	0.06	39.58	1.46	0.03	0.45	26.20	0.00	0.13	0.00	0.00	0.00	0.00	91.50
762040	intense ad, cd, chl alteration	GGF M4	chl, cd, py, po	euhedral	22.99	0.05	0.04	37.77	1.14	2.29	0.45	26.67	0.09	0.01	0.00	0.02	0.04	0.02	91.58

Abbreviations: ad = andalusite, chl = chlorite, cd = chloritoid, py = pyrite, po = pyrrhotite, intlck = interlocking, repl = replacement

*All iron as Fe^{2+}

**Note low totals due to uncalculated H_2O contents

Appendix A6: Detection limits of major and trace elements

XRF Major and trace element analysis (University of Tasmania)

Element	Detection limit (wt.%)
SiO_2	0.01
TiO_2	0.01
Al_2O_3	0.01
FeO*	0.01
MnO	0.01
MgO	0.01
CaO	0.01
Na_2O	0.01
K_2O	0.01
P_2O_5	0.01
LOI	0.01
S	0.01

Element	Detection limit (ppm)
La	2
Ce	4
Nd	2
Nb	0.5
Zr	1
Sr	1
Cr	1
Ba	4
Sc	2
V	1.5
Sn	1
Cu	2
Pb	1.5
Zn	1
Ni	1
Y	1
Rb	1

Trace elements by ICP-MS (Analabs, Perth)

Element	Detection limit (ppm)
Ag	0.1
As	1
Bi	0.1
Mo	0.1
Cd	0.1
Sb	0.1
Cs	0.05
Tl	0.5
Th	0.05
U	0.05

Appendix A6.1: Major and trace element analyses of least altered lithologies from the Golden Grove and Scuddles Formations

	GGF M6: Breccia and siltstone								GGF M6: Tuffaceous sandstone				GGF M5: Tuffaceous sandstone							
SAMPLE	760364ii	760364i	769162	769341	769343	760231	769336	Average	760491(i)	760491(ii)	760445	Average	760233	760376	769065	769286	769288	769331	769278	Average
DDH	GG134	GG134	GG157	GG045	GG045	GG132	GG045		GG165	GG165	GG165		GG132	GG134	GG027	GG070	GG070	GG045	GG070	
depth	130.1	130.1	279.4	415.2	428.6	380.4	384.0		247.3	247.3	402.9		399.3	253.0	364.5	429.1	465.2	333.0	360.1	
SiO_2	55.76	64.36	59.71	63.54	70.64	83.84	84.05	68.84	55.22	59.31	66.14	60.22	71.32	66.82	66.77	68.92	65.60	63.04	64.83	66.76
TiO_2	0.35	0.31	0.25	0.32	0.07	0.18	0.08	0.22	0.63	0.68	0.13	0.48	0.30	0.36	0.24	0.28	0.28	0.27	0.22	0.28
Al_2O_3	12.96	9.22	10.88	8.87	1.28	4.85	2.87	7.28	12.41	12.43	5.40	10.08	11.41	9.96	10.38	11.37	10.54	11.23	9.31	10.60
FeO*	19.80	16.96	17.21	15.25	6.91	7.19	7.30	12.95	17.44	16.93	18.48	17.62	6.26	13.54	13.70	11.17	14.21	17.33	13.90	12.87
MnO	0.14	0.11	0.03	0.08	0.03	0.06	0.07	0.07	0.22	0.17	0.05	0.15	0.15	0.05	0.05	0.05	0.07	0.05	0.02	0.06
MgO	5.30	3.78	7.39	3.40	0.33	1.44	0.70	3.19	5.45	5.65	1.74	4.28	1.43	5.46	4.85	3.74	5.19	3.95	7.09	4.53
CaO	0.06	0.17	<	0.19	0.33	0.08	0.09	0.13	2.12	0.30	0.05	0.82	1.89	0.09	<	0.03	0.10	0.00	0.03	0.30
Na_2O	<	<	<	<	<	0.03	0.11	0.02	0.05	0.05	<	0.03	0.11	0.03	0.03	0.14	0.03	<	0.05	0.06
K_2O	<	<	<	<	0.06	0.14	0.22	0.06	0.20	0.06	<	0.09	2.41	<	0.02	0.82	<	0.03	<	0.47
P_2O_5	0.03	0.05	<	0.05	<	0.02	0.04	0.03	0.08	0.07	<	0.05	0.04	0.08	<	0.03	0.04	<	<	0.03
LOI	4.43	4.71	4.35	4.18	5.55	1.74	3.00	3.99	4.80	4.18	6.06	5.01	3.74	3.72	3.58	3.16	3.65	3.67	4.12	3.66
S	0.21	2.48	<	2.36	8.55	0.06	2.44	2.30	0.89	0.03	6.82	2.58	0.09	<	<	<	<	<	<	<
TOTAL	98.89	100.14	99.84	98.75	97.90	99.57	98.72	99.12	98.62	99.83	98.12	98.86	99.06	100.12	99.62	99.71	99.72	99.60	99.58	99.63
La	30	21	36	10	<	7	5	16	6	3	17	9	26	23	30	30	23	29	34	28
Ce	57	40	67	19	<	9	11	29	14	9	33	19	55	43	63	58	45	56	61	54
Nd	26	19	34	9	<	4	3	14	7	3	16	9	28	23	40	29	22	29	27	28
Nb	9.0	4.9	10.7	5.6	<	1.4	1.7	4.8	5.5	3.2	4.6	4.4	12.0	7.5	10.5	11.0	9.7	10.4	8.3	9.9
Zr	277	141	304	126	10	34	38	133	113	83	131	109	321	221	295	308	286	305	246	283
Sr	2	1	<	1	4	2	6	2	4	1	2	2	24	2	<	8	2	<	<	5
Cr	14	65	3	30	6	17	7	20	80	88	4	57	3	3	2	2	2	3	2	2
Ba	5	7	7	<4	<	8	21	7	33	12	6	17	357	6	11	170	4	11	5	80
Sc	23	18	7	21	<	8	4	12	37	36	9	27	10	21	7	10	9	9	9	11
V	64	53	2	92	22	44	16	42	205	209	6	140	4	2	<	2	4	<	<	2
Sn	7.3	7.1	7.0	32.1	151.7	4.0	3.0	30.3	5.0	4.0	2.5	3.8	3.0	3.0	5.0	4.0	3.0	5.0	4.0	3.9
Cu	21.0	925.0	5.0	266.0	210.0	10.0	240.0	239.6	56.0	21.0	135.0	70.7	19.0	4.0	5.0	5.0	5.0	5.0	15.0	8.3
Pb	29.0	213.0	4.0	25.0	226.0	8.0	533.0	148.3	38.0	10.0	19.0	22.3	27.0	4.0	3.0	9.0	12.0	6.0	3.0	9.1
Zn	445	445	187	22700	101600	730	858	18138	453	425	194	357	491	133	230	74	212	211	451	257
Ni	23	23	2	Zn intf	Zn intf	5	12	9	46	52	2	33	1	3	2	1	1	<	2	1
Y	47	25	59	26	2	7	9	25	15	15	26	19	66	48	69	67	59	71	59	63
Rb	<	<	<	<	2	4	5	2	5	1	<	2	82	<	<	17	<	<	<	14
Ag	2.7	24.0	0.2	1.1	5.2	0.3	4.1	5.4	1.4	0.3	0.4	0.7	0.4	0.1	0.1	0.1	0.2	0.1	<	0.1
As	28	58	1	26	61	3	40	31	50	48	24	41	4	<	1	4	4	<	<	2
Bi	0.6	5.4	<	3.0	7.8	0.2	10.2	3.9	0.8	0.1	1.7	0.9	<	<	<	<	<	<	<	0.0
Mo	1.0	1.0	1.3	0.8	0.4	0.4	1.3	0.9	0.6	<	0.5	0.4	0.3	0.8	1.1	0.9	0.9	0.9	4.2	1.3
Cd	0.8	9.1	0.2	72.8	323.0	2.6	5.0	59.1	0.2	0.1	0.2	0.2	1.2	<	0.1	0.2	<	<	0.2	0.2
Sb	0.8	4.0	1.9	2.2	3.0	0.7	2.5	2.2	2.9	1.6	1.7	2.1	1.4	0.6	1.1	1.0	0.8	1.5	0.8	1.0
Cs	0.07	0.07	0.21	0.09	0.06	0.09	0.18	0.11	0.17	0.15	0.08	0.13	0.63	0.26	0.21	0.60	0.70	0.26	0.13	0.40
Tl	<	<	<	<	1.5	0.6	0.7	0.4	0.6	<	<	0.2	1.3	<	<	<	<	<	<	0.2
Th	6.87	3.78	6.52	2.87	0.20	1.24	0.93	3.20	2.97	1.74	2.87	2.53	6.29	4.98	6.12	6.65	5.95	6.41	5.48	5.98
U	1.42	0.80	1.56	0.65	0.06	0.30	0.27	0.72	0.62	0.41	0.61	0.55	1.39	1.02	1.35	1.37	1.28	1.33	1.18	1.27

FeO* indicates total iron as Fe^{2+}; analyses are un-normalised, < indicates below detection; Zn intf = not determined due to zinc interference, LOI=loss on ignition

'Average' denotes the average values for each lithology as shown, major elements, LOI and S in wt.%, trace elements in ppm

Appendix A6.1: Major and trace element analyses of least altered lithologies from the Golden Grove and Scuddles Formations

	GGF M4: breccia			GGF M4: Quartz sandstone							GGF M1: Tuffaceous pebble breccia										
SAMPLE	769056	769155	Average	769150	769072	760375	769089	769269	760357	Average	769049	769142	769146	769148	769254	769255	769258	769259	762018	769325	Average
DDH	GG027	GG157		GG157	GG027	GG134	GG038	GG070	GG118		GG027	GG157	GG157	GG157	GG070	GG070	GG070	GG070	GG148	GG045	
depth	296.7	228.6		211.7	517.3	245.2	218.3	308.5	262.1		251.9	109.6	157.1	198.6	118.0	168.1	244.0	248.8	400.7	255.5	
SiO_2	29.57	69.23	49.40	45.69	66.96	77.05	49.55	27.40	38.23	50.81	75.55	73.64	78.48	51.69	74.34	78.29	83.69	57.70	80.11	73.05	72.65
TiO_2	0.81	0.13	0.47	0.34	0.23	0.17	0.57	0.42	0.43	0.36	0.26	0.27	0.20	0.51	0.33	0.19	0.19	0.49	0.29	0.32	0.31
Al_2O_3	16.40	5.07	10.74	12.93	9.34	6.90	14.85	18.14	16.93	13.18	7.21	8.53	6.35	15.23	8.58	6.54	4.91	13.52	8.94	9.76	8.96
FeO*	26.30	10.17	18.24	24.59	13.95	11.44	20.54	28.78	31.85	21.86	10.29	10.10	8.14	18.80	9.18	8.58	6.50	16.46	4.42	9.21	10.17
MnO	0.05	<	0.03	0.03	0.04	0.03	0.05	0.03	0.06	0.04	0.03	0.04	0.02	0.06	0.03	0.02	0.02	0.05	0.02	0.05	0.03
MgO	13.28	10.75	12.02	8.52	5.18	2.20	7.67	15.86	5.52	7.49	3.44	4.13	3.20	7.73	3.71	3.09	2.25	6.35	2.00	3.52	3.94
CaO	2.59	0.18	1.39	0.06	0.03	0.00	0.21	0.03	0.00	0.06	0.04	<	0.06	<	0.08	0.03	<	0.04	0.05	0.14	0.04
Na_2O	0.06	0.03	0.05	<	<	<	<	<	<	<	0.04	0.04	0.05	0.06	0.06	0.03	0.04	0.07	0.21	0.11	0.07
K_2O	<	<	<	<	<	0.03	<	<	<	<	0.01	0.20	0.15	0.26	0.58	0.09	0.09	0.38	1.44	0.70	0.39
P_2O_5	0.05	<	0.03	<	<	<	0.16	<	<	<	0.04	<	0.02	<	0.05	0.03	<	0.04	0.04	<	0.03
LOI	10.56	3.81	7.19	6.94	3.73	2.33	5.46	9.13	5.36	5.49	2.70	2.99	2.71	5.41	2.60	2.55	1.90	4.58	2.05	2.87	3.04
S	<	0.02	<	<	<	<	<	<	<	<	<	<	0.52	0.06	<	0.14	<	<	<	0.04	0.08
TOTAL	99.69	99.39	99.54	99.17	99.50	100.16	99.07	99.80	98.40	99.35	99.61	99.94	99.38	99.75	99.54	99.44	99.61	99.68	99.57	99.74	99.63
La	22	14	18	33	22	23	19	38	30	27	13	22	20	36	15	14	33	25	14	23	21
Ce	43	25	34	56	43	43	39	74	53	51	25	39	40	57	28	26	50	38	27	40	37
Nd	18	14	16	27	19	19	20	36	25	24	12	17	16	26	13	12	22	17	13	19	17
Nb	3.8	4.8	4.3	9.6	9.6	7.0	10.4	16.2	11.8	10.8	5.8	6.7	5.1	7.6	5.6	4.1	3.4	6.2	5.7	6.4	5.7
Zr	135	137	136	287	260	179	302	472	366	311	152	189	139	233	162	131	98	162	178	188	163
Sr	9	<	5	2	2	2	4	3	2	3	<	2	3	5	5	2	2	5	42	5	7
Cr	42	2	22	3	3	2	3	4	3	3	2	3	3	104	4	2	2	29	3	6	16
Ba	7	<	3	10	9	8	7	9	10	9	5	48	34	59	277	17	17	78	246	136	92
Sc	38	6	22	15	7	4	32	14	12	14	10	10	8	25	13	8	6	27	13	14	13
V	242	<	121	<	2	<	13	<	<	2	7	13	3	72	11	5	9	103	8	12	24
Sn	9.8	3.0	6.4	1.7	5.0	4.0	18.0	7.7	6.3	7.1	3.0	2.0	2.0	5.0	2.0	2.0	1.0	5.0	2.0	3.0	2.7
Cu	30.0	97.0	63.5	12.0	5.0	51.0	8.0	10.0	11.0	16.2	4.0	6.0	19.0	10.0	7.0	11.0	4.0	9.0	9.0	4.0	8.3
Pb	<	2.0	1.0	<	9.0	7.0	2.0	3.0	2.0	3.8	4.0	1.5	5.0	5.0	3.0	4.0	4.0	4.0	7.0	3.0	4.1
Zn	157	68	113	84	379	162	46	93	73	140	45	38	22	61	29	22	30	93	24	31	40
Ni	37	2	20	2	2	1	3	3	3	2	2	3	2	17	2	2	3	12	2	3	5
Y	34	27	31	51	56	42	59	52	64	54	21	28	22	36	22	21	12	50	28	39	28
Rb	<	<	0	<	<	<	<	<	<	0	<1	4	3	4	13	2	2	8	31	15	8
Ag	<	<	0.0	0.2	0.1	0.1	0.2	0.2	0.1	0.2	<	0.1	0.1	0.2	<	<	<	<	0.1	<	0.1
As	5	<	3	4	2	<	1	20	8	6	<	<	4	2	<	<	<	2	<	<	1
Bi	0.5	0.2	0.4	0.5	<	0.2	0.3	<	<	0.2	0.1	<	0.5	1.1	<	0.1	0.1	0.2	0.2	3.3	0.6
Mo	2.7	2.3	2.5	2.3	2.0	0.9	6.3	0.1	1.8	2.2	3.2	12.5	1.6	42.9	2.6	1.0	3.9	2.0	1.6	1.1	7.2
Cd	0.3	0.1	0.2	0.2	0.2	0.2	0.2	0.2	0.2	0.2	<	<	<	0.2	0.1	<	<	4.4	<	<	0.5
Sb	1.7	0.7	1.2	0.6	0.9	0.6	0.9	1.3	1.6	1.0	0.6	0.2	1.0	0.7	0.2	0.2	0.2	0.6	0.4	0.3	0.4
Cs	1.67	0.14	0.91	0.15	0.32	0.18	0.43	0.35	0.20	0.27	0.13	0.13	0.31	0.77	0.41	0.19	0.18	0.45	0.63	0.72	0.39
Tl	<	<	0.0	<	<	<	<	<	<	0.0	<	<	<	<	<	<	<	<	<	<	0.0
Th	5.50	2.87	4.19	6.43	5.58	3.83	7.58	11.40	8.47	7.22	4.27	5.04	4.01	6.07	4.32	3.71	2.72	4.01	4.77	5.07	4.40
U	1.45	0.73	1.09	1.42	1.16	0.97	1.80	3.64	2.05	1.84	0.99	1.35	0.88	1.66	1.07	0.89	0.75	1.06	1.17	1.31	1.11

FeO* indicates total iron as Fe^{2+}; analyses are un-normalised, < indicates below detection; Zn intf = not determined due to zinc interference, LOI=loss on ignition

'Average' denotes the average values for each lithology as shown, major elements, LOI and S in wt.%, trace elements in ppm

Appendix A6.1: Major and trace element analyses of least altered lithologies from the Golden Grove and Scuddles Formations

	SCF M2: DAC3 dacite												Dacite intrusions			SCF M2: RD2 rhyodacite				
SAMPLE	760207	760214	760486	760447	769073	769074	769075	769279	769294	769328	769347	Average	769076	769278	Average	760211	760215	760217	760218	760219
DDH	GG132	GG132	GG165	GG165	GG027	GG027	GG027	GG070	GG070	GG045	GG045		GG027	GG138		GG132	GG132	GG132	GG132	GG132
depth	240.2	319.9	190.7	424.2	571.0	587.7	630.9	375.2	551.2	286.2	460.4		667.5	286.3		297.5	329.7	347.2	360.2	364.5
SiO_2	68.00	71.86	64.30	63.75	66.09	66.78	66.43	65.92	60.62	65.21	58.65	65.27	68.07	66.85	67.46	81.98	80.70	71.81	64.08	72.26
TiO_2	0.43	0.45	0.39	0.36	0.39	0.35	0.38	0.37	0.53	0.35	0.40	0.40	0.43	0.38	0.41	0.39	0.35	0.39	0.48	0.40
Al_2O_3	13.92	14.75	14.02	14.06	14.58	14.37	14.57	14.26	14.21	13.97	13.46	14.21	14.80	14.81	14.81	11.95	11.23	12.29	15.38	12.21
FeO*	3.87	5.71	4.07	3.92	3.47	3.96	3.40	3.85	4.94	3.80	5.20	4.20	3.54	3.68	3.61	0.11	2.17	4.73	6.40	7.71
MnO	0.07	0.04	0.08	0.14	0.06	0.10	0.08	0.14	0.08	0.10	0.21	0.10	0.02	0.04	0.03	0.00	0.01	0.11	0.17	0.10
MgO	1.92	1.27	2.47	3.07	2.03	2.58	2.38	2.69	3.68	2.59	2.77	2.48	2.53	2.32	2.43	0.05	0.63	1.34	2.60	1.66
CaO	3.19	0.15	5.16	3.64	3.88	2.93	2.93	2.86	4.63	3.37	6.21	3.54	0.99	2.67	1.83	0.15	0.12	2.36	2.33	0.31
Na_2O	0.59	0.64	1.11	0.61	0.80	0.84	0.64	0.63	1.16	0.55	0.82	0.91	6.35	2.04	4.20	0.91	0.62	0.42	0.37	0.31
K_2O	2.71	1.95	1.25	2.75	2.65	2.46	2.92	2.79	1.82	2.99	2.29	2.39	0.22	2.02	1.12	2.05	2.02	2.17	2.68	1.80
P_2O_5	0.10	0.12	0.09	0.10	0.10	0.10	0.11	0.10	0.16	0.10	0.11	0.11	0.11	0.11	0.11	0.10	0.08	0.08	0.11	0.09
LOI	4.74	2.66	6.46	7.48	5.63	5.38	5.72	5.91	7.90	6.87	9.81	6.08	2.57	4.55	3.56	1.64	1.82	3.87	5.16	2.76
S	0.18	0.19	0.02	0.06	<	<	0.06	0.15	<	<	0.06	0.06	0.50	0.08	0.29	<	0.15	0.13	0.19	0.64
TOTAL	99.54	99.60	99.40	99.88	99.68	99.85	99.56	99.52	99.73	99.90	99.93	99.69	99.63	99.47	99.55	99.33	99.75	99.57	99.76	99.61
La	21	10	21	17	17	17	19	19	20	14	17	17	19	18	18	8	25	24	29	26
Ce	39	22	37	32	32	34	35	32	38	29	32	33	39	34	37	18	57	46	62	51
Nd	14	10	15	12	13	11	14	12	16	11	13	13	14	14	14	9	27	22	29	25
Nb	5.7	5.4	4.3	5.2	5.4	4.8	5.0	5.4	6.5	4.1	5.4	5.2	6.2	5.0	5.6	10.2	8.9	9.7	13.9	10.6
Zr	152	155	145	148	151	145	152	150	166	145	156	152	157	152	154	262	234	264	337	259
Sr	78	38	86	54	60	53	41	43	66	43	57	63	192	56	124	56	41	39	26	19
Cr	46	47	64	27	28	28	30	30	89	30	54	44	62	32	47	6	6	7	8	13
Ba	578	166	218	380	337	343	434	534	443	509	387	420	1288	411	850	220	261	269	252	168
Sc	10	12	12	9	10	9	9	8	14	9	12	10	10	9	10	11	12	14	15	15
V	69	71	76	51	51	51	51	49	86	49	58	61	65	52	58	35	22	25	28	26
Sn	1.0	1.0	2.0		2.0	1.0	1.0	2.0	2.0	2.0	2.0	1.4	<	1.0	0.5	<	2.0	2.0	3.0	6.0
Cu	13.0	34.0	16.0	7.0	15.0	5.0	5.0	13.0	21.0	11.0	20.0	15.1	18.0	70.0	44.0	5.0	28.0	24.0	19.0	7.0
Pb	7.0	15.0	26.0	17.0	19.0	25.0	22.0	7.0	11.0	9.0	13.0	14.8	8.0	7.0	7.5	16.0	23.0	43.0	128.0	94.0
Zn	45	194	249	108	79	120	168	51	92	31	122	110	47	53	50	3	82	220	250	207
Ni	33	39	47	20	20	23	18	16	57	19	32	31	52	19	36	14	5	7	11	4
Y	13	14	12	10	11	10	11	10	13	9	13	12	11	10	11	57	43	48	107	46
Rb	74	48	31	77	79	70	81	68	49	75	57	64	5	52	29	49	49	54	66	43
Ag	0.1	0.3	0.1		<	<	<	<	<	<	0.1	0.1	0.2	<	0.1	0.1	0.7	0.5	1.3	0.9
As	1	48	2	4	<	<	2	3	<	<	7	6	4	2	3	30	14	10	32	82
Bi	0.3	0.1	<	<	<	<	<	0.1	<	<	<	0.0	0.1	0.1	0.1	<	<	<	<	<
Mo	0.2	1.1	0.7	0.1	1.8	0.1	0.8	0.7	2.0	0.7	0.5	0.8	0.2	0.6	0.4	2.5	0.9	1.1	2.9	0.3
Cd		0.2	0.1	0.1	0.2	0.2	0.1	<	0.1	<	0.1	0.1	<	<	0.0	<	<	0.4	0.3	0.2
Sb	1.1	1.6	1.4	0.7	0.7	0.8	1.2	0.5	1.2	0.9	1.8	1.0	2.0	0.6	1.3	1.0	3.3	2.0	3.2	2.9
Cs	1.37	0.97	1.09	1.18	1.21	1.13	1.30	1.09	1.91	1.15	1.15	1.22	0.43	0.94	0.69	1.28	1.05	0.96	1.06	0.64
Tl	<	0.5	1.0	1.0		<	0.6	<	<	<	<	0.3	<	<	0.0	<	0.7	1.2	2.5	2.3
Th	5.93	6.33	5.27	5.35	5.61	5.38	5.62	5.40	5.21	5.07	4.51	5.48	6.58	5.73	6.16	7.89	6.70	6.74	8.75	7.03
U	1.41	1.67	1.18	1.28	1.31	1.33	1.33	1.27	1.16	1.25	1.10	1.31	1.52	1.34	1.43	1.96	1.54	1.78	2.31	1.62

FeO* indicates total iron as Fe^{2+}; analyses are un-normalised, < indicates below detection; Zn intf = not determined due to zinc interference, LOI=loss on ignition

'Average' denotes the average values for each lithology as shown, major elements, LOI and S in wt.%, trace elements in ppm

Appendix A6.1: Major and trace element analyses of least altered lithologies from the Golden Grove and Scuddles Formations

	SCF M2; RD2 rhyodacite						Dolerite intrusions		
SAMPLE	760487	760488	769302	769303	769346	Average	769144	769145	Average
DDH	GG165	GG165	GG095	GG095	GG045		GG157	GG157	
depth	222.7	234.5	295.3	378.4	443.8		137.5	142.6	
SiO_2	75.36	65.57	69.98	78.47	74.54	73.48	48.35	47.06	47.71
TiO_2	0.36	0.33	0.38	0.38	0.41	0.39	0.83	1.36	1.10
Al_2O_3	11.43	10.46	11.30	12.14	12.81	12.12	14.85	13.66	14.26
FeO*	3.51	5.05	2.25	0.65	5.22	3.78	12.59	16.66	14.63
MnO	0.06	0.17	0.15	0.05	0.04	0.09	0.19	0.22	0.21
MgO	1.61	2.56	0.65	0.12	1.25	1.25	8.00	5.15	6.58
CaO	1.48	6.08	5.90	1.65	0.21	2.06	10.62	10.93	10.78
Na_2O	0.38	0.27	0.64	0.53	0.48	0.49	1.51	0.22	0.87
K_2O	2.13	1.71	2.23	2.75	2.08	2.16	<	<	<
P_2O_5	0.09	0.07	0.08	0.08	0.10	0.09	0.05	0.10	0.08
LOI	3.32	7.63	6.14	2.84	2.59	3.78	2.90	3.82	3.36
S	0.03	<	0.02	0.12	0.12	0.14	0.13	0.31	0.22
TOTAL	99.73	99.90	99.70	99.66	99.73	99.67	99.90	99.18	99.54
La	23	20	20	20	30	22	2	8	5
Ce	47	41	42	44	63	47	7	17	12
Nd	22	20	20	22	29	22	4	15	9
Nb	9.9	8.8	9.7	10.3	10.9	10.3	1.9	6.9	4.4
Zr	241	237	252	254	272	261	47	85	66
Sr	20	22	53	41	28	35	138	347	242
Cr	7	8	6	6	8	8	418	25	221
Ba	386	318	434	300	343	295	9	<	4
Sc	11	12	13	11	13	13	41	23	32
V	21	21	21	23	26	25	261	254	257
Sn	3.0	3.0	3.0	2.0	2.0	2.6	2.0	3.0	2.5
Cu	70.0	8.0	19.0	11.0	45.0	23.6	101.0	211.0	156.0
Pb	23.0	23.0	26.0	25.0	16.0	41.7	3.0	6.0	4.5
Zn	118	148	112	12	161	131	103	126	115
Ni	4	6	9	6	9	8	151	91	121
Y	35	37	43	45	45	51	18	25	22
Rb	51	45	64	77	49	55	<	<	0
Ag	0.4	0.2	0.4	1.4	0.3	0.6	<	0.2	0.1
As	4	1	<	18	7	20	3	3	3
Bi	<	<	<	<	0.1	0.0	<	0.2	0.1
Mo	0.6	0.2	0.6	1.5	0.8	1.1	0.2	0.3	0.3
Cd	<	0.1	0.4	<	<	0.1	0.2	0.3	0.3
Sb	1.6	1.6	0.5	1.9	2.5	2.1	0.8	0.6	0.7
Cs	0.89	0.64	1.05	0.94	0.97	0.95	0.11	0.15	0.13
Tl	2.1	1.7	<	0.6	0.5	1.2	<	<	0.0
Th	6.40	5.87	6.47	5.92	7.22	6.90	0.33	0.97	0.65
U	1.54	1.41	1.51	1.50	1.74	1.69	0.07	0.23	0.15

FeO* indicates total iron as Fe^{2+}; analyses are un-normalised, < indicates below detection; Zn intf = not determined due to zinc interference, LOI=loss on ignition

'Average' denotes the average values for each lithology as shown, major elements, LOI and S in wt.%, trace elements in ppm

Appendix A6.2: Major and trace element analyses of altered volcaniclastic rocks from the Golden Grove Formation

	GGF M6 : M1 Marker chert bands					GGF M6 : M1 Marker chlorite bands							GGF M6 : Si-rich	GGF M6 : Chlorite alteration			
SAMPLE	SCD007ii	SCD005ii	760490ii	762064ii	Average	SCD007i	SCD005iii	SCD005i	760490i	760366	762064i	Average	760230	760436	760373	760433	Average
DDH	Scuddles	Scuddles	GG165	GG099		Scuddles	Scuddles	Scuddles	GG165	GG134	GG099		GG132	GG165	GG134	GG165	
depth			243.7	157.8					243.7	163.1	157.8		374.6	357.2	224.6	337.1	
SiO_2	79.84	86.86	76.09	81.31	81.03	39.24	48.28	35.53	16.65	61.56	71.73	45.50	60.74	29.09	56.77	54.05	46.64
TiO_2	<	<	0.02	0.00	0.01	0.16	0.65	0.46	0.32	0.27	0.16	0.34	0.24	0.08	0.07	0.36	0.17
Al_2O_3	0.06	0.08	0.35	0.20	0.17	3.62	13.16	11.33	6.08	6.72	5.20	7.69	3.03	2.38	2.13	12.44	5.65
FeO*	5.23	2.89	5.86	10.17	6.04	34.49	18.42	24.00	24.39	23.34	13.94	23.10	8.39	42.25	21.75	24.23	29.41
MnO	0.20	0.13	0.32	0.07	0.18	0.80	0.19	0.38	1.02	0.32	0.04	0.46	0.03	0.09	0.30	0.30	0.23
MgO	2.01	0.66	1.88	0.36	1.23	5.13	4.14	5.99	7.62	2.67	2.13	4.61	0.95	1.21	2.25	3.16	2.21
CaO	4.47	3.70	5.86	0.35	3.60	4.77	4.45	7.75	16.64	0.08	0.04	5.62	0.03	0.03	3.56	0.09	1.23
Na_2O	<	<	<	<	0.00	0.08	0.17	0.12	0.12	<	<	0.08	<	<	<	<	<
K_2O	<	<	<	0.00	0.00	0.00	1.52	0.29	0.00	0.00	0.00	0.30	0.06	0.01	0.01	0.00	0.01
P_2O_5	<	<	0.01	0.01	0.01	0.18	0.19	0.12	0.13	0.04	0.02	0.11	0.02	0.03	0.01	0.05	0.03
LOI	7.39	4.99	8.84	4.99	6.55	9.11	8.32	12.81	22.42	4.15	3.86	10.11	6.22	19.53	9.03	4.44	11.00
S	0.21	0.16	0.26	6.41	1.76	0.80	0.04	0.17	0.28	0.77	3.40	0.91	9.97	27.66	7.75	1.36	12.26
TOTAL	99.22	99.32	99.23	98.54	99.08	97.62	99.54	98.85	95.46	99.30	98.47	98.21	97.80	95.14	96.69	99.71	97.18
La	<	<	4	<	1	7	17	7	15	8	<	9	7	<	10	35	15
Ce	<	<	7	<	2	28	34	16	27	14	<	20	12	<	23	63	28
Nd	<	<	2	<	0	4	16	7	12	3	<	7	4	<	9	26	12
Nb	<	<	<	<	0.0	<	9.7	2.4	1.7	2.1	<	2.7	<	<	2.5	9.0	3.8
Zr	3	2	9	2	4	23	228	63	52	71	14	75	38	7	64	275	115
Sr	9	31	7	2	12	15	52	70	22	1	2	27	4	3	14	3	7
Cr	3	2	4	26	9	25	12	242	26	44	1521	312	11	552	2	16	190
Ba	<	<	3	13	4	8	290	64	9	7	14	65	<	6	8	11	8
Sc	<	<	2	<	1	12	29	45	22	16	10	22	5	6	<	12	6
V	3	2	15	3	6	49	58	177	113	49	83	88	62	47	3	34	28
Sn	2.0	1.0	1.0	16.6	5.2	<	2.1	<	2.8	4.9	25.2	5.8	124.7	3.7	73.3	20.9	32.6
Cu	64.0	132.0	176.0	8300.0	2168.0	101.0	110.0	43.0	386.0	39.0	10620.0	1883.2	1500.0	2800.0	2077.0	3830.0	2902.3
Pb	9.0	170.0	4.0	20.0	50.8	3.0	11.0	30.0	7.0	<	28.0	13.2	688.0	231.0	14.0	59.0	101.3
Zn	39	553	39	235	217	206	288	531	228	1255	205	452	143240	1062	4420	835	2106
Ni	6	9	3	46	16	22	14	45	25	25	65	33	Zn intf	87	Zn intf	12	33
Y	4	8	6	2	5	17	50	23	29	8	5	22	8	3	17	71	30
Rb	<	<	<	<	0	<	35	6	<	<	<	7	2	<	<	<	0
Ag	0.2	0.7	1.1	7.1	2.3	0.3	0.3	0.3	2.5	0.5	8.8	2.1	33.8	9.1	7.5	7.9	8.2
As	91	32	10	54	47	5080	21	8	150	596	43	983	192	454	24	21	166
Bi	<	0.4	<	8.2	2.2	<	0.2	0.2	0.1	<	2.6	0.5	17.2	49.6	1.5	0.5	17.2
Mo	0.2	0.3	0.4	0.3	0.3	0.2	1.0	0.4	0.4	0.2	1.0	0.5	0.4	4.3	0.9	6.3	3.8
Cd	<	5.0	0.1	1.3	1.6	0.2	0.3	1.7	0.3	4.6	1.0	1.4	473.0	3.0	33.5	1.9	12.8
Sb	4.5	2.1	1.1	3.1	2.7	7.7	1.8	2.0	2.2	1.4	1.9	2.8	11.6	13.9	2.4	4.0	6.8
Cs	<	<	<	<	0.00	0.12	0.62	0.35	<	<	<	0.18	0.05	0.06	0.06	0.17	0.10
Tl	<	<	<	<	0.0	<	2.7	0.6	<	<	<	0.6	8.0	0.6	<	<	0.2
Th	<	<	0.12	<	0.03	0.63	5.53	1.45	1.70	2.06	0.38	1.96	1.19	0.08	1.41	6.63	2.71
U	<	<	<	<	0.00	0.18	1.09	0.34	0.26	0.46	0.09	0.40	0.30	0.08	0.32	1.66	0.69

FeO* indicates total iron as Fe^{2+}; analyses are un-normalised, < indicates below detection; Zn intf = not determined due to zinc interference, LOI=loss on ignition.

'Average' denotes the average values for each alteration type sample group as shown; major elements, LOI and S in wt.%, trace elements in ppm.

Appendix A6.2: Major and trace element analyses of altered volcaniclastic rocks from the Golden Grove Formation (*continued*)

	GGF M5 : Carbonate nodular alteration					GGF M4 : Chlorite alteration				GGF M4 : Magnetite			GGF M6 : Andalusite alteration				GGF M4 : Siliceous nodules		
SAMPLE	760411	SCDOO1	760410	769066	Average	769151	769061	769053	Average	760356	769077	Average	760465	760441	760434	Average	769174	769267	Average
DDH	GG127	Scuddles	GG127	GG027		GG157	GG027	GG027		GG118	GG027		GG160	GG165	GG165		GG162	GG070	
depth	179.4		179.0	369.5		269.8	336.7	287.3		250.5	280.4		332.1	379.9	339.3		285.4	303.4	
SiO_2	54.72	58.07	60.42	71.08	61.07	22.10	18.72	33.30	24.71	42.11	14.95	28.53	18.03	10.92	17.68	15.54	55.04	49.75	52.40
TiO_2	0.19	0.30	0.29	0.16	0.24	0.38	0.09	0.62	0.36	0.07	0.10	0.09	0.51	0.13	0.75	0.46	0.25	0.33	0.29
Al_2O_3	7.25	11.81	11.31	9.35	9.93	14.63	3.26	18.23	12.04	2.49	3.25	2.87	18.19	4.49	11.35	11.34	10.39	12.74	11.57
FeO*	7.67	5.74	9.50	11.74	8.66	37.56	68.28	31.15	45.66	41.04	57.52	49.28	45.00	56.11	52.68	51.26	17.53	20.10	18.82
MnO	0.13	0.01	0.03	0.05	0.06	0.07	0.02	0.06	0.05	0.11	0.20	0.16	0.16	0.20	0.25	0.20	0.04	0.04	0.04
MgO	11.13	15.21	11.91	3.81	10.52	12.67	7.23	8.98	9.63	4.43	5.31	4.87	4.94	3.62	5.14	4.57	9.49	8.89	9.19
CaO	6.37	1.12	0.35	0.00	1.96	0.02	0.60	0.31	0.31	1.59	5.91	3.75	0.01	0.55	0.20	0.25	0.91	0.77	0.84
Na_2O	0.04	0.05	0.03	0.06	0.05	<	<	<	0.00	<	<	<	<	<	<	<	0.04	0.06	0.05
K_2O	0.00	0.00	0.00	0.22	0.06	0.00	0.00	0.00	0.00	0.00	0.00	0.00	0.00	0.00	0.00	0.00	0.00	0.00	0.00
P_2O_5	0.03	0.01	0.03	0.01	0.02	0.02	0.02	0.19	0.08	0.02	0.17	0.10	0.03	0.03	0.13	0.06	0.01	0.01	0.01
LOI	10.90	7.07	5.76	3.18	6.73	9.63	1.51	6.73	5.96	6.66	11.37	9.02	10.39	17.69	7.17	11.75	5.61	6.46	6.04
S	0.23	0.01	<	<	0.06	4.19	0.00	0.02	1.40	0.85	0.09	0.47	12.39	24.19	7.17	14.58	0.02	<	0.02
TOTAL	98.43	99.39	99.63	99.66	99.28	98.36	99.73	99.64	99.24	98.55	98.78	98.67	97.35	94.84	98.05	96.75	99.31	99.16	99.24
La	20	26	30	24	25	48	12	41	34	8	21	14	54	35	40	43	25	28	26
Ce	43	52	57	48	50	60	19	73	51	8	29	19	97	53	68	73	46	54	50
Nd	23	25	30	22	25	26	10	36	24	3	15	9	48	23	33	35	21	25	23
Nb	8.2	11.5	10.9	8.9	9.9	12.5	<	8.5	7.0	2.0	<	1.0	16.5	3.0	2.0	7.2	9.3	11.3	10.3
Zr	217	339	315	243	279	365	83	199	216	61	66	64	495	115	100	237	270	312	291
Sr	50	4	3	4	15	4	4	4	4	12	26	19	4	4	2	3	6	5	5
Cr	2	2	3	2	2	4	5	10	6	4	4	4	9	11	8	9	2	3	3
Ba	3	12	4	67	21	16	<	10	9	4	<	2	4	<	<	1	5	8	6
Sc	12	12	9	5	9	15	7	36	19	6	10	8	24	7	48	26	9	11	10
V	4	7	7	<	4	2	<	47	16	2	6	4	13	4	213	77	<	<	0
Sn	3.0	3.0	3.0	4.0	3.3	10.8	9.0	7.4	9.0	4.4	11.6	8.0	1.0	4.2	138.0	47.7	4.0	1.8	2.9
Cu	32.0	4.0	4.0	4.0	11.0	10070.0	18.0	41.0	3376.3	204.0	37.0	120.5	347.0	4390.0	377.0	1704.7	217.0	6.0	111.5
Pb	8.0	2.0	4.0	4.0	4.5	8.0	<	2.0	3.3	<2	2.0	1.0	19.0	315.0	2662.0	998.7	5.0	<	2.5
Zn	161	27	217	208	153	151	63	612	275	55	31	43	361	4970	18900	8077	53	81	67
Ni	2	1	2	2	2	3	1	4	3	<2	2	1	3	Zn intf	Zn intf	1	1	2	2
Y	60	73	72	58	66	45	19	41	35	19	18	19	118	32	26	59	55	53	54
Rb	<	<	<	4	1	<1	1	<1	0	<	<	<	<	<	<	0	<	<	0
Ag	0.6	0.1	0.2	0.1	0.3	1.0	<	0.1	0.4	0.1	<	0.1	1.0	16.4	9.2	8.9	0.2	0.1	0.2
As	3	5	<	<	2	5	<	<	2	<	21	11	43	844	8	298	1	12	7
Bi	0.3	<	<	<	0.1	11.3	0.1	7.5	6.3	0.6	17.5	9.1	6.4	123.0	23.6	51.0	0.3	0.1	0.2
Mo	0.1	<	0.3	1.2	0.4	3.1	3.2	10.4	5.6	0.3	28.4	14.4	2.7	5.0	0.3	2.7	5.1	2.4	3.8
Cd	0.1	<	<	0.1	0.1	1.0	0.3	0.8	0.7	0.2	0.2	0.2	0.3	15.1	67.8	27.7	0.3	0.1	0.2
Sb	1.2	1.9	0.7	1.4	1.3	0.9	4.2	1.5	2.2	3.9	5.5	4.7	3.8	12.0	4.8	6.9	1.0	1.2	1.1
Cs	0.19	2.43	0.24	0.24	0.78	0.22	0.19	0.59	0.33	0.06	0.10	0.08	0.42	0.07	0.08	0.19	0.15	0.25	0.20
Tl	<	<	<	<	0.0	<	<	<	0.0	<	<	<	<	<	1.6	0.5	<	<	<
Th	4.26	6.45	6.36	5.18	5.56	8.37	1.83	4.65	4.95	1.25	1.42	1.34	11.30	2.71	2.55	5.52	5.81	6.83	6.32
U	0.87	1.46	1.33	1.12	1.20	2.02	0.42	1.31	1.25	0.30	0.46	0.38	3.10	0.91	0.50	1.50	1.54	1.55	1.55

FeO* indicates total iron as Fe^{2+}; analyses are un-normalised, < indicates below detection; Zn intf = not determined due to zinc interference, LOI=loss on ignition.

'Average' denotes the average values for each alteration type sample group as shown; major elements, LOI and S in wt.%, trace elements in ppm.

Appendix A7.1

Grid line geometry specifications used in Surfer (v. 6.2, Golden Software Incorporated) to generate contoured east-west sections, plan projections and north-south long sections. The method used linear kriging with the specifications listed below.

Composite section 18,300 N (C zone only)

Northing	>18,200 N	<18,400 N		(100 m window)
	minimum	**maximum**	**grid (metres)**	**line spacing**
East	4,774	4,907	5	27
RL	9,964	10,217	5	51

Section 18,280 N

Northing	>18,260 N	<18,300 N		(20 m window)
	minimum	**maximum**	**grid (metres)**	**line spacing**
East	4,790	5,060	5	55
RL	9,900	10,270	5	73

Section 18,360 N

Northing	>18,340 N	<18,380 N		(20 m window)
	minimum	**maximum**	**grid (metres)**	**line spacing**
East	4,945	5,085	5	29
RL	9,930	10,260	5	67

Section 18,480 N

Northing	>18,460 N	<18,500 N		(20 m window)
	minimum	**maximum**	**grid (metres)**	**line spacing**
East	5,017	5,130	5	23
RL	9,933	10,237	5	62

Section 18,560 N

Northing	>18,540 N	<18,580 N		(20 m window)
	minimum	**maximum**	**grid (metres)**	**line spacing**
East	5,034	5,141	5	22
RL	9,962	10,242	5	56

Level Plan 10,150 RL

RL	>10,100 RL	<10,200 RL		(50 m window)
	minimum	**maximum**	**grid (metres)**	**line spacing**
North	18,067	18,766	5	140
East	4,774	5,126	5	71

Composite Long Projection 5,000 E

East	>4,800 E	<5,150 E		(200 m window)
	minimum	**maximum**	**grid (metres)**	**line spacing**
North	18,100	18,700	5	160
RL	9,900	10,270	5.1	101

Appendix A7.2

Drill holes used in metal ratios, contour plots and relational metal diagrams.

The upper Zn-rich ore zone in GGF M6

Composite section 18,300 N (100 m window)

G96/141	G96/152	G96/166	G96/179	G96/188
G96/142	G96/153	G96/167	G96/180	G96/189
G96/143	G96/154	G96/168	G96/181	G96/190
G96/144	G96/158	G96/169	G96/182	G96/191
G96/145	G96/159	G96/170	G96/183	G96/192
G96/146	G96/160	G96/171	G96/184	G96/193
G96/147	G96/161	G96/172	G96/185	G96/194
G96/148	G96/162	G96/173	G96/186	G96/195
G96/149	G96/163	G96/174	G96/187	G96/196
G96/150	G96/164	G96/178	G96/188	G96/197
G96/151	G96/165			

The upper Zn- and Cu-rich stockwork zone across GGF M6 and GGF M4

Section 18,280 N (20 m window)

G96/94	G96/149	G96/162	G96/173	G96/187
G96/95	G96/150	G96/163	G96/174	G96/188
G96/96	G96/151	G96/164	G96/178	G96/189
G96/97	G96/152	G96/165	G96/179	G96/190
G96/98	G96/153	G96/166	G96/180	G96/191
G96/99	G96/154	G96/167	G96/181	G96/192
G96/100	G96/158	G96/168	G96/182	G96/193
G96/101	G96/159	G96/169	G96/183	G96/194
G96/102	G96/160	G96/170	G96/184	G96/195
G96/103	G96/161	G96/171	G96/185	G96/196
		G96/172	G96/186	G96/197

The lower Cu-rich ore zone in GGF M4

Section 18,360 N (20 m window)

G96/77	G96/80	G96/82	G96/84	GG184
G96/78	G96/81	G96/83	G96/85	GG185
G96/79				

Section 18,480 N (20 m window)

G96/52	G96/57	G96/107	G96/112	G96/137
G96/53	G96/58	G96/108A	G96/113	G96/138A
G96/54	G96/59	G96/109	G96/114	G96/139
G96/55	G96/60	G96/110	G96/115	G96/140
G96/56	G96/67	G96/111	G96/136A	

Section 18,560 N (20 m window)

G96/35	G96/40	G96/122	G96/127	G96/131
G96/36	G96/41	G96/123	G96/128	G96/132
G96/37	G96/42	G96/124	G96/129	G96/133
G96/38	G96/116	G96/125	G96/129A	G96/134
G96/39	G96/121	G96/126	G96/130	G96/135

Appendix A7.2 *(continued)*

Plan Projection 10,150 RL (50 m window)

G96/1	G96/37	G96/90	G96/120	G96/164
G96/2	G96/38	G96/91	G96/121	G96/169
G96/3	G96/39	G96/96	G96/122	G96/170
G96/7	G96/44	G96/97	G96/123	G96/171
G96/8	G96/45	G96/99	G96/124	G96/172
G96/10A	G96/46	G96/100	G96/127	G96/180
G96/11	G96/47	G96/104	G96/128	G96/181
G96/12	G96/52	G96/105	G96/129A	G96/182
G96/15	G96/53	G96/106	G96/130	G96/183
G96/16	G96/54	G96/107	G96/131	G96/187
G96/17	G96/55	G96/108A	G96/132	G96/188
G96/20	G96/61	G96/110	G96/136A	G96/191
G96/21	G96/62	G96/111	G96/139	G96/192
G96/22	G96/63	G96/112	G96/140	G96/193
G96/23	G96/69	G96/113	G96/142	G96/196
G96/27	G96/80	G96/114	G96/143	GG173
G96/28	G96/81	G96/115	G96/149	GG176
G96/29	G96/83	G96/116	G96/150	GG184
G96/30	G96/84	G96/117	G96/151	GG187
G96/35	G96/88	G96/118	G96/160	GG188
G96/36	G96/89	G96/119	G96/163	

Long Projection 5,000 E (200 m window)

G96/1	G96/40	G96/83	G96/124	G96/171
G96/2	G96/41	G96/84	G96/125	G96/172
G96/3	G96/42	G96/85	G96/126	G96/173
G96/4	G96/43	G96/86	G96/127	G96/174
G96/5	G96/44	G96/87	G96/128	G96/178
G96/6	G96/45	G96/88	G96/129A	G96/179
G96/7	G96/46	G96/89	G96/130	G96/180
G96/8	G96/47	G96/90	G96/131	G96/181
G96/9	G96/48	G96/91	G96/132	G96/182
G96/10	G96/49	G96/92	G96/133	G96/183
G96/11	G96/51	G96/93	G96/134	G96/184
G96/12	G96/52	G96/94	G96/135	G96/185
G96/13	G96/53	G96/95	G96/136A	G96/186
G96/14	G96/54	G96/96	G96/137	G96/187
G96/15	G96/55	G96/97	G96/138A	G96/188
G96/16	G96/56	G96/98	G96/139	G96/189
G96/17	G96/57	G96/99	G96/140	G96/190
G96/18	G96/58	G96/100	G96/141	G96/191
G96/19	G96/59	G96/101	G96/142	G96/192
G96/20	G96/60	G96/102	G96/143	G96/193
G96/21	G96/61	G96/103	G96/149	G96/194
G96/22	G96/62	G96/104	G96/150	G96/195
G96/23	G96/63	G96/105	G96/151	G96/196
G96/24	G96/64	G96/106	G96/152	G96/197
G96/25	G96/65	G96/107	G96/153	GG172
G96/26	G96/66	G96/108A	G96/154	GG173
G96/27	G96/67	G96/110	G96/158	GG174
G96/28	G96/68	G96/111	G96/159	GG175X
G96/29	G96/69	G96/112	G96/160	GG176
G96/30	G96/70	G96/113	G96/161	GG177
G96/31	G96/71	G96/114	G96/162	GG181
G96/32	G96/72	G96/115	G96/163	GG182
G96/33	G96/73	G96/116	G96/164	GG183
G96/34	G96/74	G96/117	G96/165	GG184
G96/35	G96/77	G96/118	G96/166	GG185
G96/36	G96/78	G96/119	G96/167	GG186
G96/37	G96/79	G96/120	G96/168	GG187
G96/38	G96/80	G96/121	G96/169	GG188
G96/39	G96/81	G96/122	G96/170	GG189
	G96/82	G96/123		

Appendix A7.3

Details of the MZC drill hole database used in Zn and Cu ratio diagrams, contour diagrams and scatter diagrams. Examples of drill hole nomenclature is given below.

G96/111	underground diamond drill hole completed during the 1994-1997 feasibility study
GG111	surface diamond drill hole completed during the 1994-1997 feasibility study

Logging codes used by MZC geologists to classify ore types are listed in Table A7.1.

Table A7.1: Ore classification used by MZC at the Gossan Hill deposit

MZC Code	description	% total sulphide	% sulphide	% magnetite
MS	massive sulphide	>90 %		-
MSS	massive sphalerite	>90 %	>30 % sphalerite	-
MSO	massive sphalerite-pyrite	>90 %	10-30 % sphalerite	-
MSP	massive pyrite	>90 %	<10 % sphalerite	-
			<5 % chalcopyrite	-
MSC	massive pyrite-chalcopyrite	>90 %	>5 % chalcopyrite	-
MM	massive magnetite	<10 %		>90 %
MMC	massive magnetite-chalcopyrite	<10 %	>5 % chalcopyrite	>90 %
BS	semi-massive sulphide	50-90 %		-
BSS	semi-massive sphalerite	50-90 %	<10 % sphalerite	-
BSP	semi-massive pyrite	50-90 %	<50 % pyrite	-
BSC	semi-massive chalcopyrite	50-90 %	<5 % chalcopyrite	-
BSM	semi-massive sulphide-magnetite	50-90 %		<50 %
BMS	semi-massive magnetite-sulphide	<50 %		50-90 %
BMSC	semi-massive magnetite-sulphide-chalcopyrite	<50 %	<5 % chalcopyrite	50-90 %
BMC	semi-massive magnetite-chalcopyrite	<10 %	>5 % chalcopyrite	50-90 %
SS	stringer mineralisation	variable	variable	variable

For the purpose of metal contouring in this thesis, the MZC ore classification codes were simplified. Ores were divided firstly on the basis of lithology and their occurrence within the upper or lower ore zones:

GGF M6	upper ore zone	bedded epiclastic-tuffaceous wall rock host sequence
GGF M4	lower ore zone	bedded tuffaceous wall rock host sequence

For both the upper and lower ore zones, the ore types were subdivided into 6 major classifications as listed in Table A7.2, based on the major ore mineral and irrespective of Cu concentrations.

Table A7.2: Subdivision of the MZC ore code classification in to the six categories used in metal ratio plots, contour and scatter diagrams.

Code	description	MZC codes
MSS	sphalerite dominated ore	MSS, BSS, MSO
MSP	pyrite dominated ore	MS, MSC ,BS, BSC, BSP, BSM, BSMC, BPM, BSS
MM	magnetite dominated ore	MM, MMP, MMC, BM, BMC, BMS, BMSC
SS	stringer mineralisation (magnetite and pyrite-rich)	SS
SF	unmineralised wall rock either GGF M6 or M4	M6, M4

Appendix A7.4

Zn ratio and Zn-Pb metal variation for the different ore types and wall rock in GGF M6. Data used is MZC assay data from a composite section along 18,300N (GGF M6) and drill holes along this section are listed in Appendix A7.2. SD = standard deviation. Values of Zn and Pb less than 0.02 % are not plotted.

(a) GGF M6 Zn ratio and Zn-Pb variation in massive sphalerite

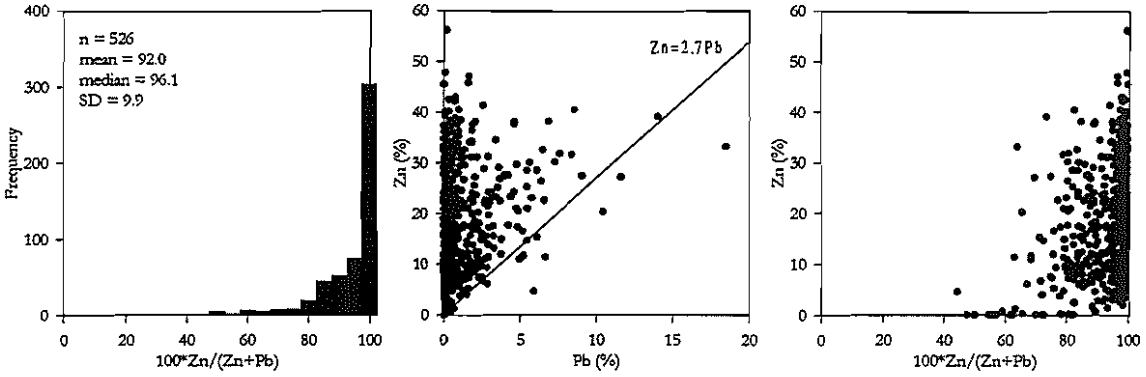

(b) GGF M6 Zn ratio and Zn-Pb variation in massive pyrite

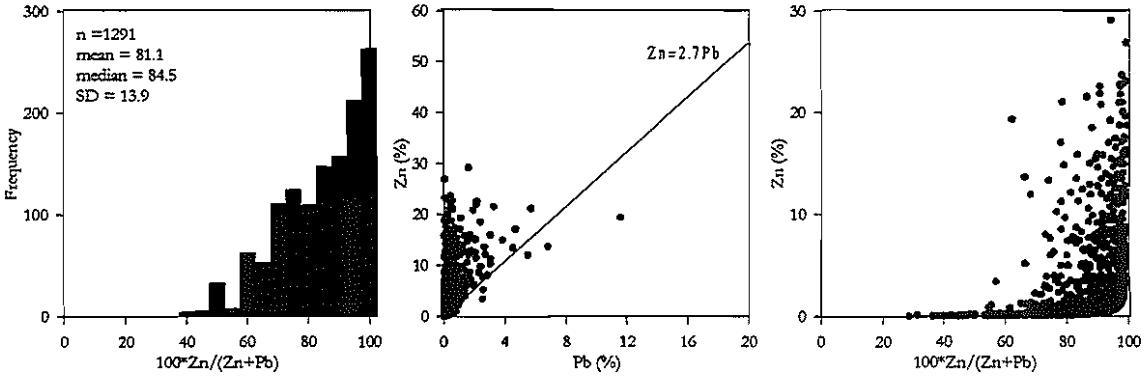

(c) GGF M6 Zn ratio and Zn-Pb variation in stringer vein zones

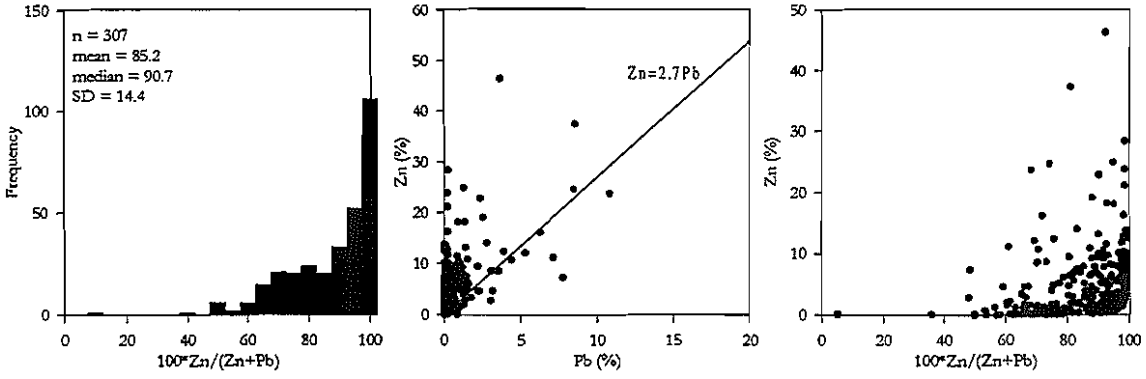

(d) GGF M6 Zn ratio and Zn-Pb variation in the wall rock

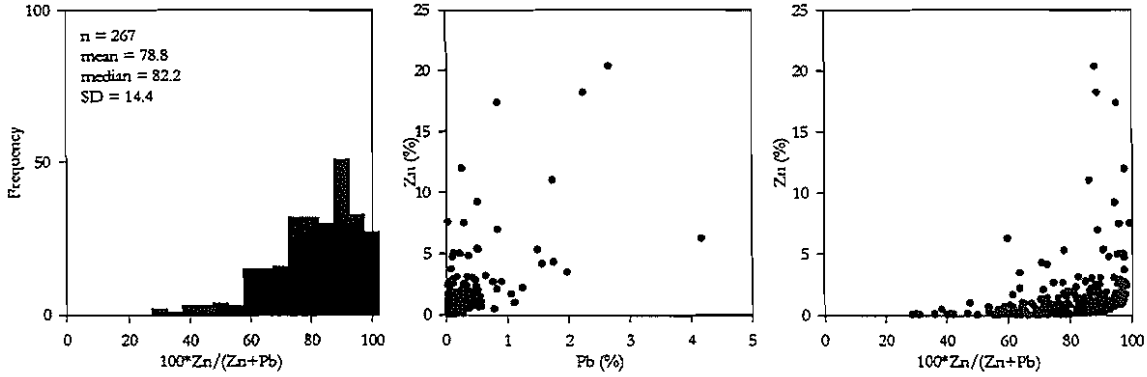

Appendix A7.4 (continued)

Cu ratio and Cu-Zn metal variation for the different ore types and wall rock in GGF M6. Data used is MZC assay data from a composite section along 18,300N (GGF M6) and drill holes along this section are listed in Appendix A7.2. SD = standard deviation. Values of Cu and Zn less than 0.02 % are not plotted.

(e) GGF M6 Cu ratio and Cu-Zn variation in massive sphalerite

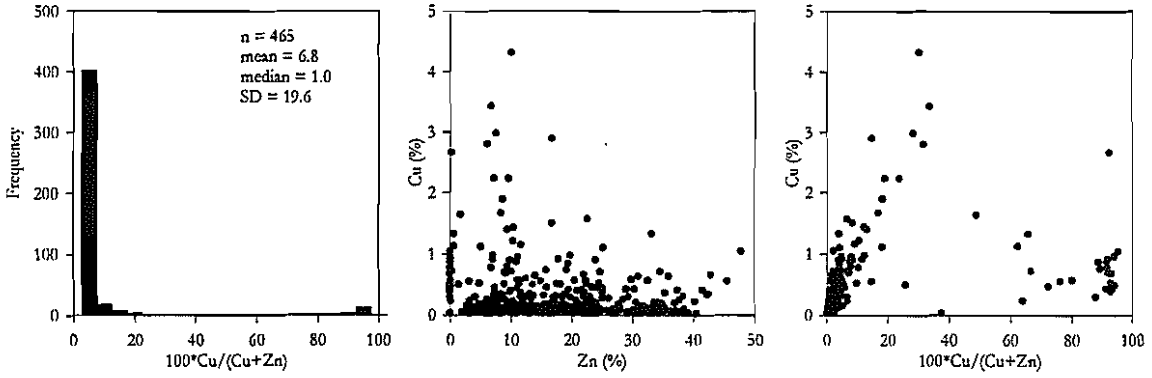

(f) GGF M6 Cu ratio and Cu-Zn variation in massive pyrite

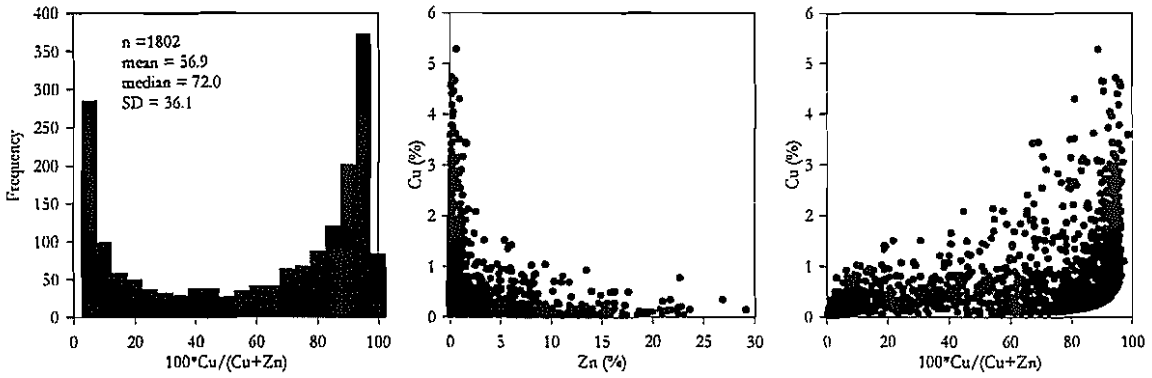

(g) GGF M6 Cu ratio and Cu-Zn variation in stringer mineralisation

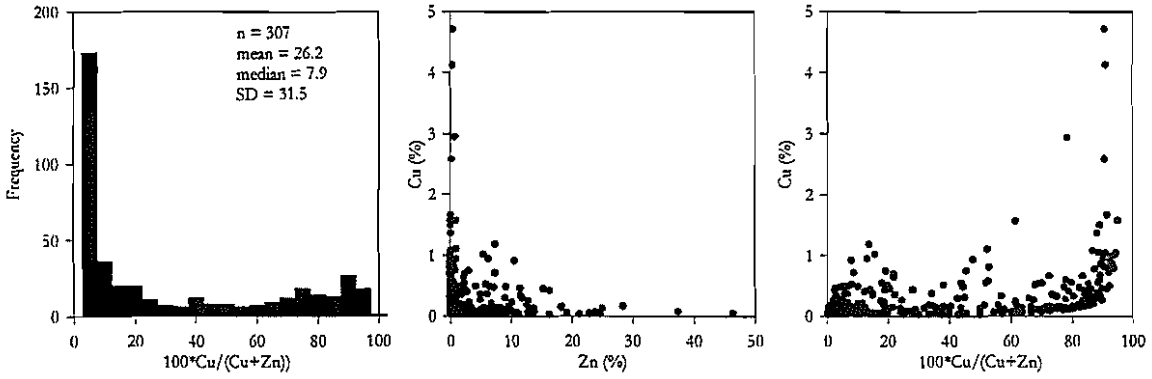

(h) GGF M6 Cu ratio and Cu-Zn variation in the wall rock

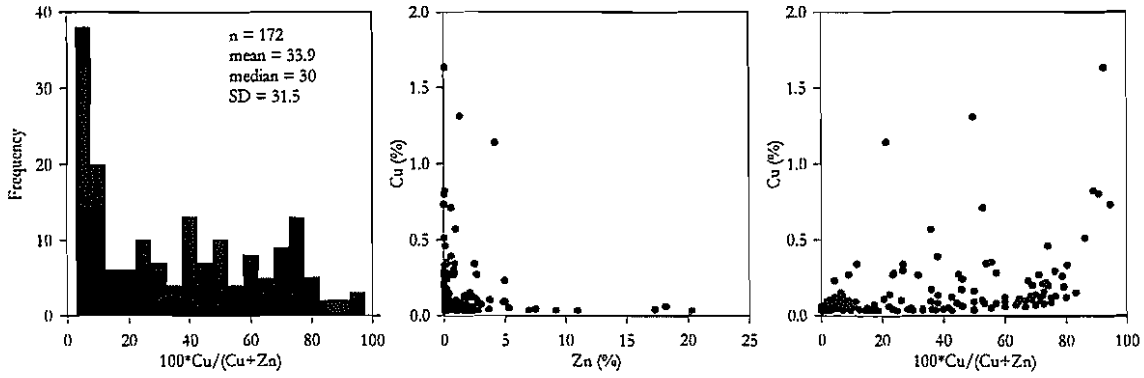

Appendix A7.5

Zn ratio and Zn-Pb metal variation for the different ore types and wall rock in GGF M4. Data used is MZC assay data from east-west sections 18,480 N and 18,560 N (GGF M4) and drill holes along this section are listed in Appendix A7.2. SD = standard deviation. Values of Zn and Pb less than 0.02 % are not plotted.

(a) GGF M4 Zn ratio and Zn-Pb variation in massive pyrite

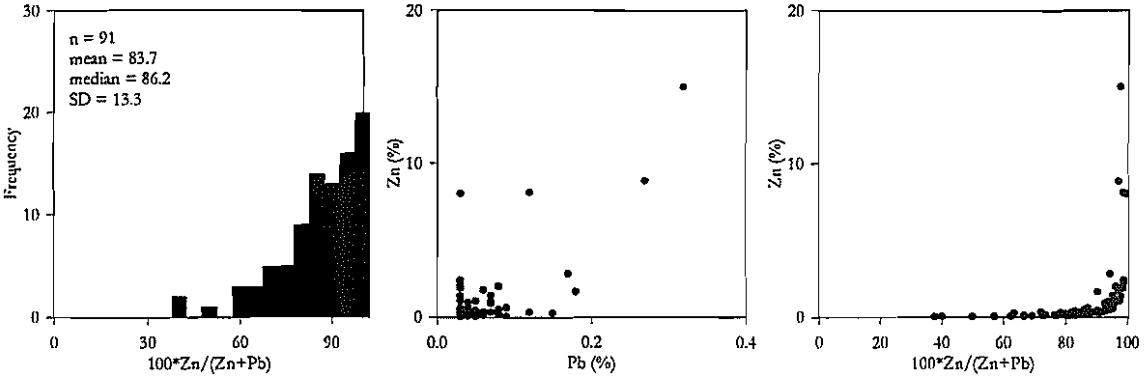

(b) GGF M4 Zn ratio and Zn-Pb variation in massive magnetite

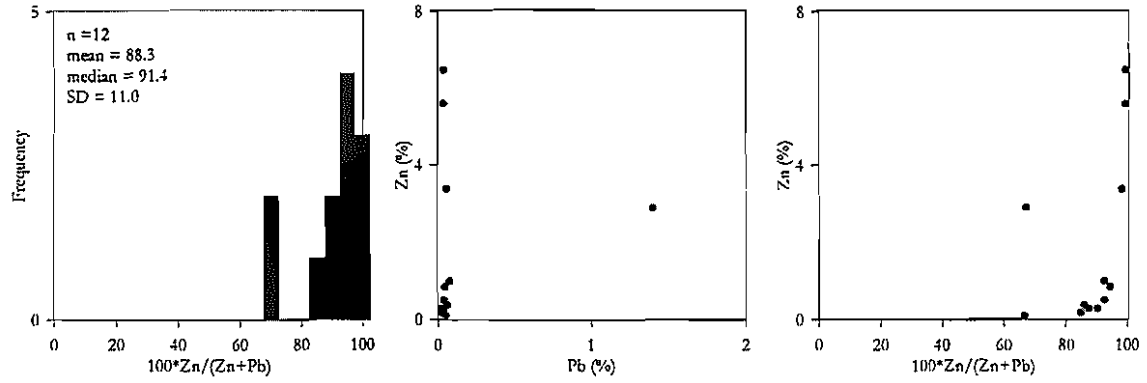

(c) GGF M4 Zn ratio and Zn-Pb variation in stringer vein zones

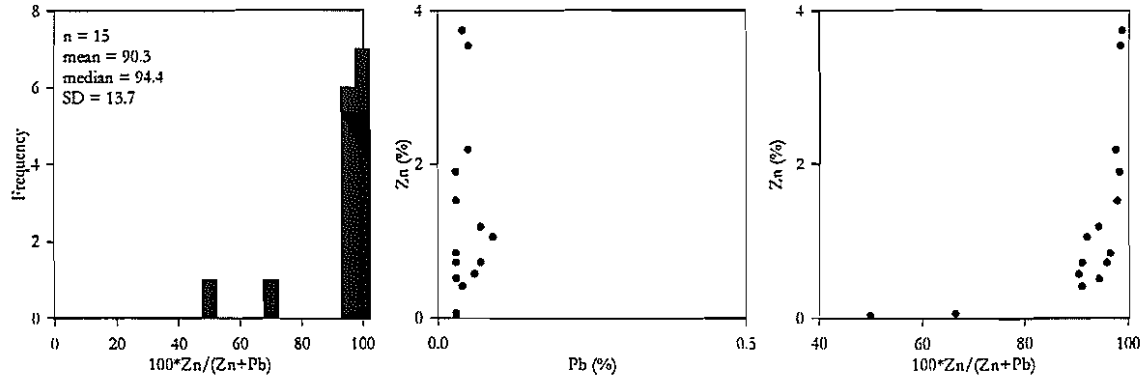

(d) GGF M4 Zn ratio and Zn-Pb variation in the wall rock

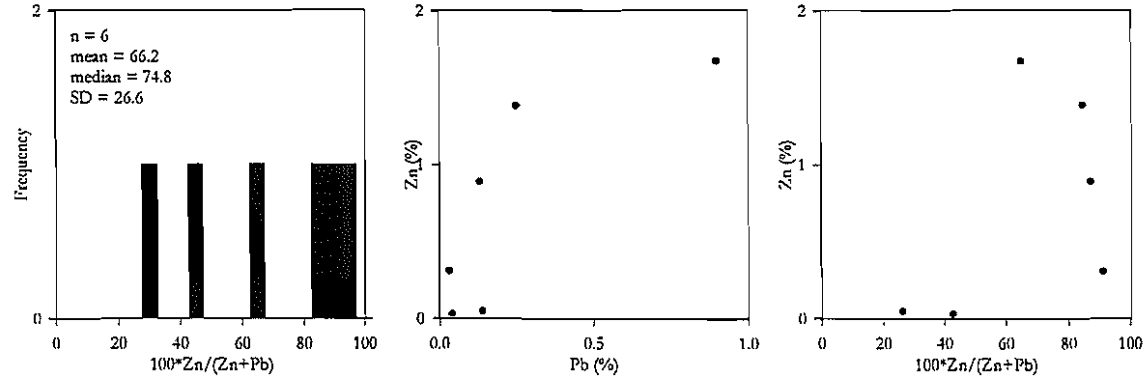

Appendix A7.5 (continued)

Cu ratio and Cu-Zn metal variation for the different ore types and wall rock in GGF M4. Data used is MZC assay data from east-west sections 18,480 N and 18,560 N (GGF M4) and drill holes along this section are listed in Appendix A7.2. SD = standard deviation. Values of Cu and Zn less than 0.02 % are not plotted.

(e) GGF M4 Cu ratio and Cu-Zn variation in massive pyrite

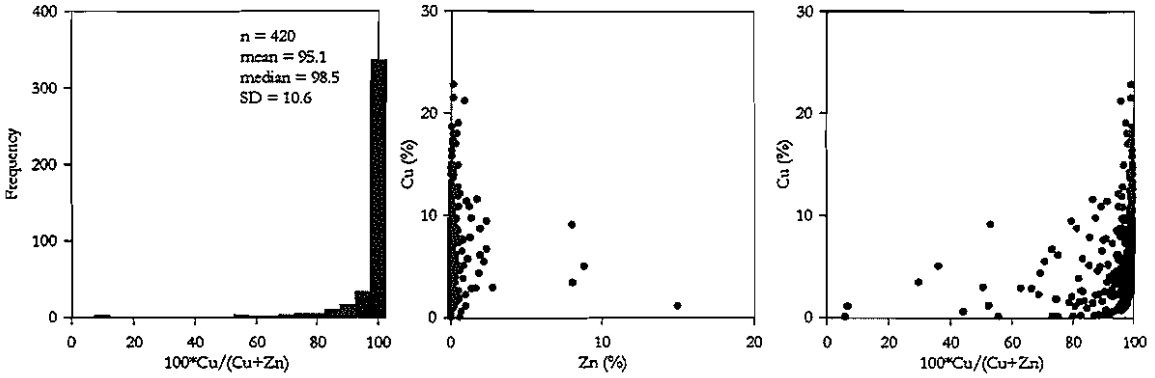

(f) GGF M4 Cu ratio and Cu-Zn variation in massive magnetite

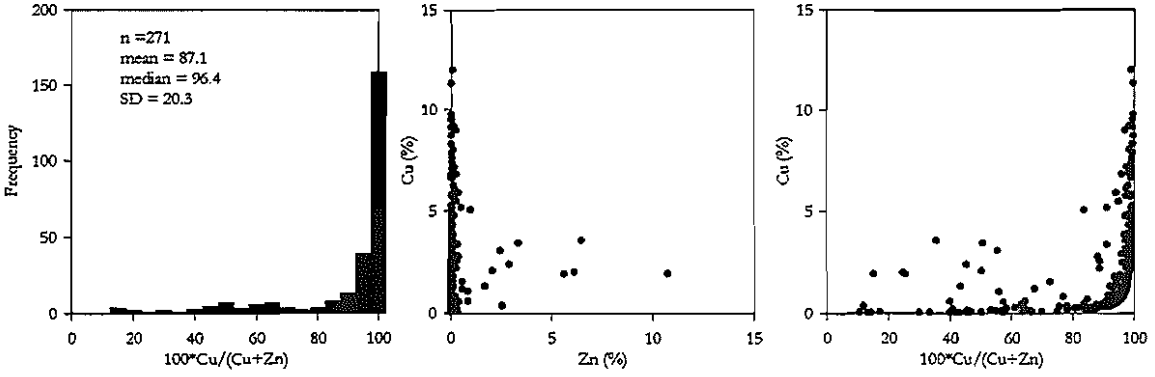

(g) GGF M4 Cu ratio and Cu-Zn variation in stringer vein zones

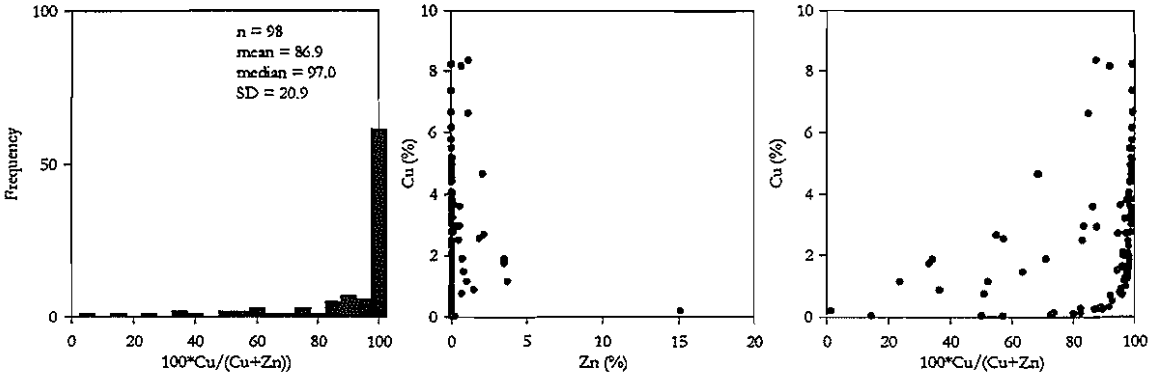

(h) GGF M4 Cu ratio and Cu-Zn variation in the wall rock

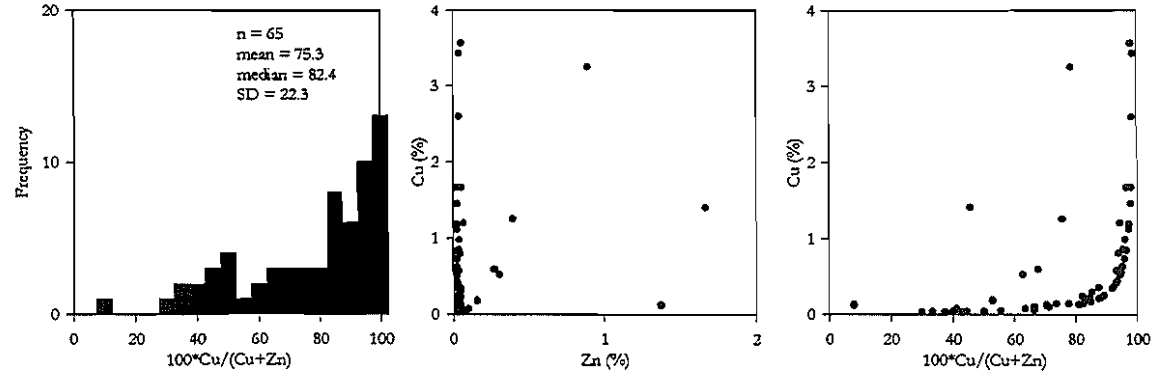

Appendix A8.1: Sulphur isotope data from sulphides at Gossan Hill

								$\delta^{34}S_{CDT}$ (per mil)					T ° C			
Sample	Description	Method	Strata	Geology	Drill Hole	Depth	Vein Type	py	sp	ga	cp	po	sp-ga	py-cp	py-po	py-sp
760222	banded rd mas sp with minor mgt and si wall rock clasts	C	M6	MSS	GG132	368.9			1.8							
760224	rx c.g mas sp minor mgt	C	M6	MSS	GG132	370.0			1.5							
760225	mas f.g sp-py	C	M6	MSS	GG132	370.5		6.1	2.0							-2
760226	py-sp in intense si wall rock	C	M6	MPY	GG132	371.0			4.7							
760227	mas py-sp	C	M6	MPY	GG132	371.7		7.8	3.0			5.0			54	-23
760228	bn mas sp-py with ds mgt	C	M6	MSS	GG132	373.2		3.1	3.1							
760230	large py in py-sp vein in intense si wall rock	C	M6	STZ	GG132	374.6	IV (B)	3.8	3.6							
760362	rx rd c.g mas sp-ga-py-cp with minor mgt	C	M6	MSS	GG134	124.6			3.0	1.2			354			
760364	py euhedra in bedded polymict breccia	C	M6	WR	GG134	130.1		0.7								
760366	intense chl alteration with disseminated mgt-py-po	C	M6	WR	GG134	163.1		3.8				2.8			255	
760367	rx rd-bn mas sp-py (-chl)	C	M6	MSS	GG134	169.2		3.5	3.8							
760368	nodular py in intense py-chl altered wall rock	C	M6	WR	GG134	199.3		2.2								
760370	semi-mas py-mgt (-si)	C	M6	MPY	GG134	205.2		2.9								
760371	mgt-py-co stringer vein in chl wall rock	C	M6	STZ	GG134	211.4	IV (A)	1.9								
760372	py-mgt-chl-co vein in mas py-mgt	C	M6	STZ	GG134	221.1	IV (A)	3.6								
760373	py-sp-chl-co vein in intense si wall rock	C	M6	STZ	GG134	224.6	IV (B)	4.1	3.1							283
760374	py-mgt vein in intene si wall rock	C	M6	STZ	GG134	225.7		3.5								
760417	rd-or f.g. mas sp-py	C	M6	MSS	GG165	271.0		3.3	3.7							
760418	bn rx mas sp in vein	C	M6	STZ	GG165	272.2	IV (B)		3.3							
760419	bn rx mas sp	C	M6	MSS	GG165	273.9			3.4							
760420	rd-bn rx mas sp with py bands	C	M6	MSS	GG165	277.0		3.0	3.1							
760421	f.g mas py with minor sp	C	M6	MPY	GG165	282.0		4.0	3.0							269
760423	f.g mas py with minor sp	C	M6	MPY	GG165	288.2		2.7								
760424	c.g. mas py	C	M6	MPY	GG165	293.2		2.5								
760425 (i)	f.g py aggregate in c.g. mas py	C	M6	MPY	GG165	296.4		3.1								
760425 (ii)	c.g. py rim to f.g aggregate in mas py	C	M6	MPY	GG165	296.4		3.1								
760425 (iii)	c.g. inner py rim to f.g py aggregate in mas py	C	M6	MPY	GG165	296.4		3.0								
760425 (iv)	c.g. outer py rim to f.g. py aggregate in mas py	C	M6	MPY	GG165	296.4		3.5								
760426	mas py cut by sp veins	C	M6	MPY	GG165	302.0	IV (B)	3.2	2.8							555
760428	mas sp-py-cp	C	M6	MSS	GG165	307.4		2.0	1.7							850
760430	disseminated py in c.g. sandstone	C	M6	WR	GG165	314.9		2.2								
760431	py vein through pebble breccia	C	M6	STZ	GG165	319.6	IV (B)	1.9								
760432	bn sp-co (-mgt) vein in intense chl wall rock	C	M6	STZ	GG165	331.6	IV (A)		3.2							

Abbreviations: C = conventional analysis, LA = laser ablation, M6 = Member 6 in the Golden Grove Formation, MPY = massive pyrite, MSS = massive sphalerite, STZ = stringer zone, WR = wall rock, ga = galena, tc = talc
py = pyrite, sp = sphalerite, cp = chalcopyrite, po= pyrrhotite, chl = chlorite, si = siliceous, mas = massive, mgt = magnetite, co = carbonate, f.g = fine grained, c.g = coarse grained, rx = recrystallised, rd = red, bn = brown, or = orange.
Note: formational temperature estimates only given where the $\delta^{34}S$ sulphide values have equilibrium (i.e., py > sp > cp > ga) and the difference is greater than 0.3 per mil due to analytical uncertainty

Appendix A8.1: Sulphur isotope data from sulphides at Gossan Hill *(continued)*

								$\delta^{34}S_{CDT}$ (per mil)					T ° C			
Sample	Description	Method	Strata	Geology	Drill Hole	Depth	Vein Type	py	sp	ga	cp	po	sp-ga	py-cp	py-po	py-sp
760436	py-po stringer vein in intense chl	C	M6	STZ	GG165	357.2	IV (B)	2.1								
760438	py vein in intense si wall rock	C	M6	STZ	GG165	365.5	IV (B)	2.1								
760440	nodular py in intense si-chl wall rock	C	M6	WR	GG165	377.0		1.8								
760441	tabular py grains disseminated in intense chl wall rock	C	M6	WR	GG165	379.9		1.7								
760442 (i)	f.g disseminated py in intense chl wall rock	C	M6	WR	GG165	380.3		2.1								
760442 (ii)	c.g. disseminated py in intense chl wall rock	C	M6	WR	GG165	380.3		1.6								
760443	py-mgt-co disseminations in chl wall rock	C	M6	WR	GG165	385.0		1.7								
760445	disseminated py grains in intense si wall rock	C	M6	WR	GG165	402.9		3.3								
760446	disseminated py in semi-mas mgt	C	M6	WR	GG165	424.2		2.4								
769054	py-chl-mgt vein in mas py	C	M4	STZ	GG027	288.6	IV (A)	1.9								
769057	mas py with disseminated mgt	C	M4	MPY	GG027	307.9		2.9								
769058	mas py with disseminated mgt	C	M4	MPY	GG027	313.6		3.4								
769151	co-py-cp-mgt vein in intense chl wall rock	C	M4	STZ	GG157	269.8	IV (A)	2.0				1.5			497	
769152	co-cp-po-py vein in intense chl wall rock	C	M4	STZ	GG157	219.9	IV (A)	2.1			1.7			911		
769153	disseminated cp in intense tc-chl alteration	C	M4	WR	GG157	222.8					1.6					
769209	py-po-mgt-chl-co vein in intense si wall rock	C	M5	STZ	GG139	223.8	IV (A)	1.8								
769260	mas cp-py	C	M4	MPY	GG070	263.7		1.5			1.7					
769263	cp-co-py-mgt vein in massive py-cp	C	M4	STZ	GG070	270.4	IV (A)	2.2			2.2					
769264	py-po-chl diffuse vein	C	M4	STZ	GG070	271.9	IV (A)	2.0								
769265	py-cp-co vein in mas mgt	C	M4	STZ	GG070	280.0	IV (A)	1.7			1.6					
769271	nodular py in vein in mas mgt-tc	C	M4	STZ	GG070	327.7	III	1.8								
769272	tc-co-chl-cp-po vein in intense tc-chl	C	M4	STZ	GG070	330.6	IV (A)				1.2					
769273	tc-py-po-co-cp-chl vein in intense chl	C	M4	STZ	GG070	333.3	IV (A)	1.0								
769274	chl-py vein in intense chl	C	M4	STZ	GG070	333.6	III	1.7								
769275	nodular py in py-tc-cp-po-chl vein	C	M4	STZ	GG070	342.7	IV (A)	0.5			1.3					
769280	cp-co-py vein cutting mas mgt	C	M4	STZ	GG070	383.3	IV (A)				1.3	1.6				
769281	nodular pyrite in a py-chl vein in mas mgt	C	M4	STZ	GG070	389.7	III	2.4								
769289	disseminated py-po in quartz sandstone	C	M4	WR	GG070	475.8		1.4								
769290	cp-py-co-po vein in intense si wall rock	C	M5	STZ	GG070	482.7	IV (A)	0.9			1.3					
769326	chl-cp-co-py vein in mas mgt	C	M4	STZ	GG045	265.9	IV (A)				1.7					
769327	co-py-mgt-po vein in intense chl wall rock	C	M4	STZ	GG045	269.3	IV (A)					2.2				
769334	py vein in intense si wall rock	C	M5	STZ	GG045	374.1	IV (B)	0.8								
769336	py-co-chl-mgt vein in intense si wall rock	C	M5	STZ	GG045	384.0	IV (A)	2.3								

Abbreviations: C = conventional analysis, LA = laser ablation, M6 = Member 6 in the Golden Grove Formation, MPY = massive pyrite, MSS = massive sphalerite, STZ = stringer zone, WR = wall rock, ga = galena, tc = talc

py = pyrite, sp = sphalerite, cp = chalcopyrite, po= pyrrhotite, chl = chlorite, si = siliceous, mas = massive, mgt = magnetite, co = carbonate, f.g = fine grained, c.g = coarse grained, rx = recrystallised, rd = red, bn = brown, or = orange.

Note: formational temperature estimates only given where the $\delta^{34}S$ sulphide values have equilibrium (i.e., py > sp > cp > ga) and the difference is greater than 0.3 per mil due to analytical uncertainty

Appendix A8.1: Sulphur isotope data from sulphides at Gossan Hill *(continued)*

								$\delta^{34}S_{CDT}$ (per mil)					T ° C			
Sample	Description	Method	Strata	Geology	Drill Hole	Depth	Vein Type	py	sp	ga	cp	po	sp-ga	py-cp	py-po	py-sp
769340(i)	py-chl vein in bedded sandstone	C	M6	STZ	GG045	411.9	III	1.0								
769340(ii)	chl-py-co-mgt vein in bedded sandstone	C	M6	STZ	GG045	411.9	IV (A)	1.7								
769343	sp vein in intense si wall rock	C	M6	STZ	GG045	428.6	IV (B)		1.2							
760383	disseminated py; large zoned py-rx euhedral core	LA	M6	WR	GG136	138.7		-0.3								
760383	disseminated py; large zoned py-skeletal rim to core	LA	M6	WR	GG136	138.7		0.5								
760383	disseminated py; large zoned py-outer skeletal rim	LA	M6	WR	GG136	138.7		1.6								
760383	disseminated py; large zoned dark py-mid rim	LA	M6	WR	GG136	138.7		0.3								
760362	rx sp-cp-ga	LA	M6	MSS	GG134	124.6			1.8	0.0			362			
760362	rx sp-cp-ga	LA	M6	MSS	GG134	124.6			2.4							
760444	nodular py in mas py (rx 1 mm grain)	LA	M6	MPY	GG165	395.6		-0.7								
760444	fractured py aggregate in mas py	LA	M6	MPY	GG165	395.6		-1.0								
760367	c.g mas sp-py	LA	M6	MSS	GG134	169.2		1.4	4.5							
760419	mas sp with ds py	LA	M6	MSS	GG165	273.9		2.5	2.4							
760225	bn-rd mas rx sp with disseminated py	LA	M6	MSS	GG132	370.5		0.6	5.1							
760225	bn-rd mas rx sp with disseminated py	LA	M6	MSS	GG132	370.5			3.0							
760426	mas py veined by dk rd c.g. rx sp	LA	M6	MPY	GG165	302.0		0.9	2.6							
760426	mas py veined by dk rd c.g. rx sp	LA	M6	MPY	GG165	302.0		0.2								
760438	py-po-co-mgt vein in chl (euhedral py)	LA	M6	STZ	GG165	365.5	IV (A)	-0.2				-4.8			-18	
760438	py-po-co-mgt vein in chl (euhedral py)	LA	M6	STZ	GG165	365.5	IV (A)	1.6								
760227	mas c.g. banded py with disseminated mgt	LA	M6	MPY	GG132	371.7		-0.3								
760227	mas c.g. banded py with disseminated mgt	LA	M6	MPY	GG132	371.7		6.3	2.6							12
769281	eu py in py-chl vein in mas mgt	LA	M4	STZ	GG070	389.7	III	1.5								
769281	eu py in py-chl vein in mas mgt	LA	M4	STZ	GG070	389.7	III	3.0								
769290	cp aggregates in py-po-cp-co-qz vein in intense si	LA	M5	STZ	GG070	482.7	IV (A)				-0.3					
769290	cp aggregates in py-po-cp-co-qz vein in intense si	LA	M5	STZ	GG070	482.7	IV (A)	0.7			3.1	-0.5			227	
769185	py aggregate in co-py-po-cp vein in intense chl	LA	M4	MPY	GG162	335.6	IV (A)	2.8			1.7	0.5		361	87	
769152	co-py-cp-po vein in intense chl	LA	M4	STZ	GG157	219.9	IV (A)	0.7			0.4	-1.6			90	
769170	spongy py grain in mas py	LA	M4	MPY	GG162	246.8		1.0								
769170	eu py grain in mas py	LA	M4	MPY	GG162	246.8		0.7								
769264	py-chl vein cut by co-py-mgt vein (subhedral py)	LA	M4	STZ	GG070	271.9	III	0.6			2.1					

Abbreviations: C = conventional analysis, LA = laser ablation, M6 = Member 6 in the Golden Grove Formation, MPY = massive pyrite, MSS = massive sphalerite, STZ = stringer zone, WR = wall rock, ga = galena, tc = talc
py = pyrite, sp = sphalerite, cp = chalcopyrite, po= pyrrhotite, chl = chlorite, si = siliceous, mas = massive, mgt = magnetite, co = carbonate, f.g = fine grained, c.g = coarse grained, rx = recrystallised, rd = red, bn = brown, or = orange.

Note: formational temperature estimates only given where the $\delta^{34}S$ sulphide values have equilibrium (i.e., py > sp > cp > ga) and the difference is greater than 0.3 per mil due to analytical uncertainty

Appendix A9.1: Oxygen, hydrogen and carbon isotope results

Sample	Description	Strata	δD_{SMOW} (‰)	$\delta^{18}O_{SMOW}$ (‰)	$\delta^{13}C_{PDB}$ (‰)
Magnetite					
760374	Sulphide vein (Type V(A)): py-po-mgt-chl-co	M6		3.9	
760432	Sulphide vein (Type V(A)): sp-mgt-po-chl-co	M6		3.4	
760459	Massive py: disseminated mgt	M6		3.2	
760461	Massive py-sp: disseminated mgt	M6		-1.0	
769100	Massive mgt-chl	M4*		-3.7	
769125	Massive mgt-co: granular texture	M4*		-3.7	
769325	Massive mgt-co: banded	M4*		-0.3	
769327	Intense chlorite with disseminated mgt and co	M4		-3.6	
Whole Rock					
760209	Massive quartz-feldspar phyric rhyodacite	RD2		8.7	
760374	Pervasive intense si alteration of sst	M6		17.4	
760490	M1 Marker: chert in banded co-qz-chl	M6		10.2	
Chlorite					
760374	Sulphide vein (TypeV(A)): py-po-chl-mgt-co	M6	-69.4	2.0	
760392	Sulphide vein (Type V(A)): cp-co-py-po in massive mgt	M6	-76.0	0.1	
760432	Sulphide vein (Type V(A)): sp-mgt-po-chl-co	M6	-61.9	1.3	
769137	Co-chl vein cutting intense si sst	M4	-66.6	-0.7	
769150	Intense chlorite alteration in qz sst	M4	-72.6	0.6	
769243	Py-chl vein (Type III)	M4	-64.9	-0.6	
769276	Chl vein in intense chl sst	M4	-67.2	0.5	
769327	Intense chlorite alteration with disseminated mgt and co	M4	-67.9	1.9	
Carbonate					
760251	Nodular co alteration in si tuffaceous sst	M5		10.7	-1.4
760490	M1 Marker: bedded qz, co, chl	M6		9.0	-3.6
762006	Co vein cutting po-co-py veins	M4		7.9	-4.3
762057	Nodular co in si tuffaceous sandstone	M5		7.9	-3.8
769083	Disseminated co in chlorite	M4		10.1	-4.2
769093	Py-co vein in intense chlorite	M4		6.8	-3.4
769137	Co-chl vein (Type III) cutting intense si sst	M4		8.7	-4.9
769152	Co-cp vein in massive chlorite	M4		6.9	-3.2
769156	Semi-massive mgt-co	M4*		5.9	-3.7
769217	Sulphide vein (Type V(A)) co-chl-py-po-mgt	M4		8.3	-3.0
769232	Massive mgt-co: co vein through mgt	M4*		6.9	-5.4
769233	Sulphie vein (Type V(A)) co-py-cp-mgt	M4		6.9	-5.4
769244	Massive mgt-co: disseminated chl	M4*		7.4	-3.8
769275	Sulphide vein: (Type IV) py-co-chl	M4		7.2	-3.8
769280	Sulphide vein (Type V(A)): cp-co-py-po in massive mgt	M4		7.0	-5.5
769308	Pumiceous sst with strong co alteration	M6		8.0	-3.3
769319	Massive mgt-co: banded and colloform	M4*		8.8	-3.9
769325	Massive mgt-co: banded	M4*		7.3	-3.2
769327	Intense chlorite with disseminated mgt and co	M4*		7.7	-4.0
769149(i)	Massive co: recrystallised	M4		6.7	-2.4
769149(ii)	Massive co: fine-grained	M4		6.5	-5.7

Abbreviations: mgt = magnetite, py = pyrite, sp = sphalerite, co = carbonate, chl = chlorite, po = pyrrhotite, si = siliceous alteration, cp = chlacopyrite, qz = quartz, sst = sandstone, M4* indicates massive magnetite in GGF M4